Transactions of the ASME

Journal of Applied Mechanics

Published Quarterly by The American Society of Mechanical Engineers

VOLUME 48 • NUMBER 2 • JUNE 1981

Journal of Applied Mechanics (ISSN 0021-8936) is edited and published quarterly at the offices of The American Society of Mechanical Engineers, United Engineering Center, 345 E. 47th St., New York, N. Y. 10017. ASME-TWX No. 710-581-5267, New York. Second Class postage paid at New York, N. Y., and at additional mailing offices.

CHANGES OF ADDRESS must be received at Society headquarters seven weeks before they are to be effective. Please send old label and new address.

PRICES: To members, $30.00, annually; to nonmembers, $60.00. Single copies $20.00 each. Add $5.00 for postage to countries outside the United States and Canada.

INDEXED by the Engineering Index, Inc.

TECHNICAL PAPERS

(Contents continued on Page 456)

CONTENTS (CONTINUED)

BRIEF NOTES

DISCUSSIONS

BOOK REVIEWS

(Contents continued on inside Back Cover)

ERRATA

J. S. Yu

Professor,
Department of Mechanical Engineering,
School of Engineering,
West Virginia Institute of Technology,
Montgomery, W. Va. 25136
Mem. ASME

Dispersion in Laminar Flow Through Tubes by Simultaneous Diffusion and Convection

The dispersion of a small quantity of a solute initially injected into a round tube in which steady-state laminar flow exists is critically examined. It is shown that the mean solute concentration profile is far from being symmetric at small dimensionless times after injection. The mean concentration and the axial location at the peak of the profile are presented in detail as functions of time for flow with various Peclet numbers. It is suggested that such results may be useful for determining either the molecular diffusion coefficient or the mean flow velocity or both from experimental measurements. A previously established criterion in terms of the Peclet number for determining the minimum dimensionless time required for applying Taylor's theory of dispersion is graphically illustrated. Although the complete generalized dispersion equation of Gill's model is exact, the truncated two-term form of it with time-dependent coefficients is exact only asymptotically at large values of time; however, at small Peclet numbers, the two-term approximation is shown graphically to be reasonably satisfactory over all values of time. The exact series solution is compared with the solution of Tseng and Besant through the use of Fourier transform.

Introduction

The problem of dispersion of a miscible material is a round straight tube in which fully developed laminar flow exists has been analytically studied by many authors. Taylor [1], who initiated the study of this problem, showed in an intuitive analysis that, for given prescribed initial conditions, the cross-sectional mean concentration of the solute after some time has elapsed spreads out longitudinally in a coordinate moving with the mean flow velocity according to Fick's second law of diffusion with a constant effective dispersion coefficient which, subsequently improved by Aris [2], is completely determined by the tube diameter, the flow velocity, and the molecular diffusion coefficient. Aris, and afterward Gill, et al. [3, 4], from a different appraoch, has proved that Taylor's analysis with the correct effective dispersion coefficient is valid strictly asymptotically at large values of time. The latter authors, through examples with initial solute inputs in the form of a slug of finite axial extension, also specified the minimum values of time beyond which Taylor's analysis is considered to be useful. Such specifications cannot be regarded as adequately general and therefore the question on the time limit for applying Taylor's theory of dispersion still remains to be answered.

In a previous paper [5], the criterion for the validity of Taylor's analysis has been established on a more rigorous basis. It will be graphically demonstrated that Taylor's model of laminar dispersion is valid for all practical purposes when $Dt/a^2 \gtrsim 0.7$, where D is the molecular diffusion coefficient, a the radius of the tube, and t is the length of time after introduction of the solute into the tube. The molecular diffusion coefficients in gases at moderate pressures and temperatures are of the order of 0.1 cm^2/sec. If the dispersive flow takes place in a tube of 0.1 cm in radius with an average flow velocity of 10 cm/sec, the foregoing criterion yields a time $t \sim 0.07$ sec and the length of the tube required is in centimeters. Thus, for gaseous dispersion, Taylor's theory can be used with complete confidence from the experimental viewpoint. The ratio of the diffusion coefficients in liquids to those in gases at normal conditions is 10^{-4} or smaller. For dispersion of liquids with the same flow velocity in the same size of tube, Taylor's theory then applies at a time $t \sim 700$ sec and a tube in excess of 70 meters in length becomes necessary. The theory of laminar dispersion in tubes does not account for the effect of gravity on the concentration distribution of the solute. Even though the excessive requirement of tube length can be managed in experiments, it is highly unlikely that analytical predictions can be made to meaningfully compare with experimental results observed beyond such a long time period unless gravity is properly included in the theoretical analysis. What is needed is a method of solution of the diffusion-convection equation that is valid at small values of time. Nevertheless, Taylor made experimental measurements successfully comparable with his analysis on the dispersion of potassium permanganate solution in water flowing in a tube with a radius as small as 0.025 cm.

Lighthill [6] has given a solution specifically developed for short

Contributed by the Applied Mechanics Division for publication in the JOURNAL OF APPLIED MECHANICS.

Discussion on this paper should be addressed to the Editorial Department, ASME, United Engineering Center, 345 East 47th Street, New York, N. Y. 10017, and will be accepted until September 1, 1981. Readers who need more time to prepare a Discussion should request an extension from the Editorial Department. Manuscript received by ASME Applied Mechanics Division, April, 1979.

durations of time after solute injection. The solution, obtained under the assumption that longitudinal molecular diffusion can be ignored, has a time limit no longer than that required by the solute in the flow field to reach the flow boundary by molecular diffusion in the radial direction. Indeed, the solution is only valid asymptotically at small times when the concentration distribution is exclusively governed by convective transport.

The approach of Gill, et al. [7, 8], and the present method are shown to be equivalent in reference [9] where the dispersion coefficients required in Gill's general equations governing the mean transverse mean concentration are evaluated systematically in an algebraic manner on the basis of the present analysis. DeGance and Johns [10] also rigorously justified Gill's theory and approached the same problem by expanding the local concentration in Hermite polynomials in the axial coordinate. By truncating the general equation beyond the second axial derivative, however, the resulting equation becomes quite limited in utility. Booras and Krantz [11], on the ground that for power-law non-Newtonian fluids the concentration distribution due to pure convection can be highly unsymmetrical, seriously questioned the general validity at small times of this truncated two-term dispersion model. The present numerical calculation shows that for dispersion in liquids, Gill's two-term equation is applicable at large times; it is an excellent approximation at times much smaller than that required by Taylor's analysis, however, when the effect due to convective transport becomes comparable to that due to molecular diffusion.

At small times, distribution of the mean concentration does not follow Fick's law of diffusion. This problem has been brought up by Aris [2] and studied by Chatwin [12] who, for the case of an initial concentrated input distributed uniformly over the tube cross section, presented a solution showing the asymmetrical nature of the mean concentration profiles at later times. The solution, however, is incorrect in detail except at large times when the concentration profile becomes nearly symmetric about the point moving with the average flow velocity. For an initial input in the form of a uniform slug, Hunt [13] developed an approximate solution for the local solute concentration by using the first-order perturbation method through asymptotic boundary matching with the unperturbed pure-convection concentration profile. The solution was first thought to be a fair approximation at small times for flow with large Peclet numbers. It turned out, however, that the technique of asymptotic matching introduced too large an effect due to molecular diffusion on the concentration distribution of the solute [5]. Hunt's solution, therefore, can not be regarded as quantitatively valid in general at small times.

In a recent paper, the present author provided a general method of solution to the basic diffusion-convection equation without imposing any arbitrary assumptions [5]. Without the use of the approximation for the higher order coefficients of the Bessel functions in the series expansion for the local concentration, the present method of solution is equivalent to the eigenvalue and eigenvector approach used by Tseng and Besant [14, 15]. A comparison of the two methods is given in the Appendix of this paper. The method is mathematically rigorous and computationally systematic. In reference [5], typical mean concentration profiles predicted by the various theories for the case of a concentrated initial input are compared, and the time limit of Taylor's analysis is established. This paper presents the detailed calculations showing the eventual approach to normal distribution of the solute concentration when the initial input is in a concentrated form. It is to be noted that for this form of input the theory of Taylor and of the two-term dispersion model of Gill, et al., invariably predict a concentration distribution symmetric about the point moving with the average flow velocity.

Basic Equation and Solution

The diffusion-convection equation for fully developed laminar flow satisfied by the local solute concentration $C(z, r, t)$ which is considered to be symmetrical about the center line of the tube is

$$\frac{\partial C}{\partial t} + U\left(1 - \frac{r^2}{a^2}\right)\frac{\partial C}{\partial z} = D\left[\frac{\partial^2 C}{\partial z^2} + \frac{1}{r}\frac{\partial}{\partial r}\left(r\frac{\partial C}{\partial r}\right)\right] \tag{1}$$

Here D is the molecular diffusion coefficient, a the radius of the tube, U the flow velocity at the center line, and z, r, and t are the axial distance, radial distance, and time, respectively. For flow in tubes with no sorption at the walls, the boundary condition is

$$\frac{\partial C}{\partial r} = 0 \quad \text{at} \quad r = a, \tag{2}$$

and for a concentrated solute input of mass unity uniformly distributed over the cross section of the tube, the initial condition may be written as

$$C(z, r, 0) = \delta(z)/\pi a^2. \tag{3}$$

where $\delta(z)$ is the Dirac delta function.

Upon using the dimensionless variables

$$\tau = Dt/a^2, \quad \xi = r/a, \quad \zeta = \frac{1}{a\,\mathrm{Pe}}(z - 0.5Ut), \tag{4}$$

where $\mathrm{Pe} = aU/D$ is the diffusion Peclet number, and the dimensionless concentration

$$\Psi(\zeta, \xi, \tau) = \pi a^3 C \tag{5}$$

we have the diffusion-convection equation in the form

$$\frac{\partial \Psi}{\partial \tau} = \frac{1}{\mathrm{Pe}^2}\frac{\partial^2 \Psi}{\partial \zeta^2} + \frac{1}{\xi}\frac{\partial}{\partial \xi}\left(\xi\frac{\partial \Psi}{\partial \xi}\right) - \left(\frac{1}{2} - \xi^2\right)\frac{\partial \Psi}{\partial \zeta}, \tag{6}$$

and the initial and boundary conditions

$$\Psi(\zeta, \xi, 0) = \delta(\zeta)/\mathrm{Pe}, \tag{7}$$

$$\frac{\partial \Psi}{\partial \xi} = 0 \quad \text{at} \quad \xi = 1. \tag{8}$$

The solution of equation (6) satisfying the boundary condition (8) is formulated as

$$\Psi(\zeta, \xi, \tau) = \sum_{n=0}^{\infty} \psi_n(\zeta, \tau) J_0(\beta_n \xi)/J_0(\beta_n), \tag{9}$$

where $J_0(x)$ is the Bessel function of zeroth order and β_n, arranged in increasing order of magnitude by starting with $\beta_0 = 0$, are the non-negative zeros of the first-order Bessel function $J_1(x)$.

The expansion representing the local concentration given by equation (9) is complete. An exact determination of the local concentration, however, requires the complete solution of the functions $\psi_n(\zeta, \tau)$ to all orders determined from an infinite set of interrelating differential equations which are obtained by substituting equation (9) into equation (6) and ultimately eliminating from the resulting equation the radial variable ξ by integration through the use of the orthogonal relations of Bessel functions. Such a procedure, although exact in the sense of convergence in the mean, has proved to be rather ineffective [16].

The present author showed in a recent paper [5] that, for any given Pe and τ, if the conditions

$$\beta_N{}^2\tau \gg 1, \tag{10a}$$

and

$$\frac{\beta_N{}^4}{|J_0(\beta_N)|}\exp\left(-\beta_N{}^2\tau\right) < \frac{8\sqrt{\pi^3\tau}}{\mathrm{Pe}}, \tag{10b}$$

of which the first is a necessary and the second a sufficient condition, are satisfied, then an approximate determination of the functions $\psi_n(\zeta, \tau)$ can be obtained from the linear equations

$$\frac{\partial \psi_n}{\partial \tau} = -\beta_n{}^2\psi_n - \sum_{m=0}^{N-1} c_{nm}\frac{\partial \psi_m}{\partial \zeta} - \left[\frac{1}{\mathrm{Pe}^2}\delta_{nm} + k_{nm}{}^{(N)}\right]\frac{\partial^2 \psi_m}{\partial \zeta^2}, \quad n \le N - 1, \tag{11}$$

and

$$\psi_n = -\sum_{m=0}^{N-1} c_{nm} \frac{\partial \psi_m}{\partial \zeta}, \quad n \geq N, \tag{12}$$

where δ_{nm} is the Kronecker delta,

$$c_{nm} = 2 \int_0^1 \xi \left\{\frac{1}{2} - \xi^2\right\} \frac{J_0(\beta_n \xi) J_0(\beta_m \xi)}{J_0(\beta_n) J_0(\beta_m)} \tag{13}$$

and

$$k_{nm}{}^{(N)} = \sum_{l=N}^{\infty} c_{nl} c_{lm} / \beta_l{}^2. \tag{14}$$

At very large values of dimensionless time such that the conditions, obtained by setting $N = 1$ in (10a) and (10b),

$$\tau \gg 1/\beta_1{}^2, \tag{15a}$$

and

$$\frac{1}{\sqrt{\tau}} \exp(-\beta_1{}^2 \tau) < \frac{8\sqrt{\pi^3}}{\beta_1{}^4 \, \mathrm{Pe}} |J_0(\beta_1)| \tag{15b}$$

are satisfied, equation (11) for the determination of the function $\psi_0(\zeta, \tau)$, which is the mean concentration over the cross section of the tube, becomes

$$\frac{\partial \psi_0}{\partial \tau} = \left[\frac{1}{\mathrm{Pe}^2} + k_{00}{}^{(1)}\right] \frac{\partial^2 \psi_0}{\partial \zeta^2}. \tag{16}$$

Noting that

$$c_{0l} = c_{l0} = -\frac{4}{\beta_l{}^2}, \quad l \geq 1, \tag{17}$$

and thus

$$k_{00}{}^{(1)} = \sum_{l=1}^{\infty} c_{0l} c_{l0} = 16 \sum_{l=1}^{\infty} \beta_l{}^{-6}, \tag{18}$$

it is seen that the change of the mean concentration obeys Fick's law in a coordinate moving at a speed equal to the mean velocity of flow with an effective constant dispersion coefficient

$$\frac{1}{\mathrm{Pe}^2} + 16 \sum_{l=1}^{\infty} \beta_l{}^{-6}$$

and the mean concentration becomes normal in distribution if the initial concentration is symmetric about the origin. Equation (16) is identical to that obtained by Taylor in his original analysis [1]. Although condition (15b) may be overly restrictive at very small values of dimensionless time (see Fig. 6), it represents the sufficient condition under which Taylor's equation may be used with complete confidence.

For a delta function initial concentration input given by equation (7), the initial conditions for the functions ψ_n are

$$\psi_0(\zeta, 0) = \delta(\zeta)/\mathrm{Pe},$$

$$\psi_n(\zeta, 0) = 0, \quad n \geq 1. \tag{19}$$

The solutions of equations (11) can be determined by employing the methods of Fourier and Laplace transforms. These can be written as

$$\psi_n(\zeta, \tau) = \frac{(-1)^n}{2\pi \, \mathrm{Pe}} \sum_{j=0}^{N-1} \int_{-\infty}^{\infty} \left(\frac{B_n}{A'}\right)_j \exp[a_j \tau + i(b_j \tau + \omega \zeta)] d\omega,$$

$$n = 0, 1, \ldots\ldots, N-1, \tag{20}$$

where $i = \sqrt{-1}$, $a_j + ib_j$ are the N distinct zeros, i.e., $p = a_j + ib_j$ which are functions of the real variable ω, of the $N \times N$ determinant

$$A = \left| \left(p + \beta_m{}^2 + \frac{\omega^2}{\mathrm{Pe}^2}\right) \delta_{mn} + \omega^2 k_{mn}{}^{(N)} + i\omega c_{mn} \right|,$$

$$m, n = 0, 1, \ldots\ldots N-1, \tag{21}$$

$$A' = dA/dp, \tag{22}$$

B_n is the complementary minor of the $(n+1)$th element in the first row ($m = 0$) of determinant A, that is, the determinant formed from A by striking out the first row and $(n+1)$th column, and $(B_n/A')_j$ is the ratio of B_n and A' when both are evaluated at $p = a_j + ib_j$.

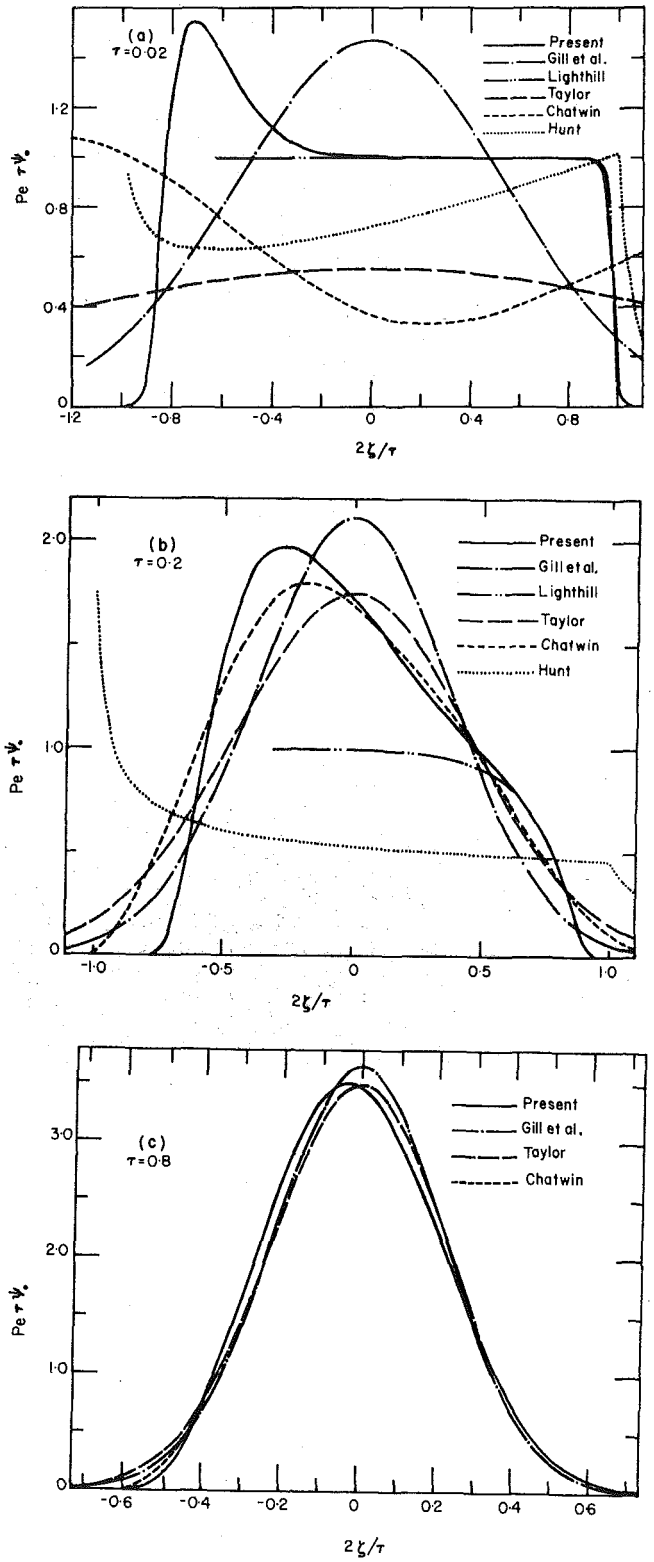

Fig. 1 Typical comparison of transverse mean concentration profiles predicted by different methods for flow with large Peclet numbers, Pe = 10,000, at τ = 0.02, 0.2, and 0.8

Discussion of Results

The zeros of determinant A defined by equation (21) can readily

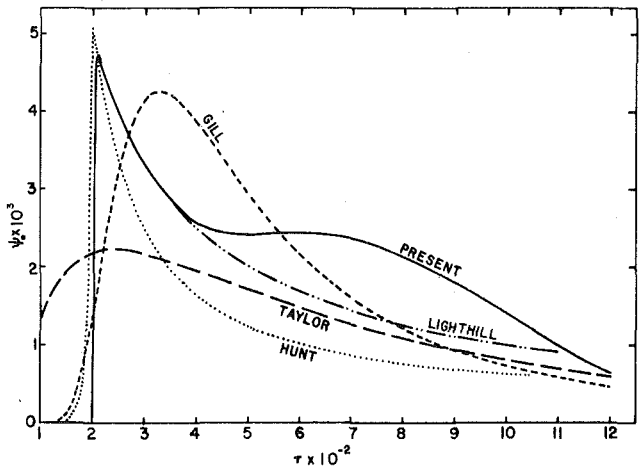

Fig. 2 Comparison of time-concentration curves predicted by different solutions at z/a Pe = 0.02 for flow with Pe = 10,000

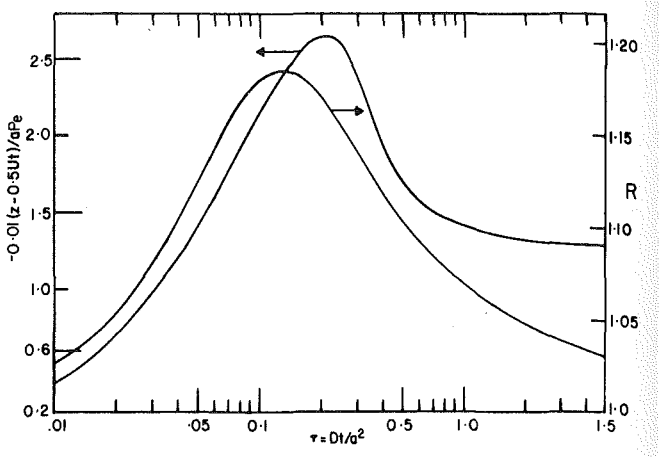

Fig. 3. Curves showing the peak location of the transverse mean concentration and the ratio R defined by equation (23) as functions of the dimensionless time, Pe = 10,000

be computed by using standard computer subroutines [5] and the evaluation of the improper integrals given by equation (20) for the determination of the functions $\psi_n(\xi, \tau)$ can be accurately performed through the method of fast Fourier transform [17]. Under the requirement given by condition (10a), the effective orders of approximation used in the calculations are made at least equal to the order N required to satisfy condition (10b) which under all cases gives a value of N sufficiently good for practical purposes.

For the purpose of investigating the approach to normal distribution, the function $\psi_0(\zeta, \tau)$, which is the mean concentration obtained by averaging the local concentration over the cross-sectional area of the tube, is calculated in detail. Figs. 1, with Pe = 10,000, show typical comparisons of the mean concentration profiles predicted by the various methods at different dimensionless times for flow with large Peclet numbers. Another comparison of these solutions is illustrated in Fig. 2 which shows the mean concentration of the solute when recorded in the course of time at a fixed axial location z/a Pe = 0.02. Lighthill's solution, specifically developed for small times, is seen here near the front of the profile indeed the result which would arise if longitudinal molecular diffusion were ignored. The solution of Hunt, on the other hand, shows too excessive a dispersion of the solute by molecular diffusion. It has been shown by detailed numerical comparisons [5] that the solutions by Taylor, Chatwin, and the solution of Gill's truncated two-term equation are in general asymptotically valid at large values of time. For flow with small Peclet numbers (Pe $\sim$ 15, see Fig. 7), however, the results obtained by Gill's solution are reasonably satisfactory over the entire time domain. The present result reveals that the concentration distribution at small times is indeed far from being symmetric and a peak of the concentration profile always shows up at an axial location somewhat downstream of, and only asymptotically approaches the section moving with the mean flow velocity. This result confirms Chatwin's observation [12] that, because of radial diffusion and interaction of the solute with the wall, the concentration distribution at small times should invariably be asymmetric while satisfying the requirement, for the case of an initial solute input uniform over the cross section of the tube, that the first moment of the mean concentration distribution is zero about the origin in the moving axial coordinate [2]. For the purpose of checking the correctness of the present method of solution, and thus the accuracy of the calculated results, the first moment of the computed concentration distribution has been evaluated by using the IMSL subroutines DCSQDU and ICSICU which are based on the method of cubic spline approximation [18, 19]; the result is essentially zero and therefore is not presented here. The ratio of the amount of solute in the region downstream to that in the region upstream of the mean flow position

$$R = \int_{-\infty}^{0} \psi_0 d\zeta \Big/ \int_{0}^{\infty} \psi_0 d\zeta \qquad (23)$$

is plotted in Fig. 3 as a function of time for flow with Pe = 10,000. Initially $R = 1$ for the concentrated input considered in this paper. The variation of R as illustrated, hitting a peak value of almost 1.2, clearly shows the importance of the detailed interplay between molecular diffusion and convective transport at small values of time. Since the first moment of the mean concentration distribution is zero, the mean concentration profile, therefore, eventually becomes symmetric about the plane moving with the mean flow velocity. Also plotted in Fig. 3, for flow with the same Peclet number, is the distance from the mean flow position, in unit of the tube radius a, of the peak location of the concentration profile as a function of time. It is clearly seen that the peak first moves rapidly downstream, reaches a maximum distance in the course of time, and then very slowly moves toward the origin, as is expected due to the eventual approach to symmetry of the concentration profile, in the moving reference frame. Since the present analysis is exact, the consistency as shown in Fig. 3 between the variation of R and the change of the peak location shows that the present calculational procedure is correct and accurate.

Collectively, for flow with Peclet numbers in the range of 5 < Pe < 10,000, the distance between the point of solute injection and the peak location of the mean concentration profile, measured in unit of $0.5Ut$, is plotted in Fig. 4 as a function of the dimensionless time. It is clearly seen from this graph that for flow with low Peclet numbers (Pe $\sim$ 10), the peak location may be identified with the section moving with the average flow velocity with little error. For flow with high Peclet numbers, however, these two locations become significantly different, especially at a dimensionless time smaller than that given by equation (15b).

In experiments for flow with known tube radius a, if the peak location z at a time t is accurately detected, then the result shown in Fig. 4 suggests a method for determining the molecular diffusion coefficient with known flow velocity, and vice versa, without quantitatively measuring the concentration of the solute at the peak location. For example, if U is known and from the experimental measurement $2z/Ut = 1.5$, then Pe $\tau = 0.75a/z$ and a trial-and-error method along the line $2z/Ut = 1.5$ in Fig. 4 will enable Pe and τ to be determined separately. The desired molecular diffusion coefficient can then be calculated from either the value of τ or the value of Pe so obtained. To determine the flow velocity with known molecular diffusion coefficient, a similar procedure may be applied along a constant Dt/a^2 line with a value given by the measured time. The method becomes particularly simple for the time range in which the ratio $2z/Ut$ is practically independent of the Peclet number but a function of τ only. In this case the curve labeled with Pe $\geq$ 10,000 applies and thus no trial-and-error is required for determining the pertinent physical quantity. This case apparently is important for dispersion in liquids where the Peclet number is usually quite large.

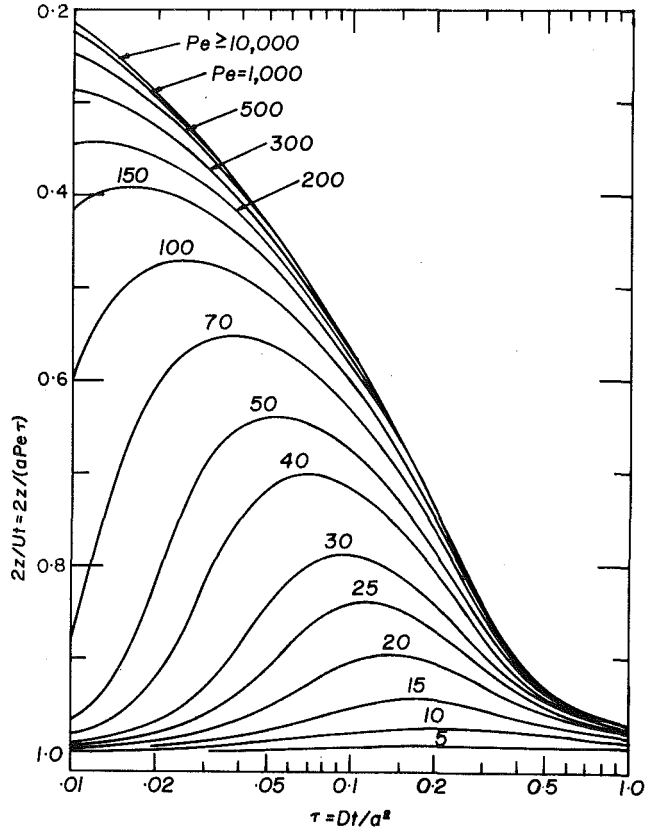

Fig. 4 Locations of maximum mean concentration as functions of the dimensionless time for flow with various Peclet numbers

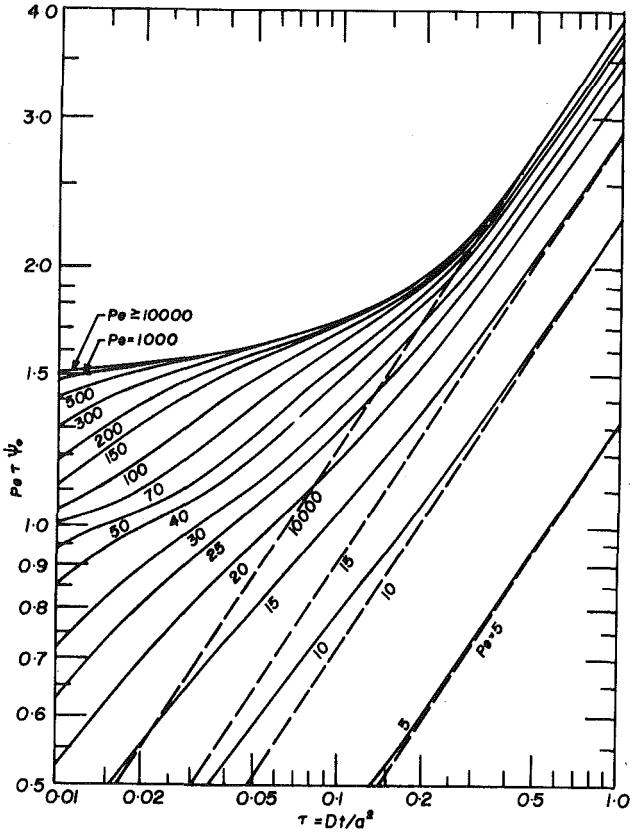

Fig. 5 Dimensionless peak mean concentration as function of dimensionless time for flow with various Peclet numbers; - - - -, peak mean concentration given by Taylor's solution at locations moving with mean flow velocity

The product Pe $\tau\psi_0$ at the peak of the mean concentration profile is plotted in Fig. 5 as a function of the dimensionless time τ for various values of the Peclet numbers. Also plotted in Fig. 5 for Pe = 5, 10, 15, and Pe ≥ 10,000, are the peak values of Pe $\tau\psi_0$ predicted by Taylor's theory at locations moving with the mean flow velocity. It is clearly seen from this comparison that, unless the value of the Peclet number is very small, Taylor's theory is strictly valid asymptotically at large values of the dimensionless time.

The practical usefulness of the results given in Fig. 5 is similar to that in Fig. 4 if the peak mean concentration ψ_0 is measured at a known value of time τ. When both ψ_0 and z/a at the peak are experimentally determined at a recorded time, then, by applying a trial procedure, Figs. 4 and 5 jointly can be used for the calculation of both the flow velocity and the molecular diffusion coefficient D. The results given by the curves for Pe ≥ 10,000 should be useful for dispersion in liquids with large Peclet numbers.

In order to see how effective condition (15*b*) is in specifying the limit of the dimensionless time above which Taylor's theory becomes valid, Fig. 6 compares the dimensionless time determined from condition (15*b*) (treated as an equation) and that required for Taylor's theory to yield the specified percentages of the presently calculated mean concentration at the peak locations of the presently determined mean concentration profiles. For flow with very low Peclet numbers, it is seen here that the time limit is somewhat overestimated. The reason for this is that, when convective transort becomes comparable with molecular diffusion in the process of modifying the solute concentration, the axial concentration gradient persists to remain significantly large for a relatively long period of time after solute injection and the assumption used in the original derivation of inequality (15*b*) that the axial concentration gradient be small [5] becomes overly stringent under this condition. The overall comparison shows, however, condition (15*b*), when viewed as an inequality, is a reasonably effective criterion.

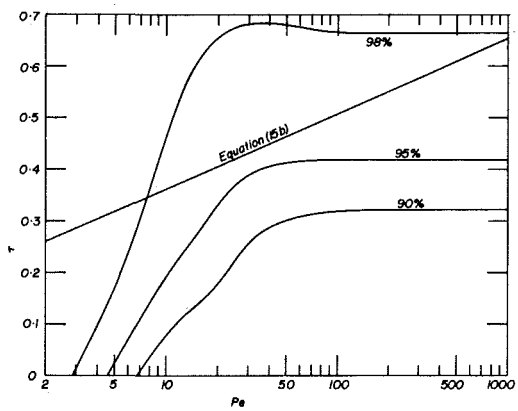

Fig. 6 Graphical illustration showing the effectiveness of inequality (15*b*) as a sufficient condition for the validity of Taylor's theory; the specified percentage is equal to the ratio of the mean concentration given by Taylor's solution and that given by the present method, both evaluated at the peak locations of the presently calculated concentration profiles

Taylor's theory ignores the effect on the concentration distribution due to molecular diffusion in the longitudinal direction. It assumes that, in a coordinate moving with the mean flow velocity, change in concentration due to convective transport (axial gradient assumed to be radially independent) in the bulk of the tube is everywhere instantaneously balanced by molecular diffusion in the radial direction (see equation (19) in reference [1]). The assumption imposes too rapid a radial diffusion, and as a result, the overall dispersion of the solute in the tube is overestimated. Fig. 6 shows, however, Taylor's assumption is realistically valid at a dimensionless time $\tau > 0.7$ over the entire range of Peclet numbers.

As mentioned previously the general equation of Gill, et al. [3, 7],

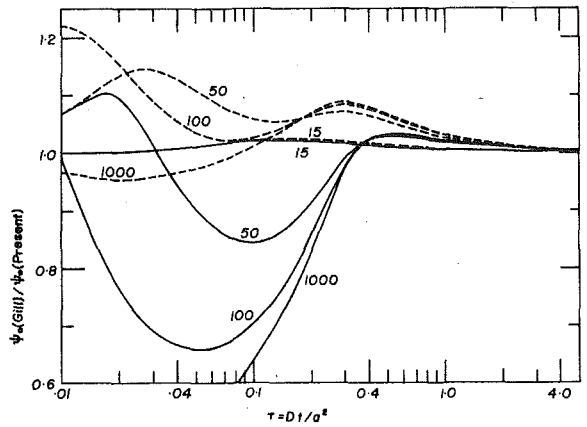

Fig. 7 Comparison of results given by the two-term approximation of Gill, et al., and that given by the present method for flow with specified Peclet numbers. The dashed line gives the ratio of the peak mean concentration given by Gill's method to that of the presently determined concentration profiles; the solid line gives the ratio of the mean concentrations when both are evaluated at the peak location of the presently determined concentration profile.

is exact, but the truncated two-term approximation to the general equation is much easier to use. Therefore, it is also of interest to compare the present results with the solution of the two-term dispersion equation of Gill for the case with a concentrated initial input. Such a comparison is made in the form of Fig. 7 where it is plotted, for Pe = 15, 50, 100, and 1000, (*a*) the ratio of the peak mean concentration obtained by Gill's method to that of the presently calculated concentration profiles, and (*b*) the ratio of the mean concentrations obtained by Gill's and the present method when both are evaluated at the presently determined peak locations. From this comparison, though limited in the range of graphical display, it is seen that the degree of genuineness predicted by Gill's two-term model of dispersion at small dimensionless times depends sharply on the value of the diffusive Peclet numbers. For flow with large Peclet numbers (e.g., Pe = 1000) Gill's two-term model yields reasonable values for the peak mean concentration even though the location of the peaks is incorrectly locked up at the moving origin at all times. For flow with small Peclet numbers (e.g., Pe = 15), Fig. 7 shows that both concentration ratios are reasonably close to unity throughout the entire range of time. The discrepancy for flow with large Peclet numbers apparently comes from neglecting the higher-order terms in Gill's generalized dispersion equation for the change in the transverse mean concentration.

Conclusion

The problem of laminar dispersion in round tubes, subject to axially symmetric and square-integrable initial conditions, has been solved analytically. The series expansion for the local concentration converges in the mean and, therefore, by increasing the number of terms in the series, the computed result can be made as accurate as is desired. The number of terms required for a close representation of the true concentration is effectively specified by inequalities (10*a*) and (10*b*). A FORTRAN computer program has been completed which, subject to either a concentrated or a slug initial solute input, can be used to determine the concentration distribution in either Newtonian or non-Newtonian fluids. The program can easily be extended to handle nonuniform initial conditions.

Acknowledgment

The author appreciates greatly the instructive criticism and helpful comments given by Prof. W. N. Gill of SUNY at Buffalo prior to the publication of this paper. The graphical results reported in this paper were computed by the WVNET Computer System through the Computer Center at West Virginia Institute of Technology.

References

1 Taylor, G. I., "Dispersion of Soluble Matter in Solvent Flowing Slowly Through a Tube," *Proceedings of the Royal Society*, London, Series A, Vol. 219, 1953, pp. 186–203.

2 Aris, R., "On the Dispersion of a Solute in a Fluid Flowing Through a Tube," *Proceedings of the Royal Society*, London, Series A, Vol. 235, 1956, pp. 67–77.

3 Gill, W. N., "A Note on the Solution of Transient Dispersion Problems," *Proceedings of the Royal Society*, London, Series A, Vol. 298, 1967, pp. 335–339.

4 Gill, W. N., and Ananthakrishnan, V., "Laminar Dispersion in Capillary Tubes: The Slug Stimulus," *AIChE Journal*, Vol. 13, No. 4, 1967, pp. 801–807.

5 Yu, J. S., "On Laminar Dispersion for Flow Through Round Tubes," ASME JOURNAL OF APPLIED MECHANICS, Vol. 46, No. 4, 1979, pp. 750–756.

6 Lighthill, M. J., "Initial Development of Diffusion in Poiseuille Flow," *Journal of Institute of Mathematics and Its Applications*, Vol. 2, 1966, pp. 97–108.

7 Gill, W. N., and Sankarasubramanian, R., "Exact Analysis of Unsteady Convective Diffusion," *Proceedings of the Royal Society*, London, Series A, Vol. 316, 1970, pp. 341–350.

8 Gill, W. N., and Sankarasubramanian, R., "Dispersion of a Nonuniform Slug in Time-Dependent Flow," *Proceedings of the Royal Society*, London, Series A, Vol. 322, 1971, pp. 101–117.

9 Author's Closure to Discussion by W. N. Gill and R. S. Subramanian on "On Laminar Dispersion for Flow Through Round Tubes," ASME JOURNAL OF APPLIED MECHANICS, Vol. 47, Dec. 1980, pp.

10 DeGance, A. E., and Johns, L. E., "On the Construction of Dispersion Approximations to the Solution of the Convective Diffusion Equation," *AIChE Journal*, Vol. 26, No. 3, 1980, pp. 411–419, and other works, by these authors cited in this paper.

11 Booras, G. S., and Krantz, W. B., "Dispersion in the Laminar Flow of Power-Law Fluids Through Straight Tubes," *Industrial and Engineering Chemistry Fundamentals*, Vol. 15, No. 4, 1976, pp. 249–254.

12 Chatwin, P. C., "The Approach to Normality of the Concentration Distribution of a Solute in a Solvent Flowing Along a Straight Pipe," *Journal of Fluid Mechanics*, Vol. 43, Part 2, 1970, pp. 321–352.

13 Hunt, B., "Diffusion in Laminar Pipe Flow," *International Journal of Heat and Mass Transfer*, Vol. 20, 1977, pp. 393–401.

14 Tseng, C. M., and Besant, R. W., "Dispersion of a Solute in Fully Developed Laminar Tube Flow," *Proceedings of the Royal Society*, London, Series A, Vol. 317, 1970, pp. 91–99.

15 Tseng, C. M., and Besant, R. W., "Transient Heat and Mass Transfer in Fully Developed Laminar Tube Flows," *International Journal of Heat and Mass Transfer*, Vol. 15, 1972, pp. 203–215.

16 Yu, J. S., "An Approximate Analysis of Laminar Dispersion in Circular Tubes," ASME JOURNAL OF APPLIED MECHANICS, Vol. 43, Series E, No. 4, 1976, pp. 537–542.

17 Brigham, E. O., *Fast Fourier Transform*, 1974, Prentice-Hall, Englewood Cliffs, N.J.

18 IMSL Library 1, Edition G, 1977, International Mathematical and Statistical Library, Inc.

19 Ahlberg, J., Nilson, E., and Walsh, J., *The Theory of Splines and Their Applications*, 1967, Academic Press.

APPENDIX

Comparison With Method by Tseng and Besant [14, 15]

The technique used by Tseng and Besant for solving equation (6) by starting with the particular solution (equation (4) in reference [14]) and then going through the evaluation of the eigenvalues and eigenvectors of the characteristic equation has essentially the same basis as the present method without using the approximation specified by equation (12).

The functions $\psi_n(\zeta, \tau)$ defined in the series expansion for the local concentration given by equation (9) satisfy the equations [5]

$$\frac{\partial \psi_n}{\partial \tau} = \frac{1}{\mathrm{Pe}^2}\frac{\partial^2 \psi_n}{\partial \zeta^2} - \beta_n{}^2 \psi_n - \sum_{m=0}^{\infty} c_{nm}\frac{\partial \psi_m}{\partial \zeta}, \qquad n = 0, 1, 2, \ldots\ldots \quad (24)$$

Let ϕ_n be the Fourier transform of ψ_n, namely,

$$\phi_n(\omega, \tau) = \frac{1}{\sqrt{2\pi}}\int_{-\infty}^{\infty} \psi_n e^{-i\omega\zeta}\, d\zeta. \quad (25)$$

Then the Fourier transform of equation (24) is

$$\frac{d\phi_n}{d\tau} = -\frac{\omega^2}{\mathrm{Pe}^2}\phi_n - {\beta_n}^2\phi_n - i\omega \sum_{m=0}^{\infty} c_{nm}\phi_m, \tag{26}$$

which is a set of linear equations with constant coefficients parametrically dependent on the variable ω, and therefore has a solution of the form

$$\phi_n = \exp\left[-\left(\frac{\omega^2}{\mathrm{Pe}^2} + {\beta_n}^2 + \lambda\right)\tau\right]. \tag{27}$$

Substituting equation (27) into equation (26) yields the system of algebraic equations

$$\sum_{m=0}^{\infty} (i\omega c_{nm} - \lambda\delta_{nm})\phi_m = 0, \qquad n = 0, 1, 2, \ldots\ldots \tag{28}$$

The eigenvalue $\lambda_0, \lambda_1, \lambda_2, \ldots\ldots$ can therefore be determined from the characteristic equation

$$|i\omega c_{nm} - \lambda\delta_{nm}| = 0, \tag{29}$$

and the solution to equation (26) associated with eigenvalue λ_m can be written as

$$\phi_{nm} = \exp\left[-\left(\frac{\omega^2}{\mathrm{Pe}^2} + {\beta_n}^2 + \lambda_m\right)\tau\right]. \tag{30}$$

By linearly combining all the ϕ_{nm}'s, the general solution to equation (24) can be obtained by applying the inverse Fourier transform, namely,

$$\psi_n(\zeta, \tau) = \frac{1}{\sqrt{2\pi}} \sum_{m=0}^{\infty} \int_{-\infty}^{\infty} f_{nm} \exp\left[-\left(\frac{\omega^2}{\mathrm{Pe}^2} + {\beta_n}^2 + \lambda_m\right)\tau + i\omega\zeta\right] d\omega. \tag{31}$$

For any prescribed initial distribution $\psi_n(\zeta, 0)$, the axial derivatives

$$\psi_n^{(k)}(\zeta, 0) = \frac{d^k}{d\zeta^k}\psi_n(\zeta, 0), \quad k = 0, 1, 2, \ldots\ldots\ldots, \tag{32}$$

can be evaluated to all orders. Use of equation (32) in equation (31) gives

$$\psi_n^{(k)}(\zeta, 0) = \frac{1}{\sqrt{2\pi}} \sum_{m=0}^{\infty} \int_{-\infty}^{\infty} (i\omega')^k f_{mn} e^{i\omega'\zeta} d\omega'. \tag{33}$$

Multiply equation (33) by $\exp(-i\omega\zeta)/\sqrt{2\pi}$ and integrate over ζ to get

$$\frac{1}{\sqrt{2\pi}} \int_{-\infty}^{\infty} \psi_n^{(k)}(\zeta, 0) e^{-i\omega\zeta} d\zeta = (i\omega)^k \sum_{m=0}^{\infty} f_{nm}, \tag{34}$$

which can be used to determine f_{nm} as functions of ω. Such a procedure for the determination of f_{nm}, however, can be completely bypassed if Laplace transform is applied to equation (26).

Substitution of equation (31) into equation (9) gives the local concentration in the form

$$\Psi(\zeta, \xi, \tau) = \frac{1}{\sqrt{2\pi}} \sum_{n=0}^{\infty} \sum_{m=0}^{\infty} (-1)^n \frac{J_0(n\xi)}{J_0(\beta_n)} \int_{-\infty}^{\infty} f_{nm} \exp\left[-\left(\frac{\omega^2}{\mathrm{Pe}^2} + {\beta_n}^2 + \lambda_m\right)\tau + i\omega\zeta\right] d\omega, \tag{35}$$

which is formally the same as equation (7) in reference [14] or equation (21) in reference [15]; the only difference is that Tseng and Besant chose to express the functions f_{nm} in terms of the eigenvectors of equation (28). The aforementioned formulation is made in an axial coordinate moving with the mean flow velocity and therefore the content of the present characteristic equation (29) is not identical to that given by Tseng and Besant. Had the comparison been made in the fixed coordinate and the term ${\beta_n}^2$ been included as part of the eigenvalue λ, then the two characteristic equations would have agreed in all algebraic detail.

Tseng and Besant presented their calculated transverse mean concentration distributions at dimensionless times $\tau \leqslant 2.5 \times 10^{-7}$ with a Peclet number Pe = 10 000 for a concentrated initial input (Fig. 10 in reference [15]). At such small times the departure of the actual concentration distribution from that due to pure convection should be small. The transverse average thus should be roughly constant within the range $|\zeta|/\tau \leqslant 0.5$ and zero elsewhere [1]. Instead, Fig. 10 in reference [15] showed that the mean concentration peaks at $\zeta = 0$ and decreases steadily as the distance from the mean position ($\zeta = 0$) increases. The method of solution used by these authors, as has been shown previously, is equivalent to that used in the present paper. Figs. 1 at $\tau = 0.02$ shows that the front portion of the profile should be flat, especially if the time is smaller. Such discrepancy in the calculated results, perhaps, serves to indicate that their computational accuracy for the evaluation of the eigenvalues and eigenvectors should be reexamined.

M. B. Stewart
Department of Mechanical and Industrial Engineering, University of Illinois at Urbana-Champaign, Urbana, Ill. 61801
Assoc. Mem. ASME

F. A. Morrison, Jr.
Lawrence Livermore National Laboratory, University of California, Livermore, Calif. 94550
Mem. ASME

Droplet Dynamics in Creeping Flows

The accelerated motion of a liquid droplet is investigated analytically. The equation of motion is developed through an analysis of the internal and external fluid motions. Response to step changes in applied force and external fluid velocity are determined. Oscillating forces and velocities are treated and frequency response characteristics found. In the appropriate limits, the results reduce to the known behavior of bubbles or rigid particles.

Introduction

The relative motion between a droplet and the surrounding fluid is of interest for a variety of reasons. Heat and mass transfer, fuel burning rates, coagulation, and dissipation are enhanced by the disparate motions produced by fluid acceleration. We seek here to describe this motion when a spherical droplet moves at low Reynolds number through the fluid about it. In contrast with the steadily moving droplet, sufficiently large surface tension is required to maintain the spherical form of an accelerating droplet.

By analyzing the coupled motions within and about the droplet, a unified theory is produced which reduces to descriptions of bubble or rigid particle motions in the appropriate limits. We are concerned here with describing the effect of the viscous internal response on motion in stationary or accelerating fluids, in response to steady or fluctuating forces.

Much earlier work has examined the responses of either rigid or inviscid spheres in creeping fluids. While the motions of bubbles and solid spheres differ significantly, little attention has been devoted to a rigorous analysis of the accelerating fluid sphere whose viscosity lies between these extremes. Sy and Lightfoot [1] examined the response of a spherical liquid drop to a step application of a constant force. As discussed later, their model differs from that presented here. Droplet response to accelerating flow is of particular interest; no previous investigations have accounted for the effects of internal circulation.

The Transient Velocity Distribution

We consider the rectilinear transient motion of a spherical droplet immersed in a second fluid. The fluids are incompressible and Newtonian with constant, but different, viscosities. The equation of motion of the droplet is developed by analyzing the coupled fluid motion within and about the droplet. At the small Reynolds numbers treated here, the convective acceleration is neglected in both fluids but local acceleration is retained.

This axisymmetric motion is governed by

$$E^2\left(E^2-\frac{1}{\nu_e}\frac{\partial}{\partial t}\right)\psi_e=0 \tag{1}$$

in the external fluid and

$$E^2\left(E^2-\frac{1}{\nu_i}\frac{\partial}{\partial t}\right)\psi_i=0 \tag{2}$$

in the droplet. ψ is the Stokes stream function, t is the time, and ν is the kinematic viscosity. The subscripts denote the fluid. E^2 is the Stokes stream function operator.

In spherical (r, θ, λ) coordinates, this operator is

$$E^2=\frac{\partial^2}{\partial r^2}+\frac{\sin\theta}{r^2}\frac{\partial}{\partial\theta}\left[\frac{1}{\sin\theta}\frac{\partial}{\partial\theta}\right] \tag{3}$$

r is the distance from the droplet center and θ, the polar angle. The local velocity components in these coordinates are

$$v_r=\frac{-1}{r^2\sin\theta}\frac{\partial\psi}{\partial\theta}\qquad v_\theta=\frac{1}{r\sin\theta}\frac{\partial\psi}{\partial r} \tag{4}$$

At this point, our analysis already differs from the earlier work of Sy and Lightfoot [1]. In their treatment of transient creeping flow about fluid spheres, the same equation is used for both fluids, no distinction being made between kinematic viscosities. They distinguish between viscosities only later in the application of a boundary condition. Consequently, our relations reduce to theirs only in a few limits.

We will first examine the flow when the frame of the fluid far from the droplet is an inertial frame. In this frame, the stream function approaches a constant as the fluid velocity far from the droplet vanishes.

$$\psi_e\to 0\quad\text{as}\quad r\to\infty \tag{5}$$

The boundary conditions at the droplet surface are also expressed

Contributed by the Applied Mechanics Division of THE AMERICAN SOCIETY OF MECHANICAL ENGINEERS, and presented at the 1981 Joint ASME/ASCE Applied Mechanics, Fluids Engineering, and Bioengineering Conference, University of Colorado, Boulder, Colo., June 22–27, 1981.

Discussion on this paper should be addressed to the Editorial Department, ASME, United Engineering Center, 345 East 47th Street, New York, N. Y. 10017, and will be accepted until September 1, 1981. Readers who need more time to prepare a Discussion should request an extension from the Editorial Department. Manuscript received by ASME Applied Mechanics Division, January, 1980; final revision, December, 1980. Paper No. 81-APM-29.

as seen by an observer in this frame. The droplet moves with a relative velocity u. Neither fluid crosses the moving spherical droplet surface. In each case, the relative normal velocity vanishes there, yielding

$$\psi_e + \frac{u\,a^2 \sin^2\theta}{2} = 0 \quad \text{at} \quad r = a \tag{6}$$

and

$$\psi_i + \frac{u\,a^2 \sin^2\theta}{2} = 0 \quad \text{at} \quad r = a \tag{7}$$

The droplet surface, r equal to a, is not a stream surface in this frame.

The tangential velocities of the two fluids are equal at the interface. In terms of the stream function

$$\frac{\partial \psi_e}{\partial r} = \frac{\partial \psi_i}{\partial r} \quad \text{at} \quad r = a \tag{8}$$

The tangential stresses generated by fluid motion balance at the interface,

$$\sigma_{\theta r,e} = \sigma_{\theta r,i} \quad \text{at} \quad r = a. \tag{9}$$

The final condition is the boundedness of interior fluid velocities at the origin.

The motions, within and about the droplet, are coupled and must be found together. In certain physical limits, the motions uncouple. As the interior viscosity increases without bound, the interior becomes rigid. As the interior viscosity vanishes (the bubble limit), the interfacial tangential stress vanishes. In this case, the exterior motion may again be found without reference to the interior flow [2].

The transient coupled motions are perhaps most readily found through use of a Laplace transform with respect to time. Denoting a transformed quantity with a bar, we have

$$\bar{\psi}(s) = \int_0^\infty f(t) \exp(-st)\, dt. \tag{10}$$

Solutions of equations (1) and (2) are found by using an angular dependence indicated by equations (6) and (7) and factoring the resulting fourth-order ordinary differential equation in r into two second-order differential equations. The resulting equations are

$$\left(\frac{d^2}{dr^2} - \frac{2}{r^2}\right)\bar{\psi}_1 = 0 \tag{11}$$

and

$$\left(\frac{d^2}{dr^2} - \frac{2}{r^2} - \frac{s}{\nu}\right)\bar{\psi}_2 = 0. \tag{12}$$

The general solution then is a sum of

$$\bar{\psi}_1 = [A\,r^2 + B\,r^{-1}] \sin^2\theta \tag{13}$$

and

$$\bar{\psi}_2 = \left[C\left(\sqrt{\frac{s}{\nu}} - \frac{1}{r}\right)\exp\left(r\sqrt{\frac{s}{\nu}}\right) + D\left(\sqrt{\frac{s}{\nu}} + \frac{1}{r}\right)\exp\left(-r\sqrt{\frac{s}{\nu}}\right)\right]\sin^2\theta. \tag{14}$$

The constants in both fluids result from the boundary and boundedness conditions. For the exterior fluid, equation (5) yields,

$$A_e = C_e = 0 \tag{15}$$

while boundedness at the origin requires

$$B_i = 0 \tag{16}$$

and

$$C_i = D_i. \tag{17}$$

The remaining coefficients are more compactly expressed by first defining the viscosity ratio

$$\gamma = \mu_e/\mu_i \tag{18}$$

and other dimensionless quantities. γ goes to 0 in the rigid limit and ∞ in the bubble limit.

$$\Delta = \left[\left(2 - 3\gamma - \gamma a\sqrt{\frac{s}{\nu_e}}\right)\left(3 - 3a\sqrt{\frac{s}{\nu_i}} + a^2\frac{s}{\nu_i}\right) + a^2\frac{s}{\nu_i}\left(1 - a\sqrt{\frac{s}{\nu_i}}\right)\right]\exp\left(a\sqrt{\frac{s}{\nu_i}}\right) - \left[\left(2 - 3\gamma - \gamma a\sqrt{\frac{s}{\nu_e}}\right) \times \left(3 + 3a\sqrt{\frac{s}{\nu_i}} + a^2\frac{s}{\nu_i}\right) + a^2\frac{s}{\nu_i}\left(1 + a\sqrt{\frac{s}{\nu_i}}\right)\right] \times \exp\left(-a\sqrt{\frac{s}{\nu_i}}\right) \tag{19}$$

and

$$\Sigma = 1 - \gamma\left(1 + a\sqrt{\frac{s}{\nu_e}}\right)\left[\left(-3 + 3a\sqrt{\frac{s}{\nu_i}} - a^2\frac{s}{\nu_i}\right)\exp\left(a\sqrt{\frac{s}{\nu_i}}\right) + \left(3 + 3a\sqrt{\frac{s}{\nu_i}} + a^2\frac{s}{\nu_i}\right)\exp\left(-a\sqrt{\frac{s}{\nu_i}}\right)\right]\Big/\Delta \tag{20}$$

In the fluid about the droplet,

$$B_e = -\frac{1}{2}\bar{u}\,a^3\left[1 + 3\Sigma\left(1 + a\sqrt{\frac{s}{\nu_e}}\right)\Big/\left(a^2\frac{s}{\nu_e}\right)\right] \tag{21}$$

and

$$D_e = \frac{3}{2}\bar{u}\,a^3\Sigma\exp\left(a\sqrt{\frac{s}{\nu_e}}\right)\Big/\left(a^2\frac{s}{\nu_e}\right) \tag{22}$$

while the coefficients

$$A_i = -\frac{1}{2}\bar{u}\left[1 + 3\gamma\left(1 + a\sqrt{\frac{s}{\nu_e}}\right)\left(\left(1 - a\sqrt{\frac{s}{\nu_i}}\right)\exp\left(a\sqrt{\frac{s}{\nu_i}}\right) - \left(1 + a\sqrt{\frac{s}{\nu_i}}\right)\exp\left(-a\sqrt{\frac{s}{\nu_i}}\right)\right)\Big/\Delta\right] \tag{23}$$

and

$$C_i = D_i = -\frac{3}{2}\bar{u}\,a^3\gamma\left(1 + a\sqrt{\frac{s}{\nu_e}}\right)\Big/\Delta \tag{24}$$

describe motion within the droplet.

When γ increases without bound, the exterior stream function in the gas bubble limit [2] is recovered. The velocity distribution about a rigid sphere is produced when γ vanishes.

As the droplet velocity approaches a steady value, the stream function approaches the value given by the final limit theorem, the Hadamard [3]-Rybczynski [4] stream function.

Motion in a Stationary Fluid

The accelerating droplet experiences an unsteady force exerted by the surrounding fluid. This force on a spherical body in the axisymmetric creeping flow is [5], independent of the interfacial boundary conditions,

$$\bar{f} = -\pi\rho_e a s\int_0^\pi\left(a\frac{\partial\bar{\psi}_{e,1}}{\partial r} + 2\bar{\psi}_{e,2}\right)\sin\theta\, d\theta \tag{25}$$

ρ_e is the density of the exterior fluid. In terms of the coefficients of the exterior stream function, this force becomes

$$\bar{f} = -\frac{4}{3}\pi\rho_e\, s\left[-B_e + 2D_e\left(1 + a\sqrt{\frac{s}{\nu_e}}\right)\exp\left(-a\sqrt{\frac{s}{\nu_e}}\right)\right] \tag{26}$$

This force, together with any externally applied force F on the droplet, produce acceleration of the droplet

$$\bar{f} + \bar{F} = m_i\, s\bar{u} \tag{27}$$

The droplet mass is m_i. Correspondingly, we have m_e as the displaced mass. Combining equations (27) and (26), the externally applied force is related to the droplet velocity by

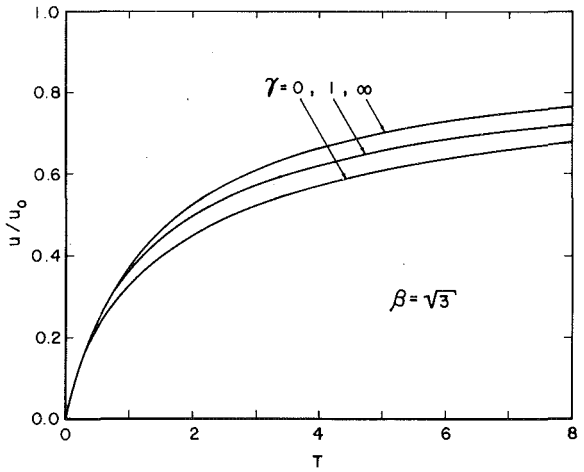

Fig. 1 Step change in the applied force on a neutrally buoyant droplet

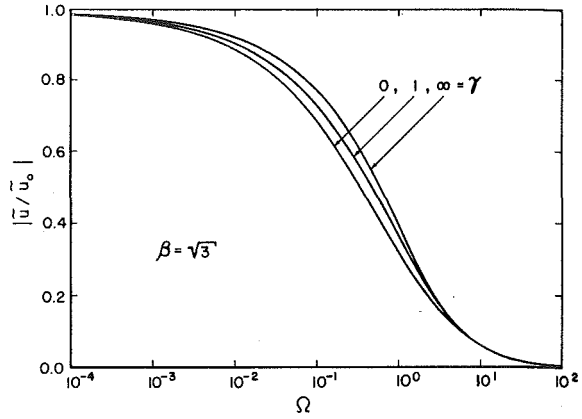

Fig. 2 Oscillating applied force on a neutrally buoyant droplet

$$\bar{F} = \left(m_i + \frac{m_e}{2}\right) s\bar{u} + 6\pi\mu_e a\bar{u}\left(1 + a\sqrt{\frac{s}{\nu_e}}\right)\Sigma \tag{28}$$

Only the factor, Σ, defined by equation (20), distinguishes this relation from its rigid sphere counterpart.

When the internal viscosity increases without bound, we invert to find the force on an accelerating rigid sphere

$$\bar{F} = \left(m_i + \frac{m_e}{2}\right)\frac{du}{dt} + 6\pi\mu_e au + \frac{9m_e}{2a}\sqrt{\frac{\nu_e}{\pi}}\int_0^t \frac{du/d\tau}{\sqrt{t-\tau}}\,d\tau \tag{29}$$

The relation is well known [6, 7]. The integral expression, usually designated the Basset term, originated with Boussinesq [8].

When the internal viscosity and mass vanish, we recover the Morrison and Stewart [2] expression for accelerating creeping response of a bubble.

$$F + \frac{a}{3\sqrt{\pi\nu_e}}\int_0^t \frac{dF/d\tau}{\sqrt{t-\tau}}\,d\tau = \frac{m_e}{2}\frac{du}{dt} + 4\pi\mu_e au + \frac{3m_e}{a}\sqrt{\frac{\nu_e}{\pi}}\int_0^t \frac{du/d\tau}{\sqrt{t-\tau}}\,d\tau + \frac{m_e a}{6\sqrt{\pi\nu_e}}\int_0^t \frac{d^2u/d\tau^2}{\sqrt{t-\tau}}\,d\tau \tag{30}$$

The general expression (28) obtained here would have no simple interpretation if inverted. Instead, we examine the response to a set of basic inputs. For this purpose, the following dimensionless parameters are introduced.

Using a relaxation time

$$\alpha = \frac{(m_i + m_e/2)}{6\pi\mu_e a} \tag{31}$$

we define a dimensionless time

$$T = t/\alpha \tag{32}$$

and

$$S = \alpha s \tag{33}$$

The density ratio is described by

$$\beta = \frac{a}{\sqrt{\alpha\nu_e}} = \left[\frac{9m_e}{2m_i + m_e}\right]^{1/2} \tag{34}$$

which takes on the values 0, $\sqrt{3}$, and 3 when the droplet mass is, respectively, much greater than, equal to, and much less than the displaced mass.

Expressing equation (28) in dimensionless form, we first can invert numerically [9] to find the response to a step change F in the applied force. Some results for a neutrally buoyant droplet are shown in Fig. 1 and illustrate the effect of droplet viscosity on the response. The velocity is expressed as a fraction of the final steady velocity u_0. The final velocity is

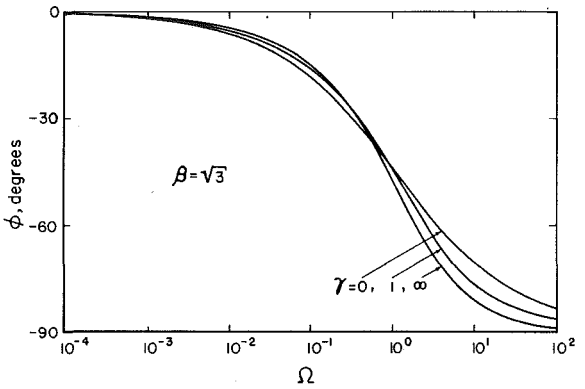

Fig. 3 Oscillating applied force on a neutrally buoyant droplet

$$(1+\gamma)F/6\pi\mu_e a(1+2\gamma/3).$$

The initial droplet response is revealed by expanding the transformed velocity in negative powers of the Laplace parameter, then inverting. The result is

$$u/u_0 = \frac{1+2\gamma/3}{1+\gamma}\left[T - \frac{4\beta\sqrt{\gamma(9-\beta^2)/2}}{3\sqrt{\pi}\,(\gamma\beta + \sqrt{\gamma(9-\beta^2)/2})}\,T^{3/2} + \ldots\right] \tag{35}$$

in dimensionless form. The initial acceleration is simply the ratio of the applied force to the apparent mass.

The approach to steady state is shown using the Bromwich [10] expansion in positive powers of $\sqrt{S}$. For long times,

$$u/u_0 = 1 - \beta\frac{(1+2\gamma/3)}{(1+\gamma)}\frac{1}{\sqrt{\pi T}} + \ldots \tag{36}$$

In dimensional form, the dominant term in the approach to steady state had no viscosity ratio dependence.

The sinusoidal steady-state response to an oscillating force is readily obtained using the Fourier transform

$$\tilde{u} = \int_{-\infty}^{\infty} u\exp(-i\omega t)\,dt \tag{37}$$

where i denotes $\sqrt{-1}$ and ω is the frequency. The Fourier transformed relation is simply equation (28) with $i\omega$ in place of s. Results are conveniently presented as a function of the dimensionless frequency

$$\Omega = a^2\omega/9\nu_e \tag{38}$$

Figs. 2 and 3 show the steady-state response to an oscillating force. The magnitude of the response monotonically decreases as the fre-

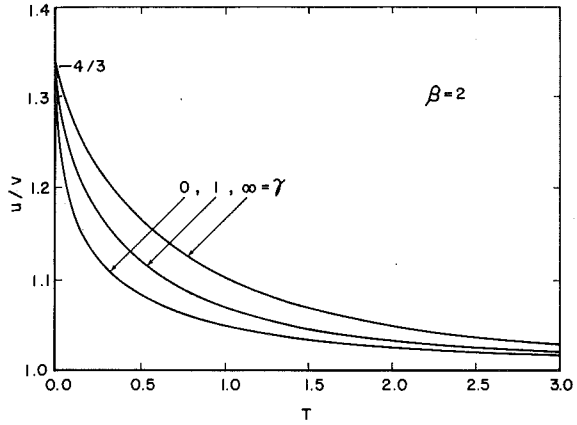

Fig. 4 Step change in the fluid velocity about a lighter droplet

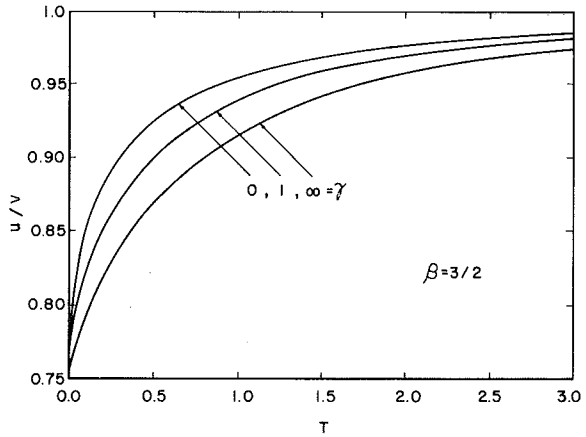

Fig. 5. Step change in the fluid velocity about a heavier droplet

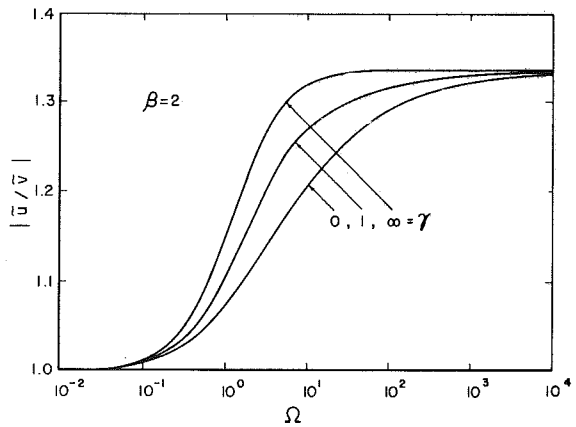

Fig. 6. Oscillating fluid about a lighter droplet

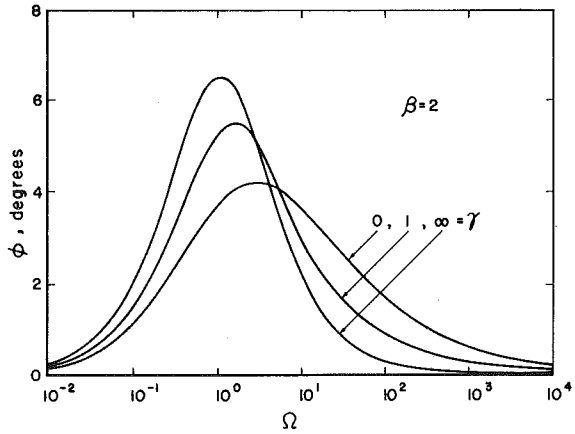

Fig. 7 Oscillating fluid about a lighter droplet

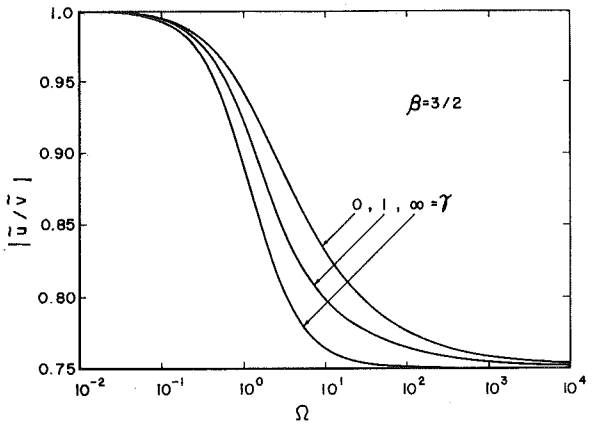

Fig. 8 Oscillating fluid about a heavier droplet

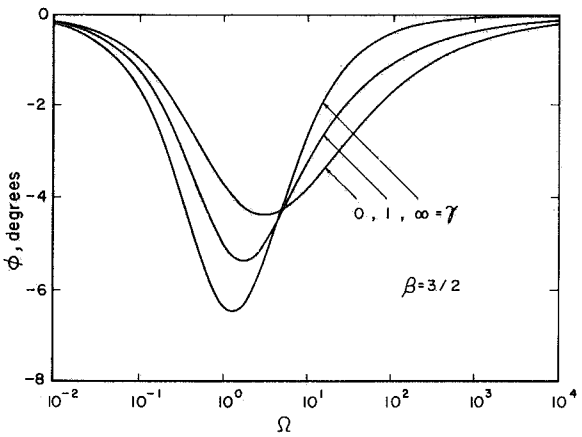

Fig. 9 Oscillating fluid about a heavier droplet

quency increases. The droplet lags behind the force, the phase angle approaching negative 90° for large frequency. This same behavior is seen at all mass ratios and viscosity ratios.

Motion in an Accelerating Fluid

The response to an accelerating external fluid is very different in character. This response can be found by a straightforward procedure. Let v be the external fluid velocity far from the droplet. Then $\bar{u}$ in the coefficients of equation (26) is replaced by the relative velocity $\bar{u} - \bar{v}$. The externally applied force $\bar{F}$ is, in this case, the force $m_e s\bar{v}$ resulting from the pressure gradient in the surrounding fluid. With these changes, we have in place of equation (28),

$$m_e s\bar{v} = m_i s\bar{u} + m_e s(\bar{u} - \bar{v})/2 + 6\pi\mu_e a(\bar{u} - \bar{v})\,(1 + a\sqrt{s/\nu_e})\Sigma \tag{39}$$

A different format is used to display response to an accelerating fluid.

Whereas the response to a specified force is qualitatively similar for all mass ratios, the response to an accelerating fluid differs significantly. The neutrally buoyant droplet moves exactly with an accelerating surrounding fluid. Lighter and heavier droplets move relative to the fluid.

Fig. 4 shows the response of a light droplet to a step change in fluid velocity. The droplet immediately assumes a velocity equal to $\beta^2/3$ of the fluid velocity, then uniformly decelerates to the velocity of the surrounding fluid. The heavier droplet, whose response appears in Fig. 5, also has a step change to $\beta^2/3$ of the external fluid velocity. In this instance, that change is less than the change of the surrounding fluid so the droplet continues to accelerate. In both cases, increased droplet viscosity produces a more rapid response.

Figs. 6 and 7 show the steady-state motion of a light droplet in an oscillating fluid. Lighter droplets ($\beta > \sqrt{3}$) have velocity magnitudes greater than the surrounding fluid and phase angles leading that fluid. For low frequencies, the velocity ratio is one and the phase angle zero. The phase angle reaches a peak at an intermediate frequency whose value depends on the viscosity ratio. At high frequencies, the phase angle again approaches zero and the magnitude ratio approaches $\beta^2/3$.

Heavier droplets differ by lagging the surrounding fluid and by having magnitude ratios less than unity decreasing to $\beta^2/3$ with increasing frequency. See Figs. 8 and 9.

In both cases, the velocity difference and the peak phase angle change increase as droplet viscosity decreases. The location of the peak phase angle varies only slightly with viscosity ratio, occurring at higher frequencies for more viscous droplets.

Discussion

Droplet viscosity and density through their influence on fluid motion about the droplets, significantly influence accelerated droplet motion. The response to a variety of inputs has been examined and the effects of viscosity and density discussed. The general character of the response for any mass or viscosity ratio can be elicited from the curves presented.

References

1 Sy, F., and Lightfoot, E. N., "Transient Creeping Flow Around Fluid Spheres," *AIChE Journal*, Vol. 17, 1971, pp. 177–181.

2 Morrison, F. A., Jr., and Stewart, M. B., "Small Bubble Motion in an Accelerating Liquid," ASME JOURNAL OF APPLIED MECHANICS, Vol. 43, 1976, pp. 399–403.

3 Hadamard, J., "Mouvement Permanent Lent d'une Sphère Liquide et Visqueuse dans un Liquide Visqueux," *Comptes Rendus*, Vol. 152, 1911, pp. 1735–1738.

4 Rybczynski, W., "Über die Fortschreitende Bewegung einer Flüssigen Kugel in einem zahen Medium," *Bulletin Internationale de L'Académie des Sciences de Cracovie*, 1911, pp. 40–46.

5 Morrison, F. A., Jr., "The Force on an Accelerating Body in Axisymmetric Creeping Flow," *Journal of Applied Mathematics and Physics (ZAMP)*, Vol. 23, 1972, pp. 333–336.

6 Basset, A. B., *A Treatise on Hydrodynamics*, Vol. II, Dover, New York, 1961 (original Deighton, Bell Edition, 1888).

7 Fuchs, N. A., *The Mechanics of Aerosols*, Pergamon Press, New York, 1964.

8 Boussinesq, J. V., *Theorie Analytique de la Chaleur*, Vol. II, Gauthier-Villars, Paris, 1903.

9 Bellman, R., Kalaba, R. E. and Lockett, J., *Numerical Inversion of the Laplace Transform*, Elsevier, Amsterdam, 1966.

10 Bromwich, T. J.I'a., "Symbolical Methods in the Theory of Conduction of Heat," *Proceedings of the Cambridge Philosophical Society*, Vol. 20, 1921, pp. 411–427.

T. Y. Han[2]
Research Assistant.
Assoc. Mem. ASME

W. L. Chow
Professor of Mechanical Engineering.
Mem. ASME

Department of Mechanical and Industrial Engineering,
University of Illinois at Urbana-Champaign,
Urbana, Ill. 61801

The Study of Sluice Gate and Sharp-Crested Weir Through Hodograph Transformations[1]

The problems of sluice gate and sharp crested weir were studied through hodograph transformations. Numerical calculations of the stream function in terms of hodograph variables were carried out after the hodographs were transformed into rectangles. Results were compared with the available experimental data and other results of calculations. Favorable agreement in all cases substantiated the fact that the method of hodograph transformation is effective in dealing with these problems strongly influenced by gravitation.

Introduction

Hydrodynamic free surface flow problems under the influence of the gravitational field have not been thoroughly examined. Due to their more difficult and complicated nature, solutions for problems of sluice gates and sharp-crested weirs have not been well established. The basic difficulty in solving these problems lies in the fact that the unknown free surface is no longer a boundary of constant speed as a result of gravitation. Thus the determination of the free surface as a part of the solution of these problems always involves a nonlinear coupling relationship along the boundary through the Bernoulli's principle.

Approximate methods were developed earlier by Marchi [2], Melkonian [3], Gurevich [4], and Benjamin [5] for the problem of sluice gate by neglecting the existence of the upstream free surface. These methods usually consisted of successive applications of conformal transformation, after adopting an approximate analytic expression for the velocity variation along the free surface in the hodograph plane. Other analytical work on the problems of jet streams under the influence of gravitation was carried out by Keller and Weitz [6], Clarke [7], and later Keller and Geer [8]. Upon selecting the thin jet thickness as a small parameter which is inversely proportional to the Froude number of the approaching flow, solutions based on asymtotic expansions were obtained by Clarke for the problem of free overfall which are, respectively, valid for upstream and downstream flow regions. The primary restriction of these methods is that the asymptotic expansion is accurate only for small gravitational effects.

The sharp-crested weir is commonly employed as a device for flow measurement, and is also of fundamental importance as its free surface profile provides the basis for the design of spillways. An early results for the sharp-crested weir with infinite weir height was obtained by McNown, Hsu, and Yih [9] through relaxational calculations. Recently, a finite-element method and its generalization were applied to the flow over a spillway by Ikegawa and Washizu [10] and to flow problems with a free surface under gravity by Varoglu and Finn [11].

The method of hodograph transformation has not been extensively explored for engineering purposes, since the final physical configuration corresponding to an indirect solution is often not of practical interest. However, it was recently found that this type of problem dominated by the influence of gravitation can be effectively dealt with through hodograph transformations. The problem of an imcompressible fluid discharging from a horizontal channel [12] and the problem of a free overfall [13] have been worked out satisfactorily. It was recognized that even with the strong influence of the gravitational field, the stream function can be determined in the transformed hodograph plane through numerical calculations.

It is the intention of this paper to demonostrate the usefulness of this approach to obtain solutions for the sluice gate and the sharp-crested weir. Results of these calculations would provide useful information for the design of hydraulic devices. Comparisons between the present results of calculations and available experimental data would also substantiate the merits of the method of hodograph transformation.

Theoretical Considerations

Sluice Gate. Referring to Fig. 1(a) where the configuration of a sluice gate is depicted, it is required, for a given uniform upstream approaching flow condition and gate angle α, to solve the flow field throughout the region including the corresponding gate opening Y_D and the free surface boundaries. It is well known that the action of the

[1] This work is based on a PhD thesis by the first author [1].

[2] Present Address, Research Associate, Department of Mechanical Engineering, University of California, Berkeley, Calif. 94720.

Contributed by the Applied Mechanics Division of THE AMERICAN SOCIETY OF MECHANICAL ENGINEERS, and presented at the 1981 Joint ASME/ASCE Applied Mechanics, Fluids Engineering, and Bioengineering Conference, University of Colorado, Boulder, Colo., June 22–27, 1981.

Discussion on this paper should be addressed to the Editorial Department, ASME, United Engineering Center, 345 East 47th Street, New York, N.Y. 10017, and will be accepted until September 1, 1981. Readers who need more time to prepare a Discussion should request an extension from the Editorial Department. Manuscript received by ASME Applied Mechanics Division, April, 1980; final revision, November, 1980. Paper No. 81-APM-23.

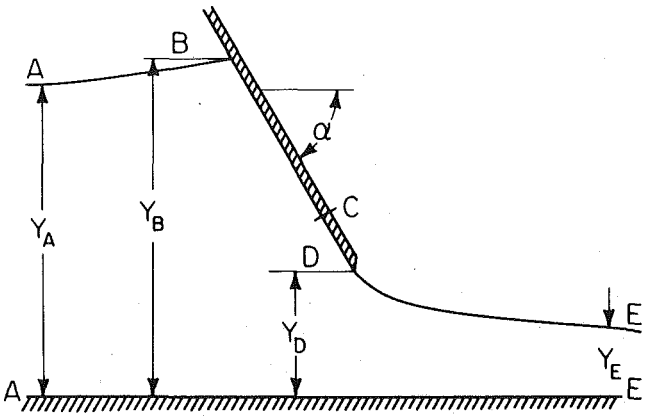

1a.

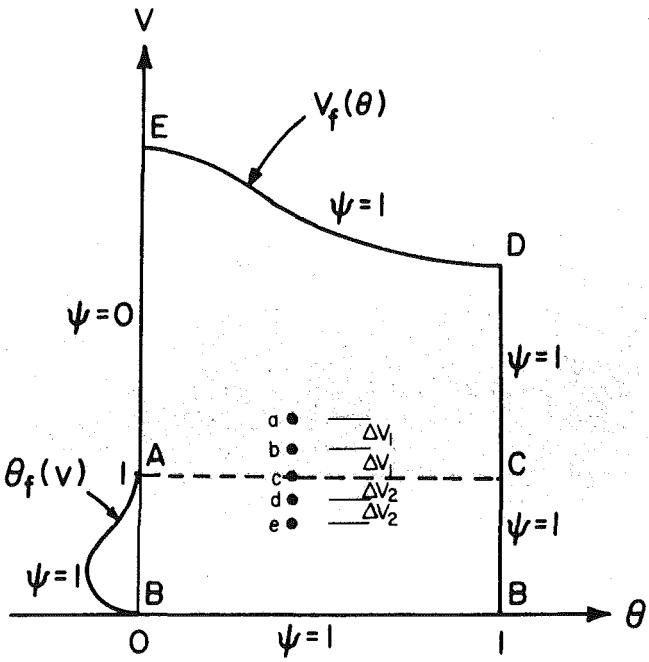

1b.

Fig. 1 The sluice gate and its hodograph

sluice gate would bring forth a flow transition from an upstream uniform subcritical flow to a downstream uniform supercritical flow. The influence of the gate obstruction extends to far upstream and downstream positions, and uniform flows with a hydrostatic pressure distribution are only possible at these locations.

From conservational principles, it can be shown that the flow depth ratio Y_E, already normalized by Y_A, satisfies a cubic algebraic equation given by

$$Y_E{}^3 - \left(1 + \frac{Fr_A{}^2}{2}\right)(Y_E{}^2) + \frac{Fr_A{}^2}{2} = 0$$

with

$$Fr_A = V_A/\sqrt{gY_A},$$

and the correct solution for Y_E is given by

$$Y_E = \frac{1}{V_E} = \frac{1 + \sqrt{1 + 8/Fr_A{}^2}}{4/Fr_A{}^2} \tag{1}$$

where V_E is already normalized by V_A.

For any point along the free surface, the velocity ratio is related to its elevation Y through the Bernoulli's principle expressed as

$$v = \sqrt{1 + \frac{2}{Fr_A{}^2}(1 - y)} \tag{2}$$

Obviously, the elevation of the stagnation point B is given by

$$Y_B = 1 + \frac{Fr_A{}^2}{2} \tag{2a}$$

It has been established [14] from the basic principles that the governing stream function for the incompressible potential flow shall satisfy, in the hodograph variables, the equation given by

$$v^2\psi_{vv} + v\psi_v + \frac{\psi_{\theta\theta}}{\alpha^2} = 0 \tag{3}$$

where ψ, v, θ are already normalized by the upstream flow quantities and $(-\alpha)$, respectively, so the values of ψ and θ vary from zero to unity. It has also been derived that the dimensionless coordinates in the physical plane satisfy the pair of differential equations given by

$$dx = \left(\frac{\cos(-\alpha\theta)}{\alpha v^2}\psi_\theta - \frac{\sin(-\alpha\theta)}{v}\psi_v\right)dv - \left(\alpha\cos(-\alpha\theta)\,\psi_v + \frac{\sin(-\alpha\theta)}{v}\psi_\theta\right)d\theta \tag{4}$$

$$dy = \left(\frac{\sin(-\alpha\theta)}{\alpha v^2}\psi_\theta + \frac{\cos(-\alpha\theta)}{v}\psi_v\right)dv - \left(\alpha\sin(-\alpha\theta)\,\psi_v - \frac{\cos(-\alpha\theta)}{v}\psi_\theta\right)d\theta \tag{5}$$

The corresponding hodograph of this problem is shown in Fig. 1(b), where the functions $V_f(\theta)$ and $\theta_f(v)$ pertaining to the free surfaces in the v, θ-plane are yet unknown. One possible approach of transforming the hodograph into rectangles is to subdivide the hodograph into two parts along a horizontal line through the points A and C as shown in Fig. 1(b) and each part of the hodograph may be subsequently transformed into rectangles.

One now introduces the transformations for the upper part of the domain according to

$$q_1 = \frac{v - 1}{v_f(\theta) - 1}$$
$$\beta_1 = \theta \tag{6}$$

and for the lower part of the domain according to

$$q_2 = v$$
$$\beta_2 = \frac{\theta - \theta_f(v)}{1 - \theta_f(v)} \tag{7}$$

The hodograph in the q, β-plane now assumes the shape of a square as shown in Figs. 2(a) and 2(b). Under these transformations, equations (3)–(5) would change, respectively, into

$$\psi_{q_1q_1}\left\{\frac{[q_1(v_f - 1) + 1]^2}{(v_f - 1)^2} + \left[\frac{q_1 v_f'}{\alpha(v_f - 1)}\right]^2\right\} - \psi_{\beta_1q_1}\left\{\frac{2q_1 v_f'}{(v_f - 1)\alpha^2}\right\} + \frac{1}{\alpha^2}\psi_{\beta_1\beta_1} + \psi_{q_1}\left\{\frac{q_1(v_f - 1) + 1}{v_f - 1} + \frac{q_1[2v_f'^2 - v_f''(v_f - 1)]}{\alpha^2(v_f - 1)^2}\right\} = 0 \tag{8}$$

$$dx = A(v_f - 1)\,dq_1 + (Aq_1 v_f' + B)\,d\beta_1 \tag{9}$$

and

$$dY = C(v_f - 1)\,dq_1 + (Cq_1 v_f' + D)\,d\beta_1 \tag{10}$$

for the upper domain, where $v_f'(\theta)$ and $v_f''(\theta)$ denote the first and

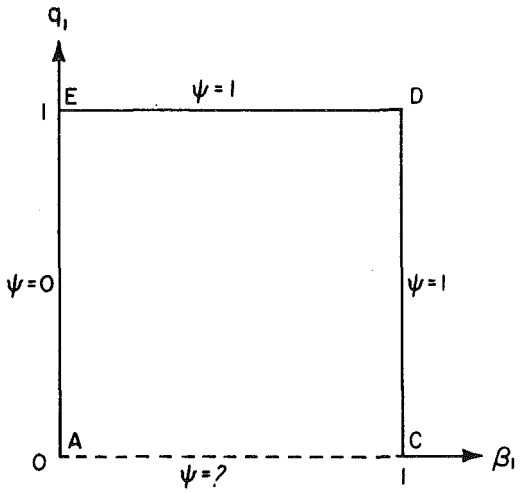

2a.

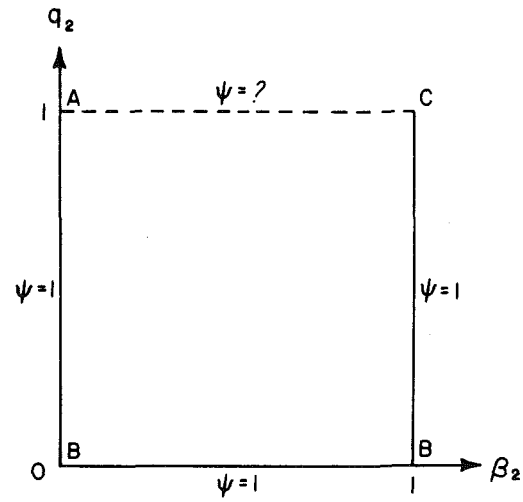

2b.

Fig. 2 The hodograph in the q, β-plane

second derivatives of the function $v_f(\theta)$, against its argument, respectively,

$$A = \frac{\cos(-\alpha\beta_1)}{\alpha[q_1(v_f-1)+1]^2}\left(\psi_{\beta_1} - \frac{q_1 v_f'}{v_f - 1}\psi_{q_1}\right) - \frac{\sin(-\alpha\beta_1)\,\psi_{q_1}}{[q_1(v_f-1)+1](v_f-1)} \tag{11}$$

$$B = \frac{-\alpha\cos(-\alpha\beta_1)}{v_f-1}\psi_{q_1} - \frac{\sin(\alpha\beta_1)}{q_1(v_f-1)+1}\left(\psi_{\beta_1} - \frac{q_1 v_f'}{v_f-1}\psi_{q_1}\right) \tag{12}$$

$$C = \frac{\sin(-\alpha\beta_1)}{\alpha[q_1(v_f-1)+1]^2}\left(\psi_{\beta_1} - \frac{q_1 v_f'}{v_f-1}\psi_{q_1}\right) + \frac{\cos(-\alpha\beta_1)\,\psi_{q_1}}{[q_1(v_f-1)+1](v_f-1)} \tag{13}$$

$$D = \frac{-\alpha\sin(-\alpha\beta_1)}{v_f-1}\psi_{q_1} + \frac{\cos(-\alpha\beta_1)}{q_1(v_f-1)+1}\left(\psi_{\beta_1} - \frac{q_1 v_f'}{v_f-1}\psi_{q_1}\right) \tag{14}$$

and

$$q_2^2\psi_{q2q2} + \psi_{\beta2q2}\left\{\frac{2q_2^2\,\theta_f'[\beta_2-1]}{1-\theta_f}\right\} + \psi_{\beta2\beta2}\left\{\frac{1}{\alpha^2(1-\theta_f)^2} + \left[\frac{\theta_f'\,q_2(\beta_2-1)}{1-\theta_f}\right]^2\right\} + q_2\psi_{q_2} + \psi_{\beta_2}\left\{\frac{\theta_f'\,q_2(\beta_2-1)}{1-\theta_f} + \frac{(\beta_2-1)\,q_2^2\,[\theta_f''(1-\theta_f)+2\theta_f'^2]}{(1-\theta_f)^2}\right\} = 0 \tag{15}$$

$$dx = [E + F\,\theta_f'(1-\beta_2)]\,dq_2 + F(1-\theta_f)\,d\beta_2 \tag{16}$$

$$dY = [G + H\,\theta_f'(1-\beta_2)]\,dq_2 + H(1-\theta_f)\,d\beta_2 \tag{17}$$

for the lower domain, where $\theta_f'(v)$ and $\theta_f''(v)$ denote the first and second derivatives of the function $\theta_f(v)$, against its argument respectively, and

$$E = \frac{\cos\{-\alpha[\theta_f + (1-\theta_f)\beta_2]\}}{q_2^2\alpha(1-\theta_f)}\psi_{\beta_2} - \frac{\sin\{-\alpha[\theta_f + (1-\theta_f)\beta_2]\}}{q_2} \times\left[\psi_{q_2} + \psi_{\beta_2}\frac{\theta_f'(\beta_2-1)}{1-\theta_f}\right] \tag{18}$$

$$F = -\alpha\cos\{-\alpha[\theta_f + (1-\theta_f)\beta_2]\}\left[\psi_{q_2} + \psi_{\beta_2}\frac{\theta_f'(\beta_2-1)}{1-\theta_f}\right] - \frac{\sin\{-\alpha[\theta_f + (1-\theta_f)\,\beta_2]\}}{q_2(1-\theta_f)}\psi_{\beta_2} \tag{19}$$

$$G = \frac{\sin\{-\alpha[\theta_f + (1-\theta_f)\beta_2]\}}{q_2^2\alpha(1-\theta_f)}\psi_{\beta_2} + \frac{\cos\{-\alpha[\theta_f + (1-\theta_f)\beta_2]\}}{q_2} \times\left[\psi_{q_2} + \psi_{\beta_2}\frac{\theta_f'(\beta_2-1)}{1-\theta_f}\right] \tag{20}$$

$$H = -\alpha\sin\{-\alpha[\theta_f + (1-\theta_f)\beta_2]\}\left[\psi_{q_2} + \psi_{\beta_2}\frac{\theta_f'(\beta_2-1)}{(1-\theta_f)}\right] + \frac{\cos\{-\alpha[\theta_f + (1-\theta_f)\beta_2]\}}{q_2(1-\theta_f)}\psi_{\beta_2} \tag{21}$$

Sharp-Crested Weir. The configuration of a sharp-crested weir is depicted in Fig. 3, where an initially uniform flow with a hydrostatic pressure distribution approaches a weir. The lower streamline stagnates at the point B and leaves the weir tangentially afterwards, reaching its maximum elevation at the crest D and forming a free streamline. The top streamline drops continuously toward the weir as a result of acceleration. It should be noted, however, that for a given set of upstream flow conditions, there is only one set of the height Y_c and the angle α of the weir.

The corresponding hodograph of this problem is shown in Fig. 3(b) where the velocity and the streamline angle have been normalized already by v_A and $(-\alpha)$, respectively. With the given approaching flow conditions, $v_f(\theta)$, $v_l(\theta)$, and $v_u(\theta)$ are all unknown. It is obvious that the idea of subdividing the hodograph is needed to solve this problem. A simple scheme is to divide the hodograph along the vertical line AD. It was learned later [1] that it would be necessary to cut along a horizontal line AC' so that the point A became a grid point after the transformation to avoid "haunting" pattern during iteration of the weir height. The hodograph now consists of three parts; each of them can be transformed into a rectangle for the benefit of computation.

A transformation for the right part of the domain is introduced according to

$$\omega = 1/v \tag{22}$$

and

$$q_1 = \frac{\omega - \omega_l(\theta)}{\omega_u(\theta) - \omega_l(\theta)}, \qquad \beta_1 = \frac{\alpha}{\pi/2}\theta \tag{23}$$

where $\omega_u(\theta)$ and $\omega_l(\theta)$ are the corresponding images of the upper and lower free streamlines in the ω, θ-plane (Fig. 4(a)). The hodograph in the q_1, β_1, plane now has the shape of the square as shown in Fig. 4(b), and equations (3)–(5) would change, respectively, into

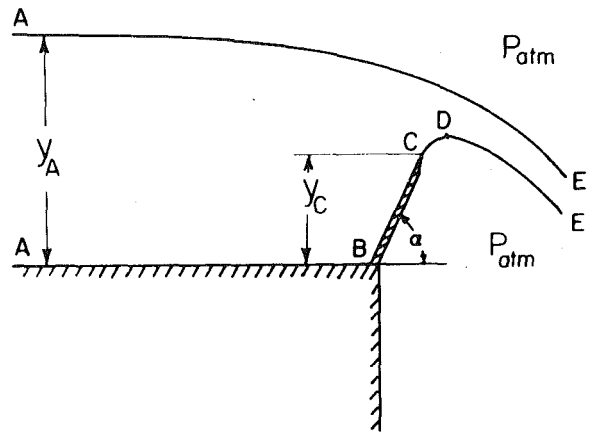

3a.

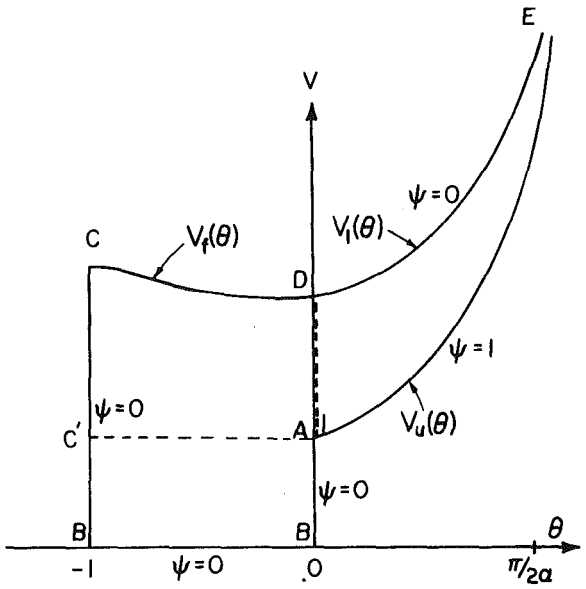

3b.

Fig. 3 A sharp-crested weir and its hodograph

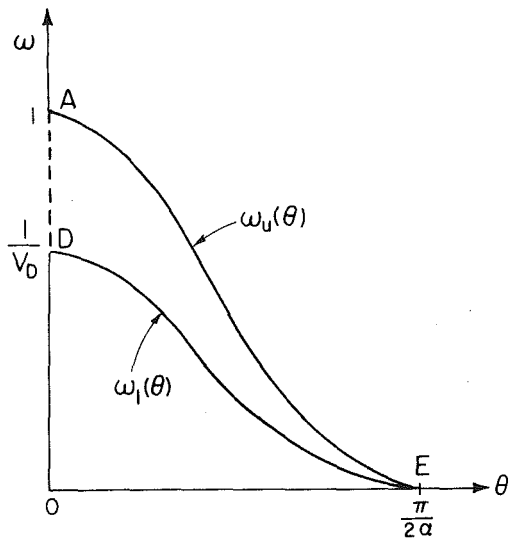

4a.

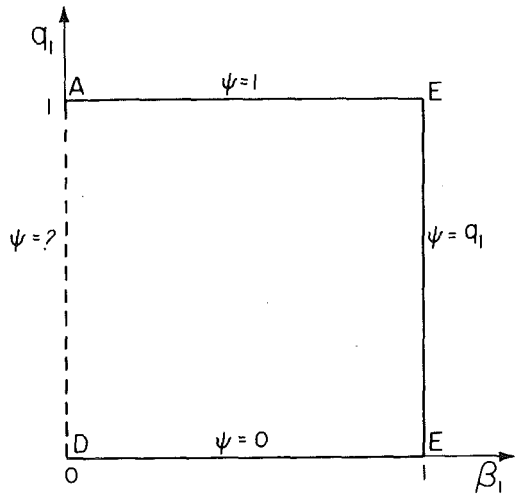

4b.

Fig. 4 The hodograph in the ω,θ and q_1, β_1-planes

$$\psi_{q_1q_1}\left\{\frac{[\omega_l + q_1(\omega_u - \omega_l)]^2}{(\omega_u - \omega_l)^2} + \left[\frac{(q_1 - 1)\omega_l' - q_1\omega_u'}{\frac{\pi}{2}(\omega_u - \omega_l)}\right]^2\right\}$$
$$+ \psi_{\beta_1q_1}\left\{\frac{8(q_1 - 1)\omega_l' - 8q_1\omega_u'}{\pi^2(\omega_u - \omega_l)}\right\} + \frac{4}{\pi^2}\psi_{\beta_1\beta_1}$$
$$+ \psi_{q_1}\left\{\frac{\omega_l + q_1(\omega_u - \omega_l)}{\omega_u - \omega_l} + \frac{8(\omega_l' - \omega_u')}{\pi^2(\omega_u - \omega_l)^2}[(q_1 - 1)\,\omega_l' - q_1\omega_u'] + \frac{4}{\pi^2(\omega_u - \omega_l)}[(q_1 - 1)\,\omega_l'' - q_1\omega_u'']\right\} = 0 \quad (24)$$

$$dx = A(\omega_u - \omega_l)\,dq_1 + \{A[\omega_l' - q_1(\omega_u' - \omega_l')] + B\}\,d\beta_1 \quad (25)$$

$$dy = C(\omega_u - \omega_l)\,dq_1 + \{C[\omega_l' - q_1(\omega_u' - \omega_l')] + D\}\,d\beta_1 \quad (26)$$

where ω_l', ω_l'', ω_u', and ω_u'' denote the first and second derivatives of functions $\omega_l(\theta)$ and $\omega_u(\theta)$ and

$$A = \frac{-\cos\left(-\frac{\pi}{2}\beta_1\right)}{\pi/2}\left\{\psi_{\beta_1} - \psi_{q_1}\frac{\omega_l' + q_1(\omega_u' - \omega_l')}{\omega_u - \omega_l}\right\} - \frac{[\omega_l + q_1(\omega_u - \omega_l)]\sin\left(-\frac{\pi}{2}\beta_1\right)}{\omega_u - \omega_l}\psi_{q_1} \quad (27)$$

$$B = \frac{\frac{\pi}{2}[\omega_l + q_1(\omega_u - \omega_l)]^2\cos\left(-\frac{\pi}{2}\beta_1\right)}{\omega_u - \omega_l}\psi_{q_1}$$
$$- [\omega_l + q_1(\omega_u - \omega_l)]\sin\left(-\frac{\pi}{2}\beta_1\right)$$
$$\times\left\{\psi_{\beta_1} - \psi_{q_1}\frac{\omega_l' + q_1(\omega_u' - \omega_l')}{\omega_u - \omega_l}\right\} \quad (28)$$

$$C = \frac{-\sin\left(-\frac{\pi}{2}\beta_1\right)}{\frac{\pi}{2}}\left\{\psi_{\beta_1} - \psi_{q_1}\frac{\omega_l' + q_1(\omega_u' - \omega_l')}{\omega_u - \omega_l}\right\}$$
$$+ \frac{[\omega_l + q_1(\omega_u - \omega_l)]\cos\left(-\frac{\pi}{2}\beta_1\right)\psi_{q_1}}{\omega_u - \omega_l} \quad (29)$$

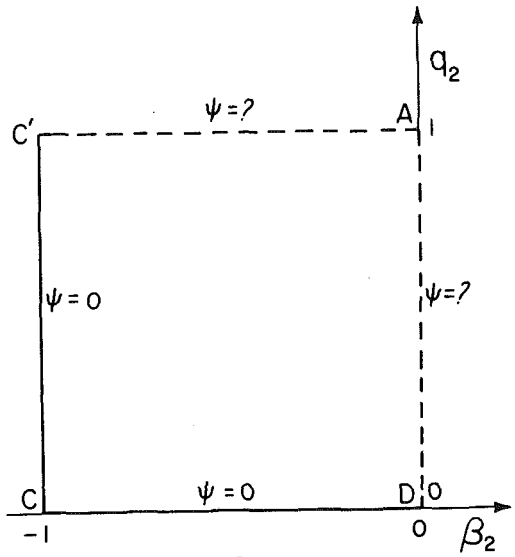

5a.

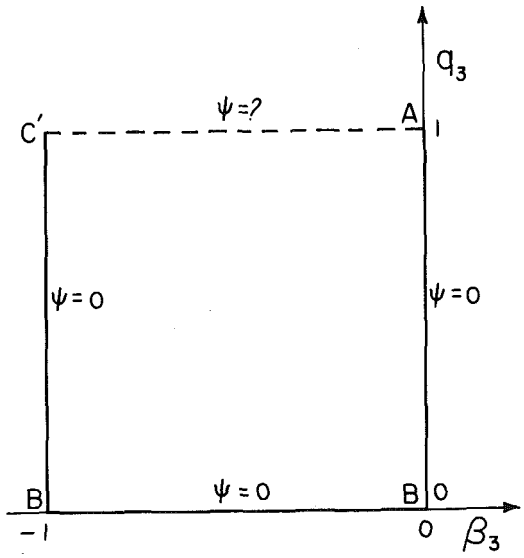

5b.

Fig. 5 The hodograph in the q_2, β_2 and q_3, β_3-planes

$$D = \frac{\frac{\pi}{2}[\omega_l + q_1(\omega_u - \omega_l)]^2 \sin\left(-\frac{\pi}{2}\beta_1\right)}{\omega_u - \omega_l} \times \psi_{q_1} + [\omega_l + q_1(\omega_u - \omega_l)] \cos\left(-\frac{\pi}{2}\beta_1\right) \times \left\{\psi_{\beta_1} - \psi_{q_1}\frac{\omega_l' + q_1(\omega_u' - \omega_l')}{\omega_u - \omega_l}\right\} \quad (30)$$

Upon introducing the transformation for the left-upper part of the hodograph according to

$$q_2 = \frac{\upsilon - \upsilon_f(\theta)}{1 - \upsilon_f(\theta)}$$
$$\beta_2 = \theta \quad (31)$$

it becomes, in the q_2, β_2-plane, also a square as shown in Fig. 5(a). The governing equations would also change, respectively, into

$$\psi_{q_2q_2}\left\{\left(q_2 + \frac{\upsilon_f}{1-\upsilon_f}\right)^2 + \left\{\frac{[q_2-1]\upsilon_f}{[1-\upsilon_f]\alpha}\right\}^2\right\} + \psi_{\beta_2q_2}\left\{\frac{2(q_2-1)\upsilon_f'}{\alpha^2(1-\upsilon_f)}\right\} + \frac{1}{\alpha^2}\psi_{\beta_2\beta_2} + \psi_{q_2}\left\{q_2 + \frac{\upsilon_f}{1-\upsilon_f} + \frac{2(q_2-1)\upsilon_f'^2}{\alpha^2(1-\upsilon_f)^2} + \frac{(q_2-1)\upsilon_f''}{\alpha^2(1-\upsilon_f)}\right\} = 0 \quad (32)$$

(Cont.)

$$dx = E(1-\upsilon_f)\,dq_2 + [E(1-q_2)\,\upsilon_f' + F]\,d\beta_2 \quad (33)$$

$$dy = G(1-\upsilon_f)\,dq_2 + [G(1-q_2)\upsilon_f' + H]\,d\beta_2 \quad (34)$$

where $\upsilon_f'(\theta)$ and $\upsilon_f''(\theta)$ denotes the first and second derivatives of the function $\upsilon_f(\theta)$, and

$$E = \frac{\cos(-\alpha\beta_2)}{\alpha[\upsilon_f + q_2(1-\upsilon_f)]^2}\left\{\psi_{\beta_2} + \frac{(q_2-1)\,\upsilon_f'}{1-\upsilon_f}\psi_{q_2}\right\} - \frac{\sin(-\alpha\beta_2)}{[\upsilon_f + q_2(1-\upsilon_f)]}\frac{\psi_{q_2}}{[1-\upsilon_f]} \quad (35)$$

$$F = \frac{-\alpha\cos(-\alpha\beta_2)}{1-\upsilon_f}\psi_{q_2} - \frac{\sin(-\alpha\beta_2)}{\upsilon_f + q_2(1-\upsilon_f)} \times \left[\psi_{\beta_2} + \frac{(q_2-1)\upsilon_f'}{1-\upsilon_f}\psi_{q_2}\right] \quad (36)$$

$$G = \frac{\sin(-\alpha\beta_2)}{\alpha[\upsilon_f + q_2(1-\upsilon_f)]^2}\left\{\psi_{\beta_2} + \frac{(q_2-1)\upsilon_f'}{1-\upsilon_f}\psi_{q_2}\right\} + \frac{\cos(-\alpha\beta_2)\,\psi_{q_2}}{[\upsilon_f + q_2(1-\upsilon_f)][1-\upsilon_f]} \quad (37)$$

$$H = \frac{-\alpha\sin(-\alpha\beta_2)}{1-\upsilon_f}\psi_{q_2} + \frac{\cos(-\alpha\beta_2)}{\upsilon_f + q_2(1-\upsilon_f)} \times \left\{\psi_{\beta_2} + \frac{(q_2-1)\upsilon_f'}{1-\upsilon_f}\psi_{q_2}\right\} \quad (38)$$

No transformation is needed for the left-lower part of the hodograph. Equations (3)–(5), the original hodograph equations, can be directly employed for the calculation of the stream function.

Methods of Calculations and Results

It is obvious that values of the stream function are completely specified on the boundaries of all the hodographs except along the lines of division which are intentionally introduced to facilitate transformation. Although the stream function is unknown along these boundaries, it is the common boundary to the two adjacent domains and must have the same value of the stream function. In fact these values are to be determined through the condition that the normal derivatives of the stream function in the original hodograph plane should be continuous. Taking Fig. 1(b) for the sluice gate as an example, one may impose this condition as

$$\left.\frac{\partial\psi}{\partial\upsilon}\right|_{AC}^{\text{upper}} = \left.\frac{\partial\psi}{\partial\upsilon}\right|_{AC}^{\text{lower}} \quad (39)$$

and these partial derivatives may be represented by their corresponding one-sided finite-difference expressions. It may be easily shown [1], that the value of the stream function ψ_c on the boundary can be found from

$$\psi_c = \frac{(4\psi_b - \psi_a)\,\Delta\upsilon_2 + (4\psi_d - \psi_e)\Delta\upsilon_1}{3(\Delta\upsilon_1 + \Delta\upsilon_2)} \quad (40)$$

where $\Delta\upsilon_1$ and $\Delta\upsilon_2$ are the corresponding numerical grid spacings for the upper and lower domains, and ψ_d, ψ_e must be obtained from interpolation for this particular situation. Similar schemes are followed for all the other common boundaries of the adjacent hodographs.

To initiate the numerical calculations, values of the stream function along these common boundaries must be known, and these values may be obtained from a crude interpolation. These values will be revised and updated according to the foregoing scheme in the midst of calculations. Methods of calculations for the sluice gate and the sharp-crested weir are separately discussed as follows:

1 For the sluice gate, with a given upstream flow condition and an arbitrary gate opening, functions $\upsilon_f(\theta)$ and $\theta_f(\upsilon)$ are initially unknown, and their initial values are estimated through simple polynomial functions. The stream function within the square domains of

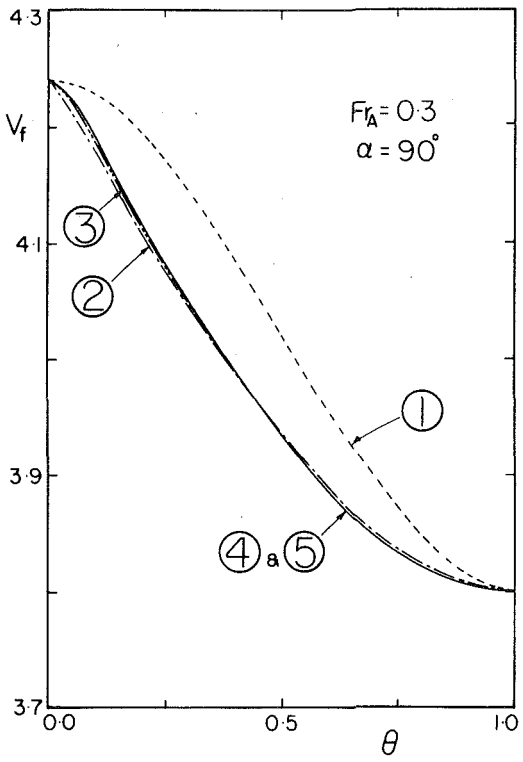

Fig. 6 Values of $v_f(\theta)$ at successive iterations

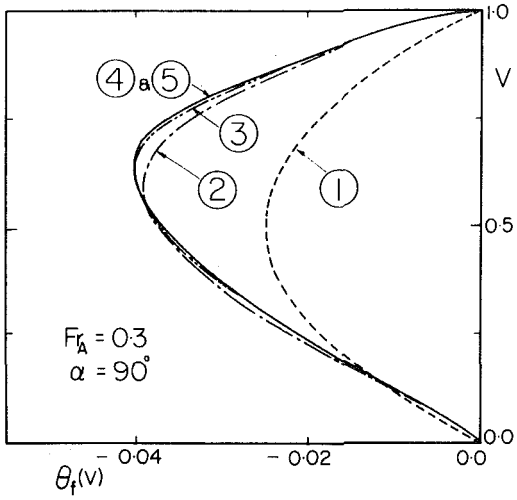

Fig. 7 Values of $\theta_f(v)$ at successive iterations

Fig. 2 may be determined from equations (8) and (15) through the Successive-Over-Relaxation scheme (SOR). Once its value at every grid point within the domain does not vary more than an arbitrarily selected small number (e.g., 10^{-4}), the derivatives of ψ_{β_1}, ψ_{β_2}, ψ_{q_1}, and ψ_{q_2} may be evaluated along the boundaries AB and DE, and their profiles in the physical plane may be traced through numerically integrating equations (9), (10), (16), and (17). These profiles of the free streamline would yield a revised form for $v_f(\theta)$ according to equation (2) for the flow downstream of the sluice gate, and a revised form for $\theta_f(v)$ for the flow upstream of the sluice gate according to

$$\theta_f(v) = \frac{\tan^{-1}\dfrac{dy_e}{dx}}{-\alpha} \tag{41}$$

where dx was obtained from equation (16) and dY_e was obtained directly from Bernoulli's principle through

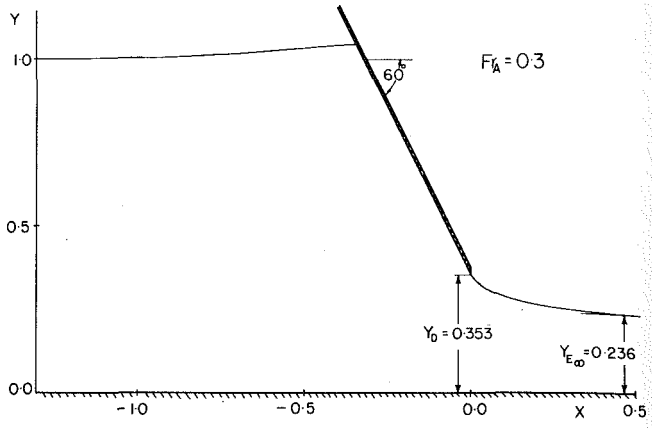

Fig. 8 Free surface profiles for $Fr_A = 0.3$, $\alpha = 60°$

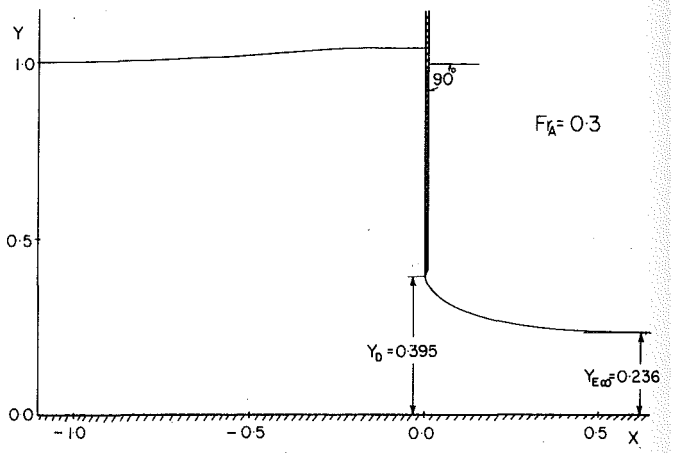

Fig. 9 Free surface profiles for $Fr_A = 0.3$, $\alpha = 90°$

$$dY_e = -q_2\, Fr_A{}^2\, dq_2 \tag{42}$$

The foregoing process of calculations may be repeated until $v_f(\theta)$ and $\theta_f(v)$ employed for the calculations agree with that produced from tracing within an arbitrarily small margin (e.g., 1×10^{-3}) at every grid point along the free streamline. For flows with low Froude number Fr_A, iteration of $v_f(\theta)$ and $\theta_f(v)$ is a rapidly convergent process. Figs. 6 and 7 clearly illustrate this feature. For Fr_A greater than 0.37, some difficulty in convergence of $\theta_f(v)$ function has been observed. The tendency of divergence of $\theta_f(v)$ function, especially for high values of Fr_A, will be discussed later.

So far, these calculations are carried out with an arbitrary gate opening, and the asymptotic height Y_E obtained from the free surface tracing would in general not agree with the results from equation (1). It is natural to expect that the gate opening Y_D should be adjusted until the correct asymptotic height Y_E is obtained. Again determination of Y_D must be based on iterations and it is a rapidly converging process. Only three iterations are usually required to determine its value within an accuracy of 10^{-3}. Figs. 8–10 present the established final profiles of the free surfaces for the cases of $Fr_A = 0.3$ with $\alpha =$ 60°, 90°, and 120°. Fig. 11 shows the pressure distribution in the vicinity of the gate for the case $Fr_A = 0.3$, $\alpha = 90°$. It is interesting to observe that drastic modification of the hydrostatic pressure distribution occurs only within a relatively small region. Fig. 12 presents the established gate opening. Fig. 13 presents the obtained $\theta_f(v)$-values for $Fr_A = 0.1$ at different α angles. For small α angles or larger Fr_A-values, sharp variations of $\theta_f(v)$ near the stagnation point have been observed. Under this situation, evaluation of $\theta_f'(v)$ and

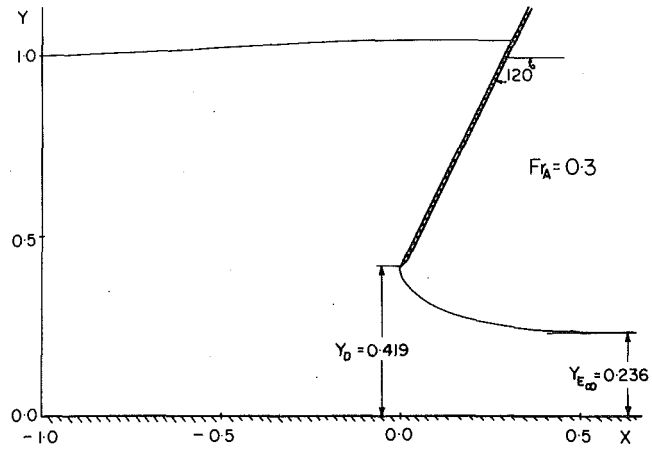

Fig. 10 Free surface profiles for $Fr_A = 0.3$, $\alpha = 120°$

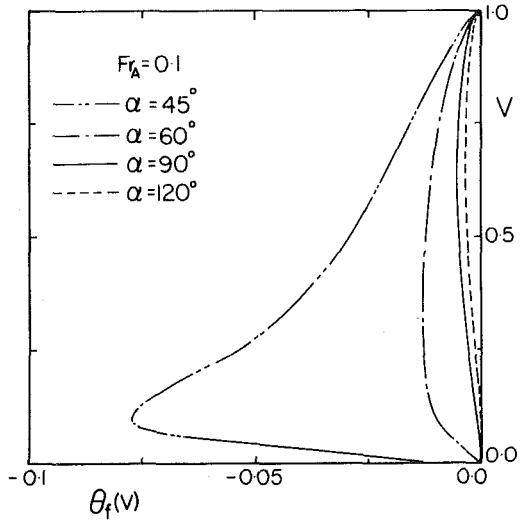

Fig. 13 $\theta_f(v)$ function for $Fr_A = 0.1$

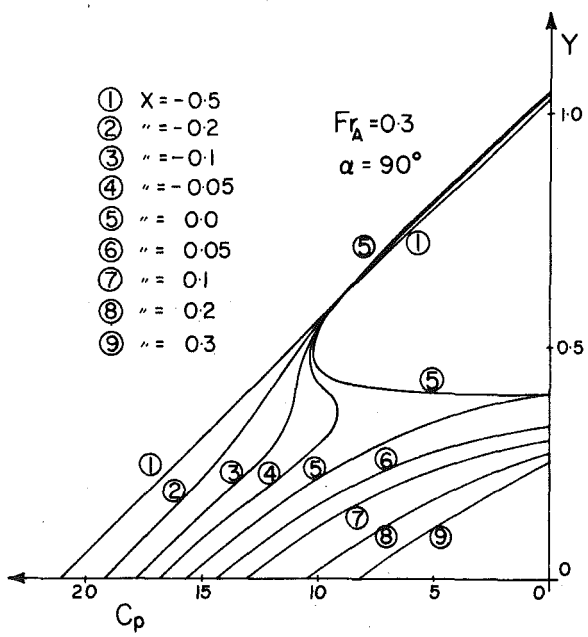

Fig. 11 Pressure distributions for a sluice gate

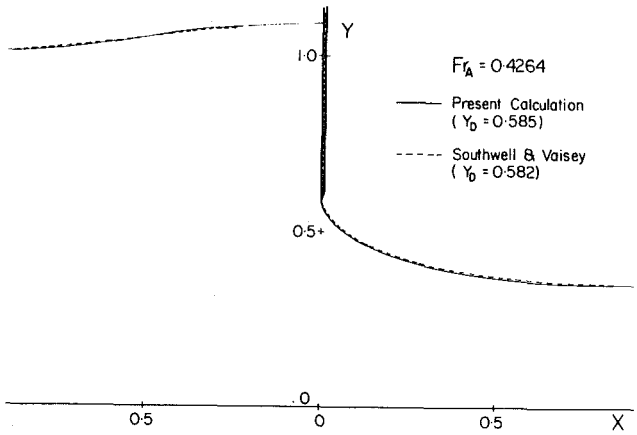

Fig. 14 Comparison with Southwell and Vaisey's results

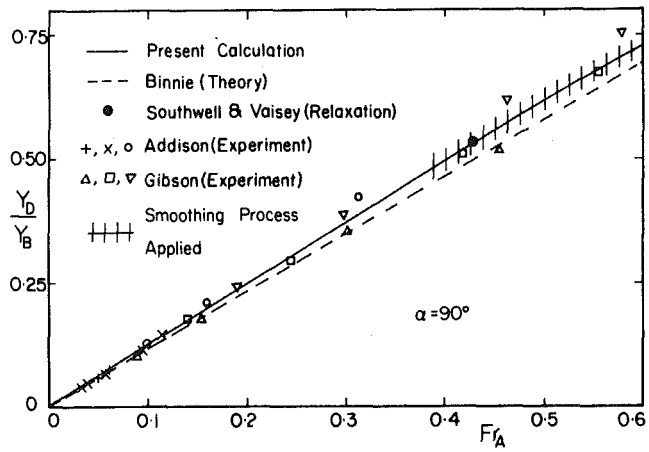

Fig. 12 The gate opening for various Fr_A values

$\theta_f''(v)$ through numerical differentiation may not be accurate, which would directly influence the stream function calculations and the convergence of $\theta_f(v)$. Smoothing process of $\theta_f'(v)$ and $\theta_f''(v)$ was introduced to effect convergence by taking average values of θ_f' and θ_f'' between two adjacent grid points successively. However, for Fr_A greater than 0.6, it becomes impossible to obtain a stable solution even with repeated application of this smoothing process. Thus, within the range of Fr_A between 0.37 and 0.6, results were obtained with minimum number of applications of this smoothing process to $\theta_f'(v)$ and $\theta_f''(v)$ for convergence purpose. Fig. 14 presents the free jet profiles for $Fr_A = 0.4264$ along with previous results by Southwell and Vaisey [15]. It is appropriate to remark that in all calculations required to solve these problems on the basis of hodograph transformation, the unknown functions such as $\theta_f(v)$ and $v_f(\theta)$ must be determined through iterations. While these functions including their first and secondary derivatives are imbedded in the main differential equation of the stream function, it is clear that the exact solution of the problem would produce matching and convergence of these functions and their derivatives up to any order under the present method of treatment. Since the secondary derivatives are the highest order of differentiation of these functions directly involved in these calculations, four levels of convergence requirement may be imposed; namely, convergence to (*i*) the secondary derivative, (*ii*) the first derivative, (*iii*) the function itself, and (*iv*) the integrated profile (e.g., the free surface of the present problem) produced from these functions. It is obvious that due to the error of numerical differentiation, imposition of con-

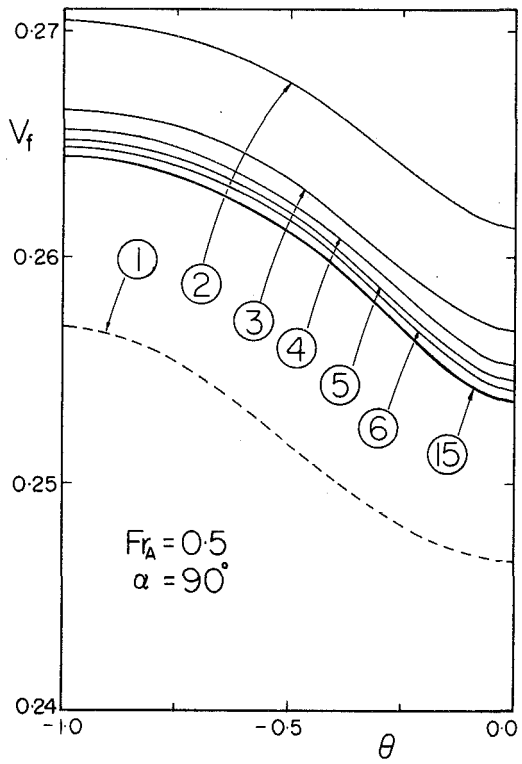

Fig. 15 Values of $v_f(\theta)$ for a sharp-crested weir at various iterations

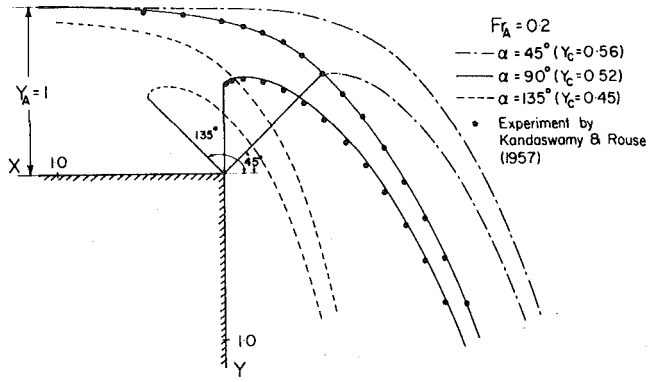

Fig. 17 Configurations of free surfaces at $Fr_A = 0.2$

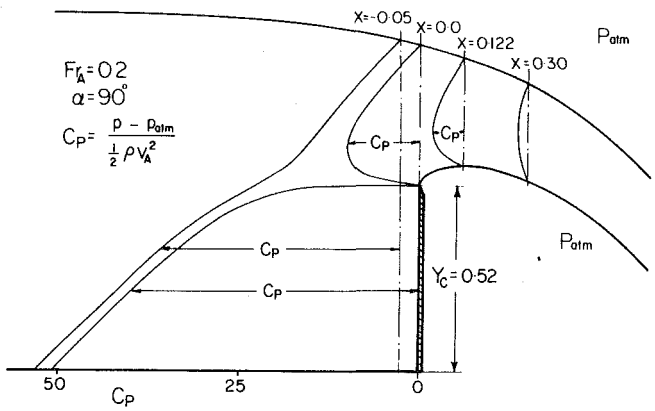

Fig. 18 Pressure distributions for a sharp-crested weir

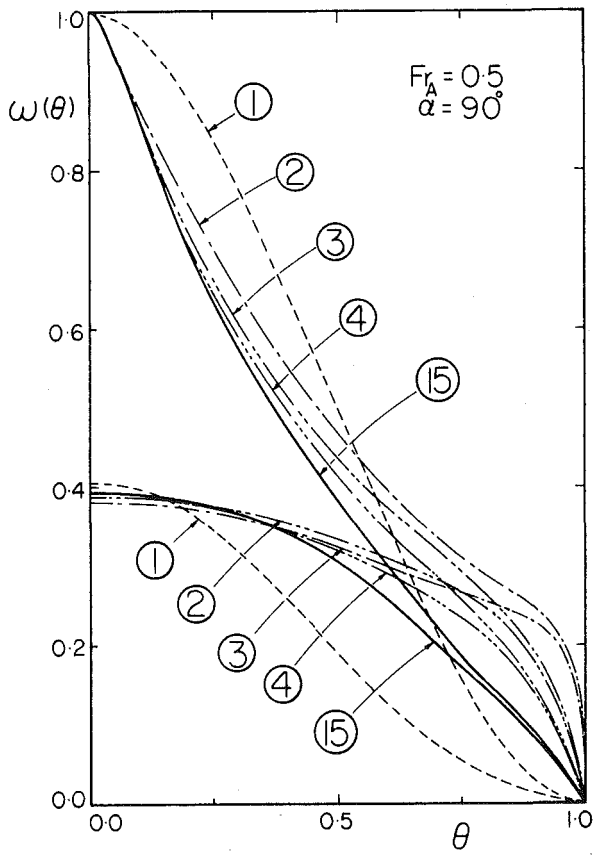

Fig. 16 $\omega_u(\theta)$ and $\omega_l(\theta)$ at various iterations

vergence of the secondary derivative may not lead to any solution to the problem, and the convergence of function itself seems to be the reasonable but nevertheless arbitrary choice. It may be anticipated that in some of these calculations, convergence of certain integrated profiles can be accepted as satisfactory. Southwell and Vaisey's results as shown in Fig. 14 are obviously based on such a criterion.

2 Calculations of the sharp-crested weirs follows essentially a similar scheme. For a given upstream flow condition, and an arbitrarily selected weir height Y_c, $v_f(\theta)$, $\omega_u(\theta)$, $\omega_l(\theta)$ were initially assumed as simple polynomial functions. The stream function within the subdivided domains may be determined from Equations (3), (24), and (32) through the SOR scheme. Once the value of the stream function is stabilized for every grid-point, the profiles of the free streamlines in the physical plane may be traced by integrating numerically the equations (4), (5), (25), (26), (33), and (34). The corresponding height of the weir may also be determined through these tracing procedures.

The new profiles of the free streamline and the weir height would yield revised forms of $v_f(\theta)$, $\omega_l(\theta)$, and $\omega_u(\theta)$ through equations (2) and (22). This process is repeated until functions $v_f(\theta)$, $\omega_l(\theta)$, and $\omega_u(\theta)$ introduced for the calculations also match with those from streamline tracing within a margin of 10^{-3} for every grid point. As shown in Figs. 15 and 16, this is clearly a rapidly convergent process. Note that variation of v_f in Fig. 15 on the vertical axis is a result of the adjustment of the weir height. Fig. 17 shows the profiles of the flow at different α values at $Fr_A = 0.2$. Fig. 18 shows the pressure distribution across the flow. Fig. 19, presents the weir height against Fr_A for the purpose of comparison.

With a relaxation factor of 1.7, and a 20 × 20 uniform grid, one typical case of the sluice gate takes 5 sec on the cyber 175 computing

system, while 12 sec are needed for the computation of a sharp-crested weir, as a result of more subdivisions of its hodograph.

Comparison of Results, Discussion

When a sluice gate is lowered into a stream of an open horizontal channel flow, the effects of its obstruction would extend to far upstream and downstream distances. The upstream free surface rises in the neighborhood of the obstruction and a stagnation point B occurs at a height Y_B above the channel bed. From the experimental results of Binnie [16], such a rise of level on the sluice gate was not observed. Instead whether the sluice gate is vertical or inclined, in front of it, a sharply defined zone of eddy was found. On the surface it appeared that flow moves in the direction opposite to the main stream indicating a rolling up motion. Downstream of the gate, the free surface should drop sharply and level off subsequently at the mathematically infinite but physically finite distance from the gate. In reality, the minimum height of the free surface is affected by the growth of the boundary layer along the bed and the entrainment of the air along the free surface. Accurate comparison of the free surface profiles with the experimental data becomes an enormous task where detailed experimental information must be obtained. Additional considerations of the viscous effect along the bed has been carried out [1] and will not be discussed here.

Southwell and Vaisey [15] obtained the solution of this problem through the relaxation calculations for the case of $Fr_A = 0.4264$. Present calculations are compared with their results in Fig. 14. The difference of free surface profiles between the two calculations is less than one percent including the estimated gate opening height. Fig. 12 presents the gate openings for various approaching values of Fr_A in comparison with the experimental data by Gibson [17] and Addison [18]. The limiting expression of the gate opening when Fr_A approaches zero, was obtained by Binnie [16]. This straight-line relationship, ($Y_D/Y_B = 1.157\, Fr_A$), is also plotted as a dotted line and is seen to hold well up to relatively large values of Fr_A. The present results agree with the experimental data over the wide range of Fr_A and is located, in general somewhat above Binnie's straight-line relationship.

A considerable amount of effort went into the study of the effect of the free surface upstream of the gate. For all the convergent results obtained, it may be observed that the influence of existence of the upstream free surface is indeed small. In that sense, a previous results [12] obtained for an enclosed channel flow with $Cp_a = 0$ should provide a crude approximate for the flow field downstream of the sluice gate.

For the sharp-crested weir, the free surface profiles for $Fr_A = 0.2$ are compared in Fig. 17 with the experimental data by Kandaswamy and Rouse [19]. Remarkably good agreement between them is observed. Similarly, good agreement between their data and calculated results for $Fr_A = 0.7$ has also been observed [1] and is not reported here. Fig. 19 shows the comparison of the weir height with the data from USBR [20] and Kandaswamy and Rouse, whose data on weir height is extracted from their presentation of the discharge coefficient. Present results generally agree very well with the experimental data over a wide range of Fr_A ($0.06 \leq Fr_A \geq 0.989$. When Fr_A is less than 0.06 computed weir-height begins to deviate from the experimental data. As a result of a relatively large contraction of the free streamline in this case, the profile of $v_u(\theta)$ in Fig. 3(b) increases so rapidly that accurate matching along the cut may not be possible. According to the experimental results of Kandaswamy and Rouse, the height of weir is decreasing rapidly near the critical initial condition and eventually the flow approaches a free overfall. Present calculations always consider the existence of a stagnation point and thus do not produce this limiting configuration as a free overfall. This was the subject of an early investigation [13]. It has been mentioned therein that a subcritical approaching flow in a free overfall is not likely to occur for steady inviscid flow. It is shown in the Appendix that its nonexistence is also supported from the numerical calculations.

On the basis of all evidence presented so far, it is obvious that the method of hodograph transformation is very effective in dealing with problems when they are strongly influenced by gravitation. Although this method invariably involves with the determination of the hodograph boundary function, such as $v_f(\theta)$ or $\theta_f(v)$, and its derivatives, through iterations, the experience obtained up to the present indicates that the secondary derivatives of these functions are always small. The only situation that a divergent trend has been observed in computations so far is the $\theta_f(v)$ associated with the free surface ahead of the sluice gate under the conditions of relatively large subcritical Fr_A values. It should be noted that since the free surface streamline must stagnate at the gate, the influence of this compression process spreads further upstream as Fr_A assumes larger values and the corresponding gate opening also increases. On the other hand, it is known that as the approaching flow reaches the critical flow condition, the only possible solution is that the gate opening should be unity, so that there is no stagnant process and the flow is uniform everywhere-the trivial solution. If the present flow pattern with the stagnant process can be extended to high subcritical Fr_A-values the steady inviscid flow would exhibit a discontinuous solution pattern at or near the critical approaching Flow. This is probably the reason why convergent solutions cannot be reached for cases of large subcritical Fr_A-values. How far one may obtain convergent solutions depends upon individual's art of smoothing out the irregular variations of the derivative functions and the criterion imposed to define a convergent solution. It is believed that the range of Fr_A may be extended to higher values than reported here, if one imposes agreement of the upstream free surface profiles between successive iterations. It is also proper to remark that no experimental data in the literature for Fr_A-values larger than 0.6 have been found.

It has been recently learned that this method is equally effective in dealing with flow geometries with curved solid boundaries.

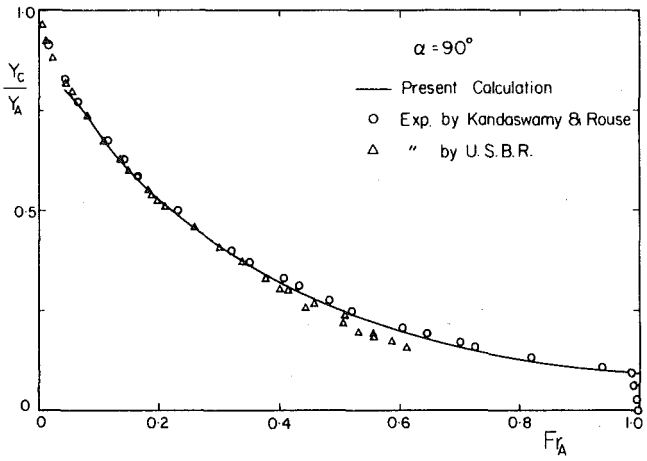

Fig. 19 Comparison of weir height with the experimental data

Acknowledgment

This work was partially supported by the U.S. Army Research Office through Research Grant No. DAAG 29-79-C-0184.

References

1 Han, T., "Applications of Hodograph Transformations to Hydrodynamic Problems Influenced by Gravitation," PhD Thesis, Department of Mechanical Engineering, University of Illinois, Urbana, Ill., Oct. 1979.

2 Marchi, E., "Sue fernomenidi efflusso piano da luci a bottente," *Ann. Mat. Pura ed Appl.*, Vol. 35, 1953, pp. 321–341.

3 Melkonian, G. I., *Izv. Akad. Nauk Armenian SSR, Ser. Phys.-Mat. Nauk*, Vol. 10, No. 3, 1957.

4 Gurevich, M. I., and Pykhteev, G. N., "Approximate Solution of the Problem of Flow of a Heavy Incompressible Fluid From Under a Sluice Gate," *PMTF (Akad. Nauk)*, Vol. 2, 1960, pp. 3–14.

5 Benjamin, T. B., "One the Flow in Channels When Rigid Obstacles Are Placed in the Stream," *Journal of Fluid Mechanics*, Vol. 1, July 1956, pp. 227–248.

6 Keller J, B., and Weitz, M. L., "A Theory of Thin Jets," *Proceedings of the 9th International Congress on Applied Mechanics*, Brussels, 1, 1957, pp. 316–323.

7 Clarke, N. S., "On Two-Dimensional Inviscid Flow in a Waterfall," *Journal of Fluid Mechanics*, Vol. 22, 1965, pp. 359–369.

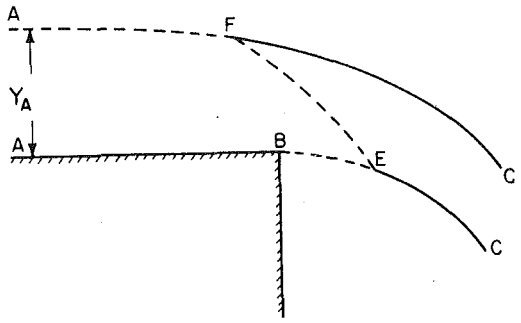

Fig. 20(*a*) The free overfall

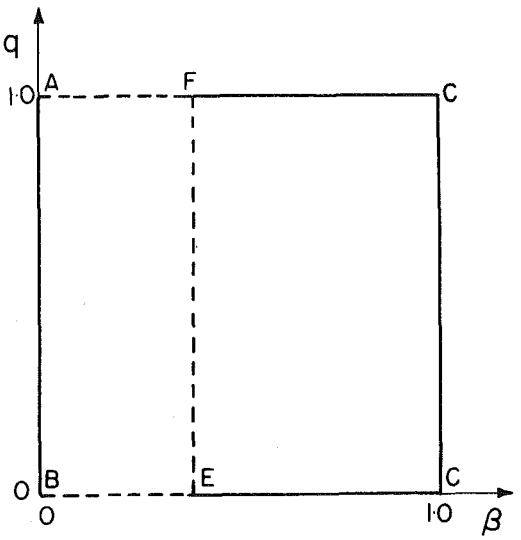

Fig. 20(*b*) The hodograph

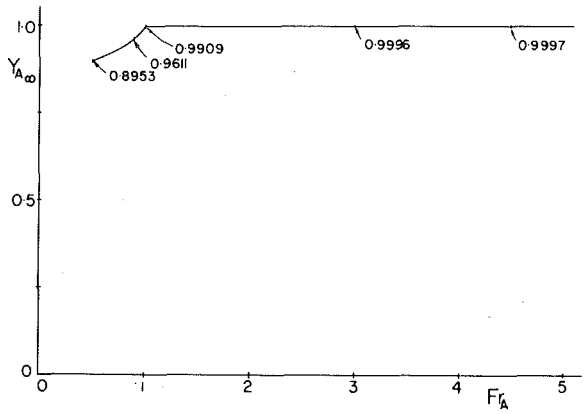

Fig. 21 Values of Y_A reflecting accuracy of calculations for free overfall

8 Keller, J. B., and Geer, J., "Flows of Thin Streams With Free Boundaries," *Journal of Fluid Mechanics*, Vol. 59, 1973, pp. 417–432.

9 McNown, J. S., Hsu, E. Y., and Yih, C. S., "Applications of the Relaxation Technique in Fluid Mechanics," *Transactions of ASCE.*, Vol. 120, 1955.

10 Ikegawa, M., and Washizu, K., "Finite-Element Method Applied to Analysis of Flow Over a Spillway Crest," *International Journal of Numerical Method in Engineering*, Vol. 6, 1973, pp. 179–189.

11 Varoglu, E., and Finn, W., "Variable Domain Finite-Element Analysis of Free Surface Gravity Flow," *Computer and Fluids*, Vol. 6, 1978, pp. 103–114.

12 Chow, W. L., Han, T., and Wu, C., "Hydrodynamic Solution for Incompressible Flow as Influenced by Gravitation," *AIAA Journal*, Vol. 16, No. 10, 1978, pp. 1097–1098.

13 Chow, W. L., and Han T., "Inviscid Solution for the Problem of Free Overfall," ASME JOURNAL OF APPLIED MECHANICS, Vol. 46, Mar. 1979, pp. 1–5.

14 Shapiro, A. H., *The Dynamics and Thermodynamics of Compressible Fluid Flow*, Vol. 1, The Ronald Press, Co., New York, 1953, pp. 338–341.

15 Southwell, R. V., and Vaisey, G., "Relaxation Methods Applied to Engineering Problems: XII, Fluid Motions Characterized by Free Streamlines," *Philosophical Transactions of the Royal Society*, London, Series A, Vol. 240, 1946, pp. 117–161.

16 Binnie, A. M., "The Flow of Water Under a Sluice Gate," *Quarterly Journal of Mechanics and Applied Mathematics*, Vol. V, Pt. 4, 1952, pp. 395–407.

17 Gibson, A. H., "Experiments on the Coefficients of Discharge Under Rectangular Sluice Gates," *Proceedings, Institution of Civil Engineering*, Vol. 207, 1920, pp. 427.

18 Addison, H., "Supplementary Notes on Flow Through Model Sluices," *Journal of the Institution of Civil Engineering*, Vol. 8, 1938, pp. 53–72.

19 Kandaswamy, P. K., and Rouse, H., "Characteristics of Flow Over Terminal Weirs and Sills," *Proceedings of the ASCE*, Hydraulics Division, N.Y., Vol. 4, 1957.

20 "Studies of Crests for Overall Dams," Bulletin 3, Part IV, Boulder Canyon Project Final Reports, Bureau of Reclamation, 1948

APPENDIX

On the Evidence of the Nonexistence of Subcritical Approaching Flow for a Free Overfall

For an inviscid flow over a free overfall as shown in Fig. 20(*a*), it was shown [13] that the corresponding hodograph can be transformed into a square as shown in Fig. 20(*b*) and the governing stream function can be determined through SOR calculations. After its value throughout the domain is stabilized ($\epsilon = 10^{-4}$), the location of the top free streamline *AFC* with respect to the lower free streamline *BEC* can be determined by performing a numerical integration of the coordinates along the path *BEF* in the hodograph plane. This integration also provides a check of the accuracy of numerical calculations of the stream function. By extending this integration back to the point *A* in the hodograph, the total change of the vertical location from *B* to *A* in the physical plane should be unity. Indeed, such a check has been carried out and the error (deviation away from unity) is shown in Fig 21. For supercritical and critical approaching flows, the errors seem to be tolerable. However, a drastic increase in error occurs as soon as the approaching flow becomes subcritical.

It is well known that for the flow with a given stagnation pressure, critical approaching flow condition yields a maximum possible rate of flow. While the gravity provides the only motivating force for the flow of a overfall, in the absence of any restriction, such as frictional force or partial obstruction, the flow would continuously adjust until a critical approaching flow is reached. Thus a steady inviscid flow of a free overfall with a subcritical approaching flow seems to be nonexistent. It is of course rewarding to see that the numerical calculations produce unacceptable errors under these conditions, and are thus compatible with the physical situation. It is nevertheless interesting to observe from the point of view of numerical calculations that the error starts to accumulate in such a fashion as soon as Fr_A becomes subcritical, especially after the stream function value has been stabilized throughout the region.

S. Krenk

Risø National Laboratory,
DK-4000, Roskilde,
Denmark

Creeping Viscous Flow Around a Heat-Generating Solid Sphere

The velocity field for creeping viscous flow around a solid sphere due to a spherically symmetric thermal field is determined and a simple thermal generalization of Stokes' formula is obtained. The velocity field due to an instantaneous heat source at the center of the sphere is obtained in closed form and an application to the storage of heat-generating nuclear waste is discussed.

1 Introduction

A solid heat-generating sphere surrounded by an infinite viscous fluid will create convective flow due to the thermal expansion and the induced buoyancy of the surrounding fluid. In addition the sphere itself may be subject to a buoyancy force due to a density difference between the sphere and the surrounding medium. A solution is presented under the assumption of creeping flow. In the limiting case of zero heat generation the well-known result of Stokes is recovered.

First, the field equations are stated and the approximations identified. Then the flow corresponding to a step function variation of the density is derived, and the resulting force on the sphere evaluated. This solution is integrated to yield the flow due to a continuous temperature distribution, and the flow induced by the temperature field from an instantaneous point heat source is considered in some detail.

One of the main results is the equilibrium velocity of the sphere. This velocity is of interest in connection with storage of nuclear waste in salt, and its magnitude and time-dependence are evaluated for a specific set of parameters.

2 The Field Equations

When only small changes from the reference density ρ_0 at temperature T_0 occur, the density is

$$\rho \simeq [1 - \alpha(T - T_0)]\rho_0 \tag{1}$$

where α is the volumetric expansion coefficient.

The assumption of creeping flow (inertial terms neglected) can now be used in connection with the Boussinesq approximation (fluid-density changes ignored except in the buoyancy term) to obtain the continuity equation

$$\partial v_i/\partial x_i = 0 \tag{2}$$

and the equation of motion

$$\mu \frac{\partial^2 v_i}{\partial x_j \partial x_j} - \frac{\partial p}{\partial x_i} - \alpha(T - T_0)\rho_0 g_i = 0 \tag{3}$$

where v_i is the velocity vector, μ the dynamic viscosity, p the pressure, and g_i the acceleration of gravity.

In the present case of spherically symmetric geometry, where the equations have been linearized through the assumption of creeping flow, the Boussinesq approximation amounts to neglecting the radial flow induced by thermal expansion. Due to the spherical symmetry of this flow it does not contribute to the resulting force on the sphere, and it will therefore not be discussed further here.

3 Flow for Step Variation of the Density

The problem under consideration has been reduced to finding a solution to (2) and (3) in the infinite domain outside a sphere of radius a_0 corresponding to a spherically symmetric temperature field generated by heat sources inside the sphere. The general solution is found as an integral of a particular solution corresponding to a temperature discontinuity ΔT at a spherical surface of radius a, Fig. 1.

Let a Cartesian coordinate system $\{x_i\}$, $i = 1, 2, 3$, be fixed at the center of the solid sphere with radius a_0 and the x_1-axis pointing downwards, whereby $g_i = (g, 0, 0)$. The field equations to be solved are the continuity equation (2),

$$\mu \frac{\partial^2 v_i}{\partial x_j \partial x_j} - \frac{\partial p}{\partial x_i} - \alpha\rho_0 \Delta T g_i = 0, \quad a_0 < r < a \tag{4}$$

and

$$\mu \frac{\partial^2 v_i}{\partial x_j \partial x_j} - \frac{\partial p}{\partial x_i} = 0, \quad a < r \tag{5}$$

where $r^2 = x_i x_i$.

The boundary conditions are no slipping at $r = a_0$,

$$v_i(a_0) \equiv 0, \qquad i = 1, 2, 3 \tag{6}$$

and v_i approaching a constant velocity $(U, 0, 0)$ at infinity,

Contributed by the Applied Mechanics Division for publication in the JOURNAL OF APPLIED MECHANICS.

Discussion on this paper should be addressed to the Editorial Department, ASME, United Engineering Center, 345 East 47th Street, New York, N. Y. 10017, and will be accepted until September 1, 1981. Readers who need more time to prepare a Discussion should request an extension from the Editorial Department. Manuscript received by ASME Applied Mechanics Division, June, 1980; final revision, October, 1980.

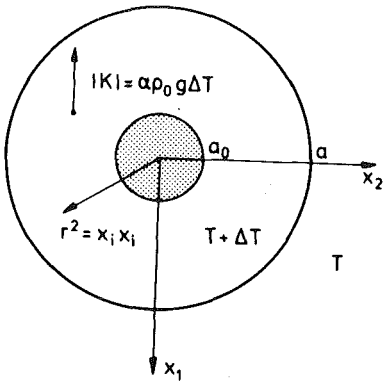

Fig. 1 Solid sphere and discontinuity surface

$$v_i \to \delta_{1i} U, \qquad r \to \infty \tag{7}$$

A positive value of U implies that the solid sphere moves upward relative to the material at infinity. At $r = a$, continuity conditions are imposed on the velocity and the stress vector,

$$v_i(a+) = v_i(a-) \tag{8}$$

$$\sigma_{ij}(a+)x_j = \sigma_{ij}(a-)x_j \tag{9}$$

It is noted that (8) does not restrict exchange of material between the two domains of different temperature. This exchange does not change the temperature field, because the convective terms have been assumed small in the *final solution.*

The solution is easily constructed by use of particular solutions given by Lamb, [1, Section 337], for domains inside and outside a spherical boundary. For $a_0 < r < a$, contributions from both types of solution must be represented.

$$v_i(x_j) = \left(\frac{A'r^5}{30\mu} - \frac{Ar^2}{6\mu} + B\right)\frac{\partial}{\partial x_i}\left(\frac{x_1}{r^3}\right) + \delta_{1i}\left(\frac{A'r^2}{6\mu} + B' + \frac{2A}{3\mu r}\right), \quad a_0 < r < a \tag{10}$$

The radial flow takes the simple form

$$v^r(x_j) = \left(\frac{A'r^2}{10\mu} + B' + \frac{A}{\mu r} - \frac{2B}{r^3}\right)\left(\frac{x_1}{r}\right), \quad a_0 < r < a \tag{11}$$

and the stress vector on a spherical surface is

$$\sigma_i^r(x_j) = -p_0'\left(\frac{x_i}{r}\right) + \left[\left(\frac{3A'}{10} - \frac{K}{3}\right)r^4 + Ar - \frac{6\mu B}{r}\right]\frac{\partial}{\partial x_i}\left(\frac{x_1}{r^3}\right) + \delta_{1i}\left(\frac{Kr}{3} - \frac{A}{r^2}\right), \quad a_0 < r < a \tag{12}$$

Here K has been introduced as

$$K = \alpha\rho_0 g\Delta T \tag{13}$$

Outside the discontinuity the solution is of the form

$$v_i(x_j) = -\left(\frac{Cr^2}{6\mu} - D\right)\frac{\partial}{\partial x_i}\left(\frac{x_1}{r^3}\right) + \delta_{1i}\left(U + \frac{2C}{3\mu r}\right), \quad a < r \tag{14}$$

The radial flow is

$$v^r(x_j) = \left(U + \frac{C}{\mu r} - \frac{2D}{r^3}\right)\left(\frac{x_1}{r}\right), \quad a < r \tag{15}$$

and the stress vector on a spherical surface

$$\sigma_i^r(x_j) = -p_0\left(\frac{x_i}{r}\right) + \left(Cr - \frac{6\mu D}{r}\right)\frac{\partial}{\partial x_i}\left(\frac{x_1}{r^3}\right) - \delta_{1i}\frac{C}{r^2}, \quad a < r \tag{16}$$

The conditions (6)–(9) can all be satisfied leading to

$$A' = \frac{2}{3}K \tag{17}$$

$$B' = U - \frac{Ka^2}{3\mu} \tag{18}$$

$$A = -\frac{3}{2}U\mu a_0 + \frac{1}{6}Ka_0(3a^2 - a_0^2) \tag{19}$$

$$B = -\frac{1}{4}Ua_0^3 + \frac{Ka_0^3}{60\mu}(5a^2 - 3a_0^2) \tag{20}$$

$$C = -\frac{3}{2}U\mu a_0 - \frac{1}{6}(2a^3 - 3a_0a^2 + a_0^3) \tag{21}$$

$$D = -\frac{1}{4}Ua_0^3 - \frac{K}{60\mu}(2a^5 - 5a_0^3a^2 + 3a_0^5) \tag{22}$$

$$p_0' = p_0 \tag{23}$$

The resulting force on the solid sphere $r < a_0$ is found by integrating (12) over the surface $r = a_0$. Due to symmetry it is clear that only the x_1 component will be different from zero. Only the factor to δ_{1i} contributes.

$$P = 6\pi\mu a_0 U - 2\pi K a_0(a^2 - a_0^2) \tag{24}$$

If U is considered as the equilibrium velocity, the result may be written in the form

$$U = \frac{1}{6\pi\mu a_0}[P + 2\pi\alpha\rho_0 g\Delta T a_0(a^2 - a_0^2)] \tag{25}$$

where P is the buoyancy of the solid sphere. For $\Delta T = 0$ or $a = a_0$ Stokes' result is recovered.

4 Continuous Temperature Fields

The equilibrium velocity U due to a continuous temperature distribution follows from (25) by integration.

$$U = \frac{1}{6\pi\mu a_0}\left[P - 2\pi\alpha\rho_0 g a_0 \int_{a_0}^{\infty}(a^2 - a_0^2)\frac{dT(a)}{da}da\right] \tag{26}$$

After integration by parts the result is

$$U = \frac{1}{6\pi\mu a_0}\left[P + 2\pi\alpha\rho_0 g a_0 \int_{a_0}^{\infty} aT(a)da\right] \tag{27}$$

The influence of the temperature field is an increased buoyancy proportional with the first moment of the temperature. Thus a finite equilibrium velocity requires $T(a)a^2 \to 0$ for $a \to \infty$ and thereby excludes consideration of the steady-state temperature field.

It is convenient to represent the heat flux from the sphere by superposition of the fluxes from a continuous distribution of instantaneous point heat sources at $r = 0$ in an infinite medium with homogeneous thermal properties. The instantaneous release of the amount of heat q at the time $t = 0$ at $r = 0$ leads to the temperature field, [2, p. 256],

$$T(a, t) = \frac{q}{\rho_0 c}(2\pi\kappa t)^{-3/2}e^{-a^2/4\kappa t} \tag{28}$$

where $\kappa = k/\rho_0 c$, c is the specific heat and k is the thermal conductivity. Substitution of (28) in (27) yields the equilibrium velocity

$$U(t) = \frac{1}{6\pi\mu a_0}\left[P + \frac{\alpha q g}{c}\frac{a_0}{\sqrt{\pi\kappa t}}e^{-a_0^2/4\kappa t}\right] \tag{29}$$

It is interesting to compare the time development of the heat generated velocity, U, with the temperature, T, and heat flux, h, at $r = a_0$. In terms of the dimensionless time

$$\tau = \frac{4\kappa t}{a_0^2} \tag{30}$$

the expressions are

$$U(\tau) = \frac{1}{3\pi^{3/2}}\frac{\alpha q g}{c\mu a_0}\tau^{-1/2}e^{-1/\tau} \tag{31}$$

$$T(a_0, \tau) = \frac{1}{\pi^{3/2}}\frac{q}{\rho_0 c a_0^3}\tau^{-3/2}e^{-1/\tau} \tag{32}$$

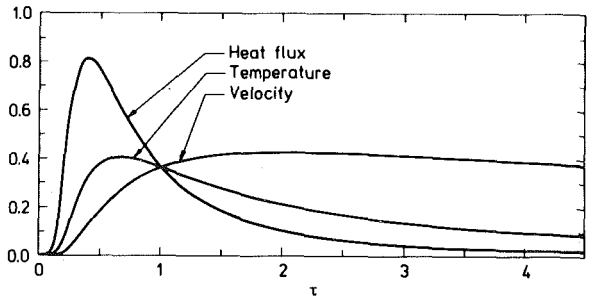

Fig. 2 Time-dependence of heat flux and temperature at $r = a_0$ and thermally induced velocity

$$h(a_0, \tau) = \frac{2}{\pi^{3/2}} \frac{qk}{\rho_0 c a_0^4} \tau^{-5/2} e^{-1/\tau} \tag{33}$$

The time-dependent factors are shown in Fig. 2. It is seen that the release of heat from the domain $r \leq a_0$ is concentrated within the time interval $0 \leq \tau \lesssim 1.5$, while the heat generated velocity prevails for a much longer time. When calculating the velocity it may therefore be an acceptable approximation to represent the heat generation inside the solid sphere by a point source.

The flow field due to a continuous temperature field is found by integration of the step function solution from Section 3. It is convenient to separate the part of the flow which is proportional to U. This part of the solution is proportional to Stokes' solution but with the velocity U given by (27).

In terms of the dimensionless coordinates $\xi_i = x_i/a_0$ and $\eta = r/a_0$ this part of the solution is

$$v_i^U(\xi_j) = U\left\{\frac{1}{4}(\eta^2 - 1)\frac{\partial}{\partial \xi_i}\left(\frac{\xi_1}{\eta^3}\right) + \delta_{1i}\frac{\eta - 1}{\eta}\right\} \tag{34}$$

The remaining part of the flow field is found by integrating (17)–(20) from r to infinity and (21), (22) from a_0 to r. The result is

$$v_i^T(x_j) = \frac{\alpha \rho_0 g}{\mu}\left\{\frac{1}{6}\left[-(r^2 - a_0^2)a_0 \int_{a_0}^{\infty} aT(a)da + \int_{a_0}^{r}(r^2a^2 - a^4)T(a)da\right]\frac{\partial}{\partial x_i}\left(\frac{x_1}{r^3}\right) + \delta_{1i}\frac{2}{3}\left[\frac{a_0}{r}\int_{a_0}^{\infty} aT(a)da - \int_r^{\infty} aT(a)da - \frac{1}{r}\int_{a_0}^{r} a^2 T(a)da\right]\right\} \tag{35}$$

When the temperature field (28) is used in (35) the result can be expressed in terms of elementary functions and the error function, erf ( ).

$$v_i^T(\xi_j) = \frac{1}{(2\pi)^{3/2}}\frac{\alpha q g}{c\mu a_0}\left\{\left[-\tau^{1/2}e^{-1/\tau} + \eta\tau^{1/2}e^{-\eta^2/\tau} + \pi^{1/2}\left(\frac{1}{3}\eta^2 - \frac{1}{2}\tau\right)(\operatorname{erf}(\eta\tau^{-1/2}) - \operatorname{erf}(\tau^{-1/2}))\right]\frac{\partial}{\partial \xi_i}\left(\frac{\xi_1}{\eta^3}\right) - \delta_{1i}\frac{4}{3}\frac{\pi^{1/2}}{\eta}(\operatorname{erf}(\eta\tau^{-1/2}) - \operatorname{erf}(\tau^{-1/2}))\right\} \tag{36}$$

The radial velocity from (34) and (36) is proportional with $\cos\theta = \xi_1/\eta$ but is otherwise only a function of η and τ. It is therefore a simple matter to determine the stream function $\psi(\xi_i, \tau)$, which is $-(2\pi)^{-1}$ times the flux through the spherical cap $\eta = (\xi_i\xi_i)^{1/2}$, $0 < \theta < \arccos(\xi_1/\eta)$. The result follows immediately from (36) by replacing the factor $\cos\theta$ with

$$-r^2 \int_0^{\arccos(\xi_1/\eta)} \cos\theta \sin\theta \, d\theta = -\tfrac{1}{2} r^2 \sin^2\theta \tag{37}$$

in the radial velocity.

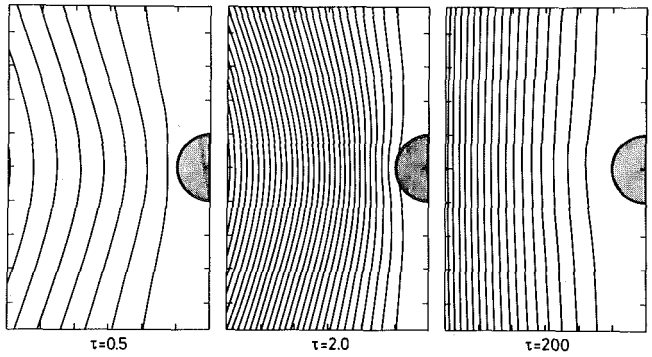

Fig. 3 Streamlines for instantaneous point heat source

Table 1 Sample parameters

Density	$\rho_0 = 2150$ kg/m^3
Thermal expansion	$\alpha = 1.2{\cdot}10^{-4}$/K
Specific heat	$c = 900$ J/kgK
Thermal conductivity	$k = 4.5$ W/mK
Viscosity	$\mu = 5.0{\cdot}10^{14}$ Ns/m^2
Canister density	$\rho_c = 4100$ kg/m^3
Radius	$a_0 = 0.665$ m
Heat-generation rate	$q_0 = 3.5$ kW

$$\psi(\xi_i, \tau) = -\left\{U(\tau)\frac{2\eta^3 - 3\eta^2 + 1}{2\eta} + \frac{1}{\pi}\frac{\alpha q g}{c\mu a_0}\left[\frac{1}{\eta}\sqrt{\frac{\tau}{2\pi}}(e^{-1/\tau} - \eta e^{-\eta^2/\tau}) - \frac{\eta^2 - \frac{1}{2}\tau}{\sqrt{2}\eta}(\operatorname{erf}(\eta\tau^{-1/2}) - \operatorname{erf}(\tau^{-1/2}))\right]\right\}\frac{a_0^2}{2}\sin^2\theta \tag{38}$$

The stream function corresponding to a situation with the sphere moving with velocity $-U(\tau)$ and the medium at rest at infinity follows from (38) by addition of the stream function

$$\psi(\xi_i, \tau) = \tfrac{1}{2} U(\tau) a_0^2 \eta^2 \sin^2\theta \tag{39}$$

Fig. 3 shows the normalized stream function for $\tau = 0.5, 2.0, 200$. The figure clearly shows the concentration of the velocity field around the sphere, while the velocity of the sphere is increasing, i.e., $\tau < 2.0$.

5 Nuclear Waste Example

As an example the formula (27) is used to evaluate the velocity of a heat-generating nuclear waste canister deposited in rock salt. This problem has been treated by Dawson and Tillerson [3] using finite-element calculations in a finite geometry. A set of typical parameters is given in Table 1.

The heat generation is assumed to be of the form

$$q(\tau) = q_0 \exp\left(-\ln 2 \frac{t}{T_{1/2}}\right) = q_0 \exp\left(-\ln 2 \frac{\tau}{\tau_{1/2}}\right) \tag{40}$$

where

$$\tau_{1/2} = \frac{4\kappa T_{1/2}}{a_0^2} = 1.99 \cdot 10^4 \tag{41}$$

corresponds to a half-life $T_{1/2} = 30$ years for the parameters of Table 1. In view of this large time scale the approximation with a point source is quite adequate for the evaluation of the equilibrium velocity, and the result follows by integration of (29).

$$U(\tau) = \frac{2}{9}\frac{a_0^2 g}{\mu}(\rho_0 - \rho_c) + \frac{\alpha q_0 \rho_0 g a_0}{12\pi^{3/2}\mu k}\int_0^{\tau} s^{-1/2} e^{-1/s} \exp\left(-\frac{\tau - s}{\tau_{1/2}}\ln 2\right) ds \tag{42}$$

Numerical evaluation is facilitated by using the fact that due to the large value of $\tau_{1/2}$ the interval of integration may be divided into two parts, an interval $0 < s < \tau_*$ where the last factor is nearly constant, and the remaining interval $\tau_* < s < \tau$ where $e^{-1/s} \simeq 1$. The first integral can then be evaluated in closed form by use of formula 3.461-5 from [4], and the second is simplified.

$$I \simeq \exp\left(-\frac{\tau}{\tau_{1/2}} \ln 2\right)\left[\int_0^{\tau_*} s^{-1/2} e^{-1/s} ds + \int_{\tau_*}^{\tau} s^{-1/2} \exp\left(\frac{s}{\tau_{1/2}} \ln 2\right) ds\right]$$

$$= 2 \exp\left(-\frac{\tau}{\tau_{1/2}} \ln 2\right)\left[\sqrt{\tau_*}\, e^{-1/\tau_*} - \sqrt{\pi}\, \mathrm{erfc}\left(\frac{1}{\sqrt{\tau_*}}\right) + \int_{\sqrt{\tau_*}}^{\sqrt{\tau}} \exp\left(\frac{p^2}{\tau_{1/2}} \ln 2\right) dp\right] \quad (43)$$

The integral including the factor $(12\pi^{3/2})^{-1}$ is shown in Fig. 4 for $\tau_{1/2}$ given by (41) and $\tau_* = 100$. For these parameters the relative error involved in the approximation (43) is less than 0.005.

Fig. 4 shows both the thermal and the buoyancy contribution in the unit pm/s (10^{-12} m/s) and the time scale in years. The actual velocity is the difference between the two full curves. After a few years the thermally induced upward velocity will dominate for about 185 years. The maximum upward velocity is 3.36 pm/s = 0.106 m/1000 years. Although this velocity may be somewhat overestimated due to the infinite geometry, it is well below the steady-state velocity 26.5 pm/s obtained by Dawson and Tillerson [3] using finite elements.

The sensitivity of the velocity to the time scale of the heat generation is illustrated by the two dashed curves corresponding to $T_{1/2}$ = 40 years and the heat generation either with the same initial rate of production (the upper curve) or the same total production (the lower curve).

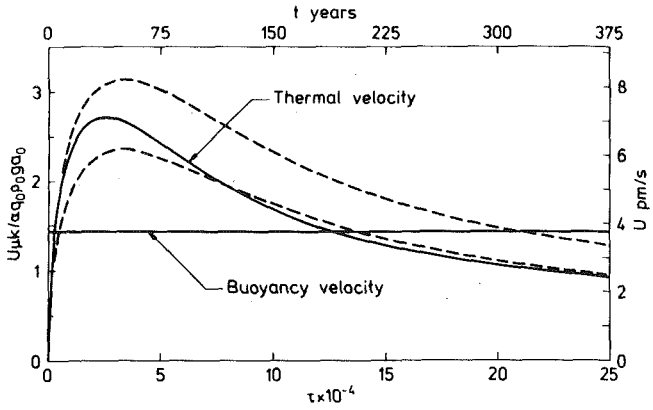

Fig. 4 Thermal and buoyancy velocities for nuclear waste canister

Acknowledgment

The author is grateful to Dr. Henrik Schmidt for providing the computer plots of the streamlines.

References

1 Lamb, H., *Hydrodynamics*, Dover, New York, 1932.

2 Carslaw, H. S., and Jaeger, J. C., *Conduction of Heat in Solids*, Clarendon Press, Oxford, 1959.

3 Dawson, P. R., and Tillerson, J. R., "Nuclear Waste Canister Thermally Induced Motion," Report Sand-78-0566, Sandia Laboratories, June 1978.

4 Gradshteyn, I. S., and Ryzhik, I. M., *Table of Integrals, Series, and Products*, Academic Press, New York, 1965.

V. K. Garg
Professor.
Mem. ASME

S. C. Gupta[1]
Senior Research Assistant.

Department of Mechanical Engineering,
Indian Institute of Technology
Kanpur, P.O. IIT Kanpur 208016, India

Stability of Developing Flow in a Pipe—Nonparallel Effects

A theoretical investigation into the linear, spatial instability of the developing flow in a rigid circular pipe, incorporating the effects of nonparallelism of the main flow, has been made at several axial locations. The velocity profile in the developing flow region is obtained by a finite-difference method assuming uniform flow at the entry to the pipe. For the stability analysis, the continuity and momentum equations have been integrated separately using fourth-order Runge-Kutta integration scheme and applying selectively the Gram-Schmidt orthonormalization procedure to circumvent the parasitic error-growth problem. It is found that the critical frequency, obtained from different growth rates, decreases first sharply and then gradually with increasing $\overline{X}$, *where* $\overline{X} = x/aR = X/R$; *x being the streamwise distance measured from the pipe inlet, a being the radius of the pipe, and R the Reynolds number based on a and average velocity of flow. However, the critical Reynolds number versus* $\overline{X}$ *curves pass through a minima. The minimum critical Reynolds number corresponding to* $g_\psi(\overline{X}, O)$, *the growth rate of stream function at the pipe axis, to* $g_E(\overline{X})$, *the growth rate of energy density, and to the parallel flow theory are 9700 at* $\overline{X} = 0.00325$, *11,000 at* $\overline{X} = 0.0035$, *and 11,700 at* $\overline{X} = 0.0035$, *respectively. It is found that the actual developing flow remains unstable over a larger inlet length of the pipe than its parallel-flow approximate. The first instability of the flow on the basis of* $g_\psi(\overline{X}, O)$, $g_E(\overline{X})$ *and the parallel flow theory, is found to occur in the range* $30 \leq X \leq 36$, $35 \leq X \leq 43$, *and* $36 \leq X \leq 45$, *respectively. The critical Reynolds numbers obtained on the basis of* $g_\psi(\overline{X}, O)$ *are closest to the experimental values.*

Introduction

It is well known that the fully developed flow in a rigid circular pipe is theoretically found to be stable to all infinitesimal disturbances [1–3], and the experimentally observed instability of the Hagen-Poiseuille flow is attributed either to the finite amplitude of the disturbances [4] or to the instability of the boundary layer inside the pipe in the developing flow region [5, 6]. While Tatsumi [5] and Huang and Chen [6] considered the temporal stability of the developing flow in a pipe, Gupta and Garg [7] have recently compared the spatial stability results for velocity profiles obtained from the methods of Hornbeck [8] and Sparrow, et al. [9], and have found that stability results for the velocity profile obtained from the Hornbeck method, hereafter referred to as the Hornbeck profile, are closer to the experimental results of Sarpkaya [10]. However, the critical Reynolds numbers for the Hornbeck profile, though much smaller than those for the Sparrow, et al., profile, are higher than the corresponding values obtained experimentally at all axial locations. This difference may be attributed to the fact that Gupta and Garg [7] assumed the flow to be parallel which is really not true in the developing flow region.

It may be noted that while Sparrow, et al., linearized the inertia terms in the Navier-Stokes equations for the developing flow in a pipe, Hornbeck carried out a finite-difference solution of the boundary-layer equations for the developing flow. Besides yielding a more accurate velocity distribution [11, 12], the latter is also at least one order of magnitude faster (computationally) than the former.

For the developing flow in a pipe, Shen, et al. [13], did consider the effect of the radial component of velocity on the otherwise parallel-flow temporal stability analysis of the Sparrow, et al., profile and found that the minimum critical Reynolds number dropped to 19,670 from the value of 19,900 for the parallel-flow theory. In comparison to this, Gupta and Garg found a minimum critical Reynolds number of 11,700 for the Hornbeck profile. Since Shen, et al., did not consider all nonparallel effects, e.g., the effects of streamwise variation of the wave number, eigenfunction, and growth rate, it is not surprising that they found only small differences from the parallel-flow stability characteristics. The flow in the developing region is essentially one of boundary-layer type, and we know that for the boundary-layer flow

[1] Presently, Reader, Department of Mechanical Engineering, University of Jodhpur, Jodhpur, India.

Contributed by the Applied Mechanics Division of THE AMERICAN SOCIETY OF MECHANICAL ENGINEERS, and presented at the 1981 Joint ASME/ASCE Applied Mechanics, Fluids Engineering, and Bioengineering Conference, University of Colorado, Boulder, Colo., June 22–27, 1981.

Discussion on this paper should be addressed to the Editorial Department, ASME, United Engineering Center, 345 East 47th Street, New York, N. Y. 10017, and will be accepted until September 1, 1981. Readers who need more time to prepare a Discussion should request an extension from the Editorial Department. Manuscript received by ASME Applied Mechanics Division, March, 1980; final revision, August, 1980. Paper No. 81-APM-13.

over a flat plate, the parallel-flow theory predicts a critical Reynolds number that is about 30 percent larger than the experimentally measured value [14, 15]. Shen [16] has shown, theoretically, that the effect of nonparallelism of the flow is, in general, to widen the unstable region and to reduce the critical Reynolds number. Therefore, we investigate here the stability of the developing flow in a rigid circular pipe while retaining its true nonparallel character. The analysis follows that of Saric and Nayfeh [17] but some details are given since cylindrical geometry is involved here.

Analysis

We consider the flow of an incompressible, viscous fluid in the inlet region of a rigid, circular pipe of radius a and define the following nondimensional variables:

$$Y = \frac{y}{a},\ T = \frac{tu_a}{a},$$
$$U = \frac{\tilde{u}}{u_a},\ V = \frac{\tilde{v}}{u_a},\ P = \frac{\tilde{p}}{\rho u_a^2},\ R = \frac{u_a a}{\nu}, \tag{1}$$

where y is the radial distance measured from the axis of the pipe, $\tilde{u}$ and $\tilde{v}$ are the streamwise and radial components of velocity at any point (x, y) in the flow field and at any time t, u_a is the average velocity of the flow, $\tilde{p}$ is the pressure at any section x, and ρ and ν are, respectively, the density and kinematic viscosity of the fluid. Spielberg and Timan [18] have shown that Squire's theorem [19] is not applicable in the case of axisymmetric flows. However, the following analysis is carried out for an axisymmetric disturbance since the results of Huang and Chen [6] show that very near the entry section (up to $\overline{X} \simeq 0.0038$) the developing flow is more unstable to axisymmetric disturbances. This happens because the main flow in this region is of the boundary-layer type for which Squire's theorem does hold. Therefore, an axisymmetric, infinitesimally small disturbance with nondimensional velocity components $u(X, Y, T)$ and $v(X, Y, T)$ and dimensionless pressure $p(X, Y, T)$ is superimposed on the main flow. Substituting for the resultant flow in the Navier-Stokes equations, using continuity and momentum equations for the main flow and neglecting the nonlinear terms in u and v, we get the following single equation:

$$\frac{\partial \eta}{\partial T} + U\frac{\partial \eta}{\partial X} + V\frac{\partial \eta}{\partial Y} + u\frac{\partial H}{\partial X} + v\frac{\partial H}{\partial Y} = \frac{1}{R}\left[\frac{\partial^2 \eta}{\partial Y^2} + \frac{3}{Y}\frac{\partial \eta}{\partial Y} + \frac{\partial^2 \eta}{\partial X^2}\right], \tag{2}$$

where

$$\eta = \frac{1}{Y}\left(\frac{\partial u}{\partial Y} - \frac{\partial v}{\partial X}\right) \quad \text{and} \quad H = \frac{1}{Y}\left(\frac{\partial U}{\partial Y} - \frac{\partial V}{\partial X}\right).$$

It is well known that for the developing flow in a pipe $U(X, Y)$ and $V(X, Y)$ are slowly varying functions of X. To express this slow variation we introduce another independent variable X_1 along X-direction such that

$$X_1 = \epsilon X, \tag{3}$$

where ϵ is a small dimensionless parameter which characterizes the nonparallelism of the flow; its value depends upon the geometry and Reynolds number of the flow. For truly parallel flow ϵ is zero. The dependence of ϵ on the Reynolds number for any given geometry of the flow may be obtained from the order of terms expressing the boundary-layer effect on the velocity field [17, 20]. From the series expression for the velocity at the center line of the pipe [21], we note that $\epsilon = R^{-1/2}$. The other reason in support of this choice is that in the initial entry length, where the effect of nonparallelism of the flow is most expected, the flow is more or less of the bounday-layer type and for boundary-layer flow, $\epsilon = R^{-1/2}$ [17, 22]. Though ϵ and R are related, we may treat them as independent in the expansions that follow. By doing this we are, in fact, solving the problem on ϵ-R plane instead of on a single curve and thus the real solution is contained in the family of fictitious extensions over all ϵ and R.

The disturbance stream function can be taken as

$$\psi(X_1, Y, T) = [\phi_0(X_1, Y) + \epsilon\phi_1(X_1, Y) + \ldots]e^{i\theta}, \tag{4}$$

where

$$\frac{\partial \theta}{\partial X} = k_0(X_1), \quad \frac{\partial \theta}{\partial T} = -\omega,$$

with ω real. Here ω is the dimensionless frequency of the disturbance, the real part of k_0 is the wave number and its imaginary part is the spatial growth rate. Substituting equation (4) into equation (2), and equating coefficients of like powers of ϵ we obtain

Order ϵ^0:

$$L(\phi_0) \equiv \left[D^4 - 2k_0^2 D^2 + k_0^4 - \frac{2}{Y}D^3 + \frac{3}{Y^2}D^2 + \left(\frac{2k_0^2}{Y} - \frac{3}{Y^3}\right)D - iR\left\{(k_0 U - \omega)\left(D^2 - k_0^2 - \frac{D}{Y}\right) - k_0 Y D(DU/Y)\right\}\right]\phi_0 = 0, \tag{5}$$

with the boundary conditions [6]

$$\phi_0 = D\phi_0 = 0 \quad \text{at} \quad Y = 0 \quad \text{and} \quad Y = 1.$$

Order ϵ:

$$L(\phi_1) = R\left[B_1\frac{\partial \phi_0}{\partial X_1} + B_2\frac{\partial}{\partial X_1}\left(D^2\phi_0 - \frac{1}{Y}D\phi_0\right) + \left(B_3\phi_0 - \frac{B_4}{Y}D\phi_0 + B_4 D^2\phi_0\right)\frac{dk_0}{dX_1} + B_5\phi_0 + B_6 D\phi_0 + B_7 D^2\phi_0 + VD^3\phi_0\right], \tag{6}$$

with the boundary conditions

$$\phi_1 = D\phi_1 = 0 \quad \text{at} \quad Y = 0 \quad \text{and} \quad Y = 1,$$

where

$$\left.\begin{aligned} B_1 &= 2k_0\omega - 3k_0^2 U - D^2 U + \frac{DU}{Y} + \frac{4ik_0^3}{R}, \\ B_2 &= U - \frac{4ik_0}{R}, \\ B_3 &= \omega - 3Uk_0 + 6ik_0^2/R, \\ B_4 &= -2i/R, \\ B_5 &= \frac{2}{Y}k_0^2 V, \\ B_6 &= -D^2 V - \frac{1}{Y}DV - k_0^2 V + \frac{4V}{Y^2}, \\ B_7 &= -\frac{3}{Y}V, \quad \text{and} \quad D \equiv \partial/\partial Y. \end{aligned}\right\} \tag{7}$$

The eigenvalue problem defined by (5) is the familiar Orr-Sommerfeld problem for the parallel flow. In equation (6), which gives first-order corrections over the parallel flow theory, we note that the first two terms on the right-hand side represent the effects of the axial variation of the amplitude of the stream function for the disturbance, the third accounts for the axial variation of the wave number and of the spatial growth rate, and the remaining four terms represent the effects of the radial velocity component of the main flow; the last being the only effect considered by Shen, et al. [13].

For given values of ω, R, and $U(X_1, Y)$, the solution of the eigenvalue problem (5) may be expressed as

$$\phi_0(X_1, Y) = A(X_1)\beta(Y; X_1), \tag{8}$$

where β is the eigenfunction, and the amplitude function $A(X_1)$ is given by

$$\frac{dA}{dX_1} = ik_1(X_1)A,$$

where

$ik_1 = b_2(X_1)/b_1(X_1)$,

$$b_1(X_1) = -\int_0^1 \left[B_1\beta + B_2\left(D^2\beta - \frac{1}{Y}D\beta\right)\right]\beta^* dY,$$

$$b_2(X_1) = \int_0^1 \left[\left(B_1 - \frac{B_2}{Y^2} + D^2U + \frac{1}{Y}DU\right)\beta^* + \left(2DU + \frac{B_2}{Y}\right)D\beta^* + B_2D^2\beta^*\right]\frac{\partial\beta}{\partial X_1}dy + \int_0^1 \left[\left\{B_3\beta + B_4\left(D^2\beta - \frac{1}{Y}D\beta\right)\right\}\frac{dk_0}{dX_1} + B_5\beta + B_6D\beta + B_7D^2\beta + VD^3\beta\right]\beta^* dY, \quad (9)$$

where $\beta^*(Y; X_1)$ is the adjoint eigenfunction corresponding to the eigenvalue k_0. The solution of equation (9) is

$$A(X_1) = A_0 \exp\left[i\int k_1(X_1)dX_1\right], \quad (10)$$

where A_0 is an arbitrary constant of integration.

Equations for evaluation of $\partial\beta/\partial X_1$, and dk_0/dX_1 (required for finding $b_2(X_1)$) are

$$L\left(\frac{\partial\beta}{\partial X_1}\right) = A_1 + A_2\,(dk_0/dX_1), \quad (11a)$$

with the boundary conditions

$$\frac{\partial\beta}{\partial X_1} = D\left(\frac{\partial\beta}{\partial X_1}\right) = 0 \quad \text{at} \quad Y = 0, 1, \quad (11b)$$

where

$$A_1 = iRk_0\left[\left(D^3V - \frac{3DV}{Y^2} + \frac{3V}{Y^3} + k_0^2DV\right)\beta - \left(D^2\beta - \frac{1}{Y}D\beta\right)\left(DV + \frac{V}{Y}\right)\right],$$

$$A_2 = 4k_0\left(D^2\beta - k_0^2\beta - \frac{1}{Y}D\beta\right) + iR\left[U\left(D^2\beta - \frac{1}{Y}D\beta\right) + \beta\left(2k_0\omega - 3Uk_0^2 - D^2U + \frac{1}{Y}DU\right)\right], \quad (11c)$$

and

$$\frac{dk_0}{dX_1} = -\int_0^1 A_1\beta^* dY \Big/ \int_0^1 A_2\beta^* dY. \quad (12)$$

Knowing dk_0/dX_1 from (12), $\partial\beta/\partial X_1$ can be evaluated from the integration of equation (11).

We note from this analysis that the effects of nonparallelism of the flow are to make the eigenvalue k_0 a function of X_1, to produce a correction $\epsilon k_1(X_1)$ to k_0 and to make the mode shape β vary in the axial direction.

Computational Procedure

For the reasons given in Antia [23], we solved the following three equations:

$$D\bar{v} + \frac{\bar{v}}{Y} + ik_0\bar{u} = 0,$$

$$D^2\bar{u} + \frac{D\bar{u}}{Y} - A\bar{u} - R\bar{v}DU - ik_0\bar{P} = 0,$$

$$D\bar{P} + A\bar{v} + ik_0D\bar{u} = 0, \quad (13)$$

where

$$A = k_0^2 + iR(k_0U - \omega), \bar{P} = R\bar{p},$$

with the boundary conditions

$$\bar{v} = D\bar{u} = 0 \quad \text{at} \quad Y = 0,$$

$$\bar{u} = \bar{v} = 0 \quad \text{at} \quad Y = 1,$$

instead of the equation (5) for the eigenvalue k_0. These equations are obtained by taking the infinitesimal disturbance as

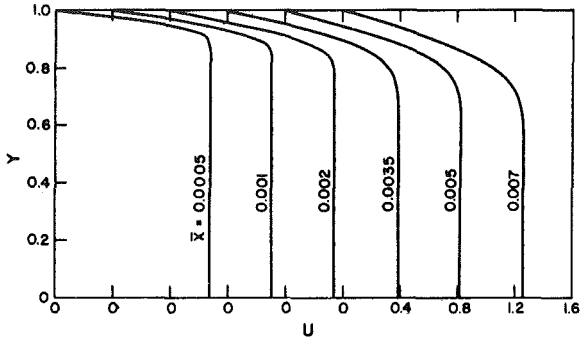

Fig. 1 Velocity profiles at several axial locations

$$[u, v, p] = [\bar{u}(Y), \bar{v}(Y), \bar{p}(Y)] \exp\{i(k_0X - \omega T)\} \quad (14)$$

and assuming the flow to be parallel.

The main flow velocity field (Fig. 1) was found using the Hornbeck method and equations (13) were integrated using the fourth-order Runge-Kutta method. The eigenvalue, k_0, was found in an iterative procedure using Muller's method [24] for fast convergence. With k_0, β and its derivatives known, a procedure similar to the foregoing one was used to solve the adjoint equations

$$D\bar{v}^* + \frac{\bar{v}^*}{Y} + ik_0\bar{u}^* = 0,$$

$$D^2\bar{u}^* + \frac{D\bar{u}^*}{Y} - A\bar{u}^* + ik_0\bar{P}^* - ik_0\left(D\bar{v}^* + \frac{\bar{v}^*}{Y}\right) = 0,$$

$$D\bar{P}^* - A\bar{v}^* + R\bar{u}^*DU = 0, \quad (15)$$

with the boundary conditions

$$D\bar{u}^* = \bar{v}^* = 0 \quad \text{at} \quad Y = 0,$$

$$\bar{u}^* = \bar{v}^* = 0 \quad \text{at} \quad Y = 1 \text{ (no-slip condition)}. \quad (16)$$

Since the eigenvalue for the main and adjoint problems is the same, no iteration is necessary while solving equations (15) and (16).

With k_0, β, and β^* known, dk_0/dX_1 is calculated by using fifth-order composite Newton-Cotes quadrature formula [25] for finding the integrals in equation (12) numerically. The values of $\partial\beta/\partial X_1$ are then given by the integration of equation (11a). It may be noted that the integrands in equation (12) vanish at $Y = 0$.

From the solution of equations (13), $k_0(X_1)$, $\beta(Y; X_1)$ and its Y derivatives were also obtained for a given ω and R at three axial locations $\overline{X} - \delta\overline{X}$, $\overline{X}$, and $\overline{X} + \delta\overline{X}$; $\delta\overline{X}$ taken as 10^{-5}. Using central differences, $\delta k_0/\delta X_1$ and $\delta\beta/\delta X_1$ were then obtained. It was found that the values of $\delta k_0/\delta X_1$ and dk_0/dX_1 were in agreement within computational accuracy; also $\partial\beta/\partial X_1$ and $\delta\beta/\delta X_1$ were in agreement at every point in the domain.

Calculations were performed on a DEC 1090 computer that carries 17 digits in double precision mode. Step size for the Runge-Kutta method was taken as 0.0025 and selective application of the Gram-Schmidt orthonormalization technique was used to keep the solution vectors linearly independent during numerical integration; details being available in Garg [26].

Growth Rates and Modified Wave Number

Shen [16] has suggested use of the growth rate based on the energy density E for determining the neutral stability characteristics of the nonparallel flows. This growth rate is given by

$$g_E(X) \equiv \frac{1}{2}E^{-1}\frac{dE}{dX} = -(k_0 + \epsilon k_1)_i + \frac{\epsilon}{2c}\frac{\partial c}{\partial X_1}, \quad (17)$$

where

$$c = \int_0^1 \frac{1}{Y}\left[|D\beta|^2 + |k_0|^2\,|\beta|^2\right]dY, \quad (18)$$

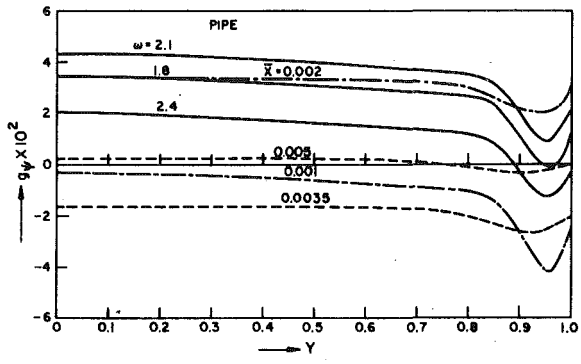

Fig. 2 Variation of g_ψ with Y for various $\bar{X}$, R, and ω. —, $\bar{X} = 0.001$; - - -, $\bar{X} = 0.002$; - - -, $\bar{X} = 0.0035$

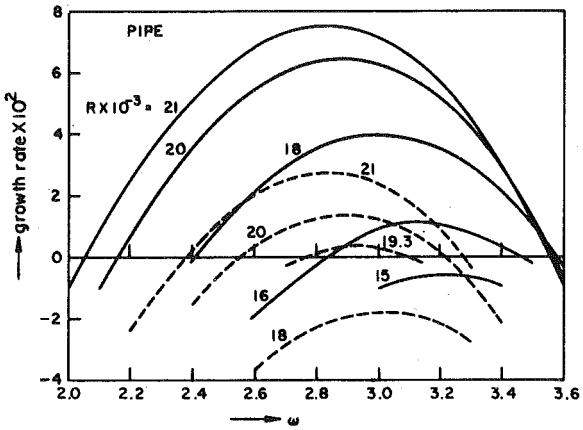

Fig. 3 Various growth rates at $\bar{X} = 0.0005$ and different R. —, $g_\psi(\bar{X}, 0)$; - - -, g_E

$$E = \frac{1}{2}\int_0^1 2\pi Y(\overline{u^2} + \overline{v^2})dY, \tag{19}$$

and subscript i denotes the imaginary part of the complex quantity. It is well known [20] that for a nonparallel flow the growth rates are functions of both the streamwise and radial coordinates. Also, the different flow quantities have different growth rates and, therefore, will have different neutral curves. Apparently, one may choose any of the growth rates for the purpose of finding the critical Reynolds number and other stability characteristics but if the experimental data for comparison are available, one must obviously use the growth rate of the same flow quantity as that which was observed. The only experimental work on the stability analysis of the developing flow in rigid circular pipe is due to Sarpkaya [10]. Though he mentions that the streamwise component of the disturbance velocity was measured at different radii, he neither reported its magnitude nor the radii at which measurements were made. Since these details could not be obtained [27], it was decided to compute several growth rates. Neutral curves were found on the basis of g_E and values of g_ψ and g_u at the pipe axis since g_ψ and g_u are functions of Y also. Here, g_ψ is the growth rate for disturbance stream function and g_u is that for the streamwise component of velocity. It can be easily seen that at the pipe axis, $g_u(X, 0) = g_\psi(X, 0)$. Further, since the velocity field was obtained at a given $\bar{X}$ instead of X, all growth rates have been obtained for a given $\bar{X}$ value and, therefore, they are, hereafter, referred to as function of $\bar{X}$. The modified wave number for any disturbance property Q is obtained from

$$\text{wave number} = \partial[\arg(Q)]/\partial X, \tag{20}$$

where arg (Q) represents the phase of Q. One, therefore, gets different wave numbers for different disturbance properties. The modified wave numbers are, however, little different from the parallel-flow wave number k_{0r}. Therefore, the modified wave numbers, though computed, are not reported here.

Results

Growth rates based on u, ψ, and E were obtained at $\bar{X} = 0.0005$, 0.001, 0.002, 0.0035, 0.005, and 0.007. Fig. 2 shows the growth rate based on ψ as a function of Y for different combinations of $\bar{X}$, R, and ω. It is observed that in the region near the pipe wall the dependence of g_ψ on Y is quite strong, the maximum growth rate occurs at the pipe axis, and while g_ψ decreases gradually and uniformly with Y up to the boundary-layer edge for all combinations of $\bar{X}$, R, and ω, its variation beyond the boundary-layer edge depends upon the value of $\bar{X}$ and upon the position of the $(\omega - R)$ point relative to the neutral curve on the $\omega - R$ plot. If the selected combination lies close to the neutral curve, g_ψ decreases suddenly near the boundary-layer edge and then increases near the pipe wall; the magnitude of the depression decreases as $\bar{X}$ increases or as one goes into the stable region away from the neutral curve. Maximum depression in the growth rate curve at any $\bar{X}$ and R is found to occur at frequencies midway between those

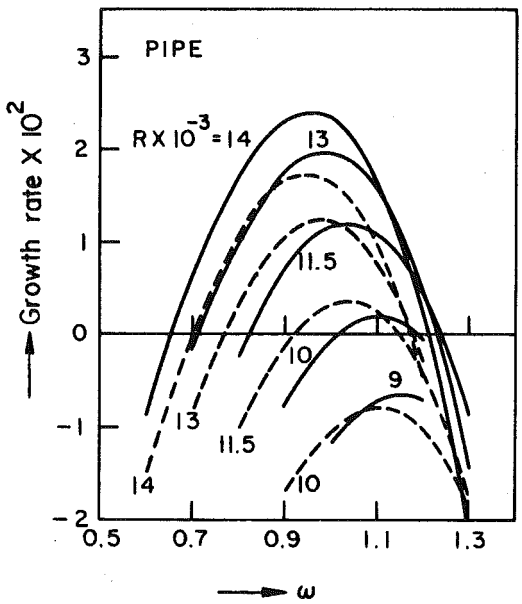

Fig. 4 Various growth rates at $\bar{X} = 0.0035$ and different R. —, $g_\psi(\bar{X}, 0)$; - - -, g_E

corresponding to the upper and lower branches of the neutral curve. The location of this depression shifts with R and ω at a fixed $\bar{X}$.

Figs. 3–5 show the variation of $g_\psi(\bar{X}, 0)$ and $g_E(\bar{X})$ with ω at $\bar{X} =$ 0.0005, 0.0035, and 0.007, respectively, for different Reynolds numbers. Similar curves were obtained at other values of $\bar{X}$. It is observed that for any ω at a given $\bar{X}$ and R, $g_\psi(\bar{X}, 0)$ is greater than g_E and is positive for the widest range of frequencies. One can also obtain from these figures the neutral curves for the different flow quantities. Fig. 6 shows these neutral curves, at different $\bar{X}$, based on (*i*) $g_\psi(\bar{X}, 0)$; (*ii*) $g_E(\bar{X})$; (*iii*) the parallel-flow theory (i.e., when the imaginary part of k_0 is zero). It is observed that the neutral curves are different for different flow quantities. In comparison to the results for the parallel-flow theory, the nonparallel effects make the flow unstable at lower Reynolds number and for a wider range of frequencies. The actual amount of such an effect depends on the choice of the growth rate used for determining the neutral curve. The growth rate $g_\psi(\bar{X}, 0)$ gives the minimum critical Reynolds number at all $\bar{X}$.

Fig. 7 shows the variation of the critical frequency, ω_c, and the critical Reynolds number, R_c, as obtained on the basis of $g_\psi(\bar{X}, 0)$, g_E, and the parallel-flow theory against $\bar{X}$. It is observed that the critical frequency, obtained from the different growth rates, decreases first sharply and then gradually with increasing $\bar{X}$ in the entry region; ω_c

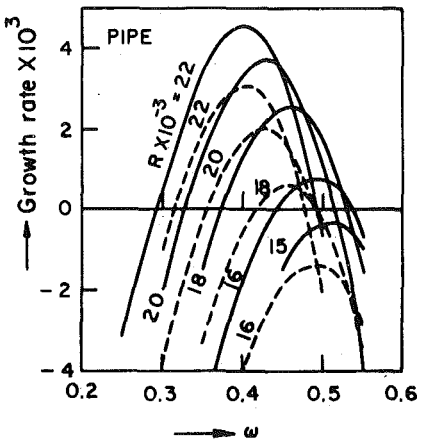

Fig. 5 Various growth rates at $\bar{X} = 0.007$ and different R. —, $g_\psi(\bar{X}, 0)$; - - -, g_E

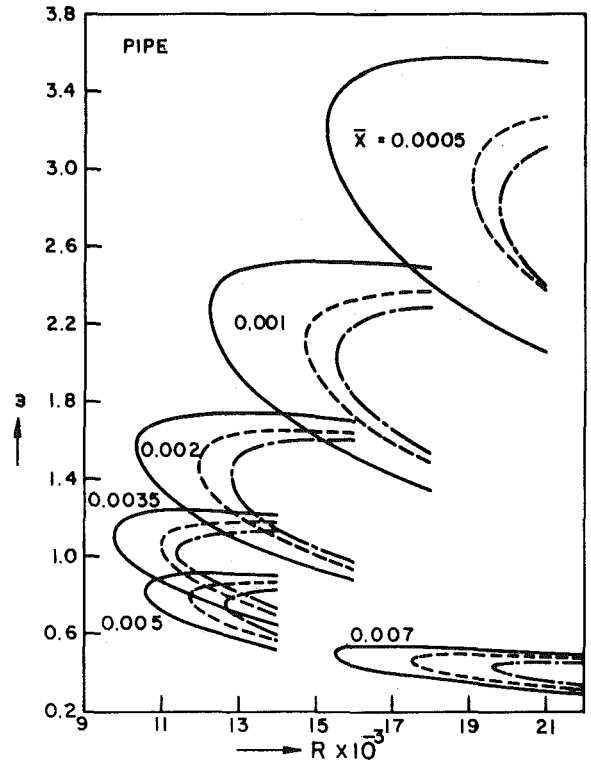

Fig. 6 Neutral curves at various $\bar{X}$. —, based on $g_\psi(\bar{X}, 0)$; - - -, based on g_E; - · -, based on parallel-flow theory

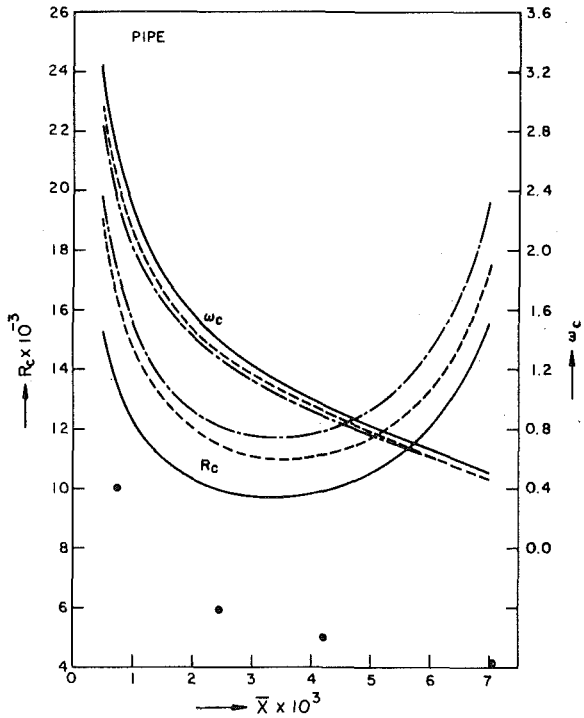

Fig. 7 Variation of R_c and ω_c with $\bar{X}$. —, based on $g_\psi(\bar{X}, 0)$; - - -, based on g_E; - · -, based on parallel-flow theory; ⊙ experimental data [10] for R_c

obtained from $g_\psi(\bar{X}, 0)$ being maximum and that from the parallel-flow theory being minimum. However the R_c versus $\bar{X}$ curves pass through a minima. The minimum critical Reynolds number corresponding to $g_\psi(\bar{X}, 0)$, $g_E(\bar{X})$, and to the parallel-flow theory are 9700 at $\bar{X} = 0.00325$, 11,000 at $\bar{X} = 0.0035$, and 11,700 at $\bar{X} = 0.0035$, respectively. In comparison to the results based on $g_\psi(\bar{X}, 0)$ and $g_E(\bar{X})$, the parallel flow theory overpredicts the critical Reynolds number by 29.8 percent and 3.7 percent, respectively, at $\bar{X} = 0.0005$, by 20.0 percent and 6.4 percent, respectively, at $\bar{X} = 0.0035$, and by 26.5 percent and 12.0 percent, respectively, at $\bar{X} = 0.007$. This implies that the R_c versus $\bar{X}$ curves obtained on the basis of nonparallel theory are flatter than those corresponding to the parallel-flow theory; R_c does increase beyond $\bar{X} = 0.0035$ but not so sharply as for the parallel-flow theory. Physically, it means that the developing flow is unstable over a larger inlet length of the pipe. The first instability of the flow, on the basis of $g_\psi(\bar{X}, 0)$, g_E, and the parallel-flow theory, is found to occur in the range $30 \leq X \leq 35$, $35 \leq X \leq 43$, and $36 \leq X \leq 45$, respectively.

Also shown on Fig. 7 are the critical Reynolds numbers obtained experimentally by Sarpkaya [10] for axisymmetric disturbances. The first instability was experimentally observed to occur in the range $45 \leq X \leq 75$. We note that R_c versus $\bar{X}$ curve obtained on the basis of $g_\psi(\bar{X}, 0)$ is closest to these data; the experimentally obtained critical Reynolds numbers being lower than those obtained from the nonparallel theory. As Sarpkaya himself noted, his critical Reynolds number may be low due to the superposition of some nonaxisymmetric disturbances on the axisymmetric disturbance as well as due to a higher initial disturbance level than that warranted by the linear theory used here. Moreover, the radii at which the streamwise component of the disturbance velocity was measured by him is not known. There is, therefore, the need for a more carefully conducted experimental study before any meaningful comparison can be made with the theoretical results presented here.

Conclusions

Nonparallel effects on the stability of developing flow in a pipe have been studied at several axial locations. The results are found to be quite different from those obtained from the parallel flow theory.

It has been found that the critical frequency, obtained from different growth rates, decreases first sharply and then gradually with increasing $\bar{X}$. However, the critical Reynolds number versus $\bar{X}$ curves pass through a minima. The minimum critical Reynolds number corresponding to $g_\psi(\bar{X}, 0)$, $g_E(\bar{X})$, and the parallel-flow theory are 9700 at $\bar{X} = 0.00325$, 11,000 at $\bar{X} = 0.0035$, and 11,700 at $\bar{X} = 0.0035$, respectively. In comparison to the results based on $g_\psi(\bar{X}, 0)$ and $g_E(\bar{X})$, the parallel-flow theory overpredicts the critical Reynolds number by 29.8 percent and 3.7 percent, respectively, at $\bar{X} = 0.0005$, by 20.0 percent and 6.4 percent, respectively, at $\bar{X} = 0.0035$, and by 26.5 percent and 12.0 percent, respectively, at $\bar{X} = 0.007$. The R_c versus $\bar{X}$ curves obtained on the basis of nonparallel theory are flatter than those obtained from the parallel-flow theory and, therefore, the actual flow remains unstable over a larger inlet length of the pipe than its parallel-flow approximate. The first instability of the flow, on the

basis of $g_\psi(\overline{X}, 0)$, $g_E(\overline{X})$, and the parallel-flow theory, is found to occur in the range $30 \leq X \leq 35$, $35 \leq X \leq 43$, and $36 \leq X \leq 45$, respectively. The R_c versus $\overline{X}$ curve obtained on the basis of $g_\psi(\overline{X}, 0)$ is closest to the experimental data of Sarpkaya [10].

Acknowledgments

This research forms a part of the PhD thesis submitted by S. C. Gupta to the Mechanical Engineering Department, Indian Institute of Technology Kanpur.

References

1 Corcos, G. M., and Sellars, J. R., "On the Stability of Fully Developed Flow in a Pipe," *Journal of Fluid Mechanics*, Vol. 5, 1959, pp. 97–112.

2 Garg, V. K., and Rouleau, W. T., "Linear Spatial Stability of Pipe Poiseuille Flow," *Journal of Fluid Mechanics*, Vol. 54, 1972, pp. 113–127.

3 Gill, A. E., "The Least Damped Disturbance to Poiseuille Flow in a Circular Pipe," *Journal of Fluid Mechanics*, Vol. 61, 1973, pp. 97–107.

4 Leite, R. J., "An Experimental Investigation of the Stability of Poiseuille Flow," *Journal of Fluid Mechanics*, Vol. 5, 1959, pp. 81–97.

5 Tatsumi, T., "Stability of the Laminar Inlet-Flow Prior to the Formation of Poiseuille Regime, II," *Journal of Physical Society of Japan*, Vol. 7, 1952, pp. 495–502.

6 Huang, L. M., and Chen, T. S., "Stability of Developing Pipe Flow Subjected to Nonaxisymmetric Disturbances," *Journal of Fluid Mechanics*, Vol. 63, 1974, pp. 183–193.

7 Gupta, S. C., and Garg, V. K., "Effect of Velocity Distribution on the Stability of Developing Flow in a Pipe," *Physics of Fluids*, Vol. 24, 1981.

8 Hornbeck, R. W., "Laminar Flow in Entrance Region of a Pipe, *Applied Science Research*, Section A, Vol. 13, 1963, pp. 224–232.

9 Sparrow, E. M., Lin, S. H., and Lundgren, T. S., "Flow Development in the Hydrodynamic Entrance Region of Tubes and Ducts," *Physics of Fluids*, Vol. 7, 1964, pp. 338–347.

10 Sarpkaya, T., "A Note on the Stability of Developing Laminar Pipe Flow Subjected to Axisymmetric and Nonaxisymmetric Disturbances," *Journal of Fluid Mechanics*, Vol. 68, 1975, pp. 345–351.

11 Crane, C. M., and Burley, D. M., "Numerical Studies of Laminar Flow in Ducts and Pipes," *Journal of Computation and Applied Mathematics*, Vol. 2, 1976, pp. 95–101.

12 Shah, R. K., "A Correlation for Laminar Hydrodynamic Entry Length Solutions for Circular and Noncircular Ducts," *Journal of Fluids Engineering*, Vol. 100, 1978, pp. 177–179.

13 Shen, F. C. T., Chen, T. S., and Huang, L. M., "The Effect of Mainflow Radial Velocity on the Stability of Developing Laminar Pipe Flow," JOURNAL OF APPLIED MECHANICS, Vol. 43, 1976, pp. 209–212.

14 Schubauer, G. B., and Skramstad, H. K., "Laminar Boundary Layer Oscillations and Transition on a Flat Plate," *Journal of the Aeronautical Sciences*, Vol. 14, 1947, pp. 69–78.

15 Ross, J. A., et al., "The Flat Plate Boundary Layer, Part 3, Comparison of Theory With Experiment," *Journal of Fluid Mechanics*, Vol. 43, 1970, pp. 819–832.

16 Shen, S. F., "Some Considerations on the Laminar Stability of Time-Dependent Basic Flows," *Journal of the Aeronautical Sciences*, Vol. 28, 1961, pp. 397–404.

17 Saric, W. S., and Nayfeh, A. H., "Nonparallel Stability of Boundary Layer Flows," *Physics of Fluids*, Vol. 18, 1975, pp. 945–950.

18 Spielberg, K., and Timan, H., "On Three and Two-Dimensional Disturbances of Pipe Flow," ASME JOURNAL OF APPLIED MECHANICS, Vol. 27, 1960, pp. 381–389.

19 Squire, H. B., "On the Stability for Three-Dimensional Disturbances of Viscous Fluid Flow Between Parallel Walls," *Proceedings of the Royal Society*, London, Series A, Vol. 142, 1933, pp. 621–628.

20 Bouthier, M., "Stabilite 'Lineaire des E' coulements presque Paralliles, II, La Couche Limite de Blasius," *Journal de Mecanique*, Vol. 12, 1973, pp. 75–95.

21 Goldstein, S., ed., *Modern Developments in Fluid Dynamics*, Vol. II, Dover Publications, 1965, p. 305.

22 Gaster, M., "On the Effects of Boundary Layer Growth on Flow Stability," *Journal of Fluid Mechanics*, Vol. 66, 1974, pp. 465–480.

23 Antia, H. M., "Finite Difference Method for Generalized Eigenvalue Problem in Ordinary Differential Equations," *Journal of Computational Physics*, Vol. 30, 1979, pp. 283–295.

24 Muller, D. E., "A Method for Solving Algebraic Equations Using an Automatic Computer," *Mathematical Tables and Other Aides to Computation*, Vol. 10, 1956, pp. 208–215.

25 Ralston, A., *A First Course in Numerical Analysis*, McGraw-Hill, International Student Edition, 1965, pp. 114–119.

26 Garg, V. K., "Improved Shooting Techniques for Linear Boundary-Value Problems," *Computer Methods in Applied Mechanics and Engineering*, Vol. 22, 1980, pp. 87–99.

27 Sarpkaya, T., Private Communication, 1979.

M. Toren[1]
Adjunct Senior Lecturer.

A. Solan
Professor.
Mem. ASME

Faculty of Mechanical Engineering,
Technion—Israel Institute of Technology,
Haifa, Israel

Rotating Compressible Flow Over the Edge of a Finite Disk

Numerical and asymptotic solutions of the similarity equations governing the laminar compressible rotating flow near the edge of a finite disk are presented for a wide range of the Prandtl and Eckert numbers and the disk-to-external flow ratios of azimuthal velocity and temperature. By appropriate transformations, the compressible flow is reduced to a formulation similar to that of the incompressible flow. Wall heating and dissipation effects are shown to be equivalent to an increment of the velocity of the disk in the sense opposite to that of the outer flow. In the limit of small velocity or temperature difference between the disk and the outer flow, the solutions show how an Ekman layer is started at the edge.

Introduction

The boundary-layer equations governing the incompressible, laminar, rotating flow over a finite disk can be reduced near the disk edge to a set of similarity equations which determine the initial growth of the boundary layer [1, 2]. The conditions under which such similarity solutions fail to exist for a disk rotating in the opposite sense to that of the external flow were considered by Bodonyi and Stewartson [3]. Numerical solutions of these equations were used in studies of the boundary-layer development on a finite disk in a rotating fluid [4–6]. For the compressible *isothermal* flow the solution was shown by the present authors [7] to be quite similar to that of the incompressible flow. However, neither the heat transfer in incompressible flow, nor the fully compressible flow have been examined in any systematic way. In particular, it is important to know the conditions under which initial (edge) similarity solutions do exist, especially in view of the nonexistence of solutions of the terminal (axis) similarity of the energy equation for an infinite rotating disk [8, 9] when the axial velocity component is directed away from the disk. Even in such cases the edge similarity solution is needed for starting the solution (not necessarily of boundary-layer type) for the flow and temperature field over the whole disk.

In this paper we consider the generalization of the initial similarity problem for the fully compressible, laminar flow with heat transfer for the whole range of the governing parameters, namely, the Prandtl and Eckert numbers, σ, α and the disk to outer flow ratios of the azimuthal velocity V_w and temperature T_w. Numerical solutions of this two-point boundary-value problem are presented together with asymptotic analytical solutions for high, low, and unity Prandtl numbers, Eckert numbers of order one, and velocity ratios from zero to almost unity (small perturbation). We consider first the *uncoupled* flow and energy equations describing heat transfer in an incompressible flow. In this context particular attention is paid to the small-perturbation flow of a disk rotating slightly slower than the outer flow. The solution of this case shows that the boundary layer thickness and the radial mass flow depend upon the Rossby number to $\frac{1}{4}$ power. This initial boundary-layer flow should eventually develop into the Ekman layer as it moves radially inwards toward the axis. The solution of the energy equation for the incompressible flow exhibits the trends of the classical boundary-layer theory for high, unity, and low Prandtl numbers. The heat-transfer coefficient is proportional to the Rossby number to $\frac{1}{4}$ power, thus illustrating the analogy between momentum and heat transfer. Further, the fully compressible flow (*coupled equations*) is considered and the influence of dissipation and wall heating is analyzed for different values of the Prandtl number. For most of these cases the compressible flow can be reduced by suitable transformations to that of an equivalent incompressible flow, thus showing clearly the influence of compressibility on the flow field and heat transfer. Wall heating and dissipation effects are shown to be analogous to a negative increment of the disk rotation in the equivalent incompressible flow. Due to an increase in temperature the density is decreased near the disk surface and the effect of the externally imposed pressure gradient is enhanced, resulting in an acceleration of the fluid radially inward. The solutions presented here can be used in the study of heat and mass transfer in shrouded disk systems for both compressible and incompressible flows.

Governing Equations

The boundary layer equations for rotating, steady, axisymmetric, laminar, compressible flow over a finite disk of radius $\bar{a}$ are

[1] During 1980–1981, EPRI, P. O. Box 10412, Palo Alto, Calif. 94304

Contributed by the Applied Mechanics Division of THE AMERICAN SOCIETY OF MECHANICAL ENGINEERS, and presented at the 1981 Joint ASME/ASCE Applied Mechanics, Fluids Engineering, and Bioengineering Conference, University of Colorado, Boulder, Colo., June 22–27, 1981.

Discussion on this paper should be addressed to the Editorial Department, ASME United Engineering Center, 345 East 47th Street, New York, N.Y. 10017, and will be accepted until September 1, 1981. Readers who need more time to prepare a Discussion should request an extension from the Editorial Department. Manuscript received by ASME Applied Mechanics Division, May, 1980; final revision, September, 1980. Paper No. 81-APM-19.

$$\bar{\rho}\left(\bar{u}\frac{\partial\bar{u}}{\partial\bar{r}}+\bar{w}\frac{\partial\bar{u}}{\partial\bar{z}}-\frac{\overline{V}^2}{\bar{r}}\right)=-\frac{\partial\bar{p}}{\partial\bar{r}}+\frac{\partial}{\partial\bar{z}}\left(\bar{\mu}\frac{\partial\bar{u}}{\partial\bar{z}}\right) \tag{1}$$

$$\bar{\rho}\left(\bar{u}\frac{\partial\overline{V}}{\partial\bar{r}}+\bar{w}\frac{\partial\overline{V}}{\partial\bar{z}}+\frac{\bar{u}\overline{V}}{\bar{r}}\right)=\frac{\partial}{\partial\bar{z}}\left(\bar{\mu}\frac{\partial\overline{V}}{\partial\bar{z}}\right) \tag{2}$$

$$\frac{\partial\bar{p}}{\partial\bar{z}}=0 \tag{3}$$

$$\bar{\rho}\bar{c}_p\left(\bar{u}\frac{\partial\overline{T}}{\partial\bar{r}}+\bar{w}\frac{\partial\overline{T}}{\partial\bar{z}}\right)-\bar{u}\frac{\partial\bar{p}}{\partial\bar{r}}=\frac{\partial}{\partial\bar{z}}\left(\bar{k}\frac{\partial\overline{T}}{\partial\bar{z}}\right)+\bar{\mu}\left[\left(\frac{\partial\bar{u}}{\partial\bar{z}}\right)^2+\left(\frac{\partial\overline{V}}{\partial\bar{z}}\right)^2\right] \tag{4}$$

$$\frac{1}{\bar{r}}\frac{\partial}{\partial\bar{r}}(\bar{\rho}\bar{r}\bar{u})+\frac{\partial}{\partial\bar{z}}(\bar{\rho}\bar{w})=0 \tag{5}$$

$$\bar{p}=\bar{\rho}\bar{R}\overline{T} \tag{6}$$

The bar denotes dimensional variables. In these equations $\bar{r}$ and $\bar{z}$ are cylindrical coordinates in a stationary frame with the origin at the center of the disk. The radial, axial, and azimuthal velocity components are $\bar{u}$, $\bar{w}$ and $\overline{V}$, respectively; $\bar{p}$, $\bar{\rho}$, and $\overline{T}$ denote pressure, density, and temperature. We assume an ideal gas with gas constant $\bar{R}$, constant heat capacity $\bar{c}_p$, Prandtl number σ, and dynamic viscosity $\bar{\mu}\propto\overline{T}$.

The angular velocity of the disk $\bar{\Omega}_w$ and its temperature $\overline{T}_w$ are prescribed. The boundary conditions at the disk surface are thus

$$\bar{z}=0:\quad \bar{u}=\bar{w}=0;\quad \overline{V}=\overline{V}_w=\bar{\Omega}_w\bar{r};\quad \overline{T}=\overline{T}_w \tag{7}$$

Far from the disk the fluid is isothermal at temperature $\overline{T}_1$ and rotating with a constant angular velocity $\bar{\Omega}_1$,

$$\bar{z}\to\infty:\quad \bar{u}=\bar{w}=0;\quad \overline{V}=\overline{V}_1=\bar{\Omega}_1\bar{r};\quad \overline{T}=\overline{T}_1 \tag{8}$$

Thus the pressure in the outer flow is given by $\partial\bar{p}/\partial\bar{r}=\bar{\rho}_1\bar{r}\bar{\Omega}_1^2=\bar{\rho}_1\overline{V}_1^2/\bar{r}$. We now use a Dorodnitsyn-Howarth transformation of the axial coordinate

$$Y=\int_0^{\bar{z}}(\bar{\rho}/\bar{\rho}_1)d\bar{z}=\int_0^{\bar{z}}(\overline{T}_1/\overline{T})d\bar{z} \tag{9}$$

and introduce a stream function $\bar{\psi}$ such that

$$\bar{u}=\frac{1}{\bar{r}}\frac{\bar{\rho}_1}{\bar{\rho}}\frac{\partial\bar{\psi}}{\partial\bar{z}}=\frac{1}{\bar{r}}\frac{\partial\bar{\psi}}{\partial Y} \tag{10}$$

Thus (1)–(4) may be written as

$$\frac{1}{\bar{r}}\frac{\partial\overline{\Psi}}{\partial Y}\frac{\partial}{\partial\bar{r}}\left(\frac{1}{\bar{r}}\frac{\partial\bar{\psi}}{\partial Y}\right)-\frac{1}{\bar{r}}\frac{\partial\bar{\psi}}{\partial\bar{r}}\frac{\partial}{\partial Y}\left(\frac{1}{\bar{r}}\frac{\partial\bar{\psi}}{\partial Y}\right)-\frac{\overline{V}^2}{\bar{r}}=-\frac{\overline{T}}{\overline{T}_1}\frac{\overline{V}_1^2}{\bar{r}}+\bar{\nu}_1\frac{\partial^2}{\partial Y^2}\left(\frac{1}{\bar{r}}\frac{\partial\bar{\psi}}{\partial Y}\right) \tag{11}$$

$$\frac{1}{\bar{r}}\frac{\partial\bar{\psi}}{\partial Y}\frac{\partial\overline{V}}{\partial\bar{r}}-\frac{1}{\bar{r}}\frac{\partial\bar{\psi}}{\partial\bar{r}}\frac{\partial\overline{V}}{\partial Y}+\frac{1}{\bar{r}^2}\frac{\partial\bar{\psi}}{\partial Y}\overline{V}=\bar{\nu}_1\frac{\partial^2\overline{V}}{\partial Y^2} \tag{12}$$

$$\frac{1}{\bar{r}}\frac{\partial\bar{\psi}}{\partial Y}\frac{\partial\overline{T}}{\partial\bar{r}}-\frac{1}{\bar{r}}\frac{\partial\bar{\psi}}{\partial\bar{r}}\frac{\partial\overline{T}}{\partial Y}-\frac{1}{\bar{r}^2}\frac{\partial\bar{\psi}}{\partial Y}\frac{\overline{T}}{\bar{c}_p\overline{T}_1}\overline{V}_1^2=\frac{\bar{\nu}_1}{\sigma}\frac{\partial^2\overline{T}}{\partial Y^2}+\frac{\bar{\nu}_1}{\bar{c}_p}\left[\frac{\partial}{\partial Y}\left(\frac{1}{\bar{r}}\frac{\partial\bar{\psi}}{\partial Y}\right)^2+\left(\frac{\partial\overline{V}}{\partial Y}\right)^2\right] \tag{13}$$

where $\bar{\nu}=\bar{\mu}/\bar{\rho}$. We note that the radial pressure gradient term on the right side of (12) is enhanced by the factor $\overline{T}/\overline{T}_1$ representing a change in density due to temperature variations. Finally, we introduce an edge similarity transformation of Stewartson type [2], and dimensionless variables

$$\eta=\left(\frac{\bar{\Omega}_1}{\bar{\nu}_1}\right)^{1/2}Y\xi^{-1/4};\quad \xi=1-\bar{r}/\bar{a} \tag{14}$$

$$\left.\begin{aligned}\bar{\psi}&=\bar{a}^2(\bar{\Omega}_1\bar{\nu}_1)^{1/2}\xi^{3/4}\psi(\eta)\\ \overline{V}&=\bar{a}\bar{\Omega}_1V(\eta)=\bar{a}\bar{\Omega}_1[1-v(\eta)]\\ \overline{T}&=\overline{T}_1[1+t(\eta)]\end{aligned}\right\} \tag{15}$$

In the following we shall use both V—the azimuthal velocity ratio and v—the azimuthal velocity difference, where $V=1-v$. In terms of these variables the momentum and energy balances become

$$\psi'''-\tfrac{3}{4}\psi\psi''+\tfrac{1}{2}\psi'^2=1+t-V^2 \tag{16}$$

$$V''-\tfrac{3}{4}\psi V'=0 \tag{17}$$

$$t''-\tfrac{3}{4}\sigma\psi t'+\alpha\sigma V'^2=0 \tag{18}$$

where $'\equiv d/d\eta$, and $\alpha=\bar{\Omega}_1^2\bar{a}^2/\bar{c}_p\overline{T}_1-(\gamma-1)\mathbf{M}^2$ is the Eckert number, closely related to the Mach number $\mathbf{M}$. The boundary conditions are

$$\left.\begin{aligned}&\psi(0)=\psi'(0)=0;\quad V(0)=V_w=1-v_w;\quad t(0)=t_w=T_w-1\\ &\psi'(\infty)=0;\qquad\quad V(\infty)=1;\qquad\quad t(\infty)=0\end{aligned}\right. \tag{19}$$

where $T_w=\overline{T}_w/\overline{T}_1$ and $V_w=\overline{V}_w/\bar{a}\bar{\Omega}_1$.

The momentum equations (16) and (17) are quite similar to those of the incompressible case [6], the only difference being in the pressure gradient term $1+t$ in the radial equation (16) which reduces to unity for an incompressible flow. This term couples the energy equation with the momentum equations. Thus compressibility effects are due to changes in density caused by temperature variations across the boundary layer, driven by wall heating or cooling (when $t_w\neq 0$) or by dissipation (when $\alpha\neq 0$) through the energy balance which consists of heat diffusion, convection, and dissipation. Note that temperature changes due to pressure work do not appear in the edge similarity transformed equations. Thus the isothermal compressible flow defined by zero dissipation with no wall heating ($t_w=\alpha=0$) is identical with the incompressible flow field in this transformation.

In equations (16)–(19) the four governing parameters are: the disk-to-external flow velocity ratio V_w (or the difference $v_w=1-V_w$), the temperature difference t_w, the Eckert number α, and the Prandtl number σ. Some significant values of these parameters and their physical meaning are given as follows:

Velocity Ratio:	$V_w<0$,	disk rotating in opposite sense to the outer fluid, not considered here in detail;
	$=0$,	stationary disk;
	$\sim 1-\epsilon$, $\epsilon\ll 1$,	small perturbation (velocity);
	>1,	outward radial flow, no initial similarity.
Temperature Excess:	$t_w<0$,	wall cooling
	$=\epsilon$,	$\lvert\epsilon\rvert\ll 1$; small perturbation (thermal);
	$=0$,	disk at the same temperature as the outer fluid.
	>0,	wall heating.
Dissipation:	$\alpha=0$,	no dissipation;
	$=\epsilon$,	$\epsilon\ll 1$, small perturbation (dissipative);
	$=0(1)$,	moderate dissipation;
Prandtl Number:	$\sigma\ll 1$,	thick thermal layer;
	$=1$,	equal thermal and viscous boundary-layer thickness;
	$\gg 1$,	thin thermal layer.

The most interesting results of the solution, beside velocity and temperature profiles, are the momentum and heat fluxes at the solid boundary and mass flux in the boundary layer, which are related to $\psi''(0)$, $V'(0)$, $\psi(\infty)$, and $t'(0)$. The effect of compressibility on these quantities and on the very existence of the edge similarity solutions are of both theoretical and practical interest in the solution of shrouded disk problems.

A double integration of (16), following [6], shows that

$$\frac{3}{8}\psi^2(\infty)+\int_0^\infty d\eta'\int_0^{\eta'}\left[V^2-1-t+\frac{5}{4}\psi'^2\right]d\eta=0 \tag{20}$$

and from (17) we see that V is monotonic. For zero dissipation $\alpha=0$, (18) shows that the temperature is monotonic also and in this case there are no solutions of the boundary-value problem when $V_w^2>1+t_w$. This condition should be compared with the equivalent condi-

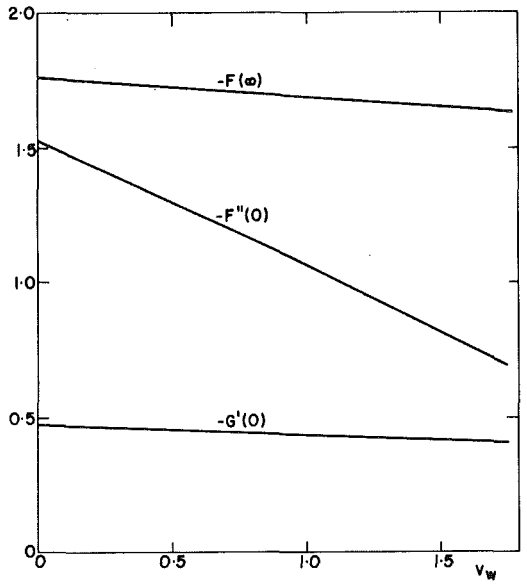

Fig. 1 Incompressible flow

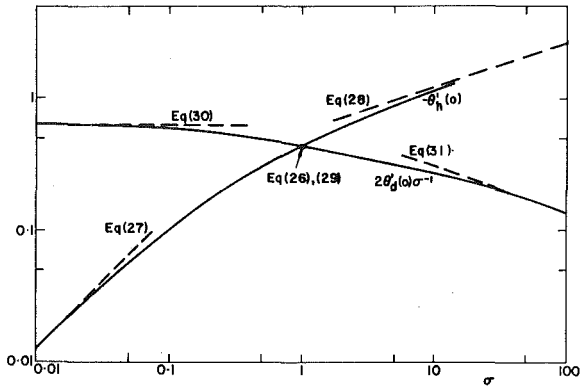

Fig. 2 Heat transfer in incompressible flow over a stationary disk ($V_w = 0$); — Numerical solution of the complete system (16)–(19); - - - - Asymptotic solutions

tion for the incompressible case, i.e., $V_w > 1$. We note that in the compressible case with zero dissipation, a solution is possible even if the azimuthal velocity of the disk is higher than that of the outer flow, provided the disk is sufficiently heated ($t_w > 1$)!

In the following we first briefly review the incompressible flow and present solutions of the heat transfer problem, dealing separately with wall heating and dissipation effects. Then, the fully compressible flow is solved for small and finite perturbations and different values of σ, using classical methods [10, 11] of boundary-layer theory. All numerical solutions were obtained by an optimization algorithm for boundary-value problems.

Incompressible Flow

The momentum equations (16), (without the compressibility term t) and (17) are uncoupled from the energy equation (18). Solutions of these equations for different values of $V_w = 1 - v_w$ both positive and negative, which were published before [2–6], were reproduced as a check of the numerical method. The transformation:

$$\psi = v_w^{1/4} F(\tilde{\eta}); \quad v = v_w G(\tilde{\eta}); \quad \eta = v_w^{-1/4}\tilde{\eta} \tag{21}$$

in (16), (17), and (19), yields

$$F''' - \tfrac{3}{4}FF'' + \tfrac{1}{2}F'^2 = 2G - v_w G^2 \quad (' \equiv d/d\tilde{\eta}) \tag{22}$$

$$G'' - \tfrac{3}{4}FG' = 0 \tag{23}$$

$$\left.\begin{aligned} G(0) = 1; \quad G(\infty) = 0 \\ F(0) = F'(0) = 0; \quad F'(\infty) = 0 \end{aligned}\right\} \tag{24}$$

In the small perturbation limit ($v_w \to 0$), this transformation removes v_w from the equation (22) and from the whole system. The numerical solution for this case yields

$$v_w \to 0: \quad F(\infty) = -1.759; G'(0) = -0.4769; F''(0) = -1.527$$

This describes the initial growth of the boundary layer which will develop eventually into the classical Ekman layer for a slower disk as we move radially inward. We note that the initial similarity solution is still nonlinear (as opposed to the Ekman solution) and that v_w plays the role of a Rossby number. In general, the dependence of stress components and mass flux on v_w is

$$\psi''(0) = F''(0)v_w^{3/4}; \quad v'(0) = G'(0)v_w^{5/4}; \quad \psi(\infty) = F(\infty)v_w^{1/4}$$

Thus the mass flux is of the order of the Rossby number v_w to the $\frac{1}{4}$ power.

Numerical results of the system (22)–(24) are shown in Fig. 1. (Stewartson's stationary disk is represented by

$$v_w = 1: \quad F(\infty) = -1.6916, G'(0) = -0.43985, F''(0) = -1.0681).$$

These results, presented in [6] in terms of unscaled variables equivalent to our ψ, v, η, were recomputed here and are presented in terms of the v_w—scaled variables $F, G, \tilde{\eta}$. Note that in the present scaling $F(\infty)$ and $G'(0)$ are nearly independent of v_w and all three variables fall on almost straight lines.

Heat Transfer in Incompressible Flow. The energy equation (18) is linear and its solution can be written as

$$t = t_w\theta_h(\eta) + \alpha\theta_d(\eta) \tag{25}$$

Here θ_h, θ_d represent wall heating and dissipation contributions. The separation of the equations for θ_h and θ_d and their formal solutions in terms of integrals of ψ are straightforward. Numerical results for a wide range of σ are shown in Fig. 2, together with asymptotic solutions for limiting values of σ as listed in the following.

Wall Heating Effects. $\sigma = 1$. The azimuthal momentum and energy equations are identical in this case and the temperature is linearly dependent on the azimuthal velocity

$$\theta_h = \frac{\cdot v}{v_w}: \quad \theta'_h(0) = \frac{v'(0)}{v_w} = G'(0)v_w^{1/4} \tag{26}$$

and the dependence of $\theta'_h(0)$ on v_w is closely related to that of $v'(0)$—see Fig. 1.

$\sigma \to 0$. The thermal layer is much thicker $0(\sigma^{-1})$ than the viscous layer, therefore we can assume $\psi \sim \psi(\infty)$ and the solution is

$$\theta_h = \exp\left[\tfrac{3}{4}\sigma\psi(\infty)\eta\right]; \quad \theta'_h(0) = \tfrac{3}{4}\sigma\psi(\infty) = \tfrac{3}{4}\sigma v_w^{1/4}F(\infty) \tag{27}$$

$\sigma \to \infty$. The thermal layer is much thinner $0(\sigma^{-1/3})$ than the viscous one, therefore we can assume $\psi \sim \frac{1}{2}\psi''(0)\eta^2$ and the solution is now

$$\theta_h = 1 - P\left(\frac{1}{3}; -\frac{1}{8}\sigma\psi''(0)\eta^3\right); \theta'_h(0) = \frac{\sigma^{1/3}}{2\Gamma(4/3)}[\psi''(0)]^{1/3}$$

$$= \frac{\sigma^{1/3}}{2\Gamma(4/3)} v_w^{1/4}[F''(0)]^{1/3} \tag{28}$$

Here $P(a,x)$ is the incomplete Gamma function [12].

From (26)–(28) and Fig. 1 it is seen that $\theta'_h(0)$ is roughly proportional to $v_w^{1/4}$ for all values of σ because $G'(0)$, $F(\infty)$, and $[F''(0)]^{1/3}$ are weakly dependent on v_w. Note the momentum and heat transfer analogy in this case. The asymptotic behavior for both high and low σ is shown by dashed lines in Fig. 2.

Effects of Viscous Dissipation. $\sigma = 1$. The solution is

$$\theta_d = \tfrac{1}{2}v(v_w - v) = \tfrac{1}{2}v_w^2 G(1 - G);$$
$$\theta'_d(0) = -\tfrac{1}{2}v_w v'(0) = -\tfrac{1}{2}v_w^{9/4}G'(0) \tag{29}$$

The dependence of $\theta'_d(0)$ on v_w is closely related to that of $v'(0)$—see Fig. 1. Due to the fact that $G'(0)$ is a weak function of v_w, $\theta'_d(0)$ is roughly proportional to $v_w^{9/4}$; this result should be compared with that of (26) which shows that $\theta'_h(0) \propto v_w^{1/4}$.

$\sigma \to 0$. In this case two regions must be considered: an inner layer $\eta = 0(1)$ in which convection is negligible and an outer layer $\eta = 0(\sigma^{-1})$ in which dissipation is negligible. Thus

$$\theta'_d(0) = \sigma \int_0^\infty d\eta v'^2 = \sigma v_w^{9/4} \int_0^\infty d\tilde{\eta} G'^2(\tilde{\eta}) \tag{30}$$

For a stationary disk a numerical integration yields $v_w = 1$: $\theta'_d(0) = 0.322\ \sigma$.

$\sigma \to \infty$. Again two layers are matched to obtain the solution. The outer layer $\eta = 0(1)$ is characterized by negligible heat conduction. Matching the layers we obtain:

$$\theta'_d(0) = \left[-\frac{1}{8}\psi''(0)\right]^{-1/3} \Gamma\left(\frac{4}{3}\right) v'^2(0)\sigma^{2/3}$$

$$= -\frac{1}{2}\Gamma\left(\frac{4}{3}\right)\sigma^{2/3} v_w^{9/4}[F''(0)]^{1/3} G'^2(0) \tag{31}$$

The main factor of the functional dependence of $\theta'_d(0)$ on v_w from (29), (30), and (31) is $v_w^{9/4}$. The asymptotic behaviour of $\theta'_d(0)$ for both high and low σ is shown by dashed lines in Fig. 2 for stationary disk ($v_w = 1$).

Compressible Flow Field

We consider now the coupled system of equations (16)–(19). We present numerical and analytical solutions for $\sigma = 1, 0, \infty$ obtained by reducing the problems to incompressible flows using suitable transformations. Special attention is paid to small perturbation cases.

$\sigma = 1$. *Small Perturbation $t_w, v_w \ll 1$.* The centrifugal term—v^2 in (16) and the dissipation term $\alpha\sigma v'^2$ in (18) are negligible (the latter provided α is not too large). Due to the fact that the energy and azimuthal equations are identical in this case, one can use a generalized (temperature plus azimuthal velocity) variable of the form

$$X = v + \tfrac{1}{2}t \tag{32}$$

This satisfies

$$\frac{v}{v_w} = \frac{t}{t_w} = \frac{X}{X_w}$$

Combining the energy and azimuthal momentum equations we obtain

$$\psi''' - \tfrac{3}{4}\psi\psi'' + \tfrac{1}{2}\psi'^2 = 2X \tag{33}$$

$$X'' - \tfrac{3}{4}\psi X' = 0 \tag{34}$$

$$\psi(0) = \psi'(0) = 0; \quad X(0) = X_w = v_w + \tfrac{1}{2}t_w$$

$$\psi'(\infty) = 0; \quad X(\infty) = 0 \tag{35}$$

The problem is thus reduced to that of an *equivalent incompressible* flow over a disk rotating with an azimuthal velocity difference (relative to the outer flow) larger than that of the original disk by an amount $\frac{1}{2}t_w$, i.e., $v_{w,\mathrm{eq}} = X_w = v_w + \frac{1}{2}t_w$ (or $V_{w,\mathrm{eq}} = 1 - X_w$). The physics behind this compressibility effect due to wall heating is quite clear. Wall heating ($t_w > 0$) will cause an increase in temperature and a decrease in density near the disk surface. Thus the centrifugal force is reduced near the disk surface and the driving force of the boundary-layer flow, i.e., the difference between the externally imposed pressure gradient and the centrifugal force is increased relative to the incompressible case. In other words wall heating is equivalent to a reduction in the velocity of the disk in a way quite similar to the corresponding Ekman layer [8]. Cooling the disk has of course the opposite effect.

A transformation similar to (21), with X_w replacing v_w, i.e.,

$$\psi = X_w^{1/4} F(\tilde{\eta}); \quad X = X_w G(\tilde{\eta}); \quad \eta = X_w^{-1/4}\tilde{\eta} \tag{36}$$

reduces the system (33)–(35) to the form of (22)–(24). This enables us to use the solution of (22)–(24) obtained for the incompressible flow with small v_w and shows that wall heating will increase the radial mass flux and the boundary-layer thickness by the factor $(1 + \frac{1}{2}(t_w/v_w))^{1/4}$. Moreover, the stress components and the heat transfer at the wall are increased by compressibility, as shown by

$$\psi''(0) = X_w^{3/4} F''(0); \quad v'(0) = X_w^{1/4} v_w G'(0); \quad t'(0) = X_w^{1/4} t_w G'(0) \tag{37}$$

This solution shows how a *compressible* Ekman layer is started at the edge. The condition under which the small perturbation solution fails to exist is found easily from the equivalent incompressible flow field which states that there is no similarity solution if the velocity of the disk exceeds unity, i.e., the velocity difference is less or equal to zero. In terms of physical variables this means that for

$$X_w = v_w + \tfrac{1}{2}t_w \le 0 \quad \text{or} \quad T_w \le 2V_w - 1 \tag{38}$$

no solution of the edge similarity type is possible. The physical significance of (38) is that cooling ($t_w < 0$) has an effect similar to increasing the velocity of the disk. Therefore, above a limiting value of cooling, $t_w = -2v_w$, the radial mass flux is reversed as for the flow over a faster disk. For $v_w = 0$, i.e., a disk rotating with the same velocity as the fluid, a boundary-layer flow is induced by thermal driving only if $t_w > 0$.

Finite t_w, v_w. No Dissipation, $\alpha = 0$. With the generalized variable X defined in (32) and the transformation (36) the problem is again reduced to the solution of the incompressible flow (22)–(24) with v_w replaced in (22) by $v_{w,\mathrm{eq}} = v_w^2/X_w = v_w(1 + \frac{1}{2}(t_w/v_w))^{-1}$. Thus, in addition to the compressibility effect defined by the transformation (32) which was explained before, we find also a decrease of the centrifugal term in the radial momentum balance. In terms of the corresponding incompressible case, it is equivalent to an increase of the azimuthal velocity of the disk—an effect opposing the first one described by (36).

Thus nonlinearity tends to decrease the main compressibility effect due to wall heating. The existence condition (38) is still valid. It is interesting to note that for wall cooling ($t_w < 0$) the velocity of the equivalent disk in incompressible flow is reduced ($v_{w,\mathrm{eq}}$ increased) and eventually it may become negative ($v_{w,\mathrm{eq}} > 1$), i.e., the equivalent disk is rotating in opposite sense to the original one! Clearly, the rotation in the physical space does not change. Let us illustrate the solution by means of a numerical example: We consider a stationary disk $v_w = 1$ heated to a temperature 50 percent higher than that of the external fluid, i.e., $t_w = 0.5$. In this case the velocity difference of the disk in the equivalent incompressible flow is $v_{w,\mathrm{eq}} = 0.8$ ($V_{w,\mathrm{eq}} = 0.2$) and the generalized variable at the wall is $X_w = 1.25$. The numerical values of interest are

$$\psi(\infty) = -1.8036, \quad \psi''(0) = -1.3763,$$
$$v'(0) = -0.4738, \quad t'(0) = -0.2368.$$

These values (confirmed by a fully numerical computation) should be compared with those given in the foregoing for an incompressible flow over a stationary disk. It is clear that the first effect is stronger than the second; thus the overall effect of compressibility and wall heating is to increase mass, heat, and momentum transport in the boundary layer. It is possible to solve in a similar way the general case with dissipation.

Finite t_w, v_w With Dissipation. The generalized variable now takes the form

$$X = v + \tfrac{1}{2}t + \tfrac{1}{4}\alpha v^2 \tag{39}$$

and the relation between temperature and azimuthal velocity is

$$t = \frac{t_w}{v_w} v + \tfrac{1}{2}\alpha v(v_w - v) \tag{40}$$

The transformation (36) with $X_w = v_w + \frac{1}{2}t_w + \frac{1}{4}\alpha v_w^2$ will reduce also this problem to the solution of an equivalent incompressible flow of the type (22)–(24). The velocity of the equivalent disk is now

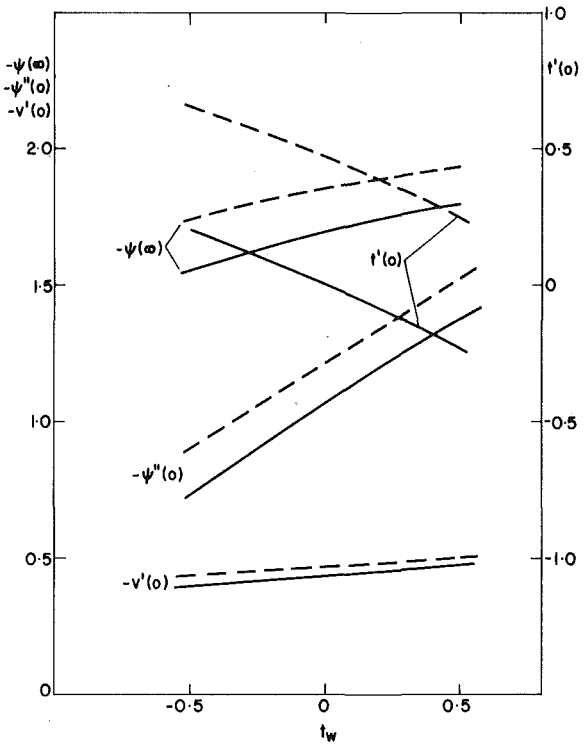

Fig. 3 Compressible flow — $\alpha = 0$; - - - - $\alpha = 2$

$$v_{w,\mathrm{eq}} = \frac{v_w^2(1+\frac{1}{2}\alpha)}{X_w} = v_w \frac{1+\frac{1}{2}\alpha}{1+\frac{1}{2}\frac{t_w}{v_w}+\frac{1}{4}\alpha v_w} \tag{41}$$

The influence of dissipation is equivalent to an additional wall heating, i.e., an increase of the wall temperature by the amount $\frac{1}{2}\alpha v_w^2$. For $\alpha \to 0$ this solution reduces to that of wall heating without dissipation. For highly dissipative systems or when the wall heating is negligible $v_{w,\mathrm{eq}}$ may exceed unity, i.e., the "equivalent disk" is rotating in an opposite sense to that of the physical problem. Let us consider a numerical example: a stationary disk ($v_w = 1$) without wall heating ($t_w = 0$) and unit Eckert number ($\alpha = 1$). The equivalent disk velocity is now $v_{w,\mathrm{eq}} = 1.2$, i.e., the equivalent disk is rotating in the opposite sense with $V_{w,\mathrm{eq}} = -0.2$. Using the numerical results of Bodonyi and Stewartson [6] for opposite rotating incompressible flow we obtain

$$\psi(\infty) = -1.7728; \quad \psi''(0) = -1.1115; \quad v'(0) = -0.4558; \quad t'(0) = 0.2279$$

These values were checked by a fully numerical computation of (16)–(19). This example illustrates that the equivalence between thermal and shear driving in this rotating flow can be extended to the "opposite rotation" range. In other words a sufficiently high heating (due to dissipation in this case) will be equivalent, from the point of view of the second (nonlinear) compressibility effect, to applying an additional counter-rotation to the disk.

Numerical results are presented in Fig. 3 for $\alpha = 0$ and 2 as plots of the mass, momentum, and heat-transfer coefficients versus wall temperature t_w. From these graphs it is seen that the effect of cooling or heating the disk to 50 percent and 150 percent of the fluid temperature, respectively, is almost linear for all transport coefficients, and from other numerical results (not shown) the same is true for dissipation effects up to $\alpha = 2$. The heat-transfer coefficient is the most affected by compressibility and the tangential stress is only slightly changed by wall heating and dissipation.

The existence conditions for the general case with $\sigma = 1$, obtained from the equivalent incompressible flow, is $v_{w,\mathrm{eq}} > 0$. Thus, for $v_{w,\mathrm{eq}} < 0$, i.e.,

$$X_w = v_w + \tfrac{1}{2}t_w + \tfrac{1}{4}\alpha v_w < 0$$

there will be no boundary-layer solution of edge similarity type. For a disk rotating with the same velocity as the external fluid ($v_w = 0$) a boundary-layer flow exists if the disk is heated. Another limitation to be considered—again from the equivalence with the incompressible flow—is that found by Bodonyi and Stewartson in [6] for an opposite sense of rotation of the disk, which states that for $v_w \gtrsim 3.066$ ($V_w < -2.066$) there will be no similarity solution. Applying it to the general case we obtain the existence condition

$$v_{w,\mathrm{eq}} = \frac{1+\frac{1}{2}\alpha}{1+\frac{1}{2}\frac{t_w}{v_w}+\frac{1}{4}\alpha v_w} < 3.066$$

which states that the solution exists when the disk is cooled up to a certain limit, depending upon its velocity and Eckert number value.

$\sigma \to 0$. We have two layers: an inner, viscous, layer $\eta = 0(1)$ and an outer, thermal layer $\eta = 0(\sigma^{-1})$. Within the inner layer temperature changes are $0(\sigma)$ and therefore negligible in the momentum equations. The solution of the inner layer must satisfy the boundary conditions at $\eta = 0$.

In the outer layer we define a new coordinate $\eta_0 = \sigma\eta$ to obtain the equations which constitute a geostrophic momentum balance and a thermal conduction—convection balance.

$$2v - v^2 + t = 0; \quad \psi = \text{constant}$$

$$t'' - \tfrac{3}{4}\psi t' = 0 \tag{42}$$

with the boundary conditions at $\eta_0 \to \infty$. Matching with the inner layer yields the boundary conditions at $\eta_0 = 0$ for the outer layer and those at $\eta \to \infty$ for the inner one. These conditions for the inner layer read

$$\psi'(\infty) = 0; \quad v(\infty) = 1 - (1+t_w)^{1/2}; \quad t(\infty) = t_w + 0(\sigma) \tag{43}$$

Note that the azimuthal velocity has an overshoot at the edge of the inner layer. The inner solution can now be found by reducing the problem to an equivalent incompressible flow (34)–(37):

$$\psi = (1+t_w)^{1/4} v_{w,\mathrm{eq}}^{1/4} F(\tilde{\eta}); \quad v = 1 - [1 - v_{w,\mathrm{eq}} G(\tilde{\eta})](1+t_w)^{1/2}$$

$$\eta = \tilde{\eta}(1+t_w)^{-1/4} v_{w,\mathrm{eq}}^{-1/4} \tag{44}$$

$$v_{w,\mathrm{eq}} = 1 - (1-v_w)(1+t_w)^{-1/2} \quad \text{or} \quad V_{w,\mathrm{eq}} = V_w T_w^{-1/2} \tag{45}$$

Compressibility effects on the flow field in this case come mainly from wall heating because dissipation effects are $0(\sigma)$ and their influence is limited to heat transfer at the wall. Increasing wall temperature is equivalent to a decrease of the velocity of the disk and correspondingly an increase of the mass and momentum transport in the boundary layer. Cooling ($t_w < 0$, $T_w < 1$) has an opposite effect, i.e., it is equivalent to an increase of the velocity of the disk.

The existence conditions are found from the equivalent incompressible flow which requires that $v_{w,\mathrm{eq}} > 0$, i.e.,

$$1 - v_w < (1+t_w)^{1/2} \quad \text{or} \quad V_w < T_w^{1/2}$$

(Although (17) does not hold in this case for the *equivalent* flow and the azimuthal velocity is not monotonic, the existence condition is still valid.) The solution of the energy equation is quite similar to that of the incompressible case. The temperature is obtained by matching inner and outer values of the function $t(\eta)$ and its derivative at $\eta \to \infty$, $\eta_0 \to 0$. The final result for the heat transfer at the wall is

$$t'(0) = \tfrac{3}{4}\sigma(1+t_w)^{1/4} V_{w,\mathrm{eq}}^{1/4} F(\infty) t_w - \alpha\sigma(1+t_w)^{5/4} v_{w,\mathrm{eq}}^{9/4} \int_0^\infty d\tilde{\eta} G'^2(\tilde{\eta}) \tag{46}$$

The first term on the right-hand side of (46) is contributed by wall heating and the second by dissipation. Thus the inner layer is almost isothermal (at wall temperature) in this case, the main compressibility factor being the wall heating, while dissipation affects only the heat

transfer at the disk surface. The outer layer is characterized by a geostrophic (momentum) balance and its main function is to adjust the azimuthal velocity overshoot at the edge of the inner layer and the temperature difference between the disk and outer fluid.

$\sigma \to \infty$. *Wall Heating, No Dissipation.* The solution is quite similar to that of the incompressible case. In the outer layer $\eta = 0(1)$ the energy equation is reduced to $t' = 0$ with the boundary condition $t(\infty) = 0$ i.e., the outer layer is isothermal which means, in our case, incompressible. The temperature variations take place within the inner layer $\eta = 0(\sigma^{-1/3})$. Using the inner layer variable $\eta_i = \sigma^{1/3}\eta$ and the definition (25) of θ_h, the incompressible flow and its solution (28) are recovered. Formally, the flow variables are obtained from an expansion in negative powers of σ, viz.,

$$\psi = \sigma^{-2/3}\psi_1(\eta_i) + \sigma^{-1}\psi_2(\eta_i) + \ldots \tag{47}$$

$$v = v_w + \sigma^{-1/3}v_1(\eta_i) + \ldots \tag{48}$$

The solution of the first-order flow equations is

$$\psi_1 = \tfrac{1}{2}\psi''(0)\eta^2; \qquad v_1 = v'(0)\eta \tag{49}$$

and the solution of the leading order energy equation is identical with that of the incompressible case. In conclusion, for large Prandtl number, compressibility effects due to wall heating are not felt in the first-order solution due to the fact that the outer (momentum) layer is isothermal (i.e., incompressible), the inner (thermal) layer is very thin and its flow values are imposed by the outer layer.

Concluding Remarks

Compressible edge-similarity solutions were found for a wide range of the governing parameters V_w, T_w, α, and σ and existence conditions were established. These solutions can be used to start computations of the rotating flow field over a finite disk; even in cases for which the solutions for the central part of the disk are not of boundary-layer type. This applies also to heat transfer problems in shrouded disk systems for both compressible and incompressible flow.

For the small-perturbation, incompressible case, the viscous boundary-layer thickness and the radial mass flow are related to $v_w^{1/4}$. In our case v_w is the Rossby number and the solution shows how an Ekman layer starts at the edge of the disk. It turns out that for finite perturbations, the flow variables (stresses at the disk surface, radial mass flow) when normalized by suitable power of v_w in the same manner as the small perturbation case, show an almost linear dependence on v_w up to $v_w \sim 2$ even when the disk is rotating in opposite sense to the fluid.

For a compressible flow, wall heating and dissipation effects are equivalent to a decrease in the velocity of the disk thus increasing stresses and mass flow. Wall heating and dissipation effects are equivalent to a negative increment of the velocity of the disk in a virtual incompressible flow. Thus thermally driven flows can be produced even when the disk is rotating with the same or higher velocity than the outer fluid provided the disk is heated to a sufficiently high temperature. Cooling the disk has an opposite effect, equivalent to an increase of the velocity of the disk thus suppressing the boundary-layer flow.

Acknowledgment

This research was partially supported by the Technion Fund for the Encouragement of Research (Grant No. 030-278).

References

1 Schultz-Grunow, F., "Der Reibungswiderstand rotierender Scheiben in Gehäusen," *Zeitschrift für Angewandte Mathematik und Mechanik*, Vol. 15, 1935, pp. 191–204.

2 Stewartson, K., *On Rotating Laminar Boundary Layers*, Freiberg Symposium Boundary Layer Research, Springer-Verlag, 1958, pp. 59–71.

3 Bodonyi, R. J., and Stewartson, K., "Boundary-Layer Similarity Near the Edge of a Rotating Disk," ASME JOURNAL OF APPLIED MECHANICS, Vol. 42, 1975, pp. 584–590.

4 Mack. L. M., "The Laminar Boundary Layer on a Disk of Finite Radius in a Rotating Flow—Part 1," Jet Propulsion Laboratory, Pasadena, Calif., T.R. 32-324, May 1962.

5 Rogers, M. H., and Lance, G. N., "The Boundary Layer on a Disk of Finite Radius in a Rotating Fluid," *Quarterly Journal of Mechanics and Applied Mathematics*, Vol. 17, Part 3, 1964, pp. 319–330.

6 Belcher, R. J., Burggraf, O. R., and Stewartson, K., "On Generalized-Vortex Boundary Layers," *Journal of Fluid Mechanics*, Vol. 52, Part 4, 1972, pp. 753–780.

7 Toren, M., and Solan, A., "Laminar Boundary Layer on a Finite Disk in a Rotating Compressible Isothermal Flow," ASME *Journal of Fluids Engineering*, Vol. 101, June 1979, pp. 166–172.

8 Riley, N., "Thermally Induced Boundary-Layer Flows in a Rotating Environment," *Journal of Fluid Mechanics*, Vol. 29, Part 2, 1967, pp. 241–257.

9 Olander, R. D., "Unsteady Heat and Mass Transfer in the Rotating-Disk—Revolving—Fluid System," *International Journal of Heat and Mass Transfer*, Vol. 5, 1962, pp. 825–836.

10 Stewartson, K., *The Theory of Laminar Boundary Layers in Compressible Fluids*, Oxford Mathematical Monographs, Oxford, 1965.

11 Riley, N., "The Heat Transfer From a Rotating Disk," *Quarterly Journal of Mechanics and Applied Mathematics*, Vol. XVII, Pt. 3, 1964, pp. 331–349.

12 Abramovitz, M., and Stegun, J., eds., *Handbook of Mathematical Functions*, Dover Publications, Inc., New York, p. 260.

J. N. Tokis
Professor,
Department of Physics,
Higher School of Engineering
Technologists of KATEE,
Koukouli, Patras, Greece

G. C. Pande
Visiting Professor,
Department of Mechanics,
University of Patras,
Patras, Greece

Unsteady Hydromagnetic Flow Near a Moving Porous Plate

Unsteady two-dimensional flow of a viscous incompressible and electrically conducting fluid near a moving porous plate of infinite extent in presence of a transverse magnetic field is investigated. Solution of the problem in closed form is obtained with the help of Laplace transform technique, when the plate is moving with a velocity which is an arbitrary function of time and the magnetic Prandtl number is unity. Three particular cases of physical interest are also discussed.

1 Introduction

The study concerning the effect of fluctuations of the external stream on unsteady hydromagnetic boundary-layer flow has stimulated considerable interest due to its important applications in cosmic fluid dynamics, meteorology, solar physics and in the motions of the Earth's core (Cramer and Pai [1]).

This important phenomenon was studied by many authors by formulating simple models and studying the behavior either for hydrodynamic or magnetohydrodynamic case. Some of the authors are Rossow [2], Watson [3], Ludford [4], and Axford [5].

Recently, Puri and Kulshrestha [6] investigated the motion of unsteady hydromagnetic boundary-layer flow in a rotating medium ignoring the effect of induced magnetic field. This problem in the absence of rotation has been studied by Tokis [7]. Pande, et al. [8, 9], studied similar problem by formulating a simple idealized model system in which the induced magnetic field is not neglected, and it is shown that how does the induced magnetic field affect the motion.

In the present paper, we generalize the works of Pande, et al. [9], and Tokis [7] for the case in which we envisage two distinct effects of the magnetic field and the porosity (injection/suction) as a coupled moving system. General solution of the problem is obtained with the help of the Laplace transform when the magnetic Prandtl number is unity. Further, in order to demonstrate the application of the results obtained here, we consider three cases, e.g., impulsive motion, accelerated motion, and decaying oscillatory motion. These motions prescribe physically acceptable different time-dependent forms to arbitrary velocity $-U_0 f(t)$ of the porous plate or of the arbitrary velocity $U_0 f(t)$ of external stream, where U_0 is a constant velocity and $f(t)$ a nondimensional function of the time t. Finally, the results thus obtained are discussed in Section 6.

Contributed by the Applied Mechanics Division for publication in the JOURNAL OF APPLIED MECHANICS.

Discussion on this paper should be addressed to the Editorial Department, ASME, United Engineering Center, 345 East 47th Street, New York, N. Y. 10017, and will be accepted until September 1, 1981. Readers who need more time to prepare a Discussion should request an extension from the Editorial Department. Manuscript received by ASME Applied Mechanics Division, August, 1980.

2 Mathematical Analysis

We take the coordinate origin O at an arbitrary point on an infinite porous plate, which is taken to be an electrical insulator. Cartesian coordinate system has been used with axes Ox' and Oy' along and perpendicular to the plate, respectively. We consider an electrically conducting, viscous, incompressible fluid filling the semi-infinite space $y' > 0$; which is in contact with the plate at $y' = 0$. The plate is initially at rest and then it is suddenly accelerated with a velocity $-U_0 f(t')$, in its own plane along the negative x'-axis (Puri and Kulshrestha [6]). On the physical ground of the problem all the quantities are assumed to be functions of the space coordinate y' and time t' only; so that the velocity $\mathbf{V}'$ and the magnetic field $\mathbf{B}'$ are given, respectively, by $(u', v', 0)$ and $(B_{x'}', B_{y'}', 0)$.

The equation of continuity, on integration, gives

$$v' = \text{constant} = v_0' \text{ (say)},$$

where v_0' is the constant normal velocity of suction or injection at the plate according as $v_0' < 0$ or >0, respectively. Also, the divergence equation for the magnetic field gives

$$B_{y'}' = \text{constant} = B_0' \text{ (say)}$$

where B_0' is the externally applied transverse magnetic field. Under these assumptions the basic equations relevant to the problem are (Ludford [4]).

$$\frac{\partial u'}{\partial t'} + v_0' \frac{\partial u'}{\partial y'} = \nu \frac{\partial^2 u'}{\partial y'^2} + \frac{B_0'}{\rho \mu_0} \frac{\partial B_{x'}'}{\partial y'}, \tag{1}$$

$$\frac{\partial B_{x'}'}{\partial t'} + v_0' \frac{\partial B_{x'}'}{\partial y'} = \frac{1}{\sigma \mu_0} \frac{\partial^2 B_{x'}'}{\partial y'^2} + B_0' \frac{\partial u'}{\partial y'}, \tag{2}$$

$$j' = -\frac{1}{\mu_0} \frac{\partial B_{x'}'}{\partial y'}, \tag{3}$$

where j' denotes the component of electrical current density in z'-direction, ρ the fluid density, ν the kinematic coefficient of viscosity of the fluid, and μ_0 and σ are the permeability and the electrical conductivity of the fluid, respectively.

Assuming that no slipping occurs between the plate and the fluid, the appropriate initial and the boundary conditions are (also, see Puri and Kulshrestha [6])

$$u'(y',0) = 0 \quad \text{for} \quad y' \geq 0, \tag{4a}$$

$$u'(0,t') = -U_0 f(t'), \tag{4b}$$

$$u'(\infty,t') \to 0, \tag{4c}$$

where $f(t')$ is an arbitrary function of time and U_0 is a constant velocity. The appropriate boundary conditions on $\mathbf{B}'$ are

$$B_{x'}'(0,t') = 0, \quad B_{y'}'(0,t') = B_0', \tag{5a,b}$$

$$B_{x'}'(\infty,t') \to 0, \quad B_{y'}'(\infty,t') \to B_0'. \tag{6a,b}$$

On using the following nondimensional transformations

$$y = \frac{U_0}{\nu} y', \quad t = \frac{U_0^2}{\nu} t', \quad \mathbf{v} = \frac{\mathbf{v}'}{U_0}, \tag{7a,b,c}$$

$$B = \frac{B_{x'}'}{U_0(\rho\mu_0)^{1/2}}, \quad j = \frac{\nu}{U_0^2}\left(\frac{\mu_0}{\rho}\right)^{1/2} j', \tag{8a,b}$$

$$p,q = \frac{u'}{U_0} \pm \frac{B_{x'}'}{U_0(\rho\mu_0)^{1/2}} \equiv u \pm B, \tag{9a,b}$$

$$m_1,m_2 = \frac{v_0'}{U_0} \pm \frac{B_0'}{U_0(\rho\mu_0)^{1/2}} \equiv v_0 \pm B_0, \tag{10a,b}$$

and assuming that the magnetic Prandtl number $P_m(=\nu\sigma\mu_0) = 1$, which is a plausible assumption in most of the hydromagnetic problems, equations (1) and (2) then become

$$\frac{\partial^2 p}{\partial y^2} - m_2 \frac{\partial p}{\partial y} - \frac{\partial p}{\partial t} = 0, \tag{11}$$

$$\frac{\partial^2 q}{\partial y^2} - m_1 \frac{\partial q}{\partial y} - \frac{\partial q}{\partial t} = 0, \tag{12}$$

which are to be solved under the boundary conditions

$$p(0,t) = q(0,t) = -f(t), \tag{13}$$

$$p(\infty,t) \to 0, \quad q(\infty,t) \to 0. \tag{14}$$

With the aid of (9) solving the equations (11) and (12) under the boundary conditions (13) and (14) with the help of the Laplace transform technique, we obtain

$$\bar{u},\bar{B} = -\frac{1}{2}\bar{f}(s)\left[\exp\left\{y\left(\frac{m_1}{2} - \left(\frac{m_1^2}{4} + s\right)^{1/2}\right)\right\} \pm \exp\left\{y\left(\frac{m_2}{2} - \left(\frac{m_2^2}{4} + s\right)^{1/2}\right)\right\}\right], \tag{15a,b}$$

where a bar over a quantity denotes its Laplace transform defined as

$$\bar{f}(s) = \int_0^\infty e^{-st} f(t)\,dt.$$

In order to determine u and B, we must find out the inverse Laplace transform of (15). We note that the right-hand side of the expression (15) is the product of the two functions of s; one of which, $\bar{f}(s)$ has a known inverse $f(t)$. Thus u and B are best obtained by using the composition product rule (also known as Duhamel theorem), namely, that

$$u(y,t) = \int_0^t u_*(y,z) f(t-z)\,dz, \tag{16a}$$

$$B(y,t) = \int_0^t B_*(y,z) f(t-z)\,dz, \tag{16b}$$

where

$$u_*(y,t),B_*(y,t) = -\frac{\mathrm{H}(t)}{4\sqrt{\pi}} y t^{-3/2}\left[\exp\left(\frac{m_1 y}{2} - \frac{m_1^2 t}{4}\right) \pm \exp\left(\frac{m_2 y}{2} - \frac{m_2^2 t}{4}\right)\right]\exp\left(-\frac{y^2}{4t}\right), \tag{17a,b}$$

$\mathrm{H}(t)$ is the Heaviside Unit function. The expressions (17) have been obtained by taking the inverse Laplace transform of (15) for the case when $f(t) = \delta(t)$; $\delta(t)$ is the Dirac delta function.

To demonstrate the applications of the results obtained in this section, we shall now consider three particular cases, in the subsequent three sections, by perscribing physically acceptable forms to $f(t)$.

3 Impulsive Motion

The case of a single impulse is considered. This corresponds to

$$f(t) = \mathrm{H}(t). \tag{18}$$

On substituting (18) into (16), we obtain the expressions for the velocity and the magnetic field as

$$u(y,t),B(y,t) = -\frac{\mathrm{H}(t)}{4}\left[\left\{\exp(m_1 y)\,\mathrm{erfc}\left(\frac{y}{2t^{1/2}} + \frac{m_1 t^{1/2}}{2}\right) + \mathrm{erfc}\left(\frac{y}{2t^{1/2}} - \frac{m_1 t^{1/2}}{2}\right)\right\} \pm \left\{\exp(m_2 y)\,\mathrm{erfc}\left(\frac{y}{2t^{1/2}} + \frac{m_2 t^{1/2}}{2}\right) + \mathrm{erfc}\left(\frac{y}{2t^{1/2}} - \frac{m_2 t^{1/2}}{2}\right)\right\}\right]. \tag{19a,b}$$

Knowing $u(y,t)$ and $B(y,t)$ from (19), we can now calculate expressions for the skin-friction and the electrical current density, in their nondimensional forms, as

$$\tau = \frac{\tau'}{\rho U_0^2} = -\frac{\mathrm{H}(t)}{4}\left[m_1\,\mathrm{erfc}\left(\frac{m_1 t^{1/2}}{2}\right) + m_2\,\mathrm{erfc}\left(\frac{m_2 t^{1/2}}{2}\right) - \frac{2}{(\pi t)^{1/2}}\left\{\exp\left(-\frac{m_1^2 t}{4}\right) + \exp\left(-\frac{m_2^2 t}{4}\right)\right\}\right], \tag{20}$$

$$j = \frac{\mathrm{H}(t)}{4}\left[m_1 \exp(m_1 y)\,\mathrm{erfc}\left(\frac{y}{2t^{1/2}} + \frac{m_1 t^{1/2}}{2}\right) - m_2 \exp(m_2 y)\,\mathrm{erfc}\left(\frac{y}{2t^{1/2}} + \frac{m_2 t^{1/2}}{2}\right) - \frac{2}{(\pi t)^{1/2}}\exp\left(\frac{y^2}{4t}\right)\left\{\exp\left(-\frac{m_1^2 t}{4}\right)\cosh\left(\frac{m_1 y}{2}\right) - \exp\left(-\frac{m_2^2 t}{4}\right)\cosh\left(\frac{m_2 y}{2}\right)\right\}\right]. \tag{21}$$

4 Accelerated Motion

Considering now an accelerated plate motion which corresponds to

$$f(t) = \frac{t}{t_0}\mathrm{H}(t), \tag{22}$$

where t_0 is a constant. In this case the expressions for the velocity and the magnetic field are given with the aid of (22) and (16), by

$$u(y,t),B(y,t) = -\frac{\mathrm{H}(t)}{4t_0}\left[\left\{\left(t + \frac{y}{m_1}\right)\exp(m_1 y) \times \mathrm{erfc}\left(\frac{y}{2t^{1/2}} + \frac{m_1 t^{1/2}}{2}\right) + \left(t - \frac{y}{m_1}\right)\mathrm{erfc}\left(\frac{y}{2t^{1/2}} - \frac{m_1 t^{1/2}}{2}\right)\right\} \pm \left\{\left(t + \frac{y}{m_2}\right)\exp(m_2 y)\,\mathrm{erfc}\left(\frac{y}{2t^{1/2}} + \frac{m_2 t^{1/2}}{2}\right) + \left(t - \frac{y}{m_2}\right)\mathrm{erfc}\left(\frac{y}{2t^{1/2}} - \frac{m_2 t^{1/2}}{2}\right)\right\}\right]. \tag{23a,b}$$

The expressions for the skin-friction and the current density are then given, respectively, by

$$\tau = -\frac{\mathrm{H}(t)}{4t_0}\left[m_1 t\,\mathrm{erfc}\left(\frac{m_1 t^{1/2}}{2}\right) + m_2 t\,\mathrm{erfc}\left(\frac{m_2 t^{1/2}}{2}\right) - \left(\frac{2}{m_1}\right)\mathrm{erf}\left(\frac{m_1 t^{1/2}}{2}\right) - \left(\frac{2}{m_2}\right)\mathrm{erf}\left(\frac{m_2 t^{1/2}}{2}\right) - 2\left(\frac{t}{\pi}\right)^{1/2}\left\{\exp\left(-\frac{m_1^2 t}{4}\right) + \exp\left(-\frac{m_2^2 t}{4}\right)\right\}\right], \tag{24}$$

$$j = \frac{H(t)}{4t_0}\left[\left(\frac{1}{m_1} + m_1 t + y\right)\exp(m_1 y)\,\mathrm{erfc}\left(\frac{y}{2t^{1/2}} + \frac{m_1 t^{1/2}}{2}\right)\right.$$
$$- \frac{(m_1 t + y)}{m_1(\pi t)^{1/2}}\exp\left(-\frac{m_1^2 t + y^2/t}{4}\right)$$
$$- \left(\frac{1}{m_2} + m_2 t + y\right)\exp(m_2 y)\,\mathrm{erfc}\left(\frac{y}{2t^{1/2}} + \frac{m_2 t^{1/2}}{2}\right)$$
$$+ \frac{(m_2 t + y)}{m_2(\pi t)^{1/2}}\exp\left(-\frac{m_2^2 t + y^2/t}{4}\right) - \frac{1}{m_1}\mathrm{erfc}\left(\frac{y}{2t^{1/2}}\,\frac{m_1 t^{1/2}}{2}\right)$$
$$- \frac{m_1 t - y}{m_1(\pi t)^{1/2}}\exp\left\{-\frac{(y/t^{1/2} - m_1 t^{1/2})^2}{4}\right\} + \frac{1}{m_2}\mathrm{erfc}\left(\frac{y}{2t^{1/2}} - \frac{m_2 t^{1/2}}{2}\right)$$
$$\left. + \frac{m_2 t - y}{m_2(\pi t)^{1/2}}\exp\left\{-\frac{(y/t^{1/2} - m_2 t^{1/2})^2}{4}\right\}\right]. \quad (25)$$

5 Decaying Oscillatory Motion

We consider the case of decaying oscillatory velocity of the plate. This corresponds to

$$f(t) = \mathrm{Re}[H(t)e^{-(\lambda^2 - i\omega)t}], \quad (26)$$

where λ and ω are real dimensionless constants. On using (26) into the equations (16), we get

$$u(y,t), B(y,t) = -\frac{H(t)}{4}\mathrm{Re}\left[e^{-(\lambda^2 - i\omega)t}\right.$$
$$\times\left\{\left(\exp\left\{y\left(\frac{m_1}{2} - a_1 - ib_1\right)\right\}\mathrm{erfc}\left\{\frac{y}{2t^{1/2}} - (a_1 + ib_1)t^{1/2}\right\}\right.\right.$$
$$+ \exp\left\{y\left(\frac{m_1}{2} + a_1 + ib_1\right)\right\}\mathrm{erfc}\left\{\frac{y}{2t^{1/2}} + (a_1 + ib_1)t^{1/2}\right\}\Big)$$
$$\pm\left(\exp\left\{y\left(\frac{m_2}{2} - a_2 - ib_2\right)\right\}\mathrm{erfc}\left\{\frac{y}{2t^{1/2}} - (a_2 + ib_2)t^{1/2}\right\}\right.$$
$$\left.\left.\left. + \exp\left\{y\left(\frac{m_2}{2} + a_2 + ib_2\right)\right\}\mathrm{erfc}\left\{\frac{y}{2t^{1/2}} + (a_2 + ib_2)t^{1/2}\right\}\right)\right\}\right], \quad (27a,b)$$

where a_1, b_1, a_2, and b_2 are constants and are given by

$$a_1, b_1 = \frac{1}{\sqrt{2}}\left[\left\{\left(\frac{m_1^2}{4} - \lambda^2 + \omega\right)^2 + \left(\frac{m_1^2}{4} - \lambda^2\right)^2\right\}^{1/2}\right], \quad (28a,b)$$

$$a_2, b_2 = \frac{1}{\sqrt{2}}\left[\left\{\left(\frac{m_2^2}{4} - \lambda^2 + \omega\right)^2 + \left(\frac{m_2^2}{4} - \lambda^2\right)^2\right\}^{1/2}\right]. \quad (29a,b)$$

Now, the nondimensional forms of the skin friction and the current density are, respectively, given by

$$\tau = \frac{H(t)}{2}\mathrm{Re}\left\{\left[(a_1 + ib_1)\,\mathrm{erf}\{(a_1 + ib_1)t^{1/2}\}\right.\right.$$
$$+ (a_2 + ib_2)\,\mathrm{erf}\{(a_2 + ib_2)t^{1/2}\} - v_0$$
$$\left.\left. + \frac{1}{(\pi t)^{1/2}}\{\exp[-(a_1 + ib_1)^2 t] + \exp[-(a_2 + ib_2)^2 t]\}\right]\right.$$
$$\left.\times\exp(-(\lambda^2 - i\omega)t)\right\}, \quad (30)$$

$$j = \frac{H(t)}{4}\mathrm{Re}\left\{\exp\{-(\lambda^2 - i\omega)t\}\left[\exp\left\{y\left(\frac{m_1}{2} - a_1 - ib_1\right)\right\}\right.\right.$$
$$\times\left\{\left(\frac{m_1}{2} - a_1 - ib_1\right)\mathrm{erfc}\left\{\frac{y}{2t^{1/2}} - (a_1 + ib_1)t^{1/2}\right\}\right.$$
$$- \frac{1}{(\pi t)^{1/2}}\exp\left\{-\left(\frac{y}{2} - a_1 t - ib_1 t\right)^2/t\right\}\Big\}$$
$$+ \exp\left\{y\left(\frac{m_1}{2} + a_1 + ib_1\right)\right\}\left\{\left(\frac{m_1}{2} + a_1 + ib_1\right)\right.$$
$$\times\mathrm{erfc}\left\{\frac{y}{2t^{1/2}} + (a_1 + ib_1)t^{1/2}\right\} - \frac{1}{(\pi t)^{1/2}}\exp\left\{-\left(\frac{y}{2} + a_1 t + ib_1 t\right)^2/t\right\}\Big\}$$
$$\left.\left. - \exp\left\{y\left(\frac{m_2}{2} - a_2 - ib_2\right)\right\}\left\{\left(\frac{m_2}{2} - a_2 - ib_2\right)\right.\right.$$
$$\times\mathrm{erfc}\left\{\frac{y}{2t^{1/2}} - (a_2 + ib_2)t^{1/2}\right\} - \frac{1}{(\pi t)^{1/2}}\exp\left\{-\left(\frac{y}{2} - a_2 t - ib_2 t\right)^2/t\right\}\Big\}$$
$$- \exp\left\{y\left(\frac{m_2}{2} + a_2 + ib_2\right)\right\}\left\{\left(\frac{m_2}{2} + a_2 + ib_2\right)\right.$$
$$\times\mathrm{erfc}\left\{\frac{y}{2t^{1/2}} + (a_2 + ib_2)t^{1/2}\right\} - \frac{1}{(\pi t)^{1/2}}\exp\left\{-\left(\frac{y}{2} + a_2 t + ib_2 t\right)^2/t\right\}\Big\}\Big]\Big\}. \quad (31)$$

(*Cont.*)

6 Conclusion

When the plate is started impulsively the expressions for velocity, magnetic field, skin-friction, and electrical current density are given, respectively, by (19*a*,*b*), (20), and (21). We observe that in the absence of the magnetic field, and with a slight adjustment, the expressions (19*a*) and (20) are identical with those of Watson [3]. Also, it is interesting to note that for large values of t, the expression for the velocity is not affected by the presence of the magnetic field.

In the case of accelerated motion, the discussion of the results of steady-state solution is the same as has been discussed earlier. Since these results and discussion are similar to those of Watson [3], we feel that any further discussion here about them is, therefore, unnecessary.

Finally, in the decaying oscillatory motion, the steady-state solution is obtained by taking $\lambda = 0$; which corresponds to the problem of flow near an oscillating porous plate. In this case the expressions for the velocity and the magnetic field (27*a*,*b*), respectively, reduce to

$$u(y,t), B(y,t) = -\frac{1}{2}\left[\exp\left\{\left(\frac{m_1}{2} - a_1\right)y\right\}\right.$$
$$\times\cos(\omega t - b_1 y) \pm \exp\left\{\left(\frac{m_2}{2} - a_2\right)y\right\}$$
$$\left.\times\cos(\omega t - b_2 y)\right], \quad (32a,b)$$

and also, the skin-friction and electrical current density for this case are given by

$$\tau = \frac{1}{2}[(a_1 + a_2 - v_0)\cos\omega t - (b_1 + b_2)\sin\omega t], \quad (33)$$

$$j = \frac{1}{2}\exp\left\{\left(\frac{m_1}{2} - a_1\right)y\right\}\left[\left(\frac{m_1}{2} - a_1\right)\cos(\omega t - b_1 y)\right.$$
$$\left. + b_1\sin(\omega t - b_1 y)\right]$$
$$- \frac{1}{2}\exp\left\{\left(\frac{m_2}{2} - a_2\right)y\right\}\left[\left(\frac{m_2}{2} - a_2\right)\cos(\omega t - b_2 y)\right.$$
$$\left. + b_2\sin(\omega t - b_2 y)\right]. \quad (34)$$

We observe that the expressions (32)–(34) are identical with those obtained by Pande, et al. [9].

Here we see that two boundary layers (or hydromagnetic boundary layers, since $P_m = 1$) exist whose thicknesses depend on the velocity of suction/injection and the strength of the applied magnetic field besides depending on some other parameters as well. In the absence of magnetic field the two boundary layers coalesce into one. We also observe that the oscillations of the plate produce wavelike disturbances within the boundary layers and the velocity decays exponentially as the distance from the plate increases. Other conclusions and discussions regarding the behaviors of the induced magnetic field, the skin friction, and the electrical current density inside the boundary layers are self-evident from the foregoing expressions and hence any further discussion about them seems to be redundant.

References

1 Cramer, K. P., and Pai, Shih-I, *Magnetofluid Dynamics for Engineers and Applied Physicists*, McGraw-Hill, New York, 1973, p. 205.

2 Rossow, V. J., "On Flow of Electrically Conducting Fluids Over a Flat Plate in the Presence of a Transverse Magnetic field," NASA Technical Note 3971, 1957.

3 Watson, J., "A Solution of the Navier-Stokes Equations Illustrating the Response of Laminar Boundary Layer to a Given Change in the External Stream Velocity," *Quarterly Journal of Mechanics and Applied Mathematics*, Vol. 11, 1958, pp. 302–325.

4 Ludford, G. S. S., "Rayleigh's Problem in Hydromagnetics: The Impulsive Motion of a Polepiece," *Archive Rat. Mech. Analysis*, Vol. 3, 1959, pp. 14–27.

5 Axford, W. I., "The Oscillating Plate Problem in Magnetohydrodynamics," *Journal of Fluid Mechanics*, Vol. 8, 1960, pp. 97–102.

6 Puri, P., and Kulshrestha, P. K., "Unsteady Hydromagnetic Boundary Layer in a Rotating Medium," ASME JOURNAL OF APPLIED MECHANICS, Vol. 43, 1976, pp. 205–208.

7 Tokis, J. N., "Hydromagnetic Unsteady Flow Due to an Oscillating Plate," *Astrophys. Space Sci.*, Vol. 58, 1978, pp. 167–174.

8 Pande, G. C., Georgantopoulos, G. A., and Goudas, C. L., "Hydromagnetic Flow Near an Oscillating Wall," *Astrophys. Space. Sci.*, Vol. 43, 1976, pp. 403–409.

9 Pande, G. C., et al., "Hydromagnetic Flow Near an Oscillating Porous Limiting Surface," *Astrophys. Space Sci.*, Vol. 51, 1977. pp. 125–134.

K. Yamagami
Graduate Student.

M. Kurashige
Assistant Professor.

Department of Mechanical Engineering II,
Faculty of Engineering,
Tohoku University,
Sendai 980, Japan

Infiltration of a Fluid Into a Dry Poro-Elastic Body

The infiltration of a fluid into a dry poro-elastic body, of infinite extent, from its cylindrical or spherical cavity and the resulting mechanical behaviors are investigated. Since the problem is a moving boundary problem, and therefore, an essentially nonlinear one, the finite-difference scheme with the aid of the boundary fixing method is applied to obtain the solution. The results thus obtained for sandstone are compared with those for a porous rigid body as well as with those in a situation where a fluid pervades the whole body from the outset. These comparisons show that the extent of the infiltration front into the body is adequately predicted by the rigid skeleton model and that the actual stress distribution is remarkably different from that which exists if fluid pervades the whole body from the outset.

Introduction

The mechanical behaviors of a poro-elastic material containing a fluid has attracted considerable attention in various fields such as soil mechanics, ground water hydrology, geophysics, seismology, biomechanics, the theory of filtration and purification, the study of machine elements, and so forth. Many basic theories [1–6] have been proposed to describe these behaviors. Among these theories, Biot's theory [2, 3] is comparatively simple and it suffices to describe the various phenomena in the field just mentioned.

As far as the authors know, all previous papers on poro-elasticity dealt with the case in which the fluid pervades the whole body, and no work has been done on the injection and infiltration of a fluid into a part of the poro-elastic material which does not yet contain the fluid. As regards infiltration problems, the effect of the elastic deformation of a porous matrix on the infiltration process has been neglected. It has not been established whether the rigid matrix theory is acceptable or not for the purpose of calculating the moving front of the injected fluid.

The present paper thus investigates how a fluid injected from a cylindrical or spherical cavity infiltrates into an infinite poro-elastic body and what deformation and stress fields the infiltration brings about. Such fluid injection and infiltration have become practical for the disposal of noxious liquid waste by pumping it into a permeable underground layer of, for instance, sandstone or limestone through a pipe. Recently, such a disposal technique is used to a considerable and broad extent by industry.

Regarding this fluid infiltration problem, the referential field is divided into two regions: one is the region where the injected fluid flows through the pores; namely, it is the region of a mixture consisting of a fluid and a solid matrix, and another is the one where the fluid has not yet penetrated into the pores. The material is regarded as homogeneous and elastic. Moreover, the boundary of separation between these two regions moves with the infiltration of the injected fluid. This problem is characterized distinctively by the possession of the moving boundary, and mathematically it belongs to the so-called moving (or free) boundary problem. Such a problem becomes perfectly nonlinear because the positions of the moving boundary are neither fixed in space nor known *a priori*. Due to this nonlinearity, the analytical solution can be found only in limited situations, for example, in Neumann's solution for the one-dimensional Stefan problem [7].

Up to now, several methods of tackling moving boundary problems have appeared. These methods can be roughly classified into three categories: analytical methods, approximate methods, and numerical methods. Using the analytical method [8, 9], the moving boundary is usually represented by the solution of a nonlinear, singular, integro-differential equation, which is not tractable. The scope within which the approximate method is applicable is restricted. However, with the recent remarkable advance of digital computers, many numerical methods based on the finite-difference scheme have been proposed. Among these methods, the boundary fixing method [10], in which Landau's transformation was adopted to immobilize the moving boundary, seems to be the most practical and superior method.

In this paper, formulating the aforementioned infiltration problem on the basis of Biot's theory, we obtained the numerical solution by using the boundary fixing method and the Crank-Nicolson finite-difference scheme. A sample calculation was performed by using material constants for sandstone infiltrated by kerosene [12]. Also, a similar infiltration problem into a porous rigid body was likewise solved for the purpose of comparison. This comparison shows that one can estimate roughly how far the moving boundary or a fluid infiltration front penetrates from the cavity into the infinite body using

Contributed by the Applied Mechanics Division for publication in the JOURNAL OF APPLIED MECHANICS.

Discussion on this paper should be addressed to the Editorial Department, ASME, United Engineering Center, 345 East 47th Street, New York, N. Y. 10017, and will be accepted until September 1, 1981. Readers who need more time to prepare a Discussion should request an extension from the Editorial Department. Manuscript received by ASME Applied Mechanics Division, April, 1980; final revision, August, 1980.

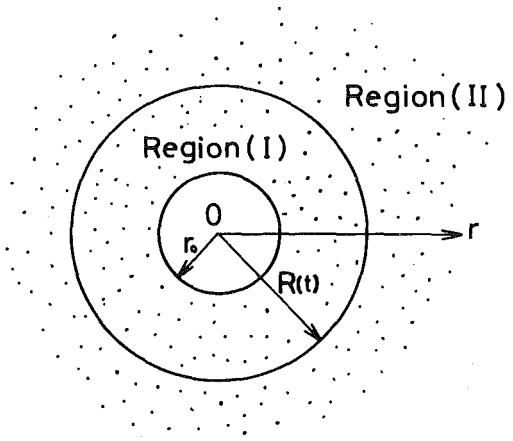

Fig. 1 *Infiltration of a fluid into a poro-elastic body, of infinite extent, from its cavity of radius r_0; the fluid infiltration front is $r = R(t)$*

the rigid skeleton model. Furthermore, we compared the results for the moving boundary problem under consideration with those in the situation where the fluid pervades the whole infinite body with a cavity from the outset. This comparison shows that the moving front has a great influence on the distribution of fluid pressure and matrix hoop stress.

Statement of Problem and Governing Equations

A schematic diagram with a coordinate system for the fluid infiltration problem is shown in Fig. 1. Consider an infinite poro-elastic body enclosing fluid in its cylindrical or spherical cavity, but without fluid in its pores. When hydraulic pressure is applied to the fluid in the cavity, the pressure injects it into the porous wall of the cavity and begins to infiltrate it through the surrounding porous body. At this stage, the relevant field can be divided into the two regions shown in Fig. 1. Region (I) already has fluid penetration but Region (II) does not. The former is regarded as a mixture composed of a solid and a fluid, while the latter is regarded as a homogeneous elastic body. The boundary of separation between these two regions moves with the infiltration of the injected fluid and its positions are not known *a priori*, depending upon the solid displacement field and the fluid dilatation field.

The cylindrical cavity and spherical cavity will be denoted by Cases 1 and 2, respectively.

As examples of practical situations, these cases may be regarded as follows. Case 1 is the situation in which the fluid is pumped through a cavity into a thick permeable layer which is confined by two slippery impermeable layers. This type of model assumes that the confining layers do not offer shear stress at their interfaces. The effect of gravity is neglected. Case 2 is similar but with the absence of the impermeable layers.

Fluid infiltration and mechanical behavior will be modeled by using Biot's theory. We neglect inertia terms.

In infiltration theories, in addition to fluid pressure, capillary pressure associated with surface tension works as the driving force for fluid motion. We neglect the capillary pressure since it is much smaller than applied fluid pressure. Furthermore, we neglect the driving force due to fluid concentration gradient which is significant only in conditions of low fluid content.

In 1955, Biot [3] proposed the linearized theory for infinitesimal deformations of a homogeneous poro-elastic medium saturated with an ideal fluid and for flows of the saturating fluid through the porous medium. Biot and Willis [11] examined the material constants involved in that theory in 1957. The basic equations in those works can be summarized with some slight changes as follows, with the use of the notations:

σ_{ij}, τ = partial stresses of the solid and fluid, respectively.
π_i = force per unit volume exerted on the solid by the fluid or, as a reaction against it, diffusion force.
u_i = displacement of the solid.
v_i = velocity of the fluid.
e_{ij} = infinitesimal strain of the solid.
e, ϵ = dilatation of the solid and fluid, respectively.
V_i = velocity of the fluid relative to that of the solid.
A, N, Q, S, b = material constants.

Kinematic Relations:

$$e_{ij} = \tfrac{1}{2}(u_{i,j} + u_{j,i}), \tag{1}$$

$$e = u_{i,i}, \tag{2}$$

$$V_i = v_i - \partial u_i/\partial t, \tag{3}$$

where, and in what follows, the sum is taken from 1–3 with respect to the repeated indices and $(\ )_{,i}$ denotes partial differentiation with respect to a Cartesian coordinate x_i.

Motion and Continuity Equations:

$$\sigma_{ji,j} + \pi_i = 0, \tag{4}$$

$$\tau_{,i} - \pi_i = 0, \tag{5}$$

$$v_{i,i} = \partial\epsilon/\partial t. \tag{6}$$

Constitutive Relations:

$$\sigma_{ij} = Ae\delta_{ij} + 2Ne_{ij} + Q\epsilon\delta_{ij}, \tag{7}$$

$$\tau = Qe + S\epsilon, \tag{8}$$

$$\pi_i = bV_i, \tag{9}$$

where δ_{ij} is the Kronecker delta. The constants N, A, Q, and S can be expressed as

$$N = \mu, \tag{10}$$

$$A = \frac{\gamma/\kappa + f^2 + (1-2f)(1-\delta/\kappa)}{\gamma + \delta - \delta^2/\kappa} - \frac{2}{3}\mu, \tag{11}$$

$$Q = \frac{f(1-f-\delta/\kappa)}{\gamma + \delta - \delta^2/\kappa}, \tag{12}$$

$$S = \frac{f^2}{\gamma + \delta - \delta^2/\kappa}, \tag{13}$$

where f is the porosity and γ is given as

$$\gamma = f(c - \delta), \tag{14}$$

where c is a compressibility coefficient of the fluid. The constants μ, κ, δ, and γ are the shear modulus of the bulk material, a coefficient of jacked compressibility, an unjacked compressibility coefficient, and a coefficient of fluid content, respectively. All these constants are measurable. The porous matrix is homogeneous, isotropic, and elastically linear.

Substituting equation (7)–(9) into equations (4) and (5), and using kinematical relations (1)–(3), gives the Navier (displacement type) equation in the form:

$$N\nabla^2\mathbf{u} + (A+N)\ \text{grad div}\ \mathbf{u} + Q\ \text{grad}\ \epsilon + b\mathbf{V} = \mathbf{0}, \tag{15}$$

$$Q\ \text{grad div}\ \mathbf{u} + S\ \text{grad}\ \epsilon - b\mathbf{V} = \mathbf{0}. \tag{16}$$

Formulation of the Problem

To the aforementioned problem, we will seek solutions for Cases 1 and 2. Due to the symmetric characteristics of the problem, we can assume

$$u_r = u(r,t), \quad v_r = v(r,t), \quad \epsilon = \epsilon(r,t) \quad \text{in Region (I)}, \tag{17}$$

$$u_r = U(r, t) \quad \text{in Region (II)}, \tag{18}$$

with respect to the cylindrical polar coordinate system (r, θ, z) for Case 1 and with respect to the spherical polar coordinate system (r, θ, ϕ) for Case 2.

Now, substituting equations (17) and (18) into equations (15), (16), and (6), we are able to obtain a set of field equations for Region (I) as follows:

$$(A + 2N)\partial\{r^{-n}\partial(r^n u)/\partial r\}/\partial r + Q\partial\epsilon/\partial r + b(v - \partial u/\partial t) = 0, \tag{19}$$

$$Q\partial\{r^{-n}\partial(r^n u)/\partial r\}/\partial r + S\partial\epsilon/\partial r - b(v - \partial u/\partial t) = 0, \tag{20}$$

$$r^{-n}\partial(r^n v)/\partial r - \partial\epsilon/\partial t = 0, \tag{21}$$

for $r_0 < r < R(t)$, where r_0 denotes the inner radius of the cavity and $R(t)$ denotes the position of the fluid infiltration front at time t. n assumes values 1 and 2 in Cases 1 and 2, respectively.

The stress-displacement relations in Region (I) are

$$\sigma_{11} = Ar^{-n}\partial(r^n u)/\partial r + 2N\partial u/\partial r + Q\epsilon, \tag{22}$$

$$\sigma_{22} = Ar^{-n}\partial(r^n u)/\partial r + 2Nu/r + Q\epsilon, \tag{23}$$

$$\sigma_{33} = Ar^{-n}\partial(r^n u)/\partial r + 2N(n-1)u/r + Q\epsilon, \tag{24}$$

$$\tau = S\epsilon + Qr^{-n}\partial(r^n u)/\partial r, \tag{25}$$

for $r_0 < r < R(t)$, where σ_{11}, σ_{22}, and σ_{33} are

$$\sigma_{11} = \sigma_{rr}, \quad \sigma_{22} = \sigma_{\theta\theta}, \quad \sigma_{33} = \sigma_{zz}, \tag{26}$$

for Case 1, and

$$\sigma_{11} = \sigma_{rr}, \quad \sigma_{22} = \sigma_{\theta\theta}, \quad \sigma_{33} = \sigma_{\phi\phi}, \tag{27}$$

for Case 2.

Since Region (II) has no fluid, the field equation for a linear elastic body holds.

$$(A_0 + 2N)\partial\{r^{-n}\partial(r^n U)/\partial r\}/\partial r = 0, \tag{28}$$

for $R(t) < r < +\infty$, where A_0 is the material constant of the poro-elastic material which contains no fluid.

The stress-displacement relations, being the same as those of an elastic body, are

$$\Sigma_{11} = A_0 r^{-n}\partial(r^n U)/\partial r + 2N\partial U/\partial r, \tag{29}$$

$$\Sigma_{22} = A_0 r^{-n}\partial(r^n U)/\partial r + 2NU/r, \tag{30}$$

$$\Sigma_{33} = A_0 r^{-n}\partial(r^n U)/\partial r + 2N(n-1)U/r, \tag{31}$$

for $R(t) < r < +\infty$, where Σ_{11}, Σ_{22}, and Σ_{33} are as follows:

$$\Sigma_{11} = \Sigma_{rr}, \quad \Sigma_{22} = \Sigma_{\theta\theta}, \quad \Sigma_{33} = \Sigma_{zz}, \tag{32}$$

for Case 1, and

$$\Sigma_{11} = \Sigma_{rr}, \quad \Sigma_{22} = \Sigma_{\theta\theta}, \quad \Sigma_{33} = \Sigma_{\phi\phi}, \tag{33}$$

for Case 2.

Let us assume that the fluid in the cavity is suddenly pressurized, and thereafter, varies as a continuous function of time $p(t)$. On the moving boundary or at the fluid infiltration front, the displacement and the traction should be continuous, and the fluid velocity should coincide with the velocity of the moving boundary. Furthermore, the solid displacement should vanish at infinity. Thus the initial and boundary conditions for equations (19)–(33) are reduced to

$$u = 0 \quad (r_0 < r < R(0)) \qquad \text{at} \quad t = 0, \tag{34}$$

$$\sigma_{11} = -(1-f)p(t), \quad \tau = -fp(t) \qquad \text{at} \quad r = r_0, \tag{35}$$

$$u = U \qquad \text{at} \quad r = R(t), \tag{36}$$

$$\sigma_{11} = \Sigma_{11}, \quad \tau = 0 \qquad \text{at} \quad r = R(t), \tag{37}$$

$$dR/dt = v \qquad \text{at} \quad r = R(t), \tag{38}$$

$$U = 0 \qquad \text{at} \quad r \to +\infty. \tag{39}$$

Nondimensionalization

Here, we introduce the nondimensional variables to facilitate the analysis:

$$\left.\begin{aligned} &\bar{u} = \frac{S}{r_0 p_0}u, \quad \bar{\epsilon} = \frac{S}{p_0}\epsilon, \quad \bar{v} = \frac{r_0 b}{p_0}v, \quad \bar{U} = \frac{S}{r_0 p_0}U, \\ &\bar{r} = r/r_0, \quad \bar{t} = \frac{S}{r_0^2 b}t, \quad \bar{R} = R/r_0, \\ &(\bar{\sigma}_{11}, \bar{\sigma}_{22}, \bar{\sigma}_{33}, \bar{\tau}, \bar{\Sigma}_{11}, \bar{\Sigma}_{22}, \bar{\Sigma}_{33}) \\ &\qquad = (\sigma_{11}, \sigma_{22}, \sigma_{33}, \tau, \Sigma_{11}, \Sigma_{22}, \Sigma_{33})/p_0. \end{aligned}\right\} \tag{40}$$

For simplicity, the bars on the nondimensional quantities will be omitted in the following. Using these nondimensional variables, the field equations are rewritten as

$$(E + G)\partial\{r^{-n}\partial(r^n u)/\partial r\}/\partial r + H\partial\epsilon/\partial r + (v - \partial u/\partial t) = 0, \tag{41}$$

$$H\partial\{r^{-n}\partial(r^n u)/\partial r\}/\partial r + \partial\epsilon/\partial r - (v - \partial u/\partial t) = 0, \tag{42}$$

$$r^{-n}\partial(r^n v)/\partial r - \partial\epsilon/\partial t = 0, \tag{43}$$

for $1 < r < R(t)$,

$$(E_0 + G)\partial\{r^{-n}\partial(r^n U)/\partial r\}/\partial r = 0, \tag{44}$$

for $R(t) < r < +\infty$.

The constitutive relations are rewritten as

$$\sigma_{11} = Er^{-n}\partial(r^n u)/\partial r + G\partial u/\partial r + H\epsilon, \tag{45}$$

$$\sigma_{22} = Er^{-n}\partial(r^n u)/\partial r + Gu/r + H\epsilon, \tag{46}$$

$$\sigma_{33} = Er^{-n}\partial(r^n u)/\partial r + G(n-1)u/r + H\epsilon, \tag{47}$$

$$\tau = \epsilon + Hr^{-n}\partial(r^n u)/\partial r, \tag{48}$$

for $1 < r < R(t)$, and

$$\Sigma_{11} = E_0 r^{-n}\partial(r^n U)/\partial r + G\partial U/\partial r, \tag{49}$$

$$\Sigma_{22} = E_0 r^{-n}\partial(r^n U)/\partial r + GU/r, \tag{50}$$

$$\Sigma_{33} = E_0 r^{-n}\partial(r^n U)/\partial r + G(n-1)U/r, \tag{51}$$

for $R(t) < r < +\infty$. Furthermore, the initial and boundary conditions are

$$u = 0 \quad (1 < r < R(0)) \quad \text{at } t = 0, \tag{52}$$

$$\sigma_{11} = -(1-f)p(t)/p_0, \quad \tau = -fp(t)/p_0 \quad \text{at } r = 1, \tag{53}$$

$$u = U \quad \text{at} \quad r = R(t), \tag{54}$$

$$\sigma_{11} = \Sigma_{11}, \quad \tau = 0 \quad \text{at} \quad r = R(t), \tag{55}$$

$$dR/dt = Pv \quad \text{at} \quad r = R(t), \tag{56}$$

$$U = 0 \quad \text{at} \quad r \to +\infty, \tag{57}$$

where p_0 is the reference pressure. The nondimensional constants appearing in equations (41)–(51) and P in equation (56) are defined as

$$E = A/S, \quad G = 2N/S, \quad H = Q/S, \quad E_0 = A_0/S, \quad P = p_0/S. \tag{58}$$

Reduction of the Field Equations to a Single Equation and the Fixing of the Moving Boundary

It is convenient to reduce the system of the simultaneous partial differential equations (41)–(43) for Region (I) to a single equation. In order to do so, let us express the solutions of that system in terms of a scalar function $\Phi(r, t)$:

$$u = -\frac{(H+1)^2}{E+G-H^2}r^{-n}\Phi - rf_1(t)/(n+1) - f_2(t)/r^n, \tag{59}$$

$$\epsilon = \frac{(E+G+H)(H+1)}{E+G-H^2}r^{-n}\partial\Phi/\partial r - f_1(t), \tag{60}$$

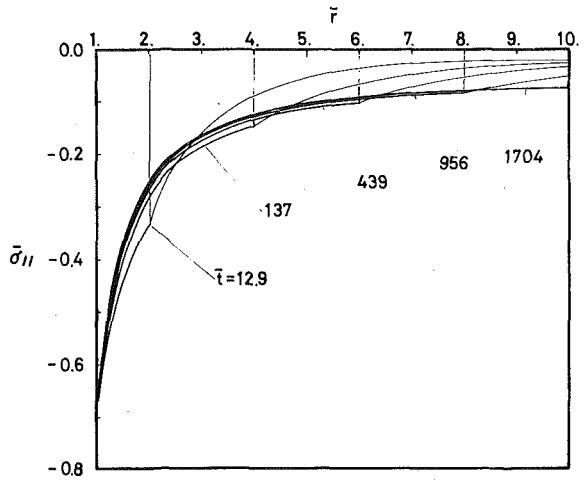

Fig. 2 Distribution of radial stress $\bar{\sigma}_{11}$ at various times for Case 1

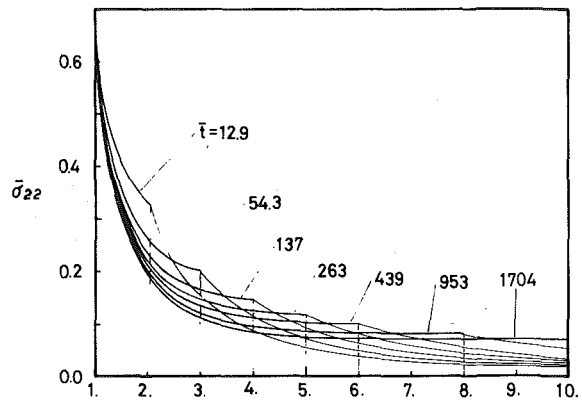

Fig. 3 Distribution of circumferential stress $\bar{\sigma}_{22}$ at various times for Case 1

$$V = \frac{(E+G+H)(H+1)}{E+G-H^2} r^{-n} \partial\Phi/\partial t - r\dot{f}_1(t)/(n+1) - \dot{f}_2(t)/r^n, \tag{61}$$

with $f_1(t)$ and $f_2(t)$ being unknown functions, where the dots denote differentiation with respect to the nondimensional time t. These solutions satisfy the continuity equation (43) automatically. From the remaining field equations (41) and (42), we obtain the following single equation for the function $\Phi(r, t)$:

$$\partial^2\Phi/\partial r^2 - \frac{n}{r}\partial\Phi/\partial r = \frac{E+G+2H+1}{E+G-H^2}\partial\Phi/\partial t. \tag{62}$$

The field equation (44) for Region (II) has a general solution

$$U = rF_1(t)/(n+1) + F_2(t)/r^n, \tag{63}$$

where $F_1(t)$ and $F_2(t)$ are also unknown. The unknown functions $f_1(t)$, $f_2(t)$, $F_1(t)$, and $F_2(t)$ are determined by the boundary conditions (53)–(57) as follows:

$$f_1(t) = 0, \tag{64}$$

$$f_2(t) = -\frac{1}{nG}p(t)/p_0 - \frac{(H+1)^2}{E+G-H^2}\Phi(1, t), \tag{65}$$

$$F_1(t) = 0, \tag{66}$$

$$F_2(t) = \frac{(H+1)^2}{E+G-H^2}\{\Phi(1, t) - \Phi(R, t)\} + \frac{1}{nG}p(t)/p_0. \tag{67}$$

The solutions (59)–(61) and (63) with (64)–(67) are easily proved to satisfy the boundary conditions (54) and (57) automatically. Using equations (45), (48), and (49), the remaining initial and boundary conditions can be expressed in terms of $\Phi(r, t)$. Thus the equation system for $\Phi(r, t)$ is obtained as follows:

$$\partial^2\Phi(r, s)/\partial r^2 - \frac{n}{r}\partial\Phi(r, s)/\partial r = \partial\Phi(r, s)/\partial s, \tag{68}$$

$$\partial\Phi(1, s)/\partial r = -\frac{f}{H+1}p(s)/p_0, \tag{69}$$

$$\partial\Phi(R, s)/\partial r = 0, \tag{70}$$

$$\frac{1}{n+1}R^{n+1} = P\left\{\frac{(E+G+H)(H+1)}{E+G-H^2}\Phi(R, s) + \frac{(H+1)^2}{E+G-H^2}\Phi(1, s) + \frac{1}{nG}p(s)/p_0\right\} + \frac{1}{n+1}R(0)^{n+1}, \tag{71}$$

$$\Phi(r, 0) = 0 \quad (1 < r < R(0)), \tag{72}$$

with

$$s = \frac{E+G-H^2}{E+G+2H+1}t. \tag{73}$$

In order to avoid the complexity of the finite-difference procedures due to the moving boundary, let us introduce the following variable transformation [10]:

$$\eta = (r-1)/(R-1). \tag{74}$$

This transformation fixes the moving boundary on the η-coordinate. Making use of the foregoing variable, the reduced equation system (68)–(72) is changed into:

$$\partial\Phi(\eta, s)/\partial s = \frac{1}{(R-1)^2}\partial^2\Phi(\eta, s)/\partial\eta^2 - \frac{1}{R-1}\left\{\frac{n}{1+\eta(R-1)} - \eta\dot{R}\right\}\partial\Phi(\eta, s)/\partial\eta \quad (0 < \eta < 1), \tag{75}$$

$$\partial\Phi(0, s)/\partial\eta = -\frac{f}{H+1}(R-1)p(s)/p_0, \tag{76}$$

$$\partial\Phi(1, s)/\partial\eta = 0, \tag{77}$$

$$\frac{1}{P(n+1)}R^{n+1} = \frac{(E+G+H)(H+1)}{E+G-H^2}\Phi(1, s) + \frac{(H+1)^2}{E+G-H^2}\Phi(0, s) + \frac{1}{nG}p(s)/p_0 + \frac{1}{P(n+1)}R(0)^{n+1}, \tag{78}$$

$$\Phi(\eta, 0) = 0 \quad (0 < \eta < 1). \tag{79}$$

Numerical Example

In order to examine some features of the problem of the fluid infiltration into a poro-elastic body, we solve numerically the equation system (75)–(79) by applying the Crank-Nicolson finite-difference scheme. Because of the characteristics of the finite-difference scheme, we need to start from the stage where the fluid slightly penetrates into the surrounding porous solid from the cavity wall. We started by putting $R(0) = 1.1$.

For the numerical calculations, it is sufficient to specify the numerical values of $f, \nu, c/\kappa, \delta/\kappa$. We used the following values, which were computed from the data given for sandstone and kerosene by [12, 13]: $f = 0.26, \nu = 0.2, c/\kappa = 4.2, \delta/\kappa = 0.18$. The fluid dilatation caused by the reference pressure p_0 was taken as $p_0 c = 5 \times 10^{-2}$, and the input function $p(t)/p_0$ was specialized to the form: $p(t)/p_0 = 1 - e^{-\alpha t}$ with $\alpha = 10$.

The results are shown in Figs. 2–8, where the bars on the nondimensional quantities are resumed.

Figs. 2–4 show the spatial distribution of the radial stress $\bar{\sigma}_{11}$, and hoop stress $\bar{\sigma}_{22}$ for the solid, and the fluid stress $\bar{\tau}$, respectively, for Case 1 with the nondimensional time $\bar{t}$ taken as the parameter. In the first two figures, each curve has discontinuity in its gradient at the fluid infiltration front. The curves behind the infiltration front show

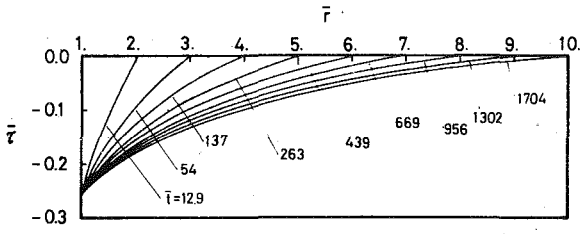

Fig. 4 Distribution of fluid stress $\bar{\tau}$ at various times for Case 1

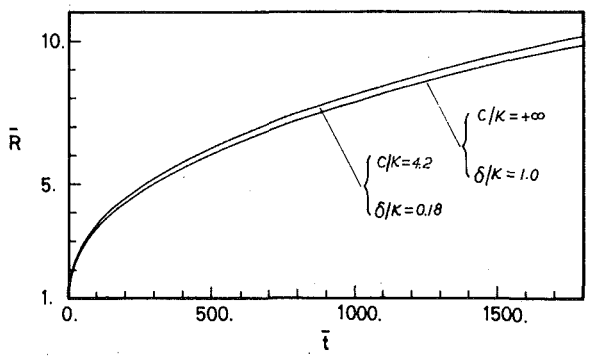

Fig. 5 Position of a fluid infiltration front for Case 1 in comparison with the rigid skelton case

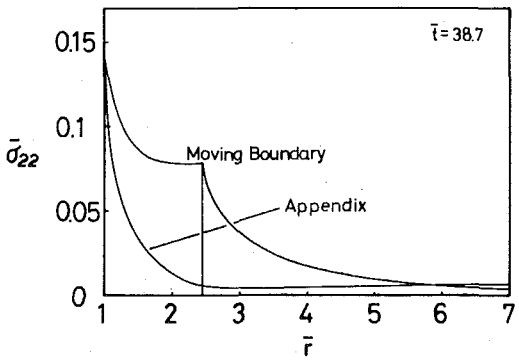

Fig. 6 Distribution of radial stress $\bar{\sigma}_{11}$ for Case 2 in comparison with that in a situation where a fluid pervades the whole body from the outset

the stresses in Region (I), and the curves ahead of the front show the ones in Region (II).

Fig. 4 shows the distribution of fluid stress $\bar{\tau}$ for Class 1. The fluid stress increases monotonically from the negative value $\bar{\tau} = -0.26$ and vanishes at the fluid infiltration front.

The time history of the position of the fluid infiltration front for sandstone and kerosene is compared with that for a porous rigid body and kerosene in Fig. 5 as to Case 1. As mentioned before, $c/\kappa = 4.2$ and $\delta/\kappa = 0.18$ for the former case, while the limiting case of the rigid skeleton is obtained by putting $c/\kappa \to +\infty$ and $\delta/\kappa = 1$. The input function $p(t)/p_0$ and the reference fluid dilatation $p_0 c$ are the same for both cases.

Initially the front progresses rapidly and later it does steadily. The front in the sandstone goes ahead of that in the rigid body, but the difference is rather small. Therefore, to estimate roughly how far the front penetrates into the body, even the rigid skelton model may be a sufficient alternative to the poro-elastic model for the sandstone.

In Figs. 6–8, the stress distributions in the solid and fluid at $\bar{t} = 38.7$ for the situation considered here are contrasted with those for situation where the fluid pervades the whole infinite poro-elastic body from

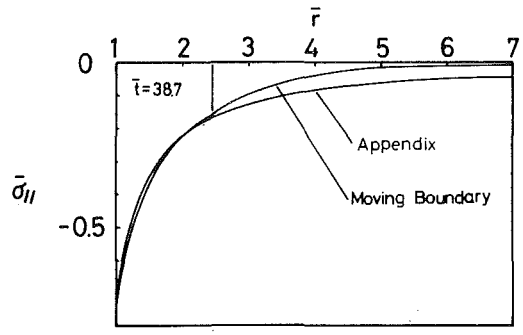

Fig. 7 Distribution of circumferential stress $\bar{\sigma}_{22}$ for Case 2 in comparison with that in a situation where a fluid pervades the whole body from the outset

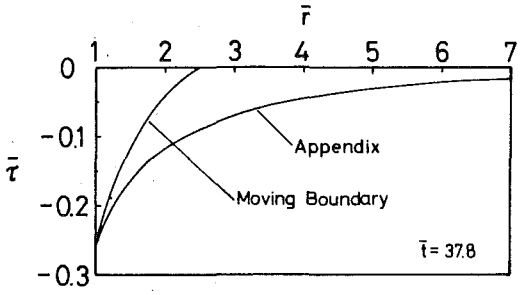

Fig. 8 Distribution of fluid stress $\bar{\tau}$ for Case 2 in comparison with that in a situation where a fluid pervades the whole body from the outset

the outset as to Case 2. The analytical solution for the latter situation can be easily obtained and is shown in the Appendix.

The difference in the radial stress distribution between the situation considered here and the situation where the fluid pervades the whole body from the outset is rather small, while the differences in the hoop stress and fluid stress distributions are remarkable. Therefore, the analytical solution given in the Appendix cannot be an alternative to the solution for the infiltration problem, no matter how simply the analytical solution is obtained.

Conclusion

The infiltration of a fluid into a dry poro-elastic body with a cylindrical or spherical cavity has been examined by the boundary fixing method and Crank-Nicolson finite-difference scheme. The following conclusion can be drawn:

1 The stress distribution in the body has discontinuity in its gradient at the fluid infiltration front.

2 The extent of the infiltration front into the body is adequately predicted by the rigid skelton model.

3 The actual stress distribution is remarkably different from that which exists if fluid pervades the whole body from the outset. The stress solution obtained using the latter model is not a good solution for the infiltration problem.

Acknowledgments

The authors wish to express their gratitude to Prof. A. Atsumi of Tohoku University for his valuable advice and encouragement throughout the progress of this investigation. They are also indebted to the referee for his helpful and important comments. The expense for this study was funded from the Scientific Research Fund of the Ministry of Education for fiscal 1979.

References

1 Terzaghi, K., "Die Berechnung der Durchassigkeitsziffer des Tones aus dem Verlauf der Hydrodynamischen Spannungsercheinungen," *Sitzungsber. Akad. Wiss. Wien Math.-Naturwiss. Kl.*, Abt. 2A, 132, 105, 1923.

2 Biot, M. A., "General Theory of Three-Dimensional Consolidation," *Journal of Applied Physics*, Vol. 12, 1941, pp. 155–164.
3 Biot, M. A., "Theory of Elasticity and Consolidation for a Porous, Anisotropic Solid," *Journal of Applied Physics*, Vol. 26, 1955, pp. 182–185.
4 Bowen, R. M., and Wiese, J. C., "Diffusion in Mixtures of Elastic Materials," *International Journal of Engineering Sciences*, Vol. 7, 1969, pp. 689–722.
5 Bowen, R. M., "Theory of Mixtures," *Continuum Physics*, Vol. 3, ed., Eringen, A. C., New York-London, Academic Press, 1976, pp. 1–127.
6 Crochet, M. J., and Naghdi, P. M., "On Constitutive Equations for Flow of Fluid Through an Elastic Solid," *International Journal of Engineering Sciences*, Vol. 4, 1966, pp. 383–401.
7 Carslaw, H. S., and Jaeger, J. C., *Conduction of Heat in Solid*, 2nd ed., Clarendon Press, Oxford, 1959, pp. 282–296.
8 Kolodner, I. I., "Free Boundary Problem for Heat Equation With Applications to Problems of Change of Phase," *Communications on Pure and Applied Mathematics*, Vol. IX, 1956, pp. 1–31.
9 Friedman, A., "Free Boundary Problems for Paribolic Equations I. Melting of Solids," *Journal of Mathematics and Mechanics*, Vol. 8, No. 4, 1959, pp. 499–517.
10 Saitoh, T., "Numerical Method for Multidimensiol Freezing Problems in Arbitrary Domains," ASME *Journal of Heat Transfer*, Vol. 100, 1978, pp. 294–299.
11 Biot, M. A., and Willis, D. G., "The Elastic Coefficients of the Theory of Consolidation," ASME JOURNAL OF APPLIED MECHANICS, Vol. 24, 1957, pp. 594–601.
12 Fatt, I., "The Biot-Willis Elastic Coefficients for a Sandstone," ASME JOURNAL OF APPLIED MECHANICS, Vol. 26, 1959, pp. 296–297.
13 Rice, J. R., and Cleary, M. P., "Some Basic Stress Diffusion Solutions for Fluid-Saturated Elastic Porous Media With Compressible Constituents," *Reviews of Geophysics and Space Physics*, Vol. 14, No. 2, 1976, pp. 227–241.

APPENDIX

We can easily obtain an analytical solution for a problem similar to Case 2 except where a fluid pervades the whole body from the outset. The equation to be solved is the same as in (68) and the boundary conditions and initial condition are

$$\sigma_{11} = -(1-f)p(t)/p_0, \quad \tau = -fp(t)/p_0 \quad \text{at} \quad r = 1, \tag{80}$$

$$\sigma_{11} = 0, \tau = 0 \quad \text{at} \quad r \to +\infty, \tag{81}$$

$$u = 0 \quad \text{at} \quad t = 0 \quad \text{for} \quad 1 < r < +\infty. \tag{82}$$

The solution for the equation system (68) and (80)–(82) is

$$\Phi(r, s) = f/(H+1)\left[\int_0^s (1 - e^{-\bar{\alpha}u}) \operatorname{erfc}\left(\frac{r-1}{2\sqrt{s-u}}\right) du + r\int_0^s (1 - e^{-\bar{\alpha}u}) \exp\left\{-\frac{(r-1)^2}{4(s-u)}\right\} \Big/ \sqrt{\pi(s-u)}\, du\right], \tag{83}$$

where erfc ( ) is the complementary error function and

$$\bar{\alpha} = \frac{E+G+2H+1}{E+G-H^2}\alpha. \tag{84}$$

Rafael F. Diaz-Munio
Graduate Student.

L. Carter Wellford, Jr.
Associate Professor.

Department of Civil Engineering,
University of Southern California,
University Park,
Los Angeles, Calif. 90007

A Finite-Element Singular-Perturbation Technique for Convection-Diffusion Problems

Part 1: The One-Dimensional Case

Approximation procedures for the solution of convection-diffusion equations, occurring in various physical problems, are considered. Several finite-element algorithms based on singular-perturbation methods are proposed for the solution of these equations. A method of variational matched asymptotic expansions is employed to develop shape functions which are particularly useful when convection effects dominate diffusion effects in these problems. When these shape functions are used, in conjunction with the standard Galerkin method, to solve convection-diffusion equations, increased solution accuracy is obtained. Numerical results for various one-dimensional problems are presented to establish the workability of the developed methods.

Introduction

In fluid mechanics problems in which convection effects dominate diffusion effects, standard numerical techniques—centered finite-difference models and finite-element Galerkin methods—have failed to produce reasonable solutions. Convergence at optimum rates can be obtained with these approximation procedures; however, if normal mesh spacings are used, the absolute error is large and often physically unreasonable oscillatory solutions are obtained.

In order to overcome these difficulties, techniques of "upwinding" [1] have been introduced by practitioners of the finite-difference method. These procedures produce noncentered finite-difference schemes in which the bias in the algorithm depends on the direction of the flow. Since finite-element Galerkin procedures, used in conjunction with standard shape functions, result in centered discretizations and corresponding poor numerical results, it has become necessary to develop finite-element equivalents of the upwind difference algorithms.

A technique using the weighted residual method, in conjunction with upwind weights, has been proposed in [2–5]. Hughes [6, 7] has introduced a method of solution in which reduced integration, in conjunction with a moving quadrature point, is used to produce an upwinding effect. Kikuchi [8] has introduced an artificial viscosity technique for this type of problem, and Barrett [9] has developed a procedure in which exponential basis functions are used in finite-element algorithms.

In this paper a solution technique, based on the standard Galerkin method, is introduced for the convection-diffusion problem. The approach advocated here is traditional in all respects except for the choice of shape functions to be employed in the analysis. The shape functions are constructed by a procedure which can be characterized as a finite-element method of matched asymptotic expansions. These shape functions can account for variable coefficients and zeroth-order terms in the differential equations. In addition, they can be used in conjunction with distorted elements and multidimensional problems.

As the diffusion effects in the problem increase or as the mesh discretization parameter decreases, the constructed shape functions approach the standard forms. However, when convection effects are important and when normal mesh spacings are employed, the shape functions are quite different as compared to those used in classical finite-element approximations for self-adjoint problems. The use of these special shape functions produces an upwinding effect in the discrete equations and a corresponding increase in solution accuracy.

The Physical Problem

Consider a one-dimensional domain $I = [a, b]$. Let x denote the coordinate of a particular point in I. Then the convection-diffusion problem in one-dimension can be stated as follows:

Presented at the Symposium on Finite-Element Methods for Convection Dominated Flows, at the 1979 Winter Annual Meeting, New York, N.Y., December 2–7, 1979 and contributed by the Applied Mechanics Division for publication in the JOURNAL OF APPLIED MECHANICS.

Discussion on this paper should be addressed to the Editorial Department, ASME, United Engineering Center, 345 East 47th Street, New York, N.Y. 10017, and will be accepted until September 1, 1981. Readers who need more time to prepare a Discussion should request an extension from the Editorial Department. Manuscript received by ASME Applied Mechanics Division, December, 1979; final revision, September, 1980.

$$\begin{cases} \epsilon \dfrac{d^2\phi}{dx^2} + u\dfrac{d\phi}{dx} + g\phi = 0 \\ \phi(a) = p \\ \phi(b) = q \end{cases} \tag{1}$$

Normally, the parameter ϵ is a diffusion coefficient, u is related (through a minus sign) to velocity, and g is associated with transient or linearized convective effects.

Singular-Perturbation Procedures

The problem (1) is a singular-perturbation problem. If the value of the diffusion coefficient ϵ is small compared to the coefficient u, this problem is of boundary-layer type with boundary layers occurring either at $x = a$ or at $x = b$, or at both positions, depending on the variation of u with x. A method of analysis which combines the finite-element discretization technique and the singular-perturbation method can be introduced to solve this type of problem. In this procedure, the spatial domain I is first subdivided into finite elements I_e. Then, singular-perturbation methods are used in the construction of the discrete equations on the local elements. When the local equations are assembled and the resulting system is solved, the entire finite-element solution is obtained.

In this paper, this approach, involving the application of singular perturbations on a local level, is employed. It will be assumed in this development that ϵ is a small, positive constant, while coefficients u and g are variable. Let the typical element be defined by $I_e = [x_e, x_e + h]$. Let a natural coordinate system be established in the element. The natural coordinate is denoted ξ and is defined on the mapped element $\bar{I}_e = [-1, 1]$. The mapping between the natural coordinate ξ and the physical coordinate x takes the following form:

$$x = x_e + (\xi + 1)\frac{h}{2} \tag{2}$$

The local problem, equivalent to the original formulation (1), can be established by making use of the transformation (2). If $\phi(\xi)$, $u(\xi)$, and $g(\xi)$ denote the transformed dependent variable and variable coefficients, the following problem can be formulated:

$$\begin{cases} \bar{\epsilon}\dfrac{d^2\phi}{d\xi^2} + \bar{u}(\xi)\dfrac{d\phi}{d\xi} + \bar{g}(\xi)\phi = 0 \quad \text{on} \quad \bar{I}_e \\ \phi(-1) = \bar{p} \\ \phi(1) = \bar{q} \end{cases} \tag{3}$$

where

$$\bar{\epsilon} = \frac{\epsilon}{h}$$

$$\bar{u}(\xi) = \frac{u(\xi)}{2}$$

$$\bar{g}(\xi) = \frac{g(\xi)h}{4}$$

Clearly, the mapped local problem (3) has a different character as compared to the original global problem (1). If ϵ is small compared to u, the solution of the original global problem (1) will be of boundary-layer type. Similarly, if $\bar{\epsilon}$ is small compared to $\bar{u}$, the local problem (3) will have a solution with a boundary layer. However, $\bar{\epsilon}$ varies inversely with h, and $\bar{g}$ is proportional to h. Thus, if the element size h is large and if ϵ and u have values which would lead to a boundary-layer-type global solution, the local element will have a solution of boundary-layer type. However, no matter how small ϵ is compared to u, as h approaches zero, the element boundary layer disappears. In fact, in the limit as h approaches zero, the local solution becomes a harmonic function.

On the typical element, there exist three solution regions. A boundary layer may occur on the right-hand side of the element if u is negative there. In addition, a boundary layer may occur on the left-hand side of the element if u is positive at that end of the element. Thus two "inner" boundary-layer regimes exist near the element boundaries. In addition, an "outer" solution region exists away from the boundary layers. Essentially, this region occupies the center of the element. Grasman and Matkowsky [10] have introduced an asymptotically valid solution for a differential equation with three similar solution regions. In the notation employed in this paper, the solution of Grasman and Matkowsky can be stated as follows:

$$\phi(\xi) = \underbrace{c\phi_0(\xi)}_{\substack{\text{outer} \\ \text{solution}}} + (\bar{p} - c\phi_0(-1))\underbrace{e^{-\bar{u}(-1)(1+\xi)/\bar{\epsilon}}}_{\substack{\text{left boundary-} \\ \text{layer solution}}} + (\bar{q} - c\phi_0(1))\underbrace{e^{\bar{u}(1)(1-\xi)/\bar{\epsilon}}}_{\substack{\text{right boundary-} \\ \text{layer solution}}} \tag{4}$$

In this equation the outer solution and boundary-layer solutions are defined by perturbation methods. In particular, the outer solution $\phi_0(\xi)$ satisfies the following equation:

$$\bar{u}(\xi)\frac{d\phi_0}{d\xi} + \bar{g}(\xi)\phi_0 = 0.$$

Thus

$$\phi_0(\xi) = \exp\left(-\int_0^{\xi} \frac{\bar{g}(s)}{\bar{u}(s)}\,ds\right)$$

The constant c in expression (4) must be defined in such a way that the boundary-layer solutions match the outer solution in some appropriate sense.

An assumption implicit in the use of the matched asymptotic expansion solution (4) is that $\bar{u}(-1) > 0$ and $\bar{u}(1) < 0$. In this case boundary layers exist at each end of the element. However, if $\bar{u}(-1) \leq 0$ and $\bar{u}(1) < 0$, a boundary layer exists on the right-hand side only, and the following matched solution is a valid restriction of (4):

$$\phi(\xi) = c\phi_0(\xi) + \tfrac{1}{2}(1 - \xi)(\bar{p} - c\phi_0(-1)) + (\bar{q} - c\phi_0(1))e^{\bar{u}(1)(1-\xi)/\bar{\epsilon}} \tag{5}$$

Similarly, if $\bar{u}(-1) > 0$ and $\bar{u}(1) \geq 0$, a boundary layer exists on the left-hand side of the element only, and the appropriate matched asymptotic solution is defined as follows:

$$\phi(\xi) = c\phi_0(\xi) + (\bar{p} - c\phi_0(-1))e^{-\bar{u}(-1)(1+\xi)/\bar{\epsilon}} + \tfrac{1}{2}(1 + \xi)(\bar{q} - c\phi_0(1)) \tag{6}$$

In the remainder of this paper numerical algorithms will be constructed using a procedure which is based on the general solution (4). When appropriate, similar algorithms can be obtained using the special formulas (5) and (6). The techniques, required to analyze those special cases, are a straightforward modification of the methods to be presented here.

The Definition of Finite-Element Shape Functions Via Singular Perturbations

The singular-perturbation solutions discussed in the previous section can be used in the construction of shape functions for finite-element convection-diffusion models. The use of these solutions seems appropriate since they are asymptotically exact on the elements and, thus, should provide accurate results. However, there are certain difficulties involved in using these functions in finite-element analyses. Asymptotically, as $\bar{\epsilon} \to 0$ the singular-perturbation solutions satisfy the boundary conditions at the ends of the elements. However, for large $\bar{\epsilon}$ these boundary conditions are not satisfied. This is a problem since in finite-element work finite values of $\bar{\epsilon}$ are often used. In fact, as $h \to 0$ in a finite-element model, $\bar{\epsilon} \to \infty$.

To overcome these difficulties alternate singular-perturbation solutions can be defined. An alternate version of (4), satisfying the appropriate boundary conditions, takes the following form:

$$\phi(\xi) = c\phi_0(\xi) + \tfrac{1}{2}(\bar{p} - c\phi_0(-1))(1 - \xi)e^{-|\bar{u}(-1)|(1+\xi)/\bar{\epsilon}} + \tfrac{1}{2}(\bar{q} - c\phi_0(1))(1 + \xi)e^{-|\bar{u}(1)|(1-\xi)/\bar{\epsilon}} \tag{7}$$

It should be noted that, in this expression, the absolute value of $\bar{u}$ was employed. This change was incorporated in order to insure that a

potential boundary layer exists at each end of the element. Because of this modification, the solution (7) can be used even when $\bar{u}(-1) < 0$ or $\bar{u}(1) > 0$. The matching criteria, to be introduced subsequently, will effectively determine which of the potential boundary layers is real, and it will give the real boundary layers more weight in the solution.

The interpolation functions for the one-dimensional problem can be obtained by defining $\bar{p}$ and $\bar{q}$ in (7) in such a way that the following condition is satisfied:

$$\psi_i(\lambda_k) = \delta_{ik}$$

where $\lambda_k = (-1)^k$, $k = 1, 2$. The resulting shape functions take the following form:

$$\psi_i(\xi) = \chi_{1i}(\xi)c_i + \chi_{2i}(\xi) \qquad i = 1, 2, (i \text{ not summed}) \tag{8}$$

where

$$\chi_{1i}(\xi) = \phi_0(\xi) - \frac{1}{2}\sum_{k=1}^{2} \phi_0(\lambda_k)(1 + \lambda_k\xi) \exp\left\{-\frac{|\bar{u}(\lambda_k)|(1 - \lambda_k\xi)}{\bar{\epsilon}}\right\}$$

$$\chi_{2i}(\xi) = \frac{1}{2}(1 + \lambda_i\xi) \exp\left\{-\frac{|\bar{u}(\lambda_i)|(1 - \lambda_i\xi)}{\bar{\epsilon}}\right\}$$

Variational Matching Procedures

The finite-element interpolation functions defined in (8) involve undetermined constants c_i. These parameters define the relative importance of the outer and boundary-layer solutions in the overall local element solution. These parameters could be chosen in many different ways. However, a useful criteria to use in defining c_1 and c_2 is to require that, in some approximate variational sense, $\psi_1(\xi)$ and $\psi_2(\xi)$ satisfy the differential equation $(3)_1$ within the element. This is, in a finite-element setting, the analog of the variational matching criteria first proposed by Grasman and Matkowsky [10], in the context of analytical singular perturbation methods.

In order to provide a concise notation for the discussion of the variational matching procedures certain integral expressions can be introduced. Let the L_2 inner product $(.\,,.)$ be defined in the following way:

$$(v, w) = \int_{-1}^{1} v(\xi)w(\xi)d\xi$$

In addition, certain bilinear forms denoted $a(.\,,.)$ and $b(.\,,.)$ will be utilized in subsequent developments. These bilinear forms have the following definitions:

$$a(v,w) = \left(\bar{\epsilon}\frac{d^2v}{d\xi^2} + \bar{u}\frac{dv}{d\xi} + \bar{g}v, \bar{\epsilon}\frac{d^2w}{d\xi^2} + \bar{u}\frac{dw}{d\xi} + \bar{g}w\right)$$

$$b(v,w) = \int_{-1}^{1}\left[\bar{\epsilon}\frac{dv}{d\xi}\frac{dw}{d\xi} + \frac{\bar{u}(\xi)}{2}\left(v\frac{dw}{d\xi} + w\frac{dv}{d\xi}\right) + \left(\frac{\bar{u}(\xi)^2}{2\bar{\epsilon}} + \frac{1}{2}\frac{d\bar{u}(\xi)}{d\xi} - \bar{g}(\xi)\right)vw\right] \exp\left(\frac{1}{\bar{\epsilon}}\int_0^{\xi}\bar{u}(s)ds\right)d\xi$$

Many different variational techniques can be employed to match the inner boundary-layer solutions with the outer solution in the sense previously defined. In this analysis, the following four techniques have been found to be useful:

1 Averaging Method. The differential equation $(3)_1$ is satisfied in the average sense over I_e.

$$\left(\bar{\epsilon}\frac{d^2\chi_{1i}}{d\xi^2} + \bar{u}\frac{d\chi_{1i}}{d\xi} + \bar{g}\chi_{1i}, 1\right)c_i = -\left(\bar{\epsilon}\frac{d^2\chi_{2i}}{d\xi^2} + \bar{u}\frac{d\chi_{2i}}{d\xi} + \bar{g}\chi_{2i}, 1\right)$$

$$i = 1, 2, (i \text{ not summed}) \tag{9}$$

2 Point Collocation Method. The differential equation $(3)_1$ is satisfied at a collocation point ξ^* ($\xi^* = 0$ seems to produce the best results).

$$\left[\bar{\epsilon}\frac{d^2\chi_{1i}}{d\xi^2}(\xi^*) + \bar{u}(\xi^*)\frac{d\chi_{1i}}{d\xi}(\xi^*) + \bar{g}(\xi^*)\chi_{1i}(\xi^*)\right]c_i = -\left[\bar{\epsilon}\frac{d^2\chi_{2i}}{d\xi^2}(\xi^*) + \bar{u}(\xi^*)\frac{d\chi_{2i}}{d\xi}(\xi^*) + \bar{g}(\xi^*)\chi_{2i}(\xi^*)\right]$$

$$i = 1, 2, (i \text{ not summed}) \tag{10}$$

3 Least-Squares Method. The differential equation $(3)_1$ is satisfied in the least-squares sense.

$$a(\chi_{1i}, \chi_{1i})c_i = -a(\chi_{1i}, \chi_{2i}) \quad i = 1, 2, (i \text{ not summed}) \tag{11}$$

4 A Method Based on a Variational Principle for Singular Perturbation Problems. The differential equation $(3)_1$ is an Euler equation of $b(\phi, \phi)$ [10]. Thus the constants c_i can be defined by insisting that $b(\psi_i, \psi_i)$ take on a stationary value as the scalars are varied.

$$b(\chi_{1i},\chi_{1i})c_i = -b(\chi_{1i},\chi_{2i}) \quad i = 1, 2, (i \text{ not summed}) \tag{12}$$

The Finite-Element Galerkin Method

The local shape functions $\psi_i(\xi)$ can be converted to global shape functions $\Psi_i(x)$ using standard assembly procedures. Then the scalar function ϕ can be defined in terms of the global shape functions Ψ_i and the nodal values of the scalar Φ_i by $\phi = \Psi_i\Phi_i$. Finally, the finite-element Galerkin procedure can be used to develop the following system of discrete equations defining the Φ_i variable:

$$K_{ji}\Phi_i = 0$$

The global stiffness matrix K_{ji} is obtained by the assembly of local stiffness matrices K_{eji} defined as follows:

$$K_{eji} = \int_{I_e}\left[\epsilon\frac{d\psi_j}{dx}\frac{d\psi_i}{dx} - u\psi_j\frac{d\psi_i}{dx} - g\psi_j\psi_i\right]dx = \int_{-1}^{1}\left[\frac{2\epsilon}{h}\frac{d\psi_j}{d\xi}\frac{d\psi_i}{d\xi} - u\psi_j\frac{d\psi_i}{d\xi} - \frac{gh}{2}\psi_j\psi_i\right]d\xi \tag{13}$$

Consider a particular class of problems. This class of problems is obtained from $(3)_1$ by setting $g = 0$ and making u a constant. Shape functions which represent exact solutions to this type of problem can be easily constructed [9]. A typical shape function ψ_1 is defined as follows:

$$\psi_1(x) = \frac{1 - e^{u(h-x)/\epsilon}}{1 - e^{uh/\epsilon}} \tag{14}$$

If shape functions of the form of (14) are employed to solve the class of constant coefficient problems with $g = 0$, the resulting solutions are exact. For this reason these shape functions could be called the "exact shape functions." The terms in the "exact" local matrix K_{eji} can be constructed by introducing (14) in (13). For example, the term in the first row and first column, denoted Z_1, of the exact coefficient matrix, is

$$Z_1 = -\frac{ue^{uh/\epsilon}}{1 - e^{uh/\epsilon}}$$

An expression, similar to Z_1, can be obtained when the singular-perturbation shape functions (8) are introduced in (13). The term in the first row and first column, denoted W_1, of the singular-perturbation coefficient matrix is defined as follows:

$$W_1 = E_1c_1^2 + E_2c_1 + E_3$$

where

$$E_1 = \frac{\bar{\epsilon}e^{-2A}}{2}\left[\left(2 + 4A + \frac{1}{A}\right)\sinh(2A) + (2 + 4A)\cosh(2A) - 4(1 + A)^2 + \frac{4}{3}A^2\right]$$

$$E_2 = 2\bar{\epsilon}Se^{-A}[\sinh(A) + \cosh(A)] - \frac{\bar{\epsilon}e^{-2A}}{2}\left[\left(2 + 4A\right.\right.$$

$$+ 4S + \frac{1}{A}\Big) \sinh(2A) + (2 + 4A + 4S)\cosh(2A) - 4(1 + A)^2 + \frac{4}{3}A^2\Big]$$

$$E_3 = \frac{\bar{\epsilon}e^{-2A}}{2}\Big[\Big(2A + 2S + \frac{1}{2A} + 1\Big)\sinh(2A) + (2A + 2S + 1)\cosh(2A)\Big]$$

$$S = \bar{u}/\bar{\epsilon};\ A = |\bar{u}|/\bar{\epsilon}$$

In order to evaluate the error in the approximations, it is useful to have an expression for the optimum constant c_1. This is the constant $c_{1\ \mathrm{opt}}$ which produces exact solutions at the nodes of a finite-element mesh. As a criteria to define $c_{1\ \mathrm{opt}}$, it is sufficient to require that the term in the first row and first column of the coefficient matrix (this is the term associated with $\psi_1(\xi)$ and, thus, with c_1) be the same when either the singular perturbation shape functions or the exact shape functions are used in the analysis. The use of this criteria implies that, when $c_1 = c_{1\ \mathrm{opt}}$, the following relationship must hold:

$$W_1 = Z_1$$

or

$$E_1 c_{1\ \mathrm{opt}}^2 + E_2 c_{1\ \mathrm{opt}} + E_3 - Z_1 = 0 \tag{15}$$

This equation has two roots. The values of the two roots depend on the magnitude of u but not on its sign. The parameter $c_{1\ \mathrm{opt}}$ must be identified with one of the roots. The particular root, with which $c_{1\ \mathrm{opt}}$ should be identified, depends on the sign of u, according to the following rule:

$$c_{1\ \mathrm{opt}} = \frac{-E_2 + \sqrt{E_2^2 - 4E_1(E_3 - Z_1)}}{2E_1}, \qquad u < 0$$

$$c_{1\ \mathrm{opt}} = \frac{-E_2 - \sqrt{E_2^2 - 4E_1(E_3 - Z_1)}}{2E_1}, \qquad u > 0 \tag{16}$$

A similar analysis can be used to define $c_{2\ \mathrm{opt}}$. In this case, the parameter $c_{2\ \mathrm{opt}}$ is defined in a way such that the term in the second row and second column of the coefficient matrix is exact. It has been found that as long as $g(\xi) = 0$, the following relationship holds:

$$c_{2\ \mathrm{opt}} = 1 - c_{1\ \mathrm{opt}} \tag{17}$$

The constants, determined by variational matching, can be compared to the optimum constants to assess the workability of the approximate matching procedures. A particular case was chosen for the comparison. In this case $u = -1$. In Fig. 1, the optimum and approximate values for c_1 are plotted versus $\bar{\epsilon}$. It has been found that oscillatory solutions can occur when c_1 values less than the optimum ones are utilized. For this reason, the averaging procedure has been judged to be the most effective technique. Using the averaging method the computed c_1 values are always close to but greater than the optimum values.

The shape functions which can be obtained using the c_1 and c_2 parameters can take many forms. Suppose the coefficients in $(3)_1$ are constant with $g = 0$ and $u = -1$. Then, the shape function ψ_1, defined using the optimum constant in conjunction with (8), takes the form shown in Fig. 2. If the problem has a variable coefficient quite different shape functions are obtained. Consider the case when $u(\xi) = -\xi$ and $g(\xi) = 0$. In this variable coefficient situation, the values of c_1 and c_2 must be defined by some approximate procedure (the optimum constants are not known for this case). In this particular problem, all four variational matching procedures give the same constants ($c_1 = c_2 = 0.5$). The resulting shape functions are pictured in Fig. 3. In this particular variable coefficient case boundary layers appear on both ends of the element.

Numerical Integration Technique

When u and g are variable coefficients, it is useful to employ nu-

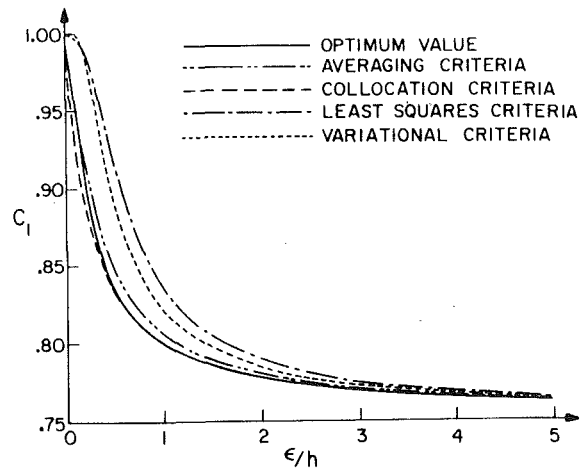

Fig. 1 Comparison of optimum and approximate values for c_1 ($u = -1$, $g = 0$)

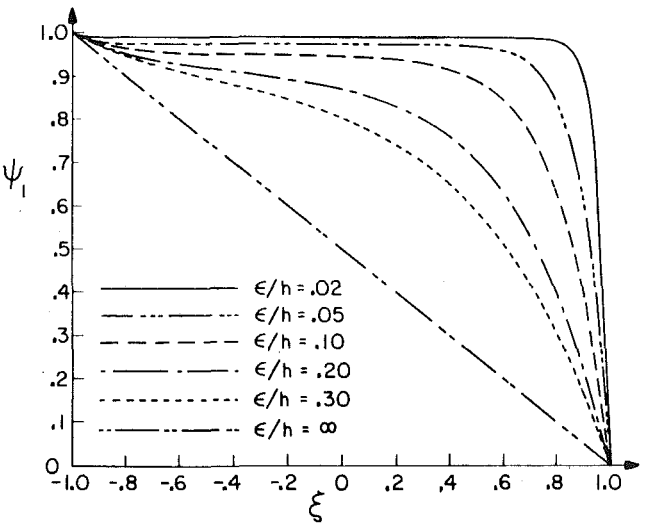

Fig. 2 Singular-perturbation shape functions for various values of $\bar{\epsilon}$ ($u = -1$, $g = 0$)

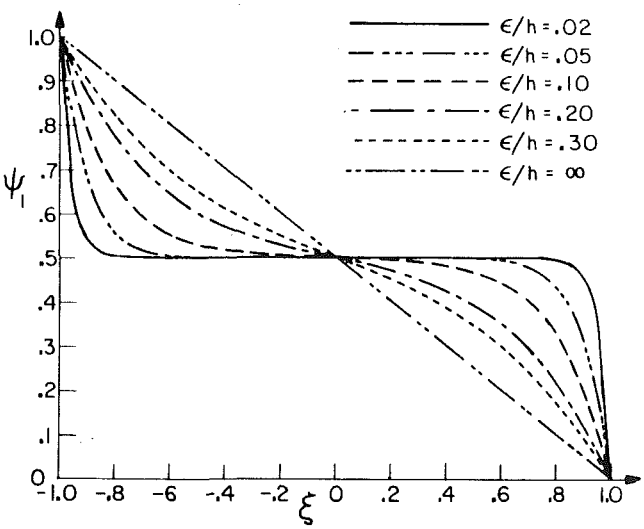

Fig. 3 Singular-perturbation shape functions for various values of $\bar{\epsilon}$ ($u(\xi) = -\xi$, $g = 0$)

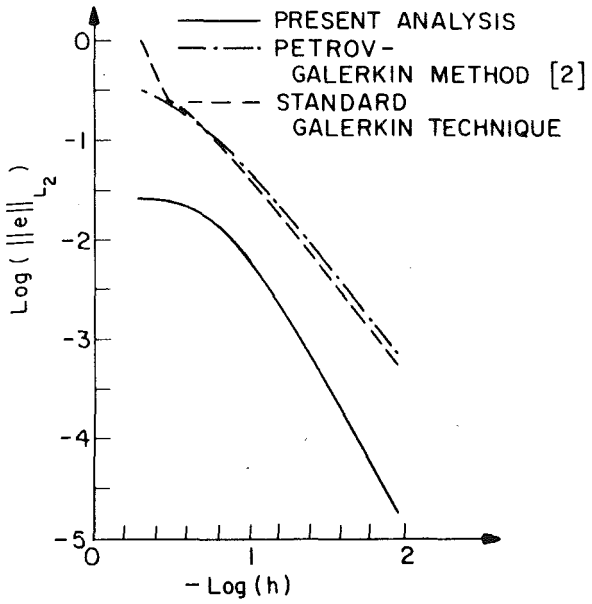

Fig. 4 Global L_2 error for various methods ($\epsilon = 0.05$)

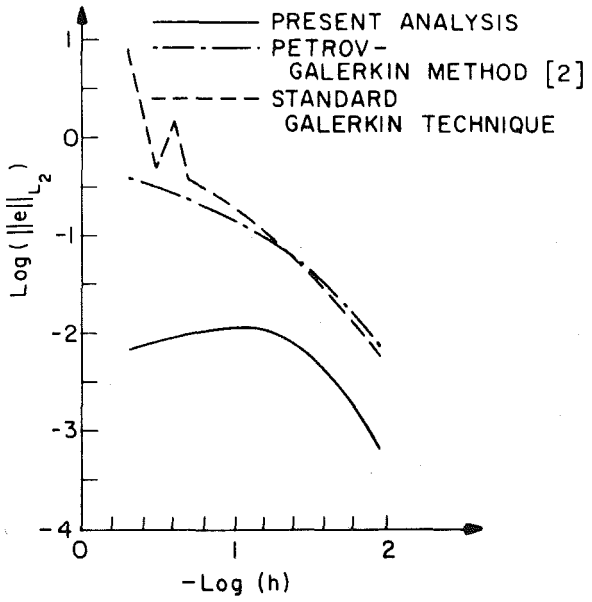

Fig. 5 Global L_2 error for various methods ($\epsilon = 0.01$)

merical integration techniques in the evaluation of the entries in matrix K_{eji}. In this work a quadrature rule, which is exact in the case when u and g are constant, has been employed. This technique is based on a two point Gaussian quadrature formula [11] for integrals of the following form:

$$I_n = \int_{-1}^{1} \xi^n e^{\alpha\xi} d\xi$$

In this quadrature rule the Gauss points $\xi_{1,2}$ and weights $w_{1,2}$ are defined as follows:

$$\xi_{1,2} = \frac{d \pm \sqrt{d^2 - 4r}}{2}$$

$$w_1 = \frac{I_0}{\xi_1 - \xi_2}\left(\frac{I_1}{I_0} - \xi_2\right) e^{-\alpha\xi_1}$$

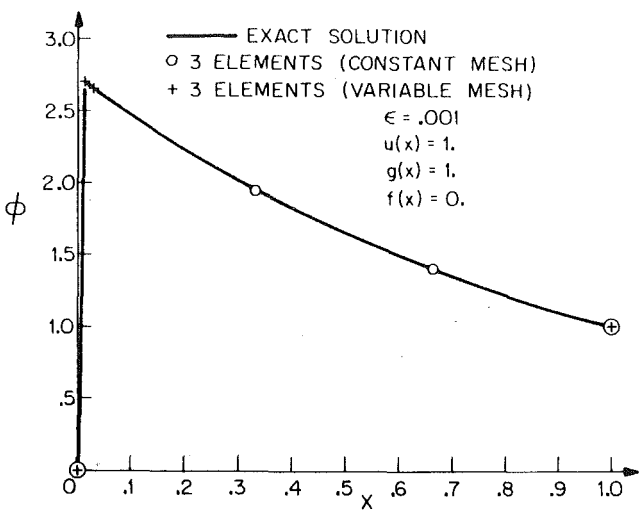

Fig. 6 Singular-perturbation solutions—a constant coefficient case

$$w_2 = \frac{I_0}{\xi_2 - \xi_1}\left(\frac{I_1}{I_0} - \xi_1\right) e^{-\alpha\xi_2}$$

where

$$d = \frac{I_0 I_3 - I_1 I_2}{I_0 I_2 - I_1^2}; \quad r = \frac{I_1 I_3 - I_2^2}{I_0 I_2 - I_1^2};$$

$$I_0 = \frac{1 - e^{-2\beta}}{\beta e^{-\beta}}; \quad I_1 = \frac{1 + e^{-2\beta}}{\alpha e^{-\beta}} - \frac{I_0}{\alpha};$$

$$I_2 = I_0 - \frac{2I_1}{\alpha}; \quad I_3 = I_1 + \frac{I_0 - 3I_2}{\alpha}; \quad \beta = |\alpha|.$$

For $\beta > 5$, multiply by $e^{-\beta}$ to avoid overflows and use asymptotic formulas in the analysis.

Numerical Experiments

In order to assess the accuracy of the finite-element algorithm, the problem (1) was solved on the interval $I = [0, 1]$. Various choices of the parameters ϵ, u, and g were employed, and in all cases the boundary values were defined by $p = 0$ and $q = 1$. Initially the constant coefficient case with $g = 0$ was considered. When optimum values were employed for the constants, c_i, the singular-perturbation algorithm produced exact solutions at the nodes. This occurred no matter what values were used for ϵ, u, and h. The approximate variational matching schemes produced inexact finite-element solutions; however, the answer obtained using these techniques were quite reasonable.

While the computed solutions for the constant coefficient problem (with $g = 0$) were exact at the nodes, they were not exact within the elements. The global L_2 error was used to define the error in matching the solution within the elements. In Figs. 4 and 5 the global L_2 error, for various choices of ϵ, is plotted for the standard Galerkin method, the Petrov-Galerkin method [2], and the singular-perturbation technique defined with optimum constants. The singular-perturbation shape functions produce a significant reduction in the error within the elements.

In Fig. 6 the solution to a problem with constant coefficients and a nonzero g term is presented. In Fig. 7 a solution for the constant coefficient differential equation $\epsilon\phi'' + u\phi' + g\phi = f$ is pictured. In Figs. 8–11 the solutions to various problems with variable coefficients are presented. In these variable coefficient solutions the averaging procedure was used to determine the constants c_i.

The most difficult variable coefficient problems seem to be those in which u changes sign within the domain. In these cases the slope of the u curve seems to have a great effect on the accuracy of the singular-perturbation finite-element solutions. A case in which u has a

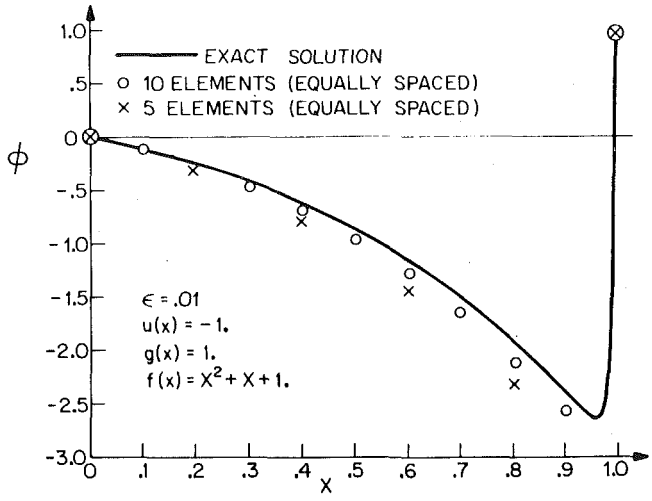

Fig. 7 Singular-perturbation solutions—a nonhomogeneous equation

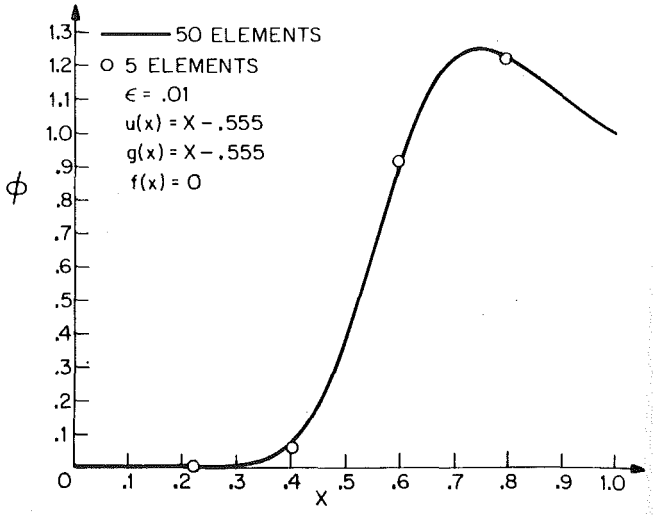

Fig. 10 Singular-perturbation solutions—a case with variable g term and right-hand side boundary layer

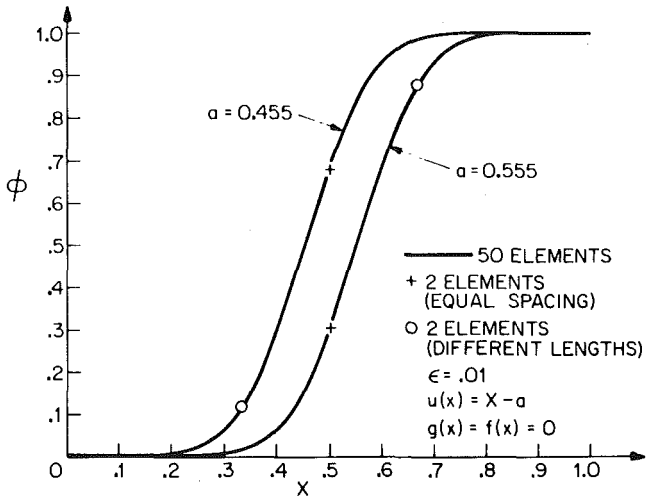

Fig. 8 Singular-perturbation solutions—variable coefficient cases with internal boundary layers

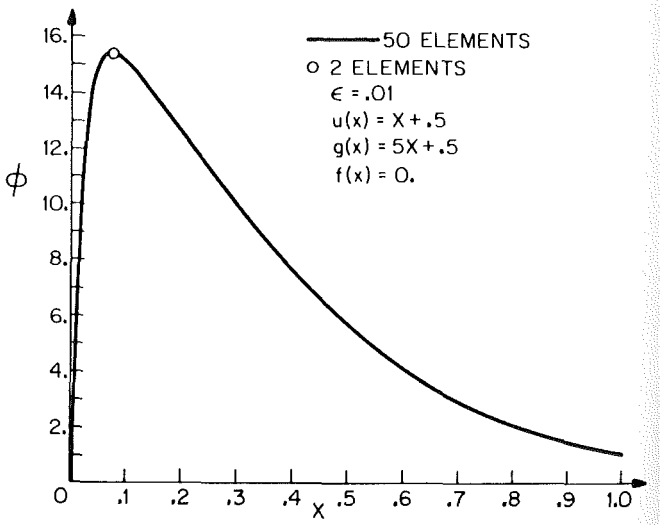

Fig. 11 Singular-perturbation solutions—a case with variable g term and left-hand side boundary layer

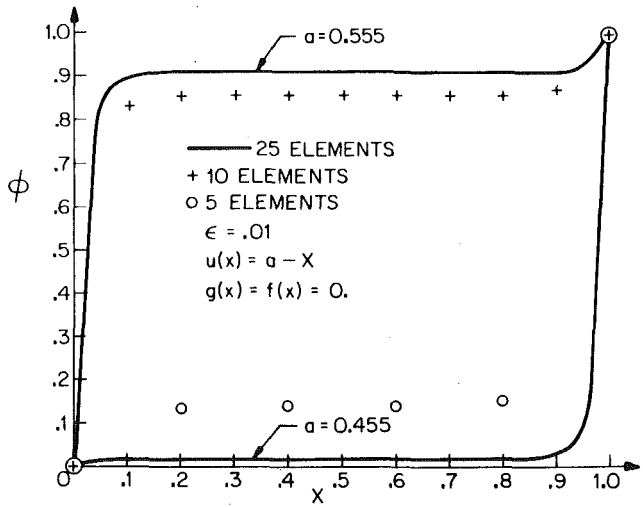

Fig. 9 Singular-perturbation solutions—variable coefficient cases with external boundary layers

positive slope is pictured in Fig. 8. In this case the solution has an interior boundary layer centered at the point of change in sign of u. The corresponding singular perturbation shape functions have a corresponding boundary layer in the center region of the elements. As can be seen from Fig. 8, the finite-element procedure works very well in this positive slope case. However, when the slope of u is negative, the situation is quite different. A typical case of this kind is pictured in Fig. 9. From Fig. 9, it can be seen that, when the slope of u is negative, slight changes in the point at which u changes sign cause large changes in the solution, and a movement of the boundary layer from one end of the domain to the other occurs. The problem is very sensitive to changes in u, and this sensitivity manifests itself as error in the numerical solution.

References

1 Roache, P. J., *Computational Fluid Dynamics*, Hermosa Publishers, Albuquerque, New Mex., 1972.

2 Christie, I., et al., "Finite-Element Methods for Second-Order Equations With Significant First Derivatives," *International Journal Num. Meth. Eng.*, Vol. 10, 1976, pp. 1389–1396.

3 Heinrich, J. C., et al., "An Upwind Finite-Element Scheme for Two-Dimensional Convective Transport Equations," *International Journal Num. Meth. Eng.*, Vol. 11, 1977, pp. 131–143.

4 Heinrich, J. C., and Zienkiewicz, O. C., "Quadratic Finite-Element Schemes for Two-Dimensional Convective Transport Problems," *International Journal Num. Meth. Eng.*, Vol. 11, 1977, pp. 1831–1844.

5 Zienkiewicz, O. C., and Heinrich, J. C., "The Finite-Element Method and Convection Problems in Fluid Mechanics," *Finite Elements in Fluids*, Vol. 3, ed., Gallagher, R. H., et al., Wiley, London, 1978, pp. 1–22.

6 Hughes, T. J. R., "A Simple Scheme for Developing 'Upwind' Finite Elements," *International Journal Num. Meth. Eng.*, Vol. 12, 1978, pp. 1359–1365.

7 Hughes, T. J. R., Liu, W. K., and Brooks, A., "Finite-Element Analysis of Incompressible Viscous Flows by the Penalty Function Formulation," *Journal Computational Physics*, Vol. 30, 1979, pp. 1–60.

8 Kikuchi, F., "Discrete Maximum Principle and Artificial Viscosity in Finite-Element Approximations to Convective Diffusion Problems," Institute of Space and Aeronautical Science, University of Tokyo, Report No. 550, 1977, pp. 153–166.

9 Barrett, K. E., "Finite-Element Analysis for Flow Between Rotating Discs Using Exponentially Weighted Basis Functions," *International Journal Num. Meth. Eng.*, Vol. 11, 1977, pp. 1809–1817.

10 Grasman, J., and Matkowsky, B. J., "A Variational Approach to Singularly Perturbed Boundary-Value Problems for Ordinary and Partial Differential Equations With Turning Points," *SIAM Journal Applied Mathematics*, Vol. 32, 1977, pp. 588–597.

11 Atkinson, J.D., and Hughes, T. J. R., "Upwind Finite-Element Schemes for Convective-Diffusive Equations," Charles Kolling Research Lab., Technical Note C-2, Department of Mechanical Engineering, University of Sydney, Dec. 1977.

Rafael F. Diaz-Munio
Graduate Student.

L. Carter Wellford, Jr.
Associate Professor.

Department of Civil Engineering,
University of Southern California,
University Park,
Los Angeles, Calif. 90007

A Finite-Element Singular-Perturbation Technique for Convection-Diffusion Problems

Part 2: Two-Dimensional Problems

Approximation procedures for the solution of two-dimensional convection-diffusion problems are introduced. In these procedures finite-element techniques are utilized. The developed solution algorithms are based on a variational method of matched asymptotic expansions. When these techniques are used in conjunction with standard Galerkin methods, to solve convection-diffusion equations, highly accurate solutions are obtained. Numerical results for certain two-dimensional problems are presented to establish the accuracy of the proposed procedures.

Introduction

In Part 1 of this paper [1], singular perturbation techniques were used to develop finite-element approximations for certain convection-diffusion problems. In particular, a method of variational matched asymptotic expansions was employed to construct shape functions which, within the elements, are almost exact solutions to the homogeneous convection-diffusion equations. These shape functions were used, in conjunction with the standard Galerkin method, to solve various one-dimensional problems. In this second part of the paper, the previously developed singular perturbation techniques are extended to two-dimensional cases.

The Physical Problem

Consider a domain $\Omega \subset R^2$. Let (x, y) be the coordinates of points in Ω. Let $\phi(x, y)$ be a scalar function defined on Ω. In addition, let $\partial\Omega$ denote a boundary on Ω with normal n. The boundary segment $\partial\Omega_1$ denotes a portion of $\partial\Omega$ on which ϕ is specified, and the boundary segment $\partial\Omega_2$ is a portion of $\partial\Omega$ on which $\partial\phi/\partial n$ is specified. The boundary $\partial\Omega = \partial\Omega_1 \cup \partial\Omega_2$. Then, the convection-diffusion problem is posed as follows:

$$\begin{cases} \epsilon\left(\dfrac{\partial^2\phi}{\partial x^2} + \dfrac{\partial^2\phi}{\partial y^2}\right) + u\dfrac{\partial\phi}{\partial x} + v\dfrac{\partial\phi}{\partial y} + g\phi = 0 & \text{on } \Omega \\ \phi = t_1 & \text{on } \partial\Omega_1 \\ \dfrac{\partial\phi}{\partial n} = t_2 & \text{on } \partial\Omega_2 \end{cases} \quad (1)$$

where t_1 represents the specified ϕ values on $\partial\Omega_1$ and t_2 represents the specified values of flux on $\partial\Omega_2$. Normally, the parameter ϵ is a diffusion coefficient, u and v are related (through a minus sign) to velocity components in the x and y-directions, and g is associated with transient or linearized convective effects.

Singular-Perturbation Shape Functions for Two-Dimensional Problems

Singular-perturbation shape functions for two-dimensional problems can be defined in various ways. In this work, two methods will be employed. In the first method, two-dimensional shape functions are defined as a tensor product of the one-dimensional shape functions introduced in [1]. Generally, the resulting finite-element approximation is *nonconforming*. However, in the limit as the element size approaches zero, this model is conforming. Thus it could be called *asymptotically conforming*. The second technique involves matching boundary layer and outer solutions for the two-dimensional problem using various variational matching procedures. This method is an extension of the technique introduced for the one-dimensional problem. It allows the development of *conforming* shape functions in two dimensions, regardless of the size of the particular element being analyzed.

Consider a mapped element $\bar{\Omega}_e$ as shown in Fig. 1. The standard

Presented at the Symposium on Finite-Element Methods for Convection Dominated Flows, at the 1979 Winter Annual Meeting, New York, N.Y., December 2–7, 1979 and contributed by the Applied Mechanics Division for publication in the JOURNAL OF APPLIED MECHANICS.

Discussion on this paper should be addressed to the Editorial Department, ASME, United Engineering Center, 345 East 47th Street, New York, N.Y. 10017, and will be accepted until September 1, 1981. Readers who need more time to prepare a Discussion should request an extension from the Editorial Department. Manuscript received by ASME Applied Mechanics Division, December, 1979; final revision, September, 1980.

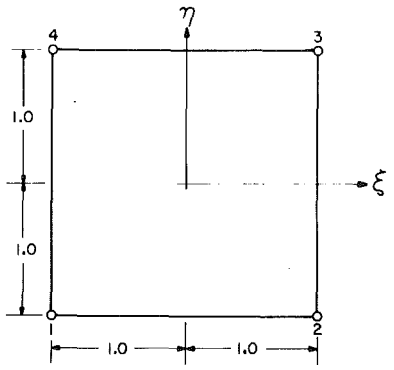

Fig. 1 Mapped element $\bar{\Omega}_e$

bilinear shape functions $\mu_i(\xi, \eta)$, defined on $\bar{\Omega}_e$, take the following form:

$$\mu_1(\xi, \eta) = \tfrac{1}{4}(1 - \xi)(1 - \eta)$$
$$\mu_2(\xi, \eta) = \tfrac{1}{4}(1 + \xi)(1 - \eta)$$
$$\mu_3(\xi, \eta) = \tfrac{1}{4}(1 + \xi)(1 + \eta)$$
$$\mu_4(\xi, \eta) = \tfrac{1}{4}(1 - \xi)(1 + \eta) \tag{2}$$

In addition, consider a four node quadrilateral element Ω_e defined in the physical plane. The coordinates of the ith node of Ω_e are denoted (x_i, y_i). A mapping between the physical element Ω_e and the mapped element $\bar{\Omega}_e$ can be constructed using standard isoparametric techniques

$$x = \mu_i(\xi, \eta)x_i$$
$$y = \mu_i(\xi, \eta)y_i \tag{3}$$

As a measure of the element sizes in the x and y-directions, a natural definition can be introduced

$$h_x = 2\left.\frac{\partial x}{\partial \xi}\right|_{\substack{\xi=0\\ \eta=0}} = 2\frac{\partial \mu_i}{\partial \xi}(0, 0)x_i$$
$$h_y = 2\left.\frac{\partial y}{\partial \eta}\right|_{\substack{\xi=0\\ \eta=0}} = 2\frac{\partial \mu_i}{\partial \eta}(0, 0)y_i$$

Finally, the following parameters can be defined in terms of h_x and h_y:

$$\bar{\epsilon}_x = \frac{\epsilon}{h_x}$$
$$\bar{\epsilon}_y = \frac{\epsilon}{h_y}$$
$$\bar{u}(\xi, \eta) = \frac{u(\xi, \eta)}{2}$$
$$\bar{v}(\xi, \eta) = \frac{v(\xi, \eta)}{2} \tag{4}$$
$$\bar{g}_x(\xi, \eta) = \frac{g(\xi, \eta)h_x}{8}$$
$$\bar{g}_y(\xi, \eta) = \frac{g(\xi, \eta)h_y}{8}$$

where ϵ is the positive constant diffusion coefficient defined in (1), and $u(\xi, \eta)$, $v(\xi, \eta)$, and $g(\xi, \eta)$ are the mappings of the variable coefficients introduced in (1).

Two sets of shape functions are utilized in modeling the dependent variable ϕ on the two-dimensional element. The first set of shape functions is denoted β_i. They are associated with the ξ coordinate and are defined as follows:

$$\beta_i(\xi) = \chi_{1i}(\xi)c_{1i} + \chi_{2i}(\xi) \quad i = 1, 2, (i \text{ not summed}) \tag{5}$$

where

$$\chi_{1i}(\xi) = \nu(\xi) - \frac{1}{2}\sum_{k=1}^{2}\nu(\lambda_k)(1 + \lambda_k\xi) \times \exp\left\{-\frac{|\bar{u}(\lambda_k, 0)|(1 - \lambda_k\xi)}{\bar{\epsilon}_x}\right\}$$
$$\chi_{2i}(\xi) = \frac{1}{2}(1 + \lambda_i\xi)\exp\left\{-\frac{|\bar{u}(\lambda_i, 0)|(1 - \lambda_i\xi)}{\bar{\epsilon}_x}\right\}$$
$$\lambda_k = (-1)^k$$
$$\nu(\xi) = \exp\left(-\int_0^{\xi}\frac{\bar{g}_x(s, 0)}{\bar{u}(s, 0)}ds\right)$$

The $\beta_i(\xi)$ expressions are designed to be singular-perturbation shape functions, in the sense defined in [1], for the following problem:

$$\bar{\epsilon}_x\frac{d^2\phi}{d\xi^2} + \bar{u}(\xi, 0)\frac{d\phi}{d\xi} + \bar{g}_x(\xi, 0)\phi = 0 \tag{6}$$

These shape functions depend on the values of the variable coefficients evaluated on the $\eta = 0$ line crossing the center of the element. If the variable coefficients are, for example, known only at the nodes of the element, they can be computed on the $\eta = 0$ line by interpolation, prior to the construction of the shape functions. The constants c_{11} and c_{12} in (5) can be defined by insuring that, in some sense, the $\beta_i(\xi)$ shape functions satisfy (6) within the element. The techniques, defined in [1], involving variational matching and optimum constants are useful in this regard. In particular, if $\bar{g}_x(\xi, 0) = 0$, if $\bar{u}(\xi, 0)$ is a constant, and if the following identification of parameters is employed:

$$\bar{\epsilon} = \bar{\epsilon}_x$$
$$\bar{u} = \bar{u}(\xi, 0)$$

the optimum values for c_{11} and c_{12} can be obtained using equations (16) and (17) in [1].

The second set of shape functions is denoted τ_j. They are associated with the η coordinates and are defined as follows:

$$\tau_j(\eta) = \mu_{1j}(\eta)c_{2j} + \mu_{2j}(\eta) \quad j = 1, 2, (j \text{ not summed}) \tag{7}$$

where

$$\mu_{1j}(\eta) = \alpha(\eta) - \frac{1}{2}\sum_{k=1}^{2}\alpha(\lambda_k)(1 + \lambda_k\eta)\exp\left\{-\frac{|\bar{u}(0, \lambda_k)|(1 - \lambda_k\eta)}{\bar{\epsilon}_y}\right\}$$
$$\mu_{2j}(\eta) = \frac{1}{2}(1 + \lambda_j\eta)\exp\left\{-\frac{|\bar{u}(0, \lambda_j)|(1 - \lambda_j\eta)}{\bar{\epsilon}_y}\right\}$$
$$\alpha(\eta) = \exp\left(-\int_0^{\eta}\frac{\bar{g}_y(0, s)}{\bar{v}(0, s)}ds\right)$$

The $\tau_j(\eta)$ shape functions are designed to be singular-perturbation shape functions, in the sense that, on the element level, they satisfy the following equation approximately:

$$\bar{\epsilon}_y\frac{d^2\phi}{d\eta^2} + \bar{v}(0, \eta)\frac{d\phi}{d\eta} + \bar{g}_y(0, \eta)\phi = 0$$

The $\tau_j(\eta)$ shape functions depend on the values of certain variable coefficients on the line $\xi = 0$ passing through the center of the element. If necessary, these coefficient values can be obtained from nodal values of the variable coefficients by interpolation. The c_{21} and c_{22} parameters must be defined by variational matching procedures, etc. These techniques are the same as those introduced for the one-dimensional problem.

Two-dimensional shape functions $\gamma_k(\xi, \eta)$, associated with the four nodes of the element pictured in Fig. 1, can be defined as a tensor product of $\beta_i(\xi)$ and $\tau_j(\eta)$. The following model results:

$$\gamma_1(\xi, \eta) = \beta_1(\xi)\tau_1(\eta)$$
$$\gamma_2(\xi, \eta) = \beta_2(\xi)\tau_1(\eta)$$
$$\gamma_3(\xi, \eta) = \beta_2(\xi)\tau_2(\eta)$$
$$\gamma_4(\xi, \eta) = \beta_1(\xi)\tau_2(\eta) \tag{8}$$

As $h_x \to 0$ and $h_y \to 0$ (or $\bar{\epsilon}_x \to \infty$ and $\bar{\epsilon}_y \to \infty$), $\gamma_k(\xi, \eta) \to \mu_k(\xi, \eta)$. That is, the two-dimensional singular perturbation shape functions approach the bilinear shape functions. Thus the functions γ_k are asymptotically conforming. However, for large values of h_x and h_y, these shape functions are nonconforming, relative to the solution space associated with the variational problem.

A second method can be utilized to develop shape functions suitable for the two-dimensional finite-element analysis. In this technique, two-dimensional inner boundary-layer solutions, corresponding to the four nodes of the element, and a two-dimensional outer solution are defined. The outer solution is denoted $\omega(\xi, \eta)$ and the inner solutions are labeled $\omega_i(\xi, \eta)$. The inner and outer solutions can be matched, using variational matching procedures, to obtain realistic shape functions for the two-dimensional problem. Utilizing the same notation as was employed in discussing the tensor product formulation, the shape functions, defined by two-dimensional variational matching, are denoted $\gamma_k(\xi, \eta)$. The typical function $\gamma_1(\xi, \eta)$, associated with the first node in the element, takes the following form:

$$\gamma_1(\xi, \eta) = c_1\omega(\xi, \eta) + \tfrac{1}{4}(1 - c_1\omega(-1, -1))(1 - \xi)(1 - \eta)\omega_1(\xi, \eta) - \frac{c_1\omega(1, -1)}{4}(1 + \xi)(1 - \eta)\omega_2(\xi, \eta) - \frac{c_1\omega(1, 1)}{4}(1 + \xi)(1 + \eta)\omega_3(\xi, \eta) - \frac{c_1\omega(-1, 1)}{4}(1 - \xi)(1 + \eta)\omega_4(\xi, \eta)$$

Various choices are possible for the outer solution $\omega(\xi, \eta)$ and the boundary-layer solutions $\omega_i(\xi, \eta)$, to be used in forming $\gamma_k(\xi, \eta)$. The inner and outer solutions could be defined so as to mimic, as closely as possible, the corresponding terms in the tensor product model. The following expressions, for ω and ω_i, result from this type of analysis:

$$\omega(\xi, \eta) = \nu(\xi)\alpha(\eta)$$

$$\omega_1(\xi, \eta) = e^{-|\bar{u}(-1,-1)|(1+\xi)/\bar{\epsilon}_x} e^{-|\bar{v}(-1,-1)|(1+\eta)/\bar{\epsilon}_y}$$

$$\omega_2(\xi, \eta) = e^{-|\bar{u}(1,-1)|(1-\xi)/\bar{\epsilon}_x} e^{-|\bar{v}(1,-1)|(1+\eta)/\bar{\epsilon}_y}$$

$$\omega_3(\xi, \eta) = e^{-|\bar{u}(1,1)|(1-\xi)/\bar{\epsilon}_x} e^{-|\bar{v}(1,1)|(1-\eta)/\bar{\epsilon}_y}$$

$$\omega_4(\xi, \eta) = e^{-|\bar{u}(-1,1)|(1+\xi)/\bar{\epsilon}_x} e^{-|\bar{v}(-1,1)|(1-\eta)/\bar{\epsilon}_y}$$

In order to obtain the final form of $\gamma_1(\xi, \eta)$, the constant c_1 must be defined. This constant can be identified using a two-dimensional approximate variational matching technique. A similar procedure can be employed to obtain the remainder of the shape functions $\gamma_k(\xi, \eta)$. For finite h_x and h_y, the resulting model is not conforming. However, the model is asymptotically conforming, and, in the limit as h_x and h_y approach 0, $\gamma_k(\xi, \eta) \to \mu_k(\xi, \eta)$—the bilinear shape functions.

An alternate model can be obtained by defining the outer solution ω and the inner solutions ω_i so that, in the case when $g(\xi, \eta) = 0$, the shape functions are conforming for any values of h_x and h_y. The following expressions seem to preserve the character of the solution, while yielding a conforming element:

$$\omega(\xi, \eta) = \exp\left(-\frac{g(0,0)}{\frac{2u(0,0)}{h_x} + \frac{2v(0,0)}{h_y}}[\xi + \eta]\right)$$

$$\omega_1(\xi, \eta) = e^{-\Omega(-1,-1)(1+\xi)(1+\eta)}$$

$$\omega_2(\xi, \eta) = e^{-\Omega(1,-1)(1-\xi)(1+\eta)}$$

$$\omega_3(\xi, \eta) = e^{-\Omega(1,1)(1-\xi)(1-\eta)}$$

$$\omega_4(\xi, \eta) = e^{-\Omega(-1,1)(1+\xi)(1-\eta)}$$

$$\Omega(\xi, \eta) = \frac{|\bar{u}(\xi, \eta)|}{\bar{\epsilon}_x} + \frac{|\bar{v}(\xi, \eta)|}{\bar{\epsilon}_y}$$

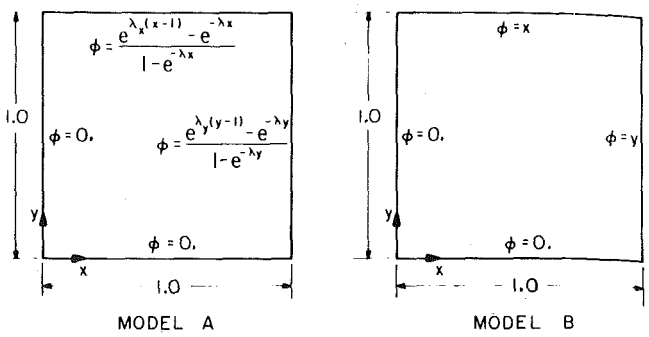

Fig. 2 Physical models employed to test the two-dimensional algorithms

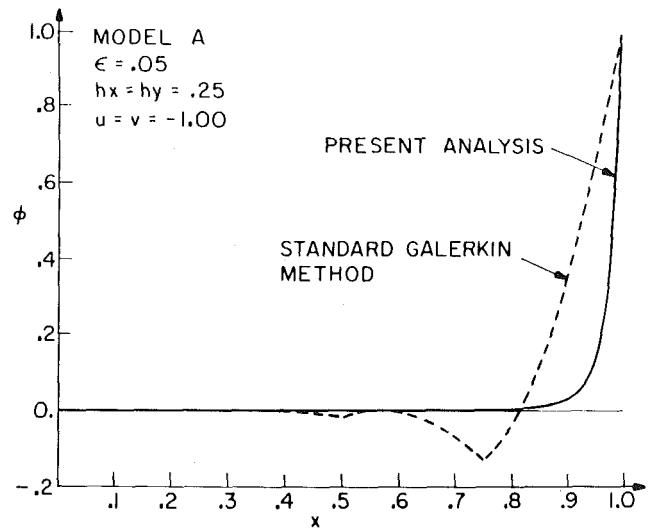

Fig. 3 Two-dimensional finite-element solutions for ϕ on the line $y = x$ ($h_x = h_y = 0.25$, Model A)

Two-Dimensional Finite-Element Galerkin Techniques

The problem (1) can be solved by the finite-element Galerkin procedure, using the shape function $\gamma_k(\xi, \eta)$ to define ϕ and using the shape functions $\mu_k(\xi, \eta)$ to define the geometric mappings. The local shape functions $\gamma_k(\xi, \eta)$ defined on $\bar{\Omega}_e$ can be mapped to local shape functions $\gamma_k(x, y)$ defined on Ω_e by using the isoparametric transformation (3). Global shape functions $\Gamma_k(x, y)$ defined on Ω can be obtained from the local shape functions $\gamma_k(x, y)$ using standard assembly procedures. The finite-element Galerkin model for problem (1), defined in terms of the global shape functions, takes the following form:

$$\int_\Omega \left[\epsilon\left(\frac{\partial^2\phi}{\partial x^2} + \frac{\partial^2\phi}{\partial y^2}\right) + u(x, y)\frac{\partial\phi}{\partial x} + v(x, y)\frac{\partial\phi}{\partial y} + g(x, y)\phi\right]\Gamma_k dx dy = 0 \quad (9)$$

For simplicity, it is assumed that $\partial\Omega_2 = 0$. Thus only kinematic boundary conditions are applied, and $\Gamma_k = 0$ on $\partial\Omega$. The dependent variable ϕ can be defined in terms of the singular perturbation shape functions Γ_j as follows:

$$\phi = \Gamma_j\Phi_j \quad (10)$$

where Φ_j is the dependent variable at global node j. Introducing (10) in (9) and using the Green's theorem to simplify the resulting expression, the following algorithm is obtained:

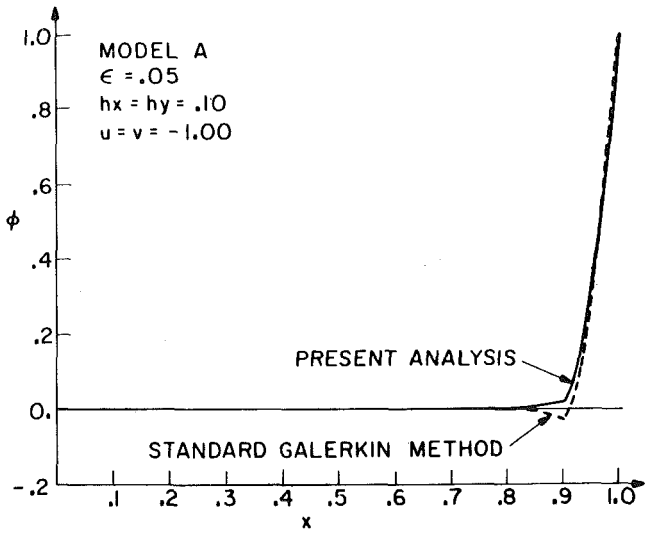

Fig. 4 Two-dimensional finite-element solutions for ϕ on the line $y = x$ ($h_x = h_y = 0.10$, Model *A*)

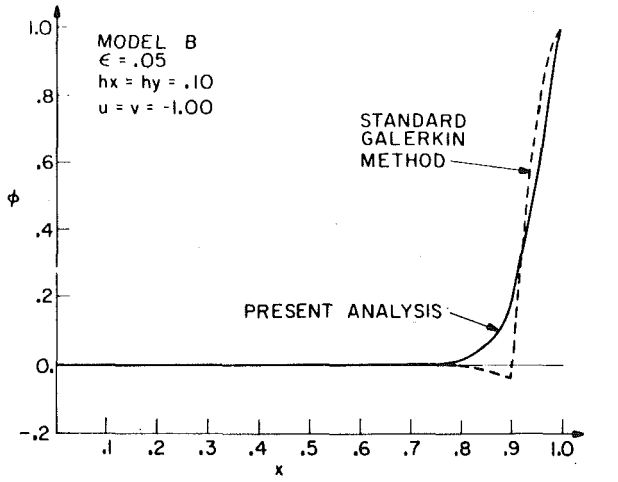

Fig. 6 Two-dimensional finite-element solutions for ϕ on the line $y = x$ ($h_x = h_y = 0.10$, Model *B*)

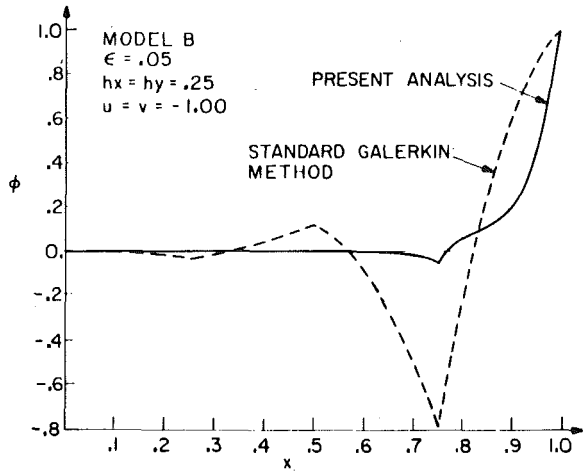

Fig. 5 Two-dimensional finite-element solutions for ϕ on the line $y = x$ ($h_x = h_y = 0.25$, Model *B*)

$$K_{kj}\Phi_j = 0 \tag{11}$$

where

$$K_{kj} = \int_\Omega \left[\epsilon \left(\frac{\partial \Gamma_k}{\partial x}\frac{\partial \Gamma_j}{\partial x} + \frac{\partial \Gamma_k}{\partial y}\frac{\partial \Gamma_j}{\partial y} \right) - u(x,y)\Gamma_k \frac{\partial \Gamma_j}{\partial x} - v(x,y)\Gamma_k \frac{\partial \Gamma_j}{\partial y} - g(x,y)\Gamma_k\Gamma_j \right] dxdy$$

This system of equations defines the values of ϕ at the global nodes of the mesh. Normally the matrix K_{kj} is defined by assembling similar local coefficient matrices constructed on the elements Ω_e. These local coefficient matrices are normally determined using numerical integration techniques in the mapped plane $\bar{\Omega}_e$. In transforming the local integrals similar to (11) from Ω_e to $\bar{\Omega}_e$, the transformation (3) involving the bilinear shape functions is employed.

Numerical Experiments for the Two-Dimensional Problem

In order to evaluate the accuracy of the two-dimensional finite-element algorithm composed of (8) and (11), two typical problems were solved. These problems are denoted *A* and *B*. In these calculations Ω was assumed to be a square region with unit area, and the boundary conditions were defined as shown in Fig. 2. In this figure, $\lambda_x = u/\epsilon$ and $\lambda_y = v/\epsilon$.

The coefficients were assumed to be constant with $\epsilon = 0.05$, $u = v = -1$, and $g = 0$. A uniform mesh of finite elements was constructed on the square domain Ω. The algorithm composed of (8) and (11) was used to obtain the approximate solutions for various values of h_x and h_y. In Figs. 3 and 4, the approximate solution defined by singular perturbation is compared to the standard Galerkin solution. In these figures, the approximations for ϕ, on the diagonal line $y = x$ in the domain Ω, are plotted versus x.

The exact solution for this problem takes the following form:

$$\phi = \left[\frac{e^{\lambda_x(x-1)} - e^{-\lambda_x}}{1 - e^{-\lambda_x}} \right] \left[\frac{e^{\lambda_y(y-1)} - e^{-\lambda_y}}{1 - e^{-\lambda_y}} \right]$$

For the problem *A*, the singular perturbation finite-element solution matched the exact solution at all nodes of the mesh. Similar results, for problem *B*, are presented in Figs. 5 and 6. The exact solution for problem *B* was not determined; however, it is clear that the finite-element singular perturbation model is not exact for this choice of boundary conditions. Even though, for model *B*, the finite-element singular perturbation algorithm was not exact, the resulting solution is considerably smoother and more reasonable than the one obtained using the standard Galerkin method.

In these calculations, typical isoparametric techniques were utilized. The numerical integrations were carried out employing the Gauss quadrature formulas for exponentials defined in [1].

Reference

1 Diaz-Munio, R. F., and Wellford, L. C., "A Finite-Element Singular-Perturbation Technique for Convection-Diffusion Problems; Part 1: The One-Dimensional Case," ASME JOURNAL OF APPLIED MECHANICS, Vol. 48, 1981, pp. 265–271.

M. A. Eisenberg
Professor.
Mem. ASME

C.-F. Yen
Research Associate.

Department of Engineering Sciences,
University of Florida,
Gainesville, Fla. 32611

A Theory of Multiaxial Anisotropic Viscoplasticity

A theory of anisotropic viscoplasticity is developed. It is compared with and shown to reduce to existing theories under appropriate restrictions. The theory accommodates anisotropic hardening laws which, by means of Lagrangian mappings in stress space, incorporate experimentally observed yield surface distortion as well as kinematic and isotropic flow-induced changes. The theory is applied to the prediction of flow surfaces in tension-torsion space.

1 Introduction

The classical plasticity and rheological theories recognize exclusively the path-dependent and rate-dependent nature of inelastic deformation, respectively. In general, both dependencies are manifest. However, for specific materials subject to a restricted range of environmental conditions the basic hypotheses of one or the other of the foregoing theories may be approximated with sufficient accuracy for a given application. To address the problems where such approximation is not obtained a variety of more ambitious constitutive theories have been proposed: among them, the theory of viscoplasticity. Perzyna [1] identifies theories which attempt to describe two classes of behavior: elastic/viscoplastic and elastic-viscoplastic. The former represents inviscid elastic response, while the latter, for which Naghdi and Murch [2] use the more descriptive label viscoelastic/plastic, assumes viscoelastic behavior for all stress states. The viscoplasticity theories to be discussed are restricted to the elastic/viscoplastic class.

The theory, rooted in the works of Bingham [3] and Hohenemser and Prager [4], has been extensively developed and popularized by Perzyna in a series of papers dating to 1963 [5]. It is assumed that there exists a yield function

$$F = f/\kappa - 1 \tag{1}$$

where F, f, and κ are scalar functions of inelastic strain, $\epsilon^p_{ij} = \epsilon_{ij} - \epsilon^e_{ij}$, and possible internal state variables which summarize the history of deformation. The functions F and f also depend upon stress σ_{ij} such that

$$F \leqq 0, \quad f \leqq \kappa \tag{2}$$

define in stress space the region of elastic response. The inelastic strains are then obtained by integrating

$$\dot{\epsilon}^p_{ij} = \gamma_o \langle \Phi(F) \rangle (\partial f/\partial \sigma_{ij}) \sigma^*_{pq}$$

where $\langle\ \rangle$ are Macaulay brackets, γ_0 and Φ are scalar material response functions, and σ^*_{pq} is the point in stress space at which the derivative is defined.

The viscoplasticity theory, to be completed, must address the following questions:

(*A*) How are Φ and γ_0 to be determined?
(*B*) How shall σ^*_{pq} be defined?
(*C*) What is the form of the initial quasi-static yield surface?
(*D*) How does the quasi-static yield surface translate, rotate, and/or deform as the inelastic deformation proceeds?

Questions (*A*) and (*B*) are treated in Sections 2 and 4 in which the uniaxial response and the multiaxial generalization thereof are discussed. Questions (*C*) and (*D*) are treated in Sections 3 and 5, in which the problem of hardening is discussed and specialized results are given. In Section 6 the theory is specialized to the tension-torsion space, and in Section 7 surfaces of constant offset strain and constant stiffness are calculated.

2 Uniaxial Flow Rules

Consider a quasi-static stress-strain curve (Fig. 1, $OA'BE$) $\sigma^* = g^*(\epsilon^p)$, which is obtained by loading at extremely slow stress rates. That is, each increment of stress is applied after the total plastic strain due to the previous stress increment has had time to develop fully. Thus the quasi-static stress-strain curve may be interpreted as a sequence of equilibrium states such that plastic flow occurs at finite loading rates when the flow condition $\sigma > g^*(\epsilon^p)$ is satisfied. Obviously, the equilibrium stress-strain curve coincides with the upper bound of the elastic region, which is bounded from below by the curve ($FA''CG$), $\sigma^{**} - \epsilon^p$.

To describe the rate effects we may use the constitutive equation proposed by Malvern [6] for the uniaxial work-hardening case

$$E\dot{\epsilon} = \dot{\sigma} + \Phi(\sigma, \epsilon) \tag{4}$$

Contributed by the Applied Mechanics Division of THE AMERICAN SOCIETY OF MECHANICAL ENGINEERS, and presented at the 1981 Joint ASME/ASCE Applied Mechanics, Fluids Engineering, and Bioengineering Conference, University of Colorado, Boulder, Colo., June 22–27, 1981.

Discussion on this paper should be addressed to the Editorial Department, ASME, United Engineering Center, 345 East 47th Street, New York, N. Y. 10017, and will be accepted until September 1, 1981. Readers who need more time to prepare a Discussion should request an extension from the Editorial Department. Manuscript received by ASME Applied Mechanics Division, March, 1980; final revision, August, 1980. Paper No. 81-APM-21.

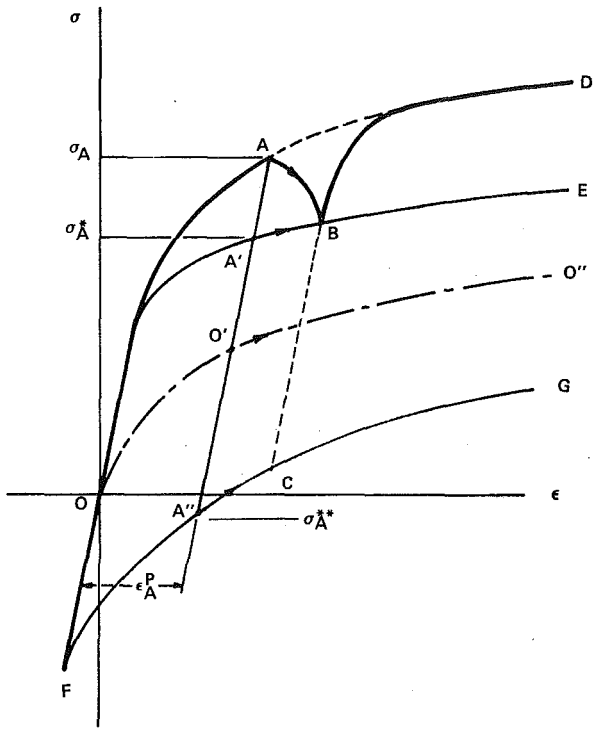

Fig. 1 Schematic illustration of rate-dependent uniaxial stress-strain response

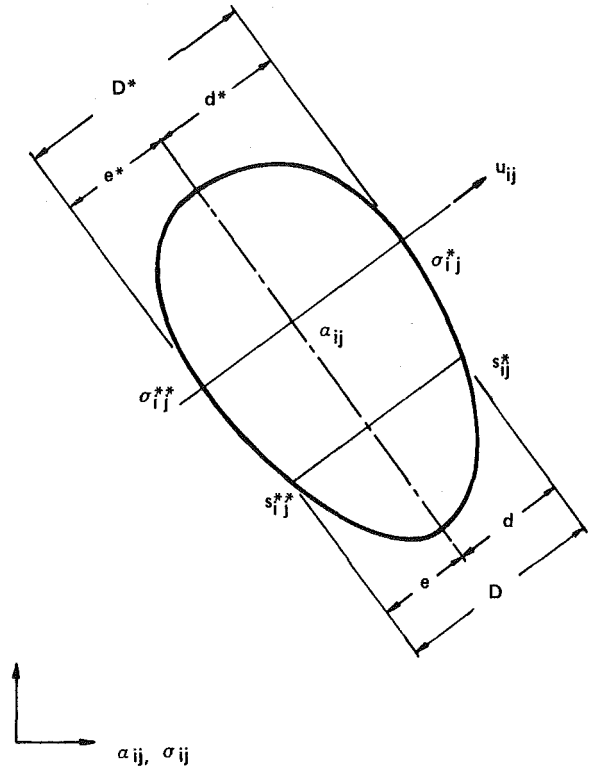

Fig. 2 The deformed yield surface in deviatoric stress space

where E is the elastic modulus and $\dot{\epsilon}^p = \Phi/E$. When the quasi-static stress-plastic strain curve is used as a relaxation boundary or reference curve, (4) may be rewritten in the form

$$E\dot{\epsilon} = \dot{\sigma} + \Phi(H) \tag{5}$$

$$H = \sigma - \sigma^* = \sigma - g^*(\epsilon^p) \tag{6}$$

where H is the overstress, i.e., the excess of the instantaneous stress over the stress on the quasi-static curve evaluated at the same plastic strain.[1] The stress state σ^*, which corresponds to σ, is called the *quasi-static loading point*. For simplicity, we consider the special case

$$\dot{\epsilon} = \dot{\sigma}/E + \bar{k}(H)^{\bar{n}} \tag{7}$$

where $\bar{k}$ and $\bar{n}$ are material constants. The quasi-static stress rate σ^* is related to the plastic strain by

$$\dot{\epsilon}^p = \dot{\sigma}^*/E^p \tag{8}$$

where the quasi-static plastic tangent modulus E^p is the derivative of g^*.

In Fig. 1, OAD represents the stress-strain curve at a given strain rate, $\sigma_A - \sigma_A^*$ is the overstress at time t_A, and curves $OO'O''$ and $FA''G$ represent the change in the "center" α and the lower bound σ^{**} of the elastic region with strain. They may be computed, respectively, by

$$\dot{\alpha} = \dot{\sigma}^* - \dot{d}^* \tag{9}$$

and

$$\dot{\sigma}^{**} = \dot{\sigma}^* - \dot{D}^* \tag{10}$$

where d^* and D^* (see Fig. 2) are the forward part of the width (in the loading direction) and the width of the elastic region. The definition of the center α is discussed in the next section.

[1] In [6] the overstress is defined by the total strain.

At a particular loading point A in Fig. 1, the corresponding quasi-static loading point A', the center of the yield surface O, and the lower bound of the elastic limit A'' are determined by the plastic strain ϵ_A^p. If at point A the stress is gradually decreased, the overstress $H = \sigma - \sigma^*$ decreases while the plastic strain continues to increase until the point B is reached. If, at point B, the strain rate imposed during the segment OA is reimposed, the new stress-strain path will have an initial slope equal to the elastic modulus, and the curve will approach the original path OAD gradually, while the quasi-static curve follows the original path OBE. From Fig. 1 other features of viscoplastic flow such as creep and relaxation can be seen to follow from (7).

3 Hardening Rules

Before generalizing the flow law to the multiaxial case it is appropriate to discuss the representation of the yield surface and its translation, growth, and distortion during the flow process. Henceforth all second rank tensors which represent stress or strain-like quantities shall be assumed to represent deviatoric quantities unless otherwise indicated.

For the purpose of describing the modification of subsequent yield surfaces during plastic flow, let S_{ij} and s_{ij} be corresponding deviatoric stress states on the initial and the subsequent yield surfaces, respectively. If a Lagrangian description of the yield surface is used, then the motion $s_{ij} = s_{ij}(S_{kl}, t)$ gives the position s_{ij} at time t occupied by a point on the subsequent yield surface whose initial position is at S_{ij}. Thus the elastic domain, bounded by the yield surface, can be envisaged as a deformable continuum in stress space.

Let the current stress deviator be σ_{ij} and let the quasi-static stress deviator be σ_{ij}^*. Two equally plausible definitions of σ_{ij}^* are possible,

σ_{ij}^*: The point on the yield surface closest to σ_{ij}. That is, the line of action of the normal (if defined) to the yield surface $n_{ij}(\sigma_{kl}^*)$ passes through σ_{ij};

σ_{ij}^*: The intersection of the yield surface and the radial line segment $\sigma_{ij} - \alpha_{ij}$, where α_{ij} represents the position of the center of the yield surface in deviatoric stress space.

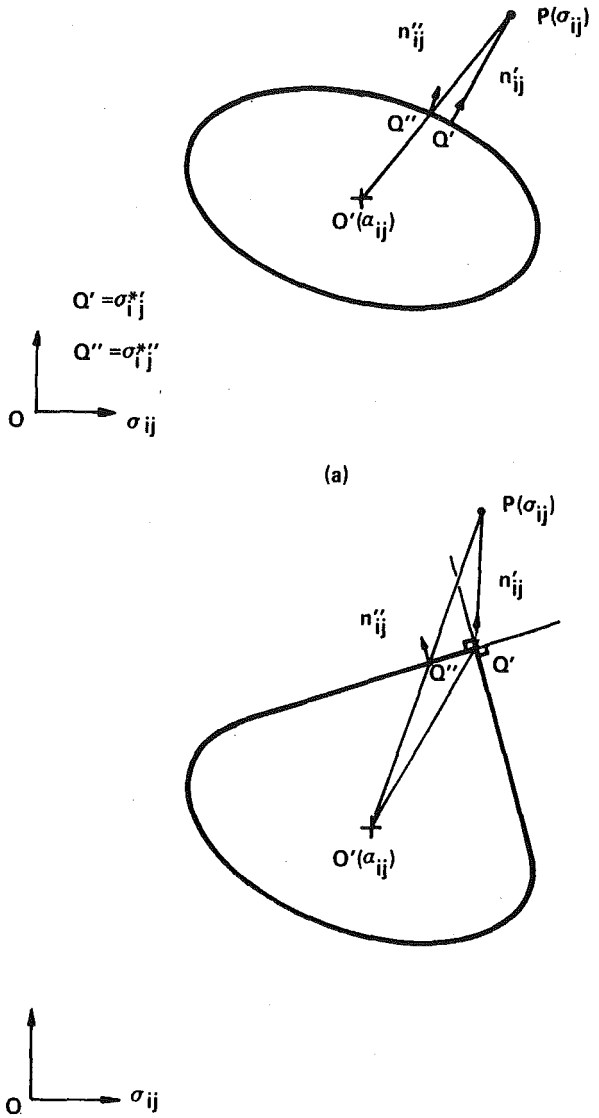

Fig. 3 Geometric interpretations of the quasi-static loading points for (*a*) regular yield surface and (*b*) corner of singular yield surface

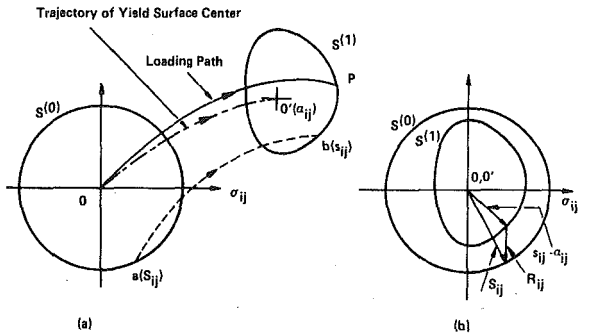

Fig. 4 A schematic representation of the deformation and translation of the yield surface

The locations of σ^*_{ij} are denoted by points Q on Figs. 3(a) and 3(b) for regular and singular yield surfaces, respectively. For most surfaces there is little difference in the positions calculated by the alternative definitions. For our immediate purposes let the loading be quasi-static so that σ_{ij} and σ^*_{ij} coincide.

To describe both deformation and translation of the yield surface during the plastic flow, the subsequent yield state s_{ij} (see Fig. 4) may be referred back to its initial yield state S_{ij} by

$$s_{ij} - \alpha_{ij} + R_{ij} = S_{ij} \tag{11}$$

where R_{ij} is a measure of the deformation of the yield surface. In general, R_{ij} is a function of S_{ij} and the history of material deformation. Fig. 4(a) represents a typical deformation and translation of a yield surface. The subsequent yield surface, $S^{(1)}$, has been created from the initial yield surface, $S^{(0)}$, by loading very slowly along the path OP. The path of a "material" stress point on the yield surface is given by ab. In accordance with Lagrangian description, the stress states at points a and b are denoted by S_{ij} and s_{ij}, respectively. In Fig. 4 the two surfaces are superposed by subtracting α_{ij} from s_{ij}. For an initial Mises surface

$$f(S_{ij}) = \tfrac{1}{2} S_{ij} S_{ij} = \kappa_0^2 \tag{12}$$

where κ_0 represents the size of the initial yield surface. From (11) and (12)

$$\tfrac{1}{2}(s_{ij} - \alpha_{ij} + R_{ij})(s_{ij} - \alpha_{ij} + R_{ij}) = \kappa_0^2 \tag{13}$$

For the special case of combined kinematic and isotropic hardening, the isotropic deformation (expansion or contraction) of the yield surface with respect to its center may be represented by defining the tensor R_{ij} in (11) to be proportion to S_{ij}. Thus (11) becomes

$$(1 + \delta)(s_{ij} - \alpha_{ij}) = S_{ij} \tag{14}$$

Now, the subsequent yield surface becomes, from (13),

$$\tfrac{1}{2}(1 + \delta)^2 (s_{ij} - \alpha_{ij})(s_{ij} - \alpha_{ij}) = \kappa_0^2 \tag{15}$$

where κ_0 is the initial size of the yield surface and δ is a scalar functional of the history of plastic deformation. The current size κ of the yield surface is given by $\kappa = \kappa_0/(1 + \delta)$. The pure kinematic hardening and pure isotropic hardening models may be obtained by setting $R_{ij} = 0$ and $\alpha_{ij} = 0$, respectively.

To complete the hardening rule one must determine the rate of change of size by specifying $\dot{\delta}$ as a function of the deformation. If the direction of motion of the center is parallel to a specified unit vector ν_{ij}, then

$$\dot{\alpha}_{ij} = \dot{\mu} \nu_{ij} \tag{16}$$

where the scalar quantity $\dot{\mu}$ may be determined from the consistency condition [7]. For the special case (15)

$$\dot{\mu} = \frac{(\sigma^*_{ij} - \alpha_{ij})\dot{\sigma}^*_{ij} + \dfrac{\dot{\delta}}{1 + \delta}(\sigma^*_{ij} - \alpha_{ij})(\sigma^*_{ij} - \alpha_{ij})}{(\sigma^*_{kl} - \alpha_{kl})\nu_{kl}} \tag{17}$$

The direction of ν_{ij} may be defined in a variety of ways [8, 9], all of which are equivalent to the loading direction in deviatoric stress space for proportional loading of an initial Mises surface.

The general form of the hardening law (11) is capable of describing not only the translation and dilatation (or contraction) of the elastic region but the experimentally observed distortion [10–15] as well. Generally, the yield surface deformation includes the development of a region of high curvature on the forward part (the part directed toward the loading point) of the yield surface; a flattening of the rear part of the surface; and a reduction of the width of the yield surface in the direction of monotonic loading. Usually zero cross effect is observed. That is, the yield strengths in directions orthogonal to the direction of loading do not change. To incorporate such phenomena we generalize a rule proposed by Phillips and his coworkers [11, 12, 16].

Let

$$\dot{R}_{ij} = -\dot{\lambda} u_{ij} \tag{18}$$

where u_{ij} is a unit vector whose possible directions are the same as

those of ν_{ij} and where $\dot{\lambda}$ is a scalar functional representing the nonuniform deformation of the yield surface. From (18) and the material derivative of (11),

$$\dot{\lambda} = (\dot{s}_{ij} - \dot{\alpha}_{ij})u_{ij} \tag{19}$$

Let the yield surface be divided in two parts separated by the hyperplane in Fig. 2, which contains the center of the yield surface α_{ij} and is perpendicular to the direction of deformation u_{ij}. The points on the forward and rear parts of the yield surface obey the inequalities

$$(s_{ij} - \alpha_{ij})u_{ij} \geq 0 \quad \text{and} \quad (s_{ij} - \alpha_{ij})u_{ij} < 0 \tag{20}$$

respectively. Thus the distances d and e (see Fig. 2) measured from typical stress points on the forward and rear parts of the yield surface to the dividing plane are given by

$$\begin{Bmatrix} d \\ -e \end{Bmatrix} = (s_{ij} - \alpha_{ij})u_{ij} \tag{21}$$

Let u_{ij} be approximately constant during an incremental loading event. Then from (19) and (21), we obtain

$$\dot{\lambda} = \dot{d}, \qquad \dot{\lambda} = -\dot{e} \tag{22}$$

on the forward and rear parts of the yield surface. To a first approximation let

$$\dot{d} = \dot{A}d, \quad \dot{e} = \dot{B}e \tag{23}$$

where A and B are independent of position on their respective portions of the yield surface. For monotonic loading, higher curvature is observed to develop in the forward part of the yield surface, thus $\dot{A} > \dot{B}$. To determine the appropriate expressions for $\dot{A}$ and $\dot{B}$, it is assumed that

$$\dot{A} = g_1\dot{\gamma}, \qquad \dot{B} = g_2\dot{\gamma} \tag{24}$$

where

$$(\dot{\gamma})^2 \equiv \tfrac{2}{3}\dot{\epsilon}^p_{ij}\dot{\epsilon}^p_{ij} \tag{25}$$

In general, g_1 and g_2 are scalar functionals of the history of the deformation.

For proportional loading of an initial Mises surface, $u_{ij} = \nu_{ij} = l_{ij}$, a unit vector in the loading direction, and so

$$\dot{s}_{ij} - \dot{\alpha}_{ij} - \begin{Bmatrix} \dot{d} \\ -\dot{e} \end{Bmatrix} l_{ij} = 0 \tag{26}$$

Equation (26) may be integrated to obtain

$$s_{ij} - \alpha_{ij} - \begin{Bmatrix} d - d_0 \\ e - e_0 \end{Bmatrix} l_{ij} = S_{ij} \tag{27}$$

where d_0 and e_0 are evaluated at the beginning of the loading event during which $\Delta\gamma_1$ plastic strain is accumulated. Also from (21), (23), and (24),

$$d = d_0 \exp\left[\int_0^{\Delta\gamma_1} g_1 d\gamma\right] \tag{28}$$

The unit change in dimension of the yield surface is given by

$$g_1^* = \frac{d - d_0}{d} = 1 - \exp\left[-\int_0^{\Delta\gamma_1} g_1 d\gamma\right] \tag{29}$$

Similarly,

$$e = e_0 \exp\left[-\int_0^{\Delta\gamma_1} g_2 d\gamma\right] \tag{30}$$

$$g_2^* = \frac{e - e_0}{e} = 1 - \exp\left[-\int_0^{\Delta\gamma_1} g_2 d\gamma\right] \tag{31}$$

From (21), (27), (29), and (31)

$$s_{ij} - \alpha_{ij} - g(s_{kl} - \alpha_{kl})l_{kl}l_{ij} = S_{ij} \tag{32}$$

where g assumes the values g_1^* and g_2^* on the front and rear surfaces, respectively. Equation (32) may be written as

$$s_{ij} - \alpha_{ij} - L_{ijkl}(s_{kl} - \alpha_{kl}) = S_{ij} \tag{33}$$

where L_{ijkl} assumes different forms on the front and rear surfaces. In general, after n linear loading trajectories L_{ijkl} assumes $2n$ different values on $2n$ subdomains of the surface and the description becomes quite complex [9].

However, a considerable simplification of the proposed hardening rule may be achieved by assuming only one deformation rate, i.e., $\dot{A} = \dot{B}$. With this approximation, the subsequent yield surface represents an ellipsoid in six-dimensional deviatoric stress space. The deformation of the yield surface is given by the fourth-order tensor L_{ijkl}, which is single-valued over the entire surface. For the initial Mises yield condition, the subsequent yield surface is now

$$\tfrac{1}{2}[s_{ij} - \alpha_{ij} - L_{ijkl}(s_{kl} - \alpha_{kl})][s_{ij} - \alpha_{ij} - L_{ijkl}(s_{kl} - \alpha_{kl})] = \kappa_0^2 \tag{34}$$

By computing the material time derivative of (34), we obtain

$$\dot{s}_{ij} - \dot{\alpha}_{ij} - \dot{L}_{ijkl}(s_{kl} - \alpha_{kl}) - L_{ijkl}(\dot{s}_{kl} - \dot{\alpha}_{kl}) = 0 \tag{35}$$

From (11), (18), (21), and (23) and the assumption of a single hardening rate $\dot{A}$,

$$\dot{s}_{ij} - \dot{\alpha}_{ij} - \dot{A}(s_{kl} - \alpha_{kl})u_{kl}u_{ij} = 0 \tag{36}$$

From (35) and (36),

$$\dot{A}(s_{mn} - \alpha_{mn})u_{mn}u_{ij} + \dot{L}_{ijkl}(s_{kl} - \alpha_{kl}) - \dot{A}(s_{pq} - \alpha_{pq})u_{pq}u_{rs}L_{ijrs} = 0 \tag{37}$$

Note that L_{ijkl} is independent of position on the yield surface. Thus, based on (37), $\dot{L}_{ijkl}$ may be defined by

$$\dot{L}_{ijkl} = \dot{K}_{ij}u_{kl} \tag{38}$$

where $\dot{K}_{ij}$ may be obtained by substituting (38) into (37) and eliminating the scalar quantity $(s_{kl} - \alpha_{kl})u_{kl}$. That is,

$$\dot{L}_{ijkl} = \dot{K}_{ij}u_{kl} = \dot{A}[u_{ij} - L_{ijmn}u_{mn}]u_{kl} \tag{39}$$

The scalar quantity $\dot{\mu}$ may be computed from the consistency condition at the active stress point, $s_{ij} = \sigma^*_{ij}$. Then, from (16), (34), and (39), we obtain

$$\dot{\mu} = \frac{s^*_{ij}\dot{\sigma}^*_{ij} - \dot{A}S^*_{kl}(u_{kl} - L_{klmn}u_{mn})u_{pq}(\sigma^*_{pq} - \alpha_{pq}) + S^*_{st}L_{stuv}\dot{\sigma}^*_{uv}}{(S^*_{pq} + S^*_{uv}L_{uvpq})\nu_{pq}} \tag{40}$$

where

$$S^*_{ij} = \sigma^*_{ij} - \alpha_{ij} - L_{ijkl}(\sigma^*_{kl} - \alpha_{kl}) \tag{41}$$

In its specialized form, the simplified hardening rule is similar to Baltov and Sawczuk's [17] anisotropic hardening rule, which also includes a combination of kinematic hardening, rigid body rotation, and symmetric deformation of the yield surface.

4 Multiaxial Flow Rules

The theory of viscoplasticity may be formulated by generalizing Malvern's one-dimensional model into multiple-dimensional constitutive relations. Generalization of the uniaxial theory required the specification of two key features: the direction of the viscoplastic strain rate, $\dot{\epsilon}^p_{ij}$, and the magnitude of the overstress.

Perzyna's version of the theory of viscoplasticity [5] is based on the existence of a yield function, (1), in deviatoric stress space. The region of elastic response is defined by (2) and the viscoelastic strain rate is given by (3), where the derivative is defined at $\sigma^*_{ij} = \sigma_{ij}$.

At the loading point outside the yield surface, $f > \kappa$, the dynamic loading surface is given by $f = C^*$, an isotropic expansion of the subsequent yield surface, and from equation (3), the viscoplastic strain

rate is defined to be normal to the dynamic loading surface. The overstress H is defined by

$$H = C^* - \kappa \tag{42}$$

which is independent of position on a given dynamic loading surface.

In [5], the theory is only proposed for isotropic hardening. However, it may be extended to any of the existing hardening rules by specifying the quasi-static loading point σ^*_{ij} properly.

As an alternative to Perzyna's theory, Phillips and Wu [18] proposed that the overstress H be defined as the perpendicular distance in the deviatoric space from the loading point σ_{ij} to the yield surface. Thus the quasi-static loading point σ^*_{ij} is given by

$$\sigma^*_{ij} = \sigma_{ij} - Hn_{ij}(\sigma^*_{pq}) \tag{43}$$

and

$$H = (\sigma_{ij} - \sigma^*_{ij})n_{ij}(\sigma^*_{pq}) \tag{44}$$

where $n_{ij}(\sigma^*_{pq})$ is, for smooth yield surfaces without corners, an uniquely defined unit normal vector to the yield surface at σ^*_{pq}.

To take into account the possibility of the existence of corners on the yield surface, one alternative is to assume the existence of a dynamic loading surface which is everywhere parallel to the static yield surface and at a constant distance equal to the overstress H. The viscoplastic strain rate is assumed to be normal to both the dynamic loading surface and to the regular regime of the yield surface. When the quasi-static loading point is at a singular point on the yield surface the plastic strain rate direction is defined uniquely by the normal to the dynamic loading surface. The constitutive relation is then of the form

$$\dot{\epsilon}^p_{ij} = \gamma\langle\Phi(H)\rangle n_{ij}(\sigma^*_{pq}) = \gamma\langle\Phi(H)\rangle n_{ij}(\sigma_{pq}) \tag{45}$$

From (45)

$$\sqrt{2}\, I^p_2 \equiv (\dot{\epsilon}^p_{ij}\dot{\epsilon}^p_{ij})^{1/2} = \gamma\langle\Phi(H)\rangle \tag{46}$$

which may be inverted to obtain

$$H = \langle\Phi\rangle^{-1}\left[\frac{\sqrt{2}}{\gamma} I^p_2\right] \tag{47}$$

Equations (43) and (47) now define the dynamic loading surface at each value of viscoplastic strain rate.

From the foregoing discussion, it can be seen that the primary role of the dynamic loading surface in Phillips and Wu's theory is to define the direction of $\dot{\epsilon}^p_{ij}$ at points which correspond to the corners of the yield surface.

In the current work, the effective overstress H is defined by the distance between the loading point σ_{ij} and the quasi-static loading point σ^*_{ij}. That is,

$$H = [\tfrac{3}{2}(\sigma_{ij} - \sigma^*_{ij})(\sigma_{ij} - \sigma^*_{ij})]^{1/2} \quad \text{for} \quad (\sigma_{ij} - \sigma^*_{ij})n_{ij}(\sigma^*_{pq}) > 0 \tag{48}$$

Otherwise, $H = 0$. The yield surface is given at σ^*_{ij} by an equation of the form

$$f(\sigma^*_{ij} - \alpha_{ij}) = \kappa_0^2 \tag{49}$$

where the quasi-static loading point σ^*_{ij} is determined in one of the two ways discussed at the beginning of Section 3 and illustrated in Fig. 3.

The rate-dependent flow rule now may be expressed by

$$\dot{\epsilon}^p_{ij} = \sqrt{\tfrac{3}{2}}\,\langle\Phi(H)\rangle v_{ij}(\sigma^*_{pq}) \tag{50}$$

where $\Phi(H)$ is given by equation (7), and the unit vector $v_{ij}(\sigma^*_{pq})$ is determined by one of two criteria:

(*a*) If $n_{ij}(\sigma^*_{pq})$ is uniquely defined, then

$$v_{ij}(\sigma^*_{pq}) = n_{ij}(\sigma^*_{pq}) \tag{51}$$

(*b*) If $n_{ij}(\sigma^*_{pq})$ is not uniquely defined, then

$$v_{ij}(\sigma^*_{pq}) = h_{ij}(\sigma^*_{pq}) \tag{52}$$

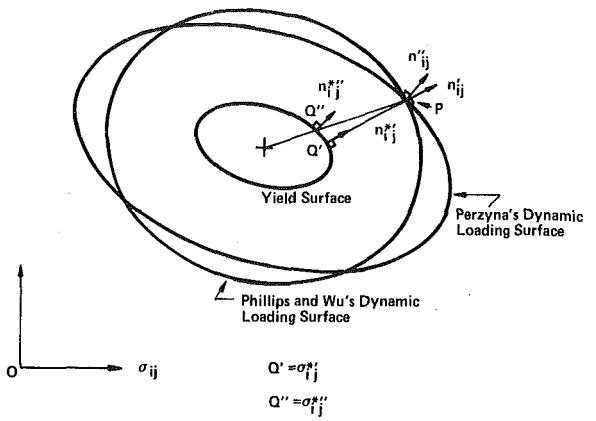

Fig. 5 Comparison of the generalized Perzyna's and Phillips and Wu's theories of viscoplasticity

where

$$h_{ij} = (\sigma_{ij} - \sigma^*_{ij})/H \tag{53}$$

Note that the use of the loading point of the first kind ($\sigma^{*'}_{ij}$) leads to a theory which is essentially equivalent to Phillips and Wu's version of viscoplasticity—although the concept of a dynamic loading surface is not introduced. Note also, that a theory based on equation (50) and the quasi-static loading point of the second kind ($\sigma^{*''}_{ij}$) is similar to Perzyna's theory, since $n_{ij}(\sigma^{*''}_{pq}) = n_{ij}(\sigma_{pq})$, where $n_{ij}(\sigma_{pq})$ is the unit normal to Perzyna's dynamic loading surface, $f(\sigma_{ij} - \alpha_{ij}) = C^*$. However, in the present theory the quasi-static loading point of the second kind, $\sigma^{*''}_{ij}$, is computed as the intersection of the yield surface and the line connecting the loading point and the center of the yield surface. That is,

$$\sigma^{*''}_{ij} - \alpha_{ij} = C(\sigma_{ij} - \alpha_{ij}) \tag{54}$$

By substituting equation (54) into (49) C may be determined. Thus the overstress given by (54) is, in general, position-dependent, while Perzyna's overstress given by equation (42) is not.

Fig. 5 shows the differences between the predictions of Phillips and Wu's and Perzyna's theories of viscoplasticity. At the loading point P, the unit vectors n'_{ij} and n''_{ij} are the unit normals to Phillips and Wu's and Perzyna's dynamic loading surfaces, respectively. Note that $n^{*'}_{ij}$ is parallel to n'_{ij} and $n^{*''}_{ij}$ is parallel to n''_{ij}.

For many cases, the alternative theories predict identical results and, in most situations, what differences there are, are small. However, the determination of $\sigma^{*''}_{ij}$ by (54) and (49) is computationally simpler than that of the first kind. To determine $\sigma^{*'}_{ij}$, minimize H by introducing the Lagrangian multiplier λ, to obtain

$$\frac{\partial H}{\partial \sigma^*_{ij}} + \lambda \frac{\partial f(\sigma^*_{pq} - \alpha_{pq})}{\partial \sigma^*_{ij}} = 0 \tag{55}$$

In six-dimensional deviatoric stress space, equations (49) and (55) give six equations with six independent unknowns, λ and $\sigma^{*'}_{ij}$. By solving these six simultaneous equations, $\sigma^{*'}_{ij}$ may be obtained.

5 A Specific Constitutive Law

To illustrate the application of the flow law developed in Section 4, consider the simplified hardening rule described at the end of Section 3. Then, at the quasi-static loading point, $s_{ij} = \sigma^*_{ij}$, the yield surface given by (34) may be written as

$$f(S^*_{ij}) = \tfrac{1}{2} S^*_{ij}S^*_{ij} = \kappa_0^2 \tag{56}$$

where

$$S^*_{ij} = \sigma^*_{ij} - \alpha_{ij} - L_{ijkl}(\sigma^*_{kl} - \alpha_{kl}) \tag{57}$$

The unit normal to the yield surface at σ^*_{ij} becomes

$$n_{ij} = \frac{\partial f/\partial \sigma^*_{ij}}{(\partial f/\partial \sigma^*_{pq}\partial f/\partial \sigma^*_{pq})^{1/2}} = \frac{Z_{ij}}{\overline{Z}} \tag{58}$$

where

$$Z_{ij} = S^*_{ij} - S^*_{kl}L_{klij} \tag{59}$$

$$\overline{Z} = (Z_{ij}Z_{ij})^{1/2} \tag{60}$$

The rate-dependent flow rule given by (50) and (51) becomes

$$\dot{\epsilon}^p_{ij} = \sqrt{\frac{3}{2}}\langle\Phi(H)\rangle\frac{Z_{ij}}{\overline{Z}} \tag{61}$$

From (61) and (25)

$$\dot{\gamma} = \Phi(H) \tag{62}$$

The translation of the yield surface is given by (16) in which $\dot{\mu}$ may be rewritten from (40) together with (39) and (59)

$$\dot{\mu} = \frac{Z_{ij}\dot{\sigma}^*_{ij} - S^*_{kl}\dot{L}_{klmn}(\sigma^*_{mn} - \alpha_{mn})}{Z_{pq}\nu_{pq}} \tag{63}$$

Note that ν_{pq} must be specified and L_{ijkl} is given by equation (39). To complete the computation of $\dot{\mu}$ we must relate the flow law to the quasi-static stress-strain law or relaxation boundary. The classical rate-independent flow law requires that

$$\dot{\epsilon}^p_{ij} = \frac{1}{K}\dot{\sigma}_{kl}n_{kl}n_{ij} \tag{64}$$

Thus, from (58) and (64), we obtain the rate-independent analog of (61),

$$\dot{\epsilon}^p_{ij} = \frac{(\dot{\sigma}^*_{kl}Z_{kl})Z_{ij}}{K(\overline{Z})^2} \tag{65}$$

From (25) and (65)

$$\dot{\gamma} = \sqrt{\frac{3}{2}}\frac{\dot{\sigma}^*_{kl}Z_{kl}}{E^p\overline{Z}} \tag{66}$$

Since $E^p = 3/2\,K$. Thus (62) and (66) imply that

$$\dot{\sigma}^*_{kl}Z_{kl} = \sqrt{\frac{2}{3}}E^p\overline{Z}\langle\Phi(H)\rangle \tag{67}$$

and thus, from (63) and (67),

$$\dot{\mu} = \frac{\sqrt{\frac{2}{3}}E^p\overline{Z}\langle\Phi(H)\rangle - S^*_{kl}\dot{L}_{klmn}(\sigma^*_{mn} - \alpha_{mn})}{Z_{pq}\nu_{pq}} \tag{68}$$

The remaining unknown quantities are C and $\dot{\sigma}^*_{ij}$. By substituting equation (54) into (56), C is obtained

$$C = \left[\frac{\kappa_0^2}{\frac{1}{2}S^{**}_{ij}S^{**}_{ij}}\right]^{1/2} \tag{69}$$

where

$$S^{**}_{ij} = \sigma_{ij} - \alpha_{ij} - L_{ijkl}(\sigma_{kl} - \alpha_{kl}) \tag{70}$$

Then, the quasi-static stress rate $\dot{\sigma}^*_{ij}$ may be computed by differentiating (54). That is,

$$\dot{\sigma}^*_{ij} = \dot{C}(\sigma_{ij} - \alpha_{ij}) + C\dot{\sigma}_{ij} + (1 - C)\dot{\alpha}_{ij} \tag{71}$$

where $\dot{C}$ may be calculated by substituting (71) into (67). That is,

$$\dot{C} = \frac{\sqrt{\frac{2}{3}}E^p\overline{Z}\langle\Phi(H)\rangle - (1 - C)Z_{ij}\dot{\alpha}_{ij} - CZ_{kl}\dot{\sigma}_{kl}}{(\sigma_{mn} - \alpha_{mn})Z_{mn}} \tag{72}$$

This completes the formulation of the constitutive equations for the proposed model of viscoplasticity combined with the simplified hardening rule. Here the definition of the second kind for the quasistatic loading point $\sigma^{*'}_{ij}$ is used. In numerical simulations of stress control tests, the independent variables σ_{ij} are specified at a succession of small time increments, then the successive increments of the dependent variables ϵ^p_{ij}, L_{klmn}, α_{ij}, C, and σ^*_{ij} are computed from equations (60), (39), (68), (72), and (71), respectively. In the next section these governing equations for combined tension-compression and torsion loading will be given. Then, together with the proper expressions for $\dot{A}$, $\Phi(H)$, and E^p, flow surfaces for pure aluminum are computed in Section 7.

6 Application to Tension-Torsion Loading

In this section, the deviatoric quantities are denoted by the conventional $(^-)$ notation, and summations are carried out over the range 1 to 5, unless otherwise indicated. The range of free subscripts is similarly defined. By using vector notation for nonzero components of the second-order tensors, we have

$$\{\overline{\sigma}\} = \{\tfrac{2}{3}\sigma, -\tfrac{1}{3}\sigma, -\tfrac{1}{3}\sigma, \tau, \tau\}, \{\overline{\sigma}^*\} = \{\tfrac{2}{3}\sigma^*, -\tfrac{1}{3}\sigma^*, \tau^*, \tau^*\},$$

and

$$\{\epsilon^p\} = \{\epsilon^p_x, -\tfrac{1}{2}\epsilon^p_x, -\tfrac{1}{2}\epsilon^p_x, \epsilon^p_{xy}, \epsilon^p_{xy}\}$$

The unit vectors $\overline{u}_{ij}$ and $\overline{\nu}_{ij}$ are denoted by

$$\{\overline{u}\} = \{\tfrac{2}{3}u_x, -\tfrac{1}{3}u_x, -\tfrac{1}{3}u_x, u_{xy}, u_{xy}\}$$

and

$$\{\overline{\nu}\} = \{\tfrac{2}{3}\nu_x, -\tfrac{1}{3}\nu_x, -\tfrac{1}{3}\nu_x, \nu_{xy}, \nu_{xy}\},$$

where $\frac{2}{3}u_x^2 + 2u_{xy}^2 = 1$ and $\frac{2}{3}\nu_x^2 + 2\nu_{xy}^2 = 1$.

Write (39) and (57) in contracted notation,

$$\dot{\overline{L}}_{ij} = \dot{A}[\overline{u}_i - \overline{L}_{ij}\overline{u}_k]\overline{u}_j \tag{73}$$

and

$$\dot{\overline{S}}^*_i = (\dot{\overline{\sigma}}^*_i - \dot{\overline{\alpha}}_i) - L_{ij}(\dot{\overline{\sigma}}^*_j - \dot{\alpha}_j) \tag{74}$$

where $\{\overline{S}^*_i\} = \{\frac{2}{3}S^*_x, -\frac{1}{3}S^*_x, -\frac{1}{3}S^*_x, S^*_{xy}, S^*_{xy}\}$ and $\{\overline{\alpha}\} = \{\frac{2}{3}\alpha, -\frac{1}{3}\alpha, -\frac{1}{3}\alpha, \beta, \beta\}$. Noting the initial zero value of L_{ij} for initial isotropic material and $\overline{u}_2 = \overline{u}_3 = -\frac{1}{2}\overline{u}_1$ and $\overline{u}_4 = \overline{u}_5$, we conclude from (73) and (74),

$$\dot{\overline{L}}_{2j} = \dot{\overline{L}}_{3j} = -\tfrac{1}{2}\dot{\overline{L}}_{1j}, \dot{\overline{L}}_{i2} = \dot{\overline{L}}_{i3} = -\tfrac{1}{2}\dot{\overline{L}}_{i1}, \dot{\overline{L}}_{5j} = \dot{\overline{L}}_{4j}, \dot{\overline{L}}_{i5} = \dot{\overline{L}}_{i4} \tag{75}$$

Similar restrictions apply to $\overline{L}_{ij}$. The four independent components of the deviatoric tensor $\overline{L}_{ij}$ are given in terms of the corresponding nondeviatoric components by

$$\{\overline{L}_{11}, \overline{L}_{14}, \overline{L}_{41}, \overline{L}_{44}\} = \{\tfrac{4}{9}L_{x,x}, \tfrac{2}{3}L_{x,xy}, \tfrac{2}{3}L_{xy,x}, L_{xy,xy}\} \tag{76}$$

From (76), equation (74) provides two independent equations in $\sigma - \tau$ space,

$$\begin{Bmatrix}\dot{S}^*_x\\ \dot{S}^*_{xy}\end{Bmatrix} = \begin{Bmatrix}\dot{\sigma}^* - \dot{\alpha}\\ \dot{\tau}^* - \dot{\beta}\end{Bmatrix} - \begin{bmatrix}L_{x,x} & L_{x,xy}\\ L_{xy,x} & L_{xy,xy}\end{bmatrix}\begin{Bmatrix}\frac{2}{3}(\dot{\sigma}^* - \dot{\alpha})\\ 2(\dot{\tau}^* - \dot{\beta})\end{Bmatrix} \tag{77}$$

From (56), the yield surface is

$$(S^*_x)^2 + 3(S^*_{xy})^2 = 3\kappa_0^2 \tag{78}$$

By denoting $\{\overline{Z}\} = \{\frac{2}{3}Z_x, -\frac{1}{3}Z_x, -\frac{1}{3}Z_x, Z_{xy}, Z_{xy}\}$, (59) reduces to

$$\begin{Bmatrix}Z^*_x\\ Z^*_{xy}\end{Bmatrix} = \begin{Bmatrix}S^*_x\\ S^*_{xy}\end{Bmatrix} - \begin{bmatrix}L_{x,x} & L_{x,xy}\\ L_{xy,x} & L_{xy,xy}\end{bmatrix}\begin{Bmatrix}\frac{2}{3}S^*_x\\ 2\,S^*_{xy}\end{Bmatrix} \tag{79}$$

From (79), the rate-dependent flow rule (61) gives

$$\begin{Bmatrix}\dot{\epsilon}^p_x\\ \dot{\epsilon}^p_{xy}\end{Bmatrix} = \frac{\langle\Phi(H)\rangle}{(Z_x^2 + 3Z_{xy}^2)^{1/2}}\begin{Bmatrix}Z_x\\ \frac{3}{2}Z_{xy}\end{Bmatrix} \tag{80}$$

where H is given by (48)

$$H = [(\sigma - \sigma^*)^2 + 3(\tau - \tau^*)^2]^{1/2} \tag{81}$$

From (73),

$$\begin{aligned}
\dot{L}_{x,x} &= \dot{A}[(1 - \tfrac{2}{3}L_{x,x})u_x^2 - 2L_{x,xy}u_xu_{xy}]\\
\dot{L}_{x,xy} &= \dot{A}[(1 - \tfrac{3}{2}L_{x,x})u_xu_{xy} - 2L_{x,xy}u_{xy}^2]\\
\dot{L}_{xy,x} &= \dot{A}[-\tfrac{2}{3}L_{xy,x}u_x^2 + (1 - 2L_{xy,xy})u_xu_{xy}]\\
\dot{L}_{xy,xy} &= \dot{A}[-\tfrac{2}{3}L_{xy,x}u_xu_{xy} + (1 - 2L_{xy,xy})u_{xy}^2]
\end{aligned} \tag{82}$$

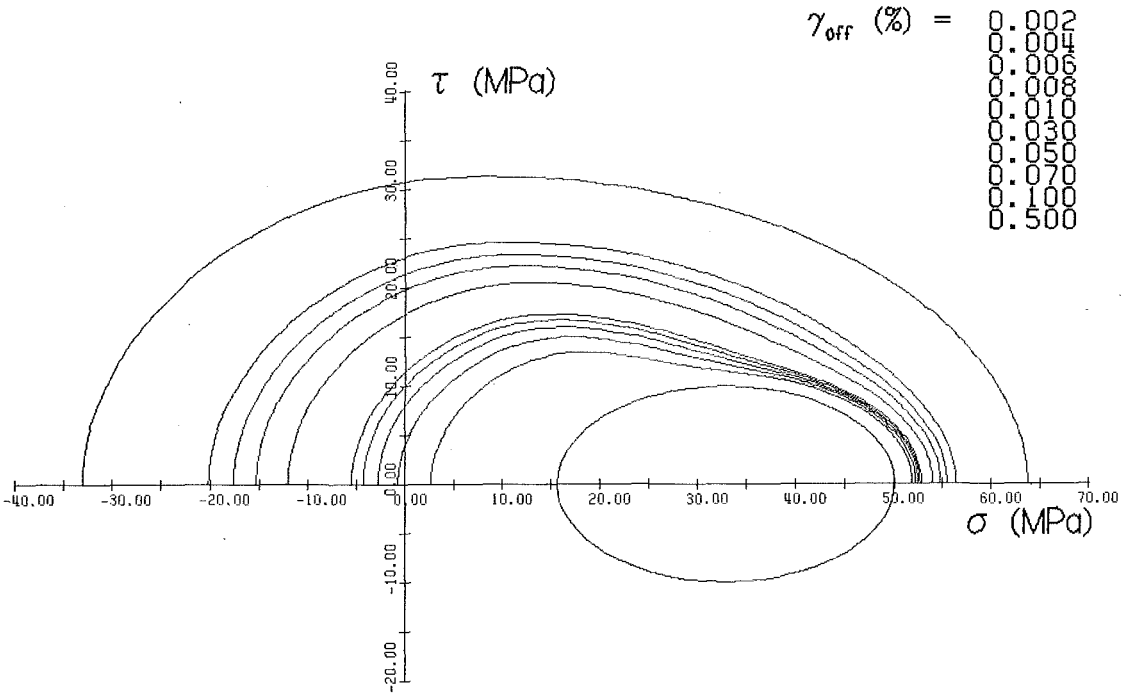

Fig. 6 Rate-dependent offset surfaces following 0.2 percent tensile plastic prestrain

where $\dot{A}$ is given by (24) and, for 1100 aluminum at room temperature [9]

$$g_1 = -a_1 b_1 \gamma^{b_1 - 1} \tag{83}$$

where

$$\begin{aligned} a_1 &= 4345,\ b_1 = 0.9767 \quad \text{for } \gamma \geq 150 \times 10^{-6} \\ a_1 &= 1.338, b_1 = 0.0584 \quad \text{for } \gamma < 150 \times 10^{-6} \end{aligned} \tag{84}$$

The accumulated inelastic strain rate $\dot{\gamma}$ is

$$\dot{\gamma} = (\dot{\epsilon}_x^p + \tfrac{1}{3}\dot{\epsilon}_{xy}^p)^{1/2} = \frac{\dot{\sigma}^* Z_x + 3\dot{\tau}^* Z_{xy}}{(Z_x^2 + 3Z_{xy}^2)^{1/2}} \tag{85}$$

The kinematic rule for the yield surface is defined by (16),

$$\begin{Bmatrix} \dot{\alpha} \\ \dot{\beta} \end{Bmatrix} = \dot{\mu} \begin{Bmatrix} \nu_x \\ \nu_{xy} \end{Bmatrix} \tag{86}$$

where, from (68),

$$\begin{aligned} \mu = \{ & E^p (Z_x + 3Z_{xy}^2)^{1/2} \langle \Phi(H) \rangle \\ & - \tfrac{2}{3}[S_x^* \dot{L}_{x,x}(\sigma^* - \alpha) + 3S_x^* \dot{L}_{x,xy}(\tau^* - \beta) \\ & + S_{xy}^* \dot{L}_{xy,x}(\sigma^* - \alpha) + 9S_{xy}^* \dot{L}_{xy,xy}(\tau^* - \beta)]\}/(Z_x \nu_x + Z_{xy} \nu_{xy}) \end{aligned} \tag{87}$$

According to equation (71), the quasi-static stress rates $(\dot{\sigma}^*, \dot{\tau}^*)$ are

$$\begin{aligned} \dot{\sigma}^* &= \dot{C}(\sigma - \alpha) + C\dot{\sigma} + (1 - C)\dot{\alpha} \\ \dot{\tau}^* &= \dot{C}(\tau - \beta) + C\dot{\tau} + (1 - C)\dot{\beta} \end{aligned} \tag{88}$$

where, from (69) and (70),

$$C = \frac{\sqrt{3}\,\kappa_0}{[(S_x^{**})^2 + 3(S_{xy}^{**})^2]^{1/2}} \tag{89}$$

and

$$\begin{Bmatrix} S_x^{**} \\ S_{xy}^{**} \end{Bmatrix} = \begin{bmatrix} \frac{3}{2} - L_{x,x} & L_{xy,x} \\ L_{xy,x} & \frac{1}{2} - L_{xy,xy} \end{bmatrix} \begin{Bmatrix} \frac{2}{3}(\sigma - \alpha) \\ 2(\tau - \beta) \end{Bmatrix} \tag{90}$$

and from (72),

$$\dot{C} = \frac{\frac{3}{2}E^p(Z_x^2 + 3Z_{xy}^2)\langle \Phi(H) \rangle - (1 - C)(Z_x \dot{\alpha} + 3Z_{xy}\dot{\beta}) - C(Z_x \dot{\sigma} + 3Z_{xy}\dot{\beta})}{[(\sigma - \alpha)Z_x + 3(\tau - \beta)Z_{xy}]} \tag{91}$$

For stress control loading programs, $\dot{\sigma}$ and $\dot{\tau}$ are specified. After choosing the proper directions for $\bar{u}_{ij}$ and $\bar{v}_{ij}$, the incremental quantities of the 13 dependent variables, ϵ_x^p, ϵ_{xy}^p, ϵ_x, ϵ_{xy}, γ, $L_{x,x}$, $L_{x,xy}$, $L_{xy,x}$, $L_{xy,xy}$, α, β, σ^*, and τ^*, can be sequentially integrated from the corresponding differential equations (77)–(91). Note that at the onset of inelastic flow, we have $(\sigma^*, \tau^*) = (\sigma, \tau)$, and also initial zero values for $\bar{L}_{ij}$, α, and β.

For strain control loading programs, $\dot{\epsilon}_x$ and $\dot{\epsilon}_{xy}$ are specified. A similar procedure can be specified for this case.

7 Flow Surfaces

For simplicity consider the case of initial tensile loading followed by probes directed radially outward from the center of the first subsequent yield surface. Let the hardening law be pure kinematic hardening of a Mises surface. Under these conditions it can be shown that the alternative definitions of kinematic hardening direction reduce to the loading direction $\{l_x, l_{xy}\} = \{\dot{\sigma}/\bar{l}, \dot{\tau}/\bar{l}\}$, where $\bar{l} = \frac{2}{3}(\dot{\sigma}^2 + 3\dot{\tau}^2)^{1/2}$.

One can compute the rate-dependent offset surfaces of constant plastic strain accumulation and the constant tangent modulus surfaces. Along a probing path, the points on a rate-dependent offset surface and on the corresponding quasi-static offset surface are the loading point and its corresponding quasi-static loading point for which the designated amount of offset strain is accumulated. The points on a rate-dependent constant tangent modulus surface are similarly defined. In this section the rate-dependent tangent modulus is defined by the ratio of the effective stress rate and the effective plastic strain rate, i.e., $\dot{\bar{\sigma}}/\dot{\gamma}$. Then from equation (62), the rate-dependent tangent modulus becomes $\bar{\sigma}/\Phi(H)$. The function Φ is determined from (5) and (7). For the 1100 aluminum considered herein, $1/\bar{k} = 237\ \text{MPa}^{\bar{n}}\cdot\text{min}$ and $\bar{n} = 2.86$. Also $\epsilon^p = (\sigma/\hat{k})^{1/\hat{n}}$, $E^p = \hat{k}\hat{n}\gamma^{\hat{n}-1}$ where $\hat{n} = 0.1014$ and $\hat{k} = 126$ MPa.

Figs. 6 and 7 illustrate the two families of surfaces of rate-dependent

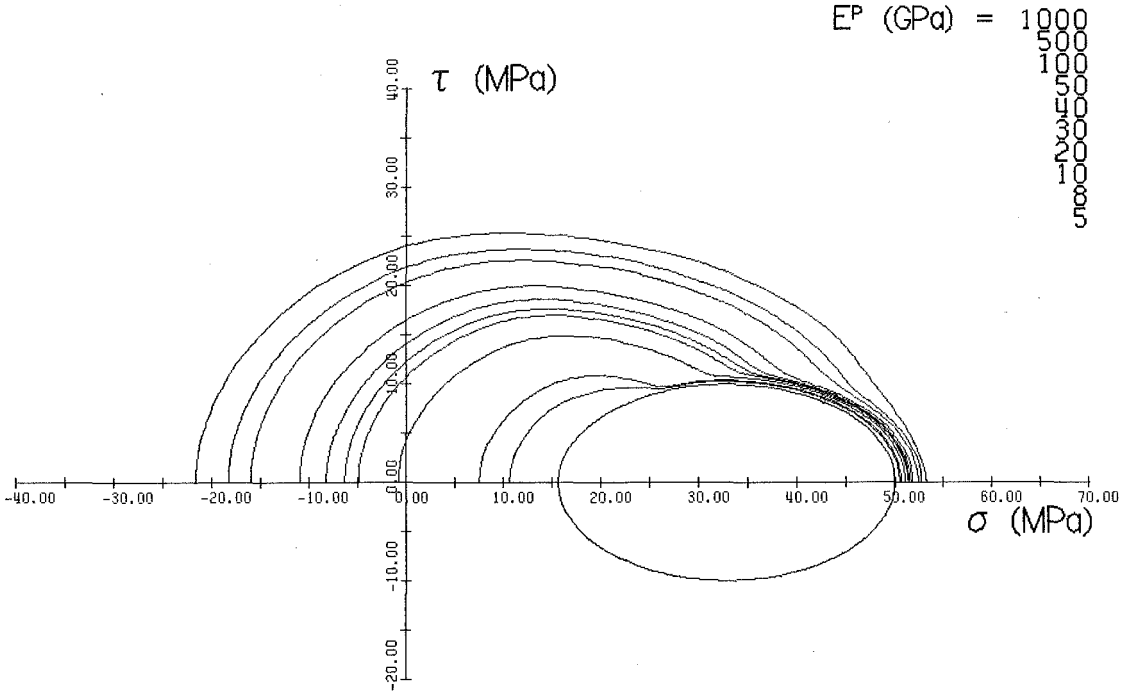

Fig. 7 Rate-dependent tangent modulus surfaces following 0.2 percent tensile plastic prestrain

offset surfaces and tangent modulus surfaces, respectively. The initial loading is such that 0.2 percent of plastic strain is obtained in uniaxial tension. The surfaces are computed by incorporating the pure kinematic hardening rule into the rate-dependent flow rule for a constant stress rate of 0.345 MPa/min (50 psi/min). The offset strains range from 0.002 to 0.5 percent, and the tangent modulus from 1000 GPa to 5 GPa. Fifteen probing paths are computed and then the surfaces are completed by interpolation. It can be seen that the rate-dependent offset surfaces are similar to those reported by Williams and Svensson [19]. The surfaces are significantly distorted for small offset strain and tend to be isotropic for large offset strain. The tangent modulus surfaces tend to become isotropic for small tangent moduli, while the surfaces of large tangent moduli show significant distortion and local concavities. Although the concept of a family of constant modulus surfaces proposed by Mroz [20] has been widely applied to formulate theories of cyclic plasticity [21, 22], no biaxial experiments to determine such surfaces have been reported.

8 Closure

In the preceding sections a theory of viscoplasticity capable of incorporating anisotropic hardening in a most general sense has been presented. The theory has been shown to reduce to those of Perzyna [5] and Phillips and Wu [18] under appropriate restrictions, and it has been applied to simple loading conditions in tension-torsion. The specific form of the calculated offset surfaces depends on the underlying quasi-static stress-strain curve during load reversal, the detailed description of which is presented in [9] and in a forthcoming paper in which the application of the theory to cyclic loading processes is explored. Similarly, the application of the theory in its more general form (Sections 3 and 4) to the description of yield surface distortion and studies of the effects of choice of direction of ν_{ij} and u_{ij} [8] are to be found in [9] and forthcoming papers.

9 Acknowledgment

The authors thank the National Science Foundation, under whose auspices much of the foregoing work was accomplished.

References

1 Perzyna, P., "Fundamental Problems in Viscoplasticity," *Advances in Applied Mechanics,* Vol. 9, 1966, pp. 244–377.

2 Naghdi, P. M., and Murch, S. A., "On the Mechanical Behavior of Viscoelastic/Plastic Solids," ASME JOURNAL OF APPLIED MECHANICS, Vol. 30, 1963, pp. 321–328.

3 Bingham, E. C., *Fluidity and Plasticity,* McGraw-Hill, New York, 1922.

4 Hohenemser, K., and Prager, W., "Über die Ansätze der Mechanik isotroper Kontinua," *Zeitschrift für Angewandte Mathematik und Mechanik,* Vol. 12, 1932, pp. 216–226.

5 Perzyna, P., "The Constitutive Equations for Rate Sensitive Plastic Materials," *Quarterly of Applied Mathematics,* Vol. 20, 1963, pp. 321–332.

6 Malvern, L. E., "The Propagation of Longitudinal Waves of Plastic Deformation in a Bar of Material Exhibiting a Strain-Rate Effect," ASME JOURNAL OF APPLIED MECHANICS, Vol. 18, 1951, pp. 203–208.

7 Prager, W., "Recent Developments in the Mathematical Theory of Plasticity," *Journal of Applied Physics,* Vol. 20, 1949, pp. 235–241.

8 Eisenberg, M. A., "Multiaxial Viscoplasticity," *Recent Advances in Engineering Sciences, Proc. 15th Annual SES,* 1978, pp. 473–477.

9 Yen, C. F., *On the Theory of Cyclic Viscoplasticity,* Dissertation, University of Florida, Gainesville, 1979.

10 Phillips, A., Liu, C. S., and Justusson, J. W., "An Experimental Investigation of Yield Surfaces at Elevated Temperatures," *Acta Mechanica,* Vol. 14, 1972, pp. 119–146.

11 Phillips, A., and Tang, J. L., "The Effect of Loading Path on the Yield Surface at Elevated Temperatures," *International Journal of Solids and Structures,* Vol. 8, 1972, pp. 463–474.

12 Phillips, A., and Kasper, R., "On the Foundations of Thermoplasticity—An Experimental Investigation," ASME JOURNAL OF APPLIED MECHANICS, Vol. 40, 1973, pp. 891–896.

13 Phillips, A., Tang, J. L., and Ricciuti, M., "Some New Observations on Yield Surfaces," *Acta Mechanica,* Vol. 20, 1974, pp. 23–29.

14 Ivey, H. J., "Plastic Stress-Strain Relations and Yield Surfaces for Aluminum Alloys," *Journal of the Mechanical Engineering Sciences,* Vol. 3, 1961, pp. 15–31.

15 Naghdi, P. M., Essenberg, F., and Koff, W., "An Experimental Study of Initial and Subsequent Yield Surfaces in Plasticity," ASME JOURNAL OF APPLIED MECHANICS, Vol. 25, 1959, pp. 77–87.

16 Phillips, A. and Weng, G. J., "An Analytical Study of an Experimentally Verified Hardening Law," ASME JOURNAL OF APPLIED MECHANICS, Vol. 42, 1975, pp. 375–378.

17 Baltov, A., and Sawczuk, A., "A Rule of Anisotropic Hardening," *Acta Mechanica,* Vol. 1, 1965, pp. 81–92.

18 Phillips, A., and Wu, H. C., "A Theory of Viscoplasticity," *International Journal of Solids and Structures,* Vol. 9, 1973, pp. 15–30.

19 Williams, J. F., and Svensson, N. L., "Effect of Tensile Prestrain on the Yield Locus of 1100-F Aluminum," *Journal of Strain Analysis,* Vol. 5, 1970, pp. 128–139.

20 Mroz, Z., "On the Description of Anisotropic Workhardening," *Journal of the Mechanics and Physics of Solids,* Vol. 15, 1967, pp. 163–175.

21 Peterson, M., and Popov, E. P., "Constitutive Relations for Generalized Loadings," *Proceedings, Engineering Mechanics Division, ASCE,* Vol. 103, 1977, pp. 611–627.

22 Jhansale, H. R., and Sharma, S. K., "Inelastic Behavior of Structural Metals Under Complex Cyclic Loading," Paper No. 77-366, *AIAA/ASME 18th Structures, Structural Dynamics and Materials Conference,* San Diego, Calif., 1977.

J. Casey[1]
Assoc. Mem. ASME

P. M. Naghdi
Fellow ASME

Department of Mechanical Engineering,
University of California,
Berkeley, Calif. 94720

On the Characterization of Strain-Hardening in Plasticity

In the context of a purely mechanical, rate-type theory of elastic-plastic materials and utilizing a strain space formulation introduced in [1], this paper is concerned mainly with developments pertaining to strain-hardening behavior consisting of three distinct types of material response, namely, hardening, softening, and perfectly plastic behavior. It is shown that such strain-hardening behavior may be characterized by a rate-independent quotient of quantities occurring in the loading criteria of strain space and the corresponding loading conditions of stress space. With the use of special constitutive equations, the predictive capability of the results obtained are illustrated for strain-hardening response and saturation hardening in a uniaxial tension test.

1 Introduction

Within the scope of a rate-type mechanical theory of elastic-plastic materials, Naghdi and Trapp [1] have recently discussed the advantages of formulating plasticity theory relative to yield (or loading) surfaces in *strain* space (rather than *stress* space). We adopt here the loading criteria of the strain space formulation as primary and derive the associated loading conditions in stress space. By comparing the local motion of the loading surface in stress space to that of the loading surface in strain space during loading, we find that three distinct types of material response representing hardening, softening, and perfectly plastic behavior can be defined in a natural way. For convenience, these three types of response will be referred to collectively as strain-hardening behavior. The development leading to the latter, as well as illustrative examples of the results for special constitutive equations, are the main objectives of the present paper. As in [1], we confine attention to the purely mechanical theory of elastic-plastic materials, and base our development on the rate-type stress space formulation of Green and Naghdi [2, 3][2] and on the alternative strain space formulation introduced by Naghdi and Trapp [1].

By way of motivation, consider the response of a typical ductile metal in a one-dimensional simple tension test in which the strain may be moderately large. Let e and s stand, respectively, for the component e_{11} of the Lagrangian strain tensor and the component s_{11} and symmetric Piola-Kirchhoff stress tensor. Fig. 1 shows a plot of the stress s versus the strain e for the one-dimensional homogeneous simple tension test. From the origin 0 to the elastic limit (identified by the point 1) the material is elastic, stress strictly increases[3] with

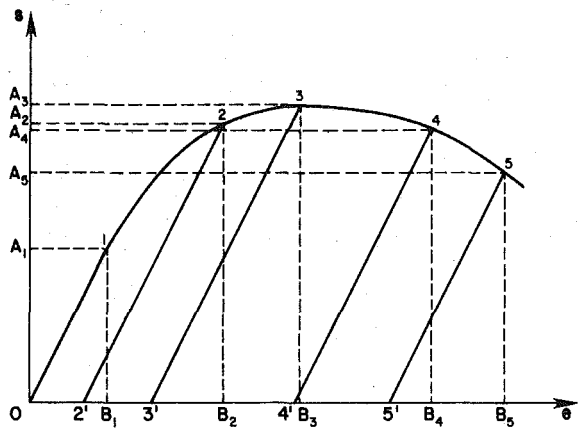

Fig. 1 Idealized stress-strain diagram for a typical ductile metal. As the points 1, 2, 3, 4, 5 of the stress-strain curve are successively transversed, the locus of the yield point on the e-axis moves outwards through B_1, B_2, B_3, B_4, and B_5, respectively, while the corresponding locus of the yield point on the s-axis first moves upwards through A_1, A_2 to A_3, and it then moves downwards through A_4 and A_5. All unloading curves are drawn parallel to the linear elastic segment 1-0 and hysteresis is ignored.

[1] Now in the Department of Mechanical Engineering, University of Houston, Houston, Texas 77004.

[2] The theory proposed in [2, 3] is a general thermodynamical theory of elastic-plastic materials. The development in [1] is carried out within a purely mechanical framework which can readily be interpreted in terms of the isothermal case of the thermodynamical theory.

Contributed by the Applied Mechanics Division of THE AMERICAN SOCIETY OF MECHANICAL ENGINEERS, and presented at the 1981 Joint ASME/ASCE Applied Mechanics, Fluids Engineering, and Bioengineering Conference, University of Colorado, Boulder, Colo., June 22–27, 1981.

Discussion on this paper should be addressed to the Editorial Department, ASME, United Engineering Center, 345 East 47th Street, New York, N. Y. 10017, and will be accepted until September 1, 1981. Readers who need more time to prepare a Discussion should request an extension from the Editorial Department. Manuscript received by ASME Applied Mechanics Division, February, 1980; final revision, December, 1980. Paper No. 81-APM-26.

[3] Recall that a real-valued function f defined on some interval $\mathcal{I}$ of the real line is *increasing* if $f(x_2) \geqq f(x_1)$ whenever x_1 and x_2 belong to $\mathcal{I}$ and $x_2 \geqq x_1$. A function f is *strictly increasing* if $f(x_2) > f(x_1)$ whenever $x_2 > x_1$. Similarly, f is *decreasing* if $x_2 \geqq x_1$ implies $f(x_2) \leqq f(x_1)$ and *strictly decreasing* if $x_2 > x_1$ implies $f(x_2) < f(x_1)$.

strain, there is no plastic straining and unloading takes place along 1–0. On the rising portion 1–3 (excluding point 3) of the s–e curve both stress and plastic strain strictly increase with strain. Unloading from a point such as 2 takes place along 2–2′ leaving a plastic strain of amount 02′. At point 3, s attains its maximum value.[4] On the falling portion 3–4–5 (excluding point 3) of the s-e curve, stress strictly decreases with strain, but plastic strain continues to strictly increase. Associated with each point of the segment 1–5 in Fig. 1, there is a unique yield point on the s-axis (i.e., in stress space) and a unique yield point on the e-axis (i.e., in strain space). For the points 1, 2, 3, 4, 5 these are denoted by A_1, A_2, A_3, A_4, A_5 and B_1, B_2, B_3, B_4, B_5, respectively. The points A_1 and B_1 are the initial yield points. As the segment 1–5 of the stress-strain curve is traversed, the locus of the yield point on the s-axis differs characteristically from that of the yield point on the e-axis, in that the former reverses its direction of motion while the latter does not.

The usual loading criteria of the stress space formulation of plasticity theory, when applied to the one-dimensional case under discussion, require that the plastic strain rate be nonzero whenever the yield point on the s-axis is moving upwards, and be zero when it is stationary. It is further stipulated that the yield point on the s-axis cannot move downwards while tension is being applied. These criteria are consistent with the results of the tensile test for the rising portion 1–3 of the stress-strain curve, both for paths of the type 1–2 and paths of the type 2–2′. They also demand the correct kind of behavior for paths of the type 4–4′ issuing from points on the falling portion 3–5 of the stress-strain curve. However, they are clearly inadequate for paths of the type 3–4 because the yield point on the s-axis does move downwards for any such path; and, as was pointed out in [1], plastic strain is observed to be strictly increasing in this region. On the other hand, again with reference to the one-dimensional case under discussion, the loading criteria of the strain space formulation require that the plastic strain rate be nonzero whenever the yield point on the e-axis is moving outwards and that it be zero whenever this yield point is stationary. It is further required that the yield point on the e-axis cannot move inwards while extension is occurring. These requirements are consistent with the behavior represented in Fig. 1. Thus the plastic strain is strictly increasing along the paths 1–2 and 3–4 and is constant along the paths 2–2′ and 4–4′.

In order to provide a background for some subsequent developments, it is desirable to make further observations regarding the stress-strain curve in Fig. 1. In the context of the classical infinitesimal theory, we recall the relations

$$e = e_e + e_p, \quad e_e = s/E, \tag{1}$$

where e_e and e_p are abbreviations for the components e^e_{11} and e^p_{11} of the elastic and plastic strains, respectively, and E (>0) is Young's modulus. We note that

$$\frac{de}{ds} = \frac{de_e}{ds} + \frac{de_p}{ds}, \quad \frac{de}{de_e} = \frac{de}{ds}\left(\frac{de_e}{ds}\right)^{-1} = 1 + \frac{de_p}{de_e}. \tag{2}$$

Now with the use of $de_e/ds = 1/E > 0$ and $(2)_2$, we have

$$\frac{de}{ds} > 0 \text{ if and only if } \frac{de}{de_e} > 0, \quad \frac{de}{ds} < 0 \text{ if and only if } \frac{de}{de_e} < 0. \tag{3}$$

On the rising portion of the s-e curve $de/ds > 0$ (or equivalently $ds/de > 0$), on the falling portion $de/ds < 0$ ($ds/de < 0$) and de/ds at point 3 becomes unbounded. Then, at a point A on the portion 1–5 of the s-e curve, with the help of (2) and (3) it is readily seen that

$$1 + \frac{de_p}{de_e}\begin{cases} > 0 \text{ if and only if } A \text{ is on the rising portion of the curve,} \\ < 0 \text{ if and only if } A \text{ is on the falling portion of the curve,} \end{cases} \tag{4}$$

while $1 + de_p/de_e$ becomes unbounded at point 3.

After recalling the main features of the purely mechanical theory of elastic-plastic materials from [1–3][5] in Section 2, a quotient $\hat{f}/\hat{g}$ of quantities which are derived from the loading functions f in stress space, and g in strain space, is introduced. It is noteworthy that while $\hat{f}$ involves the time rate of the stress tensor and $\hat{g}$ the time rate of the strain tensor, the quotient $\hat{f}/\hat{g}$ is independent of rates. In the latter part of Section 2, using an equation obtained with the help of a physically plausible work assumption introduced by Naghdi and Trapp in [4], we derive a geometrically revealing expression for the quotient $\hat{f}/\hat{g}$ [see equation (32)]. Next (Section 3), in terms of the quotient $\hat{f}/\hat{g}$, definitions are provided (see (43)) for strain-hardening behavior, i.e., for hardening, softening, and perfectly plastic behavior, and their geometrical implications are examined. It is demonstrated that, while during loading the yield surface in strain space is always moving outwards locally, the corresponding yield surface in stress space may concurrently be moving outwards, inwards, or may be stationary depending on whether the material is hardening, softening, or exhibiting perfectly plastic behavior. Because of our definitions (43), a variety of functions associated with material behavior and deriving from $\hat{f}/\hat{g}$ or $\hat{f}$ are found to be positive, negative, or zero according as a material exhibits hardening, softening, or perfectly plastic behavior. To avoid undue repetition, we introduce the abbreviation (44) and denote such conditions by the letter H. Any function that satisfies conditions H can be used to characterize strain-hardening behavior. By considering the limiting behavior of $\hat{f}/\hat{g}$, we also examine (in the context of the developments of the present paper) the phenomenon of saturation hardening studied previously by Caulk and Naghdi [5]. Definitions for saturation behavior are given at the end of Section 3.

The results in Sections 2 and 3 hold in the context of the nonlinear theory, but in the remainder of the paper attention is confined to *small* deformations of elastic-plastic materials. In order to demonstrate the predictive capability of the strain-hardening characterization developed in Section 3, special sets of constitutive equations are utilized in Sections 4 and 5 to discuss, respectively, strain-hardening response and saturation hardening under uniaxial loading.

For the particular constitutive equations utilized in Section 4, a rate-independent characterization of strain-hardening behavior is provided in terms of a certain combination ($2\beta + \psi\phi$) of material constants. Moreover, it is shown that both the time rate of work-hardening ($\dot{\kappa}$) and the time rate of tension ($\dot{s}$) may be used to characterize strain-hardening behavior. While the quotient $\hat{f}/\hat{g}$ involves the coefficient ψ as well as the derivatives of strains with respect to stress (see equation (64)), it is shown that for a certain special case, the quotient $\hat{f}/\hat{g}$ may be expressed (see equation (65a)) in terms of quantities appearing in (2)–(4) recorded earlier in this section. An examination of details of the solution in Section 4 shows that in uniaxial tension and in the sense of our definitions, linear elastic behavior is followed for perfectly plastic behavior by a horizontal stress-strain curve, while hardening behavior is represented by a straight line lying above, and softening by a straight line lying below the perfectly plastic line.

Finally, in Section 5, we consider another set of constitutive equations having in particular a loading function employed by Caulk and Naghdi [5] in their discussion of hardening response in small deformation of metals. Again it is shown that a number of different functions can be used to characterize strain-hardening behavior. Moreover, it is demonstrated that the quotient $\hat{f}/\hat{g}$ may be calculated in uniaxial tension from a knowledge of the slope de/ds, found from the stress-strain curve, and the elastic constants, namely, Young's modulus E and the shear modulus μ, and thus may be easily identified experimentally. Although our characterization of strain-hardening is, in general, different from that discussed previously by Caulk and Naghdi [5], the two sets of results are in agreement for the class of materials for which detailed comparisons with experiments were

[4] As was observed by Naghdi and Trapp [1, p. 789], the maximum of the s–e curve corresponds to a point which is still in the rising portion of the engineering stress (π) versus engineering strain (ϵ) curve. The maximum of the π–ϵ curve, where necking begins, corresponds to a point on the falling portion of the s–e curve.

[5] While some of the formulas in Section 2 may appear to be repetitions of those in [1], our starting point and some of our conclusions differ from [1] and for clarity we have repeated these formulas.

undertaken in [5]. In this connection see equations (88), which also include a simple expression in terms of material coefficients for the saturation hardening constant.

2 The Quotient $\hat{f}/\hat{g}$ of Quantities Occurring in Loading Criteria

Let the motion of a body be referred to a fixed system of rectangular Cartesian axes and let the position of a typical particle in the present configuration at time t be designated by $x_i = \chi_i(X_A, t)$, where X_A is a reference position of the particle. Throughout the paper, lower case Latin indices are associated with the spatial coordinates x_i and assume the values 1, 2, 3. Similarly, upper case Latin indices are associated with the material coordinates X_A and take the values 1, 2, 3. We also adopt the usual convention of summation over repeated indices.

We define a symmetric Lagrangian strain tensor by $e_{KL} = \frac{1}{2}(F_{iK}F_{iL} - \delta_{KL})$, where $F_{iK} = \partial\chi_i/\partial X_K$ is the deformation gradient relative to reference position and δ_{KL} is the Kronecker symbol. The six-dimensional Euclidean vector space formed from the components e_{KL} is called strain space. The components of the symmetric Piola-Kirchhoff stress tensor are denoted by s_{MN} and the six-dimensional Euclidean space formed from these components is called stress space.

We now summarize the main ingredients of the purely mechanical rate-type theory of a finitely deforming elastic-plastic solid and base our treatment on the work of Green and Naghdi [2, 3] and Naghdi and Trapp [1]. In addition to the strain tensor e_{KL}, we assume the existence of a symmetric[6] second-order tensor-valued function $e^p_{KL} = e^p_{KL}(X_A, t)$ called the plastic strain at X_A and t, and a scalar-valued function $\kappa = \kappa(X_A, t)$ called a measure of work-hardening. It is assumed that the stress s_{MN} is given by the constitutive equation

$$s_{MN} = \hat{s}_{MN}(\mathcal{U}), \quad \mathcal{U} = \{e_{KL}, e^p_{KL}, \kappa\}, \tag{5}$$

and that for fixed values of e^p_{KL} and κ, $(5)_1$ possesses an inverse of the form

$$e_{MN} = \hat{e}_{MN}(\mathcal{V}), \quad \mathcal{V} = \{s_{KL}, e^p_{KL}, \kappa\}. \tag{6}$$

The response functions $\hat{s}_{MN}$ and $\hat{e}_{MN}$ in (5) and (6) are taken to be smooth.

We admit the existence of a continuously differentiable scalar-valued yield (or loading) function $g(\mathcal{U})$ such that, for fixed values of e^p_{KL} and κ, the equation

$$g(\mathcal{U}) = 0 \tag{7}$$

represents a closed orientable hypersurface $\partial\mathscr{E}$ of dimension five enclosing a region $\mathscr{E}$ of strain space. The function g is chosen so that $g(\mathcal{U}) < 0$ for all points in the interior of the region $\mathscr{E}$. The hypersurface $\partial\mathscr{E}$ is called the yield (or loading) surface in strain space. Corresponding to a motion χ_i, we may associate with each particle of the body a continuous oriented curve C_e in strain space. This curve will be called a strain trajectory. The strain trajectories are restricted to lie initially in $\mathscr{E}$ or on its surface $\partial\mathscr{E}$, i.e.,

$$g(\mathcal{U}) \leqq 0 \tag{8}$$

initially on C_e.

The constitutive equations for $\dot{\kappa}$ and $\dot{e}^p_{KL}$ are [1]

$$\dot{\kappa} = \mathscr{C}_{KL}\dot{e}^p_{KL}, \tag{9}$$

and

$$\dot{e}^p_{KL} = \begin{cases} 0 & \text{if } g < 0, & (a) \\ 0 & \text{if } g = 0 \text{ and } \hat{g} < 0, & (b) \\ 0 & \text{if } g = 0 \text{ and } \hat{g} = 0, & (c) \\ \lambda\rho_{KL}\hat{g} & \text{if } g = 0 \text{ and } \hat{g} > 0, & (d) \end{cases} \tag{10}$$

where $\mathscr{C}_{KL} = \bar{\mathscr{C}}_{KL}(\mathcal{U})$ is a symmetric tensor-valued function, a superposed dot indicates material time differentiation,

$$\hat{g} = \frac{\partial g}{\partial e_{MN}}\dot{e}_{MN}, \tag{11}$$

and where $\lambda = \bar{\lambda}(\mathcal{U})$ and $\rho_{KL} = \bar{\rho}_{KL}(\mathcal{U})$ are,[7] respectively, a scalar-valued function and a symmetric tensor-valued function. The quantity $\hat{g}$ is the inner product of the tangent vector $\dot{e}_{MN}$ to a strain trajectory C_e and the vector $\partial g/\partial e_{MN}$. When $g = 0$ and at least one component of $\partial g/\partial e_{MN} \neq 0$, $\hat{g}$ gives the inner product of $\dot{e}_{MN}$ and the outward normal vector to the yield surface $\partial\mathscr{E}$, where the notation $\partial g/\partial e_{MN}$ stands for the symmetric form $\frac{1}{2}(\partial g/\partial e_{MN} + \partial g/\partial e_{NM})$. The conditions involving g and $\hat{g}$ in (10) are the loading criteria of the strain space formulation. Using conventional terminology, these four conditions in the order listed correspond to (a) an elastic state (or point in strain space); (b) unloading from an elastic-plastic state, i.e., a point in strain space for which $g = 0$; (c) neutral loading from an elastic-plastic state; and (d) loading from an elastic-plastic state. We assume that the coefficient of $\hat{g}$ in ($10d$) is nonzero on the yield surface and, without loss in generality, we then set

$$\rho_{KL} \neq 0, \quad \lambda > 0. \tag{12}$$

In order to provide a geometrical interpretation of the conditions (10), we need to record the material time derivative of the loading function, namely,

$$\dot{g} = \hat{g} + \frac{\partial g}{\partial e^p_{KL}}\dot{e}^p_{KL} + \frac{\partial g}{\partial \kappa}\dot{\kappa}, \tag{13}$$

where (11) has been used. It follows from (7), (9), and ($10a$) that in an elastic state the strain trajectory C_e lies in the interior of $\mathscr{E}$, which is referred to as the elastic region in strain space, and the yield surface $\partial\mathscr{E}$ remains stationary. Similarly, by (7), (9), ($10b$), and (13), during unloading the strain trajectory C_e intersects the yield surface $\partial\mathscr{E}$ and is moving in an inwardly direction, with the function g decreasing, while $\partial\mathscr{E}$ itself remains stationary. Likewise, from (7), (9), ($10c$), and (13) during neutral loading the strain trajectory C_e lies in the yield surface $\partial\mathscr{E}$ while the latter remains stationary and $\dot{g} = 0$. Finally, from (7), (9), ($10d$), and (13) during loading the strain trajectory C_e intersects $\partial\mathscr{E}$ and is moving in an outwardly direction. It is stipulated in this case that $\partial\mathscr{E}$ is locally pushed outwards by the strain trajectory C_e so that[8]

$$\dot{g} = 0, \tag{14}$$

if $g = 0, \hat{g} > 0$. Thus positive values of the function g can never be reached on a strain trajectory and the condition (8) holds for all time. It follows from (9), ($10d$), (13), and (14) that during loading

$$\hat{g}\left\{1 + \lambda\rho_{KL}\left(\frac{\partial g}{\partial e^p_{KL}} + \frac{\partial g}{\partial \kappa}\mathscr{C}_{KL}\right)\right\} = 0. \tag{15}$$

Therefore, since the coefficient of $\hat{g}$ is independent of $\dot{e}_{MN}$, we have

$$1 + \lambda\rho_{KL}\left(\frac{\partial g}{\partial e^p_{KL}} + \frac{\partial g}{\partial \kappa}\mathscr{C}_{KL}\right) = 0 \tag{16}$$

at all points on the yield surface $\partial\mathscr{E}$ through which loading can occur. We note that equations $(5)_1$ and $(6)_1$ hold during loading, neutral loading, unloading, and in an elastic state.

For a given motion χ_i and an associated strain trajectory C_e we may utilize the constitutive equations $(5)_1$, (9), and (10), together with appropriate initial conditions for e^p_{KL} and κ, to obtain the corresponding stress trajectory C_s, a continuous oriented curve in stress

[6] In [4], Naghdi and Trapp have shown that the symmetry of e^p_{KL} follows from a physically plausible work assumption which will be discussed at the end of this section.

[7] Our notation λ corresponds to $\bar{\lambda}$ in [1].

[8] In the literature on plasticity this is called the "consistency" condition, namely, that loading from an elastic-plastic state leads to another elastic-plastic state. For references and background information in the context of a stress space formulation, see, for example, Naghdi [6, Pages 141, 137].

space. In a similar fashion $(6)_1$ may be used to obtain C_e from C_s. Furthermore, for a given loading function $g(\mathcal{U})$, with the aid of $(6)_1$, we can obtain a corresponding function $f(\mathcal{V})$ through the formula

$$g(\mathcal{U}) = g(\hat{e}_{KL}(\mathcal{V}), e^p_{KL}, \kappa) = f(\mathcal{V}), \tag{17}$$

where the variables $\mathcal{U}$ and $\mathcal{V}$ are defined by $(5)_2$ and $(6)_2$, respectively. Conversely, $(5)_1$ may be used to obtain g from f. Because of the assumed smoothness of $(6)_1$, for fixed values of e^p_{KL} and κ, the equation

$$f(\mathcal{V}) = 0 \tag{18}$$

represents a hypersurface $\partial\mathcal{S}$ in stress space having the same geometrical properties as the hypersurface $\partial\mathcal{E}$ in strain space. The region enclosed by $\partial\mathcal{S}$ is denoted $\mathcal{S}$. It follows from (17) that a point in strain space belongs to the region $\mathcal{E}$ (i.e., $g(\mathcal{U}) \leqq 0$) if and only if the corresponding point in stress space satisfies $f(\mathcal{V}) \leqq 0$ and hence belongs to $\mathcal{S}$. Similarly, by (17) and (18) a point in strain space belongs to the yield surface $\partial\mathcal{E}$ (i.e., $g = 0$) if and only if the corresponding point in stress space belongs to $\partial\mathcal{S}$ (i.e., $f = 0$). Hence, we refer to the interior of $\mathcal{S}$ as the elastic region in stress space, and to $\partial\mathcal{S}$ as the yield (or loading) surface in stress space. We have seen that (8) holds for all t. Therefore, by (17), every stress trajectory C_s is restricted to lie in $\mathcal{S}$ or on its surface $\partial\mathcal{S}$ and positive values of f can never be reached. We note that any function of variables $\mathcal{U}$ can be written as a different function of variables $\mathcal{V}$ and vice versa, e.g., $\mathcal{C}_{KL} = \overline{\mathcal{C}}_{KL}(\mathcal{U}) = \tilde{\mathcal{C}}_{KL}(\mathcal{V})$ which occurs in (9).

In [1] a comparative basis was provided between the two independent sets of loading criteria for the stress space and the strain space formulations. A correspondence between the two sets of loading criteria was established for all conditions except that during loading. The approach in the present paper differs from that of [1] in that the loading criteria of the strain space formulation are regarded as primary and associated loading conditions in stress space are deduced from the former.[9] Although in the examination of the loading criteria our starting point and conclusions are different, the arguments employed parallel those of [1]. Thus, taking the material time derivative of (17) and making use of (13), we obtain

$$\dot{f} = \hat{f} + \frac{\partial f}{\partial e^p_{KL}}\dot{e}^p_{KL} + \frac{\partial f}{\partial \kappa}\dot{\kappa} = \hat{g} + \frac{\partial g}{\partial e^p_{KL}}\dot{e}^p_{KL} + \frac{\partial g}{\partial \kappa}\dot{\kappa}, \tag{19}$$

where

$$\hat{f} = \frac{\partial f}{\partial s_{MN}}\dot{s}_{MN}. \tag{20}$$

The quantity $\hat{f}$ is, of course, the inner product of the tangent vector $\dot{s}_{MN}$ to a stress trajectory C_s and the vector $\partial f/\partial s_{MN}$. In view of (19)

$$\hat{f} = \hat{g} \quad \text{if} \quad \dot{e}^p_{KL} = 0 \text{ and } \dot{\kappa} = 0. \tag{21}$$

Considering an elastic state, $f = g < 0$, $(10a)$ holds, $\dot{\kappa} = 0$ by (9) and hence $\hat{f} = \hat{g}$ by (21). Since the yield surface $\partial\mathcal{E}$ in strain space is stationary so also is the yield surface $\partial\mathcal{S}$ in stress space. The stress trajectories remain in the interior of $\mathcal{S}$. It is clear from (9), $(10b)$, (17), and (21) that[10] $f = 0$ and $\hat{f} < 0$ if $g = 0$ and $\hat{g} < 0$. In this case ($g = 0$, $\hat{g} < 0$) the stress trajectory C_s intersects $\partial\mathcal{S}$ and is directed inwards, with the function f decreasing in value, while $\partial\mathcal{S}$ itself remains stationary. It follows from (9), $(10c)$, (17), and (21) that[11] $f = 0$ and $\hat{f} = 0$ if $g = 0$ and $\hat{g} = 0$. In this case ($g = 0, \hat{g} = 0$) the stress trajectory C_s lies in the surface $\partial\mathcal{S}$ which remains stationary and $\dot{f} = 0$.

In the case of loading from an elastic-plastic state, it follows from (9), $(10d)$, and (19) that

$$\frac{\hat{f}}{\hat{g}} = 1 + \lambda\rho_{KL}\left\{\left(\frac{\partial g}{\partial e^p_{KL}} - \frac{\partial f}{\partial e^p_{KL}}\right) + \left(\frac{\partial g}{\partial \kappa} - \frac{\partial f}{\partial \kappa}\right)\mathcal{C}_{KL}\right\}, \quad (g = 0, \hat{g} > 0). \tag{22}$$

In the developments that follow, the quotient $\hat{f}/\hat{g}$ can be expressed in a number of different forms. In order to establish one such form we note that by (17), $(5)_1$, $(6)_1$ and the chain rule of differentiation

$$\begin{aligned} \frac{\partial g}{\partial e^p_{KL}} - \frac{\partial f}{\partial e^p_{KL}} &= \frac{\partial f}{\partial s_{MN}}\frac{\partial \hat{s}_{MN}}{\partial e^p_{KL}} = -\frac{\partial g}{\partial e_{MN}}\frac{\partial \hat{e}_{MN}}{\partial e^p_{KL}}, \\ \frac{\partial g}{\partial \kappa} - \frac{\partial f}{\partial \kappa} &= \frac{\partial f}{\partial s_{MN}}\frac{\partial \hat{s}_{MN}}{\partial \kappa} = -\frac{\partial g}{\partial e_{MN}}\frac{\partial \hat{e}_{MN}}{\partial \kappa}. \end{aligned} \tag{23}$$

With the use of (23), (22) can be rewritten as

$$\begin{aligned} \frac{\hat{f}}{\hat{g}} &= 1 + \lambda\rho_{KL}\frac{\partial f}{\partial s_{MN}}\left\{\frac{\partial \hat{s}_{MN}}{\partial e^p_{KL}} + \frac{\partial \hat{s}_{MN}}{\partial \kappa}\mathcal{C}_{KL}\right\} \\ &= 1 - \lambda\rho_{KL}\frac{\partial g}{\partial e_{MN}}\left\{\frac{\partial \hat{e}_{MN}}{\partial e^p_{KL}} + \frac{\partial \hat{e}_{MN}}{\partial \kappa}\mathcal{C}_{KL}\right\}, \quad (g = 0, \hat{g} > 0). \end{aligned} \tag{24a}$$

Another useful form of the quotient $\hat{f}/\hat{g}$ that may be derived from (22) with the help of $(12)_2$ and (16) is

$$\begin{aligned} \frac{\hat{f}}{\hat{g}} &= -\lambda\rho_{KL}\left\{\frac{\partial f}{\partial e^p_{KL}} + \frac{\partial f}{\partial \kappa}\mathcal{C}_{KL}\right\} \\ &= \frac{\rho_{KL}\left\{\dfrac{\partial f}{\partial e^p_{KL}} + \dfrac{\partial f}{\partial \kappa}\mathcal{C}_{KL}\right\}}{\rho_{MN}\left\{\dfrac{\partial g}{\partial e^p_{MN}} + \dfrac{\partial g}{\partial \kappa}\mathcal{C}_{MN}\right\}}, \quad (g = 0, \hat{g} > 0). \end{aligned} \tag{24b}$$

Since the right-hand side of $(24b)_2$ is independent of rates, it is clear that the quotient $\hat{f}/\hat{g}$ is independent of rates and has the same value for all strain trajectories through a given elastic-plastic point on $\partial\mathcal{E}$. Also, in view of (17), $\hat{f}/\hat{g}$ is dimensionless. Clearly a knowledge of all constitutive equations is required for the calculation of $\hat{f}/\hat{g}$.

We now turn to the work assumption of Naghdi and Trapp [4, 7]. Starting with the assumption that the external work done on an elastic-plastic body in any smooth homogeneous cycle of deformation is nonnegative, it was demonstrated[12] in [4] that

$$\left\{\frac{\partial \hat{s}_{MN}}{\partial e^p_{KL}} + \frac{\partial \hat{s}_{MN}}{\partial \kappa}\mathcal{C}_{KL}\right\}\dot{e}^p_{KL}\dot{e}_{MN} \leqq 0 \tag{25}$$

during loading or neutral loading, i.e., when $g = 0$, $\hat{g} \geqq 0$. In the case of neutral loading it follows from $(10c)$ that the left-hand side of (25) vanishes and (25) is satisfied trivially, while in the case of loading, it follows from $(10d)$ and $(12)_2$ that (25) becomes

$$\left\{\frac{\partial \hat{s}_{MN}}{\partial e^p_{KL}} + \frac{\partial \hat{s}_{MN}}{\partial \kappa}\mathcal{C}_{KL}\right\}\rho_{KL}\dot{e}_{MN} \leqq 0 \tag{26}$$

with $g = 0$ and $\hat{g} > 0$. The coefficient of $\dot{e}_{MN}$ in (26) is itself independent of $\dot{e}_{MN}$ and the inequality must hold for all choices of $\dot{e}_{MN}$ that satisfy $\hat{g} > 0$. Therefore, by the same argument used in Section 5 of [4], we deduce that

$$\left\{\frac{\partial \hat{s}_{MN}}{\partial e^p_{KL}} + \frac{\partial \hat{s}_{MN}}{\partial \kappa}\mathcal{C}_{KL}\right\}\rho_{KL} = -\gamma^*\frac{\partial g}{\partial e_{MN}} \tag{27}$$

evaluated on the yield surface $g = 0$, where the scalar function γ^* satisfies

$$\gamma^* = \overline{\gamma}^*(\mathcal{U}) \geqq 0. \tag{28}$$

We emphasize that (27) holds even for a motion that is not homogeneous.[13]

[9] These derived conditions are not the same as the loading criteria usually assumed in the stress space formulation.

[10] In [1] it was possible to prove the converse of this statement because of the *independent* loading criteria that were assumed in the stress-space formulation. It will become clear presently that in the context of this paper the converse statement does not hold.

[11] See the previous footnote.

[12] See equations (5.2), (5.3), and (4.11) of [4]; the notation H_{MN} in [4] corresponds to $\mathcal{C}_{MN}$ in the present paper.

[13] For a discussion of this point, see [4, p. 40] or [7, p. 63].

In order to compare (27) with the results of [4] we multiply on both sides of (27) by $\lambda\hat{g}$ and utilize (10d) to obtain

$$\left\{\frac{\partial \hat{s}_{MN}}{\partial e^p_{KL}} + \frac{\partial \hat{s}_{MN}}{\partial \kappa}\, e_{KL}\right\} \dot{e}^p_{KL} = -\lambda\gamma^*\hat{g}\,\frac{\partial g}{\partial e_{MN}}, \quad (g = 0, \hat{g} > 0). \tag{29}$$

Recalling the restrictions $(12)_2$ and (28), we define a function γ by[14]

$$\gamma = \lambda\gamma^*\hat{g} \geqq 0 \tag{30}$$

and from (29) obtain

$$\left\{\frac{\partial \hat{s}_{MN}}{\partial e^p_{KL}} + \frac{\partial \hat{s}_{MN}}{\partial \kappa}\, e_{KL}\right\} \dot{e}^p_{KL} = -\gamma\,\frac{\partial g}{\partial e_{MN}}, \quad (g = 0, \hat{g} > 0). \tag{31}$$

Equation (31) is the same as (5.4) of [4]. We note that (31) involves rates, while (27) does not. We have shown that (27) implies (31). Conversely, it follows at once from (10d) and $(12)_2$ that (31) implies (27) with $\gamma^* = \gamma/\lambda\hat{g}$, as in (30).

From (27) and $(24a)_1$ follows an expression for $\hat{f}/\hat{g}$ in the form:

$$\frac{\hat{f}}{\hat{g}} = 1 - \lambda\gamma^*\Lambda, \quad (g = 0, \hat{g} > 0), \tag{32}$$

where

$$\Lambda = \frac{\partial f}{\partial s_{MN}}\,\frac{\partial g}{\partial e_{MN}}, \quad (g = f = 0). \tag{33}$$

The quantity Λ represents the inner product of the normal to the yield surface $\partial\mathcal{S}$ in stress space and the normal to the yield surface $\partial\mathcal{E}$ in strain space.

For some purposes it is convenient to express the constitutive equation $(5)_1$ in terms of an equivalent set of kinematical variables in the form

$$s_{MN} = \bar{s}_{MN}(e_{KL} - e^p_{KL}, e^p_{KL}, \kappa). \tag{34}$$

Suppose that the partial derivatives $\partial\hat{s}_{MN}/\partial e_{KL}$ possess the symmetries[15] $\partial\hat{s}_{MN}/\partial e_{KL} = \partial\hat{e}_{KL}/\partial e_{MN}$. Then, in a manner similar to that in [4, Section 5], from (27) we obtain[16]

$$-\rho_{PQ} + \frac{\partial \hat{e}_{PQ}}{\partial s_{MN}}\left\{\frac{\partial \bar{s}_{MN}}{\partial e^p_{KL}} + \frac{\partial \bar{s}_{MN}}{\partial \kappa}\, e_{KL}\right\}\rho_{KL} = -\gamma^*\,\frac{\partial f}{\partial s_{PQ}}, \quad (g = f = 0). \tag{35}$$

It is clear from (35), (30), (10d), and (12) that if the response function $\bar{s}_{MN}$ in (34) is independent of its second and third arguments, i.e., if $\partial\bar{s}_{MN}/\partial e^p_{KL} = 0$, $\partial\bar{s}_{MN}/\partial\kappa = 0$, then

$$\rho_{KL} = \gamma^*\,\frac{\partial f}{\partial s_{KL}} \neq 0, \quad \dot{e}^p_{KL} = \gamma\,\frac{\partial f}{\partial s_{KL}}, \quad (g = 0) \tag{36}$$

and ρ_{KL} is directed along the normal to the yield surface $\partial\mathcal{S}$ in stress space, as also is $\dot{e}^p_{KL}$ during loading. It follows from $(36)_1$ and (28) that in this case

$$\gamma^* > 0, \quad (g = 0) \tag{37}$$

and hence, during loading, in view of (30) and $(12)_2$

$$\gamma > 0 \tag{38}$$

also. When ρ_{KL} satisfies $(36)_1$, (16) can be written as

$$1 + \lambda\gamma^*\,\frac{\partial f}{\partial s_{KL}}\left\{\frac{\partial g}{\partial e^p_{KL}} + \frac{\partial g}{\partial \kappa}\, e_{KL}\right\} = 0, \quad (g = 0). \tag{39}$$

The last result can be used to solve for the product $\lambda\gamma^*$ and (30) then gives γ. Also, we may set γ^* equal to an arbitrary positive scalar-valued function of the variables $\mathcal{U}$ and then use (39) to determine λ. Thus, in the special case in which $\bar{s}_{MN}$ in (34) depends only on its first argument, no constitutive equation is needed for ρ_{KL}.

We observe that when ρ_{KL} satisfies $(36)_1$, then $(24b)_1$ may be used to express $\hat{f}/\hat{g}$ as

$$\hat{f}/\hat{g} = \lambda\gamma^*\Gamma, \quad (g = 0, \hat{g} > 0), \tag{40}$$

where

$$\Gamma = -\frac{\partial f}{\partial s_{KL}}\left\{\frac{\partial f}{\partial e^p_{KL}} + \frac{\partial f}{\partial \kappa}\, e_{KL}\right\}, \quad (g = 0). \tag{41}$$

Also, in view of (32), (40), (37), and $(12)_2$,

$$0 < \frac{1}{\lambda\gamma^*} = \Gamma + \Lambda, \quad \frac{\hat{f}}{\hat{g}} = \frac{\Gamma}{\Gamma + \Lambda}, \quad (g = 0, \hat{g} > 0). \tag{42}$$

3 Strain-Hardening Behavior and Its Geometrical Interpretation

The quotient $\hat{f}/\hat{g}$ which occurs in $(24b)_2$ and related equations in Section 2, is utilized here to define three distinct types of strain-hardening response for an elastic-plastic material. These definitions are as follows: An elastic-plastic material is said to be *hardening*, *softening* or exhibiting *perfectly plastic* behavior during loading $(g = 0, \hat{g} > 0)$ according to whether[17]

$$\begin{aligned} &(a) \quad \hat{f}/\hat{g} > 0 \quad \text{(for hardening)},\\ &(b) \quad \hat{f}/\hat{g} < 0 \quad \text{(for softening)},\\ &(c) \quad \hat{f}/\hat{g} = 0 \quad \text{(for perfectly plastic)}. \end{aligned} \tag{43}$$

We emphasize that a condition of loading, i.e., $g = 0$ and $\hat{g} > 0$, is always presupposed in the definitions (43). It is worth observing from $(24b)_2$ that once ρ_{KL}, e_{KL}, g, and $(6)_1$ are specified, then the strain-hardening response is also known.

We now provide a geometrical interpretation of the definitions (43). We recall that during loading, since $g = 0, \hat{g} > 0$, and $\dot{g} = 0$, the strain trajectory C_e is intersecting the yield surface $\partial\mathcal{E}$ and locally pushing it outwards. Since $g = 0$ and $\dot{g} = 0$ it follows from (17) and (19) that $f = 0$ and $\dot{f} = 0$ also, and the corresponding stress trajectory C_s is intersecting the yield surface $\partial\mathcal{S}$ in stress space. If the material is hardening, (43a) holds and the stress trajectory C_s is directed outwards and is pushing the surface $\partial\mathcal{S}$ locally outwards. But, (43b) holds if the material is softening and the stress trajectory is directed inwards and is pulling the surface $\partial\mathcal{S}$ locally inwards. In perfectly plastic behavior when (43c) holds, the stress trajectory continues to lie on the yield surface $\partial\mathcal{S}$ which is stationary.

Thus while during loading the strain trajectory C_e is always pushing the yield surface $\partial\mathcal{S}$ in strain space locally outwards, the corresponding yield surface $\partial\mathcal{S}$ in stress space may be moving concurrently outwards, inwards, or may be stationary depending on the type of strain-hardening response being exhibited. The actual occurrence of such behavior has been indicated in Section 1 with reference to the simple tension test. The usual stress space formulation of plasticity theory introduces *a priori* loading criteria in stress space and stipulates that during loading the yield surface in stress space can never move inwards. Viewed in the context of the present development, the usual stress space formulation of plasticity is seen to include only a hardening-type response and to exclude softening and perfectly plastic responses.[18] Fig. 2 illustrates the three types of material behavior defined by (43).

[14] The function γ on the right-hand side of (31) depends on the variables e_{MN}, e^p_{MN}, κ, and $\dot{e}_{MN}$.

[15] This is equivalent to the condition that $\hat{s}_{MN}$ be derivable from a potential, as indeed is the case in the general thermodynamical theory (see Section 4 of [3]) of which the present development may be regarded as corresponding to the isothermal case. The existence of a potential in the purely mechanical theory can also be demonstrated by an argument based on the work postulate of [4].

[16] The symmetry of ρ_{KL} and hence e^p_{KL} follows from (35). See [4, Section 5].

[17] Since $\hat{g}$ is always positive in (43), we could use only $\hat{f}$ in providing the foregoing definitions. But the use of the quotient $\hat{f}/\hat{g}$ which is rate-independent, is preferable in general. For certain purposes, however, it is useful to employ only $\hat{f}$ as in $(58)_3$ and (59) of Section 4.

[18] In the context of the present paper, it is not possible to formulate loading criteria in stress space using only f and $\hat{f}$.

Table 1 Summary of loading criteria in strain space and associated conditions in stress space

Elastic	$g < 0$	implies	$f < 0$
Unloading	$g = 0, \quad \hat{g} < 0$	implies	$f = 0, \quad \hat{f} < 0$
Neutral loading	$g = 0, \quad \hat{g} = 0$	implies	$f = 0, \quad \hat{f} = 0$
Loading	$g = 0, \quad \hat{g} > 0$ { (a) hardening; (b) softening; (c) perfectly plastic }	implies	{ $f = 0, \ \hat{f} > 0$; $f = 0, \ \hat{f} < 0$; $f = 0, \ \hat{f} = 0$

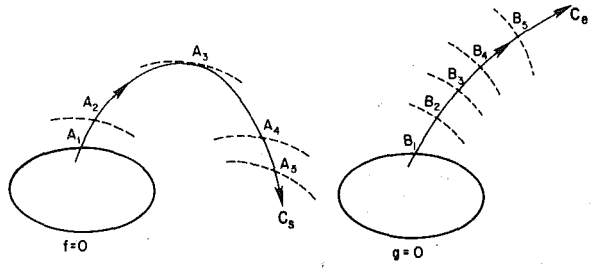

Fig. 2 A sketch indicating the motion of yield surfaces in stress space and strain space. During loading the yield surface $\partial\mathcal{E}$ in strain space moves outwards with the strain trajectory C_e through positions such as B_1, B_2, B_3, B_4, B_5. The corresponding yield surface $\partial\mathcal{S}$ in stress space moves outwards through positions such as A_1 and A_2 during hardening behavior, is stationary in positions of the type A_3 during perfectly plastic behavior, and moves inwards through positions such as A_4 and A_5 during softening behavior.

The definitions for hardening, softening, and perfectly plastic behavior introduced in (43) require the use of yield surfaces both in strain space and stress space. However, it may be noted that our terminology for softening and hardening seems to be consistent with the geometrical sense of these terms employed in a stress space formulation by Edelman and Drucker [8]; see Fig. 5 of their paper. Also, Prager [9] employs the terms hard and soft with reference to material behavior, but this sense of these terms differs from ours: In [9], a hard material is one whose stress-strain curve always lies above a given straight line (representing linear elastic response) with the deviation from linear behavior increasing for larger deformation; a soft material is one whose stress-strain curve always lies below the straight line with the deviation increasing for larger deformation.

In what follows, we frequently need to refer to a set of conditions which must be satisfied by various functions and material coefficients, and which arise from characterization of strain-hardening response. To avoid undue repetition we denote this set of conditions by H and write

$$H: \begin{cases} > 0 \text{ if and only if the material is hardening,} & (a) \\ < 0 \text{ if and only if the material is softening,} & (b) \\ = 0 \text{ if and only if the material is exhibiting perfectly plastic behavior.} & (c) \end{cases} \tag{44}$$

Returning to the definitions (43) and recalling $(24b)_1$ and $(12)_2$, it is seen that

$$-\rho_{KL}\left\{\frac{\partial f}{\partial e^p_{KL}} + \frac{\partial f}{\partial \kappa}\, \mathcal{C}_{KL}\right\} \text{ satisfies conditions } H. \tag{45}$$

It is worth mentioning that the usual treatment of an elastic-perfectly plastic material (see, for example, [2, Section 9]) in stress space requires the use of a yield condition of the form $f(s_{KL}) = \text{constant}$ and the quantity on the left-hand side of (45) indeed vanishes identically in this case.

With the use of the definitions $(43a, b)$, we now obtain an expression for the rate of plastic strain which is valid in regions of hardening and softening behavior only. Thus, by $(10d)$, (12), $(24b)_1$ and $(43a)$, in a region of hardening $\dot{e}^p_{KL}$ can be related to $\hat{f}$ through the expression

$$\dot{e}^p_{KL} = \lambda \rho_{KL} \frac{\hat{f}}{\hat{f}/\hat{g}} = -\frac{\rho_{KL}\hat{f}}{\rho_{MN}\left\{\dfrac{\partial f}{\partial e^p_{MN}} + \dfrac{\partial f}{\partial \kappa}\, \mathcal{C}_{MN}\right\}} \neq 0 \tag{46}$$

with $(43a)$ and $(45a)$ holding,[19] while in a region of softening $\dot{e}^p_{KL}$ is again given by (46) but now with $(43b)$ and $(45b)$ holding; in both cases, the sign of the coefficient of ρ_{KL} in (46) is positive. For perfectly plastic behavior, it is clear from $(10d)$, $(24b)_1$, $(43c)$, and $(45c)$ that $\dot{e}^p_{KL}$ cannot be expressed as a product involving $\hat{f}$ and must be calculated from $(10d)$. For convenience, a summary of the relationships between the loading criteria in strain space and the associated conditions in stress space is provided in Table 1.

In the remainder of this section, we discuss some special cases of the foregoing results which are of particular interest in view of their simplicity. The first two of these (see Cases (a) and (b) below) examine the consequences on strain-hardening behavior of certain restrictions on the stress response functions $\hat{s}_{MN}$ in $(5)_1$ and $\bar{s}_{MN}$ in (34). The third (see Case (c) below) pertains to a limiting behavior of strain-hardening response, i.e., saturation hardening and softening.

Case (a). Consider the special case of $(5)_1$ for which the stress response is independent of its last two arguments, i.e.,

$$\frac{\partial \hat{s}_{MN}}{\partial e^p_{KL}} = 0, \quad \frac{\partial \hat{s}_{MN}}{\partial \kappa} = 0. \tag{47a}$$

When conditions $(47a)$ are satisfied, $(5)_1$ may be replaced by an equation of the form

$$s_{MN} = \bar{s}_{MN}(e_{KL}). \tag{47b}$$

We observe that $(47b)$ has the same form as the stress constitutive equation of a nonlinear elastic solid. For an elastic-plastic material whose stress constitutive equation is $(47b)$, the stress tensor s_{MN} is determined once the motion χ_i of the body is specified. This should be contrasted with the general case for which the differential equations (9) and (10) must be solved before s_{MN} can be calculated. A further interesting feature of elastic-plastic materials for which $(47a)_{1,2}$ hold is that their hardening response is extremely limited. Thus, by $(47a)$ and (23), we have

$$\frac{\partial g}{\partial e^p_{KL}} = \frac{\partial f}{\partial e^p_{KL}}, \quad \frac{\partial g}{\partial \kappa} = \frac{\partial f}{\partial \kappa}$$

and hence by $(24a)$ or (22)

$$\hat{f}/\hat{g} = 1. \tag{48}$$

Recalling the definitions (43), it is clear that a material for which $(47)_{1,2}$ hold can never exhibit softening or perfectly plastic behavior. If conditions $(47a)_{1,2}$ are satisfied and if $\partial g/\partial e_{MN} \neq 0$, it follows from (27) and (30) that

[19] The equation number $(45a)$ refers to (45) along with part (a) of condition H.

$$\gamma^* = 0, \quad \gamma = 0. \tag{49}$$

Conversely, if $(49)_1$ is satisfied so is $(49)_2$ and then (48) holds by virtue of (32).

It is clear from the results of the foregoing special case that in order to construct a general theory of elastic-plastic materials, it is necessary to include e^p_{KL} and κ (or at least one of them) in the list of arguments of the stress response function $\hat{s}_{MN}$. Otherwise, the strain-hardening behavior will be too restrictive.

Case (b). Consider the special case of (34) for which the stress response is independent of its last two arguments. In this case, the results (36) to (42) hold. It then follows from (37), (40), (43), and $(12)_2$ that

$$\Gamma \text{ satisfies conditions } H. \tag{50}$$

With the use of $(36)_1$ and (40), in a region of hardening or softening (46) becomes

$$\dot{e}^p_{KL} = \frac{\hat{f}}{\Gamma}\frac{\partial f}{\partial s_{KL}} \neq 0, \tag{51a}$$

while it follows from (50c), (42), $(36)_1$, and (10*d*) that in a region of perfectly plastic behavior

$$\dot{e}^p_{KL} = \frac{\hat{g}}{\Lambda}\frac{\partial f}{\partial s_{KL}} \neq 0. \tag{51b}$$

Case (c). Caulk and Naghdi [5] have previously introduced a definition of saturation hardening in connection with their discussion of hardening response in cyclic loading of metallic materials (see equation (19) in [5]). In view of the definitions (43), it is of interest to reexamine here the notion of saturation hardening. Thus, for our present purpose, an elastic-plastic material is said to exhibit saturation hardening along a strain trajectory C_e (or a stress trajectory C_s) if and only if there exists a constant K_h such that [20]

$$\lim_{t\to\infty} \hat{f}/\hat{g} = K_h > 0 \quad (g = 0, \hat{g} > 0). \tag{52a}$$

Similarly a material exhibits saturation softening along a strain trajectory C_e if and only if there exists a constant K_s such that

$$\lim_{t\to\infty} \hat{f}/\hat{g} = K_s < 0 \quad (g = 0, \hat{g} > 0). \tag{52b}$$

In order to indicate the relationship between the definition (52*a*) of saturation hardening and that given by Caulk and Naghdi [5, equation (19)], we observe that if during loading the limit as $t \to \infty$ of $\dot{\kappa}$ is zero on some strain trajectory C_e, then assuming $(12)_2$ to hold in the limit, it follows from (9) and (10*d*) that on C_e:

$$\lim_{t\to\infty} \rho_{KL}\mathcal{C}_{KL} = 0.$$

Consequently, by $(24b)_2$ on C_e:

$$\lim_{t\to\infty}\frac{\hat{f}}{\hat{g}} = \lim_{t\to\infty}\frac{\rho_{KL}\dfrac{\partial f}{\partial e^p_{KL}}}{\rho_{MN}\dfrac{\partial g}{\partial e^p_{MN}}},$$

if this limit exists. The latter limit may be positive, negative, or zero depending on the limiting value of $-\rho_{KL}/(\partial f/\partial e^p_{KL})$, in view of (45).

We close this section with some remarks on certain other approaches which have been used in connection with the characterization of strain-hardening.

One approach, that of Palmer, Maier, and Drucker [10] is based on a "plastic work" criterion. In the notation of the present paper, the procedure of [10] amounts to stipulating that the scalar $\dot{s}_{KL}\dot{e}^p_{KL}$ is positive for hardening and negative for softening. However, such a criterion leads to ambiguities since $\dot{s}_{KL}\dot{e}^p_{KL}$ vanishes for both perfectly plastic behavior and neutral loading (and in an elastic state as well).

Another approach is that of Hill [11].[21] Hill confines his discussion to a special class of constitutive equations which may be derived from (34) when $\bar{s}_{MN}$ is independent of its last two arguments. While Hill considers flow rules in both strain space and stress space,[22] his stress space flow rules are anomalous; and, in particular, his flow rule for perfectly plastic behavior involves an indeterminacy in strain rate (and hence also in plastic strain rate). The reason for these anomalies is that Hill does not regard the loading criteria of strain space as primary.

To elaborate, although Hill [11, p. 245] speaks of a condition of "continued plastic flow," his flow rules 1), 2), 3) are not consistent with the requirement that $\hat{g}$ be positive.[23] In particular, if $\hat{g} > 0$ and $\hat{f}/\hat{g} > 0$, then the first part of flow rule 1) corresponding to $\hat{f} < 0$ can never apply. Hill's flow rule 2) involves a "double-valued" inverse. Again, if the condition $\hat{g} > 0$ is enforced no such anomaly occurs. Finally, in the case 3) of perfectly plastic behavior, the first part of the flow rule corresponding to $\hat{f} < 0$ should be omitted and instead of the second part of the flow rule which involves an indeterminacy, the flow rule of the strain space formulation should be retained.[24] The indeterminacy in Hill's flow rule 3) results from the fact that the determinant of $\mathbf{L}$ (in equation (4) of [11]) vanishes for perfectly plastic behavior.

Setting aside the matter of incorrectness of the flow rules in [11], we now wish to relate Hill's quantity $1\text{-}\boldsymbol{\ell}'\boldsymbol{\lambda}$ to the quotient $\hat{f}/\hat{g}$ of the present paper. Consider the stress constitutive equation in the alternative forms (5) and (34). By applying the chain rule to these equations, $(24)_1$ may be expressed as

$$\frac{\hat{f}}{\hat{g}} = 1 - \lambda\rho_{KL}\frac{\partial g}{\partial e_{KL}} + \lambda\rho_{KL}\frac{\partial f}{\partial s_{MN}}\left\{\frac{\partial \bar{s}_{MN}}{\partial e^p_{KL}} + \frac{\partial \bar{s}_{MN}}{\partial \kappa}\mathcal{C}_{KL}\right\}.$$

In [11], Hill defines strain-hardening, strain softening, and perfectly plastic behavior in accordance with whether $\lambda\rho_{KL}(\partial g/\partial e_{KL})$ is less than, greater than or equal to unity. Such a characterization is clearly not adequate for a general elastic-plastic material of the type being treated in the present paper. If, however, we confine attention to the special class of constitutive equations for which the function $\bar{s}_{MN}$ in (34) is independent of its last two arguments, then $\hat{f}/\hat{g}$ reduces to $1 - \lambda\rho_{KL}(\partial g/\partial e_{KL})$. Indeed, as we have indicated above (see (36)–(42) and Case (*b*) of the present section), when $\bar{s}_{MN}$ is independent of its last two arguments, the work assumption of Naghdi and Trapp [4, 7] implies the normality condition $(36)_1$ on ρ_{KL}, and instead of $\hat{f}/\hat{g}$, the simpler quantity Γ in (41) can be used to characterize strain-hardening behavior. Furthermore, in a region of hardening and in a region of softening the flow rule for plastic strain rate may be written in the stress space form (51*a*), while in a region of perfectly plastic behavior it reduces to the strain space form (51*b*).

4 Strain-Hardening Response for Special Constitutive Equations

We consider now in some detail the nature of the hardening response in small deformation of metals whose behavior is characterized

[20] In the definitions (52*a*, *b*) we have excluded for convenience the equality sign. If the limit of the left-hand sides of (52*a*, *b*) is zero, we say that the material saturates to a perfectly plastic behavior.

[21] Hill's paper [11] was brought to our attention by a referee after the present paper was submitted for publication.

[22] Actually, Hill [11] employs strain-rate and stress-rate space in conjunction with a constitutive equation for an objective stress rate.

[23] Hill's $\boldsymbol{\lambda}$, $\boldsymbol{\ell}$, $\mathbf{m}$, $\boldsymbol{\ell}'\boldsymbol{\epsilon}$, $\mathbf{m}'\mathbf{s}$ correspond to our $\lambda\rho_{KL}$, $\partial g/\partial e_{KL}$, $\partial f/\partial s_{KL}$, $\hat{g}$, $\hat{f}$, respectively. As will be shown presently, for the case discussed by Hill, the quotient $\hat{f}/\hat{g}$ of the present paper reduces to Hill's $1\text{-}\boldsymbol{\ell}'\boldsymbol{\lambda}$.

[24] As we have observed in the present paper (see the paragraph containing (46)) one *can* go over to the flow rules of stress space (involving $\hat{f}$) in a region of hardening ($\hat{g} > 0, \hat{f} > 0$) and in a region of softening ($\hat{g} > 0, \hat{f} < 0$), although even then one must retain the loading conditions of strain space. In the case of perfectly plastic behavior, however, one must retain (10*d*), the flow rule of the strain space formulation, which gives a determinate plastic strain rate once the motion χ_i is specified.

by a simple set of constitutive equations appropriate for elastic-plastic materials which are homogeneous and initially isotropic in their reference state. First, we recall that the infinitesimal elastic strain tensor is defined by $e^e_{KL} = e_{KL} - e^p_{KL}$ and note that with $e^p_{KL} = 0$ in the reference configuration, $e^e_{KL} = 0$ also there. It is convenient to utilize a standard decomposition for second-order tensors. Thus, for example, in the case of the stress tensor, we have

$$s_{KL} = \bar{s}\delta_{KL} + \tau_{KL}, \quad \bar{s} = \tfrac{1}{3}s_{KK},$$

where $\bar{s}\delta_{KL}$ is the spherical part of s_{KL}, τ_{KL} is the deviatoric (traceless) part of s_{KL} and $\bar{s}$ is the mean normal stress. In a similar manner we decompose e_{KL}, e^p_{KL}, e^e_{KL} into spherical parts $\bar{e}\delta_{KL}$, $\bar{e}^p\delta_{KL}$, $\bar{e}^e\delta_{KL}$ and deviatoric parts γ_{KL}, γ^p_{KL}, γ^e_{KL}.

Let the stress response function in $(5)_1$ be specified by generalized Hooke's law, namely,

$$\tau_{KL} = 2\mu\gamma^e_{KL}, \quad \bar{s} = 3k\bar{e}^e, \tag{53}$$

and the coefficient function $\mathcal{C}_{KL}$ for the rate of work-hardening response in (9) in the form [12]

$$\mathcal{C}_{KL} = \beta\tau_{KL} + \phi\bar{s}\delta_{KL}, \tag{54}$$

where μ (> 0) is the shear modulus, k (> 0) the bulk modulus and β and ϕ are constants. With the use of the decompositions just noted, the loading functions $f(\mathcal{V})$ and $g(\mathcal{U})$ can be written as different functions $\bar{f}(\tau_{MN}, \bar{s}, \gamma^p_{MN}, \bar{e}^p, \kappa)$ and $\bar{g}(\gamma_{MN}, \bar{e}, \gamma^p_{MN}, \bar{e}^p, \kappa)$. In this section, we restrict attention to special loading functions of the form

$$f(\mathcal{V}) = \bar{f}(\tau_{MN}, \bar{s}, \gamma^p_{MN}, \bar{e}^p, \kappa) = \tau_{KL}\tau_{KL} + 3\psi\bar{s}^2 - \kappa,$$

$$g(\mathcal{U}) = \bar{g}(\gamma_{MN}, \bar{e}, \gamma^p_{MN}, \bar{e}^p, \kappa)$$
$$= 4\mu^2(\gamma_{KL} - \gamma^p_{KL})(\gamma_{KL} - \gamma^p_{KL}) + 27\psi k^2(\bar{e} - \bar{e}^p)^2 - \kappa, \tag{55}$$

where ψ is a constant and where (17) and (53) have been used.[25] Utilizing formulas of the type[26]

$$\frac{\partial f}{\partial s_{MN}} = \frac{\partial \bar{f}}{\partial \tau_{MN}} - \frac{1}{3}\left(\frac{\partial \bar{f}}{\partial \tau_{KK}} - \frac{\partial \bar{f}}{\partial \bar{s}}\right)\delta_{MN} \tag{56}$$

and recalling (20) and (11), it can be easily shown that

$$\frac{\partial f}{\partial s_{MN}} = 2(\tau_{MN} + \psi\bar{s}\delta_{MN}), \quad \hat{f} = 2(\tau_{MN}\dot{\tau}_{MN} + 3\psi\bar{s}\dot{\bar{s}}),$$

$$\hat{g} = 2(2\mu\tau_{MN}\dot{\gamma}_{MN} + 9\psi k\bar{s}\dot{\bar{e}}) = \hat{f} + 2(2\mu\tau_{MN}\dot{\gamma}^p_{MN} + 9\psi k\bar{s}\dot{\bar{e}}^p) \tag{57}$$

and the expressions for $\partial g/\partial e_{MN}$ and $\partial f/\partial e^p_{MN}$ may be obtained similarly. We recall that during loading $\hat{g}$ is positive while $g = f = \hat{g} = \hat{f} = 0$. Keeping this in mind, it follows from $(55)_1$ and $(57)_2$ that during loading

$$\tau_{KL}\tau_{KL} + 3\psi\bar{s}^2 - \kappa = 0, \quad 2(\tau_{KL}\dot{\tau}_{KL} + 3\psi\bar{s}\dot{\bar{s}}) - \dot{\kappa} = 0, \quad \hat{f} = \dot{\kappa} \tag{58}$$

and hence by the definitions (43),

$$\dot{\kappa} \text{ and } (\tau_{MN}\dot{\tau}_{MN} + 3\psi\bar{s}\dot{\bar{s}}) \text{ both satisfy conditions } H. \tag{59}$$

Clearly for the special constitutive equations used in this section, in view of $(58)_3$ and (59), the strain-hardening behavior may be characterized by $\dot{\kappa}$.

The stress response (53) may be regarded as a special case of that in (34) with the last two arguments absent; and, in addition, the symmetry conditions mentioned following (34) are satisfied by (53). Hence, in addition to (36)–(42) the special results obtained at the end of Section 3 [see Case (b) following equation (49)] remain valid here.

Thus, using (54) and (55), from (33), (41), and formulas of the type (56) and $(57)_1$ and recalling that $\partial f/\partial s_{KL} \neq 0$ by $(36)_1$, we obtain

$$\Lambda = 4(2\mu\tau_{KL}\tau_{KL} + 9\psi^2 k\bar{s}^2) > 0, \quad \Gamma = 2(\beta\tau_{KL}\tau_{KL} + 3\psi\phi\bar{s}^2). \tag{60}$$

With the use of (60), $\lambda\gamma^*$ and $\hat{f}/\hat{g}$ may be obtained at once from (42). Moreover, in this case, since $\hat{f}/\hat{g}$ is always < 1 the degree of hardening behavior is limited. Also, remembering (50), we observe that in this case the right-hand side of $(60)_2$ provides a rate-independent characterization of strain hardening. Constitutive equations for the rate of plastic strain or equivalently for $\dot{\bar{e}}^p$ and $\dot{\gamma}^p_{KL}$ simplify and may now be obtained from ($51a$) in a region of hardening or softening and from ($51b$) in a region of perfectly plastic behavior.

Since our development in Sections 2 and 3 began with the strain space (rather than the stress space) formulation as primary and since the quotient $\hat{f}/\hat{g}$ is used to define strain hardening, it is desirable to examine the predictions of various theoretical results in the case of the familiar one-dimensional tension test. To this end, consider a homogeneous deformation sustained by a uniaxial tension $s_{11} = s = \hat{s}(t)$ along the X_1-axis. Then, using a matrix representation for τ_{KL}, we have

$$\|\tau_{KL}\| = \frac{s}{3}\|b_{KL}\|, \quad \bar{s} = \frac{s}{3} \gtreqless 0, \quad \|b_{KL}\| = \begin{Vmatrix} 2 & 0 & 0 \\ 0 & -1 & 0 \\ 0 & 0 & -1 \end{Vmatrix}, \tag{61}$$

where for brevity we have introduced the constant matrix $\|b_{KL}\|$. Assuming that initial yield occurs at a value s_0 of s and a value $\kappa_0 > 0$ of κ, the solution can be obtained in a straightforward manner. We omit details, but record here some of the results of interest:[27]

$$\kappa = \tfrac{1}{3}s^2(2+\psi), \quad \kappa_0 = \tfrac{1}{3}s_0^2(2+\psi), \quad 2+\psi > 0, \quad s_0 > 0, \tag{62a}$$

$$s > 0, \quad \kappa > 0, \quad \dot{e}^p_{11} > 0 \quad \text{when} \quad g = 0, \hat{g} > 0, \tag{62b}$$

$$\text{Both } \dot{s} \text{ and } (2\beta + \psi\phi) \text{ satisfy conditions } H. \tag{62c}$$

We postpone a discussion of perfectly plastic behavior until later in this section but consider further calculations for the other two types of behavior: In a region of hardening or softening, the elastic and plastic strains are

$$\bar{e}^e = \frac{s}{9k}, \quad \|\gamma^e_{KL}\| = \frac{s}{6\mu}\|b_{KL}\|, \tag{63a}$$

$$\bar{e}^p = \frac{s - s_0}{9k^*}, \quad \|\gamma^p_{KL}\| = \frac{s - s_0}{6\mu^*}\|b_{KL}\|, \tag{63b}$$

$$\|e^p_{KL}\| = \frac{s - s_0}{E^*}\begin{Vmatrix} 1 & 0 & 0 \\ 0 & -\nu^* & 0 \\ 0 & 0 & -\nu^* \end{Vmatrix}$$

$$\frac{de^p_{11}}{ds} \text{ and } \frac{d\gamma^p_{11}}{ds} \begin{cases} > 0 \text{ if and only if the material is hardening,} \\ < 0 \text{ if and only if the material is softening,} \end{cases} \tag{63c}$$

where the constants ν^*, E^*, μ^*, and k^* are defined by

$$\nu^* = \frac{1-\psi}{2+\psi}, \quad E^* = \frac{3(2\beta + \psi\phi)}{2(2+\psi)^2},$$

$$\mu^* = \frac{E^*}{2(1+\nu^*)} = \frac{2+\psi}{6}E^*, \tag{63d}$$

$$k^* = \frac{E^*}{3(1-2\nu^*)} = \frac{2+\psi}{9\psi}E^* \quad (\psi \neq 0)$$

and

$$E^* \text{ and } \mu^* \text{ satisfy conditions } H, \tag{63e}$$

[25] The loading function $(55)_1$ does not depend explicitly on plastic strain, but includes a dependency on mean normal stress. When $\psi = 0$ and $\kappa =$ constant, $(55)_1$ reduces to the usual von Mises yield function. A loading function of the type $(55)_1$ was previously employed by Green and Naghdi [12].

[26] It is understood that in line with the summation convention, our notation $\partial\bar{f}/\partial\tau_{KK}$ in (56) stands for the sum $\partial\bar{f}/\partial\tau_{11} + \partial\bar{f}/\partial\tau_{22} + \partial\bar{f}/\partial\tau_{33}$.

[27] It is clear from (10), $(62a)_3$, $(62b)_1$, and the expression $\hat{f} = (2/3)(2+\psi)s\dot{s}$, that during neutral loading, it is necessary to have $\dot{s} = 0$ and during unloading it is necessary to have $\dot{s} < 0$. In this connection, recall Table 1 and the discussion following (21).

while

$$\hat{g} = \frac{2}{3} s\dot{s}(2+\psi)\left[1 + \frac{2(4\mu + 3\psi^2 k)}{2\beta + \psi\phi}\right] > 0. \tag{63f}$$

The constants in (63d) have been defined analogously to the corresponding constants in linear elasticity, e.g., $\mu = E/2(1+\nu)$, $k = E/3(1-2\nu)$, where ν is Poisson's ratio. In the special case that $\psi = 0$, $\nu = 1/2$ and the expressions for E^*, μ^* simplify while $k^* \to \infty$ as $\psi \to 0$. Continuing our discussion of hardening and softening behavior, it can be shown that when $\psi \neq 0$ (see the Appendix for details) the quotient $\hat{f}/\hat{g}$ can be written as

$$1 > \frac{\hat{f}}{\hat{g}} = \frac{2+\psi}{\frac{1}{3}\,\mathrm{tr}\left(2\left\|\frac{d\gamma_{KL}}{ds}\right\|\left\|\frac{d\gamma^e_{KL}}{ds}\right\|^{-1} + \psi\frac{d\bar{e}}{ds}\left(\frac{d\bar{e}^e}{ds}\right)^{-1}\|\delta_{KL}\|\right)}, \tag{64}$$

where tr stands for the trace operator. In the special case when $\nu^* = \nu$, (64) reduces to (see the Appendix for details)

$$1 > \frac{\hat{f}}{\hat{g}} = \left[E\frac{de}{ds}\right]^{-1} = \left[1 + \frac{de_p}{de_e}\right]^{-1} \tag{65a}$$

and by (43a,b)

$$\frac{de}{ds} \text{ and } \left(1 + \frac{de_p}{de_e}\right) \begin{cases} > 0 \text{ if and only if the material is hardening,} \\ < 0 \text{ if and only if the material is softening,} \end{cases} \tag{65b}$$

where as in Section 1, we have again used the notation $e = e_{11}$, $e_e = e^e_{11}$, $e_p = e^p_{11}$.

Before closing this section, it is desirable to elaborate briefly on some features of the foregoing results for uniaxial tension, which have been obtained with the use of a special set of constitutive equations. With reference to all three types of strain hardening response defined in (43), it is clear that during loading e^p_{11} is strictly increasing with time by virtue of $(62b)_3$. Moreover, according to (62c) the time rate of stress may be used to characterize strain-hardening behavior in uniaxial tension and a characterization of the same behavior is provided by the combination $(2\beta + \psi\phi)$ of the constitutive coefficients. While the elastic moduli E, μ are always positive, it follows from (63e) that the constants E^*, μ^* are positive for hardening and negative for softening behavior. In the special case of $\nu^* = \nu$, it is clear from (65a) that the quotient $\hat{f}/\hat{g}$ can be expressed in terms of quantities (2)–(4) and indeed (65b) corresponds to the behavior summarized in (4) for uniaxial tension.[28] Furthermore, with $\psi = 0$ in $(55)_1$, the plastic volume change or equivalently $\bar{e}^p$ vanishes also. The strain-hardening response is then characterized by β, in view of (62c). Also, in a region of hardening or softening the quotient $\hat{f}/\hat{g}$ reduces to (see the Appendix for details)

$$\frac{\hat{f}}{\hat{g}} = \left[3\mu\frac{d\gamma}{ds}\right]^{-1}, \tag{66}$$

where we have put $\gamma = \gamma_{11}$ and $\gamma^e = \gamma^e_{11}$.

The significance of the strain space formulation in the case of elastic-perfectly plastic materials was pointed out in [1]. Since the quotient $\hat{f}/\hat{g}$ is used here to define various types of hardening response, it is desirable to indicate the reduction of the present development to the usual perfectly plastic behavior in uniaxial tension. First, we observe that during loading ($g = 0, \hat{g} > 0$) for perfectly plastic behavior $\hat{f}/\hat{g} = \Gamma = 0$ by (43c) and (42). It then follows that $\dot{\kappa} = 0$, $\kappa = \kappa_0$, $s = s_0$ by $(58)_3$ and $(62a)_{1,2}$ and that, in view of $(62b)_3$, e^p_{11} is strictly increasing with time.[29] Thus, in the context of the present paper, the uniaxial stress-strain curve for elastic-perfectly plastic behavior consists of a linearly elastic portion followed by a horizontal portion and as time progresses the locus of e^p_{11} moves outward along the abscissa of the s-e curve. This is in agreement with the usual characterization of perfectly plastic behavior in uniaxial tension. We also note that an examination of the solution given by (63a, b) and (63e) easily reveals that hardening (softening) is represented in a stress-strain diagram by a straight line which lies above (below) the horizontal perfectly plastic line. Indeed, since $e_{11} = s/E + (s - s_0)/E^*$, then $de_{11}/ds = 1/E + 1/E^*$ and by standard results for inequalities it follows from (63e) that

$$\infty > \frac{de_{11}}{ds} > \max\left\{\frac{1}{E}, \frac{1}{E^*}\right\} \text{ if the material is hardening,}$$

$$\frac{1}{E} > \frac{de_{11}}{ds} > \frac{1}{E^*} > -\infty \quad \text{if the material is softening.}$$

Moreover,

$$\infty > \frac{de_{11}}{ds} > \frac{1}{E} \text{ implies that the material is hardening,}$$

$$-\infty < \frac{de_{11}}{ds} < \frac{1}{E} \text{ implies that the material is softening,}$$

and it is at once clear by comparing the constant slope de_{11}/ds with the inverse $1/E$ of the elastic modulus whether the material is hardening or softening.

5 Saturation Hardening

As in Section 4, we again restrict attention to small deformations of elastic-plastic materials, which are homogeneous and initially isotropic in their reference configuration. We also assume that there is no plastic volume change so that $\bar{e}^p = 0$ in the notation of Section 4. For a fairly large class of metallic materials, it is well known that the stress-strain curves of uniaxial cyclic loading attain—after several cycles—saturation hardening. The purpose of this section is to indicate how the development of Sections 2 and 3 can be used to characterize a hardening response that includes saturation behavior and to compare the results with those of Caulk and Naghdi [5].

Starting with a fairly general discussion of loading functions contained in the paper of Green and Naghdi [2], for initially isotropic materials Caulk and Naghdi [5] derived a loading function in the form (see [5, equations $(40)_1$ and $(56)_1$])

$$f(\mathcal{V}) = \bar{f}(\tau_{MN}, \gamma^p_{MN}, \kappa) = \tau_{KL}\tau_{KL} - \alpha\tau_{KL}\gamma^p_{KL} + \sigma\gamma^p_{KL}\gamma^p_{KL} - \kappa,$$
$$g(\mathcal{U}) = \bar{g}(\gamma_{MN}, \gamma^p_{MN}, \kappa) = 4\mu^2(\gamma_{KL} - \gamma^p_{KL})(\gamma_{KL} - \gamma^p_{KL}) - 2\alpha\mu\,(\gamma_{KL} - \gamma^p_{KL})\gamma^p_{KL} + \sigma\gamma^p_{KL}\gamma^p_{KL} - \kappa, \tag{67}$$

where α and σ are constants and where (53) has been used in writing $(67)_2$. It should be noted that the loading functions $(67)_{1,2}$ depend explicitly on γ^p_{KL} but not on the mean normal stress $\bar{s}$. Here we also adopt $(67)_{1,2}$ but, instead of the hardening response assumed in [5], we specify the coefficient function $\mathcal{C}_{KL}$ in (9) by

$$\mathcal{C}_{KL} = \hat{\beta}(\kappa)\tau_{KL} + \hat{\eta}(\kappa)\gamma^p_{KL}, \tag{68}$$

which is different from that used in Section 4. The constitutive assumption for $\mathcal{C}_{KL}$ in [5] is similar to (68) but with $\hat{\beta}(\kappa)$ and $\hat{\eta}(\kappa)$ specified

$$\hat{\beta}(\kappa) = \frac{\kappa - \kappa_s}{\kappa_0 - \kappa_s}\beta, \quad \hat{\eta}(\kappa) = \frac{\kappa - \kappa_s}{\kappa_0 - \kappa_s}\eta, \tag{69}$$

where β and η are constants, κ_0 is the value of κ at initial yield and κ_s is the saturation value of κ. Since the stress response (53) is used in

[28] Recall that the special constitutive equations employed in this section are not sufficiently general to predict all details of the stress-strain curve in Fig. 1. Indeed, different choices of the combination $(2\beta + \psi\phi)$ of the coefficients (appropriate for different materials) yield stress-strain curves consisting of straight line segments which correspond to the rising and falling portions of the curve in Fig. 1.

[29] In the case of perfectly plastic behavior in uniaxial tension, (51b) reduces to an identity unless the motion is specified.

this section, in addition to (36)–(42), all the results stated under Case (*b*) at the end of Section 3 are also valid here.

To facilitate the discussion that follows and for later reference, we record the expressions

$$\begin{aligned}
&\frac{\partial f}{\partial s_{MN}} = 2\tau_{MN} - \alpha\gamma^p_{MN} \neq 0,\\
&\frac{\partial g}{\partial e_{MN}} = 2\mu\frac{\partial f}{\partial s_{MN}} \neq 0, \quad (g = 0),\\
&\hat{f} = (2\tau_{MN} - \alpha\gamma^p_{MN})\dot{\tau}_{MN},\\
&\hat{g} = 2\mu(2\tau_{MN} - \alpha\gamma^p_{MN})\dot{\gamma}_{MN}\\
&\quad = \hat{f} + 2\mu(2\tau_{MN} - \alpha\gamma^p_{MN})\dot{\gamma}^p_{MN},
\end{aligned} \tag{70}$$

which have been obtained with the use of formulas of the type (56) along with (20), (11), $(36)_1$, and (37). With the help of (70) and recalling the definitions (33) and (41), Λ and Γ are given by

$$\begin{aligned}
&\Lambda = \mu\frac{\partial f}{\partial s_{KL}}\frac{\partial f}{\partial s_{KL}} = 2\mu(2\tau_{KL} - \alpha\gamma^p_{KL})(2\tau_{KL} - \alpha\gamma^p_{KL}) > 0,\\
&\Gamma = (2\tau_{KL} - \alpha\gamma^p_{KL})\{(\alpha + \hat{\beta}(\kappa))\tau_{KL} - (2\sigma - \hat{\eta}(\kappa))\gamma^p_{KL}\},
\end{aligned} \tag{71}$$

Thus, based on the constitutive equations assumed in this section, Λ is 2μ times the square of the magnitude of the normal to the yield surface $\partial\mathcal{S}$ in stress space. Having obtained the results $(71)_{1,2}$, $\lambda\gamma^*$ can be calculated from $(42)_1$ and it then follows from (32) that the quotient $\hat{f}/\hat{g}$ must satisfy the inequality

$$\hat{f}/\hat{g} < 1, \tag{72}$$

which limits the extent of the hardening behavior. The restriction (72), in turn, places an upper bound of unity on the value of the saturation constant K_h in (52*a*) so that

$$0 < K_h \leqq 1. \tag{73}$$

Expressions for $\dot{\gamma}^p_{KL}$ can now be easily calculated from (51*a*) in a region of hardening or softening and from (51*b*) in a region of perfectly plastic behavior.

Given the constitutive assumptions employed in this section, the results $(71)_{1,2}$ and the restrictions (72) and (73) are valid for any small elastic-plastic deformations. In the rest of this section, however, we again confine attention to a homogeneous deformation sustained by uniaxial tension (61). Since plastic volume change $\bar{e}^p = 0$, $\bar{e}^e = \bar{e}$ is given by $(63a)_1$. Again, as in $(1)_1$, for convenience we use the notation $e = e_{11}$, $e_e = e^e_{11}$, $e_p = e^p_{11}$and write

$$\|\gamma^p_{KL}\| = \tfrac{1}{2}\, e_p\|b_{KL}\|,$$

where the constant matrix $\|b_{KL}\|$ is defined by $(61)_3$. Also, from $(70)_{1,3,4}$, (61), and $(1)_2$, we deduce that

$$\begin{aligned}
&\hat{f} = (\tfrac{4}{3}s - \alpha e_p)\dot{s}, \quad \hat{g} = (\tfrac{4}{3}s - \alpha e_p)\{E\dot{e} + (3\mu - E)\dot{e}_p\},\\
&\tfrac{4}{3}s - \alpha e_p \neq 0 \ (g = 0).
\end{aligned} \tag{74}$$

At initial yield $e_p = 0$ and $\kappa_0 = \frac{2}{3}s_0^2 > 0$ by virtue of $(74)_3$ and $(67)_1$. Hence, on the yield surface ($g = 0$), $\frac{4}{3}s - \alpha e_p$ must be positive. From this last result, along with (30) and $(36)_2$, we have $\dot{e}_p > 0$ during loading and therefore e_p is strictly increasing with time. Further, from the definition (43), and the positivity of the coefficient of $\dot{s}$ in $(74)_1$, it follows that $\dot{s}$ must satisfy the conditions in (44). The above results may be summarized as follows[30]

$$\begin{aligned}
&\tfrac{4}{3}s - \alpha e_p > 0, \quad \dot{e}_p > 0,\\
&\dot{s} \text{ satisfies conditions } H.
\end{aligned} \tag{75}$$

While $(75)_2$ holds during all three types of strain-hardening behavior defined in (43), it follows at once from $(75)_3$ and $(1)_2$ that $\dot{e}_e$ also satisfies conditions H.

[30] The inequality $(75)_1$, together with $(74)_1$ and (10), imply the following: During neutral loading it is necessary that $\dot{s} = 0$, while during unloading it is necessary that $\dot{s} < 0$.

For uniaxial tension under discussion, the quantities Λ and Γ in $(71)_{1,2}$ reduce to

$$\begin{aligned}
&\Lambda = 3\mu(\tfrac{4}{3}s - \alpha e_p)^2 > 0, \quad \Gamma = (\tfrac{4}{3}s - \alpha e_p)\bar{\Gamma},\\
&\bar{\Gamma} = (\alpha + \hat{\beta}(\kappa))s - \tfrac{3}{2}(2\sigma - \hat{\eta}(\kappa))e_p,
\end{aligned} \tag{76}$$

where for later convenience we have introduced the quantity $\bar{\Gamma}$ defined by $(76)_3$. Further, from (50), $(76)_2$, and $(75)_1$ follows the result

$$\bar{\Gamma} \text{ satisfies conditions } H. \tag{77}$$

Also, the expression for the plastic strain rate $\dot{e}_p$ in a region of hardening or softening can be written as

$$\dot{e}_p = \frac{\frac{4}{3}s - \alpha e_p}{\bar{\Gamma}}\,\dot{s}. \tag{78a}$$

If $\bar{\Gamma} \neq -E(\frac{4}{3}s - \alpha e_p)$, (78*a*) may be written as

$$\dot{e}_p = \left[1 + \frac{\bar{\Gamma}}{E(\frac{4}{3}s - \alpha e_p)}\right]^{-1}\dot{e}, \tag{78b}$$

which is similar in form to that obtained in [5] and where the relation $s = E(e - e_p)$ has been used in deriving (78*b*). In fact, if the coefficient functions $\hat{\beta}$ and $\hat{\eta}$ which occur in $\bar{\Gamma}$ are specialized to those given by (69), then (78*b*) reduces to that in [5, equation (80)]. The value $\bar{\Gamma} = -E(\frac{4}{3}s - \alpha e_p)$ corresponds to a special softening behavior in which $\dot{e} = 0$, $\dot{s} = -E\dot{e}_p$.

The result $(75)_3$ enables us to calculate the slopes de/ds, de_p/ds explicitly as functions of s, e_p, κ. Thus, with the use of (1), (78*a*) and chain rule of differentiation, in a region of hardening or softening we have

$$\frac{de}{ds} = \frac{1}{E} + \frac{de_p}{ds}, \quad \frac{de_p}{ds} = \frac{\frac{4}{3}s - \alpha e_p}{\bar{\Gamma}} \tag{79}$$

It follows from (79), $(75)_1$, and (77) that

$$\begin{aligned}
&\infty > \frac{de_p}{ds} > 0,\\
&\qquad \infty > \frac{de}{ds} > \max\left\{\frac{1}{E}, \frac{de_p}{ds}\right\} > 0 \text{ if the material is hardening,}\\
&-\infty < \frac{de_p}{ds} < 0, \quad \frac{1}{E} > \frac{de}{ds} > \frac{de_p}{ds} \text{ if the material is softening.}
\end{aligned} \tag{80a}$$

Moreover,

$$\begin{aligned}
&\infty > \frac{de}{ds} > \frac{1}{E}\left(\text{or equivalently } \infty > \frac{de_p}{ds} > 0\right) \text{ implies hardening,}\\
&-\infty < \frac{de}{ds} < \frac{1}{E}\left(\text{or equivalently } -\infty < \frac{de_p}{ds} < 0\right) \text{ implies softening.}
\end{aligned} \tag{80b}$$

Since $de_e/ds = 1/E$ which is always positive, we may write $de_p/de_e = E\, de_p/ds$, $de/de_e = E\, de/ds$ and then obtain explicit expressions for these derivatives from (79). It is evident that conditions of the type indicated in (80) for de_p/ds also hold for de_p/de_e. It follows from (42), (76), and $(79)_2$ that in a region of hardening or softening

$$1 > \frac{\hat{f}}{\hat{g}} = \left[1 + 3\mu\frac{de_p}{ds}\right]^{-1} = \left[1 + \frac{d\gamma^p_{11}}{ds}\left(\frac{d\gamma^e_{11}}{ds}\right)^{-1}\right]^{-1}. \tag{81}$$

In view of (80*a*) and (43), (81) implies that $de_p/ds < -1/3\mu$ in a region of softening. It is clear from $(81)_1$ and (1) that a knowledge of μ, E and the slope de/ds suffices to determine $\hat{f}/\hat{g}$. If the material saturates to perfectly plastic behavior, the left-hand side of $(81)_1$, i.e., $\hat{f}/\hat{g}$ must tend to zero and hence in this case de_p/ds must become unbounded.

We now turn to a brief discussion of saturation hardening usually observed under uniaxial cyclic loading. Recalling the definitions (52*a*, *b*), from (81) we deduce that saturation hardening occurs if there exists a constant K_h such that

$$\left[1 + 3\mu\lim_{t\to\infty}\frac{de_p}{ds}\right]^{-1} = K_h, \quad \lim_{t\to\infty}\frac{de}{ds} = \frac{1}{E} + \frac{1 - K_h}{3\mu K_h}, \ (0 < K_h \leqq 1). \tag{82}$$

In order to exploit the implications of (82), we first observe that $\bar{\Gamma}$ defined by $(76)_3$ can be rewritten as

$$\bar{\Gamma} = \frac{3}{4}\left(\frac{4}{3}s - \alpha e_p\right)(\alpha + \hat{\beta}(\kappa)) + \frac{3}{2}\left(\frac{\alpha^2}{2} - 2\sigma + \hat{\eta}(\kappa) + \frac{\alpha}{2}\hat{\beta}(\kappa)\right)e_p \tag{83}$$

and then express $(79)_2$ in the form

$$\frac{de_p}{ds} = \left[\frac{3}{4}(\alpha + \hat{\beta}(\kappa)) + \frac{3}{2}\frac{\left(\frac{\alpha^2}{2} - 2\sigma + \hat{\eta}(\kappa) + \frac{\alpha}{2}\hat{\beta}(\kappa)\right)e_p}{\frac{4}{3}s - \alpha e_p}\right]^{-1}. \tag{84}$$

Consider now a special material response which corresponds to the vanishing of the numerator of the second term in the square brackets in (84), i.e.,

$$\frac{\alpha^2}{2} - 2\sigma + \hat{\eta}(\kappa) + \frac{\alpha}{2}\hat{\beta}(\kappa) = 0, \tag{85}$$

which has the same form as a particular case discussed in [5]. From $(75)_1$, $(77)_1$, (83)–(85), and (81), it can be readily concluded that

$$\alpha + \hat{\beta}(\kappa) \text{ satisfies conditions } H,$$

$$\frac{de_p}{ds} = \frac{4/3}{\alpha + \hat{\beta}(\kappa)}, \quad \frac{\hat{f}}{\hat{g}} = \left[1 + \frac{4\mu}{\alpha + \hat{\beta}(\kappa)}\right]^{-1} < 1. \tag{86}$$

Also, in view of (43b) and $(86)_2$, in a region of softening:

$$0 > \alpha + \hat{\beta}(\kappa) > -4\mu.$$

If saturation hardening occurs with $0 < K_h < 1$, then from $(82)_1$, (86), and the condition (85) we have

$$\lim_{t\to\infty} \hat{\beta}(\kappa) = \frac{4\mu K_h}{1 - K_h} - \alpha, \quad \lim_{t\to\infty} \hat{\eta}(\kappa) = -\frac{2\alpha\mu K_h}{1 - K_h} + 2\sigma, \quad (0 < K_h < 1), \tag{87}$$

while $\hat{\beta}(\kappa)$ becomes unbounded for $K_h = 1$.

We further examine saturation hardening by adopting the special coefficients (69) subject to the condition (85). When saturation is assumed to occur, the limit of the coefficients (69) as $t \to \infty$ is zero and from (85), (82), and $(86)_2$ we obtain

$$\alpha^2 = 4\sigma, \quad \alpha\beta + 2\eta = 0, \quad \lim_{t\to\infty}\frac{de}{ds} = \frac{1}{E} + \frac{4}{3\alpha}, \quad 0 < K_h = \left[1 + \frac{4\mu}{\alpha}\right]^{-1} < 1, \alpha > 0, \tag{88}$$

the first three of which are the same as those derived in [5, equations (70) and (86)].

By way of illustration, consider the 304 stainless steel whose behavior in cyclic tension-compression is discussed in [5, Section 7]. As in [5], for the 304 stainless steel, we take the values of $E = 123$ GPa and $de/ds = (3.85\ \text{GPa})^{-1}$ at initial yield and also assume the value $\nu = 0.3$ for Poisson's ratio.[31] With these values, the expressions $(79)_1$ and (81) predict that the quotient $\hat{f}/\hat{g}$ at initial yield is approximately equal to 0.027. Again using the above values, as well as $\alpha = 1.5$ (for tension), $(88)_3$ gives an approximate value of 0.008 for K_h. Thus $\hat{f}/\hat{g}$ decreases from a value of 0.027 at initial yield to a value of 0.008 at saturation. It is clear from (82) that the definition of saturation hardening given by (52a) implies that the slopes de/ds and de_p/ds tend to constant limits at saturation. In this connection, it should be noted that when $\hat{\beta}$ and $\hat{\eta}$ are of the form (69), the definition of saturation hardening used in [5] also gives constant limiting slopes.

We return once more to the perfectly plastic case, and first observe that the expression for[32] $\dot{\gamma}^p_{KL}$ can be obtained from (51b) with the use of $(70)_{1,4}$ and $(71)_1$. In view of $(75)_3$, $\dot{s} = 0$ for perfectly plastic behavior and s retains its initial yield value s_0 and, in accordance with $(75)_2$, e_p is strictly increasing with time during loading. The work-hardening parameter κ may then be obtained as a function of e_p from $g = f = 0$ with f given by $(67)_1$:

$$\kappa = \tfrac{2}{3}s_0^2 - \alpha s_0 e_p + \tfrac{3}{2}\sigma e_p^2. \tag{89}$$

By (76) and (77c), for perfectly plastic behavior it is necessary that

$$\tfrac{2}{3}(\alpha + \hat{\beta}(\kappa))s_0 - (2\sigma - \hat{\eta}(\kappa))e_p = 0 \tag{90}$$

for all e_p. We observe, however, that in view of (76) and (77c) the constant values

$$\hat{\beta}(\kappa) = -\alpha, \quad \hat{\eta}(\kappa) = 2\sigma \tag{91}$$

are sufficient for perfectly plastic behavior. It should be noted that the values (91) satisfy the condition (85).

Acknowledgment

The results reported here were obtained in the course of research supported by the U. S. Office of Naval Research under Contract N00014-75-C-0148, Project NR 064-436 with the University of California, Berkeley (U.C.B.). Also, the work of one of us (J.C.) was partially supported by a grant-in-aid from General Motors Research Laboratories to the Department of Mechanical Engineering at U.C.B.

References

1 Naghdi, P. M., and Trapp, J. A., "The Significance of Formulating Plasticity Theory With Reference to Loading Surfaces in Strain Space," *International Journal of Engineering Science*, Vol. 13, 1975, pp. 785–797.

2 Green, A. E., and Naghdi, P. M., "A General Theory of an Elastic-Plastic Continuum, *Arch. Ratl. Mech. Anal.*, Vol. 18, 1965, pp. 251–281.

3 Green, A. E., and Naghdi, P. M., "A Thermodynamic Development of Elastic-Plastic Continua, *Proceedings of the IUTAM Symposium on Irreversible Aspects of Continuum Mechanics and Transfer of Physical Characteristics in Moving Fluids*, eds., Parkus, H., and Sedov, L. I., Springer-Verlag, 1966, pp. 117–131.

4 Naghdi, P. M., and Trapp, J. A., "Restrictions on Constitutive Equations of Finitely Deformed Elastic-Plastic Materials," *Quarterly Journal of Mechanics and Applied Mathematics*, Vol. 28, 1975, pp. 25–46.

5 Caulk, D. A., and Naghdi, P. M., "On the Hardening Response in Small Deformation of Metals," ASME JOURNAL OF APPLIED MECHANICS, Vol. 45, 1978, pp. 755–764.

6 Naghdi, P. M., "Stress-Strain Relations in Plasticity and Thermoplasticity," *Proceedings of the 2nd Symposium on Naval Structural Mechanics*, held at Brown University, 1960, Pergamon Press, 1960, pp. 121–169.

7 Naghdi, P. M., and Trapp, J. A., "On the Nature of Normality of Plastic Strain Rate and Convexity of Yield Surfaces in Plasticity," ASME JOURNAL OF APPLIED MECHANICS, Vol. 42, 1975, pp. 61–66.

8 Edelman, F., and Drucker, D. C., "Some Extensions of Elementary Plasticity Theory," *Journal of The Franklin Institute*, Vol. 251, 1951, pp. 581–605.

9 Prager, W., "On Ideal Locking Materials," *Transactions of the Society of Rheology*, Vol. 1, 1957, pp. 169–175.

10 Palmer, A. C., Maier, G., and Drucker, D. C., "Normality Relations and Convexity of Yield Surfaces for Unstable Materials or Structural Elements," ASME JOURNAL OF APPLIED MECHANICS, Vol. 30, 1967, pp. 464–470.

11 Hill, R., "On the Classical Constitutive Relations for Elastic/Plastic Solids," in *Recent Progress in Applied Mechanics—The Folke Odqvist Volume*, Wiley, 1967, pp 241–249.

12 Green, A. E., and Naghdi, P. M., "A Comment on Drucker's Postulate in the Theory of Plasticity," *Acta Mechanica*, Vol. 1, 1965, pp. 334–338.

APPENDIX

We provide here details of the calculations leading to (64), (65a), and (66), and also record alternative useful forms of the quotient $\hat{f}/\hat{g}$ associated with the constitutive equations of Section 4. From (63), in a region of hardening or softening we have

[31] A value for Poisson's ratio was not needed in the calculation given in [5, Section 7]. With $\nu = 0.3$ and $E = 123$ GPa, μ is calculated to be 47.31 GPa.

[32] In fact, in the case of uniaxial tension, the resulting expression is an identity, unless the motion is specified.

$$\frac{d\bar{e}}{ds}\left(\frac{d\bar{e}^e}{ds}\right)^{-1} = 1 + \frac{d\bar{e}^p}{ds}\left(\frac{d\bar{e}^e}{ds}\right)^{-1} = 1 + \frac{k}{k^*}, \quad (\psi = 0), \tag{92}$$

$$\left\|\frac{d\gamma_{KL}}{ds}\right\| \left\|\frac{d\gamma^e_{KL}}{ds}\right\|^{-1} = \|\delta_{KL}\| + \left\|\frac{d\gamma^p_{KL}}{ds}\right\| \left\|\frac{d\gamma^e_{KL}}{ds}\right\|^{-1} = \left(1 + \frac{\mu}{\mu^*}\right)\|\delta_{KL}\|, \tag{93}$$

$$\left\|\frac{de_{KL}}{ds}\right\| \left\|\frac{de^e_{KL}}{ds}\right\|^{-1} = \|\delta_{KL}\| + \left\|\frac{de^p_{KL}}{ds}\right\| \left\|\frac{de^e_{KL}}{ds}\right\|^{-1} = \|\delta_{KL}\| + \frac{E}{E^*}\left\|\begin{matrix}1 & 0 & 0\\ 0 & \nu^*/\nu & 0\\ 0 & 0 & \nu^*/\nu\end{matrix}\right\|, \tag{94}$$

In a region of hardening or softening $\Gamma \neq 0$ by (50) and using $(42)_2$ we may write $\hat{f}/\hat{g} = (1 + \Lambda/\Gamma)^{-1}$. Then, by (60), (61), and $(62b)_1$ we have

$$\begin{aligned} 1 > \frac{\hat{f}}{\hat{g}} &= \left[1 + \frac{2(4\mu + 3\psi^2 k)}{2\beta + \psi\phi}\right]^{-1} \\ &= \left[1 + \frac{E}{3E^*}\left\{\frac{2(1+\nu^*)^2}{1+\nu} + \frac{(1-2\nu^*)^2}{1-2\nu}\right\}\right]^{-1} \\ &= \left[1 + \frac{E}{E^*}\left\{1 + \frac{2(\nu-\nu^*)^2}{(1+\nu)(1-2\nu)}\right\}\right]^{-1} \end{aligned} \tag{95}$$

and we may recall that $1 + \nu > 0, 1 - 2\nu > 0$. If $\psi \neq 0$, then $\hat{f}/\hat{g}$ may also be written as

$$1 > \frac{\hat{f}}{\hat{g}} = \left[1 + \frac{4\mu + 3\psi^2 k}{4\mu^* + 3\psi^2 k^*}\right]^{-1} = \frac{2 + \psi}{2\left(1 + \frac{\mu}{\mu^*}\right) + \psi\left(1 + \frac{k}{k^*}\right)}. \tag{96}$$

The result (64) follows at once from (92), (93), and (96). Similarly, if $\nu^* = \nu$ [or $\psi = 1 - 2\nu/(1 + \nu)$], then from (94) and (95) we obtain

$$\frac{\hat{f}}{\hat{g}} = \left[1 + \frac{E}{E^*}\right]^{-1} = \left[\frac{1}{3}\,\mathrm{tr}\left\{\|\delta_{KL}\| + \left\|\frac{de^p_{KL}}{ds}\right\| \left\|\frac{de^e_{KL}}{ds}\right\|^{-1}\right\}\right]^{-1}. \tag{97}$$

The result (65a) follows from (97) and (63a). With the use of (94) it is also possible to write (97) in terms of

$$\left\|\frac{de_{KL}}{ds}\right\| \left\|\frac{de^e_{KL}}{ds}\right\|^{-1}$$

but we do not record this here.

In the special case that $\psi = 0$, we note that by $(63d)_{2,3}$ and (93),

$$1 + 4\frac{\mu}{\beta} = \frac{1}{3}\,\mathrm{tr}\left\{\left\|\frac{d\gamma_{KL}}{ds}\right\| \left\|\frac{d\gamma^e_{KL}}{ds}\right\|^{-1}\right\} = \frac{d\gamma}{ds}\left(\frac{d\gamma^e}{ds}\right)^{-1}. \tag{98}$$

The relations $(95)_1$, (98), $(63a)_2$, and $(63b)_2$ lead to the expression (66).

K. Hashiguchi

Associate Professor,
Department of Agricultural Engineering,
Kyushu University,
Fukuoka, Japan
Mem. ASME

Constitutive Equations of Elastoplastic Materials With Anisotropic Hardening and Elastic-Plastic Transition

Constitutive equations of elastoplastic materials with anisotropic hardening and elastic-plastic transition are presented by introducing three similar surfaces, i.e., a loading surface on which a current stress exists, a subyield surface limiting a size of the loading surface and a distinct-yield surface representing a fully plastic state. The assumption of similarity of these surfaces leads the derived equations to remarkably simple forms. Also a more general rule of the kinematic hardening for the distinct-yield surface is incorporated into the constitutive equations. While they seem to be applicable to various materials, special constitutive equations of metals, for example, are derived from them and are compared with experimental data on a cyclic uniaxial loading of aluminum. A close correlation between theory and experiment is observed in this comparison.

Introduction

The author proposed previously constitutive equations of elastoplastic materials with elastic-plastic transition [1], introducing the concept of a loading surface in a subyield state. A reasonably simplified rule of kinematic hardening is incorporated into the constitutive equations. They cannot, however, describe the phenomenon that the curvature of the stress-strain curve becomes smaller in the reverse loading than in the first loading from an initial isotropic state as is observed in the stress—strain curve for the uniaxial loading of elastoplastic materials such as metals. Further, according to them, the loading along the yield surface which represents the fully plastic state brings about not a plastic deformation but an elastic deformation, since the loading surface is assumed to coincide with the yield surface in the fully plastic state. However, not only an elastic but a plastic deformation will occur in real materials subjected to such a loading.

On the other hand, the Mróz model of a field of hardening moduli [2] in which are assumed many surfaces can describe these phenomena suitably to some extent. Further, Krieg [3] and Dafalias and Popov [4] proposed independently the simplified constitutive equations in the form of the so-called two-surface theory. The former [3] formulated elastoplastic constitutive equations in concrete forms though they are confined to metals, while the latter [4] provided only a conceptional description. These constitutive equations in the two-surface theory would have similar mathematical behaviors to those of the Mróz model. The Mróz model and the Krieg or the Dafalias and Popov's two-surface theory are, however, incapable of describing suitably the elastic-plastic transition, since they assume the surface which delimits an elastic region. For instance, the reloading after a partial unloading within this surface brings about an abrupt change from the elastic to the fully plastic state.

In this paper, the elastoplastic constitutive equations which are modified to remove the aforementioned defects in the past theories are presented by formulating a simplified two-surface theory on the assumption of similarity of surfaces and then incorporating the author's previous theory with a loading surface [1] into it. Consequently, three similar surfaces are assumed; a *loading surface* on which a current stress exists, a *subyield surface* limiting the size of the loading surface and a *distinct-yield surface* representing a *fully plastic* or *distinct-yield state*. The assumption of similarity of these surfaces leads the derived constitutive equations to remarkably simple forms. And a more general rule of the kinematic hardening for the distinct-yield surface, which would be applicable to various materials including metals and granular media, is incorporated into them. Further, from them are derived special constitutive equations of metals, for example. And the adaptability of them to the description of the actual behavior of metals is examined comparing with experimental data on a cyclic unlaxial loading of aluminum which was reported by Lipkin and Swearengen [5] and quoted by Krieg [3] also to compare with his theory. In this comparison, a close correlation between theory and

Contributed by the Applied Mechanics Division for publication in the JOURNAL OF APPLIED MECHANICS.

Discussion on this paper should be addressed to the Editorial Department, ASME, United Engineering Center, 345 East 47th Street, New York, N. Y. 10017, and will be accepted until September 1, 1981. Readers who need more time to prepare a Discussion should request an extension from the Editorial Department. Manuscript received by ASME Applied Mechanics Division, June, 1980; final revision, November, 1980.

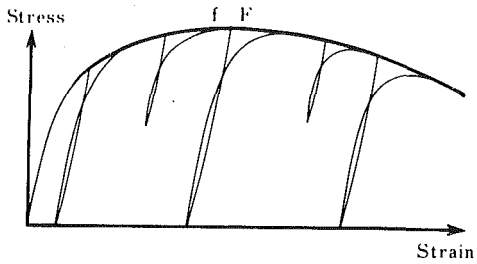

Fig. 1 The distinct-yield state ($f = F$) illustrated as the envelope curve of reloading curves

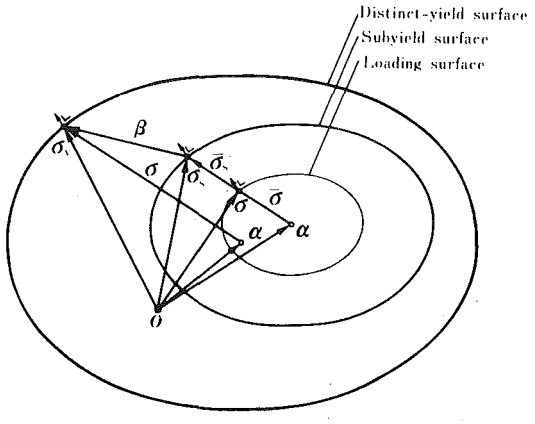

Fig. 2 The distinct-yield, the subyield and the loading surfaces

experiment is obtained by the equations proposed in the present paper better than the equations of Krieg.

Basic Constitutive Equations

A typical stress-strain curve of elastoplastic materials is schematically illustrated in Fig. 1. Assume that the surface which represents stresses in the *distinct-yield state* shown by the envelope curve of reloading curves in this figure is described by the following equation (see Fig. 2).

$$f(\boldsymbol{\sigma} - \hat{\boldsymbol{\alpha}}) - F(K) = 0 \tag{1}$$

or

$$f(\hat{\boldsymbol{\sigma}}) - F(K) = 0, \tag{2}$$

where

$$\hat{\boldsymbol{\sigma}} \equiv \boldsymbol{\sigma} - \hat{\boldsymbol{\alpha}}. \tag{3}$$

The second-order tensor $\boldsymbol{\sigma}$ is a stress, and the scalar K and the second-order tensor $\hat{\boldsymbol{\alpha}}$ are parameters to describe, respectively, the expansion or contraction and the translation of the surface. Let this surface be called a *distinct-yield surface*.

Now, we assume that the distinct-yield surface retains a similarity in a stress space. Therefore, the function f is to be a homogeneous function of its arguments. Then, let the degree of f be denoted by n.

Further, we introduce the secondary surface which is similar to the distinct-yield surface and translates within the distinct-yield surface (see Fig. 2). Hence, let the surface be described by

$$f(\boldsymbol{\sigma} - \hat{\boldsymbol{\alpha}}) - r^n F(K) = 0 \tag{4}$$

or

$$f(\bar{\boldsymbol{\sigma}}) - r^n F(K) = 0, \tag{5}$$

where we set

$$\bar{\boldsymbol{\sigma}} \equiv \boldsymbol{\sigma} - \bar{\boldsymbol{\alpha}}. \tag{6}$$

r ($0 \leqq r \leqq 1$) is a material constant and the second-order tensor $\bar{\boldsymbol{\alpha}}$ is a parameter to describe a translation of the surface. Let this surface be called a *subyield surface*.

In what follows, the parameters K, $\hat{\boldsymbol{\alpha}}$ and $\bar{\boldsymbol{\alpha}}$ are defined.

Let $\dot{K}$ where a superposed dot designates a material time derivative be a function of stress, plastic strain, and plastic strain rate $\dot{\boldsymbol{\epsilon}}^p$ in degree one, which satisfies the condition $\dot{K} = 0$ when $\dot{\boldsymbol{\epsilon}}^p = \mathbf{0}$.

Now, suppose that the current stress is on the subyield surface, and let it be denoted by $\boldsymbol{\sigma}_s$. Further, let the conjugate point on the distinct-yield surface having the same outer normal direction as that of the subyield surface at $\boldsymbol{\sigma}_s$ be designated by $\boldsymbol{\sigma}_y$.

Then, let $\dot{\hat{\boldsymbol{\alpha}}}$ be given by

$$\begin{aligned}\dot{\hat{\boldsymbol{\alpha}}} &= A \operatorname{tr}(\dot{\boldsymbol{\epsilon}}^p \mathbf{1})\mathbf{1} + B \operatorname{tr}\left(\dot{\boldsymbol{\epsilon}}^p \frac{\hat{\boldsymbol{\sigma}}_y}{|\hat{\boldsymbol{\sigma}}_y|}\right)\frac{\hat{\boldsymbol{\sigma}}_y}{|\hat{\boldsymbol{\sigma}}_y|} \\ &= A\dot{\epsilon}_v{}^p \mathbf{1} + B \operatorname{tr}\left(\dot{\boldsymbol{\epsilon}}^p \frac{\hat{\boldsymbol{\sigma}}_y}{|\hat{\boldsymbol{\sigma}}_y|}\right)\frac{\hat{\boldsymbol{\sigma}}_y}{|\hat{\boldsymbol{\sigma}}_y|}\end{aligned} \tag{7}$$

or

$$\dot{\hat{\boldsymbol{\alpha}}} = A\dot{\epsilon}_v{}^p \mathbf{1} + B \operatorname{tr}\left(\dot{\boldsymbol{\epsilon}}^p \frac{\bar{\boldsymbol{\sigma}}_s}{|\bar{\boldsymbol{\sigma}}_s|}\right)\frac{\bar{\boldsymbol{\sigma}}_s}{|\bar{\boldsymbol{\sigma}}_s|} \tag{8}$$

by the relation

$$\hat{\boldsymbol{\sigma}}_y = \frac{1}{r}\bar{\boldsymbol{\sigma}}_s \tag{9}$$

in accordance with the assumption of the similarity of the distinct-yield and the subyield surfaces. In these equations,

$$\dot{\epsilon}_v{}^p \equiv \operatorname{tr}(\dot{\boldsymbol{\epsilon}}^p), \tag{10}$$

$$\hat{\boldsymbol{\sigma}}_y \equiv \boldsymbol{\sigma}_y - \hat{\boldsymbol{\alpha}}, \bar{\boldsymbol{\sigma}}_s \equiv \boldsymbol{\sigma}_s - \bar{\boldsymbol{\alpha}}.$$

A and B are scalar functions of K and $\hat{\boldsymbol{\alpha}}$, and the notation $|\ |$ is used to represent the magnitude. In (7) or (8), the first term is added to the equation assumed in the previous paper [1], while the first and the second term would be significant for granular media and metals, respectively.

Since the subyield surface must not intersect the distinct-yield surface but can come into contact with it, the direction of the relative motion of the conjugate point $\boldsymbol{\sigma}_y$ and $\boldsymbol{\sigma}_s$ must coincide with that of the vector $\boldsymbol{\sigma}_y - \boldsymbol{\sigma}_s$ at least when $\boldsymbol{\sigma}_s$ is near to $\boldsymbol{\sigma}_y$. Then, let the following equation be assumed as is done in the Mróz model [2].

$$\dot{\boldsymbol{\beta}} = \boldsymbol{\beta}\dot{\mu}, \tag{11}$$

where $\dot{\mu}$ is a scalar parameter formulated later and we set

$$\boldsymbol{\beta} \equiv \boldsymbol{\sigma}_y - \boldsymbol{\sigma}_s \tag{12}$$

which can be written as

$$\boldsymbol{\beta} = \left(\frac{1}{r} - 1\right)\bar{\boldsymbol{\sigma}}_s + \hat{\boldsymbol{\alpha}} - \bar{\boldsymbol{\alpha}} \tag{13}$$

by (9).

Substituting (13) into (11) using (10), we have

$$\dot{\bar{\boldsymbol{\alpha}}} = (1 - r)\dot{\boldsymbol{\sigma}}_s + r\dot{\hat{\boldsymbol{\alpha}}} - r\boldsymbol{\beta}\dot{\mu}. \tag{14}$$

Differentiation of (5) with substitution of (14) yields

$$\dot{\mu} = \frac{r^{n-1}\dot{F} - \operatorname{tr}\left\{\dfrac{\partial f}{\partial \bar{\boldsymbol{\sigma}}_s}(\dot{\boldsymbol{\sigma}}_s - \dot{\hat{\boldsymbol{\alpha}}})\right\}}{\operatorname{tr}\left(\dfrac{\partial f}{\partial \bar{\boldsymbol{\sigma}}_s}\boldsymbol{\beta}\right)}. \tag{15}$$

Further, substituting (15) into (14), we obtain

$$\dot{\bar{\boldsymbol{\alpha}}} = (1 - r)\dot{\boldsymbol{\sigma}}_s + r\dot{\hat{\boldsymbol{\alpha}}} - r\boldsymbol{\beta}\frac{r^{n-1}\dot{F} - \operatorname{tr}\left\{\dfrac{\partial f}{\partial \bar{\boldsymbol{\sigma}}_s}(\dot{\boldsymbol{\sigma}}_s - \dot{\hat{\boldsymbol{\alpha}}})\right\}}{\operatorname{tr}\left(\dfrac{\partial f}{\partial \bar{\boldsymbol{\sigma}}_s}\boldsymbol{\beta}\right)}. \tag{16}$$

Finally, the plastic strain rate $\dot{\boldsymbol{\varepsilon}}^p$ is formulated in the following.

In the distinct-yield state ($\boldsymbol{\sigma}_s = \boldsymbol{\sigma}_y$), it can be obtained by differentiating (2) and substituting (7) that

$$\mathrm{tr}\left(\frac{\partial f}{\partial \hat{\boldsymbol{\sigma}}_y}\dot{\boldsymbol{\sigma}}_y\right) - \mathrm{tr}\left[\frac{\partial f}{\partial \hat{\boldsymbol{\sigma}}_y}\left\{A\dot{\varepsilon}^p \mathbf{1} + B\,\mathrm{tr}\left(\dot{\boldsymbol{\varepsilon}}^p \frac{\hat{\boldsymbol{\sigma}}_y}{|\hat{\boldsymbol{\sigma}}_y|}\right)\frac{\hat{\boldsymbol{\sigma}}_y}{|\hat{\boldsymbol{\sigma}}_y|}\right\}\right] = F'\dot{K}, \quad (17)$$

where

$$F' \equiv \frac{dF}{d\dot{K}}. \quad (18)$$

Adopting the associated flow rule

$$\dot{\boldsymbol{\varepsilon}}^p = \dot{\lambda}\frac{\partial f}{\partial \boldsymbol{\sigma}} \qquad (\dot{\lambda} > 0), \quad (19)$$

where $\dot{\lambda}$ is a proportionality factor, $\dot{\boldsymbol{\varepsilon}}^p$ is given from (17) as follows:

$$\dot{\boldsymbol{\varepsilon}}^p = \frac{\mathrm{tr}\left(\dfrac{\partial f}{\partial \hat{\boldsymbol{\sigma}}_y}\dot{\boldsymbol{\sigma}}_y\right)}{A\left\{\mathrm{tr}\left(\dfrac{\partial f}{\partial \hat{\boldsymbol{\sigma}}_y}\right)\right\}^2 + B\left\{\mathrm{tr}\left(\dfrac{\partial f}{\partial \hat{\boldsymbol{\sigma}}_y}\dfrac{\hat{\boldsymbol{\sigma}}_y}{|\hat{\boldsymbol{\sigma}}_y|}\right)\right\}^2 + F'\hat{\kappa}_y}\frac{\partial f}{\partial \hat{\boldsymbol{\sigma}}_y}, \quad (20)$$

where $\hat{\kappa}_y$ is a scalar function of stress, plastic strain and $\partial f/\partial\hat{\boldsymbol{\sigma}}_y$ in degree one given by

$$\hat{\kappa}_y = \dot{K}/\dot{\lambda}, \quad (21)$$

that is, $\hat{\kappa}_y$ is given by replacing the argument $\dot{\boldsymbol{\varepsilon}}^p$ by $\partial f/\partial\hat{\boldsymbol{\sigma}}_y$ in the function $\dot{K}$.

Now, we extend (20) to the subyield state $\boldsymbol{\sigma}_s \neq \boldsymbol{\sigma}_y$ as follows:

$$\dot{\boldsymbol{\varepsilon}}^p = Q(b)\frac{\mathrm{tr}\left(\dfrac{\partial f}{\partial \hat{\boldsymbol{\sigma}}_y}\dot{\boldsymbol{\sigma}}_s\right)}{A\left\{\mathrm{tr}\left(\dfrac{\partial f}{\partial \hat{\boldsymbol{\sigma}}_y}\right)\right\}^2 + B\left\{\mathrm{tr}\left(\dfrac{\partial f}{\partial \hat{\boldsymbol{\sigma}}_y}\dfrac{\hat{\boldsymbol{\sigma}}_y}{|\hat{\boldsymbol{\sigma}}_y|}\right)\right\}^2 + F'\hat{\kappa}_y}\frac{\partial f}{\partial \hat{\boldsymbol{\sigma}}_y}, \quad (22)$$

where b denotes

$$b \equiv \mathrm{tr}\left(\frac{\boldsymbol{\beta}}{F^{1/n}}\frac{\dfrac{\partial f}{\partial \hat{\boldsymbol{\sigma}}_y}}{\left|\dfrac{\partial f}{\partial \hat{\boldsymbol{\sigma}}_y}\right|}\right), \quad (23)$$

and Q ($0 \leqq Q \leqq 1$) is a monotonically decreasing function of b satisfying the condition

$$Q = 1 \quad \text{when} \quad b = 0. \quad (24)$$

(22) means that the plastic strain rate produced in the subyield state relates to the parameter b, i.e., the projection of the vector $\boldsymbol{\beta}/F^{1/n}$ to the outer-normal direction of the subyield surface at $\boldsymbol{\sigma}_s$.

Further, since the homogeneity of the function f and the relation (9) yield the relation

$$\frac{\partial f}{\partial \hat{\boldsymbol{\sigma}}_y} = r^{1-n}\frac{\partial f}{\partial \bar{\boldsymbol{\sigma}}_s}, \quad (25)$$

(22) can be written as

$$\dot{\boldsymbol{\varepsilon}}^p = Q\frac{\mathrm{tr}\left(\dfrac{\partial f}{\partial \bar{\boldsymbol{\sigma}}_s}\dot{\boldsymbol{\sigma}}_s\right)}{A\left\{\mathrm{tr}\left(\dfrac{\partial f}{\partial \bar{\boldsymbol{\sigma}}_s}\right)\right\}^2 + B\left\{\mathrm{tr}\left(\dfrac{\partial f}{\partial \bar{\boldsymbol{\sigma}}_s}\dfrac{\bar{\boldsymbol{\sigma}}_s}{|\bar{\boldsymbol{\sigma}}_s|}\right)\right\}^2 + r^{n-1}F'\bar{\kappa}_s}\frac{\partial f}{\partial \bar{\boldsymbol{\sigma}}_s}, \quad (26)$$

where $\bar{\kappa}_s$ stands for a function given by replacing the argument $\partial f/\partial\hat{\boldsymbol{\sigma}}_y$ by $\partial f/\partial\bar{\boldsymbol{\sigma}}_s$ in the function $\hat{\kappa}_y$.

The constitutive equations formulated in the foregoing are regarded as one of the so-called *two-surface theory*, which are considerably simplified by virtue of the similarity of the distinct-yield and the subyield surfaces. However, if the interior of the subyield surface is assumed to be an elastic region as is done on the Mróz model of a field of hardening moduli [2] and the Krieg [3] or the Dafalias and Popov [4]'s two-surface theory, the aforementioned constitutive equations cannot describe suitably the elastic-plastic transition. For instance, the reloading after a partial unloading within the subyield surface brings about a gradual transition from the elastic to the plastic state but an abrupt one. In what follows, the previous constitutive equations are extended so as to describe suitably a gradual elastic-plastic transition even in a reloading state.

In accordance with the foregoing discussion, it should be assumed that a plastic deformation occurs even in the state that a current stress exists within a subyield surface. Then, let the current stress be designated simply by $\boldsymbol{\sigma}$, and assume the following relation.

$$\dot{\boldsymbol{\sigma}}_s = H(R)\dot{\boldsymbol{\sigma}}, \quad (27)$$

where H ($0 \leqq H \leqq 1$) is a monotonically increasing function of R satisfying the condition

$$H = 1 \quad \text{when} \quad R = 1. \quad (28)$$

R ($0 \leqq R \leqq 1$) designates the ratio of the size of the third surface, which passes through $\boldsymbol{\sigma}$ and is similar to the subyield surface with respect to $\bar{\boldsymbol{\alpha}}$ (see Fig. 2) and which we call a *loading surface*, to that of the subyield surface, i.e.,

$$R \equiv \frac{1}{r}\left\{\frac{f(\bar{\boldsymbol{\sigma}})}{F}\right\}^{1/n} \quad (29)$$

in setting

$$\bar{\boldsymbol{\sigma}} \equiv \boldsymbol{\sigma} - \bar{\boldsymbol{\alpha}}. \quad (30)$$

Now, noting the homogeneity of the function f and the equations (5) and (29), we get

$$\bar{\boldsymbol{\sigma}}_s = \frac{\bar{\boldsymbol{\sigma}}}{R} \quad (31)$$

and also

$$\frac{\partial f}{\partial \bar{\boldsymbol{\sigma}}_s} = R^{1-n}\frac{\partial f}{\partial \bar{\boldsymbol{\sigma}}}. \quad (32)$$

By substituting (25), (27), (31), and (32) into (8), (13), (16), (23), and (26) for the state $R = 1$, we obtain the extended constitutive equations to the general state $0 \leqq R \leqq 1$ as follows:

$$\dot{\boldsymbol{\varepsilon}}^p = QH\frac{\mathrm{tr}\left(\dfrac{\partial f}{\partial \bar{\boldsymbol{\sigma}}}\dot{\boldsymbol{\sigma}}\right)}{A\left\{\mathrm{tr}\left(\dfrac{\partial f}{\partial \bar{\boldsymbol{\sigma}}}\right)\right\}^2 + B\left\{\mathrm{tr}\left(\dfrac{\partial f}{\partial \bar{\boldsymbol{\sigma}}}\dfrac{\bar{\boldsymbol{\sigma}}}{|\bar{\boldsymbol{\sigma}}|}\right)\right\}^2 + F'\bar{\kappa}(rR)^{n-1}}\frac{\partial f}{\partial \bar{\boldsymbol{\sigma}}}, \quad (33)$$

$$\dot{\hat{\boldsymbol{\alpha}}} = A\dot{\varepsilon}_v{}^p \mathbf{1} + B\,\mathrm{tr}\left(\dot{\boldsymbol{\varepsilon}}_v{}^p \frac{\bar{\boldsymbol{\sigma}}}{|\bar{\boldsymbol{\sigma}}|}\right)\frac{\bar{\boldsymbol{\sigma}}}{|\bar{\boldsymbol{\sigma}}|}, \quad (34)$$

$$\dot{\bar{\boldsymbol{\alpha}}} = (1-r)H\dot{\boldsymbol{\sigma}} + r\dot{\hat{\boldsymbol{\alpha}}} - r\boldsymbol{\beta}\frac{(rR)^{n-1}\dot{F} - \mathrm{tr}\left\{\dfrac{\partial f}{\partial \bar{\boldsymbol{\sigma}}}(H\dot{\boldsymbol{\sigma}} - \dot{\hat{\boldsymbol{\alpha}}})\right\}}{\mathrm{tr}\left(\dfrac{\partial f}{\partial \bar{\boldsymbol{\sigma}}}\boldsymbol{\beta}\right)}, \quad (35)$$

$$\boldsymbol{\beta} = \frac{1}{R}\left(\frac{1}{r} - 1\right)\bar{\boldsymbol{\sigma}} + \hat{\boldsymbol{\alpha}} - \bar{\boldsymbol{\alpha}}, \quad (36)$$

$$b = \mathrm{tr}\left(\frac{\boldsymbol{\beta}}{F^{1/n}}\frac{\dfrac{\partial f}{\partial \bar{\boldsymbol{\sigma}}}}{\left|\dfrac{\partial f}{\partial \bar{\boldsymbol{\sigma}}}\right|}\right), \quad (37)$$

where $\bar{\kappa}$ stands for a function given by replacing the argument $\partial f/\partial\bar{\boldsymbol{\sigma}}_s$ by $\partial f/\partial\bar{\boldsymbol{\sigma}}$ in the function $\bar{\kappa}_s$.

As a consequence of formulating (33), it follows that the associated flow rule is applied to the loading surface whose interior is not an elastic region. The applicability of this rule to the loading surface was discussed in the previous paper [6, 7].

Constitutive Equations of Metals

Based on the constitutive equations formulated in the preceding

section, constitutive equations of metals are derived in this section.

We first introduce the modified von Mises yield condition

$$\Sigma - F(\xi) = 0, \tag{38}$$

where

$$\Sigma \equiv \sqrt{\frac{3}{2}}\,|\bar{\sigma}^*|, \quad \bar{\sigma}^* \equiv \bar{\sigma} - \frac{1}{3}\,\mathrm{tr}\,(\bar{\sigma})1 \tag{39}$$

$$\dot{\xi} \equiv \sqrt{\frac{2}{3}}\,|\dot{\epsilon}^p|,$$

Hence, it follows that

$$n = 1, \qquad \bar{\kappa} = 1. \tag{40}$$

Substitution of (38) and (40) into (29) and (33)–(37) leads to

$$\dot{\epsilon}^p = \left(\frac{3}{2}\right)^2 QH \frac{\mathrm{tr}\,(\bar{\sigma}^*\dot{\sigma})}{\Sigma^2(B+F')}\bar{\sigma}^*, \tag{41}$$

$$\dot{\lambda} = \frac{3}{2} QH \frac{\mathrm{tr}\,(\bar{\sigma}^*\dot{\sigma})}{\Sigma(B+F')}, \tag{42}$$

$$\dot{\hat{\alpha}} = B\,\mathrm{tr}\left(\dot{\epsilon}^p \frac{\bar{\sigma}}{|\bar{\sigma}|}\right)\frac{\bar{\sigma}}{|\bar{\sigma}|}, \tag{43}$$

$$\dot{\bar{\alpha}} = (1-r)H\dot{\sigma} + r\dot{\hat{\alpha}} - r\beta\,\frac{\dot{F} - \frac{3}{2}\,\mathrm{tr}\left\{\frac{\bar{\sigma}^*}{\Sigma}(H\dot{\sigma} - \dot{\hat{\alpha}})\right\}}{\frac{3}{2}\,\mathrm{tr}\left(\frac{\bar{\sigma}^*}{\Sigma}\beta\right)}, \tag{44}$$

$$\beta = (1-r)\frac{F}{\Sigma}\bar{\sigma} + \hat{\alpha} - \bar{\alpha}. \tag{45}$$

$$b = \mathrm{tr}\left(\frac{\beta}{F}\frac{\bar{\sigma}^*}{|\bar{\sigma}^*|}\right), \tag{46}$$

$$R = \frac{\Sigma}{rF}, \tag{47}$$

Now, we consider the uniaxial loading of a bar. In this case, it holds that

$$\Sigma = |\bar{\sigma}_a|, \qquad \dot{\xi} = |\dot{\epsilon}_a{}^p|, \tag{48}$$

where

$$\bar{\sigma}_a \equiv \bar{\sigma}_a - \bar{\alpha}_a, \tag{49}$$

and σ_a, $\bar{\alpha}_a$, and $\dot{\epsilon}_a{}^p$ designate components of σ, $\bar{\alpha}$, and $\dot{\epsilon}^p$ along the axis, respectively.

Substituting (48) into (41)–(47), we have

$$\dot{\epsilon}_a{}^p = QH\frac{\dot{\sigma}_a}{B+F'}, \tag{50}$$

$$\dot{\lambda} = QH\frac{\bar{\sigma}_a}{|\bar{\sigma}_a|}\frac{\dot{\sigma}_a}{B+F'}, \tag{51}$$

$$\dot{\hat{\alpha}} = B\dot{\epsilon}_a{}^p, \tag{52}$$

$$\dot{\bar{\alpha}}_a = H\dot{\sigma}_a - r\frac{\bar{\sigma}_a}{|\bar{\sigma}_a|}\dot{F}, \tag{53}$$

$$\beta_a = (1-r)F\frac{\bar{\sigma}_a}{|\bar{\sigma}_a|} + \hat{\alpha}_a - \bar{\alpha}_a, \tag{54}$$

$$b = \sqrt{\frac{2}{3}}\frac{\beta_a}{F}\frac{\bar{\sigma}_a}{|\bar{\sigma}_a|}, \tag{55}$$

$$R = \frac{|\bar{\sigma}_a|}{rF}, \tag{56}$$

where $\hat{\alpha}_a$ is the component of $\hat{\alpha}$ along the axis.

Comparison With Experimental Data

In this section, how closely the foregoing constitutive equations can predict the actual behavior of metals is examined by comparing with experimental data on a cyclic uniaxial loading of aluminum. The experimental curve for the stress-strain relation of 6061-0 Aluminum subjected to a repeated uniaxial loading between −95 and +95 Mpa, measured by Lipkin and Swearengen [5], is depicted by the heavy solid line in Fig. 3. Thie material was selected for presentation because it satisfies the assumption of initial plastic isotropy. Further, the theoretical curve calculated by the present theory is depicted by the broken line, provided that this curve is supplemented by the elastic axial strain $\epsilon_a{}^e$ given by the Hooke's law

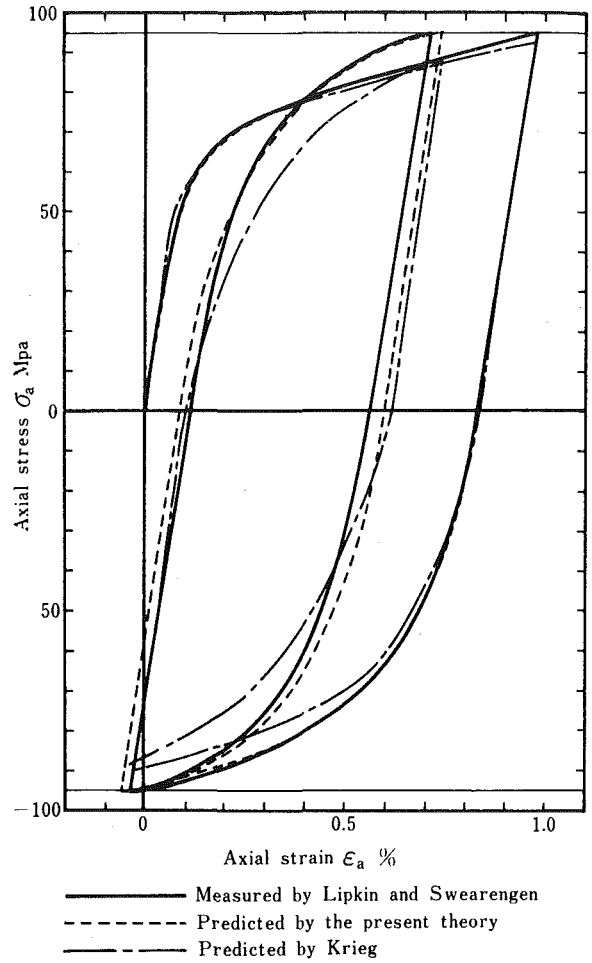

Fig. 3 Theoretical prediction of cyclic uniaxial loading behavior of 6061-0 Aluminum

$$\epsilon_a{}^e = \sigma_a/E, \tag{57}$$

where E is the Young's modulus. Functions and material constants in (41)–(47) and (57) are selected as follows:

$$\begin{aligned} F &= 88 - 26\exp(-300\xi)\ \text{Mpa}, \\ B &= 32000\xi^{0.6}\ \text{Mpa}, \\ r &= 0.7, \\ Q &= \frac{1}{1+36.7b}, \\ H &= R^{10}, \\ E &= 64000\ \text{Mpa}. \end{aligned} \tag{58}$$

The distinction between a loading ($\dot{\epsilon}^p \neq 0$) and an unloading ($\dot{\epsilon}^p = 0$) is made by the sign of $\dot{\lambda}$ as was described in the previous paper [1], while for the uniaxial loading it is made by the sign of $\bar{\sigma}_a\dot{\sigma}_a$ as is known from (51).

Theoretical curves for the relations of parameters σ_a, σ_{ya}, σ_{sa}, $\hat{\alpha}_a$, and $\bar{\alpha}_a$ versus $\epsilon_a{}^p$ are depicted by the broken line, the fine solid line, the fine chain line, the solid line and the chain line respectively in Fig. 4, where σ_{ya} and σ_{sa} are components of $\boldsymbol{\sigma}_y$ and $\boldsymbol{\sigma}_s$ along the axis, respectively.

In Fig. 3, the theoretical curve calculated by Krieg [3] with his two-surface theory is also depicted by the chain line. It does not, however, exactly satisfy the stress condition varying between −95 and +95 Mpa. The ratio of the strain rate to the stress rate becomes progressively greater as $|\sigma_a|$ comes up to the maximum value 95 Mpa. Therefore, note that the slight difference of the stress range affects considerably the magnitude of the strain calculated. On the other hand, the broken line is calculated conforming exactly to that stress condition. And yet the very close approximation throughout all deformation process is obtained by this line.

Besides, the theoretical stress-strain curve for the partial unloading from 80 Mpa (point u) to 60 Mpa (point r) and the reloading from 60 Mpa (point r) is depicted in Fig. 4 where we observe the gradual change of its slope. On the other hand, the Mróz model and the Krieg and the Dafalias and Popov's two-surface theory express not a gradual transition but an abrupt change of the stress-strain curve in which the reloading curve coincides with the unloading curve until $\sigma_a = 80$ Mpa and bents suddenly to follow the curve depicted by the direct loading without the unloading, since they assume the surface whose interior is an elastic region.

Summary and Application to the Other Material

Constitutive equations of elastoplastic materials with an anisotropic hardening (or softening) and an elastic-plastic transition have been presented. They have quite simple forms by virtue of the similarity of the assumed three surfaces, i.e., the distinct-yield, the subyield and the loading surfaces. Hence, they can be called a *three-surface theory*. Though the equations have been applied to metals and their adaptability was examined on the cyclic uniaxial loading behavior of aluminum for example, they seem to be applicable to various materials. For instance, constitutive equations of granular media which exhibit very different plastic behaviors, softening and volume change, from metals would be formulated suitably by introducing the following functions [7].

$$f(\bar{\sigma}) = p^2 + \left(\frac{\bar{\sigma}^*}{m}\right)^2, \quad F = F_0 \exp\left(-\frac{2}{\rho}\epsilon_v{}^p\right),$$

$$A = \frac{m}{\rho M}\sqrt{F}, \quad B = 0,$$

where

$$\bar{P} = \tfrac{1}{3}\,\mathrm{tr}\,(\bar{\sigma}).$$

m, M, and ρ are material constants and F_0 is an initial value of F.

Elastoplastic constitutive equations of granular media will be reported in another paper at length.

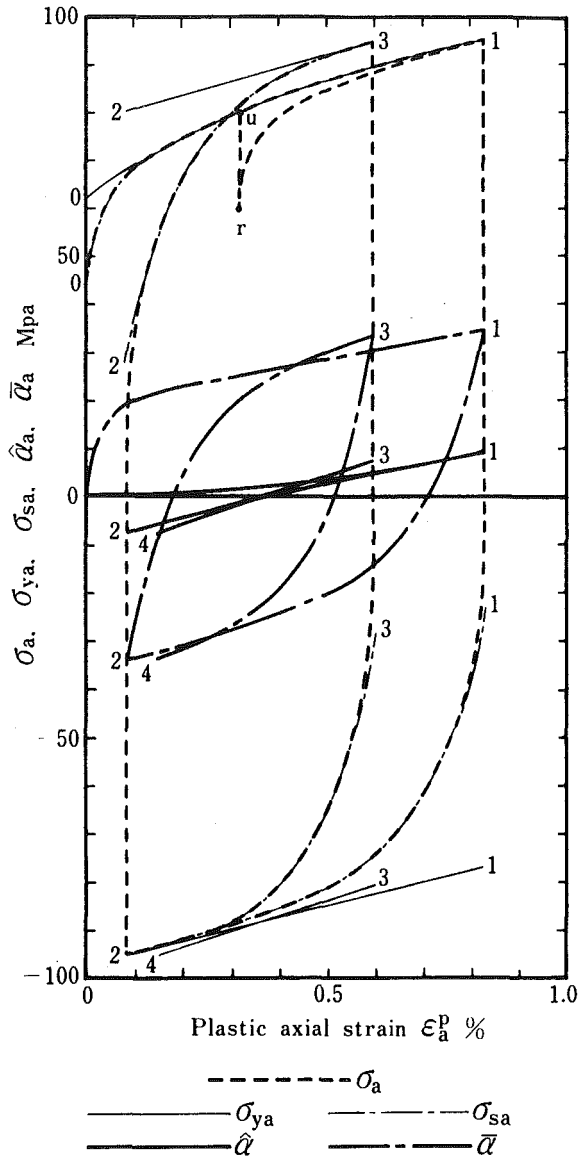

Fig. 4 Theoretical relations of σ_a, σ_{ya}, σ_{sa}, $\hat{\alpha}_a$, and $\bar{\alpha}_a$ versus $\epsilon_a{}^p$

Acknowledgment

The author wishes to express his sincere gratitude to Prof. H. Yamaguchi of the Tokyo Institute of Technology for his kind advice and many helpful discussions. The results reported here were obtained in the course of research supported by the Aid for Scientific Researches from the Ministry of Education of Japan under Grant 355220 in 1978–1979 to the author.

References

1 Hashiguchi, K., "Constitutive Equations of Elastoplastic Materials With Elastic-Plastic Transition," ASME JOURNAL OF APPLIED MECHANICS, Vol. 47, 1980, pp. 266–272.

2 Mróz, Z., "On the Description of Anisotropic Workhardening," *Journal of the Mechanics and Physics of Solids*, Vol. 15, 1967, pp. 163–175.

3 Krieg, R. D., "A Practical Two Surface Plasticity Theory," ASME JOURNAL OF APPLIED MECHANICS, Vol. 42, 1975, pp. 641–646.

4 Dafalias, Y. F., and Popov, E. P., "A Model of Nonlinearly Hardening Materials for Complex Loading," *Acta Mechanica*, Vol. 21, 1975, pp. 173–192.

5 Lipkin, J., and Swearengen, J. C., "On the Subsequent Yielding of an Aluminum Alloy Following Cyclic Prestraining," *Metallurgical Transactions*, Vol. 6, Series A, 1975, pp. 167–177.

6 Hashiguchi, K., "A Derivation of the Associated Flow Rule," *Journal of the Faculty of Agriculture*, Kyushu University, Vol. 24, 1979, pp. 75–80.

7 Hashiguchi, K., "Anisotropic Hardening Model for Granular Media, "*Proceedings of the International Symposium on Soils Under Cyclic and Transient Loading*, Swansea, 1980, pp. 469–474.

A. J. Rosakis
Research Assistant.

L. B. Freund
Professor and Chairman.
Fellow ASME.

Division of Engineering,
Brown University,
Providence, R. I. 02912

The Effect of Crack-Tip Plasticity on the Determination of Dynamic Stress-Intensity Factors by the Optical Method of Caustics

The shadow spots which are obtained in using the optical method of caustics to experimentally determine dynamic stress-intensity factors are usually interpreted on the basis of a static elastic crack model. In this paper, an attempt is made to include both crack-tip plasticity and inertial effects in the analysis underlying the use of the method in reflection. For dynamic crack propagation in the two-dimensional tensile mode which is accompanied by a Dugdale-Barenblatt line plastic zone, the predicted caustic curves and corresponding initial curves are studied within the framework of plane stress and small scale yielding conditions. These curves are found to have geometrical features which are quite different from those for purely elastic crack growth. Estimates are made of the range of system parameters for which plasticity and inertia effects should be included in data analysis when using the method of caustics. For example, it is found that the error introduced through the neglect of plasticity effects in the analysis of data will be small as long as the distance from the crack tip to the initial curve ahead of the tip is more than about twice the plastic zone size. Also, it is found that the error introduced through the neglect of inertial effects will be small as long as the crack speed is less than about 20 percent of the longitudinal wave speed.

1 Introduction

Progress toward understanding the phenomenon of dynamic crack propagation in solids has been impeded by several complicating features which are encountered in both analytical and experimental approaches. From the experimental viewpoint, the inherent time dependence of the process requires that many sequential measurements of field quantities be made in an extremely short time in a way which does not interfere with the process itself. Furthermore, the place at which field quantities are to be measured varies, often in a nonuniform way, during the course of the process. Because of this complexity, most experimental techniques for measuring crack-tip stress and deformation fields during rapid fracture are based on optics. Such methods have three main advantages:

(*i*) The techniques are full-field methods, i.e., the entire specimen is observed continuously and crack paths need not be known *a priori*.

(*ii*) There is no coupling between the optical and mechanical processes, i.e., the method of measurement does not interfere with the process being examined.

(*iii*) The response of an optical system is essentially instantaneous on the time scale of mechanical rapid fracture events.

Several optical methods have been used during the past 50 years to measure deformations in nominally elastic materials, and thereby to determine stress fields. Most of the methods are based on light wave interference principles, and their application has been confined to transparent materials, or to opaque materials coated with transparent materials.

Recently, the optical method of caustics, or the shadow spot method, was developed and applied in the investigation of nonuniform surface deformations due to stress concentrations in deformed solids [1, 2]. Details of the stress field may then be inferred from shadow spot measurements on the basis of an analytical model. The method of caustics is an exceptional method because it is based on the principles of geometrical optics, rather than light interference, and it has been successfully applied to cases of both opaque and transparent materials. The method was first used in a reflection arrangement by Theocaris [2], who studied the stress singularity in the vicinity of a stationary crack tip. Later, Theocaris and Gdoutos [3, 4] applied the method of caustics in reflection to experimentally examine the de-

Contributed by the Applied Mechanics Division for publication in the JOURNAL OF APPLIED MECHANICS.
Discussion on this paper should be addressed to the Editorial Department, ASME, United Engineering Center, 345 East 47th Street, New York, N. Y. 10017, and will be accepted until September 1, 1981. Readers who need more time to prepare a Discussion should request an extension from the Editorial Department. Manuscript received by ASME Applied Mechanics Division, October, 1980.

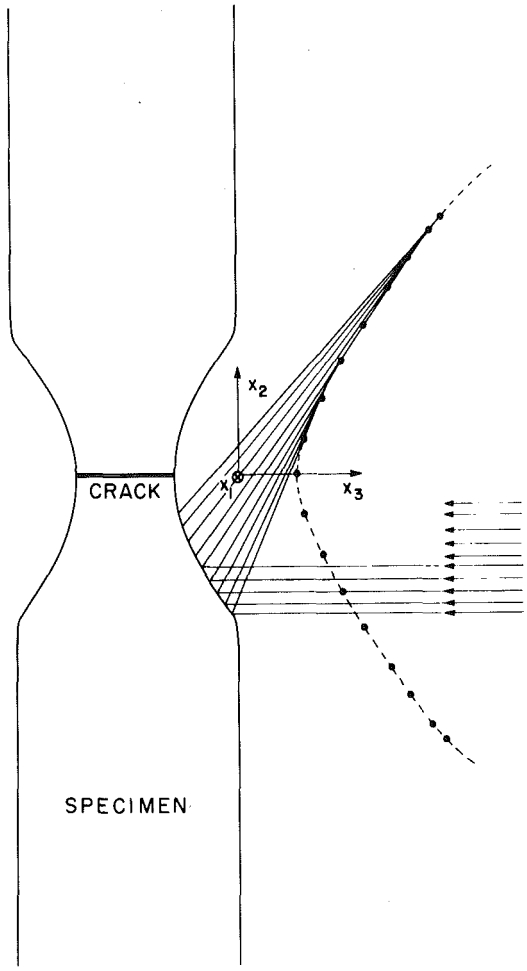

Fig. 1 Schematic of the formation of the three-dimensional caustic envelope obtained by reflection

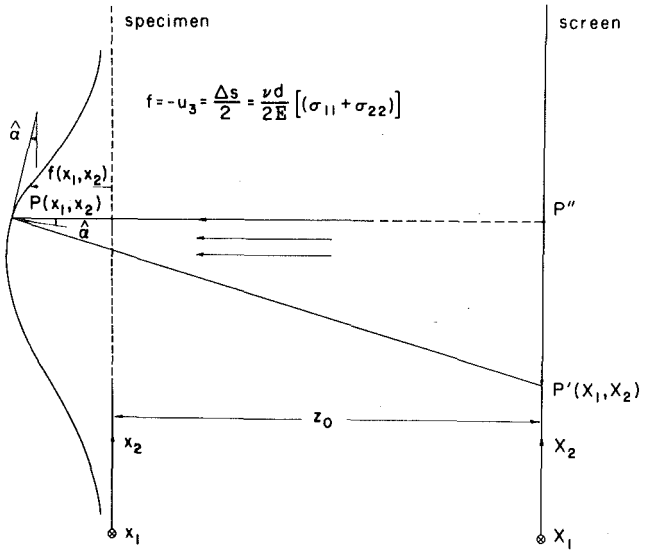

Fig. 2 Optical mapping of points $P(x_1, x_2)$ of the surface of an illuminated solid, to points $P'(X_1, X_2)$ on a screen

formation fields near the tips of stationary cracks in metal plates. In this case, which apparently was the first application of the method to metal specimens, plastic deformation occurred locally and the optical data were analyzed by assuming a plane stress Dugdale-Barenblatt model for the crack-tip plastic zones.

The method was first used in experiments involving very rapid crack propagation and stress wave loading by Kalthoff and coworkers [5] and Theocaris and coworkers [6, 7], and more recently by Goldsmith [8]. In each case, it was assumed that the elastic stress field near the tip of a rapidly growing crack in a brittle solid has precisely the same spatial variation as the elastic stress field near the tip of a stationary crack. That is, the influence of inertial effects on the spatial dependence of the crack-tip field was not taken into account. More recently, several investigators have reanalyzed the method of caustics as applied to rapid crack propagation in brittle materials, including the effect of inertia on the spatial variation of the elastic crack-tip stress field. Kalthoff, et al. [9], introduced an approximate correction factor to account for the potentially large error introduced when the static local field is used in data analysis. The exact equations of the caustic envelope formed by the reflection of parallel incident light from the surface of a specimen containing a rapidly growing crack were recently obtained by Rosakis [10] for mixed mode plane-stress crack growth. It was found that, for some typical laboratory materials used in crack propagation studies, the neglect of the influence of inertia on the crack-tip stress field could lead to errors of up to 30 to 40 percent in the value of the elastic stress-intensity factor inferred from the measured caustic diameter. A similar analysis has also been discussed by Theocaris, et al. [11].

In this paper, a first attempt is made at including plasticity effects in the analysis underlying the optical method of caustics as applied in dynamic crack propagation studies. The analysis is based on the one-dimensional line plastic zone model of Dugdale and Barenblatt. For dynamic crack propagation in the two-dimensional tensile mode which is accompanied by such a strip yield zone, the sizes and shapes of the predicted caustic curves are studied. The influence of material inertia and of the extent of the plastic zone on stress-intensity factor measurements are considered. The initial and caustic curves are found to have geometrical features quite different from those present for purely elastic crack growth, and the dependence of these features on crack speed and plastic zone size is investigated.

2 Formation of Caustics in Reflection

Consider a family of parallel light rays incident on the reflective surface $x_3 = -f(x_1, x_2)$ of an opaque material; see Fig. 1. Upon reflection from the surface, the light rays will deviate from parallelism. (In practice, the intensity of the reflected ray will be less than the intensity of the incident ray due to random scattering.) If certain geometrical conditions are met by the reflecting surface, then the family of reflected rays will have an envelope in the form of a three-dimensional surface in space. A section of such a surface is shown as the dashed curve in Fig. 1. This surface, which is called the *caustic surface*, is the locus of points of maximum luminosity (i.e., highest density of rays) in the reflected field. The reflected rays are tangent to the caustic surface. If a screen is positioned parallel to the (x_1, x_2)-plane and so that it intersects the caustic surface, then a cross section of the caustic surface can be observed as a bright curve (the so-called *caustic curve*) bordering a relatively dark region (the *shadow spot*) on the screen.

Suppose that the incident ray which is reflected from the point $P(x_1, x_2)$ on the reflecting surface will intersect the screen at the image point $P'(X_1, X_2)$; see Fig. 2. The (X_1, X_2) coordinate system is identical to the (x_1, x_2) system, except that the origin of the former has been translated to the screen. The position of the image point P' will depend on the slope of the reflecting surface at P and on the normal distance z_0 between the screen and the reflecting surface. It has been shown elsewhere [12] that the position of the image point P' on the screen has coordinates

$$X_i = x_i \pm 2z_0(\partial f/\partial x_i) \tag{1}$$

where $z_0 \gg |f|$. Equation (1) represents a mapping of points P of the reflecting surface onto points P' of the screen. The choice of sign in

(1) depends on whether the image point is a real image in front of the reflecting surface (+ sign) as is the case in Fig. 2 or a virtual image behind the reflecting surface (− sign). The use of the virtual image has certain advantages in experimental fracture mechanics, and the subsequent analysis will be based on the choice of the negative sign in (1).

If the screen intersects a caustic surface, then the resulting caustic curve on the screen is a locus of points of multiple reflection. That is, for those points on the caustic curve, the mapping (1) is not invertible and the Jacobian of the transformation must vanish, i.e.,

$$J(x_1, x_2) = \frac{\partial(X_1, X_2)}{\partial(x_1, x_2)} = 0 \tag{2}$$

The vanishing of the Jacobian is the necessary and sufficient condition for the existence of a caustic curve. The points on the reflecting surface for which $J(x_1, x_2) = 0$ are the points from which the rays forming the caustic curve are reflected. The locus of these points on the reflecting surface is the so-called *initial curve*.

3 Application of Caustics to Plane-Stress Elastodynamics

Consider a two-dimensional elastic solid occupying a region of the x_1, x_2-plane. The outer boundary is subjected to traction and/or displacement boundary conditions of a type to ensure uniqueness of solution. Suppose that a planar crack grows through the body, with the crack tip speed being v. Within the framework of the theory of plane stress, the two-dimensional displacement vector $\mathbf{u}$ is governed by the equation

$$c_l^2 \nabla(\nabla \cdot \mathbf{u}) - c_s^2 \nabla \times \nabla \times \mathbf{u} = \ddot{\mathbf{u}} \tag{3}$$

where ∇ is the two-dimensional gradient operator and the superposed dot denotes time derivative. In terms of the elastic modulus E and Poisson's ratio ν, the longitudinal and shear wave speeds for plane stress are $c_l = [E/(1 - \nu^2)\rho]^{1/2}$ and $c_s = [E/2(1 + \nu)\rho]^{1/2}$, respectively.

Any displacement vector which is derived from the longitudinal and shear wave potentials ϕ and ψ according to

$$\mathbf{u} = \nabla\phi + \nabla \times \psi; \quad c_l^2 \nabla^2 \phi - \ddot{\phi} = 0; \quad c_s^2 \nabla^2 \psi - \ddot{\psi} = 0 \tag{4}$$

satisfies (3). In plane stress, ψ has a single nonzero component which is here denoted by ψ.

Suppose now that the (x_1, x_2) coordinate system is fixed with its origin at the moving crack tip and that it is oriented so that crack growth is in the x_1-direction. Furthermore, suppose that the crack grows with constant speed, and that the geometry and applied loading are steady (i.e., independent of time) as seen by an observer moving with the crack tip. Under these circumstances, it is expected that the complete elastodynamic field is steady, so that ϕ and ψ depend only on x_1, x_2 and $(\dot{\ }) = -v\partial(\ )/\partial x_1$. Under steady conditions, the wave equations in (4) reduce to

$$\frac{\partial^2 \phi}{\partial x_1^2}\left(1 - \frac{v^2}{c_l^2}\right) + \frac{\partial^2 \phi}{\partial x_2^2} = 0 \qquad \frac{\partial^2 \psi}{\partial x_1^2}\left(1 - \frac{v^2}{c_s^2}\right) + \frac{\partial^2 \psi}{\partial x_2^2} = 0 \tag{5}$$

But each of the reduced wave equations is clearly equivalent to Laplace's equation with the x_2 coordinates scaled by the factor $\alpha_l = (1 - v^2/c_l^2)^{1/2}$ in the first case and $\alpha_s = (1 - v^2/c_s^2)^{1/2}$ in the second case. General solutions of (5) may be written immediately in the form

$$\phi = \mathrm{Re}\,[F(z_l)], \quad \psi = \mathrm{Im}\,[G(z_s)] \tag{6}$$

where $z_l = x_1 + i\alpha_l x_2$, $z_s = x_1 + i\alpha_s x_2$, and F and G are each an analytic function of its complex argument in the region occupied by the body. In any given problem, the analytic functions are determined by the boundary conditions. Although (5)–(6) have been established with reference to crack growth, it should be noted that these equations are valid for any steady plane-stress elastodynamic field.

Generally, for plane-stress crack propagation in a body which is symmetric about the crack plane, the deformation fields are a combination of two modes. The tensile mode, or Mode I, exhibits reflective symmetry with respect to the crack plane, while the shearing mode, or Mode II, is antisymmetric with respect to the crack plane. For these cases

$$F(\bar{z}_l) = \pm \overline{F(z_l)}, \quad G(\bar{z}_s) = \pm \overline{G(z_s)} \tag{7}$$

where the upper signs apply for Mode I and the lower signs for Mode II. The bar denotes complex conjugate.

Consider now a plate which has uniform thickness d in the undeformed state. If the plate is subjected to edge loading which results in a nonuniform state of plane stress, then the thickness of the deformed plate is also nonuniform. In terms of the in-plane stress components the lateral contraction is

$$f(x_1, x_2) = -u_3(x_1, x_2) = \nu d(\sigma_{11} + \sigma_{22})/2E \tag{8}$$

Clearly, the function f here is identified with the function f describing the reflecting surface in Section 2. It represents the shape of the originally plane surface which is the reflecting surface.

In terms of the stress distribution, the equations of the mapping (1) based on geometrical optics become

$$X_i = x_i - C\partial(\sigma_{11} + \sigma_{22})/\partial x_i \tag{9}$$

where $C = z_0 \nu d/E$. Thus determination of the first invariant of stress establishes the mapping, even for dynamic problems.

In terms of the displacement potential ϕ, the first stress invariant is

$$\sigma_{11} + \sigma_{22} = \frac{E}{(1 - \nu)} \nabla^2 \phi \tag{10}$$

For a steady-state deformation field translating in the x_1-direction with speed v, (5) may be employed to reduce (10) to

$$\sigma_{11} + \sigma_{22} = (1 + \nu)\rho v^2 \partial^2 \phi / \partial x_1^2 \tag{11}$$

or, in terms of the analytic function F appearing in the general solution (6),

$$\sigma_{11} + \sigma_{22} = (1 + \nu)\rho v^2\, \mathrm{Re}\,[F''(z_l)] \tag{12}$$

If the differentiation indicated in (9) is performed and the result is expressed in terms of the complex variables $Z = X_1 + iX_2$, $z = x_1 + ix_2$ then the mapping is

$$Z = z - \kappa\{\mathrm{Re}\,[F'''(z_l)] - i\alpha_l\, \mathrm{Im}\,[F'''(z_l)]\} \tag{13}$$

where $\kappa = (1 + \nu)\rho v^2 C$.

As noted in the preceding section, the condition for the existence of a caustic curve on the screen at $x_3 = -z_0$ is the vanishing of the Jacobian of the transformation (13). With reference to (2), the condition $J(x_1, x_2) = 0$ specifies the initial curve on the plane of the specimen, and the corresponding caustic curve on the screen is the map of the initial curve according to (13) onto the place of the screen. The condition that the determinant of the Jacobian matrix must vanish is

$$J = 1 + \kappa(1 - \alpha_l^2)\, \mathrm{Re}\,[F^4(z_l)] - \alpha_l^2 \kappa^2 |F^4(z_l)|^2 = 0 \tag{14}$$

where F^4 is the fourth derivative of F with respect to its argument.

The equations (13) and (14) together describe the caustic curves formed by reflection of parallel light from the surface of *any* planar elastic solid in which the elastodynamic stress distribution is steady. For any particular case, the analytic function F which appears in these equations must be determined from the geometrical configuration of the body and the boundary conditions.

In the case of elastic crack propagation, the stress field has universal spatial dependence in the vicinity of the crack tip. The only quantity which varies from one specific case to another is a scalar amplitude, the so-called elastic stress-intensity factor, which is often the parameter of fundamental interest in laboratory testing. In the context of equations (13) and (14), the function F will be known up to a scalar multiplier, the stress-intensity factor. If the crack speed, geometrical parameters, and bulk material parameters are known, the equations (13) and (14) then provide a relationship between a characteristic dimension of the caustic curve and the corresponding value of the

stress-intensity factor. Experimental measurement of this characteristic dimension provides the instantaneous value of the stress-intensity factor. The tremendous appeal of the method is due to the fact that it povides a *direct* measure of the stress-intensity factor in nominally elastic fracture. No measurement of boundary conditions or field quantities is required. The optical singularity on the screen provides the information necessary to determine the strength of the mechanical singularity in the specimen (under the assumption that the theory of plane stress provides an accurate picture of the three-dimensional deformation field).

4 Caustic Curves for the Line Plastic Zone Model

Analytical crack-tip models of a one-dimensional zone of nonlinear material response extending ahead of the tip have been proposed for plane-stress fracture of ductile sheets by Dugdale [13] and for the case of pure cleavage tensile fracture by Barenblatt, et al. [14]. The Dugdale-Barenblatt model is analyzed as an elastic crack problem in which the crack is made effectively longer by an amount R, the plastic zone size, with cohesive forces in the plastic zone acting on the prospective crack surfaces so as to restrain the opening. If small scale yielding conditions prevail then the applied loading is completely specified by an equivalent elastic stress-intensity factor, which is denoted by K_I for the plane tensile fracture model.

The analysis of the strip yield model is outlined in [15]. The (x_1, x_2) coordinate system is fixed at the tip which is moving with constant speed v in the x_1-direction. The plastic zone extends over the interval $0 < x_1 < R$. The derivation of the analytic function F, which is required to determine the caustic curves, follows closely the work of Willis [16] and employs the asymptotic result of Freund and Clifton [17]. For the case of small scale yielding and ideal plasticity, in which the cohesive tractions which resist crack opening in the plastic zone have the constant magnitude σ_0, the analytic function F is given by

$$F''(z) = \frac{2\sigma_0(1+\alpha_s^2)}{\mu\pi Q}\tan^{-1}\left[\frac{R}{z-R}\right]^{1/2} \tag{15}$$

where

$$R = \frac{\pi K_I^2}{8\sigma_0^2}, \quad Q = 4\alpha_l\alpha_s - (1+\alpha_s^2)^2 \tag{16}$$

The quantity σ_0 is identified as the uniaxial tensile flow stress of the material. The branch of $(z-R)^{1/2}$ which is positive as $z \to \infty$ along the positive real axis of the z-plane is assumed. Note that the relationship (16) between the plastic zone size and the remote stress-intensity factor is identical to the corresponding result for quasi-static deformations [18]. However, the function F is different from the corresponding quasi-static result.

Suppose now that a tensile crack is propagating in a polished plate specimen, and that the specimen is illuminated by a beam of parallel light as indicated in Fig. 1. The light will be reflected from the specimen surface and, under suitable conditions, will form a caustic curve on a screen placed at a distance z_0 from the midsurface of the specimen. The size and shape of the caustic curve will be related to the functional form of F in (15), and will depend on the parameters v, σ_0, and K_I. In what follows, the nature of the caustic curves corresponding to dynamic crack growth accompanied by a strip yield plastic zone under small scale yielding conditions is investigated. The investigation is based on the analytic function F given in (15) and (16), on the equation of the initial curve (14), and on the equation of the optical mapping (13).

Next, all lengths are normalized with respect to the plastic zone size R, and a superposed caret is used to denote normalized values of the length parameters, e.g., $\hat{z}_l = z_l/R = \hat{r}_l \exp(i\theta_l)$. If F is differentiated and is substituted into the equation for the initial curve (14), then the result in nondimensional form is

$$J(\hat{r}_l, \theta_l) = 1 - A(1-\alpha_l^2)\,\mathrm{Re}\,[G(\hat{z}_l)] - \alpha_l^2 A^2 |[G(\hat{z}_l)]|^2 = 0 \tag{17}$$

where J is now viewed as a function of the distorted polar coordinates. In (17)

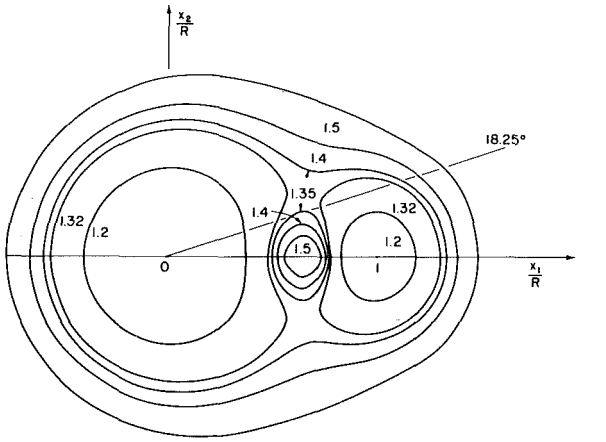

Fig. 3 Initial curves at the tips of steadily propagating cracks for five values of r/R

$$G(z) = \frac{(3z/2-1)}{z^2(z-1)^{3/2}} \qquad A = \frac{(1+\nu)\rho v^2(1+\alpha_s^2)}{\pi Q}\frac{\sigma_0 z_0 v d}{ER^2} \tag{18}$$

The mapping, which defines the caustic curves corresponding to the solution of (17), is

$$\hat{X}_1 = \hat{r}_l\cos\theta_l + \frac{A}{\hat{r}_l(\hat{r}_l^2 - 2\hat{r}_l\cos\theta_l + 1)^{1/4}} \times \cos\left[\theta_l + \frac{1}{2}\tan^{-1}\left(\frac{\hat{r}_l\sin\theta_l}{\hat{r}_l\cos\theta_l - 1}\right)\right] \tag{19a}$$

$$\alpha_l\hat{X}_2 = \hat{r}_l\sin\theta_l + \frac{\alpha_l^2 A}{\hat{r}_l(\hat{r}_l^2 - 2\hat{r}_l\cos\theta_l + 1)^{1/4}} \times \sin\left[\theta_l + \frac{1}{2}\tan^{-1}\left(\frac{\hat{r}_l\sin\theta_l}{\hat{r}_l\cos\theta_l - 1}\right)\right] \tag{19b}$$

The limiting behavior of the foregoing equations as $R \to 0$ and $v \to 0$ may be checked against the previously derived results for $R = 0$ and $v = 0$. It is easily shown that if $R \to 0$ then (19) reduce to the equations (2.9) of [10] which represent the caustic envelope for a dynamic Mode I crack propagating in a linear elastic solid. For $R \to 0$ and $v \to 0$, (19) reduce to the equation of a generalized epicycloid as predicted by the analysis of a stationary crack in a linear elastic material [2].

5 Results and Discussion

Two parameters which seem to have fundamental significance in analyzing the initial curves (17) and caustic curves (19) are the ratio of crack-tip speed to characteristic speed of the material and the ratio of initial curve "size" to plastic zone size. The former parameter represents a measure of the inertial effects, while the latter parameter represents a measure of the influence of the crack-tip plastic zone. Furthermore, the two parameters are independent of each other, in the sense that either may be varied without influencing the other. Specifically, the *inertial parameter* is v/c_l and the *plasticity parameter* is r/R, which is understood to be the solution of (17) for $\theta_l = 0$. Thus r/R is the quotient of the distance from the crack tip to the extremity of the initial curve directly ahead of the crack tip and the length of the plastic zone R.

The equation of the initial curve (17) was solved numerically by means of the Newton-Raphson procedure. First, the value of θ_l was fixed, and then all values of $\hat{r}_l$ satisfying the resulting equation were determined by Newton-Raphson iteration. This was done for a number of values of θ_l sufficient to generate the initial curves.

The computed initial curves for the case of $v/c_l = 0.2$ are shown in Fig. 3 for a range of values of r/R. The geometrical features of the initial curves are strikingly different from the features of an initial curve for an elastic crack. For values of r/R near to unity (e.g., $r/R =$

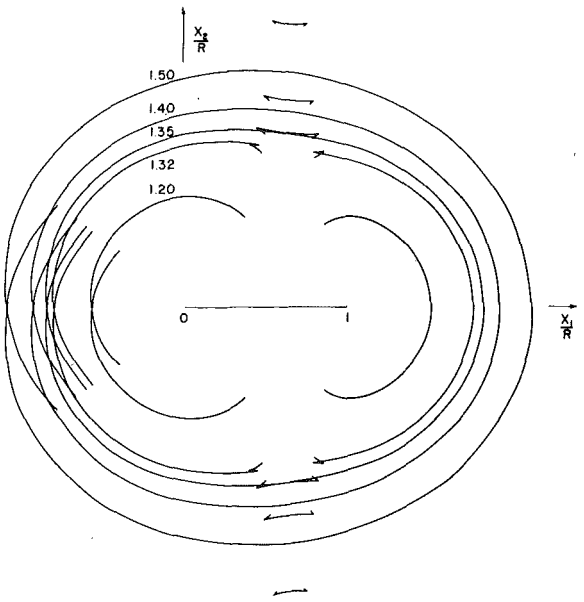

Fig. 4 Caustic curves formed by reflection from the near tip region of steadily propagating cracks corresponding to the initial curves of Fig. 3

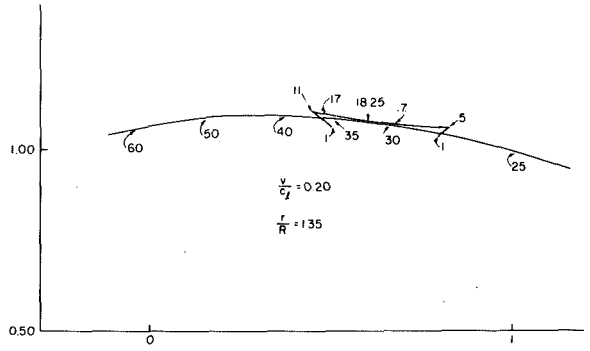

Fig. 5 A detailed view of the cusped portion of the caustic curve for $r/R = 1.35$, $v = 0.20\ c_l$, shown in Fig. 4

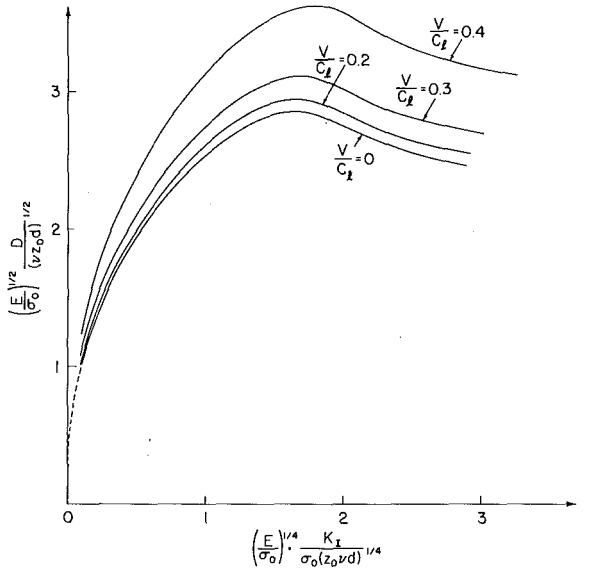

Fig. 6 Variation of the dimensionless maximum transverse diameter of the caustic curve, versus the normalized remote elastic stress-intensity factor, presented for a range of crack velocities

1.2), the individual singularities in the deformation field at the crack tip and the plastic zone tip dominate. The initial curve consists of two disjoint lobes, each roughly circular and centered at these two singularities. As r/R becomes larger, the shape of two lobes is distorted and they tend to approach each other. As seen in Fig. 3, the two lobes are almost in contact for $r/R = 1.32$. When r/R has increased to about 1.34, the two lobes have two common points. As r/R increases beyond this critical value (e.g., to $r/R = 1.35$), the initial curve again splits into two lobes. However, whereas the lobes are disjoint for $r/R < 1.34$, they are nested for $r/R > 1.34$. This nested structure is maintained as r/R is increased. For values of r/R large compared to one, the shape of the outer lobe is essentially the correct shape for a dynamic elastic crack. The inner lobe becomes very small compared to R as r/R becomes large, and is finally reduced to a point as $r/R \to \infty$.

It is a simple matter to prove that the initial curve (17) intersects the plastic zone at two points for *any* value of r/R in the range $1 < r/R < \infty$. On Im $(\hat{z}_l) = 0$ and $0 <$ Re $(\hat{z}_l) < 1$, it is clear from (18) that Re $(G) = 0$, and (17) takes on the simple form

$$(\alpha_l A)^{-2} = |G(\hat{z}_l)|^2 \tag{20}$$

The left side of (20) is, in general, a bounded positive real number. From (18), it can be seen that the right side of (20) equals zero if Re $(\hat{z}_l) = \frac{2}{3}$. Furthermore, the right side of (20) increases monotonically from zero to arbitrarily large values *either* as Re $(\hat{z}_l)$ increases from $\frac{2}{3}$ to 1 *or* as Re $(\hat{z}_l)$ decreases from $\frac{2}{3}$ to 0. Thus (20) always has one, and only one, root in the range $0 <$ Re $(\hat{z}_l) < \frac{2}{3}$, and one, and only one, root in the range $\frac{2}{3} <$ Re $(\hat{z}_l) < 1$. As $r/R \to \infty$, these two roots coalesce at $\hat{z}_l = \frac{2}{3}$. The coalescence of the two roots as $r/R \to \infty$ corresponds to the reduction of the inner loop of the initial curve to a single point as the effects of plasticity disappear.

The caustic curves corresponding to the initial curves in Fig. 3 are shown in Fig. 4. If the initial curve consists of disjoint lobes, then the resulting caustic consists of open curves (e.g., $r/R = 1.2$ in Fig. 4). As r/R approaches the transition value of 1.34, cusps are formed near the ends of the open curves. When r/R reaches the critical value of 1.34, the gap between the open curves which form the caustic closes, and as r/R increases beyond the critical value (e.g., for $r/R = 1.35$), the cusped portion of the curve splits off from the main caustic curve. A detailed view of these cusps for $r/R = 1.35$ is shown in Fig. 5, where the corresponding angle on the initial curve is identified for several points on the caustic. Note that the ends of the caustic seem to correspond to the points where the initial curve intersects the plastic zone. For $r/R \geq 1.34$, the cusped segment of the caustic arises from the small inner loop of the initial curve, and the larger smooth portion of the caustic arises from the outer loop of the initial curve. As r/R increases, the small cusped segment of the caustic curve becomes smaller and separates further from the main part of the caustic curve.

6 Interpretation of Experiments

The following discussion is based on the assumption that, in the interpretation of experimental data, the size of the caustic curve is determined by the distance between the two points on the curve which are furthest from the X_1-axis on the screen. This distance will be denoted by D. For a purely elastic Mode I crack under quasi-static conditions, the relationship

$$\left[\left(\frac{E}{\sigma_0 \nu z_0 d}\right)^{1/2} D\right] = 2.5928 \left[\left(\frac{E}{\sigma_0 \nu z_0 d}\right)^{1/4} \frac{K_I}{\sigma_0}\right]^{2/5} \tag{21}$$

between D and the Mode I stress-intensity factor K_I is well known. Although the plastic flow stress σ_0 appears in (21), it does so only through a factor common to both sides of the equation. The form of (21) was chosen because the results with plasticity effects included could be expressed best in terms of the dimensionless quantities in square brackets in (21).

For a given crack-tip speed v/c_l, both of the dimensionless quantities $D(E/\sigma_0 \nu\, z_0 d)^{1/2}$ and $(K_I/\sigma_0)(E/\sigma_0\, \nu\, z_0 d)^{1/4}$ can be determined

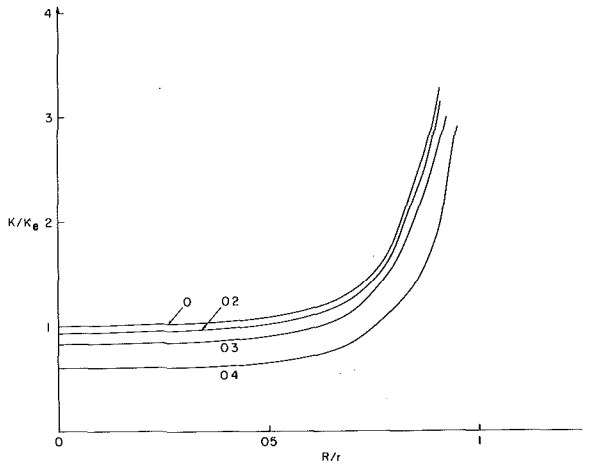

Fig. 7 Error introduced in the inferred value of K through neglect of both material inertia and plasticity effects in the analysis of experimental data

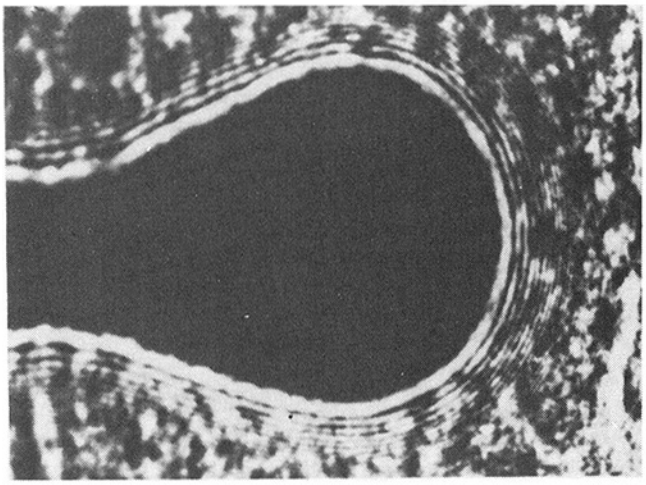

Fig. 8 Caustic formed in reflection at the tip of a propagating crack in a metallic specimen using single phase, monochromatic light

in terms of the parameter r/R, which is thus a parametric representation of the D versus K_I relationship. If the parameter r/R is eliminated (a process which can only be done numerically), then the relationship shown in Fig. 6 for four crack speeds is established. It is important to note that r/R varies alone each curve in Fig. 6, in general decreasing from left to right. The dashed curve in Fig. 6 is simply a graph of (21) which is valid for $v/c_l = 0$ and $r/R \to \infty$. As can be seen, it fits very well with the computed result for $v/c_l = 0$. It should perhaps be restated here that D is assumed to be the observed caustic size, K_I is the remote elastic stress-intensity factor within small scale yielding theory, and the relationship shown in Fig. 6 is that predicted on the basis of plane-stress theory, small scale yielding, and the Dugdale-Barenblatt one-dimensional plastic zone model. It would appear from Fig. 6 that if experimental observations are confined to cases for which $(K_I/\sigma_0)(E/\sigma_0\, \nu\, z_0\, d)^{1/4}$ is less than about 1.0, then plasticity effects need not be taken into account in the interpretation of the observations. The possibility of adjusting the value of this nondimensional parameter simply by changing z_0 is only apparent because the value of this distance is not completely arbitrary. In any experimental setup for measuring stress-intensity factors by the method of caustics, the distance z_0 must be chosen so that the initial curve lies in a region of the specimen near the crack tip where the K-dominated small scale yielding solution accurately represents the stress field. It is also observed that the influence of inertia on the D versus K_I relationship is not large if v/c_l is less than about 0.2.

Suppose now that an observed caustic of size D is interpreted in two ways. First, it is interpreted on the basis of an elastic crack model and quasi-static conditions, and the inferred value of Mode I stress-intensity factor is K_e. Alternatively, the caustic is interpreted on the basis of a dynamic line plastic zone model, and the inferred value of the Mode I stress-intensity factor in this case is simply K. The ratio K/K_e as a function of r/R is shown in Fig. 7. This result suggests that, as long as the extent of the initial curve ahead of the crack tip is at least about twice the plastic zone size, the error introduced through neglect of plasticity effects in the analysis of the data will be small. Again, this observation is based on the condition that the initial curve lies in a region of the specimen in which the K-dominated small scale yielding solution accurately represents the stress field. A qualitative discussion of this oint is included in [19]. For any extent of the plastic zone, inertial effects seem to be important only for crack speeds in excess of $0.2\, c_l$.

Finally, two photographs of caustic curves obtained in reflection for running fractures in steel specimens are shown in Figs. 8 and 9. These are preliminary photographs taken in the process of developing an experimental apparatus, and a full quantitative interpretation is not yet available. However, it does seem that the caustics are elongated in the direction of crack growth, rather than circular as they would

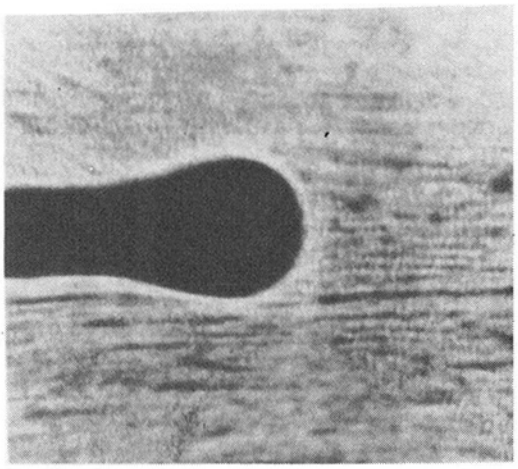

Fig. 9 Caustic formed in reflection at the tip of a propagating crack in a metallic specimen using white light

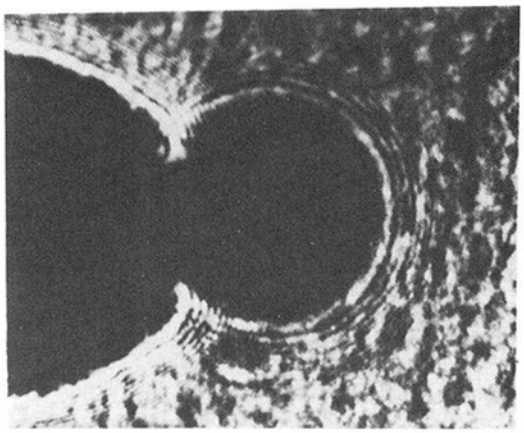

Fig. 10 Caustic at a stationary crack tip in the form of an epicycloid as predicted by elastic static analysis

be for an elastic crack as in Fig. 10. The long tail behind the main caustic curves is apparently due to the permanently deformed wake left behind as the active plastic zone passes by a material point. The Dugdale-Barenblatt crack-tip plastic zone model does not include a plastic wake effect, and no quantitative estimate of the relative size of the caustic associated with the wake region is yet available. The fringes in the optical pattern of Figs. 8 and 10 seem to be due to phase

interference. The light source used to produce the photographs shown in Figs. 8 and 10 was a laser which emits monochromatic, single phase light. The illumination outside the caustic curve results from a double reflection or mapping. That is, light waves reflected from both inside and outside the initial curve on the specimen strike the screen outside the caustic. Because of the deformation of the specimen surface, however, the light rays reflected from inside the initial curve travel a distance different from that traveled by the rays reflected from outside the initial curve. This difference in path length leads to a difference in phase at the screen which results in the observed phase interference pattern. Unlike Figs. 8 and 10, no fringes appear in the photograph in Fig. 9 because the incident light in this case was not single phase and no regular phase interference pattern could be formed.

7 Summary of Conclusions

For the line plastic zone model, the geometrical features of the initial and caustic curves are found to be strikingly different from the curves corresponding to an elastic crack. In terms of the fundamental parameters r/R and v/c, which were defined at the beginning of Section 5, the following observations are made:

1 With reference to the initial curve for $v/c = 0.2$,

(*i*) For r/R near unit, two disjoint lobes centered at $x_1 = 0$ and $x_1 = R$ are found.

(*ii*) As r/R increases from 1 to 1.34, the two lobes distort and approach each other.

(*iii*) The two lobes make contact when $r/R = 1.34$ and as r/R increases beyond 1.34, the initial curve takes the form of two nested closed curves.

(*iv*) As $r/R \to \infty$, the outer branch of the initial curve approaches the shape appropriate for a dynamic elastic crack and the inner branch shrinks to a single point on the line plastic zone.

2 With reference to the caustic curve for $v/c_l = 0.2$,

(*i*) For $1 < r/R < 1.34$, the caustic consists of two open curves.

(*ii*) As r/R increases toward 1.34, cusps are formed at the ends of the open curves and the separation distance between the two open curves decreases. The separation distance vanishes when $r/R = 1.34$.

(*iii*) For $r/R > 1.34$, the main part of the caustic is an oval curve with its longer axis in the direction of crack growth. A small secondary caustic, arising from the inner loop of the nested initial curve, splits off from the main caustic.

(*iv*) As $r/R \to \infty$, the main part of the caustic approaches the shape appropriate for a dynamic elastic crack and the secondary caustic vanishes.

3 On the basis of the line plastic zone model, plasticity effects need not be taken into account in analyzing experimental data for which $(E/\sigma_0 \nu z_0 d)^{1/4} (K_I/\sigma_0)$ is less than about 1.0.

4 The error introduced through the neglect of plasticity effects in the analysis of data will be small as long as the extent of the initial curve ahead of the crack tip is more than twice the plastic zone size.

5 Inertial effects appear to be significant for crack speeds exceeding approximately $0.2\, c_l$.

Acknowledgment

The research support of the Office of Naval Research, Structural Mechanics Program, through Grant NOOO14-78-C-51 to Brown University, is gratefully acknowledged.

References

1 Manogg, P., "Anwendung der Schattenoptik zur Untersuchung des Zerreisvorganges von Platten," Dissertationsschrift an der Universität Freiburg, 1964.

2 Theocaris, P. S., "Local Yielding Around a Crack Tip in Plexiglass," ASME JOURNAL OF APPLIED MECHANICS, Vol. 37, 1970, pp. 409–415.

3 Theocaris, P. S., and Gdoutos, E. E., "Verification of the Validity of the Dugdale-Barenblatt Model by the Method of Caustics," *Engineering Fracture Mechanics*, Vol. 6, 1974, pp. 523–535.

4 Theocaris, P. S., and Gdoutos, E. E., "The Modified Dugdale-Barenblatt Model Adapted to Various Fracture Configurations in Metals," *International Journal of Fracture*, Vol. 10, 1974, pp. 549–564.

5 Kalthoff, J. F., Winkler, S., and Beinert, J., "Dynamics Stress-Intensity Factors for Arresting Cracks in DCB specimens," *International Journal of Fracture*, Vol. 12, 1976, pp. 317–319.

6 Theocaris, P. S., "Dynamic Propagation and Arrest Measurements by the Method of Caustics on Overlapping Skew-Parallel Cracks," *International Journal of Solids and Structures*, Vol. 14, 1978, pp. 639–653.

7 Katsamanis, F., Raftopoulos, D., and Theocaris, P. S., "Static and Dynamic Stress-Intensity Factors by the Method of Transmitted Caustics," ASME *Journal of Engineering Materials and Technology*, Vol. 99, 1977, pp. 105–109.

8 Goldsmith, W., and Katsamanis, F., "Fracture of Notched Polymeric Beams Due to Central Impact," *Experimental Mechanics*, 1979, pp. 235–244.

9 Kalthoff, J. F., Beinert, J., and Winkler, S., "Influence of Dynamic Effects on Crack Arrest," EPRI 1022-1, First Semi-Annual Progress Report, Report V9/78, Institut für Festkörpermechanik, Freiburg, Germany, Aug. 1978.

10 Rosakis, A. J., "Analysis of the Optical Method of Caustics for Dynamic Crack Propagation," Report ONR-79-1 Division of Engineering Brown University, Mar. 1979, *Engineering Fracture Mechanics*, Vol. 13, 1980, pp. 331–347.

11 Theocaris, P. S., and Ioakimides, N. I., "The Equations of Caustics for Crack and other Dynamic Plane Elasticity Problems," *Engineering Fracture Mechanics*, Vol. 12, 1979, pp. 613–615.

12 Theocaris, P. S., and Gdoutos, E. E., "Surface Topology by Caustics," *Applied Optics*, Vol. 15, 1976, pp. 1629–1638.

13 Dugdale, D. S., "Yielding of Steel Sheets Containing Slits," *Journal of the Mechanics and Physics of Solids*, Vol. 8, 1960, p. 100.

14 Barenblatt, G. F., Salganik, R. I., and Cherepanov, G. P., "On the Nonsteady Motion of Cracks," *Journal of Applied Mathematics and Mechanics* (English translation of *PMM*), Vol. 26, 1962, p. 469.

15 Rosakis, A. J., and Freund, L. B., "The Effect of Crack-Tip Plasticity on the Determination of Dynamic Stress-Intensity Factors by the Optical Method of Caustics," Report N00014-78-C-0051/5, Division of Engineering, Brown University, Sept. 1980.

16 Willis, J. R., "A Comparison of the Fracture Criteria of Griffith and Barenblatt," *Journal of the Mechanics and Physics of Solids*, Vol. 15, 1967, p. 151.

17 Freund, L. B., and Clifton, R. J., "On the Uniqueness of Plane Elastodynamic Solutions for Running Cracks," *Journal of Elasticity*, Vol. 4 1974, pp. 293–299.

18 Rice, J. R., "Mathematical Analysis in the Mechanics of Fracture," *Fracture*, Vol. II, ed., Liebowitz, H., Academic Press, New York, 1968, p. 191.

19 Beinert, J., and Kalthoff, J. F., "Experimental Determination of Dynamic Stress-Intensity Factors by the Methods of Shadow Patterns," for publication in *Mechanics of Fracture*, Vol. VII, ed., Sih, G. C., Noordhoff International Publishing, Leyden, The Netherlands.

M. K. Kassir

Professor,
Department of Civil Engineering,
City College of City University
of New York,
New York, N. Y. 10031
Mem. ASME

Stress-Intensity Factor for a Three-Dimensional Rectangular Crack

An integral transform solution is developed to reduce the problem of determining the stress-intensity factor of a narrow three-dimensional rectangular crack to the solution of a Fredholm integral equation of the second kind. The crack is assumed to be embedded in an infinite elastic solid subjected to normal loading. Numerical results are presented to indicate a reduction in the value of the stress-intensity factor from the plane strain case. For an elongated rectangular crack the plane-strain stress-intensity factor is recovered.

Introduction

A problem of current interest in Fracture Mechanics is the determination of the stress-intensity factors of cracked structural components. Confining attention to embedded cracks in three-dimensional solids, analytical solutions are available to treat basic geometries like the circular, elliptical, and half-plane cracks. They involve solutions to certain half-space problems in the theory of elasticity with emphasis placed on the state of stress near the crack border. An outline of these solutions and expressions of the corresponding stress-intensity factors induced by various loading conditions are given in [1]. For flat cracks occupying other regions analytical solutions are not available and several attempts have been made to formulate the problem in term of integral equations amenable to numerical treatment (see, for example, [2–5]). Also, the nature of the singularity at the corner of a wedge-shaped crack (or punch) has been investigated in [6–8]. However, there seems to be a conspicuous lack of information in the literature concerning analytical formulation to determine the stress-intensity factor along the sides of flat rectangular crack embedded in infinitely extended solid.

It is the aim of this paper to develop an integral transform formulation to reduce the problem of determining the stress-intensity factor of a narrow rectangular crack subjected to normal loading to the solution of a standard integral equation of Fredholm type. The formulation consists of representing the components of stress and displacement in the solid in terms of double integrals containing one unknown function. By introducing the plane strain solution of a Griffith crack [9], the unknown function is shown to be governed by a Fredholm integral equation of the second kind. The example of a crack opened out by constant stress is considered in some detail. Numerical results are obtained to indicate a reduction in the value of the stress-intensity factor from the corresponding two-dimensional case. This is in agreement with the results obtained in [4, 5]. For a narrow rectangular crack the plane-strain stress-intensity factor is reached asymptotically.

Basic Equations

Consider a flat rectangular crack of sides $(2a)$ by $(2b)$ embedded in the midplane of a three-dimensional elastic solid. In terms of Cartesian coordinates (x, y, z) centered at the midpoint, the crack occupies the region $|x| \leq a$, $|y| \leq b$ of the $z = 0$ plane. Let the crack be opened out by the application of identical stresses to its surfaces. Because of symmetry, it suffices to consider the half space $z \geq 0$ with the following boundary conditions on $z = 0$:

$$\tau_{zx} = \tau_{zy} = 0, \quad \text{all } x \text{ and } y, \tag{1}$$

$$\sigma_z = -\sigma_0(x, y), \quad |x| \leq a, \quad |y| \leq b, \tag{2a}$$

$$u_z = 0, \quad |x| > a, \quad |y| > b, \tag{2b}$$

where (u_x, u_y, u_z) designate the components of the displacement vector, τ_{zx}, τ_{zy}, and σ_z denote the stresses associated with the z-plane and $\sigma_0(x, y)$ stands for the prescribed stress inside the crack surface. In addition to conditions (1) and (2), all components of displacement and stress must vanish at the remote distances.

The complete solution of this class of problems can be represented by utilizing Boussinesq's potential formulation

$$2\mu u_x = (1 - 2\nu)\frac{\partial f}{\partial x} + z\frac{\partial^2 f}{\partial x\,\partial z}, \tag{3a}$$

$$2\mu u_y = (1 - 2\nu)\frac{\partial f}{\partial y} + z\frac{\partial^2 f}{\partial y \partial z}, \tag{3b}$$

$$2\mu u_z = -2(1 - \nu)\frac{\partial f}{\partial z} + z\frac{\partial^2 f}{\partial z^2}, \tag{3c}$$

in which μ and ν denote the shearing modulus and Poisson's ratio of the material, respectively, and $f(x, y, z)$ is a harmonic function satisfying Laplace's equation in three dimensions

Contributed by the Applied Mechanics Division for publication in the JOURNAL OF APPLIED MECHANICS.

Discussion on this paper should be addressed to the Editorial Department, ASME, United Engineering Center, 345 East 47th Street, New York, N. Y. 10017, and will be accepted until September 1, 1981. Readers who need more time to prepare a Discussion should request an extension from the Editorial Department. Manuscript received by ASME Applied Mechanics Division, June, 1980; final revision, October, 1980.

$$\nabla^2 f = 0, \tag{4}$$

Some of the relevant stress components are

$$\tau_{zx} = z\frac{\partial^3 f}{\partial x^2 \partial z}, \tag{5a}$$

$$\tau_{zy} = z\frac{\partial^3 f}{\partial y^2 \partial z}, \tag{5b}$$

$$\sigma_z = -\frac{\partial^2 f}{\partial z^2} + z\frac{\partial^3 f}{\partial z^3}, \tag{5c}$$

which automatically clears the $z = 0$ surface from shearing stresses.

By the usual method of separation of the variables, a sufficiently general solution of equation (4) which is symmetric in x and y can be taken as

$$f = \int_0^\infty \int_0^\infty \frac{A(\xi, \eta)}{(\xi^2 + \eta^2)} \cos(x\xi) \cos(y\eta)\, e^{-(\xi^2+\eta^2)^{1/2} z}\, d\xi d\eta, \tag{6}$$

in which $A(\xi, \eta)$ is an unknown function and the factor $1/(\xi^2 + \eta^2)$ has been introduced for convenience. For problems possessing skew-symmetry in x and y, the cosine terms in equation (6) may be replaced by sine terms. Across the plane $z = 0$, the normal displacement and stress are

$$u_z = \frac{1-\nu}{\mu} \int_0^\infty \int_0^\infty \frac{A(\xi, \eta)}{\sqrt{\xi^2 + \eta^2}} \cos(x\,\xi) \cos(y\eta)\, d\xi\, d\eta, \tag{7a}$$

$$\sigma_z = -\int_0^\infty \int_0^\infty A(\xi, \eta) \cos(x\xi) \cos(y\eta)\, d\xi\, d\eta, \tag{7b}$$

Consequently, conditions (2) give rise to the dual integral equations

$$\int_0^\infty \int_0^\infty \frac{A(\xi, \eta)}{(\xi^2 + \eta^2)^{1/2}} \cos(x\xi) \cos(y\eta)\, d\xi\, d\eta = 0, \quad x > a, \quad y > b, \tag{8a}$$

$$\int_0^\infty \int_0^\infty A(\xi, \eta) \cos(x\xi) \cos(y\eta)\, d\xi\, d\eta = \sigma_0(x, y), \quad x \leqslant a, \quad y \leqslant b, \tag{8b}$$

for the determination of $A(\xi, \eta)$.

Reduction to an Integral Equation

With a view toward establishing the integral equation governing the unknown function, $A(\xi, \eta)$, it is convenient to express the normal stress across the crack plane in the form

$$\sigma_z(x, y, 0) = p(x)\, q(y), \quad |x| < \infty, \quad |y| < \infty, \tag{9}$$

where $p(x)$ and $q(y)$ are arbitrary functions. Inside the crack region these functions are specified (see equations (13)) while in the outside region they control the stress-intensity factor. Making use of equations (7b) and (9) and assuming the inversion of the double Fourier cosine transform, the following result is obtained:

$$A(\xi, \eta) = -\frac{4}{\pi^2} \int_0^\infty \int_0^\infty p(x)\, q(y) \cos(x\xi) \cos(y\eta)\, dx dy, \tag{10}$$

which may be abbreviated to

$$A(\xi, \eta) = -\frac{4}{\pi^2}\, p_c(\xi)\, q_c(\eta) \tag{11}$$

In equation (11), $p_c(\xi)$ and $q_c(\eta)$ designate the one-dimensional Fourier cosine transforms of the functions $p(x)$ and $q(y)$, respectively,

$$p_c(\xi) = \int_0^\infty p(x) \cos(x\xi)\, dx, \tag{12a}$$

$$q_c(\eta) = \int_0^\infty q(y) \cos(y\eta)\, dy, \tag{12b}$$

By virtue of the fact that inside the crack region, the functions $p(x)$ and $q(y)$ are specified

$$p(x) = p_0(x), \quad 0 \leqslant x \leqslant a, \tag{13a}$$

$$q(y) = q_0(y), \quad 0 \leqslant y \leqslant b, \tag{13b}$$

it immediately follows that

$$\int_0^\infty p_c(\xi) \cos(x\xi)\, d\xi = \frac{\pi}{2} p_0(x), \quad 0 \leqslant x \leqslant a, \tag{14a}$$

$$\int_0^\infty q_c(\eta) \cos(y\eta)\, d\eta = \frac{\pi}{2} q_0(y), \quad 0 \leqslant y \leqslant b, \tag{14b}$$

The next step in the analysis is to determine the corresponding relations satisfied by $p_c(\xi)$ and $q_c(\eta)$ outside the crack region. Toward this end, the relation (11) is inserted into equation (7a), and upon setting[1] $y = 0$ (in order to compute the value of the maximum stress-intensity factor), the normal displacement assumes the form

$$u_z = -\frac{4(1-\nu)}{\pi^2 \mu} \int_0^\infty p_c(\xi) \cos(x\xi)\, d\xi \int_0^\infty \frac{q_c(\eta)\, d\eta}{(\xi^2 + \eta^2)^{1/2}}, \tag{15}$$

Applying relation (12b) to equation (15), interchanging the order of integration and utilizing the result [10]

$$\int_0^\infty \frac{\cos(s\eta)\, d\eta}{(\xi^2 + \eta^2)^{1/2}} = K_0(s\xi), \quad \xi > 0, \tag{16}$$

it is found that

$$u_z = -\frac{2(1-\nu)}{\pi\mu} \int_0^\infty p_c(\xi) q_k(\xi) \cos(x\xi)\, d\xi, \tag{17}$$

where $q_k(\xi)$ denotes the relation

$$q_k(\xi) = \frac{2}{\pi} \int_0^\infty q(s) K_0(s\xi)\, ds, \tag{18}$$

In equations (16) and (18), K_0 is the modified Bessel function of the second kind of order zero. Condition (2b) when applied to the expression in equation (17) yields

$$\int_0^\infty p_c(\xi) q_k(\xi) \cos(x\xi)\, d\xi = 0, \quad x > a, \tag{19a}$$

which is the required relation outside the crack region. In exactly similar manner, the corresponding relation for $q_c(\eta)$ along the y-axis is

$$\int_0^\infty q_c(\eta) p_k(\eta) \cos(y\eta)\, d\eta = 0, \quad y > b, \tag{19b}$$

where $p_k(\eta)$ satisfies a relation identical to that expressed in equation (18) except that $q(s)$ in equation(18) should be replaced by $p(s)$.

Equations (14a) and (19a) constitute a set of standard dual integral equations with arbitrary weight function. They have the solution

$$p_c(\xi) q_k(\xi) = \int_0^\infty \phi(t)\, J_0(\xi\, t)\, dt, \tag{20}$$

where the auxiliary function, $\phi(t)$, is governed by the Fredholm equation

$$\phi(t) + \int_0^\infty \phi(\theta)\, K(\theta, t)\, d\theta = -t \int_0^t \frac{p_0(u)\, du}{(t^2 - u^2)^{1/2}}, \tag{21}$$

whose kernel is given by

$$K(\theta, t) = t \int_0^\infty s \left[\frac{1}{s\, q_k(s)} - 1\right] J_0(st)\, J_0(s\theta)\, ds, \tag{22}$$

and J_0 denotes the usual Bessel function of the first kind of order zero.

It is convenient to nondimensionalize equation (21) by substituting

$$t = ar, \quad \theta = a\rho, \quad \lambda = as$$

Moreover, suppose that the crack is opened out by a constant stress,

[1] By writing $y = \beta b, 0 \leq \beta \leq 1$, other values of the stress-intensity factor along the side of the crack can be obtained.

$p_0(x) = p_0$ (constant), then, upon introducing a new function, Φ, defined by

$$\phi(t) = \phi(ar) = -\frac{\pi}{2} p_0 a \sqrt{r}\, \Phi(r), \tag{23}$$

the integral equation (21) assumes the standard form

$$\Phi(r) + \int_0^1 \Phi(\rho)\, L(ar, a\rho)\, d\rho = \sqrt{r}\,, \tag{24}$$

in which the symmetric kernel is

$$L(ar, a\rho) = (r\rho)^{1/2} \int_0^\infty \lambda \left[\frac{1}{\left(\frac{\lambda}{a}\right) q_k\left(\frac{\lambda}{a}\right)} - 1 \right] J_0(\lambda\rho)\, J_0(\lambda r)\, d\lambda, \tag{25}$$

The next step in the analysis is to determine the function $q_k(\lambda/a)$. This will be done in the next section by assuming the plane-strain solution of a Griffith crack of length $2b$ [9].

Plane Strain Solution

A basic characteristic of any three-dimensional crack problem is the fact that the state of stress in a normal plane near a smooth crack front is essentially a plane-strain one [11]. Aside from the stress-intensity factors k_1, k_2, k_3, it can be expressed in a form independent of the applied loading and shape of the solid. Thus, for rectangular cracks with large aspect ratios, the function $q(y)$ can be considered as the normal stress, $\sigma_z(y, z)$ evaluated at $z = 0$. In the yz-plane, the appropriate crack conditions are

$$\tau_{yz}(y, 0) = 0, \qquad \text{all values of } y, \tag{26a}$$

$$\sigma_z(y, 0) = q_0(y), \quad 0 \le |y| \le b, \tag{26b}$$

$$u_z(y, 0) = 0, \qquad |y| > b, \tag{26c}$$

It is well known that the solution of this problem can be represented by

$$2\mu u_z(y, z) = \int_0^\infty [2(1 - \nu) + sz]\, B(s) \cos(sy)\, e^{-sz}\, ds, \tag{27a}$$

$$\sigma_z(y, z) = -\int_0^\infty s(1 + sz)\, B(s) \cos(sy)\, e^{-sz}\, ds, \tag{27b}$$

$$\tau_{yz}(y, z) = -z \int_0^\infty s^2 B(s) \sin(sy)\, e^{-sz}\, ds, \tag{27c}$$

where the unknown function, $B(s)$, is found from the relation

$$B(s) = -\frac{2}{\pi} \int_0^b tJ_0(st)\, dt \int_0^t \frac{q_0(y)\, dy}{(t^2 - y^2)^{1/2}}, \tag{28}$$

It follows from equation (27b) that

$$q(y) = -\int_0^\infty sB(s) \cos(sy)\, ds, \tag{29}$$

Inserting equation (29) into equation (18), making use of the result [10]

$$\int_0^\infty K_0(\xi y) \cos(sy)\, dy = \frac{\pi}{2(\xi^2 + s^2)^{1/2}}, \tag{30}$$

it is found that

$$q_k(\xi) = -\int_0^\infty \frac{sB(s)\, ds}{(s^2 + \xi^2)^{1/2}}, \tag{31}$$

Applying the relation (28) to equation (31), making a permissible change in the order of integration and noting the result

$$\int_0^\infty \frac{s\, J_0(st)\, ds}{(s^2 + \xi^2)^{1/2}} = \frac{e^{-t\xi}}{t}, \tag{32}$$

it is found that

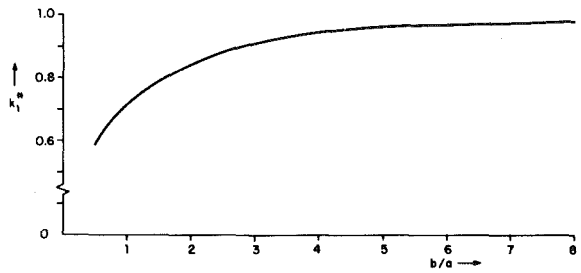

Fig. 1 Variation of K_1^* with b/a

$$q_k(\xi) = \frac{2}{\pi} \int_0^b e^{-t\xi} dt \int_0^t \frac{q_0(y)\, dy}{(t^2 - y^2)^{1/2}}, \tag{33}$$

The relation (33) determines the transform function q_k in terms of the specified stress and enables the integral equation to be solved. For the example considered earlier, $q_0(y) = 1$, and equation (33) yields

$$q_k(\xi) = \frac{1}{\xi}[1 - e^{-b\xi}], \tag{34}$$

The integral (25) now takes the form

$$L(ar, a\rho) = (r\rho)^{1/2} \int_0^\infty \frac{\lambda}{e^{(b/a)\lambda} - 1} J_0(\lambda r) J_0(\lambda\rho)\, d\lambda, \tag{35}$$

which is convergent throughout its range and can be evaluated numerically.

Stress-Intensity Factor

In order to compute the stress-intensity factor, the relation (23) is inserted into equation (20) and after performing an integration by parts it is found that

$$p_c(\xi) = -\frac{\pi a p_0}{2\xi q_k(\xi)} \left\{ \Phi(1) J_1(a\xi) + \int_0^1 sJ_1(s\xi) \frac{d}{ds}[s^{-1/2}\, \Phi(s)]\, ds \right\}, \tag{36}$$

and since

$$p(x) = \frac{2}{\pi} \int_0^\infty p_c(\xi) \cos(x\xi)\, d\xi, \tag{37}$$

it follows that

$$p(x) = -p_0 a \Phi(1) \int_0^\infty \frac{J_1(a\xi) \cos(x\xi)}{\xi\, q_k(\xi)}\, d\xi + \ldots\ldots, \tag{38}$$

where terms which are finite as $x \to a$ have been neglected. Since the singularities of the integral in equation (38) occurs at the upper limit, and as evident from equation (34) that $\xi\, q_k(\xi) \to 1$ as $\xi \to \infty$, it follows that the integral in equation (38) yields:

$$p(x) = -p_0 \Phi(1) \left[1 - \frac{x}{(x^2 - a^2)^{1/2}} \right] + \ldots\ldots, \tag{39}$$

The normal stress outside the crack can be obtained from equations (9), (28), (29), and (39). Near the crack edge it can be expressed in the standard form

$$\sigma_z(x, y, 0) = \frac{k_1}{(2\pi r)^{1/2}} + \ldots\ldots \tag{40}$$

where r is a small distance measured from any point on the side $x = a$ of the rectangle (except the corner point) and the stress-intensity factor, k_1, is given by

$$k_1 = \Phi(1)\, p_0 \sqrt{\pi a}\,, \tag{41}$$

The factor k_1 is nondimensionalized with reference to the plane-strain factor and the variation of the factor

$$k_1^* = \frac{k_1}{p_0(\pi a)^{1/2}}, \tag{42}$$

with different aspect ratios of the crack sides is shown in Fig. 1. It is evident that there is a reduction in the stress-intensity factor for the rectangular crack. For an infinite strip crack ($b \to \infty$), the integral (35) vanishes, $\Phi(1) = 1$, and the plane strain factor is reached. It should also be mentioned that the results shown in Fig. 1 agree with those obtained in [4, 5] by other methods.

Conclusion

An integral transform technique is presented to treat the problem of determining the stress-intensity factor of a three-dimensional rectangular crack embedded in an infinite elastic solid. The crack is assumed to be subjected to normal loadings. By introducing the plane strain solution across the width of the crack the stress-intensity factor along the crack length is shown to be governed by a standard Fredholm integral equation. For the particular case of constant loading, the integral equation governing the maximum value of the stress-intensity factor is solved numerically and the result indicates a reduction in the three-dimensional stress-intensity factor from the plane strain solution. As expected, for a rectangular crack with large aspect ratio (infinite strip crack), the integral equation degenerates and the stress-intensity factor becomes identical to that of the plane-strain geometry. The technique employed in this paper may also be adopted to the case of shear loading on the crack surface. However, this is left for future study.

References

1 Kassir, M. K., and Sih, G. C., *Three-Dimensional Crack Problems*, Noordhoff International Publishing. Leyden, The Netherlands, 1975.

2 Martynenko, M. D., "Some Three-Dimensional Problems on the Equilibrium of an Elastic Body Weakened by a Crack," *Prikladnaya Mekhanika*, Vol. 6, 1970, pp. 84–88 (English translation, 1970; pp. 1107–1111).

3 Andreikiv, A. E., and Stadnik, M. M., "Propagation of a Plane Crack With a Piecewise Smooth Contour," *Prikladnaya Mekhanika*, Vol. 10, 1973, pp. 50–56 (English translation, 1974, pp. 1078–1083).

4 Weaver, J., "Three-Dimensional Crack Analysis," *International Journal of Solids* and *Structures*, Vol. 13, 1977, pp. 321–330.

5 Mastrojannis, E. N., Keer, L. M., and Mura, T., "Stress-Intensity Factor for a Plane Crack Under Normal Pressure," *International Journal of Fracture*, Vol. 15, 1979, pp. 247–258.

6 Borodachev, N. M., "Contact Problem for a Stamp With a Rectangular Base," *Applied Mathematics and Mechanics (PMM)*, Vol. 40, 1976, pp. 554–560.

7 Keer, L. M., and Parihar, K. S., "A Note on the Singularity at the Corner of a Wedge-Shaped Punch or Crack," *Journal of Applied Mathematics*, SIAM, Vol. 34, 1978, pp. 297–302.

8 Pu, S. L., and Hussain, M. A., "Note on Apex Singularities of a Wedge-Shaped Crack Under All Modes," ASME JOURNAL OF APPLIED MECHANICS, Vol. 46, 1979, pp. 705–707.

9 Sneddon, I. N., and Lowengrub, M., *Crack Problems in the Classical Theory of Elasticity*, Wiley, New York, 1969.

10 Erdelyi, A., *Tables of Integral Transforms*, Vols. 1 and 2, McGraw-Hill, New York, 1954.

11 Kassir, M. K., and Sih, G. C., "Three-Dimensional Stress Distribution Around an Elliptical Crack Under Arbitrary Loadings," ASME JOURNAL APPLIED MECHANICS, Vol. 33, 1966, pp. 601–611.

C.-F. Sheng
Ingersoll-Rand Company,
Terry Division,
Windsor, Conn. 06095
Assoc. Mem. ASME

L. Wheeler
Professor,
Department of Mechanical Engineering,
University of Houston,
Houston, Tex. 77004

Crack Path Prediction for a Kinked Crack in the Neighborhood of a Circular Inclusion in an Infinite Medium

In this paper, we study the effects of the elasticity and proximity of a circular inclusion upon the fracture angle of a bent crack in the surrounding matrix. The medium is assumed to be in plane strain, and loaded in uniaxial tension by stresses acting perpendicular to the main branch of the crack. A comparison is made of fracture-angle predictions based upon current theories governing the initial fracture angle.

Introduction

Problems concerned with the branching and kinking of cracks have attracted considerable interest in recent years. Among the early publications, a key investigation is Sih's [1] work on the kinked (bent) crack in an infinite medium subject to antiplane shear deformation. For further discussion of this problem, see references [2–4] and for the related plane strain case, which is the context of the present discussion, see [3,4,5–20].

The mathematical techniques applied to these problems can be grouped into four categories. The first, and most commonly used is the Kolosov-Muskhelishvili potential formulation [5–10], where a mapping function derived by Darwin is used to transform the star-shaped crack geometry on to the unit circle. The solution is then found either by solving an integral equation or using series expansions of the complex potential functions and the mapping function.

Bilby, Cardew, and Howard [12] used an approach due to Khrapkov [11] to evaluate the stress intensity for kinked and symmetrically forked cracks. Their results agree with Chatterjee's work [8], but an incorrect comparison made by these authors led them to a 20 percent difference between their findings and those of [9]. However, the results of the present paper show them ([8, 9]) to be in agreement.

Theocaris and Ioakimidis used a method proposed by Datsyshin and Savruk [13] to solve the problems of the symmetrically branched crack [14], asymmetrically branched crack [15], and kinked crack [16]. This approach, which does not make use of conformal mapping, is applicable to problems involving essentially arbitrary crack shape.

Over the past 10 years a fourth method has come into prominence. In this approach, a crack is viewed as the locus of a dislocation pileup and the problem is reduced to the consideration of singular integral equations involving the dislocation density, which are usually solved numerically. We were led by the results in [18–20], which deal with crack branching, to employ this approach in the present investigation.

Another advantage of the method just mentioned is that it lends itself to a convenient determination of stress-intensity factors, which are needed in connection with certain of the criteria for determining fracture angle. We turn now to a discussion of these criteria.

Criteria for Mixed Mode Fracture

The current criteria can be summarized as follows:

1 Maximum normal stress criterion [21],
2 Maximum normal stress at a critical distance [22],
3 Minimum strain-energy density [23],
4 Minimum strain-energy density at a critical distance [24],
5 Maximum energy-release rate.

For an inclined straight crack in a homogeneous isotropic solid, we can find the fracture angle through

$$K_I \sin\theta + K_{II}(3\cos\theta - 1) = 0 \tag{1}$$

when Theory 1 is applied [21], whereas the second criterion gives

$$\frac{1}{\sqrt{2r_0}}\left(-\frac{3}{4}\right)\cos\frac{\theta}{2}\{K_I \sin\theta + K_{II}(3\cos\theta - 1)\} + 2A\sin\theta\cos\theta = 0. \tag{2}$$

The stress-intensity factors K_I and K_{II} are regarded as known and the constant A comes from the second-order term in the Williams

Contributed by the Applied Mechanics Division of THE AMERICAN SOCIETY OF MECHANICAL ENGINEERS, and presented at the 1981 Joint ASME/ASCE Applied Mechanics, Fluids Engineering, and Bioengineering Conference, University of Colorado, Boulder, Colo., June 22–27, 1981.
Discussion on this paper should be addressed to the Editorial Department, ASME, United Engineering Center, 345 East 47th Street, New York, N. Y. 10017, and will be accepted until September 1, 1981. Readers who need more time to prepare a Discussion should request an extension from the Editorial Department. Manuscript received by ASME Applied Mechanics Division, July, 1980; final revision, November, 1980. Paper No. 81-APM-31.

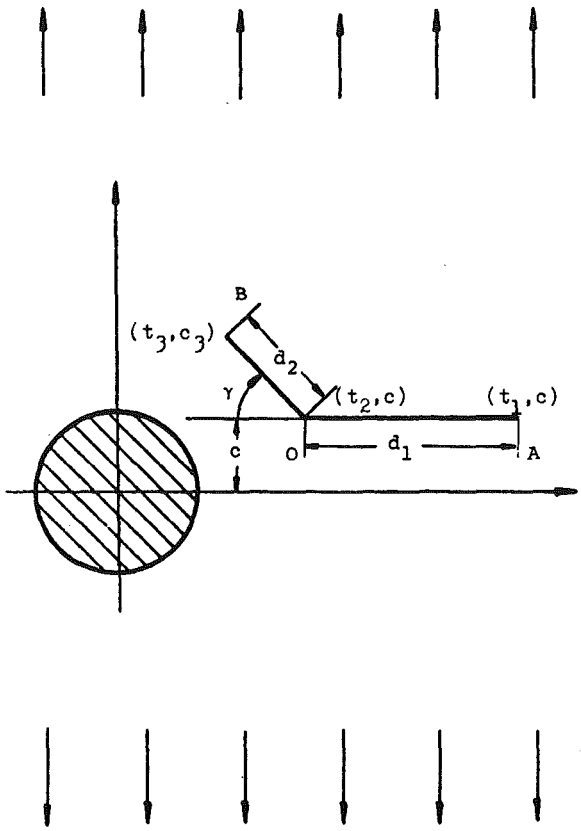

Fig. 1 Geometry of the kinked crack in the vicinity of a circular inclusion

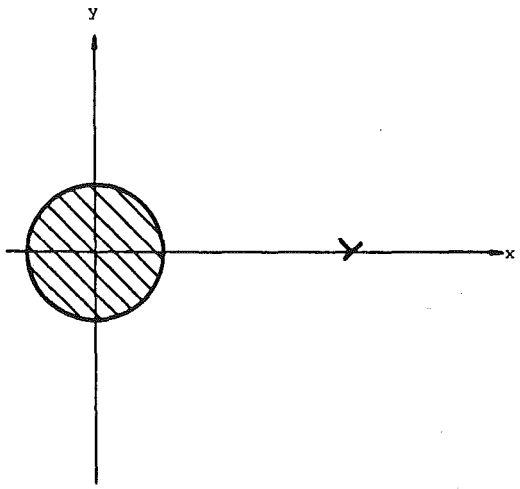

Fig. 2 Edge dislocation in the neighborhood of a circular inclusion (from [17])

crack-tip stress field. (The first term is of order $O(r^{-1/2})$, the second term is a function of θ, but not r, and the third term of order $O(r^{1/2})$.) Equation (2) is obtained by setting $(d\sigma_\theta/d\theta)(r_0, \theta) = 0$, where σ_θ denotes the circumferential stress, as calculated in [24]. The critical distance r_0 can be found experimentally and it was suggested by both Williams [22] and Sih [29] that $r_0 = 0.00787$ mm for polymethylmethacrylate.

Another controlling factor, the critical energy-release rate S_c, is used in Theory 3 [23]. The energy-release rate, S, is a direction-sensitive quantity, and the expression relevant to the present analysis is, from [23].

$$S = a_{11}K_I^2 + 2a_{12}K_IK_{II} + a_{22}K_{II}^2 \tag{3}$$

The explicit formulas for $a_{ij}(i, j = 1, 2)$ are given in [23] and will not be reproduced here. The initial fracture angle is found by setting $dS/d\theta = 0$. The resulting expression is

$$K_I^2[\sin 2\theta - (\kappa - 1)\sin\theta] + 2K_IK_{II}[2\cos 2\theta - (\kappa - 1)\cos\theta] + K_{II}^2[-3\sin 2\theta - (1 - \kappa)\sin\theta] = 0 \tag{4}$$

where κ is given in terms of Poisson's ratio as $\kappa = 3 - 4\nu$.

The strain-energy density function is related to S near the crack tip through

$$W = (S/r) + C_1(\theta) + O(r). \tag{5}$$

It is clear that sufficiently near the tip, S furnishes the information needed to find the direction of minimum W.

In the criterion which we designate as Theory 4, the effect of $C_1(\theta)$ in (5) comes into play. Rather than attempt to find this term, our approach is to resort to the expressions

$$W = \frac{1}{2E}[\sigma_{xx}^2 - 2\nu\sigma_{xx}\sigma_{yy} + \sigma_{yy}^2 + 2(1 + \nu)\sigma_{xy}^2] \tag{6}$$

for plane stress, and

$$W = \frac{1 + \nu}{2E}[(1 - \nu)(\sigma_{xx}^2 + \sigma_{yy}^2) - 2\nu\sigma_{xx}\sigma_{yy} + 2\sigma_{xy}^2] \tag{7}$$

for plane strain. We evaluate $W(r_0, \theta)$ numerically by carrying out the appropriate calculations for σ_{xx}, σ_{yy}, and σ_{xy}. We then search out the value of θ which minimizes $W(r_0, \theta)$.

The final principle is a two-dimensional version of the Griffith-Irwin "Maximum Energy-Release Criterion." The energy-release rate is given by

$$G = (1 - \nu^2)(K_I^2 + K_{II}^2)/E \quad \text{(plane strain)} \tag{8}$$

where $K_I(\theta)$ and $K_{II}(\theta)$ are stress-intensity factors for the limiting case where the length of the propagation branch goes to zero.

Formulation

The crack shown in Fig. 1 is situated in an elastic material (the "matrix") characterized by the constants (μ_1, κ_1), which is loaded at infinity by uniaxial tension perpendicular to the main branch of the crack. Near the angled tip is a bonded tubular elastic inclusion, circular in cross section and of constants (μ_2, κ_2). Here, μ_1 and μ_2 denote the shear moduli, whereas $\kappa_1 = 3 - 4\nu_1$ and $\kappa_2 = 3 - 4\nu_2$, ν_1 and ν_2 being Poisson's ratios.

The problem just stated will, for convenience, be solved by superposing the solutions of two problems. The configuration and loading for the first problem (Problem I) is as in Fig. 1, but without the crack.

In the second problem (Problem II), the geometry is the same as the main problem, but instead of loading at infinity, surface tractions are prescribed along the crack surfaces. If we require these surface tractions to be equal in magnitude and opposite in sign to the tractions obtained in Problem I, then it is clear that the stresses for the main problem result from summing those of Problems I and II. Furthermore, Problem II gives the same stress-intensity factors as the main problem.

Consider now another problem, Problem II′, having a continuous distribution of edge dislocations spread along the crack locus. If the dislocations are so distributed that the surface tractions induced along these segments are equal to what we specified in Problem II, then these two problems have identical solutions.

As a prerequisite to Problem II′, we consider the stress field produced by a single dislocation in the presence of a circular inclusion. This problem, whose configuration is shown in Fig. 2, was solved in [17]. We here cite the solution in the form given by Erdogan and Gupta [19]:

$$\sigma_{xx} = [\mu_1/\pi(\kappa_1 + 1)](H_{xx1}b_x + H_{xx2}b_y).$$
$$\sigma_{yy} = [\mu_1/\pi(\kappa_1 + 1)](H_{yy1}b_x + H_{yy2}b_y), \tag{9}$$

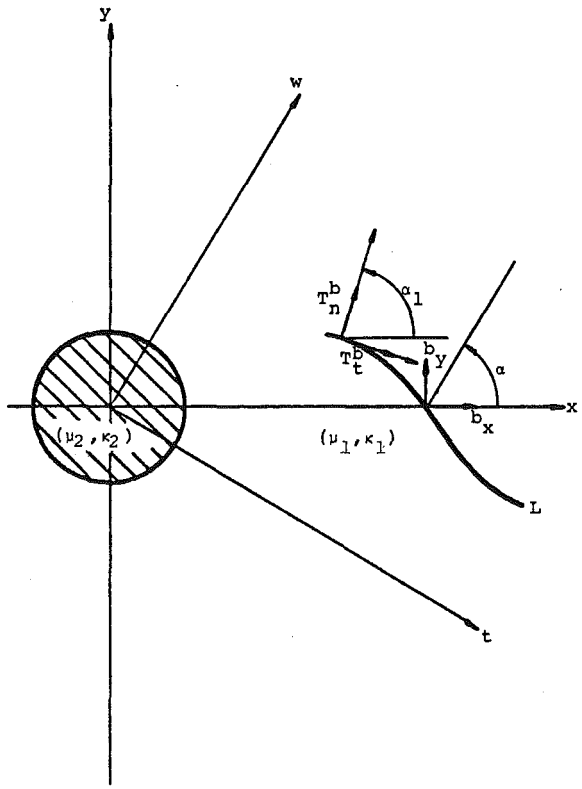

Fig. 3 Geometry showing the dislocations b_x and b_y in x-y coordinate, and a curved crack in the vicinity of a circular inclusion

$$\sigma_{xy} = [\mu_1/\pi(\kappa_1 + 1)](H_{xy1}b_x + H_{xy2}b_y). \quad (9)$$

(*Cont.*)

The quantities H_{xx1}, H_{xx2}, H_{yy1}, H_{yy2}, H_{xy1}, and H_{xy2} are written in full in [19], and b_x, b_y denote the components of the Burger vector.

The surface tractions along the crack locus which result from the foregoing stress field are

$$[\pi(\kappa_1 + 1)/\mu_1]T_n{}^b = A_{nt}b_t + A_{nw}b_w$$
$$[\pi(\kappa_1 + 1)/\mu_1]T_t{}^b = A_{tt}b_t + A_{tw}b_w \quad (10)$$

where b_t and b_w are the components of the Burger vector in the (t, w) coordinate system (see Fig. 3). The coefficients A_{nt}, A_{nw}, A_{tt}, and A_{tw} are given by

$$A_{nt} = (H_{xx1}\sin\alpha - H_{xx2}\cos\alpha)\cos^2\alpha_1 + (H_{yy1}\sin\alpha - H_{yy2}\cos\alpha)\sin^2\alpha_1 + (H_{xy1}\sin\alpha - H_{xy2}\cos\alpha)\sin 2\alpha_1,$$

$$A_{nw} = (H_{xx1}\cos\alpha + H_{xx2}\sin\alpha)\cos^2\alpha_1 + (H_{yy1}\cos\alpha + H_{yy2}\sin\alpha)\sin^2\alpha_1 + (H_{xy1}\cos\alpha + H_{xy2}\sin\alpha)\sin 2\alpha_1,$$

$$A_{tt} = [(H_{xx1} - H_{yy1})\sin\alpha - (H_{xx2} - H_{yy2})\cos\alpha](\sin 2\alpha_1/2) - (H_{xy1}\sin\alpha - H_{xy2}\cos\alpha)\cos 2\alpha_1,$$

$$A_{tw} = [(H_{xx1} - H_{yy1})\cos\alpha + (H_{xx2} - H_{yy2})\sin\alpha](\sin 2\alpha_1/2) - (H_{xy1}\cos\alpha + H_{xy2}\sin\alpha)\cos 2\alpha_1. \quad (11)$$

The $x - y$ and $t - w$ coordinates and the geometric meaning of α and α_1 are shown in Fig. 3.

Using (10) as a Green's function, we obtain four integral equations. They relate the surface tractions to the dislocation densities along the kinked crack locus.

Introduce the notation $f_1(t) = -b_t(t), f_2(t) = -b_w(t)$ for dislocation densities on line OA; $f_3(t) = -b_t(t), f_4(t) = -b_w(t)$ for densities on line OB; and define

$$\begin{bmatrix} k_{11} & k_{12} & k_{13} & k_{14} \\ k_{21} & k_{22} & k_{23} & k_{24} \\ k_{31} & k_{32} & k_{33} & k_{34} \\ k_{41} & k_{42} & k_{43} & k_{44} \end{bmatrix} = \begin{bmatrix} [-\overline{A}_{nt}]_{A,A} & [-\overline{A}_{nw}]_{A,A} & [-A_{nt}]_{A,B} & [-A_{nw}]_{A,B} \\ [-\overline{A}_{tt}]_{A,A} & [-\overline{A}_{tw}]_{A,A} & [-A_{tt}]_{A,B} & [-A_{tw}]_{A,B} \\ [-A_{nt}]_{B,A} & [-A_{nw}]_{B,A} & [-\overline{A}_{nt}]_{B,B} & [-\overline{A}_{nw}]_{B,B} \\ [-A_{tt}]_{B,A} & [-A_{tw}]_{B,A} & [-\overline{A}_{tt}]_{B,B} & [-\overline{A}_{tw}]_{B,B} \end{bmatrix} \quad (12)$$

where $[-\overline{A}_{nt}]_{\alpha,\alpha}$, $[-\overline{A}_{nw}]_{\alpha,\alpha}$, $[-\overline{A}_{tt}]_{\alpha,\alpha}$, and $[-\overline{A}_{tw}]_{\alpha,\alpha}$ ($\alpha = A$ or B) are regular parts of $[-A_{nt}]_{\alpha,\alpha}$, $[-A_{nw}]_{\alpha,\alpha}$, $[-A_{tt}]_{\alpha,\alpha}$, and $[-A_{tw}]_{\alpha,\alpha}$. The notation $[\ ]_{A,B}$, for instance, stands for the effect at a point of line OA of a continuous distribution of dislocations on line OB.

The four equations we just mentioned can be written as

$$\frac{\pi(\kappa_1+1)}{\mu_1}p_1(t) = 2\int_{t_2}^{t_1}\frac{f_2}{t_0-t}dt_0 + \int_{t_2}^{t_1}(k_{11}f_1 + k_{12}f_2)dt_0 + \int_{t_3}^{t_2}(k_{13}f_3 + k_{14}f_4)\frac{dt_0}{\cos\gamma}$$

$$\frac{\pi(\kappa_1+1)}{\mu_1}p_2(t) = 2\int_{t_2}^{t_1}\frac{f_1}{t_0-t}dt_0 + \int_{t_2}^{t_1}(k_{21}f_1 + k_{22}f_2)dt_0 + \int_{t_3}^{t_2}(k_{23}f_3 + k_{24}f_4)\frac{dt_0}{\cos\gamma}$$

$$\frac{\pi(\kappa_1+1)}{\mu_1}p_3(t) = \int_{t_3}^{t_2}\left[2\left(\frac{\sin\gamma f_3}{t_0-t} + \frac{\cos\gamma f_4}{t_0-t}\right) + k_{33}f_3 + k_{34}f_4\right]\cdot\frac{dt_0}{\cos\gamma} + \int_{t_2}^{t_1}(k_{31}f_1 + k_{32}f_2)dt_0$$

$$\frac{\pi(\kappa_1+1)}{\mu_1}p_4(t) = \int_{t_3}^{t_2}\left[2\left(\frac{\cos\gamma f_3}{t_0-t} + \frac{-\sin\gamma f_4}{t_0-t}\right) + k_{43}f_3 + k_{44}f_4\right]\cdot\frac{dt_0}{\cos\gamma} + \int_{t_2}^{t_1}(k_{41}f_1 + k_{42}f_2)dt_0 \quad (13)$$

where $-p_i(t)$ $(i = 1, 2, 3, 4)$ are surface tractions from the corresponding crack locus of Problem I.

In order to complete the formulation, we require that $\int_L d\omega = 0$, where ω denotes the relative displacement across the crack locus [28]. This condition, which is a single-valuedness condition, assumes the form

$$\int_{t_2}^{t_1}f_1(t_0)dt_0 + \int_{t_3}^{t_2}\frac{f_3(t_0)}{\cos\gamma}dt_0 = 0,$$
$$\int_{t_2}^{t_1}f_2(t_0)dt_0 + \int_{t_3}^{t_2}\frac{f_4(t_0)}{\cos\gamma}dt_0 = 0. \quad (14)$$

in the present problem.

Stress-Intensity Factors and the Standard Form of a System of Singular Integral Equations

Following the standard procedure for dealing with singular integral equations, we first define

$$g_i(t_0) = (t_0 - t_2)^\beta(t_1 - t_0)^{1/2}f_i(t_0) \quad (i = 1, 2)$$
$$g_i(t_0) = (t_2 - t_0)^\beta(t_0 - t_3)^{1/2}f_i(t_0) \quad (i = 3, 4) \quad (15)$$

so that $g_i(t_0)$ $(i = 1, 2, 3, 4)$ is Hölder continuous. The exponent β represents the strength of the corner point singularity [26]. The change of variables

$$\xi_1 = \frac{2t_0 - (t_1 + t_2)}{t_1 - t_2}$$
$$\xi_2 = -\left[\frac{2t_0 - (t_2 + t_3)}{t_2 - t_3}\right] \quad (16)$$

in (15) furnishes

$$f_i(\xi_1) = \frac{\kappa_1 + 1}{2\mu_1}\frac{h_i(\xi_1)}{(1-\xi_1)^{1/2}(1+\xi_1)^\beta} \quad (i = 1, 2) \quad (17)$$

$$f_i(\xi_2) = \frac{\kappa_1 + 1}{2\mu_1} \frac{h_i(\xi_2)}{(1-\xi_2)^{1/2}(1+\xi_2)^{\beta}} \quad (i = 3, 4) \tag{17}$$

(Cont.)

where h_i and g_i are related through

$$\frac{\kappa_1 + 1}{2\mu_1} h_i(\xi_1) = \frac{g_i(t_0(\xi_1))}{(d_1/2)^{1/2+\beta}} \quad (i = 1, 2)$$

$$\frac{\kappa_1 + 1}{2\mu_1} h_i(\xi_2) = \frac{g_i(t_0(\xi_2))}{(d_2 \cos\gamma/2)^{1/2+\beta}} \quad (i = 3, 4) \tag{18}$$

By a simple manipulation, (12) becomes

$$\pi p_1(\bar{\xi}) = \int_{-1}^{1} \left[\frac{h_2}{\xi - \bar{\xi}} + K_{11}h_1 + K_{12}h_2 + K_{13}h_3 + K_{14}h_4 \right] \cdot \frac{d\xi}{(1-\xi)^{1/2}(1+\xi)^{\beta}}$$

$$\pi p_2(\bar{\xi}) = \int_{-1}^{1} \left[\frac{h_1}{\xi - \bar{\xi}} + K_{21}h_1 + K_{22}h_2 + K_{23}h_3 + K_{24}h_4 \right] \cdot \frac{d\xi}{(1-\xi)^{1/2}(1+\xi)^{\beta}}$$

$$\pi p_3(\bar{\xi}) = \int_{-1}^{1} \left[\frac{-\sin\gamma h_3}{\xi - \bar{\xi}} - \frac{\cos\gamma h_4}{\xi - \bar{\xi}} + K_{31}h_1 + K_{32}h_2 + K_{33}h_3 + K_{34}h_4 \right] \frac{d\xi}{(1-\xi)^{1/2}(1+\xi)^{\beta}}$$

$$\pi p_4(\bar{\xi}) = \int_{-1}^{1} \left[\frac{-\cos\gamma h_3}{\xi - \bar{\xi}} + \frac{\sin\gamma h_4}{\xi - \bar{\xi}} + K_{41}h_1 + K_{42}h_2 + K_{43}h_3 + K_{44}h_4 \right] \frac{d\xi}{(1-\xi)^{1/2}(1+\xi)^{\beta}} \tag{19}$$

where

$$K_{ij} = \frac{1}{4} \begin{bmatrix} d_1k_{11} & d_1k_{12} & d_2k_{13} & d_2k_{14} \\ d_1k_{21} & d_1k_{22} & d_2k_{23} & d_2k_{24} \\ d_1k_{31} & d_1k_{32} & d_2k_{33} & d_2k_{34} \\ d_1k_{41} & d_1k_{42} & d_2k_{43} & d_2k_{44} \end{bmatrix}$$

With $d_1 = (t_1 - t_2)$, $d_2 = (t_2 - t_3)/\cos\gamma$.

Similarly, the single-valuedness condition takes the form

$$\int_{-1}^{1} [d_1h_1 + d_2h_3] \frac{d\xi}{(1-\xi)^{1/2}(1+\xi)^{\beta}} = 0$$

$$\int_{-1}^{1} [d_1h_2 + d_2h_4] \frac{d\xi}{(1-\xi)^{1/2}(1+\xi)^{\beta}} = 0 \tag{20}$$

As for the stress-intensity factors, it follows directly from the formulas for the crack-tip stress field that

$$K_{\mathrm{I}}(t_1) = \lim_{t \to t_1} [2(t - t_1)]^{1/2} p_1(t)$$

$$K_{\mathrm{II}}(t_1) = \lim_{t \to t_1} [2(t - t_1)]^{1/2} p_2(t)$$

$$K_{\mathrm{I}}(t_3) = \lim_{t \to t_3} [2(t_3 - t)/\cos\gamma]^{1/2} p_3(t)$$

$$K_{\mathrm{II}}(t_3) = \lim_{t \to t_3} [2(t_3 - t)/\cos\gamma]^{1/2} p_4(t) \tag{21}$$

By using the procedure found in [19], we arrive at

$$\frac{K_{\mathrm{I}}(t_1)}{\sigma(d_1)^{1/2}} = -\frac{h_2(1)}{2^{\beta}},$$

$$\frac{K_{\mathrm{I}}(t_3)}{\sigma(d_2)^{1/2}} = \frac{1}{2^{\beta}} (\sin\gamma h_3(1) + \cos\gamma h_4(1)).$$

$$\frac{K_{\mathrm{II}}(t_1)}{\sigma(d_1)^{1/2}} = -\frac{h_1(1)}{2^{\beta}},$$

$$\frac{K_{\mathrm{II}}(t_3)}{\sigma(d_2)^{1/2}} = \frac{1}{2^{\beta}} (\cos\gamma h_3(1) - \sin\gamma h_4(1)). \tag{22}$$

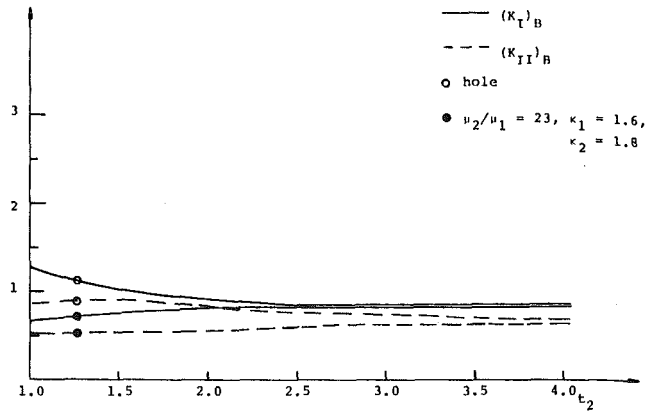

Fig. 4 Stress-intensity factors for the kinked crack tip B ($\gamma = -45°$, $d_1 = 1$, $d_2 = 0.1$, $R = 1$)

Numerical Methods and Results

After examining the various numerical methods, we decided on the closed-type (Lobatto) quadrature suggested by Ioakimidis and Theocaris [27]. This approach avoids extrapolation procedures for the estimation of the stress-intensity factors at the crack tips.

The numerical counterparts of (19) and (20) consist of $(4n - 2)$ linear equations with $4n$ unknowns (n is the number of abscissas for the integration formula). We thus require two more equations. Our scheme is to define a new function $\bar{h}_i(\xi)$ through [16]

$$\bar{h}_i(\xi) = h_i(\xi)\,(1+\xi)^{1/2-\beta} \qquad (i, = 1, 2, 3, 4) \tag{23}$$

and then replace $h_i(\xi)/(1-\xi)^{1/2}(1+\xi)^{\beta}$ in (19) and (20) by $\bar{h}_i(\xi)/(1-\xi)^{1/2}(1+\xi)^{1/2}$. This weight function $(1+\xi)^{-1/2}(1-\xi)^{-1/2}$ leads us to use the Lobatto-Chebyshev numerical integration formula of [27] to solve the present problem.

The singularities of the dislocation density functions $f_i(t)$ [$i = 1, 2, 3, 4$] are of the order $(t - t_2)^{-\beta}$, where $0 \le \beta \le \frac{1}{2}$ [26]. Therefore, the exponent $(\frac{1}{2} - \beta)$ in (23) is always greater than or equal to zero. At the corner point where $\xi = -1$, (23) gives

$$\bar{h}_i(-1) = 0 \quad (i = 1, 2, 3, 4). \tag{24}$$

The two equations needed to solve the new form of (19) and (20) ($\bar{h}_i(\xi)$ is the unknown function) may be selected from among (24). Table 1 illustrates the results for different choices of conditions in (24) in solving (19) and (20). Minor differences in stress-intensity factors occur in Cases 2 and 5. The results for other cases are indistinguishable.

The reason is simple. By requiring $\bar{h}_1(-1) = \bar{h}_3(-1) = 0$ (Case 2), we lose control over the values of dislocation density functions with the burgers vector in the $-w$-direction. In any of the four other cases, say Case 3, since we pin down the exact values of $\bar{h}_1(-1)$ for burgers vector in the $-t$-direction and $\bar{h}_4(-1)$ in the $-w$-direction, better results are anticipated.

Fig. 4 shows the effect of the proximity of an inclusion on the stress-intensity factors of a kinked crack having $d_1 = 1$, $d_2 = 0.1$, $R = 1$, and $\gamma = -45°$. Two different kinds of inclusions are considered, the first being a comparatively stiff inclusion, with material constants $\mu_2/\mu_1 = 23$, $\kappa_1 = 1.6$, and $\kappa_2 = 1.8$. The second is the special case when the inclusion becomes a hole ($\mu_2 = 0$).

The results for the stress-intensity factors plotted against γ for various inclusions are shown in Fig. 5. The point (t_2, c) is chosen close enough to the inclusion to sense its influence.

Table 2 shows the comparison among most of the results for the kinked crack problem (without inclusion) available in the literature. The present findings agree with the work of Kitagawa [10], Chatterjee [8], and Ioakimidis [16] to within 0.05 percent.

The results for normal stress σ_θ and strain-energy density W at a critical distance $r^* = 0.002$ from the crack tip are plotted as a function

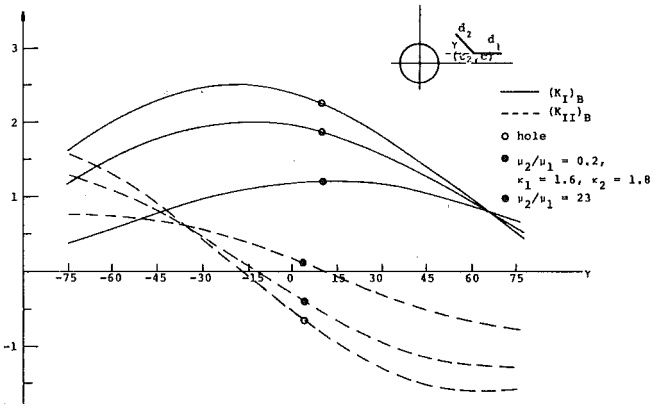

Fig. 5 Variation of the stress-intensity factors at the kinked crack tips for the angle γ varying between $-75°$ and $75°$ ($t_2 = 0.75$, $c = 0.80$, $d_2 = 0.001$, $d_1 = 1$, $R = 1$)

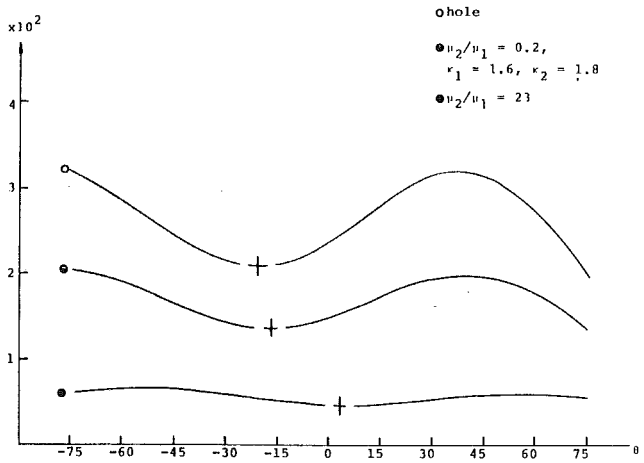

Fig. 7 Variations of the strain-energy density w at a distance r^* from the crack tip of a straight crack for θ varying between $-75°$ and $75°$ ($t_2 = 0.75$, $c = 0.80$, $r^* = 0.002$, $d_1 = 1$, $R = 1$, $\kappa_1 = 1.6$)

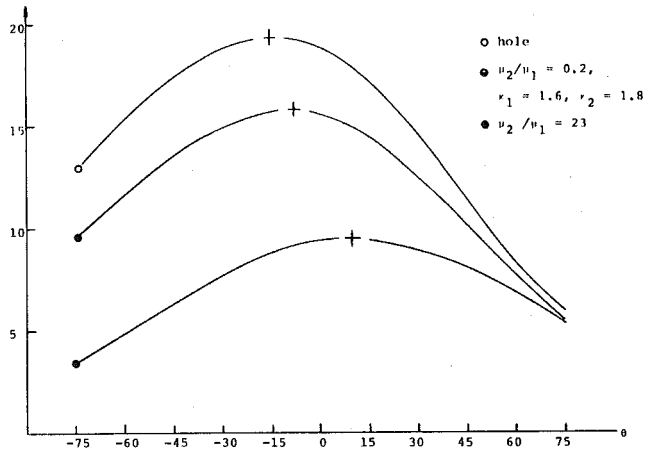

Fig. 6 Variation of the normal stress σ_θ at a distance r^* from the crack tip of a straight crack for θ varying between $-75°$ and $75°$ ($t_2 = 0.75$, $c = 0.80$, $r^* = 0.002$, $d_1 = 1$, $R = 1$)

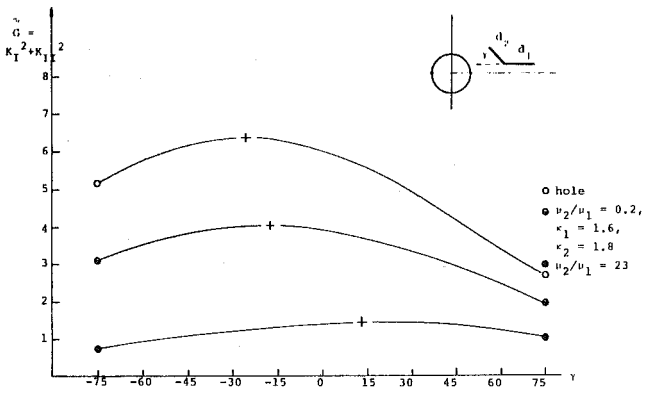

Fig. 8 Variation of the strain-energy release rate at the kinked crack tip for the angle γ varying between $-75°$ and $75°$ ($t_2 = 0.175$, $c = 0.80$, $d_2 = 0.001$, $d_1 = 1$, $R = 1$)

Table 1 $\gamma = 15°$, $d_1 = d_2 = 1$

Case	Conditions imposed	$(K_I)_A$	$(K_{II})_A$	$(K_I)_B$	$(K_{II})_B$
1	$\bar{h}_1(-1) = \bar{h}_2(-1) = 0$	1.75115	0.02867	1.66188	−0.47767
2	$\bar{h}_1(-1) = \bar{h}_3(-1) = 0$	1.73282	0.02787	1.64393	−0.47128
3	$\bar{h}_1(-1) = \bar{h}_4(-1) = 0$	1.75115	0.02867	1.66188	−0.47767
4	$\bar{h}_2(-1) = \bar{h}_3(-1) = 0$	1.75115	0.02867	1.66188	−0.47767
5	$\bar{h}_2(-1) = \bar{h}_4(-1) = 0$	1.75124	0.03054	1.66221	−0.47589
6	$\bar{h}_3(-1) = \bar{h}_4(-1) = 0$	1.75115	0.02867	1.66188	−0.47767

of angle θ and shown in Fig. 6 and Fig. 7. In these figures, a softer inclusion with material constants $\mu_2/\mu_1 = 0.2$, $\kappa_1 = 1.6$, $\kappa_2 = 1.8$ is added to the aforementioned two types of inclusion for the purpose of comparison.

The fracture angles as obtained by using the mixed-mode criteria 2 and 4 are easily inferred from Figs. 6 and 7. The results are summarized in Table 3.

Fig. 8 shows the variation of $\tilde{G}$ when γ is varied from $-75°$ to $75°$. Here $\tilde{G}$ is related to the energy-release rate G by

$$\tilde{G} = G\frac{E}{(1-\nu^2)} = K_I^2 + K_{II}^2$$

All the calculations related to criterion 5 are accomplished by assuming $d_2 = 0.01$. As one can see in Fig. 8, the peaks shift to the right as the relative stiffness μ_2/μ_1 is raised.

There is thus a tendency of soft inclusions to attract cracks, whereas a hard one tends to divert them.

In all of the work done here, we are able to infer that the softer an inclusion, the greater its tendency to serve as a crack termination site. Thus, in Fig. 5, we see the peak values of $(K_I)_B$ and the zeros of $(K_{II})_B$ shift to the left with decreasing relative stiffness. In Fig. 6, the angle of maximum normal stress decreases with μ_2/μ_1, and in Fig. 7 we see decreasing angles of minimum strain energy.

When Theories 1 and 3 are applied, it should be noted that K_I and K_{II} are associated with the tip of a straight crack, not the tip of a

Table 2 Comparison of present work with results in the literature ($d_2/d_1 = 1$)

	θ	15	30	45	60	75
$(K_I)_A$	Ref [10]			1.6129		
	Ref [8]	1.7512	1.6930	1.6127	1.5283	1.4547
	Ref [16]	1.7511	1.6928	1.6124	1.5282	1.4556
	Present work	1.7512	1.6929	1.6125	1.5282	1.4551
$(K_{II})_A$	Ref [10]			0.0262		
	Ref [8]	0.0287	0.0407	0.0261	−0.0145	−0.0701
	Ref [16]	0.0287	0.0406	0.0258	−0.0149	−0.0706
	Present work	0.0287	0.0407	0.0259	−0.0147	−0.0703
$(K_I)_B$	Ref [10]	1.6618	1.3573	0.9324	0.4867	
	Ref [8]	1.6619	1.3573	0.9322	0.4865	0.1203
	Ref [16]	1.6619	1.3571	0.9319	0.4866	0.1210
	Present work	1.6619	1.3572	0.9320	0.4866	0.1209
$(K_{II})_B$	Ref [10]	−0.4776	−0.8527	−1.0501	−1.0399	
	Ref [8]	−0.4777	−0.8528	−1.0499	−1.0392	−0.8429
	Ref [16]	−0.4777	−0.8528	−1.0498	−1.0396	−0.8455
	Present work	−0.4777	−0.8528	−1.0498	−1.0394	−0.8446

Table 3 Initial fracture angle obtained by applying different theories for two cases

		$t_2 = 0.75$ $c = 0.8$			$t_2 = 0.95$ $c = 0.6$		
μ_2/μ_1		23	0.2	0	23	0.2	0
Fracture angle θ	Theory 1	+14°	−17°	−23°	11°	−9°	−12°
	Theory 2	9°	−11°	−16°	4°	−6°	−5°
	Theory 3	14°	−17°	−22°	11°	−9°	−12°
	Theory 4	3°	−17°	−21°	2°	−11°	−12°
	Theory 5	14°	−17°	−24°	12°	−10°	−13°

kinked crack. The fracture angle θ for these two theories is also listed in Table 3.

Although an approximation (a finite length of 0.01 for the branched crack) is involved when Theory 5 is applied, the results are in good agreement with those obtained by applying Theories 1 and 3. The fracture angles predicted by Theories 2 and 4 disagree with each other and deviate a lot from the values given by applying the other three theories. Therefore, the use of Theories 2 and 4, which consider the second-order term in the crack-tip stress field in determining the initial fracture angle, is not promising here.

References

1 Sih, G. C., "Stress Distribution Near Internal Crack Tips for Longitudinal Shear Problems," ASME JOURNAL OF APPLIED MECHANICS, Vol. 32, 1965, pp. 51–58.

2 Smith, E., "A Note on Crack-Forking in Antiplane Shear Deformation," *International Journal of Fracture*, Vol. 9, 1973, pp. 181–183.

3 Wu, C. H., "Fracture Under Combined Loads by Maximum-Energy-Release-Rate Criterion," ASME JOURNAL OF APPLIED MECHANICS, Vol. 45, 1978, pp. 553–558.

4 Wu, C. H., "Elastic Problems of a Slender Z-Crack," *Journal of Elasticity*, Vol. 8, 1978, pp. 183–205.

5 Anderson, H., "Stress-Intensity Factors at the Tips of a Star-Shaped Contour in an Infinite Tensile Sheet," *Journal of the Mechanics and Physics of Solids*, Vol. 17, 1969, pp. 405–417.

6 Anderson, H., Erratum on [5], *Journal of the Mechanics and Physics of Solids*, Vol. 18, 1970, p. 437.

7 Hussian, M. A., Pu, S. L., and Underwood, G., "Strain-Energy Release Rate for a Crack Under Combined Mode I and Mode II," Technical Report, Benet Weapons Lab., Aug. 1973.

8 Chatterjee, S. N., "The Stress Field in the Neighborhood of a Branched Crack in an Infinite Sheet," *International Journal of Solid and Structures*, Vol. 11, 1975, pp. 521–538.

9 Kitagawa, H., and Yuuki, R., "Analysis of Branched Cracks Under Biaxial Stresses," *Fracture*, 1977, ed. Taplin, D. M. R., Vol. 3, University of Waterloo, Canada, 1977, pp. 201–211.

10 Kitagawa, H., Yuuki, R., and Ohira, T. "Crack-Morphological Aspects in Fracture Mechanics," *Engineering Fracture Mechanics*, Vol. 7, 1975, pp. 515–529.

11 Khrapkov, A. A., "The First Basic Problem for a Notch at the Apex of an Infinite Wedge," *International Journal of Fracture*, Vol. 7, 1971, pp. 373–382.

12 Bilby, B. A., Cardew, G. E., and Howard, I. C., "Stress-Intensity Factors at the Tips of Kinked and Forked Cracks," *Fracture*, 1977, ed., Taplin, D. M. R., Vol. 3, University of Waterloo Press, Canada, 1977, pp. 197–200.

13 Datsyshin, A. P., and Savruk, M. P., "A System of Arbitrarily Oriented Cracks in Elastic Solids," *Journal of Applied Mathematics and Mechanics (PMM)*, Vol. 38, 1974, pp. 677–686.

14 Theocaris, P. S., and Ioakimidis, N. I., "The Symmetrically Branched Crack in an Infinite Elastic Medium," *Journal of Applied Mathematics and Physics (ZAMP)*, Vol. 27, 1976, pp. 801–814.

15 Theocaris, P. S., "Asymmetric Branching of Cracks," ASME JOURNAL OF APPLIED MECHANICS, Vol. 44, 1977, pp. 611–618.

16 Ioakimidis, N. I., and Theocaris, P. S., "The Modified Lobatto-Chebyshev Method Applied to the Numerical Evaluation of Stress-Intensity Factors in Cracks With a Corner Point," Feb. 1979, private communication.

17 Dunders, J., and Mura, T., "Interaction Between an Edge Dislocation and a Circular Inclusion," *Journal of Mechanics and Physics of Solids*, Vol. 12, 1964, pp. 177–189.

18 Atkinson, C., "The Interaction Between a Crack and an Inclusion," *International Journal of Engineering Science*, Vol. 10, 1972, pp. 127–136.

19 Erdogan, F., Gupta, G. D., and Ratwani, M., "Interaction Between a Circular Inclusion and an Arbitrarily Oriented Crack," ASME JOURNAL OF APPLIED MECHANICS, Vol. 41, 1974, pp. 1007–1013.

20 Lo, K. K., "Analysis of Branched Cracks," ASME JOURNAL OF APPLIED MECHANICS, Vol. 45, 1978, pp. 797–802.

21 Erdogan, F., and Sih, G. C., "On the Crack Extension in Plates Under Plane Loading and Transverse Shear," ASME *Journal of Basic Engineering*, Vol. 85, 1963, pp. 519–525.

22 Williams, J. G., and Ewing, P. D., "Fracture Under Complex Stress—The Angled Crack Problem," *International Journal of Fracture*, Vol. 8, 1972, pp. 441–446.

23 Sih, G. C., "A Special Theory of Crack Propagation," *Methods of Analysis and Solutions of Crack Problems*, Vol. I, ed., Sih, G. C., Noordhoof International Publishing, 1973, pp. 21–45.

24 Eftis, J., Subramonian, N., and Liebowitz, H. "Crack Border Stress and Displacement Equations Revisited," *Engineering Fracture Mechanics*, Vol. 9, 1977, pp. 189–210.

25 Erdogan, F., Gupta, G. D., and Cook, T. S. "Numerical Solution of Singular Integral Equations," *Methods of Analysis and Solutions of Crack Problems*, ed., Sih, G. C. Noordhoff, Leyden, The Netherlands, 1973, Chapter 7, pp. 368–425.

26 Williams, M. L., "Stress Singularities Resulting From Various Boundary Conditions in Angular Corners of Plates in Extention," ASME JOURNAL OF APPLIED MECHANICS, Vol. 19, 1952, pp. 526–528.

27 Theocaris, P. S., and Ioakimidis, N. I. "Numerical Integration Methods for the Solution of Singular Integral Equations," *Quarterly of Applied Mathematics*, Vol. 35, 1977, pp. 173–183.

28 Bilby, B. A., and Eshelby, J. D., *Fracture*, Vol. I, ed., Liebowitz, H., Academic Press, 1968, pp. 99–182.

29 Sih, G. C. Discussion on [22], *International Journal of Fracture*, Vol. 10, 1974, pp. 261–265.

J. G. Simmonds
Professor of Applied Mathematics.
Mem. ASME

J. Duva
Department of Applied Mathematics
and Computer Science,
University of Virginia,
Charlottesville, Va. 22901

Thickness Effects Are Minor in the Energy-Release Rate Integral for Bent Plates Containing Elliptic Holes or Cracks[1]

The exact value of Sanders' path-independent, energy-release rate integral I for an infinite, bent elastic slab containing an elliptic hole is shown to be approximated by its value from classical plate theory to within a relative error of $O(h/c)F(e)$, where h is the thickness, c is the semimajor axis of the ellipse, and F is a function of the eccentricity e. This result is based on Golden'veiser's analysis of three-dimensional edge effects in plates, as developed by van der Heijden. As the elliptic hole approaches a crack, $F(e) \sim \ln(1-e)$. However, this limit is physically meaningless, because Golden'veiser's analysis assumes that h is small compared to the minimum radius of curvature of the ellipse. Using Knowles and Wang's analysis of the stresses in a cracked plate predicted by Reissner's theory, we show that the relative error in computing I from classical plate theory is only $O(h/c) \ln(h/c)$, where c is the semicrack length. Our results suggest that classical plate and shell theories are entirely adequate for predicting crack growth, within the limitations of applying any elastic theory to an inherently inelastic phenomenon.

Introduction

One computes stress-intensity factors for loaded, cracked elastic solids in the hope that, if the material is brittle, these factors may serve as a measure of the likelihood of crack growth. For infinite, elastically isotropic plates containing straight, through cracks and under simple in-plane or bending loads at infinity, stress-intensity factors may be computed from the classical two-dimensional theories of plane stress or plate bending, either as a limiting case of solutions for elliptic holes [1, 2] or directly, via singular integral equations [3].

Clearly, within the immediate vicinity of an edge, we cannot expect to infer accurately the true state of three-dimensional stress from a two-dimensional theory. This shortcoming is particularly acute in the classical theory of plate *bending* where imposition of the two contracted boundary conditions of Kirchoff at a free edge implies, except in special cases, that the twisting couple at the edge does not vanish, but is of the order of magnitude of the stress couples in the *interior* of the plate [4].

There have been two distinct approaches to correcting the deficiencies of classical bending theory. The first is due to Reissner [5–7] who has developed an *improved two-dimensional theory* wherein the classical fourth-order biharmonic equation for the midplane normal deflection w is supplemented by a second-order Helmholtz equation for a stress function ψ. Reissner's theory should predict significantly better values than the classical theory for the actual stress resultants and couples in the edge-zone because

1 It can satisfy, at a free-edge, the three conditions that the transverse shear stress resultant, the twisting couple, and the bending couple must vanish.

2 There are solutions that decay rapidly outside an edge-zone of width $O(h)$, where h is the plate thickness.

(Note that we refrain, as does Reissner, from suggesting that prediction of the thickness variation of the three-dimensional stress is improved in the edge-zone.) For the special case of beinding of an infinite plate with a circular hole, Reissner's later plate theory agrees well numerically with the essentially exact three-dimensional solution of Alblas [8].

The other approach to correcting the deficiences of classical plate theory is to recognize the three-dimensional nature of the stress distribution in the vicinity of an edge but to attempt, by a proper scaling, to reduce the governing equations to two-dimensional ones in a strip formed by the intersection of the plate with a plane perpendicular to the edge and to the midplane. The solutions to these equations as one moves toward the interior of the plate are then matched to the solutions of the classical plate equations as one moves toward the edge of

[1] This work was supported by the National Science Foundation under Grant No. MCS79-27135.

Contributed by the Applied Mechanics Division for publication in the JOURNAL OF APPLIED MECHANICS.

Discussion on this paper should be addressed to the Editorial Department, ASME, United Engineering Center, 345 East 47th Street, New York, N. Y. 10017, and will be accepted until September 1, 1981. Readers who need more time to prepare a Discussion should request an extension from the Editorial Department. Manuscript received by ASME Applied Mechanics Division, August, 1980.

the plate. This approach was pioneered by Friedrichs [9] and elaborated upon by Golden'veiser (see [8] for a list of references). Fortunately, this rather tedious work has been given a simple physical interpretation and variational formulation by Koiter and van der Heijden [8, 9].

Beginning with Knowles and Wang [10], a number of authors [11–14] have computed "improved" stress-intensity factors for cracked plates and shells using some version of Reissner's plate theory or its shallow shell analog. In contrast to the classical theory, Reissner's refined theory predicts an angular variation of the stress couples around the tip of the crack that agrees with the exact theory of antiplane strain. And in contrast to the classical eighth-order theory of shallow shells, the refined, tenth-order theory predicts identical angular variation near a crack tip for the stress resultants and couples. The bending stress-intensity factors computed from these refined theories differ significantly from those of the classical theory and thus, presumably, indicate the importance of thickness effects on crack growth predictions.

It is our contention that, *insofar as it is possible in a purely elastic theory to predict crack growth—an inelastic phenomenon—the most meaningful number to compute is the value of Sanders' path-independent, energy-release rate integral I for the expected crack growth path.* As we shall argue, the exact, three-dimensional expression for I for a cracked, bent plate is approximated by the value of I from classical plate theory to within a relative error of $O(h/c)\ln(h/c)$, where c is the half crack length. Moreover, for an infinite plate with an elliptical hole, we shall show that classical plate theory approximates I to within a relative error of $O(h/c)F(e)$, where $F(e)$ is a shape factor that approaches $\ln(1-e)$ as the eccentricity e of the ellipse approaches one.

We arrive at our conclusions by evaluating I over a path lying at an arbitrarily *large* distance from the crack. We begin with the results of a recent paper by Cheng [15] who has shown that the solution of the three-dimensional Navier equations for the bending of an elastic slab free of body forces and face tractions can be reduced to the sum of the solutions of two distinct types of two-dimensional problems. The first type involves the solution of two infinite sequences of Helmholtz equations, each admitting solutions that decay over a length equal to some numerical factor times the slab thickness. These may be called edge-zone solutions. The second type of two-dimensional problem involves the single-biharmonic equation

$$\nabla^2\nabla^2 w = 0, \tag{1}$$

where ∇^2 is the Laplacian in the midsurface of the slab. The solutions of (1) may be called interior solutions and are discussed in detail in the books by Love [16, pp. 473–487] and Lur'e [17, pp. 199–230].

In circular cylindrical coordinates (r, θ, z), the associated three-dimensional displacement components (U^i, V^i, W^i) and stress components $(\sigma^i_{rr}, \sigma^i_{r\theta}, \sigma^i_{rz})$ are given by [15, equations (39) and (40)]

$$U^i = \frac{-z}{1-\nu}\frac{\partial}{\partial r}\left\{1-\nu+\left[\frac{h^2}{4}-\frac{(2-\nu)}{6}z^2\right]\nabla^2\right\}w \tag{2}$$

$$V^i = \frac{-z}{1-\nu}\frac{1}{r}\frac{\partial}{\partial\theta}\left\{1-\nu+\left[\frac{h^2}{4}-\frac{(2-\nu)}{6}z^2\right]\nabla^2\right\}w \tag{3}$$

$$W^i = \left[1+\frac{\nu}{2(1-\nu)}z^2\nabla^2\right]w \tag{4}$$

$$\sigma^i_{rr} = -\frac{Ez}{1-\nu^2}\left\{\frac{\partial^2}{\partial r^2}+\left(\frac{1}{r}\frac{\partial}{\partial r}+\frac{1}{r^2}\frac{\partial^2}{\partial\theta^2}\right)\left[\nu-\left(\frac{h^2}{4}-\frac{2-\nu}{6}z^2\right)\nabla^2\right]\right\}w \tag{5}$$

$$\sigma^i_{r\theta} = \frac{-Ez}{1-\nu^2}\frac{\partial}{\partial r}\left(\frac{1}{r}\right)\frac{\partial}{\partial\theta}\left[(1-\nu)+\left(\frac{h^2}{4}-\frac{2-\nu}{6}z^2\right)\nabla^2\right]w \tag{6}$$

$$\sigma^i_{rz} = -\frac{E}{2(1-\nu^2)}\left(\frac{h^2}{4}-z^2\right)\frac{\partial}{\partial r}\nabla^2 w. \tag{7}$$

We emphasize that (2)–(7) are *exact* solutions of the Navier equations. We also emphasize that the boundary conditions at the edge of a hole involve all of the separated solutions of the Navier equations, so that the determination of w involves the simultaneous consideration of the edge-zone solutions. This is a key point and we shall return to it momentarily.

Sanders' energy-release integral I [18, 19] evaluated over the truncated cylinder $r = R$, $|z| \le \frac{1}{2}h$ takes the form

$$I = \tfrac{1}{2}\int_{-\frac{1}{2}h}^{\frac{1}{2}h}\int_0^{2\pi}(\sigma_{rr}\dot{U}+\sigma_{r\theta}\dot{V}+\sigma_{rz}\dot{W} - \dot{\sigma}_{rr}U-\dot{\sigma}_{r\theta}V-\dot{\sigma}_{rz}W)Rd\theta dz, \tag{8}$$

where the dot denotes the derivative with respect to some parameter that characterizes the shape of the hole. (For a hole whose cross section is always an ellipse of the same area, aligned with the x and y-axes, we shall take the parameter to be the length l of the ellipse.) In (8), $\sigma_{rr} = \sigma^i_{rr} + \sigma^e_{rr}$, $U = U^i + U^e$, etc., where the superscript e denotes an edge-zone contribution. As $R \to \infty$, the edge-zone contributions will make a transcendentally small contribution to I. But as I is path-independent, it follows that *I is determined by the interior-zone contributions alone.*

Substituting the right sides of (2)–(7) into (8), and carrying out the z integration, we obtain an expression of the form

$$I = \tfrac{1}{2}\int_0^{2\pi}(-m_r\dot{w}_{,r}-m_{r\theta}r^{-1}\dot{w}_{,\theta}+Q_r\dot{w} + \dot{m}_r w_{,r}+\dot{m}_{r\theta}r^{-1}w_{,\theta}-\dot{Q}_r w)[1+O(h^2/L^2)]Rd\theta. \tag{9}$$

Here L is the wavelength of w, defined so that $L^2\nabla^2 w$, $L^3(\nabla^2 w_{,r}, r^{-1}\nabla^2 w_{,\theta})$, $L^4(\nabla^2 w_{,rr}, r^{-1}\nabla^2 w_{,r\theta}, r^{-2}\nabla^2 w_{,\theta\theta}) = O(w)$,

$$m_r = -D[w_{,rr}+\nu(r^{-1}w_{,\theta}+r^{-2}w_{,\theta\theta})] \tag{10}$$

$$m_{r\theta} = -D(1-\nu)(r^{-1}w_{,\theta})_{,r} \tag{11}$$

$$Q_r = -D(\nabla^2 w)_{,r} \tag{12}$$

$$D = \frac{Eh^3}{12(1-\nu^2)}, \tag{13}$$

E is Young's modulus and ν is Poisson's ratio. For conciseness, we have indicated partial differentiation by a comma. Note from equation (41) of [15] that the actual bending couple acting along a circle in the midplane of the slab is given by

$$M_r = m_r + h^2 D[(8+\nu)/40][r^{-1}(\nabla^2 w)_{,r}+r^{-2}(\nabla^2 w)_{,\theta\theta}]. \tag{14}$$

If the loading on the infinite slab is such that

$$\nabla^2 w = c + O(r^{-2}) \text{ as } r \to \infty, \tag{15}$$

then as $R \to \infty$, the $O(h^2/L^2)$-terms in (9) disappear, and I reduces to precisely the form it takes in classical plate theory. This happens, for example, if the slab is subject at infinity to a pure stress couple M turning about the y-axis, in which case

$$w = -(6M/Eh^3)(x^2-\nu y^2)+O(1), \tag{16}$$

and $c = -12(1-\nu)M/Eh^3$.

It remains to investigate the influence on w of imposing exact boundary conditions at the hole rather than the approximate Kirchhoff conditions. Fortunately, Golden'veiser has carried out the rather tedious analysis that is required [20]. When all is said and done it turns out that, to a first approximation, the necessary corrections to classical plate theory are obtained merely by solving the classical plate equations subject to slightly *modified Kirchhoff conditions.* (Golden'veiser's results were given a simple energetic interpretation and derivation by Koiter and van der Heijden [8, 9]. Moreover, Reissner has shown that his latest refined two-dimensional plate theory [7] implies a set of modified Kirchhoff boundary conditions for the classical plate equations that involve a numerical constant that is remarkably close to the one coming from Golden'veiser's three-dimensional analysis. For an explanation of Golden'veiser's method in a simple nontrivial context see [4].)

The modified classical solutions for a bent, infinite plate containing an elliptic hole have been computed analytically by van der Heijden [8]. His results are expressed in terms of the two standard complex

functions of classical plate theory [21]. Our first task is to express I in terms of these.

***I* for Plate Bending in Terms of Complex Variables.** There exists a well-known duality between the theories of generalized plane stress and classical plate bending that we summarize in the following table:

Plane stress	$-F$	$\mathbf{u}$	$\hat{N}$	E	$1/Eh$	ν
Plate bending	w	$\mathbf{G}$	K	$-\hat{M}$	D	$-\nu$

(17)

Here F is Airy's stress function, $\mathbf{u}$ and $\mathbf{G}$ are, respectively, tangential displacement and moment stress function vectors, N, M, E, and K are, respectively, stress resultant and bending couple tensors and extensional and bending strain tensors, and $\hat{E} = \text{trace}\,(E)I - E^T$, etc., where I is the identity tensor and the superscript T denotes the transpose.

In the theory of plane stress,

$$I = \tfrac{1}{2}\int_C (\mathbf{T}\cdot\dot{\mathbf{u}} - \dot{\mathbf{T}}\cdot\mathbf{u})ds, \tag{18}$$

where C is a smooth closed curve and $\mathbf{T}$ is the traction vector acting across C [18]. This equation, as it stands, is not the dual of the coordinate-free form of (9). However, if the net force and moment acting over C are zero (so that F and $\mathbf{G}$ are single-valued), then by introducing stress functions and integrating by parts several times, it may be shown that (9) and (18) are indeed duals.

The theory of plane stress may be formulated in terms of complex variables. In the absence of body forces, Airy's stress function has the representation [22, equation (70.5)]

$$F = -\tfrac{1}{2}[\bar{z}\phi(z) + z\overline{\phi(z)} + \chi(z) + \overline{\chi(z)}], \tag{19}$$

where ϕ and χ are analytic functions of the complex variable $z = x + iy$. (z, of course, no longer stands for the third Cartesian coordinate.)

Sanders has shown [18] that in terms of ϕ and $\psi = \chi'$,

$$I = -2(Eh)^{-1}\mathcal{J}\int_C (\phi'\dot{\psi} + \dot{\phi}\,\psi')dz, \tag{20}$$

where $\mathcal{J}$ denotes "the imaginary part of." It now follows immediately from the duality expressed by (17) that Sanders' integral for classical plate bending has precisely the same form as (20) provided that the solution of (1) is represented in the form

$$w = \tfrac{1}{2}[\bar{z}\phi(z) + z\overline{\phi(z)} + \chi(z) + \overline{\chi(z)}] \tag{21}$$

and $(Eh)^{-1}$ is replaced by D.

Summary and Extension of van der Heijden's Results. The function

$$z = \omega(\zeta) = R(\zeta^{-1} + m\zeta), \tag{22}$$

where

$$R = \frac{a+b}{2}, \quad m = \frac{a-b}{a+b}, \tag{23, 24}$$

maps the interior of the unit circle in the complex ζ-plane onto the region in the complex z-plane exterior to the ellipse

$$\frac{x^2}{a^2} + \frac{y^2}{b^2} = 1. \tag{25}$$

The inverse of (22) is given by

$$\zeta = \Omega(z) = \frac{z - (z^2 - 4R^2m)^{1/2}}{2Rm} = Rz^{-1} + R^3mz^{-3} + O(z^{-5}), \tag{26}$$

where $\Omega(z)$ is analytic in the z-plane with a cut joining the foci of the ellipse (25).

van der Heijden considers an infinite plate with an elliptic cylindrical hole with cross section (25). A uniform stress couple of magnitude M acts at infinity about the y-axis so that (16) obtains.[2] To analyze the resulting stresses van der Heijden sets

$$\phi(\omega(\zeta)) = K[\phi_1(\zeta) + (h/R)\phi_1^*(\zeta)] \tag{27}$$

$$\psi(\omega(\zeta)) = K[\psi_1(\zeta) + (h/R)\psi_1^*(\zeta)], \tag{28}$$

where [8, equations (2.2.13) and (2.2.16)]

$$\phi_1(\zeta) = \frac{1}{2(1+\nu)}\left(\frac{1}{\zeta} + m\zeta\right)\frac{1-m}{3+\nu}\,\zeta \tag{29}$$

$$\psi_1(\zeta) = \frac{m-1}{3+\nu}\frac{\zeta(m+\zeta^2)}{\zeta^2 m - 1} + \frac{1}{1-\nu}\left(\zeta + \frac{1}{\zeta}\right), \tag{30}$$

and

$$K = -MR/2D. \tag{31}$$

ϕ_1 and ψ_1 represent the classical plate theory solutions and ϕ_1^* and ψ_1^* represent the corrections to classical plate theory that result when increments are added to the Kirchhoff boundary conditions to make them agree with Golden'veiser's modified conditions. Since ϕ_1^* and ψ_1^* correspond to self-equilibrated loads along the hole, they have series representations of the form

$$\phi_1^*(\zeta) = \sum_1^\infty \alpha_n\phi^n, \quad \psi_1^*(\zeta) = \sum_1^\infty \beta_n\zeta^n, \quad |\zeta| < 1. \tag{32, 33}$$

It turns out that *all we need from (32) and (33) in the evaluation of Sanders' integral are expressions for α_1 and β_1.* We shall compute these coefficients after we have verified this statement.

Substituting (29)–(33) into (27) and (28), we obtain, for $0 < |\zeta| < 1$,

$$\phi(\omega(\zeta)) = K[a_{-1}\zeta^{-1} + a_1\zeta + O(\zeta^3)] \tag{34}$$

$$\psi(\omega(\zeta)) = K[b_{-1}\zeta^{-1} + b_1\zeta + O(\zeta^3)], \tag{35}$$

where

$$a_{-1} = \frac{1}{2(1+\nu)}, \quad a_1 = \frac{m}{2(1+\nu)} + \frac{1-m}{3+\nu} + (h/R)\alpha_1 \tag{36, 37}$$

$$b_{-1} = \frac{1}{1-\nu}, \quad b_1 = \frac{1}{1-\nu} + \frac{m-m^2}{3+\nu} + (h/R)\beta_1. \tag{38, 39}$$

With (22) and (26), (34) and (35) take the following form outside the ellipse (25) in the z-plane:

$$\phi(z) = K[A_1z + A_{-1}z^{-1} + O(z^{-3})] \tag{40}$$

$$\psi(z) = K[B_1z + B_{-1}z^{-1} + O(z^{-3})], \tag{41}$$

where

$$A_1 = a_{-1}R^{-1}, A_{-1} = a_1R - a_{-1}mR \tag{42, 43}$$

$$B_1 = b_{-1}R^{-1}, B_{-1} = b_1R - b_{-1}mR. \tag{44, 45}$$

Computing the residue of $\phi'(z)\dot{\psi}(z) + \dot{\phi}(z)\psi'(z)$ from (40) and (41), we find that Sanders' integral (20) with $(Eh)^{-1}$ replaced by D is given by

$$I = -4\pi DK[A_1(KB_{-1})^{\cdot} - A_{-1}(KB_1)^{\cdot} + B_1(KA_{-1})^{\cdot} - B_{-1}(KA_1)^{\cdot}]. \tag{46}$$

But from (31), (36), (38), (42), and (44),

$$KB_1 = -\frac{M}{2D(1-\nu)}, \quad KA_1 = -\frac{M}{4D(1+\nu)}. \tag{47}$$

These quantities are independent of the parameters R and m that characterize the ellipse (25). Thus (46) reduces to

[2] The standard orientation, as used by Knowles and Wang [10], for example, is with the stress couple at infinity turning about the x-axis. However, for ease of transcription from and comparison with [8], we have retained van der Heijden's convention. The value of I is, of course, independent of our stress conventions.

$$I = -\frac{\pi M^2}{2D}\left[R^2\left(\frac{b_1 - mb_{-1}}{1+\nu} + 2\frac{a_1 - ma_{-1}}{1-\nu}\right)\right]. \quad (48)$$

It is useful to set

$$I = -\frac{\pi M^2 R}{2D} I_c[1 + (h/R)I_c^G], \quad (49)$$

where I_c is the dimensionless value of I from classical plate theory and $(h/R)I_c^G$ (the G is for Golden'veiser) represents the correction due to edge-effects. From (36)–(39) and (42)–(45)

$$I_c = \frac{2(1-m)}{1-\nu^2}\left[1 + \frac{(2+m)+\nu(2-m)}{3+\nu}\right]\dot{R} - \frac{R}{1-\nu^2}\left[1 + \frac{1+2m+\nu(3-2m)}{3+\nu}\right]\dot{m} \quad (50)$$

$$I_c I_c^G = \left(\frac{\beta_1}{1+\nu} + \frac{2\alpha_1}{1-\nu}\right)\dot{R} + R\left(\frac{\dot{\beta}_1}{1+\nu} + \frac{2\dot{\alpha}_1}{1-\nu}\right). \quad (51)$$

Determination of α_1 and β_1. van der Heijden has shown that [8]

$$\phi_1^* = C_* I_*(\zeta; m). \quad (52)$$

Here

$$(3+\nu)^2 C_* = \frac{384}{\pi^5}\sum_1^\infty \frac{1}{(2k-1)^5} = 1.26049\ldots, \quad (53)$$

$$I_*(\zeta; m) = \frac{1}{2\pi i}\oint_{|\sigma|=1} \frac{g(\sigma; m)d\sigma}{\sigma - \zeta}, \quad (54)^3$$

where

$$g(\sigma; m) = \frac{2}{\pi}\frac{(1-m)(\sigma^4-1)}{\sigma(\sigma^2-m)}h(\sigma; m), \quad (55)$$

and

$$h(\sigma; m) = \frac{\pi}{2}\frac{\sigma}{(\sigma^2-m)^{1/2}(1-m\sigma^2)^{1/2}} = h(\sigma^{-1}; m). \quad (56)$$

The function $h(\sigma; m)$ is analytic in the complex σ-plane, cut along the three segments $(-\infty, -1/\sqrt{m}]$, $[-\sqrt{m}, \sqrt{m}]$, $[1/\sqrt{m}, \infty)$ of the real axis. For simplicity, we assume, initially, that $0 < m < 1$. However our final results are valid for $-1 < m < 1$. This is important because with van der Heijden's loading convention, whereby the uniform stress couple at infinity turns about the y-axis, the nontrivial limiting case of a crack is obtained as $m \to -1$. That is, the ellipse approaches a slit of length $2b$ along the y-axis. The branches of $h(\sigma; m)$ are chosen so that $(1-m)^{1/2} = \sqrt{1-m}$. $I_*(\zeta; m)$ is analytic in the complex ζ-plane, cut along the segments $(-\infty, -1/\sqrt{m}]$ and $[1/\sqrt{m}, \infty)$ of the real axis. van der Heijden has shown that $I_*(\zeta; m)$ may be expressed in closed form [8, equation (III.2.13)] in terms of the complete elliptic integrals of the 1st, 2nd, and 3rd kinds:

$$K(m) = \int_0^1 \frac{dx}{\sqrt{1-x^2}\sqrt{1-m^2x^2}} \quad (57)$$

$$E(m) = \int_0^1 \sqrt{\frac{1-m^2x^2}{1-x^2}}\,dx \quad (58)$$

$$\Pi(\lambda^2; m) = \int_0^1 \frac{dx}{(1-\lambda^2x^2)\sqrt{1-x^2}\sqrt{1-m^2x^2}} = K(m) + (\lambda^2/m^2)[K(m) - E(m)] + O(\lambda^4). \quad (59)$$

$\Pi(\lambda^2; m)$ is analytic in the complex λ^2-plane, cut along the segments $(-\infty, -1]$ and $[1, \infty)$ of the real axis. For future reference, we note that [23]

$$K(m) = -\tfrac{1}{2}\ln(1-m^2) + O(1),\ mK'(m) = \frac{E(m)}{1-m^2} - K(m) \quad (60)$$

$$E(m) = O(1),\quad mE'(m) = E(m) - K(m). \quad (61)$$

It follows from (32), (52), (59), and equation (2.2.35) of [8] that

$$\alpha_1 = C_* I_*'(0; m) = \frac{4C_*}{\pi}\frac{1-m}{m^2}[K(m) - E(m)]. \quad (62)$$

van der Heijden did not derive an express for ψ_1^*, but from equation (2.1.38) of [8] and equation (79.10) of [22] we have

$$\psi_1^* = C_*\left[\frac{\zeta(\zeta^2+m)}{1-m\zeta^2}I_*'(\zeta; m) - \hat{\kappa}J_*(\zeta; m)\right], \quad (63)$$

where $\hat{\kappa} = (3+\nu)/(1-\nu)$ and

$$J_*(\zeta; m) = \frac{1}{2\pi i}\oint_{|\sigma|=1} \frac{\overline{g(\sigma; m)}}{\sigma - \zeta}d\sigma. \quad (64)$$

From (33), (63), and (64),

$$\beta_1 = C_*[mI_*'(0; m) - \hat{\kappa}J_*'(0; m)], \quad (65)$$

where

$$J_*'(0; m) = \frac{1}{2\pi i}\oint_{|\sigma|=1} \frac{\overline{g(\sigma; m)}}{\sigma^2}d\sigma. \quad (66)$$

On the unit circle $|\sigma| = 1$, (55) and (56) imply that

$$\frac{\overline{g(\sigma; m)}}{\sigma^2} = \frac{g(\sigma^{-1}; m)}{\sigma^2} = \frac{2}{\pi}\frac{(1-m)(1-\sigma^4)}{\sigma^3(1-m\sigma^2)}h(\sigma; m). \quad (67)$$

As $h(\sigma; m)$ is analytic in the annulus $\sqrt{m} < |\sigma| < 1/\sqrt{m}$, it may be represented as the sum of a function $h_<(\sigma; m)$ analytic for $|\sigma| < 1/\sqrt{m}$ and a function $h_>(\sigma; m)$ analytic for $|\sigma| > \sqrt{m}$. Explicitly, [23, equation (117.01)], [8, equation (III.2.18)],

$$h(\sigma; m) = [\Pi(m\sigma^2; m) - K(m)] + \Pi(m\sigma^{-2}; m) = h_<(\sigma; m) + h_>(\sigma; m). \quad (68)$$

The function

$$g_<^*(\sigma; m) = \frac{2}{\pi}\frac{1-m)(1-\sigma^4)}{\sigma^3(1-m\sigma^2)}h_<(\sigma; m) \quad (69)$$

is analytic in the disk $|\sigma| < 1/\sqrt{m}$, save for a simple pole at $\sigma = 0$. With the aid of (59) and (68),

$$\text{Res}\,\{g_<^*(0; m)\} = \frac{2}{\pi}\frac{1-m}{m}[K(m) - E(m)]. \quad (70)$$

The function

$$g_>^*(\sigma; m) = \frac{2}{\pi}\frac{(1-m)(1-\sigma^4)}{\sigma^3(1-m\sigma^2)}h_>(\sigma; m) \quad (71)$$

is analytic for $|\sigma| > \sqrt{m}$, save for simple poles at $\sigma = \pm 1/\sqrt{m}$ where

$$\text{Res}\,\{g_>^*(\pm 1/\sqrt{m}; m)\} = \frac{1}{\pi}\frac{1-m}{m}E(m), \quad (72)$$

where we have used the fact that $(1-m^2)\Pi(m^2, m) = E(m)$. Furthermore, as $\sigma \to \infty$,

$$g_>^*(\sigma; m) \sim \frac{2}{\pi\sigma}\frac{1-m}{m}K(m). \quad (73)$$

Thus, from (66)–(73),

$$J_*'(0; m) = \frac{1}{2\pi i}\left[\oint_{|\sigma|=1} g_<^*(\sigma; m)d\sigma + \oint_{|\sigma|=1} g_>^*(\sigma; m)d\sigma\right] = \frac{4}{\pi}\frac{1-m}{m}[K(m) - E(m)]. \quad (74)$$

Finally, inserting (62) and (74) into (65) and recalling that $\hat{\kappa} = (3+\nu)/(1-\nu)$, we have

[3] In van der Heijden's notation [8], $I_* = (1-m)I$. We have introduced I_* in place of I so that the dependence on m may be displayed explicitly.

$$\beta_1 = -\frac{8(1+\nu)C_*}{(1-\nu)}\frac{1-m}{m}[K(m)-E(m)]. \tag{75}$$

This result, combined with (62), yields

$$\frac{\beta_1}{1+\nu}+\frac{2\alpha_1}{1-\nu}=\frac{8C_*}{(1-\nu)\pi}\left(\frac{1-m}{m}\right)^2[K(m)-E(m)], \tag{76}$$

so that, with the aid of (60) and (61),

$$\left(\frac{\beta_1}{1+\nu}+\frac{2\alpha_1}{1-\nu}\right)^{\cdot}=\frac{8C_*}{(1-\nu)\pi}\left(\frac{1-m}{m^3}\right) \times\left[\left(\frac{2+2m+m^2}{1+m}\right)E(m)-2K(m)\right]\dot{m}. \tag{77}$$

Consider a class of movements in which the elliptical hole in the midplane distorts, without rotating, into another elliptical hole of equal area and take $(\ )^{\cdot} = d(\ )/dl$, where l is the length of the ellipse. (This is only one of many possible movements that, in the limit as $m \to -1$, yield the uniform extension of a crack. As equation (84) shows, $(h/R)I_c^G$, the correction to I_c, is independent of the movement of the hole.) Then

$$l = 4\int_0^{\pi/2}\sqrt{a^2\sin^2\theta + b^2\cos^2\theta}\,d\theta = 4bE(k), \tag{78}$$

where

$$k^2 = \frac{b^2-a^2}{b^2} = -\frac{4m}{(1-m)^2}. \tag{79}$$

With πab a constant, it follows readily from (23), (24), (78), and (79) that

$$\dot{R} = -\left(\frac{m}{1-m}\right)\frac{db}{dl}, \qquad \dot{m} = -\left(\frac{1+m}{R}\right)\frac{db}{dl}, \tag{80, 81}$$

where

$$\left(\frac{db}{dl}\right)^{-1} = 4\left\{E(k)-\frac{(1+m)^2}{2m}[E(k)-K(k)]\right\}. \tag{82}$$

Substituting (76), (77), and (80)–(82) into (50) and (51), we obtain

$$I_c = \frac{4(1-m)}{(3+\nu)(1-\nu)}\frac{db}{dl} \tag{83}$$

$$I_c^G = \frac{2(3+\nu)C_*}{\pi m^3}[(2+2m-m^2)K(m) - 2(1+m)E(m)] \equiv (3+\nu)^{-1}\hat{F}(m) \equiv (3+\nu)^{-1}F(e), \tag{84}$$

where

$$e = \frac{2\sqrt{-m}}{1-m}, \quad -1 \le m \le 0, \tag{85}$$

is the eccentricity of the ellipse.

As $m \to -1$, we have, with the aid of (60),

$$I_c^G \sim -\frac{(3+\nu)C_*}{\pi}\ln(1+m). \tag{86}$$

This limiting behavior is meaningless, however, because Golden'veiser's modified boundary conditions assume that the plate thickness is small compared to the minimum radius of curvature of the ellipse. Fig. 1 is a graph of $\hat{F}(m)$ which is independent of ν, as a glance at (53) and (84) shows.

***I* for a Cracked, Bent Plate Via Reissner's Theory.** Knowles and Wang [10], Wang [11], and Hartranft and Sih [12] have all used Reissner's plate theory [5] to compute stresses and stress-intensity factors along and at the tip of a crack in a plate.

The crack is represented by the segment $(-1, 1)$ of the x-axis and its edges subject to a uniform bending couple M. To compute the resulting stress field is the so-called residual problem. The stress field for a plate with a stress-free crack subject to a uniform stress couple M at infinity turning about the x-axis is obtained by adding the stress

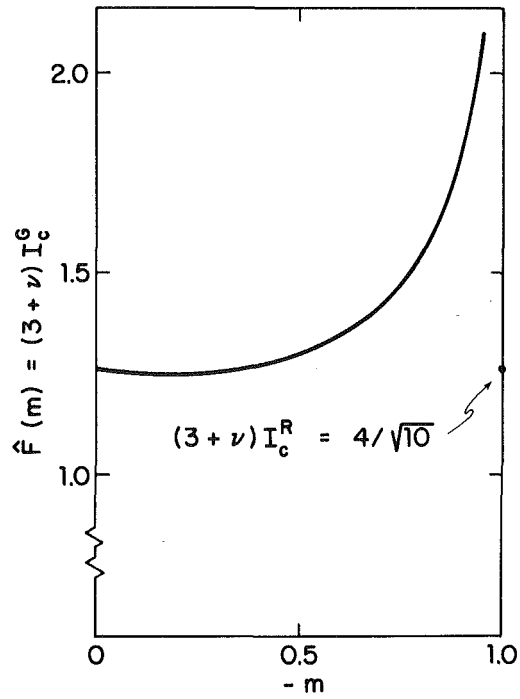

Fig. 1 Correction factors for I_c from Golden'veiser's and Reissner's theories

field for an uncracked plate to that for the residual problem. The numerical results of [11, 12] show that there are pronounced boundary-layer effects that lead to significant differences from the classical values of some of the aforementioned quantities as $h/c \to 0$. Despite this, we shall show that *Reissner's theory leads to a correction to I_c that is only of relative order $(h/c)\ln(h/c)$.*

Knowles and Wang reduced Reissner's equations for a bent, cracked plate to the following singular integral equation [10, equation (3.23)]:

$$\oint_{-1}^{1}\frac{1}{x-\xi}\left[1-\frac{2}{3+\nu}F\left(\frac{|x-\xi|}{\epsilon}\right)\right]v(\xi)d\xi = \pi x, \quad |x|<1. \tag{87}$$

Here $\epsilon = h/c\sqrt{10}$, $v(\xi)$ is an even function, $\oint$ denotes the Cauchy principal value, and

$$F(x) = \frac{4}{x^2} - 2K_2(x), \tag{88}$$

where $K_2(x)$ is the modified Bessel function.

The bending moments may be expressed in terms of $v(\xi)$ in the form [10, equation (3.17)]

$$\begin{pmatrix}M_x\\M_y\\M_{xy}\end{pmatrix} = -\frac{M}{2(3+\nu)}\int_{-1}^{1}\begin{pmatrix}m_x(x-\xi,y)\\m_y(x-\xi,y)\\m_{xy}(x-\xi,y)\end{pmatrix}v(\xi)d\xi, \tag{89}$$

where the kernels m_x, etc., are given by equations (3.16), (3.19), and (3.20) of [10]. These formulas are for the residual stress couples. The associated residual complex potentials Φ and Ψ may be computed from the formulas

$$M_y - M_x + 2iM_{xy} = 2D(1-\nu)[\bar{z}\Phi''(z) + \Psi'(z)] \tag{90}$$

$$M_x + M_y = -2D(1-\nu)[\Phi'(z) + \overline{\Phi'(z)}]. \tag{91}$$

To compute I we need only the dominant terms in the expressions for the residual stress couples as $r^2 = x^2 + y^2 \to \infty$. With $x = r\cos\theta$, $y = r\sin\theta$, we find, from (89) and equations (3.16), (3.17), (3.19), and (3.20) of [10], that

$$\begin{pmatrix} M_x \\ M_y \\ M_{xy} \end{pmatrix} \sim \frac{-M}{2(3+\nu)} \frac{p}{r^2} \begin{pmatrix} (1-\nu)(\sin^4\theta + \cos^4\theta - 6\cos^2\theta \sin^2\theta) \\ (3+\nu)(\sin^2\theta - \cos^2\theta) - 2(1-\nu)(\sin^4\theta - 3\cos^2\theta \sin^2\theta) \\ 4\cos\theta \sin\theta - 2(1-\nu)(3\cos\theta \sin^3\theta - \cos^3\theta \sin\theta) \end{pmatrix}, \quad (92)$$

where

$$P = (2/\pi) \int_{-1}^{1} v(\xi) d\xi. \quad (93)$$

Thus we do not need the complete solution of (87) but only its integral from -1 to $+1$.

Adding the stress field for the uncracked plate, $M_y = M, M_x = M_{xy} = 0$, we readily deduce from (92) the following asymptotic behavior for the associated complex potentials Φ and ψ:

$$\Phi \sim -\frac{M}{4D}\left[\frac{z}{1+\nu} - \frac{c^2 P}{(3+\nu)z}\right] \quad (94)$$

$$\Psi \sim \frac{M}{2D(1-\nu)}\left[z - \frac{(1+\nu)c^2 P}{(3+\nu)z}\right]. \quad (95)$$

It then follows from (20), with $D = (Eh)^{-1}$ and $(\ )^{\cdot} = d(\ )/dl = \frac{1}{4} d(\ )/dc$, that

$$I = -\frac{\pi M^2 c P}{2D(3+\nu)(1-\nu)}. \quad (96)$$

Remarkably, Knowles and Wang [10] were able to obtain all their analytical results using only the classical plate theory solution

$$v_0(x) = \sqrt{1-x^2}, \quad (97)$$

which satisfies (87) if one formally sets $\epsilon = 0$. Thus we must extract more information from (87). We shall proceed formally with what we hope are convincing arguments.

It is convenient to integrate both sides of (87) with respect to x, thereby obtaining the equivalent integral equation.

$$\int_{-1}^{1} [\ln|x-\xi| + (3+\nu)^{-1} G(|x-\xi|/\epsilon)] \times v(\xi) d\xi = \pi(\tfrac{1}{2}x^2 + C). \quad (98)$$

Here, C is an unknown constant,

$$G(x) = \frac{4}{x^2} - \frac{4}{x} K_1(x), \quad (99)$$

and K_1 is the modified Bessel function. From the Appendix,

$$\int_0^{\infty} G(x) dx = 2\pi. \quad (100)$$

Hence, as $\epsilon \to 0$,

$$G(|x-\xi|/\epsilon) \to \epsilon 4\pi \delta(x-\xi), \quad (101)$$

where δ is the Dirac δ-function.

Let

$$\epsilon(3+\nu)\pi\theta(x,\epsilon) = \int_{-1}^{1} G(|x-\xi|/\epsilon) v(\xi) d\xi. \quad (102)$$

Then the solution of (98) may be expressed in the form [24, equation (8-191)]

$$v(x;\epsilon) = \frac{1}{\pi}\frac{1}{\sqrt{1-x^2}}\left\{ \oint_{-1}^{1} \frac{\sqrt{1-\xi^2}\,[\xi - \epsilon\theta'(\xi;\epsilon)] d\xi}{\xi - x} + \frac{\pi}{2} P(\epsilon) \right\} = \sqrt{1-x^2} + \frac{\epsilon[Q(\epsilon) - \hat{Q}(x;\epsilon)]}{\pi\sqrt{1-x^2}}. \quad (103)$$

where

$$\epsilon Q(\epsilon) = (2/\pi) \int_{-1}^{1} [v(\xi;\epsilon) - \sqrt{1-\xi^2}] d\xi = P(\epsilon) - 1, \quad (104)$$

and

$$\hat{Q}(x;\epsilon) \equiv \oint_{-1}^{1} \frac{\sqrt{1-\xi^2}\,\theta'(\xi;\epsilon) d\xi}{\xi - x}. \quad (105)$$

(The constant C is hidden in Q.)

Because $v(x)$ represents the slope of the deformed midplane normal to the crack along the crack, $v(x) \to 0$ as $x \to \pm 1$. Therefore, the term in brackets in (103) must vanish as $x \to \pm 1$, i.e.,

$$Q(\epsilon) = \lim \hat{Q}(x;\epsilon) \quad \text{as} \quad x \to \pm 1. \quad (106)$$

This value of Q leads, via (96) and (104), to the correction predicted by Reissner's theory to the classical value of I.

To see how the limit in (106) occurs, first note that the structure of (87) and the graphs of various numerical results obtained by Wang [11] and Hartranft and Sih [12] indicate that as $\epsilon \to 0$, $v(x;\epsilon)$ exhibits a boundary layer at the crack tips. Simple order of magnitude arguments imply that the width of the boundary layer is $O(\epsilon)$ and that, in the boundary layer, v is $O(\epsilon^{1/2})$. We therefore *assume* that the solution of (87) has the form

$$v(x;\epsilon) = \sqrt{1-x^2} + \sqrt{\epsilon}\,[\hat{V}(s;\epsilon) + \hat{V}(t;\epsilon)] + \epsilon V(x;\epsilon), \quad (107)$$

where

$$x = -1 + \epsilon s = 1 - \epsilon t. \quad (108)$$

We further assume that $\hat{V}(s;\epsilon)$ and all of its derivatives are $O(1)$ for $s \geq \delta > 0$ and vanish sufficiently rapidly as $s \to \infty$.

To see the interior and boundary-layer structure of $\theta(x;\epsilon)$, rewrite (102) as follows:

$$\epsilon(3+\nu)\pi\theta(x;\epsilon) = \int_{-1}^{1} G(|x-\xi|/\epsilon)[\sqrt{1-\xi^2} + \epsilon V(\xi,\epsilon)] d\xi + \sqrt{\epsilon}\left(\int_{-1}^{-1+\sqrt{\epsilon}} + \int_{-1+\sqrt{\epsilon}}^{1-\sqrt{\epsilon}} + \int_{1-\sqrt{\epsilon}}^{1} G(|x-\xi|/\epsilon)\right) \times \left[\hat{V}\left(\frac{1+\xi}{\epsilon};\epsilon\right) + \hat{V}\left(\frac{1-\xi}{\epsilon};\epsilon\right)\right] d\xi. \quad (109)$$

Upon introducing the change of variables (108) and

$$\xi = -1 + \epsilon\sigma = 1 - \epsilon\eta, \quad (110)$$

and noting (101), we see that $\theta(x;\epsilon)$ takes the form

$$\theta(x;\epsilon) = 4\sqrt{1-x^2}/(3+\nu) + \sqrt{\epsilon}[\hat{\Theta}(s;\epsilon) + \hat{\Theta}(t;\epsilon)] + \epsilon\Theta(x;\epsilon). \quad (111)$$

This expression for $\theta(x;\epsilon)$, substituted into (105), yields, *to lowest order*,

$$\hat{Q}(x;0) = \frac{4x}{3+\nu}\ln\left(\frac{1+x}{1-x}\right) + \sqrt{2}\oint_0^{\infty} \frac{\sqrt{\sigma}\,\hat{\Theta}'(\sigma;0) d\sigma}{\sigma - s} + \sqrt{2}\oint_0^{\infty} \frac{\sqrt{\tau}\,\hat{\Theta}'(\tau;0)\, d\tau}{\tau - t} - \frac{8}{3+\nu}. \quad (112)$$

To evaluate the integrals in (112) assume that $f(\sigma) \equiv \sqrt{\sigma}\hat{\Theta}'(\sigma,0)$ can be extended to be an analytic function of the complex variable $v = \sigma + i\tau$ in a neighborhood of the positive σ-axis. Furthermore, assume that as $\sigma \to \infty, f(\sigma)\ln^{1+\delta}(\sigma) \to 0, \delta > 0$. (This is a sufficient condition; for example, for the integrals in (112) to converge.) Defining

$$F(u) = \frac{1}{2\pi i}\int_0^{\infty} \frac{f(\sigma) d\sigma}{\sigma - u}, \quad u \notin [0,\infty), \quad (113)$$

where $u = s + it$, we have, by the well-known Plemelj formulas [24, equations (8–130) and (8–131)].

$$F_+(s) + F_-(s) = \frac{1}{\pi i}\oint_0^{\infty} \frac{f(\sigma) d\sigma}{\sigma - s} \quad (114)$$

$$F_+(s) - F_-(s) = f(s), \tag{115}$$

where $F_\pm(s) = \lim F(s + it)$ as $t \to 0\pm$.

By inspection,

$$F(u) = \tfrac{1}{2}[1 + (i/\pi) \log u]f(u), \tag{116}$$

where $F(u)$ is defined in the complex u-plane cut along the positive s-axis and $\log u = \ln |u| + i\theta$, $0 \le \theta < 2\pi$. Thus, from (114),

$$\int_0^\infty \frac{\sqrt{\sigma}\hat{\Theta}'(\sigma; 0)d\sigma}{\sigma - s} = -\sqrt{s}\hat{\Theta}'(s; 0) \ln s. \tag{117}$$

As $x \to -1$, $s \to 0$, and $\ln (1 + x) = \ln (\epsilon s) \sim \ln s$. Thus, if $\hat{Q}(x; 0)$ is to have a finite limit as $x \to -1$, we must require that

$$\lim_{s \to 0} \sqrt{s}\hat{\Theta}'(s; 0) = -\frac{2\sqrt{2}}{3 + \nu}. \tag{118}$$

By symmetry, the same conclusion holds as $x \to +1$. It then follows from (106), (112), and (117) that

$$Q(\epsilon) \sim -\frac{4 \ln \epsilon}{3 + \nu} \sim \sqrt{10}\, I_c^R \ln (h/c), \tag{119}$$

and from (83), (96), (107), and (119), that

$$I \sim -\frac{\pi M^2 c}{4D} I_c[1 + I_c^R (h/c) \ln (h/c)]. \tag{120}$$

The value of I_c^R is indicated in Fig. 1.

Conclusions

Our results, derived within the framework of linear theory for the special case of bent, infinite plates, show that Sanders' energy-release integral I may be computed using classical plate theory to within a relative error of $O(h/R) \ln (h/R)$ where R is some typical geometric length associated with the undeformed midplane. The path-independence of I was crucial to our arguments. Edge-zone layers of width $O(h)$ are characteristic of shells as well as of plates. As I may be evaluated along a contour lying totally in the interior of a shell, classical shell theory—linear or nonlinear—can be expected to be entirely adequate for computing energy-release rates for slowly moving voids or cracks.

Acknowledgment

We thank Professor Koiter for pointing out to us the significance of the sections on thick plates in the books of Love and Lur'e.

References

1 Inglis, C. E., "Stresses in a Plate Due to the Presence of Cracks and Sharp Corners," *Transactions of the Institution of Naval Architects*, London, Vol. 55, 1913, pp. 219–230.

2 Goodier, J. N., "The Influence of Circular and Elliptical Holes on the Transverse Flexure of Elastic Plates," *London Philosophical Magazine*, Vol. 2, 1936, pp. 69–80.

3 Ang, D. C., and Williams, M. L., "Combined Stresses in an Orthotropic Plate Having a Finite Crack," ASME JOURNAL OF APPLIED MECHANICS, Vol. 28, 1961, pp. 372–378.

4 Simmonds, J. G., "Recent Advances in Shell Theory," *Advances in Engineering Science*, NASA CP-2001, 1976, pp. 617–626.

5 Reissner, E., "The Effect of Transverse Shear Deformation on the Bending of Elastic Plates," ASME JOURNAL OF APPLIED MECHANICS, Vol. 12, 1945, pp. 69–77.

6 Reissner, E., "On the Transverse Bending of Plates Including the Effect of Transverse Shear Deformation," *International Journal of Solids and Structures*, Vol. 11, 1975, pp. 569–573.

7 Reissner, E., "On the Theory of Transverse Bending of Elastic Plates," *International Journal of Solids and Structures*, Vol. 12, 1976, pp. 545–554.

8 van der Heijden, A. M. A., "On Modified Boundary Conditions for a Free Edge of a Shell," Thesis, Technische Hogeschool Delft, Delft University Press, 1976.

9 Koiter, W. T., and Simmonds, J. G., "Foundations of Shell Theory," *Proceedings, 13th International Congress of Theoretical and Applied Mechanics*, Springer-Verlag, 1972, pp. 150–176.

10 Knowles, J. K., and Wang, N-M., "On the Bending of an Elastic Plate Containing a Crack," *Journal of Mathematics and Physics*, Vol. 39, 1960, pp. 223–236.

11 Wang, N-M., "Effects of Plate Thickness on the Bending of an Elastic Plate Containing a Crack," *Journal of Mathematics and Physics*, Vol. 47, 1968, pp. 371–390.

12 Hartranft, R. J., and Sih, G. C., "Effect of Plate Thickness on the Bending Stress Distribution Around Through Cracks," *Journal of Mathematics and Physics*, Vol. 47, 1968, pp. 276–291.

13 Hartranft, R. J., "Improved Approximate Theories of the Bending and Extension of Flat Plates," *Plates and Shells With Cracks*, ed., Sih, G. C., Noordhoff, 1977, Chapter 2.

14 Krenk, S., "Influence of Transverse Shear on an Axial Crack in a Cylindrical Shell," *International Journal of Fracture*, Vol. 14, 1978, pp. 123–143.

15 Cheng, S., "Elasticity Theory of Plates and a Refined Theory," ASME JOURNAL OF APPLIED MECHANICS, Vol. 46, 1979, pp. 644–650.

16 Love, A. E. H., *A Treatise on the Mathematical Theory of Elasticity*, 4th ed., Dover, 1944.

17 Lur'e, A. I., *Three-Dimensional Problems of the Theory of Elasticity*, Interscience, 1964.

18 Sanders, J. L., Jr., "On the Griffith-Irwin Fracture Theory," ASME JOURNAL OF APPLIED MECHANICS, Vol. 27, 1960, pp. 352–353.

19 Simmonds, J. G., and Nicholson, J. W., "Sanders' Energy-Release Rate Integral and Conservation Laws in Finite Elastostatics," to appear in *Archive for Rational Mechanics and Analysis*.

20 Golden'veiser, A. L., "The Principles of Reducing Three-Dimensional Problems of Elasticity of Two-Dimensional Problems of the Theory of Plates and Shells," *Proceedings of the 11th International Congress on Theoretical and Applied Mechanics*, Springer-Verlag, 1966, pp. 306–311.

21 Green, A. E., and Zerna, W., *Theoretical Elasticity*, 2nd ed., Oxford University Press, 1968.

22 Sokolnikoff, I. S., *Mathematical Theory of Elasticity*, 2nd ed., McGraw-Hill, New York, 1956.

23 Byrd, P. F., and Friedman, M. D., *Handbook of Elliptic Integrals for Engineers and Scientists*, 2nd ed., revised, Springer-Verlag, 1971.

24 Carrier, G., Krook, M., and Pearson, C. E., *Functions of a Complex Variable*, McGraw-Hill, New York, 1966.

25 Abramowitz, M., and Stegun, I. A., *Handbook of Mathematical Functions*, U. S. Government Printing Office, 1964.

APPENDIX

The integral in (100) is improper, but it is only the behavior of the integrand near $x = 0$ that must be treated with some care. The following steps, that employ an integral representation for K_2 [25, equation 9.6 23] and a change of variable, should be self-evident.

$$\begin{aligned}
\frac{1}{4}\int_0^\infty G(x)dx &= \lim_{\epsilon \to 0} \int_\epsilon^\infty \left[\frac{1}{x^2} - \frac{K_2(x)}{x}\right]dx \\
&= \lim_{\epsilon \to 0}\left[\frac{1}{\epsilon} - \int_\epsilon^\infty \int_1^\infty \sqrt{t^2 - 1}\, e^{-xt}dtdx\right] \\
&= \lim_{\epsilon \to 0}\left[\int_0^\infty e^{-\epsilon t}dt - \int_1^\infty \sqrt{t^2 - 1}\int_\epsilon^\infty e^{-xt}dxdt\right] \\
&= \lim_{\epsilon \to 0}\left[\int_0^1 e^{-\epsilon t}dt + \int_1^\infty \left(1 - \frac{\sqrt{t^2 - 1}}{t}\right)e^{-\epsilon t}dt\right] \\
&= 1 + \int_0^\infty (\text{sechs} - e^{-s})ds = \tfrac{1}{2}\pi.
\end{aligned} \tag{121}$$

C. A. Anderson

Los Alamos Scientific Laboratory,
University of California,
P.O. Box 1663,
Los Alamos, New Mex. 87545
Mem. ASME

Boussinesq-Papkovich Functions for Creep Around a Spherical Cavity or a Rigid Inclusion in a Gravity-Loaded Half Space

Boussinesq-Papkovich stress functions are used to determine three-dimensional closed form solutions for steady creep around a spherical cavity or rigid inclusion in a half space under gravity loading. The ratio of cavity depth to radius is assumed to be greater than 5, and the flow law of the half space is linear, which allows for solution in terms of a finite number of spherical harmonics. Numerical results are given to show the influence of the lateral stress component at infinity, the stabilizing effect of internal cavity pressure, and buoyancy forces associated with the motion of a rigid inclusion.

Introduction

In recent years much interest has been focused on the use of underground caverns for storage of gaseous and liquid hydrocarbons and radioactive wastes. Relatively pure deposits of halite (salt) have been approved for cavern construction in certain instances, and, because of the compliant nature of the material at relatively low temperatures and stress levels, questions of creep around the cavern have arisen. Since the creep law for halite is a nonlinear (usually taken as a power law) function of the driving stress, numerical methods must be resorted to for investigation of creep and cavern stability [1,2]. Confidence in these calculations would be greatly reinforced if closed-form solutions to even the linear problem could be developed and used for comparison purposes. It is the purpose of this paper to provide such solutions for deep cavities using the elastic analogy for steady creep [3] and the Boussinesq-Papkovich stress function approach. A related problem, the motion of a rigid spherical inclusion embedded in a half space, is also studied using this method, and the Stokes solution for viscous flow about a sphere is obtained.

In the present paper we treat an idealized problem of a semi-infinite, linearly creeping body containing a spherical cavity of radius a and loaded by gravity and uniform pressure on the cavity surface. The center of the cavity is located at a depth H, and the ratio H/a is assumed to 5 or greater, whereupon stresses applied to the cavity wall are little felt on the planar boundary. The assumption is consistent with construction practice for caverns in salt domes. This considerably simplifies the analyses of Tsuchida and Nakahara [4, 5] as applied to a semi-infinite elastic body with an embedded cavity where traction boundary conditions on both the planar and cavity surfaces are satisfied exactly with the aid of Hankel transforms and relations between spherical and cylindrical harmonics.

As mentioned, the elastic problem of a spherical cavity in a half space has been treated in references [4, 5] for uniform tension applied at infinity and for the case of uniform pressure on the plane boundary or the surface of the cavity. Mitchell and Weese [6] used spherical dipolar coordinates to treat the same problems, but their results appear to differ significantly from those of [5] for the case of uniform pressure on the plane boundary. Atsumi and Itou [7] gave the elastic solution for the transversely isotropic half space under a uniform tension at infinity. Finally, there appears to be no exact solutions as yet for the case of the elastic half space with spherical cavity and loaded by a gravitational body force field, but it is clear that the method of Tsuchida and Nakahara could be used to supply such a solution.

Basic Equations

The origin of a spherical coordinate system (R, θ, ϕ) is located at a distance H from the planar surface of the half space as shown in Fig. 1. The spherical cavity is of radius a as shown, and is loaded by a uniform pressure p. The half-space material is linearly viscous with constant viscosity G. The density of the half space is ρ and under the action of the gravitational force a far field equilibrium system of stresses

$$\sigma_r = \sigma_\theta = -\lambda\rho gz, \quad \sigma_z = -\rho gz, \quad \tau_{rz} = 0 \tag{1}$$

Contributed by the Applied Mechanics Division of THE AMERICAN SOCIETY OF MECHANICAL ENGINEERS, and presented at the 1981 Joint ASME/ASCE Applied Mechanics, Fluids Engineering, and Bioengineering Conference, University of Colorado, Boulder, Colo., June 22–27, 1981.

Discussion on this paper should be addressed to the Editorial Department, ASME, United Engineering Center, 345 East 47th Street, New York, N.Y. 10017, and will be accepted until September 1, 1981. Readers who need more time to prepare a Discussion should request an extension from the Editorial Department. Manuscript received by ASME Applied Mechanics Division, February, 1980; final revision, October, 1980. Paper No. 81-APM-30.

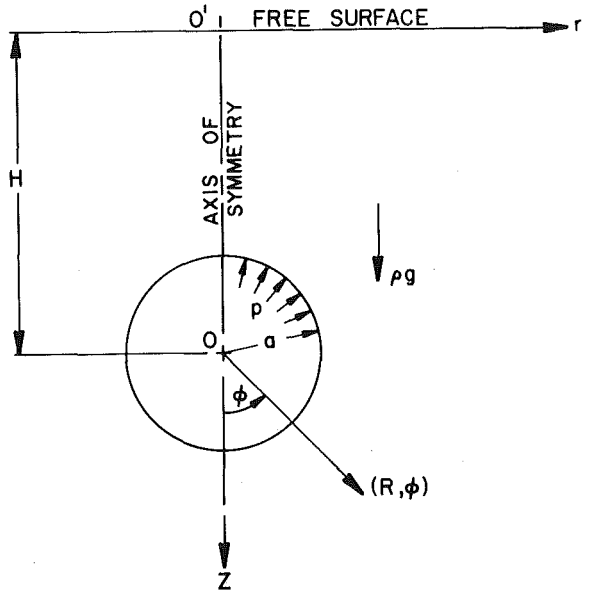

Fig. 1 Geometry of the spherical cavity problem

is developed.[1] Here, the stress components are taken with respect to a cylindrical coordinate system (r, θ, z) with origin 0′. This stress field will put tractions on the cavity surface, which will be removed by the system of stresses developed below using the Boussinesq-Papkovich stress function representation and outer spherical harmonics.

The basic equations for steady creep of a linearly viscous material are the equilibrium equations, the strain rate-velocity relations, and the constitutive equation. Under the "elastic analog" [3], these equations become the equations for linear incompressible elasticity where the elastic Poisson's ratio is taken as one half to reflect incompressibility of the creep strain rate, the viscosity becomes the shear modulus, and velocities and strain rates become displacements and strains, respectively. Elasticity solutions then carry over to linear steady creep solutions.

A general solution of the displacement equations of equilibrium for the case of axisymmetric elasticity without torsion is given in terms of Boussinesq-Papkovich stress functions χ and ψ [8]. Taking Poisson's ratio equal to one half, in spherical coordinates the velocities (u_R, w_ϕ) are given by

$$2Gu_R = \frac{\partial \chi}{\partial R} + R\cos\phi\frac{\partial \Psi}{\partial R} - \cos\phi\Psi$$
$$2Gw_\phi = \frac{1}{R}\frac{\partial \chi}{\partial \phi} + \cos\phi\frac{\partial \Psi}{\partial \phi} + \sin\phi\Psi \tag{2}$$

while the stresses $(\sigma_R, \sigma_0, \sigma_\phi, \tau_{R\phi})$ are given by

$$\sigma_R = \frac{\partial^2\chi}{\partial R^2} + R\cos\phi\frac{\partial^2\Psi}{\partial R^2} - \cos\phi\frac{\partial \Psi}{\partial R} + \frac{\sin\phi}{R}\frac{\partial \Psi}{\partial \phi}$$
$$\sigma_0 = \frac{1}{R}\frac{\partial \chi}{\partial R} + \frac{\cot\phi}{R^2}\frac{\partial \chi}{\partial \phi} + \frac{1}{R\sin\phi}\frac{\partial \Psi}{\partial \phi}$$
$$\sigma_\phi = \frac{1}{R^2}\frac{\partial^2\chi}{\partial \phi^2} + \frac{1}{R}\frac{\partial \chi}{\partial R} + \frac{\cos\phi}{R}\frac{\partial^2\Psi}{\partial \phi^2} + \frac{\sin\phi}{R}\frac{\partial \Psi}{\partial \phi} \tag{3}$$
$$\tau_{R\phi} = \frac{1}{R}\frac{\partial^2\chi}{\partial R\partial\phi} - \frac{1}{R^2}\frac{\partial \chi}{\partial \phi} + \cos\phi\frac{\partial^2\Psi}{\partial R\partial\phi} - \frac{\cos\phi}{R}\frac{\partial \Psi}{\partial \phi}$$

and where, in the absence of body forces, χ and Ψ satisfy

$$\nabla^2\chi = 0, \qquad \nabla^2\Psi = 0. \tag{4}$$

Solutions to equation (4) for the spherical cavity problem are given in terms of outer spherical harmonics possessing singularities at $R = 0$ and being regular for $R \geq a$,

$$\chi = \sum_{m=0}^{\infty} A_m \frac{P_{m(\mu)}}{R^{m+1}}, \qquad \Psi = \sum_{m=0}^{\infty} B_m \frac{P_{m(\mu)}}{R^{m+1}} \tag{5}$$

where $\mu = \cos\phi$ and P_m is the Legendre polynomial of order m.

Our objective is to produce a solution for the half-space problem that contains a cavity with no traction on the cavity boundary. This requires that we superimpose on the stress solution, equation (1), a complementary stress distribution, which annihilates the stresses on the cavity boundary produced by the solution represented by equation (1). To do this we expand the tractions $(\sigma_R, \tau_{R\phi})$ on the cavity surface caused by the stress field equation (1) in terms of Legendre polynomials and then to use the negative of the tractions as boundary conditions to determine a solution of equations (3) and (5); i.e., determine the constants A_m, B_m, $m = 0, 1, 2, \ldots$. Converting the stress state, equation (1), into spherical coordinates and spherical stress components and then expanding in Legendre polynomials gives the unique finite series representation,

$$\frac{\sigma_R(a)}{\rho gH} = \frac{1}{3}(1+2\lambda) + \frac{\kappa}{5}(3+2\lambda)P_1(\mu) + \frac{2}{3}(1-\lambda)P_2(\mu) + \frac{2\kappa}{5}(1-\lambda)P_3(\mu)$$
$$\frac{\tau_{R\phi}(a)}{\rho gH\sin\phi} = -(1-\lambda)\left\{\frac{1}{5}\kappa P_1'(\mu) + \frac{1}{3}P_2'(\mu) + \frac{2\kappa}{15}P_3'(\mu)\right\}. \tag{6}$$

In equation (6) $\kappa = a/H$. Substituting equation (5) into the first and last of equation (3), setting $R = a$ in the resulting equations, and then equating[2] to equation (6) gives a set of equations for the coefficients A_m, B_m, $m = 0, 1, 2, \ldots$.

$$A_0 = \frac{1}{18}(-7+16\lambda) \quad B_0 = \frac{\kappa}{3}$$
$$A_1 = -\frac{5}{19}(1-\lambda)\kappa \quad B_1 = \frac{5}{9}(1-\lambda)$$
$$A_2 = -\frac{2}{9}(1-\lambda) \quad B_2 = \frac{14}{57}(1-\lambda)\kappa \tag{7}$$
$$A_3 = \frac{2}{19}(1-\lambda)\kappa \quad B_3 = 0$$

The sum of this solution given by equations (2), (3), (5), and (7) and the solution given by equation (1) will correspond to the half-space solution under gravity loading and proportional lateral stress at infinity and with no traction on the cavity surface. There will, however, be traction on the planar surface. For $H/a \geq 5$ this traction will be shown to be small.

When an infinite elastic body is subjected to a uniform pressure $\mathcal{P}$ on the wall of a spherical cavity of radius a, the Boussinesq-Papkovich functions take the simple form

$$\chi = \frac{\mathcal{P}a^3}{2R}, \qquad \Psi = 0 \tag{8}$$

from which the stress components and velocities in spherical coordinates can be derived. On the plane boundary of Fig. 1 the stress components τ_{rz}, σ_z are

$$\frac{\sigma_z}{\mathcal{P}} = \frac{a^3}{2}\left\{\frac{1}{(H^2+r^2)^{3/2}} - \frac{3H^2}{(H^2+r^2)^{5/2}}\right\}, \quad \frac{\tau_{rz}}{\mathcal{P}} = \frac{3}{2}\frac{a^3Hr}{(H^2+r^2)^{5/2}}. \tag{9}$$

[1] λ is a parameter that reflects the magnitude of the lateral stress, which is also proportional to distance from the planar surface. If, for instance, $\lambda = \nu/(1-\nu)$ where ν is the elastic Poisson's ratio for the half-space material, then the lateral stress would enforce a zero lateral displacement at infinity.

[2] Recurrence relations between Legendre polynomials and their derivatives must also be used to arrive at a form consistent with the representation in equation (6).

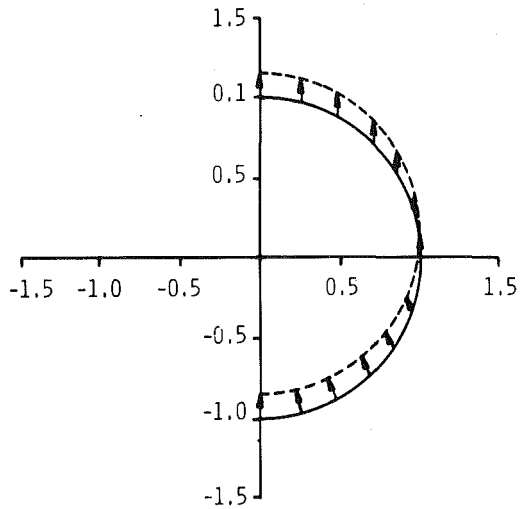

Fig. 2 Velocity field around a stabilized cavity ($p = \rho gH$) in a half space under hydrostatic loading ($\lambda = 1$)

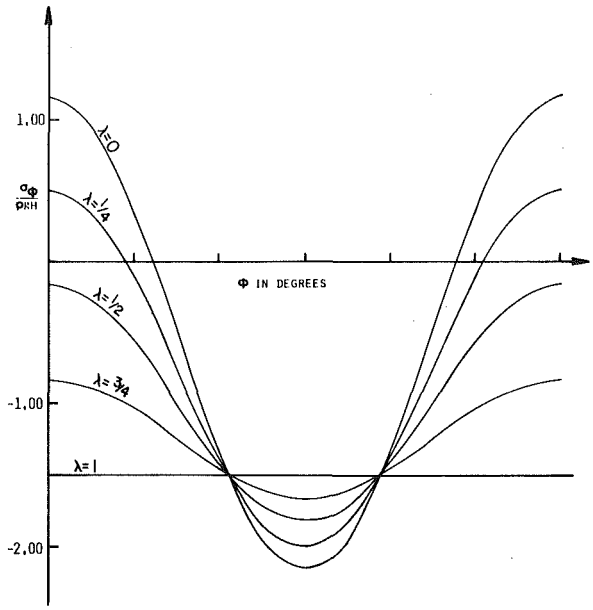

Fig. 3 Variation of hoop stress on the cavity surface for various values of λ, $\kappa = 0$

For $H/a > 5$ the stress components at the planar surface are less than one percent of the applied pressure on the cavity wall.

Numerical Results

The velocity components (u, w) corresponding to the stress state, equation (1), for a linearly viscous material of viscosity G can be shown to be (in cylindrical coordinates)

$$2Gu = \frac{1}{3}(1-\lambda)\,\rho g r z,\quad 2Gw = -\frac{1}{6}(1-\lambda)\,\rho g\,(2z^2 + r^2). \tag{10}$$

When $\lambda = 1$, the state of stress is hydrostatic and the velocity field is identically zero. Also, referring to equation (7), we see that the solution around the cavity is particularly simple since $A_0 = \frac{1}{2}$ and $B_0 = \kappa/3$ are the only nonzero coefficients in the polynomial representation. For definiteness we display this solution for pressure $\not p$ on the cavity surface and a hydrostatic gravitational loading ρg:

$$\begin{aligned}
\frac{2Gu_R}{\rho gHa} &= -\frac{1}{2}\left(1 - \frac{\not p}{\rho gH}\right)\left(\frac{a}{R}\right)^2 - \frac{2}{3}\kappa\left(\frac{a}{R}\right)\cos\phi \\
\frac{2Gw_\phi}{\rho gHa} &= \frac{1}{3}\kappa\left(\frac{a}{R}\right)\sin\phi \\
\frac{\sigma_R}{\rho gH} &= -\left[1 + \kappa\left(\frac{R}{a}\right)\cos\phi\right] + \left(1 - \frac{\not p}{\rho gH}\right)\left(\frac{a}{R}\right)^3 + \kappa\left(\frac{a}{R}\right)^2\cos\phi \\
\frac{\sigma_\Theta}{\rho gH} &= \frac{\sigma_\phi}{\rho gH} = -\left[1 + \kappa\left(\frac{R}{a}\right)\cos\phi\right] - \frac{1}{2}\left(1 - \frac{\not p}{\rho gH}\right)\left(\frac{a}{R}\right)^3
\end{aligned} \tag{11}$$

and

$$\tau_{R\phi} = 0.$$

Inspection of the radial velocity component of equation (11) shows that for deep cavities ($\kappa = a/H \ll 1$) and $\not p < \rho gH$ the deformation is essentially a uniform collapse of the cavity. Of greater interest, however, is the case when the applied cavity pressure equals the overburden pressure at the cavity equatorial plane. Here, the velocity field on the cavity wall is given by

$$\frac{2Gu_R}{\rho gHa} = -\frac{2}{3}\kappa\cos\phi,\quad \frac{2Gw_\phi}{\rho gHa} = \frac{1}{3}\kappa\sin\phi \tag{12}$$

and is a volume preserving rise of the cavity as shown in Fig. 2. This buoyancy effect had been observed previously in numerical investigation of nonlinear creep around a cavity in halite [1].

Setting $\kappa = 0$ in equation (7) gives the solution for cavity under biaxial compressive stress field ρgH and $\lambda\rho gH$ at infinity. With $A_0 = (7 + 16\lambda)/18$, $A_2 = -2(1-\lambda)/9$, and $B_1 = 5(1-\lambda)/9$ being the only nonzero coefficients, the following stress components are obtained:

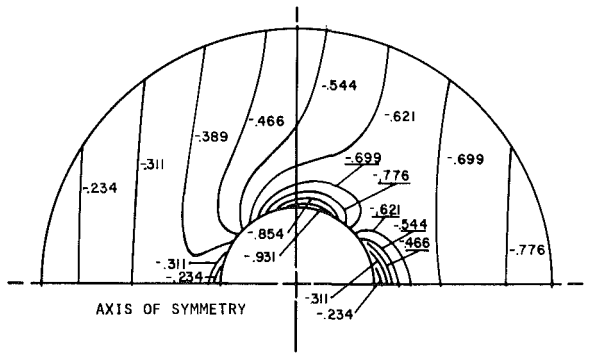

Fig. 4 Contour values of hoop stress around the cavity for $\kappa = 0.2$ and $\lambda = 0.5$

$$\begin{aligned}
\frac{\sigma_R}{\rho gH} &= -\cos^2\phi - \lambda\sin^2\phi + \frac{(1+2\lambda)}{3}\left(\frac{a}{R}\right)^3 P_0 \\
&\quad + \frac{2}{3}\left(\frac{a}{R}\right)^3\left[(-7+16\lambda)\left(\frac{a}{R}\right)^2 + 5(1-\lambda)\right]P_2 \\
\frac{\tau_{R\phi}}{\rho gH\sin\phi} &= -(1-\lambda)\cos\phi + \frac{(1-\lambda)}{9}\left(\frac{a}{R}\right)^3\left[5 - 8\left(\frac{a}{R}\right)^2\right]P_2' \\
\frac{\sigma_\phi}{\rho gH} &= -\lambda - \frac{(1+2\lambda)}{6}\left(\frac{a}{R}\right)^3 P_1' + \frac{2}{9}(1-\lambda)\left(\frac{a}{R}\right)^5 P_3' \\
\frac{\sigma_\phi}{\rho gH} &= -(\sin^2\phi + \lambda\cos^2\phi) + \frac{(4\lambda-13)}{18}\left(\frac{a}{R}\right)^3 P_0 \\
&\quad + 2(1-\lambda)\left(\frac{a}{R}\right)^5 P_2 + 5\frac{(1-\lambda)}{9}\left(\frac{a}{R}\right)^3 P_1'
\end{aligned} \tag{13}$$

Fig. 3 illustrates the variation of $\sigma_\phi/\rho gH$ around the cavity surface for $\lambda = 0, \frac{1}{4}, \frac{1}{2}, \frac{3}{4}$, and 1. The case $\lambda = 0$ agrees with the well-known solution (see reference [8], for instance) for a spherical cavity in an incompressible elastic material submitted to uniform axial compression at infinity. The stress concentration factor is 39/18 as determined by the value of σ_ϕ at the equator of the cavity.

Fig. 4 illustrates a contour plot of the hoop stress σ_θ around the cavity for $\kappa = 0.2$ and $\lambda = 0.5$, and in Fig. 5 the values of σ_θ on the

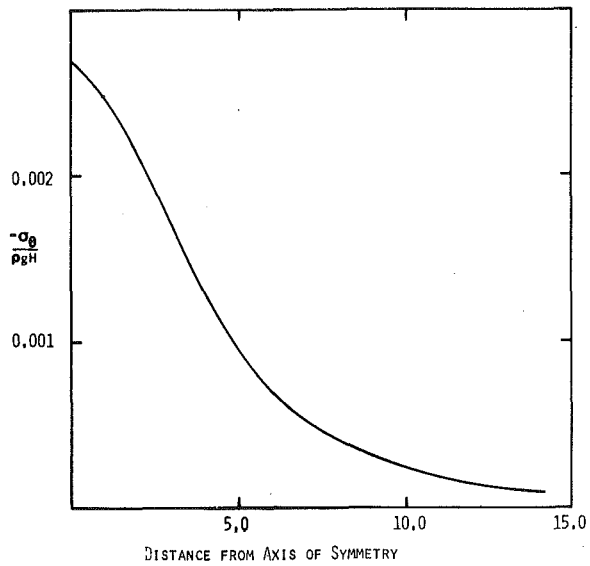

Fig. 5 Values of hoop stress on the plane surface of the half space for κ = 0.2 and λ = 0.5

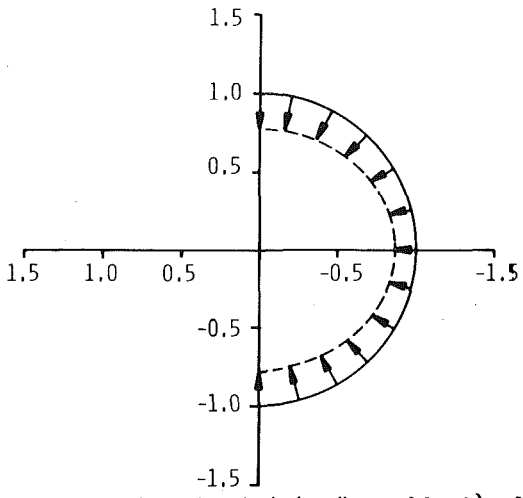

Fig. 6 Deformation of the spherical cavity, κ = 0.2 and λ = 0.5

planar surface are shown. Legendre polynomials and their derivatives up to and including order 3 are present in this solution. As can be seen from Figs. 4 and 5, the hoop stress along the planar surface is less than one percent of its maximum values on the cavity surface. Fig. 6 illustrates the deformed shape of the cavity surface for the case $\kappa = 0.2$ and $\lambda = 0.5$. The deformed shape was produced from displacements found by applying the velocity field over a time period Δt where Δt is used for scaling the resultant deformation.

The Boussinesq-Papkovich functions can also be used to obtain the solution for slow, viscous flow about a spherical inclusion in a gravity loaded half space. Here, we take $\lambda = 1$ and, hence, the velocity field away from the inclusion is identically zero. Presuming that the inclusion is rising with a velocity u_0 because its density, ρ_1, is less than that of the surrounding medium and that the inclusion is bonded to it, we must have the boundary conditions,

$$u_R = -u_0 \cos\phi, \quad w_\phi = u_0 \sin\phi \quad \text{on} \quad R = a.$$

Substituting equations (5) into equations (2) and setting equal to the foregoing velocity boundary values at $R = a$ then gives all zero coefficients except for $B_0 = 3Gu_0a/2$ and $A_1 = -Gu_0a^3/2$. The velocities and stresses in spherical coordinates are then found to be

$$u_R = \frac{u_0}{2}\left(\frac{a}{R}\right)\left[\left(\frac{a}{R}\right)^2 - 3\right]\cos\phi$$

$$w_\phi = \frac{u_0}{4}\left(\frac{a}{R}\right)\left[\left(\frac{a}{R}\right)^2 + 3\right]\sin\phi \tag{14}$$

$$\frac{\sigma_R}{\rho g H} = -\left(1 + \frac{R}{H}\cos\phi\right) + \frac{3}{2}\left(\frac{a}{R}\right)^2\left[\frac{3}{2} - \left(\frac{a}{R}\right)^2\right]\frac{Gu_0\cos\phi}{\rho g H a}$$

$$\frac{\tau_{R\phi}}{\rho g H} = -\frac{3}{4}\left(\frac{a}{R}\right)^4\frac{Gu_0\sin\phi}{\rho g H a} \tag{15}$$

$$\frac{\sigma_\phi}{\rho g H} = \frac{\sigma_0}{\rho g H} = -\left(1 + \frac{R}{H}\cos\phi\right) + \frac{3}{4}\left(\frac{a}{R}\right)^4\frac{Gu_0\cos\phi}{\rho g H a}.$$

We can calculate the force on the inclusion from the stress field, equation (15) evaluated at $R = a$ as

$$2\pi a^2 \int_0^\pi [\cos\phi\,\sigma_R - \sin\phi\,\tau_{R\phi}]\sin\phi\,d\phi.$$

Equating to the weight of the spherical inclusion then gives a relation between the velocity of rise and the density contrast $\rho - \rho_1$ as

$$u_0 = \frac{2}{9}\frac{a^2 g}{G}(\rho - \rho_1). \tag{16}$$

This formula can be reduced to the classical Stokes formula for the drag on a sphere moving slowly through a linearly viscous fluid [9].

References

1 Anderson, C. A., "An Investigation of the Steady Creep of a Spherical Cavity in a Half Space," ASME JOURNAL OF APPLIED MECHANICS, Vol. 43, 1976, pp. 254–258.

2 Anderson, C. A., and Bridwell, R. J., "A Finite-Element Method for Studying the Transient Nonlinear Thermal Creep of Geological Structures," *International Journal for Num. and Anal. Meth.*, in Geomechanics, Vol. 4, No. 3, 1980, pp. 255–276.

3 Odquist, F. K. G., *Mathematical Theory of Creep and Creep Rupture*, 2nd ed., Oxford Press, 1974.

4 Tsuchida, E., and Nakahara, I., "Three-Dimensional Stress Concentration Around a Spherical Cavity in a Semi-Infinite Elastic Body," *Bulletin of Japan Soc. Mech. Engrs.*, Vol. 13, No. 58, 1970, pp. 499–508.

5 Tsuchida, E., and Nakahara, I., "Stresses in a Semi-Infinite Body Subjected to Uniform Pressure on the Surface of the Cavity and the Plane Boundary," *Bulletin of Japan Soc. Mech. Engrs.*, Vol. 15, No. 79, 1972, pp. 1–10.

6 Mitchell, T. P., and Weese, J. A., "Stress Distribution Analyzed in Bispherical Coordinates," ASME JOURNAL OF APPLIED MECHANICS, Vol, 27, 1960, pp. 726–731.

7 Atsumi, A., and Itou, S., "Stresses in a Transversely Isotropic Half Space Having a Spherical Cavity," ASME JOURNAL OF APPLIED MECHANICS, Vol. 41, 1974, pp. 708–712.

8 Sternberg, E., and Sadowsky, M. A., "On the Axisymmetric Problem of the Theory of Elasticity for an Infinite Region Containing Two Spherical Cavities," ASME JOURNAL OF APPLIED MECHANICS, Vol. 19, 1952, pp. 19–27.

9 Landau, L., and Lifshitz, E., *Fluid Mechanics*, Pergamon Press, 1959, pp. 63–67.

F. Delale[2]
F. Erdogan
Professor of Mechanics.
Mem. ASME

Department of Mechanical Engineering
and Mechanics,
Lehigh University,
Bethlehem, Pa. 18015

Viscoelastic Analysis of Adhesively Bonded Joints[1]

In this paper an adhesively bonded lap joint is analyzed by assuming that the adherends are elastic and the adhesive is linearly viscoelastic. After formulating the general problem a specific example for two identical adherends bonded through a three parameter viscoelastic solid adhesive is considered. The standard Laplace transform technique is used to solve the problem. The stress distribution in the adhesive layer is calculated for three different external loads namely, membrane loading, bending, and transverse shear loading. The results indicate that the peak value of the normal stress in the adhesive is not only consistently higher than the corresponding shear stress but also decays slower.

1 Introduction

In its simplest form an adhesively bonded structure consists of three components of different mechanical properties, namely, the adhesive and the two adherends. Because of the nonhomogeneous nature and of the geometrical complexity of the medium, even for the linearly elastic materials the exact analytical treatment of the problem regarding the stress analysis of the structure is, in general, hopelessly complicated. The existing analytical studies are, therefore, based on certain simplifying assumptions with regard to the modeling of the adhesive and the adherends. The adherends are usually modeled as an isotropic or orthotropic membrane (e.g., [1]), a plate (e.g., [2,3]), or an elastic continuum (e.g., [4–6]). The primary physical consideration used in the selection of a particular model is generally the ratio of the thickness of the adherend to lateral dimensions of the bond region. For example, for adherends with a very small relative thickness the bending stiffness may be neglected whereas if the thickness of the adherend is not small even the plate assumption may be erroneous. As for the adhesives, generally the thickness variation of the stresses is neglected and the adhesive layer is modeled as a linear shear or a tension-shear spring.

In most applications of structural adhesives the operating temperature is such that the adhesive remains in its initial glassy stage through the entire loading period and hence it is not necessary to consider the time-dependent behavior of the stress-strain relations in performing the stress analysis of the joint. However, in certain applications, the temperature and the load duration may be such that the rheological behavior of the adhesive may no longer be negligible. In this paper the adhesively bonded joint problem is considered by assuming that the adhesive is a linear viscoelastic material.

2 Formulation of the Problem

In formulating the adhesively bonded joint problems unless the thickness of the adherends is at least two orders of magnitude smaller than the length characterizing the bond region the generalized plane stress or the membrane assumption does not seem to be very realistic. On the other hand in an adhesive joint between relatively thin adherends, even if it were possible to formulate the problem by assuming the adherends as elastic continua, the numerical analysis involve such severe convergence problems that the accuracy of the results may be highly questionable [5]. In such problems the plate assumption in modeling the adherends appears to be a fairly good compromise. Thus, in this paper, the problem will be formulated under the following primary assumptions: (*a*) the adherends are treated as linear elastic plates and the transverse shear effects are taken into account; and (*b*) the adhesive is considered as a viscoelastic solid in which the in-plane strain as well as out-of-plane strain and shear strain are assumed to be nonzero. The secondary assumptions under which the specific problem is formulated and solved simplify the analysis quite considerably but do not affect the character of the solution. These assumptions are: (*a*) the problem is one of plane strain, that is, the bonded joint is very "wide" and undergoes cylindrical bending; (*b*) the adherends have the same thickness and are made of the same material; and (*c*) the structure is a single lap joint. The elastic version of the problem neglecting the transverse shear effects in the adherends was considered in [2]. The solution of, again, the elastic problem for different adherends with a somewhat simpler adhesive model may be found in [3].[3]

[1] This work was supported by NASA-Langley under the Grant NGR 39-007-011 and by NSF under the Grant ENG 78-09737.

[2] Permanently, Faculty of Engineering and Architecture, Technical University of Istanbul, Macka, Istanbul, Turkey.

Contributed by the Applied Mechanics Division for publication in the JOURNAL OF APPLIED MECHANICS.

Discussion on this paper should be addressed to the Editorial Department, ASME, United Engineering Center, 345 East 47th Street, New York, N. Y. 10017, and will be accepted until September 1, 1981. Readers who need more time to prepare a Discussion should request an extension from the Editorial Department. Manuscript received by ASME Applied Mechanics Division, July, 1980; final revision, October, 1980.

[3] Needless to say, the problem has been very widely studied. Some references to further analytical work and to finite-element-type solutions may be found in [3].

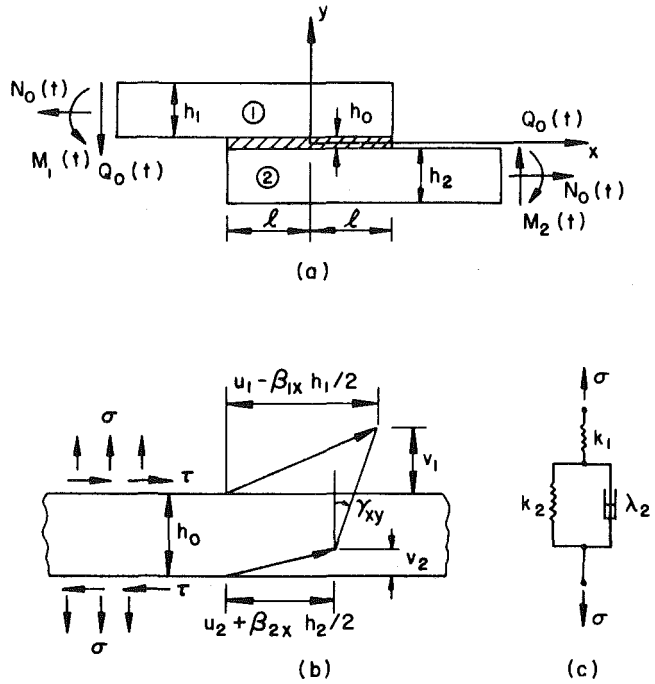

Fig. 1 Geometry of the bonded joint and the viscoelastic adhesive model

It should be pointed out that at present the continuum elasticity solution of the problem appears to be intractable. To appreciate the difficulties involved, one may refer to [4] where the elastostatic problem for a "lap joint" is considered. In [4] the problem could be solved only under rather severe simplifying assumptions. The two-dimensional elasticity problem formulated in [4] is actually that of an infinite strip $(-\infty < x < \infty, -h < y < h)$ containing two semi-infinite cracks in the midplane $(y = 0, |x| > a)$ of the strip. Uniform tension is applied at infinity to the lower half on one side (at $x = \infty$, $-h < y < 0$) and the upper half on the other $(x = -\infty, 0 < y < h)$. The problem is then solved basically as a crack problem.[4]

The geometry of the problem under consideration is shown in Fig. 1(*a*). From the equilibrium of the plate elements for the adherends 1 and 2 the following differential equations may be obtained:

$$\frac{\partial N_{1x}}{\partial x} = \tau, \quad \frac{\partial Q_{1x}}{\partial x} = \sigma, \quad \frac{\partial M_{1x}}{\partial x} = Q_{1x} - \frac{h_1 + h_0}{2}\tau, \quad (1\ a\text{–}c)$$

$$\frac{\partial N_{2x}}{\partial x} = -\tau, \quad \frac{\partial Q_{2x}}{\partial x} = -\sigma, \quad \frac{\partial M_{2x}}{\partial x} = Q_{2x} - \frac{h_2 + h_0}{2}\tau, \quad (2\ a\text{–}c)$$

where N_{ix}, Q_{ix}, M_{ix} are, respectively the standard membrane, transverse shear, and moment resultants, the index $i = 1, 2$ referring to the adherends 1 and 2, h_1, h_2, and h_0 are the thicknesses of the adherends and the adhesive as shown, and $\sigma(x, t)$ and $\tau(x, t)$ are the *interface normal and shear stresses. In modeling the adhesive it is* assumed that the stress components $\sigma_y(x, y, t) = \sigma(x, t)$ and $\tau_{xy}(x, y, t) = \tau(x, t)$ in the adhesive layer are independent of the y-coordinate.

Assuming cylindrical bending, $\epsilon_{1z} = 0$, $\epsilon_{2z} = 0$. The stress resultant-displacement relations may then be expressed as

$$\frac{\partial u_1}{\partial x} = C_1 N_{1x}, \quad \frac{\partial \beta_{1x}}{\partial x} = D_1 M_{1x}, \quad \frac{\partial v_1}{\partial x} + \beta_{1x} = \frac{Q_{1x}}{B_1}, \quad (3\ a\text{–}c)$$

$$\frac{\partial u_2}{\partial x} = C_2 N_{2x}, \quad \frac{\partial \beta_{2x}}{\partial x} = D_2 M_{2x}, \quad \frac{\partial v_2}{\partial x} + \beta_{2x} = \frac{Q_{2x}}{B_2}, \quad (4\ a\text{–}c)$$

where

$$C_i = \frac{1 - \nu_i^2}{E_i h_i}, \quad D_i = \frac{12(1 - \nu_i^2)}{E_i h_i^3}, \quad B_i = \frac{5}{6}\mu_i h_i, \quad (i = 1, 2) \quad (5\ a\text{–}c)$$

E_i, μ_i, ν_i, $(i = 1, 2)$ are the elastic constants, $u_i(x, t)$ and $v_i(x, t)$, $(i = 1, 2)$ are x and y-components of the displacement vector and β_{ix}, $(i = 1, 2)$ is the rotation of the normal to the midplane of the adherends.

It may be seen that as stated the problem has 14 unknown functions, namely, σ, τ, u_i, v_i, β_{ix}, N_{ix}, Q_{ix}, M_{ix}, $(i = 1, 2)$. Equations (1)–(4) provide 12 relations. The remaining two relations necessary to complete the formulation of the problem are obtained from the continuity conditions for the displacements in the bond region. To do this the mechanics of the adhesive layer, specifically its constitutive relations need to be considered.

Referring to Fig. 1(*b*) the average strains in the adhesive may be expressed as

$$\gamma_{xy} = \left(u_1 - \frac{h_1}{2}\beta_{1x} - u_2 - \frac{h_2}{2}\beta_{2x}\right)/h_0,$$

$$\epsilon_y = (v_1 - v_2)/h_0,$$

$$\epsilon_x = \left(\frac{\partial u_1}{\partial x} - \frac{h_1}{2}\frac{\partial \beta_{1x}}{\partial x} + \frac{\partial u_2}{\partial x} + \frac{h_2}{2}\frac{\partial \beta_{2x}}{\partial x}\right)/2 \quad (6\ a\text{–}c)$$

Noting that all the remaining strain components in the adhesive are zero and defining

$$e = (\epsilon_x + \epsilon_y)/3, \quad (7)$$

the strain tensor for the adhesive may be decomposed as follows:

$$\begin{bmatrix} \epsilon_x & \gamma_{xy}/2 & 0 \\ \gamma_{xy}/2 & \epsilon_y & 0 \\ 0 & 0 & 0 \end{bmatrix} = \begin{bmatrix} e & 0 & 0 \\ 0 & e & 0 \\ 0 & 0 & e \end{bmatrix} + \begin{bmatrix} \epsilon_x - e & \gamma_{xy}/2 & 0 \\ \gamma_{xy}/2 & \epsilon_y - e & 0 \\ 0 & 0 & -e \end{bmatrix} \quad (8)$$

Similarly, noting that $\sigma_y = \sigma$, $\tau_{xy} = \tau$, the stress tensor for the adhesive may be decomposed as

$$\begin{bmatrix} \sigma_x & \tau & 0 \\ \tau & \sigma & 0 \\ 0 & 0 & \sigma_z \end{bmatrix} = \begin{bmatrix} s & 0 & 0 \\ 0 & s & 0 \\ 0 & 0 & s \end{bmatrix} + \begin{bmatrix} \sigma_x - s & \tau & 0 \\ \tau & \sigma - s & 0 \\ 0 & 0 & \sigma_z - s \end{bmatrix} \quad (9)$$

where, the hydrostatic component of the stress tensor s is defined by

$$s = (\sigma_x + \sigma + \sigma_z)/3 \quad (10)$$

The constitutive equations of linear isotropic viscoelastic materials may be expressed in terms of either hereditary integrals by using creep compliance or relaxation functions, or differential operators[5] [7–9]. In this paper the latter approach is adopted and it is assumed that

$$P_1(s_{ij}) = Q_1(e_{ij}), \quad (i, j) = 1, 2, 3, \quad (11)$$

$$P_2(s) = Q_2(e) \quad (12)$$

where s_{ij} and e_{ij} $(i, j,) = 1, 2, 3$, are the deviatoric components of stress and strain tensors, respectively, as given by (8) and (9), s and e are defined by (10) and (7), and P_1, Q_1, P_2, and Q_2 are differential operators of the form $\sum_0^n a_k(t)\, \partial^k/\partial t^k$, the coefficients a_k being generally

[4] On the other hand in this paper the lap joint problem is formulated as a finite plate problem under certain boundary conditions. Nevertheless, qualitatively the elastic results found in this paper (equations (71) and (73)) agree with that given in [4].

[5] The two formulations are, of course, related through Laplace transforms. For example, the creep compliance $J(t)$ is the inverse Laplace transform of $\overline{P}(s)/s\overline{Q}(s)$ where P and Q are the related differential operators operating on σ and ϵ, respectively, and s is the transform variable.

functions of temperature. More explicitly, from (7)–(12) it may be seen that

$$P_1(2\sigma_x - \sigma - \sigma_z) = Q_1(2\epsilon_x - \epsilon_y), \tag{13}$$

$$P_1(2\sigma - \sigma_x - \sigma_z) = Q_1(2\epsilon_y - \epsilon_x), \tag{14}$$

$$P_1(2\sigma_z - \sigma_x - \sigma) = -Q_1(\epsilon_x + \epsilon_y), \tag{15}$$

$$P_1(\tau) = \frac{1}{2} Q_1(\gamma_{xy}), \tag{16}$$

$$P_2(\sigma_x + \sigma + \sigma_z) = Q_2(\epsilon_x + \epsilon_y). \tag{17}$$

Since $\sum_1^3 s_{ii} = 0$ and $\sum_1^3 e_{ii} = 0$, equations (13)–(15) are not linearly independent. Equation (14) may be obtained by adding (13) and (15) and will, therefore, be ignored in the remainder of the analysis.

Practical experience indicates that under a hydrostatic stress state most viscoelastic materials behave elastically. Hence, it may be assumed that

$$P_2 \equiv 1, \quad Q_2 \equiv 3K, \tag{18}$$

or

$$\sigma_x + \sigma + \sigma_z = 3K(\epsilon_x + \epsilon_y) \tag{19}$$

where K is the bulk modulus of the adhesive. Eliminating σ_x and σ_z from (13), (15), and (19) and using (6 a–c), the constitutive equations may now be written

$$3P_1\left\{K\left[\frac{1}{2}\frac{\partial u_1}{\partial x} - \frac{h_1}{4}\frac{\partial \beta_{1x}}{\partial x} + \frac{1}{2}\frac{\partial u_2}{\partial x} + \frac{h_2}{4}\frac{\partial \beta_{2x}}{\partial x} + \frac{v_1 - v_2}{h_0}\right] - \sigma\right\}$$
$$= Q_1\left\{\frac{1}{2}\frac{\partial u_1}{\partial x} - \frac{h_1}{4}\frac{\partial \beta_{1x}}{\partial x} + \frac{1}{2}\frac{\partial u_2}{\partial x} + \frac{h_2}{4}\frac{\partial \beta_{2x}}{\partial x} - \frac{2}{h_0}(v_1 - v_2)\right\} \tag{20}$$

$$P_1(\tau) = \frac{1}{2} Q_1\left\{\left[u_1 - \frac{h_1}{2}\beta_{1x} - u_2 - \frac{h_2}{2}\beta_{2x}\right]/h_0\right\} \tag{21}$$

Equations (20) and (21) with (1)–(4) provide the system of 14 relations necessary to solve for the unknown functions $\sigma, \tau, u_i, v_i, \beta_{ix}, N_{ix}, Q_{ix}$, and M_{ix}, $(i = 1,2)$.

3 Example

As an example we consider a single lap joint which consists of two identical adherends bonded through an adhesive layer which may be represented by a three-parameter viscoelastic solid (Fig. 1 (c)). For the adherends we have

$$h_1 = h_2 = h, \quad C_1 = C_2 = C = \frac{1 - \nu^2}{Eh},$$
$$D_1 = D_2 = D = \frac{12(1 - \nu^2)}{Eh^3}, \quad B_1 = B_2 = B = \frac{5}{6}\mu h. \tag{22}$$

For the adhesive, referring to Fig. 1(c) it may be shown that

$$P_1 = 1 + a_1\frac{\partial}{\partial t}, \quad Q_1 = b_0 + b_1\frac{\partial}{\partial t} \tag{23 a,b}$$

where

$$a_1 = \frac{\lambda_2}{k_1 + k_2}, \quad b_0 = \frac{k_1 k_2}{k_1 + k_2}, \quad b_1 = \frac{\lambda_2 k_1}{k_1 + k_2}. \tag{24}$$

For a nondecreasing strain under sustained load the following inequality must be satisfied:

$$b_1 > a_1 b_0. \tag{25}$$

Generally, the coefficients a_1, b_0, and b_1 are functions of temperature, hence implicitly, functions of time if the temperature does not remain reasonably constant during the period of loading. In the example considered, it is assumed that these coefficients are constant.

Through a relatively straightforward elimination, the governing equations (1)–(4), (20), and (21) can be reduced to a pair of differential equations in the unknown functions $\sigma(x,t)$ and $\tau(x,t)$. By carrying out this elimination, using (22) and the operators defined by (23) we obtain

$$\frac{\partial^2 \tau}{\partial x^2} + a_1\frac{\partial^3 \tau}{\partial x^2 \partial t} - \frac{b_0}{2h_0}\left[2C + \frac{hD}{2}(h + h_0)\right]\tau$$
$$- \frac{b_1}{2h_0}\left[2C + \frac{hD}{2}(h + h_0)\right]\frac{\partial \tau}{\partial t} = -\frac{b_0 hD}{4h_0}Q_0(t) - \frac{b_1 hD}{4h_0}\frac{dQ_0}{dt}, \tag{26}$$

$$3\frac{\partial^4 \sigma}{\partial x^4} + 3a_1\frac{\partial^5 \sigma}{\partial x^4 \partial t} + \left[\frac{h}{2}D(3K - b_0) - \frac{2}{h_0 B}(3K + 2b_0)\right]\frac{\partial^2 \sigma}{\partial x^2}$$
$$+ \left[\frac{h}{2}D(3Ka_1 - b_1) - \frac{2}{h_0 B}(3Ka_1 + 2b_1)\right]\frac{\partial^3 \sigma}{\partial x^2 \partial t}$$
$$+ \frac{2}{h_0}D(3K + 2b_0)\sigma + \frac{2}{h_0}D(3Ka_1 + 2b_1)\frac{\partial \sigma}{\partial t} = 0. \tag{27}$$

Assuming that no external transverse shear load is applied to the composite plate in $-l < x < l$ and noting that $\tau(x,t)$ is the average shear stress acting on the adhesive, referring to Fig. 1(a) the equilibrium of transverse shear resultants gives

$$Q_{1x}(x,t) + Q_{2x}(x,t) \cong Q_0(t), \quad (-l < x < l). \tag{28}$$

Equation (28) has been used in deriving (26).

The differential equations (26) and (27) are uncoupled and may easily be solved by first reducing them to ordinary differential equations through the use of Laplace transforms. Assuming that the bonded joint is initially stress-free, the functions $\sigma(x,t)$ and $\tau(x,t)$ are zero for $t < 0$ and from (26) and (27), we find

$$\frac{d^2 F}{dx^2} - \alpha^2 F = \beta \tag{29}$$

$$\frac{d^4 G}{dx^4} - 2\gamma^2\frac{d^2 G}{dx^2} + \omega^4 G = 0 \tag{30}$$

where $F(x,s)$ and $G(x,s)$ are the Laplace transforms of $\tau(x,t)$ and $\sigma(x,t)$, respectively, and

$$\alpha^2 = \frac{[4C + hD(h + h_0)](b_0 + b_1 s)}{4h_0(1 + a_1 s)}, \tag{31}$$

$$\beta = -\frac{hDQ_0(b_0 + b_1 s)}{4h_0 s(1 + a_1 s)}, \tag{32}$$

$$\gamma^2 = \frac{1}{6(1 + a_1 s)}\left\{\frac{2}{h_0 B}(3K + 2b_0) - \frac{h}{2}D(3K - b_0)\right.$$
$$\left. + s\left[\frac{2}{h_0 B}(3Ka_1 + 2b_1) - \frac{h}{2}D(3Ka_1 - b_1)\right]\right\}, \tag{33}$$

$$\omega^4 = \frac{2D}{3h_0(1 + a_1 s)}[3K + 2b_0 + s(3Ka_1 + 2b_1)]. \tag{34}$$

In the example it is assumed that the external loads are given by (see Fig. 1(a))

$$N_0(t) = N_0 \mathrm{H}(t), \quad M_1(t) = M_1 \mathrm{H}(t), \quad M_2(t) = M_2 \mathrm{H}(t),$$
$$Q_o(t) = Q_0 \mathrm{H}(t) \tag{35 a–d}$$

where $\mathrm{H}(t)$ is the Heaviside function. For example, the nonhomogeneous term β which appears in (29) and which is given by (32) is obtained by using (35d).

The general solution of (29) and (30) may be written as

$$F(x,s) = A_1 \sinh(\alpha x) + A_2 \cosh(\alpha x) - \frac{\beta}{\alpha^2}, \tag{36}$$

$$G(x,s) = A_3 \sinh(\phi_1 x) + A_4 \cosh(\phi_1 x) + A_5 \sinh(\phi_2 x)$$
$$+ A_6 \cosh(\phi_2 x) \tag{37}$$

where

$$\phi_1 = [\gamma^2 + (\gamma^4 - \omega^4)^{1/2}]^{1/2}, \quad \phi_2 = [\gamma^2 - (\gamma^4 - \omega^4)^{1/2}]^{1/2}, \tag{38}$$

and the unknown functions $A_1(s), \ldots, A_6(s)$ are determined from the boundary conditions.

The problem is solved under three separate loading conditions shown in Fig. 2.

(a) Membrane Loading (Fig. 2(a)).

For this case the boundary conditions for plates 1 and 2 are given as follows:

$$N_{1x}(l,t) = 0, \quad M_{1x}(l,t) = 0, \quad Q_{1x}(l,t) = 0, \tag{39a-c}$$

$$N_{1x}(-l,t) = N_0\mathrm{H}(t), \quad M_{1x}(-l,t) = -N_0\frac{h+h_0}{2}\mathrm{H}(t), \quad Q_{1x}(-l,t) = 0, \tag{40a-c}$$

$$N_{2x}(l,t) = N_0\mathrm{H}(t), \quad M_{2x}(l,t) = N_0\frac{h+h_0}{2}\mathrm{H}(t), \quad Q_{2x}(l,t) = 0, \tag{41a-c}$$

$$N_{2x}(-l,t) = 0, \quad M_{2x}(-l,t) = 0, \quad Q_{2x}(-l,t) = 0, \tag{42a-c}$$

Considering the symmetry of the problem in geometry and materials, after some lengthy manipulations it can be shown that (39)–(42) are equivalent to the following conditions:

$$\tau(x,t) = \tau(-x,t), \quad \int_{-l}^{l}\tau(x,t)\,dx = -N_0\mathrm{H}(t), \tag{43a,b}$$

$$\sigma(x,t) = \sigma(-x,t), \quad \int_{-l}^{l}\sigma(x,t)\,dx = 0, \tag{44a,b}$$

$$\frac{h}{2}D(3K-b_0)\sigma(l,t) + \frac{h}{2}D(3Ka_1-b_1)\frac{\partial}{\partial t}\sigma(l,t) - \frac{1}{h_0}(3K+2b_0)\left[\frac{2}{B}\sigma(l,t) + \frac{D}{2}(h+h_0)N_0\mathrm{H}(t)\right] - \frac{1}{h_0}(3Ka_1+2b_1)\left[\frac{2}{B}\frac{\partial}{\partial t}\sigma(l,t) + \frac{D}{2}(h+h_0)N_0\delta(t)\right] + 3\frac{\partial^2}{\partial x^2}\sigma(l,t) + 3a_1\frac{\partial^3}{\partial x^2\partial t}\sigma(l,t) = 0. \tag{45}$$

In this problem since $Q_0 = 0, \beta = 0$ and substituting from (36) and (37) into (43)–(45) we obtain

$$A_1(s) = 0, \quad A_2(s) = -\frac{\alpha N_0}{2s\sinh(\alpha l)},$$

$$A_3(s) = 0, \quad A_4(s) = -\frac{(h+h_0)N_0\omega^4\sinh(\phi_2 l)}{4s\phi_2\Delta_a(s)},$$

$$A_5(s) = 0, \quad A_6(s) = \frac{(h+h_0)N_0\omega^4\sinh(\phi_1 l)}{4s\phi_1\Delta_a(s)}, \tag{46}$$

where

$$\Delta_a(s) = \phi_2\cosh(\phi_1 l)\sinh(\phi_2 l) - \phi_1\sinh(\phi_1 l)\cosh(\phi_2 l). \tag{47}$$

(b) Bending (Fig. 2(b)).

For this problem the nonhomogeneous boundary conditions are

$$M_{1x}(-l,t) = M_0\mathrm{H}(t), \quad M_{2x}(l,t) = M_0\mathrm{H}(t), \tag{48a,b}$$

and the remaining stress and moment resultants at $x = \pm l$ which appear in (39)–(42) are zero. Again, considering the symmetry of the problem these conditions may be shown to be equivalent to the following:

$$\tau(x,t) = -\tau(-x,t), \tag{49}$$

$$\frac{\partial}{\partial x}\tau(l,t) + a_1\frac{\partial^2}{\partial x\partial t}\tau(l,t) = -\frac{hD}{4h_0}M_0[b_0\mathrm{H}(t) + b_1\delta(t)], \tag{50}$$

$$\sigma(x,t) = -\sigma(-x,t), \tag{51}$$

$$\int_{-l}^{l}\sigma(x,t)x\,dx = M_0\mathrm{H}(t), \tag{52}$$

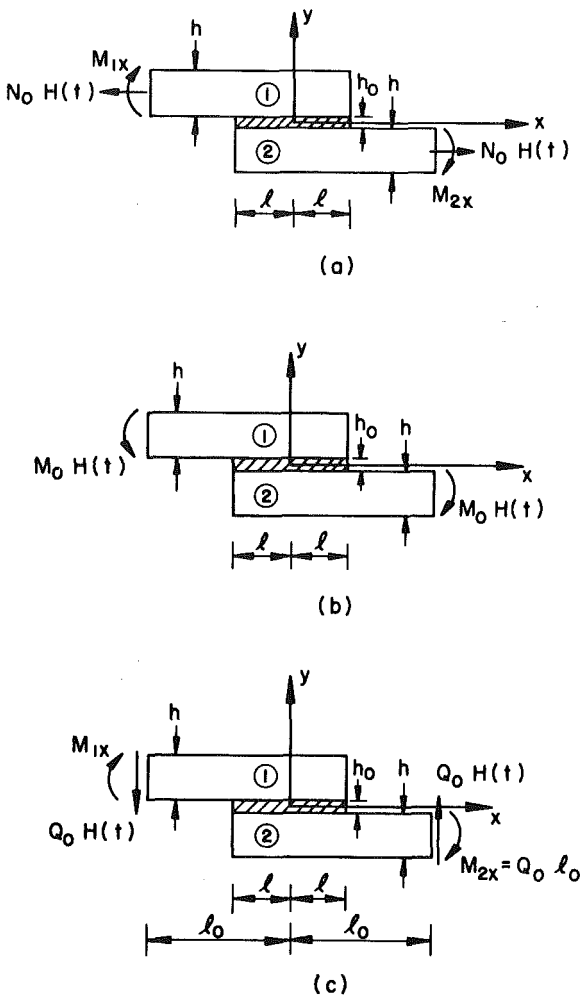

Fig. 2 The loading conditions

$$(3K-b_0)\frac{hD}{2}\sigma(l,t) + (3Ka_1-b_1)\frac{hD}{2}\frac{\partial}{\partial t}\sigma(l,t) - \frac{1}{h_0}(3K+2b_0)\left[\frac{2}{B}\sigma(l,t) + DM_0\mathrm{H}(t)\right] - \frac{1}{h_0}(3Ka_1+2b_1)\left[\frac{2}{B}\frac{\partial}{\partial t}\sigma(l,t) + DM_0\delta(t)\right] + 3\frac{\partial^2}{\partial x^2}\sigma(l,t) + 3a_1\frac{\partial^3}{\partial x^2\partial t}\sigma(l,t) = 0. \tag{53}$$

In this problem, too, $\beta = 0$, and substituting from (36) and (37) into (49)–(53) we obtain

$$A_1(s) = -\frac{hDM_0(b_0+b_1 s)}{4h_0\alpha s(1+a_1 s)\cosh(\alpha l)}, \quad A_2(s) = 0,$$

$$A_3(s) = -\frac{\omega^4 M_0\cosh(\phi_2 l)}{2s\phi_2\Delta_b(s)}, \quad A_4(s) = 0,$$

$$A_5(s) = \frac{\omega^4 M_0\cosh(\phi_1 l)}{2s\phi_1\Delta_b(s)}, \quad A_6(s) = 0$$

$$\Delta_b(s) = \phi_2\sinh(\phi_1 l)\cosh(\phi_2 l) - \phi_1\cosh(\phi_1 l)\sinh(\phi_2 l). \tag{54}$$

(c) Transverse Shear (Fig. 2(c)).

For the loading given in Fig. 2(c) the nonhomogeneous boundary conditions are

$$M_{1x}(-l,t) = -Q_0 l\mathrm{H}(t), \; Q_{1x}(-l,t) = Q_0\mathrm{H}(t), \tag{55a,b}$$

$$M_{2x}(l,t) = Q_0 l\mathrm{H}(t), \; Q_{2x}(l,t) = Q_0\mathrm{H}(t), \tag{56a,b}$$

and the remaining stress and moment resultants at $x = \pm l$ are zero. It may again be shown that these boundary conditions are equivalent to

$$\tau(x,t) = \tau(-x,t), \quad \int_{-l}^{l} \tau(x,t)dx = 0, \tag{57 a,b}$$

$$\sigma(x,t) = \sigma(-x,t), \quad \int_{-l}^{l} \sigma(x,t)dx = -Q_0 \mathrm{H}(t), \tag{58 a,b}$$

$$\frac{hD}{2}(3K - b_0)\sigma(l,t) + \frac{hD}{2}(3Ka_1 - b_1)\frac{\partial}{\partial t}\sigma(l,t)$$
$$-\frac{1}{h_0}(3K + 2b_0)\left[\frac{2}{B}\sigma(l,t) + DQ_0 l\mathrm{H}(t)\right]$$
$$-\frac{1}{h_0}(3Ka_1 + 2b_1)\left[\frac{2}{B}\frac{\partial}{\partial t}\sigma(l,t) + DQ_0 l\delta(t)\right]$$
$$+ 3\frac{\partial^2}{\partial x^2}\sigma(l,t) + 3a_1\frac{\partial^3}{\partial x^2 \partial t}\sigma(l,t) = 0. \tag{59}$$

In this case β is given by (32) and the functions $A_1(s), \ldots, A_6(s)$ are obtained as follows:

$$A_1(s) = 0, A_2(s) = \frac{\beta l}{\alpha \sinh(\alpha l)},$$
$$A_3(s) = 0, A_4(s) = \frac{Q_0[\omega^2\phi_1 \cosh(\phi_2 l) - \omega^4 l \sinh(\phi_2 l)]}{2s\phi_2\Delta_c(s)},$$
$$A_5(s) = 0, A_6(s) = -\frac{Q_0[\omega^2\phi_2 \cosh(\phi_1 l) - \omega^4 l \sinh(\phi_1 l)]}{2s\phi_1\Delta_c(s)},$$
$$\Delta_c(s) = \phi_2 \cosh(\phi_1 l)\sinh(\phi_2 l) - \phi_1 \sinh(\phi_1 l)\cosh(\phi_2 l). \tag{60}$$

4 Solution and Results

After determining the functions $A_i(s)$, $(i = 1, \ldots, 6)$ the unknown functions $\tau(x,t)$ and $\sigma(x,t)$ may be obtained by substituting from (36) and (37) into the inversion integral. In each case the constant c giving the line of integration is determined by analyzing the singular behavior of the functions $F(x,s)$ and $G(x,s)$ in the complex s-plane. Because of the existence of a number of branch points in the complex plane the exact inversion of F and G becomes very complicated and, in light of the fact that the inversion integrals can be evaluated in a straightforward manner numerically, does not seem to be worth the effort. Thus making the following change in variable

$$s = c + iy, \quad -\infty < y < \infty \tag{61}$$

the functions τ and σ may be expressed as

$$\tau(x,t) = \frac{1}{2\pi}\int_{-\infty}^{\infty} F(x, c+iy)e^{t(c+iy)}dy, \tag{62}$$

$$\sigma(x,t) = \frac{1}{2\pi}\int_{-\infty}^{\infty} G(x, c+iy)e^{t(c+iy)}dy, \tag{63}$$

It can be shown that the imaginary parts of the integrands in (62) and (63) are odd functions in y and therefore the integrals give real results.

Examining the functions F and G in the complex plane it is found that $s = 0$ is a simple pole and all the remaining singularities lie in the left-hand plane. Hence c is a positive constant. To evaluate the integrals in (62) and (63) first they are expressed in $(0, \infty)$ as follows:

$$\int_{-\infty}^{\infty} f(y)dy = \int_0^{\infty}[f(y) + f(-y)]dy. \tag{64}$$

Even though there are routine techniques for evaluating infinite integrals, it is generally a good practice to obtain the asymptotic behavior of the integrands for large values of the argument before selecting a particular technique. In the problem under consideration the integrands do not decay exponentially. Consequently, the numerical integration requires more care. One way to insure that no significant accuracy is lost due to the slow decay of integrands is to evaluate the integral in closed form for large values of the argument. For example, in the lap joint under membrane loading N_0 (Fig. 2(a)), after analyzing the asymptotic behavior of the function F, the shear stress τ may be expressed as

$$\tau(x,t) = \frac{1}{2\pi}\int_0^A [F(x, c+iy)e^{t(c+iy)} + F(x, c-iy)e^{t(c-iy)}]dy$$
$$-\frac{N_0}{2\pi}\sqrt{m/a_1}\,e^{ct}\frac{\cosh(x\sqrt{m/a_1})}{\sinh(l\sqrt{m/a_1})}\int_A^{\infty}\frac{\sin(ty)}{y}dy \tag{65}$$

where

$$m = b_1[4C + h(h + h_0)D]/(4h_0) \tag{66}$$

and A is a "large" number. The second integral is known in closed form and the first is evaluated numerically. The proper selection of A requires some trial calculations. In this problem A selected in 20 to 30 range gives good results. It may also be pointed out that the numerical calculations show the results to be insensitive to the choice of the constant c.

In the numerical example considered it is assumed that the adherends are aluminum alloy plates with the following elastic constants and dimensions (Fig. 2):

$$E = 10^7 \text{ psi} = 6.895 \times 10^{10} \text{ N/m}^2, \quad \nu = 0.3$$

$$h = 0.09 \text{ in.} = 0.229 \times 10^{-2}\text{m}, \quad l = 0.5 \text{ in.} = 1.27 \times 10^{-2}\text{m}.$$

In the three parameter viscoelastic solid adopted for the adhesive the coefficiénts which appear in the operators P_1 and Q_1 (see equations (23a, b)) are related to the constants shown in Fig. 1(c) by (24). To relate these constants to somewhat more conventional material properties consider the response of the model given in Fig. 1(c) to an input $\tau = \tau_0 \mathrm{H}(t)$ which is found to be

$$\frac{1}{2}\gamma(t) = \frac{\tau_0}{b_1}[t_0(1 - e^{-t/t_0}) + a_1 e^{-t/t_0}], \quad t_0 = \frac{b_1}{b_0} = \frac{\lambda_2}{k_2}, \tag{67}$$

where t_0 is called the retardation time. Now defining

$$\mu_0 = \frac{\tau_0}{\gamma(0^+)}, \quad \mu_\infty = \frac{\tau_0}{\gamma(\infty)} \tag{68}$$

from (67) it is seen that

$$2\mu_0 = \frac{b_1}{a_1} = k_1, \quad 2\mu_\infty = b_0 = \frac{k_1 k_2}{k_1 + k_2} \tag{69}$$

Thus the moduli μ_0 and μ_∞ and the retardation time t_0 may be selected as the three parameters representing the viscoelastic solid.

For the particular epoxy used as the adhesive the properties at $t = 0$ are assumed to be

$$h_0 = 0.004 \text{ in.} = 1.016 \times 10^{-4} \text{ m}$$
$$E_0 = 5.797 \times 10^5 \text{ psi} = 39.968 \times 10^8 \text{ N/m}^2$$
$$\mu_0 = 2.225 \times 10^5 \text{ psi} = 15.341 \times 10^8 \text{ N/m}^2$$

The bulk modulus K is assumed to be constant and may, therefore, be calculated in terms of E_0 and the shear modulus μ_0 as

$$K = \frac{E_0\mu_0}{3(3\mu_0 - E_0)} \tag{70}$$

In the example it is also assumed that

$$\mu_\infty = \mu_0/3, \quad t_0 = 4 \text{ hr}.$$

If it is assumed that the adhesive layer is linearly elastic having the constants E_a and ν_a, with the adhesive model used in this paper the solution may be obtained in a straightforward manner. For example, in the case of membrane loading described by (39)–(42) the adhesive stresses are found to be

$$\tau_e(x) = -\frac{N_0\alpha_e \cosh(\alpha_e x)}{2\sinh(\alpha_e l)}, \tag{71}$$

$$\alpha_e{}^2 = \frac{E_a}{4(1+\nu_a)h_0}[4C + hD(h + h_0)], \tag{72}$$

$$\sigma_e(x) = B_4 \cosh(m_1 x) + B_6 \cosh(m_2 x), \tag{73}$$

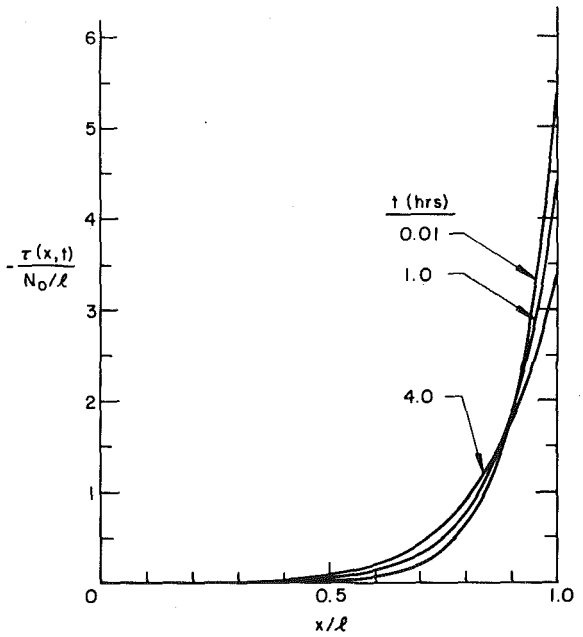

Fig. 3 The shear stress $\tau_{xy} = \tau(x, t)$ in the adhesive layer

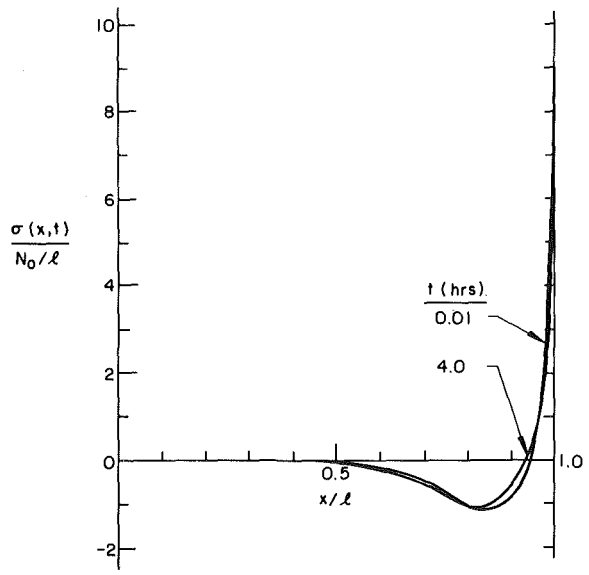

Fig. 4 The normal stress $\sigma_y = \sigma(x, t)$ in the adhesive layer

Table 1 Variation of $\tau(x, t)/(N_0/l)$ for the case of tension (t in hr)

x/ℓ \ t	0	0.01	0.1	0.5	1.0	2.0	4.0	∞
0	-2.24×10^{-4}	-2.26×10^{-4}	-2.73×10^{-4}	-5.29×10^{-4}	-9.12×10^{-4}	-1.84×10^{-3}	-4.02×10^{-3}	-0.012
0.1	-3.67×10^{-4}	-3.71×10^{-4}	-4.42×10^{-4}	-8.15×10^{-4}	-1.35×10^{-3}	-2.61×10^{-3}	-5.40×10^{-3}	-0.015
0.2	-9.81×10^{-4}	-9.95×10^{-4}	-1.16×10^{-3}	-1.98×10^{-3}	-3.10×10^{-3}	-5.53×10^{-3}	-0.010	-0.023
0.3	-2.85×10^{-3}	-2.89×10^{-3}	-3.29×10^{-3}	-5.24×10^{-3}	-7.78×10^{-3}	-0.013	-0.022	-0.041
0.4	-8.36×10^{-3}	-8.48×10^{-3}	-9.45×10^{-3}	-0.014	-0.020	-0.030	-0.048	-0.075
0.5	-0.026	-0.025	-0.027	-0.038	-0.050	-0.071	-0.101	-0.139
0.6	-0.072	-0.073	-0.078	-0.100	-0.125	-0.164	-0.213	-0.258
0.7	-0.212	-0.213	-0.224	-0.266	-0.309	-0.373	-0.441	-0.481
0.8	-0.624	-0.624	-0.641	-0.702	-0.759	-0.833	-0.891	-0.896
0.9	-1.834	-1.828	-1.838	-1.843	-1.839	-1.816	-1.757	-1.670
1.0	-5.391	-5.351	-5.265	-4.812	-4.382	-3.838	-3.366	-3.112

Table 2 Variation of $\sigma(x, t)/(N_0/l)$ for the case of tension (t in hr)

x/ℓ \ t	0	0.01	0.1	0.5	1.0	2.0	4.0	∞
0	1.01×10^{-5}	1.18×10^{-5}	2.05×10^{-5}	5.80×10^{-5}	9.57×10^{-5}	1.48×10^{-4}	1.99×10^{-4}	2.29×10^{-4}
0.1	-4.61×10^{-5}	-4.33×10^{-5}	-3.01×10^{-5}	2.77×10^{-5}	8.59×10^{-5}	1.67×10^{-4}	2.46×10^{-4}	2.92×10^{-4}
0.2	-4.45×10^{-4}	-4.38×10^{-4}	-4.12×10^{-4}	-2.90×10^{-4}	-1.69×10^{-4}	-8.28×10^{-7}	1.61×10^{-4}	2.50×10^{-4}
0.3	-2.45×10^{-3}	-2.44×10^{-3}	-2.40×10^{-3}	-2.20×10^{-3}	-2.00×10^{-3}	-1.73×10^{-3}	-1.49×10^{-3}	-1.38×10^{-3}
0.4	-0.011	-0.011	-0.011	-0.011	-0.011	-0.011	-0.011	-0.011
0.5	-0.044	-0.044	-0.044	-0.045	-0.046	-0.048	-0.049	-0.050
0.6	-0.153	-0.152	-0.154	-0.158	-0.163	-0.169	-0.174	-0.177
0.7	-0.457	-0.456	-0.460	-0.469	-0.478	-0.489	-0.498	-0.502
0.8	-1.052	-1.048	-1.052	-1.050	-1.048	-1.045	-1.040	-1.037
0.9	-0.882	-0.876	-0.866	-0.808	-0.755	-0.690	-0.639	-0.621
1.0	9.017	8.971	8.938	8.656	8.397	8.096	7.872	7.801

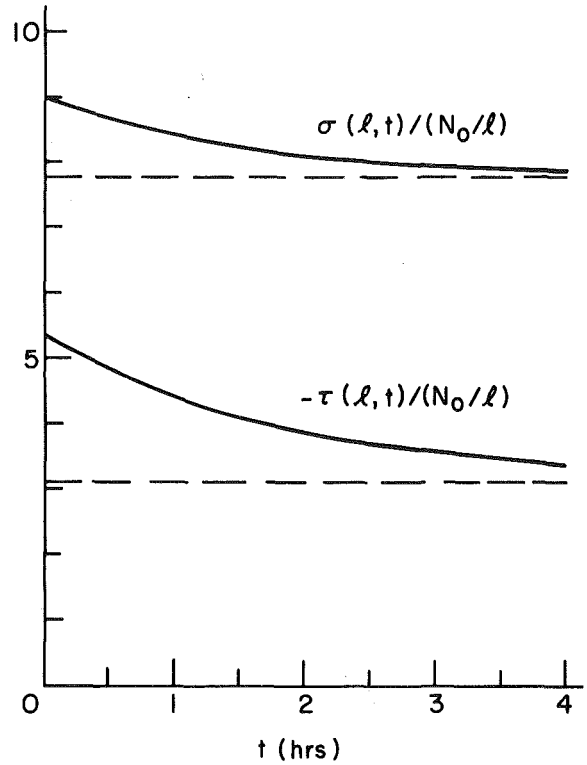

Fig. 5 Variation of maximum shear and normal stresses in the adhesive as functions of time

$$B_4 = -\epsilon_1{}^4 N_0(h + h_0)\sinh(m_2 l)/(4m_2\Delta),$$

$$B_6 = \epsilon_1{}^4 N_0(h + h_0)\sinh(m_1 l)/(4m_1\Delta),$$

$$\Delta = m_2\cosh(m_1 l)\sinh(m_2 l) - m_1\sinh(m_1 l)\cosh(m_2 l),$$

$$\epsilon_1{}^4 = \frac{2DE_a(1-\nu_a)}{h_0(1-\nu_a-2\nu_a{}^2)},$$

$$m_1 = [\gamma_1{}^2 + (\gamma_1{}^4 - \epsilon_1{}^4)^{1/2}]^{1/2}, \quad m_2 = [\gamma_1{}^2 - (\gamma_1{}^4 - \epsilon_1{}^4)^{1/2}]^{1/2},$$

$$\gamma_1{}^2 = \frac{(1-\nu_a)E_a}{(1-\nu_a-2\nu_a{}^2)}\left[\frac{1}{Bh_0} - \frac{hD\nu_a}{4(1-\nu_a)}\right]. \tag{74}$$

On the other hand, in the case of viscoelastic adhesive the elastic response for $t = +0$ and $t = \infty$ may also be determined by using the limit theorems for the inversion of Laplace transforms. For example, again for the case of membrane loading, from (36) and (46) the shear stress in the adhesive may be obtained as

$$\tau(x, +0) = -\frac{N_0\alpha_0\cosh(\alpha_0 x)}{2\sinh(\alpha_0 l)}, \tag{75}$$

$$\alpha_0{}^2 = \frac{b_1}{4h_0 a_1}[4C + hD(h + h_0)], \tag{76}$$

and

$$\tau(x, \infty) = -\frac{N_0\alpha_\infty\cosh(\alpha_\infty x)}{2\sinh(\alpha_\infty l)}, \tag{77}$$

$$\alpha_\infty{}^2 = \frac{b_0}{4h_0}[4C + hD(h + h_0)]. \tag{78}$$

Note that at $t = +0$, $\mu_a = E_a/2(1+\nu_a) = \mu_0$ and $E_a = E_0$, and from (69), (72), and (76), it follows that $\alpha_0 = \alpha_e$. Hence, the initial response given by (75) is the expected elastic solution given by (71). Similarly, at $t = \infty$, $\mu_a = \mu_\infty$, and (69), (72), and (78) show that $\alpha_\infty = \alpha_e$, and hence $\tau(x, \infty) = \tau_e(x)$. Also, it can be shown that $\sigma(x, \infty)$ corresponds to the elastic solution obtained by using $\mu_a = \mu_\infty$ and the bulk modulus of the adhesive which is assumed to be a time-independent constant.

Table 3 Variation of $\tau(x, t)/(M_0/l^2)$ for the case of bending (t in hr)

x/ℓ \ t	0.01	0.1	0.5	1.0	2.0	4.0
0.	0.	0.	0.	0.	0.	0.
0.1	-2.38×10^{-3}	-2.81×10^{-3}	-5.01×10^{-3}	-8.09×10^{-3}	-0.015	-0.029
0.2	-7.82×10^{-3}	-9.07×10^{-3}	-0.015	-0.024	-0.042	-0.077
0.3	-0.023	-0.026	-0.042	-0.062	-0.103	-0.175
0.4	-0.068	-0.076	-0.113	-0.159	-0.245	-0.382
0.5	-0.200	-0.219	-0.303	-0.401	-0.573	-0.818
0.6	-0.587	-0.629	-0.808	-1.005	-1.324	-1.720
0.7	-1.720	-1.803	-2.143	-2.495	-3.010	-3.553
0.8	-5.036	-5.171	-5.658	-6.123	-6.718	-7.185
0.9	-14.74	-14.82	-14.86	-14.83	-14.64	-14.17
1.0	-43.15	-42.46	-38.81	-35.34	-30.95	-27.14

Table 4 Variation of $\sigma(x, t)/(M_0/l^2)$ for the case of bending (t in hr)

x/ℓ \ t	0.01	0.1	0.5	1.0	2.0	4.0
0.	0.	0.	0.	0.	0.	0.
0.1	-5.94×10^{-4}	-4.84×10^{-4}	5.50×10^{-6}	5.00×10^{-4}	1.19×10^{-3}	1.88×10^{-3}
0.2	-4.72×10^{-3}	-4.45×10^{-3}	-3.19×10^{-3}	-1.93×10^{-4}	-1.85×10^{-4}	1.51×10^{-3}
0.3	-0.026	-0.026	-0.023	-0.021	-0.019	-0.016
0.4	-0.118	-0.118	-0.117	-0.116	-0.116	-0.115
0.5	-0.465	-0.469	-0.480	-0.491	-0.506	-0.521
0.6	-1.621	-1.638	-1.686	-1.733	-1.796	-1.852
0.7	-4.847	-4.891	-4.991	-5.084	-5.205	-5.301
0.8	-11.15	-11.19	-11.17	-11.15	-11.11	-11.06
0.9	-9.318	-9.209	-8.599	-8.031	-7.341	-6.802
1.0	95.43	95.09	92.09	89.33	86.13	83.75

Table 5 Variation of $\tau(x, t)/(Q_0/l)$ for the case of shearing (t in hr)

x/ℓ \ t	0.01	0.1	0.5	1.0	2.0	4.0
0.	4.030	4.030	4.028	4.025	4.017	4.000
0.1	4.029	4.029	4.027	4.021	4.011	3.989
0.2	4.024	4.023	4.016	4.007	3.988	3.949
0.3	4.009	4.006	3.990	3.969	3.928	3.854
0.4	3.964	3.956	3.919	3.873	3.787	3.649
0.5	3.832	3.813	3.729	3.631	3.459	3.214
0.6	3.445	3.404	3.225	3.027	2.709	2.312
0.7	2.312	2.229	1.890	1.537	1.022	0.479
0.8	-1.004	-1.139	-1.626	-2.091	-2.686	-3.153
0.9	-10.71	-10.79	-10.83	-10.80	-10.61	-10.14
1.0	-39.12	-38.43	-34.78	-31.31	-26.92	-23.11

Table 6 Variation of $\sigma(x, t)/(Q_0/l)$ for the case of shearing (t in hr)

x/ℓ \ t	0.01	0.1	0.5	1.0	2.0	4.0
0.	1.37×10^{-4}	2.25×10^{-4}	6.02×10^{-4}	9.78×10^{-4}	1.50×10^{-3}	2.00×10^{-3}
0.1	-3.86×10^{-4}	-2.53×10^{-4}	3.33×10^{-4}	9.21×10^{-4}	1.73×10^{-3}	2.53×10^{-3}
0.2	-4.21×10^{-3}	-3.93×10^{-3}	-2.68×10^{-3}	-1.42×10^{-3}	3.10×10^{-4}	1.98×10^{-3}
0.3	-0.024	-0.023	-0.021	-0.019	-0.016	-0.014
0.4	-0.109	-0.109	-0.107	-0.106	-0.105	-0.104
0.5	-0.433	-0.438	-0.445	-0.454	-0.466	-0.479
0.6	-1.521	-1.538	-1.578	-1.619	-1.674	-1.724
0.7	-4.595	-4.635	-4.726	-4.811	-4.921	-5.009
0.8	-10.79	-10.84	-10.83	-10.81	-10.79	-10.75
0.9	-10.47	-10.38	-9.832	-9.322	-8.707	-8.225
1.0	82.09	81.77	79.09	76.62	73.76	71.63

For the three types of loading shown in Fig. 2, the calculated results for $\tau(x, t)$ and $\sigma(x, t)$ are shown in Tables 1–6. To visualize the variation of the stresses in time and along the bond region some sample results are also given in Figs. 3–5. Figs. 3 and 4 show the distribution of shear and tensile stresses in the bond region in a single lap joint under membrane loading for some fixed values of time. As expected, there is a certain redistribution of stresses with increasing time. This may also be seen in Fig. 5 where the variation of the maximum values

of τ and σ is given. From Figs. 3–5 and Tables 1–6 it may be observed that the peak values of the tensile stress σ in the adhesive are not only higher than the corresponding shear values but also decay slower. The values τ and σ given in Tables 1 and 2 for $t = 0$ and $t = \infty$ are obtained from the elastic solutions (71) and (73) by using the bulk modulus K which is assumed to be independent of time and the corresponding μ_0 and μ_∞.

References

1 Erdogan, F., and Ratwani, M., "Stress Distribution in Bonded Joints," *Journal of Composite Materials*, Vol. 5, 1971, pp. 378–393.

2 Goland, M., and Reissner, E., "The Stresses in Cemented Joints," ASME JOURNAL OF APPLIED MECHANICS, Vol. 11, 1944, pp. A17–A27.

3 Yuceoglu, U., and Updike, D. P., "Stress Analysis of Bonded Plates and Joints," *Journal of Engineering Mechanics Division ASCE*, 1980, pp. 37–56.

4 Chang, D. J., and Muki, R., "Stress Distribution in a Lap Joint Under Tension-Shear," *International Journal of Solids and Structures*, Vol. 10, 1974, pp. 503–517.

5 Erdogan, F., and Civelek, M. B., "Contact Problem for an Elastic Reinforcement Bonded to an Elastic Plate," ASME JOURNAL OF APPLIED MECHANICS, Vol. 41, 1974, pp. 1014–1018.

6 Erdogan, F., "Fracture Problems in Composite Materials," *Journal of Engineering Fracture Mechanics*, Vol. 4, 1972, 811–840.

7 Flügge, W., *Viscoelasticity*, Springer-Verlag, 1975.

8 Pipkin, A. C., *Lectures on Viscoelasticity Theory*, Springer-Verlag, 1972.

9 Findley, W. N., Lai, J. S., and Onaran, K., *Creep and Relaxation of Nonlinear Viscoelastic Materials*, North-Holland Publ. Co., 1976.

J. Christoffersen
Professor,
Department of Solid Mechanics,
The Technical University of Denmark,
DK-2800, Lyngby, Denmark

M. M. Mehrabadi
Postdoctoral Fellow.
Assoc. Mem. ASME

S. Nemat-Nasser
Professor of Civil Engineering
and Applied Mathematics.
Mem. ASME

Department of Civil Engineering,
The Technological Institute,
Northwestern University,
Evanston, Ill. 60201

A Micromechanical Description of Granular Material Behavior

Considered is a sample of cohesionless granular material, in which the individual granules are regarded rigid, and which is subjected to overall macroscopic average stresses. On the basis of the principle of virtual work, and by an examination of the manner by which adjacent granules transmit forces through their contacts, a general representation is established for the macroscopic stresses in terms of the volume average of the (tensorial) product of the contact forces and the vectors which connect the centroids of adjacent contacting granules. Then the corresponding kinematics is examined and the overall macroscopic deformation rate and spin tensors are developed in terms of the volume average of relevant microscopic kinematical variables. As an illustration of the application of the general expressions developed, two explicit macroscopic results are deduced: (1) a dilatancy equation which both qualitatively and quantitatively seems to be in accord with experimental observation, and (2) a noncoaxiality equation which seems to support the vertex plasticity model. Since the development is based on a microstructural consideration, all material coefficients entering the results have well-defined physical interpretations.

1 Introduction

Suppose a medium consisting of rigid cohesionless granules carries a set of overall macroscopic stresses through forces transmitted across contact points on the microscopic scale. It is natural to expect that the overall macroscopic mechanical properties of this material are expressible in terms of the coefficient of contact friction, and parameters such as size and shape distributions, and the void ratio (the ratio of the void volume to the solid one). Many authors have dealt with various aspects of this rather intriguing and fundamental problem. For example, the dilatancy induced by shearing in granular masses examined by Reynolds [1], has been studied from various points of view over the past decades; see, e.g., Newland and Allely [2], Rowe [3, 4], Horne [5, 6], Satake [7], Oda [8], Matsuoka [9], and Nemat-Nasser [10], for treatments involving particulate approaches, and Drucker and Prager [11], Shield [12, 13], Drucker, et al. [14], Jenike and Shield [15], Nemat-Nasser and Shokooh [16] for a phenomenological plasticity approach, and finally see Cowin [17] for a review of microstructural continuum theories.[1] In addition, it has been experimentally verified (see, e.g., Drescher and de Josselin de Jong [19], Oda and Konishi [20], and Drescher [21]) that during the deformation of granular materials, the principal directions of the overall macroscopic stress tensor at each instant are not, in general, coincident with the principal directions of the corresponding macroscopic deformation rate. This property is usually referred to as *noncoaxiality* in the literature; for theoretical treatment of this property, see, e.g., Mandel [22], Spencer [23], de Josselin de Jong [24, 25], and Mehrabadi and Cowin [26]. All plasticity theories which are based on a *smooth* flow potential that depends only on the basic stress invariants (as well as some measures of the deformation history) yield *coaxiality* of stress and plastic deformation rate, the exception being vertex models recently discussed by Rice [27], Christoffersen and Hutchinson [28], and Mehrabadi and Cowin [29].

In this work we shall consider a sample of cohesionless granular material, in which the individual granules are regarded rigid, and which is subjected to overall macroscopic average stresses, $\bar{\sigma}_{ij}$, $i, j = 1, 2, 3$, where a fixed rectangular Cartesian coordinate system, x_i, is employed. On the basis of the principle of virtual work, Hill [30], and by an examination of the manner by which adjacent granules transmit forces through their contacts, we shall establish a general representation for the macroscopic stresses, $\bar{\sigma}_{ij}$, in terms of the volume average of the (tensorial) product of the contact forces and the vectors which connect the centroids of adjacent contacting granules; see equation (12). We shall then examine the kinematics in an effort to obtain the overall macroscopic deformation rate and spin tensors in terms of the volume average of relevant microscopic kinematical variables. For simplicity in presentation, this last program is carried out for two-dimensional problems only, although, like stresses, the deformation rate and spin tensors can be given a complete microscopic representation in three dimensions. As an illustration of the application of the general expressions developed, we shall deduce two explicit macroscopic results:

1 A dilatancy equation which both qualitatively and quantitatively seems to be in accord with experimental observation.

[1] The book edited by Cowin and Satake [18] contains a large number of relevant references.

Contributed by the Applied Mechanics Division for publication in the JOURNAL OF APPLIED MECHANICS.

Discussion on this paper should be addressed to the Editorial Department, ASME, United Engineering Center, 345 East 47th Street, New York, N.Y. 10017, and will be accepted until September 1, 1981. Readers who need more time to prepare a Discussion should request an extension from the Editorial Department. Manuscript received by ASME Applied Mechanics Division, March, 1980; final revision, August, 1980.

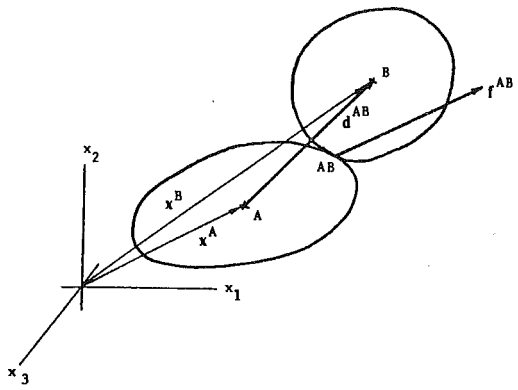

Fig. 1

2 A noncoaxiality equation which is in accord with the vertex plasticity model.

Since the development is based on a microstructural consideration, all material coefficients entering the results have well-defined physical interpretations.

In developing our kinematical relations, we are led to distinguish between contacts which are instantaneously inactive in the sense that instantaneously no sliding takes place at these points and the critical contacts at which instantaneous sliding occurs. It has been known—see, for example, Rowe [4] and Davis and Deresiewicz [31, p. 80]—that at each instant, groups of instantaneously mutually immobile granules are formed in the course of the deformation of granular masses. This is required by compatibility of the deformation, and is expected to occur even in the case of a collection of spherical granules. At each instant the groups move relative to adjacent groups, while transmitting forces through a finite number of active critical contacts with their neighbors. The structure, size, and shape of these instantaneously rigid groups change with deformation, and therefore both the density of the critical contacts and the distribution of the orientation of unit normals on these contacts change, as new critical contacts are continually developed, while some existing ones are rendered inactive. To obtain a complete solution to the problem stated at the beginning of this section, namely, to express the macroscopic deformation rates as functions of the corresponding macroscopic stress rates using a microscopic model, we first need to establish the manner by which the density of active contacts and the distribution of their unit normals evolve with deformation. The results presented in this paper, however, do not depend on this evolution, and are valid at each instant during the course of flow.

2 Representation of Stress in Granular Materials

Consider a macroscopically homogeneous element of a granular material consisting of rigid granules. The material is carrying an overall macroscopic stress $\bar{\sigma}_{ij}$ through internal forces f_i acting at the contact points. We set out to find a representation for the overall stress in terms of these contact forces.

Consider two granules, labeled A and B, with centroids at $\mathbf{x}^A$ and $\mathbf{x}^B$ and contacting each other at $\mathbf{x}^{AB}$; see Fig. 1. Let f_i^{AB} and f_i^{BA} denote, respectively, the forces exerted on grain A by grain B and vice versa. Thus

$$f_i^{AB} + f_i^{BA} = 0. \tag{1}$$

Balance of forces acting on grain A requires

$$\sum_{\beta=1}^{\kappa} f_i^{A\beta} = 0, \tag{2}$$

where κ is the coordination number for grain A, i.e., the number of grains contacting A. Balance of moments requires

$$\sum_{\beta=1}^{\kappa} f_i^{A\beta}\,(x_j^{A\beta} - x_j^A) = \sum_{\beta=1}^{\kappa} f_j^{A\beta}\,(x_i^{A\beta} - x_i^A). \tag{3}$$

Summing over all grains interior to the surface of the material, and noting that each contact point contributes with terms such as

$$f_i^{AB}\,(x_j^{AB} - x_j^A) + f_i^{BA}\,(x_j^{AB} - x_j^B),$$

we obtain

$$\sum_{\alpha=1}^{N} f_i^\alpha\, d_j^\alpha = \sum_{\alpha=1}^{N} f_j^\alpha\, d_i^\alpha, \tag{4}$$

where α stands for contacts such as AB, N is the total number of contacts in the considered volume, and where

$$d_i^{AB} = x_i^B - x_i^A \tag{5}$$

is the vector connecting the centroid of A to that of B. Note that from each pair of contact forces at a given contact point, only one enters the summations in (4) according to the choice of the vector d_j^α, that is, f_i^{AB} is chosen when $d_i^\alpha \equiv d_i^{AB}$.

Equation (4) also holds when A and B represent two instantaneously rigid groups (clusters) of grains. In this case d_i^α should be interpreted as the vector connecting the centroids of the two rigid groups. Note that then α will represent the *instantaneously critical* contact between the two rigid groups, and N will be the number of critical contacts in the considered volume. This interpretation is advantageous in two respects. First, it is generally believed that during the deformation of granular materials, at each instant granules form rigid groups (i.e., groups of mutually immobile granules) and that the overall deformation occurs by instantaneous sliding of these rigid groups against one another before they reform into new groups; see, e.g., Rowe [4] and Davis and Deresiewicz [31]. Second, the interpretation of N as the number of critical contacts will facilitate the formulation of the constitutive relations in that the overall (macroscopic) kinematical quantities involve summations over the critical contacts only.

To relate the contact forces to the overall stresses, we employ the principle of virtual work in the manner discussed by Hill [30]. Let the granular body be subjected to overall tractions T_i on its boundary S, i.e.,

$$T_i = \sigma_{ij}\nu_j \quad \text{on} \quad S, \tag{6}$$

where $\boldsymbol{\nu}$ is the exterior unit normal to S. Consider a suitably smooth overall virtual displacement, u_i, which results in the virtual displacement (separation) Δ_i^α of the αth contact forces. If the tractions, T_i, are in equilibrium with the contact forces f_i^α, then the virtual work principle requires

$$\sum_{\alpha=1}^{N} f_i^\alpha\, \Delta_i^\alpha = \frac{1}{V}\int_S T_i u_i dS. \tag{7}$$

Let the boundary displacement u_i be chosen to be linear so that

$$u_i = \phi_{ij}x_j + c_i \quad \text{on} \quad S, \tag{8}$$

where ϕ_{ij} is an arbitrary constant tensor, and $\mathbf{c}$ is a constant vector. It can be shown (see Appendix) that, to a first order of approximation, it is reasonable to set

$$\Delta_i^\alpha = \phi_{ij} d_j^\alpha. \tag{9}$$

Substituting (8) and (9) into (7), and employing the divergence theorem, we obtain

$$\phi_{ij}\left(\bar{\sigma}_{ij} - \sum_{\alpha=1}^{N} f_i^\alpha\, d_j^\alpha\right) = 0, \tag{10}$$

where

$$\bar{\sigma}_{ij} = \frac{1}{V}\int_V \sigma_{ij} dV \tag{11}$$

is the volume average of stress. Since ϕ_{ij} is an arbitrary tensor, we conclude from (10) that

$$\bar{\sigma}_{ij} = \sum_{\alpha=1}^{N} \frac{1}{2}\,(f_i^\alpha\, d_j^\alpha + f_j^\alpha\, d_i^\alpha), \tag{12}$$

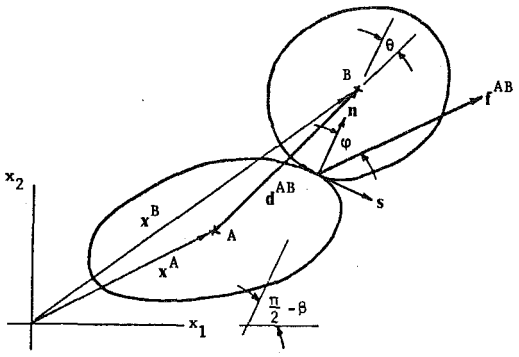

Fig. 2

where we have used the balance of moments, relation (4). It should be remarked that the virtual work principle, in the context of granular materials, has also been employed by other workers in this field. For example, Satake [7] employed this principle to define an "anisotropy tensor," and Kishino [32] used it to obtain the average stress as

$$\bar{\sigma}_{ij} = \frac{1}{V}\sum_{\alpha=1}^{M} x_i^\alpha f_j^\alpha, \tag{13}$$

where M is the number of contacts on the boundary. We note, however, that (13) can be obtained (without using the virtual work principle) by considering the relation between the volume average of stress and the integral of tractions over the surface of the body; e.g., Drescher and de Josselin de Jong [19] and Cowin [33].

Summarizing the results so far, we have obtained a relation for the balance of moments, equation (4), and a relation for overall stresses in terms of the contact forces, equation (12). These relations can be written as

$$\langle f_i d_j - f_j d_i \rangle = 0, \tag{14}$$

$$\bar{\sigma}_{ij} = \tfrac{1}{2} N \langle f_i d_j + f_j d_i \rangle, \tag{15}$$

where $\langle\ \rangle$ denotes the average over N critical contacts in a (suitably large) unit volume.[2] These relations hold in three as well as two dimensions.

For simplicity, however, we shall, from now on, restrict our attention to the two-dimensional problems. Also it is advantageous to represent (14) and (15) in terms of the unit vectors n_i^α and s_i^α which are, respectively, normal and tangent to the contact α. These unit vectors are defined by

$$\mathbf{n}^\alpha = \sin\beta^\alpha \mathbf{e}^{(1)} + \cos\beta^\alpha \mathbf{e}^{(2)} \quad \text{and} \quad \mathbf{s}^\alpha = \cos\beta^\alpha \mathbf{e}^{(1)} - \sin\beta^\alpha \mathbf{e}^{(2)}, \tag{16}$$

where $\mathbf{e}^{(1)}$ and $\mathbf{e}^{(2)}$ are orthogonal unit vectors in the direction of fixed rectangular Cartesian coordinate axes. In terms of $\mathbf{n}^\alpha$ and $\mathbf{s}^\alpha$, the interparticle force $\mathbf{f}^\alpha$ and the vector $\mathbf{d}^\alpha$ have the form

$$f_i^\alpha = f^\alpha(\cos\phi^\alpha\, n_i^\alpha + \sin\phi^\alpha s_i^\alpha), \tag{17a}$$

$$d_i^\alpha = d^\alpha(\cos\theta^\alpha n_i^\alpha + \sin\theta^\alpha s_i^\alpha), \tag{17b}$$

where f^α is the magnitude of $\mathbf{f}^\alpha$, ϕ^α is the angle between $\mathbf{f}^\alpha$ and $\mathbf{n}^\alpha$, d^α is the magnitude of $\mathbf{d}^\alpha$, and θ^α is the angle between $\mathbf{d}^\alpha$ and $\mathbf{n}^\alpha$, see Fig. 2. Substituting from (17) in (14) and (15) we obtain

$$\langle fd\sin(\phi - \theta)\rangle = 0, \tag{18}$$

$$\bar{\sigma}_{ij} = N\langle fd[\sin\phi\sin\theta\delta_{ij} + \cos(\phi+\theta)n_i n_j + \tfrac{1}{2}\sin(\phi+\theta)(n_i s_j + n_j s_i)]\rangle, \tag{19}$$

where δ_{ij} is the Kronecker delta. These relations are the two-dimensional version of the balance of moments, relation (14), and the average stress, relation (15). Some results based on (18) and (19) will be discussed in Section 4.

3 Kinematics

As mentioned earlier, the overall (macroscopic) deformation of the granular mass results from instantaneous sliding of rigid groups (or clusters) of grains. At each instant, each group consists of a collection of mutually immobile grains, which moves relative to its neighboring groups. Since a relative movement of these clusters causes changes in the magnitude and direction of the vectors $\mathbf{d}^\alpha$, we make the following simple assumption concerning the rate of change of $\mathbf{d}^\alpha$ and the resulting overall average velocity gradient tensor:

$$\dot{d}_i^\alpha = l_{ij}^\alpha d_j^\alpha, \tag{20}$$

$$\bar{L}_{ij} = \frac{1}{N}\sum_{\alpha=1}^{N} l_{ij}^\alpha, \tag{21}$$

where superposed dot denotes the rate of change, and $\bar{L}_{ij}$ is the average overall (macroscopic) velocity gradient. We further assume that the vectors $\mathbf{n}^\alpha$ and $\mathbf{s}^\alpha$ remain orthonormal, and that the vector $(1/d^\alpha)d_i^\alpha$ remains a unit vector after an (infinitesimal) increment of deformation has taken place. With these assumptions, (17b) and (16) yield

$$\dot{d}_i^\alpha = \left(\frac{\dot{d}^\alpha}{d^\alpha}\delta_{ij} + R_{ij}^\alpha\right) d_j^\alpha, \tag{22}$$

where R_{ij}^α, the spin of d_i^α, is given by

$$R_{ij}^\alpha = (\dot{\beta}^\alpha + \dot{\theta}^\alpha)(s_i^\alpha n_j^\alpha - s_j^\alpha n_i^\alpha). \tag{23}$$

Substituting for $\dot{d}_j^\alpha$ from (22) into (20) and rearranging, we obtain

$$d_j^\alpha\left(l_{ij}^\alpha - \frac{\dot{d}^\alpha}{d^\alpha}\delta_{ij} - R_{ij}^\alpha\right) = 0. \tag{24}$$

Thus l_{ij}^α has the form

$$l_{ij}^\alpha = \frac{\dot{d}^\alpha}{d^\alpha}\delta_{ij} + R_{ij}^\alpha + \dot{\gamma}^\alpha(\cos\theta^\alpha s_j^\alpha - \sin\theta^\alpha n_j^\alpha)\kappa_i^\alpha \tag{25}$$

for some scalar $\dot{\gamma}^\alpha$ and some unit vector κ_i^α. We define the angle κ^α by

$$\kappa_i^\alpha = \cos\kappa^\alpha\, n_i^\alpha + \sin\kappa^\alpha\, s_i^\alpha, \tag{26}$$

substitute from this and (23) into (25), and enter the result into (21) to obtain

$$\bar{D}_{ij} = \left(\frac{\dot{d}}{d} + \dot{\gamma}\sin\kappa\cos\theta\right)\delta_{ij} - \langle\dot{\gamma}\sin(\theta+\kappa)n_i n_j\rangle + \tfrac{1}{2}\langle\dot{\gamma}\cos(\theta+\kappa)(n_i s_j + n_j s_i)\rangle,$$

$$\bar{W}_{ij} = \langle[\dot{\beta} + \dot{\theta} - \tfrac{1}{2}\dot{\gamma}\cos(\theta-\kappa)](s_i n_j - s_j n_i)\rangle, \tag{27}$$

where, by definition, the overall deformation rate and spin tensors are

$$\bar{D}_{ij} = \tfrac{1}{2}(\bar{L}_{ij} + \bar{L}_{ji}) \quad \text{and} \quad \bar{W}_{ij} = \tfrac{1}{2}(\bar{L}_{ij} - \bar{L}_{ji}).$$

Equations (27) represent these average macroscopic kinematical quantities in terms of the microscopic kinematical variables for the considered two-dimensional model. Note that the inclusion of the as yet unknown quantities $\dot{\gamma}$ and κ_i is essential, as it bears on the compatibility of the overall deformation of the granular mass.

Before closing this section let us examine the rate of energy dissipation. To this end we assume that, at each instant, energy is being dissipated only by frictional sliding of rigid clusters of grains as they move relative to one another. A similar hypothesis has been used by others; see, e.g., Horne [5]. For the model considered here, this assumption results in

$$\bar{\sigma}_{km}\bar{D}_{km} = \sum_{\alpha=1}^{N}(\mathbf{f}^\alpha\cdot\mathbf{s}^\alpha)(\overset{\nabla}{\mathbf{d}}{}^\alpha\cdot\mathbf{s}^\alpha), \tag{28}$$

where dot denotes the scalar product, and where $\overset{\nabla}{\mathbf{d}}{}^\alpha$ defined by

[2] Henceforth, N will refer to the number of contacts per unit volume.

$$\overset{\nabla}{d}{}_i^\alpha = \dot{d}_i^\alpha - R_{ij}^\alpha d_j^\alpha, \tag{29}$$

is the (objective) rate of change of $\mathbf{d}^\alpha$ as measured by an observer rotating with $\mathbf{d}^\alpha$. Substituting from (17a) and (29) into (28) we obtain

$$\bar{\sigma}_{km}\bar{D}_{km} = N\langle (f \sin\phi \sin\theta)\dot{d}\rangle, \tag{30}$$

where (22) has been used. This is an interesting equation as it shows that frictional sliding must be accompanied by changes in the magnitude of vectors which connect the centroids of adjacent clusters of mutually immobile grains. Since this observation applies independently of shape of individual grains, it is seen that compatibility indeed requires formation of noncircular (in the two-dimensional case) groups even when the granular mass consists of a collection of cylindrical rods with circular cross sections.

4 An Example

The equations obtained in the preceeding sections for the overall stress and kinematical quantities, are rather complicated. Therefore, further insight into their physical implications requires additional simplifying assumptions. To this end consider equation (18) which is obtained from the balance of moments, and let all averages be taken over only the critical contacts; this implies that the angles ϕ^α, $\alpha = 1, 2, \ldots, N$, equal the *average* frictional angle ϕ (= constant). Then (18) becomes

$$\mu = \tan\phi = \frac{\langle fd \sin\theta\rangle}{\langle fd \cos\theta\rangle}.$$

Now, assume further that f^α and d^α, the magnitudes of the contact forces and the vectors $\mathbf{d}^\alpha$ connecting the centroids of adjacent groups, are *not* statistically correlated with the angles θ^α which define the orientation of $\mathbf{d}^\alpha$ with respect to the corresponding contact normals; see (17). Then the foregoing equation becomes

$$\mu = \tan\phi = \frac{\langle \sin\theta\rangle}{\langle \cos\theta\rangle}, \tag{31}$$

admitting the following solution:

$$a\cos\phi = \langle\cos\theta\rangle, \quad a\sin\phi = \langle\sin\theta\rangle, \tag{32}$$

for some scalar a. A more restrictive solution, of course, is

$$\theta^\alpha = \phi^\alpha = \phi \tag{33}$$

which states that at each critical contact the contact force is parallel to the line which connects the centroids of the corresponding contacting adjacent groups. For our purposes we shall consider the more general solution (32) and then later on seek to explore results stemming from assumption (33).

Let us now make a further assumption, namely, that the quantities f^α and d^α are not correlated with $\mathbf{n}^\alpha$ (and, hence, also with $\mathbf{s}^\alpha$). Then, with the aid of (32), from (19) we obtain

$$\bar{\sigma}_{ij} = 2p\{\sin^2\phi\delta_{ij} + \cos 2\phi\,\langle n_i n_j\rangle + \tfrac{1}{2}\sin 2\phi\langle n_i s_j + n_j s_i\rangle\}, \tag{34}$$

where

$$p \equiv \tfrac{1}{2}\bar{\sigma}_{kk} = \tfrac{1}{2}aN\langle fd\rangle \tag{35}$$

is the mean pressure.

Before discussing the kinematics, we pause briefly to examine some features of equation (34). Employing (16), it can be shown from (34) that

$$R \equiv \frac{\tau}{p} = \{\langle\sin 2\beta\rangle^2 + \langle\cos 2\beta\rangle^2\}^{1/2}, \tag{36}$$

$$\tan 2\psi = -\frac{\langle\sin 2\beta\rangle\cos 2\phi + \langle\cos 2\beta\rangle\sin 2\phi}{\langle\cos 2\beta\rangle\cos 2\phi - \langle\sin 2\beta\rangle\sin 2\phi} = \tan 2(\psi' - \phi), \tag{37}$$

where R is the stress ratio; and τ, ψ, and ψ' are defined by

$$2\tau^2 = \bar{\sigma}'_{ij}\bar{\sigma}'_{ij} \quad \text{or} \quad \tau = \tfrac{1}{2}(\bar{\sigma}_1 - \bar{\sigma}_2), \tag{38}$$

$$\tan 2\psi = \frac{2\bar{\sigma}_{12}}{\bar{\sigma}_{11} - \bar{\sigma}_{22}}, \tag{39}$$

$$\tan 2\psi' = -\frac{\langle\sin 2\beta\rangle}{\langle\cos 2\beta\rangle}, \tag{40}$$

where in (38), $\bar{\sigma}'_{ij} = \bar{\sigma}_{ij} - \tfrac{1}{2}\delta_{ij}\bar{\sigma}_{kk}$ is the average deviatoric stress, and $\bar{\sigma}_1$ and $\bar{\sigma}_2$ are, respectively, the major and the minor principal stresses. In the terminology of Curray [34], used by Oda [35] and Konishi [36], the quantity in the right-hand side of (36) is the "degree of concentration" or the "vector magnitude" of the contact normals (n_i^α), and ψ' defined by (40) is their preferred orientation. Konishi [36] reported measured values of the degree of concentration and the preferred orientation of the contact normals, n_i^α. His consideration, however, is based on *all* contacts rather than only the *critical* contacts which enter our work. In other words, the averages measured by Konishi are defined by (for some quantity f)

$$\langle f\rangle = \int_\Omega E(\beta)f(\beta)d\beta, \tag{41}$$

in terms of the probability density distribution of contact normals, $E(\beta)$; Oda [35]. The averages appearing in (36) and (37), on the other hand, have the form

$$\langle f\rangle = \int_\Omega E(\beta)\,P(\beta)f(\beta)d\beta, \tag{42}$$

where $P(\beta)$ is the probability of sliding; Oda [8]. In (41) and (42) Ω represents a unit circle. We recall that the macroscopic stress may be formulated either in terms of averages taken over the critical contacts only, or in terms of the averages taken over *all* contacts. In the former case we observe that the quantity $\mathbf{d}^\alpha$ then represents the vector which connects the centroids of two adjacent *clusters of mutually immobile grains,* whereas in the latter case all individual grains are included; see the discussion after (5). The two formulations are of course, equivalent.

Returning to the example, we assume that $\dot{\gamma}^\alpha\sin\kappa^\alpha$ and $\dot{\gamma}^\alpha\cos\kappa^\alpha$ appearing in (27) are not correlated with either θ^α or the unit vector $\mathbf{n}^\alpha$. Employing this assumption together with (32) we reduce (27) to

$$\bar{D}_{ij} = \left[\left\langle\frac{\dot{d}}{d}\right\rangle + \cos\phi\,\langle\dot{\gamma}\sin\kappa\rangle\right]\delta_{ij} - [\cos\phi\,\langle\dot{\gamma}\sin\kappa\rangle + \sin\phi\,\langle\dot{\gamma}\cos\kappa\rangle]$$
$$\times\langle n_i n_j\rangle + \tfrac{1}{2}[\cos\phi\,\langle\dot{\gamma}\cos\kappa\rangle - \sin\phi\,\langle\dot{\gamma}\sin\kappa\rangle]\langle n_i s_j + n_j s_i\rangle, \tag{43}$$

$$2\bar{W}_{12} = 2\langle\dot{\beta} + \dot{\theta}\rangle - [\cos\phi\langle\dot{\gamma}\cos\kappa\rangle + \sin\phi\langle\dot{\gamma}\sin\kappa\rangle]. \tag{44}$$

Similarly, employing (32) and the assumption that $f^\alpha d^\alpha$ and $\dot{d}^\alpha/d^\alpha$ are uncorrelated, it follows from the energy dissipation relation (30) that

$$\bar{\sigma}_{km}\bar{D}_{km} = aN\sin^2\phi\langle fd\rangle\left\langle\frac{\dot{d}}{d}\right\rangle = 2p\sin^2\phi\left\langle\frac{\dot{d}}{d}\right\rangle, \tag{45}$$

where (35) has been used to obtain (45).

Now components of $\langle n_i n_j\rangle$ and $\langle n_i s_j + n_j s_i\rangle$ are not all independent, as can be seen from (16). Noting this, it follows from (34) and (43) that

$$\bar{\sigma}'_{km}\bar{D}'_{km} = \frac{\tau^2}{p}[\sin\phi\langle\dot{\gamma}\cos\kappa\rangle - \cos\phi\langle\dot{\gamma}\sin\kappa\rangle], \tag{46}$$

$$\bar{\sigma}_{1k}\bar{D}_{k2} - \bar{\sigma}_{2k}\bar{D}_{k1} = -\frac{\tau^2}{p}[\cos\phi\langle\dot{\gamma}\cos\kappa\rangle + \sin\phi\langle\dot{\gamma}\sin\kappa\rangle]. \tag{47}$$

The rate of volume change is obtained from (43),

$$\bar{D}_{kk} = 2\langle\dot{d}/d\rangle + \cos\phi\langle\dot{\gamma}\sin\kappa\rangle - \sin\phi\langle\dot{\gamma}\cos\kappa\rangle. \tag{48}$$

Employing (44), (45), and (48), we eliminate the average quantities appearing in the left-hand sides of (46) and (47). The final result can be written as

$$(\sin^2\phi - R^2)\frac{1}{\tau}\bar{\sigma}'_{km}\overline{D}'_{km} = R\cos^2\phi\,\overline{D}_{kk}, \tag{49}$$

$$\overset{\nabla}{\bar{\sigma}}_{ik}\bar{\sigma}_{kj} - \bar{\sigma}_{ik}\overset{\nabla}{\bar{\sigma}}_{kj} = \frac{2\tau}{R}(\bar{\sigma}_{ik}\overline{D}_{kj} - \overline{D}_{ik}\bar{\sigma}_{kj}), \tag{50}$$

corresponding, respectively, to (46) and (47). In these relations R denotes the stress ratio defined by (36), and the stress rate, $\overset{\nabla}{\bar{\boldsymbol{\sigma}}}$, is defined by

$$\overset{\nabla}{\bar{\sigma}}_{ij} = \dot{\bar{\sigma}}_{ij} - \Omega_{ik}\bar{\sigma}_{kj} - \Omega_{jk}\bar{\sigma}_{ki}, \tag{51}$$

where $\boldsymbol{\Omega}$ is a skew-symmetric tensor with components

$$\Omega_{12} = -\Omega_{21} = \overline{W}_{12} - \langle\dot{\beta} + \dot{\theta}\rangle - \dot{\psi}. \tag{52}$$

In component form, (49) and (50) are

$$(\sin^2\phi - R^2)\{(\overline{D}_{11} - \overline{D}_{22})\cos 2\psi + 2\overline{D}_{12}\sin 2\psi] - R\cos^2\phi\,(\overline{D}_{11} + \overline{D}_{22}) = 0, \tag{53}$$

$$(\overline{D}_{11} - \overline{D}_{22})\sin 2\psi - 2\overline{D}_{12}\cos 2\psi + 2R(\overline{W}_{12} - \langle\dot{\beta} + \dot{\theta}\rangle) = 0. \tag{54}$$

These relations are similar in form to the relations developed by de Josselin de Jong [24, 25], Spencer [23], and Mehrabadi and Cowin [26, 29], using a completely different approach. In particular, de Josselin de Jong's idea of "free rotation" is clearly expressed by the quantity $-\langle\dot{\beta} + \dot{\theta}\rangle$ in (54). It is interesting to note, however, that under a steady-state circumstance when the statistics of the critical contacts remain time-invariant[3] so that $\langle\langle f\rangle\rangle^{\cdot} = \langle\dot{f}\rangle$, and when $\dot{\beta}$ and β are uncorrelated (e.g., when R = constant), then (37) yields

$$\dot{\psi} = -\langle\dot{\beta}\rangle. \tag{55}$$

If, in addition, the more restrictive assumption (33) is used instead of (32) then it follows from (52) that $\Omega_{12} = \overline{W}_{12}$ and the stress rate in (51) becomes the Jaumann rate.

Relations (49) and (50) are similar in structure to those proposed by Rice [27] for the rigid plastic yield-vertex model. However, the coefficients and the stress rate involved are different in the two models. The advantage of (49) and (50) over their counterparts in all the aforementioned works is that, due to the microstructural approach adopted here, all the macroscopic material coefficients are determined explicitly in the present work in terms of the average friction angle ϕ and the stress ratio R.

For example, since the rate of plastic work is positive,

$$\bar{\sigma}_{km}\overline{D}_{km} > 0, \tag{56}$$

it follows from (49) that

$\overline{D}_{kk} < 0$	(dilatation)	for $R > \sin\phi$,
$\overline{D}_{kk} = 0$	(no volume change)	for $R = \sin\phi$,
$\overline{D}_{kk} > 0$	(densification)	for $R < \sin\phi$,

which are in accordance with the experimental results.

5 Summary of Assumptions and Discussion

Based on the principle of virtual work, a relation for average stresses in terms of the contact forces and vectors joining the centroids of granules (or mutually immobile clusters of granules) is derived in Section 2; see equation (12). The major assumptions used to obtain this result are: (*i*) the virtual separation of two contacting granules at a typical contact point α resulting from a prescribed virtual displacement field (equation (8)) can be written by equation (9) where ϕ_{ij} is the constant virtual displacement gradient; and (*ii*) the contacts do not transmit moments (equation (3)). This last assumption yields (4) which in turn leads to a symmetric overall stress field. Of course, without this assumption, couple stresses would be present.

The "microscopic" description of the overall stress field given by (12), which holds in two as well as three dimensions, seems to be of a fundamental nature in the sense that it relates the macroscopic stress field to the microstructure (or the "fabric") of the granular mass.

In Section 3, kinematic relations for the plane deformation are developed. The involved basic assumptions are: (*i*) the rate of change of $\mathbf{d}$ (the vector joining the centroids of two contacting clusters) gives rise to a microscopic (local) velocity gradient l^{α}_{ij} whose average taken over all critical contacts results in the average overall macroscopic velocity gradient for the sample; and (*ii*) the unit vectors $\mathbf{n}^{\alpha}$ and $\mathbf{s}^{\alpha}$ (the contact normal and the sliding direction at contact α) remain orthonormal. Under these assumptions, expressions for the rate of deformation and the spin tensors are obtained in terms of the contact normals and tangents; equation (27). Also in Section 3, an hypothesis is made with regard to the rate of energy dissipation: it is assumed that energy is dissipated only by frictional sliding of rigid clusters of granules as they move relative to one another; this is given by equation (28).

Finally, an example of the class of constitutive equations which emerges from the development of Sections 2 and 3, is given in Section 4. This example is concerned with the case where the quantities of the type

$$\langle An_in_j\rangle \quad \text{or} \quad \langle B(n_is_j + n_js_i)\rangle$$

which appear in the stress equations (19) and the kinematic relations (27), can be written as

$$\langle A\rangle\langle n_in_j\rangle \quad \text{or} \quad \langle B\rangle\langle n_is_j + n_js_i\rangle.$$

It is shown that under this assumption, the resulting constitutive relations resemble those of de Josselin de Jong [24], Spencer [23], and Mehrabadi and Cowin [26]. Of course, more general constitutive relations can be obtained by assuming that A and B statistically depend on $n^{\alpha}_i n^{\alpha}_j$; see Mehrabadi, Nemat-Nasser, and Oda [37].

Acknowledgment

This work was supported by U.S. Air Force Office of Scientific Research, Grant No. AFOSR-80-0017 to Northwestern University.

References

1 Reynolds, O., "On the Dilatancy of Media Composed of Rigid Particles in Contact," *Philosophical Magazine*, Vol. 20, 1885, pp. 469–481.

2 Newland, P. L., and Allely, B. A., "Volume Changes in Drained Triaxial Tests on Granular Materials," *Géotechnique*, Vol. 7, 1957, pp. 17–34.

3 Rowe, P. W., "The Stress-Dilatancy Relations for Static Equilibrium of an Assembly of Particles in Contact," *Proceedings of the Royal Society*, London, Series A, Vol. 269, 1962, pp. 500–527.

4 Rowe, P. W., "Theoretical Meaning and Observed Values of Deformation Parameters for Soils," *Stress-Strain Behavior of Soils*, 1971, ed., Parry, R. H. G., Foulis Henley-on-Thames, pp. 143–194.

5 Horne, M. R., "The Behavior of an Assembly of Rotund, Rigid, Cohesionless Particles, I and II," *Proceedings of the Royal Society*, London, Series A, Vol. 286, 1965, pp. 62–97.

6 Horne, M. R., "The Behavior of an Assembly of Rotund, Rigid, Cohesionless Particles, III," *Proceedings of the Royal Society*, London, Series A, Vol. 310, 1969, pp. 21–34.

7 Satake, M., "Constitution of Mechanics of Granular Materials Through the Graph Theory," *Proceedings of the U.S.-Japan Seminar on Continuum Mechanical and Statistical Approaches in the Mechanics of Granular Materials*, 1978, eds., Cowin, S. C., and Satake, M., Gakujutsu Bunken Fukyukai, Tokyo, pp. 47–62.

8 Oda, M., "A Mechanical and Statistical Model of Granular Material," *Soils and Foundations*, Vol. 14, No. 1, 1974, pp. 13–27.

9 Matsouka, H., "A Microscopic Study on Shear Mechanism of Granular Materials," *Soils and Foundations*, Vol. 14, No. 1, 1974, pp. 29–43.

10 Nemat-Nasser, S., "On Behavior of Granular Materials in Simple Shear," Earthquake Research and Engineering Laboratory Technical Report No. 79-6-19, Department of Civil Engineering, Northwestern University, Evanston, Ill., 1979; *Soils and Foundations*, Vol. 20, No. 3, 1980, pp. 59–73.

11 Drucker, D. C., and Prager, W., "Soil Mechanics and Plastic Analysis or Limit Design," *Quarterly of Applied Mathematics*, Vol. 10, 1952, pp. 157–165.

[3] In general the density of the critical contacts as well as the density function defining the distribution of the critical contact normals changes with the deformation; e.g., new critical contacts are continually formed while some existing critical contacts are rendered inactive. Therefore, in general, $\langle\langle f\rangle\rangle^{\cdot} \neq \langle\dot{f}\rangle$.

12 Shield, R. T., "Mixed Boundary Value Problems in Soil Mechanics," *Quarterly of Applied Mathematics,* Vol. 11, 1953, pp. 61–75.
13 Shield, R. T., "Stress and Velocity Fields in Soil Mechanics," *Journal of Mathematics and Physics,* Vol. 33, 1957, pp. 144–156.
14 Drucker, D. C., Gibson, R. E., and Henkel, D. J., "Soil Mechanics and Work-Hardening Theories of Plasticity," *Trans. ASCE,* Vol. 122, 1957, pp. 338–346.
15 Jenike, A. W., and Shield, R. T., "On the Plastic Flow of Coulomb Solids Beyond Original Failure," ASME JOURNAL OF APPLIED MECHANICS, Vol. 26, 1959, pp. 599–602.
16 Nemat-Nasser, S., and Shokooh, A., "On Finite Plastic Flow of Compressible Materials With Internal Friction," Earthquake Research and Engineering Laboratory Technical Report No. 79-5-16, Department of Civil Engineering, Northwestern University, Evanston, Ill., 1979; *International Journal of Solids and Structures,* Vol. 16, 1980, pp. 495–514.
17 Cowin, S. C., "Microstructural Continuum Models for Granular Materials," *Proceedings of the U.S.-Japan Seminar on Continuum Mechanical and Statistical Approaches in the Mechanics of Granular Materials,* 1978, eds., Cowin, S. C., and Satake, M., Gakujutsu Bunken Fukyukai, Tokyo, pp. 162–170.
18 Cowin, S. C., and Satake, M., eds., *Proceedings of the U.S.-Japan Seminar on Continuum Mechanical and Statistical Approaches in the Mechanics of Granular Materials,* Gakujutsu Bunken Fukyukai, Tokyo, 1978.
19 Drescher, A., and de Josselin de Jong, G., "Photoelastic Verification of a Mechanical Model for the Flow of a Granular Material," *Journal of the Mechanics and Physics of Solids,* Vol. 20, 1972, pp. 337–351.
20 Oda, M., and Konishi, J., "Microscopic Deformation Mechanism of Granular Material in Simple Shear," *Soils and Foundations,* Vol. 14, No. 4, 1974, pp. 25–38.
21 Drescher, A., "An Experimental Investigation of Flow Rules for Granular Materials Using Optically Sensitive Glass Particles," *Géotechnique,* Vol. 26, 1976, pp. 591–601.
22 Mandel, J., "Sur les lignes de glissement et le calcul des déplacements dans la déformation plastique," *Comptes Rendus de l'Académie des Sciences,* Vol. 225, 1947, pp. 1272–1273.
23 Spencer, A. J. M., "A Theory of the Kinematics of Ideal Soils Under Plane Strain Conditions," *Journal of the Mechanics and Physics of Solids,* Vol. 12, 1964, pp. 337–351.
24 de Josselin de Jong, G., "The Double Sliding, Free Rotating Model for Granular Assemblies," *Géotechnique,* Vol. 21, 1971, pp. 155–163.
25 de Josselin de Jong, G., "Mathematical Elaboration of the Double Sliding, Free Rotating Model," *Archive of Mechanics,* Vol. 29, 1977, pp. 561–591.
26 Mehrabadi, M. M., and Cowin, S. C., "Initial Planar Deformation of Dilatant Granular Materials," *Journal of the Mechanics and Physics of Solids,* Vol. 26, 1978, pp. 269–284.
27 Rice, J. R., "Localization of Plastic Deformation," *Proceedings of the 14th International Congress of Theoretical and Applied Mechanics,* Vol. 1, 1976, pp. 207–220.
28 Christoffersen, J., and Hutchinson, J. W., "A Class of Phenomenological Corner Theories of Plasticity," *Journal of the Mechanics and Physics of Solids,* Vol. 27, 1979, pp. 465–487.
29 Mehrabadi, M. M., and Cowin, S. C., "Prefailure and Postfailure Soil Plasticity Models," *Journal of Engineering Mechanics Division, Trans. ASCE,* Vol. 106, 1980, pp. 991–1003.
30 Hill, R., "Elastic Properties of Reinforced Solids: Some Theoretical Principles," *Journal of the Mechanics and Physics of Solids,* Vol. 11, 1963, pp. 357–372.
31 Davis, R. A., and Deresiewicz, H., "A Discrete Probabilistic Model for Mechanical Response of a Granular Medium," *Acta Mechanica,* Vol. 27, 1977, pp. 69–89.
32 Kishino, Y., "Statistical Consideration on Deformation Characteristics of Granular Materials," *Proceedings of the U.S.-Japan Seminar on Continuum Mechanical and Statistical Approaches in the Mechanics of Granular Materials,* 1978, eds., Cowin, S. C., and Satake, M., Gakujutsu Bunken Fukyukai, Tokyo, pp. 114–122.
33 Cowin, S. C., "Effective Stress-Strain Relations for Finitely Deformed Inhomogeneous Bodies," *Mechanics Research Communications,* Vol. 4, 1977, pp. 163–169.
34 Curray, J. R., "The Analysis of Two-Dimensional Orientation Data," *Journal of Geology,* Vol. 64, 1956, pp. 117–131.
35 Oda, M., "Initial Fabrics and Their Relations to Mechanical Properties of Granular Material," *Soils and Foundations,* Vol. 12, No. 1, 1972, pp. 1–18.
36 Konishi, J., "Microscopic Model Studies on the Mechanical Behavior of Granular Materials," *Proceedings of the U.S.-Japan Seminar on Continuum Mechanical and Statistical Approaches in the Mechanics of Granular Materials,* 1978, eds., Cowin, S. C., and Satake, M., Gakujutsu Bunken Fukyukai, Tokyo, pp. 27–45.
37 Mehrabadi, M. M., Nemat-Nasser, S., and Oda, M., "On Statistical Description of Stress and Fabric in Granular Materials," Earthquake Research and Engineering Laboratory Technical Report No. 80-4-29, Department of Civil Engineering, Northwestern University, Evanston, Ill., 1980; to appear in the *International Journal for Numerical and Analytical Methods in Geomechanics.*

APPENDIX

To calculate Δ_i^α in equation (7), consider two rigid granules, denote their respective centroids by A and B, and assume that they are in contact at point C. Consider a virtual displacement field which introduces the relative displacement Δ_i^C at contact C, i.e.,

$$\Delta_i^C = u_i^{CB} - u_i^{CA}, \tag{57}$$

where $\mathbf{u}^{CA}$ and $\mathbf{u}^{CB}$ are the displacements of the contact point C when viewed as belonging to grains A and B, respectively. Since the grains are rigid, we can write, for example, for grain A,

$$u_i^{CA} = u_i^A + \omega_{ij}^{AC}(x_j^C - x_j^A), \tag{58}$$

where $\omega_{ij}^{AC} = -\omega_{ij}^{CA}$ is the rotation of C relative to A, and u_i^A is the displacement of centroid A; a similar equation applies to grain B (replace A with B in equation (58)).

Equation (57) is now written as

$$\Delta_i^C = (u_i^B - u_i^C) - (u_i^A - u_i^C) + \omega_{ij}^{CA}(x_j^C - x_j^A) - \omega_{ij}^{CB}(x_j^C - x_j^B), \tag{59}$$

where (58) is also used and u_i^C is to be defined next, and then it is assumed that the displacements and rotations, u_i^α, $\alpha = A, B$, and ω_{ij}^{CA} and ω_{ij}^{CB}, conform to some smooth fields u_i and ω_{ij}, and that $u_i^C = u_i(\mathbf{x}^C)$ is the value of u_i at the contact point C. Then we have $\omega_{ij}^{AC} = \omega_{ij}^{BC} = \omega_{ij}(\mathbf{x}^C)$, and

$$u_i^A - u_i^C = \frac{\partial u_i}{\partial x_j}(\mathbf{x}^C)(x_j^A - x_j^C) + \ldots, \tag{60}$$

with a similar expression corresponding to grain B. Hence (59) becomes

$$\Delta_i^C = \left[\frac{\partial u_i}{\partial x_j}(\mathbf{x}^C) - \omega_{ij}(x^C)\right] d_j^{AB} + \ldots, \tag{61}$$

where $d_j^{AB} = x_j^B - x_j^A$. To the first order of approximation, this is identical with equation (9), provided that we identify the quantity inside the brackets with ϕ_{ij}.

W. Dreyer

Technische Universität Berlin,
Hermann-Föttinger-Institut für
Thermo und fluiddynamik,
Strasse des 17. Juni 135,
1000 Berlin 12,
Germany

On Thermodynamics and Kinetic Theory of Ideal Rubber Membranes

Based on experimental evidence and thermodynamics it will be shown that the stored energy function of an ideal rubber membrane is determined by the entropy alone. The membrane is represented by a two-dimensional surface for the purposes of thermodynamics, and its thickness is taken into account by a scalar parameter so that incompressibility of the membrane can be described. The entropy of the membrane is calculated from a kinetic model and hence results the surface stress as a function of temperature and deformation for arbitrary shape of the membrane.

1 Introduction

The subject of this paper is the application of thermodynamics of two-dimensional surfaces to ideal rubber membranes. Just as in bulk rubber the thermodynamic theory is supported by arguments from the kinetic theory of rubber.

A continuum theory of bulk bodies has been applied to ideal rubber membranes by Kubo [1], Adkins and Rivlin [2], et al., with good results for spherical and cylindrical membranes. However, it seems impossible to extend those approaches to arbitrary shapes of the membrane because of the difficulty of determining the hydrostatic pressure in the membrane. This difficulty is explained in Section 2.

The present approach is given entirely in terms of thermodynamics of two-dimensional surfaces and there is no problem in considering membranes of arbitrary shapes. The formulation of a thermodynamic theory of a two-dimensional surface implies the definition of a surface entropy, which must be determined by a constitutive relation. This constitutive relation is derived here from a variant of Kuhn's [3] kinetic theory of rubber. It seemed necessary at the beginning to modify Kuhn's theory to take care of the fact that in a thin membrane the rubber molecules are strung out along the membrane. It turned out in the end that the effect of curvature was minimal. This is explained in Section 4.

The concept of two-dimensional surfaces is familiar in thermodynamics of thin bodies (e.g., see Wang and Cross [4, 5], Green, Naghdi, and Wainwright [6]). In particular the paper of Green, Naghdi, and Wainwright deals with an elastic Cosserat surface. The authors assign a director to every surface point, so that the surface can support couple stresses.

Rubber membranes do not support couple stresses and therefore director fields are not needed. What *is* needed in rubber is a scalar thickness parameter among the state variables, because otherwise the incompressibility of rubber would not reflect itself in the two-dimensional theory.

However, if the director field in the Cosserat theory is replaced by the scalar field of the thickness parameter, the present theory can be classified as a spherical case of a Cosserat surface (e.g., see [6]).

2 Phenomenology and Existing Theories of Rubber Membranes

Rubber is an isotropic incompressible material, distinguished from other such materials by the fact that its stress is proportional to the temperature.

The pecularities of the stress-strain relation of a rubber membrane are best illustrated by the dependence of the pressure difference $[p] = p_I - p_E$ between the interior and exterior of a spherical rubber balloon on its radius r. Qualitatively this dependence is plotted as the solid curve in Fig. 1 where R is the radius of the balloon in the unloaded reference configuration.

Attempts to describe this curve include those by Kubo [1] and Adkins and Rivlin [2], both of which approach the problem by use of the ideas of continuum mechanics of bulk bodies, but in a different manner.

Both approaches start from the momentum balance in equilibrium, viz.,

$$\oint\!\!\!\!\!\!\int t_{ij} n_j dF = 0 \tag{1}$$

and from the representation

$$t_{ij} = -P\delta_{ij} + aB_{ij} + b(B^2)_{ij} \tag{2}$$

of the stress t_{ij} in an isotropic incompressible body. P is the hydrostatic pressure which must be calculated from the balance of momentum and the boundary conditions and B_{ij} is the left Cauchy-Green tensor, while a and b may be scalar functions of temperature T. The dotted line in Fig. 1 results from setting $b = 0$. Kubo has only considered the case $b = 0$, but in principle his method would also work for the general case. Rubber with $b = 0$ and a = constant is usually called ideal rubber.

Contributed by the Applied Mechanics Division for publication in the JOURNAL OF APPLIED MECHANICS.

Discussion on this paper should be addressed to the Editorial Department, ASME, United Engineering Center, 345 East 47th Street, New York, N. Y. 10017, and will be accepted until September 1, 1981. Readers who need more time to prepare a Discussion should request an extension from the Editorial Department. Manuscript received by ASME Applied Mechanics Division, July, 1979; final revision, March, 1980.

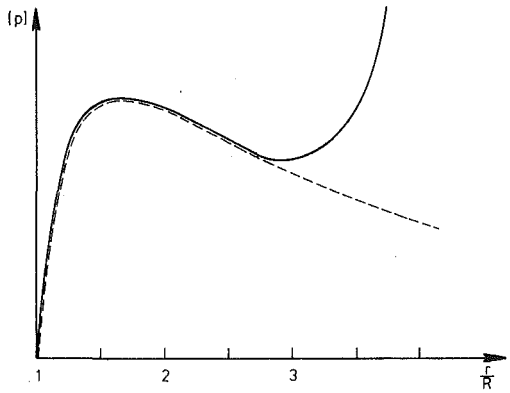

Fig. 1

Kubo's method starts by considering the membrane first as a bulk body and calculates P from $\partial t_{ij}/\partial x_j = 0$ in the body and from $(t_{ij}n_j)_I = -(pn_i)_I$ and $(t_{ij}n_j)_E = -(pn_i)_E$ on its surfaces. Subsequently Kubo lets the width of the membrane tend to zero. This method is excellent, except that it turns out to be extremely difficult to determine P in the case of complex shapes of the membrane.

The method of Adkins and Rivlin avoids the aforementioned difficulty of Kubo's approach, because they determine P from the requirement

$$t_{rr} \to 0 \quad \text{as} \quad \delta \to 0, \tag{3}$$

where t_{rr} is the normal stress and δ is the thickness of the balloon. Thus Adkins and Rivlin obtain

$$P = aB_{rr} + b(B^2)_{rr} \tag{4}[1]$$

and they proceed as follows:

1 They define a surface stress

$$t_s^{i\Delta} = \int_0^\delta t^{i\Delta} dr \quad (\Delta = \Theta, \Phi),$$

2 They integrate $\partial t_{ij}/\partial x_j = 0$ over the width of the membrane and obtain

$$t^{i\Delta}_{s;\Delta} + t^{ir}(\delta) - t^{ir}(0) = 0, \tag{5}[2]$$

3 With the boundary conditions

$$(t^{ij}n^j)_I = -(pn^i)_I, \quad (t^{ij}n^j)_E = -(pn^i)_E \tag{6}$$

they get

$$t^{i\Delta}_{s;\Delta} - [p]n^i = 0. \tag{7}$$

Thus Adkins and Rivlin start out with arguments from the theory of elasticity of bulk bodies and they arrive at an equation of balance of momentum for a two-dimensional surface in equilibrium (see, equation (11)).

However, the approach by Adkins and Rivlin is not without problems, because the boundary conditions (6) will not in general be compatible with (3).

Even so the assumption (3) may be justified in approximate form as follows. From Kubo's arguments we may determine t_{rr} and obtain—in the limit of a thin membrane—the value $t_{rr} = \frac{1}{2}(p_I + p_E)$. Setting t_{rr} equal to zero, Adkins and Rivlin neglect the effect of $(p_I + p_E)$ on the deformation of the membrane; indeed, in most cases the values of t_{rr} are small as compared to the coefficients a and b in (2).

[1] r, Θ, Φ are the polar coordinates appropriate to a spherical balloon.

[2] A semicolon denotes the covariant derivative with respect to the surface coordinates Θ and Φ.

3 Thermodynamics

(a) Fields of Thermodynamics in an Incompressible Membrane. For the purpose of thermodynamics we represent the membrane by a two-dimensional surface whose particles are characterized by the surface parameters U^Γ ($\Gamma = 1, 2$).

The objective of thermodynamics of membranes is the determination of the fields

Surface Mass Density

$$\rho_s(U^\Gamma, t), \tag{8}_1$$

Motion

$$x^i(U^\Gamma, t), \tag{8}_2$$

Absolute Surface Temperature

$$T_s(U^\Gamma, t), \tag{8}_3$$

for all times. x^i determines the position of a surface particle in a Cartesian frame.

Experience shows that incompressibility of a body, i.e., constancy of volume and density, strongly influences its mechanical behavior and that is true for membranes as well as for bulk bodies. However, the two-dimensional surface has no volume and therefore it would seem impossible to describe the influence of incompressibility in a thermodynamic theory of two-dimensional surfaces. We can get around this difficulty, by introducing an additional surface field, called

Thickness Parameter

$$\delta(U^\Gamma, t) \tag{8}_4$$

such that

$$\rho_s = \rho\delta, \tag{9}$$

where ρ is the volume density within the membrane. Thus incompressibility of the membrane is expressed by setting ρ_s/δ constant, and the model of a two-dimensional surface is preserved.

For the determination of the fields (8) it is necessary to have field equations and these are derived from the equations of balance of mechanics and thermodynamics which we proceed to write down next.

(b) Equations of Balance. We consider the membrane immersed in an inviscid heat-conducting fluid. The membrane is impermeable and moves with the velocity $V_\nu(U^\Gamma, t)$ and its mean and Gaussian curvatures are k_M and k_G, respectively. While $x^i(U^\Gamma, t)$ determines the position of the membrane in its present configuration κ_t we introduce $X^A(U^\Gamma)$ for its position in a reference configuration κ_0.

The equations of balance of mass, momentum, and internal energy read[3]

$$\frac{\partial \rho_s}{\partial t} + (V^\Gamma_{;\Gamma} - 2k_M V_\nu)\rho_s = 0, \tag{10}$$

$$\rho_s \frac{\partial v^i_s}{\partial t} - t^{i\Delta}_{s;\Delta} - [-p\nu^i] = 0, \tag{11}$$

$$\rho_s \frac{\partial \epsilon_s}{\partial t} + q^\Delta_{s;\Delta} + [q^j\nu^j] = t^{i\Delta}_s \frac{\partial v^i_s}{\partial U^\Delta} = \frac{1}{2}\frac{\partial g_{\Delta\Gamma}}{\partial t} S^{\Delta\Gamma} + S^\Delta\left(b_{\Delta\Gamma}V^\Gamma + \frac{\partial V_\nu}{\partial U^\Delta}\right). \tag{12}$$

The field equations for the determination of the thickness parameter δ follows from (9) and (10), because the volume density is constant. It reads

$$\frac{\partial \delta}{\partial t} + (V^\Gamma_{;\Gamma} - 2k_M V_\nu)\delta = 0 \tag{13}$$

The newly introduced notation in (10)–(13) and further quantities

[3] e.g., see [7, p. 233].

relevant to the future development of the theory may be read off from the following list:

$\tau^i_\Delta = \dfrac{\partial x^i}{\partial U^\Delta}$	Tangent vector in κ_t to coordinate lines U^Δ = constant
$\nu^i = \dfrac{\epsilon^{ijk}\tau^j_1\tau^k_2}{\lvert\epsilon^{ijk}\tau^i_1\tau^k_2\rvert}$	Normal vector to the surface in κ_t
$T^A_\Delta = \dfrac{\partial X^A}{\partial U^\Delta}$	Tangent vectors in κ_0 to coordinate lines U^Δ = constant
$N^A = \dfrac{\epsilon^{ABC}T^B_1T^C_2}{\lvert\epsilon^{ABC}T^B_1T^C_2\rvert}$	Normal vector to the surface in κ_0
$g_{\Delta\Gamma} = \tau^i_\Delta\tau^i_\Gamma$	Metric tensor in κ_t
$b_{\Delta\Gamma} = \dfrac{\partial\tau^i_\Delta}{\partial U^\Gamma}\nu^i$	Curvature tensor in κ_t
$G_{\Delta\Gamma} = T^A_\Delta T^A_\Gamma$	Metric tensor in κ_0
$B_{\Delta\Gamma} = \dfrac{\partial T^A_\Delta}{\partial U^\Gamma}N^A$	Curvature tensor in κ_0
$v^i_s = \dfrac{\partial x^i(U^\Gamma, t)}{\partial t} = V^\Gamma\tau^i_\Gamma + V_\nu\nu^i$	Decomposition of the velocity v^i_s of a surface particle
$t^{i\Delta}_s = S^{\Delta\Gamma}\tau^i_\Gamma + S^\Delta\nu^i$	Decomposition of the surface stress $t^{i\Delta}_s$
$[p]$	Pressure jump across the surface
ϵ_s	Specific internal energy of the surface
q^Δ_s	Normal component of the heat flux
$[q^j\nu^j]$	across the surface

For later use we list the identity (e.g., see [8, p. 500])

$$V^\Gamma_{;\Gamma} - 2k_MV_\nu = \frac{1}{2g}\frac{\partial g}{\partial t}, \tag{14}$$

where g is the determinant of $g_{\Delta\Gamma}$.

(c) Constitutive Equations. To obtain field equations the equations of balance must be supplemented by constitutive relations for the following quantities:

$$S^{\Delta\Gamma}, S^\Delta, q^\Delta_s, \epsilon_s, p^\pm, q^{j\pm}.$$

These are constitutive quantities and they can be split into two groups:

The first group consists of $S^{\Delta\Gamma}$, S^Δ, q^Δ_s, ϵ_s and we assume that in a homogenous, isotropic, thermoelastic, incompressible membrane these quantities are related to the fields ρ_s, x^i, T_s, and δ by the equations

$$s^{\Delta\Gamma} = s^{\Delta\Gamma}\left(\rho_s, \delta, g_{\Lambda\Sigma}, G_{\Lambda\Sigma}, b_{\Lambda\Sigma}, B_{\Lambda\Sigma}, T_s, \frac{\partial T_s}{\partial U^\Lambda}\right),$$

$$\text{where } s^{\Delta\Gamma} = s^{\Gamma\Delta} \tag{15}_1$$

$$s^\Delta = 0, \tag{15}_2$$

$$q^\Delta_s = q^\Delta_s\left(\rho_s, \delta, g_{\Lambda\Sigma}, G_{\Lambda\Sigma}, b_{\Lambda\Sigma}, B_{\Lambda\Sigma}, T_s, \frac{\partial T_s}{\partial U^\Lambda}\right), \tag{15}_3$$

$$\epsilon_s = \epsilon_s\left(\rho_s, \delta, g_{\Lambda\Sigma}, G_{\Lambda\Sigma}, b_{\Lambda\Sigma}, B_{\Lambda\Sigma}, T_s, \frac{\partial T_s}{\partial U^\Lambda}\right). \tag{15}_4$$

$S^\Delta = 0$ and the symmetry of $S^{\Delta\Gamma}$ are typical for a *membrane* theory and they distinguish this theory from a *shell* theory. The metric tensors $g_{\Lambda\Sigma}$ and $G_{\Lambda\Sigma}$ together form a measure for the deformation of the membrane from its reference configuration.

The second group of constitutive equations consists of $p^\pm$ and $q^{i\pm}$. These quantities may depend on the same variables that occur in (15) and, in addition, on the variables that determine the state of the fluid on side + or −, respectively, of the surface.

Insertion of the constitutive equations into the equations of balance leads to a set of six field equations for the six fields ρ_s, x^i, T_s, and δ. A solution of these field equations is called a *thermodynamic process*.

However, the explicit form of the constitutive equations is not known and we rely upon the entropy principle to introduce restrictions on the generality of the constitutive functions.

(d) Entropy Principle and Its Consequences. The entropy principle used here is an adaption to two-dimensional surfaces of the one proposed by Müller [9] for bulk bodies. It reads

(i) The entropy of a membrane—represented as before by a two-dimensional surface—is an additive quantity so that it obeys an equation of balance

$$\rho_s\frac{\partial\eta_s}{\partial t} + \phi^\Delta_{s;\Delta} + [\phi^j\nu^j] = \sigma_s. \tag{16}$$

(ii) The specific entropy η_s and the surface flux ϕ^Δ_s of the entropy are constitutive quantities. In particular we assume that η_s is given by

$$\eta_s = \eta_s\left(\rho_s, \delta, g_{\Delta\Gamma}, G_{\Delta\Gamma}, b_{\Delta\Gamma}, B_{\Delta\Gamma}, T_s, \frac{\partial T_s}{\partial U^\Delta}\right) \tag{17}$$

in a thermoelastic membrane of the type considered here. ϕ^Δ_s is taken to be equal to the heat flux q^Δ_s divided by temperature

$$\phi^\Delta_s = q^\Delta_s/T_s. \tag{18}$$[4]

The entropy flux ϕ^j of the fluids on either side of the membrane is given by (see [9])

$$\phi^j = q^j/T, \tag{19}$$

where T is the absolute temperature of those fluids.

(iii) The production density σ_s of the entropy is non-negative for each thermodynamic process

$$\rho_s\frac{\partial\eta_s}{\partial t} + \phi^\Delta_{s;\Delta} + [\phi^j\nu^j] \geqq 0. \tag{20}$$

Insertion of (17) and (18) with $(15)_3$ into this inequality leads to an expression on its lefthand side that is linear in the derivatives

$$\frac{\partial\rho_s}{\partial t}, \frac{\partial\delta}{\partial t}, \frac{\partial\rho_s}{\partial U^\Gamma}, \frac{\partial\delta}{\partial U^\Gamma}, \frac{\partial^2x^i}{\partial U^\Gamma\partial U^\Delta}\tau^i_\Sigma, \frac{\partial v^i_s}{\partial t}, \frac{\partial V^\Gamma}{\partial U^\Delta}, \frac{\partial V_\nu}{\partial U^\Delta},$$
$$\frac{\partial^2V_\nu}{\partial U^\Delta\partial U^\Gamma}, \frac{\partial T_s}{\partial t}, \frac{\partial^2T_s}{\partial t\partial U^\Gamma}, \frac{\partial^2T_s}{\partial U^\Gamma\partial U^\Delta}, \frac{\partial^3x^i}{\partial U^\Gamma\partial U^\Delta\partial U^\Sigma}. \tag{21}$$

But several of these derivatives are constrained by the field equations (10)–(13) and we rely on the method of Lagrange multipliers to take care of those constraints. This method was introduced by Liu [10] and according to him we may replace the entropy inequality (20) by the new inequality

$$\rho_s\frac{\partial\eta_s}{\partial t} + \phi^\Delta_{s;\Delta} + [\phi^j\nu^j] - \Lambda^{\rho_s}\left(\frac{\partial\rho_s}{\partial t} + (V^\Gamma_{;\Gamma} - 2k_MV_\nu)\rho_s\right)$$
$$- \Lambda^{v^i_s}\left(\rho_s\frac{\partial v^i_s}{\partial t} - t^{i\Delta}_{s;\Delta} - [-p\nu^i]\right)$$
$$- \Lambda^{\epsilon_s}\left(\rho_s\frac{\partial\epsilon_s}{\partial t} + q^\Delta_{s;\Delta} + [q^j\nu^j] - \frac{1}{2}\frac{\partial g_{\Delta\Gamma}}{\partial t}S^{\Delta\Gamma} - S^\Delta\left(b_{\Delta\Gamma}V^\Gamma + \frac{\partial V_\nu}{\partial U^\Delta}\right)\right)$$
$$- \Lambda^\delta\left(\frac{\partial\delta}{\partial t} + (V^\Gamma_{;\Gamma} - 2k_MV_\nu)\delta\right) \geqq 0 \tag{22}$$

[4] It is possible to derive (18) from the assumption that ϕ^Δ_s is a constitutive quantity of the same type as $(15)_3$ provided that ϕ^Δ_s and q^Δ_s are linear functions of $T_{s,\Delta}$. For brevity we anticipate that result by assuming (18).

and require that this new inequality be satisfied for all analytic fields of

$$\rho_s(U^\Gamma, t), x^j(U^\Gamma, t), T_s(U^\Gamma, t), \delta(U^\Gamma, t).$$

The newly introduced quantities Λ^{ρ_s}, $\Lambda^{v_s^i}$, Λ^{ϵ_s}, and Λ^δ are called Lagrange multipliers by Liu and they may depend on all variables in the constitutive relations and on v_s^i.

The exploitation of this inequality is cumbersome but it follows the, by now, standard procedure. Some of the results may be used to identify the Lagrange multipliers:

$$\Lambda^{\rho_s} = \rho_s\left(\frac{\partial \eta_s}{\partial \rho_s} - \Lambda^{\epsilon_s}\frac{\partial \epsilon_s}{\partial \rho_s}\right), \quad \Lambda^{v_s^i} = 0, \quad \Lambda^{\epsilon_s} = \frac{1}{T_s}$$

$$\Lambda^\delta = \rho_s\left(\frac{\partial \eta_s}{\partial \delta} - \Lambda^{\epsilon_s}\frac{\partial \epsilon_s}{\partial \delta}\right). \tag{23}$$

After some calculation one concludes that η_s and ϵ_s are independent of $\partial T_s/\partial U^\Delta$ and the curvature tensor $b_{\Delta\Gamma}$ and that the derivatives of η_s and ϵ_s with respect to ρ_s, $g_{\Delta\Gamma}$, T_s, and δ are related by the equations

$$\frac{\partial \epsilon_s - T_s\eta_s}{\partial T_s} = -\eta_s, \quad -\left(\rho_s^2\frac{\partial \epsilon_s - T_s\eta_s}{\partial \rho_s} + \rho_s\delta\frac{\partial \epsilon_s - T_s\eta_s}{\partial \delta}\right)g^{\Delta\Gamma} + 2\rho_s\frac{\partial \epsilon_s - T_s\eta_s}{\partial g_{\Delta\Gamma}} = S^{\Delta\Gamma} \tag{24}$$

So far constraints on the derivatives $\partial\rho_s/\partial t$, $\partial\delta/\partial t$, $\partial g_{\Delta\Gamma}/\partial t$ have been taken into account by use of Lagrange multipliers. But the field equations (10) and (13) upon integration imply constraints on ρ_s, δ, and $g_{\Delta\Gamma}$ themselves, namely,

$$\rho_s = \rho_s^{\kappa 0}\sqrt{\frac{G}{g}}, \quad \delta = \delta^{\kappa 0}\sqrt{\frac{G}{g}}, \tag{25}$$

where G is the determinant of $G_{\Delta\Gamma}$. The identity (14) was used to derive (25). Thus it is possible to replace ϵ_s, $(\rho_s, \delta, g_{\Delta\Gamma}, T_s, G_{\Delta\Gamma}, B_{\Delta\Gamma})$ and $\eta_s(\rho_s, \delta, g_{\Delta\Gamma}, T_s, G_{\Delta\Gamma}, B_{\Delta\Gamma})$ by functions $\hat{\epsilon}_s$ and $\hat{\eta}_s$ of $g_{\Delta\Gamma}$, T_s, $G_{\Delta\Gamma}$, $B_{\Delta\Gamma}$ only and the relations (24) may thus be shortened to

$$\frac{\partial \hat{\epsilon}_s - T_s\hat{\eta}_s}{\partial T_s} = -\hat{\eta}_s, \quad 2\rho_s\frac{\partial \hat{\epsilon}_s - T_s\hat{\eta}_s}{\partial g_{\Delta\Gamma}} = S^{\Delta\Gamma}. \tag{26}$$

These two equations imply an integrability condition for $\hat{\epsilon}_s - T_s\hat{\eta}_s$, viz.,

$$\frac{\partial \hat{\epsilon}_s}{\partial g_{\Delta\Gamma}} = \frac{1}{2\rho_s}\left(S^{\Delta\Gamma} - T_s\frac{\partial S^{\Delta\Gamma}}{\partial T_s}\right). \tag{27}$$

As was mentioned in the Introduction as a basic observation with rubber, the stress of rubber is proportional to the temperature T_s. Therefore we conclude from (27) that the internal energy of rubber is independent of deformation. This is a most remarkable property of rubber, because it implies that the stress is determined by the specific entropy alone rather than by the specific values of both entropy and internal energy.

Indeed, by $(26)_2$ we have

$$S^{\Delta\Gamma} = -2\rho_s^{\kappa 0}T_s\sqrt{\frac{G}{g}}\frac{\partial \hat{\eta}_s}{\partial g_{\Delta\Gamma}}. \tag{28}$$

This formula forms the basis for the further development of the theory in the next chapter.

For future reference, I emphasize that, while the entropy principle forbids the dependence of η_s on $b_{\Delta\Gamma}$ it may still depend on the curvature tensor $B_{\Delta\Gamma}$ in the *reference* configuration. Thus $S^{\Delta\Gamma}$ may depend on $B_{\Delta\Gamma}$ as well.

3 Kinetic Theory of Rubber Membranes

(a) Scope of This Chapter. The objective of this chapter is the calculation of the stress-deformation relation in a rubber membrane. This goal can be reached by the calculation of the specific entropy η_s from a kinetic theory, because, by (28) the knowledge of η_s implies the knowledge of $S^{\Delta\Gamma}$.

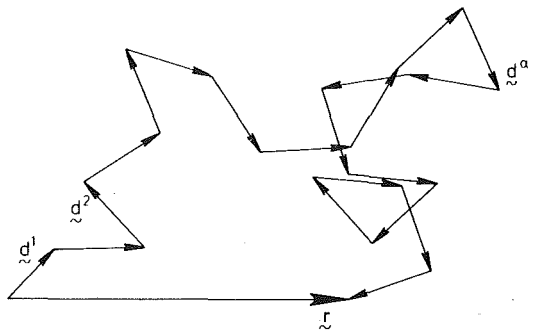

Fig. 2

The basis for the calculation of η_s is the idea—proposed by Kuhn [3] and reviewed by Treloar [11]—that a rubber molecule forms a long entangled chain whose links are randomly oriented. The entropy of such a chain will be determined first.

The membrane particle in this model is represented by a network of such chains. The entropy of a particle results by the summation of the entropies of its chains.

(b) Entropy of a Single Rubber Molecule. The individual links of the chain, which represent the rubber molecule in Kuhn's model, can be oriented randomly as shown schematically in Fig. 2. The macrostate of this chain may be given by the euclidean distance r of its ends and a typical microstate is given by assigning a direction vector $\mathbf{d}^\alpha$ $(\alpha = 1, 2, \ldots, N)$ to each link.

When $N_\mathbf{d}$ is the number of links pointing in the direction $\mathbf{d}$, the number of possibilities to realize a macrostate $\mathbf{r}$ is given by

$$R = \frac{N!}{\prod_\mathbf{d} N_d!}, \quad \text{where} \quad \sum_\mathbf{d} N_\mathbf{d} = N \quad \text{and} \quad \sum_\mathbf{d} \mathbf{d}b = \mathbf{r}. \tag{29}$$

b is the length of one link. This number R determines the equilibrium entropy by Boltzmann's formula

$$H = k \ln R, \tag{30}$$

where k is the Boltzmann constant.

The entropy turns out to be fairly insensitive to different assumptions about the possible direction which might be assumed by the individual links of the chain. Indeed, in a strongly entangled chain with the four different choices

(i) $\mathbf{d} = (\pm\mathbf{e}_1)$

(ii) $\mathbf{d} = (\pm\mathbf{e}_1, \pm\mathbf{e}_2)$,

(iii) $\mathbf{d} = d_1\mathbf{e}_1 + d_2\mathbf{e}_2$,

(iv) $\mathbf{d} = d_1\mathbf{e}_1 + d_2\mathbf{e}_2 + d_3\mathbf{e}_3$,

where $\mathbf{e}_j$ is an orthonormal base, lead to similar entropies namely,

$$H_{(\beta)} = k\left(N\ln a_\beta - b_\beta\frac{r^2}{Nb^2}\right). \quad (\beta = i), ii), iii), iv)) \tag{31}$$

In particular the dependence of H on r and N is the same in all four cases and the coefficients b_β are all of the order of magnitude 1, while a_β is an unimportant constant.

(c) Entropy of a Membrane Particle. (α) *Tangential and Normal Chains.* A membrane particle must be visualized as a network of rubber molecules. Let there be n such chains in a particle. When the idea of the membrane as a two-dimensional surface is taken seriously, all parts of the network have to lie on that surface. In Section (β) we shall indeed exploit that idea and calculate the entropy which is contributed by such tangential chains.

However, just like in thermodynamics of membranes we have to account for the incompressibility of the rubber and this will make it necessary to attribute a thickness to the membrane. In the model this thickness is taken into consideration by allowing parts of the chains

to lie in the direction normal to the membrane. The contributions of these normal chains to the entropy of the particle is calculated in Section γ.

(β) *The Entropy of a Particle Due to Tangential Chains.* If N_τ is the number of the links of a chain which are constrained to lie on a line of the two-dimensional surface, it can be shown that the entropy of the chain is given by

$$H_\tau(\lambda, N_\tau) = k\left(N_\tau \ln 2 - \frac{\lambda^2}{2N_\tau b^2}\right). \tag{32}^5$$

λ is the length of the chain along the line, rather than the euclidean distance of the ends.

If the chain is free to choose between different lines connecting the ends along the surface, it will choose the geodesic, because this makes H_τ a maximum.

Four assumptions precede the calculation of the entropy of a network of tangential chains:

(*i*) All n chains of one particle have the same number of links. Thus the entropy $\mathcal{H}_\tau$ of the particle reads

$$\mathcal{H}_\tau = \sum_{i=1}^{n} H_\tau(\lambda^i, N_\tau^i) = \sum_{i=1}^{n} H_\tau(\lambda^i) = \sum_{\lambda} H_\tau(\lambda) Z(\lambda), \tag{33}$$

where $Z(\lambda)$ is the number of chains with the length λ.

(*ii*) In the reference configuration κ_0 the number $Z(L)$ is proportional to the number of possibilities $R = e^{1/k\, H_\tau}$ to realize the length L:

$$Z_{\kappa_0}(L) = Ce^{1/k\, H_\tau(L)}. \tag{34}^6$$

It follows that

$$Z_{\kappa_t}(\ell) = Z_{\kappa_0}(L) \tag{35}$$

holds, because the number of chains does not change in the deformation.

(*iii*) The deformation of the end to end distance of the chains is affine to the membrane particle.

(*iv*) For the calculation of the entropy of the tangential chains it is useful to imagine that one end of each of the n chains in a membrane particle with coordinates U^Γ lies in a central point P. The other end lies at Θ^1, Θ^2 in the reference configuration κ_0 and at ϑ^1, ϑ^2 in the deformed configuration κ_t where Θ^Γ and ϑ^Γ are geodesic coordinates within the particle with the origin at P.[7] This means that the chains are situated on certain lines Θ^Γ = constant and ϑ^Γ = constant. For simplicity we choose the Θ^Γ's as polar geodesic coordinates such that in κ_0 the chain lies along a line θ^2 = constant and L is equal to θ^1.

We assume that the number of end points between Θ^Γ and $\theta^\Gamma + d\Theta^\Gamma$ in κ_0 is proportional to the element of area $\sqrt{G}\, d\Theta^1 d\Theta^2$. A corresponding assumption applies to $\kappa_t(\Theta)$ and thus we have

$$Z_{\kappa_0}(L) = z_{\kappa_0}(L) \underset{(\Theta)}{\sqrt{G}}\, d\Theta^1 d\Theta^2 \text{ and } Z_{\kappa_t}(\ell) = z_{\kappa_t}(\ell) \underset{(\vartheta)}{\sqrt{g}} d\vartheta^1 d\vartheta^2; \tag{36}$$

$G_{\Delta\Gamma}$ and $g_{\Delta\Gamma}$ are the metric tensors of the parameters nets Θ^Γ and ϑ^Γ.

Therefore, by (33), the entropy of a particle in the deformed configuration reads

$$\mathcal{H}_\tau^{\kappa_t} = \int H_\tau(\ell) z_{\kappa_t}(\ell) \underset{(\vartheta)}{\sqrt{g}} d\vartheta^1 d\vartheta^2, \tag{37}$$

where $\ell = \underset{(\vartheta)}{\sqrt{g_{\Delta\Gamma}\vartheta^\Delta \vartheta^\Gamma}}$. By assumption (*iv*) we may write (35) with (34) as

$$z_{\kappa_t}(\ell) \underset{(\vartheta)}{\sqrt{g}}\, d\vartheta^1 d\vartheta^2 = C\, e^{1/kH_\tau(L)} \underset{(\Theta)}{\sqrt{G}}\, d\Theta^1 d\Theta^2 \tag{38}$$

and C has the value

$$C = \frac{n}{\int_{(\Theta)} e^{1/kH_\tau(L)} \sqrt{G}\, d\Theta^1 d\Theta^2}, \tag{39}$$

because the total number of chains in the particle is n. Thus we have

$$\mathcal{H}_\tau^{\kappa_t} = n \frac{\int_{(\Theta)} H_\tau(\ell) e^{1/kH_\tau(L)} \sqrt{G}\, d\Theta^1 d\Theta^2}{\int_{(\Theta)} e^{1/kH_\tau(L)} \sqrt{G}\, d\Theta^1 d\Theta^2}; \tag{40}$$

ℓ is related to L by assumption (*iii*) in a complex manner which is specified in [12]. Furthermore $G_{\Delta\Gamma}$ is related to $G_{\Delta\Gamma}$ and its first two derivatives by the equation

$$\underset{(\Theta)}{G_{\Delta\Gamma}} = \begin{pmatrix} 1 & 0 \\ 0 & (\Theta^1)^2 - \tfrac{1}{3}\, K_G (\Theta^1)^4 \end{pmatrix}_{\Delta\Gamma} \tag{41}$$

where K_G is the Gaussian curvature of the membrane particle U^Γ in κ_0.

Integration of (40) leads to the following expression for the entropy of the tangential chains of the particle U^Γ:

$$\mathcal{H}_\tau^{\kappa_t} = nk\{N_\tau \ln 2 - \tfrac{1}{2}\, g_{\Delta\Gamma} G^{\Delta\Gamma}(1 - \tfrac{1}{6}\, N_\tau b^2 K_G)\} \tag{42}$$

and we conclude that the entropy of the particle U^Γ depends on the values of $g_{\Delta\Gamma}(U^\Sigma)$ and $G_{\Delta\Gamma}(U^\Sigma)$ *and* on the second derivatives of $G_{\Delta\Gamma}(U^\Sigma)$ as represented by K_G.

(γ) *The Entropy of a Particle Due to Normal Chains.* To account for the thickness we assume a part of each chain to be normal to the membrane. The number of normal links is denoted by N_ν. The entropy of a normal chain is, according to Section (α),

$$H_\nu^{\kappa_t}(r_{\kappa_t}, N_\nu) = k\left(N_\nu \ln 2 - \frac{r_{\kappa_t}^2}{2N_\nu b^2}\right), \tag{43}$$

where $\mathbf{r}_{\kappa_t}$ is the distance vector of the ends of the chain which is parallel to the normal $\boldsymbol{\nu}$ of the membrane particle.

Just like for the tangential chain we assume affine deformation of the chain length and the membrane thickness, such that

$$r_{\kappa_t} = \frac{\delta}{\delta_{\kappa_0}} r_{\kappa_0}, \tag{44}$$

where δ is the thickness parameter introduced in $(8)_4$.

In addition we assume—again like for the tangential chains—that in the reference configuration κ_0 the number of chains with the length r_{κ_0} is proportional to the number of ways to realize this distance. Therefore the mean value of $r_{\kappa_0}^2$ is

$$\overline{r_{\kappa_0}^2} = N_\nu b^2 \tag{45}$$

and, by (43) and (44), the mean value of $H_\nu^{\kappa_t}$ is

$$\overline{H_\nu^{\kappa_t}} = k\left(n_\nu \ln 2 - \frac{1}{2}\left(\frac{\delta}{\delta_{\kappa_0}}\right)^2\right). \tag{46}$$

By $(25)_2$ we obtain

$$\overline{H_\nu^{\kappa_t}} = k\left(N_\nu \ln 2 - \frac{1}{2}\frac{G}{g}\right) \tag{47}$$

and, since the membrane particle contains n chains, the entropy of the normal chains of the particle is given by

$$\mathcal{H}_\nu^{\kappa_t} = n\,\overline{H_\nu^{\kappa_t}} = nk\left(N_\nu \ln 2 - \frac{1}{2}\frac{G}{g}\right). \tag{48}$$

(δ) *Entropy of a Membrane Particle.* The entropy of the membrane particle in the deformed configuration is the sum of $\mathcal{H}_\tau^{\kappa_t}$ and $\mathcal{H}_\nu^{\kappa_t}$ derived in the foregoing. If M denotes the mass of a chain we obtain the specific entropy of the membrane in the form

$$\eta_s = \frac{k}{M}\left(N \ln 2 - \tfrac{1}{2}\, g_{\Delta\Gamma} G^{\Delta\Gamma}(1 - \tfrac{1}{6}\, N_\tau b^2 K_G) - \tfrac{1}{2}\frac{G}{g}\right). \tag{49}$$

---

[5] This case corresponds to choice (*i*) in the Section (*b*). Proof of the formula (32) can be found in [12].

[6] The geodesic length λ will be denoted by L in the reference configuration κ_0 and by ℓ in the present configuration κ_t.

[7] Thus the particle U^Γ is put under a magnifying glass and its different points are labeled by Θ^Γ and ϑ^Γ, respectively, in κ_0 and κ_t.

We conclude that this result is consistent with the thermodynamic result according to which η_s is independent of the curvature tensor $b_{\Delta\Gamma}$ in the present configuration κ_t. In the contrary, thermodynamics allows a dependence of η_s on the curvature tensor $B_{\Delta\Gamma}$ in the reference configuration κ_0 and this dependence is indeed realized by the kinetic theory, because η_s in (49) depends on K_G. However, the dependence on K_G is weak indeed, because $N_\tau b^2 K_G \ll 1$ under all realistic circumstances. We are then left with the formula

$$\eta_s = \frac{k}{M}\left(N \ln 2 - \tfrac{1}{2}\left(g_{\Delta\Gamma}G^{\Delta\Gamma} + \frac{G}{g}\right)\right). \tag{50}$$

It is easy to confirm that

$$\eta_s^{\kappa_t} - \eta_s^{\kappa_0} < 0, \tag{51}$$

so that the reference configuration has the biggest entropy.

(d) Surface Stress of a Membrane Particle. Insertion of η_s from (50) into the thermodynamic relation (20) for the surface stress leads to

$$S^{\Delta\Gamma} = \frac{\rho_s^{\kappa_0} k T_s}{M}\sqrt{\frac{G}{g}}\left(G^{\Delta\Gamma} - \frac{G}{g}g^{\Delta\Gamma}\right). \tag{52}$$

Experiments with spherical membranes show that this formula is valid for deformations up to 250 percent.[8] This restriction of the range of validity is due to the assumptions which have led to (50). In particular at large deformations the assumption of a strong entanglement of the chains is no longer valid.

The formula (52) shows that the temperature dependence of $S^{\Delta\Gamma}$ is linear as it must be according to observations related in the Introduction.

It remains to be shown that the aforementioned expression for $S^{\Delta\Gamma}$ is compatible with the observations reported in Fig. 1. To this end we consider the case of a spherical membrane which is deformed by an increase of the radius. In this case

$$g_{\Delta\Gamma} = \begin{pmatrix} r^2 & 0 \\ 0 & r^2\sin^2\Theta \end{pmatrix}_{\Delta\Gamma}, \quad G_{\Delta\Gamma} = \begin{pmatrix} R^2 & 0 \\ 0 & R^2\sin^2\Theta \end{pmatrix}_{\Delta\Gamma},$$

$$b_{\Delta\Gamma} = \begin{pmatrix} r & 0 \\ 0 & r\sin^2\Theta \end{pmatrix}_{\Delta\Gamma} \tag{53}$$

holds, so that

$$\eta_s = \frac{k}{M}\left(N \ln 2 - \frac{r^2}{R^2} - \frac{1}{2}\frac{R^4}{r^4}\right), \tag{54}$$

$$S^{\Delta\Gamma} = \frac{\rho_s^{\kappa_0} k T_s}{M}\frac{1}{r^2}\begin{pmatrix} 1 - \dfrac{R^6}{r^6} & 0 \\ 0 & \left(1 - \dfrac{R^6}{r^6}\right)\dfrac{1}{\sin^2\Theta} \end{pmatrix}^{\Delta\Gamma} \tag{55}$$

The equation of balance of momentum in equilibrium is expressed by the two equations

$$S^{\Delta\Gamma}_{;\Gamma} = 0 \quad \text{and} \quad [p] = S^{\Delta\Gamma}b_{\Delta\Gamma} \tag{56}$$

and insertion of (55) shows that $(56)_1$ is identically satisfied while $[p]$ is given by

$$[p] = 2\frac{\rho_s^{\kappa_0} k T_s}{M}\frac{1}{r}\left(1 - \left(\frac{R}{r}\right)^6\right). \tag{57}$$

This function can be compared directly with the curves of Fig. 1 and it turns out that (57) with an appropriate factor coincides with the dashed curve of Fig. 1. This curve is confirmed by experiments up to $r/R \approx 2{,}5$ which is the range where we expect this theory to hold).[9]

If one follows the derivation of the expression (57) for $[p]$ closely, one finds that the summand $(R/r)^6$ in (57) results from the contribution of the normal chains. It is thus seen that the contribution of the normal chains dominates the behavior of the membrane at small deformations. In particular, this term guarantees the existence of a configuration for which $[p] = 0$ and $S^{\Delta\Gamma} = 0$ this is the configuration where $r = R$. The effect of the tangential chains dominates the behavior of the membrane at large deformations to the right of the maximum in Fig. 1.

In the stress-free configuration $r = R$ the entropy (54) has a maximum. Here again we conclude that the contribution of the normal chains is most important. Indeed, if it were absent, the maximum of the entropy would occur at $r = 0$ and the membrane would therefore contract to a point.

Acknowledgment

I am indebted to Prof. I. Müller for most valuable discussions and help with the English wording.

References

1 Kubo, R., "Large Elastic Deformation of Rubber," *Journal of The Physical Society of Japan,* Vol. 3, 1948, pp. 312–315.

2 Adkins, J. E., and Rivlin, R. S., "Large Elastic Deformations of Isotropic Materials," *Philosophical Transactions of the Royal Society,* London, Series A, Vol. 244, 1951, pp. 505–531.

3 Kuhn, W., "Beziehungen zwischen Molekülgröße, statistischer Molekülgestalt und elastischer Eigenschaften hochpolymerer Stoffe," *Kolloid Zeitschrift,* Band 76, 1936, pp. 258–271.

4 Wang, C.-C., and Cross, J. J., "Universal Solutions for Isotropic Elastic Membranes," *Archive for Rational Mechanics and Analysis,* Vol. 65, 1977, pp. 73–86.

5 Wang, C.-C., and Cross, J. J., "On the Field Equations of Motion for a Smooth Materially Uniform, Elastic Shell," *Archive for Rational Mechanics and Analysis,* Vol. 65, 1977, pp. 57–72.

6 Green, A. E., and Naghdi, P. M., and Wainwright, W. L., "A General Theory of a Cosserat Surface," *Archive for Rational Mechanics and Analysis,* Vol. 20, 1965, pp. 287–308.

7 Aris, R., *Vectors, Tensors, and the Basic Equations of Fluid Mechanics,* Prentice-Hall, Englewood Cliffs, N. J., 1962.

8 Truesdall, C., and Toupin, R., *Handbuch der Physik,* Vol. III/1, 1960, p. 500.

9 Müller, I., *Thermodynamik,* Bertelsmann Universitätsverlag, Germany 1973.

10. Liu, I-Shi, "Method of Lagrange Multipliers for Exploitation of the Entropy Inequality," *Archive for Rational Mechanics and Analysis,* Vol. 46, 1072, pp. 131–148.

11 Treloar, L. R. G., *The Physics of Rubber Elasticity,* Clarendon Press, Oxford, Great Britain, 1975.

12 Dreyer, W., "Zur Thermodynamik und Kinetischen Theorie von Gummimembranen," *Diplomwork,* Paderborn, Germany, 1979.

13 Treloar, L. R. G., "Strains in an Inflated Rubber Sheet, and the Mechanism of Bursting," *Transactions of the Institute of Rubber Industries,* Vol. 19, 1944, pp. 201–212.

[8] e.g., see [13].

[9] A material for which (57) holds is often called ideal rubber.

M. Kurashige

Assistant Professor,
Department of Mechanical Engineering II,
Faculty of Engineering,
Tohoku University,
Sendai 980, Japan

Instability of a Transversely Isotropic Elastic Slab Subjected to Axial Loads

After obtaining the relations between incremental stresses and incremental strains, we analyzed the instability problem stated in the title on the basis of Biot's mechanics of incremental deformations. The slab, made of a hypothetical transversely isotropic compressible elastic material, is assumed to be stronger in its transverse direction than in its axial direction. The analysis shows that, no matter what the anisotropy strength of the slab is or its thickness is, it can become unstable under tension as well as under compression. The critical load is higher for the stronger anisotropy in the compressive case, while it is lower for the stronger anisotropy in the tensile case. In other words, the reinforcement in the "wrong" direction weakens the slab under tension with respect to its stability. Furthermore, the weakly anisotropic slab can become unstable only after the axial resultant force reaches its maximum, while the strongly anisotropic slab can lose its stability before the force reaches its maximum.

1 Introduction

By "instability" of an elastic body we understand here a situation when for certain prescribed boundary loads there exist several adjacent states of displacement that are in equilibrium with these loads. The smallest load (stress) at which this state is possible is called the "critical" load.

There are many papers concerning instability problems, even if we direct our attention to an elastic slab or a thick plate or a rectangular block under axial loads. Most of these papers considered a slab made of a general or special incompressible isotropic material [1–6]; the special one is of the neo-Hookean or Mooney-Rivlin type. Unlike these, Southwell [7] and Kerr [8] treated the case in which the stresses and strains, whatever their magnitude, are connected by Hooke's law, and Hill and Hutchinson [9], and Young [10] considered a wide class of materials that is initially isotropic or orthotropic with respect to the geometric axes, incompressible, and incrementally linear. The compressible isotropic case was investigated by Burgess and Levinson [11]. Furthermore, the author [12] examined the instability of a slab of a compressible isotropic elastic material reinforced by inextensible completely flexible fibers.

Wesolowski [1] paid special attention to the instability of a slab subjected to a tensile axial load, and found that instability would arise only after the applied force reaches its maximum. This conclusion was also reached by Hill and Hutchinson [9]. In contrast to their conclusion, it follows from [12], though not explicitly stated, that the fiber-reinforced slab under tension loses its stability though the tensile resultant force has no maximum.

Here we thus examine the instability of a transversely isotropic compressible elastic slab subjected to uniform axial loads. The slab is assumed to be stronger in its transverse direction than in its axial direction, and to be in a plane strain state both prior to and after becoming unstable.

In the next section, we first obtain the relations between incremental stresses and incremental strains by taking the material time derivative of the stress-deformation equations of transversely isotropic, compressible, elastic solids. The incremental stresses are defined as the product of the time increment and the objective corotational stress rate, so that they are identical with those in Biot's mechanics of incremental deformations [13].

A special form of the strain-energy function for a transversely isotropic, compressible, elastic material is proposed in Section 3. The stress-deformation relations resulting from the proposed form of the strain-energy function contain the following two special cases: those of the isotropic Blatz-Ko foam rubber [15] and the idealized fiber-reinforced Blatz-Ko foam rubber [12].

Next, using the derived incremental stress-incremental strain relations and the proposed form of the strain-energy function, we solved the aforementioned instability problem on the basis of Biot's mechanics of incremental deformations [13]; the equilibrium equations for incremental stresses are regarded as equations of neutral equilibrium for examining the stability of the finite, uniform, axial extension or contraction of the slab. The buckling condition comes about in consequence of the fact that there must exist nontrivial solutions for the infinitesimal deformations superposed upon the uniform extension or contraction.

Some numerical results in the last section show that the

Contributed by the Applied Mechanics Division for publication in the JOURNAL OF APPLIED MECHANICS.

Discussion on this paper should be addressed to the Editorial Department, ASME, United Engineering Center, 345 East 47th Street, New York, N. Y. 10017, and will be accepted until September 1, 1981. Readers who need more time to prepare a Discussion should request an extension from the Editorial Department. Manuscript received by ASME Applied Mechanics Division, March, 1980; final revision, July, 1980.

transversely isotropic, elastic slab under compression, including the isotropic case, becomes unstable at a certain critical load for all wavelength-to-thickness ratios l/h. The critical load decreases for the larger ratios. On the other hand, when the load is tensile, the slab becomes unstable for all wavelength-to-thickness ratios l/h and for all anisotropy strength parameters k. The critical load decreases and is asymptotic to that of the idealized fiber-reinforced slab according to the increase in the anisotropy strength; in other words, the fiber-reinforcement in the transverse or wrong direction weakens the slab under tensile load with respect to its stability. Furthermore, the critical load does not depend on the wavelength-to-thickness ratios for the anisotropy strength parameter $k > k_0 \simeq 0.86$, but does depend on these ratios for the anisotropy parameter $k < k_0$. Finally, for the anisotropy parameter $k < k_0$ including the isotropic case $k = 0$, the slab under tension loses its stability after the axial resultant force reaches its maximum, while for the parameter $k > k_0$, the slab under tension becomes unstable before the resultant force reaches its maximum.

2 Incremental Stress-Incremental Strain Relations

Let $\mathbf{x}$ and $\mathbf{x}$ be the positions occupied by a material point X in a fixed reference configuration and in the present configuration, respectively. Identify the position $\mathbf{x}$ with the deformation function, and the particle velocity $\mathbf{v}$ is given by $\mathbf{v} = d\mathbf{x}/dt$. The deformation gradient $\mathbf{F}$ and the velocity gradient $\mathbf{L}$ are defined as

$$\mathbf{F} = \partial \mathbf{x}/\partial \mathbf{X}, \quad \mathbf{L} = \partial \mathbf{v}/\partial \mathbf{x}, \tag{1}$$

between which there is the relation

$$\mathbf{L} = \dot{\mathbf{F}}\,\mathbf{F}^{-1}. \tag{2}$$

In terms of these gradients, we may express the right and left Cauchy-Green deformation tensors, $\mathbf{C}$ and $\mathbf{B}$, the deformation rate tensor $\mathbf{D}$, and the spin tensor $\mathbf{W}$ as

$$\begin{aligned} &\mathbf{C} = \mathbf{F}^T\mathbf{F}, \qquad &&\mathbf{B} = \mathbf{F}\mathbf{F}^T, \\ &\mathbf{D} = (\mathbf{L} + \mathbf{L}^T)/2, \quad &&\mathbf{W} = (\mathbf{L} - \mathbf{L}^T)/2. \end{aligned} \tag{3}$$

In the foregoing equations and also in what follows, $(\dot{\ })$ denotes the material time derivative, $(\ )^T$ and $(\ )^{-1}$ the transpose and the inverse of the tensor, respectively.

Further, let $\mathbf{H}_a$ denote three mutually orthogonal unit vectors in the reference configuration. Analytically,

$$\partial \mathbf{H}_a/\partial t = \mathbf{o}, \quad \partial \mathbf{H}_a/\partial \mathbf{X} = \mathbf{o}, \quad \text{tr}\,(\mathbf{H}_a \otimes \mathbf{H}_b) = \delta_{ab}, \tag{4}$$

where tr $(\ )$ denotes the trace and $(\ )\otimes(\ )$ the tensor product. The symbol δ_{ab} is the Kronecker delta. The indices a and b take on the values 1, 2, 3. The deformation carries the vectors $\mathbf{H}_a$ into the vectors

$$\mathbf{h}_a = \mathbf{F}\mathbf{H}_a, \tag{5}$$

in terms of which the six scalars are defined as

$$\Gamma_{ab} = \text{tr}\,(\mathbf{h}_a \otimes \mathbf{h}_b). \tag{6}$$

If the transversely isotropic material considered here has a strain-energy function, the function W should depend on the deformations only through the five invariants of $\mathbf{C}$

$$\begin{aligned} &\text{I} = \text{tr}\,\mathbf{C}, \quad \text{II} = \tfrac{1}{2}\{(\text{tr}\,\mathbf{C})^2 - \text{tr}\,\mathbf{C}^2\}, \quad \text{III} = \det \mathbf{C}, \\ &\text{IV} = \Gamma_{cc}, \quad V = \Gamma_{ca}\Gamma_{ca}, \quad \text{(no sum on } c) \end{aligned} \tag{7}$$

under rotations about the preferred direction $\mathbf{H}_c$ [14]; that is,

$$W = W(\text{I, II, III, IV, V}). \tag{8}$$

In equations (7) and in what follows, the double suffix notation for summation is applied to the indices but not to the index c. The stress-deformation relations for the transversely isotropic, compressible, elastic material are given by [14] as

$$\mathbf{T} = \Phi_0\mathbf{I} + \Phi_1\mathbf{B} + \Phi_{-1}\mathbf{B}^{-1} + \Phi_2\mathbf{h}_c\otimes\mathbf{h}_c + \Phi_3(\mathbf{B}\mathbf{h}_c\otimes\mathbf{h}_c + \mathbf{h}_c\otimes\mathbf{B}\mathbf{h}_c), \tag{9}$$

where $\mathbf{T}$ is the Cauchy stress tensor, $\mathbf{I}$ the unit tensor, and the response coefficients $\Phi_k = \Phi_k(\text{I,II,III,IV,V})$, $(k = -1,0,1,2,3)$ are expressed in terms of the strain-energy function W as

$$\begin{aligned} &\Phi_0 = (2/\sqrt{\text{III}})(\text{II}\partial_{\text{II}}W + \text{III}\partial_{\text{III}}W), \quad \Phi_1 = (2/\sqrt{\text{III}})\partial_{\text{I}}W, \\ &\Phi_{-1} = -2\sqrt{\text{III}}\,\partial_{\text{II}}W, \quad \Phi_2 = (2/\sqrt{\text{III}})\partial_{\text{IV}}W, \quad \Phi_3 = (2/\sqrt{\text{III}})\partial_V W. \end{aligned} \tag{10}$$

Here and henceforth, ∂_{I}, ∂_{II}, etc., denote the partial differentiation with respect to the respective invariants. If the material is initially unstressed,

$$\partial_{\text{I}}W + 2\partial_{\text{II}}W + \partial_{\text{III}}W = 0, \quad \partial_{\text{IV}}W + 2\partial_V W = 0, \tag{11}$$

when $\text{I} - 3 = \text{II} - 3 = \text{III} - 1 = \text{IV} - 1 = \text{V} - 1 = 0$.

From equations (1)–(6), we can easily obtain the following formulas:

$$\begin{aligned} &\dot{\mathbf{B}} = (\mathbf{D}\mathbf{B} + \mathbf{B}\mathbf{D}) + (\mathbf{W}\mathbf{B} - \mathbf{B}\mathbf{W}), \quad \dot{\mathbf{C}} = 2\mathbf{F}^T\mathbf{D}\mathbf{F}, \\ &\dot{\mathbf{h}}_a = (\mathbf{D} + \mathbf{W})\mathbf{h}_a, \quad \dot{\Gamma}_{ab} = 2\,\text{tr}\,(\mathbf{D}\mathbf{h}_a\otimes\mathbf{h}_b), \end{aligned} \tag{12}$$

and we define the incremental stress tensor $\mathbf{s}$, the incremental strain tensor $\mathbf{e}$, and the incremental rotation tensor $\boldsymbol{\omega}$ as

$$\mathbf{s} = \dot{\mathbf{T}}\Delta t, \quad \mathbf{e} = \mathbf{D}\Delta t, \quad \boldsymbol{\omega} = \mathbf{W}\Delta t, \tag{13}$$

where Δt is a time increment and $\dot{\mathbf{T}} = \dot{\mathbf{T}} - \mathbf{W}\mathbf{T} + \mathbf{T}\mathbf{W}$ the objective corotational stress-rate tensor.

Differentiate the stress-deformation relations (9) with (10) and (8) with respect to time t and then use the formulas (12) and the definitions (13), and we are to obtain the relations between the incremental stresses and the incremental strains

$$\begin{aligned} \mathbf{s} = {} &\Phi_1(\mathbf{e}\mathbf{B} + \mathbf{B}\mathbf{e}) - \Phi_{-1}(\mathbf{e}\mathbf{B}^{-1} + \mathbf{B}^{-1}\mathbf{e}) + \Phi_2(\mathbf{e}\mathbf{h}_c\otimes\mathbf{h}_c + \mathbf{h}_c\otimes\mathbf{e}\mathbf{h}_c) \\ &+ \Phi_3\{(\mathbf{e}\mathbf{B} + 2\mathbf{B}\mathbf{e})\mathbf{h}_c\otimes\mathbf{h}_c + \mathbf{h}_c\otimes(\mathbf{e}\mathbf{B} + 2\mathbf{B}\mathbf{e})\mathbf{h}_c \\ &+ \mathbf{B}\mathbf{h}_c\otimes\mathbf{e}\mathbf{h}_c + \mathbf{e}\mathbf{h}_c\otimes\mathbf{B}\mathbf{h}_c\} + 2\,\text{tr}\,(\mathbf{e}\mathbf{B})\partial_{\text{I}}\mathbf{E} \\ &+ 2\{\text{II}\,\text{tr}\,\mathbf{e} - \text{III}\,\text{tr}\,(\mathbf{e}\mathbf{B}^{-1})\}\partial_{\text{II}}\mathbf{E} + 2\text{III}(\text{tr}\,\mathbf{e})\partial_{\text{III}}\mathbf{E} \\ &+ 2\,\text{tr}\,(\mathbf{e}\mathbf{h}_c\otimes\mathbf{h})\partial_{\text{IV}}\mathbf{E} + 2\,\text{tr}\,(\mathbf{B}\mathbf{h}_c\otimes\mathbf{e}\mathbf{h}_c + \mathbf{e}\mathbf{h}_c\otimes\mathbf{B}\mathbf{h}_c)\partial_V\mathbf{E}, \end{aligned} \tag{14}$$

where $\mathbf{E}(\text{I, II, III, IV, V})$ is given by

$$\mathbf{E} = \Phi_0\mathbf{I} + \Phi_1\mathbf{B} + \Phi_{-1}\mathbf{B}^{-1} + \Phi_2\mathbf{h}_c\otimes\mathbf{h}_c + \Phi_3(\mathbf{B}\mathbf{h}_c\otimes\mathbf{h}_c + \mathbf{h}_c\otimes\mathbf{B}\mathbf{h}_c). \tag{15}$$

3 A Special Form of the Strain-Energy Function

Blatz and Ko [15] proposed a particular form of the strain-energy function for an isotropic, compressible, elastic material, which they adopted in an attempt to characterize the experimental data obtained in tests on foam rubber. This particular form of the strain-energy function is, according to our notation,

$$W = \tfrac{1}{2}\mu\{(\text{II}/\text{III} - 3) + 2(\sqrt{\text{III}} - 1)\}, \tag{16}$$

where μ is a material constant. From this follows

$$\mathbf{T} = \mu\left(\mathbf{I} - \frac{1}{\sqrt{\text{III}}}\mathbf{B}^{-1}\right). \tag{17}$$

In the previous paper [12], the author considered, in connection with the instability problem, the reinforcement of this Blatz-Ko foam rubber by the inextensible, completely flexible fibers along the preferred direction. The stress-deformation relations for this idealized fiber-reinforced Blatz-Ko foam rubber are given, with the help of the theory of ideal fiber-reinforced composites [16, 17], as

$$\mathbf{T} = \mu\left(\mathbf{I} - \frac{1}{\sqrt{\text{III}}}\mathbf{B}^{-1}\right) - Q\mathbf{h}_c\otimes\mathbf{h}_c, \tag{18}$$

with the kinematical internal constraint

$$\text{tr}\,(\mathbf{h}_c\otimes\mathbf{h}_c) = 1, \tag{19}$$

if the preferred direction is given by $\mathbf{H}_c$. The last term on the right-hand side of equation (18) represents the reaction stresses due to the internal constraint.

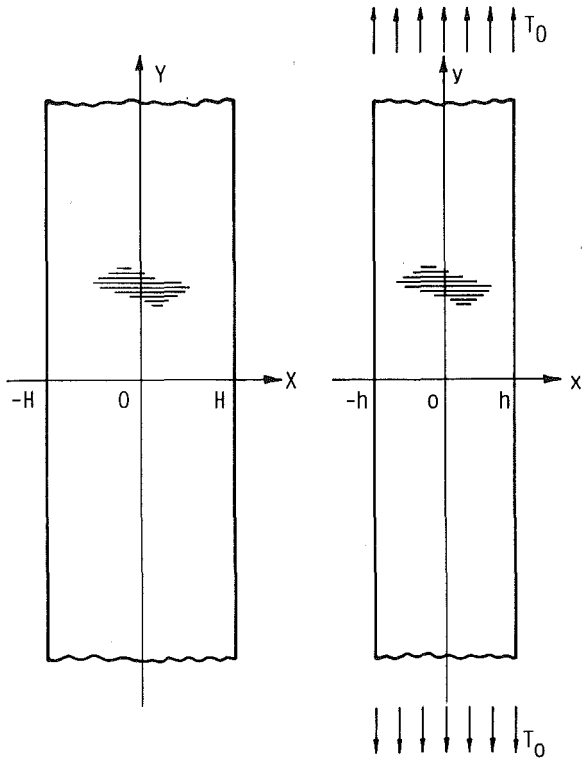

Fig. 1 Transversely isotropic slabs before loading and under axial loads

Here, let us consider the Blatz-Ko foam rubber reinforced by "extensible" fibers along the preferred direction $\mathbf{H}_c$, and let us treat this rubber as a transversely isotropic material possessing rotational symmetry relative to the direction $\mathbf{H}_c$. As one of the simplest forms of the strain energy function for such a transversely isotropic rubber, we consider the following special one:

$$W = \tfrac{1}{2}\mu\{(\mathrm{II}/\mathrm{III} - 3) + 2(\sqrt{\mathrm{III}} - 1) + \tfrac{1}{2}k(\mathrm{IV} - 1)^2\}, \tag{20}$$

where $k \geqq 0$ is an additional material constant characterizing the reinforcement by extensible fibers or the strength of the anisotropy. Henceforth, let us refer to this constant as an anisotropy parameter. This function satisfies the natural state conditions (11). It follows from equations (20), (9), and (10) that

$$\mathbf{T} = \mu\left\{\mathbf{I} - \frac{1}{\sqrt{\mathrm{III}}}\mathbf{B}^{-1} + \frac{k}{\sqrt{\mathrm{III}}}(\mathrm{IV} - 1)\mathbf{h}_c \otimes \mathbf{h}_c\right\}. \tag{21}$$

This stress-deformation equation coincides with equation (17) in the limit $k \to 0$. On the other hand, when $k \to \infty$ and tr $(\mathbf{h}_c \otimes \mathbf{h}_c) \to 1$, this equation agrees with equation (18), provided that

$$\mu \lim_{k\to\infty} k(\mathrm{IV} - 1)/\sqrt{\mathrm{III}} = -Q. \tag{22}$$

This limiting provision may be intuitively understood to be reasonable from equations (5)–(7) and (19). For the specified strain-energy function (20), the incremental stress-incremental strain relations (14) and (15) reduce to

$$\mathbf{s} = (\mu/\sqrt{\mathrm{III}})[\mathbf{e}\mathbf{B}^{-1} + \mathbf{B}^{-1}\mathbf{e} + \mathbf{B}^{-1}\,\mathrm{tr}\,\mathbf{e} + k\{2\mathbf{h}_c \otimes \mathbf{h}_c\,\mathrm{tr}\,(\mathbf{e}\mathbf{h}_c \otimes \mathbf{h}_c) + (\mathrm{IV} - 1)(\mathbf{e}\mathbf{h}_c \otimes \mathbf{h}_c + \mathbf{h}_c \otimes \mathbf{e}\mathbf{h}_c - \mathbf{h}_c \otimes \mathbf{h}_c\,\mathrm{tr}\,\mathbf{e})\}]. \tag{23}$$

This equation also agrees, when $k \to \infty$, tr $(\mathbf{h}_c \otimes \mathbf{h}_c) \to 1$ and tr $(\mathbf{e}\mathbf{h}_c \otimes \mathbf{h}_c) \to 0$, with the counterpart of the theory for ideal fiber-reinforced composites, provided that

$$\mu \lim_{k\to\infty} k\{2\,\mathrm{tr}\,(\mathbf{e}\mathbf{h}_c \otimes \mathbf{h}_c) - (\mathrm{IV} - 1)\,\mathrm{tr}\,\mathbf{e}\}/\sqrt{\mathrm{III}} = -q, \tag{24}$$

where q is the indeterminate incremental reaction stress due to the inextensible constraint.

4 Deformation and Stress in a Slab Under Axial Loads

Let (X, Y, Z) and (x, y, z) denote, respectively, the material coordinates and the spatial coordinates, with the bases $(\mathbf{i}, \mathbf{j}, \mathbf{k})$, of a point when referred to the same Cartesian system. Consider an infinite elastic slab of thickness $2H$ in its natural state and having a thickness of $2h$ when subjected to the uniform axial stress T_0 at infinity, as shown in Fig. 1; the strain-energy function of its material has the form like in equation (20), and the symmetry axis is in the X-direction. That is,

$$\mathbf{H}_c = \mathbf{i}. \tag{25}$$

Furthermore, the slab is assumed to be free from tractions on its $x = \pm h$ boundaries and to be in a plane strain state with $\lambda_3 = 1$.

Denote the principal stretches in the X, Y, and Z-directions as λ_1, λ_2, λ_3, respectively, and the deformation gradient is clearly

$$\mathbf{F} = \lambda_1\mathbf{i}\otimes\mathbf{i} + \lambda_2\mathbf{j}\otimes\mathbf{j} + \mathbf{k}\otimes\mathbf{k}, \tag{26}$$

from which follow

$$\mathbf{B} = \lambda_1^2\mathbf{i}\otimes\mathbf{i} + \lambda_2^2\mathbf{j}\otimes\mathbf{j} + \mathbf{k}\otimes\mathbf{k} \tag{27}$$

and

$$\mathrm{I} = \lambda_1^2 + \lambda_2^2 + 1, \quad \mathrm{II} = \lambda_1^2 + \lambda_2^2 + \lambda_1^2\lambda_2^2, \quad \mathrm{III} = \lambda_1^2\lambda_2^2, \quad \mathrm{IV} = \lambda_1^2, \quad \mathrm{V} = \lambda_1^4. \tag{28}$$

wherein we have used equations (3), (5)–(7), and (25). Substituting equations (26)–(28) into equation (21) yields, with the aid of equation (5),

$$T_{xx} = \mu[1 - \lambda_1^{-3}\lambda_2^{-1} + k\lambda_1\lambda_2^{-1}(\lambda_1^2 - 1)],$$
$$T_{yy} = \mu(1 - \lambda_1^{-1}\lambda_2^{-3}), \tag{29}$$
$$T_{zz} = \mu(1 - \lambda_1^{-1}\lambda_2^{-1}).$$

These are the nonzero components of the Cauchy stress tensor $\mathbf{T}$. From the condition of traction-free boundaries and from the loading condition at infinity, we get

$$\lambda_2 - \lambda_1^{-3} + k\lambda_1(\lambda_1^2 - 1) = 0 \tag{30}$$

and

$$T_0 = \mu(1 - \lambda_1^{-1}\lambda_2^{-3}). \tag{31}$$

5 Instability of the Slab

In order to examine whether the finite deformation and the stresses of the slab obtained in the previous section are statically stable or not, let us superpose an infinitesimal plane deformation on that finite deformation. Equilibrium equations for incremental stresses due to the superposed infinitesimal deformation are regarded as equations of neutral equilibrium for examining this stability.

As shown by Bažant [18], the incremental stresses defined by Biot [13] are identical with those defined as the product of a time increment and the objective corotational stress rate. Therefore, it may be preferable to adopt Biot's formulation of the infinitesimal deformations of continuous bodies under initial stresses from among various mathematical formulations. The equilibrium equations for the incremental deformations in rectangular Cartesian coordinates are

$$\partial s_{ij}/\partial x_j + T_{jk}\partial\omega_{ik}/\partial x_j + T_{ik}\partial\omega_{jk}/\partial x_j - e_{jk}\partial T_{ik}/\partial x_j = 0, \tag{32}$$

where s_{ij}, e_{ij}, and ω_{ij} are the Cartesian components of $\mathbf{s}$, $\mathbf{e}$, and $\boldsymbol{\omega}$ defined by equations (13). The incremental boundary forces per unit initial area are

$$\Delta f_i = (s_{ij} + T_{kj}\omega_{ik} + T_{ij}e_{kk} - T_{ik}e_{jk})n_j, \tag{33}$$

where n_j is a unit normal to the initial boundary surface. In equations (32) and (33), the sum is taken from 1 to 3 with respect to the repeated indices.

For the sake of simplicity, the superposed deformation is also as-

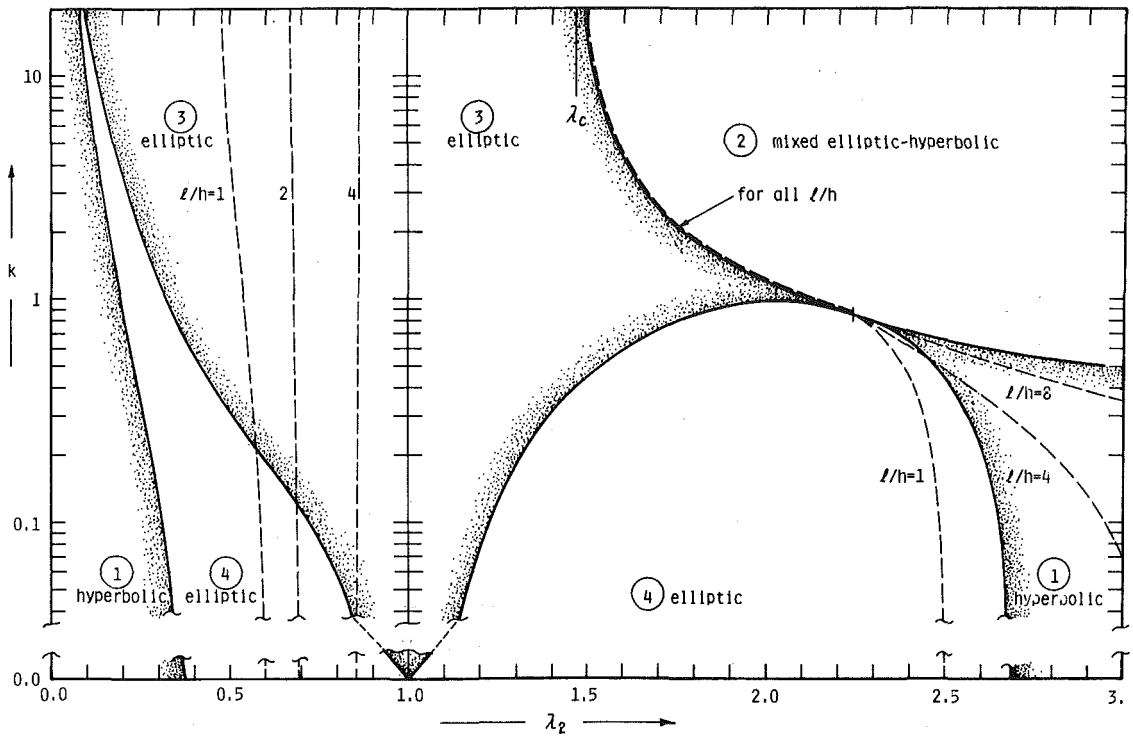

Fig. 2 Classification of equations (36) in a $k - \lambda_2$ plane and critical axial stretch curves $\lambda_2 = \lambda_{2c}$ represented by dashed curves

sumed to be in a plane strain state. Consequently, the components of incremental displacement are given by

$$u = u(x, y), \quad v = v(x, y), \quad w = 0. \tag{34}$$

These equations and equations (25)–(29) reduce the incremental stress-incremental strain relations (23) to the forms

$$\begin{aligned} s_{xx} &= \phi_{11} e_{xx} + \phi_{12} e_{yy}, \\ s_{yy} &= \phi_{22} e_{yy} + \phi_{21} e_{xx}, \\ s_{xy} &= \phi_0 e_{xy}, \end{aligned} \tag{35}$$

where

$$\begin{aligned} \phi_{11} &= \mu(\lambda_1\lambda_2)^{-1}\{3\lambda_1^{-2} + k\lambda_1^2(3\lambda_1^2 - 1)\}, \\ \phi_{22} &= \mu(\lambda_1\lambda_2)^{-1}(3\lambda_2^{-2}), \\ \phi_{12} &= \mu(\lambda_1\lambda_2)^{-1}\{\lambda_1^{-2} - k\lambda_1^2(\lambda_1^2 - 1)\}, \\ \phi_{21} &= \mu(\lambda_1\lambda_2)^{-1}\lambda_2^{-2}, \\ \phi_0 &= \mu(\lambda_1\lambda_2)^{-1}\{(\lambda_1^{-2} + \lambda_2^{-2}) + k\lambda_1^2(\lambda_1^2 - 1)\}. \end{aligned} \tag{36}$$

Substituting equations (29) and (35) into equations (32), we obtain a set of governing equations in terms of the incremental displacement components u and v:

$$\begin{aligned} \psi_{11}\partial^2 u/\partial x^2 + \partial^2 u/\partial y^2 + \psi_{12}\partial^2 v/\partial x\,\partial y &= 0, \\ \psi_{22}\partial^2 v/\partial x^2 + \partial^2 v/\partial y^2 + \psi_{21}\partial^2 u/\partial x\,\partial y &= 0, \end{aligned} \tag{37}$$

where

$$\begin{aligned} \psi_{11} &= 3 + k\lambda_1^4(3\lambda_1^2 - 1), \\ \psi_{22} &= \tfrac{1}{3}\{1 + k\lambda_1^2\lambda_2^2(\lambda_1^2 - 1)\}, \\ \psi_{12} &= \lambda_1^2(\lambda_1^{-2} + \lambda_2^{-2}), \\ \psi_{21} &= \tfrac{1}{3}\lambda_2^2(\lambda_1^{-2} + \lambda_2^{-2}). \end{aligned} \tag{38}$$

Since the slab is free from tractions, the incremental boundary forces (33) should vanish at $x = \pm h$; using equations (29)–(31), (34)–(36), and (38), we obtain

$$\begin{aligned} \psi_{11}\partial u/\partial x + \psi_0 \partial v/\partial y = 0 \quad &\text{at} \quad x = \pm h, \\ \partial u/\partial y + \partial v/\partial x = 0 \quad &\text{at} \quad x = \pm h, \end{aligned} \tag{39}$$

where

$$\psi_0 = 1 - k\lambda_1^4(\lambda_1^2 - 1). \tag{40}$$

The differential equations (37) have the following formal solutions for the antisymmetric mode:

$$\begin{aligned} u &= \{A_1 \cos(\zeta_1\pi x/l) + A_2 \cos(\zeta_2\pi x/l)\} \cos(\pi y/l), \\ v &= \{A_1\kappa_1 \sin(\zeta_1\pi x/l) + A_2\kappa_2 \sin(\zeta_2\pi x/l\} \sin(\pi y/l), \end{aligned} \tag{41}$$

where A_1 and A_2 are integral constants, and l is the half wavelength in the axial direction. The constants ζ_1 and ζ_2 are given by

$$\zeta_\alpha = [\{-b - (-1)^\alpha(b^2 - 4a)^{1/2}\}/(2a)]^{1/2} \quad (\alpha = 1, 2), \tag{42}$$

which are two of the four roots for the algebraic equation

$$a\zeta^4 + b\zeta^2 + 1 = 0 \tag{43}$$

with the coefficients

$$a = \psi_{11}\psi_{22}, \quad b = \psi_{11} + \psi_{22} - \psi_{12}\psi_{21}. \tag{44}$$

Furthermore, the constants κ_1 and κ_2 are given by

$$\kappa_\alpha = (\psi_{11}\zeta_\alpha^2 + 1)/(\psi_{12}\zeta_\alpha) \quad (\alpha = 1, 2). \tag{45}$$

On reference to the boundary conditions (39), the solutions in (41) yield homogeneous linear algebraic equations with respect to the unknowns A_1 and A_2. For a nontrivial set of solutions of these equations, the determinant of the coefficients must vanish, resulting in the following buckling expression:

$$\begin{aligned} &(\psi_{11}\zeta_1 - \psi_0\kappa_1)(1 - \kappa_1\zeta_1)^{-1} \tan(\zeta_1\pi h/l) \\ &\quad - (\psi_{11}\zeta_2 - \psi_0\kappa_2)(1 - \kappa_2\zeta_2)^{-1} \tan(\zeta_2\pi h/l) = 0. \end{aligned} \tag{46}$$

The counterparts of equations (41) and (46) for the symmetric mode are

$$\begin{aligned} u &= \{A_1 \sin(\zeta_1\pi x/l) + A_2 \sin(\zeta_2\pi x/l)\} \cos(\pi y/l), \\ v &= -\{A_1\kappa_1 \cos(\zeta_1\pi x/l) + A_2\kappa_2 \cos(\zeta_2\pi x/l)\} \sin(\pi y/l), \end{aligned} \tag{47}$$

Table 1 Classification of equations (36)

Region in Fig.2	ζ_1 and ζ_2		Type of eqs. (36)
①	Both real	$b^2-4a>0$, $a>0$, $b<0$	Hyperbolic
②	Real and purely imaginary	$a<0$	Mixed hyperbolic-elliptic
③	Both purely imaginary	$b^2-4a>0$, $a>0$, $b>0$	Elliptic
④	Both complex	$b^2-4a<0$	Elliptic

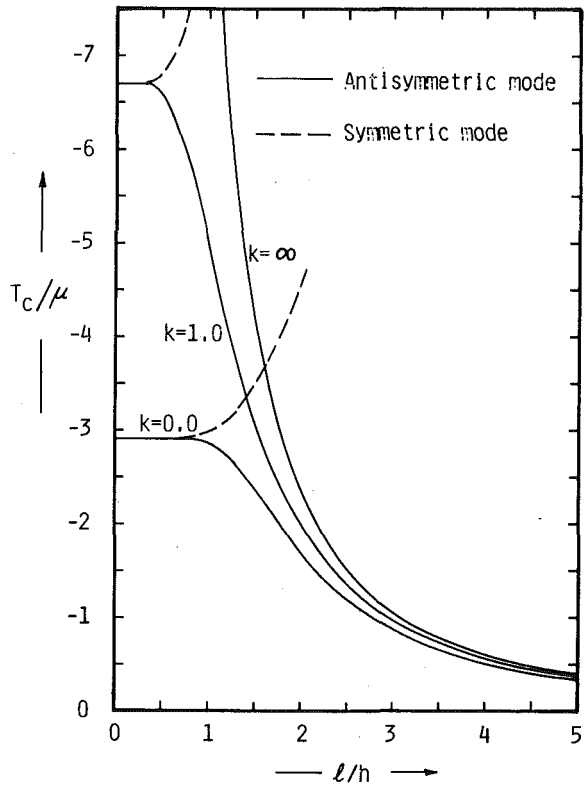

Fig. 3 Critical load under compression

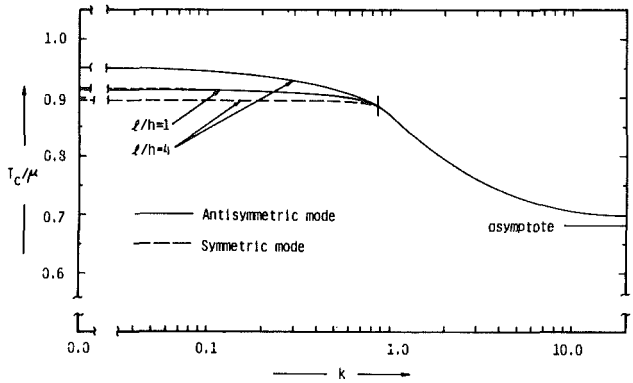

Fig. 4 Critical load under tension as a function of anisotropy parameter

and

$$(\psi_{11}\zeta_1 - \psi_0\kappa_1)(1-\kappa_1\zeta_1)^{-1}/\tan(\zeta_1\pi h/l) - (\psi_{11}\zeta_1 - \psi_0\kappa_2)(1-\kappa_2\zeta_2)^{-1}/\tan(\zeta_2\pi h/l) = 0, \quad (48)$$

where the constants ζ_1, ζ_2, κ_1, κ_2 are given by equations (43) and (45) again.

The solutions (41) and (47), and therefore the equations in (46) and (48) as well, are formal expressions and may be rewritten in other forms depending on what type the differential equations (37) are classified into. This classification can be carried out according to whether the two roots ζ_1 and ζ_2 are both real, real and purely imaginary, both purely imaginary, or both complex. This is summarized in Table 1 and shown in Fig. 2; the $k - \lambda_2$ plane is divided into several regions, marked from ① to ④, by solid curves.

6 Numerical Computations

From equation (30) it follows that λ_2 is a single-valued function of λ_1. The use of this in equation (46) [or (48)] then gives an equation for λ_1 which has multiple roots. After these are found for the given l/h and k, we choose a root such that λ_2 is nearest to unity (the maximum for compression and the minimum for tension), say λ_{2c}. The axial load corresponding to this root obtained through equation (31) is a critical, or buckling load, such as T_c.

However, for the case of tensile loads and when $k > k_0 \simeq 0.86$, a set of roots λ_2 corresponding to the multiple roots λ_1 does not have a minimum but an infimum, as is proved by examining equation (46) [or (48)] in the region ② in detail. This infimum is given by the equation $a = 0$ instead of equation (46) [or (48)] and falls on the ②–③ boundary in Fig. 2. That is, this boundary is a locus of points of accumulation of roots λ_2 of equation (46) [or (48)]. We regard the corresponding load for this infimum as a critical value, such as T_c again.

In Fig. 2, the dashed curves represent the $\lambda_2 = \lambda_{2c}$ curves for some wavelength-to-thickness ratios. For the compressive case ($\lambda_2 < 1$), all these curves are within the ellipticity regions ③ and ④. For the tensile case ($\lambda_2 > 1$), the curves are on the ②–③ boundary, within the ellipticity region ④, or even within the hyperbolicity region ①. Within this hyperbolicity region, there might be hyperbolic solutions possibly carrying weak discontinuities or strong discontinuities, though we have assumed continuously differentiable solutions from the outset. These possible discontinuities lie beyond our scope. The vertical line marked λ_c in the upper middle of the figure is an asymptote of the ②–③ boundary curve and at the same time an asymptote of the $\lambda_2 = \lambda_{2c}$ curve. The approximate value of λ_c is given as 1.466 in [12].

For the compressive case, Fig. 3 shows how the critical load depends upon the wavelength-to-thickness ratio l/h for the anisotropy parameters $k = 0.0$, 1.0, ∞, meaning isotropy, transverse isotropy, and ideal fiber-reinforcement, respectively. The slab becomes unstable for all $l/h > 0$. In particular, the transversely isotropic slab, including the isotropic case, becomes unstable for $l/h \to 0$. The critical load in this limit coincides with that of a "surface instability" of an elastic half space. The critical load for the antisymmetric mode, which is smaller than for the symmetric mode, decreases according to the increase in l/h. The stronger anisotropy makes the critical load higher; in other words, a stronger reinforcement makes the critical load higher.

For the tensile case, Figs. 4 and 5 show how the critical load depends on the anisotropy strength k and the wavelength-to-thickness ratio

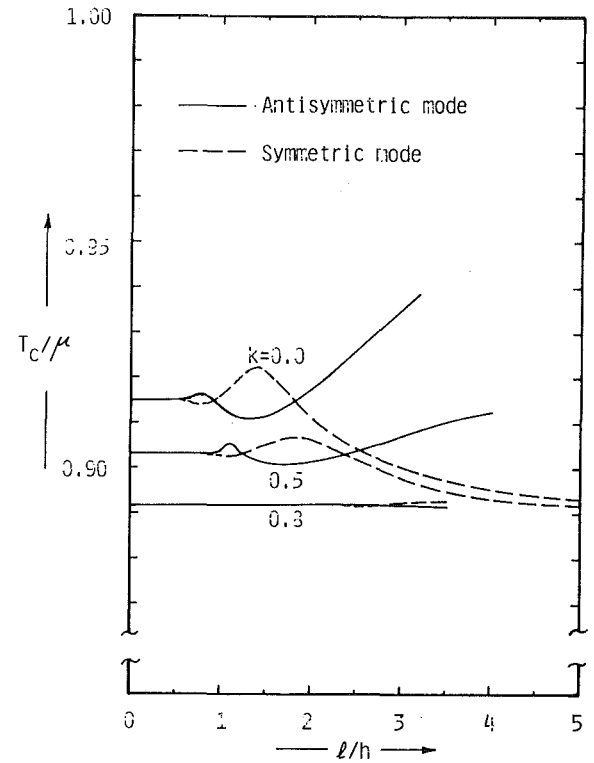

Fig. 5 Critical load under tension as a function of wavelength-to-thickness ratio

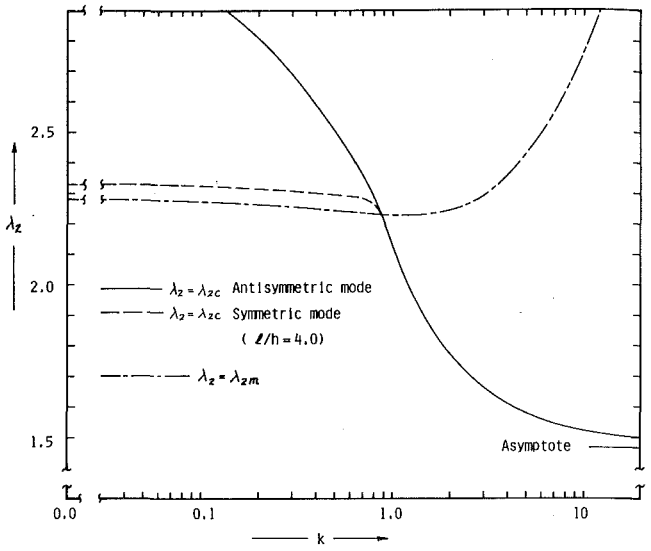

Fig. 6 Critical stretch and the stretch corresponding to the maximum resultant force

l/h. In spite of the tensile load, the slab becomes unstable for all $l/h \geqq 0$ and for all $k \geqq 0$. For $k > k_0 \simeq 0.86$, the critical load does not depend on l/h but does depend on l/h for $k < k_0$. This dependence on l/h for $k < k_0$ is shown in Fig. 5; the incipient instability occurs for the antisymmetric mode for some values of l/h and for the symmetric mode for other values of l/h. Furthermore, the critical load decreases according to the increase in k; in other words, the reinforcement in the transverse or "wrong" direction weakens the slab in regard to its stability. The asymptotic critical load in the limit $k \to \infty$ is $T_{0c} = \mu(1 - \lambda_c^{-3})$ [12].

Fig. 6 shows the $\lambda_2 = \lambda_{2c}$ curves and the $\lambda_2 = \lambda_{2m}$ curve with λ_{2m} being the value the principal stretch in the axial direction assumes when the tensile resultant force

$$F = 2H\lambda_1 T_0 \tag{49}$$

reaches its maximum. For $k < k_0$, $\lambda_{2c} > \lambda_{2m}$. This means that, for the anisotropy that is weaker than when $k = k_0$, the instability can arise only after the resultant force reaches its maximum. This is the same conclusion as that reached by Wesolowski [1] and Hill and Hutchinson [9]. In contrast to that conclusion, for $k > k_0$, $\lambda_{2c} > \lambda_{2m}$. That is, for the anisotropy that is stronger than when $k = k_0$, the instability can occur before the resultant force reaches its maximum.

Acknowledgment

The author wishes to express his sincere gratitude to Prof. A. Atsumi of Tohoku University for his valuable advice and encouragement. He also wishes to express his thanks to the two referees for their helpful and important comments.

References

1 Wesolowski, Z., "Stability in Some Cases of Tension in the Light of Finite Strain," *Archiwum Mechaniki Stosowanej*, Vol. 14, 1962, pp. 875–900.

2 Biot, M. A., "Exact Theory of Buckling of a Thick Slab," *Applied Scientific Researches*, Vol. A12, 1963, pp. 182–198.

3 Levinson, M., "Stability of a Neo-Hookean Rectangular Parallelepiped," *Journal of Mechanics and Physics of Solids*, Vol. 16, 1968, pp. 403–415.

4 Nowinski, J. L., "On the Elastic Stability of Thick Columns," *Acta Mechanica*, Vol. 7, 1969, pp. 279–286.

5 Wu, C.-H., and Widera, O. E., "Stability of Thick Rubber Solid Subjected to Pressure Loads," *International Journal of Solids and Structures*, Vol. 5, 1969, pp. 1107–1117.

6 Sawyers, K. N., and Rivlin, R. S., "Bifurcation Conditions for a Thick Elastic Plate Under Thrust," *International Journal of Solids and Structures*, Vol. 10, 1974, pp. 483–501.

7 Southwell, R. V., "On the General Theory of Elastic Stability," *Philosophical Transactions of the Royal Society*, Series A, Vol. 213, 1913, pp. 187–244.

8 Kerr, A. D., "On the Instability of Elastic Solids," *Proceedings of the 4th U. S. National Congress of Applied Mechanics*, 1962, pp. 647–656.

9 Hill, R., and Hutchinson, J. W., "Bifurcation Phenomena in the Plane Tension Test," *Journal of Mechanics and Physics of Solids*, Vol. 23, 1975, pp. 239–264.

10 Young, N. J. B., "Bifurcation Phenomena in the Plane Compression Test," *Journal of Mechanics and Physics of Solids*, Vol. 24, 1976, pp. 77–91.

11 Burgess, I. W., and Levinson, M., "The Instability of Slightly Compressible Rectangular Rubberlike Solids Under Biaxial Loadings," *International Journal of Solids and Structures*, Vol. 8, 1972, pp. 133–148.

12 Kurashige, M., "Instability of a Fiber-Reinforced Elastic Slab Subjected to Axial Loads," ASME JOURNAL OF APPLIED MECHANICS, Vol. 46, 1979, pp. 838–843.

13 Biot, M. A., *Mechanics of Incremental Deformations*, Wiley, New York, 1965.

14 Ericksen, J. L., and Rivlin, R. S., "Large Elastic Deformations of Homogeneous Anisotropic Materials," *Journal of Rational Mechanics and Analysis*, Vol. 3, 1954, pp. 281–301.

15 Blatz, P. J., and Ko, W. L., "Application of Finite Elasticity Theory to the Deformation of Rubbery Materials," *Transactions of the Society of Rheology*, Vol. 6, 1962, pp. 223–251.

16 Pipkin, A. L., "Finite Deformations of Ideal Fiber-Reinforced Composites," *Composite Materials*, Vol. 2, ed., Sendeckyj, G. P., Academic Press, New York, 1974, pp. 251–308.

17 Spencer, A. J. M., *Deformation of Fiber-Reinforced Materials*, Clarendon Press, Oxford, 1972.

18 Bažant, Z. P., "A Correlation Study of Formulations of Incremental Deformation and Stability of Continuous Bodies," ASME JOURNAL OF APPLIED MECHANICS, Vol. 38, 1971, pp. 919–928.

W. J. Fenner[2]
Graduate Student.
Assoc. Mem. ASME

C. H. Wu
Professor.
Mem. ASME

Department of Materials Engineering,
University of Illinois at Chicago Circle,
Box 4348,
Chicago, Ill. 60680

Large Plane-to-Surface Deformations of Membranes With Inclusion[1]

For large deformations, the strain-energy density function for a neo-Hookean membrane is dominated by the sum of squares of the two principal stretch ratios. This property reduces the displacement equations of equilibrium for the class of problems considered to three uncoupled linear equations. The nonlinear coupling appears only in the algebraic stress calculations. In light of the scarcity of exact solutions to nontrivial problems, the approximate but explicit solutions obtained here should be of some practical value.

1 Introduction

The theory of the finite deformation of a nonlinearly elastic membrane has been studied by many authors (see [1–5], for example). Because of the nonlinearity of the equations involved, the application of the theory to particular problems is in general very difficult. Aside from the few simple problems solved by a semi-inverse approach (see [6], for example), exact solutions are few.

In the context of the theory of plane stress, the solutions to the class of axisymmetric problems, originally studied by Rivlin and Thomas [1], may be considered exact in that the governing equations may be reduced to two uncoupled first-order ordinary differential equations. This reduction was accomplished by Yang [7]. The class of solutions obtained by Varley and Cumberbatch [8] is exact, but is based on an assumed special strain-energy density function.

In the general case where at least either the undeformed or the deformed surface is not a plane, the number of exact solutions is even fewer. Axisymmetric deformations of initially cylindrical membranes may be solved exactly [9–12]. These are perhaps the only nontrivial additions to the semi-inverse solutions mentioned in [6]. Effective numerical formulations for a large number of nontrivial problems, however, can be found in [13–15].

For very large deformations, explicit asymptotic solutions are very often possible. The needed asymptotic analysis depends very much on the type of membrane material involved (see [16–20], for example). A summary of this discussion may be found in [21] in which the reduction of Wang and Shield [17] was generalized to plane-to-surface deformations. This simplification is extremely significant in that it reduces a nonlinear problem to one that is even simpler than a linear problem. This is illustrated by the many problems solved in [17] and a recent solution by Wu [22]. The solutions given in this paper give another indication of the usefulness of the reduction.

2 Nonlinear Membrane Theory

Consider an elastic membrane surface characterized by a constant thickness H and a characteristic linear dimension R. The membrane is made of a neo-Hookean material with an elastic constant C_1. We shall use R and RHC_1 as a length scale and a force scale, respectively, and shall henceforth be dealing with dimensionless quantities only.

Let $x_i = x^i$ be a set of rectangular cartesian coordinates with unit vectors $\mathbf{e}_i = \mathbf{e}^i$. The position vector $\mathbf{x} = \mathbf{Z}$ of a point on a surface S may be expressed in terms of two surface coordinates $\theta^\alpha = \theta_\alpha$. Specifically, we write

$$\mathbf{Z} = \mathbf{Z}(\theta^\alpha) = Z^i(\theta_\alpha)\mathbf{e}_i = Z_i(\theta_\alpha)\mathbf{e}^i \tag{1}$$

The covariant base vectors $\mathbf{A}_\alpha$ and the components $A_{\alpha\beta}$ and $A^{\alpha\beta}$ of the metric tensors are

$$\mathbf{A}_\alpha = \mathbf{Z}_{,\alpha} = Z^i_{,\alpha}\mathbf{e}_i \tag{2}$$

$$A_{\alpha\beta} = \mathbf{A}_\alpha \cdot \mathbf{A}_\beta, \tag{3}$$

$$A^{\alpha\beta} = {}_\alpha{}^{-1}\, e^{\alpha\lambda}\, e^{\beta\mu} A_{\lambda\mu}, \tag{4}$$

where $e^{\alpha\beta}$ are the components of the two-dimensional alternator, and

$$A = \det [A_{\alpha\beta}]. \tag{5}$$

Suppose that the surface S is deformed to a new surface s. Let $\mathbf{x} = \mathbf{z}$ be the position vector of a point on s which, in the undeformed state, had position $\mathbf{Z}$. The deformation may be defined by

$$\mathbf{z} = \mathbf{z}(\theta_\alpha) = z^i(\theta_\alpha)\mathbf{e}_i = z_i(\theta_\alpha)\mathbf{e}^i. \tag{6}$$

On the deformed surface s, the base vectors $\mathbf{a}_\alpha$ and the components

[1] The work reported here was supported by NSF under Grant CME-7905462.

[2] Presently, Hunter Corporation, Hammond, Ind.

Contributed by the Applied Mechanics Division for publication in the JOURNAL OF APPLIED MECHANICS.

Discussion on this paper should be addressed to the Editorial Department, ASME, United Engineering Center, 345 East 47th Street, New York, N. Y. 10017, and will be accepted until September 1, 1981. Readers who need more time to prepare a Discussion should request an extension from the Editorial Department. Manuscript received by ASME Applied Mechanics Division, July, 1980.

$a_{\alpha\beta}$ and $a^{\alpha\beta}$ of the metric tensors may be derived from (2)–(5) by replacing the kernel letters by their lower case counterparts.

Let dL and dl be, respectively, the arc elements on S and s. Then

$$\Lambda^2 = \left(\frac{dl}{dL}\right)^2 = (a_{\alpha\beta} d\theta^\alpha d\theta^\beta)/(A_{\alpha\beta} d\theta^\alpha d\theta^\beta) \tag{7}$$

where Λ is the stretch ratio. The two invariants I and J of (7) are

$$I = \Lambda_1^2 + \Lambda_2^2 = A^{\alpha\beta} a_{\alpha\beta} \tag{8}$$

$$J = \Lambda_1^2 \Lambda_2^2 = a/A \tag{9}$$

where Λ_1 and Λ_2 are the principal stretch ratios. For a neo-Hookean membrane subjected to large deformation, the dimensionless strain-energy density W per unit area of the undeformed surface may be approximated by

$$W = I - 2. \tag{10}$$[3]

For zero body force and surface load, the three displacement equations of equilibrium are [21]

$$\frac{\partial}{\partial\theta_\alpha}\left(\frac{\partial W}{\partial z^i_{,\alpha}} A^{1/2}\right) = 0 \tag{11}$$

which, for W defined by (10), become

$$\frac{\partial}{\partial\theta_\alpha}\left(A^{1/2} A^{\alpha\beta} \frac{\partial z_i}{\partial\theta_\beta}\right) = 0. \tag{12}$$

If the undeformed surface S is in the plane $Z_3 = 0$, and if Z_1 and Z_2 are taken as the surface coordinates, then (12) becomes

$$\left(\frac{\partial^2}{\partial Z_1^2} + \frac{\partial^2}{\partial Z_2^2}\right) z_i = 0. \tag{13}$$

Let $\mathbf{t}\, dl$ be the traction vector on the deformed line element dl. Then

$$\mathbf{t} = 2A^{1/2} A^{\alpha\delta} e_{\alpha\beta} \frac{d\theta^\beta}{dl} \mathbf{a}_\delta. \tag{14}$$

The line elements along the coordinate curves are

$$dl_\alpha = a_{\alpha\alpha}^{1/2}\, d\theta^\alpha \qquad \text{(no sum)}. \tag{15}$$

Substituting (15) into (14), we obtain the traction vectors

$$\mathbf{t}_\alpha = 2A^{1/2} A^{\gamma\delta} e_{\gamma\alpha} \frac{1}{a_{\alpha\alpha}^{1/2}} \mathbf{a}_\delta \qquad \text{(no sum on } \alpha) \tag{16}$$

3 Elliptic Inclusion

We begin by introducing two complex variables

$$Z = Z_1 + iZ_2, \tag{17}$$

$$\zeta = \zeta_1 + i\zeta_2 = \rho e^{i\theta} \quad (\rho \geq 1, \quad 0 \leq \theta \leq 2\pi), \tag{18}$$

and a transformation

$$Z = \Omega(\zeta) = \zeta + m/\zeta \quad (-1 \leq m \leq 1). \tag{19}$$

The parameters ρ and θ define a set of curvilinear coordinates in the Z-plane. We choose them as the surface coordinates introduced in Section 2 and write

$$\theta_1 = \theta^1 = \rho, \qquad \theta_2 = \theta^2 = \theta. \tag{20}$$

In terms of the curvilinear coordinates, we may characterize an elliptical annulus by the expression

$$1 \leq \rho \leq k \tag{21}$$

where $\rho = 1$ defines the boundary of the inclusion and $\rho = k$ the outer boundary. The shape of the inclusion depends on the choice of m:

$$m = \begin{cases} -1 & \text{line inclusion of length 4 on the } Z_2\text{-axis.} \\ 0 & \text{circular inclusion of radius 1.} \\ +1 & \text{line inclusion of length 4 on the } Z_1\text{-axis.} \end{cases}$$

For large values of k, the outer boundary is almost circular. Our objective is to determine the deformation of the membrane due to the application of certain displacement boundary conditions specified along the inclusion boundary $\rho = 1$ as well as the outer boundary $\rho = k$.

Let $\boldsymbol{\epsilon}_i$ be a set of body-axes attached to the inclusion such that $\boldsymbol{\epsilon}_i$ coincide with $\mathbf{e}_i$ in the undeformed configuration. The set of body-axes is rotated through the sequence of Euler-angle rotations: ϕ about $\boldsymbol{\epsilon}_3$, γ about $\boldsymbol{\epsilon}_1$, and ψ about $\boldsymbol{\epsilon}_3$. The effect of these rotations may be characterized by a matrix $\mathbf{R}$ with components $R_{lm} = R^{lm}$ defined by

$$\begin{aligned}
R_{11} &= \cos\phi\cos\psi - \sin\psi\sin\phi\cos\gamma \\
R_{12} &= \sin\phi\cos\psi + \sin\psi\cos\phi\cos\gamma \\
R_{13} &= \sin\psi\sin\gamma \\
R_{21} &= -\cos\phi\sin\psi - \cos\psi\sin\phi\cos\gamma \\
R_{22} &= -\sin\phi\sin\psi + \cos\psi\cos\phi\cos\gamma \\
R_{23} &= \cos\psi\sin\gamma \\
R_{31} &= \sin\phi\sin\gamma \\
R_{32} &= -\cos\phi\sin\gamma \\
R_{33} &= \cos\gamma
\end{aligned} \tag{22}$$

The matrix $\mathbf{R}$ satisfies the relation $\mathbf{R}^T = \mathbf{R}^{-1}$. If $\mathbf{u}$ is a vector with representations

$$\mathbf{u} = u^i \mathbf{e}_i = u_i \mathbf{e}^i = \mu^i \boldsymbol{\epsilon}_i = \mu_i \boldsymbol{\epsilon}^i, \tag{23}$$

then

$$\mu^i = R^{ij} u_j, \quad u^i = R^{ji} \mu_j. \tag{24}$$

The boundary conditions along the inclusion boundary $\rho = 1$ are those effected by a rigid-body translation $\Delta_i \mathbf{e}^i$ and a rigid-body rotation characterized by $\mathbf{R}$. We have

$$z_j = \Delta_j + R_{1j} Z_1 + R_{2j} Z_2 \tag{25}$$

or

$$z_j = \Delta_j + R_j Z + \overline{R}_j \overline{Z} \tag{26}$$[4]

where

$$R_j = \tfrac{1}{2}(R_{1j} - iR_{2j}). \tag{27}$$

The conditions along the outer boundary $\rho = k$ are assumed to be of the following form:

$$z_j = \Gamma_j Z + \overline{\Gamma}_j \overline{Z} \tag{28}$$

where the Γ's are expressed in terms of three parameters λ_1, λ_2, and β by the expressions

$$\Gamma_1 = \tfrac{1}{4}[(\lambda_1 + \lambda_2) + (\lambda_1 - \lambda_2)e^{-i2\beta}], \tag{29}$$

$$\Gamma_2 = \frac{i}{4}[(\lambda_1 - \lambda_2)e^{-i2\beta} - (\lambda_1 + \lambda_2)], \tag{30}$$

$$\Gamma_3 = 0. \tag{31}$$

This choice is motivated by the observation that as $k \to \infty$, λ_1 and λ_2 are just the constant principal stretch ratios Λ_1 and Λ_2 at infinity, and β is simply the angle between the Z_1-axis and the Λ_1-direction.

[3] The complete expression is $W = I + J^{-1} - 3$. A discussion on various restrictions on the applicability of (10) may be found in [21].

[4] $(\bar{\ })$ = complex conjugate of $(\ )$

The functions z_i must now be determined to satisfy (13), (26), and (28). The solution is elementary and the result is

$$z_j = \Delta_j \left(1 - \frac{1}{\ln k} \ln \rho\right) + b_j \zeta + \bar{b}_j \bar{\zeta} + \frac{d_j}{\zeta} + \frac{\bar{d}_j}{\bar{\zeta}} \tag{32}$$

where

$$b_j = \frac{1}{k^2 - 1} [(k^2 \Gamma_j + m\bar{\Gamma}_j) - (R_j + m\bar{R}_j)], \tag{33}$$

$$d_j = \frac{1}{k^2 - 1} [-(k^2 \bar{\Gamma}_j + m\Gamma_j) + k^2(\bar{R}_j + mR_j)]. \tag{34}$$

We proceed to calculate a number of quantities pertinent to the solution.

Using the parametric representation defined by (19) and (20), we have

$$A_{11} = \frac{1}{\rho^2} A_{22} = \frac{1}{\rho} A^{1/2} = 1 - 2\frac{m}{\rho^2} \cos 2\theta + \frac{m^2}{\rho^4}, \tag{35}$$

$$A_{12} = A^{12} = 0. \tag{36}$$

The traction acting on the membrane along the inclusion boundary may be calculated from (16). It is

$$-\mathbf{t}_2 \, dl_2 = -2 \left(A^{1/2} A^{11} \frac{\partial z_l}{\partial \rho}\right)_{\rho=1} \mathbf{e}_l \, d\theta$$

$$= 2 \left[\frac{\Delta_l}{\ln k} - (b_l - \bar{d}_l) e^{i\theta} - (\bar{b}_l - d_l) e^{-i\theta}\right] \mathbf{e}_l \, d\theta. \tag{37}$$

The total force that must be applied on the inclusion is just

$$\mathbf{F} = \int -\mathbf{t}_2 \, dl_2 = \frac{4\pi}{\ln k} \Delta_l \mathbf{e}^l. \tag{38}$$

Let $\mathbf{C}$ be the total couple that must be applied on the inclusion. Then

$$\mathbf{C} = c_l \boldsymbol{\epsilon}^l = C_l \mathbf{e}^l$$

$$= \oint \mathbf{z} \times (-\mathbf{t}_2 \, dl_2) - \boldsymbol{\Delta} \times \mathbf{F} \tag{39}$$

where $\mathbf{z}$ is the position vector defined by (26). The explicit results for the components C_l are

$$C_1 = \frac{2\pi}{k^2 - 1} \{R_{13} (1 + m) (k^2 + m) (\lambda_1 - \lambda_2) \sin 2\beta$$

$$- R_{23} (1 - m) (k^2 - m) [(\lambda_1 - \lambda_2) \cos 2\beta - (\lambda_1 + \lambda_2)]\}, \tag{40}$$

$$C_2 = -\frac{2\pi}{k^2 - 1} \{R_{13} (1 + m) (k^2 + m) [(\lambda_1 + \lambda_2) + (\lambda_1 - \lambda_2)$$

$$\times \cos 2\beta] + R_{23} (1 - m) (k^2 - m) (\lambda_1 - \lambda_2) \sin 2\beta\}, \tag{41}$$

$$C_3 = -\frac{2\pi}{k^2 - 1} [(1 + m) (k^2 + m) \{R_{11}(\lambda_1 - \lambda_2) \sin 2\beta$$

$$- R_{12}[(\lambda_1 + \lambda_2) + (\lambda_1 - \lambda_2) \cos 2\beta]\} - (1 - m) (k^2 - m)$$

$$\{R_{21}[(\lambda_1 - \lambda_2) \cos 2\beta - (\lambda_1 + \lambda_2)] + R_{22}(\lambda_1 - \lambda_2) \sin 2\beta\}] \tag{42}$$

The components c_l may be calculated by using (24).

Traction vectors along the coordinate curves may be calculated by using (16). They are

$$\mathbf{t}_1 = \frac{2}{\rho} a_{11}^{-1/2} \mathbf{a}_2 = -\frac{2}{\rho} a_{11}^{-1/2} z_{l,2} \mathbf{e}_l, \tag{43}$$

$$\mathbf{t}_2 = 2\rho a_{22}^{-1/2} \mathbf{a}_1 = 2\rho a_{22}^{-1/2} z_{l,1} \mathbf{e}_l. \tag{44}$$

Along the inclusion boundary $\rho = 1$, the traction is

$$\mathbf{t}_2 = 2(1 - 2m \cos 2\theta + m^2)^{-1/2} \mathbf{a}_1|_{\rho=1} \tag{45}$$

where the condition $A_{22} = a_{22}$ for $\rho = 1$ has been used in the derivation. The tangential and normal tractions along the inclusion are just

$$T = \mathbf{t}_2 \times a_{22}^{-1/2} \mathbf{a}_2 = 2a_{22}^{-1} a_{12}, \tag{46}$$

$$N = (\mathbf{t}_2 \times \mathbf{t}_2 - T^2)^{1/2} = 2a_{22}^{-1} a^{1/2}, \tag{47}$$

where $a_{\alpha\beta}$ can be explicitly obtained by using (32), but the lengthy algebraic expressions are not given here.

4 Examples

Pulling and Twisting of a Circular Inclusion. The membrane is uniformly stretched at the outer boundary with $\lambda_1 = \lambda_2 = \lambda$, and the inclusion is pulled out of the plane by a force $F\mathbf{e}_3$ and a couple $C\mathbf{e}_3$. Setting

$$m = \beta = \psi = \gamma = \Delta_1 = \Delta_2 = 0, \tag{48}$$

$$\Delta_3 = \frac{F}{4\pi} \ln k, \tag{49}$$[5]

we obtain

$$z_1 = f_1(\rho) \cos \theta + f_2(\rho) \sin \theta, \tag{50}$$

$$z_2 = f_1(\rho) \sin \theta - f_2(\rho) \cos \theta, \tag{51}$$

$$z_3 = \frac{F}{4\pi} \ln k - \frac{F}{4\pi} \ln \rho, \tag{52}$$

where

$$f_1(\rho) = \frac{k^2\lambda - \cos \phi}{k^2 - 1} \rho - \frac{k^2 (\lambda - \cos \phi)}{k^2 - 1} \frac{1}{\rho}, \tag{53}$$

$$f_2(\rho) = \frac{\sin \phi}{k^2 - 1} \left(\rho - \frac{k^2}{\rho}\right). \tag{54}$$

The couple C is related to the Euler angle ϕ by the expression

$$C = \frac{8\pi k^2 \lambda}{k^2 - 1} \sin \phi. \tag{55}$$

For this problem, the curvilinear coordinates are the polar coordinates in the undeformed configuration, i.e.,

$$\mathbf{A}_1 = \mathbf{e}_\rho, \qquad \mathbf{A}_2 = \rho \mathbf{e}_\theta, \tag{56}$$

where $\mathbf{e}_\rho$ and $\mathbf{e}_\theta$ are unit vectors. We further introduce a set of body-polar coordinates with unit vectors $\boldsymbol{\epsilon}_\rho$ and $\boldsymbol{\epsilon}_\theta$ defined by

$$\boldsymbol{\epsilon}_\rho = \cos \phi \, \mathbf{e}_\rho + \sin \phi \, \mathbf{e}_\theta, \tag{57}$$

$$\boldsymbol{\epsilon}_\theta = -\sin \phi \, \mathbf{e}_\rho + \cos \phi \mathbf{e}_\theta. \tag{58}$$

It follows from the explicit expressions (50)–(52) that

$$\mathbf{a}_1 = (f_1' \cos \phi - f_2' \sin \phi) \boldsymbol{\epsilon}_\rho$$

$$- (f_1' \sin \phi + f_2' \cos \phi) \boldsymbol{\epsilon}_\theta - \frac{F}{4\pi\rho} \mathbf{e}_3, \tag{59}$$

$$\mathbf{a}_2 = (f_1 \sin \phi + f_2 \cos \phi) \boldsymbol{\epsilon}_\rho + (f_1 \cos \phi - f_2 \sin \phi) \boldsymbol{\epsilon}_\theta, \tag{60}$$

where primes denote differentiation with respect to ρ.

At the inclusion boundary $\rho = 1$, we have

$$\mathbf{a}_1 = \frac{2k^2\lambda \cos \phi - (k^2 + 1)}{k^2 - 1} \boldsymbol{\epsilon}_\rho - \frac{2k^2\lambda}{k^2 - 1} \sin \phi \, \boldsymbol{\epsilon}_\rho - \frac{F}{4\pi} \mathbf{e}_3 \tag{61}$$

$$\mathbf{a}_2 = \boldsymbol{\epsilon}_\theta \tag{62}$$

and

$$a_{11} = \frac{[2k^2\lambda \cos \phi - (k^2 + 1)]^2 + 4k^4\lambda^2 \sin^2 \phi}{(k^2 - 1)^2} + \left(\frac{F}{4\pi}\right)^2, \tag{63}$$

$$a_{12} = -\frac{2k^2\lambda}{k^2 - 1} \sin \phi, \quad a_{22} = 1, \tag{64}$$

$$a = \frac{[2k^2\lambda \cos \phi - (k^2 + 1)]^2}{(k^2 - 1)^2} + \left(\frac{F}{4\pi}\right)^2. \tag{65}$$

A thin membrane wrinkles when one of the principal stresses becomes

[5] c.f. (38).

zero. For membrane materials defined by (10), wrinkling occurs when

$$a = \Lambda_1^2 \Lambda_2^2 = 0. \tag{66}$$

It follows from (65) that for plane-to-plane deformation, $F = 0$, the condition

$$\phi \leq \cos^{-1} \frac{k^2 + 1}{2k^2 \lambda} \tag{67}^6$$

must be satisfied to avoid wrinkling. If F is not zero, then a is always positive. Condition (67) simply indicates the maximum rotation of the inclusion before the membrane begins to wrap around the inclusion. This follows from the fact that the traction vector along the inclusion is $\mathbf{t}_2 = 2\mathbf{a}_1$ which becomes tangent to the inclusion boundary when ϕ satisfies the equality of (67).

Line Inclusion. In view of the arrangement that the Euler angle γ is a rotation about the ϵ_1 body-axis, we must choose the line inclusion to coincide with the ϵ_2-axis and hence $m = -1$. We shall restrict ourselves to the case $\phi = \psi = \beta = 0$. Then

$$z_1 = \Delta_1 \left(1 - \frac{1}{\ln k} \ln \rho\right) + \lambda_1 \left(\rho - \frac{1}{\rho}\right) \cos \theta, \tag{68}$$

$$z_2 = \Delta_2 \left(1 - \frac{1}{\ln k} \ln \rho\right) + \left\{\left[\frac{(k^2+1)\lambda_2}{k^2-1} - \frac{2\cos\gamma}{k^2-1}\right]\rho - \left[\frac{(k^2+1)\lambda_2}{k^2-1} + \frac{2k^2}{k^2-1}\cos\gamma\right]\frac{1}{\rho}\right\} \sin\theta, \tag{69}$$

$$z_3 = \Delta_3 \left(1 - \frac{1}{\ln k} \ln \rho\right) - \frac{2\sin\gamma}{k^2-1}\left(\rho - \frac{k^2}{\rho}\right) \sin\theta. \tag{70}$$

The force acting on the inclusion is just (38), while the couple is given by the expression

$$\mathbf{C} = \frac{8\pi\lambda_2(k^2+1)}{k^2-1} \sin\gamma\, \mathbf{e}_1 \tag{71}$$

We now examine the property of the solution for $Z_1 = 0$ and $0 < Z_2 - 2 \ll 1$. Setting $\theta = \pi/2$ and $(\rho - 1) = (Z_2 - 2)^{1/2}$ in the various expressions, we obtain

$$A_{11} = A_{22} = 4(Z_2 - 2) \tag{72}$$

$$A_{11} = \left(\frac{\Delta_1}{\ln k}\right)^2 + \left(\frac{\Delta_2}{\ln k} - 2\frac{k^2+1}{k^2-1}\lambda_2 - 2\cos\gamma\right)^2 + \left(\frac{\Delta_3}{\ln k} + 2\frac{k^2+1}{k^2-1}\sin\gamma\right)^2 \tag{73}$$

$$A_{22} = 4\lambda_1^2 (Z_2 - 2), \quad A_{12} = 0 \tag{74}$$

It follows that ahead of the splinter tip $Z_1 = 0$ and $Z_2 = 2$, the principal stretch ratios are

$$\Lambda_1 = (a_{22}/A_{22})^{1/2} = \lambda_1, \tag{75}$$

$$\Lambda_2 = (a_{11}/A_{11})^{1/2} = a_{11}^{1/2}/2(Z_2 - 2)^{1/2}, \tag{76}$$

where Λ_2 has the familiar singularity.

[6] c.f. [17].

References

1 Rivlin, R. S., and Thomas, A. G., "Large Elastic Deformations of Isotropic Materials. VIII. Strain Distribution Around a Hole in a Sheet," *Philosophical Transactions of the Royal Society*, London, Series A, Vol. 243, 1951, pp. 289–298.

2 Adkins, J. E., and Rivlin, R. S., "Large Elastic Deformations of Isotropic Materials IX. The Deformation of Thin Shells," *Philosophical Transactions of the Royal Society*, London, Series A, Vol. 244, 1952, pp. 505–531.

3 Green, A. E., and Adkins, J. E., *Large Elastic Deformations and Nonlinear Continuum Mechanics*, Oxford University Press, London, 1960.

4 Corneliussen, A. H., and Shield, R. T., "Finite Deformation of Elastic Membranes With Application to the Stability of an Inflated and Extended Tube," *Arch. Rational Mech. and Analysis*, Vol. 7, 1961, pp. 273–304.

5 Stoker, J. J., *Topics in Nonlinear Elasticity*, Courant Institute of Mathematical Sciences, 1964.

6 Green, A. E., and Zerna, W., *Theoretical Elasticity*, Oxford University Press, London, 1954.

7 Yang, W. H., "Stress Concentration in a Rubber Sheet Under Axially Symmetric Stretching," ASME JOURNAL OF APPLIED MECHANICS, Vol. 34, 1967, pp. 943–947.

8 Varley, E., and Cumberbatch, E., "The Finite Deformation of an Elastic Material Surrounding an Elliptical Hole," Symposium on Finite Elasticity Theory, AMD, Vol. 27, ASME, 1977.

9 Wu, C. H., "Tube to Annulus—An Exact Nonlinear Membrane Solution," *Quarterly of Applied Mathematics*, Vol. 27, 1970, pp. 489–496.

10 Kydoniefs, A. D., and Spencer, A. J. M., "Finite Axisymmetric Deformations of an Initially Cylindrical Elastic Membrane," *Quarterly Journal of Mechanics and Applied Mathematics*, Vol. 22, 1969, pp. 87–95.

11 Kydoniefs, A. D., "Finite Axisymmetric Deformations of an Initially Cylindrical Elastic Membrane Enclosing a Rigid Body," *Quarterly Journal of Mechanics and Applied Mathematics*, Vol. 22, 1969, pp. 319–331.

12 Pipkin, A. C., "Integration of an Equation in Membrane Theory," *ZAMP*, Vol. 19, 1968, pp. 818–819.

13 Yang, W. H., and Feng, W. W., "On Axisymmetrical Deformations of Nonlinear Membranes," ASME JOURNAL OF APPLIED MECHANICS, Vol. 37, 1970, pp. 1002–1011.

14 Yang, W. H., and Lu, C. H., "General Deformations of Neo-Hookean Membranes," ASME JOURNAL OF APPLIED MECHANICS, Vol. 40, 1973, pp. 9–12.

15 Feng, W. W., Tielking, J. T., and Huang, P., "The Inflation and Contact Constraint of a Rectangular Mooney Membrane," ASME JOURNAL OF APPLIED MECHANICS, Vol. 41, 1974, pp. 979–984.

16 Foster, H. O., "Very Large Deformations of Axially Symmetric Membranes Made of Neo-Hookean Material," *International Journal of Engineering Science*, Vol. 5, 1967, pp. 95–117.

17 Wong, F. S., and Shield, R. T., "Large Plane Deformations of Thin Elastic Sheets of Neo-Hookean Material," *ZAMP*, Vol. 20, 1969, pp. 176–199.

18 Isaacson, E., "The Shape of a Balloon," *Comm. Pure Appl. Math.*, Vol. 18, 1965, pp. 163–166.

19 Wu, C. H., "Spherelike Deformations of a Balloon," *Quarterly of Applied Mathematics*, Vol. 30, 1972, pp. 183–194.

20 Wu, C. H., and Perng, D. Y. P., "On the Asymptotically Spherical Deformations of Arbitrary Membranes of Revolution Fixed Along an Edge and Inflated by Large Pressure—A Nonlinear Boundary Layer Phenomenon," *SIAM Journal of Applied Mathematics*, Vol. 23, 1972, pp. 133–152.

21 Wu, C. H., "Large Finite Strain Membrane Problems," *Quarterly of Applied Mathematics*, Vol. 36, 1979, pp. 347–359.

22 Wu, C. H., "Sutures in Stretched Membranes," *Quarterly of Applied Mathematics*, Vol. 38, 1980, pp. 109–119.

M. Taya
Assistant Professor,
Department of Mechanical
and Aerospace Engineering,
University of Delaware,
Newark, Del. 19711
Assoc. Mem. ASME

T. Mura
Professor,
Department of Civil Engineering,
The Technological Institute,
Northwestern University,
Evanston, Ill. 60201
Mem. ASME

On Stiffness and Strength of an Aligned Short-Fiber Reinforced Composite Containing Fiber-End Cracks Under Uniaxial Applied Stress[1]

One of the experimental findings on short-fiber reinforced composite materials is that the fiber-ends act as a crack initiator. The effect of the fiber-end crack on the overall stiffness and the strength of the composite are investigated here. A particular emphasis is placed upon the weakening longitudinal Young's modulus by the fiber-end crack which is assumed to be penny-shaped. The energy release rate of the penny-shaped crack at the fiber-end under a uniaxial applied stress is also calculated for a fracture criterion. It is assumed in our theoretical model that short-fibers are all aligned in the loading direction and the penny-shaped crack at the fiber-end extends in the direction perpendicular to the fiber axis. Our analytical technique is a combination of Eshelby's equivalent inclusion method and Mori-Tanaka's back stress analysis so that our results are valid even for large volume fraction of fibers.

Introduction

The stress-strain curve of a short-fiber reinforced composite consists of two stages; (*i*) linear stage and (*ii*) nonlinear stage. A typical stress-strain curve of this nature is shown in Fig. 1 [1], where variation of the tangent modulus and the corresponding acoustic emission are also given. In these figures the nonlinear stage can further be divided into two stages, hence we have three stages 1, 2, and 3. Assisted by the acoustic emission result one can conclude that the linear stage (stage 1) is due to elastic deformation of the composite with perfect interfacial bonding, whereas during the nonlinear stage (stages 2 and 3) the stiffness of the composite is reduced until the composite fails in a brittle manner due to the debonding at fiber-ends and the propagation of the fiber-end cracks. During stage 3 the microcracks are expected to be abundant in the matrix so that some of the microcracks cut through adjacent fibers. Observation of a fractured composite has revealed [1] that the fiber-end crack grows radially and propagates into the matrix followed by a final failure.

Based on the foregoing experimental findings, a number of problems and corresponding theoretical models have been proposed [4]. In this paper we focus on the strength and stiffness at the early part of stage 2 just after the fiber-end crack is initiated. We will compute the energy-release rate of the fiber-end crack and the longitudinal Young's modulus of the composite under uniaxial applied stress. The fiber-end crack can be simulated by a penny-shaped crack based on the experimental findings [1].

The energy-release rate of a penny-shaped crack in a pure matrix has been computed by a number of researchers [5–8]. However, the problem of a penny-shaped crack at a fiber-end has not been solved mainly due to the complexity of its geometry (see Fig. 2), except for the case of a penny-shaped crack located in the matrix and surrounded by fibers which are not in contact with the penny-shaped crack [9], and for the 2-D crack meeting a continuous fiber at a right angle [10]. There are three methods for evaluating the energy-release rate of crack: (*i*) stress-intensity factor approach; (*ii*) J-integral approach, and (*iii*) total potential energy approach by use of the equivalent inclusion method. The first two approaches require a detailed information of stress and strain field, whereas in the third approach a computation of the total potential energy of the composite containing cracks is only the work to be done. For the computation

[1] This research was supported by NSF under Grant No. CME-7918249.
Contributed by the Applied Mechanics Division for publication in the JOURNAL OF APPLIED MECHANICS.
Discussion on this paper should be addressed to the Editorial Department, ASME, United Engineering Center, 345 East 47th Street, New York, N.Y. 10017, and will be accepted until September 1, 1981. Readers who need more time to prepare a Discussion should request an extension from the Editorial Department. Manuscript received by ASME Applied Mechanics Division, June, 1980; final revision, September, 1980.

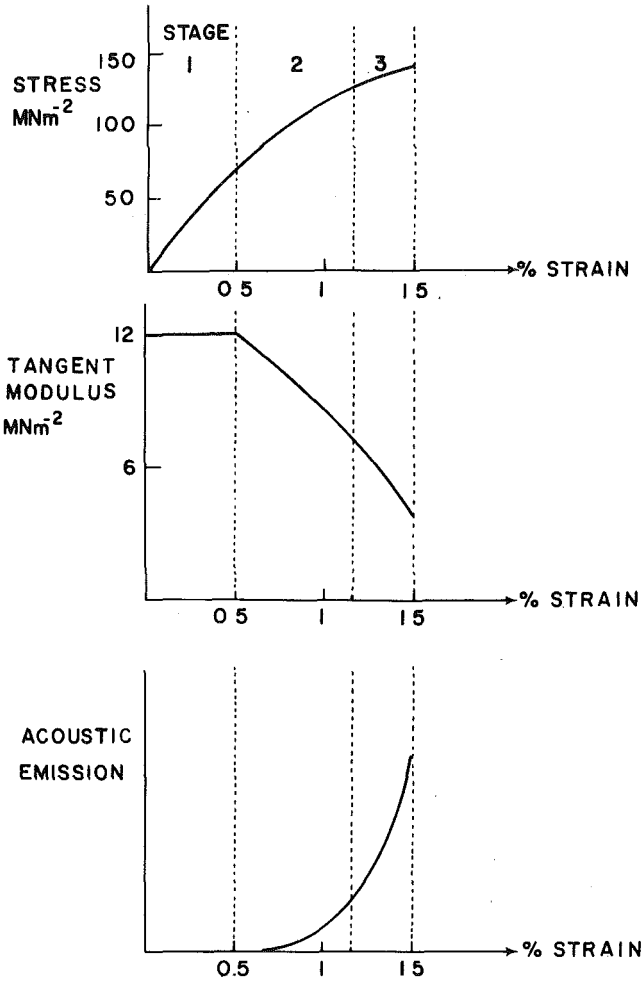

Fig. 1 A typical stress-strain curve with acoustic emission for a short-fiber-reinforced composite [1]

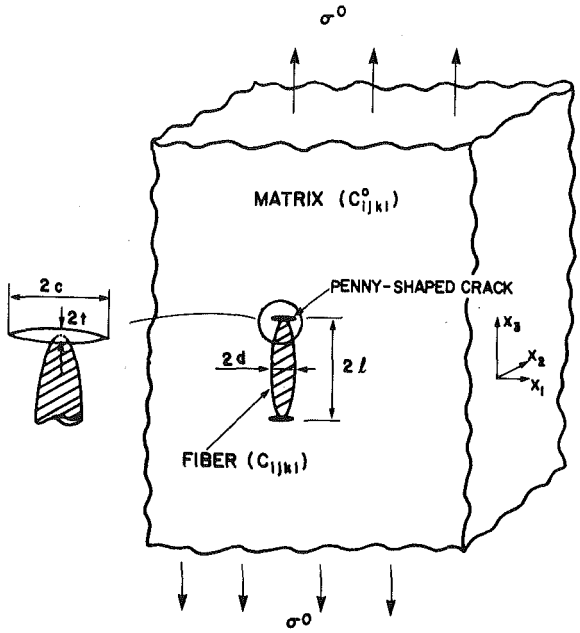

Fig. 2 A theoretical model

of a penny-shaped crack at a fiber-end, the total potential energy approach may require the least effort in the computation if one can find a simple method to compute the total potential energy of the composite containing fiber-end cracks. The equivalent inclusion method of Eshelby [2] is such a simple method by which we can compute energy-release rate in terms of the equivalent eigenstrains defined in the fiber and crack. This method also provides the overall stiffness of the composite weakened by fiber-end cracks.

A prediction of the overall stiffness of a composite has been well studied in the last two decades. However, a perfect bonding at the matrix-fiber interface was always assumed in the aforementioned model. If a volume fraction of fiber is small and fiber-end cracks are of small size, the interaction between fibers can be neglected. If the volume fraction is not small, the Eshelby's equivalent inclusion method can be modified such that the interaction is counted by an average back stress. The back stress can be again evaluated in terms of the eigenstrains as Mori and Tanaka [3] did.

The overall stiffness of a composite weakened by fiber-end cracks can be obtained by use of the modified Eshelby's equivalent method.

A Theoretical Model

A theoretical model considered in this paper is shown in Fig. 2 where the axis of uniaxial loading and fiber is along the x_3-direction. It is assumed in our model that the fiber is an ellipsoid elongated in the x_3-axis (the major axis l and the minor axis d) and the penny-shaped crack is also an ellipsoid but elongated in the x_1 and x_2-directions (the major axis c and the minor t). The stiffness tensors of the matrix and the fiber which are linear isotropic, are denoted by C^0_{ijkl} and C_{ijkl}, respectively. For later convenience the domain of the fiber and crack are denoted by Ω_f and Ω_c, respectively.

As an analytical tool we use "Eshelby's equivalent inclusion method" [2] by which an inhomogeneity is replaced by an inclusion with C^0_{ijkl} and unknown eigenstrain components. The eigenstrains in Ω_f and Ω_c are denoted by ϵ^*_{ij} and ϵ^{**}_{ij}, respectively. Once ϵ^*_{ij} and ϵ^{**}_{ij} are solved, we can compute the energy-release rate of a penny-shaped crack, G, and the longitudinal Young's modulus of a composite weakened by penny-shaped cracks at fiber-ends, E_L.

Energy-Release Rate of a Penny-Shaped Crack at the Fiber-End. The energy-release rate of a penny-shaped crack can be defined as

$$G = \left|\frac{\partial P}{\partial c}\right| \tag{1}$$

where P is the total potential energy; elastic energy plus the potential energy due to applied stress σ^0. Following Eshelby, the total potential energy P is given by

$$P = P_0 + E_{\text{int}} \tag{2}$$

where P_0 is the total potential energy without any inhomogeneity and E_{int} is called "the interaction energy" between the applied stress and the inhomogeneity. For our problem, E_{int} consists of two parts; E_{int} due to ϵ^*_{ij}, (E^*_{int}), and that due to ϵ^{**}_{ij}, (E^e_{int}). However, ϵ^*_{ij} has no contribution to $\partial P/\partial c$ since ϵ^*_{ij} is independent of c. Thus G is reduced to

$$G = \left|\frac{\partial E^e_{\text{int}}}{\partial c}\right| \tag{3}$$

where E^e_{int} is expressed by [2]

$$E^e_{\text{int}} = -\tfrac{1}{2}\,\sigma^0 \epsilon^{**}_{33}\, V_c$$

where V_c is the volume of a penny-shaped crack. We note in passing that there is an alternative way of defining the energy release rate of a penny-shaped crack [8, 11]. That is, G is given by $c\,|\partial P/\partial c|$ instead of equation (1); hence the dimension of G becomes "force." The energy-release rate G so defined is rather convenient if one would like to try to relate G to the energy conservation laws explored by Knowles and Steinberg [12].

The Longitudinal Young's Modulus of a Composite Weakened by Penny-Shaped Cracks at Fiber-Ends. There are basically two methods to compute the overall stiffness of a composite: (*i*) to compute the average stress and strain, and (*ii*) to compute the elastic energy. We take the latter approach to utilize the Eshelby's equivalent inclusion method. Under the assumption that the applied stress σ^0 in the x_3-direction (along the fiber axis) is kept constant, the equivalence of the elastic energy yields

$$\frac{\sigma^{0^2}}{2E_L} V = \frac{\sigma^{0^2}}{2E_0} V - E^c_{\text{int}} - E^f_{\text{int}} \tag{5}$$

where E_0 is Young's modulus of the matrix, E^c_{int} is given by equation (4) and E^f_{int} is defined by

$$E^f_{\text{int}} = -\tfrac{1}{2}\,\sigma^0 \epsilon^*_{33}\, V_f \tag{6}$$

and where V and V_f are the volume of a composite and fibers, respectively.

In computing G and E_L, we have only to solve for ϵ^*_{ij} and ϵ^{**}_{ij}. The method of solving for ϵ^*_{ij} and ϵ^{**}_{ij} as well as the computation of G and E_L will be discussed in the following section.

Solution Procedure

Two problems are solved successively in this section. The first problem is to find eigenstrain ϵ^*_{ij} and the disturbed stress σ^f_{ij} in Ω_f for an infinite elastic body containing fibers and subjected to the uniaxial applied stress σ^0. In the first problem the fiber-end crack is not considered for obtaining ϵ^*_{ij}, but the interaction between fibers is taken into account by the back stress analysis [3].

In the second problem the disturbed stress σ^c_{ij} in Ω_c is obtained in terms of ϵ^{**}_{ij} which is eigenstrain in Ω_c and still unknown. On the other hand, in the first problem the disturbed stress just outside the fiber-end, $\bar{\sigma}^f_{ij}$ is expressed in terms of σ^f_{ij} which is a function of ϵ^*_{ij}, C^0_{ijkl}, C_{ijkl}, and the geometry of the fiber [13–15]. Then, the total stress σ^t_{ij} in Ω_c, vanish:

$$\sigma^t_{ij} = \sigma^0_{ij} + \sigma^c_{ij}\,(\epsilon^{**}_{kl}) + \bar{\sigma}^f_{ij}\,(\epsilon^*_{kl}, C^0_{klmn}, C_{klmn}, l/d) = 0 \tag{7}$$

Thus we can solve for ϵ^{**}_{kl} from equation (7). The use of equation (7) implies that the interaction between fiber and a fiber-end crack is taken into account to some extent.

Computation of ϵ^*_{ij} and σ^f_{ij}. Based on the Eshelby's equivalent inclusion method and Mori and Tanaka's method on back stress analysis, we assume that the averaged disturbed stress in the matrix, $\langle \sigma_{ij} \rangle_M$ is given by

$$\langle \sigma_{ij} \rangle_M = C^0_{ijkl} \tilde{\epsilon}_{kl} \tag{8}$$

The equivalent inclusion method yields in Ω_f

$$\begin{aligned} \sigma^0_{ij} + \sigma_{ij} &= C^0_{ijkl}\,(\epsilon^0_{kl} + \tilde{\epsilon}_{kl} + \epsilon_{kl} - \epsilon^*_{kl}) \\ &= C_{ijkl}\,(\epsilon^0_{kl} + \tilde{\epsilon}_{kl} + \epsilon_{kl}) \end{aligned} \tag{9}$$

where

$$\begin{aligned} C^0_{ijkl} &= \lambda^0\,\delta_{ij}\,\delta_{kl} + \mu^0\,(\delta_{ik}\,\delta_{jl} + \delta_{il}\,\delta_{kj}) \\ C_{ijkl} &= \lambda \delta_{ij}\,\delta_{kl} + \mu(\delta_{ik}\,\delta_{jl} + \delta_{il}\,\delta_{kj}) \\ \epsilon_{kl} &= S_{klmn}\,\epsilon^*_{mn} \\ \sigma^0_{ij} &= C^0_{ijkl}\,\epsilon^0_{kl} \end{aligned} \tag{10}$$

From equations (9), $(10)^{3,4}$ we have in Ω_f

$$\sigma^f_{ij} = C^0_{ijkl}\,(\tilde{\epsilon}_{kl} + S_{klmn}\,\epsilon^*_{mn} - \epsilon^*_{kl}) \tag{11}$$

S_{klmn} in equation $(10)^3$ is called "the Eshelby's tensor" and is a function of C^0_{ijkl} and the geometry of the fiber, l/d. Explicit expressions for S_{klmn} are given in Appendix. In equation $(10)^{1,2}$ δ_{ij} is the Kronecker's delta, and λ^0 (λ) and μ^0 (μ) are the Lamé constants of the matrix (fiber). The geometry of fiber and the direction of applied stress (see Fig. 2 excluding a crack) yield two nonvanishing components of ϵ^*_{ij}, ϵ^*_{11} (or ϵ^*_{22}) and ϵ^*_{33}. An integration of the disturbed stress over the entire domain of a composite (V) yields

$$(1-f)\,\langle \sigma_{ij} \rangle_M + f \langle \sigma_{ij} \rangle_I = 0 \tag{12}$$

where f is a volume fraction of fiber, the symbol $\langle \sigma_{ij} \rangle$ indicates the volume average of σ_{ij}, and the subscripts M and I are for the matrix and the inclusion (fiber in our problem), respectively. A substitution of equations (8) and (11) into (12) yields

$$C^0_{ijkl}\,\tilde{\epsilon}_{kl} + f C^0_{ijkl}\,(S_{klmn}\,\epsilon^*_{mn} - \epsilon^*_{kl}) = 0 \tag{13}$$

By setting $ij = 11$ and 33 in equation (9), we obtain

$$C_{11}\,\epsilon^*_{11} + C_{12}\,\epsilon^*_{33} = -2D_1 e^0_{11} - e^0_{33} \tag{14}$$

$$C_{21}\,\epsilon^*_{11} + C_{22}\,\epsilon^*_{33} = -2e^0_{11} - D_2 e^0_{33} \tag{15}$$

where

$$\begin{aligned} C_{11} &= \frac{1}{2(1-\nu_0)}\left\{-1 + 6\nu_0 - \frac{2}{(\alpha^2-1)} + 3(1-2\nu_0)g\right\} \\ &\quad + \frac{1}{2(1-\nu_0)}\left(\frac{\mu-\mu_0}{\lambda-\lambda_0}\right)\left[1 + 2\nu_0 + \left\{1 - 2\nu_0 - \frac{3}{(\alpha^2-1)}\right\}g\right] \\ &\quad + 2\left(\frac{\lambda^0+\mu^0}{\lambda-\lambda^0}\right) \\ C_{12} &= 1 - \left(\frac{1-2\nu_0}{1-\nu_0}\right)g + \frac{1}{2(1-\nu_0)}\left(\frac{\mu-\mu^0}{\lambda-\lambda^0}\right)\left[-\frac{2\alpha^2}{(\alpha^2-1)}\right. \\ &\quad \left. + \left\{\frac{3\alpha^2}{(\alpha^2-1)} - (1-2\nu_0)\right\}g\right] + \frac{\lambda^0}{(\lambda-\lambda^0)} \\ C_{12} &= \frac{1}{2(1-\nu_0)}\left\{-1 + 6\nu_0 - \frac{2}{(\alpha^2-1)} + 3(1-2\nu_0)g\right\} \\ &\quad + \frac{2\lambda^0}{(\lambda-\lambda^0)} + \frac{2}{(1-\nu_0)}\left(\frac{\mu-\mu^0}{\lambda-\lambda^0}\right)\left[-(1-2\nu_0) - \frac{1}{(\alpha^2-1)}\right. \\ &\quad \left. + \left\{1 - 2\nu_0 + \frac{3}{2(\alpha^2-1)}\right\}g\right] \\ C_{22} &= 1 - \left(\frac{1-2\nu_0}{1-\nu_o}\right)g + \left(\frac{\lambda^0+2\mu^0}{\lambda-\lambda^0}\right) \\ &\quad + \frac{1}{(1-\nu_0)}\left(\frac{\mu-\mu^0}{\lambda-\lambda^0}\right)\left[1 - 2\nu_0 + \frac{(3\alpha^2-1)}{(\alpha^2-1)}\right. \\ &\quad \left. - \left\{1 - 2\nu_0 + \frac{3\alpha^2}{(\alpha^2-1)}\right\}g\right] \end{aligned} \tag{16}$$

$$\begin{aligned} D_1 &= 1 + \left(\frac{\mu-\mu^0}{\lambda-\lambda^0}\right) \\ D_2 &= 1 + 2\left(\frac{\mu-\mu^0}{\lambda-\lambda^0}\right) \end{aligned} \tag{17}$$

and where g is given in the Appendix, and

$$e^0_{ij} = \epsilon^0_{ij} + \tilde{\epsilon}_{in} \tag{18}$$

Noting that $\epsilon^0_{11} = -\nu_o \sigma_o / E_0$, $\epsilon^0_{33} = \sigma_0/E_0$, we solve for ϵ^*_{11} and ϵ^*_{33} in equations (14) and (15) to obtain

$$\epsilon^*_{11} = \frac{B_1}{A}\tilde{\epsilon}_{11} + \frac{B_2}{A}\tilde{\epsilon}_{33} + \frac{\sigma_0}{E_0}\frac{(B_2 - \nu_0 B_1)}{A} \tag{19}$$

$$\epsilon^*_{33} = \frac{B_3}{A}\tilde{\epsilon}_{11} + \frac{B_4}{A}\tilde{\epsilon}_{33} + \frac{\sigma_0}{E_0}\frac{(B_4 - \nu_0 B_3)}{A} \tag{20}$$

where

$$\begin{aligned} A &= C_{11}C_{22} - C_{21}C_{12} \\ B_1 &= 2(C_{12} - D_1 C_{22}) \\ B_2 &= D_2 C_{12} - C_{22} \\ B_3 &= 2(D_1 C_{21} - C_{11}) \\ B_4 &= C_{21} - D_2 C_{11} \end{aligned} \tag{21}$$

Next we solve for unknown $\tilde{\epsilon}_{ij}$ by equation (13). After some algebraic computation, we obtain

$$\tilde{\epsilon}_{11} = f\frac{S_1\sigma_0}{SE_0} \tag{22}$$

$$\tilde{\epsilon}_{33} = f\frac{S_2\sigma_0}{SE_0} \tag{23}$$

where

$$S_1 = \left\{\frac{2\nu_0}{(1-2\nu_0)} + f\frac{(H_{11}B_2 + H_{12}B_4)}{A}\right\} \times \frac{\{H_{21}(B_2 - \nu_0 B_1) + H_{22}(B_4 - \nu_0 B_3)\}}{A} - \left\{\frac{2(1-\nu_0)}{(1-2\nu_0)} + f\frac{(H_{21}B_2 + H_{22}B_4)}{A}\right\} \times \frac{\{H_{11}(B_2 - \nu_0 B_1) + H_{12}(B_4 - \nu_0 B_3)\}}{A}$$

$$S_2 = \left\{\frac{4\nu_0}{(1-2\nu_0)} + f\frac{(H_{21}B_1 + H_{22}B_3)}{A}\right\} \times \frac{\{H_{11}(B_2 - \nu_0 B_1) + H_{12}(B_4 - \nu_0 B_3)\}}{A} - \left\{\frac{2}{(1-2\nu_o)} + f\frac{(H_{11}B_1 + H_{12}B_3)}{A}\right\} \times \frac{\{H_{21}(B_2 - \nu_0 B_1) + H_{22}(B_4 - \nu_0 B_3)\}}{A}$$

$$S = \left\{\frac{2}{(1-2\nu_0)} + f\frac{(H_{11}B_1 + H_{12}B_3)}{A}\right\}\left\{\frac{2(1-\nu_0)}{(1-2\nu_0)} + f\frac{(H_{21}B_2 + H_{22}B_4)}{A}\right\} - \left\{\frac{4\nu_0}{(1-2\nu_0)} + f\frac{(H_{21}B_1 + H_{22}B_3)}{A}\right\} \times \left\{\frac{2\nu_0}{(1-2\nu_0)} + \frac{f(H_{11}B_2 + H_{12}B_4)}{A}\right\} \tag{24}$$

and where

$$H_{11} = 2\left\{\frac{2\nu_0}{(1-2\nu_0)}(S_{1111} + S_{1122} + S_{3311} - 1) + S_{1111} + S_{1122} - 1\right\}$$

$$H_{12} = \frac{2\nu_0}{(1-2\nu_0)}(2S_{1133} + S_{3333} - 1) + 2S_{1133}$$

$$H_{21} = \frac{4\nu_0}{(1-2\nu_0)}(S_{1111} + S_{1122} + S_{3311} - 1) + 4S_{3311}$$

$$H_{22} = \frac{2\nu_0}{(1-2\nu_0)}(2S_{1133} + S_{3333} - 1) + 2(S_{3333} - 1) \tag{25}$$

Thus the eigenstrain in Ω_f, ϵ^*_{ij} can be computed explicitly from equations (19), (20), (22), and (23) as

$$\epsilon^*_{11} = \left\{\frac{(B_2 - \nu_0 B_1)}{A} + \frac{f(B_1S_1 + B_2S_2)}{AS}\right\}\frac{\sigma^0}{E_0} \tag{26}$$

$$\epsilon^*_{33} = \left\{\frac{(B_4 - \nu_0 B_3)}{A} + \frac{f(B_3S_1 + B_4S_2)}{AS}\right\}\frac{\sigma^0}{E_0} \tag{27}$$

It should be noted that for a small f the terms carying f can be neglected and we recover the results for ϵ^*_{11} and ϵ^*_{33} by the Eshelby's method (without the back stress analysis).

From equations (11), (22), (23), (26), and (27), we can compute σ^f_{ij} in Ω_f as

$$\sigma^f_{11} = -\frac{(1-f)}{(1+\nu_0)(1-2\nu_0)}\frac{(S_1 + \nu_0)S_2)\sigma^0}{S} \tag{28}$$

$$\sigma^f_{33} = -\frac{(1-f)}{(1+\nu_0)(1-2\nu_0)}\frac{\{2\nu_0S_1 + (1-\nu_0)S_2\}\sigma^0}{S} \tag{29}$$

Computation of ϵ^{**}_{33}. In order to compute ϵ^{**}_{ij} by use of equation (7), we obtain first σ^c_{ij} and $\overline{\sigma}^f_{ij}$. Here we have considered only the interaction between a fiber and its end crack. Following the equivalent inclusion method, we have in Ω_c:

$$\sigma^c_{ij} = C^0_{ijkl}\,(S_{klmn}\,\epsilon^{**}_{mn} - \epsilon^{**}_{kl}) \tag{30}$$

where S_{ijkl} in equation (30) is the Eshelby's tensor for a penny-shaped crack and its nonvanishing components are given by

$$S_{1111} = S_{2222} = \frac{(13-8\nu_0)}{32(1-\nu_0)}\left(\frac{t}{c}\right)$$

$$S_{3333} = 1 - \frac{(1-2\nu_0)\pi}{4(1-\nu_0)}\left(\frac{t}{c}\right)$$

$$S_{1122} = S_{2211} = -\frac{(1-8\nu_0)\pi}{32(1-\nu_0)}\left(\frac{t}{c}\right)$$

$$S_{1133} = S_{2233} = -\frac{(1-2\nu_0)\pi}{8(1-\nu_0)}\left(\frac{t}{c}\right)\left\{1 - \frac{4}{\pi(1-2\nu_0)}\left(\frac{t}{c}\right)\right\}$$

$$S_{3311} = S_{3322} = \frac{\nu_0}{(1-\nu_0)}\left\{1 - \frac{(1+4\nu_0)\pi}{8\nu_0}\left(\frac{t}{c}\right)\right\} \tag{31}$$

where c and t are the major and minor axes of an ellipsoidal penny-shaped crack (see Fig. 2), and $c \gg t$ is assumed.

Next we obtain the stress just outside the fiber end, $\overline{\sigma}^f_{ij}$ expressed in terms of σ^f_{ij}, C^0_{ijkl}, and ϵ^*_{ij}. The relation between the stress jump across the interface of an inclusion and eigenstrain ϵ^*_{ij} in the inclusion can be written as [2, 13–15];

$$\overline{\sigma}^f_{ij} - \sigma^f_{ij} = C^0_{ijkl}\{-C^0_{pqmn}\epsilon^*_{mn}M_{kp}n_qn_l + \epsilon^*_{kl}\} \tag{32}$$

where

$$M_{kp} = \frac{1}{\mu^0}\left\{\delta_{kp} - \frac{n_kn_p}{2(1-\nu_0)}\right\} \tag{33}$$

and where n_i is the ith component of an unit vector outer normal to the inclusion, and is given by, at the fiber-end

$$\mathbf{n} = (0, 0, 1). \tag{34}$$

With equation, (34), equation (32) yields

$$\overline{\sigma}^f_{11} = \sigma^f_{11} + 2\mu^0\left(\frac{1+\nu_0}{1-\nu_0}\right)\epsilon^*_{11} \tag{35}$$

$$\overline{\sigma}^f_{33} = \sigma^f_{33} \tag{36}$$

A substitution of σ^c_{ij} and $\overline{\sigma}^f_{ij}$ (equations (26)–(30), (35), and (36)) into equation (7) yields

$$\epsilon^{**}_{33} = 4(1-\nu_0^2)\,(1+F)\left(\frac{c}{\pi t}\right)\frac{\sigma^0}{E_0} \tag{37}$$

where

$$F = -\frac{(1-f)}{(1+\nu_0)(1-2\nu_0)}\frac{\{2\nu_0S_1 + (1-\nu_0)S_2\}}{S} \tag{38}$$

Computation of Energy-Release Rate G. The interaction energy between the uniaxial applied stress σ^0 and eigenstrain in Ω_c, ϵ^{**}_{ij} is given by equation (4). Thus E^c_{int} can be expressed as

$$E^c_{\text{int}} = -\frac{1}{2}\sigma^0\epsilon^{**}_{33}\,V_c = -\frac{8}{3}\frac{\sigma_0^2c^3(1-\nu_0^2)}{E_0}(1+F) \tag{39}$$

where $V_c = 4\pi c^2t/3$ is used. From equations (3) and (39) the energy-release rate of a penny-shaped crack at fiber-end, G is obtained as

$$G = \frac{8\sigma_0^2\,c^2(1-\nu_0^2)}{E_0}(1+F) \tag{40}$$

Computation of Longitudinal Young's Modulus E_L. By assuming that the major axis of the penny-shaped crack c is equal to the minor axis of the fiber d (this is reasonable at the early part of stage 2), we can solve for E_L through equations (4)–(6), and (37)

$$\frac{E_L}{E_0} = \frac{1}{1+\eta f} \tag{41}$$

where

$$\eta = \frac{(B_4 - \nu_0 B_3)}{A} + f\frac{(B_3 S_1 + B_4 S_2)}{AS} + \frac{8(1-\nu_0^2)(1+F)}{\pi\alpha} \quad (42)$$

Results and Discussion

We take $\nu_0 = 0.35$ and $\nu = 0.3$ throughout our computation. The major parameters are hence l/d, E/E_0, and f.

Energy-Release Rate G. When a penny-shaped crack is embedded in a pure matrix; $E/E_0 = 1$, $\nu = \nu_0$, a simple computation yields

$$F = 0 \quad (43)$$

In this case equations (39) and (40) are reduced by

$$E^c_{\text{int}} = -\frac{8\sigma_0^2 c^3(1-\nu_0^2)}{3E_0} \quad (44)$$

$$G_0 = \frac{8\sigma_0^2 c^2(1-\nu_0^2)}{E_0} \quad (45)$$

where G for the case of pure matrix surrounding a penny-shaped crack is set as G_0.

Equation (44) has been obtained by Sack [16] and Eshelby [2].[2] Irwin [5] derived crack-extension force f for a penny-shaped crack:

$$f = \frac{4\sigma_0^2 c(1-\nu_0^2)}{\pi E_0} \quad (46)$$

In order to obtain 3-dimensional energy-release rate for a penny-shaped crack, we multiply f by $2\pi c$ to recover equation (45).

In the case of a penny-shaped crack at a fiber-end, the energy-release rate G is computed and the results are plotted in Fig. 3 where the solid and dashed curves are for small f (= 0.05) and large f (= 0.20), respectively. Also two cases of l/d; 10 and 100, are focused on in order to study the effect of l/d on G. It follows from Fig. 3 that the energy-release rate G increases as the stiffness of the fiber increases compared with that of the matrix, but its values will reach the asymptotic ones at large E/E_0. The larger the aspect ratio of the fiber, the larger is the value of G. This is more enhanced for smaller f. As for the range of the parameters of a typical commercial short fiber composite, $l/d = 50 \sim 100$, $E/E_0 = 000$, $f = 0.2 \sim 0.3$. Then the corresponding energy-release rate $G \approx 5G_0$.

It should be noted that the present results for G are valid for the early part of stage 2 deformation where the magnitude of a penny-shaped crack at the fiber-end is considered to be small, i.e., the radius of the crack c being approximately equal to that of the fiber d. When a penny-shaped crack is extended in the matrix to a large extent such that the order of c becomes that of the fiber length l, the following two cases are identified as important problems to be solved:

(i) A penny-shaped crack extends in the matrix, but does not touch the neighboring fibers.

(ii) A penny-shaped crack is arrested by the neighboring fibers.

Even though the geometry of the first case is similar to the present model (Fig. 2), we cannot use the present method to obtain the energy-release rate of the crack because the present method neglects the interaction between cracks and also that between a penny-shaped crack and the neighboring fibers.[3] The second case is reduced to a problem of a crack meeting the fiber-matrix interface at a right angle. Both cases are now under investigation by one of the present authors.

Longitudinal Young's Modulus E_L. The values of E_L normalized by the matrix Young's modulus E_0 are computed by equations (41) as a function of f for the following three cases:

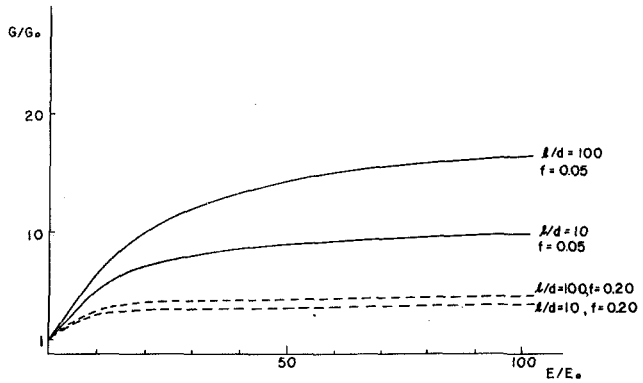

Fig. 3 The energy-release rate of a penny-shaped crack at a fiber-end, G normalized by that in a pure matrix (without fibers), G_0 versus E/E_0

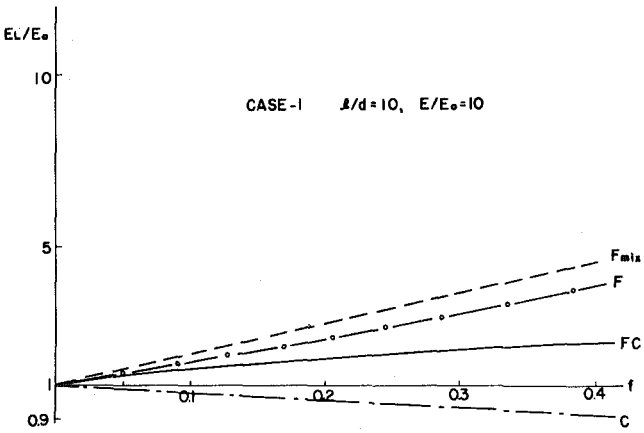

Fig. 4 The longitudinal Young's modulus of a composite, E_L normalized by the matrix Young's odulus E_0 versus f for Case 1: $l/d = 10$, $E/E_0 = 10$

Case 1: $l/d = 10$, $E/E_0 = 10$
Case 2: $l/d = 10$, $E/E_0 = 100$
Case 3: $l/d = 100$, $E/E_0 = 100$

The results are plotted by the solid curves in Figs. 4–6 for Cases 1, 2, and 3, respectively. In order to check the validity of our results, two extreme cases are investigated; (i) to compute E_L when the penny-shaped crack at the fiber-end, and (ii) to compute E_L when the existence of the fiber is neglected, i.e., the composite contains only penny-shaped cracks. Obviously the first and second cases yield a kind of the upper and lower bound on E_L, the longitudinal Young's modulus of the composite containing fibers and fiber-end cracks. Furthermore two methods are used to compute E_L for the first case: (a) law of mixture and (b) the modified Eshelby's method (the present method). For our convenience, four methods to compute E_L are categorized as

Method F_{mix}: To compute E_L of the composite with *fibers only* by law of mixture

$$\frac{E_L}{E_0} = \frac{E}{E_0} f + 1 - f \quad (47)$$

Method F: To compute E_L of the composite with *fibers only* by the present method

$$\frac{E_L}{E_0} = \frac{1}{1+\eta_F f}$$

$$\eta_F = \frac{B_4 - \nu_0 B_3}{A} + f\frac{(B_3 S_1 + B_4 S_2)}{AS} \quad (48)$$

[2] There is a misprint in the expression of E^c_{int} on Page 394 of reference [2].

[3] We thank Prof. A. S. Kobayashi for his valuable comments on the validity of the present model.

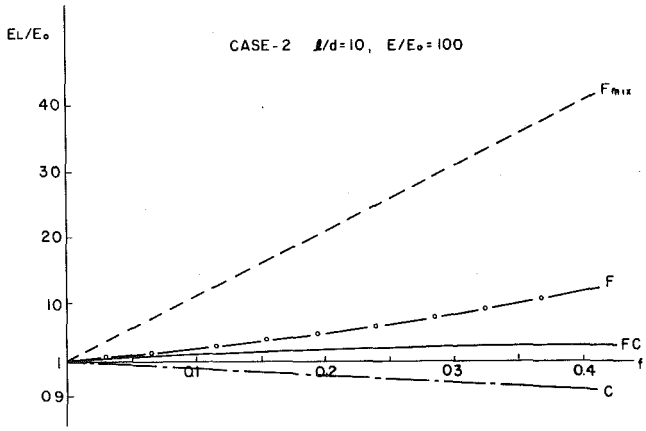

Fig. 5 The longitudinal Young's modulus of a composite, E_L normalized by the matrix Young's Modulus E_0 versus f for Case 2: $l/d = 10$, $E/E_0 = 100$

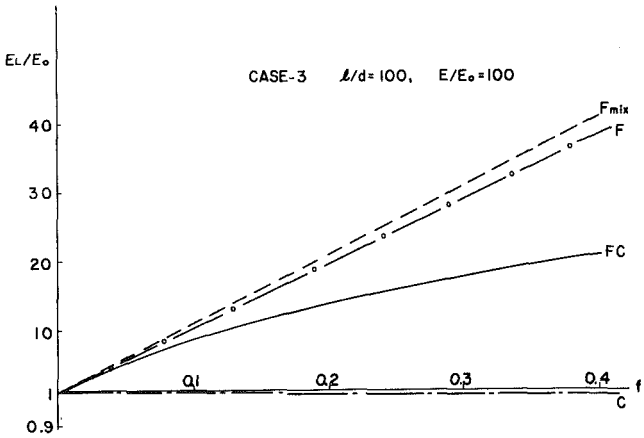

Fig. 6 The longitudinal Young's modulus for a composite, E_L normalized by the matrix Young's modulus E_0 versus f for Case 3: $l/d = 100$, $E/E_0 = 100$

Method FC: To compute E_L of the composite with *fibers and fiber-end cracks* by the present method (equations (41) and (42))

Method C: To compute E_L of the composite with *penny-shaped cracks only* by

$$\frac{E_L}{E_0} = \frac{1}{1 + \dfrac{8(1-\nu_0^2)}{\alpha\pi} f} \tag{49}$$

The results by equations (47)–(49) are plotted by the dashed (F_{mix}), dash-circle (F), and dash-dot curves (C) in Figs. 4–6. It should be noted that the validity of Method FC (the present results) is correlated to that of Method F since both of them are based on the present method.

It can be seen from Figs. 4–6 that the present results (FC) remain always between the curves F and C for various values of l/d and E/E_0. Thus the validity of the present results is justified.

Next the degree of the reduction in E_L of the composite due to fiber-end cracks is studied. To this end E_L obtained by Method F is assumed to be the correct longitudinal Young's modulus before fiber-end cracks are initiated. Then we compute the ratio $(E_L)_{FC}$ to $(E_L)_F$ where the subscripts FC and F denote, respectively, the composite with fibers and fiber-end cracks, and that with fibers only. The results of $(E_L)_{FC}/(E_L)_F$ are plotted for a fixed $l/d = 50$ (in Fig. 7) and $E/E_0 = 50$ (in Fig. 8) with f being a parameter. It follows from Figs. 7 and 8 that the larger f (or E/E_0) is, or the smaller l/d is, more reduction in the longitudinal stiffness of the composite due to fiber-end cracks is expected.

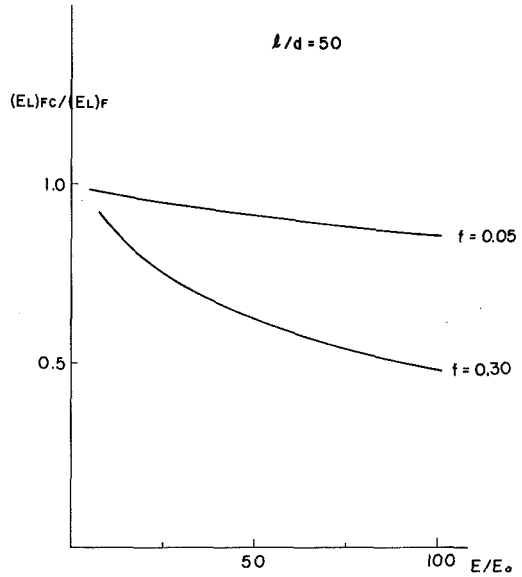

Fig. 7 E_L weakened by fiber-end cracks, $(E_L)_{FC}$ normalized by E_L of a composite without fiber-end cracks, $(E_L)_F$ versus E/E_0 for $l/d = 50$

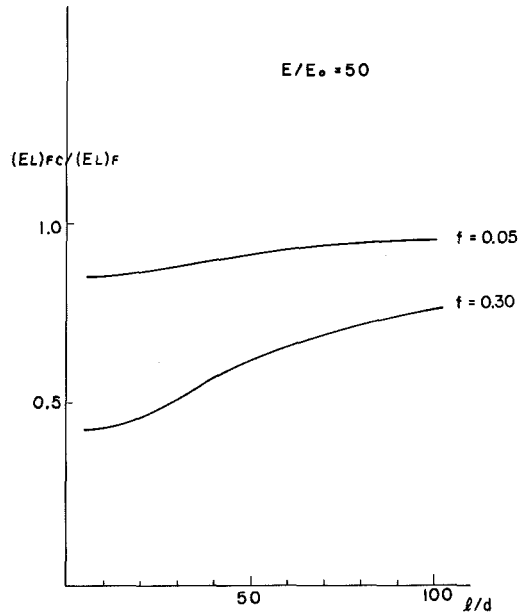

Fig. 8 E_L weakened by fiber-end cracks, $(E_L)_{FC}$ normalized by E_L of a composite without fiber-end cracks, $(E_L)_F$ versus E/E_0 for $E/E_0 = 50$

References

1 Curtis, R. T., Bader, M. G., and Bailey, J. E., "The Stiffness and Strength of a Polyamide Thermoplastic Reinforced With Glass and Carbon Fibers," *Journal of Material Science*, Vol. 13, 1978, pp. 377–390.

2 Eshelby, J. D., "The Determination of the Elastic Field of an Ellipsoidal Inclusion, and Related Problems," *Proceedings of the Royal Society*, London, Series A, Vol. 241, 1957, pp. 376–396.

3 Mori, T., and Tanaka, K., "Average Stress in Matrix and Average Elastic Energy of Materials With Misfitting Inclusions," *Acta Metallurgica*, Vol. 21, May 1973, pp. 571–574.

4 Taya, M., and Chou, T. W., "On a Path-Dependence of 3-D J-Integrals Applied to Fiber-End Cracks in Composites," 16th Annual Meeting Society of Engineering Science, Northwestern University, Sept. 1979, p. 81 of the Abstract.

5 Irwin, G. R., "Crack Extension Force for a Part-Through Crack in a

Plate," ASME JOURNAL OF APPLIED MECHANICS, Vol. 29, Dec. 1962, pp. 651–654.

6 Kassir, M. K., and Sih, G. C., "Three-Dimensional Stress Distribution Around an Elliptical Crack Under Arbitrary Loadings," ASME JOURNAL OF APPLIED MECHANICS, Vol. 33, 1966, pp. 601–611.

7 Mura, T., and Lin, S. C., "Thin Inclusions and Cracks in an Isotropic Media," ASME JOURNAL OF APPLIED MECHANICS, Vol. 41, 1974, pp. 209–214.

8 Budiansky, B., and O'Connel, R. J., "Elastic Moduli of a Cracked Solid," *International Journal of Solids and Structures*, Vol. 12, 1976, pp. 81–97.

9 Pacella, A. H., and Erdogan, F., "A Penny-Shaped Crack in a Filament-Reinforced Matrix-II. The Crack Problem," *International Journal of Solids and Structures*, Vol. 10, 1974, pp. 807–819.

10 Sanchez-Moya, V., and Pipkin, A. C., "Energy-Release Rate for Cracks in Ideal Composites," *International Journal of Solids and Structurers*, Vol. 13, 1977, pp. 571–578.

11 Budiansky, B., and Rice, J. R., " Conservation Laws and Energy-Release Rates," ASME JOURNAL OF APPLIED MECHANICS, Vol. 40, Mar. 1973, pp. 201–203.

12 Knowles, J. K., and Sternberg, E., "On a Class of Conservation Laws in Linearized and Finite Elastostatics," *Archive for Rational Mechanics and Analysis*, Vol. 44, No. 3, 1972, pp. 187–211.

13 Mura, T., and Cheng, P. C., "The Elastic Field Outside an Ellipsoidal Inclusion", ASME JOURNAL OF APPLIED MECHANICS, Vol. 44, Dec. 1977, pp. 591–594.

14 Hill, R., "Discontinuity Relations in Mechanics on Solids," in *Progress in Solid Mechanics* 2, eds. Sneddon, I.N., and Hill, R., North-Holland, Amsterdam, 1961, pp. 245–276.

15 Walpole, L. J., "The Elastic Field of an Inclusion in an Anisotropic Medium," *Proceedings of the Royal Society*, London, Series A, Vol. 300, 1967, pp. 270–289.

16 Sack, R. A., "Extension of Griffith's Theory of Rupture to Three Dimensions," *Proceedings of the Physical Society*, London, Vol. 58, 1946, pp. 729–736.

APPENDIX

The Eshelby's tensor S_{ijkl} for an ellipsoidal fiber with major axis l and minor axis d are expressed by

$$S_{1111} = S_{2222} = \frac{3}{8(1-\nu)}\frac{\alpha^2}{(\alpha^2-1)} + \frac{1}{4(1-\nu_0)}\left\{1 - 2\nu_0 - \frac{9}{4(\alpha^2-1)}\right\}g$$

$$S_{3333} = \frac{1}{2(1-\nu_0)}\left[\left[1 - 2\nu_0 + \frac{(3\alpha^2-1)}{(\alpha^2-1)} - \left\{1 - 2\nu_0 + \frac{3\alpha^2}{(\alpha^2-1)}\right\}g\right]\right]$$

$$S_{1122} = S_{2211} = \frac{1}{4(1-\nu_0)}\left\{\frac{\alpha^2}{2(\alpha^2-1)} - (1-2\nu_0) - \frac{3}{4(\alpha^2-1)}g\right\}$$

$$S_{1133} = S_{2233} = -\frac{1}{2(1-\nu_0)}\frac{\alpha^2}{(\alpha^2-1)} + \frac{1}{4(1-\nu_0)}\left\{\frac{3\alpha^2}{(\alpha^2-1)} - (1-2\nu_0)\right\}g$$

$$S_{3311} = S_{3322} = -\frac{1}{2(1-\nu_0)}\left\{1 - 2\nu_0 + \frac{1}{(\alpha^2-1)}\right\} + \frac{1}{2(1-\nu_0)}\left\{1 - 2\nu_0 + \frac{3}{2(\alpha^2-1)}\right\}g$$

where ν_0 is Poisson's ratio of a matrix, α is aspect ratio of a fiber $(=l/d)$, and g is given by

$$g = \frac{\alpha}{(\alpha^2-1)^{3/2}}\{\alpha(\alpha^2-1)^{1/2} - \cosh^{-1}\alpha\}$$

B. Prasad

Engineering and Research Staff,
Metallurgy Department,
Ford Motor Company,
P. O. Box 2053,
Dearborn, Mich. 48121
Mem. ASME

On the Stability of a Composite Beam With Initial Stress to Moving Loads

When an axial compressive force is present, the wavelength of a propagating free wave in a beam rapidly decreases [1]. The conventional Bernoulli-Euler beam equations are often not adequate for determining dynamic behavior of a composite beam with initial stress due to a moving load. However, for the stability of the composite beam, when it is expressed in a nondimensional form, it is shown here that both the systems (Bernoulli-Euler beam and Timoshenko beam) behave identically. The investigation is based on the equations derived by Sun [2] for a composite beam wherein each constituent layer of the composite beam is regarded as a Timoshenko beam. The beam consists of five stiff layers and four soft layers.

Analytical expressions of the critical velocity as a function of initial axial stress and foundation modulus parameters are derived for the composite beam. Critical velocities are also obtained on the basis of Bernoulli-Euler beam equations and the results compared.

Analysis Based on Microstructure Theory

Sun [2] has proposed a microstructure theory, for a laminated beam under initial stress, consisting of a large number of alternating layers of two different elastic materials. The equations of motion are expressed as

$$b_1\frac{\partial^2 w}{\partial x^2} - b_2\frac{\partial \psi}{\partial x} - b_3\frac{\partial \phi}{\partial x} + \frac{P}{\xi} = b_4\frac{\partial^2 w}{\partial t^2} \tag{1}$$

$$b_2\frac{\partial w}{\partial x} + b_5\frac{\partial^2 \psi}{\partial x^2} - b_6\psi - b_7\frac{\partial^2 \phi}{\partial x^2} + b_8\phi = b_9\frac{\partial^2 \psi}{\partial t^2} - b_{10}\frac{\partial^2 \phi}{\partial t^2} \tag{2}$$

$$b_3\frac{\partial w}{\partial x} - b_7\frac{\partial^2 \psi}{\partial x^2} + b_8\psi + b_{11}\frac{\partial^2 \phi}{\partial x^2} - b_{12}\phi = -b_{10}\frac{\partial^2 \psi}{\partial t^2} + b_{13}\frac{\partial^2 \phi}{\partial t^2} \tag{3}$$

All quantities entering these equations are defined in [2].

If the beam is supported on a Winkler-type foundation (with stiffness k and damping constant β_0) and is subjected to a load F_0 moving with a constant velocity v, the quantity p in equation (1) becomes

$$p(x,t) = F_0\,\delta(x - vt) - kw - \beta_0\frac{\partial w}{\partial t} \tag{4}$$

Stipulating a steady-state solution with $r = x - vt$,

$$n = \sigma_1{}^0A_1 + \sigma_2{}^0A_2; \quad W = w/r_1; \quad R = r/r_1$$

and assuming that dependent variables W, ϕ, and ψ and their first derivatives approach zero at infinity, the solutions of (1)–(3) may be constructed with the use of Fourier transform technique.

Introducing the following nondimensional quantities

$$N_1 = \frac{\sigma_1{}^0}{G_1}, N_2 = \frac{\sigma_2{}^0}{G_2}, v_0 = \sqrt{G_2/\rho_2}, F^* = \frac{F_0}{(b_1 - n)\xi} \tag{5}$$

$$\alpha = \frac{kr_1{}^2}{(b_1 - n)\xi}, \beta = \frac{\beta_0 r_1 v_0}{2\xi(b_1 - n)}, \Gamma = \frac{G_1}{G_2}, \lambda = \frac{\rho_1}{\rho_2} \tag{6}$$

$$\theta = \frac{v}{v_0}, \eta = \frac{d_1}{d_1 + d_2}, \xi = \frac{h}{d_1 + d_2}, \eta_0 = \frac{b_1}{(b_1 - n)} \tag{7}$$

$$\eta_1 = \frac{(b_1 - n)}{b_2}, \eta_2 = \frac{b_5}{(b_1 - n)r_1{}^2},$$

$$\eta_3 = \frac{b_7}{(b_1 - n)r_1{}^2}, \eta_4 = \frac{b_{11}}{(b_1 - n)r_1{}^2} \tag{8}$$

$$\alpha_1 = \frac{(b_1 - n)}{b_4 v_0{}^2}, \alpha_2 = \frac{b_5}{b_9 v_0{}^2}, \alpha_3 = \frac{b_7}{b_{10} v_0{}^2}, \alpha_4 = \frac{b_{11}}{b_{13} v_0{}^2} \tag{9}$$

and following the procedure similar to reference [3], the transformed solutions for $\overline{W}, \overline{\psi}$, and $\overline{\phi}$ can be expressed as

$$\overline{W} = \frac{F^*(s^4p_4 + s^2p_2 + 1)}{\Delta_0} \tag{10}$$

$$\overline{\psi} = \frac{F^* is(s^2p_5 + 1)}{\Delta_0} \tag{11}$$

$$\overline{\phi} = \frac{F^* is(s^2p_6 + 1)}{\Delta_0} \tag{12}$$

where

$$\Delta_0 = (s^2p_1 - 2\beta\theta is + \alpha)(s^4p_4 + s^2p_2 + 1) - s^2(s^2p_3 + 1) \tag{13}$$

is a sixth-order polynomials, in s, with real and imaginary coefficients.

Determination of Resonant Speeds

The characteristic equation, Δ_0, equation (13) can be replaced with

Contributed by the Applied Mechanics Division of THE AMERICAN SOCIETY OF MECHANICAL ENGINEERS, and presented at the 1981 Joint ASME/ASCE Applied Mechanics, Fluids Engineering, and Bioengineering Conference, University of Colorado, Boulder, Colo., June 22–27, 1981.

Discussion on this paper should be addressed to the Editorial Department, ASME, United Engineering Center, 345 East 47th Street, New York, N. Y. 10017, and will be accepted until September 1, 1981. Readers who need more time to prepare a Discussion should request an extension from the Editorial Department. Manuscript received by ASME Applied Mechanics Division, October, 1979; final revision, October, 1980. Paper No. 81-APM-25.

real coefficients by making a simple substitution, $q = is$. The result is, after rearrangement,

$$\Delta_0 = [-q^6 p_1 p_4 - 2\beta\theta p_4 q^5 - (p_3 - p_1 p_2 - \alpha p_4) q^4 + 2\beta\theta p_2 q^3 - (p_1 + \alpha p_2 - 1) q^2 - 2\beta\theta q + \alpha] \quad (14)$$

The true critical velocities for the composite beam occur for the cases when the characteristic equation (13) possesses double roots, $s = \pm a, \pm a, \pm ib$. This is a limiting form of Case 3 mentioned in reference [3, Table 1] which is in general of the type; $\pm a_1, \pm a_2$, and $\pm ib_3$.

For this particular case the inversion integrals are of the form

$$\int_{-\infty}^{\infty} \frac{dx}{(s-a)^2} \quad \text{and} \quad \int_{-\infty}^{\infty} \frac{dx}{(s+a)^2} \quad (15)$$

where s and a are both real.

It is well known that an integral of the type (15) does not exist even in the sense of a Cauchy principal value. It was discussed in [3] that such nonexistence of a solution to a physical problem, implies a resonance, in the sense that the displacement becomes unbounded. The value of the load velocity parameter θ, which yields an integral of the type (15) defines the critical load velocities.

The characteristic equation Δ_0 for $\beta = 0$ can be written as

$$s^6 p_1 p_4 - s^4 (p_3 - p_1 p_2 - p_4) + s^2 (p_1 + \alpha p_2 - 1) + \alpha = 0 \quad (16)$$

Imposing the condition of double roots and eliminating b, one can find using equation (16), a condition in terms of θ, which is

$$3a^4 + 2e_2 a^2 + e_3 = 0 \quad (17)$$

where a^2 is obtained as

$$a^2 = (e_3 e_2 - 9e_4)/(6e_3 - 2e_2^2) \quad (18)$$

and e_2, e_3, e_4 are defined as

$$e_2 = (p_1 p_2 + \alpha p_4 - p_3)/p_1 p_4 \quad (19)$$

$$e_3 = (p_1 + \alpha p_2 - 1)/p_1 p_4 \quad (20)$$

and

$$e_4 = \alpha/p_1 p_4 \quad (21)$$

$p_1, p_2 \ldots p_4$ are functions of only the load velocity parameter θ. They are defined in reference [3]. Real values of θ for which equation (17) is satisfied, are the resonant speeds.

Comparison of Critical Velocities

A periodically layered composite beam of two elastic materials, Fig. 1, can also be considered as a homogeneous beam without microstructure with its effective moduli so determined that it predicts the gross or net behavior of the composite beam. A very widely used approach in evaluating the gross elastic property of a composite material is the rule of mixtures, through which the effective Young's modulus and the effective shear modulus are obtained as [5]

$$E = \eta E_1 + (1-\eta) E_2; \quad G = \eta G_1 + (1-\eta) G_2 \quad (22)$$

Taking the effective mass density and the effective initial stress to be

$$\rho = \eta\rho_1 + (1-\eta)\rho_2; \quad \sigma^0 = \eta\sigma_1{}^0 + (1-\eta)\sigma_2{}^0 \quad (23)$$

we can then regard the composite beam as an equivalent homogeneous beam. Based on the analysis of an Bernoulli-Euler differential equation of a beam which is given as

$$EI \frac{d^2 w}{dx^2} - \sigma^0 A \frac{d^2 w}{dx^2} + m \frac{d^2 w}{dt^2} + kw = p\delta(x,t) \quad (24)$$

(σ^0 is a tensile axial stress and m is the mass per unit length), Kerr [4] has given an expression for the critical velocity of the beam subjected to a unfiorm tensile stress σ^0 as

$$v_{cr} = \left[\sqrt{\frac{4kEI}{m^2} + \frac{\sigma^0 A}{m}}\right]^{1/2} \quad (25)$$

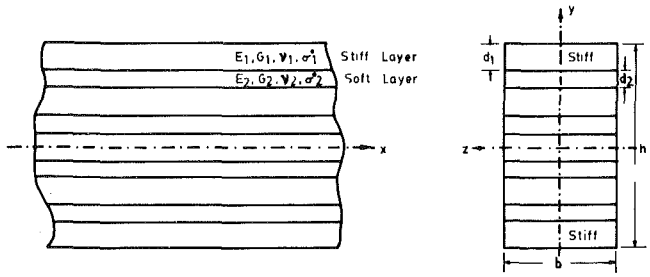

Fig. 1 Layout of composite beam

Dividing both sides of the equation (25) by v_0 and replacing m by pA, we get

$$v_{cr}/v_0 = \theta_{cr} = \left[2\sqrt{\frac{kEI}{\rho^2 A^2 v_0{}^4}} + \frac{\sigma^0}{\rho v_0{}^2}\right]^{1/2} \quad (26)$$

Utilizing the properties of the equivalent homogeneous beam characterized by equations (22)–(23) and the relations,

$$\frac{A_1}{A} = \frac{\eta}{\xi}; \quad \frac{A_2}{A} = \frac{1-\eta}{\xi}; \quad \frac{Ar_1{}^2}{I} = \left(\frac{\eta}{\xi}\right)^2 \quad (27)$$

We can express the equation (26) in terms of nondimensional constants; some are defined in equations (5)–(9). Defining some additional ones as

$$\delta_1 = \frac{\sigma^0}{\rho v_0{}^2} = \frac{N\alpha_1}{\kappa} \quad \text{and} \quad \delta_2 = \frac{E(b_1 - n)\xi}{\rho^2 A v_0{}^4}$$

We thus have for $N_1 = N_2 = N$

$$\theta_{cr} = \left[2\left(\frac{\xi}{\eta}\right)\sqrt{\alpha\delta_2} + N\alpha_1/\kappa\right]^{1/2} \quad (28)$$

It is clear from equation (28) that the effect of compressive initial axial stress is to decrease the critical velocity of the Bernoulli-Euler beam; a phenomenon which is also observed with equation (17). It is therefore of interest to compare the critical velocities and its dependence on α and N derived in the previous section with that predicted by Kerr [4] using the Bernoulli-Euler beam equations. It may be noticed that in the case of the Bernoulli-Euler beam formulation, the expression for N_{cr} can be obtained easily from (28) by setting $\theta_{cr} \to 0$, i.e.,

$$N_{cr} = -2\kappa\xi\sqrt{\alpha\delta_2}/(\eta\alpha_1) \quad (29)$$

Also when $N_1 = N_2 = 0$, equation (28) reduces to

$$\theta_{cr|_{N=0}} = \left[2\left(\frac{\xi}{\eta}\right)\sqrt{\alpha\delta_2}\right]^{1/2} \quad (30)$$

Using equations (29) and (30), equation (28) can be rewritten in the following form:

$$\frac{\theta^2_{cr}}{\theta^2_{cr|_{N=0}}} + \frac{N}{N_{cr}} = 1 \quad (31)$$

Since N is negative, a positive fraction for N/N_{cr} denotes the fraction of compressive stress value.

It can be noticed that the relationship between $\theta_{cr}/\theta_{cr|_{N=0}}$ and N/N_{cr} is independent of α. A question can be raised whether a similar relationship exist for the composite beam formulation. It does not seem apparent looking at the expression (17) that such a relationship would exist. However, it has been verified numerically that the plots between $\theta_{cr}/\theta_{cr|_{N=0}}$ and N/N_{cr} for the Sun's derivation are identical with that of Bernoulli-Euler beam formulation. It has also been observed with considerable interest that such a relationship is independent of α, the foundation modulus parameter. A graphical representation of equation (31) is shown in Fig. 2 for a composite beam consisting of five stiff layers and four soft layers (sketched in Fig. 1).

$\Gamma = 100, \lambda = 2, \eta = 0.8, \xi = 4.8, \nu_1 = 0.2, \nu_2 = 0.35, \kappa = 0.822$

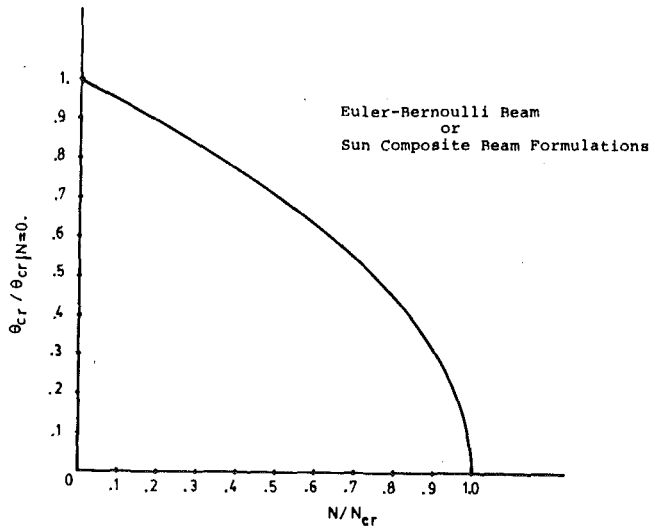

Fig. 2 Relationship between the ratios of critical velocity versus initial axial force

These parameters are the same as originally used in references [2, 3] for plotting the dispersion curves for the flexural waves.

Results and Discussion

It has been observed from Fig. 2 that the ratios of the critical velocities $\theta_{cr}/\theta_{cr}|_{N=0}$ when plotted against N/N_{cr} are independent of the magnitude of the foundation modulus parameters, α on which beam is supported. It is interesting to note that the relationship is valid for composite beam theory, wherein each lamina is considered as Timoshenko beam, as well as the equivalent modulus theory based on Bernoulli-Euler beam equations. Fig. 3 shows the effect of critical velocity on the magnitude of the initial axial force N, when they are plotted in unscaled terms. Three curves are plotted for three representative values of $\alpha(\alpha = 0.1, 0.5$ and $1.0)$. It is observed from this figure that the behaviors of θ_{cr} versus N are dependent on the values of α. Similar type of curves though not shown here (see reference [6]) has been found based on the Bernoulli-Euler beam theory which also depends on α. The ratio of N/N_{cr} when plotted against $\theta_{cr}/\theta_{cr}|_{N=0}$ (as shown in Fig. 2) has however, the effect of coalescing all the different curves (shown in Fig. 3) into a single one.

Concluding Remarks

The expression of the true critical velocity of a composite beam is obtained in terms of elastic modulus (α) and initial stress (N) parameters. In deriving such expression as shown here (as opposed to reference [4] for the Bernoulli-Euler beam) it is not essential to find analytical solutions, i.e., the inverse Fourier transforms of the response quantities. The results of this investigation show some interesting features like the one shown in Fig. 2, which indicates that not only the independency of the scaled variables exists with respect to α (foundation modulus parameter) but also with respect to the basic mathematical systems (Bernoulli-Euler or composite beams) from which it is derived. The relationship between the unscaled variables however, has different (see Fig. 3) behaviors.

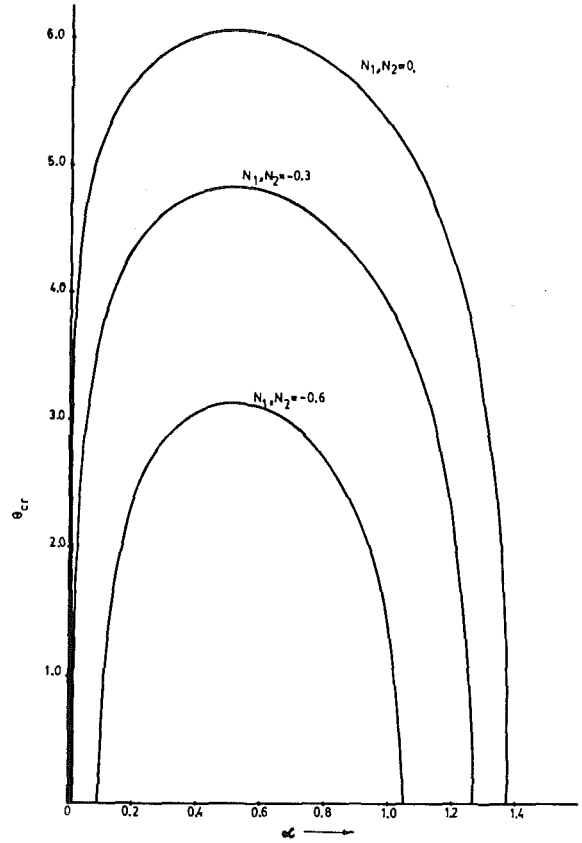

Fig. 3 Dependence of critical velocity θ_{cr} on the foundation modulus

References

1 Herrmann, G., and Armerakas, A. E., "Vibration and Stability of Plates Under Initial Stress," *Journal of Engineering Mechanics Division, ASCE*, Vol. 86, 1960, pp. 65.

2 Sun, C. T., "On the Equations for a Composite Beam Under Initial Stress," *International Journal of Solids and Structures*, Vol. 8, No. 3, 1972, pp. 385–399.

3 Prasad, B., and Herrmann, G., "Response of a Laminated Beam to a Moving Load," *AIAA Journal*, Vol. 15, No. 10, Oct. 1977, pp. 1424–1431.

4 Kerr, A. D., "The Continuously Supported Rail Subjected to an Axial Force and Moving Load," *International Journal of Mechanical Sciences*, Vol. 14, 1972, pp. 71–78.

5 Voigt, W., *Lehrbuch des Kristallphysik*, Teubner, 1928, pp. 962.

6 Prasad, B., and Garg, V. K., "Stability of a Timoshenko Beam Under Initial Stress to a Moving Load," *Proceedings of the 16th Midwestern Conference*, September 19–21, 1979.

C. W. Bert
Perkinson Professor of Engineering.
Mem. ASME

J. N. Reddy[1]
Associate Professor.
Mem. ASME

W. C. Chao[2]
Graduate Research Assistant.

V. S. Reddy[3]
Graduate Research Assistant.

School of Aerospace, Mechanical, and Nuclear Engineering,
The University of Oklahoma,
Norman, Okla. 73019

Vibration of Thick Rectangular Plates of Bimodulus Composite Material

A finite-element analysis is carried out for small-amplitude free vibration of laminated, anisotropic, rectangular plates having arbitrary boundary conditions, finite thickness shear moduli, rotatory inertia, and bimodulus action (different elastic properties depending upon whether the fiber-direction strain is tensile or compressive). The element has five degrees of freedom, three displacements and two slope functions, per node. An exact closed-form solution is also presented for the special case of freely supported single-layer orthotropic and two-layer, cross-ply plates. This solution provides a benchmark to evaluate the validity of the finite-element analysis. Both solutions are compared with numerical results existing in the literature for special cases (all for ordinary, not bimodulus, materials), and good agreement is obtained.

Introduction

Structural uses have been increasing for laminates consisting of multiple layers of fiber-reinforced composite materials. Consequently, there is an increasing need for realistic mathematical modeling of the material behavior for incorporation in static and dynamic structural analyses. Certain fiber-reinforced materials have been found experimentally to exhibit quite different elastic behavior depending upon whether the fiber-direction strain (ϵ_f) is tensile or compressive [1–3]. Examples of such materials are tire cord-rubber, reinforced solid propellants, and some biological tissues. Although the stress-strain behavior of such materials is actually curvilinear, it is often approximated as being bilinear, with different slopes (elastic properties) depending upon the sign of ϵ_f. Thus they are called bimodulus composite materials.

The limited number of previous bimodulus-material plate analyses were reviewed in [4–6], and all were limited to static analyses. The present work is believed to be the first vibrational analysis of such plates. The present work is not limited to just thin plates of isotropic bimodulus material; rather it is applicable to moderately thick plates laminated of orthotropic bimodulus material. Two formulations are presented and solved: one is a finite-element formulation with five degrees of freedom per node, and the other is an exact closed-form solution.

Classical Formulation and Closed-Form Solution

Mindlin's linear dynamic theory [7] of moderately thick plates was first extended to plates laminated of ordinary (not bimodulus) monoclinic elastic material by Yang, Norris, and Stavsky [8]. Later, Wang and Chou [9] showed that a slightly different version of the Yang, Norris, and Stavsky theory, presented by Whitney and Pagano [10], is more accurate than the original version [8]. Here, this class of theory is extended to bimodulus-material laminates.

Numerous mathematical models have been introduced to describe the mechanical behavior of bimodulus materials; five of them were discussed in [11]. The model used here is the fiber-governed model introduced in [12], where this model was shown to agree well with experimental results reported in [2]. Thus we take the generalized Hooke's law for the in-plane action in each layer (l) to be of the following bimodular form:

$$\begin{Bmatrix} \sigma_x \\ \sigma_y \\ \tau_{xy} \end{Bmatrix} = \begin{bmatrix} Q_{11kl} & Q_{12kl} & Q_{16kl} \\ Q_{12kl} & Q_{22kl} & Q_{26kl} \\ Q_{16kl} & Q_{26kl} & Q_{66kl} \end{bmatrix} \begin{Bmatrix} \epsilon_x \\ \epsilon_y \\ \gamma_{xy} \end{Bmatrix} \tag{1}$$

Here, the origin of a Cartesian coordinate system is taken to be in the midplane (xy-plane) of the plate with the z-axis being normal to this

[1] Presently, Professor of Engineering Science and Mechanics, Virginia Polytechnic Institute and State University, Blacksburg, Va.
[2] Presently, Graduate Assistant, Engineering Science and Mechanics, Virginia Polytechnic Institute and State University, Blacksburg, Va.
[3] Presently, Structures Engineer, Lear Fan Corp., Reno, Nev.

Contributed by the Applied Mechanics Division of THE AMERICAN SOCIETY OF MECHANICAL ENGINEERS, and presented at the 1981 Joint ASME/ASCE Applied Mechanics, Fluids Engineering, and Bioengineering Conference, University of Colorado, Boulder, Colo., June 22–27, 1981.
Discussion on this paper should be addressed to the Editorial Department, ASME, United Engineering Center, 345 East 47th Street, New York, N. Y. 10017, and will be accepted until September 1, 1981. Readers who need more time to prepare a Discussion should request an extension from the Editorial Department. Manuscript received by ASME Applied Mechanics Division, June, 1980; final revision, October, 1980. Paper No. 81-APM-28.

plane and directed positive downward. The stresses (σ_x, σ_y, τ_{xy}) and engineering strains (ϵ_x, ϵ_y, γ_{xy}) are denoted in the usual fashion, and the Q's are the plane-stress-reduced stiffnesses (symmetric array). The first two subscripts of the Q's are the contracted forms used in anisotropic elasticity [13] and composite-material mechanics [14]. Here, the third subscript (k) refers to the sign of the fiber-direction strain ($k = 1$ for tension and $k = 2$ for compression), and l refers to the layer number ($l = 1, 2, \ldots, n$, where n is the total number of layers). The thickness shear behavior is assumed to be unaffected by bimodular action; thus these stresses are governed by the same stress-strain relations used in [10].

The force and moment resultants, each per unit length, are expressed in terms of stresses in the usual fashion [10]. The displacement components, u, v, and w in the x, y, and z-directions, respectively, are expressed in terms of midplane displacements u^0, v^0, w, and slope functions ψ_x and ψ_y as in [10]. Then, the constitutive equations for an unsymmetric cross-ply laminate are

$$\begin{Bmatrix} N_x \\ N_y \\ N_{xy} \\ M_x \\ M_y \\ M_{xy} \end{Bmatrix} = \begin{bmatrix} A_{11} & A_{12} & 0 & B_{11} & B_{12} & 0 \\ A_{12} & A_{22} & 0 & B_{12} & B_{22} & 0 \\ 0 & 0 & A_{66} & 0 & 0 & B_{66} \\ B_{11} & B_{12} & 0 & D_{11} & D_{12} & 0 \\ B_{12} & B_{22} & 0 & D_{12} & D_{22} & 0 \\ 0 & 0 & B_{66} & 0 & 0 & D_{66} \end{bmatrix} \begin{Bmatrix} u^0_{,x} \\ v^0_{,y} \\ v^0_{,x} + u^0_{,y} \\ \psi_{x,x} \\ \psi_{y,y} \\ \psi_{y,x} + \psi_{x,y} \end{Bmatrix} \tag{2}$$

and

$$\begin{Bmatrix} Q_y \\ Q_x \end{Bmatrix} = \begin{bmatrix} S_{44} & 0 \\ 0 & S_{55} \end{bmatrix} \begin{Bmatrix} w_{,y} + \psi_y \\ w_{,x} + \psi_x \end{Bmatrix} \tag{3}$$

Here, differentiation is denoted by a comma, i.e., $(\ )_{,x} \equiv \partial(\ )/\partial x$, and the extensional, flexural-extensional coupling, and flexural stiffnesses of the laminate are defined by

$$(A_{ij}, B_{ij}, D_{ij}) = \int_{-h/2}^{h/2} (Q_{ij})(1, z, z^2)dz, \quad i, j = 1, 2, 6 \tag{4}$$

Also, the thickness shear stiffnesses of the laminate are defined by

$$S_{ii} = K_i^2 \int_{-h/2}^{h/2} C_{ii}\, dz, \quad i = 4, 5 \tag{5}$$

where the K_i^2 are the thickness shear correction coefficients, which can be determined by various approaches, cf. [15]. In addition to performing the integrations in a piecewise manner from layer to layer, one also has to take into consideration the possibility of different elastic properties (tension or compression) within a layer. This procedure is explained in detail for a two-layer cross-ply laminate in the Appendix.

The equations of motion in terms of the force and moment resultants as given in [10] are used. Then substituting the plate constitutive equations (2) and (3) into the equations of motion, we obtain them to be as given by equations (15) in [10].

The boundary conditions on all edges are freely supported (simply supported without in-plane normal restraint). Along the edges at $x = 0$ and $x = a$,

$$w = \psi_y = M_x = v^0 = N_x = 0$$

Along the edges at $y = 0$ and $y = b$, (6)

$$w = \psi_x = M_y = u^0 = N_y = 0$$

The governing equations and the boundary conditions (6) are exactly satisfied in closed form by the following set of functions:

$$\begin{aligned} u^0 &= U \cos \alpha x \sin \beta y\, e^{i\omega t} \\ v^0 &= V \sin \alpha x \cos \beta y\, e^{i\omega t} \\ w &= W \sin \alpha x \sin \beta y\, e^{i\omega t} \\ h\psi_y &= Y \sin \alpha x \cos \beta y\, e^{i\omega t} \\ h\psi_x &= X \cos \alpha x \sin \beta y\, e^{i\omega t} \end{aligned} \tag{7}$$

Here, ω is the natural frequency associated with the mode having axial and transverse wave numbers m and n, and

$$\alpha \equiv m\pi/a, \quad \beta \equiv \eta\pi/b \tag{8}$$

where a and b are plate dimensions in the x and y-directions, respectively.

Substituting solutions (7) into the governing equations [10], we obtain

$$[C_{kl}] \begin{Bmatrix} U \\ V \\ W \\ Y \\ X \end{Bmatrix} = \begin{Bmatrix} 0 \\ 0 \\ 0 \\ 0 \\ 0 \end{Bmatrix}, \qquad k, l = 1, 2, 3, 4, 5 \tag{9}$$

where C_{kl} is a 5×5 symmetric matrix containing the following elements:

$$\begin{aligned}
&C_{11} \equiv -A_{11}\alpha^2 - A_{66}\beta^2 + P\omega^2; \quad C_{12} \equiv -(A_{12} + A_{66})\alpha\beta; \quad C_{13} \equiv 0 \\
&C_{14} \equiv -[(B_{12} + B_{66})/h]\alpha\beta; \quad C_{15} \equiv -(B_{11}/h)\alpha^2 - (B_{66}/h)\beta^2 + (R/h)\omega^2 \\
&C_{22} \equiv -A_{66}\alpha^2 - A_{22}\beta^2 + P\omega^2; \quad C_{23} \equiv 0 \\
&C_{24} \equiv -(B_{66}/h)\alpha^2 - (B_{22}/h)\beta^2 + (R/h)\omega^2; \quad C_{25} \equiv C_{14} \\
&C_{33} \equiv -(S_{55}\alpha^2 + S_{44}\beta^2 - P\omega^2); \quad C_{34} \equiv -(S_{44}/h)\beta \\
&C_{35} \equiv -(S_{55}/h)\alpha; \quad C_{44} \equiv -(D_{66}/h^2)\alpha^2 - (D_{22}/h^2)\beta^2 - (S_{44}/h^2) + (I/h^2)\omega^2 \\
&C_{45} \equiv -[(D_{12} + D_{66})/h^2]\alpha\beta \\
&C_{55} \equiv -(D_{11}/h^2)\alpha^2 - (D_{66}/h^2)\beta^2 - (S_{55}/h^2) + (I/h^2)\omega^2
\end{aligned} \tag{10}$$

Here, P, R, and I are the respective normal, coupling, and rotatory inertias as defined in [10]. The frequency ω is determined by setting $|C_{kl}| = 0$.

To determine the z-position of the fiber-direction neutral surface, one sets

$$\epsilon_f = \epsilon_f^0 + z\kappa_f = 0$$

or (11)

$$z_{nf} = -\epsilon_f^0/\kappa_f.$$

Thus $z_{nx} = hU/X$ and $z_{ny} = -hV/Y$. An iterative procedure is used to obtain the final displacement ratios and corresponding frequency.

Finite-Element Formulation

An exact closed-form solution to the governing equations [10] can be obtained only under special conditions of geometry, edge conditions, loadings, and lamination. Here, we present a simple finite-element formulation which does not have any limitations (except for those implied in the formulation of the governing equations) [16].

Suppose that the region $\mathbb{R}$ is subdivided into a finite number N of subregions: finite elements, $\mathbb{R}_e (e = 1, 2, \ldots, N)$. Over each element, the generalized displacements (u^0, v^0, w, ψ_x, ψ_y) are interpolated according to

$$\begin{aligned}
u^0 &= \sum_i^r u_i \phi_i^1, \quad v^0 = \sum_i^r v_i \phi_i^1, \quad w = \sum_i^s w_i \phi_i^2 \\
\psi_x &= \sum_i^p \psi_{x_i} \phi_i^3, \quad \psi_y = \sum_i^p \psi_{y_i} \phi_i^3
\end{aligned} \tag{12}$$

where ϕ_i^α ($\alpha = 1, 2, 3$) is the interpolation function corresponding to the ith node in the element. Note that the in-plane displacements, the transverse displacement, and the slope functions are approximated by different sets of interpolation functions. Although this generality is included in the formulation (to indicate the fact that such independent approximations are possible), we dispense with it in the interest of simplicity when the element is actually programmed and

Table 1 Fundamental natural frequencies ($m = n = 1$) of rectangular antisymmetric cross-ply plates at different aspect ratios and thicknesses ($E_{11}/E_{22} = 40$, $G_{12}/E_{22} = G_{13}/E_{22} = G_{23}/E_{22} = 0.5$, $\nu_{12} = 0.25$, $K_4^2 = K_5^2 = 5/6$)*

Aspect ratio a/b	Dimensionless frequency $\omega(b/\pi)^2(P/D_{22})^{1/2}$				
	Thin-plate theory [18]	b/h = 50		b/h = 10	
		C.F.	F.E.	C.F.	F.E.
0.5	2.24	2.400	2.421	1.942	1.946
1.0	0.865	0.858	0.877	0.794	0.799
1.5	0.65	0.656	0.668	0.612	0.615
2.0	0.606	0.604	0.617	0.565	0.569
2.5	0.59	0.590	0.599	0.548	0.552
3.0	0.580	0.578	0.591	0.541	0.544

*C.F. denotes the closed-form solution and F.E. denotes the finite-element solution.

Table 2 Fundamental natural frequencies of square antisymmetric cross-ply plates at different thicknesses ($E_{11}/E_{22} = 40$, $G_{12}/E_{22} = G_{13}/E_{22} = 1$, $G_{23}/E_{22} = 0.5$, $\nu_{12} = 0.25$, $K_4^2 = K_5^2 = 5/6$)

b/h	Dimensionless frequency $\omega b^2(P/E_{22}h^3)^{1/2}$		
	Fortier & Rossettos [19]	C.F.	F.E.
10	10.80	11.11	11.15
50	11.65	11.82	12.06

Table 3 Material properties for two tire cord-rubber, unidirectional, bimodulus composite materials[a]

Property	Aramid-Rubber		Polyester-Rubber	
	k = 1	k = 2	k = 1	k = 2
Longitudinal Young's modulus, GPa	3.58	0.0120	0.617	0.0369
Transverse Young's modulus, GPa	0.00909	0.0120	0.00800	0.0106
Major Poisson's ratio, dimensionless[b]	0.416	0.205	0.475	0.185
Longitudinal-transverse shear modulus, GPa[a]	0.00370	0.00370	0.00262	0.00267
Transverse-thickness shear modulus, GPa	0.00290	0.00499	0.00233	0.00475
Specific gravity, dimensionless	0.970		1.00	

[a] Fiber-direction tension is denoted by k = 1, and fiber-direction compression by k = 2.

[b] The minor Poisson's ratio is assumed to be given by the reciprocal relation.

[c] The longitudinal-thickness shear modulus is assumed to be equal to this one.

take $\phi_i^1 = \phi_i^2 = \phi_i^3 (r = s = p)$. Here r, s, and p denote the number of degrees of freedom for each variable. That is, the total number of degrees of freedom per element is $2r + s + 2p$.

Substituting equations (12) into the Galerkin integrals associated with the governing equations [10], which must also hold in each element $\mathbb{R}_e$,

$$\int_{\mathbb{R}_e} [L]\{\delta\}\{\phi\}dxdy = 0 \tag{13}$$

and using integration by parts once (to distribute the differentiation equally between the terms in each expression), we obtain

$$\begin{bmatrix} [K^{11}] & [K^{12}] & [K^{13}] & [K^{14}] & [K^{15}] \\ & [K^{22}] & [K^{23}] & [K^{24}] & [K^{25}] \\ & & [K^{33}] & [K^{34}] & [K^{35}] \\ & \text{Symmetric} & & [K^{44}] & [K^{45}] \\ & & & & [K^{55}] \end{bmatrix}_e \begin{Bmatrix} \{u\} \\ \{v\} \\ \{w\} \\ \{w_x\} \\ \{\psi_y\} \end{Bmatrix}_e = \begin{Bmatrix} 0 \\ 0 \\ 0 \\ 0 \\ 0 \end{Bmatrix} \tag{14}$$

where the $\{u\}$, $\{v\}$, etc., denote the columns of the nodal values of u, v, respectively, and the elements $K_{ij}^{\alpha\beta}(\alpha, \beta = 1, 2, \ldots, 5)$ of the symmetric stiffness matrix are given by

$$\begin{aligned}
K_{ij}^{11} &= A_{11}G_{ij}^{x} + A_{66}G_{ij}^{y} & K_{ij}^{25} &= B_{66}H_{ij}^{x} + B_{22}H_{ij}^{y} \\
K_{ij}^{12} &= A_{12}G_{ij}^{xy} + A_{66}G_{ji}^{xy} & K_{ij}^{33} &= S_{55}S_{ij}^{x} + S_{44}S_{ij}^{y} \\
K_{ij}^{13} &= 0 & K_{ij}^{34} &= S_{55}R_{ij}^{xo} \\
K_{ij}^{14} &= B_{11}H_{ij}^{x} + B_{66}H_{ij}^{y} & K_{ij}^{35} &= S_{44}R_{ij}^{yo} \\
K_{ij}^{15} &= B_{12}H_{ij}^{xy} + B_{66}H_{ji}^{xy} & K_{ij}^{44} &= D_{11}T_{ij}^{x} + D_{66}T_{ij}^{y} + S_{55}T_{ij}^{0} \\
K_{ij}^{22} &= A_{22}G_{ij}^{y} + A_{66}G_{ij}^{x} & K_{ij}^{45} &= D_{12}T_{ij}^{xy} + D_{66}T_{ji}^{xy} \\
K_{ij}^{23} &= 0 & K_{ij}^{55} &= D_{66}T_{ij}^{x} + D_{22}T_{ij}^{y} + S_{44}T_{ij}^{0} \\
K_{ij}^{24} &= B_{66}H_{ij}^{xy} + B_{12}H_{ji}^{xy}
\end{aligned} \tag{15}$$

where

$$\begin{aligned}
G_{ij}^{\xi\eta} &= \int_{\mathbb{R}_e} \phi_{i,\xi}^1 \phi_{j,\eta}^1 \, dx\, dy && (i, j = 1, 2, \ldots, r) \\
H_{ij}^{\xi\eta} &= \int_{\mathbb{R}_e} \phi_{i,\xi}^1 \phi_{j,\eta}^3 \, dx\, dy && (i = 1, 2, \ldots, r; \quad j = 1, 2, \ldots, t) \\
M_{ij}^{\xi\eta} &= \int_{\mathbb{R}_e} \phi_{i,\xi}^1 \phi_{j,\eta}^2 \, dx\, dy && (i = 1, 2, \ldots, r; \quad j = 1, 2, \ldots, s) \\
S_{ij}^{\xi\eta} &= \int_{\mathbb{R}_e} \phi_{i,\xi}^2 \phi_{j,\eta}^2 \, dx\, dy && (i, j = 1, 2, \ldots, s) \\
R_{ij}^{\xi\eta} &= \int_{\mathbb{R}_e} \phi_{i,\xi}^2 \phi_{j,\eta}^3 \, dx\, dy && (i = 1, 2, \ldots, s; \quad j = 1, 2, \ldots, t) \\
T_{ij}^{\xi\eta} &= \int_{\mathbb{R}_e} \phi_{i,\xi}^3 \phi_{j,\eta}^3 \, dx\, dy && (i, j = 1, 2, \ldots, s)
\end{aligned}$$

$$(\xi, \eta = 0, x, y) \tag{16}$$

and $G_{ij}^{xx} = G_{ij}^{x}$, etc. In the special case in which $\phi_i^1 = \phi_i^2 = \phi_i^3$, all of the matrices in equations (16) coincide.

In the present study, elements of the serendipity family are employed with the same interpolation for all of the variables. The resulting stiffness matrices are 20 by 20 for this four-node element and 40 by 40 for the eight-node element. Reduced integration [17] must be used to evaluate the matrix coefficients in equations (15). That is, if the four-node rectangular element is used, the 1×1 Gauss rule must be used in place of the standard 2×2 Gauss rule to numerically evaluate the coefficients K_{ij}.

Substituting solution (14) into equations (11), we get

$$z_{nx}^e = -u_{,x}^e/\psi_{x,x}^e; \quad z_{ny}^e = -v_{,y}^e/\psi_{y,y}^e \tag{17}$$

Numerical Results

Computations using the closed-form and finite-element solutions were carried out on an IBM 370 computer. Because there is no previous analysis for vibration of bimodulus plates, the present results could be compared only with those for rectangular plates laminated of ordinary materials. Comparisons of the results of the present analysis are displayed in Tables 1 and 2 along with the fundamental-frequency results of Jones [18] for thin plates and Fortier and Rossettos [19] for thick and thin plates. Upon comparison of the various results, we find good agreement.

As examples of some actual bimodulus materials, two composites used in automobile tires, aramid cord-rubber, and polyester cord-rubber, are selected. The material properties, listed in Table 3, are based on the experiments of Patel, et al. [2], and are the same data used in [6] with the addition of the values of specific gravity, which were estimated on the basis of the volume fractions. The numerical results for single-layer 0° orthotropic and two-layer cross-ply plates are presented in Tables 4 and 5–6, respectively, where the agreement is good.

There may be a question regarding the effect of bimodulus action on plate stiffness in different portions of each cycle of vibration. To explain this effect, we show a single-layer, bimodulus-material plate at the two extremes of its deflection in Fig. 1. The initial half cycle is depicted in Fig. 1(*a*). During this time interval, the top surface is in compression and the bottom in tension, thus causing the neutral surface for ϵ_x to be positive ($z_{nx} > 0$), i.e., below the plate midplane

Table 4 Dimensionless fiber-direction neutral-surface locations and fundamental frequencies for single-layer 0° orthotropic plates having $b/h = 10$ by two methods (closed form and finite element)

Aspect ratio a/b	$Z_x \equiv z_{nx}/h$ C.F.	$Z_x \equiv z_{nx}/h$ F.E.	$\omega b^2(P/E_{22}^C h^3)^{1/2}$ C.F.	$\omega b^2(P/E_{22}^C h^3)^{1/2}$ F.E.
		Aramid-rubber:		
0.5	0.4484	0.4484	19.065	19.255
0.7	0.4467	0.4468	11.324	11.515
1.0	0.4433	0.4435	6.877	7.062
1.4	0.4373	0.4370	4.766	4.968
2.0	0.4262	0.4302	3.688	3.856
		Polyester-rubber:		
0.5	0.3089	0.3083	25.134	23.136
0.7	0.3072	0.3071	15.058	14.421
1.0	0.3056	0.3049	8.668	8.648
1.4	0.3011	0.3013	5.421	5.533
2.0	0.2945	0.2950	3.777	3.918

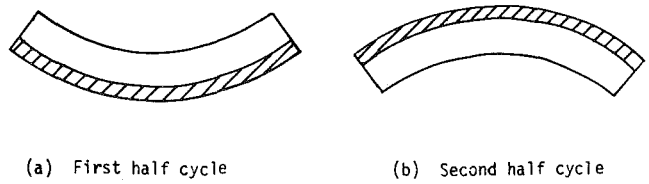

(a) First half cycle (b) Second half cycle

Fig. 1 Bimodulus action during the two half cycles of motion of a single-layer bimodulus plate; shaded material is in longitudinal tension

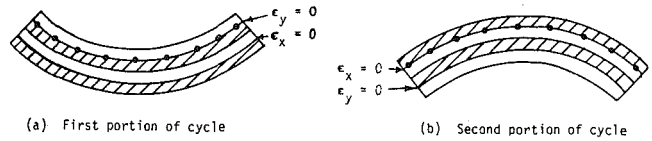

(a) First portion of cycle (b) Second portion of cycle

Fig. 2 Bimodulus action during the two portions of motion of a two-layer plate in the fundamental mode of vibration; bottom layer is in x-direction (0°), top layer is in y (90°); shaded portions are in tension in the respective fiber directions

Table 5 Dimensionless neutral-surface locations in the first and second portions of a cycle for two-layer, cross-ply plates having $b/h = 10$ by closed-form and finite-element methods*

Aspect ratio a/b	$Z_x^{(1)}$ C.F.	$Z_x^{(1)}$ F.E.	$Z_y^{(1)}$ C.F.	$Z_y^{(1)}$ F.E.	$Z_x^{(2)}$ C.F.	$Z_x^{(2)}$ F.E.	$Z_y^{(2)}$ C.F.	$Z_y^{(2)}$ F.E.
				Aramid-rubber:				
0.5	0.4457	0.4458	-0.0648	-0.0660	-0.0171	-0.0170	0.4247	0.4257
0.7	0.4434	0.4436	-0.0490	-0.0491	-0.0240	-0.0238	0.4338	0.4344
1.0	0.4394	0.4394	-0.0347	-0.0344	-0.0347	-0.0346	0.4394	0.4394
1.4	0.4335	0.4337	-0.0250	-0.0249	-0.0494	-0.0497	0.4423	0.4426
2.0	0.4228	0.4237	-0.0174	-0.0175	-0.0705	-0.0700	0.4437	0.4442
				Polyester-rubber:				
0.5	0.3687	0.3691	-0.1335	-0.1295	-0.0830	-0.0825	0.3569	0.357
0.7	0.3664	0.3663	-0.1119	-0.1113	-0.0868	-0.0868	0.3603	0.360
1.0	0.3632	0.3633	-0.0960	-0.0960	-0.0959	-0.0959	0.3631	0.363
1.4	0.3589	0.3596	-0.0870	-0.0870	-0.1115	-0.112	0.3648	0.365
2.0	0.3514	0.3513	-0.0817	-0.0817	-0.1389	-0.139	0.3660	0.366

* Here $Z_x^{(1)} \equiv z_{nx}/h$ for the first portion of a cycle, etc.

Table 6 Dimensionless fundamental frequencies in the first partial cycle, second partial cycle, and complete cycle of motion for two-layer, cross-ply plates having $b/h = 10$ by closed-form and finite-element methods†

Aspect ratio a/b	$\omega_1 b^2(P/E_{22}^C h^3)^{1/2}$ C.F.	$\omega_1 b^2(P/E_{22}^C h^3)^{1/2}$ F.E.	$\omega_2 b^2(P/E_{22}^C h^3)^{1/2}$ C.F.	$\omega_2 b^2(P/E_{22}^C h^3)^{1/2}$ F.E.	$\omega b^2(P/E_{22}^C h^3)^{1/2}$ C.F.	$\omega b^2(P/E_{22}^C h^3)^{1/2}$ F.E.
				Aramid-rubber:		
0.5	19.38	20.23	13.88	14.55	16.18	16.93
0.7	11.60	12.17	9.353	9.807	10.35	10.86
1.0	7.038	7.386	7.038	7.364	7.038	7.375
1.4	4.838	5.045	6.037	6.356	5.371	5.625
2.0	3.712	3.909	5.551	5.821	4.449	4.677
				Polyester-rubber:		
0.5	19.12	19.81	15.95	16.61	17.39	18.07
0.7	11.43	11.92	10.04	10.45	10.69	11.14
1.0	7.084	7.406	7.085	7.394	7.085	7.400
1.4	5.164	5.407	5.928	6.193	5.520	5.773
2.0	4.310	4.518	5.435	5.688	4.807	5.036

† Here ω_1 and ω_2 denote the frequencies corresponding to the first and second portions of a cycle, respectively, and ω denotes the effective frequency for an entire cycle.

a certain distance. The latter half cycle is shown in Fig. 1(b). During this portion of the cycle, the top surface is now in tension and the bottom in compression, thus causing z_{nx} to be negative, i.e., to fall above the plate midplane. However, the absolute value of z_{nx} is identical to its value in the first half cycle. Thus it can be concluded that the frequency associated with the second half cycle is identical to that of the first half cycle and either modal shape, Fig. 1(a) or 1(b), will give the same computational result for the natural frequencies.

Now consider a two-layer laminate with the bottom layer (layer $l = 1$) oriented at 0 deg and the top layer ($l = 2$) at 90 deg; see Fig. 2. Initially, as shown in Fig. 2(a), the neutral surface for ϵ_x falls below the interface, within the 0-deg layer, while the neutral surface for ϵ_y falls above the interface, completely within the 90-deg layer. In the latter portion of the cycle, Fig. 2(b), the ϵ_x neutral surface falls outside of the 0-deg layer, and the ϵ_y neutral surface falls outside of the 90-deg layer. Thus compressive properties are used for the entire 0-deg layer, and tensile ones for the 90-deg layer.

From the foregoing considerations for a two-layer cross-ply laminate, it is clear that the plate stiffnesses acting in the two portions of a cycle are different and thus the associated frequencies are also different, except in the case of a square plate. We denote the frequencies associated with the two portions of a vibration cycle by ω_1 and ω_2; then the corresponding time intervals over which the two portions take place are π/ω_1 and π/ω_2, respectively. Thus the total period for a complete cycle is $\pi(\omega_1^{-1} + \omega_2^{-1})$. The average frequency (ω) over the entire cycle is 2π divided by the period:

$$\omega^{-1} = (1/2)(\omega_1^{-1} + \omega_2^{-1}) \tag{18}$$

Thus the computational procedure used for a cross-ply plate is to calculate ω_1 and ω_2 associated with modal shapes shown in Figs. 2(a) and 2(b), respectively, and then to apply equation (18).

The question arises as to the possibility of a discontinuity in energy at the junction of the two portions of a cycle. At this instant in the cycle, the displacement is zero and the velocity is maximum (because each individual portion is simple harmonic). Since the mass is unchanged, equating kinetic energies of the two portions implies equating maximum velocities. Thus

$$\omega_1 W_1 = \omega_2 W_2 \quad \text{or} \quad \omega_2/\omega_1 = W_1/W_2 \tag{19}$$

where W_1 and W_2 are the amplitudes of motion in portions 1 and 2.

Conservation of potential energy requires

$$\tfrac{1}{2}k_1W_1^2 = \tfrac{1}{2}k_2W_2^2 \quad \text{or} \quad W_1/W_2 = (k_2/k_1)^{1/2} \tag{20}$$

where k_1 and k_2 are the generalized stiffnesses corresponding to Figs. 2(*a*) and 2(*b*), respectively. However, the frequency ratio is

$$\omega_2/\omega_1 = (k_2/k_1)^{1/2} \tag{21}$$

Thus, by combining equations (20) and (21), we see that equation (19) is satisfied and thus energy is conserved in going from one portion of the cycle to the other.

There are very drastic changes in neutral-surface locations (for example, z_{nx} for aramid-rubber goes from $0.4h$ to $-0.03h$) from one cycle portion to the other. Thus a question may arise regarding a transient action. However, it should be remembered that the neutral surfaces are just boundaries between the tensile and compressive regions (analogous to the elastic-plastic boundary in elastoplastic problems) and thus have no mass.

Concluding Remarks

A finite element has been developed to analyze the small-deflection free vibration of laminated, anisotropic, rectangular thick plates of bimodulus material. The results obtained agree well with those of an exact, closed-form solution derived for such a plate freely supported on all four edges. Thus it is concluded that the element has been validated and may be used for computations involving more complicated boundary conditions.

Acknowledgments

The authors are grateful to the Office of Naval Research, Structural Mechanics Program, for financial support through Contract N00014-78-C-0647 and to the University's Merrick Computing Center for providing computing time. The skillful computational assistance of M. Kumar is also greatly appreciated.

References

1 Clark, S. K., "The Plane Elastic Characteristics of Cord-Rubber Laminates," *Textile Research Journal*, Vol. 33, No. 4, Apr. 1963, pp. 295–313.

2 Patel, H. P., Turner, J. L., and Walter, J. D., "Radial Tire Cord-Rubber Composites," *Rubber Chemistry and Technology*, Vol. 49, 1976, pp. 1095–1110.

3 Bert, C. W., "Micromechanics of the Different Elastic Behavior of Filamentary Composites in Tension and Compression," *Mechanics of Bimodulus Materials*, AMD Vol. 33, ASME, N. Y., Dec. 1979, pp. 17–28.

4 Reddy, J. N., and Bert, C. W., "Analyses of Plates Constructed of Fiber-Reinforced Bimodulus Materials," *Mechanics of Bimodulus Materials*, AMD Vol. 33, ASME, N. Y., Dec. 1979, pp. 67–83.

5 Bert, C. W., Reddy, V. S., and Kincannon, S. K., "Deflection of Thin Rectangular Plates of Cross-Plied Bimodulus Material," *Journal of Structural Mechanics*, Vol. 8, 1980, pp. 347–364.

6 Bert, C. W., et al., "Analysis of Thick Rectangular Plates Laminated of Bimodulus Composite Materials," *Proceedings, AIAA/ASME/ASCE/AHS 21st Structures, Structural Dynamics and Materials Conference*, Seattle, Wash., May 12–14, 1980, Part 1, pp. 177–186.

7 Mindlin, R. D., "Influence of Rotatory Inertia and Shear on Flexural Motions of Isotropic Elastic Plates," ASME JOURNAL OF APPLIED MECHANICS, Vol. 18, Mar. 1951, pp. 31–38.

8 Yang, P. C., Norris, C. H., and Stavsky, Y., "Elastic Wave Propagation in Heterogeneous Plates," *International Journal of Solids and Structures*, Vol. 2, 1966, pp. 665–684.

9 Wang, A. S. D., and Chou, P. C., "A Comparison of Two Laminated Plate Theories," ASME JOURNAL OF APPLIED MECHANICS, Vol. 39, June 1972, pp. 611–613.

10 Whitney, J. M., and Pagano, N. J., "Shear Deformation in Heterogeneous Anisotropic Plates," ASME JOURNAL OF APPLIED MECHANICS, Vol. 37, Dec. 1970, pp. 1031–1036.

11 Bert, C. W., "Recent Advances in Mathematical Modeling of the Mechanics of Bimodulus, Fiber-Reinforced Composite Materials," *Proceedings, 15th Annual Meeting, Society of Engineering Science*, Gainesville, Fla., Dec. 4–5, 1978, pp. 101–106.

12 Bert, C. W., "Models for Fibrous Composites With Different Properties in Tension and Compression," ASME *Journal of Engineering Materials and Technology*, Vol. 99, No. 4, Oct. 1977, pp. 344–349.

13 Lekhnitskii, S. G., *Theory of Elasticity of an Anisotropic Elastic Body*, English translation, Holden-Day, San Francisco, 1963.

14 Jones, R. M., *Mechanics of Composite Materials*, McGraw-Hill, New York, 1975.

15 Whitney, J. M., "Shear Correction Factors for Orthotropic Laminates Under Static Loads," ASME JOURNAL OF APPLIED MECHANICS, Vol. 40, Mar. 1973, pp. 302–304.

16 Reddy, J. N., "A Penalty-Plate Bending Element for the Analysis of Laminated Anisotropic Composite Plates," *International Journal for Numerical Methods in Engineering*, Vol. 15, No. 8, Aug. 1980, pp. 1187–1206.

17 Zienkiewicz, O. C., Taylor, R. L., and Too, J. M., "Reduced Integration Technique in General Analysis of Plates and Shells," *International Journal for Numerical Methods in Engineering*, Vol. 3, 1971, pp 575–586.

18 Jones, R. M., "Buckling and Vibration of Unsymmetrically Laminated Cross-Ply Rectangular Plates," *AIAA Journal*, Vol. 11, No. 12, Dec. 1973, pp. 1626–1632.

19 Fortier, R. C., and Rossettos, J. N., "On the Vibration of Shear Deformable Curved Anisotropic Composite Plates," ASME JOURNAL OF APPLIED MECHANICS, Vol. 40, Mar. 1973, pp. 299–301.

20 Reddy, J. N., et al., "Thermal Bending of Thick Rectangular Plates of Bimodulus Material," *Journal of Mechanical Engineering Science*, to appear.

APPENDIX

Derivation of the Plate Stiffnesses for a Two-Layer Cross-Ply Laminate of Bimodulus Material

In problems involving laminates comprised of bimodulus-material layers, it is necessary to evaluate the integral forms appearing in the definitions of the plate stiffnesses, equations (4). The derivation presented here is for a two-layer cross-ply laminate.

Each layer has the same thickness, $h/2$, and the same orthotropic elastic properties with respect to the fiber direction. Because each layer is oriented at either 0° or 90° to the x-axis, there are no sitffnesses with subscripts 16 and 26. The bottom layer, with fibers oriented parallel to the x-axis, is denoted as layer 1, i.e., $l = 1$ in Q_{ijkl}, and occupies the thickness space from $z = 0$ to $z = h/2$, where z is measured positive downward from the midplane. The top layer, with fibers oriented at 90°, is denoted as layer 2, i.e., $l = 2$, and occupies the thickness space from $z = -h/2$ to $z = 0$.

Because there are two different neutral surfaces (associated with strains in the respective x and y-directions) and two different layers, there are four distinct cases depending upon the combination of signs of the dimensionless neutral surfaces ($Z_x = z_{nx}/h$ and $Z_y = z_{ny}/h$). These cases are designated as follows:

Case 1:	$0.5 > Z_x > 0$,	$-0.5 < Z_y < 0$
Case 2:	$-0.5 < Z_x < 0$,	$0.5 > Z_y > 0$
Case 3:	$0.5 > Z_x > 0$,	$0.5 > Z_y > 0$
Case 4:	$-0.5 < Z_x < 0$,	$-0.5 < Z_y < 0$

In Case 1, the upper portion (from $z = -h/2$ to $z = z_{ny}$) of the top layer ($l = 2$) is in compression ($k = 2$ in Q_{ijkl}) in its fiber direction (y-axis), and the lower portion ($z = z_{ny}$ to 0) of the top layer is in tension ($k = 1$). Also, the inner portion of the bottom layer ($l = 1$), from $z = 0$ to $z = z_{nx}$, is in compression ($k = 2$) in its fiber direction (x-axis), and the outer portion (from z_{nx} to $h/2$) of layer 1 is in tension ($k = 1$). Thus the general integral expression for A_{ij}, in equation (4), can be taken as the sum of the integrals for each of these regions:

Case 1. $(0.5 > Z_x > 0, -0.5 < Z_y < 0)$:

$$A_{ij} = \int_{-h/2}^{h/2} Q_{ijkl}\,dz$$

$$= \int_{-h/2}^{z_{ny}} Q_{ij22}\,dz + \int_{z_{ny}}^{0} Q_{ij12}\,dz + \int_{0}^{z_{nx}} Q_{ij21}\,dz + \int_{z_{nx}}^{h/2} Q_{ij11}\,dz \tag{22}$$

Because the planar reduced stiffnesses Q_{ijkl} are each, respectively, constant in the appropriate regions, equation (22) can be integrated to the following:

$$A_{ij} = (Q_{ij22} + Q_{ij11})(h/2) + (Q_{ij21} - Q_{ij11})z_{nx} + (Q_{ij22} - Q_{ij12})z_{ny} \tag{23}$$

or

$$A_{ij} = (1/2)(Q_{ij22} + Q_{ij11}) + (Q_{ij21} - Q_{ij11})Z_x + (Q_{ij22} - Q_{ij12})Z_y \quad (24)$$

Similarly

$$B_{ij} = \int_{-h/2}^{h/2} zQ_{ijkl}\,dz$$

$$= \int_{-h/2}^{z_{ny}} zQ_{ij22}\,dz + \int_{z_{ny}}^{0} zQ_{ij12}\,dz + \int_{0}^{z_{nx}} zQ_{ij21}\,dz + \int_{z_{nx}}^{h/2} zQ_{ij11}\,dz \quad (25)$$

$$= (-Q_{ij22} + Q_{ij11})(h^2/8) + (Q_{ij21} - Q_{ij11})(z_{nx}^2/2) + (Q_{ij22} - Q_{ij12})(z_{ny}^2/2) \quad (26)$$

or

$$B_{ij}/h = (1/8)(-Q_{ij22} + Q_{ij11}) + (Q_{ij21} - Q_{ij11})(Z_x^2/2) + (Q_{ij22} - Q_{ij12})(Z_y^2/2) \quad (27)$$

Also

$$D_{ij} = \int_{-h/2}^{h/2} z^2 Q_{ijkl}\,dz$$

$$= \int_{-h/2}^{z_{ny}} z^2 Q_{ij22}\,dz + \int_{z_{ny}}^{0} z^2 Q_{ij12}\,dz + \int_{0}^{z_{nx}} z^2 Q_{ij21}\,dz + \int_{z_{nx}}^{h/2} z^2 Q_{ij11}\,dz \quad (28)$$

$$= (Q_{ij22} + Q_{ij11})(h^3/24) + (Q_{ij21} - Q_{ij11})(z_{nx}^3/3) + (Q_{ij22} - Q_{ij12})(z_{ny}{}^3/3) \quad (29)$$

or

$$D_{ij}/h = (1/24)(Q_{ij22} + Q_{ij11}) + (Q_{ij21} - Q_{ij11})(Z_x^3/3) + (Q_{ij22} - Q_{ij12})(Z_y^3/3) \quad (30)$$

Similarly

Case 2. $(-0.5 < Z_x < 0, 0.5 > Z_y > 0)$:

$$A_{ij}/h = (Q_{ij11} + Q_{ij22})/2 + (Q_{ij22} - Q_{ij12})Z_x + (Q_{ij21} - Q_{ij11})Z_y$$

$$B_{ij}/h^2 = (Q_{ij11} - Q_{ij22})/8 + (Q_{ij22} - Q_{ij12})(Z_x^2/2) + (Q_{ij21} - Q_{ij11})(Z_y^2/2)$$

$$D_{ij}/h^3 = (Q_{ij11} + Q_{ij22})/24 + (Q_{ij22} - Q_{ij12})(Z_x^3/3) + (Q_{ij21} - Q_{ij11})(Z_y^3/3) \quad (31)$$

Case 3. $(0.5 > Z_x > 0, 0.5 > Z_y > 0)$:

$$A_{ij}/h = (Q_{ij11} + Q_{ij22})/2 + (Q_{ij21} - Q_{ij11})Z_x$$

$$B_{ij}/h^2 = (Q_{ij11} - Q_{ij22})/8 + (Q_{ij21} - Q_{ij11})(Z_x^2/2)$$

$$D_{ij}/h^3 = (Q_{ij11} + Q_{ij22})/24 + (Q_{ij21} - Q_{ij11})(Z_x^3/3) \quad (32)$$

Case 4. $(-0.5 < Z_x < 0, -0.5 < Z_y < 0)$:

$$A_{ij}/h = (Q_{ij11} + Q_{ij22})/2 + (Q_{in22} - Q_{ij12})Z_y$$

$$B_{ij}h^2 = (Q_{ij11} - Q_{ij22})/8 + (Q_{ij22} - Q_{ij12})(Z_y^2/2)$$

$$D_{ij}/h^3 = (Q_{ij11} + Q_{ij22})/24 + (Q_{ij22} - Q_{ij12})(Z_y^3/3) \quad (33)$$

In the presence of excessively high in-plane loads, such as those due to heating to a high average temperature [20] or due to large deflections, the neutral surfaces can go outside of the thickness of the laminate and, thus, make it act as if it were homogeneous. However, this does not occur for small-deflection free vibrations and thus the equations for these cases are not presented here.

Single 0° Layer. $(|Z_x| < 0.5)$

Here, all four cases collapse to only one, with these results:

$$A_{ij}/h = (Q_{ij11} + Q_{ij21})/2 + (Q_{ij21} - Q_{ij11})Z_x$$

$$B_{ij}/h^2 = (Q_{ij11} - Q_{ij21})/8 + (Q_{ij21} - Q_{ij11})Z_x^2/2$$

$$D_{ij}/h^3 = (Q_{ij11} + Q_{ij21})/24 + (Q_{ij21} - Q_{ij11})Z_x^3/3 \quad (34)$$

N. Sugimoto

Research Associate,
Department of Mechanical Engineering,
Faculty of Engineering Science,
Osaka University,
Toyonaka, Osaka 560, Japan

Nonlinear Theory for Flexural Motions of Thin Elastic Plate

Part 1: Higher-Order Theory

This paper develops a comprehensive higher-order theory for flexural motions of a thin elastic plate, in which the effect of finite thickness of the plate and that of small but finite deformation are taken into account. Based on the theory of nonlinear elasticity for a homogeneous and isotropic solid, the nonlinear equations for the flexural motions coupled with the extensional motions are systematically derived by the moment asymptotic expansion method. Denoting by ϵ the ratio of the thickness of the plate to a characteristic wavelength of flexural motions, an order of characteristic deflection is assumed to be ϵ^2 and that of a characteristic strain ϵ^3. The displacement and stress components are sought consistently up to the next higher-order terms than those in the classical theory.

Introduction

The classical theory for flexural motions of an elastic plate [1–3] can give an adequate description for a sufficiently thin plate whose deflection is much smaller than the thickness of the plate. But as a characteristic wavelength of flexural motions diminishes and the plate can no longer be regarded sufficiently thin, the effect of finite thickness comes to play an important role and then the classical theory becomes inadequate. Also a similar limitation of the theory occurs in a case of flexural bending of a plate with small cutouts whose linear dimension is not large enough compared with the thickness. In these cases, a refined theory is then required to include the effect of finite thickness of the plate. The investigations toward this refinement were first made by Reissner [4] and Mindlin [5] under the name of the effects of shear deformation and of rotatory inertia and since then, they have been made by many authors [6–15]. In this paper, such a theory including the effect of finite thickness is called a higher-order theory for the thin plate theory as a lowest-order one.

On the other hand, the effect of finite deformation plays an important role in such a geometrical configuration as a thin plate whose linear dimension is much smaller than the others. Under the assumption that the plate is thin and flexural deflection is as large as the thickness, von Karman [1–3, 16] derived the nonlinear equations which couple the deflection with the in-plane displacements. Although, in von Karman's theory, the effect of finite thickness of the plate is neglected, it often happens in actual situations (such as vibration or impact) that the effect becomes as important as the effect of finite deformation. But most of the higher-order theories just quoted have been concerned with the linear theory and little attention has been paid to the nonlinear theory. The purpose of this paper is to develop a comprehensive higher-order theory for flexural motions of a thin elastic plate, taking account of the effect of finite thickness and that of small but finite deformation.

To do so, we start from the theory of nonlinear elasticity [3, 17–19], assuming that a plate is of a homogeneous and isotropic elastic solid. In developing the higher-order theory, it should be noted that there exist two important parameters. One is ϵ which specifies the order of the thickness of the plate, i.e., $\epsilon = O(H/L)$, H and L being, respectively, the thickness of the plate and a characteristic wavelength of flexural motions. The other is δ which specifies the order of deflection of the plate, i.e., $\delta = O(W/L)$, W being a characteristic deflection. In the classical linear theory, both ϵ and δ are assumed to be sufficiently small, while in von Karman's theory, W/H is assumed to be of order of unity so that $\delta \sim \epsilon$. In addition to ϵ and δ, another practical parameter is γ which specifies an order of a characteristic strain. As is well known, the characteristic strain in flexural motions takes place in the in-plane bending strain and γ is roughly estimated as $\gamma = O(U/L)$, U being a characteristic in-plane displacement. According to Kirchhoff's hypothesis [1–3], U can be estimated as $U \sim WH/L$ and therefore $\gamma \sim U/L \sim WH/L^2 \sim W/L \cdot H/L \sim \delta\epsilon$. Thus the characteristic strain in von Karman's theory is found to be of order of ϵ^2. The present paper is concerned with the flexural motions in which ϵ and δ are small but finite. For definiteness, δ is chosen as a typical case to be ϵ^2, i.e., $\gamma \sim \epsilon^3$.

In deriving approximate equations, there are two useful methods available in addition to the variational methods on which the work of Reissner [4, 6] and Librescu [13] is based. The variational method is simple to use when deriving only the lowest-order approximation, but it has a disadvantage in that it lacks systematic consistency in

Contributed by the Applied Mechanics Division for publication in the JOURNAL OF APPLIED MECHANICS.

Discussion on this paper should be addressed to the Editorial Department, ASME, United Engineering Center, 345 East 47th Street, New York, N. Y. 10017, and will be accepted until September 1, 1981. Readers who need more time to prepare a Discussion should request an extension from the Editorial Department. Manuscript received by ASME Applied Mechanics Division, December, 1979; final revision, August, 1980.

developing the higher-order theory compared with the two methods described as follows. One of these methods is the direct asymptotic expansion method used by Friedrichs and Dressler [7], Reissner [9], Gol'denveizer [10], and Widera [12]. By this method, the displacements and stresses are sought in the form of expansion by the small parameter ϵ. After introducing the expansion into the equations of motion and equating like powers of ϵ, sequences of the system of equations are solved by a step-by-step integration. Although Friedrichs and Dressler and Gol'denveizer indicated the procedure, explicit results are not given. Reissner carried the expansion to higher order, but he obtained the result that the higher-order deflection is also governed by the classical plate equation, though the displacements and stresses are consistently sought up to the higher-order terms in the ϵ^2-expansion. This result is due to the fact that neither inertia nor applied stresses at both faces of the plate are taken into account. Widera also developed the higher-order theory for the dynamic problem, but it still remains essentially within classical theory because he proceeded to only the second-order problem. For the consistent derivation of the linear higher-order theory, it is necessary to proceed to the third-order problem and the ϵ^2-expansion is relevant.

The other method is the moment asymptotic expansion method by Tiffen [8], Novotny [11], and Lo, et al. [15]. This method assumes that the displacements can be expanded into a power series of the transverse coordinate of the plate around the middle surface. After taking the moments of the equations of motion with respect to the transverse coordinate, and substituting the expansion into the averaged quantities over the thickness such as total in-plane forces, bending or twisting moments, etc., the coefficients of the series are successively determined in terms of the displacements of the middle surface up to any order desired. Because Tiffen treated all quantities in the averaged form only, he obtained very complicated results. The method by Lo, et al., lacks systematic consistency since the expansion is truncated without any positive reason being given. Novotny, who developed a nonlinear theory for thin shells, first expanded the displacements and stresses in terms of a small parameter and later expanded them in the transverse coordinate. This method is located between the direct and the moment methods, but it is too complicated. The two asymptotic methods should be equivalent in principle. Since the direct method gives successive closed systems of equations to determine higher-order terms, it is not deemed suitable for the present purpose which is to derive the compact higher-order equations and the moment method is employed in this paper.

By use of this method, higher-order equations for the behavior of the middle surface are derived systematically up to terms next higher in order to the classical theory. In the course of developing it, the displacements and stresses are consistently sought in terms of the displacements of the middle surface up to at least $O(\delta\epsilon^3)$. If the nonlinear terms are ignored and the linear higher-order theory is concerned, it is found that the ϵ^2-expansion is legitimate. Furthermore if plane harmonic waves are considered in the linear higher-order theory thus derived, it can readily be verified that the dispersion relation of this theory corresponds to the exact Rayleigh-Lamb frequency equation [20, 21] up to the second-order terms. On the other hand, it is found that the effect of small but finite deformation arises in the form of the total curvature of the plate just as in von Karman's theory. It should be noted that the effect of material nonlinearity becomes the secondary effect compared with that of geometrical nonlinearity. Even if the fact that the third-order elastic constants are usually greater than the Lamé constants (e.g., 10–10^2 times) is taken into consideration, the effect still remains weak in the present problem. Thus it is concluded that the effect of material nonlinearity plays a less important role in such flexural motions of long wavelengths ($\epsilon \ll 1$). This should be compared with the case of the high frequency wave propagation ($\epsilon \gtrsim 1$) [19].

Finally, it should be remarked that the present higher-order theory does not presuppose the existence of an edge. Therefore as it usually happens, the present theory alone cannot always constitute a full plate problem. In such a case, a sort of boundary-layer theory must be developed near the edge. This point will be discussed in Part 2 of this paper.

Basic Equations

Let us consider the basic equations which govern a behavior of an elastic solid [3, 17–19]. Here we assume that the plate is of a homogeneous and isotropic elastic solid and that dynamic deformations take place adiabatically. The basic equations then consist of the equations of motion and the constitutive equations. We employ the Lagrangian formulation in a rectangular coordinate system X_i (i = 1, 2, 3) and the usual Cartesian tensor notation. The in-plane coordinates of the plate are designated by X_1 and X_2, while the transverse coordinate normal to the middle surface of the plate is designated by X_3. The equations of motion can be simply expressed as

$$u_{i,tt} = L_{ik,X_k}, \qquad (i = 1, 2, 3) \tag{1}$$

where u_i and L_{ij} represent the displacement vector and the Lagrangian stress tensor, respectively; the comma "," implies the partial differentiation with respect to the subscript(s) indicated after the comma, t being time; the repeated index k implies the summation over 1, 2, 3. The Lagrangian stress tensor is related to the Kirchhoff's stress tensor K_{ij} through

$$L_{ij} = (\delta_{ik} + u_{i,X_k})K_{kj}, \qquad (i, j = 1, 2, 3) \tag{2}$$

where δ_{ij} is the Kronecker delta symbol. Note here that K_{ij} is a symmetric tensor, but L_{ij} is asymmetric generally. All quantities are normalized by the characteristic wavelength and the velocity of shear waves $(\mu/\rho_0)^{1/2}$, μ and ρ_0 being, respectively, the usual Lamé constant (the modulus of rigidity) and the density in the reference state.

The equations of motion are supplemented by the following constitutive equations in the form of the power series with respect to the Lagrangian strain tensor E_{ij}:

$$K_{ij} = \lambda I\delta_{ij} + 2E_{ij} + [lI^2 - (2m - n)II]\delta_{ij} + (2m - n)IE_{ij} + nE_{ik}E_{kj} + \ldots, \qquad (i, j = 1, 2, 3) \tag{3}$$

with the Lagrangian strain tensor given by

$$2E_{ij} = u_{i,X_j} + u_{j,X_i} + u_{k,X_i}u_{k,X_j}, \quad (i, j = 1, 2, 3) \tag{4}$$

where $\lambda[=2\sigma/(1 - 2\sigma)]$ is another Lamé constant normalized by μ, σ being Poisson's ratio and l, m, and n are the third-order elastic constants (Murnaghan constants) normalized by μ. Here I and II are, respectively, the first and the second invariants of E_{ij} defined by $I = E_{ii}$, and $II = (E_{ii}E_{jj} - E_{ij}E_{ij})/2$.

It is assumed that both faces of the plate are free from a tangential traction, but subject to normal stresses q_+ and q_- on the upper and lower surfaces, respectively. The boundary conditions can then be expressed as

$$L_{13} = L_{23} = 0 \quad \text{and} \quad L_{33} = q_{\pm}, \quad \text{at} \quad X_3 = \pm\epsilon h/2 \tag{5}$$

where ϵh is the normalized thickness of the plate, and the parameter ϵ is introduced to specify the order of thickness of the plate, h being of $O(1)$.

We remark here that, in the subsequent sections, the coordinates X_1, X_2, and X_3 are replaced by x, y, and z and the subscripts 1, 2, and 3 of the vector or the tensor are also replaced by x, y, and z, respectively.

Derivation of Approximate Equations

Let us now derive by the moment asymptotic expansion method approximate equations describing the nonlinear flexural motions. Since a thin plate ($\epsilon \ll 1$) is considered, the displacement components in equations (1)–(5) are sought in the following power series in the transverse coordinate z around a uniform state:

$$\begin{aligned} u_x &= \delta(u_0 + u_1 z + u_2 z^2 + u_3 z^3 + \ldots), \\ u_y &= \delta(v_0 + v_1 z + v_2 z^2 + v_3 z^3 + \ldots), \\ u_z &= \delta(w_0 + w_1 z + w_2 z^2 + w_3 z^3 + w_4 z^4 + \ldots), \end{aligned} \tag{6}$$

where $|z| \leqq \epsilon h/2$ and the small parameter δ implies the order of

nonlinearity; u_i, v_i, and w_i ($i = 0, 1, 2, \ldots$) depend on x, y, and t and their order of magnitude is assumed, for the moment, to be of $O(1)$. Also it is assumed that the differentiation of u_i, v_i, and w_i ($i = 0, 1, 2, \ldots$) with respect to x and y does not change the original order of them, e.g., $w_{0,x} \sim w_{0,y} \sim w_0 \sim O(1)$, etc.

Multiplying each of the x, y, and z components of the equations of motion (1) by z^n ($n = 0, 1, 2, \ldots$), respectively, and integrating with respect to z over the thickness (i.e., taking the moments of equations (1)), the following systems of equations are successively obtained:

$$U^{(n)}_{x,tt} = N^{(n)}_{xx,x} + N^{(n)}_{xy,y} - nN^{(n-1)}_{xz}, \tag{7}$$

$$U^{(n)}_{y,tt} = N^{(n)}_{yx,x} + N^{(n)}_{yy,y} - nN^{(n-1)}_{yz}, \tag{8}$$

$$U^{(n)}_{z,tt} = N^{(n)}_{zx,x} + N^{(n)}_{zy,y} - nN^{(n-1)}_{zz} + Q^{(n)}, \quad (n = 0, 1, 2, \ldots) \tag{9}$$

with

$$U^{(n)}_i = \int_{-\epsilon h/2}^{\epsilon h/2} u_i z^n dz,$$

$$N^{(n)}_{ij} = \int_{-\epsilon h/2}^{\epsilon h/2} L_{ij} z^n dz, \ (N^{(-1)}_{iz} \equiv 0) \ (i, j = x, y, z) \tag{10, 11}$$

and

$$Q^{(n)} = \epsilon^n (h/2)^n [q_+ + (-1)^{n+1} q_-], \quad (n = 0, 1, 2, \ldots) \tag{12}$$

where the boundary conditions (5) have been used in carrying out the integration. Equations (7)–(9) will be referred to as the nth-order moment equations hereafter. To derive approximate equations, the order of the applied stressed $q_\pm$ must be specified. Since the applied stresses are usually smaller than the in-plane stresses (of $O(\delta\epsilon)$), we assume in the following analysis that $q_\pm$ are of $O(\delta\epsilon^3)$ and therefore $Q^{(n)}$ is of $O(\delta\epsilon^{n+3})$.

Lowest-Order Approximation. We first seek the lowest-order approximation which is equivalent to the classical linear theory. Introducing (6) into (11) and neglecting all higher-order terms, the lowest-order expressions for $N^{(0)}_{ij}$ ($i, j = x, y, z$) become

$$\begin{aligned}
N^{(0)}_{xx} &= \delta\epsilon h[(\lambda + 2)u_{0,x} + \lambda(v_{0,y} + w_1)], \\
N^{(0)}_{xy} &= \delta\epsilon h(u_{0,y} + v_{0,x}), \\
N^{(0)}_{xz} &= N^{(0)}_{zx} = \delta\epsilon h(u_1 + w_{0,x}), \\
N^{(0)}_{zz} &= \delta\epsilon h[(\lambda + 2)w_1 + \lambda(u_{0,x} + v_{0,y})],
\end{aligned} \tag{13}$$

where the explicit forms of $N^{(0)}_{yx}$, $N^{(0)}_{yy}$, $N^{(0)}_{yz}$, and $N^{(0)}_{zy}$ are omitted because they can readily be recovered from $N^{(0)}_{xy}$, $N^{(0)}_{xx}$, $N^{(0)}_{xz}$, and $N^{(0)}_{zx}$, respectively, by the symmetric transposition between x and y and between u and v. Similarly the lowest-order expressions for $N^{(1)}_{ij}$ ($i, j = x, y, z$) become

$$\begin{aligned}
N^{(1)}_{xx} &= \delta\epsilon^3(h^3/12)[(\lambda + 2)u_{1,x} + \lambda(v_{1,y} + 2w_2)], \\
N^{(1)}_{xy} &= \delta\epsilon^3(h^3/12)(u_{1,y} + v_{1,x}), \\
N^{(1)}_{xz} &= N^{(1)}_{zx} = \delta\epsilon^3(h^3/12)(2u_2 + w_{1,x}), \\
N^{(1)}_{zz} &= \delta\epsilon^3(h^3/12)[2(\lambda + 2)w_2 + \lambda(u_{1,x} + v_{1,y})],
\end{aligned} \tag{14}$$

and the lowest-order expressions for $N^{(2)}_{ij}$ ($i, j = x, y, z$) become

$$\begin{aligned}
N^{(2)}_{xx} &= \delta\epsilon^3(h^3/12)[(\lambda + 2)u_{0,x} + \lambda(v_{0,y} + w_1)], \\
N^{(2)}_{xy} &= \delta\epsilon^3(h^3/12)(u_{0,y} + v_{0,x}), \\
N^{(2)}_{xz} &= N^{(2)}_{zx} = \delta\epsilon^3(h^3/12)(u_1 + w_{0,x}), \\
N^{(2)}_{zz} &= \delta\epsilon^3(h^3/12)[(\lambda + 2)w_1 + \lambda(u_{0,x} + v_{0,y})].
\end{aligned} \tag{15}$$

Here, and hereafter, the symmetric forms are also omitted for the same reason as for $N^{(0)}_{ij}$.

From the first-order moment equations, it is found that

$$\begin{aligned}
&u_1 = -w_{0,x} + O(\epsilon^2), \quad v_1 = -w_{0,y} + O(\epsilon^2), \\
&w_1 = -\lambda/(\lambda + 2)(u_{0,x} + v_{0,y}) + O(\epsilon^2) = -\sigma/(1 - \sigma)D_0 + O(\epsilon^2),
\end{aligned} \tag{16}$$

where $D_0 = u_{0,x} + v_{0,y}$. Note here that these relations for u_1 and v_1 are nothing but Kirchhoff's hypothesis used in the classical linear theory of the thin plate.

Next, from the second-order moment equations and the relations (16), it is also found that

$$\begin{aligned}
&u_2 = \sigma/[2(1 - \sigma)]D_{0,x}, \quad v_2 = \sigma/[2(1 - \sigma)]D_{0,y}, \\
&w_2 = \sigma/[2(1 - \sigma)]\Delta w_0 - (1 - 2\sigma)/[8(1 - \sigma)]w_{0,tt},
\end{aligned} \tag{17}$$

where equations (7) and (8) with $n = 0$ have been employed in deriving u_2 and v_2; Δ denotes the two-dimensional Laplacian defined by $\Delta = \partial^2/\partial x^2 + \partial^2/\partial y^2$. We note here that the second term in w_2 is, as will be found later, inaccurate because $w_{0,tt}$ is of $O(\epsilon^2)$. By virtue of the relations (16) and (17), $N^{(0)}_{xz}$ in equation (7) with $n = 1$ can be expressed in terms of w_0 as

$$N^{(0)}_{xz} = \delta\epsilon^3(h^3/12)\{-2/(1 - \sigma)\Delta w_{0,x} + (2 - 3\sigma)/[2(1 - \sigma)]w_{0,ttx}\}. \tag{18}$$

Noting that $N^{(0)}_{xz} = N^{(0)}_{zx}$ and $N^{(0)}_{yz} = N^{(0)}_{zy}$ within this lowest-order approximation, equation (9) with $n = 0$ yields

$$\begin{aligned}
\delta\epsilon h w_{0,tt} + \delta\epsilon^3(h^3/12)w_{2,tt} = \delta\epsilon^3(h^3/12)\{&-2/(1 - \sigma)\Delta\Delta w_0 \\
&+ (2 - 3\sigma)/[2(1 - \sigma)]\Delta w_{0,tt}\} + Q^{(0)}.
\end{aligned} \tag{19}$$

Since $Q^{(0)}$ is assumed to be of $O(\delta\epsilon^3)$, it can readily be seen that $w_{0,tt}$ is of $O(\epsilon^2)$ and hence equation (19) becomes

$$w_{0,tt} + \epsilon^2 h^2/[6(1 - \sigma)]\Delta\Delta w_0 = \epsilon^2 q, \tag{20}$$

where $q = Q^{(0)}/(\delta\epsilon^3 h) = (q_+ - q_-)/(\delta\epsilon^3 h)$. This equation is well known as Lagrange's equation for the flexural motions [1–3, 20].

On the other hand, upon substitutions of w_1 into $N^{(0)}_{xx}$ and $N^{(0)}_{yy}$, Poisson's equations for the extensional motions [1–3, 20] can immediately be derived from equations (7) and (8) with $n = 0$:

$$u_{0,tt} = 2/(1 - \sigma)(u_{0,x} + \sigma v_{0,y})_{,x} + (u_{0,y} + v_{0,x})_{,y} \tag{21}$$

$$v_{0,tt} = (u_{0,y} + v_{0,x})_{,x} + 2/(1 - \sigma)(v_{0,y} + \sigma u_{0,x})_{,y} \tag{22}$$

Thus Lagrange's equation and Poisson's equations have been obtained as the lowest-order approximation of the present analysis.

Higher-Order Approximation. We now proceed to derive the higher-order approximate equations by reviving the neglected terms in equations (20)–(22). Since only the lowest-order terms have been considered so far, the relation $\delta \sim \epsilon^2$ has not yet been positively employed. Furthermore, the order of u_0 and v_0 has been temporarily assumed to be of $O(1)$. But in order to take account of the effect of small but finite deformation, it becomes necessary to specify their order of magnitude.

The effect of nonlinearity comes from two origins, one due to the finite geometrical deformation and the other due to the deviation from Hooke's law. The former nonlinearity causes first, through the Lagrangian strain tensor, extensional stresses whose order is estimated as $O(\delta^2)$. On the other hand, the order of the latter material nonlinearity causes, through the constitutive equations, extensional stresses which are estimated as of $O(l\delta^2\epsilon^2, m\delta^2\epsilon^2, n\delta^2\epsilon^2)$ from the present strain level $\gamma = O(\delta\epsilon)$. But since the Murnaghan constants l, m, and n (normalized by μ) are usually much greater than unity (e.g., 10–10^2), the order of material nonlinearity cannot readily be estimated as $O(\delta^2\epsilon^2)$, but depends on the relative order of l, m, n, and ϵ. For the plausible value of ϵ (10^{-1}–10^{-2} say), it is appropriate that the Murnaghan constants should be estimated as $O(\epsilon^{-1})$. Under this assumption, the effect of geometrical nonlinearity is still dominant over the material one. Since the extensional motions concerned with here are assumed to be caused by finite flexural motions only, u_0 and v_0 are primarily induced by the effect of geometrical nonlinearity of $O(\delta^2)$. Thus u_0 and v_0 must be taken to be of $O(\delta)$ because the extensional strains and stresses are of $O(\delta u_0, \delta v_0)$. By this fact, it is found from relations (16) and (17) that w_1, u_2, and v_2 are also of $O(\delta)$. In the following analysis, u_0 and v_0 are replaced by δu_0 and δv_0 to specify their order explicitly and a similar replacement is made for w_1, u_2, and v_2.

Making use of the lowest-order approximation and the assumption $\delta \sim \epsilon^2$, $N^{(0)}_{ij}$ ($i, j = x, y, z$) and $N^{(1)}_{ij}$ ($i, j = x, y$) can be evaluated up to terms next higher in order to the lowest-order approximation as

$$\begin{aligned}
N^{(0)}_{xx} = {} &\delta^2\epsilon h[(\lambda + 2)u_{0,x} + \lambda(v_{0,y} + w_1)] \\
&+ \delta^2\epsilon h[(\lambda + 1)(w_{0,x})^2 + \lambda(w_{0,y})^2] + O(\delta^2\epsilon^3, \delta^3\epsilon),
\end{aligned} \tag{23}$$

$$N_{xy}^{(0)} = \delta^2\epsilon h(u_{0,y} + v_{0,x}) + \delta^2\epsilon h w_{0,x}w_{0,y} + O(\delta^2\epsilon^3, \delta^3\epsilon),$$

$$N_{zx}^{(0)} = N_{xz}^{(0)} + \delta^3\epsilon h\{[(\lambda + 2)u_{0,x} + \lambda(v_{0,y} + w_1)]w_{0,x} + (\lambda + 1)[(w_{0,x})^2 + (w_{0,y})^2]w_{0,x} + (u_{0,y} + v_{0,x})w_{0,y}\} + O(\delta^3\epsilon^3),$$

$$N_{zz}^{(0)} = \delta^2\epsilon h\{(\lambda + 2)w_1 + \lambda(u_{0,x} + v_{0,y}) + (\lambda + 1)[(w_{0,x})^2 + (w_{0,y})^2]\} + O(\delta^2\epsilon^3, \delta^3\epsilon),$$

$$N_{xx}^{(1)} = \delta\epsilon^3(h^3/12)[(\lambda + 2)u_{1,x} + \lambda(v_{1,y} + 2w_2)] + \delta\epsilon^5(h^5/80)[(\lambda + 2)u_{3,x} + \lambda(v_{3,y} + 4w_4)] + O(\delta\epsilon^7, \delta^3\epsilon^3),$$

$$N_{xy}^{(1)} = \delta\epsilon^3(h^3/12)(u_{1,y} + v_{1,x}) + \delta\epsilon^5(h^5/80)(u_{3,y} + v_{3,x}) + O(\delta\epsilon^7, \delta^3\epsilon^3) \quad (23)$$

(*Cont.*)

Let us now first derive the higher-order approximate equation for the flexural motions. Following the same procedure as in deriving equation (20), we have from equation (9) with $n = 0$,

$$\delta\epsilon h w_{0,tt} + \delta\epsilon^3(h^3/12)w_{2,tt} = \delta\epsilon^3(h^3/12)[(\lambda + 2)\Delta D_1 + 2\lambda\Delta w_2 - D_{1,tt}] + \delta\epsilon^5(h^5/80)[(\lambda + 2)\Delta D_3 + 4\lambda\Delta w_4 - D_{3,tt}] + \delta^3\epsilon h(R_{x,x} + R_{y,y}) + Q^{(0)} + O(\delta\epsilon^7, \delta^3\epsilon^3), \quad (24)$$

where the definition of D_i ($i = 1, 3$) is given by $D_i = u_{i,x} + v_{i,y}$ and R_x and R_y are defined as

$$R_x = \{(\lambda + 2)u_{0,x} + \lambda(v_{0,y} + w_1) + (\lambda + 1)[(w_{0,x})^2 + (w_{0,y})^2]\}w_{0,x} + (u_{0,y} + v_{0,x})w_{0,y},$$

$$R_y = (u_{0,y} + v_{0,x})w_{0,x} + \{(\lambda + 2)v_{0,y} + \lambda(u_{0,x} + w_1) + (\lambda + 1)[(w_{0,x})^2 + (w_{0,y})^2]\}w_{0,y}. \quad (25)$$

On the other hand, the equations for the extensional motions are derived from equations (7) and (8) with $n = 0$. From equation (7), we have

$$\delta^2\epsilon h u_{0,tt} = \delta^2\epsilon h\{[(\lambda + 2)u_{0,x} + \lambda(v_{0,y} + w_1)]_{,x} + (u_{0,y} + v_{0,x})_{,y}\} + \delta^2\epsilon h\{[(\lambda + 1)(w_{0,x})^2 + \lambda(w_{0,y})^2]_{,x} + (w_{0,x}w_{0,y})_{,y}\} + O(\delta^2\epsilon^3, \delta^3\epsilon), \quad (26)$$

and the symmetric equation for v_0 from equation (8) with $n = 0$. To complete equations (24) and (26), u_3, v_3, and w_4 must be evaluated within the lowest order, while u_1, v_1, w_1, *and* w_2 must be evaluated up to the second-order terms. Following the same procedure as before, we have from the first and the third-order moment equations,

$$u_3 = (2 - \sigma)/[6(1 - \sigma)]\Delta w_{0,x} \quad \text{and} \quad v_3 = (2 - \sigma)/[6(1 - \sigma)]\Delta w_{0,y}. \quad (27)$$

By virtue of these relations and the first-order moment equations, u_1, v_1, and w_1 can be expressed up to the second-order terms as

$$u_1 = -w_{0,x} - \epsilon^2h^2/[4(1 - \sigma)]\Delta w_{0,x},$$
$$u_1 = -w_{0,y} - \epsilon^2h^2/[4(1 - \sigma)]\Delta w_{0,y},$$
$$w_1 = -\sigma/(1 - \sigma)D_0 - [(w_{0,x})^2 + (w_{0,y})^2]/[2(1 - \sigma)]. \quad (28)$$

In order to obtain w_2 up to the second order and w_4 to the lowest order, the fourth-order moment equations are necessary. From equation (9) with $n = 2$ and that with $n = 4$, they can be expressed as

$$w_2 = \sigma/[2(1 - \sigma)]\Delta w_0 + (1 - 2\sigma)/[4(1 - \sigma)]w_{0,tt} + \epsilon^2h^2/[16(1 - \sigma)^2]\Delta\Delta w_0,$$
$$w_4 = -(1 + \sigma)/[24(1 - \sigma)]\Delta\Delta w_0. \quad (29)$$

Thus we have determined the coefficients of z^n in the expansion (6) as far as equations (24) and (26) are concerned. The displacement and Kirchhoff's stress components are then evaluated from those expressions up to $O(\delta\epsilon^3)$ at least and their explicit representation is given in the Appendix. If the terms with δ^2 in those expressions are neglected (which corresponds to the linear higher-order theory), it is found that the displacement and stress components are expanded by the ϵ^2-power, since z is considered to be of $O(\epsilon)$ and the ϵ^2-expansion is relevant to derive the linear higher-order theory. Furthermore, if the static problem with no applied stresses on the faces of the plate is considered, the present results agree with Reissner's results [9][1] after expanding $w_0 = w_0^{(0)} + \epsilon^2w_0^{(2)} + \ldots$.

Upon substitution of the expressions just obtained into equations (24) and (26), we have for the flexural motions,

$$w_{,tt} + \epsilon^2\alpha^2\Delta\Delta w - \epsilon^2\beta_1^2\Delta w_{,tt} + \epsilon^4\beta_2^2\Delta\Delta\Delta w = \epsilon^2 q + \delta^2(R_{x,x} + R_{y,y}) + O(\epsilon^6), \quad (30)$$

with

$$R_x = \nu[2(u_{,x} + \sigma v_{,y}) + (w_{,x})^2 + (w_{,y})^2]w_{,x} + (u_{,y} + v_{,x})w_{,y},$$
$$R_y = (u_{,y} + v_{,x})w_{,x} + \nu[2(v_{,y} + \sigma u_{,x}) + (w_{,x})^2 + (w_{,y})^2]w_{,y}, \quad (31)$$

where $\alpha^2 = h^2/[6(1 - \sigma)]$, $\beta_1^2 = h^2(2 - \sigma)/[24(1 - \sigma)]$, $\beta_2^2 = h^4(8 - 3\sigma)/[240(1 - \sigma)^2]$ and $\nu = 1/(1 - \sigma)$. Here, and hereafter, the subscript (0) of u_0, v_0, and w_0 is omitted.

On the other hand, we have for the extensional motions,

$$u_{,tt} = 2\nu(u_{,x} + \sigma v_{,y})_{,x} + (u_{,y} + v_{,x})_{,y} + \nu[(w_{,x})^2 + \sigma(w_{,y})^2]_{,x} + (w_{,x}w_{,y})_{,y} + O(\epsilon^2), \quad (32)$$

$$v_{,tt} = (u_{,y} + v_{,x})_{,x} + 2\nu(v_{,y} + \sigma u_{,x})_{,y} + (w_{,x}w_{,y})_{,x} + \nu[(w_{,y})^2 + \sigma(w_{,x})^2]_{,y} + O(\epsilon^2), \quad (33)$$

Equation (30) together with equations (32) and (33) are the required higher-order equations for the flexural motions in which the effect of finite thickness and that of small but finite deformation are taken into account.

If the nonlinear terms are completely ignored, equations (30)–(33) decouple and reduce to the linear higher-order equation for flexural motions and Poisson's equations for extensional motions. Equation (30) in this linearized version is given by

$$w_{,tt} + \epsilon^2\alpha^2\Delta\Delta w - \epsilon^2\beta_1^2\Delta w_{,tt} + \epsilon^4\beta_2^2\Delta\Delta\Delta w = \epsilon^2 q + O(\epsilon^6). \quad (34)$$

Since the present theory is valid only for $\epsilon \ll 1$, equation (34), which apparently is a sixth-order differential equation, can also be rewritten by using the lowest-order approximation (20) as

$$w_{,tt} + \epsilon^2\alpha^2\Delta\Delta w - \epsilon^2\beta^2\Delta w_{,tt} = \epsilon^2 q - \epsilon^4\beta'^2\Delta q + O(\epsilon^6), \quad (35)$$

where $\beta^2 = \beta_1^2 + \beta_2^2/\alpha^2 = h^2(17 - 7\sigma)/[60(1 - \sigma)]$ and $\beta'^2 = \beta_2^2/\alpha^2 = h^2(8 - 3\sigma)/[40(1 - \sigma)]$. This suggests that equation (34) should be essentially regarded as the fourth-order equation. As will be discussed in Part 2, the order of this differenttial equation has a very important bearing on an appropriate number of boundary conditions to be imposed on it. We note here that in the static case with no applied stresses $q_\pm$ on the both faces of the plate, equations (34) and (35) degenerate to the classical plate equation, which is consistent with Reissner's result [9].

Next, if we assume no applied stresses and look for plane harmonic wave solutions of equation (34) which vary like $\exp[i(kx - \omega t)]$, the direction of wave propagation being chosen as the x-axis and k and ω being the wave number and the frequency, we have the dispersion relation for flexural waves

$$\omega^2 = \frac{\epsilon^2\alpha^2k^4 - \epsilon^4\beta_2^2k^6}{1 + \epsilon^2\beta_1^2k^2} \cong \frac{\epsilon^2h^2}{6(1 - \sigma)}k^4 - \frac{\epsilon^4h^4(17 - 7\sigma)}{360(1 - \sigma)^2}k^6 + \ldots. \quad (36)$$

This expression is exactly equivalent to that obtained by the ϵ^2-expansion of the frequency ω in Rayleigh-Lamb frequency equation for the flexural waves up to the second-order term [20, 21],[2]

[1] Reissner's results contain errors in his expressions (18*a*, *b*, *c*), which are corrected by $\nu_z \to -\nu_z$.

[2] This expression can also be obtained equivalently by expanding ω in powers of k around $\omega = k = 0$ after setting $\epsilon = 1$.

$$\tan(\epsilon ah/2)/\tan(\epsilon bh/2) = -[4k^2ab/(b^2-k^2)^2], \quad (37)$$

where $a^2 = (1-2\sigma)/[2(1-\sigma)]\omega^2 - k^2$ and $b^2 = \omega^2 - k^2$. Thus it is verified that the present higher-order theory is consistent with the exact three-dimensional linear elastic theory up to terms next higher in order to those of the classical theory. It should be noted that relation (36) is valid only for $k \ll \epsilon^{-1}$ and the dispersion relation of equation (34) and that of equation (35) are equivalent within this range of k. However, we remark that the latter dispersion relation $\omega^2 = \epsilon^2\alpha^2k^4/(1 + \epsilon^2\beta^2k^2)$, rather than the former, exhibits a qualitatively good agreement with the exact Rayleigh-Lamb frequency equation beyond the range of validity for k. Namely, it exhibits a saturation of the phase velocity as $k \to \infty$.

Since the time variation of the flexural motions is small, i.e., $w_{,tt} \sim O(\epsilon^2)$, the inertia terms of the extensional motions caused by the flexural motions are also supposed to be small. Physically, it is interpreted in such a way that the velocity of the extensional waves $c[=(2\nu)^{1/2}]$ is so fast compared with that of the flexural waves (of $O(\epsilon^2)$) that the static equilibrium for the extensional motions is quickly attained. If a new time variable t' focusing on the slow flexural motions is introduced as $t' = \epsilon t$, the inertia terms $\partial^2u/\partial t^2$ and $\partial^2v/\partial t^2$ becomes $\epsilon^2\partial^2u/\partial t'^2$ and $\epsilon^2\partial^2v/\partial t'^2$, respectively. Thus, as far as the terms of $O(1)$ are concerned in equations (32) and (33), they are reduced to the two-dimensional static problem in which the stress function f can be introduced through the following definitions:

$$\begin{aligned} 2\nu(u_{,x} + \sigma v_{,y}) + \nu[(w_{,x})^2 + \sigma(w_{,y})^2] &= f_{,yy}, \\ 2\nu(v_{,y} + \sigma u_{,x}) + \nu[(w_{,y})^2 + \sigma(w_{,x})^2] &= f_{,xx}, \\ u_{,y} + v_{,x} + w_{,x}w_{,y} &= -f_{,xy}. \end{aligned} \quad (38)$$

By virtue of the stress function f, equations (30)–(33) can be rewritten as

$$\begin{aligned} w_{,t't'} + \alpha^2\Delta\Delta w - \epsilon^2\beta^2\Delta w_{,t't'} &= q - \epsilon^2\beta'^2\Delta q \\ &+ (\delta/\epsilon)^2(f_{,yy}w_{,xx} + f_{,xx}w_{,yy} - 2f_{,xy}w_{,xy}), \end{aligned} \quad (39)$$

and

$$\Delta\Delta f = 2(1+\sigma)[(w_{,xy})^2 - w_{,xx}w_{,yy}], \quad (40)$$

where the lowest-order approximation (20) has been used. It can readily be seen that the finite deflection causes in-plane displacements in the form of the total curvature of the plate just as in von Karman's theory.

In concluding this paper, we again remark about the effect of material nonlinearity. As was already mentioned, the effect first causes in K_{xx}, K_{xy}, and K_{yy} extensional stresses of $O(l\delta^2\epsilon^2, m\delta^2\epsilon^2, n\delta^2\epsilon^2)$ and flexural stresses of $O(l\delta^3\epsilon, m\delta^3\epsilon, n\delta^3\epsilon)$. In the present analysis, however, the extensional stresses due to the effect of geometrical nonlinearity are taken up to $O(\delta^2)$, while the flexural stresses are taken up to $O(\delta\epsilon^3)$ (Appendix). Thus it is found that the effect of material nonlinearity is higher order if l, m, and n remain less than ϵ^{-2}. If, on the other hand, it happens that l, m, and $n \geqq \epsilon^{-2}$, account would have to be taken of the effect of material nonlinearity as well as that of geometrical one. Although this process is straightforward, the results are too complicated to be reproduced here.

Finally, we note that the present analysis is concerned with the case in which $\delta \sim \epsilon^2$, but can be extended to the case with $\epsilon^3 < \delta < \epsilon$. In equation (24), it can be seen that next higher-order terms due to the effect of finite thickness are of $O(\delta\epsilon^7)$, while next higher order nonlinear terms are of $(\delta^3\epsilon^3)$. Therefore in order that the higher-order equation (30) is still valid even if the condition $\delta \sim \epsilon^2$ is relaxed, it is necessary that $\epsilon^3 < \delta < \epsilon$. But it should be noted that the effect of material nonlinearity of $O(l\delta^3\epsilon^3, m\delta^3\epsilon^3, n\delta^3\epsilon^3)$ in $N^{(1)}_{xx}$, $N^{(1)}_{xy}$, and $N^{(1)}_{yy}$ become important near the upper limit of $\delta(\delta \lesssim \epsilon)$, if l, m, and n are greater than $(\epsilon/\delta)^2$.

Acknowledgments

The author would like to express his hearty thanks to Prof. T. Kakutani for his stimulating discussion and kind inspection of the manuscript. The author also would like to express his gratitude to the editors and the reviewers for a number of comments and criticisms which led to the improvement of the original manuscript.

This work has been partially supported by THE SAKKOKAI FOUNDATION, Tokyo, Japan.

References

1 Love, A. E. H., *A Treatise on the Mathematical Theory of Elasticity*, Cambridge University Press, Cambridge, 1927.

2 Timoshenko, S., and Woinowsky-Krieger, S., *Theory of Plates and Shells*, McGraw-Hill, New York, 1959.

3 Fung, Y. C., *Foundations of Solid Mechanics*, Prentice-Hall, Englewood Cliffs, N. J., 1965.

4 Reissner, E., "The Effect of Transverse Shear Deformation on the Bending of Elastic Plates," ASME JOURNAL OF APPLIED MECHANICS, Vol. 12, 1945, pp. A-69–A-77.

5 Mindlin, R. D., "Influence of Rotatory Inertia and Shear on Flexural Motions of Isotropic Elastic Plates," ASME JOURNAL OF APPLIED MECHANICS, Vol. 18, 1951, pp. 31–38.

6 Reissner, E., "On Bending of Elastic Plates," *Quarterly of Applied Mathematics*, Vol. 5, 1947, pp. 55–68.

7 Friedrichs, K. O., and Dressler, R. F., "A Boundary Layer Theory for Elastic Plates," *Communications on Pure and Applied Mathematics*, Vol. 14, 1961, pp. 1–33.

8 Tiffen, R., "An Investigation of the Transverse Displacement Equation of Elastic Plate Theory," *Quarterly Journal of Mechanics and Applied Mathematics*, Vol. 14, 1961, pp. 59–74.

9 Reissner, E., "On the Derivation of Boundary Conditions for Plate Theory," *Proceedings of the Royal Society*, London, Series A, Vol. 276, 1963, pp. 178–186.

10 Gol'denveizer, A. L., "Derivation of an Approximate Theory of Bending of a Plate by the Method of Asymptotic Integration of the Equations of the Theory of Elasticity," *Journal of Applied Mathematics and Mechanics*, Vol. 26, 1962, pp. 1000–1025 (*PMM*, Vol. 26, 1962, pp. 668–686).

11 Novotny, B., "On the Asymptotic Integration of the Three Dimensional Nonlinear Equations of Thin Elastic Shells and Plates," *International Journal of Solids and Structures*, Vol. 6, 1970, pp. 433–451.

12 Widera, O. E., "An Asymptotic Theory for the Motion of Elastic Plates," *Acta Mechanica*, Vol. 9, 1970, pp. 54–66.

13 Librescu, L. I., "Some Results Concerning the Refined Theory of Elastic Multilayered Shells," *Revue Roumaine de Sciences and Techniques*, Vol. 20, 1975, pp. 93–105, pp. 285–296.

14 Reissner, E., "On Transverse Bending of Plates Including the Effect of Transverse Shear Deformation," *International Journal of Solids and Structures*, Vol. 11, 1975, pp. 569–573.

15 Lo, K. H., Christensen, R. M., and Wu, E. M., "A High-Order Theory of Plate Deformation," ASME JOURNAL OF APPLIED MECHANICS, Vol. 44, 1977. pp. 663–668.

16 von Karman, T., "Festigkeitsprobleme im Maschinenbau," *Encyklopadie der Mathematischen Wissenschaften*, Vol. IV, 1910, pp. 311–385.

17 Eringen, A. C., *Nonlinear Theory of Continuous Media*, McGraw-Hill, New York, 1962.

18 Bland, D. R., *Nonlinear Dynamic Elasticity*, Blaisdell, Waltham, England, 1969.

19 Sugimoto, N., and Hirao, M., "Nonlinear Mode Coupling of Elastic Waves," *Journal of the Acoustical Society of America*, Vol. 92, 1977, pp. 23–32.

20 Achenbach, J. D., *Wave Propagation in Elastic Solids*, North-Holland, Amsterdam, 1973.

21 Miklowitz, J., *The Theory of Elastic Waves and Waveguides*, North-Holland, Amsterdam, 1978.

APPENDIX

Explicit Representation of Displacement and Kirchhoff's Stress Components

$$\begin{aligned} u_x &= -\delta\left\{\left[w_{,x} + \frac{\epsilon^2h^2}{4(1-\sigma)}\Delta w_{,x}\right]z - \frac{(2-\sigma)}{6(1-\sigma)}\Delta w_{,x}z^3\right\} + \delta^2u, \\ u_z &= \delta\left\{w + \left[\frac{\sigma}{2(1-\sigma)}\Delta w + \frac{\epsilon^2h^2}{16(1-\sigma)^2}\Delta\Delta w + \frac{\epsilon^2(1-2\sigma)}{4(1-\sigma)}w_{,t't'}\right]z^2 \right. \\ &\quad \left. - \frac{1+\sigma}{24(1-\sigma)}\Delta\Delta wz^4\right\} - \delta^2\left\{\frac{1}{2(1-\sigma)}[2\sigma(u_{,x} + v_{,y}) \right. \\ &\quad \left. + (w_{,x})^2 + (w_{,y})^2]z\right\}, \\ K_{xx} &= -\delta\left\{\frac{2}{(1-\sigma)}(w_{,xx} + \sigma w_{,yy}) + \frac{\epsilon^2h^2}{4(1-\sigma)^2}[(2-\sigma)\Delta w_{,xx} \right. \\ &\quad \left. + \sigma\Delta w_{,yy}] - \frac{\epsilon^2\sigma}{(1-\sigma)}w_{,t't'}\right\}z \end{aligned} \quad (41)$$

$$+\frac{\delta}{3(1-\sigma)}[2\Delta\Delta w-(2-\sigma)\Delta w_{,yy}]z^3+\frac{\delta^2}{(1-\sigma)}[2(u_{,x}+\sigma v_{,y})$$
$$+(w_{,x})^2+\sigma(w_{,y})^2],$$
$$K_{zz}=\delta\left\{\epsilon^2\left[w_{,t't'}+\frac{h^2}{4(1-\sigma)}\Delta\Delta w\right]z-\frac{1}{3(1-\sigma)}\Delta\Delta w z^3+\epsilon^3\frac{ph}{2}\right\},$$
$$K_{xy}=-\delta\left\{\left[2w_{,xy}+\frac{\epsilon^2h^2}{2(1-\sigma)}\Delta w_{,xy}\right]z-\frac{(2-\sigma)}{3(1-\sigma)}\Delta w_{,xy}z^3\right\}$$
$$+\delta^2(u_{,y}+v_{,x}+w_{,x}w_{,y}) \qquad (41)\ (Cont.)$$

$$K_{xz}=\delta\left(z^2-\frac{\epsilon^2h^2}{4}\right)\left[\frac{1}{(1-\sigma)}\Delta w_{,x}+\frac{\epsilon^2h^2(2-\sigma)}{8(1-\sigma)^2}\Delta\Delta w_{,x}\right.$$
$$\left.-\frac{\epsilon^2}{2(1-\sigma)}w_{,t't'x}\right]-\delta\left(z^4-\frac{\epsilon^4h^4}{16}\right)\frac{\Delta\Delta w_{,x}}{6(1-\sigma)}, \qquad (41)\ (Cont.)$$

where $z\sim O(\epsilon)$ and $ph=2Q^{(1)}/(\delta\epsilon^4h)=(q_++q_-)/(\delta\epsilon^3)$; the subscript (0) of u_0, v_0, and w_0 is dropped and the explicit forms of u_y, K_{yy}, and K_{yz} are omitted because they are easily reproduced from u_x, K_{xx}, and K_{xz}.

N. Sugimoto

Research Associate,
Department of Mechanical Engineering,
Faculty of Engineering Science,
Osaka University,
Toyonaka, Osaka 560, Japan

Nonlinear Theory for Flexural Motions of Thin Elastic Plate

Part 2: Boundary-Layer Theory Near the Edge

This paper deals with, as a continuation of Part 1 of this series, the boundary-layer theory for flexural motions of a thin elastic plate. In the framework of the higher-order theory developed in Part 1, three independent boundary conditions at the edge of the plate are too many to be imposed on the essentially fourth order differential equations. To overcome this difficulty, a boundary layer appearing in a narrow region adjacent to the edge is introduced. Using the matched asymptotic expansion method, uniformly valid solutions for a full plate problem are sought. The boundary-layer problem consists of the torsion problem and the plane problem. Three types of the edge conditions are treated, the built-in edge, the free edge, and the hinged edge. Depending on the type of edge condition, the nature of the boundary layer is characterized. After solving the boundary-layer problem, "reduced" boundary conditions relevant to the higher-order theory are established.

Introduction

In Part 1, [1] of this paper, a higher-order theory for flexural motions of a thin elastic plate was developed including both the effects of finite thickness of the plate and of small but finite deformation. To apply the theory to actual problems, it is then required to specify boundary conditions along an edge of the plate. The analysis in Part 1, however, does not presuppose the presence of an edge explicitly. It only assumes that

1 A characteristic wavelength of flexural motions L is greater than a thickness of the plate H (i.e., $O(H/L) = \epsilon \ll 1$).

2 A characteristic deflection of the plate W is smaller than the thickness (i.e., $O(W/H) = O(W/L \cdot L/H) = \delta/\epsilon \ll 1$).

3 δ is of order of ϵ^2.

If boundary conditions would be imposed, it usually happens that the constraint along the edge invalidates the previous three assumptions.

To elucidate this situation, let us first start from the linear higher-order theory for flexural motions. Since in the linear theory, flexural motions and extensional motions can be treated separately, together with the boundary conditions inclusive, we take up only flexural motions here. From the standpoint of three-dimensional elasticity theory, three independent boundary conditions must be satisfied along the edge of the plate. For example, suppose a semi-infinite plate whose edge condition is the built-in type (the edge is located at $y = 0$, say). Then it is reasonable, since the plate is thin, to impose three boundary conditions averaged over the thickness; that is, no averaged deflection, $\overline{u}_z = \delta\{w + \epsilon^2\sigma h^2/[24(1-\sigma)]\Delta w + \ldots\} = 0$, and no averaged rotations $\overline{\omega}_x$ and $\overline{\omega}_y$ about the x and y-axes, $\overline{\omega}_{x(y)} = \overline{(\text{rot } u/2)}_{x(y)} = (-1)\delta\{w_{,y(x)} + \epsilon^2(2+\sigma)h^2/[24(1-\sigma)]\Delta w_{,y(x)} + \ldots\} = 0$, (-1) being only for $\overline{\omega}_y$ and the averaged quantity $\overline{(\ldots)}$ being defined as $\overline{(\ldots)} = \int_{-\epsilon h/2}^{\epsilon h/2}(\ldots)dz/(\epsilon h)$ (see the Appendix of Part 1). In the classical linear theory ($\epsilon \to 0$), the conditions $\overline{u}_z = 0$ and $\overline{\omega}_y = 0$ degenerate into one condition $w = 0$, and only two independent conditions can be imposed. This is consistent with the fourth-order differential equation of the classical thin plate theory. In the present higher-order theory, however, they no longer degenerate into two conditions. Since the higher-order equation for flexural motions (equation (34) in Part 1) is apparently of sixth order, it seems possible to impose the foregoing three conditions. But for the fulfillment of the conditions, there arises a solution which varies rapidly, i.e., $\partial w/\partial x \sim \partial w/\partial y \sim O(\epsilon^{-1})$ and invalidates Assumption 1, since the highest derivative in the higher-order equation contains the coefficient with the smaller parameter ϵ^4 than other terms. Thus the higher-order theory becomes invalid. But this does not imply that when an edge is present, the higher-order theory is invalid everywhere in the plate, because the validity of the initial three assumptions is still physically expected in a region away from the edge. It rather implies that the higher-order equation should not be regarded as the sixth order, but as the fourth order and that three boundary conditions are too many. Thus there arises a discrepancy between the conditions to be satisfied actually at the edge and those relevant to the higher-order theory. For the present weakly nonlinear problem, since the flexural and extensional motions are coupled, they are no longer treated separately. The boundary conditions should thus be imposed on the total motions. For the coupled higher-order equations, on the other hand, it is considered legitimate that two boundary conditions should be imposed on each equation. To bridge the gap between the actual

Contributed by the Applied Mechanics Division for publication in the JOURNAL OF APPLIED MECHANICS.

Discussion on this paper should be addressed to the Editorial Department, ASME, United Engineering Center, 345 East 47th Street, New York, N. Y. 10017, and will be accepted until September 1, 1981. Readers who need more time to prepare a Discussion should request an extension from the Editorial Department. Manuscript received by ASME Applied Mechanics Division, December, 1979; final revision, August, 1980.

boundary conditions and the "reduced" boundary conditions relevant to the higher-order **theory,** it is necessary to introduce the idea of a boundary layer appearing in a narrow region adjacent to the edge.

The idea of the boundary layer was first introduced by Friedrichs and Dressler [2] to explain the relevant stress boundary conditions for the classical plate equation. As is well known, three independent boundary conditions (bending moment, twisting moments, and shear force) are too many to be imposed. They showed by the asymptotic expansion method that the two conditions for the twisting moment and shear force should be replaced by one modified condition, although this result has already been pointed out by Kirchhoff and later Kelvin and Tait based on the Saint-Venant's principle [3, 4]. In a similar manner, Gol'denveizer [5] also developed the boundary-layer theory to confirm the classical boundary conditions for various edge conditions. Recently Reissner [6] considered the boundary-layer effect in his original manner. It is to be noted, however, that the aforementioned analyses referred to are restricted to linear theory. The purpose of this paper is to extend the analysis to the weakly nonlinear case, and to investigate systematically the boundary-layer effect on the higher-order theory. After solving the boundary-layer problem, the reduced boundary conditions for the higher-order theory are established.

Since the boundary layer is supposed to develop in a narrow region along the edge, the full plate theory is divided into two parts. One part is for the boundary layer in which the effect of the constraint at the edge is dominant, while the other is for the interior region in which the effect of edge conditions is tempered through the boundary layer. In the interior region, the higher-order theory described in Part 1 is taken to be valid. To develop the boundary-layer theory, a matched asymptotic expansion method [7–9] is used. To achieve a proper description of the narrow layer, new stretched coordinate are introduced. The equations in the new coordinates consist of the torsion problem and the plane problem. Solutions are sought so that they may match with the interior solutions at the limit between the boundary layer and the interior region. Three types of edge conditions are treated in the following: the built-in edge, the free edge, and the hinged edge. It is found that the type of boundary layer is different depending on the edge conditions. For the built-in edge, there first appears the plain strain boundary layer, while for the free edge, the torsion boundary layer first. For the hinged edge, however, it is found that no boundary layer arises. After seeking boundary-layer solutions, the reduced boundary conditions for the interior equations (the higher-order equations in Part 1) are established. It is then revealed from these conditions that, if the boundary layer arises, its effect gives rise to $O(\epsilon)$-corrections in the interior solutions. Although the effect of finite thickness is of $O(\epsilon^2)$ in the interior equations, the effect affects the interior solutions primarily through the boundary layer. This should be compared with the case in which no boundary layer arises. Finally, we remark that the stress distribution in the boundary layer can easily be obtained, but explicit results are not given here and left for a subsequent paper.

Basic Equations

Since the complete set of basic equations has already been given in Part 1 [1], we only briefly make reference to them. The same notation is also used so that each quantity having already appeared there is referred to without a comment. The same rectangular coordinate system is also used with the in-plane coordinates designated by x and y and the transverse coordinate by z.

Let a semi-infinite plate occupy the region, $y \geqq 0$ and $-\epsilon h/2 \leqq z \leqq \epsilon h/2$, and let the boundary be located at $y = 0$ and $-\infty < x < \infty$. The boundary layer is assumed to develop in a narrow region adjacent to the edge, $0 \leqq y \lesssim y_b$ and $-\epsilon h/2 \leqq z \leqq \epsilon h/2$. Here, y_b is the width of the boundary layer in the y-direction whose order is comparable with the thickness of the plate. It is therefore appropriate to introduce, instead of y and z, new stretched coordinates η and ζ defined by

$$\eta = y/\epsilon \quad \text{and} \quad \zeta = z/\epsilon, \tag{1}$$

where y and z are already normalized by the characteristic wavelength of the flexural motions.

By means of the new coordinates η and ζ, the equations of motion can be rewritten as

$$\epsilon u_{i,tt} = \epsilon L_{ix,x} + L_{iy,\eta} + L_{iz,\zeta} \quad (i = x, y, z) \tag{2}$$

where, as in Part 1, the comma implies the partial differentiation with respect to the subscript(s) indicated after the coma.

In Part 1, the displacement components have been treated as the basic dependent variables. In the following, however, it is advantageous to work with the stress tensor, especially Kirchhoff's stress tensor. Thus the equations of motion can be expressed as

$$\begin{aligned} K_{iy,\eta} + K_{iz,\zeta} = {} & \epsilon u_{i,tt} - \epsilon K_{ix,x} \\ & - (\epsilon u_{i,x} K_{xx} + u_{i,\eta} K_{yx} + u_{i,\zeta} K_{zx})_{,x} \\ & - \epsilon^{-1} [(\epsilon u_{i,x} K_{xy} + u_{i,\eta} K_{yy} + u_{i,\zeta} K_{zy})_{,\eta} \\ & + (\epsilon u_{i,x} K_{xz} + u_{i,\eta} K_{yz} + u_{i,\zeta} K_{zz})_{,\zeta}], \quad (i = x, y, z) \end{aligned} \tag{3}$$

When the analysis is carried out with Kirchhoff's stress tensor, the compatibility conditions are required to determine the displacements uniquely. The six necessary and sufficient compatibility conditions are derived in the Appendix A:

$$\begin{aligned} \tilde{\Delta} K_{xy} + \epsilon^2 K_{xy,xx} + \epsilon \Theta_{,x\eta} &= \epsilon^2 P_{xy}, & \tilde{\Delta} K_{xx} + \epsilon^2 K_{xx,xx} + \epsilon^2 \Theta_{,xx} &= \epsilon^2 P_{xx}, \\ \tilde{\Delta} K_{zx} + \epsilon^2 K_{zx,xx} + \epsilon \Theta_{,x\zeta} &= \epsilon^2 P_{zx}, & \tilde{\Delta} K_{yy} + \epsilon^2 K_{yy,xx} + \Theta_{,\eta\eta} &= \epsilon^2 P_{yy}, \\ \tilde{\Delta} K_{yz} + \epsilon^2 K_{yz,xx} + \Theta_{,\eta\zeta} &= \epsilon^2 P_{yz}, & \tilde{\Delta} K_{zz} + \epsilon^2 K_{zz,xx} + \Theta_{,\zeta\zeta} &= \epsilon^2 P_{zz}, \end{aligned} \tag{4}$$

where $\tilde{\Delta} = \partial^2/\partial\eta^2 + \partial^2/\partial\zeta^2$ and $\Theta = (K_{xx} + K_{yy} + K_{zz})/(1 + \sigma)$. Once Kirchhoff's stress tensor is known and therefore the Lagrangian strain tensor is known from the constitutive equations, the displacement components are derived from the following relations:

$$\begin{aligned} 2u_{x,x} &= 2E_{xx} - u_{k,x} u_{k,x}, & u_{x,\eta} + \epsilon u_{y,x} &= 2\epsilon E_{xy} - u_{k,x} u_{k,\eta}, \\ 2u_{y,\eta} &= 2\epsilon E_{yy} - \epsilon^{-1} u_{k,\eta} u_{k,\eta}, & u_{x,\zeta} + \epsilon u_{z,x} &= 2\epsilon E_{xz} - u_{k,x} u_{k,\zeta}, \\ 2u_{z,\zeta} &= 2\epsilon E_{zz} - \epsilon^{-1} u_{k,\zeta} u_{k,\zeta}, & u_{y,\zeta} + u_{z,\eta} &= 2\epsilon E_{yz} - \epsilon^{-1} u_{k,\eta} u_{k,\zeta}. \end{aligned} \tag{5}$$

where the repeated index k implies summation over x, y, and z.

Boundary-Layer Theory

By the matched asymptotic expansion method [7–9], the boundary-layer solutions are sought in the following form:

$$\begin{aligned} u_i &= \delta(\tilde{u}_i^{(0)} + \epsilon \tilde{u}_i^{(1)} + \epsilon^2 \tilde{u}_i^{(2)} + \epsilon^3 \tilde{u}_i^{(3)} + \ldots), \\ E_{ij} &= \delta(\epsilon \tilde{E}_{ij}^{(1)} + \epsilon^2 \tilde{E}_{ij}^{(2)} + \epsilon^3 \tilde{E}_{ij}^{(3)} + \ldots), \\ K_{ij} &= \delta(\epsilon \tilde{K}_{ij}^{(1)} + \epsilon^2 \tilde{K}_{ij}^{(2)} + \epsilon^3 \tilde{K}_{ij}^{(3)} + \ldots), \\ L_{ij} &= \delta(\epsilon \tilde{L}_{ij}^{(1)} + \epsilon^2 \tilde{L}_{ij}^{(2)} + \epsilon^3 \tilde{L}_{ij}^{(3)} + \ldots), \\ & \qquad (i, j = x, y, z) \end{aligned} \tag{6}$$

where δ has already been assumed to be ϵ^2 and the tilde implies a quantity pertaining to the boundary layer and each quantity is assumed to depend on x, η, ζ, and t. It should be remarked that E_{ij}, K_{ij}, and L_{ij} $(i, j = x, y, z)$ begin with terms of $O(\delta\epsilon)$ because the characteristic strain and stress concerned with here have been assumed to be of $O(\delta\epsilon)$. According to the matched asymptotic expansion method, the infinity $\eta = \infty$ in the boundary layer corresponds to $y = 0$ in the interior solutions. The boundary-layer solutions therefore should be obtained so that they may be matched at $\eta = \infty$ with the interior solutions at $y = 0$. To do so, the displacement components in the interior solutions are expanded in the following form:

$$u = u^{(0)} + \epsilon u^{(1)} + \epsilon^2 u^{(2)} + \ldots,$$
$$v = v^{(0)} + \epsilon v^{(1)} + \epsilon^2 v^{(2)} + \ldots,$$
$$w = w^{(0)} + \epsilon w^{(1)} + \epsilon^2 w^{(2)} + \ldots, \quad (7)$$

where $u^{(k)}$, $v^{(k)}$, and $w^{(k)}$ ($k = 0, 1, 2, \ldots$) depend on x, y, and t.

The interior solutions at the matching region ($\eta = \infty, y = 0$) can be obtained by substituting (7) into the interior solutions (see the Appendix in Part 1) and expanding them around $y = 0$. After setting $y = \epsilon\eta$ and $z = \epsilon\zeta$ in the expansions thus obtained, the interior solutions with which the boundary-layer solutions should be matched at $\eta = \infty$ are given by

$$u_{i\infty} = \delta(\bar{u}_{i\infty}^{(0)} + \epsilon\bar{u}_{i\infty}^{(1)} + \epsilon^2\bar{u}_{i\infty}^{(2)} + \ldots),$$
$$K_{ij\infty} = \delta(\epsilon\tilde{K}_{ij\infty}^{(1)} + \epsilon^2\tilde{K}_{ij\infty}^{(2)} + \epsilon^3\tilde{K}_{ij\infty}^{(3)} + \ldots), \quad (i, j = x, y, z) \quad (8)$$

where $\bar{u}_{i\infty}^{(k)}$ and $\tilde{K}_{ij\infty}^{(k)}$ ($k = 0, 1, 2, \ldots$) are evaluated at $y = 0$. At the actual edge $\eta = 0$, on the other hand, three types of the boundary conditions are treated in the following analysis: the built-in edge, the free edge, and the hinged edge. For the built-in edge, the boundary conditions are given in terms of displacement components as

$$u_x = u_y = u_z = 0 \quad \text{at} \quad \eta = 0, \quad (9)$$

and for the free edge, they are given in terms of stress components as

$$L_{xy} = L_{yy} = L_{zy} = 0 \quad \text{at} \quad \eta = 0. \quad (10)$$

For the hinged edge, it is difficult, especially in the nonlinear case, to specify the boundary conditions in the form of the displacement and/or the stress components. This is discussed later. In addition to the conditions at $\eta = 0$ and $\eta = \infty$, the conditions at the upper and lower faces of the plate are required. They are nothing but those for the interior solutions. For the boundary-layer solutions as well, it is thus assumed that

$$L_{xz} = L_{yz} = 0 \quad \text{at} \quad \zeta = \pm h/2, \quad (11a,b)$$

but L_{zz} is employed in the following expansion form:

$$L_{zz} = \delta\epsilon^3[\tilde{q}_{\pm}(x) + \epsilon\tilde{q}_{\pm,y}(x)\eta + \epsilon^2\tilde{q}_{\pm,yy}(x)\eta^2/2 + \ldots]_{y=0}. \quad (11c)$$

Case of Built-In Edge. Although the case of built-in edge is treated first, the imposition of the boundary condtions at $\eta = 0$ is suspended for a while so that the following analysis may be valid not only for the built-in edge but also for the other edge conditions. Substituting (6) into the basic equations and collecting terms with the same power of ϵ, we have successive systems of equations. In this process, it is assumed that the time derivative $\partial/\partial t$ is also of $O(\epsilon)$ just as in the interior solutions.

Zeroth-Order Problem. Since we are concerned with the case in which all stress and strain components at this order vanish, all basic equations except (5) are satisfied identically. The equations for the displacement components are then given by

$$\bar{u}_{x,x}^{(0)} = \bar{u}_{x,\eta}^{(0)} = \bar{u}_{x,\zeta}^{(0)} = \bar{u}_{y,\eta}^{(0)} = \bar{u}_{y,\zeta}^{(0)} + \bar{u}_{z,\eta}^{(0)} = \bar{u}_{z,\zeta}^{(0)} = 0. \quad (12)$$

Imposing the matching conditions at $\eta = \infty$, i.e., $\bar{u}_{x\infty}^{(0)} = \bar{u}_{y\infty}^{(0)} = 0$ and $\bar{u}_{z\infty}^{(0)} = w^{(0)}$, we have

$$\bar{u}_x^{(0)} = \bar{u}_y^{(0)} = 0 \quad \text{and} \quad \bar{u}_z^{(0)} = w^{(0)}, \quad (13)$$

where it should be noted that $w^{(0)}$ is evaluated at $y = 0$ and therefore it depends on x and t only.

First-Order Problem.

$$\tilde{K}_{xy,\eta}^{(1)} + \tilde{K}_{xz,\zeta}^{(1)} = \tilde{K}_{yy,\eta}^{(1)} + \tilde{K}_{yz,\zeta}^{(1)} = \tilde{K}_{yz,\eta}^{(1)} + \tilde{K}_{zz,\zeta}^{(1)} = 0. \quad (14a,b,c)$$

This system of equations is supplemented by the following compatibility conditions:

$$\tilde{\Delta}\tilde{K}_{xy}^{(1)} = \tilde{\Delta}\tilde{K}_{xz}^{(1)} = \tilde{\Delta}\tilde{K}_{xx}^{(1)} = 0,$$
$$\tilde{\Delta}\tilde{K}_{yy}^{(1)} + \tilde{\Theta}_{,\eta\eta}^{(1)} = \tilde{\Delta}\tilde{K}_{zz}^{(1)} + \tilde{\Theta}_{,\zeta\zeta}^{(1)} = \tilde{\Delta}\tilde{K}_{yz}^{(1)} + \tilde{\Theta}_{,\eta\zeta}^{(1)} = 0, \quad (15)$$

where $\tilde{\Theta}^{(1)} = (\tilde{K}_{xx}^{(1)} + \tilde{K}_{yy}^{(1)} + \tilde{K}_{zz}^{(1)})/(1 + \sigma)$.

In addition, the displacement components are governed by

$$2\bar{u}_{x,x}^{(1)} = [\tilde{K}_{xx}^{(1)} - \sigma(\tilde{K}_{yy}^{(1)} + \tilde{K}_{zz}^{(1)})]/(1 + \sigma),$$
$$\bar{u}_{x,\eta}^{(1)} = \bar{u}_{y,\eta}^{(1)} = \bar{u}_{z,\zeta}^{(1)} = \bar{u}_{x,\zeta}^{(1)} + \bar{u}_{z,x}^{(0)} = \bar{u}_{y,\zeta}^{(1)} + \bar{u}_{z,\eta}^{(1)} = 0. \quad (16)$$

These equations should be solved in the semi-infinite strip region, i.e., $0 \leqq \eta < \infty$ and $-h/2 \leqq \zeta \leqq h/2$ under the relevant boundary conditions specified along the boundary of the region. It can readily be seen that equations (14)–(16) can be split into two separate problems. Equation (14a) constitutes a torsion problem for the strip region, while (14b, c) constitute a plane strain problem. As will be seen later, however, it is not an exact plane strain problem.

In order to solve these equations, it is convenient to introduce the following stress functions $\tilde{\psi}^{(1)}$ and $\tilde{\varphi}^{(1)}$ so that the stresses derived from them may vanish at $\eta = \infty$:

$$\tilde{K}_{xy}^{(1)} = \tilde{K}_{xy\infty}^{(1)} - \tilde{\psi}_{,\zeta}^{(1)}, \quad \tilde{K}_{xz}^{(1)} = \tilde{\psi}_{,\eta}^{(1)},$$
$$\tilde{K}_{yy}^{(1)} = \tilde{K}_{yy\infty}^{(1)} - \tilde{\varphi}_{,\zeta\zeta}^{(1)}, \tilde{K}_{zz}^{(1)} = -\tilde{\varphi}_{,\eta\eta}^{(1)}, \quad \tilde{K}_{yz}^{(1)} = \tilde{\varphi}_{,\eta\zeta}^{(1)}, \quad (17)$$

where the matching conditions at $\eta = \infty$ are given by

$$\tilde{K}_{xy\infty}^{(1)} = -2w_{,xy}^{(0)}\zeta, \quad \tilde{K}_{xz\infty}^{(1)} = 0,$$
$$\tilde{K}_{yy\infty}^{(1)} = -W_y^{(0)}\zeta, \quad \tilde{K}_{yz\infty}^{(1)} = \tilde{K}_{zz\infty}^{(1)} = 0, \quad (18)$$

$W_y^{(0)}$ being defined by $W_y^{(0)} = 2(w_{,yy}^{(0)} + \sigma w_{,xx}^{(0)})/(1 - \sigma)$. It can readily be seen that (17) can of course satisfy equation (14). Furthermore, it follows from the compatibility conditions that the stress functions must satisfy the following equations:

$$\tilde{\Delta}\tilde{\psi}^{(1)} = c(x, t), \quad \tilde{\Delta}\tilde{\Delta}\tilde{\varphi}^{(1)} = 0, \quad (19), (20)$$

where c is an arbitrary function of x and t, but must be taken zero in light of the boundary conditions at $\eta = \infty$. Solving $\tilde{\Theta}^{(1)}$ from equation (15) yields

$$\tilde{\Theta}^{(1)} = -\tilde{\Delta}\tilde{\varphi}^{(1)} + \alpha^{(1)}\eta + \beta^{(1)}\zeta + \gamma^{(1)}, \quad (21)$$

where $\alpha^{(1)}$, $\beta^{(1)}$, and $\gamma^{(1)}$ are arbitrary functions of x and t only, which should be determined from the matching condition for $\tilde{K}_{xx}^{(1)}$. Since $\tilde{K}_{xx\infty}^{(1)}$ is given by $\tilde{K}_{xx\infty}^{(1)} = -W_x^{(0)}\zeta$, $W_x^{(0)}$ being defined as $W_x^{(0)} = 2(w_{,xx}^{(0)} + \sigma w_{,yy}^{(0)})/(1 - \sigma)$, it is found that $\alpha^{(1)} = \gamma^{(1)} = 0$ and $\beta^{(1)} = -2\Delta w^{(0)}/(1 - \sigma)$, where Δ is defined as $\Delta = \partial^2/\partial x^2 + \partial^2/\partial y^2|_{y=0}$. This Δ should not be confused with $\tilde{\Delta} = \partial^2/\partial\eta^2 + \partial^2/\partial\zeta^2$. Thus $\tilde{K}_{xx}^{(1)}$ can be obtained as

$$\tilde{K}_{xx}^{(1)} = -W_x^{(0)}\zeta - \sigma\tilde{\Delta}\tilde{\varphi}^{(1)}. \quad (22)$$

As the problems are formulated in terms of the stress functions, the boundary conditions must also be expressed in terms of the stress functions. For $\tilde{\psi}^{(1)}$, the boundary conditions are expressed as

$$\eta \to \infty, \quad \tilde{\psi}_{,\eta}^{(1)}, \tilde{\psi}_{,\zeta}^{(1)} \to 0, \quad \zeta = \pm h/2, \tilde{\psi}_{,\eta}^{(1)} = 0, \quad (23a,b)$$

and for $\tilde{\varphi}^{(1)}$, they are given by

$$\eta \to \infty, \tilde{\varphi}_{,\eta\eta}^{(1)}, \tilde{\varphi}_{,\zeta\zeta}^{(1)}, \tilde{\varphi}_{,\eta\zeta}^{(1)} \to 0, \quad \zeta = \pm h/2, \quad \tilde{\varphi}_{,\eta\eta}^{(1)} = \tilde{\varphi}_{,\eta\zeta}^{(1)} = 0, \quad (24a,b)$$

where the conditions at $\eta = 0$ are left open for a while for the reason mentioned before. Although the conditions (23a) and (24a) imply that as $\eta \to \infty$, $\tilde{\psi}^{(1)}$ and $\tilde{\varphi}^{(1)}$ approach, respectively, $\tilde{\psi}^{(1)} \to c_0$ and $\tilde{\varphi}^{(1)} \to c_1\eta + c_2\zeta + c_3$, where c_0, c_1, c_2, and c_3 being arbitrary functions of x and t, they can be set equal to zero without loss of generality. Therefore (23b) and (24b) at $\zeta = \pm h/2$ are replaced by $\tilde{\psi}^{(1)} = 0$ and $\tilde{\varphi}^{(1)} = \tilde{\varphi}_{,\zeta}^{(1)} = 0$, respectively.

It should be remarked here that the two stress functions thus introduced represent the boundary-layer solutions. It should also be noted, even though it seems trivial, that even if the two stress functions are set equal to zero identically, the stresses (17) can satisfy equations (14)–(15). Therefore, if the stresses and/or the displacements can satisfy the boundary conditions at $\eta = 0$ without any introduction $\tilde{\psi}^{(1)}$ and $\tilde{\varphi}^{(1)}$, the interior solutions invade the boundary layer. This case should then be interpreted as no boundary layer appearing.

The displacement components are obtained from equations (16). By making use of the matching conditions,

$$\tilde{u}_{x\infty}^{(1)} = -w_{,x}^{(0)}\zeta, \quad \tilde{u}_{y\infty}^{(1)} = -w_{,y}^{(0)}\zeta, \quad \tilde{u}_{z\infty}^{(1)} = w^{(1)} + w_{,y}^{(0)}\eta, \tag{25}$$

they are sought as $\tilde{u}_i^{(1)} = \tilde{u}_{i\infty}^{(1)}$ $(i = x, y, z)$. We remark here that $\tilde{\varphi}^{(1)}$ itself does not affect $\tilde{u}_x^{(1)}$. Therefore $\tilde{u}_x^{(1)}$ is free from the boundary-layer solutions. Such a plane problem may be called a plane strain problem, although it is not so in a strict sense because the displacements derived from $\tilde{\varphi}^{(1)}$ ($\tilde{u}_{yh}^{(2)}$ and $\tilde{u}_{zh}^{(2)}$) depend on x parametrically.

Second-Order Problem.

$$\tilde{K}_{xy,\eta}^{(2)} + \tilde{K}_{xz,\zeta}^{(2)} = -\tilde{K}_{xx,x}^{(1)} = W_{x,x}^{(0)}\zeta + \sigma\tilde{\Delta}\tilde{\varphi}_{,x}^{(1)}, \tag{26a}$$

$$\tilde{K}_{yy,\eta}^{(2)} + \tilde{K}_{yz,\zeta}^{(2)} = -\tilde{K}_{xy,x}^{(1)} = 2w_{,xxy}^{(0)}\zeta + \tilde{\psi}_{,x\zeta}^{(1)}, \tag{26b}$$

$$\tilde{K}_{yz,\eta}^{(2)} + K_{zz,\zeta}^{(2)} = -\tilde{K}_{zx,x}^{(1)} = -\tilde{\psi}_{,x\eta}^{(1)}. \tag{26c}$$

The following analysis can be executed in quite an analogous manner to that demonstrated for the first-order problem. It is therefore only briefly described.

To solve equations (26*a*), a stress function $\tilde{\psi}^{(2)}$ is introduced in view of the matching conditions as

$$\tilde{K}_{xy}^{(2)} = \tilde{K}_{xy\infty}^{(2)} + \tilde{\varphi}_{,x\eta}^{(1)} + (1-\sigma)\int_\eta^\infty \tilde{\Delta}\tilde{\varphi}^{(1)}{}_{,x}d\eta - \tilde{\psi}_{,\zeta}^{(2)},$$

$$\tilde{K}_{xz}^{(2)} = \tilde{K}_{xz\infty}^{(2)} + \tilde{\varphi}_{,x\zeta}^{(1)} + \tilde{\psi}_{,\eta}^{(2)}, \tag{27}$$

with

$$\tilde{K}_{xy\infty}^{(2)} = -2w_{,xy}^{(1)}\zeta - 2w_{,xyy}^{(0)}\eta\zeta + u_{,y}^{(0)} + v_{,x}^{(0)} + w_{,x}^{(0)}w_{,y}^{(0)},$$

$$\tilde{K}_{xz\infty}^{(2)} = \Delta w_{,x}^{(0)}\,(\zeta^2 - h^2/4)/(1-\sigma). \tag{28}$$

The function $\tilde{\psi}^{(2)}$ is specified from the compatibility conditions by $\tilde{\Delta}\tilde{\psi}^{(2)} = 0$. Noting that $\tilde{L}_{xz}^{(2)} = \tilde{K}_{xz}^{(2)}$ for this order, the boundary conditions for $\tilde{\psi}^{(2)}$ are given by the same conditions as for $\tilde{\psi}^{(1)}$ (23*a*, *b*).

For equations (26*b*, *c*), on the other hand, a stress function $\tilde{\varphi}^{(2)}$ can also be introduced through the relations

$$\tilde{K}_{yy}^{(2)} = \tilde{K}_{yy\infty}^{(2)} - 2\int_\eta^\infty \tilde{\psi}_{,x\zeta}^{(1)}d\eta - \tilde{\varphi}_{,\zeta\zeta}^{(2)},$$

$$\tilde{K}_{zz}^{(2)} = -\tilde{\varphi}_{,\eta\eta}^{(2)}, \quad \tilde{K}_{yz}^{(2)} = \tilde{K}_{yz\infty}^{(2)} - \tilde{\psi}_{,x}^{(1)} + \tilde{\varphi}_{,\eta\zeta}^{(2)}, \tag{29}$$

with

$$\tilde{K}_{yy\infty}^{(2)} = -W_y^{(1)}\,\zeta - W_{y,y}^{(0)}\,\eta\zeta + [2(v_{,y}^{(0)} + \sigma u_{,x}^{(0)}) + (w_{,y}^{(0)})^2 + \sigma(w_{,x}^{(0)})^2]/(1-\sigma),$$

$$\tilde{K}_{zz\infty}^{(2)} = 0, \quad \tilde{K}_{yz\infty}^{(2)} = \Delta w_{,y}^{(0)}\,(\zeta^2 - h^2/4)/(1-\sigma). \tag{30}$$

Here, and hereafter, the definitions $W_y^{(k)} = 2(w_{,yy}^{(k)} + \sigma w_{,xx}^{(k)})/(1-\sigma)$ $(k = 1, 2, \ldots)$ are used and a similar definition $W_x^{(k)} = 2(w_{,xx}^{(k)} + \sigma w_{,yy}^{(k)})/(1-\sigma)$ $(k = 1, 2, \ldots)$ will be used as follows. It is found from the compatibility conditions that $\tilde{\varphi}^{(2)}$ must also satisfy $\tilde{\Delta}\tilde{\Delta}\tilde{\varphi}^{(2)} = 0$. Since $\tilde{K}_{yz}^{(2)} = \tilde{L}_{yz}^{(2)}$ and $\tilde{K}_{zz}^{(2)} = \tilde{L}_{zz}^{(2)}$, the boundary conditions for $\tilde{\varphi}^{(2)}$ are given by the same conditions as for $\tilde{\varphi}^{(1)}$, (24*a*, *b*). The remaining stress component $\tilde{K}_{xx}^{(2)}$ is matched with $\tilde{K}_{xx\infty}^{(2)}$ and given by

$$\tilde{K}_{xx}^{(2)} = -W_x^{(1)}\zeta - W_{x,y}^{(0)}\eta\zeta + 2\int_\eta^\infty \tilde{\psi}_{,x\zeta}^{(1)}d\eta + [2(u_{,x}^{(0)} + \sigma v_{,y}^{(0)}) + (w_{,x}^{(0)})^2 + \sigma(w_{,y}^{(0)})^2]/(1-\sigma) - \sigma\tilde{\Delta}\tilde{\varphi}^{(2)}. \tag{31}$$

The displacement components, on the other hand, are obtained, after being matched with the interior solutions as

$$\tilde{u}_x^{(2)} = u^{(0)} - w_{,x}^{(1)}\zeta - w_{,xy}^{(0)}\eta\zeta + \int_\eta^\infty \tilde{\psi}_{,\zeta}^{(1)}\,d\eta,$$

$$\tilde{u}_y^{(2)} = v^{(0)} - w_{,y}^{(1)}\zeta - w_{,yy}^{(0)}\eta\zeta + \tilde{u}_{yh}^{(2)},$$

$$\tilde{u}_z^{(2)} = w^{(2)} + w_{,y}^{(1)}\eta + w_{,yy}^{(0)}\eta^2/2 + \sigma/[2(1-\sigma)]\Delta w^{(0)}\zeta^2 + \tilde{u}_{zh}^{(2)}, \tag{32}$$

where $\tilde{u}_{yh}^{(2)}$ and $\tilde{u}_{zh}^{(2)}$ denote, respectively, the displacement components derived from $\tilde{\varphi}^{(1)}$. Since the displacements thus derived are always accompanied by an arbitrary rigid body motion, we determine them so as to be free from the rigid body motion. Thus these displacement components are taken to be damped out as $\eta \to \infty$.

Third-Order Problem.

$$\tilde{K}_{xy,\eta}^{(3)} + \tilde{K}_{xz,\zeta}^{(3)} = -\tilde{K}_{xx,x}^{(2)} - (\tilde{u}_{x,\zeta}^{(1)}\tilde{K}_{zy}^{(1)})_{,\eta} - (\tilde{u}_{x,\zeta}^{(1)}\tilde{K}_{zz}^{(1)})_{,\zeta} \tag{33a}$$

$$\tilde{K}_{yy,\eta}^{(3)} + \tilde{K}_{yz,\zeta}^{(3)} = -\tilde{K}_{xy,x}^{(2)} - (\tilde{u}_{y,\zeta}^{(1)}K_{zy}^{(1)})_{,\eta} - (\tilde{u}_{y,\zeta}^{(1)}\tilde{K}_{zz}^{(1)})_{,\zeta} \tag{33b}$$

$$\tilde{K}_{yz,\eta}^{(3)} + \tilde{K}_{zz,\zeta}^{(3)} = \tilde{u}_{z,t't'}^{(0)} - \tilde{K}_{xz,x}^{(2)} - (\tilde{u}_{z,x}^{(0)}\tilde{K}_{xy}^{(1)} + \tilde{u}_{z,\eta}^{(1)}\tilde{K}_{yy}^{(1)})_{,\eta} - (\tilde{u}_{z,x}^{(0)}\tilde{K}_{xz}^{(1)} + \tilde{u}_{z,\eta}^{(1)}\tilde{K}_{yz}^{(1)})_{,\zeta} \tag{33c}$$

where t' is defined as $t' = \epsilon t$. The stress functions $\tilde{\psi}^{(3)}$ and $\tilde{\varphi}^{(3)}$ for this problem can be introduced as follows:

$$\tilde{K}_{xy}^{(3)} = \tilde{K}_{xy\infty}^{(3)} + \tilde{\varphi}_{,x\eta}^{(2)} + (1-\sigma)\int_\eta^\infty \tilde{\Delta}\tilde{\varphi}_{,x}^{(2)}d\eta - \tilde{\psi}_{,\zeta}^{(3)},$$

$$\tilde{K}_{xz}^{(3)} = K_{xz\infty}^{(3)} + \tilde{\varphi}_{,x\zeta}^{(2)} - 2\int_\eta^\infty \tilde{\psi}_{,xx}^{(1)}\,d\eta + \tilde{\psi}_{,\eta}^{(3)},$$

$$\tilde{K}_{yy}^{(3)} = \tilde{K}_{yy\infty}^{(3)} - 2\int_\eta^\infty \tilde{\psi}_{,x\zeta}^{(2)}\,d\eta - \tilde{\varphi}_{,xx}^{(1)} + (1-\sigma)\int_\eta^\infty d\eta\int_\eta^\infty \tilde{\Delta}\tilde{\varphi}_{,xx}^{(1)}\,d\eta - \tilde{\varphi}_{,\zeta\zeta}^{(3)},$$

$$\tilde{K}_{zz}^{(3)} = \tilde{K}_{zz\infty}^{(3)} - \tilde{\varphi}_{,xx}^{(1)} - \tilde{\varphi}_{,\eta\eta}^{(3)},$$

$$\tilde{K}_{yz}^{(3)} = \tilde{K}_{yz\infty}^{(3)} - \tilde{\psi}_{,x}^{(2)} + \tilde{\varphi}_{,\eta\zeta}^{(3)}, \tag{34}$$

where the explicit forms of $\tilde{K}_{ij\infty}^{(3)}$ $(i, j = x, y, z)$ are omitted, but their forms are easily reproduced from the Appendix of Part 1. The stress functions thus introduced must satisfy the following equations:

$$\tilde{\Delta}\tilde{\psi}^{(3)} = -\tilde{\psi}_{,xx}^{(1)}, \quad \tilde{\Delta}\tilde{\Delta}\tilde{\varphi}^{(3)} = -2\tilde{\Delta}\tilde{\varphi}_{,xx}^{(1)}, \tag{35), (36}$$

together with the same boundary conditions as for $\tilde{\psi}^{(1)}$ and $\tilde{\varphi}^{(1)}$, respectively. It should be noted that on both surfaces of the plate, $\tilde{L}_{iz}^{(3)} = \tilde{K}_{iz}^{(3)}$ $(i = x, y, z)$ because $\tilde{K}_{iz}^{(1)}$ $(i = x, y, z)$ vanish there.

On the other hand, the third-order displacement components are calculated after matching with the interior solutions as

$$\tilde{u}_x^{(3)} = -\{w_{,x}^{(2)} + w_{,xy}^{(1)}\eta + w_{,xyy}^{(0)}\,\eta^2/2 + h^2/[4(1-\sigma)]\Delta w_{,x}^{(0)}\}\zeta + (2-\sigma)/[6(1-\sigma)] \times \Delta w_{,x}^{(0)}\,\zeta^3 + \int_\eta^\infty \tilde{\psi}_{,\zeta}^{(2)}\,d\eta - \int_\eta^\infty u_{yh,x}^{(2)}\,d\eta + u^{(1)} + u_{,y}^{(0)}\eta,$$

$$\tilde{u}_y^{(3)} = -\{w_{,y}^{(2)} + w_{,yy}^{(1)}\eta + w_{,yyy}^{(0)}\,\eta^2/2 + h^2/[4(1-\sigma)]\Delta w_{,y}^{(0)}\}\zeta + (2-\sigma)/[6(1-\sigma)] \times \Delta w_{,y}^{(0)}\,\zeta^3 + \int_\eta^\infty d\eta\int_\eta^\infty \tilde{\psi}_{,x\zeta}^{(1)}\,d\eta + v^{(1)} + v_{,y}^{(0)}\eta + \tilde{u}_{yh}^{(3)},$$

$$\tilde{u}_z^{(3)} = w^{(3)} + w_{,y}^{(2)}\eta + w_{,yy}^{(1)}\eta^2/2 + w_{,yyy}^{(0)}\eta^3/6 + \sigma/[2(1-\sigma)][\Delta w^{(1)} + \Delta w_{,y}^{(0)}\eta]\zeta^2 - 1/[2(1-\sigma)][2\sigma(u_{,x}^{(0)} + v_{,y}^{(0)}) + (w_{,x}^{(0)})^2 + (w_{,y}^{(0)})^2] + \tilde{u}_{zh}^{(3)}, \tag{37}$$

where $\tilde{u}_{yh}^{(3)}$ and $\tilde{u}_{zh}^{(3)}$ represent the displacements derived from $\tilde{\varphi}^{(2)}$.

So far we have not imposed the boundary conditions at $\eta = 0$. Thus, as stated earlier, the foregoing analysis can be applied to various edge conditions.

Let us now consider the boundary conditions for the built-in edge. Although the boundary conditions are stipulated by (9), we assume that the conditions are assigned separately as $\tilde{u}_i^{(k)} = 0$ $(i = x, y, z;\ k = 0, 1, 2, \ldots)$. From relations (13) and (25), it immediately follows that

$$w^{(0)} = w_{,y}^{(0)} = w^{(1)} = 0. \tag{38}$$

The first two conditions are nothing but the classical boundary conditions. From the second-order displacement components (32), the boundary conditions leads to

$$u^{(0)} + \int_0^\infty \tilde{\psi}_{,\zeta}^{(1)}\,d\eta = v^{(0)} - w_{,y}^{(1)}\zeta + \tilde{u}_{yh}^{(2)} = w^{(2)} + \frac{\sigma}{2(1-\sigma)}\Delta w^{(0)}\zeta^2 + \tilde{u}_{zh}^{(2)} = 0. \tag{39a,b,c}$$

As can be seen from (39), the interior solutions and the boundary layer

solutions couple with each other through the boundary conditions at $\eta = 0$. We are now in position to derive from the conditions, reduced boundary conditions at $y = 0$ for $w^{(1)}$, $w^{(2)}$, $u^{(0)}$, and $v^{(0)}$. From condition (39a), it is found after integrating over ζ ($-h/2 \leqq \zeta \leqq h/2$) that

$$u^{(0)} = \int_0^\infty \tilde{\psi}^{(1)}_{,\zeta}\, d\eta = 0. \tag{40}$$

From the latter condition, $\tilde{\psi}^{(1)}$ is taken to be zero. Therefore $\tilde{K}^{(1)}_{xy}$ and $\tilde{K}^{(1)}_{xz}$ vanish in the boundary layer since $\tilde{K}^{(1)}_{xy\infty} = 0$ from relations (38). Thus, for the built-in edge, as will be seen later, the plane strain boundary layer first appears.

Next, in order to derive the conditions for $v^{(0)}$, $w^{(1)}_{,y}$, and $w^{(2)}$, we must solve the boundary-layer equation (20) under the boundary conditions (24) and (39b,c). For this purpose, it is convenient to convert the conditions (39b,c) to those expressed in terms of the stress function $\tilde{\varphi}^{(1)}$. From the relations between the displacement and stress components (Appendix B), they are rewritten as

$$\tilde{u}^{(2)}_{yh,\zeta\zeta} = (2-\sigma)\,\tilde{\varphi}^{(1)}_{,\eta\zeta\zeta}/2 + (1-\sigma)\,\tilde{\varphi}^{(1)}_{,\eta\eta\eta}/2 = 0,$$
$$\tilde{u}^{(2)}_{zh,\zeta} = -\sigma/(1-\sigma)\Delta w^{(0)}\zeta = \sigma\tilde{\varphi}^{(1)}_{,\zeta\zeta}/2 - (1-\sigma)\,\tilde{\varphi}^{(1)}_{,\eta\eta}/2. \tag{41}$$

Following the procedure developed in the Appendix B, $\tilde{\varphi}^{(1)}$ can be obtained [in this case, noting that $w^{(0)}_{,xx} = 0$, $\alpha = 2\sigma/(1-\sigma)^2 w^{(0)}_{,yy}$ and $\beta = 0$]. Thus, from the expressions (78), $v^{(0)}$, $w^{(1)}_{,y}$, and $w^{(2)}$ are determined as

$$v^{(0)} = w^{(1)}_{,y} + \kappa_1 h w^{(0)}_{,yy} = w^{(2)} + \kappa_2 h^2 w^{(0)}_{,yy} = 0, \tag{42}$$

with the coefficients κ_1 and κ_2 given by

$$\kappa_1 = \frac{24\sigma^2}{(1-\sigma)^2}\left[\sum_{n=1,3,5}^{\infty}\frac{B_n'}{(n\pi)^2} - c_2 B_s'\right],$$
$$\kappa_2 = \frac{\sigma}{40(1-\sigma)} - \frac{24\sigma(2-\sigma)}{(1-\sigma)^2}\left[\sum_{n=1,3,5}^{\infty}\frac{A_n'}{(n\pi)^2} - c_1 A_s'\right]. \tag{43}$$

In order to derive the condition for $w^{(2)}_{,y}$, we must proceed to the third-order problem. Then the condition for $w^{(2)}_{,y}$ is similarly determined from $\tilde{u}^{(3)}_y = 0$ at $\eta = 0$ and given by

$$w^{(2)}_{,y} + \kappa_1 h w^{(1)}_{,yy} + \kappa_3 h^2 w^{(0)}_{,yyy} = 0, \tag{44}$$

with

$$\kappa_3 = \frac{8+\sigma}{40(1-\sigma)} + \frac{24\sigma(2-\sigma)}{(1-\sigma)^2}\left[\sum_{n=1,3,5}^{\infty}\frac{B_n''}{(n\pi)^2} - c_2 B_s''\right]. \tag{45}$$

We remark here that the remaining condition $\tilde{u}^{(3)}_z = 0$ is used to determine $w^{(3)}$, while the condition $\tilde{u}^{(3)}_x = 0$ is used to give the boundary condition for $\tilde{\psi}^{(2)}$ at $\eta = 0$. Thus conditions (38), (40), and (42)–(45) constitute the reduced boundary conditions for the interior equations at $y = 0$. These conditions can alternatively be written in a compact form in light of the expansion (7) as

$$w_{,y} + \epsilon\kappa_1 h w_{,yy} + \epsilon^2\kappa_3 h^2 w_{,yyy} = w + \epsilon^2\kappa_2 h^2 w_{,yy} = 0,$$

and

$$u = v = 0. \tag{46}$$

Case of Free Edge. For the free edge, three stress components (10) vanish along the edge and these conditions are assigned separately as $\tilde{L}^{(k)}_{xy} = \tilde{L}^{(k)}_{yy} = \tilde{L}^{(k)}_{zy} = 0$ ($k = 1, 2, 3, \ldots$). By taking the moments of the conditions, they can also be expressed in terms of the averaged quantities as

$$Q^{(k)}_i = \int_{-h/2}^{h/2}\tilde{L}^{(k)}_{iy}\,d\zeta = 0, \quad M^{(k)}_{jy} = \int_{-h/2}^{h/2}\zeta\tilde{L}^{(k)}_{jy}\,d\zeta = 0,$$
$$(i = x, y, z,\ j = x, y;\ k = 1, 2, 3, \ldots) \tag{47}$$

where $Q^{(k)}_x$ and $Q^{(k)}_y$ denote the resultant in-plane forces on the edge, while $Q^{(k)}_z$, $M^{(k)}_{xy}$, and $M^{(k)}_{yy}$ denote, respectively, the transverse shearing force, the twisting moment, and the bending moment.

Noting that $\tilde{L}^{(1)}_{iy} = \tilde{K}^{(1)}_{iy}(i = x, y, z)$, and $\int_{-h/2}^{h/2}\zeta\tilde{\varphi}^{(1)}_{,\zeta\zeta}d\zeta = \int_{-h/2}^{h/2}\tilde{\varphi}^{(1)}_{,\eta}d\zeta = 0$, the boundary conditions are given by

$$M^{(1)}_{yy} = -h^3/[6(1-\sigma)]\,(w^{(0)}_{,yy} + \sigma\, w^{(0)}_{,xx}) = 0, \tag{48a}$$

$$M^{(1)}_{xy} = -h^3 w^{(0)}_{,xy}/6 - \int_{-h/2}^{h/2}\zeta\tilde{\psi}^{(1)}_{,\zeta}\,d\zeta = 0, \quad Q^{(1)}_z = 0, \tag{48b,c}$$

where $Q^{(1)}_i$ ($i = x, y$) are automatically satisfied. By the condition (48a), $\tilde{K}^{(1)}_{yy\infty}$ becomes zero and therefore all boundary conditions for $\tilde{\varphi}^{(1)}$ vanish. Thus $\tilde{\varphi}^{(1)}$ is taken to be zero throughout the boundary layer. Condition (48b) should be interpreted as the condition which determines the boundary-layer solution $\tilde{\psi}^{(1)}$. For $\tilde{L}^{(1)}_{xy}$ to be free, it is required that

$$\tilde{\psi}^{(1)}_{,\zeta} = -2w^{(0)}_{,xy}\zeta \quad \text{at} \quad \eta = 0. \tag{49}$$

After solving equation (19) subject to this condition together with (23), $\tilde{\psi}^{(1)}$ can be obtained as

$$\tilde{\psi}^{(1)} = 8w^{(0)}_{xy}h^2\sum_{m=0}^{\infty}\frac{(-1)^m}{\pi^3(2m+1)^3}$$
$$\times\cos[\pi(2m+1)\zeta/h]\exp[-\pi(2m+1)\eta/h]. \tag{50}$$

Thus it is found that, for the free edge, the torsion boundary layer appears first.

Next from the boundary conditions for $M^{(2)}_{yy}$, $M^{(2)}_{xy}$, and $Q^{(2)}_z$, it follows that

$$M^{(2)}_{yy} = -h^3/[6(1-\sigma)](w^{(1)}_{,yy} + \sigma w^{(1)}_{,xx}) + 2\int_0^\infty d\eta\int_{-h/2}^{h/2}\tilde{\psi}^{(1)}_{,x}\,d\zeta = 0, \tag{51a}$$

$$M^{(2)}_{xy} = -h^3 w^{(1)}_{,xy}/6 - \int_{-h/2}^{h/2}\zeta\tilde{\psi}^{(2)}_{,x}\,d\zeta = 0, \tag{51b}$$

$$Q^{(2)}_z = -h^3/[6(1-\sigma)]\Delta w^{(0)}_{,y} - \int_{-h/2}^{h/2}\zeta\tilde{\psi}^{(1)}_{,x}\,d\zeta = 0. \tag{51c}$$

Eliminating $\tilde{\psi}^{(1)}$ from (48b) and (51c), we find that the well-known classical boundary condition is obtained

$$w^{(0)}_{,yyy} + (2-\sigma)w^{(0)}_{,xxy} = 0. \tag{52}$$

After substituting $\tilde{\psi}^{(1)}$ into $M^{(2)}_{yy}$, we have the higher-order boundary condition for $w^{(1)}$:

$$w^{(1)}_{,yy} + \sigma\, w^{(1)}_{,xx} - 192\kappa(1-\sigma)hw^{(0)}_{,xxy} = 0, \tag{53}$$

where

$$\kappa = \sum_{m=0}^{\infty}[\pi(2m+1)]^{-5}.$$

From the remaining boundary conditions, $Q^{(2)}_x = Q^{(2)}_y = 0$, we have

$$u^{(0)}_{,y} + v^{(0)}_{,x} + w^{(0)}_{,x}w^{(0)}_{,y} = 0,$$
$$v^{(0)}_{,y} + \sigma u^{(0)}_{,x} + [(w^{(0)}_{,y})^2 + \sigma(w^{(0)}_{,x})^2]/2 = 0. \tag{54}$$

Another boundary condition for $w^{(1)}$ can be similarly derived from $M^{(2)}_{xy}$ and $Q^{(3)}_z$ by eliminating $\tilde{\psi}^{(2)}$ and is given by

$$w^{(1)}_{,yyy} + (2-\sigma)w^{(1)}_{,xxy} = 0. \tag{55}$$

This condition together with (53) constitute the reduced boundary condition for $w^{(1)}$.

We now proceed to derive the conditions for $w^{(2)}$. From the condition $M^{(3)}_{yy} = 0$, we have easily one of the conditions

$$w^{(2)}_{,yy} + \sigma w^{(2)}_{,xx} - \sigma w^{(0)}_{,t't'}/2 + 1/[40(1-\sigma)]h^2[(4+\sigma^2)w^{(0)}_{,xxyy}$$
$$+ (8-3\sigma)w^{(0)}_{,yyyy}] - 192\kappa(1-\sigma)hw^{(1)}_{,xxy} = 0. \tag{56}$$

The other boundary condition for $w^{(2)}$ could be obtained by proceeding to the fourth-order problem to eliminate $\tilde{\psi}^{(3)}$ from $M^{(3)}_{xy} = Q^{(4)}_z = 0$. But we choose another way to achieve it. From the z-component of the equations of motion for the fourth order, we have

$$\tilde{L}^{(4)}_{zy,\eta} + \tilde{L}^{(4)}_{zz,\zeta} = \tilde{u}^{(1)}_{z,t't'} - \tilde{L}^{(3)}_{zx,x}. \tag{57}$$

Integrating this and (33a) over the thickness, and noting that $\tilde{L}^{(3)}_{zx} =$

$\tilde{K}^{(3)}_{xz} - w^{(0)}_{,y}(2w^{(0)}_{,xy}\zeta + \tilde{\psi}^{(1)}_{,\zeta}) - w^{(0)}_{,x}W^{(0)}_{x}\zeta$ and $\tilde{L}^{(3)}_{xy} = \tilde{K}^{(3)}_{xy}$, it follows after integrating with respect to η that

$$Q^{(4)}_z + M^{(3)}_{xy,x} = h(w^{(0)}_{,t't'y} + h^2W^{(0)}_{x,xxy}/12 - \tilde{q}_{,y})\eta^2/2 + h(w^{(1)}_{,t't'} + h^2W^{(1)}_{x,xx}/12)\eta - 2\int_\eta^\infty d\eta\int_\eta^\infty d\eta\int_{-h/2}^{h/2}\tilde{\psi}^{(1)}_{,xxx}\,d\zeta - \int_\eta^\infty d\eta\int_{-h/2}^{h/2}\sigma\zeta\tilde{\Delta}\tilde{\varphi}^{(2)}_{,xx}d\zeta + \text{constant}, \quad (58)$$

where $\tilde{q} = (\tilde{q}_+ - \tilde{q}_-)/h$ and the constant should be determined from the boundary conditions at $\eta = 0$. Since $Q^{(4)}_z = M^{(3)}_{xy} = 0$ at $\eta = 0$, we have

$$\text{constant} = 2\int_0^\infty d\eta\int_\eta^\infty d\eta\int_{-h/2}^{h/2}\tilde{\psi}^{(1)}_{,xxx}d\zeta + \int_0^\infty d\eta\int_{-h/2}^{h/2}\sigma\zeta\tilde{\Delta}\tilde{\varphi}^{(2)}_{,xx}d\zeta = h^5w^{(0)}_{,xxxxy}/30. \quad (59)$$

where the second integral for $\tilde{\varphi}^{(2)}$ vanishes, noting that $\int_{-h/2}^{h/2}\zeta\tilde{\varphi}^{(2)}_{,\eta}d\zeta = 0$ at $\eta = 0$ from $\int_{-h/2}^{h/2}K^{(2)}_{yz}\zeta^2d\zeta = 0$ at $\eta = 0$ and the relation (52). Since expression (58) must be valid at $\eta = \infty$ where $Q^{(4)}_z$ and $M^{(3)}_{xy}$ are already known from the interior solutions, another boundary condition for $w^{(2)}$ can be obtained as

$$w^{(2)}_{,yyy} + (2-\sigma)w^{(2)}_{,xxy} - w^{(0)}_{,t't'y}/2 + (h^2/10)\{(2-\sigma)w^{(0)}_{,xxxxy} + \sigma w^{(0)}_{,xxyyy} + (8-3\sigma)/(1-\sigma)[w^{(0)}_{,yyyyy} + (2-\sigma)w^{(0)}_{,xxyyy}]/4\} = 0. \quad (60)$$

Thus (48*a*), (52)–(56), and (60) constitute the reduced boundary conditions for the free edge. These conditions can alternatively be expressed in a compact form similar to expressions (46).

Case of Hinged Edge. As already remarked, it is difficult, especially in the nonlinear case, to specify the boundary conditions for the hinged edge in terms of displacement and/or stress components. In the linear case, the boundary conditions may be given by $L_{yy} = u_x = u_z = 0$. In the nonlinear case, however, the finite flexural deformation causes extensional deformation, i.e., in-plane displacements and stresses. If the same conditions as in the linear case are applied, the hinged edge cannot support the in-plane forces, nor can slide along the edge. Thus these conditions are inappropriate and new definitions are required. It should however be remembered that, if the boundary conditions in the averaged form are imposed on the interior equations and the interior solutions can be obtained without any discrepancy, then there arises no need to introduce the boundary layer. To examine it, we now define the hinged edge in such a way that the bending moment, the averaged deflection, and the averaged rotation about y-axis vanish. Furthermore, it is assumed that the averaged translation in y-direction and the shearing force in x-direction vanish. Under these conditions, it immediately follows from the zeroth and first-order problems that

$$w^{(0)} = w^{(0)}_{,yy} + \sigma w^{(0)}_{,xx} = 0. \quad (61)$$

It is also found that these conditions can be satisfied even if boundary-layer solutions are not introduced.

Next, from the second-order problem, we find that

$$w^{(1)} = w^{(1)}_{,yy} + \sigma w^{(1)}_{,xx} = w^{(2)} = v^{(0)} = u^{(0)}_{,y} + v^{(0)}_{,x} + w^{(0)}_{,x}w^{(0)}_{,y} = 0. \quad (62)$$

For this order as well, there arises no need to introduce a boundary layer. Using these conditions in the third-order problem, we have

$$w^{(2)}_{,yy} + \sigma w^{(2)}_{,xx} = 0. \quad (63)$$

Thus it is found that in the case of the hinged edge, there appears no boundary layer. However, it should be remarked that if the definition of the hinged edge is made in a different way, there might appear a boundary layer.

Concluding Remarks

For the plate with an edge, we have derived reduced boundary conditions for the higher-order equations in the interior region by taking account of the boundary-layer effect. In the case of the built-in edge and the free edge, it is found from conditions (46), for example, that the reduced boundary conditions are subjected to the $O(\epsilon)$-corrections to the classical conditions. Therefore the effect of boundary layer gives rise to the $O(\epsilon)$-corrections in the interior solutions. But as can be seen from the higher-order equations, the effect of finite thickness gives only $O(\epsilon^2)$-corrections to the classical theory. This implies that when the boundary layer appears, the effect of finite thickness affects the interior solutions primarily through the boundary layer. These results should be compared with the case in which no boundary layer arises.

Finally it is remarked that since the main concern in this paper is to derive the reduced boundary conditions, we have not proceeded further to examine explicit stress distribution in the boundary layer. However, since the stress functions $\tilde{\psi}^{(1)}$ or $\tilde{\varphi}^{(1)}$ are already known, its explicit distribution can easily be calculated. It will be demonstrated in a subsequent paper.

Acknowledgments

The author would like to express his hearty thanks to Prof. T. Kakutani for his stimulating discussions and kind inspection of the manuscript. The author also would like to express his gratitude to the editors and the reviewers for a number of comments and criticisms which led to the improvement of the original manuscript. This work has been partially supported by THE SAKKOKAI FOUNDATION, Tokyo, Japan.

References

1 Sugimoto, N., "Nonlinear Theory for Flexural Motions of Thin Elastic Plate. Part 1: Higher-Order Theory," ASME JOURNAL OF APPLIED MECHANICS, Vol. 48, 1981, pp. 377–382.

2 Friedrichs, K. O., and Dressler, R. F., "Boundary Layer Theory for Elastic Plates," *Communications on Pure and Applied Mathematics*, Vol. 14, 1961, pp. 1–33.

3 Love, A. E. H., *A Treatise on the Mathematical Theory of Elasticity*, Cambridge University Press, Cambridge, 1927.

4 Timoshenko, S., and Woinowsky-Krieger, S., *Theory of Plates and Shells*, McGraw-Hill, New York, 1959.

5 Gol'denveizer, A. L., "Derivation of an Approximate Theory of Bending of a Plate by the Method of Asymptotic Integration of the Equations of the Theory of Elasticity," *Journal of Applied Mathematics and Mechanics*, Vol. 26, 1962, pp. 1000–1025 (*PMM*, Vol 26, 1962, pp. 668–686).

6 Reissner, E., "On the Theory of Transverse Bending of Elastic Plates," *International Journal of Solids and Structures*, Vol. 12, 1976, pp. 545–554.

7 Cole, J. D., *Perturbation Methods in Applied Mathematics*, Blaisdell, Waltham, 1968.

8 Nayfeh, A. H., *Perturbation Methods*, Wiley-Interscience, New York, 1973.

9 Bryant, R. H., and Widera, O. E., "Solution of a Class of Plane Elasticity Problems by Use of Parametric Expansion," *Revue Roumaine de Sciences Techniques*, Vol. 18, 1973, pp. 885–90.

10 Eringen, A. C., *Nonlinear Theory of Continuous Media*, McGraw-Hill, New York, 1962.

11 Benthem, J. P., "A Laplace Transform Method for the Solution of Semi-Infinite and Finite Strip Problems in Stress Analysis," *Quarterly Journal of Mechanics and Applied Mathematics*, Vol. 16, 1963, pp. 413–429.

12 Johnson, M. W., and Little, R. W., "The Semi-Infinite Elastic Strip," *Quarterly of Applied Mathematics*, Vol. 22, 1965, pp. 335–344.

13 Williams, M. L., "Stress Singularities Resulting From Various Boundary Conditions in Angular Corners of Plates in Extension," ASME JOURNAL OF APPLIED MECHANICS, Vol. 19, 1952, pp. 526–528.

APPENDIX *A*

Compatibility Conditions for Finite Lagrangian Strain Tensor

The compatibility conditions for the finite Lagrangian strain tensor are given in [10]:

$$E_{ij,kl} + E_{kl,ij} - E_{il,kj} - E_{kj,il} + R_{iklj} = 0, \quad (i, j, k, l = 1, 2, 3) \quad (64)$$

with

$$R_{iklj} = (\delta_{rs} + 2E_{rs})^{-1}[(E_{ir,j} + E_{jr,i} - E_{ij,r})(E_{ks,l} + E_{ls,k} - E_{kl,s}) - (E_{ir,l} + E_{lr,i} - E_{il,r})(E_{ks,j} + E_{js,k} - E_{kj,s})], \quad (65)$$

where $E_{ij,kl}$ stands for $\partial^2E_{ij}/\partial X_k\partial X_l$, etc., and the suffix 1, 2, and 3

correspond, respectively, to x, y, and z in the main text. Out of 81 conditions, there are six necessary and sufficient compatibility conditions to determine the displacement components uniquely. These compatibility conditions can be rewritten in terms of Kirchhoff's stress tensor by use of the constitutive equations. Since it has already been remarked that the effect of material nonlinearity does not play a dominant role in such flexural motions, we employ here the generalized Hooke's law neglecting the material nonlinearity. The six compatibility conditions are given in terms of Kirchhoff's stress tensor as

$$K_{ij,ll} + K_{ll,ij}/(1+\sigma) = X_{i,j} + X_{j,i} + \sigma/(1-\sigma)\,(X_{l,l} - R_{mllm})\delta_{ij} - 2R_{illj} = P_{ij}, \quad (66)$$

where $X_i = K_{ij,j} = u_{i,tt} - (u_{i,k}K_{kj})_{,j}$.

APPENDIX B

Solution of Biharmonic Equation

We consider the biharmonic equation in the semi-infinite rectangular strip region ($0 \leqq \eta < \infty$, $-h/2 \leqq \zeta \leqq h/2$) [11, 12]:

$$\phi_{,\eta\eta\eta\eta} + 2\phi_{,\eta\eta\zeta\zeta} + \phi_{,\zeta\zeta\zeta\zeta} = 0, \quad (67)$$

with the boundary conditions given by

$$\eta = 0, \quad (1-\sigma)\,\phi_{,\eta\eta} - \sigma\phi_{,\zeta\zeta} = (1-\sigma)\alpha\zeta,$$
$$(1-\sigma)\,\phi_{,\eta\eta\eta} + (2-\sigma)\phi_{,\eta\zeta\zeta} = (1-\sigma)\beta\zeta,$$
$$\eta \to \infty, \quad \phi \to 0, \quad \zeta = \pm h/2, \quad \phi = \phi_{,\zeta} = 0, \quad (68)$$

where α and β are constants. The boundary conditions at $\eta = 0$ are derived from the relations between the displacement and stress components as

$$2u_{y,\eta} = \sigma\phi_{,\eta\eta} - (1-\sigma)\phi_{,\zeta\zeta}, \quad 2u_{z,\zeta} = \sigma\phi_{,\zeta\zeta} - (1-\sigma)\phi_{,\eta\eta}, \quad u_{y,\zeta} + u_{z,\eta} = \phi_{,\eta\zeta}. \quad (69)$$

To solve the biharmonic equation, we employ a Laplace transform method defined by

$$\hat{\phi}(p,\zeta) = \int_0^\infty \phi(\eta,\zeta)e^{-p\eta}\,d\eta. \quad (70)$$

In transforming equation (67), it is required to specify ϕ and $\phi_{,\eta}$ at $\eta = 0$. If they are known, $\phi_{,\eta\eta}$ and $\phi_{,\eta\eta\eta}$ at $\eta = 0$ are immediately obtained from the conditions (68). But ϕ and $\phi_{,\eta}$ at $\eta = 0$ are the quantities to be obtained after the full solution is completed. We therefore assume the form of ϕ and $\phi_{,\eta}$ at $\eta = 0$, and determine it consistently so that the solution may satisfy the boundary condition as $\eta \to \infty$. For selection of the form assumed, it should be remarked that stress singularities usually arise at two corners ($\eta = 0$ and $\zeta = \pm h/2$). Keeping this in mind, ϕ and $\phi_{,\eta}$ are assumed, respectively, to be composed of two parts, one being the regular part and the other the singular part producing the stress singularities at the corners. The regular parts are expanded into the Fourier series after extending them into the region ($0 \leqq \eta < \infty$, $-3h/2 \leqq \zeta \leqq -h/2$) as the even function with respect to $\zeta = -h/2$. Furthermore, noting that ϕ is an odd function with respect to $\zeta = 0$, ϕ and $\phi_{,\eta}$ are assumed as follows:

$$\phi(0,\zeta) = \sum_{n=1,3,5}^{\infty} a_n \cos[n\pi(\zeta/h + 1/2)] + a_s\phi^{(s)}(\zeta/h),$$
$$\phi_{,\eta}(0,\zeta) = \sum_{n=1,3,5}^{\infty} b_n \cos[n\pi(\zeta/h + 1/2)] + b_s\phi_{,\eta}^{(s)}(\zeta/h), \quad (71)$$

with

$$\phi^{(s)}(\zeta/h) = (1/2 - \zeta/h)^{\lambda+1} - (1/2 + \zeta/h)^{\lambda+1} + (\lambda+1)\zeta/h,$$
$$\phi_{,\eta}^{(s)}(\zeta/h) = (1/2 - \zeta/h)^{\lambda} - (1/2 + \zeta/h)^{\lambda} + \lambda\zeta/h, \quad (72)$$

where the summation is taken over the odd numbers and a_n, a_s, b_n, and b_s are the real constants to be determined so that the solution may satisfy the boundary condition as $\eta \to \infty$. Here $\phi^{(s)}$ and $\phi_{,\eta}^{(s)}$ are the terms which produce the stress singularities at the corners, a_s and b_s being the strength of the singularity, and the power of the stress singularity λ ($0 < \mathrm{Re}\,\lambda < 1$) is determined from the following characteristic equation for the corner singularity with one side built-in and the other free [13]:[1]

$$\sin^2(\pi\lambda/2) = 4(1-\sigma)^2/(3-4\sigma) - \lambda^2/(3-4\sigma). \quad (73)$$

It should be noted that $\phi^{(s)}$ and $\phi_{,\eta}^{(s)}$ are nonsingular themselves and therefore the preceding Fourier series in (71) could represent them. But unless the singular parts are included, the Fourier series for the stress components would not converge uniformly.

After effecting the Laplace transform, we have

$$\hat{\phi}(p,\zeta) = \left(\frac{\alpha}{p^3} + \frac{\beta}{p^4}\right)\left[\zeta + \frac{2}{\sin(ph) - ph}\left\{\frac{ph^2}{4}\sin\left(\frac{ph}{2}\right)\sin(p\zeta) - \left[\sin\left(\frac{ph}{2}\right) - \frac{ph}{2}\cos\left(\frac{ph}{2}\right)\right]\zeta\cos(p\zeta)\right\}\right]$$
$$+ \sum_{n=1,3,5}^{\infty} \frac{1}{[p^2 - (n\pi/h)^2]^2}\left\{\left[p^3 - \frac{(2-\sigma)}{(1-\sigma)}\left(\frac{n\pi}{h}\right)^2 p\right]a_n + \left[p^2 + \frac{\sigma}{(1-\sigma)}\left(\frac{n\pi}{h}\right)^2\right]b_n\right\}\left[\cos\left[n\pi\left(\frac{\zeta}{h} + \frac{1}{2}\right)\right]\right.$$
$$+ \frac{2}{\sin(ph) - ph}\left\{\left[\cos\left(\frac{ph}{2}\right) - \frac{ph}{2}\sin\left(\frac{ph}{2}\right)\right]\sin(p\zeta) - p\cos\left(\frac{ph}{2}\right)\zeta\cos(p\zeta)\right\}\Bigg] + \hat{\phi}^{(s)}(p,\zeta)$$
$$- \frac{2}{\sin(ph) - ph}\left[\hat{\phi}^{(s)}\left(p,\frac{h}{2}\right)\left\{\left[\cos\left(\frac{ph}{2}\right) - \frac{ph}{2}\sin\left(\frac{ph}{2}\right)\right]\sin(p\zeta) - p\cos\left(\frac{ph}{2}\right)\zeta\cos(p\zeta)\right\}\right.$$
$$\left. - \hat{\phi}_{,\zeta}^{(s)}\left(p,\frac{h}{2}\right)\left\{\frac{h}{2}\cos\left(\frac{ph}{2}\right)\sin(p\zeta) - \sin\left(\frac{ph}{2}\right)\zeta\cos(p\zeta)\right\}\right], \quad (74)$$

with $\hat{\phi}^{(s)}(p,\zeta)$ defined by

$$\hat{\phi}^{(s)}(p,\zeta) = a_s\int_0^\zeta \{[(2-\sigma)/(1-\sigma)G_1(\zeta,\xi,p) - 1/[2(1-\sigma)]G_2(\zeta,\xi,p)\}\phi^{(s)}(\xi/h)d\xi$$
$$+ b_s\int_0^\zeta \{[-\sigma/(1-\sigma)G_1(\zeta,\xi,p) + 1/[2(1-\sigma)]G_2(\zeta,\xi,p)\}\phi_{,\eta}^{(s)}(\xi/h)/p\,d\xi, \quad (75)$$

where $G_1(\zeta,\xi,p) = \sin[p(\zeta-\xi)]$ and $G_2(\zeta,\xi,p) = \sin[p(\zeta-\xi)] - p(\zeta-\xi)\cos[p(\zeta-\xi)]$. The function $\hat{\phi}(p,\zeta)$ has simple poles at zeros of equation $\sin(ph) - ph = 0$, $\pm p_k$ and $\pm p_k^*$ ($k = 1, 2, 3, \ldots$; $p_k \neq 0$), where p_k^* being the complex conjugate of p_k, but not at $p = 0$ and $p = \pm n\pi/h$ ($n = 1, 3, 5, \ldots$). Since ϕ is assumed to be damped out as $\eta \to \infty$, it is necessary that the residues at $p = p_k$ and p_k^* ($\mathrm{Re}\,p_k > 0$; $k = 1, 2, 3, \ldots$) must vanish. From these conditions, a_n, a_s, b_n, and b_s are determined by

$$\sum_{n=1,3,5}^{\infty} \frac{1}{[q_k^2 - (n\pi)^2]^2}\left\{\left[q_k^3 - \frac{(2-\sigma)}{(1-\sigma)}(n\pi)^2 q_k\right]a_n + \left[q_k{}^2 + \frac{\sigma}{(1-\sigma)}(n\pi)^2\right]hb_n\right\} + \left[\frac{1}{2\cos^2(q_k/2)}\hat{\phi}_{1,\zeta}^{(s)}(q_k) - \hat{\phi}_1^{(s)}(q_k)\right]a_s + \left[\frac{1}{2\cos^2(q_k/2)}\hat{\phi}_{2,\zeta}^{(s)}(q_k) - \hat{\phi}_2^{(s)}(q_k)\right]hb_s$$
$$+ \frac{1}{2}\left(\frac{\alpha h^3}{q_k^3} + \frac{\beta h^4}{q_k^4}\right)\tan^2\left(\frac{q_k}{2}\right) = 0, \quad (k = 1, 2, 3, \ldots) \quad (76)$$

where $q_k = p_k h$ and $\hat{\phi}_i^{(s)}(q_k)$ and $\hat{\phi}_{i,\zeta}^{(s)}(q_k)$ ($i = 1, 2$) are defined as $\hat{\phi}(p_k, h/2) = a_s h\hat{\phi}_1^{(s)}(q_k) + b_s h^2\hat{\phi}_2^{(s)}(q_k)$ and $\hat{\phi}_{,\zeta}^{(s)}(p_k, h/2) = a_s\hat{\phi}_{1,\zeta}^{(s)}(q_k) + b_s h\hat{\phi}_{2,\zeta}^{(s)}(q_k)$. Solving a_n, a_s, b_n, and b_s from these equations, we have $\phi(\eta,\zeta)$ by the inversion formula and complete the boundary layer

[1] This λ should not be confused with the Lamé constant used in the main text.

solution. In order to derive the reduced boundary conditions only, however, we do not solve the solution explicitly. Noting that u_y, u_z, and ϕ are assumed to be damped out exponentially as $\eta \to \infty$, the displacement components at $\eta = 0$ are given by

$$u_y(0, \zeta) = \frac{\sigma}{2}\phi_{,\eta} + \frac{1-\sigma}{2}\int_0^\infty \phi_{,\zeta\zeta}d\eta = \frac{\sigma}{2}\phi_{,\eta} + \frac{1-\sigma}{2}\lim_{p\to 0}\hat{\phi}_{,\zeta\zeta},$$

$$u_z(0, \zeta) = \frac{2-\sigma}{2}\phi_{,\zeta} + \frac{1-\sigma}{2}\int_0^\infty \eta\phi_{,\zeta\zeta\zeta}d\eta = \frac{2-\sigma}{2}\phi_{,\zeta} - \frac{1-\sigma}{2}\lim_{p\to 0}\frac{d}{dp}\hat{\phi}_{,\zeta\zeta\zeta}. \quad (77)$$

Expressing the solutions a_n, a_s, b_n, and b_s as $a_{n(s)} = \alpha h^3 A'_{n(s)} + \beta h^4 A''_{n(s)}$ and $b_{n(s)} = \alpha h^2 B'_{n(s)} + \beta h^3 B''_{n(s)}$, (77) can be written as

$$u_y = \left\{\frac{(1-\sigma)\beta h^2}{80} - 12\sigma\left[\sum_{n=1,3,5}^{\infty}\frac{(\alpha h B'_n + \beta h^2 B''_n)}{(n\pi)^2} - c_2(\alpha h B'_s + \beta h^2 B''_s)\right]\right\}\zeta - \frac{(1-\sigma)\beta}{12}\zeta^3,$$

$$u_z = \frac{(1-\sigma)\alpha h^2}{80} - 12(2-\sigma)\left[\sum_{n=1,3,5}^{\infty}\frac{(\alpha h^2 A'_n + \beta h^3 A''_n)}{(n\pi)^2} - c_1(\alpha h^2 A'_s + \beta h^3 A''_s)\right] - \frac{(1-\sigma)\alpha}{4}\zeta^2, \quad (78)$$

where the coefficients c_1 and c_2 are given by

$$c_1 = \int_0^{1/2}\xi\phi^{(s)}(\xi)d\xi, \quad c_2 = \int_0^{1/2}\xi\phi^{(s)}_{,\eta}(\xi)d\xi. \quad (79)$$

Thus the displacement components at $\eta = 0$ [for example, (39*b*,*c*)] should be determined so that they may be consistent with expressions (78) and then the reduced boundary conditions are derived.

J. Tani

Assistant Professor,
Institute of High Speed Mechanics,
Tohoku University,
Sendai, Japan
Mem. ASME

Dynamic Stability of Truncated Conical Shells Under Pulsating Torsion

The dynamic stability of clamped, truncated conical shells under periodic torsion is analyzed by the Galerkin method in conjunction with Hsu's results. The instability regions of practical importance are clarified for relatively low frequency ranges. Numerical results indicate that under the purely periodic torsion only the combination instability region exists but that with an increase in the static torsion the principal instability region becomes most significant. The relative openness of the instability regions is found to depend sensitively on the circumferential phase difference of two vibration modes excited simultaneously at the resonance with the same circumferential wave number.

Introduction

It is of great technical importance to clarify the dynamic stability for the design of lightweight structures under pulsating load. Hence, numerous references can be found in an excellent review article by Hsu [1] and a brilliant book by Evan-Iwanowski [2].

Since a conical shell is one of the basic elements of lightweight structures, a variety of researches have been made on this subject. For example, the dynamic stability of conical shells under pulsating pressure has been studied by Alfutov and Razumeev [3], Kornecki [4], and Tani [5, 6]. The dynamic stability of truncated conical shells under periodic axial load has been treated by Tani [7, 8]. As far as the author is aware, however, no results exist in the case of truncated conical shells under pulsating torsion.

This paper is concerned with the dynamic stability of clamped, truncated conical shells subjected to both static and periodic torsions. The Donnell-type equations modified with the transverse inertia force are used. The problem is solved by first applying the Galerkin method and then using Hsu's general result for the stability of coupled Hill's equations [9]. Through detailed calculations, the instability regions of practical importance, associated with both principal and combination resonances, are determined for relatively low frequency ranges.

The simultaneous action of the static torsion and the circumferential phase difference of two vibration modes excited simultaneously at the resonance are found to exert the significant effect on the relative openness of the instability regions.

Contributed by the Applied Mechanics Division for publication in the JOURNAL OF APPLIED MECHANICS.

Discussion on this paper should be addressed to the Editorial Department, ASME, United Engineering Center, 345 East 47th Street, New York, N. Y. 10017, and will be accepted until September 1, 1981. Readers who need more time to prepare a Discussion should request an extension from the Editorial Department. Manuscript received by ASME Applied Mechanics Division, August, 1980.

Basic Equations and Boundary Conditions

Assume that a truncated conical shell with slant length l, thickness h, base circle radius r, and semi-vertex angle α is subjected to periodic torsion $T = T_0 + T_1 \cos \Omega t$ applied along the edges, where T_0, T, Ω, and t are static torsion, a amplitude of periodic torsion, a angular frequency, and time, respectively. The coordinate system is taken as shown in Fig. 1. When the problem is restricted to relatively low frequency ranges where flexural vibrations of thin shells are dominant, effects of transverse shear deformation and in-plane as well as rotatory inertia forces can be neglected. Hence, in the unperturbed motion, the shell executes a simple torsional vibration with the stress resultants as given by

$$N_{s0} = N_{\theta 0} = 0, \quad N_{s\theta 0} = \frac{T_0 + T_1 \cos \Omega t}{2\pi s^2 \sin^2 \alpha} \tag{1}$$

Next, consider the perturbed motion of the shell. With U, V, and W denoting the small incremental displacement components and F the stress function for the incremental stress resultants, the governing equations are given by the modified Donnell-type equations including the effect of transverse inertia force as

$$\nabla^4 F + \frac{Eh \cot \alpha}{s} W_{,ss} = 0 \tag{2}$$

$$\mu h W_{,tt} + D\nabla^4 W - \frac{\cot \alpha}{s} F_{,ss} - 2N_{s\theta 0}\left(\frac{1}{s} W_{,\phi}\right)_{,s} = 0 \tag{3}$$

where

$$\nabla^2 = \frac{\partial^2}{\partial s^2} + \frac{1}{s}\frac{\partial}{\partial s} + \frac{1}{s^2}\frac{\partial^2}{\partial \phi^2}, \quad \phi = \theta \sin \alpha$$

In the foregoing, $D = Eh^3/12(1 - \nu^2)$ is the flexural rigidity of the shell, and E, ν, and μ are Young's modulus, Poisson's ratio, and the mass density of the shell, respectively, while subscripts following a comma stand for differentiation. The relations between the stress function and the stress resultants are

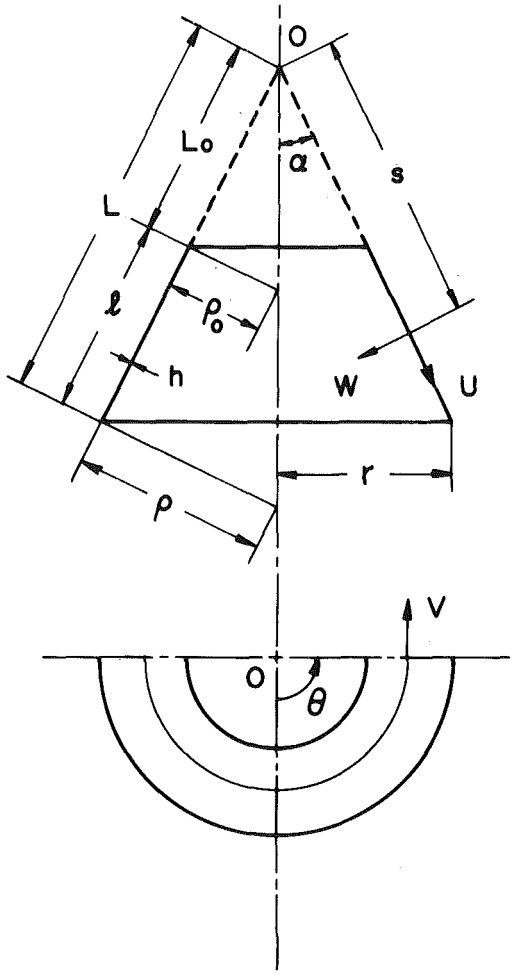

Fig. 1 Coordinates and nomenclature of the truncated conical shell

$$N_s = \frac{1}{s}F_{,s} + \frac{1}{s^2}F_{,\phi\phi}, \quad N_\theta = F_{,ss}, \quad N_{s\theta} = -\left(\frac{1}{s}F_{,\phi}\right)_{,s} \tag{4}$$

while the displacement components are related to the stress resultants by

$$EhU_{,s} = N_s - \nu N_\theta, \quad \frac{Eh}{s}(U + V_{,\phi} - W\cot\alpha) = N_\theta - \nu N_s$$

$$\frac{Eh}{s}(U_{,\phi} - V + sV_{,s}) = 2(1+\nu)N_{s\theta} \tag{5}$$

For the boundary conditions at $s = L_0$ and L, the following case will be considered:

$$U = V = W = W_{,s} = 0 \tag{6}$$

Here, the following coordinate transformation and nondimensional notations are introduced for convenience.

$$x = \log\frac{s}{L}, \quad f = \frac{e^{-x}F}{Eh^2L\cot\alpha}, \quad \tau = t/L^2\sqrt{\frac{D}{\mu h}}$$

$$\omega = \Omega L^2\sqrt{\frac{\mu h}{D}}, \quad w = \frac{W}{h}, \quad (u, v) = (U, V)/h\cot\alpha$$

$$(n_x, n_\phi, n_{x\phi}) = \frac{L}{Eh^2\cot\alpha}(N_s, N_\theta, N_{s\theta}), \quad \gamma = \frac{L_0}{L}$$

$$Z = \sqrt{1-\nu^2}\,\frac{L^2}{\rho h}, \quad (q_0, q_1) = \frac{(T_0, T_1)}{T_{cr}}$$

$$T_{cr} = \frac{2\pi k_s\gamma^2 D}{L^2} \tag{7}$$

In the foregoing, γ and Z are a truncation ratio and a shape factor of the conical shell, respectively, and T_{cr} is a buckling torsion load with a relevant parameter k_s. Further, q_0 and q_1 are the static and periodic load intersities normalized by T_{cr}, respectively, while ω is an exciting frequency parameter. With these notations, the preceding equations can be rewritten as follows:

$$\left\{\frac{\partial^4}{\partial x^4} - 2\frac{\partial^2}{\partial x^2} + 1 + \frac{\partial^2}{\partial\phi^2}\left(2\frac{\partial^2}{\partial x^2} + 2 + \frac{\partial^2}{\partial\phi^2}\right)\right\}f = w_{,x} - w_{,xx} \tag{8}$$

$$\bar{L}(wf) \equiv w_{,\tau\tau} + e^{-4x}\bar{\nabla}^4 w - 12Z^2e^{-2x}(f_{,x} + f)_{,x} - 2k_s(q_0 + q_1\cos\omega\tau)e^{-4x}(w_{,x} - w)_{,\phi} = 0 \tag{9}$$

$$n_x = e^{-x}(f + f_{,x} + f_{,\phi\phi}), \quad n_\phi = e^{-x}(f + f_{,x})_{,x}$$

$$n_{x\phi} = -e^{-x}f_{,x\phi} \tag{10}$$

$$u_{,x} = e^x(n_x - \nu n_\phi), \quad u - w + v_{,\phi} = e^x(n_\phi - \nu n_x)$$

$$v_{,\phi} + v_{,x} - v = 2(1+\nu)e^x n_{x\phi} \tag{11}$$

$$u = v = w = w_{,x} = 0 \quad \text{at} \quad x = \log\gamma, 0 \tag{12}$$

where

$$\bar{\nabla}^4 \equiv \frac{\partial^4}{\partial x^4} - 4\frac{\partial^3}{\partial x^3} + 4\frac{\partial^2}{\partial x^2} + \frac{\partial^2}{\partial\phi^2}\left(2\frac{\partial^2}{\partial x^2} - 4\frac{\partial}{\partial x} + 4 + \frac{\partial^2}{\partial\phi^2}\right)$$

Under the boundary condition (12), equations (8) and (9) have, in general, only bounded solutions for w and f, and the unperturbed motion is stable. However, under specific combinations of q_0, q_1 and ω, the governing equations have a solution w increasing indefinitely with time τ, leading to the dynamic instability of the shell. The problem consists of determining the boundaries dividing the stability and instability regions in the space of q_0, q_1, and ω, when the values for the shell geometry Z, γ, and α, Poisson's ratio ν and the wave number N are prescribed.

Method of Solution

Considering the boundary condition (12), we put w as

$$w = \sum_m (C_{m-1} - C_{m+1})\{a_m(\tau)\cos N\theta + b_m(\tau)\sin N\theta\}$$

$$C_m = \cos(\beta_m x), \quad \beta_m = m\pi/\log\gamma, \quad (m = 1, 2, 3, \cdots) \tag{13}$$

where $a_m(\tau)$ and $b_m(\tau)$ are unknown time functions and N is the number of circumferential waves. Substituting equation (13) into equation (8), we can obtain the general solution f of equation (8) as follows:

$$f = \{f_1e^{(\eta+1)x} + f_2e^{-(\eta+1)x} + f_3e^{(\eta-1)x} + f_4e^{-(\eta-1)x}\}\cos N\theta + \{g_1e^{(\eta+1)x} + g_2e^{-(\eta+1)x} + g_3e^{-(\eta+1)x} + g_4e^{-(\eta-1)x}\}\sin N\theta + \sum_m \{\beta_{m-1}G_{m-1}(\beta_{m-1}C_{m-1} - S_{m-1}) - \beta_{m+1}G_{m+1}(\beta_{m+1}C_{m+1} - S_{m+1})\}(a_m\cos N\theta + b_m\sin N\theta) \tag{14}$$

where f_1 to f_4 and g_1 to g_4 are arbitrary time functions, η is a wave number parameter and

$$\eta = N/\sin\alpha, \quad S_m = \sin(\beta_m x)$$

$$G_m = 1/\{\beta_m{}^2 + (\eta+1)^2\}\{\beta_m{}^2 + (\eta-1)^2\}$$

Substituting equations (10), (13), and (14) into equation (11), and solving for u and v, we can determine the arbitrary time functions $f_{1\sim4}$ and $g_{1\sim4}$ so as to satisfy the boundary condition (12).

Thus we have obtained the expressions for w and f satisfying both the compatibility and boundary conditions exactly. To determine the unknown time functions $a_m(\tau)$ and $b_m(\tau)$ contained in these expressions, the Galerkin method is applied to the remaining basic equation (9), which leads to the following sets of conditions:

$$\int_0^{2\pi}\int_0^{\log\gamma}\bar{L}(w,f)(C_{n-1}-C_{n+1})\begin{Bmatrix}\cos N\theta\\ \sin N\theta\end{Bmatrix}e^{2x}dxd\theta=0,$$

$$(n=1,2,3\cdots) \quad (15)$$

Substituting equations (13) and (14) in these conditions (15) and integrating, we finally obtain two sets of the equations of motion in terms of $a_m(\tau)$ and $b_m(\tau)$ as

$$\sum_m\{M_{nm}a_{m,\tau\tau}+R_{nm}a_m+k_s(q_0+q_1\cos\omega\tau)P_{nm}b_m\}=0$$

$$\sum_m\{M_{nm}b_{m,\tau\tau}+R_{nm}b_m-k_s(q_0+q_1\cos\omega\tau)P_{nm}a_m\}=0$$

$$(m,n=1,2,3,\ldots) \quad (16)$$

where

$$M_{nm}=\{1-(-1)^{n+m}\gamma^2\}(D_{n,m-1}-D_{n,m+1})$$

$$R_{nm}=Z^2\{(A_{n-1}+A_{n+1})\delta_{m,n}-A_{n-1}\delta_{m,n-2}-A_{n+1}\delta_{m,n+2}+H_{nm}(\eta)+H_{nm}(-\eta)\}-\{1-(-1)^{n+m}\gamma^2\}(B_{n,m-1}-B_{n,m+1})$$

$$P_{nm}=\{1-(-1)^{n+m}\gamma^2\}(E_{n,m-1}-E_{n,m+1}) \quad (17)$$

In the foregoing, $\delta_{n,m}$ is the Kronecker delta, while A_n, $B_{n,m}$, $D_{n,m}$, $E_{n,m}$, $H_{n,m}$ are complicated functions of the truncation ratio γ, the shape factor Z, Poisson's ratio ν, the wave number parameter η (or N), m, and n, For completeness, these actual expressions are given in the Appendix 1.

Putting $Z=0$ and $\eta=N$ in equations (17), these equations agree precisely with those for the problem of annular plates [10].

Upon omitting the inertia terms as well as those with periodic coefficients, and putting $a_m(\tau)\equiv a_{m0}$, $b_m(\tau)\equiv b_{m0}$ and $q_0=1$ in equations (16), we have two sets of the homogeneous linear equations in a_{m0} and b_{m0} as

$$\sum_m\left\{R_{nm}\begin{pmatrix}a_{m0}\\ b_{m0}\end{pmatrix}\pm k_sP_{nm}\begin{pmatrix}b_{m0}\\ a_{m0}\end{pmatrix}\right\}=0, \quad (m,n=1,2,3,\cdots) \quad (18)$$

From these equations, the buckling coefficient k_s, the wave number N_s and the buckling mode can be determined for each specified conical shell, with the usual procedure for the buckling problem.

Further, upon omitting the terms with periodic coefficients and putting $a_m(\tau)\equiv a_{m1}\cos\omega\tau$ and $b_m(\tau)\equiv b_{m1}\cos\omega\tau$, equations (16) lead to

$$\sum_m\left\{(R_{nm}-\omega^2M_{nm})\begin{pmatrix}a_{m1}\\ b_{m1}\end{pmatrix}\pm k_sq_0P_{nm}\begin{pmatrix}b_{m1}\\ a_{m1}\end{pmatrix}\right\}=0,$$

$$(m,n=1,2,3,\cdots) \quad (19)$$

Equating to zero the determinant of the coefficients of these equations, we can determine, for each wave number N, the nondimensional natural frequencies ω_i $(i=1,2,3,\cdots)$ and the corresponding eigenvectors ϕ_{ij} $(i,j=1,2,3,\cdots)$, under the effect of the static torsion q_0. The indices i $(=1,2,3,\cdots)$ designate the axial mode of vibration, representing the number of half waves in the axial direction.

Here, it should be noted that in addition of $a_{11}=1$, the other condition is required to determine the eigenvectors ϕ_{ij}, because of the use of equation (13). Hence, the following condition is added:

$$w_{,xx}=0 \quad \text{at} \quad x=\log\gamma, \quad \theta=\theta_0 \quad (20)$$

This condition represents that a nodal line of the vibration mode develops from a position (γ, θ_0) on the top edge of the truncated conical shell in the axial direction. Further, this condition makes it possible to designate the circumferential phase difference ϵ of two vibration modes with the same circumferential wave number which excited simultaneously at the resonance.

Now we will proceed to examine the stability of equations (16). Transforming the generalized coordinates a_m and b_m to the normal coordinates d_i by making use of the eigenvectors ϕ_{ij}, we obtain the following set of coupled Mathieu equations in the standard form:

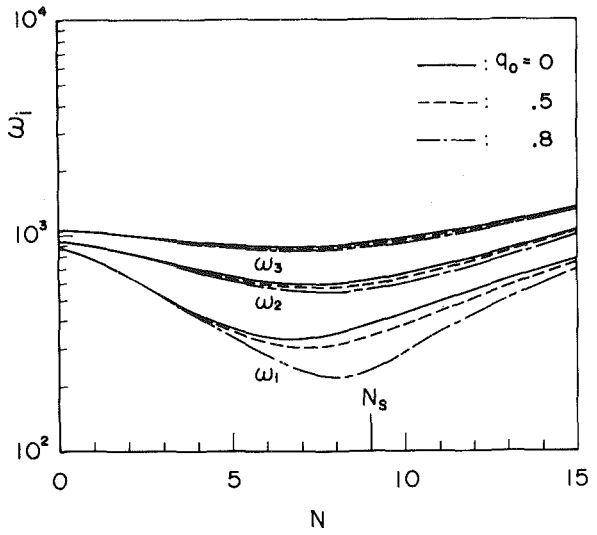

Fig. 2 Effect of static torsion on the natural frequencies in the case with $\gamma = 0.5$ and $Z = 191$

$$d_{i,\tau\tau}+\omega_i{}^2d_i+q_1\cos\omega\tau\sum_j Q_{ij}d_j=0$$

$$Q_{ij}=Q_{ji}=k_s\sum_k\sum_l\psi_{ki}P_{kl}\psi_{lj}$$

$$\psi_{ji}=\phi_{ij}\Big/\sqrt{\sum_k\sum_l\phi_{ik}M_{kl}\phi_{il}}$$

$$(i,j,k,l=1,2,3,\cdots) \quad (21)$$

The stability of the foregoing equations has been studied by Hsu in detail [9]. According to his first approximation analysis, equations (21) have instability regions of combination resonance type when ω is in the neighborhood of $\omega_i+\omega_j$, the boundaries of which are given by

$$\frac{\omega}{\omega_{ij}}=1\pm\theta_{ij}q_1, \quad (i,j=1,2,3,\cdots)$$

$$\omega_{ij}=\omega_i+\omega_j, \quad \theta_{ij}=\frac{|Q_{ij}|}{2\omega_{ij}\sqrt{\omega_i\omega_j}} \quad (22)$$

In the foregoing, ω_{ij} and θ_{ij} are a central frequency and a relative openness parameter of the instability region, respectively. Equations (21) have also principal instability regions at $\omega\cong 2\omega_i$, the boundaries of which are given by putting $i=j$ in equation (22).

For the small exciting force q_1, the foregoing instability regions will be of most practical importance. Hence, the consideration of the secondary instability will be omitted in the present analysis.

Numerical Results and Discussions

On the basis of the preceding analyses, detailed calculations are carried out for the conical shells with the truncation ratio $\gamma=0.5$ and the shape factor $Z=191$. Poisson's ratio ν is assumed to be 0.3. Practically accurate solutions are obtained by taking 20 terms for each unknown parameter a_m and b_m. Additional cases with $Z=57.2, 644$ and $\gamma=0.5$ are also treated.

Buckling Load and Natural Frequency. To check the computer program, the buckling load parameter k_s, the corresponding wave number parameter η_s and the natural frequency of the first order ω_1 are first determined for the conical shells treated in references [11, 12]. A comparison of the present and previous results is shown in the Appendix 2 (Tables 2 and 3). It is found that the present results are in good agreement with the previous ones.

Next, the buckling load parameter k_s and the corresponding wave number N_s in the cases of three kinds as adopted here are determined with the results listed in Table 1.

Moreover, with the effect of the static torsion q_0 taken into con-

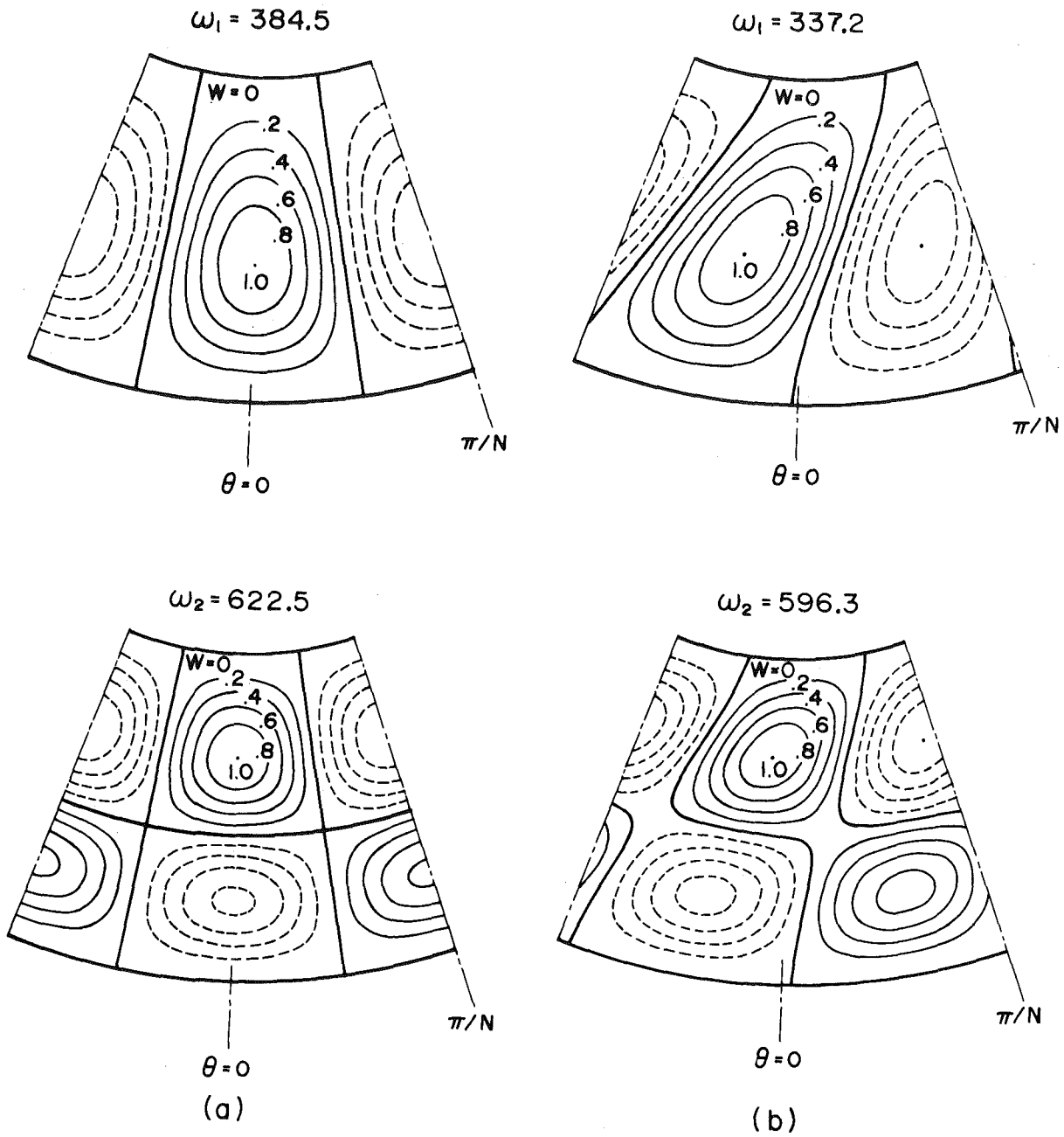

Fig. 3 Waveforms of the natural mode of vibration in the case with $\gamma = 0.5$, $Z = 191$, and $N = 9$: (*a*) $q_0 = 0$, (*b*) $q_0 = 0.5$

Table 1 Buckling load and the corresponding wave number in each case: $\nu = 0.3$, $\gamma = 0.5$

L/h	$(\rho + \rho_0)/2h$	α	Z	k_s	N_s
200	500	73.3°	57.2	256.7	8
200	150	45.0	191	472.3	9
600	400	41.6	644	1064	12

sideration, the natural frequencies w_i ($i = 1, 2, 3$) in each case are determined for each wave number N by using the values of k_s as given in Table 1. A typical result for the case with $\gamma = 0.5$ and $Z = 191$ is shown in Fig. 2. It will be seen that for the same wave number N, natural frequencies decrease with the increase in the static torsion. This tendency is most pronounced for those of first order ω_1, especially when the wave number is in the vicinity of buckling wave number N_s. This results agree with those obtained by Weingarten [13].

The effect of the static torsion on the natural modes of the first and second orders is also investigated. The typical results for the case with $\gamma = 0.5$, $Z = 191$, $N = 9$ ($\equiv N_s$), and $\theta_0 = \pi/2N$ are shown in Fig. 3, with the contour lines with the maximum amplitude of the deflection w taken as unity. It will be seen that, with the application of the static torsion, the axial nodal lines are obliquely rotated in the loading direction and that the wave pattern for ω_1 becomes almost identical with that for the static buckling (see reference [11]).

Instability Regions. First, the variation of the relative openness θ_{ij} of instability regions with the circumferential phase difference ϵ of two vibration modes exciting simultaneously at the resonance is examined by using the eigenvectors ϕ_{ij} obtained along with the calculation of natural frequencies ω_i. This is because two vibration modes, having the same circumferential wave number but having the

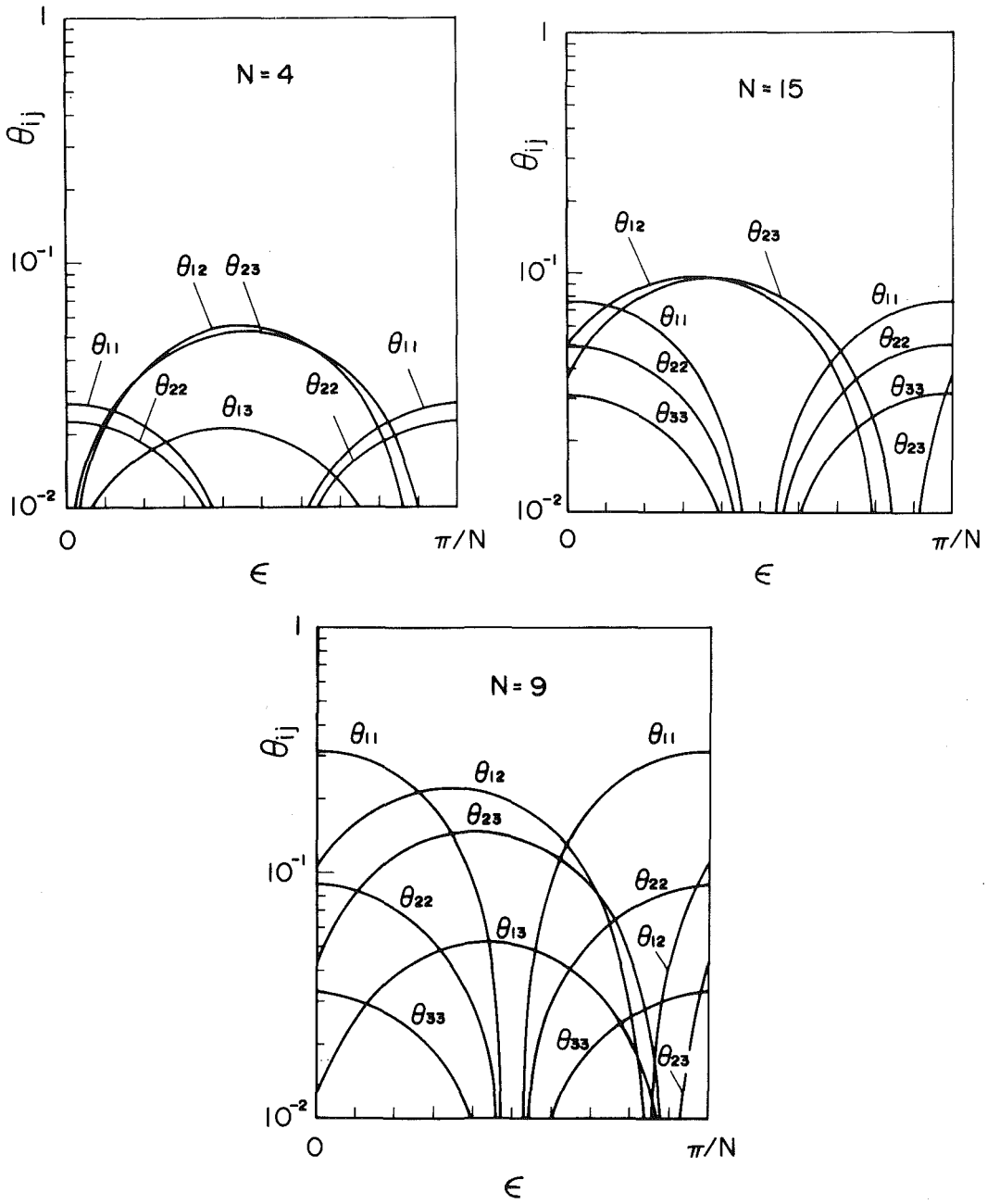

Fig. 4 Relation between relative openness and circumferential phase difference in the case with $\gamma = 0.5$, $Z = 191$, and $q_0 = 0.5$

different circumferential phase, may be excited simultaneously at the resonance. As a typical example, the results for the case with $\gamma = 0.5$, $Z = 191$, and $q_0 = 0.5$ are shown in Fig. 4. In this figure, the instability regions with θ_{ij} less than 10^{-2} are omitted as they will be of less practical importance. From this figure, the following is observed. The relative openness of the combination instability region θ_{ij} $(i \neq j)$ is widest when the value of the circumferential phase difference ϵ is in the vicinity of $\pi/2N$. On the other hand, that of the principal instability region θ_{ij} $(i = j)$ is widest when the value of ϵ is equal to 0 and π/N. The value of the relative openness θ_{ij} depends on the circumferential wave number N which two vibration modes excited simultaneously have equally.

Next, with the effect of the static torsion taken into consideration, the instability regions are determined for the same shape of shells under the loads $q_0 = 0$, 0.25, 0.5, and 0.75. These results are shown in Fig. 5. In this figure and the following, the relative openness θ_{ij} *represents the maximum value with respect to the circumferential phase* difference. Only the instability regions with $\theta_{ij} \geqq 10^{-2}$ are considered for natural frequencies up to the third order of axial modes. From this figure, one can easily find the location and the relative openness of the instability regions, together with the wave number as well as the modes of the excited vibration. The following observations can be made. Under the purely periodic torsion without the static one, one has only the instability regions of combination resonance type, in which two modes of vibration of ith and jth axial orders are parametrically excited. To judge from the magnitude of the relative openness θ_{ij}, the instability region associated with (i, j) as (1, 2) is of most practical importance. The relative openness θ_{12} has a maximum when the wave number N is near the buckling wave number N_s. Under the simultaneous action of the static torsion, one has the principal instability regions with $i = j$, besides the combination instability regions with $i \neq j$. With an increase in the static torsion, the

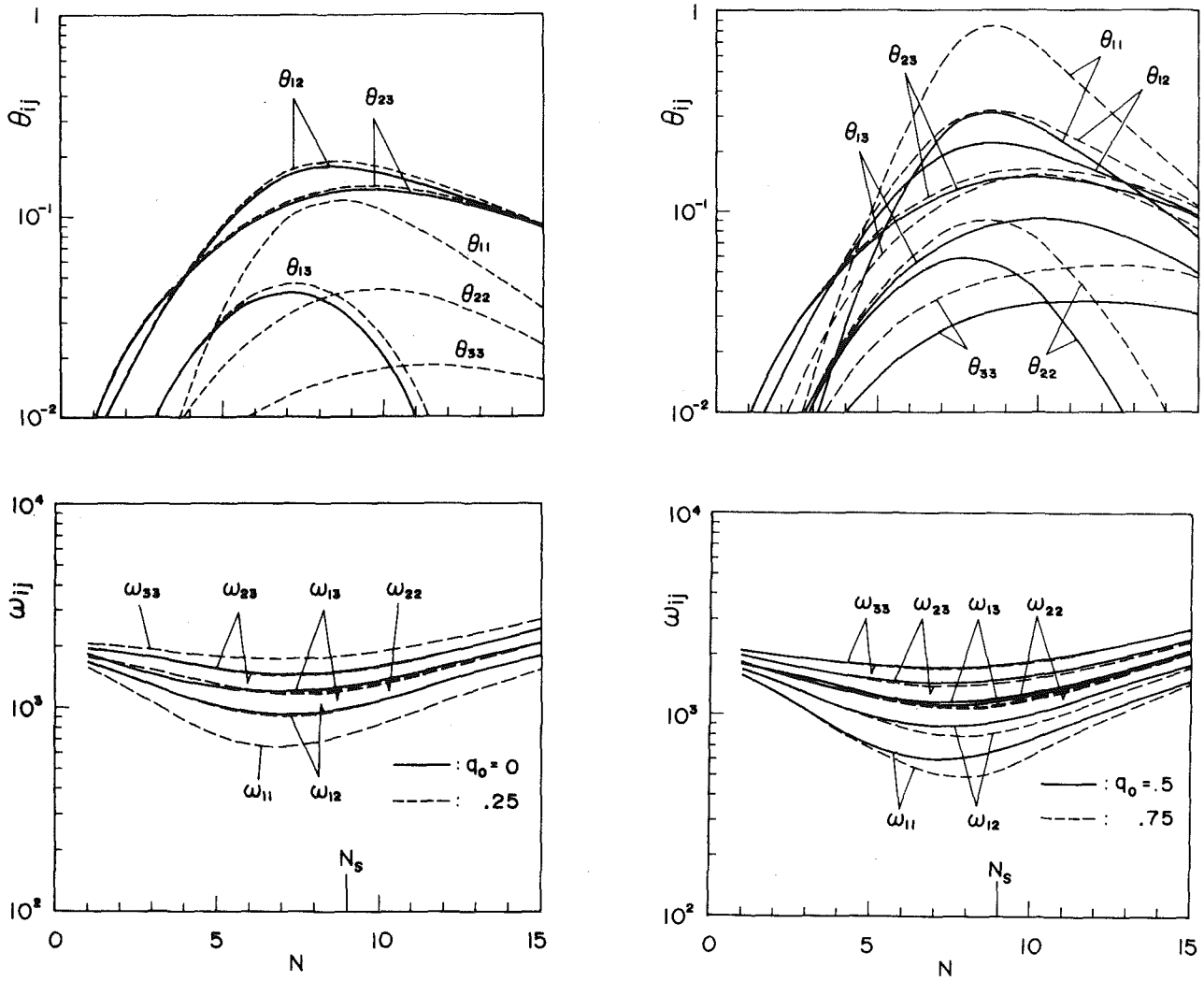

Fig. 5 Effect of static torsion on the central frequency and the relative openness of the instability regions: $\gamma = 0.5$, $Z = 191$

relative openness of the principal instability regions θ_{ij} $(i = j)$, especially θ_{11}, grows rapidly, while that for the combination type θ_{ij} $(i \neq j)$ remains almost unchanged. When the static torsion exceeds one half of the buckling load, the principal instability region for the vibration mode of the first order, associated with the wave number around N_s, is of most importance. The central frequencies ω_{ij} of each instability region are shifted toward the lower frequency with the static torsion.

To check the influence of the shell geometry, the instability regions for the cases with $Z = 57.2, 644$ and $\gamma = 0.5$ are determined with the results shown in Figs. 6 and 7. In these cases, two loading conditions are considered: $q_0 = 0$ and 0.5. It can be seen from these figures that with the change in the shape factor Z, the magnitude of the central frequencies ω_{ij} together with the dependence on wave number N are changed significantly, obviously due to the variations in the natural frequencies. However, no substantial changes are observed in the magnitude and in the wave number dependence of the relative openness θ_{ij}. It was omitted to illustrate the effect of the truncation ratio γ, but the same tendency was observed. Hence, it is to be noted that the main remarks on the instability regions stated in the forgoing are still valid irrespective of the shell geometry.

Conclusions

On the basis of the dynamic version of the Donnell-type equations, the dynamic stability of clamped, truncated conical shells subjected to both static and periodic torsion has been theoretically studied within relatively low frequency ranges. The main results obtained here may be summarized as follows:

1 Under the purely periodic torsion only the combination instability region exists, while the simultaneous action of the static torsion gives rise to the principal instability region also.

2 With the increase in the static torsion, the relative openness of the principal instability region, especially that for the vibration mode of the first order, grows rapidly, while that of the combination type remains almost unchanged. When the static torsion exceeds one half of the buckling load, the principal instability region for the vibration mode of the first order, associated with the wave number around the buckling one is of most importance.

3 The relative openness of the instability regions depends sensitively on the circumferential phase difference of two vibration modes excited simultaneously at the resonance with the same circumferential wave number.

4 The aforementioned conclusions are valid irrespective of the shell geometry.

5 The magnitude of the central frequencies and its dependence on wave number are changed significantly with the change in the shell geometry.

Acknowledgment

The author wishes to express his gratitude to Prof. N. Yamaki,

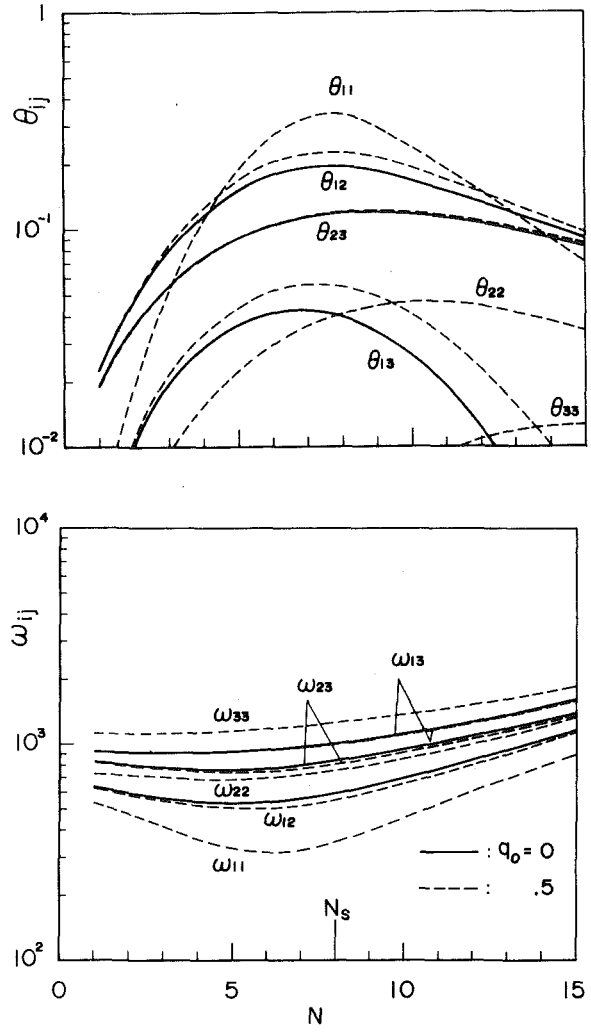

Fig. 6 Central frequency and the relative openness of the instability regions: $\gamma = 0.5$, $Z = 57.2$

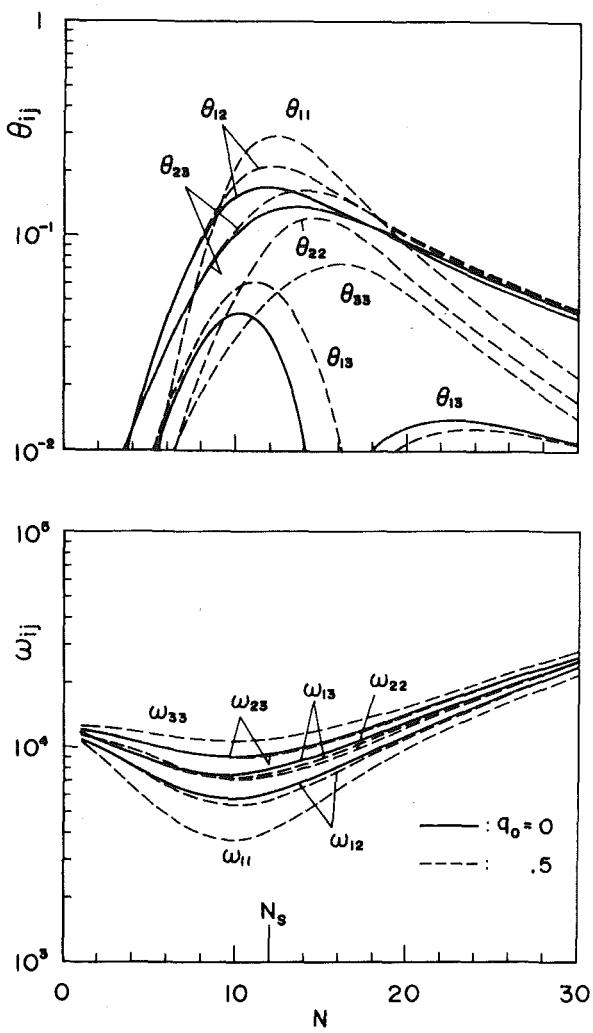

Fig. 7 Central frequency and the relative openness of the instability regions: $\gamma = 0.5$, $Z = 644$

Tohoku University, for his valuable advice and encouragement throughout the present study.

References

1 Hsu, C. S., "On Parametric Excitation and Snap-Through Stability Problems of Shells," *Thin Shell Structures: Theory, Experiment and Design*, eds., Fung, Y. C., and Sechler, E. E., Prentice-Hall, Englewood Cliffs, N. J., 1973, pp. 103–131.

2 Evan-Iwanowski, R. M., *Resonance Oscillations in Mechanical Systems*, Elsevier, 1976, pp. 251–281.

3 Alfutov, N. A., and Razumeev, V. F., "Dynamic Stability of a Conical Shell Supported on One End and Loaded by Axisymmetric Pressure" (in Russian), *Izvestia Akademiia Nauk, SSSR Otdel Teckhnitshoskikh Nauk*, Vol. 11, 1955, pp. 161–165.

4 Kornecki, A., "Dynamic Stability of Truncated Conical Shells Under Pulsating Pressure," *Israel Journal of Technology*, Vol. 4, 1966, pp. 110–120.

5 Tani, J., "Dynamic Stability of Truncated Conical Shells Under Periodic External Pressure," *The Report of the Institute of High Speed Mechanics*, Tohoku University, Japan, Vol. 28, 1973, pp. 135–147.

6 Tani, J., "Influence of Deformations Before Instability on the Parametric Instability of Conical Shells Under Periodic Pressure," *Journal of Sound and Vibration*, Vol. 45, 1976, pp. 253–258.

7 Tani, J., "Dynamic Instability of Truncated Conical Shells Under Periodic Axial Load," *International Journal of Solids and Structures*, Vol. 10, 1974, pp. 169–176.

8 Tani, J., "Influence of Deformations Prior to Instability on the Dynamic Instability of Conical Shells Under Periodic Axial Load," ASME JOURNAL OF APPLIED MECHANICS, Vol. 43, 1976, pp. 87–91.

9 Hsu, C. S., "On the Parametric Excitation of a Dynamic System Having Multiple Degrees of Freedom," ASME JOURNAL OF APPLIED MECHANICS, Vol. 30, 1963, pp. 367–372.

10 Tani, J., "Dynamic Stability of Annular Plates Under Pulsating Torsion," ASME JOURNAL OF APPLIED MECHANICS, Vol. 47, 1980, pp. 595–600.

11 Yamaki, N., and Tani, J., "Buckling of Truncated Conical Shells Under Torsion," *Zeitschrift für Angewandte Mathematik und Mechanik*, Heft 49, 1969, pp. 471–480.

12 Tani, J., "Free Transverse Vibrations of Truncated Conical Shells," *The Report of the Institute of High Speed Mechanics*, Tohoku University, Japan, Vol. 24, 1971, pp. 87–110.

13 Weingarten, V. I., "Vibration of Conical Shells Subjected to Torsion," *Journal of the Engineering Mechanics Division, Proceedings of the ASCE*, Vol. 94, 1968, pp. 47–55.

APPENDIX 1

For completeness, actual expressions of the coefficients appearing in equations (19) are given in the following:

$$A_n = 3\pi n^3 G_n (1 + \beta_n{}^2) 4\beta_n$$

$$B_{n,m} = n(\beta_m{}^2 + \eta^2)[(4 + \beta_m{}^2 - \eta^2)(4 + \beta_m{}^2 + \beta_{n-1}{}^2)(4 + \beta_m{}^2 + \beta_{n+1}{}^2) + 4\beta_m{}^2\{\eta^2(4 + \beta_m{}^2) - \beta_{n-1}{}^2\beta_{n+1}{}^2\}]/\lambda_{nm}$$

$$D_{n,m} = \beta_n{}^2\{(4 + \beta_m{}^2 + \beta_{n-1}{}^2)(4 + \beta_m{}^2 + \beta_{n+1}{}^2) - 4\beta_m{}^2(4 + \beta_m{}^2)\}/n\lambda_{nm}$$

$$E_{n,m} = n\eta[(2+\beta_m{}^2)(4+\beta_m{}^2+\beta_{n-1}{}^2)(4+\beta_m{}^2+\beta_{n+1}{}^2) - 2\beta_m{}^2\{\beta_m{}^2(4+\beta_m{}^2)+\beta_{n-1}\beta_{n+1}\}]/\lambda_{nm}$$

$$\lambda_{mn} = (4+\beta_{m+n-1}{}^2)(4+\beta_{m-n+1}{}^2)(4+\beta_{m+n+1}{}^2) \times (4+\beta_{m-n-1}{}^2)$$

$$H_{mn}(\eta) = 12\beta_m\beta_n\eta(\eta+1)^2[[(1+\nu)(2+\nu)\{1+(-1)^n\gamma^{\eta+1}\} \times [\{\gamma^{-2}-(-1)^m\gamma^{-\eta+1}\}K_m{}^{(1)}+(3-\nu)\{\gamma^{-2\eta} - (-1)^m\gamma^{n-1}\}K_m{}^{(2)}-(1+\nu)(\eta-1)\{1-(-1)^m\gamma^{-\eta-1}\}K_m{}^{(3)}] + \{1+(-1)^n\gamma^{-\eta-1}\}[(3-\nu)\{\gamma^{\eta}-(-1)^m\gamma^{-\eta+1}\}K_m{}^{(1)} + \{(1+\nu)^2\eta^2+8(1-\nu)\}\{\gamma^2-(-1)^m\gamma^{\eta-1}\}K_m{}^{(2)} + (1+\nu)(\eta-1)\{1-(-1)^m\gamma^{\eta+1}\}K_m{}^{(4)}]]/\chi_m$$

$$\chi_m = \eta(1+\nu)\{(\eta+1)^2+\beta_{m-1}{}^2\}\{(\eta-1)^2+\beta_{m-1}{}^2\}\{(\eta+1)^2+\beta_{m+1}{}^2\} \times \{(\eta-1)^2+\beta_{m+1}{}^2\}\{(\eta+1)^2+\beta_{n-1}{}^2\}\{(\eta+1)^2+\beta_{n+1}{}^2\} \times [\{(1+\nu)^2+(\eta^2+1)+(3-\nu)^2\}(\gamma-\gamma^{-1})^2 - (3-\nu)^2(\gamma^{\eta}-\gamma^{-\eta})^2]$$

$$K_m{}^{(1)} = 2(1-\eta^2)(\eta-1)\{(1+\nu)\eta+4\}I_m - \{(1+\nu)(2+\nu)\eta^2 + (2\nu^2+3\nu-3)\eta+4\}J_m$$

$$K_m{}^{(2)} = 2(1-\eta^2)(1-\nu)I_m + \{1+(2+\nu)\eta\}J_m$$

$$K_m{}^{(3)} = 2(1-\eta^2)(1+\eta)I_m + \{1-(2+\nu)\nu\}J_m$$

$$K_m{}^{(4)} = 2(1-\eta^2)(\eta-1)\{(1+\nu)\eta-4\}I_m - \{(1+\nu)(2+\nu)\eta^2 - (2\nu^2+3\nu-3)\eta+4\}J_m$$

$$I_m = \beta_m{}^2(1+m^{-2})+1+\eta^2$$

$$J_m = \beta_{m-1}{}^2\beta_{m+1}{}^2-(1-\eta^2)^2$$

APPENDIX 2

Table 2 Buckling load and the corresponding wavenumber parameter in each case: $\nu = 0.3$. (The value of η is assumed to be able to change continuously.)

		Present		Reference [11]	
γ	Z	k_s	η_s	k_s	η_s
0.2	10	41.55	3.05	41.55	3.05
	100	124.2	6.33	124.3	6.43
	1000	608.6	13.6	608.6	13.4
0.5	10	188.8	5.68	188.8	5.69
	100	326.7	9.58	326.8	9.58
	1000	1454	21.8	1454	21.8
0.8	10	1781	17.0	1781	16.9
	100	1840	17.8	1839	17.8
	1000	3624	32.8	3623	32.8

Table 3 Natural frequencies of the first order: $\nu = 0.3$, $Z = 932$, $\gamma = 0.438$, $\alpha = 20°$

N	2	3	4	5	6
Present	1737	1131	837.5	744.6	788.1
Reference [12]	1736	1131	837.0	744.0	787.4

N	7	8	9	10	11
Present	899.1	1042	1210	1403	1617
Reference [12]	898.2	1041	1209	1400	1614

J. Tani

Assistant Professor,
Institute of High Speed Mechanics,
Tohoku University,
Sendai, Japan
Mem. ASME

Elastic Instability of a Heated Annular Plate Under Lateral Pressure

On the basis of the dynamic version of the nonlinear von Karman equations, a theoretical analysis is performed on the elastic instability of a uniformly heated, thin, annular plate which has suffered a finite axisymmetric deformation due to lateral pressure. The linear free vibration problems around the finite axisymmetric deformation of the plate are solved by a finite-difference method. By examining the frequency spectrum with various asymmetric modes, the critical temperature rise under which the axisymmetric deformation becomes unstable due to the bifurcation buckling is determined, which is found to jump up to 7.2 times within a range of very small lateral pressure.

Introduction

The large axisymmetric deflection of thin annular plates under various lateral loads and boundary conditions has been studied by numerous researchers [1–8]. Moreover, the axisymmetric postbuckling behavior of the annular plate with the free inner edge and subjected to uniform compressive thrust at the clamped-movable outer edge has been studied by Huang [9, 10], and Uthgenannt and Brand [11]. The axisymmetric postbuckling behavior of heated annular plates with both edges clamped or simply supported has been studied by Pal [12]. Recently, the author examined the thermal buckling of a clamped annular plate with axisymmetric initial deflection [13] and the elastic instability of a clamped annular plate under uniform compressive thrust and lateral pressure [14]. The latter results of the author's studies showed that there are two ranges of the combined loads under which the axisymmetric deformation of the plate becomes unstable.

The object of the present paper is to study the elastic instability of a uniformly heated, thin, circular annular plate which has suffered a finite axisymmetric deformation due to lateral pressure. The material properties of the perfectly clamped annular plate are assumed to be independent of temperature. A finite-difference method is applied to the dynamic version of the nonlinear von Karman plate theory. By examining a continuous variation of the asymmetric linear natural frequencies in the neighborhood of the axisymmetric finite equilibrium state, one may detect the unstable axisymmetric deformation of the plate. Through the numerical results, it is shown in this case also that there are two ranges of the magnitude of combined loads under which the axisymmetric deformation of the plate becomes unstable due to the bifurcation buckling.

Basic Equations and Boundary Conditions

Consider that a thin, isotropic annular plate with thickness h, inner radius a, outer radius b is heated uniformly and subjected to a uniform lateral pressure p. Assume that its temperature rise T above the unstrained state is constant throughout the plate and that its material properties, i.e., Young's modulus E, Poisson's ratio ν, the mass density ρ, and the thermal expansion coefficient α are independent of temperature. The coordinate system is taken as shown in Fig. 1. The transverse displacement of the midplane and the stress function for stress resultants are denoted by W and F, respectively. As a basis for the analysis of the asymmetric small vibration of the plate in the neighborhood of nonlinear axisymmetric equilibrium state, we use the dynamic version of von Karman's equations. These equations are given in nondimensional form as follows:

$$\nabla^4 f = -\frac{12}{x}\left(w_{,x} + \frac{1}{x}w_{,\theta\theta}\right)w_{,xx} + \frac{12}{x^2}\left(w_{,x\theta} - \frac{1}{x}w_{,\theta}\right)^2$$

$$\nabla^4 w = \frac{1}{x}\left(f_{,x} + \frac{1}{x}f_{,\theta\theta}\right)w_{,xx} + \frac{1}{x}f_{,xx}\left(w_{,x} + \frac{1}{x}w_{,\theta\theta}\right) \tag{1}$$

$$-2\left(\frac{1}{x}f\right)_{,x\theta}\left(\frac{1}{x}w\right)_{,x\theta} + \bar{p} - w_{,\tau\tau} \tag{2}$$

$$u_{,x} + \frac{1}{2}(w_{,x})^2 = \frac{1}{12}\left(\frac{1}{x}f_{,x} + \frac{1}{x^2}f_{,\theta\theta} - \nu f_{,xx} + \bar{t}\right)$$

$$v_{,\theta} + u + \frac{1}{2x}(w_{,\theta})^2 = \frac{x}{12}\left[f_{,xx} - \frac{\nu}{x}\left(f_{,x} + \frac{1}{x}f_{,\theta\theta}\right) + \bar{t}\right]$$

$$v_{,\theta} + xv_{,x} - v + w_{,x}w_{,\theta} = -\frac{1+\nu}{6}x\left(\frac{1}{x}f_{,\theta}\right)_{,x} \tag{3}$$

Contributed by the Applied Mechanics Division for publication in the JOURNAL OF APPLIED MECHANICS.

Discussion on this paper should be addressed to the Editorial Department, ASME, United Engineering Center, 345 East 47th Street, New York, N. Y. 10017, and will be accepted until September 1, 1981. Readers who need more time to prepare a Discussion should request an extension from the Editorial Department. Manuscript received by ASME Applied Mechanics Division, July, 1980.

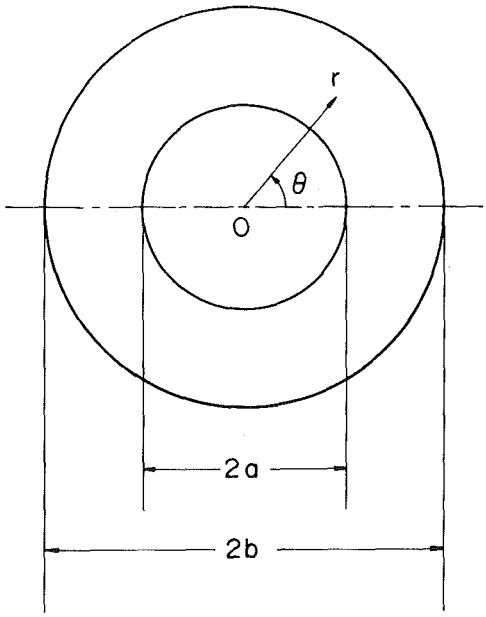

Fig. 1 Dimensions and coordinate system of the annular plate

where subscripts following a comma stand for partial differentiation and

$$\nabla^2 = \frac{\partial^2}{\partial x^2} + \frac{1}{x}\frac{\partial}{\partial x} + \frac{1}{x^2}\frac{\partial^2}{\partial \theta^2}$$

In these equations, the nondimensional quantities are related to the corresponding physical ones through the following relations:

$$x = \frac{r}{b}, \quad \gamma = \frac{a}{b}, \quad (u, v) = \frac{b(1-\nu^2)}{h^2}(U, V)$$
$$w = \frac{\sqrt{1-\nu^2}}{h} W, \quad f = \frac{F}{D}, \quad \tau = \frac{t}{b^2}\sqrt{\frac{D}{\rho h}}$$
$$\bar{t} = \frac{\alpha b^2 h E T}{D}, \quad \bar{p} = \sqrt{1-\nu^2}\frac{p b^4}{D h} \tag{4}$$

in which γ is a ratio of inner to outer radii, $D = Eh^3/12(1-\nu^2)$ is the flexural rigidity of the plate and t is time. The displacements of the midplane in the radial and circumferential directions are denoted by U and V, respectively.

Assuming that the annular plate is perfectly clamped along both edges, we have the following boundary conditions as $x = \gamma$, and 1.

$$u = v = w = w_{,x} = 0 \tag{5}$$

Denoting the time-independent, nonlinear, axisymmetric deformation state by $u_0(x)$, $w_0(x)$, and $f_0(x)$, the relevant equations are obtained from equations (1)–(3) and (5).

$$x\left[\frac{1}{x}(x\eta)_{,x}\right]_{,x} = -6\zeta^2 \tag{6}$$

$$x\left[\frac{1}{x}(x\zeta)_{,x}\right]_{,x} = \eta\zeta + \frac{1}{2}x^2\bar{p} \tag{7}$$

$$\eta_{,x} - \frac{\nu}{x}\eta + \bar{t} = 0, \quad \zeta = 0 \quad \text{at} \quad x = \gamma, 1 \tag{8}$$

where

$$\eta = f_{0,x}, \quad \zeta = w_{0,x}$$

In order to analyze the asymmetric small free vibration of the plate in the vicinity of an axisymmetric equilibrium state, we assume u, v, w, and f in the form

$$u = u_0(x) + u_1(x)\cos N\theta e^{i\omega\tau}, \; v = v_1(x)\sin N\theta e^{i\omega\tau}$$
$$w = w_0(x) + w_1(x)\cos N\theta e^{i\omega\tau}, \; f = f_0(x) + f_1(x)\cos N\theta e^{i\omega\tau} \tag{9}$$

where N and ω are the number of circumferential waves and a circular frequency, respectively, while u_1, v_1, w_1, and f_1 are infinitesimal quantities.

The equations governing the asymmetric small free vibration of the plate in the neighborhood of the axisymmetric equilibrium state are obtained by substituting equation (9) into equations (1)–(3) and (5), subtracting the equations of axisymmetric deformation from resulting equations and retaining only the linear terms in the infinitesimal quantities. This leads to

$$\nabla_1^4 f_1 = -\frac{12}{x}\left[\zeta w_{1,xx} + \left(w_{1,x} - \frac{N^2}{x}w_1\right)\zeta_{,x}\right] \tag{10}$$

$$\nabla_1^4 w_1 = \frac{1}{x}\left[\zeta f_{1,xx} + \left(f_{1,x} - \frac{N^2}{x}f_1\right)\zeta_{,x} + \eta w_{1,xx} + \left(w_{1,x} - \frac{N^2}{x}w_1\right)\eta_{,x}\right] + \omega^2 w_1 \tag{11}$$

$$u_{1,x} + \zeta w_{1,x} = \frac{1}{12}\left(\frac{1}{x}f_{1,x} - \frac{N^2}{x^2}f_1 - \nu f_{1,xx}\right)$$
$$N v_1 + u_1 = \frac{x}{12}\left[f_{1,xx} - \nu\left(\frac{1}{x}f_{1,x} - \frac{N^2}{x^2}f_1\right)\right]$$
$$-N u_1 + x v_{1,x} - v_1 - N\zeta\omega_1 = \frac{N(1+\nu)}{6}\left(f_{1,x} - \frac{1}{x}f_1\right) \tag{12}$$

$$u_1 = v_1 = w_1 = w_{1,x} = 0 \quad \text{at} \quad x = \gamma, 1 \tag{13}$$

where

$$\nabla_1^2 = \frac{d^2}{dx^2} + \frac{1}{x}\frac{d}{dx} - \frac{N^2}{x^2}$$

With equation (12), equation (13) becomes, at $x = \gamma$ and 1,

$$w_1 = w_{1,x} = 0, \quad x^2 f_{1,xx} - \nu(x f_{1,x} - N^2 f_1) = 0$$
$$x^3 f_{1,xxx} - (1 - \nu + 2N^2 + \nu N^2)x f_{1,x} + 3N^2 f_1 = 0 \tag{14}$$

Numerical Procedures and Results

The details of the numerical procedures used in this study were described in reference [15] and will not be repeated here. The system of nonlinear differential equations (6)–(8) governing the axisymmetric deformation was solved by Newton's method, in which the direct solution of the nonlinear system is replaced by the solution of a sequence of linear correctional equations. These equations, as well as the eigenvalue problem posed by equations (10), (11), and (14) were solved by central differencing and the application of Potters' algorithm [16]. Iterative calculations of Newton's method were done until the condition $|\delta y^{(n)}/y^{(n)}| \leqq 10^{-4}$ was satisfied, where $\delta y^{(n)}$ and $y^{(n)}$ correspond to the values of correction term and solution of n iteration at each station, respectively. A mesh of 100 points on the interval of $(1-\gamma)$ was considered in the finite-difference method.

When the values for the radius ratio γ, Poisson's ratio ν, and the load parameters $\bar{t}$ and $\bar{p}$ are given, we can determine the eigenvalues, i.e., the natural frequencies ω in this case for each circumferential wave number N. If the square of any natural frequency thus obtained is negative, the corresponding original axisymmetric deformation will be unstable. Hence, the branching of the asymmetric equilibrium state from the axisymmetric one may take place at the state where one of the natural frequency becomes zero.

As a numerical example, we take an annular plate with $\gamma = 0.5$ and $\nu = 0.3$.

Fig. 2 shows the variation of the square of the first order of natural frequencies with the wave numbers $N = 2, 3, 4$, and 5 as a function of the temperature rise $\bar{t}$ for the plate under $\bar{p} = 30$. From this figure, it can be seen that there are the ranges in which the square of the natural frequencies corresponding to $N = 3$ and 4 becomes negative. Hence, the axisymmetric deformation is unstable between two circle marks, i.e., A ($\bar{t}_{cr} \equiv \bar{t} = 104.5$) and B ($\bar{t}_{cr} \equiv \bar{t} = 113.2$). When the temperature rises from the unstrained state of the plate, the branching

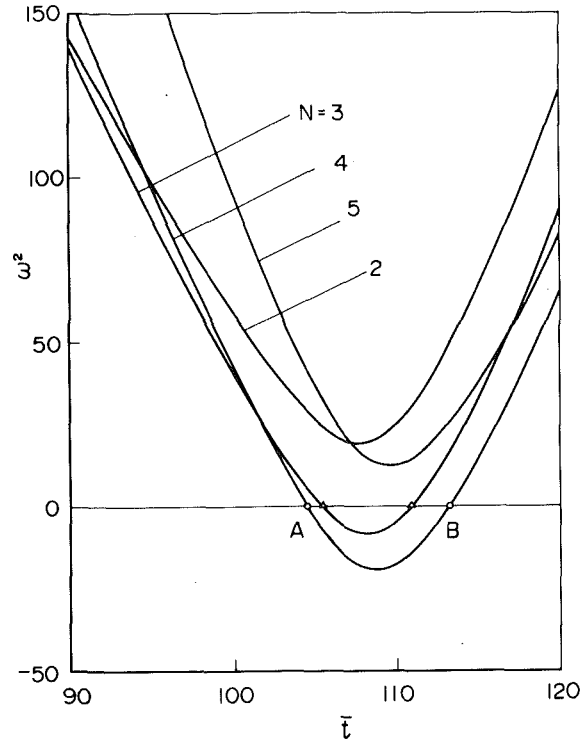

Fig. 2 Relations between the temperature rise and the square of the first order of natural frequencies with various wave numbers: $\gamma = 0.5$, $\bar{p} = 30$

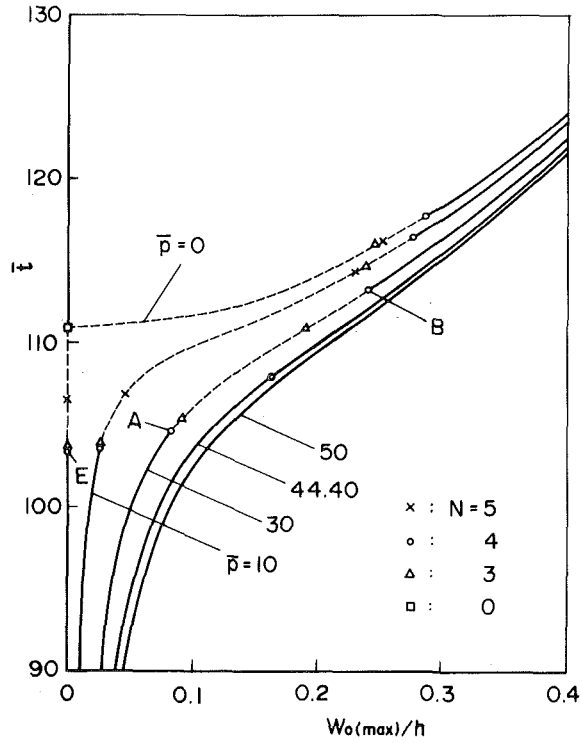

Fig. 4 Relations between the temperature rise and the maximum value of the axisymmetric deflection: $\gamma = 0$, $\bar{p} = 0 \sim 50$

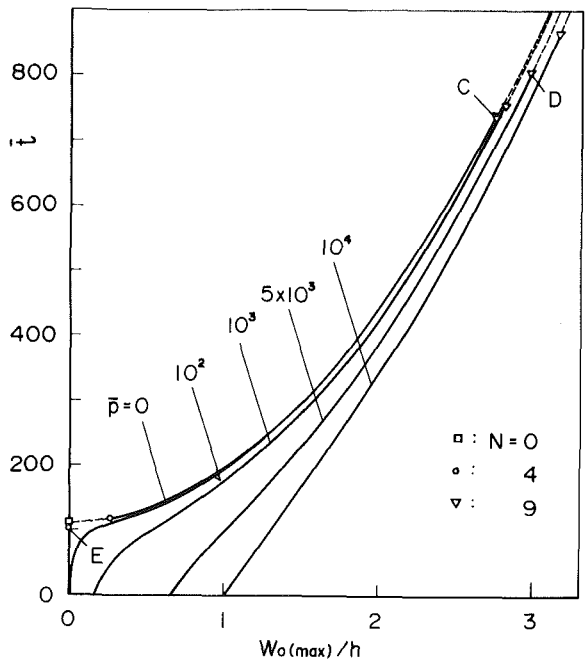

Fig. 3 Relations between the temperature rise and the maximum value of the axisymmetric deflection: $\gamma = 0.5$, $\bar{p} = 0 \sim 10^4$

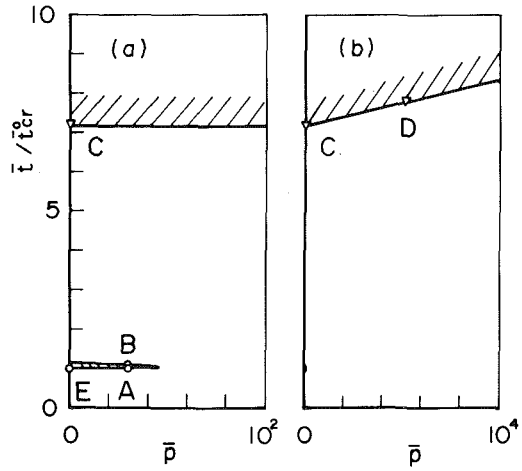

Fig. 5 Instability regions for the axisymmetric deformation: $\gamma = 0.5$

of the asymmetric equilibrium state with $N = 4$ from the axisymmetric one occur at the point A. If the axisymmetric equilibrium state were realized at a temperature rise beyond the point B, the branching of the asymmetric equilibrium state with $N = 4$ from the axisymmetric one will take place at the point B, during a fall in temperature.

Fig. 3 shows the relations between the temperature rise and the maximum value of the axisymmetric deformation for various values of pressure. Detailed results for the cases when $\bar{p}$ is less than 50 are shown in Fig. 4. In these figures, small circles, triangles, squares, and so on, denote the branching points, while broken lines correspond to the unstable axisymmetric equilibrium states in which the square of some natural frequencies becomes negative. The points A and B in Fig. 4 indicate the location of the corresponding points in Fig. 2, respectively. The bifurcation buckling with the indicated wave number N may occur at the branching points corresponding to ends of the broken lines. The following may be observed from these figures. The asymmetric bifurcation buckling of the annular plate without lateral pressure occurs at the point E with $\bar{t}^0_{cr} = 103.4$ and $N = 4$. For the annular plate under $\bar{p} \leq 44.40$, the axisymmetric deformation becomes unstable near $\bar{t}^0_{cr}$. When the temperature rise becomes higher than $7.2\,\bar{t}_{cr}{}^0$, the bifurcation buckling with $N = 9$ occurs and the axi-

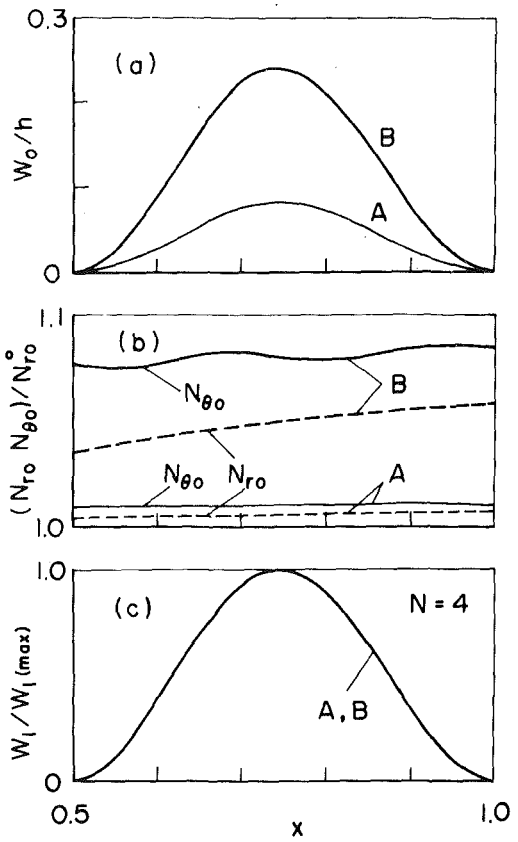

Fig. 6 Distributions of (*a*) axisymmetric deflection, (*b*) axisymmetric radial and hoop stress resultants just before buckling, and (*c*) bifurcation buckling deflection: $\bar{p} = 30$, *A* ($\bar{t}_{cr} = 10.45$), *B* ($\bar{t}_{cr} = 113.2$)

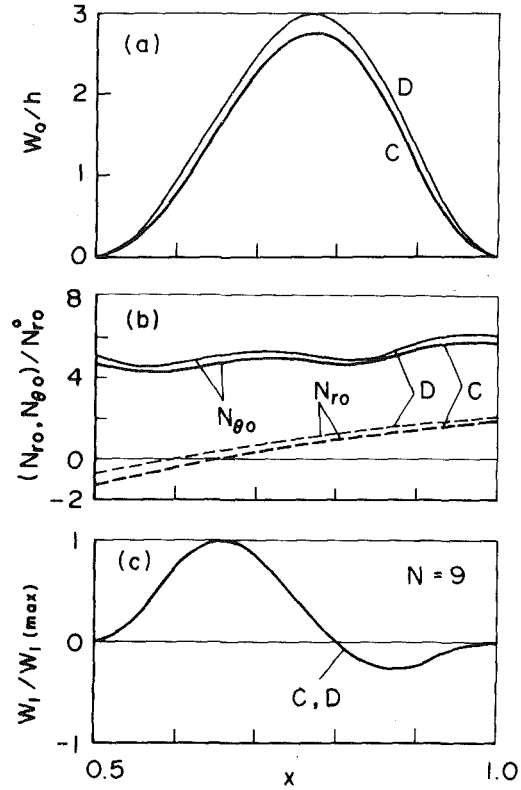

Fig. 7 Distributions of (*a*) axisymmetric deflection, (*b*) axisymmetric radial and hoop stress resultants just before buckling, and (*c*) bifurcation buckling deflection, *C* ($\bar{p} = 0$, $\bar{t}_{cr} = 740.4$), D ($\bar{p} = 5000$, $\bar{t}_{cr} = 806.6$)

symmetric deformation becomes unstable. From the results stated in the foregoing, the relation between the temperature rise and pressure destabilizing the axisymmetric deformation is determined with the results as illustrated in Figs. 5. Fig. 5(*a*) shows a part of Fig. 5(*b*) after magnification. In these figures, the shaded ranges show the combined loads destabilizing the axisymmetric deformation. The points *A*, *B*, *C*, *D*, and *E* indicate the location of the corresponding points in the foregoing figures, respectively. From these figures, the following observations may be made for the annular plate here considered. The instability region near $\bar{t}^0_{cr}$ exists only for the plate under pressure less than 44.40. The temperature rise $\bar{t}_{cr}$ which gives rise to the bifurcation buckling jumps up to 7.2 $\bar{t}^0_{cr}$, and then gradually increases with pressure.

Figs. 6 and 7 show the distributions of (*a*) the axisymmetric deflection, (*b*) the axisymmetric radial and circumferential stress resultants, N_{r0} and $N_{\theta 0}$, just before bifurcation buckling, and (*c*) the buckling deflection for the plates under $\bar{p} = 30$ and those under $\bar{p} =$ 5000 and 0, respectively. In these figures, $x = 0.5$ and 1 in the abscissa correspond to the inner and outer edges of the annular plate, while N^0_{r0} stands for the axisymmetric compressive radial stress resultant at the buckling temperature rise $\bar{t}^0_{cr}$ of the heated annular plate without lateral pressure, Moreover, the cases *A*, *B*, *C*, and *D* indicate the states of the corresponding points in the foregoing figures, respectively. It is to be noted that for the heated plate without lateral pressure, N^0_{r0} is equal to the circumferential stress resultant $N^0_{\theta 0}$ at buckling, as the plate is in a state of uniform compression. It will be seen from Fig. 6(*b*) that the circumferential compressive stress resultant $N_{\theta 0}$ becomes larger than the radial stress resultant N_{r0}, as the buckling temperature rise $\bar{t}_{cr}$ increases from *A* to *B*. From Fig. 7(*b*), this tendency will be seen to be especially marked in the case with high pressure. From Fig. 6(*c*), it will be observed that both buckling deflections at the points *A* ($\bar{t}_{cr} = 104.5$, $N = 4$) and *B* ($\bar{t}_{cr} = 113.2$, $N =$ 4) almost agree with that of the point *E* ($\bar{t}^0_{cr} = 103.4$, $N = 4$). Fig. 7(*c*) indicates that the buckling deflections at the points *C* ($\bar{t}_{cr} = 7404$, $N = 9$) and *D* ($\bar{t}_{cr} = 806.6$, $N = 9$) almost agree, and have many waves in the circumferential direction and two half waves in the radial direction. Judging from these figures the bifurcation buckling for the plate under high pressure appears to be caused by the large circumferential stress.

Conclusions

The elastic instability of a uniformly heated circular annular plate under lateral pressure is studied by examining the linear free vibration in the vicinity of the finite axisymmetric equilibrium state. Main results obtained through the calculations for the radius ratio $\gamma = 0.5$ are summarized as follows:

1 The combination of the temperature rise and lateral pressure destabilizing the axisymmetric deformation of the annular plate exists always for the higher temperature than 7.2 times the buckling one $\bar{t}^0_{cr}$ of the annular plate without lateral pressure.

2 The bifurcation buckling due to the higher temperature rise than 7.2 $\bar{t}^0_{cr}$, is caused by the large hoop stress and has many circumferential waves. This buckling temperature rise $\bar{t}_{cr}$ increases with pressure.

3 Besides the forestated one, the annular plate under very small pressure gives rise to the buckling with a few circumferential waves due to the temperature rise near $\bar{t}^0_{cr}$.

Acknowledgment

The author would like to express his appreciation to Prof. N. Yamaki, Tohoku University, for his instructive suggestions and discussions on the present study. The author also wishes to thank heartily Prof. G. A. Wempner for his kind comment.

References

1 Wempner, G. A., and Schmidt, R., "Large Symmetric Deflections of Annular Plates," ASME JOURNAL OF APPLIED MECHANICS, Vol. 25, 1958, pp. 449–452.

2 Tamate, T., and Abé, H., "Large Deflections of Thin Annular Plates Under Uniform Pressure With Outer Edge Clamped," *Transactions of the Japan Society of Mechanical Engineers* (in Japanese), Vol. 30, 1964, pp. 828–834.

3 Hart, V. G., and Evans, D. J., "Nonlinear Bending of an Annular Plate by Transverse Edge Forces," *Journal of Mathematics and Physics*, Vol. 43, 1964, pp. 275–303.

4 Sherbourne, A. N., and Lennox, W. C., "Elastic, Large Deflections of Annular Membranes," *Journal of Engineering Mechanics Division, ASCE*, Vol. 92, 1966, pp. 75–99.

5 Koenig, H. A., Llorens, R. E., and Chou, P. C., "Finite Deflections of an Elastic Circular Plate With a Central Hole," ASME JOURNAL OF APPLIED MECHANICS, Vol. 36, 1969, pp. 285–291.

6 Llorens, R. E., and Koenig, H. A., "An Asymptotic Solution for the Large Deflection of a Circular Plate With a Central Hole," *International Journal of Nonlinear Mechanics*, Vol. 7, 1972, pp. 337–343.

7 William, J. H., III, and Peddieson, J., Jr., "Finite Deflections of Annular Membranes," *Journal of the Industrial Mathematical Society*, Vol. 27, 1977, pp. 75–86.

8 Tielking, J. T., "Axisymmetric Bending of Annular Plates," ASME JOURNAL OF APPLIED MECHANICS, Vol. 45, 1978, pp. 834–838.

9 Huang, C. L., "Postbuckling of an Annulus," *AIAA Journal*, Vol. 11, 1973, pp. 1608–1612.

10 Huang, C. L., "On Postbuckling of Orthotropic Annular Plates," *International Journal of Nonlinear Mechanics*, Vol. 10, 1975, pp. 63–74.

11 Uthgenannt, E. B., and Brand, R. S., "Postbuckling of Orthotropic Annular Plates," ASME JOURNAL OF APPLIED MECHANICS, Vol. 40, 1973, pp. 559–564.

12 Pal, M. C., "Large Deformations of Heated Circular Plates," *Acta Mechanica*, Vol. 8, 1969, pp. 82–103.

13 Tani, J., "Thermal Buckling of an Annular Plate With Axisymmetric Initial Deflection," ASME JOURNAL OF APPLIED MECHANICS, Vol. 45, 1978, pp. 693–695.

14 Tani, J., "Elastic Instability of an Annular Plate Under Uniform Compression and Lateral Pressure," ASME JOURNAL OF APPLIED MECHANICS, Vol. 47, 1980, pp. 591–594.

15 Tani, J., "Influence of Prebuckling Deformations on the Buckling of Truncated Conical Shells Under Axial Compression," *Transactions of the Japan Society of Aeronautical and Space Sciences*, Vol. 16, 1973, pp. 232–245.

16 Potters, M. L., "A Matrix Method for the Solution of a Second-Order Difference Equation in Two Variables," Report MR19 Mathematich Centrum, Amsterdam, The Netherlands, 1955.

S. F. Masri
Professor.
Mem. ASME

Y. A. Mariamy
Graduate Student.

J. C. Anderson
Associate Professor.

Department of Civil Engineering,
University of Southern California,
Los Angeles, Calif. 90007

Dynamic Response of a Beam With a Geometric Nonlinearity

Analytical and experimental studies were made of the dynamic response of a system with a geometric nonlinearity, which is encountered in many practical engineering applications. An exact solution was derived for the steady-state motion of a viscously damped Bernoulli-Euler beam with an unsymmetric geometric nonlinearity, under the action of harmonic excitation. Experimental measurements of a mechanical model under harmonic as well as random excitation verified the analytical findings. The effect of various dimensionless parameters on the system response was determined.

1 Introduction

The problem of forced vibration of a dynamic system with motion-limiting stops is of great importance in many practical engineering applications. For example, this problem is encountered in such cases as

1 The effect of gapped supports on the response of piping systems in nuclear power plants subjected to postulated rupture conditions.

2 The vibration of mechanical equipment possessing dead space nonlinearities.

3 The vibration isolation of dynamic systems mounted on resilient supports with motion-limiting stops.

Several investigators have conducted numerous analytical, numerical, and experimental studies of dynamic systems with geometric nonlinearities and, in some cases, with material nonlinearities (see, for example [1–10]). However, closed-form solutions are lacking, particularly for nonlinear continuous systems.

For better determination of the dynamic response of real nonlinear structural systems, this study is concerned with the "exact" solution for the steady-state motion of a harmonically excited, viscously damped Bernoulli-Euler beam with an unsymmetrical geometric nonlinearity located at an arbitrary point along its span.

The formulation of the problem and the solution algorithm are presented in Section 2; the experimental studies that were conducted are given in Section 3; and the application of the analytical results to investigate the effects of various system parameters is discussed in Section 4.

Contributed by the Applied Mechanics Division for publication in the JOURNAL OF APPLIED MECHANICS.

Discussion on this paper should be addressed to the Editorial Department, ASME, United Engineering Center, 345 East 47th Street, New York, N. Y. 10017, and will be accepted until September 1, 1981. Readers who need more time to prepare a Discussion should request an extension from the Editorial Department. Manuscript received by ASME Applied Mechanics Division, March 1980; final revision, September, 1980.

2 Analytical Studies

Formulation. The model of the system under consideration is shown in Fig. 1. It consists of a viscously damped continuous Bernoulli-Euler beam of mass $M(x)$ and stiffness $EI(x)$ which is separated by a gap d from an elastic stop located at a distance h from the beam support point. The elastic stop has a stiffness K_t. Although Fig. 1 shows a cantilever beam, the method of solution is applicable to beams with arbitrary boundary conditions.

The motion of the system in Fig. 1 is governed by the partial differential equation

$$L^*[W(x,t)] + \frac{\partial}{\partial t} C[W(x,t)] + M(x) \frac{\partial^2 W(x,t)}{\partial t^2} = F(x,t) \quad (1)$$

over the length L of the beam, where

L^* = a linear, homogeneous, self-adjoint differential operator of order $2p$ with respect to spatial coordinate x that specifies the stiffness distribution of the beam.

C = an operator that is a linear combination of operator L^* and function M, viz.,

$$C = \alpha M + \beta L^* \quad (2)$$

M = a function that specifies the mass distribution of the beam.

$F(x, t)$ is a harmonically varying load equal to

$$F(x) \cos \omega t \quad (3)$$

with

$$F(x) = \Omega^2 S_0 M(x) \quad (4)$$

for base excitation.

Steady-State Solution. Experimental studies of the system under consideration indicate that the predominant type of response under harmonic excitation is that in which the beam contacts the elastic stop, and the conditions of the system are repeated, once per cycle,

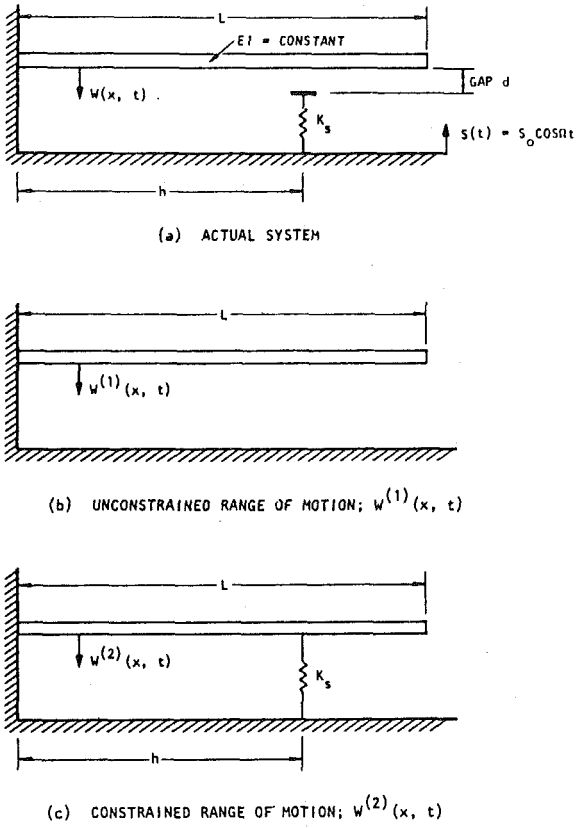

Fig. 1 Regimes of motion of elastic beam with geometric nonlinearity: (*a*) Actual system; (*b*) Unconstrained range of motion; $W^{(1)}(x,t)$; (*c*) Constrained range of motion; $W^{(2)}(x,t)$

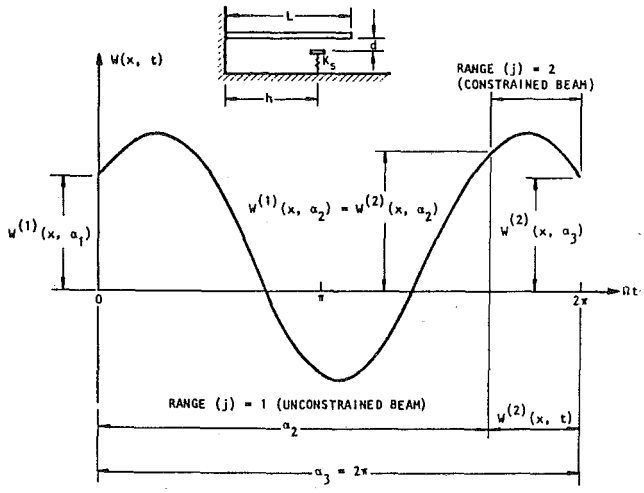

Fig. 2 Ranges of motion of the steady-state solution

of the excitation. A typical segment of the time-history of such steady-state motion during one period of the excitation is illustrated in Fig. 2.

The steady-state solution of the system shown in Fig. 1(*a*) consists of two segments corresponding to $W^{(1)}(h, t) \leq d$, i.e., when there is no contact between the beam and the elastic stop (the spring), and $W^{(2)}(h, t) \geq d$, i.e., the solution region in which the beam and the elastic stop are in contact (see Figs. 1(*b*, *c*)). The solution should satisfy certain conditions of continuity of the displacement and velocity of the system at times of release and contact for one cycle. These conditions may be stated as follows:

(*a*) Everywhere along the beam, the displacement $W^{(1)}(x, \alpha_2)$ and velocity $\dot{W}^{(1)}(x, \alpha_2)$ at the end of the first region of solution (the no-contact solution region) should be equal to the corresponding displacement and velocity, respectively, at the beginning of the second solution region.

(*b*) Everywhere along the beam, the displacement $W^{(1)}(x, \alpha_1)$ and velocity $\dot{W}^{(1)}(x, \alpha_1)$ at the beginning of the first solution region should equal the displacement $W^{(2)}(x, \alpha_3)$ and velocity $\dot{W}^{(2)}(x, \alpha_3)$, respectively, at the end of the second solution region (contact region).

(*c*) At the point of contact between the beam and the elastic stop, the displacements $W^{(1)}(h, \alpha_1)$, $W^{(1)}(h, \alpha_2)$, $W^{(2)}(h, \alpha_2)$, and $W^{(2)}(h, \alpha_3)$ at the beginning and the end of both solution regions should be equal to the gap d.

Thus the steady-state solution must satisfy the following conditions:

$$W^{(1)}(x, \alpha_2) = W^{(2)}(x, \alpha_2) \equiv W_2(x) \tag{5}$$

$$\dot{W}^{(1)}(x, \alpha_2) = \dot{W}^{(2)}(x, \alpha_2) \equiv \dot{W}_2(x) \tag{6}$$

$$W^{(2)}(x, \alpha_3) = W^{(1)}(x, \alpha_1) \equiv W_1(x) \tag{7}$$

$$\dot{W}^{(2)}(x, \alpha_3) = \dot{W}^{(1)}(x, \alpha_1) \equiv \dot{W}_1(x) \tag{8}$$

$$W^{(2)}(x, \alpha_3)\,|_{x=h} = W^{(1)}(x, \alpha_1)\,|_{x=h} = W_1(h) = d \tag{9}$$

$$W^{(1)}(x, \alpha_2)\,|_{x=h} = W^{(2)}(x, \alpha_2)\,|_{x=h} = W_2(h) = d \tag{10}$$

Solution Procedure. Referring to Fig. 2, let $\phi_i^{(j)}(x)$ be the ith eigenfunction associated with the homogeneous equation of the undamped system for the jth solution region and assume that the eigenfunctions satisfy the orthogonality condition

$$\int_0^L \phi_i^{(j)}(x) M(x) \phi_s^{(j)}(x) dx = \delta_{is} M_i^{(j)} \tag{11}$$

and

$$\int_0^L \phi_i^{(j)}(x) L^*[\phi_s^{(j)}(x)] dx = \delta_{is} K_i^{(j)} \tag{12}$$

where δ_{is} is the Kronecker delta, and $M_i^{(j)}$ and $K_i^{(j)}$ are, respectively, the generalized mass and generalized stiffness of the ith mode for solution region j.

Using the normal-mode approach, the solution for region j can be written as

$$W^{(j)}(x, t) = \sum_{i=1}^{\infty} \phi_i^{(j)}(x) q_i^{(j)}(t) \tag{13}$$

where $j = 1$ or 2, depending on the solution region.

Then, substituting for $W^{(j)}(x, t)$ into equation (1) leads to

$$M_i^{(j)} \ddot{q}_i^{(j)}(t) + C_i^{(j)} \dot{q}_i^{(j)}(t) + K_i^{(j)} q_i^{(j)}(t) = Q_i^{(j)}(t) = \left[\int_0^L \phi_i^{(j)}(x) f_i^{(j)}(x) dx \right] \cos(\Omega t + \alpha_0) \tag{14}$$

where α is a phase angle related to the origin t_0 by $\alpha_0 = \Omega t_0$.

The solution of equation (14) is

$$\begin{aligned} q_i^{(j)}(t) = {} & \exp\left[-\frac{\zeta_i^{(j)}}{r_i^{(j)}} (\Omega t - \alpha_j) \right] \\ & \times \left\{ q_i^{(j)}(\alpha_j) \left\{ \frac{1}{\eta_i^{(j)}} \left[\zeta_i^{(j)} \sin \frac{\eta_i^{(j)}}{r_i^{(j)}} (\Omega t - \alpha_j) + \eta_i^{(j)} \cos \frac{\eta_i^{(j)}}{r_i^{(j)}} (\Omega t - \alpha_j) \right] \right\} + \dot{q}_i^{(j)}(\alpha_j) \right\} \\ & \times \left\{ \frac{1}{\omega_i^{(j)} \eta_i^{(j)}} \sin \frac{\eta_i^{(j)}}{r_i^{(j)}} (\Omega t - \alpha_j) \right\} \\ & + \sin \theta_i^{(j)} \left\{ \frac{A_i^{(j)}}{\eta_i^{(j)}} r_i^{(j)} \sin \frac{\eta_i^{(j)}}{r_i^{(j)}} (\Omega t - \alpha_j) \right\} \end{aligned} \tag{15}$$

$$+ \cos\theta_i^{(j)} \left\{ -\frac{A_i^{(j)}}{\eta_i^{(j)}} \left[\zeta_i^{(j)} \sin\frac{\eta_i^{(j)}}{r_i^{(j)}}(\Omega t - \alpha_j) + \eta_i^{(j)} \cos\frac{\eta_i^{(j)}}{r_i^{(j)}}(\Omega t - \alpha_j) \right] \right\} + A_i^{(j)} \cos(\Omega t + \tau_i^{(j)}) \quad (15)\ (Cont.)$$

where

$$\omega_i^{(j)} = \sqrt{K_i^{(j)}/M_i^{(j)}}, \quad \zeta_i^{(j)} = C_i^{(j)}/2\sqrt{K_i^{(j)}M_i^{(j)}}$$

$$\eta_i^{(j)} = \sqrt{1 - [\zeta_i^{(j)}]^2}, \quad r_i^{(j)} = \Omega/\omega_i^{(j)}$$

$$A_i^{(j)} = (f_i^{(j)}K_i^{(j)})/\sqrt{(1 - [r_i^{(j)}]^2)^2 + (2\zeta_i^{(j)}r_i^{(j)})^2}$$

$$f_i^{(j)} = \int_0^L \phi_i^{(j)}(x) f^{(j)}(x)\,dx$$

$$\tau_i^{(j)} = \alpha_0 - \gamma_i^{(j)},$$

$$\gamma_i^{(j)} = \tan^{-1}\{2\zeta_i^{(j)}r_i^{(j)}/(1 - [r_i^{(j)}]^2)\}$$

subject to the conditions $\alpha_j \le \Omega t \le \alpha_{j+1}$ where $\alpha_1 = 0$, $\theta_i^{(j)} = \tau_i^{(j)} + \alpha_j$ and $\alpha_j = \Omega t_j$, $\alpha_2 \equiv$ unknown to be determined, $\alpha_3 = 2\pi$.

The velocity of the system is given by

$$\begin{aligned}\dot{q}_i^{(j)}(t) = \exp\left[-\frac{\zeta_i^{(j)}}{r_i^{(j)}}(\Omega t - \alpha_j)\right] &\times \left\{ q_i^{(j)}(\alpha_j) \left\{ -\frac{\omega_i^{(j)}}{\eta_i^{(j)}} \sin\frac{\eta_i^{(j)}}{r_i^{(j)}}(\Omega t - \alpha_j) \right\} \right. \\ &+ \dot{q}_i^{(j)}(\alpha_j) \left\{ -\frac{1}{\eta_i^{(j)}} \left[\zeta_i^{(j)} \sin\frac{\eta_i^{(j)}}{r_i^{(j)}}(\Omega t - \alpha_j) \right.\right. \\ &\left.\left. - \eta_i^{(j)} \cos\frac{\eta_i^{(j)}}{r_i^{(j)}}(\Omega t - \alpha_j) \right] \right\} \\ &+ \sin\theta_i^{(j)} \left\{ -\frac{\omega_i^{(j)} r_i^{(j)} A_i^{(j)}}{\eta_i^{(j)}} \left[\zeta_i^{(j)} \sin\frac{\eta_i^{(j)}}{r_i^{(j)}} \right.\right. \\ &\times (\Omega t - \alpha_j) - \eta_i^{(j)} \cos\frac{\eta_i^{(j)}}{r_i^{(j)}}(\Omega t - \alpha_j) \left.\left.\right] \right\} \\ &+ \cos\theta_i^{(j)} \left\{ \frac{\omega_i^{(j)} A_i^{(j)}}{\eta_i^{(j)}} \sin\frac{\eta_i^{(j)}}{r_i^{(j)}}(\Omega t - \alpha_j) \right\} \Bigg\rangle \\ &- \Omega A_i^{(j)} \sin(\Omega t + \tau_i^{(j)}) \quad (16)\end{aligned}$$

subject to the condition

$$\alpha_j \le \Omega t \le \alpha_{j+1}.$$

Evaluating equations (15) and (16) at $\Omega t = \alpha_{j+1}$ yields

$$q_i^{(j)}(\alpha_{j+1}) = S1_i^{(j)} q_i^{(j)}(\alpha_j) + S2_i^{(j)} \dot{q}_i^{(j)}(\alpha_j) + S5_i^{(j)} \sin\theta_i^{(j)} + S6_i^{(j)} \cos\theta_i^{(j)} + S7_i^{(j)} \cos(\alpha_{j+1} + \tau_i^{(j)}) \quad (17)$$

and

$$\dot{q}_i^{(j)}(\alpha_{j+1}) = S3_i^{(j)} q_i^{(j)}(\alpha_j) + S4_i^{(j)} \dot{q}_i^{(j)}(\alpha_j) + S8_i^{(j)} \sin\theta_i^{(j)} + S9_i^{(j)} \cos\theta_i^{(j)} + S10_i^{(j)} \sin(\alpha_{j+1} + \tau_i^{(j)}) \quad (18)$$

where all the undefined symbols are related to the parameters in equation (15).

The solution for $j = 1$ is subject to the condition

$$\alpha_1 \le \Omega t \le \alpha_2 \quad (19)$$

and the solution for $j = 2$ is subject to the condition

$$\alpha_2 \le \Omega t \le \alpha_3. \quad (20)$$

Initially, the unknowns of the motion are $W_1(x)$, $W_2(x)$, $\dot{W}_1(x)$, $\dot{W}_2(x)$, α_0, and α_2. With some effort (see Appendix), the use of the orthogonality conditions in equations (11) and (12), together with the steady-state conditions as expressed by equations (5)–(10) and with equations (17) and (18), will eventually lead to a set of two coupled nonlinear algebraic equations of the form

$$g_1(\alpha_0, \alpha_2) = 0 \quad (21a)$$

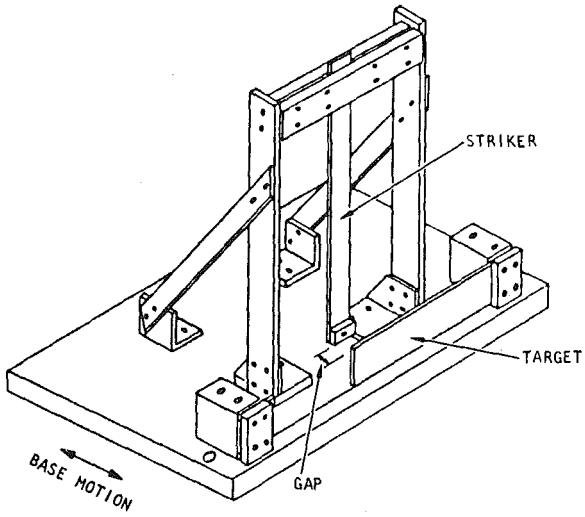

Fig. 3 Model configuration

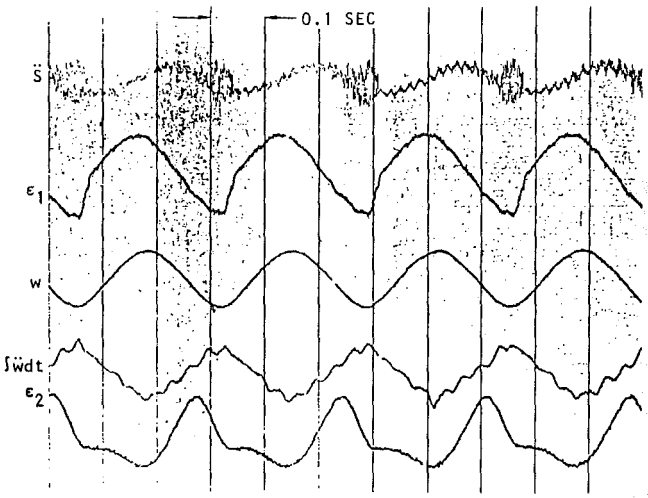

Fig. 4 Steady-state excitation and forced nonlinear response of beam/target system; $\Omega/2\pi = 30.4$ Hz

$$g_2(\alpha_0, \alpha_2) = 0 \quad (21b)$$

that involve only the two unknowns α_0 and α_2.

Once the system properties are specified, equations (21) can be solved by conventional numerical techniques to yield the values of α_0 and α_2. The rest of the unknowns of the motion can then be found by back substitution.

3 Experimental Studies

The model shown in Fig. 3 was used to investigate the range of validity of the analytical results, and to evaluate the effects of system parameters. The striker and target beams were made from sheets of mild steel. In addition to a number of strain gages that were mounted on the beams, several vibration pickups were attached to the test fixtures and the vibration exciter (which furnished base motion) to monitor the system response.

Vibration Test Procedure. In a typical test, the gap clearance d was set to a specific value, the shaker base amplitude level S_0 was selected, and the shaker frequency was set to a given frequency value Ω. The excitation and the system response were then measured and recorded. Measurements were made of the following quantities:

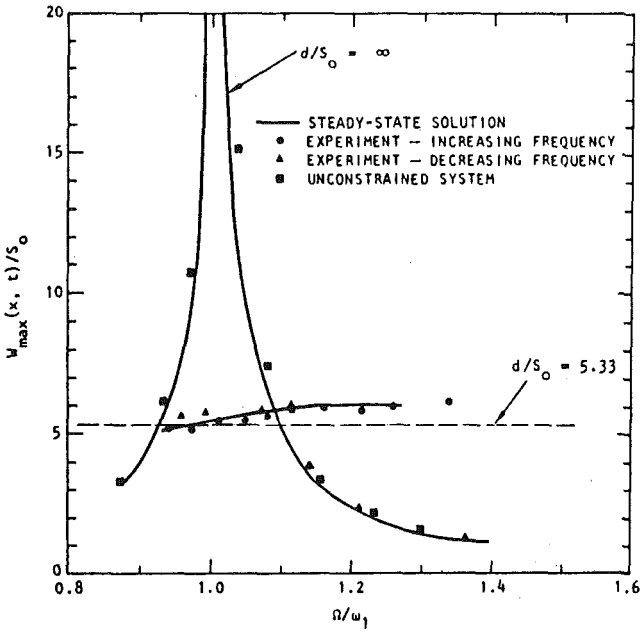

Fig. 5 Comparison between theory and experiment of the response of a continuous system with a gap: $K^* = 25$, $\zeta_0 \approx 0.02$, clearance ratio $d/S_0 = 3.33$

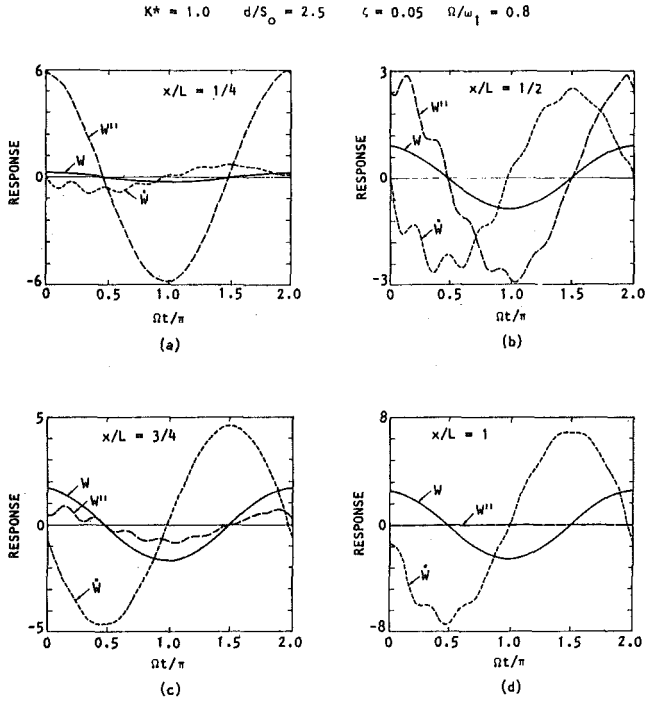

Fig. 6 Construction of a typical solution

$\ddot{S}(t)$ = sinusoidal base acceleration = $-\Omega^2 S_0 \sin \Omega t$.
$W(x, t)$ = displacement at chosen stations along the beam.
$\dot{W}(x, t)$ = velocity at chosen stations along the beam.
$\epsilon_1(x, t)$ = striker beam strain at the chosen stations.
$\epsilon_2(x, t)$ = target beam strain at a station chosen along the target beam.

The excitation frequency Ω was then increased to some value Ω_1 and the same response parameters were measured and recorded again. Due to the nonlinearity of the system parameters, the response was determined for both increasing and decreasing excitation frequency values that spanned a range of ±50 percent with respect to ω_1, the fundamental frequency of the striker beam.

Sample time histories of representative response quantities are shown in Fig. 4. The striker beam displacement was measured with an optical displacement follower, and the corresponding velocity was found by integrating the beam acceleration.

Reduced Vibration Data. The data discussed in the section, "Vibration Test Procedure," were reduced to a more meaningful form by introducing the following dimensionless ratios:

Ω/ω_1 = excitation frequency ratio = exciting frequency/natural frequency of striker beam.
d/S_0 = clearance ratio = size of gap between striker and target beam/amplitude of a sinusoidal base motion.
K_t/K_s = stiffness ratio = target beam stiffness/striker beam stiffness = K^*.
W_{max}/S_0 = amplification ratio = peak S-S amplitude of striker beam/amplitude of sinusoidal base motion.
ζ = ratio of critical damping corresponding to the first mode

Typical frequency response results are shown in Fig. 5.

4 Applications

Cantilever Beam With a Stop. In order to apply the present theory to a specific beam/stopper system, the striker beam mode shapes in both ranges of the motion must be determined. Consider, for example, a cantilever beam with an elastic stop at its free end (i.e., $h/L = 1$ in Fig. 1). The modal frequencies and shapes of the beam in the unconstrained range of the motion (range 1 in Fig. 2) are readily available in standard vibration books. In the range of motion where the beam and stopper are connected, the natural frequencies and mode shapes can be found by using a procedure similar to that in [11, 12].

The damping parameters α and β can be related to the frequencies and ratios of critical damping of two modes m and n by [13]

$$\alpha = (2\zeta_m - \beta\omega_m)\omega_m \tag{22}$$

and

$$\beta = 2(\zeta_n\omega_n - \zeta_m\omega_m)(\omega_n{}^2 - \omega_m{}^2). \tag{23}$$

In the present study, the values of α and β were determined from equations (22) and (23) so as to make ζ_1 and ζ_2 the damping ratios of the first two modes of vibration of the unconstrained region of solution, equal to $\zeta_0 \cong$ constant. The damping ratio $\zeta_i{}^{(j)}$ for each mode of both solution regions is then determined by the following equation:

$$\zeta_i{}^{(j)} = 0.5\left[\frac{\alpha}{\omega_i{}^{(j)}} + \beta\omega_i{}^{(j)}\right] \tag{24}$$

Steady-State Response. Typical time histories of the steady-state solutions for an arbitrary set of parameters are illustrated in Fig. 6, where the displacement $W(x, t)$, the velocity $\dot{W}(x, t)$, and the curvature $W''(x, t)$ at different stations along the striker beam length are shown for one period of the excitation. For this case the dimensionless stiffness ratio is $K^* = 1$, the dimensionless gap size is $d/S_0 \approx 2.5$, the ratio of critical damping in the first two modes is $\zeta_0 = 0.05$, and the harmonic excitation has a frequency of 0.8 of the fundamental frequency of the striker beam. Five modes were used in the calculations.

The contribution of the higher modes to the response is clear in all the time histories shown in Fig. 6, as was the case in the experimental results shown in Fig. 4. Note also that the qualitative behavior of the beam response agrees with reality:

1 The stress (curvature) is zero at the free end and increases as x/L approaches zero, the beam's fixed boundary.

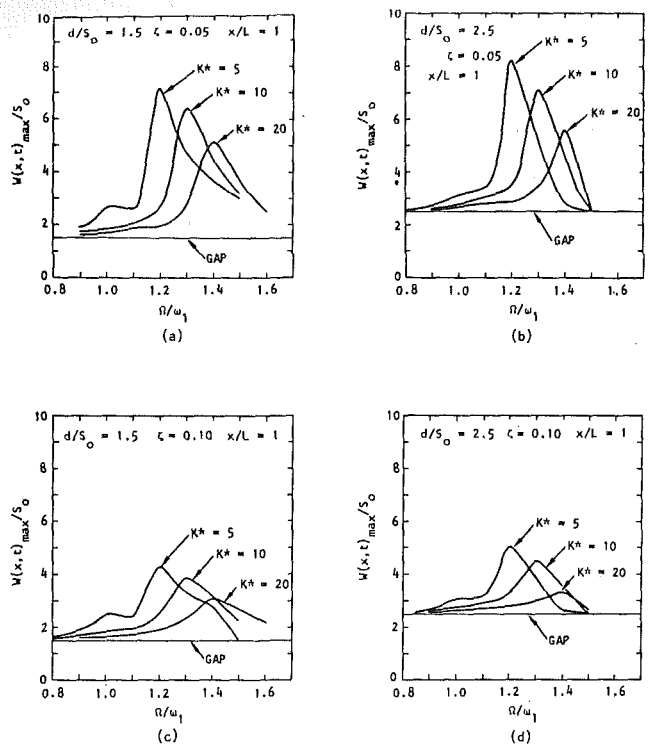

Fig. 7 Maximum positive peak response for $\zeta = 0.05, 0.10$; clearance ratio $d/S_0 = 1.5, 2.5$; $K^* = 5, 10, 20$

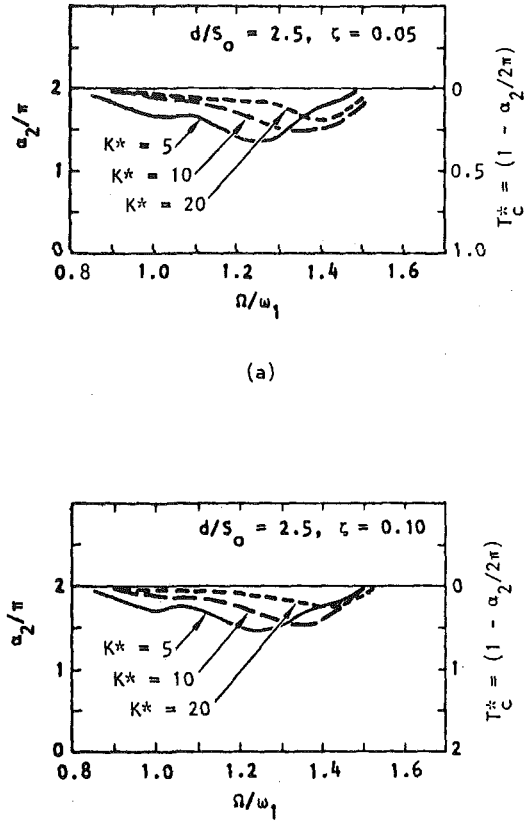

Fig. 8 Variation of dimensionless contact time with frequency ratio; $d/S_0 = 2.5$; $K^* = 5, 10, 20$; $\zeta = 0.5, 0.10$

2 The ratios of the peak response at different locations along the beam approximately correspond to the same ratios associated with the first modes.

3 The major contribution from the higher harmonics (more significant in the case of velocity and stress) is due to the second beam mode which for the present example is $\omega_2/\omega_1 \approx 6/1$.

Additional qualitative features of interest in the results shown in Fig. 6 are that

1 The beam conditions at $\Omega t \approx 0$ match those at the end of a period $\Omega t = 2\pi$, as required by the steady-state solution.

2 The transients induced by the contact with the elastic stop start to decay at $\Omega t = 0$ upon the separation of the beam and its target, thus attenuating (at an exponential rate determined by ζ_0) the contribution of the higher harmonics to a negligible amount within a period of $\approx 0.75\ T_1$.

3 The sharpest velocity change occurs at the contact point.

4 The amount of penetration $(W(L, t) - d)$ during contact at $x/L = 1$, as well as the duration of contact, is relatively small.

If the striker and target beams are of comparable stiffness (i.e., $K^* = 1$), a more reasonable analytical model would treat both striker and target as beams.

In a comparison of theoretical and experimental results shown in Fig. 5, note the qualitative difference in the response of the system with increasing and decreasing excitation frequency. Keeping in mind that the beam/target system is essentially a nonlinear system with hardening restoring force characteristics, one would expect such a system to exhibit "jump" phenomena associated with the "backbone curve" related to the frequency response of the nonlinear Duffing oscillator [14]. Moreover, it is known that the amplitude-frequency relationship of the Duffing oscillator will result in a backbone curve that tends to "rotate" clockwise as the nonlinearity of a hardening system is increased, thus shifting the jump point associated with increasing excitation frequency to a higher frequency value. These observations apply, in a qualitative sense, to the amplitude-frequency curve of the beam/target system.

It is seen from Fig. 5 that the peak beam/target response occurs at a frequency ratio significantly higher than unity; this again is consistent with the behavior of the hardening Duffing oscillator, whose peak response is known to decrease in amplitude but occur at an ever-increasing frequency value as the magnitude of the nonlinearity increases [14].

In Fig. 7 the effects of the dimensionless target stiffness ratio K^*, dimensionless gap size d/S_0, and beam damping ratio ζ on the peak response of the free end of the example cantilever beam are shown over a relatively wide excitation frequency band. The maximum response peaks are markedly affected by the target stiffness and inherent striker beam damping, but less by the gap size. The reduction of the maximum peaks with increasing target stiffness and the shift in frequency where the peaks occur with increasing K^* are indeed consistent with the behavior expected of such systems for the reasons just discussed.

Since the system under discussion has an unsymmetric nonlinearity (a one-sided stop), one would not expect the beam motion to be symmetric with respect to its equilibrium position. Nonetheless, for the range of parameters under discussion, the positive peak response very nearly equals the corresponding negative one at all locations along the beam. Of course, the main reason for this behavior is that since the beam displacement is periodically constrained to a certain amplitude every system period, the "initial conditions" at the end of the contact period cannot propagate in time (under periodic excitation, a lightly damped dynamic system will require a time $t/T_1 \gg 1$ to reach steady-state values).

Fig. 7 also demonstrates that as K^* and the damping ratio increase, the ability of the elastic stop to reduce peak response decreases; for example, a fourfold increase of K^* from 5 to 20 changes the peak response in Fig. 7(*a*) by the ratio $\approx 7/5$, or 1.4. Thus, in practical engi-

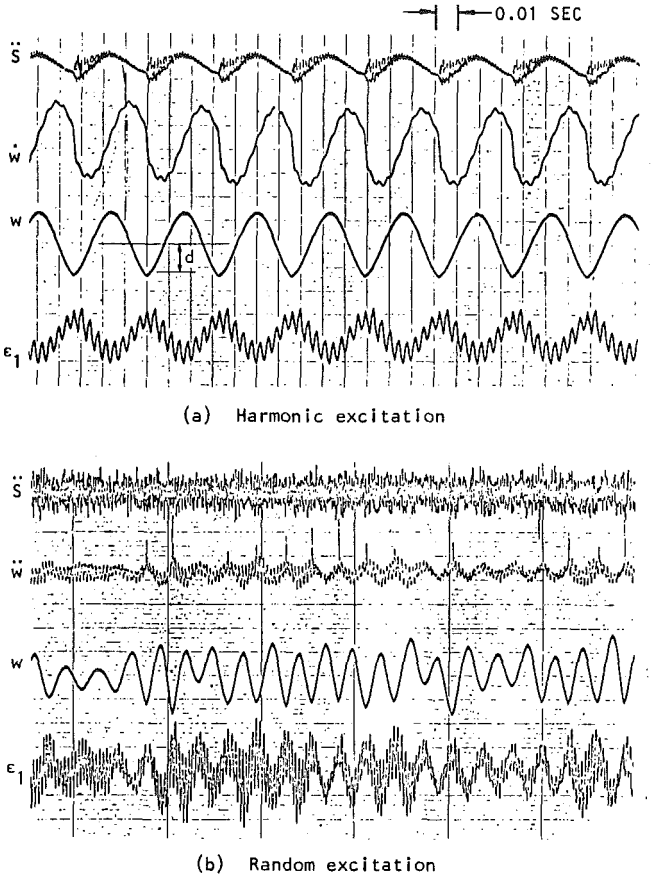

Fig. 9 Response of beam model; (*a*) Harmonic excitation; (*b*) Random excitation

neering applications, little additional control of the beam response can be gained by stiffening the stop beyond a certain level.

Note that if the gap becomes progressively smaller while all other parameters remain constant, the amount of penetration ($W_{max} - d$) increases. Penetration also increases if damping is decreased and excitation levels are increased while gap size remains constant.

The variation of the dimensionless contact time T_c^* with excitation frequency ratio is shown in Fig. 8. Keeping in mind that α_2 is a measure of the fraction of the excitation period during which the beam is not in contact with the stop, then $T_c^* \equiv 1 - \alpha_2/(2\pi)$ is the fraction of the excitation period during which contact does occur. The curves in Fig. 8 indicate that T_c^* varies from 0 for $0.9 \gtrsim \Omega/\omega_1 \gtrsim 1.5$ to about 0.25 (a quarter of an excitation period) at frequency values corresponding to the peaks of W_{max} as shown in Fig. 7. Comparison of the results shown in Figs. 7 and 8, makes clear that the amount of penetration and duration of contact have similar (nonlinear) dependence on the other system characteristics.

Referring back to the jump phenomenon shown in Fig. 5, it was found that the width of the frequency band over which unstable behavior occurs is dependent on a number of factors such as gap size, stiffness ratio, amount of inherent damping, rate of change of the exciting frequency, etc. This fact has important ramifications for the behavior of the beam/target system under arbitrary transient excitation, particularly stochastic excitations. Fig. 9 shows the nonlinear dynamic response of the beam/target system under stationary random excitation. In addition to the richness of the various response quantities with higher-mode contributions, it is interesting to note that beam/target impacts persist for a long time even after the excitation level that induced the onset of such impacts has dropped to much lower levels. If the same excitation levels were applied to the linear system (i.e., without the target), it would not generate a relative beam motion that exceeds the available gap.

The relatively simple example studied has some of the basic features of nuclear power plant piping systems with snubbers. Based on the analytical and experimental results shown here, it is clear that caution should be exercised in analyzing nonlinear systems of the type previously discussed. This is particularly true where repetitive impact-induced stresses are a concern, such as in cases where low-cycle fatigue is significant.

Regarding the "exact" solution in this paper, it is worth noting that in nonlinear systems periodic forcing inputs do not always lead to periodic solutions. One case in point is the class of strange attractor solutions [15–17] that have been found recently in both theoretical and experimental studies in which nonperiodic, bounded, chaotic motions can occur under periodic excitation. Ueda [15], for example, has found such solutions for a single equilibrium point system with strong nonlinearity.

5 Summary and Conclusions

An "exact" closed-form analytical solution for the steady-state motion of a viscously damped Bernoulli-Euler beam with an unsymmetric geometric nonlinearity was derived using a modified normal mode approach. The elastic beam was assumed to have uniform properties and arbitrary boundary conditions, and was subjected to a harmonic excitation. The geometric nonlinearity consisted of an elastic spring placed at some arbitrary location within the span of the beam and separated from the beam by a certain gap.

Experimental studies with a mechanical model were performed to verify the validity of the analytical solution and also to investigate the effect of system parameters under both harmonic and random excitation. A fairly good agreement between the theoretical and experimental results was achieved.

The effects of various dimensionless system parameters (such as excitation frequency, damping, target stiffness ratio, and gap size) on the system displacement, velocity, and stress at various locations along the beam were investigated and found to be significant.

Acknowledgment

This study was supported in part by a contract from the U.S. Nuclear Regulatory Commission. The assistance of D. Oba in the preparation of the manuscript is appreciated.

References

1 Den Hartog, J. P., and Heiles, R. M., "Forced Vibrations With Nonlinear Spring Constants," ASME JOURNAL OF APPLIED MECHANICS, Vol. 3, 1936, pp. 127–130.

2 Lee, W. F. Z., and Saibel, E., "Free Vibrations of Constrained Beams," ASME JOURNAL OF APPLIED MECHANICS, Vol. 19, 1952.

3 Iwan, W. D., "Steady-State Dynamic Response of a Limited Slip System," ASME JOURNAL OF APPLIED MECHANICS, Vol. 35, 1968, pp. 322–326.

4 Watanabe, T., "Forced Vibration of Continuous Systems With Nonlinear Boundary Conditions," ASME *Journal of Mechanical Design*, Vol. 100, No. 3, July 1978, pp. 487–491.

5 Moreadith, F. L., et al., "Structural Analysis and Design of Pipe Whip Restraints," *Structural Design of Nuclear Power Plants*, Vol. 2, ASCE, Dec. 1973.

6 Anderson, J. C., and Singh, A. K., "Inelastic Response of Nuclear Piping Subjected to Rupture Forces," ASME *Journal of Pressure Vessel Technology*, Vol. 98, No. 2, May 1976.

7 Kotwicki, P. J., Chang, K. C., and Johnson, E. R., "Effects of Restraint Stiffness and Gap on the Dynamic Response of Piping Systems," Third U.S. National Congress on Pressure Vessels and Piping, ASME, San Francisco, June 25–29, 1979.

8 Onesto, A. T., "A Snubber Response Sensitivity Study," Third U.S. National Congress on Pressure Vessels and Piping, ASME, San Francisco, June 25–29, 1979.

9 Graham, D., and McRuer, D., *Analysis of Nonlinear Control Systems*, Wiley, New York, 1961.

10 Tseng, W. Y., and Dugungi, J., "Nonlinear Vibrations of a Buckled Beam Under Harmonic Excitation," ASME JOURNAL OF APPLIED MECHANICS, Vol. 38, June 1971, pp. 467–476.

11 Young, D., "Vibration of a Beam With Concentrated Mass, Spring, and Dashpot," ASME JOURNAL OF APPLIED MECHANICS, Vol. 70, Mar. 1948, pp. 65–72.

12 Gorman, D. J., *Free Vibration Analysis of Beams and Shafts*, Wiley, New York, 1975.

13 Rosenblueth, E., and Newmark, N., *Fundamentals of Earthquake Engineering*, Prentice-Hall, Englewood Cliffs, N.J., 1971.

14 Caughey, T. K., "The Existence and Stability of Ultraharmonics and Subharmonics in Forced Nonlinear Oscillations," ASME JOURNAL OF APPLIED MECHANICS, Vol. 21, Dec. 1954, pp. 327–335.
15 Ueda, Y., "Randomly Transitional Phenomena in the System Governed by Duffing's Equation," *Journal of Statistical Physics*, Vol. 20, No. 2, 1979, pp. 181–196.
16 Holmes, P. J., "A Nonlinear Oscillator With a Strange Attractor," *Philosophical Transactions of the Royal Society*, London, Vol. 292, No. 1394, Oct. 1979, pp. 419–448.
17 Moon, F. C., and Holmes, P. J., "A Magnetoelastic Strange Attractor," *Journal of Sound and Vibration*, Vol. 65(2), 1979, pp. 275–296.

APPENDIX

Derivation of Equations (21)

Multiplying both sides of equations (17) and (18) by $\phi_i^{(j)}(x)$ and summing over i with $j = 1, 2$ yields the following:

$$\sum_i \phi_i^{(1)}(x)\{S1_i^{(1)}q_{i1} + S2_i^{(1)}\dot{q}_{i1} + S5_i^{(1)}\sin\theta_i^{(1)} + S6_i^{(1)}\cos\theta_i^{(1)} + S7_i^{(1)}\cos(\alpha_2+\tau_i^{(1)})\} = W_2(x) = \sum_i \phi_i^{(2)}(x)q_{i2} \quad (25)$$

$$\sum_i \phi_i^{(1)}(x)\{S3_i^{(1)}q_{i1} + S4_i^{(1)}\dot{q}_{i1} + S8_i^{(1)}\sin\theta_i^{(1)} + S9_i^{(1)}\cos\theta_i^{(1)} + S10_i^{(1)}\sin(\alpha_2+\tau_i^{(1)})\} = \dot{W}_2(x) = \sum_i \phi_i^{(2)}(x)\dot{q}_{i2} \quad (26)$$

$$\sum_i \phi_i^{(2)}(x)\{S1_i^{(2)}q_{i2} + S2_i^{(2)}\dot{q}_{i2} + S5_i^{(2)}\sin\theta_i^{(2)} + S6_i^{(2)}\cos\theta_i^{(2)} + S7_i^{(2)}\cos(\alpha_3+\tau_i^{(2)})\} = W_1(x) = \sum_i \phi_i^{(1)}(x)q_{i1} \quad (27)$$

$$\sum_i \phi_i^{(2)}(x)\{S3_i^{(2)}q_{i2} + S4_i^{(2)}\dot{q}_{i2} + S8_i^{(2)}\sin\theta_i^{(2)} + S9_i^{(2)}\cos\theta_i^{(2)} + S10_i^{(2)}\sin(\alpha_3+\tau_i^{(2)})\} = \dot{W}_1(x) = \sum_i \phi_i^{(1)}(x)\dot{q}_{i1} \quad (28)$$

where

$$q_{i1} = q_i^{(1)}(\alpha_1) \quad (29)$$

$$q_{i2} = q_i^{(2)}(\alpha_2) \quad (30)$$

$$\dot{q}_{i1} = \dot{q}_i^{(1)}(\alpha_1) \quad (31)$$

$$\dot{q}_{i2} = \dot{q}_i^{(2)}(\alpha_2) \quad (32)$$

Using equations (13), (17), and (18), together with equations (9) and (10), yields

$$\sum_i \phi_i^{(2)}(h)q_i^{(2)}(\alpha_3) = \sum_i \phi_i^{(2)}(h)\{S1_i^{(2)}q_{i2} + S2_i^{(2)}\dot{q}_{i2} + S5_i^{(2)}\sin\theta_i^{(2)} + S6_i^{(2)}\cos\theta_i^{(2)} + S7_i^{(2)}\cos(\alpha_3+\tau_i^{(2)})\} = d \quad (33)$$

$$\sum_i \phi_i^{(1)}(h)q_i^{(1)}(\alpha_2) = \sum_i \phi_i^{(1)}(h)\{S1_i^{(1)}q_{i1} + S2_i^{(1)}\dot{q}_{i1} + S5_i^{(1)}\sin\theta_i^{(1)} + S6_i^{(1)}\cos\theta_i^{(1)} + S7_i^{(1)}\cos(\alpha_2+\tau_i^{(1)})\} = d \quad (34)$$

Using equation (26), together with the orthogonality condition of equations (11) and (12), yields

$$\dot{q}_{l2} = \frac{1}{M_l^{(2)}}\sum_m [C1_{lm}q_{m1} + C2_{lm}\dot{q}_{m1} + C3_{lm}\sin\theta_m^{(1)} + C4_{lm}\cos\theta_m^{(1)} + C5_{lm}\sin(\alpha_2+\tau_m^{(1)})] \quad (35)$$

Similarly, equation (25) yields

$$q_{l2}' = \frac{1}{M_l^{(2)}}\sum_i [C6_{li}q_{i1} + C7_{li}\dot{q}_{i1} + C8_{li}\sin\theta_i^{(1)} + C9_{li}\cos\theta_i^{(1)} + C10_{li}\cos(\alpha_2+\tau_i^{(1)})] \quad (36)$$

Substituting for $\dot{q}_{l2}$ and q_{l2} from equations (35) and (36) into equations (27)–(32) yields

$$\sum_j [h1_jq_{j1} + h2_j\dot{q}_{j1} + h3_j\sin\theta_j^{(1)} + h4_j\cos\theta_j^{(1)} + h5_j\cos(\alpha_2+\tau_j^{(1)}) + h6_j\sin(\alpha_2+\tau_j^{(2)}) + h7_j\sin\theta_j^{(2)} + h8_j\cos\theta_j^{(2)} + h9_j\cos(\alpha_3+\tau_j^{(2)})] = \sum_i \phi_i^{(1)}(x)q_{i1} = W_1(x) \quad (37)$$

$$\sum_p [h10_pq_{p1} + h11_p\dot{q}_{p1} + h12_p\sin\theta_p^{(1)} + h13_p\cos\theta_p^{(1)} + h14_p\cos(\alpha_2+\tau_p^{(1)}) + h15_p\sin(\alpha_2+\tau_p^{(1)}) + h16_p\sin\theta_p^{(2)} + h17_p\cos\theta_p^{(2)} + h18_p\sin(\alpha_3+\tau_p^{(1)})] = \sum_p \phi_p^{(1)}(x)\dot{q}_{p1} = \dot{W}_1(x) \quad (38)$$

and

$$\sum_k [h19_kq_{k1} + h20_k\dot{q}_{k1} + h21_k\sin\theta_k^{(1)} + h22_k\cos\theta_k^{(1)} + h23_k\cos(\alpha_2+\tau_k^{(1)}) + h24_k\sin(\alpha_2+\tau_k^{(1)}) + h25_k\sin\theta_k^{(2)} + h26_k\cos\theta_k^{(2)} + h27_k\cos(\alpha_3+\tau_k^{(2)})] = d \quad (39)$$

Also, equation (33) can be written as

$$\sum_i [h28_iq_{i1} + h29_i\dot{q}_{i1} + h30_i\sin\theta_i^{(1)} + h31_i\cos\theta_i^{(1)} + h32_i\cos(\alpha_2+\tau_i^{(1)})] = d \quad (40)$$

From the definition of $\tau_i^{(j)}$ and $\theta_i^{(j)}$,

$$\theta_i^{(j)} = \alpha_0 + (\alpha_j - \gamma_i^{(j)}). \quad (41)$$

Making use of trigonometric identities to express sin and cos of $\theta_i^{(j)}$ in terms of α_0 and α_j, then equations (37)–(40) become

$$\sum_j [h1_jq_{j1} + h2_j\dot{q}_{j1} + h50_j\sin\alpha_0 + h51_p\cos\alpha_0] = \sum_j \phi_j^{(1)}(x)q_{j1} \quad (42)$$

$$\sum_p [h10_pq_{p1} + h11_p\dot{q}_{p1} + h52_p\sin\alpha_0 + h53_p\cos\alpha_0] = \sum_p \phi_p^{(1)}(x)q_{p1} \quad (43)$$

$$h19_kq_{k1} + h20_k\dot{q}_{k1} + h60_1\sin\alpha_0 + h61_k\cos\alpha_0 = d \quad (44)$$

$$h28_iq_{i1} + h29_i\dot{q}_{i1} + h62_i\sin\alpha_0 + h63_i\cos\alpha_0 = d \quad (45)$$

The orthogonality conditions of equations (11) and (12) can be further used with equations (42) and (43) to yield

$$q_{l1} = \sum_j [H1_{lj}q_{j1} + H2_{lj}\dot{q}_{j1} + H3_{lj}\sin\alpha_0 + H4_{lj}\cos\alpha_0] \quad (46)$$

$$q_{m1} = \sum_p [H5_{mp}\dot{q}_{p1} + H6_{mp}q_{p1} + H7_{mp}\sin\alpha_0 + H8_{mp}\cos\alpha_0] \quad (47)$$

Note that equations (44)–(47) provide four equations through which the unknowns q_{i1}, $\dot{q}_{i1}$, α_0, and α_2 can be determined.

The various undefined coefficients are omitted for the sake of brevity. In general, they are algebraic expressions involving the system parameters.

M. A. Haroun
Research Fellow and Lecturer

G. W. Housner
C. F. Braun Professor of Engineering

Department of Civil Engineering,
California Institute of Technology,
Pasadena, Calif. 91125

Earthquake Response of Deformable Liquid Storage Tanks

A method for analyzing the earthquake response of deformable, cylindrical liquid storage tanks is presented. The method is based on superposition of the free lateral vibrational modes obtained by a finite-element approach and a boundary solution technique. The accuracy of such modes has been confirmed by vibration tests of full-scale tanks. Special attention is given to the cos θ-type modes for which there is a single cosine wave of deflection in the circumferential direction. The response of deformable tanks to known ground motions is then compared with that of similar rigid tanks to assess the influence of wall flexibility on their seismic behavior. In addition, detailed numerical examples are presented to illustrate the variation of the seismic response of two different classes of tanks, namely, "tall" and "broad" tanks. Finally, the significance of the cos nθ-type modes in the earthquake response analysis of irregular tanks is briefly discussed.

Introduction

The only special feature of the earthquake-response problem, compared with any other form of dynamic loading, is that the excitation is applied in the form of support motions rather than by external loads; thus the essential subject of the present discussion is the method of defining for the tank wall the effective external load history resulting from a given form of support motion.

The hydrodynamic fluid pressure exerted on the wall of a deformable tank due to a ground motion $G(t)$ is given by the superposition of four pressure components:

- p_1 = the long period component contributed by the "convective" fluid motion (sloshing).
- p_2 = the "impulsive" fluid pressure component which varies in synchronism with the horizontal ground acceleration.
- p_3 = the short period component contributed by the $\cos\theta$-type vibrations of the tank walls.
- p_4 = the contributions of the $\cos n\theta$-type vibrations ($n \geq 2$) of the tank walls.

Each of these four pressures has a different variation with time.

It has been shown [1] that the coupling between liquid sloshing modes and shell vibrational modes is weak; and consequently, the convective dynamic pressure can be evaluated with reasonable accuracy by considering the tank wall to be rigid. It is the purpose of this paper to evaluate the hydrodynamic pressure components p_2 and p_3; to develop the effective earthquake load by employing the expression of the work done by external loads through arbitrary virtual displacements; and to obtain the time histories of shell displacements and stresses.

Coordinate System and Fundamental Assumptions

The liquid-shell system under consideration is shown in Fig. 1. It is a ground-supported, circular cylindrical, thin-walled liquid container of radius R, length L, and thickness h, with the wall connected to a rigid base. The tank is partly filled with liquid to a height H. If the tank wall is not connected to a rigid base, the strong earthquake response will be different.

A cylindrical coordinate system is used with the center of the base being the origin. The radial, circumferential, and axial coordinates are denoted r, θ, and z, respectively, and the corresponding displacement components of a point on the shell middle surface are denoted by w, v, and u, respectively. The tank is subjected to a ground motion $G(t)$ in the constant direction of $\theta = 0$.

Throughout this investigation, the liquid is assumed to be homogeneous, inviscid, and incompressible. In addition, the amplitudes of vibration are considered to be small. The strain-energy expression of the shell includes the effects of both stretching and bending. A detailed analysis of this problem is given in reference [1].

Free Lateral Vibrational Modes

The dynamic characteristics of the liquid-shell system are determined [2] by means of a discretization scheme in which the elastic shell is modeled by finite elements (refer to Fig. 2) and the liquid region is treated as a continuum by boundary solution techniques. In this approach the number of unknowns is substantially less than in those analyses where both tank wall and liquid are subdivided into finite elements.

Contributed by the Applied Mechanics Division for publication in the JOURNAL OF APPLIED MECHANICS. Was presented at the Century 2 Pressure Vessels and Piping Conference, San Francisco, Calif., August 12–15, 1980. Paper No. 80-C2/PVP-79.

Discussion on this paper should be addressed to the Editorial Department, ASME, United Engineering Center, 345 East 47th Street, New York, N.Y. 10017, and will be accepted until September 1, 1981. Readers who need more time to prepare a Discussion should request an extension from the Editorial Department. Manuscript received by ASME Applied Mechanics Division, September, 1980; final revision, January, 1981.

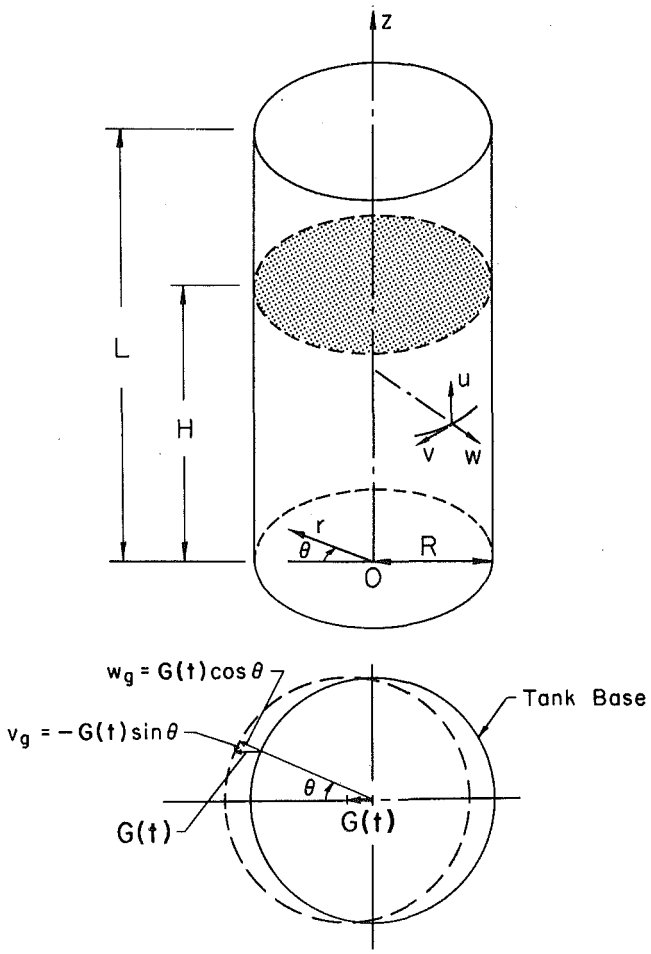

Fig. 1 Tank geometry, coordinate system, and earthquake excitation

The extremization of the appropriate variational functional leads, for each circumferential wave number n, to the following matrix equation of motion:

$$[M]\{\ddot{q}\} + [K]\{q\} = \{0\} \tag{1}$$

where $\{q\}$ is the nodal displacement vector of the shell, $[M] = [M_s] + [M_l]$; $[M_s]$ and $[M_l]$ being the consistent mass matrix of the shell and the added mass matrix of the liquid, respectively, and $[K] = [K_s] + [K_s^i]$; $[K_s]$ and $[K_s^i]$ are the shell stiffness matrix and the added stiffness matrix due to the initial hoop stress, respectively.

The resulting eigenvalue problem is solved by means of a digital computer. A comparison between the computed natural frequencies and mode shapes with those measured by vibration tests of full-scale tanks confirms the reliability of the theoretical analysis [3].

Tank Response to Earthquake Excitations

The matrix equation which governs the earthquake response of the liquid-shell system for a particular value of n can be written as

$$[M]\{\ddot{q}\} + [C]\{\dot{q}\} + [K]\{q\} = \{P_{\text{eff}}\} \tag{2}$$

where $[M]$ and $[K]$ are the mass and stiffness matrices defined in equation (1); $[C]$ is the damping matrix; and $\{P_{\text{eff}}\}$ is the effective earthquake load vector resulting from a given ground motion $G(t)$. For a perfect circular cylindrical shell, the effective earthquake load vector takes the form

$$\{P_{\text{eff}}\} = \begin{cases} -[F]\ddot{G}(t) & n = 1 \quad \text{(refer to equation (22))} \\ \{0\} & n \neq 1 \end{cases} \tag{3}$$

and consequently, the earthquake response can be obtained by superposition of the vertical modes corresponding to $n = 1$ only. Recently, shaking table experiments with aluminum tank models [4, 5] and vibration tests of full-scale tanks [3] showed that cos $n\theta$-type modes do respond to rigid base excitations; and this is attributed to noncircular imperfections of the cross section

Cos θ-Type Response to Earthquake Excitations

1 The Effective Force Vector. The total displacement vector of the shell can be considered as the sum of two components: the relative displacement vector $\{d\}$ defined by

$$\{d\} = \begin{Bmatrix} u(\theta,z,t) \\ v(\theta,z,t) \\ w(\theta,z,t) \end{Bmatrix} \tag{4}$$

and the displacement vector $\{d_g\}$ associated with the ground displacement $G(t)$; it can be written as

$$\{d_g\} = \begin{Bmatrix} 0 \\ -\sin(\theta) \\ \cos(\theta) \end{Bmatrix} G(t) \tag{5}$$

Nomenclature

$[C]$ = damping matrix
$\{d\}$ = relative displacement vector
$\{\bar{d}\}_e$ = element nodal displacement vector
$\{d_g\}$ = displacement vector associated with ground motion
e = element number
$\{F_g\}$ = inertia force vector
g = acceleration of gravity
$G(t)$ = ground displacement
h = shell thickness
H = liquid depth
H_0 = height of impulsive mass
I_1 = modified Bessel function
$[K]$ = stiffness matrix
$[K_s]$ = shell stiffness matrix
$[K_s^i]$ = shell stiffness matrix due to static hoop stress
L = shell length
L_e = length of a finite element
m = total mass of liquid
m_0 = impulsive mass
$M_{\max}$ = maximum impulsive wall moment
$[M]$ = mass matrix
$[M_l]$ = added mass matrix of liquid
$[M_s]$ = consistent mass matrix of shell
n = circumferential wave number
NEH = number of shell elements in contact with liquid
NEL = number of shell elements along its length
N_z = axial membrane force resultant
N_θ = circumferential membrane force resultant
p = hydrodynamic pressure
$\{P_{\text{eff}}\}$ = effective earthquake load vector
$\{q\}$ = shell nodal displacement vector
$Q(t)$ = base shear
$[\overset{*}{Q}]$ = modal displacement matrix
r = radial coordinate
R = tank radius
S_d = spectral displacement
t = time
u = shell axial displacement
v = shell circumferential displacement
w = shell radial displacement
W = work done by external loads
z = axial coordinate
β_j = modal participation factors
δ = variational operator
ζ_j = damping ratios
$\{\eta(t)\}$ = modal amplitude vector
θ = circumferential coordinate
ρ_l = mass density of liquid
ρ_s = mass density of shell
ϕ = liquid velocity potential function
ω_j = circular natural frequency

Subscripts

e = an element
l = liquid
max = maximum
s = shell
z = axial direction
θ = circumferential direction

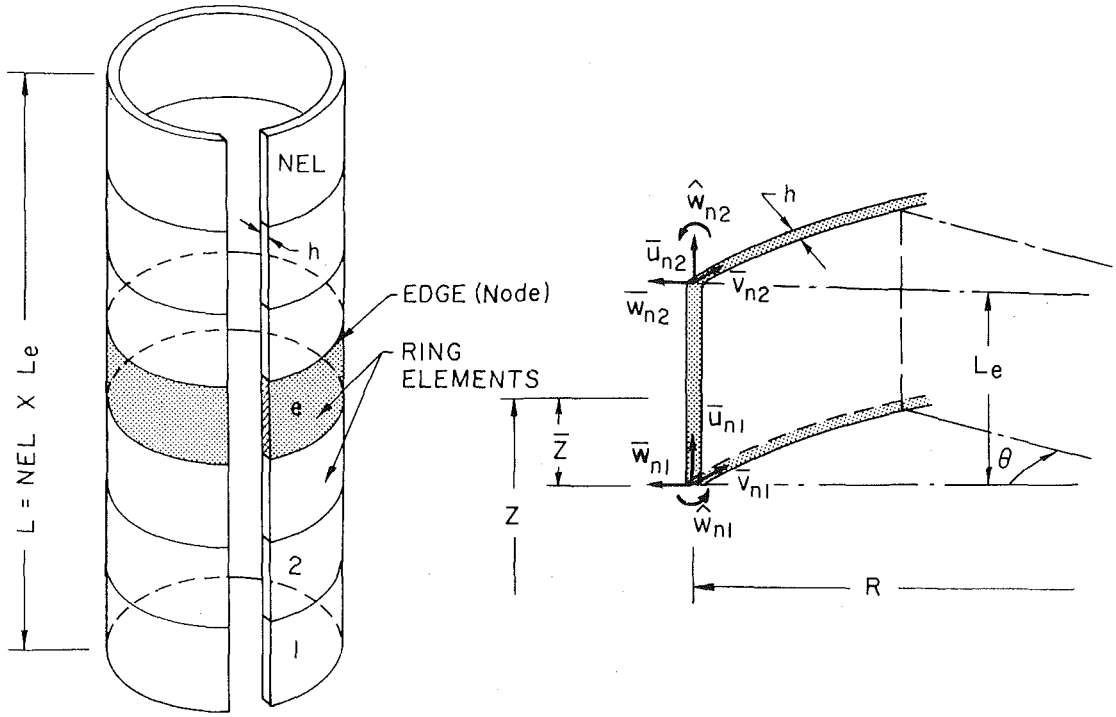

(a) Finite-element Idealization of the Shell

(b) Shell Element

Fig. 2 Finite-element definition diagram

The external forces acting on the shell due to ground motion $G(t)$ include (i) the distributed inertia force of the shell which is given by

$$\{F_g\} = -\rho_s h\{\ddot{d}_g\} = -\rho_s h\ddot{G}(t)\begin{Bmatrix} 0 \\ -\sin(\theta) \\ \cos(\theta) \end{Bmatrix} \tag{6}$$

and (ii) the hydrodynamic pressure on the wall of a similar rigid tank. This pressure can be expressed as

$$p_g(R,\theta,z,t) = -\rho_l \frac{\partial \phi}{\partial t}(R,\theta,z,t)$$

$$= -\frac{2\rho_l}{H}\sum_{i=1}^{\infty}\frac{\int_0^H \ddot{G}(t)\cos(\alpha_i x)dx}{\alpha_i\, 'I_1(\alpha_i R)} I_1(\alpha_i R)\cos(\alpha_i z)\cos(\theta)$$

$$= -\frac{2\rho_l \ddot{G}(t)}{H}\sum_{i=1}^{\infty}\frac{(-1)^{i+1}I_1(\alpha_i R)}{\alpha_i^2\, 'I_1(\alpha_i R)}\cos(\alpha_i z)\cos(\theta) \tag{7}$$

where ϕ is the velocity potential function associated with the ground motion $\ddot{G}(t)$; ρ_l is the liquid mass density; I_1 is the modified Bessel function of the first kind of order 1; and α_i are constants given by

$$\alpha_i = \frac{(2i-1)\pi}{2H} \tag{8}$$

The work done by these external loads during arbitrary virtual displacements

$$\{\delta d\} = \begin{Bmatrix} \delta u_1 \cos(\theta) \\ \delta v_1 \sin(\theta) \\ \delta w_1 \cos(\theta) \end{Bmatrix} \tag{9}$$

can be expressed as

$$\delta W = \int_0^L \int_0^{2\pi} (\{F_g\}^T\{\delta d\}) R d\theta dz + \int_0^H \int_0^{2\pi} (p_g(R,\theta,z,t)\,\delta w_1 \cos(\theta)) R d\theta dz \tag{10}$$

Substituting equations (6), (7), and (9) into equation (10) yields

$$\delta W = -\ddot{G}(t)\left\{\rho_s \pi R \int_0^L h(-\delta v_1 + \delta w_1)dz + \sum_{i=1}^{\infty} b_i \int_0^H \delta w_1 \cos(\alpha_i z)dz\right\} \tag{11}$$

where

$$b_i = \frac{2\pi R \rho_l I_1(\alpha_i R)}{\alpha_i^2 H' I_1(\alpha_i R)}(-1)^{i+1} \tag{12}$$

With the aid of the finite-element model of the shell, the first term in equation (11) becomes

$$\rho_s \pi R \int_0^L h(-\delta v_1 + \delta w_1)dz = \rho_s \pi R \sum_{e=1}^{NEL} h_e\{\delta \bar{d}\}_e^T\{\bar{f}\}_e = \{\delta q\}^T\{\bar{F}\} \tag{13}$$

where NEL is the number of shell elements along the shell length; $\{\bar{d}\}_e$ is the nodal displacement vector of the element "e"; and the vectors $\{\bar{f}\}_e$ and $\{\bar{F}\}$ are given by

$$\{\bar{f}\}_e^T = \left[0, -\frac{L_e}{2}, \frac{L_e}{2}, \frac{L_e^2}{12}, 0, -\frac{L_e}{2}, \frac{L_e}{2}, -\frac{L_e^2}{12}\right] \tag{14}$$

and

$$\{\bar{F}\} = \sum_{e=1}^{NEL} \rho_s \pi R h_e \{\bar{f}\}_e \tag{15}$$

Furthermore, the second term in equation (11) can be expressed as

$$\sum_{i=1}^{\infty} b_i \int_0^H \delta w_1 \cos(\alpha_i z) dz = \sum_{i=1}^{\infty} \sum_{e=1}^{NEH} \{\delta \bar{d}\}_e^T \{\bar{\bar{f}}\}_{ie} \tag{16}$$

where NEH is the number of shell elements in contact with the liquid and $\{\bar{\bar{f}}\}_{ie}$ is given by

$$\{\bar{\bar{f}}\}_{ie}^T = [0, 0, \bar{\bar{f}}_{i3}, \bar{\bar{f}}_{i4}, 0, 0, \bar{\bar{f}}_{i7}, \bar{\bar{f}}_{i8}]_e \tag{17}$$

in which

$$\bar{\bar{f}}_{i3} = L_e \left[-\left(\frac{1}{a_i} + \frac{6}{a_i^3}\right) \sin a_i(e-1) + \frac{12}{a_i^4} \cos a_i(e-1) - \frac{6}{a_i^3} \sin a_i e - \frac{12}{a_i^4} \cos a_i e \right];$$

$$\bar{\bar{f}}_{i4} = L_e^2 \left[-\frac{4}{a_i^3} \sin a_i(e-1) - \left(\frac{1}{a_i^2} - \frac{6}{a_i^4}\right) \cos a_i(e-1) - \frac{2}{a_i^3} \sin a_i e - \frac{6}{a_i^4} \cos a_i e \right];$$

$$\bar{\bar{f}}_{i7} = L_e \left[\frac{6}{a_i^3} \sin a_i(e-1) - \frac{12}{a_i^4} \cos a_i(e-1) + \left(\frac{1}{a_i} + \frac{6}{a_i^3}\right) \sin a_i e + \frac{12}{a_i^4} \cos a_i e \right];$$

$$\bar{\bar{f}}_{i8} = L_e^2 \left[-\frac{2}{a_i^3} \sin a_i(e-1) + \frac{6}{a_i^4} \cos a_i(e-1) - \frac{4}{a_i^3} \sin a_i e + \left(\frac{1}{a_i^2} - \frac{6}{a_i^4}\right) \cos a_i e \right];$$

$$a_i = \frac{i\pi L_e}{H} \; (i = 1, 2, \ldots) \quad \text{and} \quad e = 1, 2, \ldots, NEH. \tag{18}$$

Equation (16) can be expressed more conveniently as

$$\sum_{i=1}^{\infty} b_i \int_0^H \delta w_1 \cos(\alpha_i z) dz = \sum_{i=1}^{\infty} b_i \{\delta q\}^T \{\bar{\bar{F}}\}_i = \{\delta q\}^T \{\bar{\bar{F}}\} \tag{19}$$

where

$$\{\bar{\bar{F}}\}_i = \sum_{e=1}^{NEH} \{\bar{\bar{f}}\}_{ie} \quad \text{and} \quad \{\bar{\bar{F}}\} = \sum_{i=1}^{\infty} b_i \{\bar{\bar{F}}\}_i \tag{20}$$

It is important to note that the infinite series in equation (20) converges very rapidly and only the first few terms are needed for adequate representation of the series.

The virtual work expression can now be written as

$$\delta W = -\ddot{G}(t) \{\delta q\}^T (\{\bar{F}\} + \{\bar{\bar{F}}\}) = -\ddot{G}(t) \{\delta q\}^T \{F\} \tag{21}$$

and therefore, the effective earthquake load vector is given by

$$\{P_{\text{eff}}\} = -\{F\} \ddot{G}(t) \tag{22}$$

2 Modal Analysis. The matrix equation of motion of the liquid-shell system can be solved directly by numerical integration; however, in analyzing the earthquake response of linear structures, *it is generally more efficient to use modal superposition to evaluate* the seismic response and to carry out the analysis for only a few natural modes.

First, the nodal displacement vector of the shell is expressed as

$$\{q\} = [\overset{*}{Q}] \{\eta(t)\} \tag{23}$$

where $[Q]$ is a rectangular matrix of the order $N \times J$ which contains the modal displacement vectors associated with the lowest J natural frequencies; N is the number of degrees of freedom ($4 \times NEL$), and $\{\eta(t)\}$ is the modal amplitude vector.

Employing the orthogonality conditions of the natural modes, the undamped matrix equation of motion can be reduced to J independent differential equations for the unknowns η_j

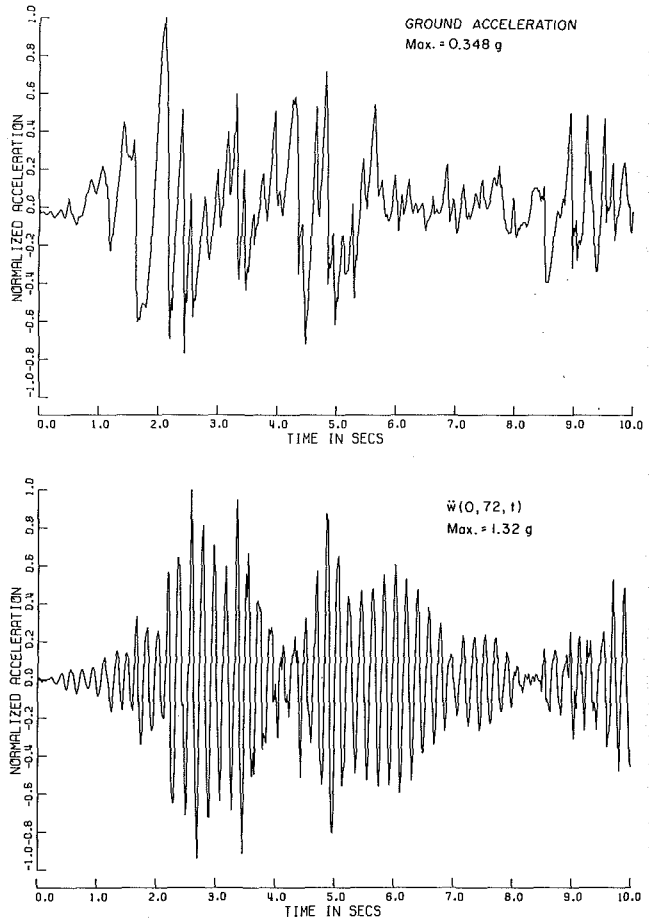

Fig. 3

$$\ddot{\eta}_j + \omega_j^2 \eta_j = -\beta_j \ddot{G}(t); \quad j = 1, 2, \ldots, J \tag{24}$$

Introducing damping into equation (24), then one can rewrite such equations as follows:

$$\ddot{\eta}_j + 2\zeta_j \omega_j \dot{\eta}_j + \omega_j^2 \eta_j = -\beta_j \ddot{G}(t); \quad j = 1, 2, \ldots J \tag{25}$$

For $\ddot{G}(t)$ given by a segmentally linear function, for $t_i \le t \le t_{i+1}$, equation (25) becomes

$$\ddot{\eta}_j + 2\zeta_j \omega_j \dot{\eta}_j + \omega_j^2 \eta_j = -\beta_j \left(\ddot{G}_i + \frac{\Delta \ddot{G}_i}{\Delta t} (t - t_i) \right) \tag{26}$$

where $\Delta \ddot{G}_i = \ddot{G}_{i+1} - \ddot{G}_i$ and $\Delta t = t_{i+1} - t_i$ = constant. The solution of equation (26) at time $t = t_{i+1}$ can be expressed in terms of that at $t = t_i$ by [6]

$$\begin{Bmatrix} \eta_{i+1} \\ \dot{\eta}_{i+1} \end{Bmatrix} = [A(\zeta, \omega, \Delta t)] \begin{Bmatrix} \eta_i \\ \dot{\eta}_i \end{Bmatrix} + [B(\zeta, \omega, \Delta t, \beta)] \begin{Bmatrix} \ddot{G}_i \\ \ddot{G}_{i+1} \end{Bmatrix} \tag{27}$$

in which the subscript j is omitted for brevity. Therefore, if the modal amplitude $\eta(t)$ and its time derivative $\dot{\eta}(t)$ are known at t_i, then the complete time history can be computed by a step-by-step application of equation (27).

3 Numerical Examples. A digital computer program has been written to compute the earthquake response of partly filled tanks by the method outlined in the preceding sections. The program obtains the free vibrational modes, formulates the generalized mass and load vectors, and computes shell nodal displacements and accelerations which are used to solve for the shell force and moment resultants, for the hydrodynamic pressures, and for base shear.

Example (1): A Tall Tank. The computer program is first utilized to estimate the earthquake response of an open top tall tank whose dimensions are: R = 24 ft (7.32m), L = 72 ft (21.96m), and h = 1 in. (2.54cm). The tank is assumed to be full of water and to be

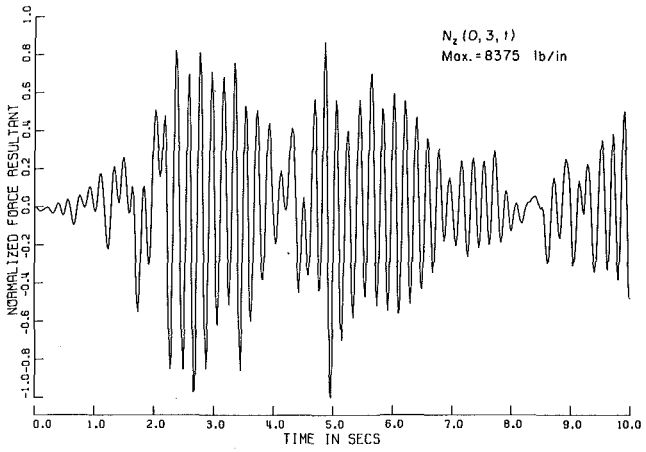

Fig. 4

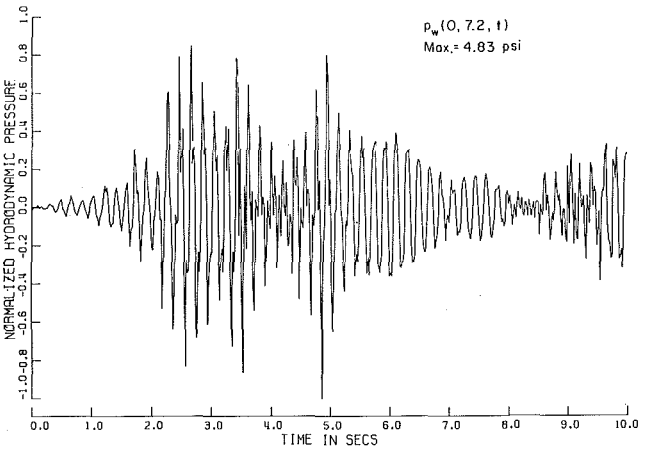

Fig. 5

subjected to the N-S component of the 1940 El Centro earthquake; only the first 10 sec of the record are employed in the analysis and this portion is displayed in Fig. 3(a). The modal damping ratios of the liquid-shell system are assumed to be 2 percent.

The time history of the relative radial component of shell acceleration at the tank top and in the $\theta = 0$ direction, $\ddot{w}(0, 72, t)$, is shown in Fig. 3(b) for comparison with the ground acceleration; it is clear that the relative acceleration is much greater than that of the ground.

The maximum relative displacement of the shell, $w_{\max}(0, 72, t)$, can be computed approximately using the El Centro response spectrum; it is given by

$$w_{\max}(0, 72, t) = \beta S_d \overset{*}{q} \tag{28}$$

where β is the earthquake participation factor of the fundamental mode; S_d is the spectral displacement corresponding to the fundamental period; and $\overset{*}{q}$ is the modal amplitude of the radial mode shape at the top of the tank. Hence, $w_{\max}(0, 72, t) = (1.55)(0.295)(1.0) = 0.457$ in. (1.16cm) which is in close agreement with the value of 0.445 in. (1.13cm) obtained by time integration of equation (27) and superposition of 4 modes of vibration. This also indicates that the displacement response of the tank is due mainly to the fundamental mode.

Having obtained the relative displacements of the shell, the force and moment resultants can be computed. Fig. 4 displays the time history of the membrane force resultant N_z computed at 3 ft (0.92m) above the base. To compare this stress with that induced in a similar rigid tank, one can make use of Housner mechanical model [7]. The elements of such model are given by $m_0 = 0.902$m and $H_0 = 0.375$H where m is the total mass of the contained liquid. The impulsive moment is therefore given by

$$M_{\max} = \left(m_0 H_0 + m_s \frac{L}{2}\right) \ddot{G}_{\max}$$

$$= 74.78 \times 10^6 \text{ lb ft } (101.5 \times 10^6 \text{ N.m}) \tag{29}$$

which produces axial membrane force resultant

$$(N_z)_{\max} = \frac{M_{\max}}{\pi R^2} = 3443.8 \text{ lb/in. } (603.3 \text{ N/m m}) \tag{30}$$

It is clear that such force resultant is much lower than that in a flexible tank. This is due to the fact that the impulsive loads arise through acceleration of the shell. If the shell is flexible, two acceleration components must be considered: (i) the acceleration of the undeformed shell, i.e., the ground acceleration, and (ii) the relative acceleration due to shell deformations. In a rigid tank, only the acceleration of the undeformed shell is considered which introduces the noticeable difference in the magnitude of shell stresses. To further clarify this point, consider, for illustration purposes, that the masses m_0 and m_s are attached to the tank wall by springs with stiffnesses that simulate the fundamental natural period of the tank. To estimate the impulsive moment, one has to employ the spectral acceleration which is 2.46 time the ground acceleration, and therefore, the maximum axial membrane force is given by

$$(N_z)_{\max} = 3443.8 \times 2.46$$

$$= 8471.8 \text{ lb/in. } (1484 \text{ N/m m})$$

which is in close agreement with that obtained by a shell analysis.

The maximum value of the membrane force resultant N_θ at a distance of 6 ft (1.83m) above the base is 2166 lb/in. (379.5 N/m m). To compare with that obtained in a similar rigid tank, one has to compute the hydrodynamic pressure. For a rigid tank, the maximum hydrodynamic pressure occurs at the bottom of the container; its value is given by [7]

$$p_d(R, 0, 0, t) = \frac{\sqrt{3}\rho_l H \ddot{G}}{2} \tanh\left(\frac{\sqrt{3}R}{H}\right)$$

$$= 4.92 \text{ psi } (33.9 \text{ kPa}) \tag{31},$$

and consequently, the maximum dynamic membrane force resultant can be computed by

$$N_\theta(0, 0, t)_{\max} = (p_d)_{\max} \cdot R$$

$$= 1417 \text{ lb/in. } (248.3 \text{ N/m m}) \tag{32}$$

which is less than that of a flexible tank.

It should be noted that the moment resultants M_z and M_θ in a tall tank have negligible effect on the extreme fiber stresses of the shell.

As is known, the impulsive hydrodynamic pressure consists of two components: one due to ground acceleration and one due to the relative acceleration of the deformed shell. The maximum value of the pressure at a distance of 7.2 ft (2.2m) above the base, due to ground acceleration only, is 3.63 psi (25 kPa) which is less than that obtained by equation (31); however, it is pointed out in [8] that the Housner model overestimates the hydrodynamic pressure for this particular H/R by about 33 percent which indicates a close agreement between the computed pressure and the "exact" pressure in rigid tanks. The time history of the additional pressure due to shell deformation at 7.2 ft (2.2m) above the base is shown in Fig. 5. Its maximum value is 1.33 times that due to ground acceleration only; however, the ratio is much larger at higher elevations. It should be noted that the maximum amplitudes of these two components of the impulsive hydrodynamic pressure do not occur, in general, at the same time.

The maximum base shear due to ground motion $(Q_g(t))_{\max}$ is in reasonable agreement with that computed for rigid tanks which is given by

Table 1 Impulsive earthquake response of a tall tank input: *N-S* component of the 1940 El Centro earthquake

	Damping			
	2%[a]	5%[b]	10%[b]	Rigid tank
Maximum radial component of shell displacement $w(0, 72, t)$ in. (cm)	0.445 (1.13)	0.344 (0.87)	0.296 (0.75)	—
Maximum axial force resultant $N_z(0, 3, t)$ lb/in. (N/m m)	8375 (1467)	6473 (1134)	5564 (974.8)	3444 (603.3)
Maximum tangential force resultant $N_\theta(0, 6, t)$ lb/in. (N/m m)	2166 (379.5)	1674 (293.3)	1439 (252.1)	1417 (248.3)
Maximum base shear $Q(t)$ lb (N)	51.08×10^5 (2.27×10^7)	39.47×10^5 (1.75×10^7)	33.94×10^5 (1.51×10^7)	27.18×10^5 (1.21×10^7)

[a] Computed by time integration.
[b] Computed by response spectrum.

$$(Q_g)_{\max} = (m_0 + m_s)\ddot{G}_{\max}$$
$$= 27.18 \times 10^5 \text{ lb } (1.21 \times 10^7 \text{N}) \quad (33)$$

The slight difference between this value and that of the present analysis is due to the fact that the Housner model overestimates the impulsive mass m_0 for tall tanks. The total impulsive base shear is also checked by the method presented in [8] where the liquid-shell system is analyzed using Flügge shell theory in combination with a Ritz-type procedure and the natural modes of vibration of uniform cantilever beams. The analysis gives a value of 52.47×10^5 lb (2.33×10^7 N) which is in close agreement with the value of 51.08×10^5 lb (2.27×10^7 N) obtained in the present analysis. It should be noted that the analysis in [8] is applicable only to uniform shells which are completely filled with liquid.

The troublesome aspect of analyzing the earthquake response of storage tanks is to define the appropriate value of damping. It can only be estimated from earthquake response of real tanks; unfortunately, seismic response data from tanks during past earthquakes are not available. Although a modal damping ratio of about 2 percent seems appropriate for the liquid-shell system, the foundation soil also dissipates energy which cannot be exactly evaluated. For illustration purposes, Table 1 presents the maximum values of the response computed for different values of damping ratio ζ; it also displays those in a similar rigid tank for comparison.

Example (2): A Tall Tank (Comparison With Shaking Table Results). To illustrate the effectiveness of the analysis under consideration, the computed earthquake response of an open top tall tank is compared with that obtained by shaking table tests [5]. The tank model was made of aluminum; its modulus of elasticity was 10×10^6 psi (6.89×10^7 kPa) and its density was 0.244×10^{-3} lb sec^2/in.^{4} (2.61×10^3 kg/m^3). The model has the following dimensions: $R = 3.875$ ft (1.18m), $L = 15$ ft (4.58m), and $h = 0.09$ in. (0.23cm) in the lower 10 ft (3.05m) of its length and $h = 0.063$ in. (0.16 cm) in the upper 5 ft (1.53m). The tank was partly filled with water to a depth of 13 ft (3.97m). The input motion was the *N-S* component of the 1940 El Centro earthquake; the time history was speeded by a factor of 1.73 and the peak acceleration was increased to 0.5g.

Table 2 presents a comparison between the computed and observed responses; it also displays the response of a similar rigid tank for comparison. Inspection of this table indicates that the computed and the observed responses are much higher than those computed for a rigid tank. It can also be seen that the seismic response of a flexible tank computed by the present method is higher than the observed response in a shaking table test. However, one must keep in mind that the input acceleration used in the calculation of the response is different from the actually applied acceleration in these tests.

Table 2 Comparison with shaking table tests [5]

	Flexible ($\zeta = 2\%$)[a] (impulsive only)	Rigid (impulsive only)	Observed[a]
Max. radial component of shell displacement $w(0, 15, t)$ in. (cm)	0.150 (0.381)	—	0.131 (0.333)
Max. axial force resultant $N_z(0, 0.625, t)$ lb/in. (N/m m)	418.1 (73.2)	155.3 (27.2)	362.6 (63.5)
Max. base shear $Q(t)$ lb (N)	3.90×10^4 (1.74×10^5)	1.79×10^4 (7.97×10^4)	2.75×10^4 (1.22×10^5)

[a] The input motion used in calculation of tank response is not identical to the actually applied shaking table acceleration.

It is found that the input acceleration used in shaking table tests does not exactly resemble the motion of the 1940 El Centro earthquake, especially at the fundamental natural frequency of the model. For such a frequency, the spectral acceleration of the actually applied motion is $0.95g$ for a 1 percent damping ratio; however, the spectral acceleration of the record employed in the calculation of the response is 1.45g for a 2 percent damping ratio. If one takes into account this difference in spectral accelerations and modifies accordingly the observed response, one can achieve a good correlation between the computed and observed responses. For example, multiplication of the observed base shear of 2.75×10^4 lb (1.22×10^5 N) by a factor of (1.45/0.95) yields a value of 4.19×10^4 lb (1.86×10^5 N) which is comparable to a computed value of 3.9×10^4 lb (1.74×10^5 N) (note that the observed base shear includes both the impulsive and convective components; however, for the problem under consideration, the convective component is much smaller than the impulsive one). The modification suggested in the foregoing yields reasonable values for all response quantities which are proportional to the acceleration; however, those quantities which are directly proportional to the spectral displacement are slightly underestimated. This indicates that the observed fundamental period is higher than the computed period by about 10 percent.

Example (3): A Broad Tank. The computer program is also used to estimate the earthquake response of an open top, fixed base, broad tank whose dimensions are: $R = 60$ ft (18.3m), $L = 40$ ft (12.2m) and $h = 1$ in. (2.54cm). The tank is assumed to be full of water and be subjected to the *N-S* component of the 1940 El Centro earthquake.

The time history of the radial component of shell acceleration at mid-height, $\ddot{w}(0, 20, t)$, is shown in Fig. 6; it should be noted that the maximum amplitude of the radial component of shell acceleration occurs near the bottom of the tank not at the top as in tall tanks as shown in Fig. 7.

The axial membrane force resultant N_z at a distance of 1.67 ft (0.51m) above the base is 1085 lb/in. (190 N/m m). The parameters of the Housner mechanical model are given by $m_0 = 0.38\ m$, $H_0 = 0.375\ H$; and therefore, the impulsive moment is

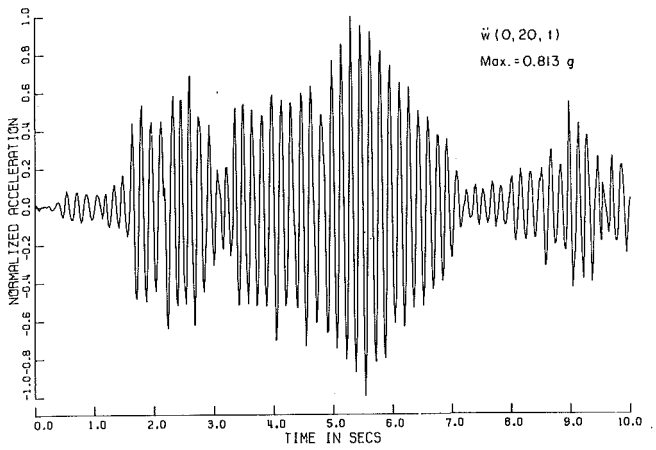

Fig. 6

$$M_{max} = \left(m_0 H_0 + m_s \frac{L}{2}\right)\ddot{G}_{max}$$

$$= 60.53 \times 10^6 \text{ lb ft } (82.15 \times 10^6 \text{ N.m})$$

and the corresponding axial membrane force resultant is 446 lb/in. (78.1 N/m m) which is much lower than that in a flexible tank. It should be noted that the computed dynamic moment resultants (M_z and M_θ) in fixed-base broad tanks are very high; however, in a real tank the wall is not rigidly "built in" at the base and this reduces local bending stresses significantly. Therefore, only the membrane stresses in a broad flexible tank are compared to those of a similar rigid tank.

The normalized hydrodynamic pressure distributions p_g and p_w due to ground motion and due to shell deformation, respectively, are plotted separately in Fig. 8; it can be seen that the pressure component p_w has an axial distribution similar to that of p_g which is in contrast to the pressure distribution in a tall tank. It should be also noted that the maximum amplitude of p_w is much higher than that of p_g. For example, $p_w(0, 4, t)_{max}$ is 9.53 psi (65.66 kPa) while $p_g(0, 4, t)_{max}$ is 4.92 psi (33.9 kPa).

Cos $n\theta$-Type Response to Earthquake Excitations

In a perfect circular tank, cos $n\theta$-type modes cannot be excited by rigid base motion; however, fabrication tolerances in civil engineering tanks permit a departure from a nominal circular cross section and this tends to excite these modes.

Little can be found in the literature about the importance of the cos $n\theta$-type modes in an earthquake response analysis. Veletsos and Turner [9] carried out an approximate investigation of the seismic response of an out-of-round tank. They computed the hydrodynamic pressure in an irregular rigid tank and applied it to a flexible tank. It should be noted, however, that the hydrodynamic pressures in a flexible tank may differ significantly than those of a rigid tank. An analysis of the effect of irregularity of the circular cross sections of flexible tanks can be found in [1] and will not be presented herein. The fact remains that the magnitude and distribution of fabrication error cannot be predicted, and consequently, only a hypothetical analysis can be made. It is also of interest to note that a recent experimental study [10] showed that buckling of full tank models depends largely on the stresses associated with the cos θ-type modes.

Conclusion

In view of the results of the study, one can conclude that the flexibility of tank walls that are anchored to a rigid base has a significant effect on the seismic response of both tall and broad tanks. These dynamic stresses are much greater than those computed assuming rigid walls.

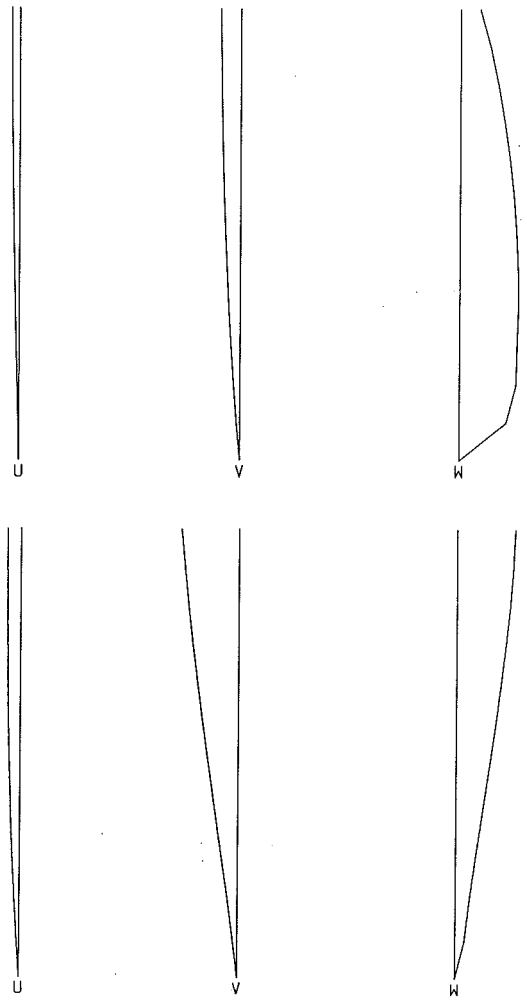

Fig. 7 Fundamental natural modes

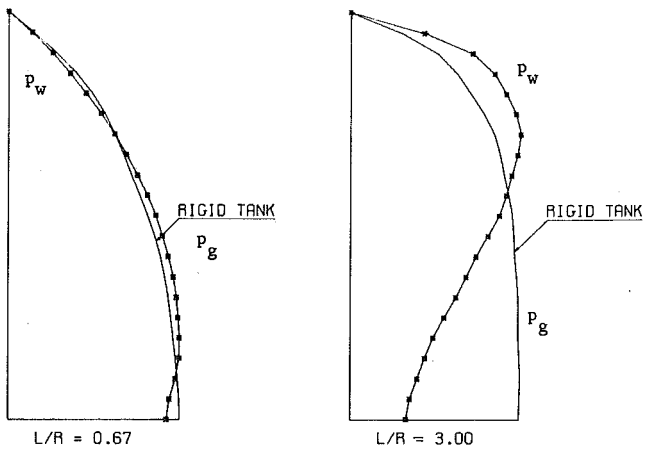

Fig. 8 Impulsive hydrodynamic pressure distribution

References

1 Haroun, M. A., "Dynamic Analyses of Liquid Storage Tanks," Earthquake Engineering Research Laboratory Report, EERL 80-4, California Institute of Technology, Feb. 1980.

2 Haroun, M. A., and Housner, G. W., "Free Lateral Vibrations of Liquid Storage Tanks," *Proceedings of the Third EMD Specialty Conference*, Austin, Texas, ASCE, Sept. 1979, pp. 466–470.

3 Housner, G. W., and Haroun, M. A., "Vibration Tests of Full-Scale Liquid Storage Tanks," *Proceedings of the Second U.S. National Conference on Earthquake Engineering*, Stanford, Calif., Aug. 1979, pp. 137–145.

4 Clough, D. P., "Experimental Evaluation of Seismic Design Methods

for Broad Cylindrical Tanks," University of California Earthquake Engineering Research Center, Report No. UC/EERC 77-10, May 1977.

5 Niwa, A., "Seismic Behavior of Tall Liquid Storage Tanks," University of California Earthquake Engineering Research Center, Report No. UC/EERC 78-04, Feb. 1978.

6 *Analyses of Strong Motion Earthquake Accelerograms, Response Spectra*, Vol. III, Part A, EERL 72–80, California Institute of Technology, Aug. 1972.

7 U.S. Atomic Energy Commission, "Nuclear Reactors and Earthquakes," TID-7024, Washington, D.C., 1963, pp. 367–390.

8 Veletsos, A. S., and Yang, J. Y., "Earthquake Response of Liquid Storage Tanks," Advances in Civil Engineering Through Engineering Mechanics, *Proceedings of the Annual EMD Specialty Conference*, Raleigh, N.C., ASCE, 1977, pp. 1–24.

9 Veletsos, A. S., and Turner, J. W., "Dynamics of Out-of-Round Liquid-Storage Tanks," *Proceedings of the Third EMD Specialty Conference*, Austin, Texas, ASCE, 1979, pp. 471–474.

10 Shih, C., and Babcock, C. D., "Scale Model Buckling Tests of a Fluid-Filled Tank Under Harmonic Excitation," presented at the 1980 Pressure Vessels and Piping Technology Conference, ASME, San Francisco, Calif., Aug. 1980, Preprint 80-C2/PVP-66.

F. Victor[1]
Research Assistant.

F. Ellyin
Professor and Head.
Mem. ASME

Structures and Solid Mechanics Section,
Department of Civil Engineering,
University of Sherbrooke,
Sherbrooke, Quebec, Canada
J1K 2R1

Acceleration of Unbalanced Rotor Through the Resonance of Supporting Structure

The dynamic response of a simple beam excited at its midspan by the action of a turbomachine secured to it, is investigated in detail. The forcing function includes transients at startup or shutdown. Effects of the shear deformation, rotatory inertia, and the internal viscous damping, which may depend on the frequency, are considered individually as well as in combined forms. The results indicate that the maximum amplitude of vibration is highly dependent on the acceleration rate through the critical frequency. There is also an apparent shift in its position as compared to the classical resonance frequency. Influences of shear deformation and rotatory inertia are significant when the supporting structure (or foundation) is relatively massive.

Introduction

The response of a simple system when subjected to a force of time-dependent frequency has been investigated in the past [1–6]. However, extension of these studies to systems with several degrees of freedom becomes extremely complicated. Furthermore, the effect of shear deformation and rotatory inertia has generally been neglected in the previous studies. In structures supporting rotating machinery these effects as well as the influence of acceleration of rotor unbalance have to be investigated.

The purpose of this paper is to study in detail the response of a beam under the action of an unbalanced rotor, starting from a position of rest and accelerating through critical frequencies. The critical frequencies are the natural frequencies of the system. The effect of various parameters such as acceleration or deceleration rates, shear deformation, rotatory inertia, and viscous damping is investigated.

Massive structures supporting turbogenerator machinery are generally composed of beam elements. A simply supported beam subjected at its midspan to an accelerating unbalanced rotor force is representative of the main load transfer member. This study is, therefore, of interest in understanding the response of structures supporting rotating machinery. It provides a method whereby effects of acceleration or deceleration through critical frequencies could be predicted. It also points out the parameters that are not generally known or considered in the present-day design practices. For example, if the design criterion is a manufacturer prescribed maximum amplitude of vibration, the designer of the support structure (foundation) must have information regarding the transients at startup or shutdown. That is, the effects of the startup regime to reach the operating frequency and its rate of decrease to arrive at a shutdown state should be studied. The steady-state analysis presently employed in the design of foundations cannot predict the maximum amplitude. This amplitude is highly dependent on the acceleration or the deceleration rate, shear deformation, and frequency-dependent damping.

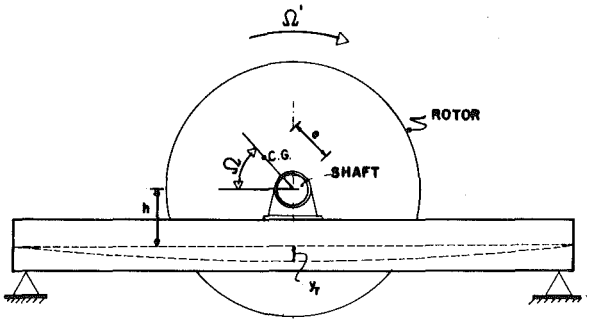

Fig. 1 A beam supporting an unbalanced rotor

Fundamental Equations and Solution

In order to appreciate the motion of a structure which is dynamically excited by a turbomachine secured to it, let us examine the behavior of a supporting element shown in Fig. 1, subjected to the action of an unbalanced rotor.

---

[1] Present address: Structural Engineer, Lemieux, Royer, Donaldson, Fields & Associés, Sherbrooke, Québec, Canada. J1J 3M7.

Contributed by the Applied Mechanics Division of THE AMERICAN SOCIETY OF MECHANICAL ENGINEERS, and presented at the 1981 Joint ASME/ASCE Applied Mechanics, Fluids Engineering, and Bioengineering Conference, University of Colorado, Boulder, Colo., June 22–27, 1981.

Discussion on this paper should be addressed to the Editorial Department, ASME, United Engineering Center, 345 East 47th Street, New York, N.Y. 10017, and will be accepted until September 1, 1981. Readers who need more time to prepare a Discussion should request an extension from the Editorial Department. Manuscript received by ASME Applied Mechanics Division, May, 1980; final revision, October, 1980. Paper No. 81-APM-24.

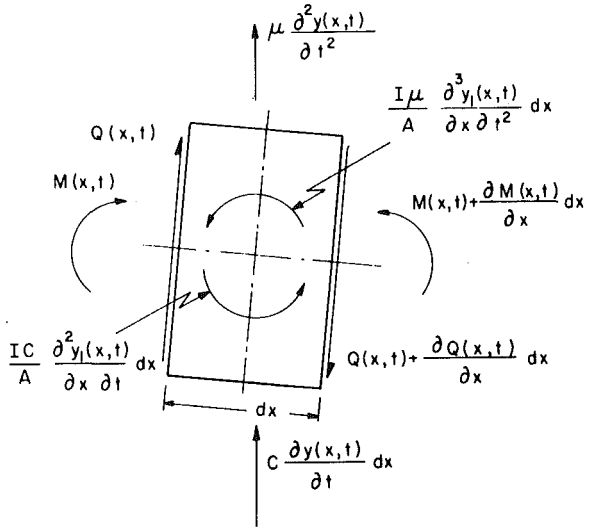

Fig. 2 Forces acting on a small element of beam

Forcing Function. The forcing function of an unbalanced rotor could be extremely complicated. It depends on the mounting details. We will assume a simple model representation (Fig. 1) of the form

$$P(t) = -m_r d^2[e \sin \Omega + h + y_r(t)]/dt^2 \tag{1}$$

where m_r is the unbalanced mass, e its eccentricity, and the remaining symbols are defined in the accompanying Nomenclature.

Carrying out the derivation at the right-hand side of equation (1), the unbalance rotor force is given by

$$P(t) = m_r e[\Omega'^2 \sin \Omega - \Omega'' \cos \Omega - y_r''(t)/e] \tag{2}$$

To simplify the study of the beam response under the action of accelerated unbalanced rotor, we will further assume that the torque applied to the rotor by the power source is constant during most of the acceleration period. The angular acceleration would also be constant, were it not for the part of the torque which is absorbed by the vibration. Due to the buildup of the vibration, a torque associated with the unbalance appears which is in opposite direction to that received from the power source. This reaction therefore reduces the angular acceleration below the ideal situation with no parasitic vibration [1]. Thus the angular travel, Ω, is assumed to vary with time according to

$$\Omega = \begin{cases} \omega_r T_1(3t^2/T_1^2 - t^3/T_1^3)/3 & \text{for } 0 \leqslant t \leqslant T_1 \\ \omega_r(t - T_1/3) & \text{for } t > T_1 \end{cases} \tag{3}$$

To utilize the formulation of the steady-state vibration, the rotor unbalance forcing function must be transformed to a set of forces, each of which has a constant circular frequency, i.e.,

$$P(t) = \sum_n [X(\omega_n) + \omega_n^2 m_r y_r(\omega_n)] \exp(i\omega_n t) \tag{4}$$

where

$$X(\omega_n) = \frac{m_r e}{T} \int_0^T [(\Omega'^2 \sin \Omega - \Omega'' \cos \Omega) \exp(-i\omega_n t)] dt \tag{5}$$

and

$$y_r(\omega_n) = \sum_n y_r(t) \cdot \exp(-i\omega_n t) \tag{6}$$

The integration appearing in equation (5) is carried out by using the Newton-Côtes rule of the fourth-order [7] and the principle of fast-fourier transform [8].

Equation of Motion. The differential equation for the damped vibration of the Timoshenko beam model is given by [9]

$$\begin{aligned} EI\partial^4 y(x,t)/\partial x^4 + \mu \partial^2 y(x,t)/\partial t^2 \\ - \frac{I\mu}{A}(1 + E/kG)\partial^4 y(x,t)/\partial x^2 \partial t^2 \\ + \frac{I\mu^2}{kGA^2} \partial^4 y(x,t)/\partial t^4 + C\partial y(x,t)/\partial t \\ - \frac{IC}{A}(1 + E/kG)\partial^3 y(x,t)/\partial x^2 \partial t \\ + \frac{IC^2}{kGA^2} \partial^2 y(x,t)/\partial t^2 + 2\frac{I\mu C}{kGA^2} \partial^3 y(x,t)/\partial t^3 = 0 \end{aligned} \tag{7}$$

For the vibration with constant circular frequency, it is possible to assume that the vibration is harmonic and the complete solution of equation (7) has the form [10]

$$\begin{aligned} y(x,t) = [a_1 \cos(\lambda_1 x/l) + a_2 \sin(\lambda_1 x/l) + a_3 \cosh(\lambda_2 x/l) \\ + a_4 \sinh(\lambda_2 x/l)] \cdot \exp(i\omega t) \end{aligned} \tag{8}$$

Applying d'Alembert's principle to the dynamic equilibrium in the vertical direction for a small element shown in Fig. 2 and using equation (8), one obtains the following relations for the bending moment and shearing force:

$$\begin{aligned} M(x,t) = \frac{EI}{l^2}[\lambda_1 \bar{\lambda}_1 a_1 \cos(\lambda_1 x/l) + \lambda_1 \bar{\lambda}_1 a_2 \sin(\lambda_1 x/l) \\ - \lambda_2 \bar{\lambda}_2 a_3 \cosh(\lambda_2 x/l) - \lambda_2 \bar{\lambda}_2 a_4 \sinh(\lambda_2 x/l)] \cdot \exp(i\omega t) \end{aligned} \tag{9}$$

$$\begin{aligned} Q(x,t) = -\frac{EI}{l^3} \bar{\lambda}_1 \bar{\lambda}_2 [\lambda_2 a_1 \sin(\lambda_1 x/l) - \lambda_2 a_2 \cos(\lambda_1 x/l) \\ + \lambda_1 a_3 \sinh(\lambda_2 x/l) + \lambda_1 a_4 \cosh(\lambda_2 x/l)] \exp(i\omega t) \end{aligned} \tag{10}$$

Nomenclature

a_i = the ith constant of integration
h = distance shown in Fig. 1
$i = \sqrt{-1}$
l = length of beam element
t = time
x = distance
y_{md} = the maximum amplitude when damping is considered
y_{mr} = the maximum amplitude when shear deformation and/or rotatory inertia effects are considered
$y_r(t)$ = the deflection at the rotor location
$y_{(x,t)}$ = the deflection at distance x and time
A = cross-sectional area
C = damping per unit length
E = Young's modulus
G = shear modulus
I = moment of inertia
k = Timoshinko shear coefficient
L = length of a simply supported beam
$R = \sqrt{I/AL^2}$
T = total time of displacement history
T_1 = acceleration time
$\gamma = ER^2/kG$
$\lambda = \frac{1}{2}[\mu\omega_n^2(1 - 2i\omega_b/\omega_n)/EI]^{1/4}$
$\lambda_1 = \lambda\{\lambda^2(R^2 + \gamma)/2 + [1 + \lambda^4(R^2 - \gamma)^2/4]^{1/2}\}^{1/2}$
$\lambda_2 = \lambda\{-\lambda^2(R^2 + \gamma)/2 + [1 + \lambda^4(R^2 - \gamma)^2/4]^{1/2}\}^{1/2}$
$\bar{\lambda}_1 = \lambda_1 - \lambda^4\gamma/\lambda_1$
$\bar{\lambda}_2 = \lambda_2 + \lambda^4\gamma/\lambda_2$
μ = mass of the beam per unit length
τ_0 = the first natural period
ω = circular frequency
ω_0 = the first critical frequency
$\omega_b = C/2\mu$
ω_i = the ith critical frequency
ω_n = the nth frequency in the series
ω_r = the operating speed of the rotor
ω_{ib} = the ith natural frequency of the simply supported beam
ω_{0r} = the first natural frequency when shear deformation and/or rotatory inertia effects are considered
Ω = angular travel of the rotor
Ω' = angular speed of the rotor
Ω_c' = the rotor speed at the maximum response amplitude
Ω'' = angular acceleration of the rotor
$\Omega_c'' = 2\omega_r\sqrt{1 - \omega_0/\omega_r}/T_1$, the angular acceleration at critical frequency

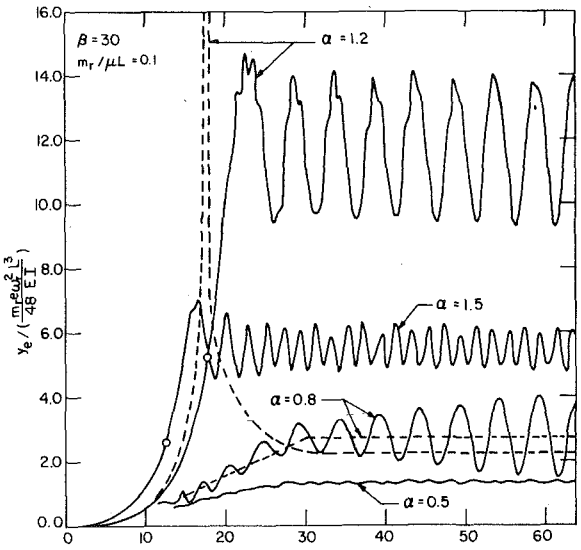

Fig. 3 Relationship between the displacement envelope at midspan, y, and the time parameter b, for various values of α

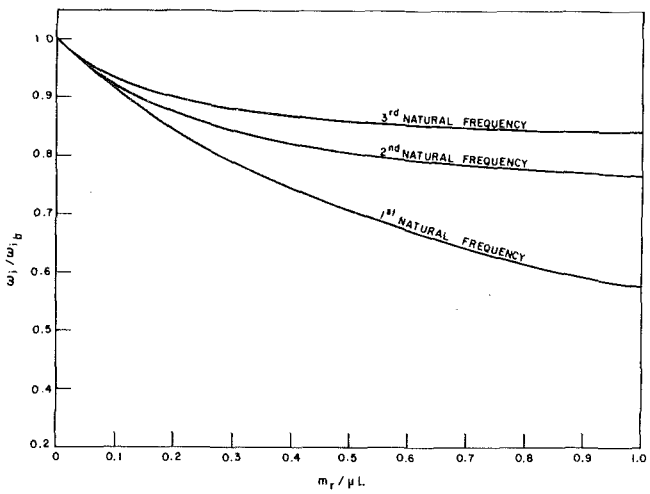

Fig. 4 The effect of unbalanced mass on the determination of natural frequencies

Using equation (8) and the boundary conditions of a simply supported beam for the symmetrical vibration modes, the coefficients of integration a_1 to a_4 can be expressed in terms of the deflection and bending slope amplitudes at the extremities of a beam element. The corresponding moments and shear forces are then obtained from equations (9) and (10). Equating each term of the forcing function, equation (4), to the difference of the shearing force at the midspan for each circular frequency, a relation is obtained between the midspan deflection and the applied force

$$y_m(t) = \frac{L^3}{48EI}\sum_n \left\{\left[\frac{3}{\Phi(\omega_n) - \lambda^4 m_r/\mu L}\right] \cdot X(\omega_n) \cdot \exp(i\omega_n t)\right\} \qquad (11)$$

in which $\Phi(\omega_n)$ is the frequency function for the nth term. It has the form of

$$\Phi(\omega_n) = \bar{\lambda}_1\bar{\lambda}_2(\lambda_1^2 + \lambda_2^2)\cosh\lambda_2\cos\lambda_1/ [\bar{\lambda}_2\cosh\lambda_2\sin\lambda_1 - \bar{\lambda}_1\sinh\lambda_2\cos\lambda_1] \qquad (12)$$

It is to be noted that the procedure described herein can be applied to analyze a framed structure subjected to any similar forcing function.

Numerical Analysis and Discussion

Response of an Ideal System. Numerical calculations have been carried out to investigate the dynamic behavior of a simply supported beam subjected to an accelerating rotor unbalance force starting from the rest. For the sake of simplicity, the deflection at the driving point will be discussed herein.

To generalize the discussion, the following dimensionless variables are introduced:

$$\alpha = \omega_r/\omega_0 \qquad \beta = T_1/\tau_0 \qquad (13a, b)$$

$$\eta = C/2\left(\mu + \frac{2m_r}{L}\right)\omega_0 \quad b = t/\tau_0 \qquad (13c, d)$$

$$\epsilon = \Omega''/\omega_0^2 \qquad \epsilon_0 = \Omega_0''/\omega_0^2 \qquad (13e, f)$$

$$\epsilon_c = \Omega_c''/\omega_0^2 \qquad (13g)$$

In the first instance an ideal case of the undamped response will be examined. The effect of rotatory inertia and shear deformation on the response of the beam will be studied later on.

Fig. 3 shows the relationship between the displacement envelope at the midspan, y_e, and the time factor, b, for $\alpha = 0.5, 0.8, 1.2$ and 1.5, respectively, $\beta = 30$ and $m_r/\mu L = 0.1$. The solid lines indicate the results obtained from the present analysis by considering the effect of acceleration. For the purpose of comparison, the envelope curves for the two cases ($\alpha = 0.8$ and 1.2) obtained through consideration of a steady-state response at a given instance are shown in dotted lines in the same figure. This type of response will be termed "instantaneous steady-state" herein.

Consider the case when the operating speed, ω_r, is less than the first critical frequency, i.e., $\alpha < 1.0$. In this case one noted that the displacement envelope oscillates around the instantaneous steady-state response envelope and the oscillation amplitude increases as the operating frequency approaches the natural frequency of the system. For those cases where the operating frequency is greater than the natural frequency of the system (i.e., $\alpha > 1.0$), the displacement envelope curves deviate considerably from that of the instantaneous steady-state response. When the instantaneous frequency, Ω', of the rotor approaches the critical frequency of the system, indicated by the "0" marks on the curves of Fig. 3, the deflection envelope as expected increases rapidly and reaches a maximum value. After this maximum has been attained, a very small amount of input energy is required to keep the system in motion. However, since there is no damping, the displacement envelope oscillates around a certain level with a maximum value slightly less than the first one already attained. This slight reduction in the maximum value for the subsequent response is due to the change in strain energy of the system resulting from the consideration of the conservation of energy. The level at which the oscillation occurs and its amplitude become smaller when the operating frequency is removed from any one of the critical frequencies, c.f., $\alpha = 1.2$ and 1.5 in Fig. 3.

It is noted that the displacement envelope in Fig. 3 especially for the case of $\alpha = 1.2$, is not a smooth curve. This phenomenon is due to the contribution of the higher modes on the response spectrum and the irregularities will diminish after the rotor attains a constant speed. It should also be noted that the maximum amplitude does not occur at the critical frequency. There is an apparent shift in its position and this shift should be kept in mind when the results of a vibration test are interpreted.

The analysis is carried out for different rotor to support beam mass ratios ($m_r/\mu L$) varying from 0.01 to 1.0. The influence of this mass ratio, as to be expected, is in the determination of the natural frequencies of the system, see Fig. 4. However, when the system response to the rotor unbalance forces is normalized as in Fig. 3, for constant values of coefficients α and β, the difference in the maximum response is within 2 percent. We will therefore, present the results for a mass ratio of $m_r/\mu L = 0.1$ which is a representative value of large turbomachine support systems.

An interesting problem is the relationship among the maximum

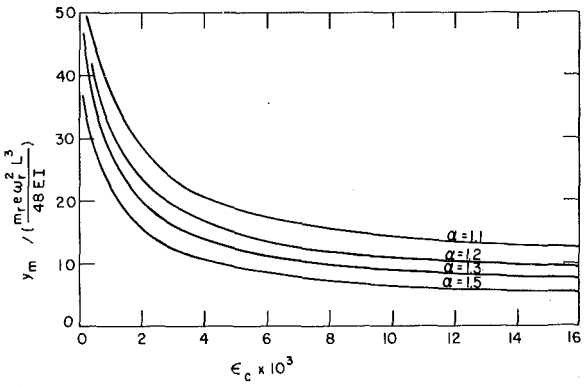

Fig. 5 Relationship between the maximum amplitude of vibration and the acceleration rate through the critical frequency, for different values of α

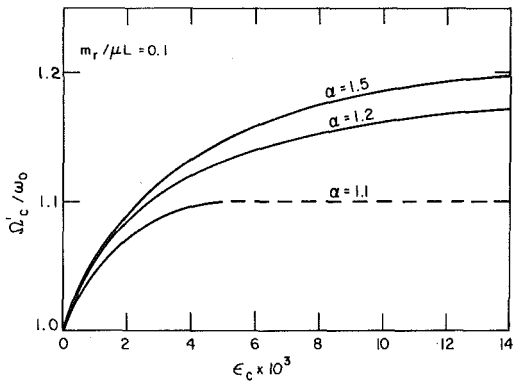

Fig. 6 The effect of acceleration rate through critical frequency on the shift of the maximum amplitude of vibration, for different values of α

amplitude of vibration, the rate at which the rotor is accelerated through the critical frequency, and the level of the operating speed from that of the critical. It is evident from Fig. 5 that the maximum amplitude, y_m, is highly dependent upon the acceleration rate through the critical frequency, i.e., the greater the acceleration through the critical frequency and/or the greater the deviation of α from unity, the smaller the maximum amplitude of the system.

Fig. 6 demonstrates the relationship between the shift of the maximum amplitude and the acceleration through the critical frequency for various levels of the operating speed. It is observed that the shift increases with the increase of the acceleration rate and/or with the increase of the frequency ratio, α. The dotted line in Fig. 6 for $\alpha = 1.1$ is intended to show that the maximum amplitude will occur for this case after the rotor speed has reached its maximum value and stabilized at that level. Note that the acceleration through resonance takes place at a value of $4.6\omega_0^2 \times 10^{-3}$ rad/sec/sec.

To eliminate the effect of the rate of change of the acceleration when passing through the critical frequency, a case of rotor unbalance with a constant acceleration is considered. The relationship between the maximum amplitude, its shift for a constant rate of acceleration is illustrated in Fig. 7. It is clear from this figure that the effect of the increasing acceleration is to diminish the maximum response amplitude, and to shift its location with respect to the critical frequency. In comparing Figs. 6 and 7, it becomes evident that a decrease of acceleration rate to achieve the operating speed would alter the location of the maximum response amplitude, displacing it toward the critical frequency.

Effect of Shear Deformation and Rotatory Inertia. Let us now examine the effect of shear deformation and rotatory inertia on the maximum amplitude of the vibrating system. It is a well known fact that the effect of shear deformation and/or rotatory inertia in a steady-state analysis is to decrease the values of the natural

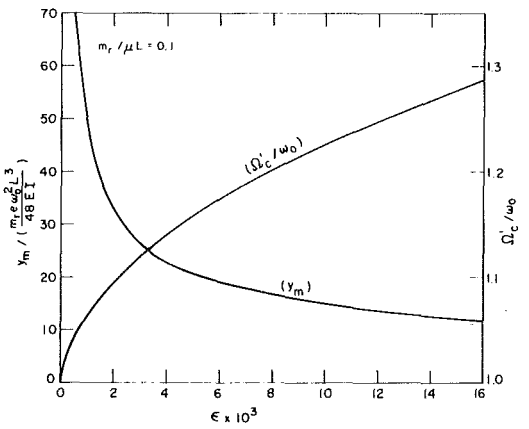

Fig. 7 Relationship between the maximum amplitude of vibration and its shift for a constant acceleration rate

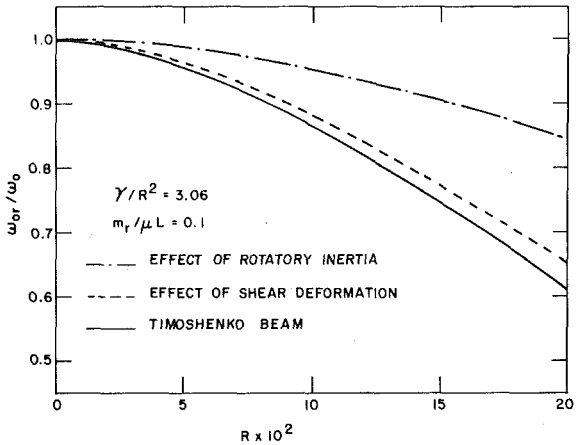

Fig. 8 The effect of the shear deformation and rotatory inertia on the first critical frequency of a simply supported beam

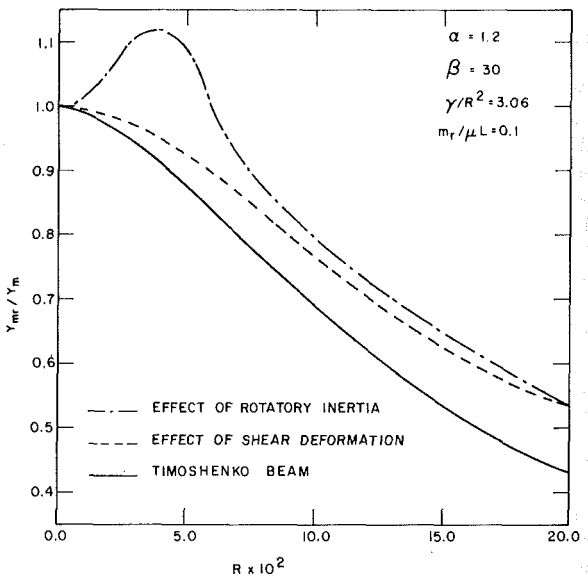

Fig. 9 The effect of shear deformation and rotatory inertia on the maximum amplitude of vibration

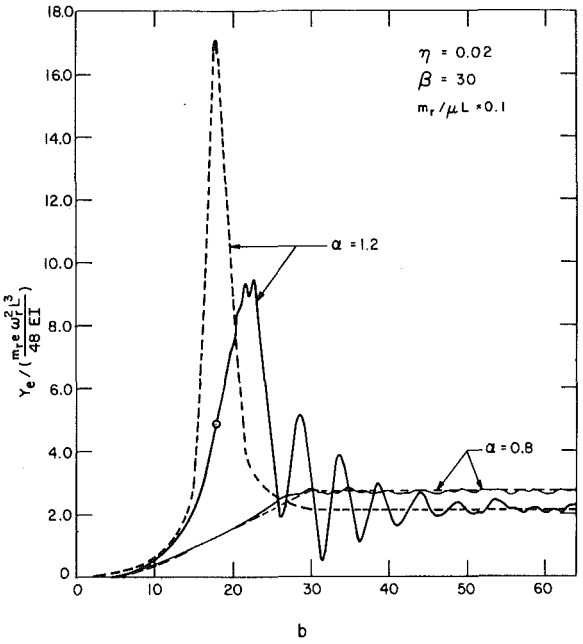

Fig. 10 Relationship between the displacement envelope at midspan, y_e, and the time parameter b, for two values of α

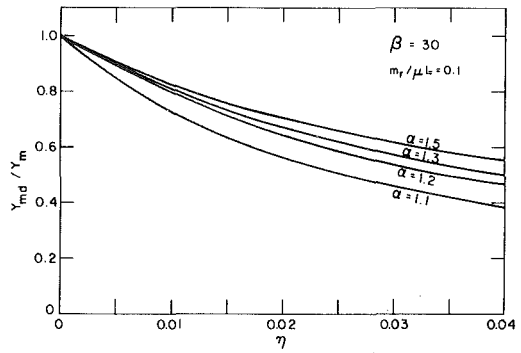

Fig. 11 Effect of damping on the maximum amplitude of vibration, for different values of α

frequencies of the system. This effect becomes more pronounced for the higher natural frequencies. Fig. 8 shows the effects of shear deformation and/or rotatory inertia on the first natural frequency for the system under consideration.

The influence of shear deformation, rotatory inertia, and their combination on the maximum amplitude of the beam subject to the action of an accelerating rotor unbalance load, is shown in Fig. 9. It is noted that this effect in general is to decrease the maximum amplitude of the beam, except for the small values of R when the rotatory inertia effect is considered alone. This general trend could be explained by observing that first, due to decrease in the value of natural frequency, the ratio between the operating speed and the natural frequency of the system is increased, thus resulting in a decreasing amplitude. The second influence is due to the higher acceleration rate when passing through the reduced natural frequency (c.f., Fig. 5).

When the effect of the rotatory inertia is examined alone, the maximum amplitude increases for small values of R, similar to that observed in a steady-state analysis. However, for higher values of R, the effect of rotatory inertia becomes similar to that of the shear deformation.

Damping Effect. The effect of the viscous damping on the dynamic response is now investigated. This effect is of prime importance in some practical cases. Fig. 10 shows the relationship between the displacement envelope and the time parameter, b, for $\alpha = 0.8$ and 1.2, $\beta = 30$, $\eta = 0.02$ and $m/\mu L = 0.1$. The solid lines are obtained from consideration of the acceleration effect, while the dotted lines are those of the instantaneous steady-state analysis. In the case when the operating frequency is less than the first critical one, the displacement envelope will be identical to that obtained from the instantaneous steady-state consideration, except for some disturbance. This disturbance is very small in comparison to that observed for the undamped case (c.f., Fig. 3).

In most practical cases, however, the operating speed is greater than the critical frequency of the system, e.g., the low-tuned foundations. In these cases, there is appreciable increase in the displacement amplitude when the instantaneous frequency of the rotor passes through the critical one. This amplitude reaches a maximum value, then it decreases rapidly to converge, with some oscillation, to the level of the steady-state amplitude at the operating speed. Note that the foregoing maximum amplitude is smaller than that of a steady-state resonance. This reduction is due to the effect of acceleration through the critical frequency.

Fig. 11 shows the influence of damping ratio, η, on the maximum amplitude for $\alpha = 1.1$, 1.2, 1.3, and 1.5, respectively, $\beta = 30$ and $m_r/\mu L = 0.1$. One notes that the greater the damping in the system, the smaller the maximum amplitude of vibration. This effect becomes more pronounced when the operating speed is in the neighborhood of any one of the critical frequencies.

From the foregoing discussion, it is evident that in the design of the supporting structure for rotating machinery such as the low-tuned turbine foundations, the effect of acceleration or deceleration of the machine speed must be taken into account. The magnification factor based on the steady-state analysis at the normal operating speed may lead to erroneous results. The maximum amplitude occurs during acceleration from position of rest to reach operating frequency or deceleration for shutdown. In these periods, the maximum amplitude of vibration is greater than that predicted by the steady-state response. The designer must acquire the speed-time relationship from the manufacturer of the machine in order to predict and design against high amplitudes which may cause damage to the machinery.

Conclusions

The following conclusions may be drawn from the results of the present work:

1 The greater the acceleration rate through the critical frequency, the smaller the maximum amplitude of vibration and the greater the shift of the position of this maximum with respect to the critical frequency (Figs. 5 and 6).

2 The maximum amplitude of vibration is dependent on the operating speed and its deviation from the critical frequency of the system.

3 Usage of the magnification factor based on the steady-state analysis at a normal operating frequency for predicting the maximum amplitude, is valid only when the operating speed is less than the first critical frequency of the system. In all other cases, the effect of the acceleration on the response should be considered.

4 In vibration tests, continuous records are often taken over a wide range of speeds. As the speed of the machine is increased or decreased, smaller amplitudes will be registered in comparison to that when the machine is held at a constant speed directly on a critical frequency. Furthermore, there is a shift in the position of the maximum amplitude with respect to the critical frequency of the system.

5 Consideration of the shear deformation and rotatory inertia effects, in general, lead to the reduction of the maximum amplitude. These effects cannot be neglected, especially in the analysis of massive structures.

6 The effect of viscous damping is to decrease the response amplitude rapidly after it has reached the maximum value. The maximum amplitude decreases with the increase of the damping in the

system. This effect becomes more pronounced when the operating speed is in the neighborhood of any one of the critical frequencies.

Acknowledgment

The results presented herein are part of a general investigation on the behavior and safety of structural systems. The research is supported, in part, by the Natural Sciences and Engineering Council Canada (Grant A-3808) and le Ministère de l'Education du Québec, Programme FCAC. The authors wish to thank the anonymous reviewer who made a valuable comment regarding the force function equation (1).

References

1 Baker, J. G., "Mathematical-Machine Determination of the Vibration of Accelerated Unbalanced Rotor," ASME JOURNAL OF APPLIED MECHANICS, Vol. 6, 1939, pp. 145–150.

2 Hother-Lushington, S., and Johnson, D. C., "The Acceleration of a Single-Degree-of-Freedom System Through Its Resonant Frequency," *Journal of the Royal Aeronautical Society*, Vol. 62, Oct. 1958, pp. 752–757.

3 Lewis, F. M., "Vibration During Acceleration Through a Critical Speed," ASME JOURNAL OF APPLIED MECHANICS, Vol. 54, 1932, pp. 253–261.

4 Suzuki, S. I., "Dynamic Behaviour of a Beam Subjected to a Force of Time-Dependent Frequency," *Journal of Sound and Vibration*, Vol. 57, 1978, pp. 59–64.

5 Suzuki, S. I., "Dynamic Behaviour of a Beam Subjected to a Force of Time-Dependent Frequency (continued)," *Journal of Sound and Vibration*, Vol. 60, 1978, pp. 417–422.

6 Suzuki, S. I., "Dynamic Behaviour of a Beam Subjected to a Force of Time-Dependent Frequency (Effects of Solid Viscosity and Rotatory Inertia)," *Journal of Sound and Vibration*, Vol. 62, 1979, pp. 157–164.

7 Sanger, J., "Numerical Analysis," *Higher Mathematics for Production Engineers*, 1st ed., Macmillan, London, 1964, pp. 115–144.

8 Rabiner, L. R., and Gold, B., "Spectrum Analysis and the Fast Fourier Transform," *Theory and Application of Digital Signal Processing*, 1st ed., Prentice-Hall, Englewood Cliffs, N.J., 1975, pp. 356–434.

9 Timoshenko, S., Young, D. H. and Weaver, W., Jr., *Vibration Problems in Engineering*, 4th ed., Wiley, New York, 1974.

10 Kolousek, V., *Dynamics in Engineering Structures*, 1st ed., Wiley, New York, 1973.

Journal of Applied Mechanics

Brief Notes

A Brief Note is a short paper which presents a specific solution of technical interest in mechanics but which does not necessarily contain new general methods or results. A Brief Note should not exceed 1500 words *or equivalent* (a typical one-column figure or table is equivalent to 250 words; a one line equation to 30 words). Brief Notes will be subject to the usual review procedures prior to publication. After approval such Notes will be published as soon as possible. The Notes should be submitted to the Technical Editor of the JOURNAL OF APPLIED MECHANICS. Discussions on the Brief Notes should be addressed to the Editorial Department, ASME, United Engineering Center, 345 East 47th Street, New York, N. Y. 10017, or to the Technical Editor of the JOURNAL OF APPLIED MECHANICS. Discussions on Brief Notes appearing in this issue will be accepted until two months after publication. Readers who need more time to prepare a Discussion should request an extension of the deadline from the Editorial Department.

Buckling of a Clamped-Hinged Circular Arch Under Gas Pressure and Related Problems

R. Schmidt[1]

The technical literature is replete with solutions to buckling problems of symmetric arches [1, 2]. On the other hand, very few cases of buckling of asymmetric arch-load systems have been investigated [1, 2]. Herein, we consider the in-plane stability (in the classical sense) of a circular elastic arch subjected to a static external gas pressure p. One end of the arch is immovably clamped and the other is immovably hinged. The cross-sectional area A of the arch rib is uniform.

The governing equations for buckling can be obtained as in [3 or 4]. They are[2]

$$\beta_1''' + b^2\beta_1' = \frac{1}{m}(cp_1 - e_1), \tag{1}$$

$$u_1' - v_1 = -ae_1, \quad v_1' + u_1 = a\beta_1, \tag{2}$$

where β_1 is the angle of rotation of a tangent to the centroidal line, $\beta_1' = d\beta_1/d\phi$, ϕ is the position angle measured clockwise from the vertical, $a \equiv R$ is the radius of the undeformed circular centroidal line, u_1 and v_1 are the buckling displacement components of a point on the centroidal line in the tangential and inward normal directions, respectively (v_0 is the prebuckling radial displacement), e_1 is a constant of integration, p_1 is a parameter related to the increase in p,

$$c = \frac{a}{EA}, \quad m = \frac{I}{a^2A}, \tag{3}$$

$$b^2 = 1 + \frac{a^3 p_{cr}}{EI}, \tag{4}$$

E is the modulus of elasticity, and I is the centroidal moment of areal inertia.

The general solution of equations (1) and (2) is

$$\beta_1' = C_2 \cos b\phi + C_3 \sin b\phi + \frac{cp_1 - e_1}{mb^2}, \tag{5}$$

Table 1 Dimensionless buckling load a^3p_{cr}/EI for different central angles 2α

2α (deg)	$\frac{a^3p_{cr}}{EI}$	2α (deg)	$\frac{a^3p_{cr}}{EI}$
20	462.17	180	5.0391
30	205.00	200	3.9740
40	114.99	220	3.1953
60	50.701	240	2.6156
80	28.204	260	2.1807
90	22.135	280	1.8569
100	17.795	300	1.6251
120	12.145	320	1.4758
140	8.7438	340	1.4047
160	6.5424	360	1.3924

$$\beta_1 = C_4 + \frac{C_2}{b}\sin b\phi - \frac{C_3}{b}\cos b\phi + \frac{(cp_1 - e_1)\phi}{mb^2}, \tag{6}$$

$$\frac{u_1}{a} = C_4 - C_5\cos\phi + C_6\sin\phi + \frac{(cp_1 - e_1)\phi}{mb^2} - \frac{C_2\sin b\phi}{b(b^2-1)} + \frac{C_3\cos b\phi}{b(b^2-1)}, \tag{7}$$

$$\frac{v_1}{a} = C_5\sin\phi + C_6\cos\phi - \frac{C_2\cos b\phi}{b^2-1} - \frac{C_3\sin b\phi}{b^2-1} + \frac{cp_1 - e_1}{mb^2} + e_1, \tag{8}$$

in which the constants $(cp_1 - e_1)/mb^2$, C_2, C_3, C_4, C_5, and C_6 are related to each other linearly by the boundary conditions

$$\beta_1 = u_1 = v_1 = 0 \text{ at } \phi = -\alpha, \tag{9}$$

$$\beta_1' = u_1 = v_1 = 0 \text{ at } \phi = \alpha, \tag{10}$$

and e_1, in (8), is neglected in comparison with e_1/mb^2, since $mb^2 \ll 1$ in the case of slender nonshallow arches buckling elastically. The resulting system of homogeneous equations yields the characteristic equation

$$\{(b^2-1)[(b^2-1)\tan\alpha - b^2\alpha] - \cot\alpha\}\sin^2 b\alpha + [(b^2-1)b^2\alpha - b^4\tan\alpha]\cos^2 b\alpha = [(b^2-1)b\alpha\cot 2\alpha - \tfrac{1}{2}b(b^2+1)]\sin 2b\alpha, \tag{11}$$

whose pertinent eigenvalues are given in Table 1.

[1] Professor of Engineering Mechanics, Department of Civil Engineering, University of Detroit, Detroit, Mich. 48221. Mem. ASME.

[2] This perturbative formulation of the arch buckling problem is subtly different from the classical formulation.

Manuscript received by ASME Applied Mechanics Division, October, 1980; final revision, January, 1981.

We observe that the critical values of the gas pressure on the clamped-hinged arches, presented in Table 1, fall between those for hingeless and one-hinged symmetrical arches [5, p. 301].

We also make use of this opportunity to correct some of the inaccuracies in the critical values quoted in the technical literature.

In [5, Table 7-2, p. 301], in the case of one-hinged arch, the values $p_{cr}a^3/EI = 162$ and 17.4 for $2\alpha = 30°$ and 90° should be replaced by 160 and 18.0, respectively, and, in the case of the three-hinged arch, the values 27.6 and 6.75 for $2\alpha = 60°$ and 120° should be replaced by 27.1 and 6.76, respectively.

In [6], the critical value of the constant-directional pressure on a semicircular two-hinged arch of constant cross section was given as $p_{cr} = 3.265\ EI/a^3$. The same authors also stated that this value constitutes the critical buckling load for a closed circular ring. Despite the fact that the critical load for a free ring has been calculated by many investigators to be $p_{cr} = 4\ EI/a^3$ (e.g., [1]), the value given in [6] was strongly defended in [7]. A recalculation by the author has yielded $p_{cr} = 3.271\ EI/a^3$ for the two-hinged semicircular arch, $p_{cr} = 4\ EI/a^3$ for the free complete ring, and $p_{cr} = 0.7014\ EI/a^3$ for the complete ring immovably clamped at a point.

Furthermore, recalculation of Table 1 of [8] has yielded: $p_{cr}a^3/EI = 74.95$, 19.59, 9.000, and 0.7014 for $\alpha = 30°$, 60°, 90°, and 180° instead of the values $p_{cr}a^3/EI = 80.5$, 19.4, 9.0, and 5.6, respectively, given in [8] for the case of constant-directional pressure on hingeless circular arches; and $p_{cr}a^3/EI = 75.06$, 20.11, 10.60, and 6.472 for $\alpha = 30°$, 60°, 90°, and 180° instead of the values $p_{cr}a^3/EI = 80.5$, 20.2, 10.9, and 6.5, respectively, presented in [8] for the case of centrally directed pressure on hingeless circular arches. Also, equation (2*b*) in [8] can be reduced from three to one term, viz.,

$$\epsilon_\theta = \frac{R\epsilon_0 + z\beta'}{R + z}.$$

Moreover, in [1, p. 2–109] and in [9], the equation

$$\epsilon = \frac{P}{2EI}\left[\frac{\alpha \tan \alpha - 2(1 - \cos \alpha)}{(3 + 2I/a^2A)\alpha \cos \alpha + (3 + \alpha \tan \alpha) \sin \alpha}\right]$$

should be replaced by, [10],

$$\epsilon = \frac{P}{2EA}\left[\frac{\alpha \tan \alpha - 2(1 - \cos \alpha)}{(3 + 2I/a^2A)\alpha \cos \alpha - (3 - \alpha \tan \alpha) \sin \alpha}\right]$$

in which the term $2I/a^2A$ may be neglected as very small in comparison with 3. The calculated graphical results are correct in both [1 and 9].

References

1 Column Research Committee of Japan, *Handbook of Structural Stability*, Corona Publishing Co., Tokyo, 1971.

2 DaDeppo, D. A., and Schmidt, R., "Stability of an Arch Under Combined Loads; Bibliography on Stability of Arches," *Industrial Mathematics, The Journal of the Industrial Mathematics Society*, Vol. 20, Part 2, 1970, pp. 71–89.

3 Schmidt, R., "Initial Postbifurcation Behavior of a One-Hinged Circular Arch," *International Journal of Mechanical Sciences*, Vol. 22, No. 8, 1980, pp. 527–533.

4 Schmidt, R., "Initial Postbuckling of Three-Hinged Circular Arch," ASME JOURNAL OF APPLIED MECHANICS, Vol. 46, No. 4, Dec. 1979, pp. 954–955.

5 Timoshenko, S. P., and Gere, J. M., *Theory of Elastic Stability*, 2nd ed., McGraw-Hill, New York, 1961.

6 Chwalla, E., and Kollbrunner, C. F., "Beiträge zum Knickproblem des Bogenträgers und des Rahmens," *Der Stahlbau*, Vol. 11, No. 10, May 1938, pp. 73–78.

7 Singer, J., and Babcock, C. D., "On the Buckling of Rings Under Constant Directional and Centrally Directed Pressure," ASME JOURNAL OF APPLIED MECHANICS, Vol. 37, No. 1, Mar. 1970, pp. 215–218.

8 Wempner, G. A., and Kesti, N. E., "On the Buckling of Circular Arches and Rings," *Proceedings of the Fourth U.S. National Congress of Applied Mechanics*, Vol. 2, ASME, 1962, pp. 843–849.

9 Schmidt, R., and DaDeppo, D. A., "Buckling of Deep Arches at Large Deflections," *AIAA Journal*, Vol. 7, No. 6, June 1969, pp. 1182–1183.

10 Schmidt, R., and DaDeppo, D. A., "Buckling and Postbuckling Behavior of High-Rise Arches With Large Prebuckling Deflections," *Industrial Mathematics, The Journal of the Industrial Mathematics Society*, Vol. 27, Part 2, 1977, pp. 61–74.

On the Savart-Masson Effect

I. Suliciu[1]

Introduction

The purpose of this Note is to show that the Savart-Masson (or stair case) effect (for a fixed previous thermomechanical history, a fixed ambient temperature, and a fixed amount of impurities) can be described by using a rate-type constitutive equation, such as that of [2] but with a variable viscosity coefficient.

Next, one describes several facts, experimentally observed, which are essentially incorporated in the proposed model (for details, see [1]):

1 This phenomenon appears as a stair case effect, at small constant rates or small increments of the applied stress, in a "soft" testing machine.

2 Some experimental results show that the jumps in strain are produced in the neighborhood of certain fixed values of stress [7, 8, 1].

3 If the stress rate $\dot{\sigma}$ exceeds a certain value, the stair case effect disappears, i.e., the $\sigma \sim \epsilon$ curve becomes a smooth curve.

4 From the experimental measurements of strain variation in time there follows that: the strain increases slowly in time on the almost vertical portions of the $\sigma \sim \epsilon$ curve; when a certain value of the stress is reached, a very fast increase of the strain is produced at almost constant stress.

5 Another experimental evidence is that the length of the horizontal steps increases when the strain increases.

The Constitutive Equation

The semilinear rate-type constitutive equation will be taken under the form

$$\dot{\sigma} = E\dot{\epsilon} - k\langle \sigma - f(\epsilon)\rangle, \tag{1}$$

where σ and ϵ are the stress and strain respectively, $E > 0$ is the Young modulus and $k > 0$ is the viscosity coefficient. The smooth curve $\sigma = f(\epsilon)$, $\epsilon \geq 0$, $\sigma \geq 0$, is an equilibrium curve (one assumes that $f(\epsilon)$ is a monotonic increasing function in this case); the way this curve is chosen will be discussed as follows. The continuous function $\langle x \rangle$ is defined as

$$\langle x \rangle = x\mathrm{H}(x), \tag{2}$$

where $\mathrm{H}(x)$ is the Heaviside function.

The solution of equation (1) with $\epsilon(t) = \epsilon_0 + at$, $a = \text{const} > 0$, $\sigma(0) = \sigma_0$ (say $\sigma_0 = f(\epsilon_0)$ and $k = \text{const} > 0$), is $\sigma = \sigma(t, a, k)$. The curve $(\epsilon_0 + at, \sigma(t, a, k))$, for $t \geq 0$, represented in the ϵ-σ plane, will be denoted by

$$\sigma = g(\epsilon, a, k). \tag{3}$$

This curve has the following properties:

$$g(\epsilon, a_2, k) > g(\epsilon, a_1, k) > f(\epsilon), \quad a_2 > a_1 > 0, \quad \epsilon > \epsilon_0 \tag{4}$$

$$g(\epsilon, a, k_2) > g(\epsilon, a, k_1) > f(\epsilon), \quad 0 < k_2 < k_1, \quad \epsilon > \epsilon_0. \tag{5}$$

The properties (4) and (5) are known properties of the constitutive equation (1). For a and k fixed for $\epsilon \gg \epsilon_0$ (i.e., for $t \gg 0$), the curve $\sigma = g(\epsilon, a, k)$ becomes (approximately) parallel to the equilibrium curve $\sigma = f(\epsilon)$, at a distance depending on a and k. For a quasi-linear rate-type constitutive equation such properties have been studied in [9].

From the foregoing remarks it is clear that the constitutive equation

[1] Department of Mathematics, Increst, B-dul Păcii 220, 77538 Bucharest, Romania.

Manuscript received by ASME Applied Mechanics Division, March, 1980; final revision, August, 1980.

We observe that the critical values of the gas pressure on the clamped-hinged arches, presented in Table 1, fall between those for hingeless and one-hinged symmetrical arches [5, p. 301].

We also make use of this opportunity to correct some of the inaccuracies in the critical values quoted in the technical literature.

In [5, Table 7-2, p. 301], in the case of one-hinged arch, the values $p_{cr}a^3/EI = 162$ and 17.4 for $2\alpha = 30°$ and 90° should be replaced by 160 and 18.0, respectively, and, in the case of the three-hinged arch, the values 27.6 and 6.75 for $2\alpha = 60°$ and 120° should be replaced by 27.1 and 6.76, respectively.

In [6], the critical value of the constant-directional pressure on a semicircular two-hinged arch of constant cross section was given as $p_{cr} = 3.265\ EI/a^3$. The same authors also stated that this value constitutes the critical buckling load for a closed circular ring. Despite the fact that the critical load for a free ring has been calculated by many investigators to be $p_{cr} = 4\ EI/a^3$ (e.g., [1]), the value given in [6] was strongly defended in [7]. A recalculation by the author has yielded $p_{cr} = 3.271\ EI/a^3$ for the two-hinged semicircular arch, $p_{cr} = 4\ EI/a^3$ for the free complete ring, and $p_{cr} = 0.7014\ EI/a^3$ for the complete ring immovably clamped at a point.

Furthermore, recalculation of Table 1 of [8] has yielded: $p_{cr}a^3/EI = 74.95$, 19.59, 9.000, and 0.7014 for $\alpha = 30°$, 60°, 90°, and 180° instead of the values $p_{cr}a^3/EI = 80.5$, 19.4, 9.0, and 5.6, respectively, given in [8] for the case of constant-directional pressure on hingeless circular arches; and $p_{cr}a^3/EI = 75.06$, 20.11, 10.60, and 6.472 for $\alpha = 30°$, 60°, 90°, and 180° instead of the values $p_{cr}a^3/EI = 80.5$, 20.2, 10.9, and 6.5, respectively, presented in [8] for the case of centrally directed pressure on hingeless circular arches. Also, equation (2*b*) in [8] can be reduced from three to one term, viz.,

$$\epsilon_\theta = \frac{R\epsilon_0 + z\beta'}{R + z}.$$

Moreover, in [1, p. 2–109] and in [9], the equation

$$\epsilon = \frac{P}{2EI}\left[\frac{\alpha \tan \alpha - 2(1 - \cos \alpha)}{(3 + 2I/a^2A)\alpha \cos \alpha + (3 + \alpha \tan \alpha) \sin \alpha}\right]$$

should be replaced by, [10],

$$\epsilon = \frac{P}{2EA}\left[\frac{\alpha \tan \alpha - 2(1 - \cos \alpha)}{(3 + 2I/a^2A)\alpha \cos \alpha - (3 - \alpha \tan \alpha) \sin \alpha}\right]$$

in which the term $2I/a^2A$ may be neglected as very small in comparison with 3. The calculated graphical results are correct in both [1 and 9].

References

1 Column Research Committee of Japan, *Handbook of Structural Stability*, Corona Publishing Co., Tokyo, 1971.

2 DaDeppo, D. A., and Schmidt, R., "Stability of an Arch Under Combined Loads; Bibliography on Stability of Arches," *Industrial Mathematics, The Journal of the Industrial Mathematics Society*, Vol. 20, Part 2, 1970, pp. 71–89.

3 Schmidt, R., "Initial Postbifurcation Behavior of a One-Hinged Circular Arch," *International Journal of Mechanical Sciences*, Vol. 22, No. 8, 1980, pp. 527–533.

4 Schmidt, R., "Initial Postbuckling of Three-Hinged Circular Arch," ASME JOURNAL OF APPLIED MECHANICS, Vol. 46, No. 4, Dec. 1979, pp. 954–955.

5 Timoshenko, S. P., and Gere, J. M., *Theory of Elastic Stability*, 2nd ed., McGraw-Hill, New York, 1961.

6 Chwalla, E., and Kollbrunner, C. F., "Beiträge zum Knickproblem des Bogenträgers und des Rahmens," *Der Stahlbau*, Vol. 11, No. 10, May 1938, pp. 73–78.

7 Singer, J., and Babcock, C. D., "On the Buckling of Rings Under Constant Directional and Centrally Directed Pressure," ASME JOURNAL OF APPLIED MECHANICS, Vol. 37, No. 1, Mar. 1970, pp. 215–218.

8 Wempner, G. A., and Kesti, N. E., "On the Buckling of Circular Arches and Rings," *Proceedings of the Fourth U.S. National Congress of Applied Mechanics*, Vol. 2, ASME, 1962, pp. 843–849.

9 Schmidt, R., and DaDeppo, D. A., "Buckling of Deep Arches at Large Deflections," *AIAA Journal*, Vol. 7, No. 6, June 1969, pp. 1182–1183.

10 Schmidt, R., and DaDeppo, D. A., "Buckling and Postbuckling Behavior of High-Rise Arches With Large Prebuckling Deflections," *Industrial Mathematics, The Journal of the Industrial Mathematics Society*, Vol. 27, Part 2, 1977, pp. 61–74.

On the Savart-Masson Effect

I. Suliciu[1]

Introduction

The purpose of this Note is to show that the Savart-Masson (or stair case) effect (for a fixed previous thermomechanical history, a fixed ambient temperature, and a fixed amount of impurities) can be described by using a rate-type constitutive equation, such as that of [2] but with a variable viscosity coefficient.

Next, one describes several facts, experimentally observed, which are essentially incorporated in the proposed model (for details, see [1]):

1 This phenomenon appears as a stair case effect, at small constant rates or small increments of the applied stress, in a "soft" testing machine.

2 Some experimental results show that the jumps in strain are produced in the neighborhood of certain fixed values of stress [7, 8, 1].

3 If the stress rate $\dot{\sigma}$ exceeds a certain value, the stair case effect disappears, i.e., the $\sigma \sim \epsilon$ curve becomes a smooth curve.

4 From the experimental measurements of strain variation in time there follows that: the strain increases slowly in time on the almost vertical portions of the $\sigma \sim \epsilon$ curve; when a certain value of the stress is reached, a very fast increase of the strain is produced at almost constant stress.

5 Another experimental evidence is that the length of the horizontal steps increases when the strain increases.

The Constitutive Equation

The semilinear rate-type constitutive equation will be taken under the form

$$\dot{\sigma} = E\dot{\epsilon} - k\langle \sigma - f(\epsilon)\rangle, \tag{1}$$

where σ and ϵ are the stress and strain respectively, $E > 0$ is the Young modulus and $k > 0$ is the viscosity coefficient. The smooth curve $\sigma = f(\epsilon)$, $\epsilon \geq 0$, $\sigma \geq 0$, is an equilibrium curve (one assumes that $f(\epsilon)$ is a monotonic increasing function in this case); the way this curve is chosen will be discussed as follows. The continuous function $\langle x \rangle$ is defined as

$$\langle x \rangle = x\mathrm{H}(x), \tag{2}$$

where $\mathrm{H}(x)$ is the Heaviside function.

The solution of equation (1) with $\epsilon(t) = \epsilon_0 + at$, $a = \text{const} > 0$, $\sigma(0) = \sigma_0$ (say $\sigma_0 = f(\epsilon_0)$ and $k = \text{const} > 0$), is $\sigma = \sigma(t, a, k)$. The curve $(\epsilon_0 + at, \sigma(t, a, k))$, for $t \geq 0$, represented in the ϵ-σ plane, will be denoted by

$$\sigma = g(\epsilon, a, k). \tag{3}$$

This curve has the following properties:

$$g(\epsilon, a_2, k) > g(\epsilon, a_1, k) > f(\epsilon), \quad a_2 > a_1 > 0, \quad \epsilon > \epsilon_0 \tag{4}$$

$$g(\epsilon, a, k_2) > g(\epsilon, a, k_1) > f(\epsilon), \quad 0 < k_2 < k_1, \quad \epsilon > \epsilon_0. \tag{5}$$

The properties (4) and (5) are known properties of the constitutive equation (1). For a and k fixed for $\epsilon \gg \epsilon_0$ (i.e., for $t \gg 0$), the curve $\sigma = g(\epsilon, a, k)$ becomes (approximately) parallel to the equilibrium curve $\sigma = f(\epsilon)$, at a distance depending on a and k. For a quasi-linear rate-type constitutive equation such properties have been studied in [9].

From the foregoing remarks it is clear that the constitutive equation

[1] Department of Mathematics, Increst, B-dul Păcii 220, 77538 Bucharest, Romania.

Manuscript received by ASME Applied Mechanics Division, March, 1980; final revision, August, 1980.

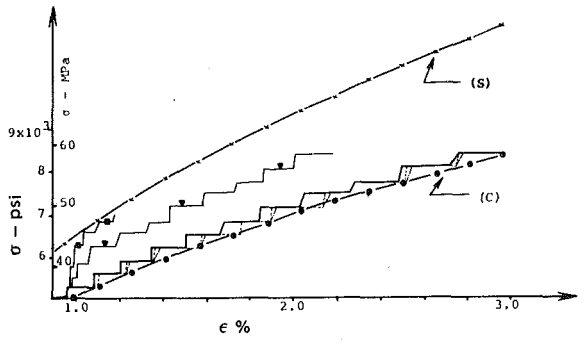

Fig. 1 Stress-strain curves for different stress rates. (The computations have been started from the state ($\epsilon = 0.908$ percent, $\sigma = 0$)). — Experimental data (Sharpe [7] test 957); —●— Equilibrium curve (C); —×— "Quasi-static" curve (S); Computed curves. ····· $\dot{\sigma}$ = 306 psi/min; —•— $\dot{\sigma}$ = 30.6 psi/min; —▼— $\dot{\sigma}$ = 3060 psi/min; —■— $\dot{\sigma}$ = 30,600 psi/min.

(1) with a variable k can model the Savart-Masson effect. In what follows, one discusses a form of the function $k = k(\epsilon, \sigma)$ which will allow the description of this effect according to Remarks 1–3 of the previous section; Remarks 4–5 will be used to check the validity of the model.

First, one will make precise the way one chooses the curve $\sigma = f(\epsilon)$ in equation (1). Remark 1 of the previous section suggests as equilibrium curve ([1, pp. 657, 42–43]) "the envelope of the bottom of the steps" of the stair case function $\sigma \sim \epsilon$ (see the full line of Fig. 1 which reproduces the experimental data of [6]). For strains between 0.3 percent and 3.0 percent, a function of the form

$$\sigma = f(\epsilon) = \beta_c \epsilon^{\alpha_c} \quad (C) \quad \beta_c = 4.05 \times 10^4 \text{ psi}, \quad \alpha_c = 0.45 \tag{6}$$

will give a good approximation as shown in Fig. 1.

For the comparison of the numerical data with the experimental data, one has selected the experimental results presented by Sharpe [6] since they are obtained on the same type of aluminum as those used in [3, 4] (cf. also [5]) but in a dynamic domain. This choice will also permit to compare the viscosity coefficient determined here with that obtained in the previously quoted papers.

The chosen viscosity coefficient will be a function of the form

$$k(\epsilon, \sigma) = k_0 + \bar{k}(\sigma)|\sigma - g(\epsilon)|, \tag{7}$$

for $f(\epsilon) = \beta_c \epsilon^{\alpha_c} \leqslant \sigma \leqslant g(\epsilon)$ and $0.003 \leqslant \epsilon \leqslant 0.03$. The curve $\sigma = g(\epsilon)$ must be chosen as the lowest possible curve obtained in a loading process with $\dot{\sigma} = c$ = constant, for which the stair case effect disappears. The fact that there exists a $c > 0$ for which the stair case effect disappears is an observed experimental behavior. Here, Bell's dynamic parabola [1]

$$\sigma = g(\epsilon) = \beta_s \epsilon^{1/2}, \quad \beta_s = 5.6 \times 10^4 \text{ psi}, \tag{8}$$

has been chosen as curve $\sigma = g(\epsilon)$. The choice (8) will give a much larger distance between the curves (C) and (S) from Fig. 1 than it (probably) is for the real body considered here but it allows us to see much better how the position of the $\sigma \sim \epsilon$ curves varies with $\dot{\sigma}$.

One denotes by σ_i, $\sigma_i < \sigma_{i+1}$, $i = 1, 2, \ldots, N-1$ the stress values where the horizontal jumps in strain take place on the $\sigma \sim \epsilon$ curve (see Fig. 1) and one chooses λ such that

$$0 < 2\lambda \ll \min_{i=1,2,\ldots,N-1} |\sigma_{i+1} - \sigma_i|.$$

The function $\bar{k}(\sigma)$ will be defined as

$$\bar{k}(\sigma) = k_1 \times \begin{cases} [\lambda^2 - (\sigma - \sigma_i)^2] & \text{if } |\sigma - \sigma_i| < \lambda, \quad i = 1,2,\ldots,N \\ 0 & \text{otherwise} \end{cases} \tag{9}$$

where k_1 = constant > 0.

With the choice (6) of the function $f(\epsilon)$ and with the choice (7) to (9) of the function $k(\epsilon, \sigma)$, the experimental facts mentioned in introduction at 1–3 are incorporated in the model. In the next section one determines, based on the experimental data of [7], the coefficients k_0, k_1, and λ such that the computed $\sigma \sim \epsilon$ curve behaves according to the experiments. As a consequence, the experimental facts mentioned in the previous section at Points 4 and 5 will be automatically described.

The Comparison Between Numerical and Experimental Data

One uses the experimental data [7] (Fig. 1) for the $\sigma \sim \epsilon$ relation, obtained for $\dot{\sigma} = 306$ psi/min. For the comparison of the experimental strain $\epsilon = \epsilon(t)$ with the computed one, the experimental data [1, 8, 10] will be used in principle only since these data are obtained in compression and torsion, respectively.

According to the previous discussion, the constitutive equation can be written as

$$E\dot{\epsilon} = \dot{\sigma} + [k_0 + \bar{k}(\sigma)|\sigma - \beta_s \epsilon^{1/2}|]\langle \sigma - \beta_c \epsilon^{\alpha_c} \rangle \tag{10}$$

where $\bar{k}(\sigma)$ is defined by formula (9).

The constants k_0, k_1, and λ were chosen as

$$k_0 = 1 \text{ (min)}^{-1}, \quad k_1 = 1 \text{ (min)}^{-1}\text{(psi)}^{-3}, \quad \lambda = 5 \text{ psi}. \tag{11}$$

Note that the constant k_0 is smaller than the dynamic viscosity coefficient [4] (cf. also [6]) by at least 6 orders of magnitude.

The experimental data of Fig. 1 show that, for strains between 1 percent and 3 percent, large increments of strain are produced for $\sigma_i(\text{psi}) \times 10^{-3} = 5.3; 5.6; 5.85; 6.25; 6.6; 6.8; 7.2; 7.5; 7.75; 8.05; 8.4$.

Note that the horizontal portion of the computed curve increases with the strain as is experimentally observed.

The choice (11) for k_1 and λ in formula (9) gives a variation for the variable viscosity coefficient $k_1\langle \lambda^2 - (\sigma - \sigma_i)^2 \rangle |\sigma - \beta_s \epsilon^{1/2}|$ that ranges from zero up to a value of the order of $10^4 (\text{min})^{-1}$. This means that the maximum value of this coefficient is by 2–3 orders of magnitude smaller than the dynamic viscosity coefficient. By integrating equation (10) where the constants are given by (9) and $\dot{\sigma} = 306$ psi/min. One gets a $\sigma \sim \epsilon$ curve which is close to the experimental one as shown in the figure. On the other hand it follows that the time necessary for the process to move on the vertical and the horizontal portions of the $\sigma \sim \epsilon$ curve is in agreement with the experimental data [1, 8, 10]. The figure also presents the behavior of $\sigma \sim \epsilon$ curves with respect to stress rate changes.

Concluding Remarks

This Note shows, in principle, that the Savart-Masson effect can be described by a rate-type constitutive equation. The viscosity coefficient has strong variations in some regions of the ϵ, σ plane that lie above the equilibrium curve $\sigma = f(\epsilon)$. The Portevin-Le Chatelier (serration) effect is also due to these variations but this assertion will be discussed elsewhere. Since the available experimental results (especially to this author) referring to a given material with a fixed previous thermomechanical history are very limited, an attempt to a deeper analysis of the structure of the viscosity coefficient $k(\epsilon, \sigma)$ could not be performed.

Acknowledgment

The idea on the possibility to describe the Savart-Masson effect by such means as presented here, appeared following a discussion with Prof. C. Foiaş from the University of Bucharest on a possible mechanism to produce earthquakes. The author is deeply indebted to Prof. C. Foiaş for that useful discussion.

References

1 Bell, F. J., "The Experimental Foundations of Solid Mechanics," *Handbuch der Physik*, VIa/1,1973, Springer-Verlag.

2 Malvern, L. E., "The Propagation of Longitudinal Waves of Plastic Deformation in a Bar of Material Exhibiting a Strain Rate Effect," ASME JOURNAL OF APPLIED MECHANICS, Vol. 18, 1951, pp. 203–208; "Plastic Wave Propagation in a Bar of a Material Exhibiting a Strain Rate Effect," *Quarterly of Applied Mathematics*, Vol. 8, 1951, pp. 405–411.

3 Cristescu, N., "A Procedure for Determining the Constitutive Equations for Materials Exhibiting Both Time-Dependent and Time-Independent

Plasticity," *International Journal of Solids and Structures*, Vol. 8, 1972, pp. 511–531.

4 Cristescu, N., and Bell, J. F., "On Unloading in the Symmetrical Impact of Two Aluminum Bars," *Inelastic Behavior of Solids*, eds., Kanninen, M. F., et al., McGraw-Hill, New York, 1970, pp. 397–421.

5 Cristescu, N., and Suliciu I., *Viscoplasticity Editura Technică*, Bucureşti, 1976 (in Romanian); to appear in English, Noordhoff, 1980.

6 Sharpe, W. N., "An Experimental Investigation of the Portevin-la Chatelier Effect in Dead Annealed Commercial Purity Aluminum," Technical Report No. 12, The Johns Hopkins University, Department of Mechanics, 1966.

7 Sharpe, W. N., "The Portevin-le Chatelier Effect in Aluminum Single Crystals and Polycrystals," *Journal of the Mechanics and Physics of Solids*, Vol. 14, 1966, pp. 187–202.

8 Dillon, O. W., "Experimental Data on Aluminum as a Mechanically Unstable Solid," *Journal of the Mechanics and Physics of Solids*, Vol. 11, 1963, pp. 289–304.

9 Gurtin, M. E., Suliciu, I., and Williams, W. O., "On Rate-Type Constitutive Equations and the Energy of Viscoelastic and Viscoplastic Materials," *International Journal of Solids and Structures*, to appear.

10 Kenig, M. J., and Dillon, O. W., Jr., "Shock Waves Produced by Small Stress Increments in Annealed Aluminum," ASME JOURNAL OF APPLIED MECHANICS, Vol. 33, 1966, pp. 907–916.

Crack-Tip Stress and Strain Singularity in Thermally Loaded Elastic-Plastic Material

S. Aoki,[1] K. Kishimoto,[2] and M. Sakata[3]

For the thermal stress problems, an elastic-plastic fracture mechanics parameter, J-integral [1] loses the property of path-independence and it is not evident if the elastic-plastic stress or strain field near a crack tip is characterizable in terms of J-integral. Recently, Wilson, et al. [2], Gurtin [3], and McCartney [4], have discussed path-independent integrals for thermoelasticity. For elastic-plastic problems, Blackburn, et al. [5], Ainsworth, et al. [6], and the present authors [7], have proposed new path-independent integrals, J^*, J_θ, and $\hat{J}$, respectively. In the present paper, the relationship between the $\hat{J}$-integral and the stress or strain near a crack tip in a thermally loaded elastic-plastic material is determined.

We consider a two-dimensional crack in an elastic-plastic body subjected to thermal stress, as shown in Fig. 1. O-X_1, X_2 is the fixed frame and Γ denotes any curve surrounding the crack tip O. A is the area surrounded by the curve Γ and the crack surfaces. For simplicity, we neglect the traction on the crack surfaces, the body forces, the inertia of material, and the fracture process region. The energy-release rate due to crack extension is given by $\hat{J}$-integral [7]:

$$\hat{J} = -\int_\Gamma T_i \frac{\partial u_i}{\partial X_1} d\Gamma + \iint_A \sigma_{ij} \frac{\partial \epsilon_{ij}}{\partial X_1} dA \tag{1}$$

where T_i is surface traction, u_i displacement, σ_{ij} stress tensor, and ϵ_{ij} strain tensor. It has been proved theoretically in the literature [7] that the $\hat{J}$-integral given by equation (1) does not lose the property of path-independence and the physical significance as the energy-release rate, even if the material is not homogeneous.

We decompose the strain ϵ_{ij} into elastic strain $\epsilon_{ij}{}^e$, thermal strain $\epsilon_{ij}{}^t$, and plastic strain $\epsilon_{ij}{}^p$.

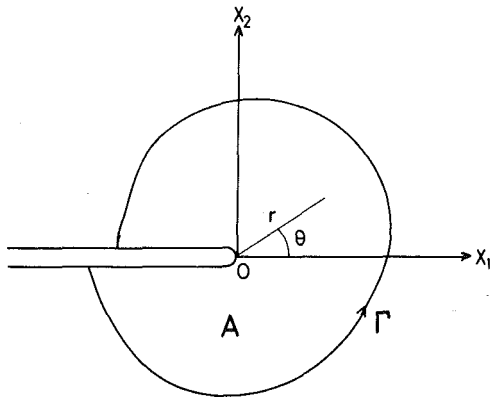

Fig. 1 Crack in elastic-plastic body subjected to thermal loading

$$\epsilon_{ij} = \epsilon_{ij}{}^e + \epsilon_{ij}{}^t + \epsilon_{ij}{}^p \tag{2}$$

In the case when the material under consideration is homogeneous, at least in the X_1-direction, equation (1) becomes

$$\hat{J} = \int_\Gamma W^e dX_2 - \int_\Gamma T_i \frac{\partial u_i}{\partial X_1} d\Gamma + \iint_A \sigma_{ij} \frac{\partial (\epsilon_{ij}{}^t + \epsilon_{ij}{}^p)}{\partial X_1} dA \tag{3}$$

where

$$W^e = \int_0^{\epsilon_{ij}{}^e} \sigma_{ij}\, d\epsilon_{ij}{}^e \tag{4}$$

We assume Γ to be a small circle of radius ρ and consider that the thermal strain $\epsilon_{ij}{}^t$ arises in proportion to temperature increment. It may be assumed that the crack-tip singularity of thermal strain does not exist in the usual circumstances and $\epsilon_{ij}{}^t$ may be neglected compared with $\epsilon_{ij}{}^e$ and $\epsilon_{ij}{}^p$ as $\rho \to 0$. In case that the elastic-plastic behavior is modeled through the deformation plasticity theory and unloading does not occur, the material can be treated as a nonlinear elastic material and hence equations (1) or (3) reduces to

$$\hat{J} = \lim_{\rho \to 0} \left[\int_\Gamma W dX_2 - \int_\Gamma T_i \frac{\partial u_i}{\partial X_1} d\Gamma \right] \tag{5}$$

where

$$W = \int_0^{\epsilon_{ij}} \sigma_{ij} d\epsilon_{ij} \tag{6}$$

Here we have assumed that the material is homogeneous in the small circle of radius ρ. From equation (5), we obtain

$$\hat{J} = \lim_{\rho \to 0} J \tag{7}$$

where J is the Rice J-integral

$$J = \int_\Gamma W dX_2 - \int_\Gamma T_i \frac{\partial u_i}{\partial X_1} d\Gamma \tag{8}$$

Since $\epsilon_{ij}{}^t$ is much smaller than the other strain components as $\rho \to 0$, the stress and strain at the vicinity of the crack tip have the HRR type [8, 9] singularity:

$$\sigma_{ij} = \sigma_Y \left(\frac{E \lim_{\rho \to 0} J}{\sigma_Y{}^2 I_n r} \right)^{1/(n+1)} \tilde{\sigma}_{ij}(\theta, n)$$

$$\epsilon_{ij} = \frac{\sigma_Y}{E} \left(\frac{E \lim_{\rho \to 0} J}{\sigma_Y{}^2 I_n r} \right)^{n/(n+1)} \tilde{\epsilon}_{ij}(\theta, n) \tag{9}$$

where (r, θ) is the polar coordinate system as shown in Fig. 1, E the Young's modulus, σ_Y the yield stress, I_n an integration constant, and

[1] Associate Professor, Department of Engineering Mechanics and Physics, Tokyo Institute of Technology, Ookayama, Meguroku, Tokyo 152, Japan.

[2] Research Associate, Department of Engineering Mechanics and Physics, Tokyo Institute of Technology, Ookayama, Meguroku, Tokyo 152, Japan.

[3] Professor, Department of Engineering Mechanics and Physics, Tokyo Institute of Technology. Ookayama, Meguroku, Tokyo 152, Japan.

Manuscript received by ASME Applied Mechanics Division, September, 1980; final revision, December, 1980.

Plasticity," *International Journal of Solids and Structures*, Vol. 8, 1972, pp. 511–531.

4 Cristescu, N., and Bell, J. F., "On Unloading in the Symmetrical Impact of Two Aluminum Bars," *Inelastic Behavior of Solids*, eds., Kanninen, M. F., et al., McGraw-Hill, New York, 1970, pp. 397–421.

5 Cristescu, N., and Suliciu I., *Viscoplasticity Editura Technică*, Bucureşti, 1976 (in Romanian); to appear in English, Noordhoff, 1980.

6 Sharpe, W. N., "An Experimental Investigation of the Portevin-la Chatelier Effect in Dead Annealed Commercial Purity Aluminum," Technical Report No. 12, The Johns Hopkins University, Department of Mechanics, 1966.

7 Sharpe, W. N., "The Portevin-le Chatelier Effect in Aluminum Single Crystals and Polycrystals," *Journal of the Mechanics and Physics of Solids*, Vol. 14, 1966, pp. 187–202.

8 Dillon, O. W., "Experimental Data on Aluminum as a Mechanically Unstable Solid," *Journal of the Mechanics and Physics of Solids*, Vol. 11, 1963, pp. 289–304.

9 Gurtin, M. E., Suliciu, I., and Williams, W. O., "On Rate-Type Constitutive Equations and the Energy of Viscoelastic and Viscoplastic Materials," *International Journal of Solids and Structures*, to appear.

10 Kenig, M. J., and Dillon, O. W., Jr., "Shock Waves Produced by Small Stress Increments in Annealed Aluminum," ASME JOURNAL OF APPLIED MECHANICS, Vol. 33, 1966, pp. 907–916.

Crack-Tip Stress and Strain Singularity in Thermally Loaded Elastic-Plastic Material

S. Aoki,[1] K. Kishimoto,[2] and M. Sakata[3]

For the thermal stress problems, an elastic-plastic fracture mechanics parameter, J-integral [1] loses the property of path-independence and it is not evident if the elastic-plastic stress or strain field near a crack tip is characterizable in terms of J-integral. Recently, Wilson, et al. [2], Gurtin [3], and McCartney [4], have discussed path-independent integrals for thermoelasticity. For elastic-plastic problems, Blackburn, et al. [5], Ainsworth, et al. [6], and the present authors [7], have proposed new path-independent integrals, J^*, J_θ, and $\hat{J}$, respectively. In the present paper, the relationship between the $\hat{J}$-integral and the stress or strain near a crack tip in a thermally loaded elastic-plastic material is determined.

We consider a two-dimensional crack in an elastic-plastic body subjected to thermal stress, as shown in Fig. 1. O-X_1, X_2 is the fixed frame and Γ denotes any curve surrounding the crack tip O. A is the area surrounded by the curve Γ and the crack surfaces. For simplicity, we neglect the traction on the crack surfaces, the body forces, the inertia of material, and the fracture process region. The energy-release rate due to crack extension is given by $\hat{J}$-integral [7]:

$$\hat{J} = -\int_\Gamma T_i \frac{\partial u_i}{\partial X_1} d\Gamma + \iint_A \sigma_{ij} \frac{\partial \epsilon_{ij}}{\partial X_1} dA \tag{1}$$

where T_i is surface traction, u_i displacement, σ_{ij} stress tensor, and ϵ_{ij} strain tensor. It has been proved theoretically in the literature [7] that the $\hat{J}$-integral given by equation (1) does not lose the property of path-independence and the physical significance as the energy-release rate, even if the material is not homogeneous.

We decompose the strain ϵ_{ij} into elastic strain $\epsilon_{ij}{}^e$, thermal strain $\epsilon_{ij}{}^t$, and plastic strain $\epsilon_{ij}{}^p$.

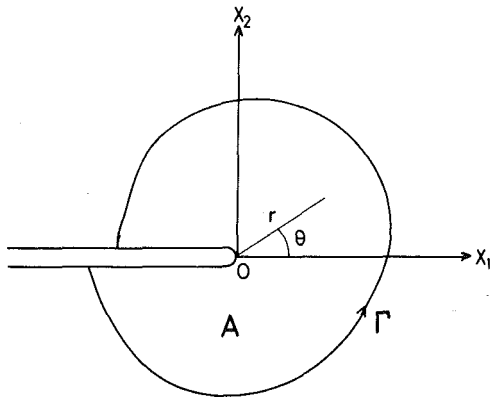

Fig. 1 Crack in elastic-plastic body subjected to thermal loading

$$\epsilon_{ij} = \epsilon_{ij}{}^e + \epsilon_{ij}{}^t + \epsilon_{ij}{}^p \tag{2}$$

In the case when the material under consideration is homogeneous, at least in the X_1-direction, equation (1) becomes

$$\hat{J} = \int_\Gamma W^e dX_2 - \int_\Gamma T_i \frac{\partial u_i}{\partial X_1} d\Gamma + \iint_A \sigma_{ij} \frac{\partial (\epsilon_{ij}{}^t + \epsilon_{ij}{}^p)}{\partial X_1} dA \tag{3}$$

where

$$W^e = \int_0^{\epsilon_{ij}{}^e} \sigma_{ij}\, d\epsilon_{ij}{}^e \tag{4}$$

We assume Γ to be a small circle of radius ρ and consider that the thermal strain $\epsilon_{ij}{}^t$ arises in proportion to temperature increment. It may be assumed that the crack-tip singularity of thermal strain does not exist in the usual circumstances and $\epsilon_{ij}{}^t$ may be neglected compared with $\epsilon_{ij}{}^e$ and $\epsilon_{ij}{}^p$ as $\rho \to 0$. In case that the elastic-plastic behavior is modeled through the deformation plasticity theory and unloading does not occur, the material can be treated as a nonlinear elastic material and hence equations (1) or (3) reduces to

$$\hat{J} = \lim_{\rho \to 0} \left[\int_\Gamma W dX_2 - \int_\Gamma T_i \frac{\partial u_i}{\partial X_1} d\Gamma \right] \tag{5}$$

where

$$W = \int_0^{\epsilon_{ij}} \sigma_{ij} d\epsilon_{ij} \tag{6}$$

Here we have assumed that the material is homogeneous in the small circle of radius ρ. From equation (5), we obtain

$$\hat{J} = \lim_{\rho \to 0} J \tag{7}$$

where J is the Rice J-integral

$$J = \int_\Gamma W dX_2 - \int_\Gamma T_i \frac{\partial u_i}{\partial X_1} d\Gamma \tag{8}$$

Since $\epsilon_{ij}{}^t$ is much smaller than the other strain components as $\rho \to 0$, the stress and strain at the vicinity of the crack tip have the HRR type [8, 9] singularity:

$$\sigma_{ij} = \sigma_Y \left(\frac{E \lim_{\rho \to 0} J}{\sigma_Y{}^2 I_n r} \right)^{1/(n+1)} \tilde{\sigma}_{ij}(\theta, n)$$

$$\epsilon_{ij} = \frac{\sigma_Y}{E} \left(\frac{E \lim_{\rho \to 0} J}{\sigma_Y{}^2 I_n r} \right)^{n/(n+1)} \tilde{\epsilon}_{ij}(\theta, n) \tag{9}$$

where (r, θ) is the polar coordinate system as shown in Fig. 1, E the Young's modulus, σ_Y the yield stress, I_n an integration constant, and

[1] Associate Professor, Department of Engineering Mechanics and Physics, Tokyo Institute of Technology, Ookayama, Meguroku, Tokyo 152, Japan.

[2] Research Associate, Department of Engineering Mechanics and Physics, Tokyo Institute of Technology, Ookayama, Meguroku, Tokyo 152, Japan.

[3] Professor, Department of Engineering Mechanics and Physics, Tokyo Institute of Technology. Ookayama, Meguroku, Tokyo 152, Japan.

Manuscript received by ASME Applied Mechanics Division, September, 1980; final revision, December, 1980.

σ_{ij} and ϵ_{ij} are dimensionless functions of θ and the hardening exponent n. The substitution of equation (7) into equation (9) leads to

$$\sigma_{ij} = \sigma_Y \left(\frac{E\hat{J}}{\sigma_Y{}^2 I_n r}\right)^{1/(n+1)} \tilde{\sigma}_{ij}(\theta,n)$$
$$\epsilon_{ij} = \frac{\sigma_Y}{E}\left(\frac{E\hat{J}}{\sigma_Y{}^2 I_n r}\right)^{n/(n+1)} \tilde{\epsilon}_{ij}(\theta,n) \quad (10)$$

Thus, for thermal stress problem, the stress and strain near the crack tip are uniquely determined by the $\hat{J}$-integral. Even in the case when the elastic-plastic behavior is best modeled with the flow theory of plasticity, the deformation near the crack-tip may be characterized by the HRR singularity (and then equation (10) may hold) except for very small region at the crack tip [10].

References

1 Rice, J. R., "A Path-Independent Integral and the Approximate Analysis of Strain Concentration by Notches and Cracks," ASME JOURNAL OF APPLIED MECHANICS, Vol. 35, 1968, pp. 379–386.

2 Wilson, W. K., and Yu, I. W., "The Use of the J-Integral in Thermal Stress Crack Problems," *International Journal of Fracture*, Vol. 15, No. 4, 1979, pp. 377–387.

3 Gurtin, M. E., "On a Path-Independent Integral for Thermoelasticity," *International Journal of Fracture*, Vol. 15, No. 5, 1979, pp. R169–R170.

4 McCartney, L. N., Discussion on "The Use of the J-Integral in Thermal Stress Crack Problem by Wilson, W. K., and Yu, I. W.," *International Journal of Fracture*, Vol. 16, No. 6, 1979, pp. R217–R221.

5 Blackburn, W. S., Jackson, A. D., and Hellen, T. K., "An Integral Associated With the State of a Crack Tip in a Nonelastic Material," *International Journal of Fracture*, Vol. 13, No. 2, 1977, pp. 183–199.

6 Ainsworth, R. A., Neale, B. K., and Prince, R. H., "Fracture Behaviour in the Presence of Thermal Strains," *Proceedings of the Institution of Mechanical Engineers*, Conference on Tolerance of Flaws in Pressurized Components, London, May 1978, p. 197; (quoted in "Methods for Post-Yield Fracture Safety Assessment," by Turner, C. E., Post-Yield Fracture Mechanics, ed., Latzko, D. G. H., London, Applied Science, 1979, Chapter 2).

7 Kishimoto, K., Aoki, S., and Sakata, M., "On Path-Independent Integral, $\hat{J}$," *Engineering Fracture Mechanics*, Vol. 13, No. 4, 1980, pp. 841–850.

8 Hutchinson, J. W., "Singular Behavior at the End of a Tensile Crack in a Hardening Material," *Journal of the Mechanics and Physics of Solids*, Vol. 16, No. 1, 1968, pp. 13–31.

9 Rice, J. R., and Rosengren, G. F., "Plane Strain Deformation Near a Crack Tip in a Power Law Hardening Material," *Journal of the Mechanics and Physics of Solids*, Vol. 16, No. 1, 1968, pp. 1–12.

10 Shih, C. F., deLorenzi, H. G., and Andrews, W. R., "Studies on Crack Initiation and Stable Crack Growth," *Elastic-Plastic Fracture*, ASTM STP 668, eds., Landes, J. D., Begley, J. A., and Clarke, G. A., American Society for Testing and Materials, 1979, pp. 65–120.

Effect of the External Load on the Thermoelastoplastic Creep Deformation

H. Ishikawa[1]

Introduction

In the author's previous papers the transient inelastic deformations of a heated circular solid [1] and hollow [2] cylinder are analyzed considering the static primary creep with Norton's law. The effect of the external load at various temperature levels on the creep deformation is discussed here in detail with the strain-hardening hypothesis for physical primary creep. The thermal and material properties are reasonably assumed to be temperature-dependent to describe precisely the actual behavior of a material at elevated temperature.

Analysis

We consider an infinite solid circular cylinder of radius a, which is initially under the mean axial stress p. Then it is subjected to an axial symmetric temperature distribution which varies with time, assuming the zero initial uniform temperature of the cylinder.

If the temperature at a generic radius r is T at time t, then the total strain should be written as

$$\epsilon_r = \epsilon_r{}^e + \int \alpha dT + \epsilon_r{}^p + \epsilon_r{}^c, \text{ etc.} \quad (1)$$

where superscripts e, p, and c denote elastic, plastic, and creep components, respectively, and α is the coefficient of thermal expansion. The time-independent plastic strain and the time-dependent creep strain should not be strictly distinguished from each other in the phenomelogical sense as the experiments show that these two components are not really different [3]. However, for convenience sake they could be separated as in (1), in engineering sense, following the customary concept [4].

The basic formulation has been given in [2] based on the incremental theory of plasticity and the Mises-Mises creep theory. Moreover, the axial strain ϵ_z is assumed not to depend on r and z, and determined from the condition of the axial force i.e., $2\pi \int_0^a \sigma_z r dr = \pi a^2 p$. Mendelson's [5] method of successive elastic solutions is used also in its modified total strain form to calculate the plastic, and creep strain increments as in [2]. Namely, using the von Mises yield criterion and the Prandtl-Reuss equations, the plastic strain increments can be obtained. The constitutive equation to calculate the plastic strain increments is the following Ramberg-Osgood stress-strain relation [6] in temperature fields

$$E\epsilon_t = \sigma_t\left[1 + \frac{3}{7}\left(\frac{\sigma_t}{\sigma_1}\right)^{q-1}\right] \quad (2)$$

where ϵ_t and σ_t are the uniaxial strain and stress, and σ_1 is the yield stress.

The creep strain increments can be presented with Mises-Mises theory of creep [7], and the equivalent creep strain increment is determined from the strain-hardening creep law that corresponds to the constant stress relation in uniaxial state [7], which shows the following physical primary creep as the constitutive equation:

$$\epsilon_t{}^c = A\,\sigma_t{}^n\, t^m, \quad m < 1 \quad (3)$$

where A, n, and m are temperature-dependent material properties.

Results

In the numerical calculations, the solid circular cylinder is divided into 80 radial increments, whereas the period during which the plastic and creep deformations proceed is divided into 200 time increments. For $q = 19$ in stress-strain relation (2), corresponding to austenitic stainless steel (ASTM 316N), we assume the coefficient of thermal expansion α, the conductivity K, the elastic modulus E and the yield stress σ_1 as

$$\alpha = 16.5 \times (1 - 5.52 \times 10^{-4} \times T) \times 10^{-6} \quad (\text{m/K}),$$
$$K = 11.0 \times (1 + 1.82 \times 10^{-3} \times T) \quad (\text{W/mK}),$$
$$E = 206 \times (1 - 5.08 \times 10^{-7} \times T^2) \times 10^9 \ (\text{N/m}^2),$$
$$\sigma_1 = 320 \times (1 - 2.05 \times 10^{-3} \times T + 3.26 \times 10^{-6} \times T^2 - 1.92 \times 10^{-9} \times T^3) \times 10^6 \ (\text{N/m}^2) \quad (4)$$

for $T < 732.2°\text{C}$,

$$A = \exp\,[(T - 1869.3)/60.39]$$
$$m = 2.398 \times 10^{-3} \times T - 0.8226, \quad n = 3.6 \times 10^{-3} \times T + 2.964,$$

and for $T \geq 732.2°\text{C}$

$$A = \exp\,[(T - 1102.3)/19.66], \quad m = 0.933, \quad n = 5.6 \quad (5)$$

[1] Presently, c/o Professor H. Lippmann, Lehrstuhl A für Mechanik, Technische Universität München, Arcisstrasse 21, 8000 Munchen 2, West Germany; after September 30, 1981, Associate Professor, Department of Mechanical Engineering II, Hokkaido University, Sapporo, 060 Japan.

Manuscript received by ASME Applied Mechanics Division, July, 1980; final revision, November, 1980.

σ_{ij} and ϵ_{ij} are dimensionless functions of θ and the hardening exponent n. The substitution of equation (7) into equation (9) leads to

$$\sigma_{ij} = \sigma_Y \left(\frac{E\hat{J}}{\sigma_Y{}^2 I_n r}\right)^{1/(n+1)} \tilde{\sigma}_{ij}(\theta,n)$$
$$\epsilon_{ij} = \frac{\sigma_Y}{E}\left(\frac{E\hat{J}}{\sigma_Y{}^2 I_n r}\right)^{n/(n+1)} \tilde{\epsilon}_{ij}(\theta,n) \quad (10)$$

Thus, for thermal stress problem, the stress and strain near the crack tip are uniquely determined by the $\hat{J}$-integral. Even in the case when the elastic-plastic behavior is best modeled with the flow theory of plasticity, the deformation near the crack-tip may be characterized by the HRR singularity (and then equation (10) may hold) except for very small region at the crack tip [10].

References

1 Rice, J. R., "A Path-Independent Integral and the Approximate Analysis of Strain Concentration by Notches and Cracks," ASME JOURNAL OF APPLIED MECHANICS, Vol. 35, 1968, pp. 379–386.

2 Wilson, W. K., and Yu, I. W., "The Use of the J-Integral in Thermal Stress Crack Problems," *International Journal of Fracture*, Vol. 15, No. 4, 1979, pp. 377–387.

3 Gurtin, M. E., "On a Path-Independent Integral for Thermoelasticity," *International Journal of Fracture*, Vol. 15, No. 5, 1979, pp. R169–R170.

4 McCartney, L. N., Discussion on "The Use of the J-Integral in Thermal Stress Crack Problem by Wilson, W. K., and Yu, I. W.," *International Journal of Fracture*, Vol. 16, No. 6, 1979, pp. R217–R221.

5 Blackburn, W. S., Jackson, A. D., and Hellen, T. K., "An Integral Associated With the State of a Crack Tip in a Nonelastic Material," *International Journal of Fracture*, Vol. 13, No. 2, 1977, pp. 183–199.

6 Ainsworth, R. A., Neale, B. K., and Prince, R. H., "Fracture Behaviour in the Presence of Thermal Strains," *Proceedings of the Institution of Mechanical Engineers*, Conference on Tolerance of Flaws in Pressurized Components, London, May 1978, p. 197; (quoted in "Methods for Post-Yield Fracture Safety Assessment," by Turner, C. E., Post-Yield Fracture Mechanics, ed., Latzko, D. G. H., London, Applied Science, 1979, Chapter 2).

7 Kishimoto, K., Aoki, S., and Sakata, M., "On Path-Independent Integral, $\hat{J}$," *Engineering Fracture Mechanics*, Vol. 13, No. 4, 1980, pp. 841–850.

8 Hutchinson, J. W., "Singular Behavior at the End of a Tensile Crack in a Hardening Material," *Journal of the Mechanics and Physics of Solids*, Vol. 16, No. 1, 1968, pp. 13–31.

9 Rice, J. R., and Rosengren, G. F., "Plane Strain Deformation Near a Crack Tip in a Power Law Hardening Material," *Journal of the Mechanics and Physics of Solids*, Vol. 16, No. 1, 1968, pp. 1–12.

10 Shih, C. F., deLorenzi, H. G., and Andrews, W. R., "Studies on Crack Initiation and Stable Crack Growth," *Elastic-Plastic Fracture*, ASTM STP 668, eds., Landes, J. D., Begley, J. A., and Clarke, G. A., American Society for Testing and Materials, 1979, pp. 65–120.

Effect of the External Load on the Thermoelastoplastic Creep Deformation

H. Ishikawa[1]

Introduction

In the author's previous papers the transient inelastic deformations of a heated circular solid [1] and hollow [2] cylinder are analyzed considering the static primary creep with Norton's law. The effect of the external load at various temperature levels on the creep deformation is discussed here in detail with the strain-hardening hypothesis for physical primary creep. The thermal and material properties are reasonably assumed to be temperature-dependent to describe precisely the actual behavior of a material at elevated temperature.

Analysis

We consider an infinite solid circular cylinder of radius a, which is initially under the mean axial stress p. Then it is subjected to an axial symmetric temperature distribution which varies with time, assuming the zero initial uniform temperature of the cylinder.

If the temperature at a generic radius r is T at time t, then the total strain should be written as

$$\epsilon_r = \epsilon_r{}^e + \int \alpha dT + \epsilon_r{}^p + \epsilon_r{}^c, \text{ etc.} \quad (1)$$

where superscripts e, p, and c denote elastic, plastic, and creep components, respectively, and α is the coefficient of thermal expansion. The time-independent plastic strain and the time-dependent creep strain should not be strictly distinguished from each other in the phenomelogical sense as the experiments show that these two components are not really different [3]. However, for convenience sake they could be separated as in (1), in engineering sense, following the customary concept [4].

The basic formulation has been given in [2] based on the incremental theory of plasticity and the Mises-Mises creep theory. Moreover, the axial strain ϵ_z is assumed not to depend on r and z, and determined from the condition of the axial force i.e., $2\pi \int_0^a \sigma_z r dr = \pi a^2 p$. Mendelson's [5] method of successive elastic solutions is used also in its modified total strain form to calculate the plastic, and creep strain increments as in [2]. Namely, using the von Mises yield criterion and the Prandtl-Reuss equations, the plastic strain increments can be obtained. The constitutive equation to calculate the plastic strain increments is the following Ramberg-Osgood stress-strain relation [6] in temperature fields

$$E\epsilon_t = \sigma_t\left[1 + \frac{3}{7}\left(\frac{\sigma_t}{\sigma_1}\right)^{q-1}\right] \quad (2)$$

where ϵ_t and σ_t are the uniaxial strain and stress, and σ_1 is the yield stress.

The creep strain increments can be presented with Mises-Mises theory of creep [7], and the equivalent creep strain increment is determined from the strain-hardening creep law that corresponds to the constant stress relation in uniaxial state [7], which shows the following physical primary creep as the constitutive equation:

$$\epsilon_t{}^c = A\,\sigma_t{}^n\, t^m, \quad m < 1 \quad (3)$$

where A, n, and m are temperature-dependent material properties.

Results

In the numerical calculations, the solid circular cylinder is divided into 80 radial increments, whereas the period during which the plastic and creep deformations proceed is divided into 200 time increments. For $q = 19$ in stress-strain relation (2), corresponding to austenitic stainless steel (ASTM 316N), we assume the coefficient of thermal expansion α, the conductivity K, the elastic modulus E and the yield stress σ_1 as

$$\alpha = 16.5 \times (1 - 5.52 \times 10^{-4} \times T) \times 10^{-6} \quad (\text{m/K}),$$
$$K = 11.0 \times (1 + 1.82 \times 10^{-3} \times T) \quad (\text{W/mK}),$$
$$E = 206 \times (1 - 5.08 \times 10^{-7} \times T^2) \times 10^9 \ (\text{N/m}^2),$$
$$\sigma_1 = 320 \times (1 - 2.05 \times 10^{-3} \times T + 3.26 \times 10^{-6} \times T^2 - 1.92 \times 10^{-9} \times T^3) \times 10^6 \ (\text{N/m}^2) \quad (4)$$

for $T < 732.2°\text{C}$,

$$A = \exp\,[(T - 1869.3)/60.39]$$
$$m = 2.398 \times 10^{-3} \times T - 0.8226, \quad n = 3.6 \times 10^{-3} \times T + 2.964,$$

and for $T \geq 732.2°\text{C}$

$$A = \exp\,[(T - 1102.3)/19.66], \quad m = 0.933, \quad n = 5.6 \quad (5)$$

---

[1] Presently, c/o Professor H. Lippmann, Lehrstuhl A für Mechanik, Technische Universität München, Arcisstrasse 21, 8000 Munchen 2, West Germany; after September 30, 1981, Associate Professor, Department of Mechanical Engineering II, Hokkaido University, Sapporo, 060 Japan.

Manuscript received by ASME Applied Mechanics Division, July, 1980; final revision, November, 1980.

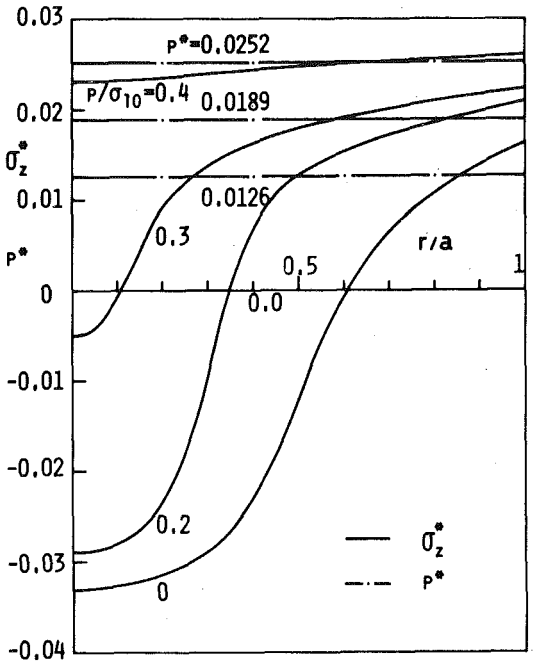

Fig. 1 Axial stress σ_z^*

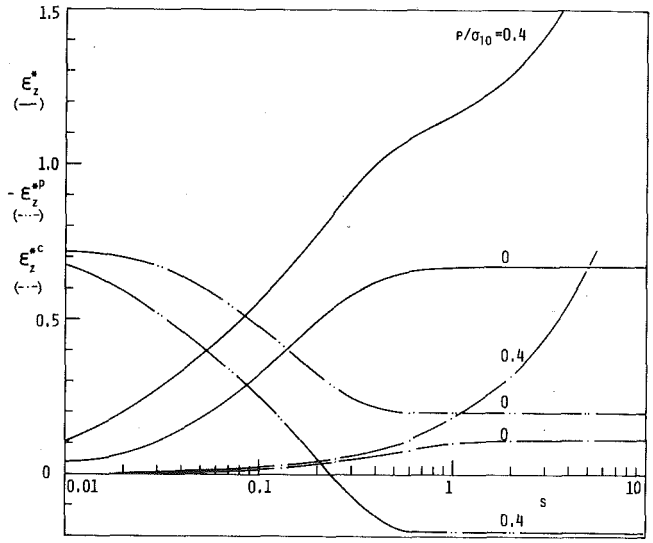

Fig. 2 Total strain ϵ_z^*, plastic strain ϵ_z^{*p}, and creep strain ϵ_z^{*c}

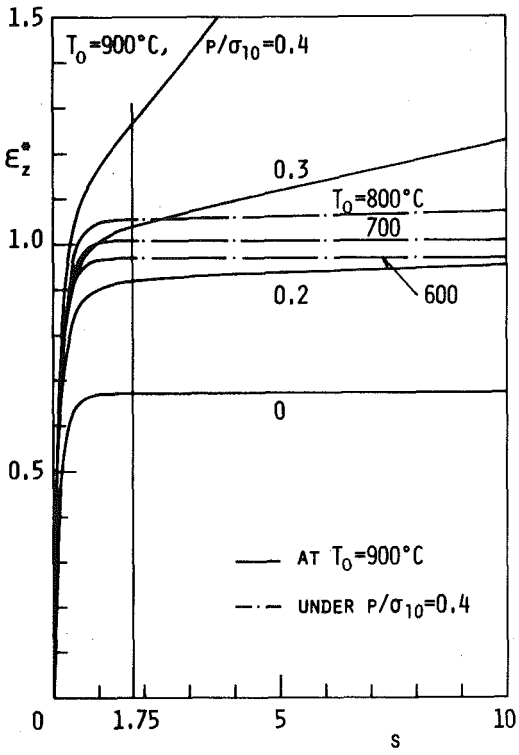

Fig. 3 Axial strain ϵ_z^*

In (4), the coefficient of thermal expansion, the conductivity, and the elastic modulus have been interporated from the data given in [8], whereas the yield stress and material properties for creep are taken from [9]. Moreover, the thermal diffusivity is taken to be $h = 5.29$ mm^2/sec from [8] and Poisson's ratio ν is assumed to be unaffected by temperature and to be equal to 0.4.

In Figs. 1–3, the nondimensional representations are used, that is, $\sigma_z^* = (1-\nu)\sigma_z/E_0\alpha_0T_0$, $p^* = (1-\nu)p/E_0\alpha_0T_0$, $\epsilon_z^* = (1-\nu)\epsilon_z/\alpha_0T_0$, and $s = (h/a^2)t$, where E_0 and α_0 are the elastic modulus and the coefficient of thermal expansion at $T = 0$ in (4), and T_0 is the constant surface temperature to which the boundary of the cylinder is suddenly exposed. Also in these Figs. 1–3, σ_{10} is the yield stress at $T = 0$ in (4). All results presented in this Note were calculated for a solid circular cylinder of radius $a = 3$ mm. Then the relation between the real time t and the dimensionless time s becomes to $t = (a^2/h)s = 1.70s$ (sec).

Fig. 1 shows the variation of σ_z with r/a for different values of the external load p/σ_{10} at time $s = 1.75$, i.e., $t = 3$ (sec), when the steady state of temperature, that is $T = 900°C$ at every place of the cylinder, is attained after subjection to rapid surface heating with the step temperature rise of $T_0 = 900°C$. With large external load ($p/\sigma_{10} = 0.4$), the other two stresses σ_r^* and σ_θ^* become almost zero because the thermal stresses caused by the variation of temperature after subjection to rapid surface heating have relaxed from the large creep strain. In the meantime, σ_z^* will be expected to be equal to its mean tensile stress p^* in the whole cylinder from the relaxation of thermal stress, and in fact for $p/\sigma_{10} = 0.4$ in Fig. 1, σ_z^* takes almost near values of $\sigma_z^* = p^* = 0.0252$. The numerals $p^* = 0.0189$ and 0.0126 in Fig. 1 correspond to the values $p/\sigma_{10} = 0.3$ and 0.2, respectively.

Fig. 2 shows the variations ϵ_z^*, ϵ_z^{*p}, and ϵ_z^{*c} at the surface of the cylinder with s for the two values of the external load, i.e., $p/\sigma_{10} = 0.4$ and 0 with the reference temperature $T_0 = 900°C$. Taking into consideration the fact that the temperature at the surface attains its constant value of $T = 900°C$ in the instant of being subjected to rapid surface heating and the fact that the total strain consists of an elastic, plastic, and creep strain together with thermal expansion, as is given in (1), it can be easily recognized from this Fig. 2 that the plastic strain, to which the special attention should be paid because of its minus sign, is dominant in the deformation of structure at the earlier stage, whereas the creep strain plays the important role after the plastic strain becomes constant, when the thermal stress is not produced any more. At $p/\sigma_{10} = 0.4$, ϵ_z^* increases with s because of the increase of creep strain, which is accompanied with the relaxation of stresses as shown in Fig. 1. On the contrary, at $p/\sigma_{10} = 0$, ϵ_z^* maintains its constant value except the earlier stage of deformation because of very little increase of creep strain. Including both results, the effect of the external load on the deformation of structure with constant $T_0 = 900°C$ is shown in Fig. 3 with the solid lines. With increase of p/σ_{10}, increases ϵ_z^* as might be expected, while the effect of the magnitude of step temperature T_0 on ϵ_z^* with constant $p/\sigma_{10} = 0.4$ is also shown in this figure with the dash-dot lines. At $T_0 = 900°C$ the extremely larger creep strain makes the outstanding characteristic in the behavior of the deformation, whereas even at $T_0 = 800°C$, the temperature should not effect much on the deformation of structure, showing the resistance of this stainless steel to creep deformation.

References

1 Ishikawa, H., "Relaxation of Termal Stress in a Circular Solid Cylinder From Creep Deformation," *Journal of Thermal Stresses*, Vol. 3, 1979, pp. 9–20.

2 Ishikawa, H., and Hata, K., "Thermoelastoplastic Creep Stress Analysis for a Thick-Walled Tube," *International Journal of Solids and Structures*, Vol. 16, No. 4, 1980, pp. 291–299.

3 Hart, E. W., "Constitutive Relations for the Nonelastic Deformation of Metals," *Journal of Engineering Materials and Technology*, Vol. 98, 1976, pp. 193–202.

4 Leckie, F. A., "Creep in Structure," ed., Hult, J., IUTAM Symposium, Gothenburg, 1970.

5 Mendelson, A., *Plasticity, Theory, and Application*, Macmillan, New York, 1968.

6 Ramberg, W., and Osgood, W. R., "Description of Stress-Strain Curves by Three Parameters," NACA TN-902, 1943.

7 Hult, J. A., *Creep in Engineering Structures*, Blaisdell, 1966.

8 Odqvist, F. K. G., *Mathematical Theory of Creep and Creep Rupture*, 2d ed., Clarendon, Oxford, 1974.

9 Kadlecek, P., "Mechanical Properties of Hot-Extruded 304N and 316N Stainless Steel Pipe," ASTM STP 522, 1973.

Some Observations in the Behavior of Laminated Composite Beams

K. M. Rao[1]

In recent years the analysis of structural members of composite materials has received the attention of many investigators. The behavior of these structural members depend on relative stiffness and thickness of layers, boundary conditions, and continuity conditions at the interfaces. Moreover accuracy of the results depend on the degree of refinement of the theory. The influence of the foregoing factors are studied by DiTaranto [1] and Rao [2] using strength of materials theory. Integral equation approach for formulating the Airy's stress function satisfying the equations of elastic anisotropic medium is suggested by Schile [4, 5]. A simple and straightforward procedure to select polynomial Airy's stress function, a special case of that of Schile [4, 5] suitable to analyze rectangular laminated beams under polynomial loading is proposed in reference [3] by the author. Here the author aims to study the influence of the aforementioned factors on the behavior of laminated composite beams using the foregoing procedure to select Airy's stress function. This refined solution, when applied to clamped-clamped laminated beam, brings out some strange and interesting observations in its behavior, and these observations are found to be contradictory to those given by elementary theories [1, 2] of certain layer-materials combinations.

Analysis

The beam shown in Fig. 1 is assumed to be made of an arbitrary number of layers N wherein each layer is of specially orthotropic medium, and the interlayer surfaces are perfectly bonded. The beam is subjected to a normal surface traction of intensity q; under these conditions each layer is in a state of generalized plane stress. The compatibility condition of nth layer of such a beam is [3]

$$\frac{\partial^4 \phi_n}{\partial x^4} + (k_{1n}^2 + k_{2n}^2)\frac{\partial^4 \phi_n}{\partial x^2 \partial y^2} + k_{1n}^2 k_{2n}^2 \frac{\partial^4 \phi_n}{\partial y^4} = 0 \qquad (1)$$

in which $\phi_n(x, y)$ is Airy's stress function, and

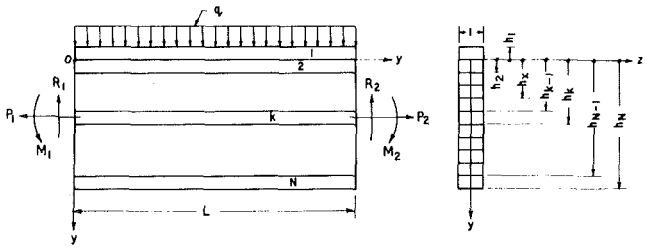

Fig. 1 Geometry of the beam

$$k_{1n}^2 + k_{2n}^2 = (2S_{12n} + S_{33n})/S_{22n}, \quad k_{1n}^2 k_{2n}^2 = S_{11n}/S_{22n} \qquad (2)$$

In equation (2), S_{11n}, S_{12n}, S_{22n}, and S_{33n} are the elastic constants of nth layer; the corresponding strain-stress relations are

$$e_{xn} = S_{11n}\sigma_{xn} + S_{12n}\sigma_{yn}, \quad e_{yn} = S_{12n}\sigma_{xn} + S_{22n}\sigma_{yn}, \quad e_{xyn} = S_{33n}\tau_{xyn} \qquad (3)$$

where e_{xn}, e_{yn}, e_{xyn} are the engineering strains, and $\sigma_{xn}, \sigma_{yn}, \tau_{xyn}$ are the stresses in nth layer. These quantities are defined by

$$e_{xn} = \frac{\partial u_n}{\partial x}, \quad e_{yn} = \frac{\partial yn}{\partial y}, \quad e_{xyn} = \frac{\partial u_n}{\partial y} + \frac{\partial v_n}{\partial x} \qquad (4)$$

$$\sigma_{xn} = \frac{\partial^2 \phi_n}{\partial y^2}, \quad \sigma_{yn} = \frac{\partial^2 \phi_n}{\partial \chi^2}, \quad \tau_{xyn} = -\frac{\partial^2 \phi_n}{\partial x \partial y} \qquad (5)$$

where $u_n(x, y)$ and $v_n(x, y)$ are the deformations along x and y-axes, respectively (Fig. 1).

According to the procedure proposed by the author [3] to select the polynomial Airy's stress function, stress function $\phi_n(x, y)$ for nth layer of the beam under uniformly distributed load is

$$\phi_n(x, y) = a_{2n}x^2/2 + b_{2n}xy + c_{2n}y^2/2 + b_{3n}x^2y/2 + c_{3n}xy^2/2 + d_{3n}y^3/6 + c_{4n}x^2y^2/2 + d_{4n}xy^3/6 + e_{4n}y^4/12 + d_{5n}x^2y^3/6 + f_{5n}y^5/20 \qquad (6)$$

in which

$$e_{4n} = -(k_{1n}^2 + k_{2n}^2)c_{4n}/k_{1n}^2 k_{2n}^2, \quad f_{5n} = -(k_{1n}^2 + k_{2n}^2)d_{5n}/k_{1n}^2 k_{2n}^2 \qquad (7)$$

and $a_{2n}, b_{2n} \ldots, f_{5n}$ are the coefficients of stress function.

The boundary and continuity conditions, to be used to evaluate the aforementioned coefficients, are

$$\sigma_{y1} = -q, \tau_{xy1} = 0 \quad \text{at} \quad y = -h1;$$

$$\sigma_{y1} = \sigma_{y2}, \tau_{xy1} = \tau_{xy2}, u_1 = u_2, v_1 = v_2 \quad \text{at} \quad y = 0;$$

$$\sigma_{yn} = \sigma_{yn+1}, \tau_{xyn} = \tau_{xyn+1}, u_n = u_{n+1}, v_n = v_{n+1} \quad \text{at} \quad y = h_n \ (n = 2, 3, .. N - 1);$$

$$\sigma_{yN} = \tau_{xyN} = 0 \quad \text{at} \quad y = hN;$$

$$\sum_{n=1}^{N} \int_{y'_{n-1}}^{y_n} (\sigma_{xn}dy, \sigma_{xn}(y - H)dy, \tau_{xyn}dy) = (P_1, -M_1, R_1) \quad \text{at} \quad x = 0 \qquad (8)$$

in which

$$H = (h_{k-1} + h_k)/2 \qquad (9)$$

indicates the location of end points of the kth layer that are constrained kinematically, and

$$y_1 = 0, \qquad y_n = h_n \quad (n = 2, 3, \ldots, N)$$

$$y'_1 = -h_1, \quad y'_2 = 0, \quad y'_{n-1} = h_{n-1} \quad (n = 3, 4, \ldots, N)$$

In the previous expressions, h_n is the distance of the farthest longitudinal surface of nth layer measured from x-axis; P_1, M_1, and R_1 are the reactions at the end $x = 0$ (Fig. 1).

[1] Assistant Professor, Department of Mechanical Engineering, I.I.T., Kharagpur-721302, India.

Manuscript received by ASME Applied Mechanics Division, May, 1980; final revision, November, 1980.

References

1 Ishikawa, H., "Relaxation of Termal Stress in a Circular Solid Cylinder From Creep Deformation," *Journal of Thermal Stresses*, Vol. 3, 1979, pp. 9–20.

2 Ishikawa, H., and Hata, K., "Thermoelastoplastic Creep Stress Analysis for a Thick-Walled Tube," *International Journal of Solids and Structures*, Vol. 16, No. 4, 1980, pp. 291–299.

3 Hart, E. W., "Constitutive Relations for the Nonelastic Deformation of Metals," *Journal of Engineering Materials and Technology*, Vol. 98, 1976, pp. 193–202.

4 Leckie, F. A., "Creep in Structure," ed., Hult, J., IUTAM Symposium, Gothenburg, 1970.

5 Mendelson, A., *Plasticity, Theory, and Application*, Macmillan, New York, 1968.

6 Ramberg, W., and Osgood, W. R., "Description of Stress-Strain Curves by Three Parameters," NACA TN-902, 1943.

7 Hult, J. A., *Creep in Engineering Structures*, Blaisdell, 1966.

8 Odqvist, F. K. G., *Mathematical Theory of Creep and Creep Rupture*, 2d ed., Clarendon, Oxford, 1974.

9 Kadlecek, P., "Mechanical Properties of Hot-Extruded 304N and 316N Stainless Steel Pipe," ASTM STP 522, 1973.

Some Observations in the Behavior of Laminated Composite Beams

K. M. Rao[1]

In recent years the analysis of structural members of composite materials has received the attention of many investigators. The behavior of these structural members depend on relative stiffness and thickness of layers, boundary conditions, and continuity conditions at the interfaces. Moreover accuracy of the results depend on the degree of refinement of the theory. The influence of the foregoing factors are studied by DiTaranto [1] and Rao [2] using strength of materials theory. Integral equation approach for formulating the Airy's stress function satisfying the equations of elastic anisotropic medium is suggested by Schile [4, 5]. A simple and straightforward procedure to select polynomial Airy's stress function, a special case of that of Schile [4, 5] suitable to analyze rectangular laminated beams under polynomial loading is proposed in reference [3] by the author. Here the author aims to study the influence of the aforementioned factors on the behavior of laminated composite beams using the foregoing procedure to select Airy's stress function. This refined solution, when applied to clamped-clamped laminated beam, brings out some strange and interesting observations in its behavior, and these observations are found to be contradictory to those given by elementary theories [1, 2] of certain layer-materials combinations.

Analysis

The beam shown in Fig. 1 is assumed to be made of an arbitrary number of layers N wherein each layer is of specially orthotropic medium, and the interlayer surfaces are perfectly bonded. The beam is subjected to a normal surface traction of intensity q; under these conditions each layer is in a state of generalized plane stress. The compatibility condition of nth layer of such a beam is [3]

$$\frac{\partial^4\phi_n}{\partial x^4} + (k_{1n}^2 + k_{2n}^2)\frac{\partial^4\phi_n}{\partial x^2\partial y^2} + k_{1n}^2 k_{2n}^2 \frac{\partial^4\phi_n}{\partial y^4} = 0 \tag{1}$$

in which $\phi_n(x, y)$ is Airy's stress function, and

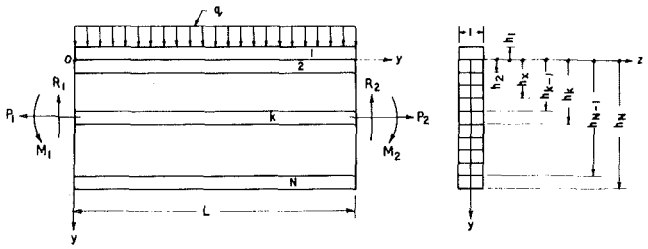

Fig. 1 Geometry of the beam

$$k_{1n}^2 + k_{2n}^2 = (2S_{12n} + S_{33n})/S_{22n}, \quad k_{1n}^2 k_{2n}^2 = S_{11n}/S_{22n} \tag{2}$$

In equation (2), S_{11n}, S_{12n}, S_{22n}, and S_{33n} are the elastic constants of nth layer; the corresponding strain-stress relations are

$$e_{xn} = S_{11n}\sigma_{xn} + S_{12n}\sigma_{yn}, \quad e_{yn} = S_{12n}\sigma_{xn} + S_{22n}\sigma_{yn}, \quad e_{xyn} = S_{33n}\tau_{xyn} \tag{3}$$

where e_{xn}, e_{yn}, e_{xyn} are the engineering strains, and σ_{xn}, σ_{yn}, τ_{xyn} are the stresses in nth layer. These quantities are defined by

$$e_{xn} = \frac{\partial u_n}{\partial x}, \quad e_{yn} = \frac{\partial yn}{\partial y}, \quad e_{xyn} = \frac{\partial u_n}{\partial y} + \frac{\partial v_n}{\partial x} \tag{4}$$

$$\sigma_{xn} = \frac{\partial^2\phi_n}{\partial y^2}, \quad \sigma_{yn} = \frac{\partial^2\phi_n}{\partial \chi^2}, \quad \tau_{xyn} = -\frac{\partial^2\phi_n}{\partial x\,\partial y} \tag{5}$$

where $u_n(x, y)$ and $v_n(x, y)$ are the deformations along x and y-axes, respectively (Fig. 1).

According to the procedure proposed by the author [3] to select the polynomial Airy's stress function, stress function $\phi_n(x, y)$ for nth layer of the beam under uniformly distributed load is

$$\phi_n(x, y) = a_{2n}x^2/2 + b_{2n}xy + c_{2n}y^2/2 + b_{3n}x^2y/2 + c_{3n}xy^2/2 + d_{3n}y^3/6 + c_{4n}x^2y^2/2 + d_{4n}xy^3/6 + e_{4n}y^4/12 + d_{5n}x^2y^3/6 + f_{5n}y^5/20 \tag{6}$$

in which

$$e_{4n} = -(k_{1n}^2 + k_{2n}^2)c_{4n}/k_{1n}^2k_{2n}^2, \quad f_{5n} = -(k_{1n}^2 + k_{2n}^2)d_{5n}/k_{1n}^2k_{2n}^2 \tag{7}$$

and $a_{2n}, b_{2n} \ldots, f_{5n}$ are the coefficients of stress function.

The boundary and continuity conditions, to be used to evaluate the aforementioned coefficients, are

$$\sigma_{y1} = -q, \tau_{xy1} = 0 \quad \text{at} \quad y = -h1;$$

$$\sigma_{y1} = \sigma_{y2}, \tau_{xy1} = \tau_{xy2}, u_1 = u_2, v_1 = v_2 \quad \text{at} \quad y = 0;$$

$$\sigma_{yn} = \sigma_{yn+1}, \tau_{xyn} = \tau_{xyn+1}, u_n = u_{n+1}, v_n = v_{n+1} \quad \text{at} \quad y = h_n \ (n = 2, 3, .. N - 1);$$

$$\sigma_{yN} = \tau_{xyN} = 0 \quad \text{at} \quad y = hN;$$

$$\sum_{n=1}^{N} \int_{y'_{n-1}}^{y_n} (\sigma_{xn}dy, \sigma_{xn}(y - H)dy, \tau_{xyn}dy) = (P_1, -M_1, R_1) \quad \text{at} \quad x = 0 \tag{8}$$

in which

$$H = (h_{k-1} + h_k)/2 \tag{9}$$

indicates the location of end points of the kth layer that are constrained kinematically, and

$$y_1 = 0, \qquad y_n = h_n \quad (n = 2, 3, \ldots, N)$$

$$y'_1 = -h_1, \quad y'_2 = 0, \quad y'_{n-1} = h_{n-1} \quad (n = 3, 4, \ldots, N)$$

In the previous expressions, h_n is the distance of the farthest longitudinal surface of nth layer measured from x-axis; P_1, M_1, and R_1 are the reactions at the end $x = 0$ (Fig. 1).

[1] Assistant Professor, Department of Mechanical Engineering, I.I.T., Kharagpur-721302, India.

Manuscript received by ASME Applied Mechanics Division, May, 1980; final revision, November, 1980.

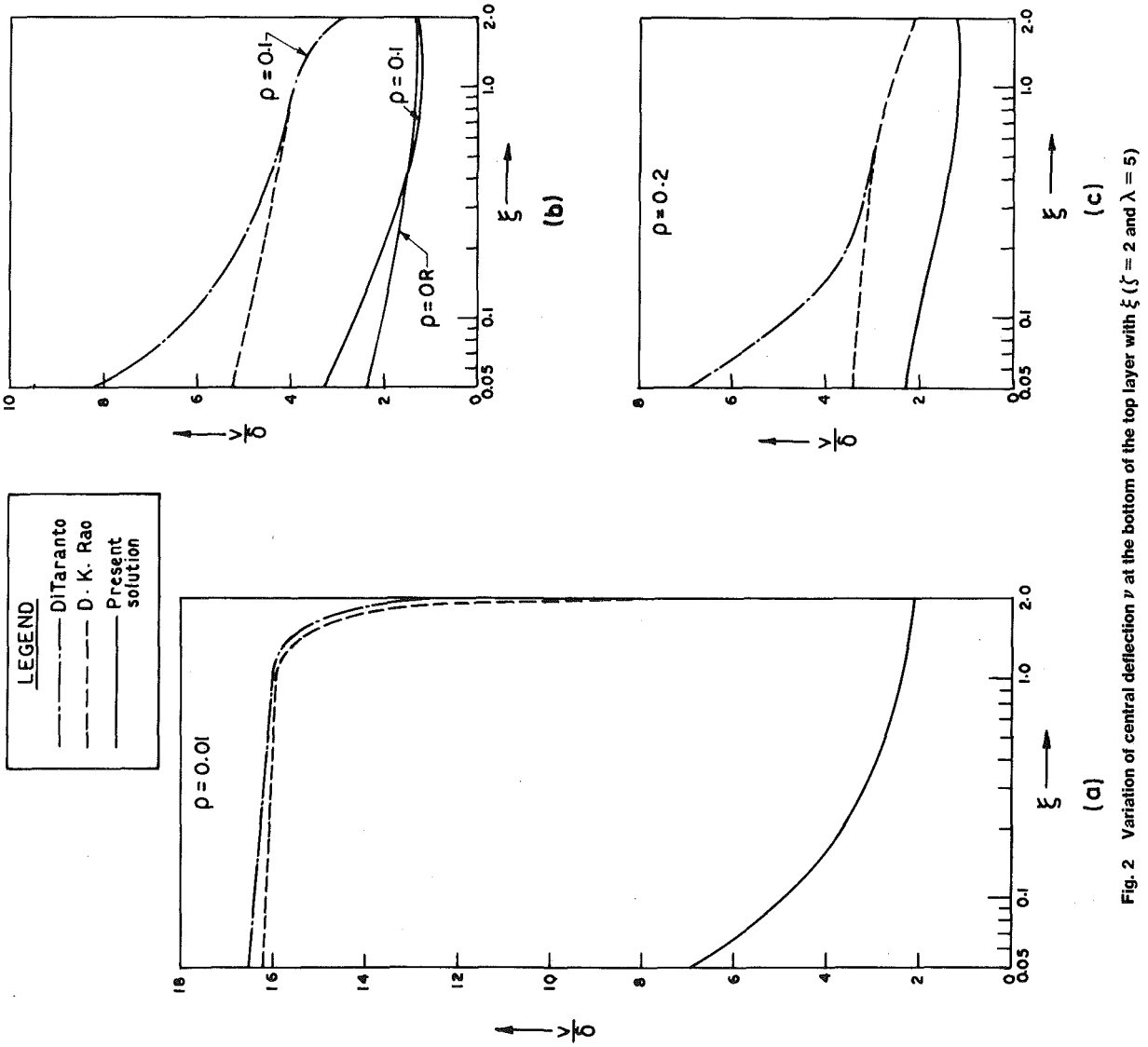

Fig. 2 Variation of central deflection v at the bottom of the top layer with ξ ($\zeta = 2$ and $\lambda = 5$)

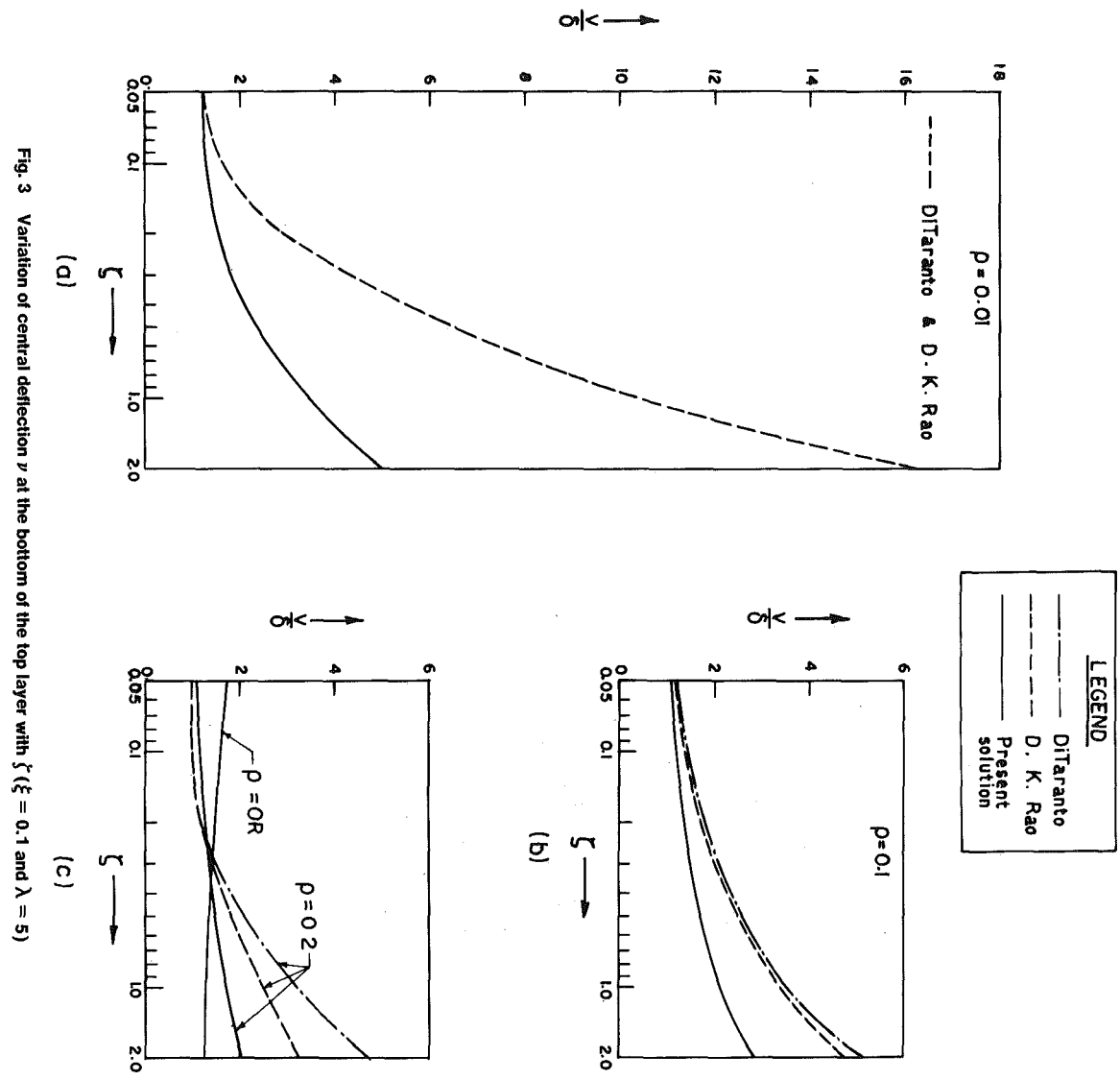

Fig. 3 Variation of central deflection v at the bottom of the top layer with ζ ($\xi = 0.1$ and $\lambda = 5$)

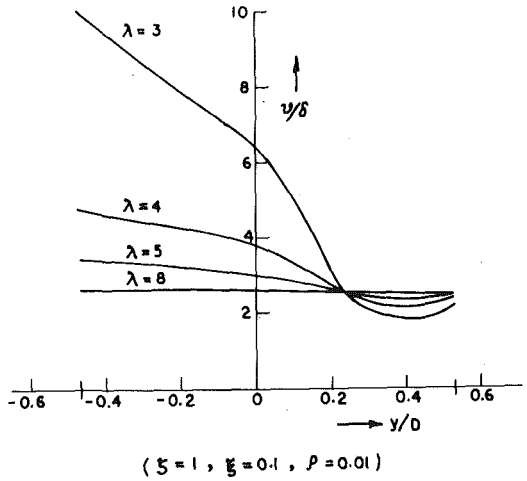

Fig. 4 Variation of central deflection v over the depth

The kinematic end conditions of a clamped-clamped beam are taken as

$$u_k = v_k = \partial v_k/\partial x = 0 \quad \text{at both ends} \quad x = 0, L \quad \text{and} \quad y = H, \quad (10)$$

where L is the span of the beam (Fig. 1).

The problem can be completely solved by evaluating the stresses σ_{xn}, σ_{yn}, and τ_{xyn}, and deformations u_n and v_n with the help of equations (3)–(6); in turn substituting these into equations (7)–(10), sufficient number of algebraic equations are obtained to solve for the constants of integration and coefficients of stress functions $\phi_n (n = 1, 2, \ldots N)$.

Results and Conclusions

The previous analysis is particularized to the case of 3-layered beam, and the numerical data of σ_x, τ_{xy}, and v is presented in Figs. 2–8. In these figures $\lambda = L/(h_1 + h_3)$, $\xi = (h_3 - h_2)/h_1$, $\zeta = h_2/h_1$ and $\rho = S_{111}/S_{112}$; *Bijk*, *Tijk*, and *Mijk* denote, respectively, the bottom, top, and middle fiber of ith layer in a beam with $\rho = 0$-jk or OR. For the beam corresponding to $\rho = 0.01$, 0.1, and 0.2, the layers are made of isotropic materials in which the top and bottom layers are of the same material and the middle layer is of comparatively flexible material; $\rho = OR$ denotes the beam in which the top, middle, and bottom layers are, respectively, of boron/epoxy, glass/epoxy, and graphite/epoxy composites, the material properties of these being taken from Jones [6]. In the graphs σ, δ, and τ signify, respectively, the normal stress in the top fiber of midsection, deflection of midsection, and maximum shear stress at one-fourth span of an equivalent Euler beam. The equivalent Euler beam is defined as one which has same outer dimensions, end conditions, and load as laminated beam, and which has the medium with Young's modulus $E = 1/S_{111}$.

The strange and interesting observations that are made by the author are as follows:

1 When the middle layer is flexible ($\rho = 0.01$), the deflection given by elasticity solution is much less than that given by elementary solution (Figs. 2 and 3). When $\rho = 0.01$, $\xi = 1$ and $\zeta = 2$ (Fig. 2), the ratio is as much as 1:7. As the elastic modulus ratio ρ tends to unity and ζ tends to zero, this deviation decreases.

2 At lower values of span-to-depth ratio ($\lambda < 8$) and $\rho = 0.01$, the deflection varies considerably over the depth (Fig. 4).

3 The normal stress σ_x given by elasticity and elementary theories differ considerably both by quantity and quality at low values of ρ (Figs. 6 and 7). The stress pattern given by elasticity solution is reversed in nature (i.e., compressive stress on convex side and tensile stress on concave side) compared to conventional stress pattern in a beam when $\rho = 0.01$. This reversed stress pattern changes to conventioned one as ρ approaches to unity (Fig. 7). For the case of orthotropic layered beam ($\rho = OR$), the stress in top layer ($M1OR$) is tensile, whereas that in bottom fiber ($B3\ OR$) changes from tensile to compression over $0.05 \leq \xi \leq 2.0$.

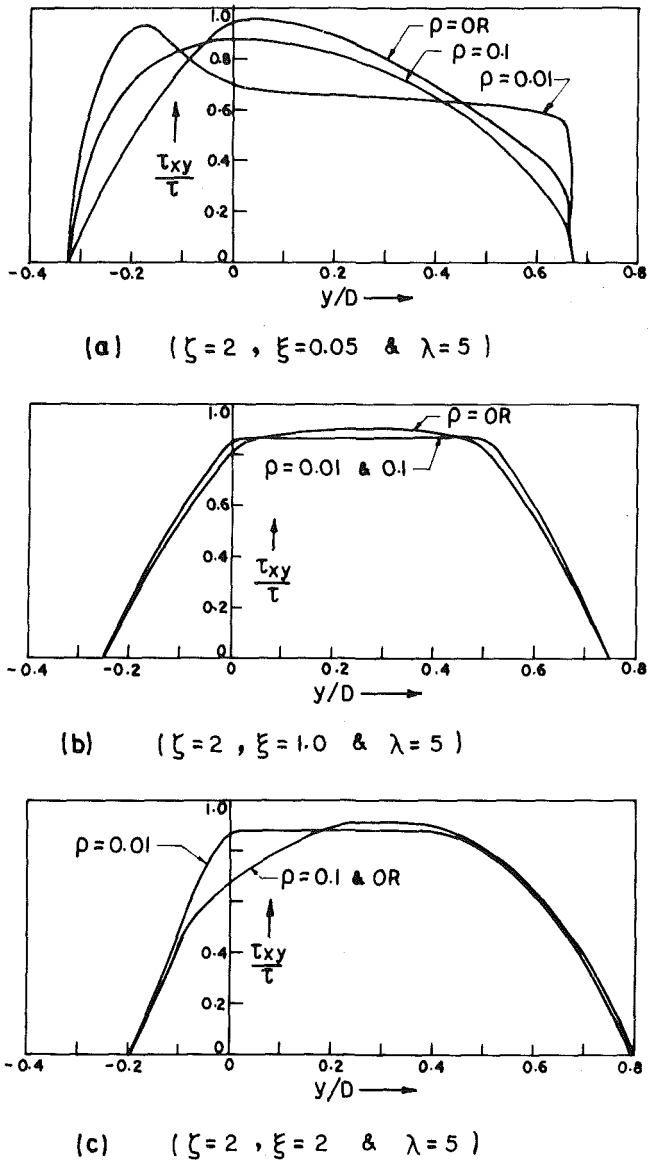

Fig. 5 Variation of shear stress τ_{xy} over the depth at one-fourth span

4 It is also observed that the reversed stress pattern in isotropic layered beam with $\rho = 0.01$ continues up to λ is about 12; and the stress on the concave side of orthotropic layered beam ($T1OR$) is tensile upto λ is about 8.

5 The inner fibers of top and bottom layers of isotropic layered beam with a very flexible middle layer are stressed more than the outer fibers, whereas generally the outer fibers of a beam are stressed more (Fig. 7).

6 In case of orthotropic layered beam, maximum value of normal stress σ_x in top layer is in the middle fiber, and that in bottom layer is in bottom fiber (Fig. 7*c*).

7 At midsection the location of the point at which σ_x is maximum is highly dependent on the parameters ρ, ξ, and ζ.

8 The stress σ_x varies linearly over the depth of each layer of isotropic layered beam; but as shown by Fig. 8. σ_x varies nonlinearly over the depth of each layer of orthotropic layered beam. For span-to-depth ratio $\lambda > 10$, even incase $\rho = OR$, σ_x varies linearly over the depth of the beam.

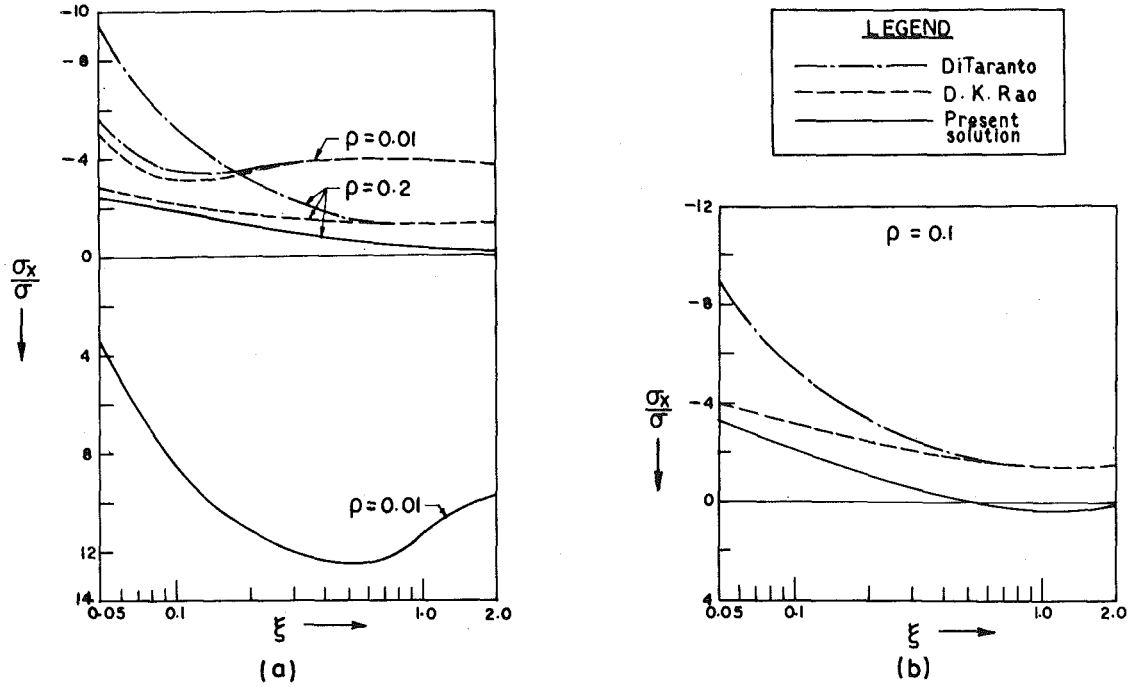

Fig. 6 Effect ξ on Stress σ_x in bottom fiber of midsection ($\zeta = 2$ and $\lambda = 5$)

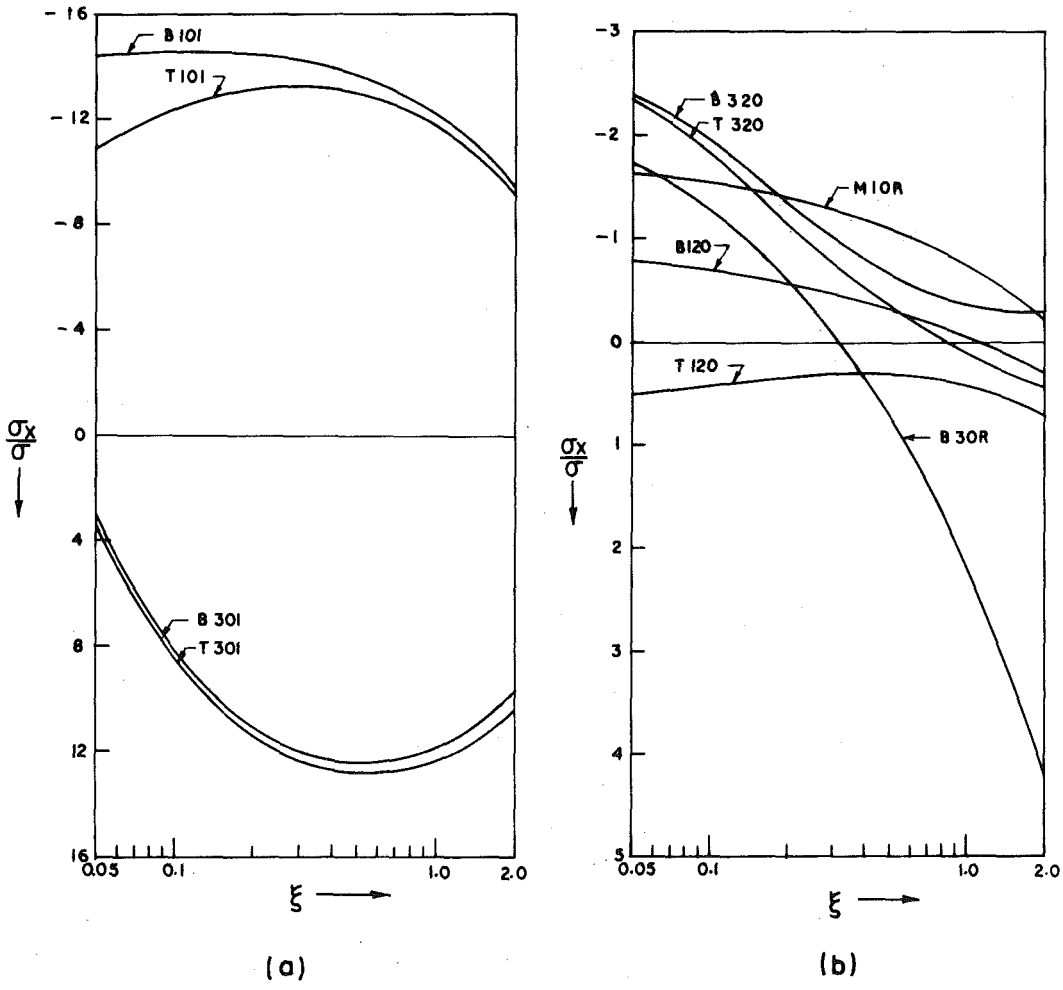

Fig. 7(a,b) Variation of σ_x with ξ at various levels of midsection ($\zeta = 2$ and $\lambda = 5$)

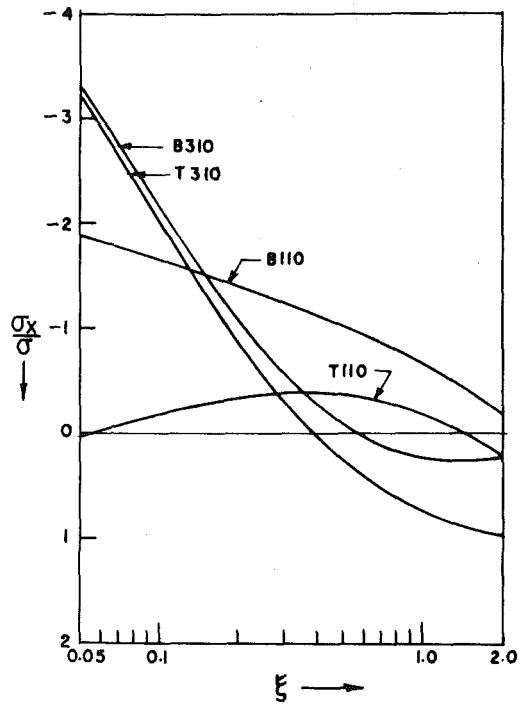

(c)

Fig. 7(c) Variation of σ_x with ξ at various levels of midsection ($\zeta = 2$ and $\lambda = 5$)

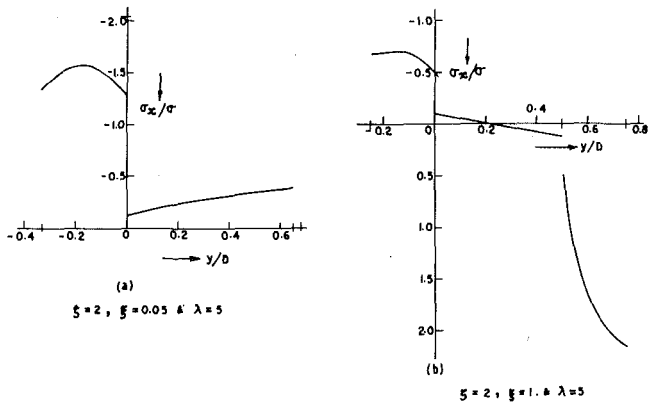

Fig. 8 Variation of σ_x over the depth

The author feels that the discrepancy in the results of elasticity and elementary solutions of a beam with flexible middle layer is due to the existence of significant amount of shear strain at the clamped ends. In the models of DiTaranto [1] and Rao [2], the shear strain is not accommodated in an element at the fixed end. But in the present model it is accommodated by the rotation of transverse fiber relative to the longitudinal fiber at the clamped end. These observations show the inadequacy of the elementary theory for the analysis of laminated beam with flexible layers.

References

1 DiTaranto, R. A., "Static Analysis of a Laminated Beam," ASME *Journal of Engineering for Industry*, Vol. 95, 1973, pp. 755–76.

2 Rao, D. K., "Static Response of Stiff-Cored Unsymmetric Sandwich Beams," ASME *Journal of Engineering for Industry*, Vol. 98, 1976, pp. 391–396.

3 Rao, K. M., "Analysis of Stresses and Deformations in Beams of Composites," PhD Thesis, I.I.T., Kharagpur, India, 1978, pp. 40–44.

4 Schile, R. D., "Laminate Elastostatistics," *International Journal of Engineering Sciences*, Vol. 9, No. 1, 1971.

5 Schile, R. D., "Elasticity Solutions for Fiber-Reinforced Polymer Composites Laminates," AFML-TR-73-115, July 1973.

6 Jones, R. M., *Mechanics of Composite Materials*, Scripta Book Co., Washington, D. C., 1975.

Drag on a Droplet in Translating Fluctuating Flow

M. B. Stewart[1] and F. A. Morrison, Jr.[2]

Introduction

A droplet in a fluctuating translating flow experiences an unsteady force exerted by the surrounding fluid. We consider low Reynolds number flow with a relative velocity $U(1 + \epsilon \exp(i\omega t))$ where ϵ is small. ω is the oscillation frequency and t is the time. We seek the effect of this small oscillation on the force imposed on an isolated spherical droplet.

Starting from Stokes classical creeping flow analysis, Proudman and Pearson [1] used matched asymptotic expansions to describe steady low Reynolds number motion past a rigid sphere. Illingworth [2] subsequently determined effects of small superimposed oscillations.

Taylor and Acrivos [3] found the analogous steady low Reynolds number extension of the Hadamard [4] and Rybczynski [5] analysis of creeping droplet motion. In this Note, we generalized Illingworth's results to include fluid spheres.

The axisymmetric flow is described using Stokes stream function ψ in spherical coordinates r, θ, ϕ. The flow of an uncompressed fluid with constant viscosity and density obeys

$$\frac{\partial}{\partial t}(E^2\psi) - J(\psi, \psi) = \nu E^4\psi \tag{1}$$

μ is the cosine of the polar angle θ and ν is the kinematic viscosity. For later convenience, we have introduced the notation

$$J(\zeta,\delta) = \frac{\partial[\zeta, (E^2\delta)/r^2\,(1-\mu^2)]}{\partial(r,\mu)} \tag{2}$$

E^2 is the Stokes stream function operator

$$E^2 = \frac{\partial^2}{\partial r^2} + \frac{1-\mu^2}{r^2}\frac{\partial^2}{\partial \mu^2} \tag{3}$$

The free-steam velocity variation suggests a stream function of the form

$$\psi = \psi_0 + \epsilon \exp(i\omega t)\psi_1 \tag{4}$$

The flow in three regions is analyzed here. Flow interior to the droplet is coupled, at the droplet radius a, to the inner flow of the exterior fluid which, in turn, is matched to the outer flow.

The dimensionless position, ρ, used for the inner flows, is r/a. The corresponding stretched coordinate, $\hat{\rho}$, of the outer flow is Re ρ. The steady flow Reynolds number, Re, is Ua/ν_e using the exterior fluid kinematic viscosity. The dimensionless inner stream functions are

[1] Department of Mechanical and Industrial Engineering, University of Illinois at Urbana—Champaign, Urbana, Ill. 61801. Assoc. Mem. ASME

[2] University of California, Lawrence Livermore National Laboratory, Livermore, Calif. 94550. Mem. ASME

Manuscript received by ASME Applied Mechanic Division, January, 1980; final revision, December, 1980.

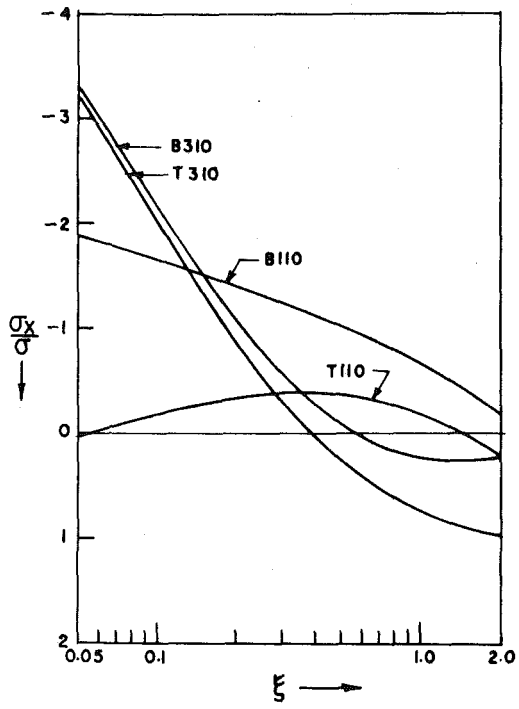

(c)

Fig. 7(c) Variation of σ_x with ξ at various levels of midsection ($\zeta = 2$ and $\lambda = 5$)

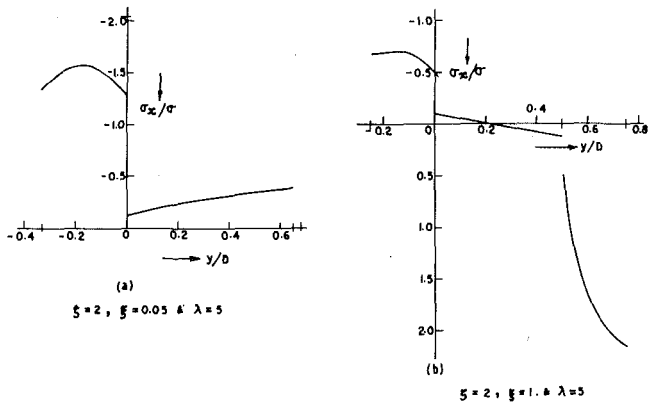

Fig. 8 Variation of σ_x over the depth

The author feels that the discrepancy in the results of elasticity and elementary solutions of a beam with flexible middle layer is due to the existence of significant amount of shear strain at the clamped ends. In the models of DiTaranto [1] and Rao [2], the shear strain is not accommodated in an element at the fixed end. But in the present model it is accommodated by the rotation of transverse fiber relative to the longitudinal fiber at the clamped end. These observations show the inadequacy of the elementary theory for the analysis of laminated beam with flexible layers.

References

1 DiTaranto, R. A., "Static Analysis of a Laminated Beam," ASME *Journal of Engineering for Industry*, Vol. 95, 1973, pp. 755–76.

2 Rao, D. K., "Static Response of Stiff-Cored Unsymmetric Sandwich Beams," ASME *Journal of Engineering for Industry*, Vol. 98, 1976, pp. 391–396.

3 Rao, K. M., "Analysis of Stresses and Deformations in Beams of Composites," PhD Thesis, I.I.T., Kharagpur, India, 1978, pp. 40–44.

4 Schile, R. D., "Laminate Elastostatistics," *International Journal of Engineering Sciences*, Vol. 9, No. 1, 1971.

5 Schile, R. D., "Elasticity Solutions for Fiber-Reinforced Polymer Composites Laminates," AFML-TR-73-115, July 1973.

6 Jones, R. M., *Mechanics of Composite Materials*, Scripta Book Co., Washington, D. C., 1975.

Drag on a Droplet in Translating Fluctuating Flow

M. B. Stewart[1] and F. A. Morrison, Jr.[2]

Introduction

A droplet in a fluctuating translating flow experiences an unsteady force exerted by the surrounding fluid. We consider low Reynolds number flow with a relative velocity $U(1 + \epsilon \exp(i\omega t))$ where ϵ is small. ω is the oscillation frequency and t is the time. We seek the effect of this small oscillation on the force imposed on an isolated spherical droplet.

Starting from Stokes classical creeping flow analysis, Proudman and Pearson [1] used matched asymptotic expansions to describe steady low Reynolds number motion past a rigid sphere. Illingworth [2] subsequently determined effects of small superimposed oscillations.

Taylor and Acrivos [3] found the analogous steady low Reynolds number extension of the Hadamard [4] and Rybczynski [5] analysis of creeping droplet motion. In this Note, we generalized Illingworth's results to include fluid spheres.

The axisymmetric flow is described using Stokes stream function ψ in spherical coordinates r, θ, ϕ. The flow of an uncompressed fluid with constant viscosity and density obeys

$$\frac{\partial}{\partial t}(E^2\psi) - J(\psi, \psi) = \nu E^4\psi \tag{1}$$

μ is the cosine of the polar angle θ and ν is the kinematic viscosity. For later convenience, we have introduced the notation

$$J(\zeta,\delta) = \frac{\partial[\zeta, (E^2\delta)/r^2\,(1-\mu^2)]}{\partial(r,\mu)} \tag{2}$$

E^2 is the Stokes stream function operator

$$E^2 = \frac{\partial^2}{\partial r^2} + \frac{1-\mu^2}{r^2}\frac{\partial^2}{\partial \mu^2} \tag{3}$$

The free-steam velocity variation suggests a stream function of the form

$$\psi = \psi_0 + \epsilon \exp(i\omega t)\psi_1 \tag{4}$$

The flow in three regions is analyzed here. Flow interior to the droplet is coupled, at the droplet radius a, to the inner flow of the exterior fluid which, in turn, is matched to the outer flow.

The dimensionless position, ρ, used for the inner flows, is r/a. The corresponding stretched coordinate, $\hat{\rho}$, of the outer flow is Re ρ. The steady flow Reynolds number, Re, is Ua/ν_e using the exterior fluid kinematic viscosity. The dimensionless inner stream functions are

[1] Department of Mechanical and Industrial Engineering, University of Illinois at Urbana—Champaign, Urbana, Ill. 61801. Assoc. Mem. ASME

[2] University of California, Lawrence Livermore National Laboratory, Livermore, Calif. 94550. Mem. ASME

Manuscript received by ASME Applied Mechanic Division, January, 1980; final revision, December, 1980.

ψ/Ua^2. These are $\tilde{\psi}$ within the droplet and $\bar{\psi}$ outside. The outer flow, far from the droplet, is described by $\hat{\psi} = \mathrm{Re}^2\psi/Ua^2$.

Accordingly, the steady flows are governed by

$$E_{\hat{\rho}}{}^4\,\hat{\psi}_0 + J_{\hat{\rho}}[\hat{\psi}_0, \hat{\psi}_0] = 0 \tag{5}$$

$$E_{\rho}{}^4\,\bar{\psi}_0 + \mathrm{Re}\, J_{\rho}[\bar{\psi}_0, \bar{\psi}_0] = 0 \tag{6}$$

and

$$E_{\rho}{}^4\,\tilde{\psi}_0 + \lambda\,\mathrm{Re}\, J_{\rho}[\tilde{\psi}_0, \tilde{\psi}_0] = 0 \tag{7}$$

λ is the ratio of external to internal kinematic viscosity.

The oscillating components satisfy

$$E_{\hat{\rho}}{}^4\,\hat{\psi}_1 + J_{\hat{\rho}}(\hat{\psi}_0, \hat{\psi}_1) + J_{\hat{\rho}}(\hat{\psi}_1, \hat{\psi}_0) - i\sigma E_{\hat{\rho}}{}^2\,\hat{\psi}_1 = 0 \tag{8}$$

$$E_{\rho}{}^4\,\bar{\psi}_1 + \mathrm{Re}\,[J_{\rho}(\bar{\psi}_0, \bar{\psi}_1) + J_{\rho}(\bar{\psi}_1, \bar{\psi}_0)] - i\sigma\,\mathrm{Re}^2\,E_{\rho}{}^2\bar{\psi}_1 = 0 \tag{9}$$

and

$$E_{\rho}{}^4\tilde{\psi}_1 + \lambda\,\mathrm{Re}\,[J_{\rho}(\tilde{\psi}_0, \tilde{\psi}_1) + J_{\rho}(\tilde{\psi}_1, \tilde{\psi}_0)] - i\sigma\lambda\,\mathrm{Re}^2\,E_{\rho}{}^2\tilde{\psi}_1 = 0 \tag{10}$$

Terms of order ϵ^2 are neglected. σ is $\omega\nu_e/U^2$, the ratio of Strouhal number to Reynolds number.

The Steady Drag Component

Taylor and Acrivos obtained a solution to equations (5)–(7) by expanding each of the steady stream functions in the manner

$$\psi_0 = \psi_{00} + \mathrm{Re}\,\psi_{01} + \ldots \tag{11}$$

The flow remains bounded at the origin and approaches uniform streaming far from the droplet. Tangential velocity and stress are continuous across the droplet surface. This surface is impervious. The flows in the exterior fluid are matched.

The zeroth-order solution in the outer steady flow represents uniform streaming. The corresponding inner flows are those of Hadamard and Rybczynski. Taylor and Acrivos obtained the first-order steady stream functions and the corresponding drag on the rigid sphere

$$F = \pi\mu_e aU\left[2\left(\frac{2\gamma+3}{\gamma+1}\right) + \frac{\mathrm{Re}}{4}\left(\frac{2\gamma+3}{\gamma+1}\right)^2 + \ldots\right] \tag{12}$$

μ_e is the external fluid viscosity and γ is the ratio of external to internal viscosity, the reciprocal of Taylor and Acrivos κ.

The Oscillating Drag Component

With this background, we address the oscillating component. Three regimes, distinguished by the magnitude of the dimensionless frequency σ are considered.

When the dimensionless frequency is much less than one, the flow is quasi-steady and the drag depends, as in a steady flow, on the instantaneous velocity. We have simply

$$F = \pi\mu_e aU\left[2\left(\frac{2\gamma+3}{\gamma+1}\right) + \frac{\mathrm{Re}}{4}\left(\frac{2\gamma+3}{\gamma+1}\right)^2 + \ldots\right]\quad[1 + \epsilon\exp(i\omega t)] \tag{13}$$

When the dimensionless frequency is large, much greater than Re^{-1}, the local acceleration dominates. This corresponds to a large Strouhal number. The convective acceleration terms in equations (9) and (10) are neglected. The transient Stokes relations apply and there is no need to match to an outer flow. As part of an analysis of droplet motion governed by the transient Stokes relations, Stewart and Morrison [6] found the drag on a droplet in an accelerating fluid. From their results, we can write an expression for the drag on a stationary droplet in an oscillating flow.

$$F = 6\pi\mu_e a\left[(1+k)\sum + \frac{k^2}{3}\right]U\epsilon\exp(i\omega t) \tag{14}$$

k^2 is $i\omega\sigma\,\mathrm{Re}^2$ and Σ is given by

$$\sum = 1 - \gamma(1+k)[(-3 + 3k\sqrt{\lambda} - k^2\lambda)\exp(k\sqrt{\lambda}) + (3 + 3k\sqrt{\lambda} + k^2\lambda)\exp(-k\sqrt{\lambda})]/\Delta \tag{15}$$

and

$$\Delta = [(2 - 3\gamma - \gamma k)(3 - 3k\sqrt{\lambda} + k^2\lambda) + k^2\lambda(1 - k\sqrt{\lambda})]\exp(k\sqrt{\lambda}) - [(2 - 3\gamma - \gamma k)(3 + 3k\sqrt{\lambda} + k^2\lambda(1 + k\sqrt{\lambda}))]\exp(-k\sqrt{\lambda}) \tag{16}$$

Combining with equation (13) gives

$$F = \pi\mu_e aU\left(2\frac{2\gamma+3}{\gamma+1} + \frac{\mathrm{Re}}{4}\left[\frac{2\gamma+3}{\gamma+1}\right]^2 + 6\left[(1+k)\sum + \frac{k^2}{3}\right]\epsilon\exp(i\omega t)\right) \tag{17}$$

When σ greatly exceeds Re^{-2}, k is large, the k^2 term dominates and the most significant part of the oscillating force does not depend on internal viscosity.

$$F = \pi\mu_e aU\left[2\frac{2\gamma+3}{\gamma+1} + \frac{\mathrm{Re}}{4}\left(\frac{2\gamma+3}{\gamma+1}\right)^2 + 2i\sigma\,\mathrm{Re}^2\,\epsilon\exp(i\omega t)\right] \tag{18}$$

We finally consider σ of order unity. In this case, local acceleration can be neglected for the inner flows, simplifying equations (9) and (10). Just as an expansion of the form (11) was useful for solving equations (5)–(7), the expansion

$$\psi_1 = \psi_{10} + \mathrm{Re}\,\psi_{11} + \ldots \tag{19}$$

can now be utilized in the solution of equation (8) together with the simplified equations (9)–(10).

The solution closely follows the rigid sphere analysis and is rather lengthy. Accordingly, only the results are presented here. Zeroth-order solutions are

$$\hat{\psi}_{10} = \hat{\psi}_{00} = \hat{\rho}^2 C_2{}^{-1/2}(\mu) \tag{20}$$

$$\bar{\psi}_{10} = \bar{\psi}_{00} = \frac{1}{2}\left(2\rho^2 - \frac{2\gamma+3}{\gamma+1}\rho + \frac{1}{\gamma+1}\rho^{-1}\right)C_2{}^{-1/2}(\mu) \tag{21}$$

$C_n{}^{-1/2}(\mu)$ is the Gegenbauer polynomial of order n and degree $-\frac{1}{2}$. Defining α as $1 + 4i\sigma$, first-order solutions are

$$\hat{\psi}_{11} = \frac{2\gamma+3}{2(\gamma+1)}\left[\left(-\hat{\rho} + \frac{1}{3}\frac{\alpha^2+\alpha+1}{\alpha+1}\hat{\rho}^2\right)C_2{}^{-1/2}(\mu) - \frac{1}{2}\hat{\rho}^2 C_3{}^{-1/2}(\mu)\right] + O(\hat{\rho}^3) \tag{22}$$

$$\bar{\psi}_{11} = \frac{2\gamma+3}{2(\gamma+1)}\frac{\alpha^2+\alpha+1}{\alpha+1}\bar{\psi}_{00} + \frac{2\gamma+3}{4(\gamma+1)}\left[\rho^2 - \frac{2\gamma+3}{2(\gamma+1)}\rho - \frac{1}{2(\gamma+1)}\rho^{-1} + \frac{(6\gamma+5)}{10(\gamma+1)^2}(1+\rho^{-2})\right]C_3{}^{-1/2}(\mu) \tag{23}$$

With this stream function, the force on the droplet is calculated.

$$F = \pi\mu_e aU\left(2\frac{2\gamma+3}{\gamma+1} + \frac{\mathrm{Re}}{4}\left(\frac{2\gamma+3}{\gamma+1}\right)^2 + 2\frac{2\gamma+3}{\gamma+1} \times\left[1 + \frac{1}{6}\frac{2\gamma+3}{\gamma+1}\frac{\alpha^2+\alpha+1}{\alpha+1}\mathrm{Re}\right]^*\epsilon\exp(i\omega t)\right) \tag{24}$$

References

1 Proudman, I., and Pearson, J. R. A., "Expansions at Small Reynolds Numbers for the Flow Past a Sphere and a Circular Cylinder," *Journal of Fluid Mechanics*, Vol. 2, 1957, pp. 237–262.

2 Illingworth, C. R., "Fluctuating Flow at Small Reynolds Numbers," *Journal of Applied Mechanics and Physics (ZAMP)*, Vol. 14, 1963, pp. 681–694.

3 Taylor, T. D., and Acrivos, A., "On the Deformation and Drag of a Falling Viscous Drop at Low Reynolds Number" *Journal of Fluid Mechanics*, Vol. 18, 1964, pp. 466–476.

4 Hadamard, J., "Mouvement Permanent Lent d'une Sphere Liquide et Visqueuse dans un Liquide Visqueux," *Comptes Rendus*, Vol. 152, 1911, pp. 1735–1738.

5 Rybczynski, W., "Über die Fortschreitende Bewegung einer Flussingen Kugel in einem zahen Medium," *Bulletin Internationale de L'Academie des Sciences de Cracovie*, 1911, pp. 40–46.

6 Stewart, M. B., and Morrison, F. A., Jr., "Droplet Dynamics in Creeping Flows," to be published in the ASME JOURNAL OF APPLIED MECHANICS.

On an Elastic Theory of Friction

N. Phan-Thien[1]

Recently, Villaggio [1] proposed an elegant and simple theory of elastic friction which is based on a reasonable definition of the limit tangential load. He argued, very correctly, that if the contact bodies deform elastically then Coulomb's, or rather Amonston's law (see [2]) should not be accepted as a postulate, but as a consequence of the elastic deformation of the contact regions. This is justifiable if the contact surfaces are not very rough so that there is no plastic deformation involved. Villaggio's starting point was the plane contact problem which was considered by Poritsky [3] using a potential analogy, refer to Fig. 1. To prevent interpenetration under the action of a normal force per unit width, N_1, it is necessary to produce over the contact band $-a \leq x \leq a$ a normal displacement over each surface whose sum is given by

$$v_1 + v_2 = W_0 - \tfrac{1}{2}\rho x^2, \tag{1}$$

where W_0 is the relative approach at $x = 0$ and ρ is given by $\rho_1 - \rho_2$, with ρ_1 and ρ_2 being the curvatures of the mating surfaces.

Poritsky [3] showed that the contact length and the relative approach are given through (there is a factor $\frac{1}{2}$ missing in various equations of Poritsky's paper)

$$a = (4N_1/\pi\rho E')^{1/2} \tag{2}$$

$$N_1 = 2\pi E' W_0/13, \tag{3}$$

where

$$\frac{1}{E'} = \frac{1-\nu_1^2}{E_1} + \frac{1-\nu_2^2}{E_2}$$

and E_i, ν_i are Young's modulus and Poisson's ratio of the body i, $i = 1, 2$.

Now a tangential force per unit width, S_1, is allowed to act on body 1. Villaggio [1] called S_1 the limit tangential load if, under its action, that part of body 2 that lies in the interval $-a \leq x \leq 0$ becomes flat. This requirement leads to [1]

$$S = \frac{4.21}{\pi^3}\frac{\rho_1\rho_2}{\rho}\left(1 + \frac{1-\nu_1^2}{1-\nu_2^2}\frac{E_2}{E_1}\right)a(N_1)N_1 \tag{4}$$

so that the coefficient of friction, $\beta = S_1/N_1$, is proportional to a (N_1) or $N_1^{1/2}$, a fact at variance with available experimental data. Note that the factor $(1-\nu_1^2)E_1/(1-\nu_2^2)E_2$ in (4) should be replaced by its inverse if it is greater than unity [1].

Notwithstanding the aforementioned drawback, Villaggio's theory appears sound and ought to be improved in order to bring it into close agreement with experimental observations.

Now, Archard [4] has pointed out that if the contact surfaces are covered with asperities, and each asperity with microasperities, and each microasperity with micro-microasperities, and so on, then such approximation gives successively a closer approximation to the law $A \propto N_1$, where A is the total contact area. This idea was exploited elegantly by Greenwood and Williamson [5] who assumed a random surface roughness. We now show that, using Greenwood and Williamson's method, Villaggio's theory can be brought into conformity with experimental data.

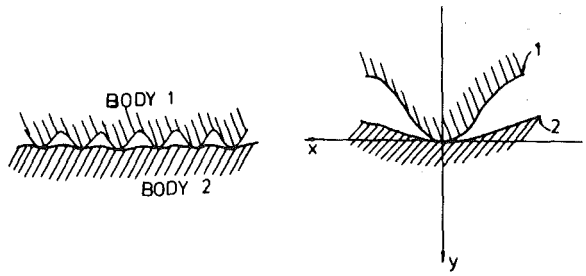

Fig. 1 Plane contact problem considered by Villaggio [1]

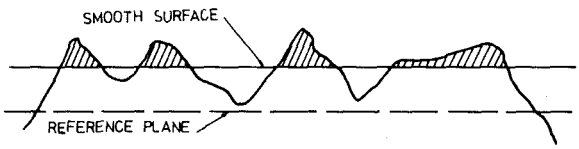

Fig. 2 Contact of rough surfaces; the load is supported by the shaded asperities

Basically we consider the contact problem between a plane and a nominal flat surface covered with plane asperities whose height is a random variable with probability density function $\phi(z)$; see Fig. 2. Here, nominal flat surfaces are defined as in Greenwood and Williamson's [5]; these surfaces have large apparent areas of contact so that the individual contacts are dispersed and the forces acting through neighboring spots do not influence each other. In effect, a collection of "dilute" indentors is considered. Mathematically we require that a characteristic wavelength of the plane asperities is large compared to the contact length a.

Since the probability of having as asperity of height greater than W_0 is given by $\int_{W_0}^{\infty}\phi(z)\,dz$, the expected normal load is

$$N = \frac{2\pi}{13}ME'\int_{W_0}^{\infty}(z - W_0)\,\phi(z)\,dz, \tag{5}$$

and the expected limit tangential load is given by, if the asperities have the same curvature ρ,

$$S = \frac{8.42}{13\pi^2}\left(\frac{8}{13}\right)^{1/2}\rho^{1/2}M\frac{E_2}{1-\nu_2^2}\int_{W_0}^{\infty}(z - W_0)^{3/2}\phi(z)\,dz, \tag{6}$$

where M is the total number of asperities.

For exponentially distributed asperity height we have $\phi(z) = \sigma^{-1}\exp(-z/\sigma)$, where σ is the mean asperity height. Also,

$$\int_{W_0}^{\infty}(z - W_0)^{\alpha}\phi(z)\,dz = \sigma^{\alpha}\Gamma(\alpha + 1)e^{-W_0/\sigma},$$

where $\Gamma(x)$ is the Gamma function. Thus the frictional coefficient is given by

[1] Department of Mechanical Engineering, The University of Sydney, New South Wales 2006, Australia.

Manuscript received by ASME Applied Mechanics Division, May, 1980; final revision, September, 1980.

3 Taylor, T. D., and Acrivos, A., "On the Deformation and Drag of a Falling Viscous Drop at Low Reynolds Number" *Journal of Fluid Mechanics*, Vol. 18, 1964, pp. 466–476.

4 Hadamard, J., "Mouvement Permanent Lent d'une Sphere Liquide et Visqueuse dans un Liquide Visqueux," *Comptes Rendus*, Vol. 152, 1911, pp. 1735–1738.

5 Rybczynski, W., "Über die Fortschreitende Bewegung einer Flussingen Kugel in einem zahen Medium," *Bulletin Internationale de L'Academie des Sciences de Cracovie*, 1911, pp. 40–46.

6 Stewart, M. B., and Morrison, F. A., Jr., "Droplet Dynamics in Creeping Flows," to be published in the ASME JOURNAL OF APPLIED MECHANICS.

On an Elastic Theory of Friction

N. Phan-Thien[1]

Recently, Villaggio [1] proposed an elegant and simple theory of elastic friction which is based on a reasonable definition of the limit tangential load. He argued, very correctly, that if the contact bodies deform elastically then Coulomb's, or rather Amonston's law (see [2]) should not be accepted as a postulate, but as a consequence of the elastic deformation of the contact regions. This is justifiable if the contact surfaces are not very rough so that there is no plastic deformation involved. Villaggio's starting point was the plane contact problem which was considered by Poritsky [3] using a potential analogy, refer to Fig. 1. To prevent interpenetration under the action of a normal force per unit width, N_1, it is necessary to produce over the contact band $-a \le x \le a$ a normal displacement over each surface whose sum is given by

$$v_1 + v_2 = W_0 - \tfrac{1}{2}\rho x^2, \tag{1}$$

where W_0 is the relative approach at $x = 0$ and ρ is given by $\rho_1 - \rho_2$, with ρ_1 and ρ_2 being the curvatures of the mating surfaces.

Poritsky [3] showed that the contact length and the relative approach are given through (there is a factor $\frac{1}{2}$ missing in various equations of Poritsky's paper)

$$a = (4N_1/\pi\rho E')^{1/2} \tag{2}$$

$$N_1 = 2\pi E' W_0/13, \tag{3}$$

where

$$\frac{1}{E'} = \frac{1-\nu_1^2}{E_1} + \frac{1-\nu_2^2}{E_2}$$

and E_i, ν_i are Young's modulus and Poisson's ratio of the body i, $i = 1, 2$.

Now a tangential force per unit width, S_1, is allowed to act on body 1. Villaggio [1] called S_1 the limit tangential load if, under its action, that part of body 2 that lies in the interval $-a \le x \le 0$ becomes flat. This requirement leads to [1]

$$S = \frac{4.21}{\pi^3}\frac{\rho_1\rho_2}{\rho}\left(1 + \frac{1-\nu_1^2}{1-\nu_2^2}\frac{E_2}{E_1}\right)a(N_1)N_1 \tag{4}$$

so that the coefficient of friction, $\beta = S_1/N_1$, is proportional to a (N_1) or $N_1^{1/2}$, a fact at variance with available experimental data. Note that the factor $(1-\nu_1^2)E_1/(1-\nu_2^2)E_2$ in (4) should be replaced by its inverse if it is greater than unity [1].

Notwithstanding the aforementioned drawback, Villaggio's theory appears sound and ought to be improved in order to bring it into close agreement with experimental observations.

Now, Archard [4] has pointed out that if the contact surfaces are covered with asperities, and each asperity with microasperities, and each microasperity with micro-microasperities, and so on, then such approximation gives successively a closer approximation to the law $A \propto N_1$, where A is the total contact area. This idea was exploited elegantly by Greenwood and Williamson [5] who assumed a random surface roughness. We now show that, using Greenwood and Williamson's method, Villaggio's theory can be brought into conformity with experimental data.

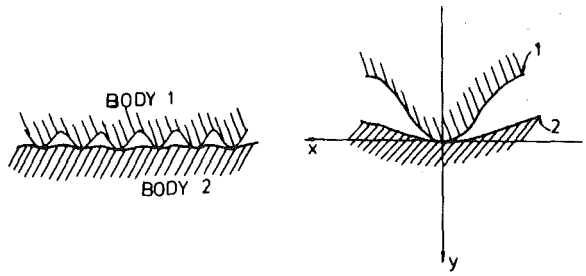

Fig. 1 Plane contact problem considered by Villaggio [1]

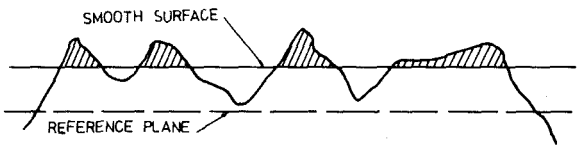

Fig. 2 Contact of rough surfaces; the load is supported by the shaded asperities

Basically we consider the contact problem between a plane and a nominal flat surface covered with plane asperities whose height is a random variable with probability density function $\phi(z)$; see Fig. 2. Here, nominal flat surfaces are defined as in Greenwood and Williamson's [5]; these surfaces have large apparent areas of contact so that the individual contacts are dispersed and the forces acting through neighboring spots do not influence each other. In effect, a collection of "dilute" indentors is considered. Mathematically we require that a characteristic wavelength of the plane asperities is large compared to the contact length a.

Since the probability of having as asperity of height greater than W_0 is given by $\int_{W_0}^{\infty}\phi(z)\,dz$, the expected normal load is

$$N = \frac{2\pi}{13}ME'\int_{W_0}^{\infty}(z - W_0)\,\phi(z)\,dz, \tag{5}$$

and the expected limit tangential load is given by, if the asperities have the same curvature ρ,

$$S = \frac{8.42}{13\pi^2}\left(\frac{8}{13}\right)^{1/2}\rho^{1/2}M\frac{E_2}{1-\nu_2^2}\int_{W_0}^{\infty}(z - W_0)^{3/2}\phi(z)\,dz, \tag{6}$$

where M is the total number of asperities.

For exponentially distributed asperity height we have $\phi(z) = \sigma^{-1}\exp(-z/\sigma)$, where σ is the mean asperity height. Also,

$$\int_{W_0}^{\infty}(z - W_0)^{\alpha}\phi(z)\,dz = \sigma^{\alpha}\Gamma(\alpha+1)e^{-W_0/\sigma},$$

where $\Gamma(x)$ is the Gamma function. Thus the frictional coefficient is given by

[1] Department of Mechanical Engineering, The University of Sydney, New South Wales 2006, Australia.

Manuscript received by ASME Applied Mechanics Division, May, 1980; final revision, September, 1980.

$$\beta = S/N$$

$$= 0.142\,(\sigma\rho)^{1/2}\left[1 + \min\left(\frac{1-\nu_1^2}{1-\nu_2^2}\frac{E_2}{E_1}, \frac{1-\nu_2^2}{1-\nu_1^2}\frac{E_1}{E_2}\right)\right] \tag{7}$$

which is in qualitative agreement with the bulk of our experimental knowledge. For a Gaussian surface roughness, β can also be approximated by (6) over several decades of the imposed normal load N.

Thus Amonton's frictional law, according to Villaggio's theory, appears to be a direct consequence of both the topology and the elastic deformation of the contact surface.

References

1 Villaggio, P., "An Elastic Theory of Coulomb Friction," *Arch. Ratl. Mech. Anal.* Vol. 70, 1979, pp. 135–143.

2 Palmer, F., "What About Friction?" *American Journal of Physics*, Vol. 17, 1949, pp. 181–187.

3 Poritsky, H., "Stresses and Deflections of Cylindrical Bodies in Contact With Application to Contact of Gears and of Locomotive Wheels," ASME JOURNAL OF APPLIED MECHANICS, Vol. 17, 1950, pp. 191–201; author's closure, 1950, pp. 466–468.

4 Archard, J. F., "Elastic Deofrmation and the Laws of Friction," *Proceedings of the Royal Society*, London, Series A, Vol. 243, 1957, pp. 190–205.

5 Greenwood, J. A., and Williamson, J. B. P., "Contact of Nominally Flat Surfaces," *Proceedings of the Royal Society*, London, Series A, Vol. 295, 1950, pp. 300–319.

Bending and Twisting of Internally Pressurized Thin-Walled Cylinder With Creep

J. H. Lau[1] and G. K. Listvinsky[2]

Introduction

A closed-form relation for the bending and twisting of a pressurized thin-walled cylinder which obeys the Bailey-Norton type isothermal power creep law with $n = 2$ is presented here. Dimensionless moment-curvature charts are also presented for various isostatic circumferential stress due to internal pressure, and isostatic shear stress due to twisting moment. The cylinder material is assumed to have identical tensile and compressive stress-strain rate relations. The derivation is based on the Bernoulli-Euler theory which stated that plane sections before bending remain plane during bending. It is assumed also that the thickness of the cylinder is so thin, compared with the inner radius, that all the nonzero stresses are uniformly distributed across the wall thickness.

The same problem without twisting moment has been studied by Edstam and Hult [1], wherein the integral equations were performed by means of Simpson's formula. It will be shown that the difference between the present solution with [1] is as high as 18 percent.

Analysis

A stationary state of creep will develop [3–5], if the average uniaxial stress-strain rate relation is

$$\dot{\epsilon} = (\sigma/m)^n, \quad n \geq 1, m > 0, \tag{1}$$

and its multiaxial counterpart

$$\dot{\epsilon}_{ij} = 3(\bar{\sigma}/m)^{n-1} S_{ij}/2m, \tag{2}$$

where

$$\bar{\sigma} = \sqrt{\tfrac{1}{2}S_{ij}S_{ij}}\,, \tag{3}$$

and $\dot{\epsilon}_{ij}$ and S_{ij} are the strain rate tensor and stress deviation tensor, respectively.

For the pressurized cylinder under consideration, cylindrical coordinates are used with z being the axial direction and r and θ being the radial and circumferential directions, respectively. The nonzero stress and strain rate components are σ_θ, σ_z, $\tau_{\theta z}$, $\dot{\epsilon}_r$, $\dot{\epsilon}_\theta$, $\dot{\epsilon}_z$, and $\dot{\gamma}_{\theta z}$. Equations (1)–(3) become

$$\dot{\epsilon} = \left\{\frac{\bar{\sigma}}{m}\right\}^2, \tag{4}$$

$$\dot{\epsilon}_z = \frac{\bar{\sigma}}{m^2}\{\sigma_z - \tfrac{1}{2}\sigma_\theta\}, \tag{5}$$

and

$$\bar{\sigma} = \sqrt{\sigma_\theta^2 - \sigma_\theta\sigma_z + \sigma_z{}^2 + 3\tau_{\theta z}{}^2}. \tag{6}$$

Since plane sections remain plane, the strain rate distribution is linear

$$\dot{\epsilon}_z = \frac{R\sin\theta}{\dot{\rho}}, \tag{7}$$

where R is the radius of the cylinder, $\dot{\rho}$ is the radius of curvature rate due to bending.

The equilibrium equations are as follows:

$$\sigma_\theta = PR/h, \quad \tau_{\theta z} = T/2\pi R^2 h, \tag{8}$$

and

$$M = R^2 h \int_0^{2\pi} \sigma_z \sin\theta d\theta, \tag{9}$$

where P is the internal pressure, T is the twisting moment, M is the bending moment, and h is the thickness of the cylinder.

Let

$$\sigma_z = \sigma_\theta/2 + f(\theta). \tag{10}$$

Then, equations (5)–(7), and (10) yield

$$f^4(\theta) + \left\{\frac{3}{4}\sigma_\theta{}^2 + 3\tau_{\theta z}{}^2\right\}f^2(\theta) - \left[\frac{m^2 R\sin\theta}{\dot{\rho}}\right]^2 = 0. \tag{11}$$

Consequently

$$f(\theta) = \sqrt{\sqrt{\left(\frac{3}{8}\sigma_\theta{}^2 + \frac{3}{2}\tau_{\theta z}{}^2\right)^2 + \left(\frac{m^2 R}{\dot{\rho}}\right)^2\sin^2\theta} - \left(\frac{3}{8}\sigma_\theta{}^2 + \frac{3}{2}\tau_{\theta z}{}^2\right)} \tag{12}$$

Substituting equations (10) and (12) into equation (9), in view of equation (8), we have

$$M = 4R^2 hm\sqrt{\eta}\int_0^{\frac{\pi}{2}} \sqrt{\sqrt{1\left(\frac{\xi}{\eta}\right)^2\sin^2\theta} - 1}\sin\theta d\theta, \tag{13}$$

where

$$\xi = R/\dot{\rho},$$

and

$$\eta = \frac{3}{8}\left\{\frac{PR}{mh}\right\}^2 + \frac{3}{2}\left\{\frac{T}{2\pi R^2 hm}\right\}^2. \tag{14}$$

Performing the integration, see Appendix, leads to

[1] Senior Engineer of Applied Physics, Ebasco Services Incorporated, New York, N. Y.

[2] Principal Engineer of Applied Physics, Ebasco Services Incorporated, New York, N. Y.

Manuscript received by ASME Applied Mechanics Division, August, 1980.

$$\beta = S/N$$

$$= 0.142\,(\sigma\rho)^{1/2}\left[1 + \min\left(\frac{1-\nu_1^2}{1-\nu_2^2}\frac{E_2}{E_1}, \frac{1-\nu_2^2}{1-\nu_1^2}\frac{E_1}{E_2}\right)\right] \tag{7}$$

which is in qualitative agreement with the bulk of our experimental knowledge. For a Gaussian surface roughness, β can also be approximated by (6) over several decades of the imposed normal load N.

Thus Amonton's frictional law, according to Villaggio's theory, appears to be a direct consequence of both the topology and the elastic deformation of the contact surface.

References

1 Villaggio, P., "An Elastic Theory of Coulomb Friction," *Arch. Ratl. Mech. Anal.* Vol. 70, 1979, pp. 135–143.

2 Palmer, F., "What About Friction?" *American Journal of Physics*, Vol. 17, 1949, pp. 181–187.

3 Poritsky, H., "Stresses and Deflections of Cylindrical Bodies in Contact With Application to Contact of Gears and of Locomotive Wheels," ASME JOURNAL OF APPLIED MECHANICS, Vol. 17, 1950, pp. 191–201; author's closure, 1950, pp. 466–468.

4 Archard, J. F., "Elastic Deofrmation and the Laws of Friction," *Proceedings of the Royal Society*, London, Series A, Vol. 243, 1957, pp. 190–205.

5 Greenwood, J. A., and Williamson, J. B. P., "Contact of Nominally Flat Surfaces," *Proceedings of the Royal Society*, London, Series A, Vol. 295, 1950, pp. 300–319.

Bending and Twisting of Internally Pressurized Thin-Walled Cylinder With Creep

J. H. Lau[1] and G. K. Listvinsky[2]

Introduction

A closed-form relation for the bending and twisting of a pressurized thin-walled cylinder which obeys the Bailey-Norton type isothermal power creep law with $n = 2$ is presented here. Dimensionless moment-curvature charts are also presented for various isostatic circumferential stress due to internal pressure, and isostatic shear stress due to twisting moment. The cylinder material is assumed to have identical tensile and compressive stress-strain rate relations. The derivation is based on the Bernoulli-Euler theory which stated that plane sections before bending remain plane during bending. It is assumed also that the thickness of the cylinder is so thin, compared with the inner radius, that all the nonzero stresses are uniformly distributed across the wall thickness.

The same problem without twisting moment has been studied by Edstam and Hult [1], wherein the integral equations were performed by means of Simpson's formula. It will be shown that the difference between the present solution with [1] is as high as 18 percent.

Analysis

A stationary state of creep will develop [3–5], if the average uniaxial stress-strain rate relation is

$$\dot{\epsilon} = (\sigma/m)^n, \quad n \geq 1, m > 0, \tag{1}$$

and its multiaxial counterpart

$$\dot{\epsilon}_{ij} = 3(\bar{\sigma}/m)^{n-1} S_{ij}/2m, \tag{2}$$

where

$$\bar{\sigma} = \sqrt{\tfrac{1}{2}S_{ij}S_{ij}}\,, \tag{3}$$

and $\dot{\epsilon}_{ij}$ and S_{ij} are the strain rate tensor and stress deviation tensor, respectively.

For the pressurized cylinder under consideration, cylindrical coordinates are used with z being the axial direction and r and θ being the radial and circumferential directions, respectively. The nonzero stress and strain rate components are σ_θ, σ_z, $\tau_{\theta z}$, $\dot{\epsilon}_r$, $\dot{\epsilon}_\theta$, $\dot{\epsilon}_z$, and $\dot{\gamma}_{\theta z}$. Equations (1)–(3) become

$$\dot{\epsilon} = \left\{\frac{\bar{\sigma}}{m}\right\}^2, \tag{4}$$

$$\dot{\epsilon}_z = \frac{\bar{\sigma}}{m^2}\{\sigma_z - \tfrac{1}{2}\sigma_\theta\}, \tag{5}$$

and

$$\bar{\sigma} = \sqrt{\sigma_\theta^2 - \sigma_\theta\sigma_z + \sigma_z{}^2 + 3\tau_{\theta z}{}^2}. \tag{6}$$

Since plane sections remain plane, the strain rate distribution is linear

$$\dot{\epsilon}_z = \frac{R\sin\theta}{\dot{\rho}}, \tag{7}$$

where R is the radius of the cylinder, $\dot{\rho}$ is the radius of curvature rate due to bending.

The equilibrium equations are as follows:

$$\sigma_\theta = PR/h, \quad \tau_{\theta z} = T/2\pi R^2 h, \tag{8}$$

and

$$M = R^2 h \int_0^{2\pi} \sigma_z \sin\theta d\theta, \tag{9}$$

where P is the internal pressure, T is the twisting moment, M is the bending moment, and h is the thickness of the cylinder.

Let

$$\sigma_z = \sigma_\theta/2 + f(\theta). \tag{10}$$

Then, equations (5)–(7), and (10) yield

$$f^4(\theta) + \left\{\frac{3}{4}\sigma_\theta{}^2 + 3\tau_{\theta z}{}^2\right\}f^2(\theta) - \left[\frac{m^2 R\sin\theta}{\dot{\rho}}\right]^2 = 0. \tag{11}$$

Consequently

$$f(\theta) = \sqrt{\sqrt{\left(\frac{3}{8}\sigma_\theta{}^2 + \frac{3}{2}\tau_{\theta z}{}^2\right)^2 + \left(\frac{m^2 R}{\dot{\rho}}\right)^2\sin^2\theta} - \left(\frac{3}{8}\sigma_\theta{}^2 + \frac{3}{2}\tau_{\theta z}{}^2\right)} \tag{12}$$

Substituting equations (10) and (12) into equation (9), in view of equation (8), we have

$$M = 4R^2 hm\sqrt{\eta}\int_0^{\frac{\pi}{2}} \sqrt{\sqrt{1\left(\frac{\xi}{\eta}\right)^2\sin^2\theta - 1}\sin\theta d\theta}, \tag{13}$$

where

$$\xi = R/\dot{\rho},$$

and

$$\eta = \frac{3}{8}\left\{\frac{PR}{mh}\right\}^2 + \frac{3}{2}\left\{\frac{T}{2\pi R^2 hm}\right\}^2. \tag{14}$$

Performing the integration, see Appendix, leads to

[1] Senior Engineer of Applied Physics, Ebasco Services Incorporated, New York, N. Y.

[2] Principal Engineer of Applied Physics, Ebasco Services Incorporated, New York, N. Y.

Manuscript received by ASME Applied Mechanics Division, August, 1980.

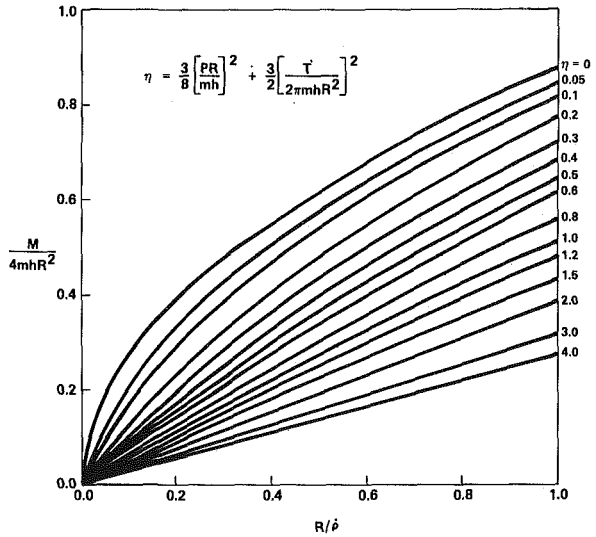

Fig. 1 Dimensionless moment—curvature rate relation for various *P* and *F*

$$\frac{M}{4R^2hm} = \frac{\sqrt{2}}{3\xi}\{\eta^2+\xi^2\}^{1/4}\left[\{\eta+\sqrt{\eta^2+\xi^2}\}F\left\{\frac{\pi}{2},k\right\} - 2\eta E\left\{\frac{\pi}{2},k\right\}\right] \tag{15}$$

where

$$k = \frac{\sqrt{2}}{2}\sqrt{1-\frac{1}{\sqrt{1+\left(\frac{\xi}{\eta}\right)^2}}} < 1, \tag{16}$$

and $F(\pi/2, k)$ and $E(\pi/2, k)$ are the complete elliptic integrals of the first and the second kinds, respectively. Equation (15) is plotted in Fig. 1 for various values of η.

Guided by Edstam and Hult [1], the "stress ratio" ϕ is defined by the relation

$$\phi^2 = \frac{\{\bar{\sigma}^{(2)}\}^2}{\{\bar{\sigma}^{(1)}\}^2}, \tag{17}$$

where

$$\{\bar{\sigma}^{(1)}\}^2 = \eta m^2\left\{2+\left(\frac{M}{\pi R^2hm}\right)^2\Big/\eta\right\} \tag{18}$$

and

$$\{\bar{\sigma}^{(2)}\}^2 = \eta m^2\{1+\sqrt{1+(\xi/\eta)^2}\}. \tag{19}$$

Consequently,

$$\phi^2 = \frac{1+\sqrt{1+(\xi/\eta)^2}}{2+(M/\pi R^2hm)^2/\eta}. \tag{20}$$

Substituting equation (20) into equation (15) leads to the interaction equation for M, P, and T. For the case, there is no twisting moment, Table 1 shows these results along with the results of (1). As can be seen that for $\phi = 0.999$, the difference between the present value with (1) is 18 percent.

Conclusions

A closed-form relation has been established for the bending and twisting of an internally pressurized thin-walled cylinder which obeys the Bailey-Norten type power law with $n = 2$. Dimensionless charts which can be used for engineering practice convenience have also been provided. The result presented herein ($n = 2$) is not only a good approximation of a wide class of materials, but also provides a standard tool for estimating the accuracy of different direct schemes such as numerical integration, finite-difference, and finite-element methods.

Table 1

θ	PR^3/M	
	Present	Edstam & Hult
0.9	0.03	0.00
0.92	0.13	*
0.95	0.24	0.22
0.96	0.28	*
0.97	0.34	*
0.98	0.42	0.43
0.99	0.56	0.58
0.992	0.60	*
0.994	0.67	*
0.995	0.71	0.73
0.996	0.76	*
0.997	0.83	*
0.998	0.94	*
0.999	1.15	1.36

* not presented

References

1 Edstam, U., and Hult, J., "Design Charts For Stationary Creep," *Recent Progress in Applied Mechanics*, ed., Broberg, Wiley, 1967.

2 Gradshteyn, I. S., and Ryzhik, I. M., *Table of Integrals Series and Products*, Academic Press, New York, 1965.

3 Hult, J., "On the Stationary of Stress and Strain Distributions in Creep," *IUTAM Proceedings of Symposium on 2nd-Order Effects in Elasticity, Plasticity, and Fluid Dynamics*, eds., Reiner, M., and Abir, D., 1965, pp. 352–361.

4 Hult, J., *Creep in Engineering Structures*, Blaisdell Publishing Company, London, 1966.

5 Rabotnov, Y. N., *Creep Problems in Structural Members*, North-Holland Publishing Company, 1969.

APPENDIX

$$M = 4R^2hm\sqrt{\eta}\int_0^{\frac{\pi}{2}}\sqrt{\sqrt{1+(\xi/\eta)^2\sin^2\theta}-1}\sin\theta d\theta$$

Let

$$\sqrt{1+(\xi/\eta)^2\sin^2\theta} = \beta$$

Then

$$M = \frac{4R^2hm\sqrt{\eta}}{(\xi/\eta)}\int_1^{\sqrt{1+(\xi/\eta)^2}}\frac{\beta\sqrt{\beta-1}\,d\beta}{\sqrt{1+(\xi/\eta)^2-\beta^2}}$$

Let

$$u = \sqrt{\beta-1} \quad \text{and} \quad dv = \frac{\beta d\beta}{\sqrt{1+(\xi/\eta)^2-\beta^2}}$$

Then, $\int u dv = uv - \int v du$ leads to

$$\frac{M(\xi/\eta)}{4R^2hm\sqrt{\eta}} = -\sqrt{(\beta-1)\{1+(\xi/\eta)^2-\beta^2\}}\Big|_1^{\sqrt{1+(\xi/\eta)^2}}$$

$$+\tfrac{1}{2}\int_1^{\sqrt{1+(\xi/\eta)^2}}\sqrt{\frac{1+(\xi/\eta)^2-\beta^2}{\beta-1}}\,d\beta$$

Note that the first term on the right-hand side is zero, and that the second term can be evaluated from [2, Page 235], then we have

$$\frac{M}{4R^2hm} = \frac{\sqrt{2}}{3\xi}\{\eta^2 + \xi^2\}^{1/4}\left[(\eta + \sqrt{\eta^2 + \xi^2})\, F\left\{\frac{\pi}{2}, k\right\} - 2\eta E\left\{\frac{\pi}{2}, k\right\}\right]$$

where

$$k = \frac{\sqrt{2}}{2}\sqrt{1 - \frac{1}{\sqrt{1 + (\xi/\eta)^2}}} < 1.$$

Inelastic Dynamic Response of Rectangular Plates by Finite Elements

K. S. Raghavan[1] and S. S. Rao[2]

Introduction

The dynamic elastoplastic behavior of rectangular plates is studied by applying finite-element idealization and numerical integration. Step-by-step response is obtained by using explicit schemes and the effects of plastic flow are incorporated through the initial strain approach. Inelastic analysis is carried out by applying the explicit elastoplastic matrix relation that relates stress increments to total strain increments. The analysis is restricted to small deformations, the material is assumed to obey the von Mises yield criterion, and the stress-strain curve is taken to be bilinear. The computational details of the analysis are given in references [1, 2].

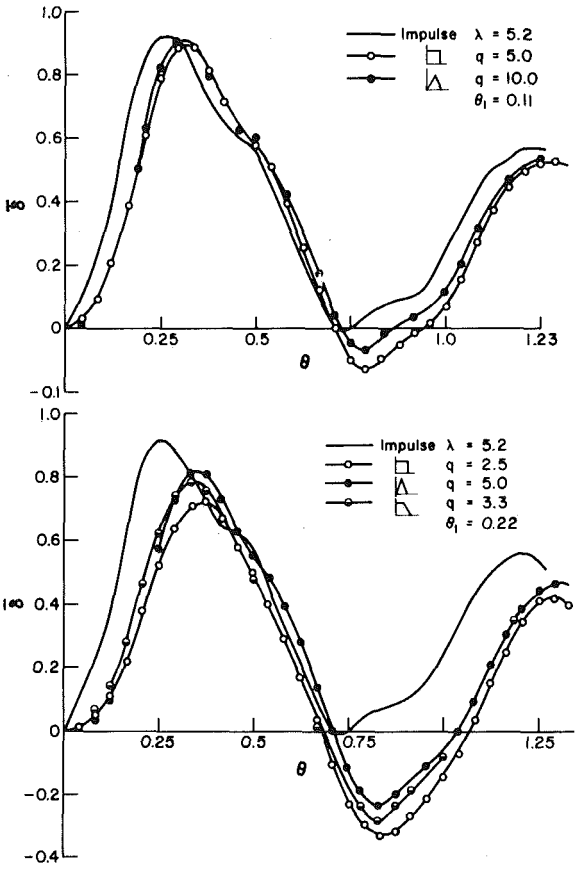

Fig. 1 Response of a clamped square plate to different pulses

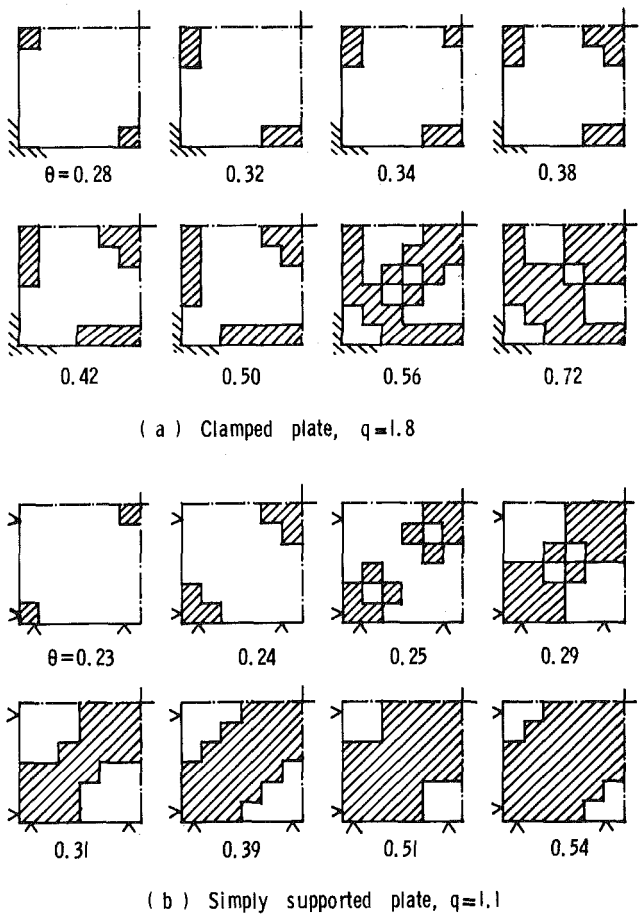

Fig. 2 Elastic-plastic boundaries for plates under uniform pressure; □ elastic, ▨ plastic

Results and Discussion

The response of rectangular plates is found using the 12-degree-of-freedom compatible element due to Bogner, et al. [3], which is based on Hermitian interpolation polynomials. Lumped mass matrix with geometric lumping was used. Responses were evaluated using a fourth-order Runge-Kutta scheme of Gill. Results are presented in Figs. 1–4 in terms of the nondimensional parameters θ, q, $\bar{\delta}$, and λ defined as $\theta = t/T_1$, $q = p/p_Y$, $\bar{\delta} = \delta/(q \cdot \delta_Y)$, $\lambda = V_0/V_r$, and $V_r = p_Y T_1/(10\, m) = k \cdot \sigma_0/[\rho E/(1-\nu^2)]^{1/2}$, where t = time, T_1 = fundamental period, p = applied distributed load, p_Y = static yield load, δ = deflection of central point, δ_Y = static deflection under p_Y, V_0 = applied uniform impulse, V_r = reference velocity, m = mass per unit area, σ_0 = yield stress, ρ = mass density, ν = Poisson's ratio, E = Young's modulus, and k is a constant. For a simply supported square plate of side a, $p_Y = M_0/(0.048\, a^2)$, $\delta_Y = 0.00406\, C_1$, $T_1 = C_2/18.73$, and $k = 0.576$ where $M_0 = \sigma_0 h^2/4$, $C_1 = p_Y a^4/D$, $c_2 = 2\pi a^2(m/D)^{1/2}$,

[1] Senior Design Engineer, R & D Division, BHEL, Hyderabad-500593, India.

[2] Professor, Department of Mechanical Engineering, Indian Institute of Technology, Kanpur-208016, India.

Manuscript received by ASME Applied Mechanics Division, December, 1978; final revision, July, 1980.

Note that the first term on the right-hand side is zero, and that the second term can be evaluated from [2, Page 235], then we have

$$\frac{M}{4R^2hm} = \frac{\sqrt{2}}{3\xi}\{\eta^2+\xi^2\}^{1/4}\left[(\eta+\sqrt{\eta^2+\xi^2})\,F\left\{\frac{\pi}{2},k\right\} - 2\eta E\left\{\frac{\pi}{2},k\right\}\right]$$

where

$$k = \frac{\sqrt{2}}{2}\sqrt{1-\frac{1}{\sqrt{1+(\xi/\eta)^2}}} < 1.$$

Inelastic Dynamic Response of Rectangular Plates by Finite Elements

K. S. Raghavan[1] and S. S. Rao[2]

Introduction

The dynamic elastoplastic behavior of rectangular plates is studied by applying finite-element idealization and numerical integration. Step-by-step response is obtained by using explicit schemes and the effects of plastic flow are incorporated through the initial strain approach. Inelastic analysis is carried out by applying the explicit elastoplastic matrix relation that relates stress increments to total strain increments. The analysis is restricted to small deformations, the material is assumed to obey the von Mises yield criterion, and the stress-strain curve is taken to be bilinear. The computational details of the analysis are given in references [1, 2].

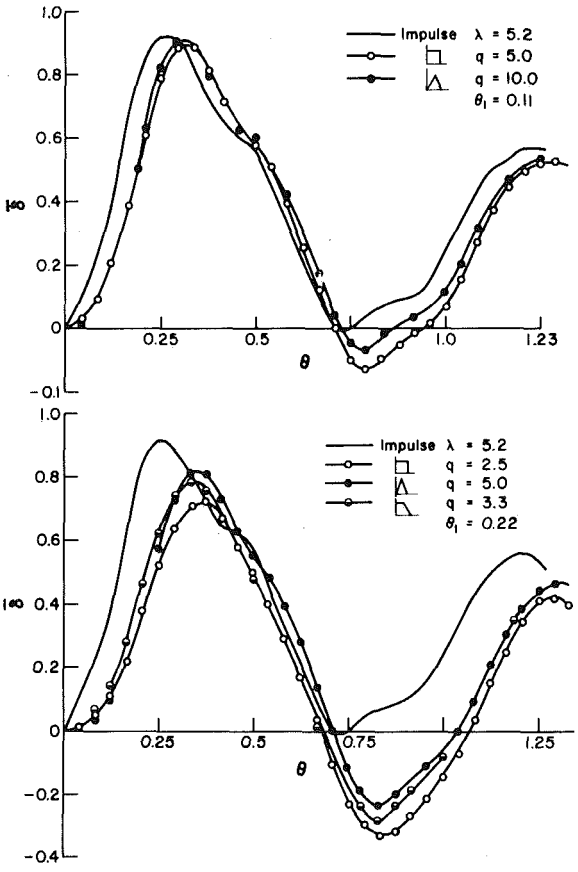

Fig. 1 Response of a clamped square plate to different pulses

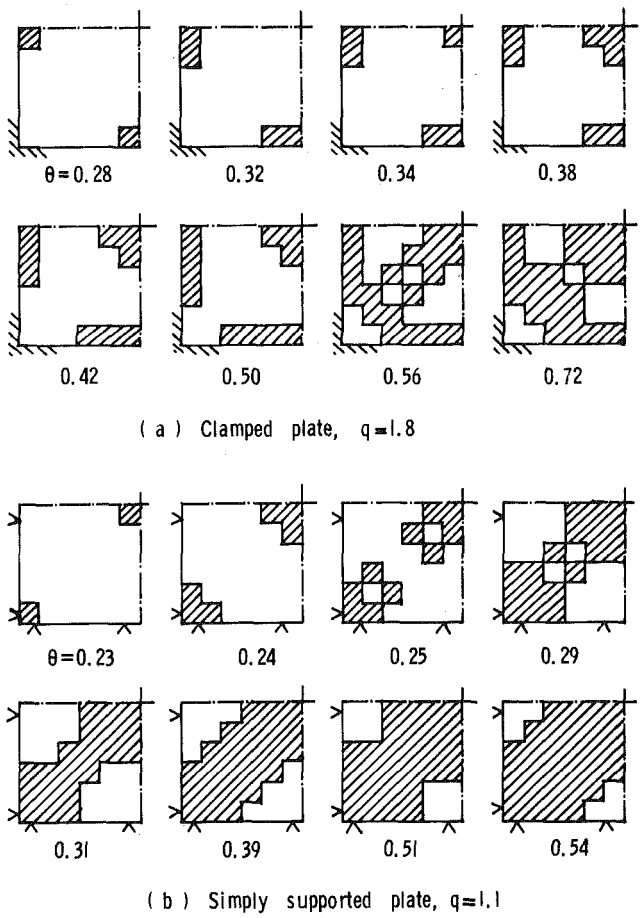

Fig. 2 Elastic-plastic boundaries for plates under uniform pressure; □ elastic, ▨ plastic

Results and Discussion

The response of rectangular plates is found using the 12-degree-of-freedom compatible element due to Bogner, et al. [3], which is based on Hermitian interpolation polynomials. Lumped mass matrix with geometric lumping was used. Responses were evaluated using a fourth-order Runge-Kutta scheme of Gill. Results are presented in Figs. 1–4 in terms of the nondimensional parameters θ, q, $\bar{\delta}$, and λ defined as $\theta = t/T_1$, $q = p/p_Y$, $\bar{\delta} = \delta/(q \cdot \delta_Y)$, $\lambda = V_0/V_r$, and $V_r = p_Y T_1/(10\,m) = k \cdot \sigma_0/[\rho E/(1-\nu^2)]^{1/2}$, where t = time, T_1 = fundamental period, p = applied distributed load, p_Y = static yield load, δ = deflection of central point, δ_Y = static deflection under p_Y, V_0 = applied uniform impulse, V_r = reference velocity, m = mass per unit area, σ_0 = yield stress, ρ = mass density, ν = Poisson's ratio, E = Young's modulus, and k is a constant. For a simply supported square plate of side a, $p_Y = M_0/(0.048\,a^2)$, $\delta_Y = 0.00406\,C_1$, $T_1 = C_2/18.73$, and $k = 0.576$ where $M_0 = \sigma_0 h^2/4$, $C_1 = p_Y a^4/D$, $c_2 = 2\pi a^2(m/D)^{1/2}$,

[1] Senior Design Engineer, R & D Division, BHEL, Hyderabad-500593, India.

[2] Professor, Department of Mechanical Engineering, Indian Institute of Technology, Kanpur-208016, India.

Manuscript received by ASME Applied Mechanics Division, December, 1978; final revision, July, 1980.

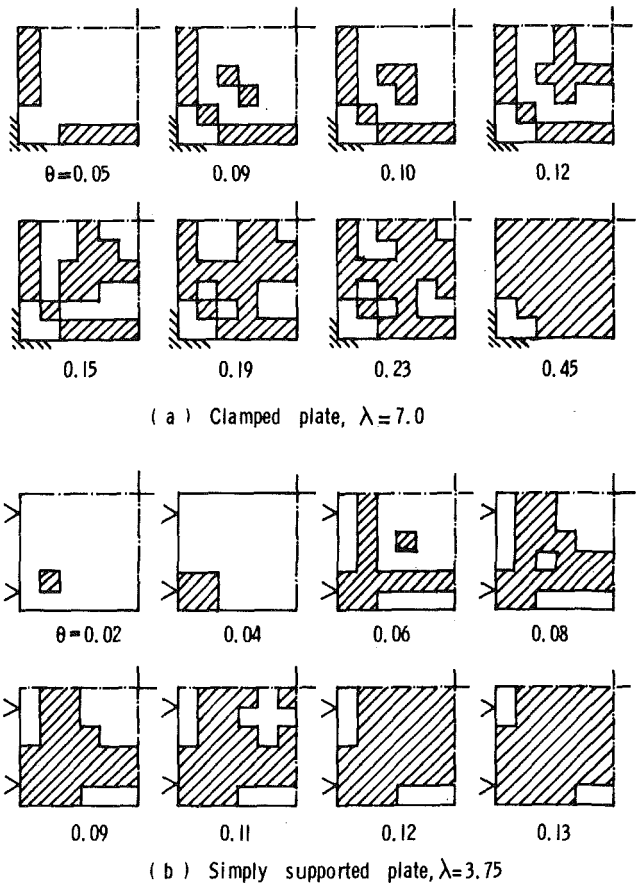

Fig. 3 Elastic-plastic boundaries for impulsively loaded plates

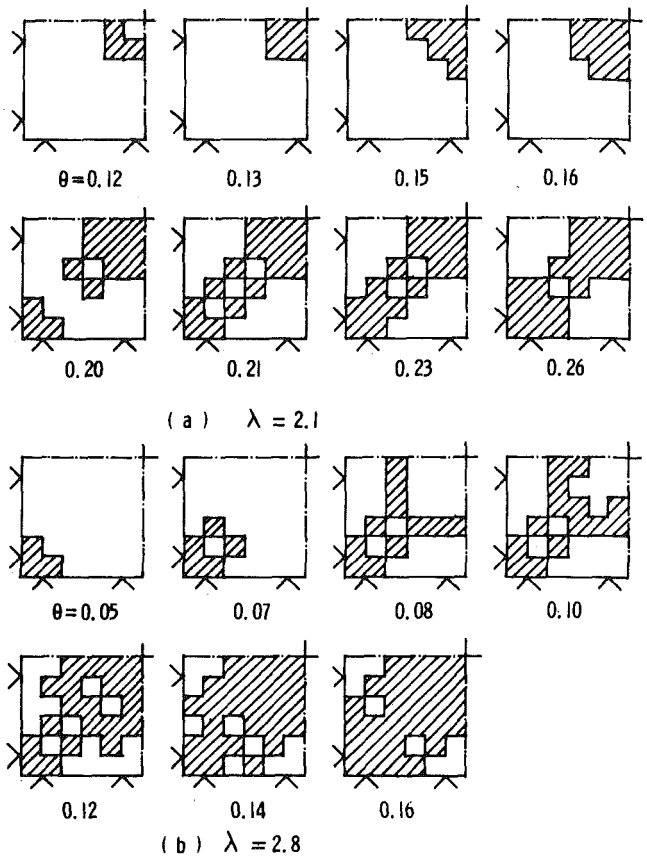

Fig. 4 Elastic-plastic boundaries for impulsively loaded simply supported plates

and $D = Eh^3/\{12\ (1 - \nu^2)\}$ where h = thickness of the plate. For a clamped plate, $p_Y = M_0/(0.053\ a^2)$, $\delta_Y = 0.00126\ C_1$, $T_1 = C_2/36$, and $k = 0.294$.

The responses of a clamped plate under the action of three different pulses are shown in Fig. 1. The pulse parameters, for comparison, are chosen on the basis of equal area and equal duration. Here the ordinate refers to the nondimensional response obtained for impulsive load. It is seen that, for a pulse period of $\theta_1 = 0.11$, the influence of pulse shape is not significant, and that for this pulse duration the impulsive approximation, predicts a response that is close to the actual one. For $\theta_1 = 0.22$, however, the influence of pulse shape is more pronounced, and, the impulsive approximation results in a large upper bound to the actual response.

In Figs. 2–4, the propagation of the plastic zones is presented for uniformly loaded and impulsively loaded plates. These results are obtained by defining yielding of the entire thickness on the basis of fully plastic moment and by using a 3 × 3 mesh and four Gaussian subdivisions in each element. In the case of uniformly loaded plates (Fig. 2) predictable patterns of plastic zones are observed. In fact they are in good agreement with the results obtained by Ang and Lopez [4] in their studies on the limit analysis of plates. In the case of impulsive load, however, no definite pattern is noticed (Fig. 3). A comparison between Figs. 3(*b*) and 4 reveals that the mode of propagation of plastic zones in an impulsively loaded plate is a function of the initial velocity (λ).

During the initial phase of the response, the nodal displacements do not conform to the static deflection shape, and at such instances the maximum moment may not be at the centre or the edges. In an impulsively loaded plate, yielding is almost instantaneous, and, it appears that because of this the plastic zones do not follow any predictable pattern.

References

1 Rao, S. S., and Raghavan, K. S., "Dynamic Response of Inelastic Thick Plates," *AIAA Journal*, Vol. 17, 1979, pp. 85–90.

2 Raghavan, K. S., "Finite-Element Studies on Inelastic Response of Beams and Plates," PhD Thesis, Indian Institute of Technology, Kanpur, India, 1977.

3 Bogner, F. K., Fox, R. L., and Schmit, L. A., Jr., "The Generation of Interelement Compatible Stiffness by the Use of Interpolation Formulas," *Matrix Methods in Structural Analysis*, AFFDL-TR-80, 1966, pp. 397–443.

4 Ang, A. H., and Lopez, L. A., "Discrete Model Analysis of Elastic Plastic plates," *Journal of Engineering Mechanics Division*, ASCE, Vol. 94, 1968, pp. 271–293.

Comments on Aleck's Stress Distribution in Clamped Plates

I. A. Blech[1] and A. A. Levi[2]

This Note reports some numerical refinements for the computed values of the coefficients in the paper entitled "Thermal Stresses in a Rectangular Plate Clamped Along an Edge," by B. J. Aleck [1],

[1] Department of Materials Engineering Technion, Israel Institute of Technology, Technion, Haifa, 32000 Israel.

[2] IBM, T. J. Watson Research Center, P.O. Box 218, Yorktown Heights, N.Y. 10598

Manuscript received by ASME Applied Mechanics Division May, 1980; final revision, October, 1980.

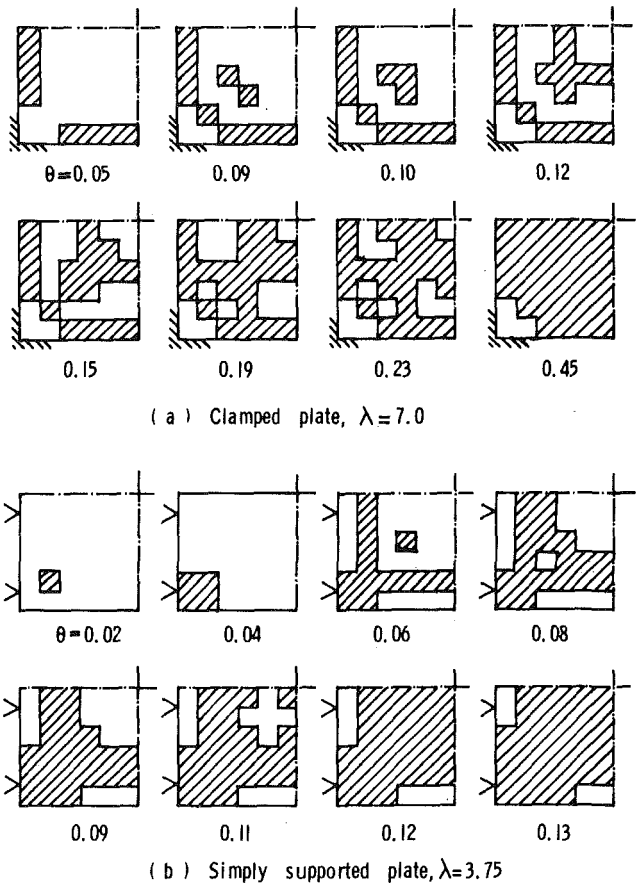

Fig. 3 Elastic-plastic boundaries for impulsively loaded plates

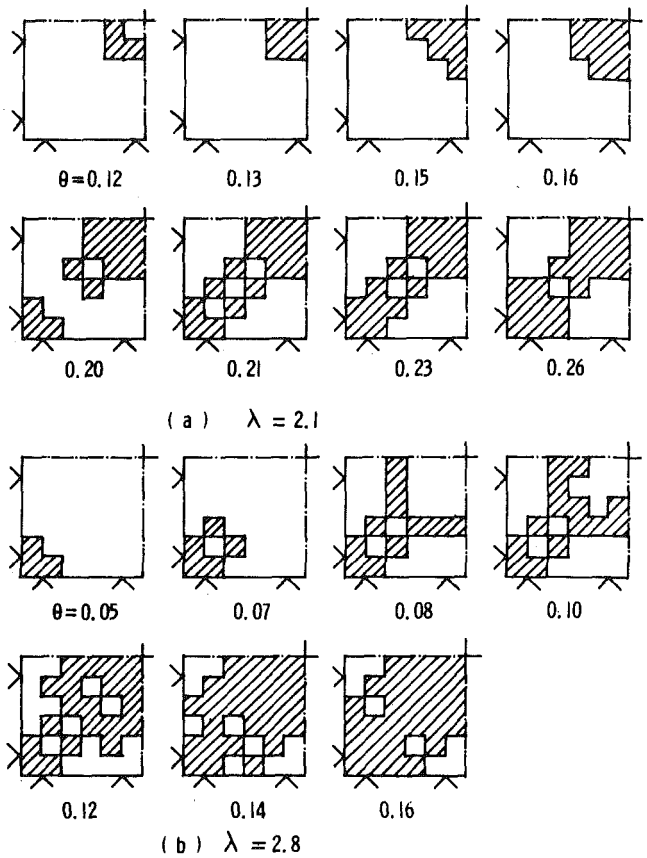

Fig. 4 Elastic-plastic boundaries for impulsively loaded simply supported plates

and $D = Eh^3/\{12\ (1 - \nu^2)\}$ where h = thickness of the plate. For a clamped plate, $p_Y = M_0/(0.053\ a^2)$, $\delta_Y = 0.00126\ C_1$, $T_1 = C_2/36$, and $k = 0.294$.

The responses of a clamped plate under the action of three different pulses are shown in Fig. 1. The pulse parameters, for comparison, are chosen on the basis of equal area and equal duration. Here the ordinate refers to the nondimensional response obtained for impulsive load. It is seen that, for a pulse period of $\theta_1 = 0.11$, the influence of pulse shape is not significant, and that for this pulse duration the impulsive approximation, predicts a response that is close to the actual one. For $\theta_1 = 0.22$, however, the influence of pulse shape is more pronounced, and, the impulsive approximation results in a large upper bound to the actual response.

In Figs. 2–4, the propagation of the plastic zones is presented for uniformly loaded and impulsively loaded plates. These results are obtained by defining yielding of the entire thickness on the basis of fully plastic moment and by using a 3 × 3 mesh and four Gaussian subdivisions in each element. In the case of uniformly loaded plates (Fig. 2) predictable patterns of plastic zones are observed. In fact they are in good agreement with the results obtained by Ang and Lopez [4] in their studies on the limit analysis of plates. In the case of impulsive load, however, no definite pattern is noticed (Fig. 3). A comparison between Figs. 3(*b*) and 4 reveals that the mode of propagation of plastic zones in an impulsively loaded plate is a function of the initial velocity (λ).

During the initial phase of the response, the nodal displacements do not conform to the static deflection shape, and at such instances the maximum moment may not be at the centre or the edges. In an impulsively loaded plate, yielding is almost instantaneous, and, it appears that because of this the plastic zones do not follow any predictable pattern.

References

1 Rao, S. S., and Raghavan, K. S., "Dynamic Response of Inelastic Thick Plates," *AIAA Journal*, Vol. 17, 1979, pp. 85–90.

2 Raghavan, K. S., "Finite-Element Studies on Inelastic Response of Beams and Plates," PhD Thesis, Indian Institute of Technology, Kanpur, India, 1977.

3 Bogner, F. K., Fox, R. L., and Schmit, L. A., Jr., "The Generation of Interelement Compatible Stiffness by the Use of Interpolation Formulas," *Matrix Methods in Structural Analysis*, AFFDL-TR-80, 1966, pp. 397–443.

4 Ang, A. H., and Lopez, L. A., "Discrete Model Analysis of Elastic Plastic plates," *Journal of Engineering Mechanics Division*, ASCE, Vol. 94, 1968, pp. 271–293.

Comments on Aleck's Stress Distribution in Clamped Plates

I. A. Blech[1] and A. A. Levi[2]

This Note reports some numerical refinements for the computed values of the coefficients in the paper entitled "Thermal Stresses in a Rectangular Plate Clamped Along an Edge," by B. J. Aleck [1],

[1] Department of Materials Engineering Technion, Israel Institute of Technology, Technion, Haifa, 32000 Israel.

[2] IBM, T. J. Watson Research Center, P.O. Box 218, Yorktown Heights, N.Y. 10598

Manuscript received by ASME Applied Mechanics Division May, 1980; final revision, October, 1980.

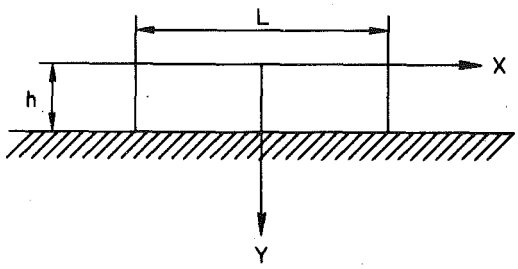

Fig. 1 Schematic diagram of a clamped plate subject to stress given by equation (1)

where the principle of least work was used to calculate the stress distribution in a clamped plate. A schematic diagram of the plate is seen in Fig. 1. The calculations are based on the assumption that the stress in the film plane σ_{xx} can be written as

$$\sigma_{xx} = f_1(x) + yf_2(x) + y^2 f_3(x) \tag{1}$$

Following Aleck's solution,

$$\frac{\sigma_{xx}}{E\Delta\alpha\Delta T} = \sum_{i=1}^{3}\sum_{j=1}^{6} A_{ij} y^{i-1} \cosh \lambda_j x - 1$$

$$\frac{\tau_{xy}}{E\Delta\alpha\Delta T} = -\sum_{i=1}^{3}\sum_{j=1}^{6} A_{ij} \frac{y^i}{i} \lambda_j \sinh \lambda_j x$$

$$\frac{\sigma_{yy}}{E\Delta\alpha\Delta T} = \sum_{i=1}^{3}\sum_{j=1}^{6} A_{ij} \frac{y^{i+1}}{i(i+1)} \lambda_j^2 \cosh \lambda_j x, \tag{2}$$

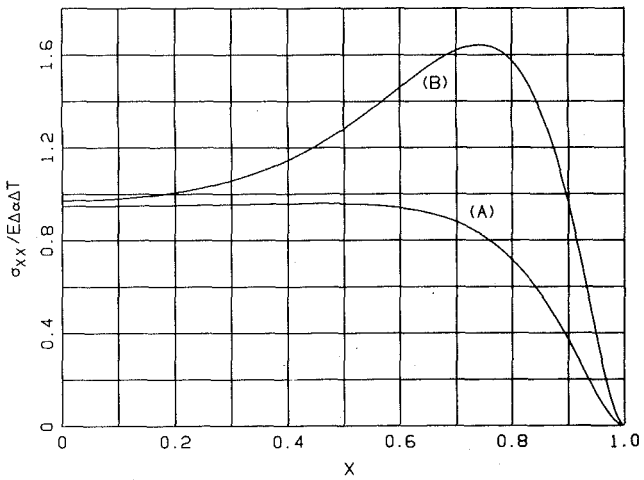

Fig. 2(a) $\sigma_{xx}/E\Delta\alpha\Delta T$ versus x

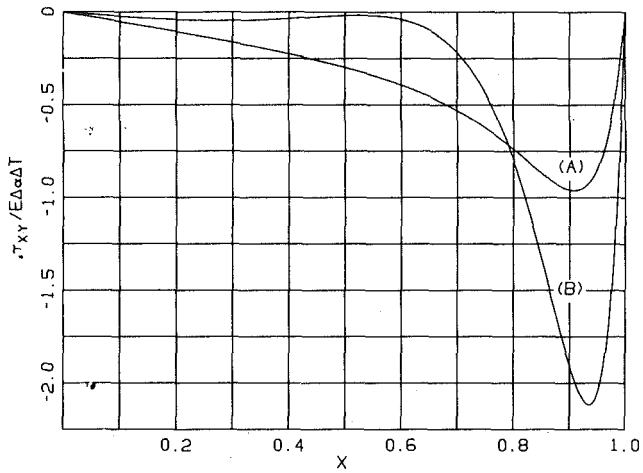

Fig. 2(b) $\tau_{xy}/E\Delta\alpha\Delta T$ versus x

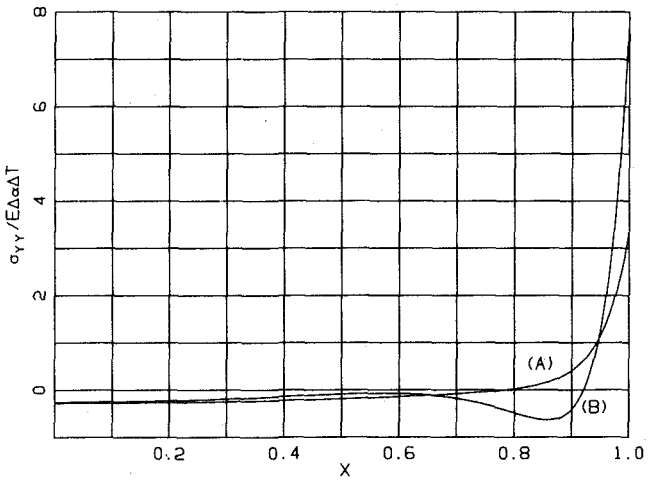

Fig. 2(c) $\sigma_{yy}/E\Delta\alpha\Delta T$ versus x

Fig. 2 Stress distribution in a clamped plate $L/2h = 1$, $\nu = 0.25$, $y = 1$ according to equation (2), (*a*) computed with coefficients of Table 1, (*b*) computed with the coefficients of Aleck's paper [1]

Table 1 Calculated values of λ_j, A_{2j}/A_{1j}, and A_{3j}/A_{1j} for $\nu = 0.25$

j	λ_j	A_{2j}/A_{1j}	A_{3j}/A_{1j}
1	21.46929445	−9.259707015	13.29296812
2	6.555641247 + 2.811853236i	−7.228832554 + 0.3938203841i	8.305571674 − 0.9943166057i
3	6.555641247 − 2.811853236i	−7.228832554 − 0.3938203841i	8.305571674 + 0.9943166057i
4	2.580328004 + 1.339360994i	−4.275900625 + 0.5528040859i	3.137293505 − 0.4612713004i
5	2.580328004 − 1.339360994i	−4.275900625 − 0.5528040859i	3.137293505 + 0.4612713004i
6	1.000579564	−0.1308266266	−0.778698474

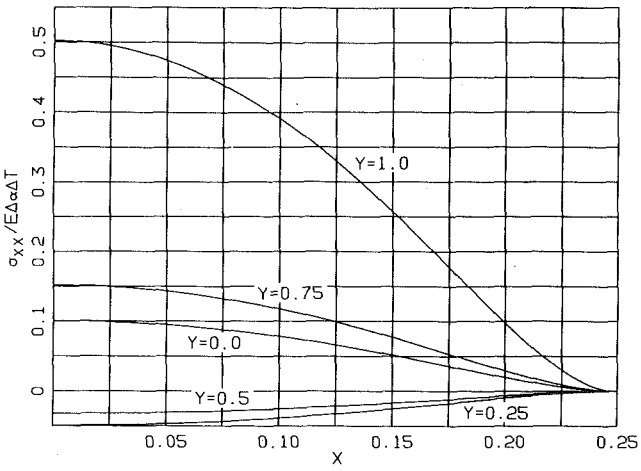

Fig. 3(*a*) $\sigma_{xx}/E\Delta\alpha\Delta T$ versus x

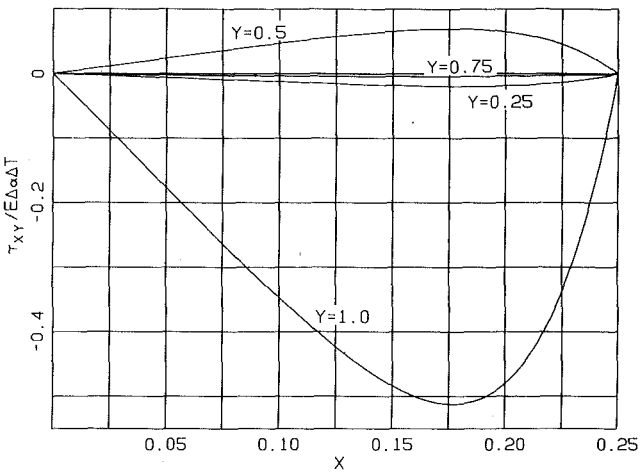

Fig. 3(*b*) $\tau_{xy}/E\Delta\alpha\Delta T$ versus x

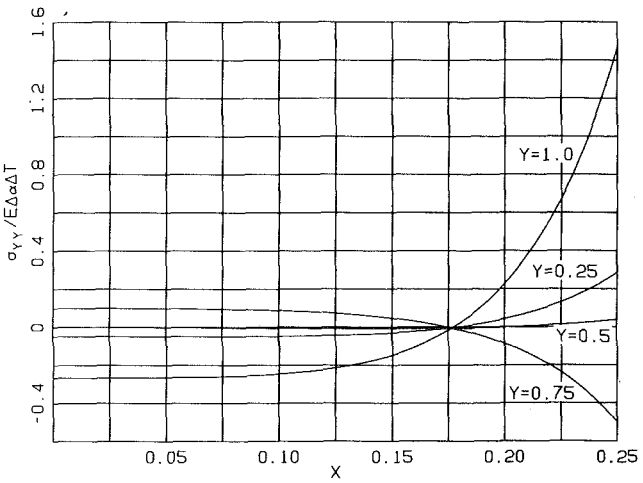

Fig. 3(*c*) $\sigma_{yy}/E\Delta\alpha\Delta T$ versus x

Fig. 3 Stress distribution in a clamped plate $L/2h = 0.25$, $\nu = 0.25$, according to equation (2)

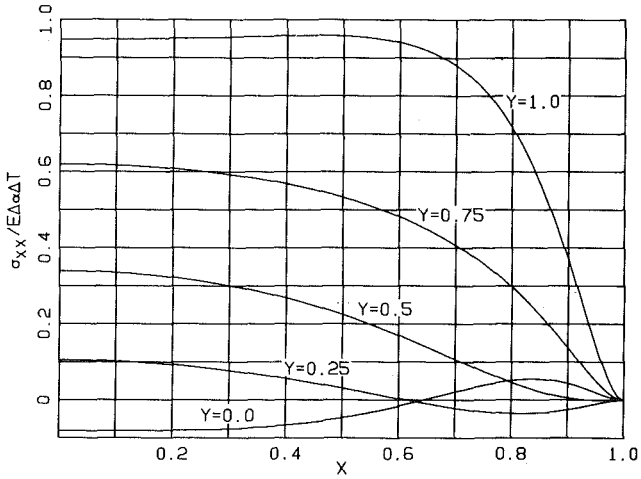

Fig. 4(*a*) $\sigma_{xx}/E\Delta\alpha\Delta T$ versus x

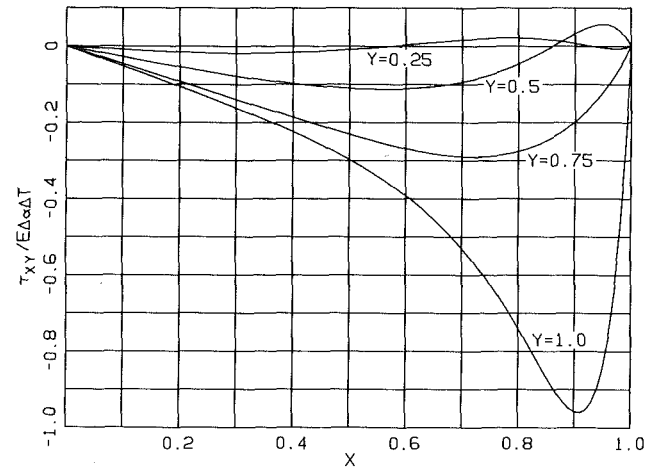

Fig. 4(*b*) $\tau_{xy}/E\Delta\alpha\Delta T$ versus x

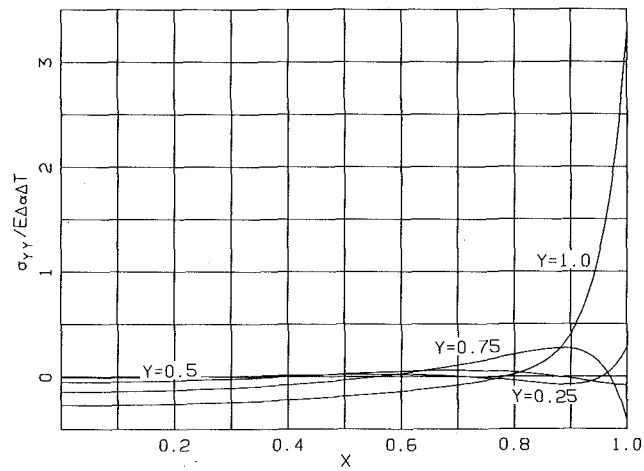

Fig. 4(*c*) $\sigma_{yy}/E\Delta\alpha\Delta T$ versus x

Fig. 4 Stress distribution in a clamped plate $L/2h = 1$, $\nu = 0.25$, according to equation (2)

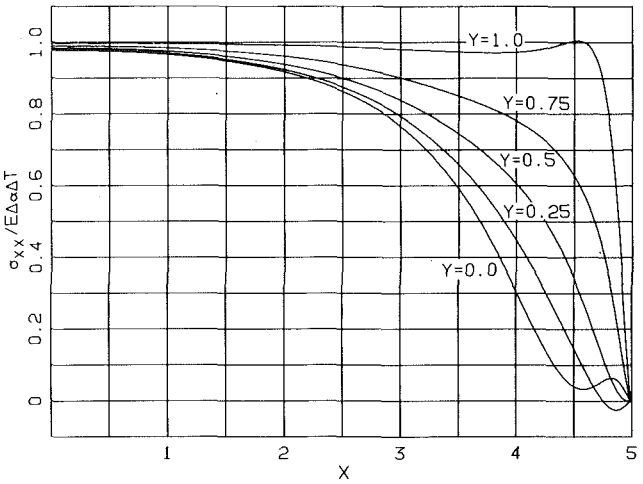

Fig. 5 (*a*) $\sigma_{xx}/E\Delta\alpha\Delta T$ versus x

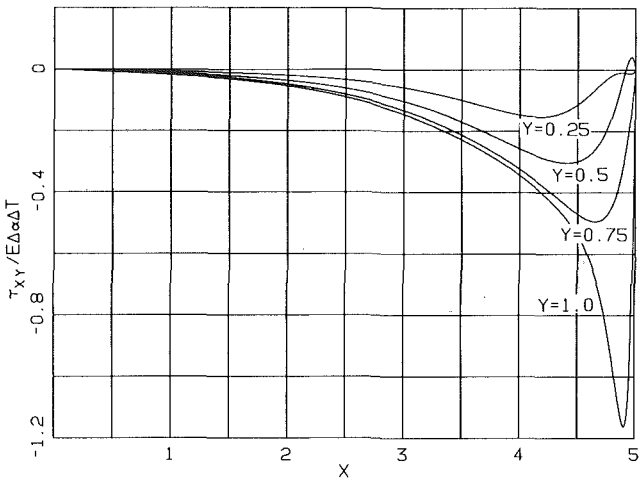

Fig. 5 (*b*) $\tau_{xy}/E\Delta\alpha\Delta T$ versus x

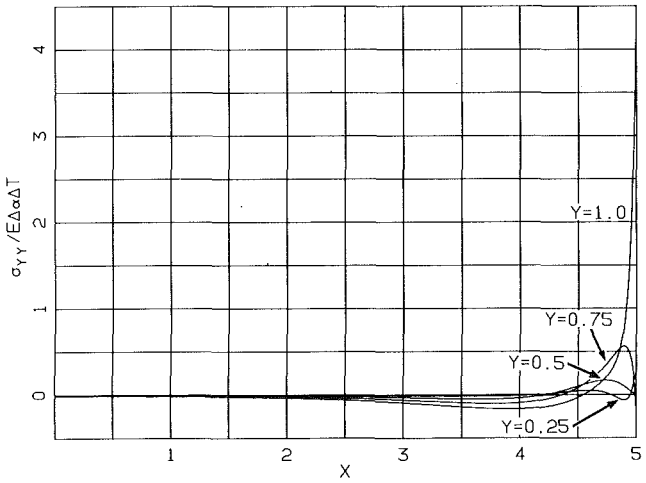

Fig. 5 (*c*) $\sigma_{yy}/E\Delta\alpha\Delta T$ versus x

Fig. 5 Stress distribution in a clamped plate $L/2h = 5$, $\nu = 0.25$, according to equation (2)

where E is the Young's modulus, $\Delta\alpha$ is the differential thermal expansion coefficient, and ΔT is the temperature difference, so that $\Delta\alpha\Delta T$ is the total thermal expansion of the plate relative to the clamping member. The nondimensional variables x and y are normalized to the plate thickness h. The coefficients A_{ij} depend on $L/2h$ and Poisson's ratio ν, and the λ_j's depend on ν.

The solution of equation (2) involves finding the condition where a determinant equals zero [1]. A computer was used to find the roots of the polynomial associated with this determinant and to determine the values for λ_j and A_{ij}. A measure of the accuracy of the calculation is how closely the determinant approaches zero upon substitution of the roots. The complex roots obtained by us result in zeros better than 10^{-12}, whereas the roots given by Aleck lead to values in the range of $7.5 \times 10^{-5} - 10^{-10}$.

Although the A_{ij}'s depend on $L/2h$, the ratios of A_{2j}/A_{1j} and A_{3j}/A_{1j} are independent of $L/2h$. Values of the coefficients λ_j, A_{2j}/A_{1j}, and A_{3j}/A_{1j} for $\nu = 0.25$ are given in Table 1.

We find that the values of λ_2 and λ_3 in particular differ from those of Aleck and consequently the coefficient ratios also differ significantly. Correspondingly, the calculated σ_{xx}, τ_{xy}, and σ_{yy} are considerably different from the previously reported values [1, 2]. In Fig. 2 we have compared the stress distribution in a clamped plate for the case of $y = 1$ and $L/2h = 1$ using our coefficients with that using Aleck's coefficients. Figs. 3, 4, and 5 show stress distributions using our coefficients over the range $0 \le y \le 1$ and $L/2h = 0.25$, 1, and 5.

Finally, the stress calculations were extended to a polynomial containing four terms,

$$\sigma_{xx} = f_1(x) + yf_2(x) + y^2f_3(x) + y^3f_4(x) \tag{3}$$

The corresponding stress equations are,

$$\frac{\sigma_{xx}}{E\Delta\alpha\Delta T} = \sum_{i=1}^{4}\sum_{j=1}^{8} A_{ij}y^{i-1}\cosh\lambda_j x - 1$$

$$\frac{\tau_{xy}}{E\Delta\alpha\Delta T} = -\sum_{i=1}^{4}\sum_{j=1}^{8} A_{ij}\frac{y^i}{i}\lambda_j \sinh\lambda_j x$$

$$\frac{\sigma_{yy}}{E\Delta\alpha\Delta T} = \sum_{I=1}^{4}\sum_{j=1}^{8} A_{ij}\frac{y^{i+1}}{i(i+1)}\lambda_j{}^2\cosh\lambda_j x \tag{4}$$

It was found that the additional term in equation (3) does not alter the stress distribution significantly.

References

1 Aleck, B. J., "Thermal Stresses in a Rectangular Plate Clamped Along an Edge," ASME JOURNAL OF APPLIED MECHANICS, *Solid-State Electronics*, Vol. 16, June 1949, pp. 118–122.

2 Zeyfang, R., "Stresses and Strains in a Plate Bonded to a Substrate: Semiconductor Devices," *Solid-State Electronics*, Vol. 14, 1971, pp. 1035–1039.

Journal of Applied Mechanics

Discussion

A Reinterpretation of the Palmgren-Miner Rule for Fatigue Life Prediction[1]

M. Ben-Amoz.[2] The author is to be commended for attempting to present a simple theory of interaction under cyclic loading that takes into account sequence-of-loading effects. Despite its apparent simplicity, the fact that the theory depends on the existence of a fatigue limit in *all* metals, raises some questions in the writer's mind which deserve discussion. This writer, unaware of the author's work, has developed in the past two years in unpublished work, a phenomenological model of metal fatigue for constant amplitude cycling, which was used as the basis for a theory of interaction under multistage loading, quite different from the author's. The writer believes that discussion of his results in this forum would be of interest to JOURNAL readers as well as to the author in clarifying the significance of the Palmgren-Miner rule and the author's own theory. For simplicity, the discussion will be confined to two-stage strain cycling, and to metals obeying the Coffin-Manson fatigue law, namely, $\Delta ep = 2\, e_f\, (2N)^{-M_1}$, where Δep is the plastic strain-range; ef, the true fracture strain and N is the fatigue life; M_1 is a constant, characteristic of the metal. In log-log coordinates, the fatigue curve for single-stage cycling is thus a straight line emanating from $\Delta ep = 2ef$ at $N = \frac{1}{2}$, as shown in Fig. 1 of this discussion. The writer, in contrast to the author's assumption, accepts the fact that some metals possess an endurance limit while others do not. Accordingly, attention will first be focused on metals without an endurance limit, in which case the straight line fatigue curve is assumed to be valid over the entire range $\frac{1}{2} \leqslant N \leqslant \infty$. Let us now consider 2-stage cycling from low to high strain amplitudes corresponding to N_2 and N_1 fatigue lives, respectively, as shown in Fig. 1. Assume that n_2 cycles are applied at the lower strain amplitude (N_2) and it is desired to determine the residual life $N_1{}^r$ at the higher amplitude (N_1). Actually, we shall seek to determine *bounds* on the residual life at the higher amplitude. In doing so, it is worth emphasizing an overlooked fact that the true fracture strain in the Coffin-Manson relation is actually a *cyclic ductility* which is *assumed* to be *approximately equal* to the monotonic ductility. In many (but not all) metals, the reduction in ductility due to cycling is quite small (but finite) so that this assumption is acceptable as an *approximation.* Keeping this fact in mind, one must allow for possibly larger reductions in cyclic ductility in some metals. Accordingly, let us assume that the residual fatigue life (RL) curve passing through $N_2{}^r = N_2 - n_2$ is parallel to the base fatigue curve, as in Fig. 1. This curve corresponds to the maximum possible reduction in cyclic ductility and thus provides one bound on the actual RL curve passing through $N_2{}^r = N_2 - n_2$. A second bound is obtained if one assumes no reduction in ductility, so that the RL curve converges to the base curve at $N = \frac{1}{2}$. Corresponding to the two RL curves, are the bounds $N_1{}^r$ min and $N_1{}^r$ max, which from simple geometric relations (in log-log coordinates) are

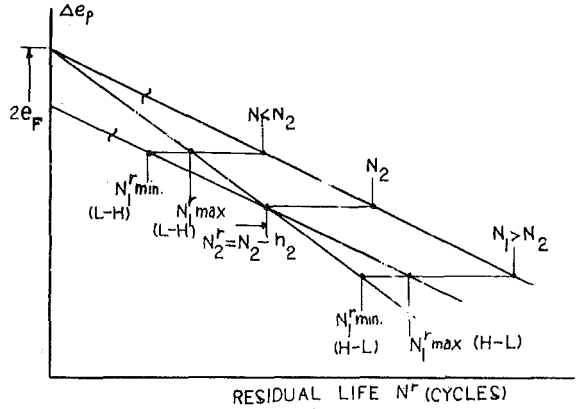

Fig. 1 Bounds on residual life curves passing through $N_2{}^r = N_2 - n_2$ for low-high (L-H) and high-low (H-L) cycling in metals without endurance limit

$$1 - \frac{n_2}{N_2} \leqslant \frac{N_1{}^r}{N_1} \leqslant \left(1 - \frac{n_2}{N_2}\right)^{\log 2N_1/\log 2N_2} \qquad (N_1 \leqslant N_2) \qquad (1)$$

It is seen that the lower bound represents the Palmgren-Miner straight line while the upper bound involves only the two endurances N_1, N_2. It is thus clear that if a metal undergoes a large reduction in ductility due to cycling, the interaction curve would approach the Palmgren-Miner line whereas if the reduction is neglibible (as in the case in most metals), the interaction curve approaches the upper bound. It is easy to show, based on Fig. 1, that by interchanging the bounds in (1), we obtain bounds for high-to-low cycling. Furthermore, the bounds (1) remain valid even if an endurance limit exists, provided *both* stages lie above or below the transition fatigue life N_T. Only in the exceptional case when one stage lies above and the other below N_T, different bounds apply. Such bounds have been established, involving N_T rather than the endurance limit, but are omitted due to space limitations.

T. Bui-Quoc.[3] The author's suggestion[1] that the linear damage (Palmgren-Miner) rule is a special case of the "generalized theory of fatigue lifetime prediction" proposed in [1] is of interest, but some features of the demonstration, in the discusser's opinion, warrant a more elaborated treatment. The major points noted are as follows:

1 What is the basis for the simplifying assumption used in the author's paper[1] that the endurance limit of a fatigued specimen is identical to that corresponding to the original material? This does not

[1] By Z. Hashin, and published in the June, 1980, issue of the ASME JOURNAL OF APPLIED MECHANICS, Vol. 47, pp. 324–328.

[2] General Electric Company, 1000 Western Ave. (240G7), Lynn, Mass. 01910.

[3] Associate Professor, Section of Applied Mechanics, Department of Mechanical Engineering, École Polytechnique, Montreal, Canada.

reflect, in general, the material behavior [2, 3] and, in fact, the strength reduction associated with the original endurance limit has been taken into consideration in several investigations [4–7].

2 In [1], the general theory has been presented with *four* alternative procedures for estimating the remaining lives of a material under multilevel loading, i.e., two types of σ-N diagram (log-log and semilog coordinates) combined with two convergence points of isodamage lines (the upper point corresponding to the ultimate tensile stress and the lower-point corresponding to the endurance limit). Experimental support has been given for one procedure only (associated with the lower convergence point) in the case of a sequence of loading with two stresses.

It appears that the estimated remaining lives depend primarily upon the convergence point consideration. As an example, for two decreasing stresses, i.e., $s_1 > s_2$, the predicted sum of life-fractions at failure, i.e., $\Sigma(n/N)$, is larger than unity with the upper-convergence-point consideration and this sum is smaller than unity when the lower-convergence point is used. What is the potential of applicability of each procedure, as well as its limitations?

Since semilog coordinates are commonly used to plot experimental results in the σ-N diagram, and since the data may be reasonably represented by a straight line in most cases, the further points in this discussion are presented on the basis of this type of plot. With this consideration, the general theory is reduced to two major alternatives characterized by the convergence points.

3 Let us examine a particular case of loading involving two *decreasing* stresses applied to a material with a typical value of $s_e = 0.4$. According to the author's paper,[1] when the two stresses are close to the ultimate tensile strength, say within 1.0–0.8, it is expected that the sum of the cycle-ratios at failure is greater than unity (upper-convergence-point method); on the other hand, when the two stresses are in the neighborhood of the endurance limit, say, within 0.6–0.4, it is expected that this sum is smaller than unity (lower-convergence-point procedure). Thus, in the middle range of stresses, i.e., 0.8–0.6, would the linear damage rule be valid? If it is not the case, how may one determine the specific stresses which delimit the two zones? How can one consider the case where the two stresses are not in the same zone?

4 Concerning the upper-convergence-point method, a similar concept has been proposed by Manson, et al. [6]. Fig. 2 of this discussion shows the method in [6] in comparison with the author's procedure for a typical case of loading (two decreasing stresses). The localization of the convergence points being of little importance for the purpose of the present discussion, the main difference between the two propositions is the starting point of the procedure to follow in order to obtain the remaining life (point A in Fig. 2). As a consequence, the estimated sum of cycle-ratios at failure given by the procedure outlined in Fig. 2(a) is opposite that obtained from the technique described by Fig. 2(b); the latter sum is in good agreement with test results reported in [2, 3]. Is there experimental evidence to support the approach in Fig. 2(a)?

5 Regarding the lower-convergence-point technique, what is the difference between the method advanced by Subramanyan [8] and the technique outlined by the author?[1]

6 An example is given in the author's paper[1] concerning the sequence of m stages of regularly increasing (or decreasing) stresses specified by two extreme levels s_1 and s_m. With m different stresses imposed (see the author's Fig. 5) there are $(m - 1)$ stress intervals, i.e.,

$$\Delta s = \frac{s_m - s_1}{m - 1}$$

It is not clear why the denominator in the author's equation (31)[1] is m.

7 It is not easy to see how the Palmgren-Miner rule is obtained as a special case (author's equations (26) and (27)) when ϕ_k = constant. Then with ϕ_k = constant (= B, say), equations (28) and (30) become

$$\phi_k = s_k - s_e = B$$

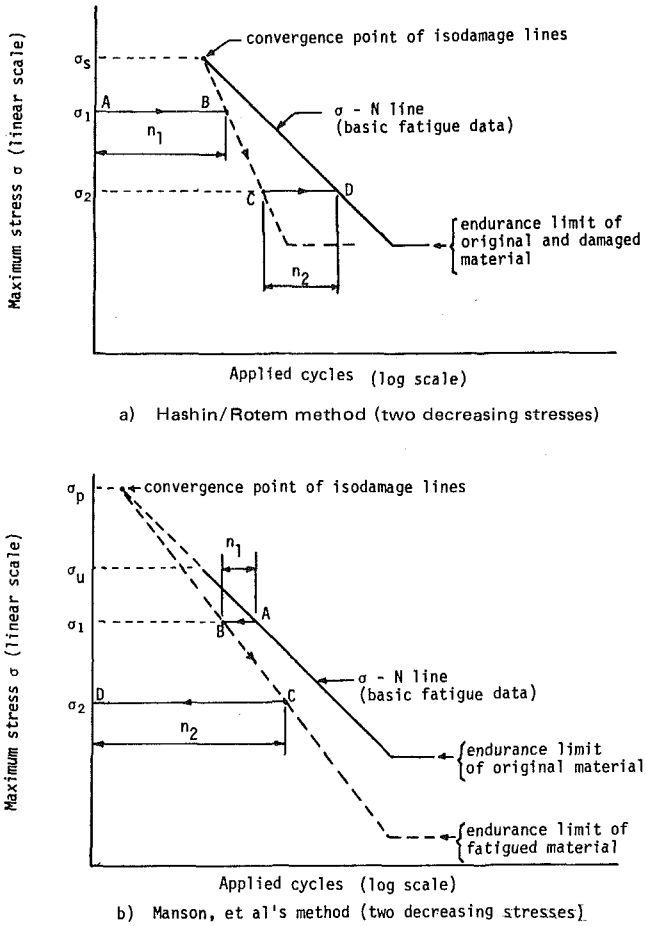

Fig. 2 Comparison between the two life-prediction methods proposed by Hashin and Manson, et al. (upper-convergence point)

$$\frac{\phi_k}{\phi_{k-1}} = \frac{\log (N_k/N_e)}{\log (N_{k-1}/N_e)} = 1$$

Thus, for a given material, since s_e (or N_e) is a fixed value, s_k (or N_k) should also be a fixed value for all stress levels considered in the sequence, according to the two foregoing equations. If there is *no* change in the stress levels, there is no cumulative damage in the usual sense requiring at least two distinct levels of solicitation. Note further that, in this case (no stress change), any fatigue damage theory yielding a normalized damage function (including stress-dependent cases) is equivalent to the linear damage rule on the basis of cycle-ratio calculations [9].

References

1 Hashin, Z., and Rotem, A., "A Cumulative Damage Theory of Fatigue Failure," *Mat. Sc. and Eng.*, Vol. 34, 1978, pp. 147–160.

2 Bennett, J. A., "A Study of the Damage Effect of Fatigue Stressing on X4130 Steel," *Proc. ASTM*, Vol. 46, 1946, pp. 693–714.

3 Manson, S. S., et al., "Further Investigation of a Relation for Cumulative Fatigue Damage in Bending," ASME *Journal of Engineering for Industry*, Vol. 87, 1965, pp. 25–35.

4 Henry, D. L., "A Theory of Fatigue Damage Accumulation in Steel," TRANS. ASME, Vol. 77, 1955, pp. 913–918.

5 Gatts, R. R., "Application of a Cumulative Damage Concept to Fatigue," ASME *Journal of Basic Engineering*, Vol. 83, 1961, pp. 529–540.

6 Manson, S. S., Nachtigall, A. J., and Freche, J. C., "A Proposed New Relation for Cumulative Fatigue Damage in Bending," *Proc. ASTM*, Vol. 61, 1961, pp. 679–703.

7 Bui-Quoc, T., et al., "Cumulative Fatigue Damage Under Stress-Controlled Conditions," ASME *Journal of Basic Engineering*, Vol. 93, 1971, pp. 691–698.

8 Subramanyan, S., "A Cumulative Damage Rule Based on the Knee Point of the S.N Curve," ASME *Journal of Engineering Materials and Technology*, Vol. 98, 1976, pp. 316–321.

9 Bui-Quoc, T., "Dommage cumulatif en fatigue," in *Fatigue des Matériaux et des Structures*, Maloine, Paris, 1980, pp. 312–342.

Author's Closure

I very much appreciate the discussers' interest and comments. May I say before attempting to answer that the present paper and its predecessor [10] should not be construed as an attempt to give a definitive solution to the cumulative damage problem. Their purpose is to present a rational point of view based on the damage curve concept and the equivalent loading postulate. Since the damage curves are not known, simple ad hoc forms have been assumed in order to obtain results. It is to be hoped and expected that better damage curves will be given in the future. The equivalent loading postulate is the key to lifetime analysis for *any* loading program, the damage curves being sufficient information for this purpose. Thus the main achievement, if any, is construction of a theory and not the actual results given. The chief shortcoming of the theory given is not in that damage curves are not sufficiently accurate or that the fatigue limit has been assumed constant, but in that scatter of data is not included.

Now to the comments of Professor Bui-Quoc considered sequentially, but first a correction in reference to his opening sentence. Whether or not this cumulative damage theory is accepted, it has been *shown*, not suggested, that it incorporates the Palmgren-Miner rule as a special case.

1 The basis for the assumption of constant fatigue limit is that no one knows its dependence on arbitrary cyclic loading histories. Discusser's references are concerned with fatigue limit dependence on simple loading histories. Such information is not sufficient for generalization of the theory to history-dependent fatigue limit.

2 As has been said previously, the damage curves are not known. It is possible to construct damage curves of second order in $\log n$ which would converge into the static ultimate *and* fatigue limit. This complicates the mathematics considerably. Linear damage curves (lines) which converge into the fatigue limit show trends observed in metals, i.e., $\Sigma n/N > 1$ for low-high two-stage loadings and the reverse for high-low loadings. Therefore they have been used (successfully) for metal fatigue data. Unidirectional fiber composites sometimes exhibit reverse trends but the evidence is not conclusive. The damage lines converging into static ultimate are thus of potential utility for such materials.

3 Again, the damage lines used should not be considered definitive. It has been shown in paper under discussion that for two-stage loading the sum of cycle ratios (*PM* coefficient) is larger than 1 for low-high and smaller than 1 for high-low when the slope of the damage curves is smaller than that of the *S-N* curve. Since such trends are generally observed in metals it seems reasonable to use this kind of damage curves for metals. The simplest such damage curves are straight lines converging into the fatigue limit.

When approaching the s-axis the damage curves must ultimately change slope and converge into the static ultimate. How and where this takes place is not known. Near the static ultimate there must be a region where the slope of the damage curves becomes larger than that of the *S-N* curve thus reversing previously described trend. However, this portion of the *S-N* curve is not well known because of the considerable scatter due to failure occurring after a small number of cycles.

4 The relation between discusser's (Bui-Quoc) Fig. 2 and our method is not clear to me, since we would use damage lines converging into the fatigue limit which is not the case in the figure. Our predictions are in good agreement with data obtained by Manson, et al., as shown in our paper.

5 I am grateful for the reference to this paper of which I was not aware. This author has also used straight damage lines converging into fatigue limit thus arriving at some of our results without, however, attempting to give underlying reasons or to develop a general theory.

6 May I be forgiven for this misprint.

7 When the ϕ_k are all constant and equal, all exponents in (26) are equal to one and the *PM* rule is obtained. When the ϕ_k are given by either of (27)–(29) they are obviously not constant.

Dr. Ben Amoz' approach and comments are interesting but are not related to the present work in obvious fashion. Our theory does *not* assume that all metals have fatigue limits as indeed it is not confined to metals. The only material information which enters into the theory is damage curves for two stage loadings and the absence of a fatigue limit will require damage curves which take this into account. Furthermore, the information contained in the Coffin-Manson fatigue law or any other such relation does not enter into the theory. It is perhaps of interest to mention that the present theory has been successfully applied to two-stage strain cycling, [11]. For such cycling a fatigue limit is not experimentally detectable but that does not mean that it does not exist. In the paper mentioned the fatigue limit was estimated on the basis of persistent slip band considerations.

References

10 Hashin, Z., and Rotem, A., "A Cumulative Damage Theory of Fatigue Failure," Materials Science and Engineering, Vol. 34, 1978, pp. 147–160.

11 Hashin, Z., and Laird, C., "Cumulative Damage Under Two Level Cycling: Some Theoretical Predictions and Test Data," *Fatigue of Engineering Materials and Structures*, Vol. 2, 1980, pp. 345–350.

The Flow of a Non-Newtonian Fluid Past Projections and Depressions[1]

Vivian O'Brien.[2] The boundary integral approach to study two-dimensional second-order fluid pressure fields is a welcome addition to more conventional finite-difference or finite-element methods. But the paper "The Flow of a Non-Newtonian Fluid Past Projections and Depressions"[1] seems to be only the introductory chapter. Undoubtedly, as the authors say, the method is applicable to more arbitrary geometries than rectangular depressions, but unfortunately such results were not described. Schubert's conformal mapping of an unbounded Couette shear flow past circular arc projections or depressions was cited, with the statement that conformal transformations "cannot be used" for internal shear flow over more arbitrary shapes. On the contrary, we have used conformal mappings to model pulsatile axisymmetric viscous flow over smoothly varying projections [1, 2]. The same analytic mapping functions can be used for corresponding two-dimensional configurations, with a uniform velocity boundary condition on the flat plane for Couette shear flow. Moreover, various numerical mappings can be applied to any shape, and the resulting transformed equations solved by finite-difference methods [3].

Lest the reader come away with some incomplete ideas regarding the present Newtonian results presented in footnote 1 for creeping Couette flow over rectangular slots, it would have been instructive to compare the calculations to earlier Stokes solutions (none cited). For example, it had been shown that circulation patterns in the slots depend on two *geometric* ratios, d/w and D/d [4], where d and w are, respectively, the depth and width of the slot depression and D is the channel depth. Not only can there be one large vortex spanning the slot or two vortices side-by-side,[1] but for fixed D/d as $d/w \to 0$ the two vortices get isolated in the corners and as $d/w \to \infty$ a vertical line of central vortices of alternate sign appears. The heights of these vortex

[1] By A. Mir-Mohamad-Sadegh and K. R. Rajagopal and published in the September, 1980, issue of the ASME JOURNAL OF APPLIED MECHANICS, Vol. 47, pp. 485–488.

[2] Applied Physics Laboratory, The Johns Hopkins University, Johns Hopkins Road, Laurel, Md. 20810.

Author's Closure

I very much appreciate the discussers' interest and comments. May I say before attempting to answer that the present paper and its predecessor [10] should not be construed as an attempt to give a definitive solution to the cumulative damage problem. Their purpose is to present a rational point of view based on the damage curve concept and the equivalent loading postulate. Since the damage curves are not known, simple ad hoc forms have been assumed in order to obtain results. It is to be hoped and expected that better damage curves will be given in the future. The equivalent loading postulate is the key to lifetime analysis for *any* loading program, the damage curves being sufficient information for this purpose. Thus the main achievement, if any, is construction of a theory and not the actual results given. The chief shortcoming of the theory given is not in that damage curves are not sufficiently accurate or that the fatigue limit has been assumed constant, but in that scatter of data is not included.

Now to the comments of Professor Bui-Quoc considered sequentially, but first a correction in reference to his opening sentence. Whether or not this cumulative damage theory is accepted, it has been *shown*, not suggested, that it incorporates the Palmgren-Miner rule as a special case.

1 The basis for the assumption of constant fatigue limit is that no one knows its dependence on arbitrary cyclic loading histories. Discusser's references are concerned with fatigue limit dependence on simple loading histories. Such information is not sufficient for generalization of the theory to history-dependent fatigue limit.

2 As has been said previously, the damage curves are not known. It is possible to construct damage curves of second order in $\log n$ which would converge into the static ultimate *and* fatigue limit. This complicates the mathematics considerably. Linear damage curves (lines) which converge into the fatigue limit show trends observed in metals, i.e., $\Sigma n/N > 1$ for low-high two-stage loadings and the reverse for high-low loadings. Therefore they have been used (successfully) for metal fatigue data. Unidirectional fiber composites sometimes exhibit reverse trends but the evidence is not conclusive. The damage lines converging into static ultimate are thus of potential utility for such materials.

3 Again, the damage lines used should not be considered definitive. It has been shown in paper under discussion that for two-stage loading the sum of cycle ratios (*PM* coefficient) is larger than 1 for low-high and smaller than 1 for high-low when the slope of the damage curves is smaller than that of the *S-N* curve. Since such trends are generally observed in metals it seems reasonable to use this kind of damage curves for metals. The simplest such damage curves are straight lines converging into the fatigue limit.

When approaching the s-axis the damage curves must ultimately change slope and converge into the static ultimate. How and where this takes place is not known. Near the static ultimate there must be a region where the slope of the damage curves becomes larger than that of the *S-N* curve thus reversing previously described trend. However, this portion of the *S-N* curve is not well known because of the considerable scatter due to failure occurring after a small number of cycles.

4 The relation between discusser's (Bui-Quoc) Fig. 2 and our method is not clear to me, since we would use damage lines converging into the fatigue limit which is not the case in the figure. Our predictions are in good agreement with data obtained by Manson, et al., as shown in our paper.

5 I am grateful for the reference to this paper of which I was not aware. This author has also used straight damage lines converging into fatigue limit thus arriving at some of our results without, however, attempting to give underlying reasons or to develop a general theory.

6 May I be forgiven for this misprint.

7 When the ϕ_k are all constant and equal, all exponents in (26) are equal to one and the *PM* rule is obtained. When the ϕ_k are given by either of (27)–(29) they are obviously not constant.

Dr. Ben Amoz' approach and comments are interesting but are not related to the present work in obvious fashion. Our theory does *not* assume that all metals have fatigue limits as indeed it is not confined to metals. The only material information which enters into the theory is damage curves for two stage loadings and the absence of a fatigue limit will require damage curves which take this into account. Furthermore, the information contained in the Coffin-Manson fatigue law or any other such relation does not enter into the theory. It is perhaps of interest to mention that the present theory has been successfully applied to two-stage strain cycling, [11]. For such cycling a fatigue limit is not experimentally detectable but that does not mean that it does not exist. In the paper mentioned the fatigue limit was estimated on the basis of persistent slip band considerations.

References

10 Hashin, Z., and Rotem, A., "A Cumulative Damage Theory of Fatigue Failure," Materials Science and Engineering, Vol. 34, 1978, pp. 147–160.

11 Hashin, Z., and Laird, C., "Cumulative Damage Under Two Level Cycling: Some Theoretical Predictions and Test Data," *Fatigue of Engineering Materials and Structures*, Vol. 2, 1980, pp. 345–350.

The Flow of a Non-Newtonian Fluid Past Projections and Depressions[1]

Vivian O'Brien.[2] The boundary integral approach to study two-dimensional second-order fluid pressure fields is a welcome addition to more conventional finite-difference or finite-element methods. But the paper "The Flow of a Non-Newtonian Fluid Past Projections and Depressions"[1] seems to be only the introductory chapter. Undoubtedly, as the authors say, the method is applicable to more arbitrary geometries than rectangular depressions, but unfortunately such results were not described. Schubert's conformal mapping of an unbounded Couette shear flow past circular arc projections or depressions was cited, with the statement that conformal transformations "cannot be used" for internal shear flow over more arbitrary shapes. On the contrary, we have used conformal mappings to model pulsatile axisymmetric viscous flow over smoothly varying projections [1, 2]. The same analytic mapping functions can be used for corresponding two-dimensional configurations, with a uniform velocity boundary condition on the flat plane for Couette shear flow. Moreover, various numerical mappings can be applied to any shape, and the resulting transformed equations solved by finite-difference methods [3].

Lest the reader come away with some incomplete ideas regarding the present Newtonian results presented in footnote 1 for creeping Couette flow over rectangular slots, it would have been instructive to compare the calculations to earlier Stokes solutions (none cited). For example, it had been shown that circulation patterns in the slots depend on two *geometric* ratios, d/w and D/d [4], where d and w are, respectively, the depth and width of the slot depression and D is the channel depth. Not only can there be one large vortex spanning the slot or two vortices side-by-side,[1] but for fixed D/d as $d/w \to 0$ the two vortices get isolated in the corners and as $d/w \to \infty$ a vertical line of central vortices of alternate sign appears. The heights of these vortex

[1] By A. Mir-Mohamad-Sadegh and K. R. Rajagopal and published in the September, 1980, issue of the ASME JOURNAL OF APPLIED MECHANICS, Vol. 47, pp. 485–488.

[2] Applied Physics Laboratory, The Johns Hopkins University, Johns Hopkins Road, Laurel, Md. 20810.

patterns depend on D/d and *also* on the shear flow velocity profile [4]. Poiseuille flow produces a slightly different circulation pattern from a Couette flow in the same geometry and thus also a different second-order fluid pressure effect [5].

The nonlinear influence of the Reynolds number is not mentioned in the paper,[1] but applies to many experimental situations. Townsend [6] has included the nonlinear convective term for second-order Poiseuille flow over slots. Perhaps the authors will demonstrate that the boundary integral method can be extended to these cases.

References

1 O'Brien, V., and Ehrlich, L. W., "Variation of Wall Shearing Stress With Arterial Geometry," *Proceedings of the 32nd Annual Conference on Engineering in Medicine and Biology*, Denver, 1979, p. 145.

2 O'Brien, V., and Ehrlich, L. W., "Pulsatile Flow Through a Constricted Artery," *Biofluid Mechanics*, Vol. 2, Schneck, D. J., ed., Plenum, New York, 1980, pp. 497–516.

3 Ehrlich, L. W., "The Numerical Solution of a Navier-Stokes Problem in a Stenosed Tube: A Danger in Boundary Approximations of Implicit Marching Schemes," *Comp. and Fluids*, Vol. 7, 1979, pp. 247–256.

4 O'Brien, V., "Closed Streamlines Associated With Channel Flow Over a Cavity," *Physics of Fluids*, Vol. 15, 1972, pp. 2089–2097.

5 Malkus, D. S., *Proceedings of the VIIth International Congress on Rheology*, Gothenberg, Sweden, 1976.

6 Townsend, P., "A Computer Model of Hole-Pressure Measurement in Poiseuille Flow of Viscoelastic Liquids," MRC Rept. 1929, 1979.

ERRATUM

Erratum on "Free Vibration of a Beam Supported by Unsymmetrical Spring Hinges," by R. C. Hibbeler, and published as a Brief Note in the June, 1975, issue of the ASME JOURNAL OF APPLIED MECHANICS, Vol. 42, pp. 501–502.

The boundary condition, equation (3), should include a minus sign, i.e.,

$$K_2 \frac{\partial}{\partial x} y(l, t) = -EI \frac{\partial^2}{\partial x^2} y(l, t) \tag{3}$$

Consequently, the frequency equation, equation (7), is then

$$2(k_n l)^2 \tan k_n l \tanh k_n l + \left(\frac{K_1 l}{EI} + \frac{K_2 l}{EI}\right)(k_n l)(\tan k_n l - \tanh k_n l) - \left(\frac{K_1 l}{EI}\right)\left(\frac{K_2 l}{EI}\right)\left(1 - \frac{1}{\cos k_n l \cosh k_n l}\right) = 0 \tag{7}$$

Table 1 is not affected significantly; however, a corrected version can be obtained from the author (P.O. Box 40141, Lafayette, La. 70504).

The author wishes to thank Messrs. G. Prathap and D. Nigogi who brought this matter to his attention.

Journal of Applied Mechanics

Book Reviews

Dynamical Systems and Evolution Equations: Theory and Applications. By J. A. Walker. Plenum Publishing Corp. New York. 1980. Pages viii–236. Price $29.50.

REVIEWED by T. K. CAUGHEY[1]

This is the first book to give a systematic account of the considerable progress which has been made in extending the geometrical methods, developed for ordinary differential equations, to systems whose evolutionary equations are partial, delay or functional differential equations. The difficulty with such systems is that their state spaces are infinite dimensional and not ideally compact, unlike ordinary differential equations where state spaces are finite dimensional.

The book is organized into five chapters. The first chapter discusses the general ideas and illustrates the techniques for finite dimensional systems. Chapters II, III, and IV extend the introductory treatment of Chapter I to a general metric space framework. Chapter II summarizes much of the mathematics needed for this extension, Chapter III discusses abstract evolution equations in Banach spaces and Chapter IV describes some of the more useful ideas of topological dynamics. The extension of Liapunov's direct method for investigating stability and asymptotic behavior by the invariance principle is studied in some detail. Attention is focused throughout the book on dynamical systems (the autonomous case) while processes (the nonautonomous case) are mentioned only briefly. Chapter V contains some recent applications of the theory to physical systems ranging from supersonic panel flutter to the stability of a nuclear reactor.

Interferometry by Holography. By U. I. Ostrovsky, M. M. Butosov, and G. V. Ostrovskaya. Springer-Verlag, Berlin, Heidelberg, New York. 1980. Pages 330. Price $35.90.

REVIEWED by F. P. CHIANG[2]

In the late sixties and early seventies there had been a saying to the effect that the only useful application of laser is in holography and the only useful application of holography is in holographic interferometry. To a certain extent the statement is still true today. Numerous articles and books have been written on the subject of holographic interferometry. However, most of them assume the reader to have a good knowledge of optics and many even assume the familiarity of communication theory. This is so, because most of the authors are electrical engineers in whose field modern optics has been residing for the past two decades. (Indeed, it is the recognition of the formal analogy between optics and communication theory that has prompted the rapid development of modern optics.) As a result mechanical engineers, material scientists, biologists, etc., who have little or no training in optics are handicapped in their quest to enter the field. It is with these people in mind that the authors have set out to write the book. In my opinion they have largely succeeded in their goal of bringing the subject matter closer to the uninitiated.

The book is divided into five chapters. The first (with 83 pages) deals with the general principles of light interference, classical interferometry, holography and holographic interferometry. The inclusion of classical interferometry is rather unique and quite useful because classical and holographic interferometric methods are closely related. The sections on holography and holographic interferometry are clearly written without the unnecessary mathematical jargon. The second chapter entitled "experimental techniques" (50 pages) gives a good account of the hardwares needed for performing holographic interferometry. Items discussed range from lasers, recording materials, and vibration tables to pinhole filters, beam splitters, and hologram fasteners. The next three chapters are on applications. The most comprehensive is the one on the "investigation of phase inhomogeneities" (Chapters 3, 86 pages) which reflects the authors personal experiences in the field. Detailed descriptions of various methods are given including many examples in the studies of plasma and gas dynamics. The next chapter (58 pages) is on the measurement of (deformation induced) displacements, generation of surface contours, and detection of flaws. The part of deformation measurement is perhaps the weakest of the entire book. Only general principle of deducing displacement vector from a deformed three-dimensional object is outlined. No discussion is given to the calculation of stress or strain; and the only quantitative example is that of a cantilever beam. The final chapter (25 pages) is on the "studies of vibration," which is perhaps the most important engineering application of holographic interferometry and is well presented in the chapter.

The book also has some other minor blemishes: there are quite a few typographical errors, the English could stand some improvement, etc., but on the whole, it is a valuable addition to the literature. I recommend it to anyone who is interested in the applications of holographic interferometry.

Rheology. Edited by G. Astarita, G. Marrucci, and L. Nicholais. *Proceedings of the Eighth International Congress of Rheology.* Naples, Italy. 1980. Plenum Publishing Corp., New York. Vol. 1, pp. xvi–421; Vol. 2, pp. xxv–677; Vol. 3, pp. xxiii–785. Price Vol. 1, $45; Vol. 2, $69.50; Vol. 3, $69.50.

REVIEWED BY R. M. CHRISTENSEN[3]

The *Proceedings* of this congress provide a useful and very broad cross section of contemporary work in rheology. The subjects span solid, fluid behavior, macroscopic, molecular scales of consideration, and experimental theoretical, and processing lines of investigation.

It is not possible to give a concise survey of the contents, it is simply too extensive. Rather, a small sampling of the papers may better serve to provide an indication of the contents. The keynote lecture of the congress was delivered by C. Truesdell, entitled "Sketch for a History of Constitutive Relations." In a lively and interesting account, the use

[1] Professor, Mail Code 104-44, California Institute of Technology, Pasadena, Calif. 91125.

[2] Senior Visiting Fellow, Physics and Chemistry of Solids, Cavendish Laboratory, Cambridge University, England (on sabbatical leave from SUNY, Stony Brook.)

[3] Lawrence Livermore Laboratory, P.O. Box 808, L-338, Livermore, Calif. 94550.

of the term constitutive relations is traced and the significance of it is assessed. The invited lectures covered a variety of subjects. For example, K. Walters and H. A. Barnes discuss the anomalous effects that are caused by lack of recognition of extensional flow behavior in some types of viscometers. In fact, if there is one subject that is receiving the major emphasis in current rheological studies it is that of extensional flows for polymer melts. The activity in this area is well represented in the *Proceedings*. An informative survey of various aspects of extensional flow is covered by C. J. S. Petrie and J. M. Dealy. T. Raible and J. Meissner present experimental results, on extensional flows, that focuses on the critically important subject of the existence or nonexistence of a stable steady state, at high rates of elongation.

In other typical areas, H. Janeschitz-Kriegl surveys flow birefringence and R. B. Bird discusses bead-spring-rod models of the kinetic theories for polymer solutions. M. J. Crochet and M. Bézy discuss numerical solutions for the die entry flow problem, while R. I. Tanner applies a finite-element approach to the die exit problem, including the consequent swelling. S. T. J. Peng developes a model for the anisotropy of thermal expansion in materials under states of large deformation.

Overall, the *Proceedings* of this congress are highly recommended to interested workers in mechanics. These three volumes provide a convenient and useful entry to much of the current work in rheology.

Creep Analysis. By H. Kraus. John Wiley & Sons. 1980. Pages xvii–250. Price $28.75.

REVIEWED BY D. L. MARRIOTT[4]

In the past decade a number of major advances have been made in creep analysis, mostly concerned with cyclic loading and with damage accumulation. Although this progress has been widely reported in scientific papers, little has been done to keep up with the current state of the art with a textbook. Several collections of papers have been published in book form, but these lack the continuity of a single author text. For these reasons Professor Kraus's book is both relevant and opportune.

Professor Kraus deliberately confines his treatment of creep to phenomenological or empirical material descriptions and concentrates on computational methods of interest to the design analyst.

All the recognized and understood creep phenomena such as steady state, transient creep, primary, secondary and tertiary phases, variable and multiaxial behavior are discussed adequately. In addition, recent progress in description of material and component behavior under variable loading is reviewed very competently. There are sections on creep ratchetting and creep fatigue interaction which form excellent introductions to these two highly topical subjects.

The main thrust of the book is toward analysis of component behavior. Professor Kraus is an acknowledged authority in the field of finite-element analysis. Not surprisingly the application of finite elements to creep problems is well done. It is obviously impossible to give a full treatment of finite-element analysis as a section of a book on creep but the basic principles are well laid out, several examples of analysis of complex structures are given, and there is useful advice for the newcomer on the availability of standard computer codes.

A large proportion of the book is given over to approximate methods of analysis such as bounding methods, and reference stress applications—the latter particularly with reference to creep rupture. The field of approximate analysis has a long history of application to creep problems. There was some opinion in the 1960's that the advent of finite-element methods would render all this effort redundant. It is interesting therefore that use of such methods is still advocated, partly because of the high cost of exact analysis, but also because of the insight into the basic structural action which is less easy to obtain by numerical methods. Professor Kraus's book is the first textbook to give a full treatment of the developments in approximate analysis which have occurred in the past 5 years.

One area, not always very well dealt with in textbooks, is the relationship between research, analysis, and design codes. Professor Kraus gives a very clear picture of recent ASME Code developments. He devotes a full section to a discussion of ASME Code Case 1592—the most authoritative guide available at present for high temperature design. This section is invaluable to the newcomer to the subject.

This book is written as an introductory text for an advanced subject. It does not claim to examine the most advanced developments in creep but is aimed more at setting down in easily understandable form, those aspects of the subject which can be used to solve current engineering problems. Its main appeal would be to structural analysts in industry, and as a textbook for graduate or senior undergraduate specialist courses. Given this objective the book is well written with clear explanations and amply supplied with worked and unworked examples. There is no doubt that this text is a welcome contribution to the literature and should become a standard introductory text.

Dislocations in Solids: Dislocations in Metallurgy. Vol. 4. Edited by F. R. N. Nabarro. North-Holland. 1979. Pages viii-464. Price $87.75.

REVIEWED: T. MURA[5]

This is the fourth of five volumes devoted to the behavior of dislocations and their influence on the properties of solids. It contains seven papers concerned with the phenomenon of slip in crystal, the predominant mechanism of the process of plastic deformation, and other processes such as precipitation and fracture. The author, title of paper, and summary of contents of each of these papers are listed as follows:

R. W. Balluffi and A. V. Granato. "Dislocations, Vacancies and Interstitials," pp. 1–133. At the present time, the authors say, there is still a serious lack of reliable and quantitative information on the interaction of vacancies and interstitials with dislocations. This is because the basic properties of the point defects themselves are not yet well enough established.

As a necessary preliminary, the authors begin with a brief account of present knowledge of the lattice properties of the vacancies and interstitials. Then, their interactions with dislocations and the manner in which they probably diffuse to and along dislocations are discussed. In the regime of low point-defect concentrations, the types of basic information on the dislocation climb, the temperature dependence of the yield stress for locked dislocations, and the striking effects in superconductors are obtained from internal friction (ultrasonic attenuation or damping) measurements.

The interaction between the hydrostatic component of the elastic stress field of the dislocation and the dilation due to the defect, electrical interactions in ionic crystals, and the localized vibrational mode interactions are discussed. Calculations of the configuration and binding energies of vacancies and interstitials in the cores of dislocations are introduced. No direct measurements have yet been made of the diffusion rates of either vacancies or interstitials along dislocations. However, several theoretical models and indirect experiments are proposed. Granato and Lücke consider a dislocation line with two types of pinning points (strong and weak pinning points) and calculate the damping and modulus changes for all frequencies.

---

[4] Visiting Associate Professor, Department of Mechanical and Industrial Engineering, University of Illinois at Urbana-Champaign, Urbana, Ill. 61801.

[5] Professor, The Technological Institute, Department of Civil Engineering, Northwestern University, Evanston, Ill. 60201.

F. Larché. "Nucleation and Precipitation on Dislocations," pp. 134–153. Dislocations can act as catalysts for nucleation of a new phase in solids. The misfit strain of a precipitate is accommodated by the strain field of the dislocation, reducing the activation energy necessary to the formation of a nucleus. The difference between coherent and incoherent interfaces is not clearly mentioned in the text from the mechanical point of view.

P. Haasen. "Solution Hardening in f.c.c. Metals," pp. 154–189. The f.c.c. metals have low values of the Peierls-Nabarro force while b.c.c. metals have its high values. The dislocation theory of solution hardening depends strongly on the crystal structure. Haasen writes for f.c.c. metals in this chapter and H. Suzuki writes for b.c.c. metals in the following chapter.

The elementary interactions between a single foreign atom and a dislocation on a nearby slip plane, the force to derive a dislocation through a solid solution at $T = 0$, temperature and inertia effects, and experimental results are treated in a very organized way.

H. Suzuki. "Solid Solution Hardening in Body-Centered Cubic Alloys," pp. 190–217. This chapter is very original in the sense that most of the materials in the text are the author's work. Nevertheless, the author gives fair credits to other researchers' papers. The author uses a new statistical method by which he calculates the average velocity of the motion of a kink overcoming a random distribution of barriers caused by solute atoms. The statistics involve finding k solute atoms in N total number of atoms entering the dislocation core and finding possible motion of a kink. His theoretical prediction for lower yield stresses of iron alloys is compared with Takeuchi's experimental results.

V. Gerold. "Precipitation Hardening," pp. 218–260. For shearable particles the author discusses the origins of the interactions between dislocations and particles through chemical, elastical, atomic ordering, and stacking fault considerations. However, our knowledge about the subject is still vague. The theories predicting the macroscopic yield stress from the interactions mentioned previously are not satisfactory when a number of dislocation-particle geometrical encountings are conceivable.

The Orowan process of the dislocation line tension for nonshearable particles is treated reasonably well in the text. However, the author's treatment on the dispersion hardening due to Orowan loops contains some ambiguities on the image stress, the average stress in the matrix and that in the inclusions. The author should have read and cited as references the celebrated papers of K. Tanaka and T. Mori, *Acta. Met.*, Vol. 18, 1970, pp. 931–941 and of T. Mori and K. Tanaka, *Acta. Met.*, Vol. 21, 1973, pp. 571–574. They correctly defined these quantities and obtained them rigorously.

Recent progress in the temperature-dependent relaxation mechanism is also not properly mentioned in the text. The author should have studied the review paper by L. M. Brown, *Proceedings, 5th International Conference Strength Metals Alloys*, 1979, p. 1551.

S. J. Basinski and Z. S. Basinski. "Plastic Deformation and Work Hardening," pp. 261–362. According to Cottrell, this subject was the first problem to be attempted by the dislocation theory of slip and may well prove to be the last to be solved. The authors completely agree with Cottrell and state that the reason lies, at least partly, in the very large number of parameters which, even in the simplest case of tensile deformation of a single crystal, include such variables as crystal orientation and purity. Since many review articles representing many points of view have been published over the years and the available experimental evidence has been documented in reasonable detail, the authors say, special consideration is given to areas where relatively recent work has in some way changed the perspective. In view of the extensive body of literature on plastic deformation, the frame of reference established here is tensile deformation of pure f.c.c. crystals, primarily Cu deformed in single glide. The article contains surface effects, transmission electron microscopy of Ge foil and of neutron irradiated Cu, latent hardening and quantitative secondary slip data, and thermal glide. Well-organized and substantial discussions follow each subject. Only very few mathematical equations appear in the whole text.

E. Smith. "Dislocations and Cracks," pp. 363–448. This chapter by E. Smith could be an excellent textbook on fracture physics for last year students in undergraduate or first year students in gradient studies. The article is well written with an interdisciplinary approach combining materials science and mechanics. Unfortunately, however, a few important subjects (e.g., stress-intensity factors in anisotropic materials, growing cracks in elastic-plastic materials) are ignored in the text. Barnett and Asaro, *Journal of Mechanics and Physics of Solids*, Vol. 20, 1972, pp. 353–366; for instance, used the dislocation model to a slit-like elastic crack in anisotropic materials and found that the stress-intensity factor is independent of the elastic moduli. The article could be richer in contents if the author further introduced the work on the growing crack by Wnuk, *Proceedings, International Conference on Dynamic Crack Propagation*, Lehigh University, 1972, pp. 273–280, Rice and Sorensen, *Journal of Mechanics and Physics of Solids*, Vol. 26, 1976, pp. 163–186; Kfouri, *Journal of Mechanics and Physics of Solids*, Vol. 27, 1979, pp. 135–150, among others.

Dislocations in Solids: Other Effects of Dislocations: Disclinations. Vol. 5. Edited by F. R. N. Nabarro. North-Holland, New York and The Netherlands. 1980. Pages viii–421. Price $78.

REVIEWED BY T. MURA[6]

This is the last of five volumes devoted to the behavior of dislocations and their influence on the properties of solids. It contains seven review papers which fall into two groups. The first group treats the influence of ordinary translational dislocations and the second group treats the theory and properties of rotational dislocations (disclinations). The author, title of paper, and summary of contents of each of these papers are listed as follows:

C. J. Humphreys. "Image of Dislocations," pp. 1–56. This chapter concentrates on the most important techniques for the imaging of dislocations and in particular upon significant recent developments which have not yet been reviewed in other publications. Early developments, up to 1964, have been covered in the book of Amelinckx (*The Direct Observation of Dislocations*, Academic Press, New York, 1964).

The article contains a simple quantitative physical explanation of the method and the theory for describing a particular imaging technique, the theory and principles of electron propagaion in crystals, the many-beam dynamical theory of electron diffraction, high-voltage electron microscopy, X-ray for bulk specimens, and recent developments in field-iron and optical microscopy.

B. Mutaftschiev. "Crystal Growth and Dislocations," pp. 57–126. Half of the chapter is devoted to the theory of crystal growth. The second part of the chapter is limited to examples of growth morphology by a dislocation mechanism. The third part deals with the generation of dislocations during crystal growth.

Within a few months of the presentation of Frank's theory (1949) for the behavior during growth of flat faces containing dislocations, the first experimental support appeared. L. J. Griffin (1950) found systems of steps corresponding exactly to the prediction of the theory by observation of the surface of natural beryl crystals by phase contrast optical microscopy. Now, however, the author says, some of the conclusions or interpretations on the crystal growth through dislocations obtained in the last decade are not as sure as they first appeared. For example, the existence of spirals with a step-height much larger than monomolecular shows that the nonsplitting of a step could not be a proof for its elementary height.

R. Labusch and W. Schröter. "Electrical Properties of Dislocations in Semiconductors," pp. 127–191. The occupation statistics and the calculation of the electrostatic potential around a

[6] Professor, The Technological Institute, Department of Civil Engineering, Northwestern University, Evanston, Ill. 60201.

charged dislocation resulting in relations between the occupation ration f (fraction of dislocation states occupied by electrons) and temperature or between the Fermi level and f are outlined and some important aspects in the application of these relations to experimental results are discussed. The problem of deriving the carrier density and f from Hall effect data is also discussed. Theoretical calculations of the free carrier mobility in deformed semiconductors are compared with experiments.

F. R. N. Nabarro and A. T. Quintanilha. "Dislocations in Superconductors," pp. 192–242. In 1968, Kojima and Suzuki, conducting tensile tests at a constant rate of strain on the Type I superconductor lead and on the Type II superconductor niobium at 4.2 K, found that the flow stress increased when superconductivity was destroyed by a magnetic field. The electron drag on the moving dislocations was absent in the superconducting state and restored by the magnetic field.

The first part of this chapter discusses the change in the mobility of ordinary dislocations of the crystal lattice of a metal when the metal becomes superconducting.

The second part of this chapter is not very closely related to the first part. It is concerned with the magnetization of a superconductor of Type II, which occurs by the motion of a lattice of flux lines through the crystal. During this process, the authors postulate, the dislocations of the crystal lattice remain fixed, and act as moderatley effective obstacles to the motion of the flux-line lattice. The nature and effect of dislocations in the lattice of flux lines in a Type II superconductor are analyzed in the last section.

M. Kléman. "The General Theory of Disclinations," pp. 243–297. The concept of disclinations (rotational dislocations) has recently found wide application in liquid crystals. Disclinations are the topoligical concepts which help in a description of broken symmetries of directional media (mesomorphic phases, surface crystals, spin lattices, etc.).

The first part of the text is devoted for explanation on the topology and geometry of disclinations. From this geometrical consideration, one can say that disclinations act as dislocation sources and sinks. Next, the energy of a disclination line in a nematic crystal is presented. Singular solutions which minimze the energy, assuming that the solutions are planar, show some geometries discussed in the first part of the text. The last part of the article describes about disclinations in cholesterics. Although the author writes another chapter on dislocations in the same volume, the article seems to need some introduction for readers to explain how disclinations are related to the physical properties of the directional media.

Y. Bouligand. "Defects and Textures in Liquid Crystals," pp. 299–347. This chapter deals with the direct observation of defects in mesmorphic media and their geometrical and topological aspects. The lamellated structure of smectics, myelinics, and cholesterics with a small helical pitch leads to textures which will be studied in terms of the geometry of parallel surfaces. The textures of nematics and weakly twisted cholesterics lead to problems of topology in director fields. Readers will be impressed by many beautiful and interesting figures and pictures.

M. Kléman. "Dislocations, Disclinations and Magnetism," pp. 349–402. The distribution of the magnetization around a dislocation or disclination becomes important when one wants to correlate the saturation law under large applied magnetic field to the defect content of the medium. The article starts with the basic concepts in domain theory and follows by the magnetoelasticity in terms of dislocation and disclination theories, the singularities which appear in spin lattices, and the interactions of lattice dislocations with the magnetic structure of a ferromagnetic crystal.

Thermal Stresses in Severe Environments. Edited by D. P. H. Hasselman and R. A. Heller. Plenum Press, New York and London. 1980. Pages X–737. Price $75.

REVIEWED BY J. L. NOWINSKI[7]

The book contains the Proceedings of the International Conference on Thermal Stresses in Materials and Structures held at Virginia Polytechnic Institute and State University in Blacksburg, Va., in 1980. The 33 contributions, most of them by the well-known experts in the field, may roughly be divided into five groups. First of these (8 papers) concerns thermal fields in specific materials such as polymeric and crystalline solids from the atomistic viewpoint; body (cylinder) with temperature-dependent properties; nonlinear composite propellants; ceramic composites; semiabsorbing materials under intense radiation; layered structures; heat-absorbing glasses; glass seals under thermal shock. The second group (5 papers) involves problems of prediction in thermoviscoplasticity; creep in jamb frames, as well as three viscoelastic analyses: of interaction effects in filled polymers, of allowable strength under variable thermal loads, and of Monte-Carlo simulation. Fracture and associated phenomena are the topics of the third group of 8 papers that include: examination of elastic-brittle materials; statistical fracture analysis; evaluation of failure probability in anisotropic structures; study of part through cracks subjected to thermal shock; investigation of effects of spatial variation of thermal conductivity; of crack healing; thermally induced stress singularities; and of instability of parallel cracks and its influence on rock geothermal energy. To the fourth group, involving dynamic and quasi-dynamic phenomena, one can include 5 papers discussing: finite wave speeds; transient and permanent thermal stresses; thermal shock of refractories; thermal shock resistance of ceramics; and, finally, thermoelastic buckling of plates. The fifth group, rather diversified in contents, takes care of 7 papers: a general survey of the present state of the field and conceivable future trends; analysis of thermomechanical parameters due to fire; life predication of heat exchangers; thermal stresses in linings of combustion engines; analysis of stresses in loft densometer mounting lug assembly; propagation of propellant separations in rocket motor grains; and estimate of storage life of some projectiles. The volume is highly recommended to those who want an up-to-date look at the research in the field.

New Approaches to Nonlinear Problems in Dynamics. Edited by Philip J. Holmes. SIAM, Philadelphia, Pa. 1980. Cloth. Pages xii and 529. Price $42.50.

REVIEWED BY P. K. C. WANG[8]

Recently, the study of nonlinear dynamical systems, in particular, bifurcation phenomena and systems with chaotic or complex behavior, has become a highly active area of research in mathematics and various branches of science and engineering. Most of the engineering studies are based on physical experimentation, stimulation, and analysis using conventional approaches such as perturbation and averaging methods. On the other hand, recent mathematical developments in this area make extensive use of concepts and results in topology and differential geometry such as the theory of differentiable manifolds which are unfamilar to most engineers. An exchange of information, ideas, and viewpoints between the mathematicians and engineers could be mutually beneficial and helpful in enriching the research in this area. In this spirit, a conference under the title of this

[7] H. Fletcher Brown Professor Emeritus, Department of Mechanical and Aerospace Engineering, University of Delaware, Newark, Del. 19711.

[8] Professor, Department of System Science, University of California, Los Angeles, Calif. 90024.

charged dislocation resulting in relations between the occupation ration f (fraction of dislocation states occupied by electrons) and temperature or between the Fermi level and f are outlined and some important aspects in the application of these relations to experimental results are discussed. The problem of deriving the carrier density and f from Hall effect data is also discussed. Theoretical calculations of the free carrier mobility in deformed semiconductors are compared with experiments.

F. R. N. Nabarro and A. T. Quintanilha. "Dislocations in Superconductors," pp. 192–242. In 1968, Kojima and Suzuki, conducting tensile tests at a constant rate of strain on the Type I superconductor lead and on the Type II superconductor niobium at 4.2 K, found that the flow stress increased when superconductivity was destroyed by a magnetic field. The electron drag on the moving dislocations was absent in the superconducting state and restored by the magnetic field.

The first part of this chapter discusses the change in the mobility of ordinary dislocations of the crystal lattice of a metal when the metal becomes superconducting.

The second part of this chapter is not very closely related to the first part. It is concerned with the magnetization of a superconductor of Type II, which occurs by the motion of a lattice of flux lines through the crystal. During this process, the authors postulate, the dislocations of the crystal lattice remain fixed, and act as moderatley effective obstacles to the motion of the flux-line lattice. The nature and effect of dislocations in the lattice of flux lines in a Type II superconductor are analyzed in the last section.

M. Kléman. "The General Theory of Disclinations," pp. 243–297. The concept of disclinations (rotational dislocations) has recently found wide application in liquid crystals. Disclinations are the topoligical concepts which help in a description of broken symmetries of directional media (mesomorphic phases, surface crystals, spin lattices, etc.).

The first part of the text is devoted for explanation on the topology and geometry of disclinations. From this geometrical consideration, one can say that disclinations act as dislocation sources and sinks. Next, the energy of a disclination line in a nematic crystal is presented. Singular solutions which minimze the energy, assuming that the solutions are planar, show some geometries discussed in the first part of the text. The last part of the article describes about disclinations in cholesterics. Although the author writes another chapter on dislocations in the same volume, the article seems to need some introduction for readers to explain how disclinations are related to the physical properties of the directional media.

Y. Bouligand. "Defects and Textures in Liquid Crystals," pp. 299–347. This chapter deals with the direct observation of defects in mesmorphic media and their geometrical and topological aspects. The lamellated structure of smectics, myelinics, and cholesterics with a small helical pitch leads to textures which will be studied in terms of the geometry of parallel surfaces. The textures of nematics and weakly twisted cholesterics lead to problems of topology in director fields. Readers will be impressed by many beautiful and interesting figures and pictures.

M. Kléman. "Dislocations, Disclinations and Magnetism," pp. 349–402. The distribution of the magnetization around a dislocation or disclination becomes important when one wants to correlate the saturation law under large applied magnetic field to the defect content of the medium. The article starts with the basic concepts in domain theory and follows by the magnetoelasticity in terms of dislocation and disclination theories, the singularities which appear in spin lattices, and the interactions of lattice dislocations with the magnetic structure of a ferromagnetic crystal.

Thermal Stresses in Severe Environments. Edited by D. P. H. Hasselman and R. A. Heller. Plenum Press, New York and London. 1980. Pages X–737. Price $75.

REVIEWED BY J. L. NOWINSKI[7]

The book contains the Proceedings of the International Conference on Thermal Stresses in Materials and Structures held at Virginia Polytechnic Institute and State University in Blacksburg, Va., in 1980. The 33 contributions, most of them by the well-known experts in the field, may roughly be divided into five groups. First of these (8 papers) concerns thermal fields in specific materials such as polymeric and crystalline solids from the atomistic viewpoint; body (cylinder) with temperature-dependent properties; nonlinear composite propellants; ceramic composites; semiabsorbing materials under intense radiation; layered structures; heat-absorbing glasses; glass seals under thermal shock. The second group (5 papers) involves problems of prediction in thermoviscoplasticity; creep in jamb frames, as well as three viscoelastic analyses: of interaction effects in filled polymers, of allowable strength under variable thermal loads, and of Monte-Carlo simulation. Fracture and associated phenomena are the topics of the third group of 8 papers that include: examination of elastic-brittle materials; statistical fracture analysis; evaluation of failure probability in anisotropic structures; study of part through cracks subjected to thermal shock; investigation of effects of spatial variation of thermal conductivity; of crack healing; thermally induced stress singularities; and of instability of parallel cracks and its influence on rock geothermal energy. To the fourth group, involving dynamic and quasi-dynamic phenomena, one can include 5 papers discussing: finite wave speeds; transient and permanent thermal stresses; thermal shock of refractories; thermal shock resistance of ceramics; and, finally, thermoelastic buckling of plates. The fifth group, rather diversified in contents, takes care of 7 papers: a general survey of the present state of the field and conceivable future trends; analysis of thermomechanical parameters due to fire; life predication of heat exchangers; thermal stresses in linings of combustion engines; analysis of stresses in loft densometer mounting lug assembly; propagation of propellant separations in rocket motor grains; and estimate of storage life of some projectiles. The volume is highly recommended to those who want an up-to-date look at the research in the field.

New Approaches to Nonlinear Problems in Dynamics. Edited by Philip J. Holmes. SIAM, Philadelphia, Pa. 1980. Cloth. Pages xii and 529. Price $42.50.

REVIEWED BY P. K. C. WANG[8]

Recently, the study of nonlinear dynamical systems, in particular, bifurcation phenomena and systems with chaotic or complex behavior, has become a highly active area of research in mathematics and various branches of science and engineering. Most of the engineering studies are based on physical experimentation, stimulation, and analysis using conventional approaches such as perturbation and averaging methods. On the other hand, recent mathematical developments in this area make extensive use of concepts and results in topology and differential geometry such as the theory of differentiable manifolds which are unfamilar to most engineers. An exchange of information, ideas, and viewpoints between the mathematicians and engineers could be mutually beneficial and helpful in enriching the research in this area. In this spirit, a conference under the title of this

[7] H. Fletcher Brown Professor Emeritus, Department of Mechanical and Aerospace Engineering, University of Delaware, Newark, Del. 19711.

[8] Professor, Department of System Science, University of California, Los Angeles, Calif. 90024.

ERRATUM

Erratum for "On the Stokes Flow of Viscous Fluids Through Corrugated Pipes," by N. Phan-Thien, and published in the December, 1980, issue of the ASME JOURNAL OF APPLIED MECHANICS, Vol. 47, pp. 961–963.

Delete the sentence containing the equation $\partial\psi/\partial r = 0$ in the Introduction. Although the boundary condition $\partial\psi/\partial r = 0$, as used by Manton [6][1] and other authors, differs on the surface from the boundary condition (3) reported in the original Note in some terms of first and second-order, both are correct for axisymmetric flows and lead to the same expression for the pressure drop enhancement.

The author regrets any inconvenience caused by the implication that the boundary conditions stated by Manton [6] are incorrect.

---

[1] Number in square bracket refers to the reference listed in the original Note.